UNIKASSEL VERSITÄT

gacm German Association for Computational Mechanics

8TH GACM COLLOQUIUM ON

COMPUTATIONAL MECHANICS

FOR YOUNG SCIENTISTS FROM ACADEMIA AND INDUSTRY

AUGUST 28TH – 30TH, 2019

UNIVERSITY OF KASSEL, GERMANY

PROCEEDINGS

EDITORS:
TOBIAS GLEIM AND STEPHAN LANGE

mechanics dynamics

TECHNISCHE MECHANIK
KONTINUUMSMECHANIK

Bibliographic information published by Deutsche Nationalbibliothek
The Deutsche Nationalbibliothek lists this publication in the Deutsche Nationalbibliografie; detailed bibliographic data is available in the Internet at http://dnb.dnb.de.

ISBN 978-3-86219-5093-9
DOI: http://dx.medra.org/10.19211/KUP9783737650939
URN: https://nbn-resolving.org/urn:nbn:de:0002-450934

www.upress.uni-kassel.de

kassel university press

Preface

This conference book contains papers presented at the 8th GACM Colloquium on Computational Mechanics for Young Scientists from Academia and Industry. The conference was held from August 28th – 30th, 2019 in Kassel, hosted by the Institute of Mechanics and Dynamics of the department for civil and environmental engineering and by the chair of Engineering Mechanics / Continuum Mechanics of the department for mechanical engineering of the University of Kassel.

The aim of the conference is, to bring together young scientits who are engaged in academic and industrial research on Computational Mechanics and Computer Methods in Applied Sciences. It provides a plattfrom to present and discuss recent results from reseach efforts and industrial applications.

In more than 150 presentations, given by young scientists, current scientific developments and advances in engineering practice in this field are presented and discussed. The contributions of the young researches are supplemented by a poster session and plenary talks from four senior scientists from academia and industry as well as from the GACM Best PhD Award winners 2017 and 2018.

We would like to thank the authors for their interesting contributions and the organizers of the 22 minisymposia for their effort making the 8th GACM Colloquium on Computational Mechanics such a successful conference.

Kassel, August 2019

Tobias Gleim
Institute of Mechanics and Dynamics

Stephan Lange
Institute of Mechanics, Chair of Engineering Mechanics/Continuum Mechanics

Overview

**Proceedings of the 8th GACM Colloquium on Computational Mechanics
for Young Scientists from Academia and Industry
August 28–30, 2019 in Kassel, Germany**

The Mechanics of Brain Development

Silvia Budday * [1]

[1]Friedrich-Alexander-University Erlangen-Nürnberg, Erlangen, Germany

Abstract. The characteristically folded surface morphology is a classical hallmark of the mammalian brain. During development, the initially smooth surface evolves into an elaborately convoluted pattern, which closely correlates with brain function and serves as a clinical indicator for pathological conditions. Here, we combine computational and experimental analyses to show that physical forces control pattern selection in the developing brain. We closely consider cellular processes during brain development to establish a mechanical model for brain growth. The model consists of a morphogenetically growing outer cortex and a stretch-induced growing inner core. Our results demonstrate that mechanical instabilities can explain cortical folding during brain development. Combining physics and biology holds promise to advance our understanding of human brain development, to enable early diagnostics of cortical malformations, and to improve treatment of neurodevelopmental disorders such as epilepsy, autism, and schizophrenia.

Introduction

Neurodevelopment involves a highly orchestrated sequence of events, which is tightly regulated by the complex interplay of various cell types and molecular factors both in space and time [2]. The first phase of brain development is characterized by cell division and cell migration, ultimately resulting in the formation of the outer cell-rich brain layer, the cortex. At the end of the neuronal migration process, its surface is still smooth. During the second phase of brain development, cortical neurons begin to interconnect and form synapses. This connectivity process results in an excessive expansion of the cortex, which is constrained by the much less growing inner core. Therefore, compressive stresses build up in the cortex, which eventually induce cortical folding as a mechanism to release the growth-induced compressive stresses [1]. Physics-based modeling can help correlate neurodevelopmental disruptions on the cellular level with structural malformations on the organ level [2]. The latter can easily be detected through modern imaging techniques.

Computational model for brain growth

We model brain growth using the nonlinear field theories of mechanics supplemented by the theory of finite growth [1]. We multiplicatively decompose the deformation gradient into an elastic and a growth contribution $\boldsymbol{F} = \boldsymbol{F}^e \cdot \boldsymbol{F}^g$. We approximate the behavior of brain tissue using a hyperelastic neo-Hookean material model with the strain energy function $\psi = 1/2\,\mu[\,\boldsymbol{F}^e : \boldsymbol{F}^e - 3 - 2\,\ln J^e\,] + 1/2\,\lambda\,\ln^2 J^e$, expressed in terms of the elastic components of the deformation gradient $\boldsymbol{F}^e$ and the Jacobian $J^e = \det\boldsymbol{F}^e$. The Piola stress then yields $\boldsymbol{P} = \boldsymbol{P}^e \cdot \boldsymbol{F}^{g-\mathrm{T}}$, where $\boldsymbol{P}^e = \partial\psi/\partial\boldsymbol{F}^e$. In the absence of volume forces, the balance of linear momentum reduces to $\mathrm{Div}\boldsymbol{P} \doteq \boldsymbol{0}$, which we solve numerically using the finite element method. We close the set of nonlinear equations by prescribing the growth contribution $\boldsymbol{F}^g$ and its evolution in time based on the cellular processes during brain development [1]. We assume that brain tissue expands isotropically and express $\boldsymbol{F}^g$ in terms of a single scalar valued growth multiplier ϑ, $\boldsymbol{F}^g = \vartheta\boldsymbol{1}$. To mimic the connectivity process during the second phase of brain development, we let the cortex grow morphogenetically in time at the constant growth rate G_c. We further assume that subcortical growth is stretch-induced (see Figure 1a), as axons grow when mechanical tension is applied. Growth is only activated if the elastic volume stretch J^e exceeds its baseline value J^0.

*Corresponding author: silvia.budday@fau.de ORCID iD: 0000-0002-7072-8174

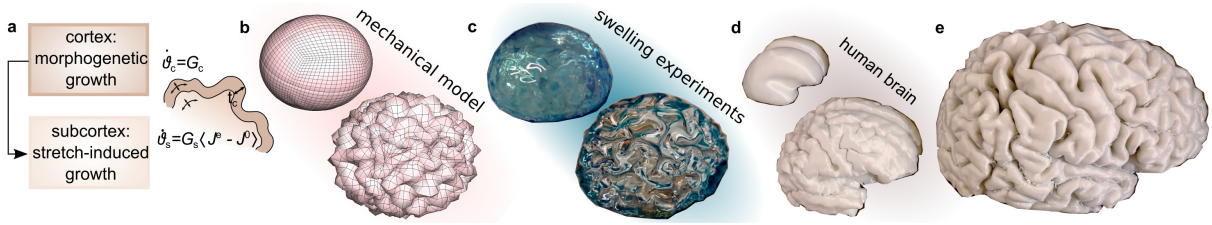

Figure 1. a) Mechanical model for brain growth. Simulation of a simplified brain geometry (b) and swelling experiments on elastomers (c) show the emergence of complex wrinkling patterns similar to those of 3D-printed brain models extracted from magnetic resonance images at different stages of human brain development, gestational week 22 and term (d), as well as at the age of 30 (e).

Experimental model for brain growth

We experimentally mimic brain folding by using soft elastomeric gels, which swell superficially when immersed in solvents [3]. We cast a simplified initial geometry of the inner core using a soft elastomer (Sylgard 184, Dowsil, mixed in a 45:1 mass ratio) and cure it at 75°C for about 30 min. After removal from the mold, the cortex layer (Sylgard 184, mixed in a 35:1 mass ratio) with blue color pigment is drop-casted, wherein each layer is cured at 75°C for about 20 min until the desired layer thickness is reached. The whole specimen is finally cured over night. To induce growth (or swelling) of the outer cortical layer, the elastomer-brain is immersed in solvent (Hexanes, Sigma-Aldrich) at room temperature for about two hours, as illustrated in Figure 1c.

Results

Figures 1d and 1e show 3D-printed human brain models extracted from magnetic resonance images at different stages of development: at gestational week 22, when the cortex is still smooth (d); at term, when all major fissures have formed (d); at the age of 30, when the brain has grown to its maximum size (e). Figures 1b and 1c impressively demonstrate that both the fairly simple mechanical model and the swelling elastomers result in complex wrinkling patterns that well resemble the morphology of mammalian brains.

Conclusion

The current work strongly suggests that mechanical instabilities are the underlying mechanism of cortical folding during brain development, and that mechanical factors play an important role in pattern selection. The mechanical model bridges the scales from cellular events such as neuronal connectivity and axon elongation to clinically relevant characteristics on the macroscopic scale, e.g. abnormal gyrification patterns, which are accessible through modern imaging techniques such as magnetic resonance imaging.

Acknowledgments

The work by Alexander Greiner and the financial support by the German Research Foundation grant STE 544/50 and the Emerging Talents Initiative (ETI) by the FAU are gratefully acknowledged.

References

[1] Silvia Budday, Paul Steinmann, and Ellen Kuhl. The role of mechanics during brain development. *J. Mech. Phys. Solids* 72 (2014), pp. 75–92.

[2] Silvia Budday, Paul Steinmann, and Ellen Kuhl. Physical biology of human brain development. *Front. Cell. Neurosci.* 9 (2015), p. 257.

[3] Tuomas Tallinen, Jun Young Chung, François Rousseau, Nadine Girard, Julien Lefèvre, and L Mahadevan. On the growth and form of cortical convolutions. *Nat. Phys.* 12.6 (2016), pp. 588–593.

**Proceedings of the 8th GACM Colloquium on Computational Mechanics
for Young Scientists from Academia and Industry
August 28–30, 2019 in Kassel, Germany**

Kino-Geometric Modeling of Proteins and Molecular Mechanisms

Dominik Budday *[1]

[1]formerly at the Chair of Applied Dynamics, Friedrich-Alexander-Universität Erlangen-Nürnberg, 91058 Erlangen, Germany

Abstract.

Proteins are dynamic biomolecules that perform an enormous variety of cellular functions on a broad range of spatio-temporal scales. Their conformational ensemble is a crucial determinant of functionality in health and disease. While experimental and computational advances have increasingly enabled atomically detailed insights into protein molecular mechanisms, the need for efficient, yet elaborate integrative computational methods to resolve functional motions across scales remains considerable. Here, we lay out a robotics-inspired, kino-geometric model that efficiently captures small- and large-scale collective motions, with dihedral angles as torsional degrees of freedom and non-covalent interactions as constraints. Using geometric tools, we decompose the biomolecules into rigid substructures and coordinated motions between them. We develop an efficient, high-dimensional motion planning algorithm dCC-RRT that integrates the principle of minimal frustration via dynamic, Clash-avoiding Constraints (dCC) into a rapidly-exploring random tree (RRT). Shown exemplarily on the enzyme Adenylate Kinase, the algorithm closely approximates its conformational transition and agrees well with motions from Molecular Dynamics simulations and experimental data, thereby providing a structural basis for allosteric networks that drive conformational change. Overall, our kino-geometric modeling approach is a robust and efficient alternative to obtain high-level insights into molecular mechanisms across scales, with broad applications in protein engineering, drug design, and human health.

Introduction

Proteins perform a tremendous variety of biological functions. Synthesized by the ribosome in our cells, they fold into rather complex, three-dimensional shapes termed their native conformation. This state, together with a subtle interplay between stability and flexibility, allows them to interact with various binding partners, such as small ligands, nucleotides or other proteins. The free-energy surface that characterizes different protein states and underlies their structural rearrangements is a critical determinant for protein functionality. Thus, efficiently and reliably characterizing the temporal and spatial distributions of protein conformational ensembles is crucial to promote our understanding of molecular mechanisms in health and disease. Although typical Molecular Dynamics (MD) based methods can provide atomically detailed trajectories, they require tremendous computational resources and tend to face limitations regarding the vast scales in space and time that are covered by protein motion. As shown in Fig. 1, these range from pico-second bond length and angle fluctuations, over side-chain flips and loop motion to rearrangements of individual protein domains or entire chains that may occur on the order of milliseconds or seconds. To mitigate these limitations, we take an alternative, time-independent approach via kinematics based analyses and conformational sampling towards high-level insights into the molecular mechanisms of protein function.

KGS – our Kino-Geometric Sampling framework

Originating in traditional robotics, our Kino-Geometric Sampling (KGS) and modeling framework efficiently captures small- and large-scale collective motions important for molecular function [2, 3, 4, 5]. As shown in Fig. 2, we model the dihedral angles ϕ, ψ, and χ of main- and side-chain covalent single bonds as d torsional degrees of freedom $\mathbf{q} \in \mathbb{T}^d$ of the molecule. Those are coupled by hydrogen bonds, disulfide

*Corresponding author: dominik.budday@fau.de ORCID iD: ORCID 0000-0002-6180-2125

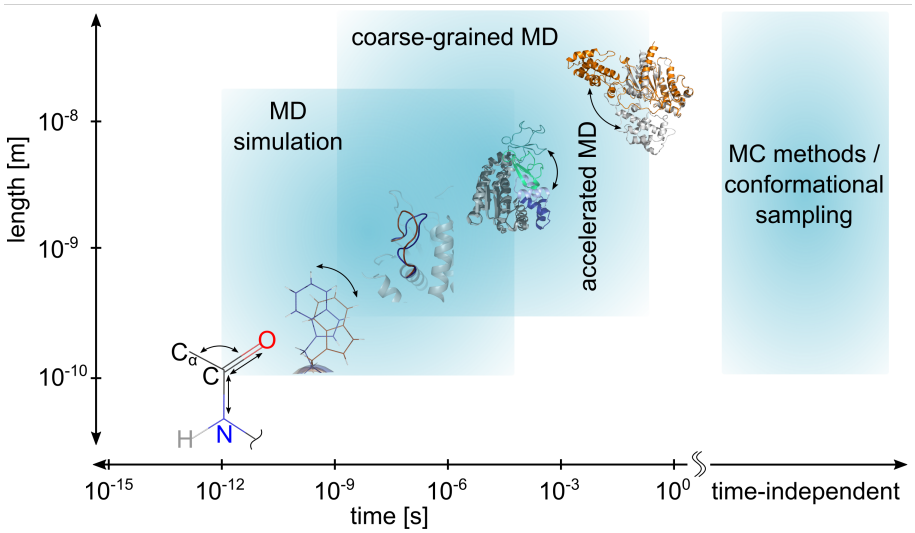

Figure 1. Spatio-temporal scales of protein motions and appropriate computational methods for their analysis.

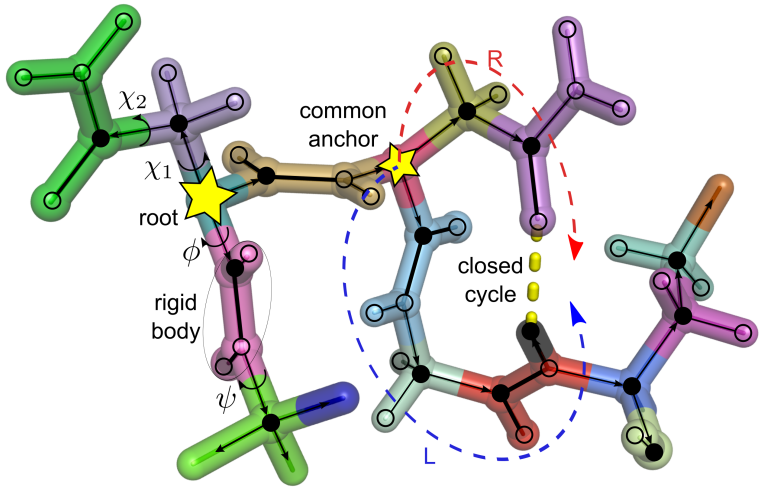

Figure 2. Protein fragment represented as a kinematic spanning tree, with dihedral angles (ϕ, ψ, χ) as degrees of freedom between rigid body vertices (individually colored) and non-covalent interactions such as hydrogen bonds (yellow dashes) encoded as geometric constraints that form closed kinematic cycles with a left (L) and right (R) branch leaving from a common anchor.

bonds, or hydrophobic forces to move in a coordinated fashion, while bond lengths and angles are fixed. We integrate these non-covalent interactions (yellow dashes) as cycle closure constraints $\mathbf{\Phi}(\mathbf{q})$, leading to a description of the molecular conformation space in terms of a constraint variety $\mathcal{Q} = \{\mathbf{q} \in \mathbb{T}^d \mid \mathbf{\Phi}(\mathbf{q}) = \mathbf{0}\}$. Introducing the constraint Jacobian $\mathbf{J}$, we obtain instantaneous (velocity) constraints

$$\frac{\mathrm{d}\mathbf{\Phi}}{\mathrm{d}t} = \mathbf{J}\dot{\mathbf{q}} \begin{cases} = \mathbf{0}, & \text{if } \dot{\mathbf{q}} \text{ constraint observing} \\ \neq \mathbf{0}, & \text{if } \dot{\mathbf{q}} \text{ constraint violating} \end{cases}$$

which characterize two disjoint, orthogonal subspaces. In this fashion, we can focus on the collective motions of dihedral angles that lie in the nullspace of $\mathbf{J}$ and preserve the global constraint network [3] (i.e. $\mathbf{J}\dot{\mathbf{q}} = \mathbf{0}$), or the ones that lie in the range of the transposed Jacobian range($\mathbf{J}^T$) and perturb constraints in a hierarchical manner [2, 5]. Coupled to sophisticated motion planning strategies, this basis allows for efficient sampling of conformational pathways between different molecular states.

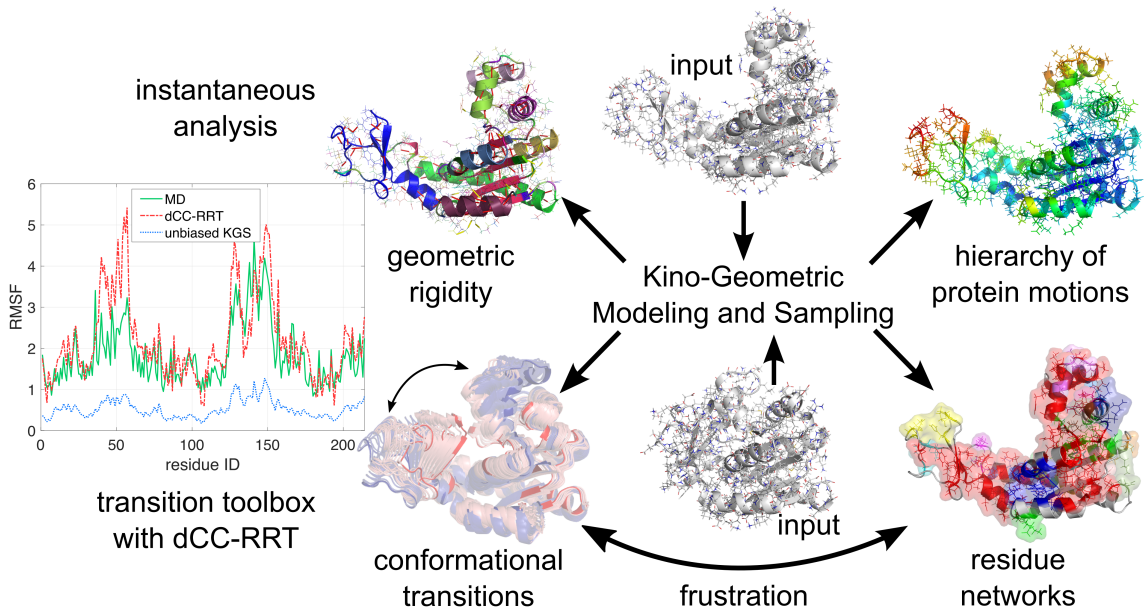

Figure 3. Exciting insights into the molecular mechanisms of ADK using Kino-Geometric Modeling and Sampling.

Results and Discussion

KGS provides insights into molecular flexibility and stability on various levels. To graphically display these capabilities, we make use of the well-studied example protein Adenylate Kinase (ADK), an important enzyme that is associated with maintaining energy levels in our cell and performs rather large opening and closing motions throughout its catalytic cycle (see e.g. [1]). Based on a deposited molecular structure from the protein data bank (PDB) (Fig. 3, top center, PDB code 4ake), KGS automatically generates a kinematic spanning tree of the molecule and identifies significant non-covalent interactions to include as constraints, based on typical geometric and energetic criteria [6] used in the protein rigidity community (see [9] for a broader review on rigidity theory applied to macromolecules). Performing geometric rigidity analysis [3] on this graph, we identify larger rigid substructures that emerge when only motions that completely respect constraints are accessible, i.e., the motions in the nullspace of $\mathbf{J}$. The top left panel in Fig. 3 displays those substructures in ADK individually colored, demonstrating relatively rigid secondary structure helices that stabilize the enzyme domains, but still allow for its characteristic opening and closing motions [1, 2]. By admitting motion modes that increasingly perturb constraints in a hierarchical fashion, we observe global motions that span the entire protein (Fig. 3, top right) [5]. The overall mobility pattern, colored by increasing atomic root-mean squared fluctuations (RMSF) from blue to red matches the enzyme domains fairly well: the stable CORE domain (mostly blue), and the more flexible LID (left) and NMP (right) binding domains (green/red) [1]. Both types of analyses are instantaneous in nature and capable to report these stability and flexibility measures in a matter of seconds.

In order to gain insights into the molecular mechanisms of activation and identify pathways between different states of the same molecule, we have integrated various sophisticated motion planning strategies in KGS. These algorithms are based on rapidly exploring random trees (RRT) [10] or Poisson planning [7], and specifically integrate the principal of minimal frustration to automatically explore energetically accessible regions of conformation space [4, 8]. This is achieved by forming dynamic Clash-avoiding Constraints (dCC) whenever two atoms are in close contact, biasing exploration towards more favorable directions. Speaking in terms of the constraint variety $\mathcal{Q}$, this approach dynamically alters its dimensions by adding constraints, allowing us to perform manifold hopping during exploration and exploiting motion where accessible. For our transition toolbox with dCC-RRT, we focus on constraint observing motions restricted to the (dynamically changing) nullspace of $\mathbf{J}$ and only include constraints from hydrogen bonds present in both conformations of interest. Providing the closed form of ADK as a second input (Fig. 3, bottom center, PDB code 1ake), KGS identifies a connective transition pathway between the open and the closed state (Fig. 3, bottom left) in a few hours [4]. Comparing RMSF from the dCC-RRT pathway to an MD trajectory (Fig. 3, center left), we observe striking qualitative and quantitative

agreement [2]. A further comparison with unbiased, unguided sampling around its open state (blue line) demonstrates very similar trends, but overall much less amplitude in motion. Clearly, cleverly designed motion planning is necessary to navigate around obstacles and widely cover conformation space. Together with our underlying KGS model, we capture similar molecular characteristics as MD, but at a much lower computational cost. On top of that, we have shown that our exploration pathways pass several experimentally determined intermediate states of ADK, further validating our motion planner dCC-RRT [4]. Clash constraints not only guide exploration towards sterically favorable conformations, but at the same time inform on residue contacts along the sampled pathways. By monitoring the list of pairwise dCC, we identify residue interaction networks that can propagate collective motion over large distances in the molecule. For ADK, the largest network shown in red spans all three protein domains and seems to be a key component for enabling its conformational change (Fig. 3, bottom right).

Overall, our results establish KGS as an efficient and insightful alternative to study molecular mechanisms across scales. As part of a larger computational pipeline for protein and nucleotide dynamics, the various results from our toolbox may serve as input to fine-tune analysis via more detailed, but costly methods such as MD, with wide applications in protein design and drug development. Source code, analysis scripts and several examples are freely available for download at `https://github.com/ExcitedStates/KGS`.

Acknowledgments

I would like to express my deep thanks to Prof. Dr.-Ing. habil. Sigrid Leyendecker and Associate Adjunct Prof. Dr. Henry van den Bedem for their continuous support and valuable guidance during my exciting time as doctoral candidate, both at the FAU in Germany as well as the SLAC National Accelerator Laboratory in the US. I gratefully acknowledge financial support by BaCaTeC (project number $7, 2014 - 1$), the DFG (project number 401512690), and the Deutsche Telekom Stiftung.

References

[1] Oliver Beckstein, Elizabeth J Denning, Juan R Perilla, and Thomas B Woolf. Zipping and unzipping of adenylate kinase: atomistic insights into the ensemble of open ↔ closed transitions. *J. Mol. Biol.* 394.1 (2009), pp. 160–176.

[2] Dominik Budday. "High-Dimensional Robotics at the Nanoscale - Kino-Geometric Modeling of Proteins and Molecular Mechanisms". PhD thesis. Friedrich-Alexander-Universität Erlangen-Nürnberg, 2019.

[3] Dominik Budday, Sigrid Leyendecker, and Henry van den Bedem. Geometric analysis characterizes molecular rigidity in generic and non-generic protein configurations. *J. Mech. Phys. Solids* 83 (2015), pp. 36–47.

[4] Dominik Budday, Rasmus Fonseca, Sigrid Leyendecker, and Henry van den Bedem. Frustration-guided motion planning reveals conformational transitions in proteins. *Proteins: Struct. Funct. Bioinf.* 85.10 (2017), pp. 1795–1807.

[5] Dominik Budday, Sigrid Leyendecker, and Henry van den Bedem. Kinematic Flexibility Analysis: Hydrogen Bonding Patterns Impart a Spatial Hierarchy of Protein Motion. *J. Chem. Inf. Model.* 58.10 (2018), pp. 2108–2122.

[6] Bassil I Dahiyat, D Benjamin Gordon, and Stephen L Mayo. Automated design of the surface positions of protein helices. *Protein Sci.* 6.6 (1997), pp. 1333–1337.

[7] Rasmus Fonseca, Dominik Budday, and Henry van den Bedem. Collision-free poisson motion planning in ultra high-dimensional molecular conformation spaces. *J. Comput. Chem.* 39.12 (2018), pp. 711–720.

[8] Amélie Héliou, Dominik Budday, Rasmus Fonseca, and Henry van den Bedem. Fast, clash-free RNA conformational morphing using molecular junctions. *Bioinformatics* 33.14 (2017), pp. 2114–2122.

[9] Susanne MA Hermans, Christopher Pfleger, Christina Nutschel, Christian A Hanke, and Holger Gohlke. Rigidity theory for biomolecules: concepts, software, and applications. *WIREs Comput. Mol. Sci.* 7.4 (2017), e1311.

[10] Steven M LaValle. *Rapidly-exploring random trees: A new tool for path planning.* Tech. rep. 98-11. Iowa State Univ., 1998.

**Proceedings of the 8th GACM Colloquium on Computational Mechanics
for Young Scientists from Academia and Industry
August 28–30, 2019 in Kassel, Germany**

Variational modeling of irreversible effects in cycled polycrystalline shape memory alloys

Johanna Waimann * [1], Klaus Hackl[2] and Philipp Junker[3]

[1]Institute of Applied Mechanics, RWTH Aachen University, Germany
[2]Institute of Mechanics of Materials, Ruhr-Universität Bochum, Germany
[3]Chair of Solid Mechanics, University of Wuppertal, Germany

Abstract. The material behavior of shape memory alloys (SMAs) is characterized by a diffusionless solid/solid phase transformation between an austenitic and several martensitic phases. Compared to transformations in classical steel, the transformation process is not only induced by thermal loading but also by mechanical loads. Due to the related properties and namely the effects of pseudoelasticity and pseudoplasticity, SMAs are very attractive materials for industrial applications. The presented work focuses the functional fatigue of this special class of materials which occurs during cyclic loading of the specimen. Three models are presented which are based on the principle of the minimum of the dissipation potential (PMDP) and take into account different aspects of the complex material behavior: a simultaneous plastic deformation, the formation of irreversible martensite during mechanical cycling and the fatigue during thermal cycling. In addition, several simulations show the functionality of the material models.

Introduction

Cyclic tension tests of SMAs show that due to some formed dislocations (cf. [5]) the material is functionally fatigued: a remaining strain is accumulating, the transformation from austenite to martensite is favored and the reverse transformation is delayed (cf. [3]). During thermal cycling the opposite effect takes place: the transformation from austenite to martensite is delayed and the back transformation is favored (see [1]).

The material models in the following sections are also presented in [6] and show different aspects of the microstructural evolution. Whereas in the first presented model the phase transformation is coupled to a formation of irreversible martensitic volume fractions, which are the direct results of the formed dislocations (see [5]), the second model displays the fatigue phenomena by considering a simultaneous plastic deformation. Thereby, a coupled dissipation function is introduced to take into account the in parallel evolving microstructural processes. The third model is additionally able to display the material's fatigue performance during thermal cycling by storage of the material's transformation history. The polycrystalline character of the examined shape memory alloys is additionally considered by an evolving orientation distribution function [4]. Each model's description is accompanied by numerical results which proof its performance.

1 Simultaneous formation of irreversible martensite

Based on the principle of the minimum of the dissipation potential, the first material model is taking into account a formation of irreversible martensite during the phase transformation between one austenitic and n martensitic phases. The transformation processes are considered by two internal variables: the reversible and the irreversible volume fractions, $\boldsymbol{\lambda}$ and $\boldsymbol{\rho}$. To additionally take into account the polycrystalline character of the examined SMAs, a third internal variable is used. The set of Euler angles $\boldsymbol{\alpha} = \{\varphi, \vartheta, \omega\}$ describes the averaged orientation of the transforming grains based on [4]. Compared to a

*Corresponding author: waimann@ifam.rwth-aachen.de ORCID iD: 0000-0002-7579-7240

grain-wise determination of the volume fractions, it enables a much faster calculation of the microstructural evolution. The used variational method, the PMDP (cf. [2]), is based on the idea of formulating a Lagrange function

$$\mathcal{L} = \dot{\Psi}\left(\boldsymbol{\varepsilon}, \theta, \boldsymbol{\alpha}, \boldsymbol{\lambda}, \boldsymbol{\rho}\right) + \mathcal{D}\left(\boldsymbol{\lambda}, \boldsymbol{\rho}, \dot{\boldsymbol{\alpha}}, \dot{\boldsymbol{\lambda}}, \dot{\boldsymbol{\rho}}\right) + \text{cons} \quad \rightarrow \min_{\dot{\boldsymbol{\alpha}}, \dot{\boldsymbol{\rho}}, \dot{\boldsymbol{\lambda}}}, \tag{1}$$

which includes the rate of the Helmholtz free energy Ψ, a dissipation function $\mathcal{D}$ and constraints which have to be fulfilled and are considered by Lagrange and Kuhn-Tucker parameters. The quantities $\boldsymbol{\varepsilon}$ and θ are the total strain and the temperature. The following minimization of $\mathcal{L}$ with respect to the rates of the internal variables directly results in evolution equations for them. Considering the microstructural effects, the Helmholtz free energy has the form

$$\Psi = \frac{1}{2}\left(\boldsymbol{\varepsilon} - \bar{\boldsymbol{\eta}}_{\mathrm{R}} - \bar{\boldsymbol{\upsilon}}_{\mathrm{R}}\right) : \bar{\mathbb{E}} : \left(\boldsymbol{\varepsilon} - \bar{\boldsymbol{\eta}}_{\mathrm{R}} - \bar{\boldsymbol{\upsilon}}_{\mathrm{R}}\right) + \bar{c} \tag{2}$$

with the effective quantities

$$\begin{aligned} \bar{\boldsymbol{\eta}}_{\mathrm{R}} &= \boldsymbol{Q}^{\mathrm{T}} \cdot \sum_{i=0}^{n} \lambda_i \boldsymbol{\eta}_i \cdot \boldsymbol{Q} & \bar{\boldsymbol{\upsilon}}_{\mathrm{R}} &= \boldsymbol{Q}^{\mathrm{T}} \cdot \sum_{i=0}^{n} \rho_i \boldsymbol{\eta}_i \cdot \boldsymbol{Q} \\ \bar{\mathbb{E}} &= \left[\sum_{i=0}^{n} \left(\lambda_i + \rho_i\right)\left(\mathbb{E}_i\right)^{-1}\right]^{-1} & \bar{c} &= \sum_{i=0}^{n} \left(\lambda_i + \rho_i\right) c_i. \end{aligned} \tag{3}$$

In Equations (2) and (3), $\boldsymbol{\eta}_i$ is the transformation strain of phase i, which is an experimentally observed quantity. Related to the irreversible volume fraction, a part of the transformation strain remains in the material, which is given by $\boldsymbol{\upsilon}_i = \rho_i \boldsymbol{\eta}_i$. By use of the rotation tensor $\boldsymbol{Q}(\boldsymbol{\alpha})$, the transformation strains are rotated in the energetically optimized averaged orientation of the transformations. The quantities $\mathbb{E}_i$ and c_i describe the stiffness and the caloric energy of the individual phases i. The in Equation (1) used function $\mathcal{D}$ denotes the energy which dissipates due to the change of the microstructure. With use of the dissipation parameter r_{T1}, the coupling parameters f and g as well as the viscous parameter r_{R}, it has the form

$$\mathcal{D} = r_{\mathrm{T1}} \sqrt{\sum_{i=0}^{n} \left(f\dot{\lambda}_i\right)^2 + \sum_{i=0}^{n} \left(g\dot{\rho}_i\right)^2} + \frac{\sqrt{2}\, r_{\mathrm{R}}}{2}\left(\dot{\varphi}^2 + \dot{\vartheta}^2 + 2\dot{\varphi}\dot{\omega}\cos\vartheta + \dot{\omega}^2\right) \tag{4}$$

and includes a rate-independent coupled approach for the part related to the transformations and a rate-dependent part for the Euler angles as defined in [4]. Considering the non-negativity of the volume fractions, mass conservation, the irreversibility and a maximum value for the stabilized martensite, the minimization of the Lagrange function results in evolution equations of elasto-plastic type for $\boldsymbol{\lambda}$ and $\boldsymbol{\rho}$

$$\dot{\lambda}_i = \frac{\beta}{f^2}\mathrm{dev}P_{\mathrm{T}i} \quad \forall\, i \in \mathcal{A}_\lambda, \qquad \dot{\rho}_i = \frac{\beta}{g^2}\mathrm{dev}P_{\mathrm{T}i} \quad \forall\, i \in \mathcal{A}_\rho \tag{5}$$

with the thermodynamic driving force $\boldsymbol{P}_{\mathrm{T}} = -\partial\Psi/\partial\boldsymbol{\lambda} = -\partial\Psi/\partial\boldsymbol{\rho}$, the consistency parameter β and the active deviator $\mathrm{dev}P_{\mathrm{T}i} = P_{\mathrm{T}i} - (\sum_{k\in\mathcal{A}_\lambda} P_{\mathrm{T}k}/f^2 + \sum_{l\in\mathcal{A}_\rho} P_{\mathrm{T}l}/g^2)/(n_{\mathcal{A}\lambda}/f^2 + n_{\mathcal{A}\rho}/g^2)$ using the sets of active phases $\mathcal{A}_\lambda$ and $\mathcal{A}_\rho$. To calculate the consistency parameter β, a Legendre transformation of the dissipation function is performed, which directly results in the yield function Φ and the Karush-Kuhn-Tucker conditions:

$$\Phi = \frac{1}{f^2}\mathrm{dev}_{\mathcal{A}}\boldsymbol{P}_{\mathrm{T}} \cdot \mathrm{dev}_{\mathcal{A}}\boldsymbol{P}_{\mathrm{T}}\Big|_{\mathcal{A}_\lambda} + \frac{1}{g^2}\mathrm{dev}_{\mathcal{A}}\boldsymbol{P}_{\mathrm{T}} \cdot \mathrm{dev}_{\mathcal{A}}\boldsymbol{P}_{\mathrm{T}}\Big|_{\mathcal{A}_\rho} - r_{\mathrm{T1}}^2 \leq 0, \qquad \beta \geq 0, \qquad \beta\Phi = 0. \tag{6}$$

Using the corresponding driving forces $\boldsymbol{P}_{\mathrm{R}} = \{P_\varphi, P_\vartheta, P_\omega\} = -\partial\Psi/\partial\boldsymbol{\alpha}$, the minimization of $\mathcal{L}$ related to the rate of the Euler angles gives evolution equations of viscous type for $\boldsymbol{\alpha}$:

$$\begin{aligned} \dot{\varphi} &= \frac{1}{\sqrt{2}r_{\mathrm{R}}}\frac{1}{1-\cos^2\vartheta}\left(P_\varphi - P_\omega\cos\vartheta\right) & \dot{\vartheta} &= \frac{1}{\sqrt{2}r_{\mathrm{R}}}P_\vartheta \\ \dot{\omega} &= \frac{1}{\sqrt{2}r_{\mathrm{R}}}\frac{1}{1-\cos^2\vartheta}\left(P_\omega - P_\varphi\cos\vartheta\right) & & \end{aligned} \quad . \tag{7}$$

Figure 1 shows the results for a cyclically loaded clamping ring. The force/displacement diagram displays the expected material behavior: an increase of the plateau stresses and an accumulating remaining

strain. In addition to that, the austenitic volume fraction at maximum load and the total irreversible martensite $\bar{\rho}$ after ten load cycles show –as a result of the coupled dissipation function– the stabilization of martensitic variants in the transforming areas. A more detailed description of the material model including a calibration, its finite element implementation and simulations as well as a comparison with experimental data is already published in [9] and [10].

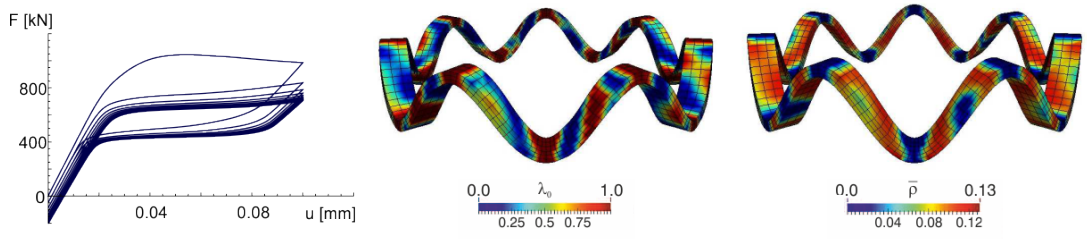

Figure 1. Simultaneous formation of irreversible martensite – cyclic loaded clamping ring: force/displacement diagram (*left*), austenitic volume fraction at maximum load (*center*), total irreversible martensitic volume fraction after ten load cycles (*right*) [10].

2 Simultaneous plastic evolution

In the second presented model, our in a chronological sense first modeling approach [8], which couples phase transformation with plasticity, is extended by the use of the evolving orientation distribution function [4] instead of the former grain-wise calculation of the microstructural evolutions. Instead of an irreversible martensitic volume fraction in the previous section, a plastic strain of every phase i given by $\boldsymbol{\varepsilon}_{\mathrm{P}i}$ is used as an internal variable. The combined dissipation function for the simultaneous processes includes now a dissipation parameter (or yield limit) which is a function of the absolute plastic strain to take into account the fatigue effect and the converging character of the material behavior. In Figure 2, the force/displacement diagram of a cyclically loaded plate with a hole as well as the related austenitic volume fraction at maximum load in the tenth cycle and the plastic strain after the same load cycle are presented. The model with simultaneous plastic deformation also shows the experimentally observed material behavior. The plastic deformations form in the arc-like transformation zone and effect the decrease of the transformation plateaus. A detailed description and several simulations for the model can be found in [8] and [6].

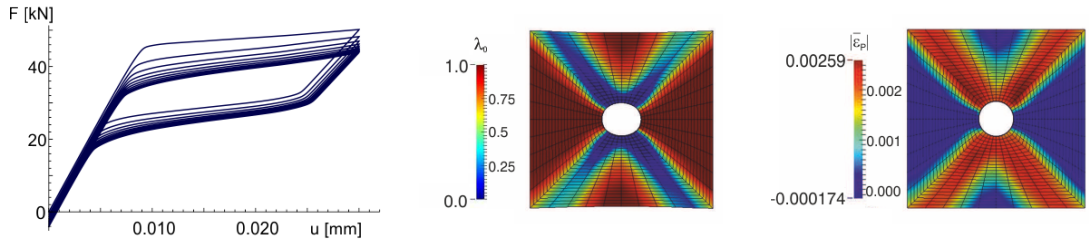

Figure 2. Simultaneous plastic evolution – cyclic loaded plate with a hole: force/displacement diagram (*left*), austenitic volume fraction at maximum load in tenth load cycle (*center*), total plastic strain after tenth cycle (*right*) [6].

3 Storage of the transformation history

Whereby the first two material models are only able to describe the functional fatigue during mechanical cycling, the last model also displays the material behavior during thermal cycling. Besides the reversible volume fraction $\boldsymbol{\lambda}$ and the set of Euler angles $\boldsymbol{\alpha}$ considering the polycrystalline structure, the transformation history of the material is stored by use of the transformation history variable ρ. To take into account the fatigue effect, an additional energy term $\Psi_{\theta\rho}(\theta, \rho)$ as well as an accumulating inelastic strain $\boldsymbol{v}(\rho)$ are used, which take into account the thermal and the transformation history's influence. First

results for the material point level are presented in Figure 3. On the left, the characteristic stress/strain diagram is presented, which again shows the effect of functional fatigue. On the right, the evolution of the austenitic volume fraction in a thermal cycling test is shown. The third model is thus also able to show the decrease of the transformation temperatures during thermal cycling, as it is observed ,e.g., in [1]. A detailed description of the model as well as its finite element implementation are presented in [6] and [7].

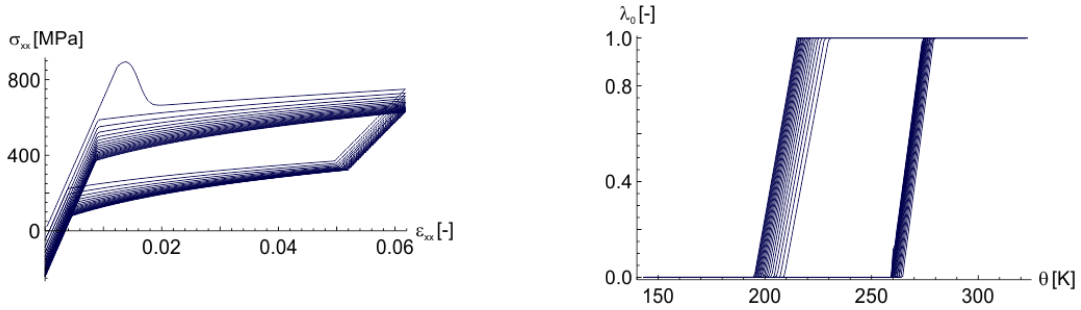

Figure 3. Storage of the transformation history – cyclic tension test: stress/strain diagram (*left*); thermal cycling test: evolution of the austenitic volume fraction (*right*) [6, 7].

Acknowledgments

I kindly acknowledge Univ.-Prof. Dr.-Ing. habil. Stefanie Reese for her support and many helpful and inspiring discussions.

References

[1] J. Burow. *Herstellung, Eigenschaften und Mikrostruktur von ultrafeinkörnigen NiTi-Formgedächtnislegierungen*. Ruhr-Universität Bochum, Diss., 2010.

[2] C. Carstensen, K. Hackl, and A. Mielke. Non–convex potentials and microstructures in finite–strain plasticity. *Proceedings of the Royal Society of London. Series A: Mathematical, Physical and Engineering Sciences* 458.2018 (2002), pp. 299–317.

[3] G. Eggeler, E. Hornbogen, A. Yawny, A. Heckmann, and M. F.-X. Wagner. Structural and functional fatigue of NiTi shape memory alloys. *Materials Science and Engineering: A* 378.1 (2004), pp. 24–33.

[4] P. Junker. A novel approach to representative orientation distribution functions for modeling and simulation of polycrystalline shape memory alloys. *International Journal for Numerical Methods in Engineering* 98.11 (2014), pp. 799–818.

[5] P. Krooß, T. Niendorf, P. M. Kadletz, C. Somsen, M. J. Gutmann, Y. I. Chumlyakov, W. W. Schmahl, G. Eggeler, and H. J. Maier. Functional Fatigue and Tension–Compression Asymmetry in [001]-Oriented Co49Ni21Ga30 High-Temperature Shape Memory Alloy Single Crystals. *Shape Memory and Superelasticity* 1.1 (2015), pp. 6–17.

[6] J. Waimann. *Variationelle Modellierung irreversibler Effekte in polykristallinen Formgedächtnislegierungen*. Ruhr-Universität Bochum, Diss., 2018.

[7] J. Waimann and P. Junker. Modeling the influence of thermal and mechanical cycling on polycrystalline shape memory alloys (2019 in preparation).

[8] J. Waimann, P. Junker, and K. Hackl. A coupled dissipation functional for modeling the functional fatigue in polycrystalline shape memory alloys. *European Journal of Mechanics-A/Solids* 55 (2016), pp. 110–121.

[9] J. Waimann, P. Junker, and K. Hackl. Modeling the Cyclic Behavior of Shape Memory Alloys. *Shape Memory and Superelasticity* (2017), pp. 1–15.

[10] J. Waimann, K. Hackl, and P. Junker. Variational modeling and finite-element simulation of functional fatigue in polycrystalline shape memory alloys. *Journal of Optimization Theory and Applications* (2019), pp. 1–27.

**Proceedings of the 8th GACM Colloquium on Computational Mechanics
for Young Scientists from Academia and Industry
August 28–30, 2019 in Kassel, Germany**

Connection between micro- and macroscales in generalized mechanics

Bilen Emek Abali * [1]

[1]Technische Universität Berlin, Institute of Mechanics MS 2, Einsteinufer 5, 10587 Berlin, Germany

Abstract. Inner structure of a material starts affecting the material response at the macroscale (length scale of the geometry), as the geometric dimensions decrease. Miniaturization in nowadays technology obliges the theory to incorporate the inner structure. Examples for these so-called metamaterials are porous structures like electrodes in batteries, 3D printed structures with varying infill ratio, foam like materials with exotic behavior. Such an extension is called generalized mechanics and various theories have been emerged, among others, strain gradient, micropolar, micromorphic theories are well known and established. Mainly two additional difficulties arise, the extension of stored energy and kinetic energy. This work highlights the possible connection between microscale (length scale of the inner structure) and macroscale leading to a better comprehension of upscaling from the microscale to the macroscale. Additional parameters emerge and their interpretation is possible by using homogenization techniques. Parameter identification is possible by a pure computational procedure of solving at micro- and macroscales. Specifically for the strain gradient theory, we demonstrate the results of a possible approach.

Introduction

Especially with additive manufacturing possibilities like in fused deposition modeling (FDM) mostly known from so-called 3D printers, an inner substructure is possible to implement in a material. Also in foam like or porous materials, where the high ratio of surface is aimed for as in the case of electrodes in a battery, an inner substructure is present within the material. We know that in crystallography, as studied in [24, 28], an inner substructure called a lattice in the atomic length scale, *microscale*, cause anisotropy in the micrometer length scale, *macroscale*. At the microscale the atomic interaction is often modeled by two body interaction scalar potentials and one of existing upscaling approaches can be used to homogenize the lattice structure, see for example the approach based on a statistical method as introduced in [12]. An analogous attempt is used for composite materials or also materials with inclusions. The microscale considers a matrix embedding fibers or voids being a heterogeneous material and it leads to a homogeneous material at the macroscale by using approaches as in [10, 11, 15, 19, 20, 26, 29, 30]. Starting with works of [8, 9, 17], a generalized mechanics is used to consider not only first but also second gradients in displacement at the macroscale such that the energy definition is discussed heavily, among others, see [1, 7, 13, 22, 23, 27]. An upscaling procedure has been proposed for generalized mechanics as well, we refer to [4, 5, 16, 21, 25].

Strain gradient theory and a computational comparison verifying its necessity

We briefly explain and then apply the method introduced in [3] for determining parameters in the case of a generalized mechanics for a porous material. Then we demonstrate the difference between solutions with strain gradient and without strain gradient computations. Consider a microscale with a distinct geometric model as seen in Fig. 1 providing a detailed internal substructure at the length scale of the microscale. For an upscaling this structure to a macroscale, it is beneficial to use a homogenization approach. Nevertheless, the first assumption for a homogenization method relies on the descriptions defined at micro- and macroscales. Often, the same material model is used at both scales; however, as analyzed in detail by [16], this fact is very questionable. Therefore, we start with an assertion that the

*Corresponding author: bilenemek@abali.org ORCID iD: 0000-0002-8735-6071

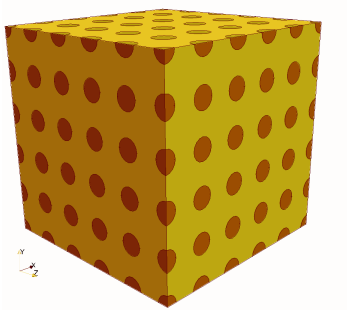

Figure 1. Microscale description of the structure, $\mathcal{B}$, with two materials indicated by different colors. If embedding material, matrix, is softer, then the round inclusions provide stiffness. On the contrary, matrix can be stiffer such that in the limiting case the inclusions can be seen as voids and the structure represents a porous foam.

micro- and macroscale material models are in general different. Consider the case that we use a first order theory, the classical case in elasticity, leading to the stored energy density, w, and stress, $\boldsymbol{\sigma}$, as follows

$$w = \varepsilon_{ij} C_{ijkl} \varepsilon_{kl} \ , \quad \sigma_{ij} = \frac{\partial w}{\partial \varepsilon_{ij}} = C_{ijkl} \varepsilon_{kl} \ , \tag{1}$$

where and henceforth we use the summation convention over repeated indices. Stiffness tensor, C_{ijkl}, denotes the material response, and we may use a linear strain measure:

$$\varepsilon_{ij} = u_{(i,j)} = \frac{1}{2}(u_{i,j} + u_{j,i}) \ , \tag{2}$$

with the partial space derivative denoted by comma. This energy is defined at the microscale, for example with two isotropic materials given by two parameters, λ, μ, as follows:

$$C_{ijkl} = \lambda \delta_{ij} \delta_{kl} + \mu \delta_{ik} \delta_{jl} + \mu \delta_{il} \delta_{jk} \ . \tag{3}$$

At the macroscale, we consider that two materials are homogenized to one single "new" material. The same energy definition might be used with different parameters, or in a more general sense, we can try to utilize an energy including strain gradients as well, considering that it be isotropic and centrosymmetric

$$\bar{w} = \varepsilon_{ij} \bar{C}_{ijkl} \varepsilon_{kl} + \varepsilon_{ij,k} \bar{D}_{ijklmn} \varepsilon_{lm,n} + \varepsilon_{ij} \bar{G}_{ijklm} \varepsilon_{kl,m} \ . \tag{4}$$

The energy densities are not equal, $w \neq \bar{w}$. In the case of an isotropic and centro-symmetric material, they read

$$\begin{aligned}
\bar{C}_{ijkl} =& c_1 \delta_{ij} \delta_{kl} + c_2 (\delta_{ik} \delta_{jl} + \delta_{il} \delta_{jk}), \\
\bar{D}_{ijklmn} =& c_3 (\delta_{ij} \delta_{kl} \delta_{mn} + \delta_{in} \delta_{jk} \delta_{lm} + \delta_{ij} \delta_{km} \delta_{ln} + \delta_{ik} \delta_{jn} \delta_{lm}) + \\
&+ c_4 \delta_{ij} \delta_{kn} \delta_{ml} + \\
&+ c_5 (\delta_{ik} \delta_{jl} \delta_{mn} + \delta_{im} \delta_{jk} \delta_{ln} + \delta_{ik} \delta_{jm} \delta_{ln} + \delta_{il} \delta_{jk} \delta_{mn}) + \\
&+ c_6 (\delta_{il} \delta_{jm} \delta_{kn} + \delta_{im} \delta_{jl} \delta_{kn}) + \\
&+ c_7 (\delta_{il} \delta_{jn} \delta_{mk} + \delta_{im} \delta_{jn} \delta_{lk} + \delta_{in} \delta_{jl} \delta_{km} + \delta_{in} \delta_{jm} \delta_{kl}) \ , \\
\bar{G}_{ijklm} =& 0 \ ,
\end{aligned} \tag{5}$$

The additional parameter tensor, $\bar{D}_{ijklmn}$, vanishes in the case that a linear elastic material model at the macroscale is adequate. Under the assumption that the energy within the structure, $\mathcal{B}$, is identical at both scales, $\int_{\mathcal{B}} w \, \mathrm{d}v = \int_{\mathcal{B}} \bar{w} \, \mathrm{d}v$, it is possible to start with known values of λ, μ at the microscale and determine values at the macroscale, c_1, c_2, $\dots c_7$. As an example we consider a porous material with Young's modulus, E_1, Poisson's ratio, ν_1, possessing voids modeled with, E_2 and ν_2 leading to

$$\lambda = \frac{E\nu}{(1+\nu)(1-2\nu)} \ , \quad \mu = \frac{E}{2(1+\nu)} \ . \tag{6}$$

We refer to [3] for details of the used algorithm determining the values compiled in Table 1. The parameters $c_\times$ in Table 1 are in the unit of force, hence, it is difficult to justify their significance. Therefore, we use a computational comparison of a beam bending experiment of this homogenized material. As experimentally proven in [6, 14, 18], a slender beam gets stiffer than calculated by using analytical methods indicating this so-called "size effect," where the strain gradient effect is of importance. We refer to [2] for details and perform simulations for two cases: one with the obtained $c_\times$ parameters and another one by setting them zero. The geometry is a simple beam of length ℓ with a squared cross sectional area of width $\ell/30$. Its length is reduced by preserving the ratio of length to width the same. Technically, we perform four computations for each case and compare the results in Table 2.

Table 1. Parameters obtained by the computational homogenization method based on [3] for the porous structure seen in Fig. 1.

E_1	E_1	$\nu_1 = \nu_2$	c_1	c_2	c_3	c_4	c_5	c_6	c_7
1 GPa	1 MPa	0.3	420 MPa	320 MPa	0.20 N	0.05 N	-0.18 N	-0.02 N	-0.02 N

Table 2. Computational comparison for different beam lengths, ℓ, simulating the two cases: case 1 is with strain gradient parameters from Table 1 and case 2 is for vanishing $c_3 = c_4 = c_5 = c_6 = c_7 = 0$

case	ℓ	tip deflection	difference
1	10 mm	0.197 mm	-
2	10 mm	0.197 mm	0%
1	1 mm	0.182×10^{-1} mm	-
2	1 mm	0.197×10^{-1} mm	8%
1	0.1 mm	0.188×10^{-2} mm	-
2	0.1 mm	0.197×10^{-2} mm	5%
1	0.01 mm	0.162×10^{-3} mm	-
2	0.01 mm	0.197×10^{-3} mm	18%

Conclusion

For technical applications getting smaller in size as a part of miniaturization, strain gradient theory becomes important. In this short note, we have briefly shown a possible consideration as well as physical interpretation of the strain gradient theory, identification of the newly introduced, as well as testing their significance by simulating the size effect dominating the material response as the dimensions reduce.

Acknowledgments

B. E. Abali's work is partly funded by a grant from the Daimler and Benz Foundation.

References

[1] B. E. Abali. Revealing the physical insight of a length-scale parameter in metamaterials by exploiting the variational formulation. *Continuum Mechanics and Thermodynamics* (2018), pp. 1–10.

[2] B. E. Abali, W. H. Müller, and F. dell'Isola. Theory and computation of higher gradient elasticity theories based on action principles. *Archive of Applied Mechanics* 87.9 (2017), pp. 1495–1510.

[3] B. E. Abali, H. Yang, and P. Papadopoulos. A Computational Approach for Determination of Parameters in Generalized Mechanics. In: *Higher Gradient Materials and Related Generalized Continua*. Ed. by H. Altenbach, W. H. Müller, and B. E. Abali. Springer Nature, Singapore, 2019. Chap. 1, pp. 1–17.

[4] H. Abdoul-Anziz and P. Seppecher. Strain gradient and generalized continua obtained by homogenizing frame lattices. *Mathematics and mechanics of complex systems* 6.3 (2018), pp. 213–250.

[5] D. Bigoni and W. J. Drugan. Analytical derivation of Cosserat moduli via homogenization of heterogeneous elastic materials. *Journal of Applied Mechanics* 74.4 (2007), pp. 741–753.

[6] C. Q. Chen, Y. T. Pei, and J. Th. M. De Hosson. Effects of size on the mechanical response of metallic glasses investigated through in situ TEM bending and compression experiments. *Acta Materialia* 58.1 (2010), pp. 189–200.

[7] V. A. Eremeyev, L. P. Lebedev, and H. Altenbach. *Foundations of Micropolar Mechanics*. Springer Science & Business Media, 2012.

[8] A. C. Eringen. Mechanics of Micromorphic Continua. In: *Mechanics of Generalized Continua*. Ed. by E. Kröner. Berlin: Springer-Verlag, 1968, pp. 18–35.

[9] A. C. Eringen and E. S. Suhubi. Nonlinear Theory of Simple Micro-elastic Solids. *International Journal of Engineering Science* 2 (1964), pp. 189–203.

[10] Z Hashin and S Shtrikman. On some variational principles in anisotropic and nonhomogeneous elasticity. *Journal of the Mechanics and Physics of Solids* 10.4 (1962), pp. 335–342.

[11] R. Hill. On Constitutive Macro-variables for Heterogeneous Solids at Finite Strain. *Proc. R. Soc. Lond. A* 326 (1972), pp. 131–147.

[12] J. H. Irving and J. G. Kirkwood. The Statistical Mechanical Theory of Transport Processes. IV. The Equations of Hydrodynamics. *The Journal of Chemical Physics* 18 (1950), pp. 817–829.

[13] E. A. Ivanova and E. N. Vilchevskaya. Micropolar continuum in spatial description. *Continuum Mechanics and Thermodynamics* 28.6 (2016), pp. 1759–1780.

[14] D. Lam, F. Yang, A. C. M. Chong, J. Wang, and P. Tong. Experiments and theory in strain gradient elasticity. *Journal of the Mechanics and Physics of Solids* 51.8 (2003), pp. 1477–1508.

[15] V. M. Levin. Determination of composite material elastic and thermoelastic constants. *Mechanics of Solids* 11.6 (1976), pp. 119–126.

[16] K. K. Mandadapu, B. E. Abali, and P. Papadopoulos. On the Polar Nature and Invariance Properties of a Thermomechanical Theory for Continuum-on-Continuum Homogenization. *arXiv preprint arXiv:1808.02540* (2018).

[17] R. D. Mindlin. Micro-structure in linear elasticity. *Archive for Rational Mechanics and Analysis* 16.1 (1964), pp. 51–78.

[18] T. Namazu, Y. Isono, and T. Tanaka. Evaluation of size effect on mechanical properties of single crystal silicon by nanoscale bending test using AFM. *Journal of Microelectromechanical Systems* 9.4 (2000), pp. 450–459.

[19] L. Nazarenko, H. Stolarski, L. Khoroshun, and H. Altenbach. Effective thermo-elastic properties of random composites with orthotropic components and aligned ellipsoidal inhomogeneities. *International Journal of Solids and Structures* 136 (2018), pp. 220–240.

[20] S. Nemat-Nasser and M. Hori. *Micromechanics: Overall Properties of Heterogeneous Materials*. Vol. 37. Elsevier, 2013.

[21] C. Pideri and P. Seppecher. A second gradient material resulting from the homogenization of an heterogeneous linear elastic medium. *Continuum Mechanics and Thermodynamics* 9.5 (1997), pp. 241–257.

[22] C. Polizzotto. A second strain gradient elasticity theory with second velocity gradient inertia–Part I: Constitutive equations and quasi-static behavior. *International Journal of Solids and Structures* 50.24 (2013), pp. 3749–3765.

[23] C. Polizzotto. A second strain gradient elasticity theory with second velocity gradient inertia–Part II: Dynamic behavior. *International Journal of Solids and Structures* 50.24 (2013), pp. 3766–3777.

[24] A. Reuss. Berechnung der Fließgrenze von Mischkristallen auf grund der Plastizitätsbedingung für Einkristalle. *ZAMM-Journal of Applied Mathematics and Mechanics/Zeitschrift für Angewandte Mathematik und Mechanik* 9.1 (1929), pp. 49–58.

[25] P. Seppecher, J.-J. Alibert, and F. dell'Isola. Linear elastic trusses leading to continua with exotic mechanical interactions. In: *Journal of Physics: Conference Series*. Vol. 319. IOP Publishing. 2011, p. 012018.

[26] B. Shafiro and M. Kachanov. Anisotropic effective conductivity of materials with nonrandomly oriented inclusions of diverse ellipsoidal shapes. *Journal of applied physics* 87.12 (2000), pp. 8561–8569.

[27] P. Steinmann. A micropolar theory of finite deformation and finite rotation multiplicative elastoplasticity. *International Journal of Solids and Structures* 31.8 (1994), pp. 1063–1084.

[28] W. Voigt. Über die Beziehung zwischen den beiden Elasticitätsconstanten isotroper Körper. *Annalen der Physik* 274.12 (1889), pp. 573–587.

[29] T. I. Zohdi. Homogenization methods and multiscale modeling. *Encyclopedia of Computational Mechanics Second Edition* (2017), pp. 1–24.

[30] T. I. Zohdi and P. Wriggers. *An Introduction to Computational Micromechanics*. Springer Science & Business Media, 2008.

**Proceedings of the 8th GACM Colloquium on Computational Mechanics
for Young Scientists from Academia and Industry
August 28–30, 2019 in Kassel, Germany**

On the modeling of microstructure influence

Arkadi Berezovski *

Tallinn University of Technology, School of Science, Tallinn, Estonia

Abstract. The mathematical structure of micromorphic elasticity is analyzed from the point of view of the internal variables theory. It is demonstrated how dispersion characteristics of governing equations depend on the choice of sign for material parameters. This choice provides the explanation of the results of direct numerical simulations of a pulse propagation in an inhomogeneous one-dimensional bar.

Introduction

There exist various methods to take into account the influence of microstructure of materials on their global behavior, e.g., distinct homogenization approaches [7, 8], strain gradient [5], micropolar, and micromorphic theories [4]. It is not easy task to choose an appropriate description due to a lack of values of material parameters. In the paper, we analyze the mathematical structure of micromorphic elasticity and its relation to the wave propagation features. For simplicity, we constrain ourself by one-dimensional setting.

1 Free energy

It is well known that linear elasticity obeys the Hooke law

$$\sigma = \rho c^2 u_x, \tag{1}$$

where σ is the stress, ρ is the density, u is the displacement, c is the elastic wave speed. The Hooke law corresponds to the free energy density in the form

$$W = \frac{\rho c^2}{2} u_x^2. \tag{2}$$

Certainly, there is no any influence of a microstructure. An extension of the free energy density is needed to include such an effect. The first possibility of such extansion is delivered by the inclusion of the strain gradient into the elastic model

$$W = \frac{\rho c^2}{2} (u_x)^2 + A u_x u_{xx} + \frac{1}{2} B (u_{xx})^2. \tag{3}$$

It should be noted that the strain gradient can be considered as an internal variable $\varphi = A/B\, u_{xx}$ [2], and the free energy density is then represented in the form

$$W = \frac{\rho c^2}{2} u_x^2 + A \varphi u_x + \frac{1}{2} B \varphi^2. \tag{4}$$

Of course, this is only the first step in the generalization of the free energy density. To go further, we consider the internal variable as a new unknown field and include space and time rates of the internal variable keeping the quadratic dependence of the free energy density

$$W = \frac{\rho c^2}{2} u_x^2 + A \varphi u_x + \frac{1}{2} B \varphi^2 + \frac{1}{2} C \varphi_x^2 + \frac{1}{2} M \varphi_t^2. \tag{5}$$

*Corresponding author: arkadi.berezovski@cs.ioc.ee

It should be noted that the last relation corresponds to the Mindlin microelasticity in one dimension if $B = -2A$ [1]

$$W = \frac{\rho c^2}{2} u_x^2 + A\varphi u_x - A\varphi^2 + \frac{1}{2} C\varphi_x^2 + \frac{1}{2} M\varphi_t^2. \tag{6}$$

2 Equations of motion

In the linear elasticity the equation of motion is the well known wave equation

$$u_{tt} = c^2 u_{xx}. \tag{7}$$

The equation of motion for the strain gradient model is extended to

$$\rho u_{tt} = \rho c^2 u_{xx} - \frac{A^2}{B} u_{xxxx}, \tag{8}$$

and in the case of internal variables we have the system of equations

$$\rho u_{tt} = \rho c^2 u_{xx} + A\varphi_x, \tag{9}$$
$$M\varphi_{tt} = C\varphi_{xx} - Au_x - B\varphi, \tag{10}$$

As previously, the choice $B = -2A$ leads to Mindlin microelasticity (and to relaxed micromorphic theory [6]) in one-dimensional setting.

2.1 Dimensionless variables

For further analysis we introduce dimensionless variables

$$U = \frac{u}{U_0}, \quad X = \frac{x}{L}, \quad T = \frac{c_0 t}{L}, \quad \varphi = \frac{U_0}{L}\Phi, \tag{11}$$

where U_0 and L are certain constants (e.g., intensity and wavelength of the initial excitation), and c_0 is the characteristic velocity.

Introducing dimensionless parameters

$$a = \frac{A}{\rho c_0^2}. \quad b = \frac{B}{\rho c_0^2}, \quad c = \frac{C}{L^2 \rho c_0^2}, \quad m = \frac{I}{L^2 \rho} \tag{12}$$

we have for the microstructure model with internal variables

$$U_{TT} = U_{XX} + a\Phi_X, \tag{13}$$
$$m\Phi_{TT} = c\Phi_{XX} - aU_X - b\Phi. \tag{14}$$

Again, the choice $b = -2a$ leads to the Mindlin microelasticity.

3 Dispersion relation

In order to study dispersive effects, we derive the dispersion relations by assuming the solutions in the form of harmonic waves

$$U(x,t) = \hat{U} e^{i(kx - \omega t)}, \quad \Phi(x,t) = \hat{\Phi} e^{i(kx - \omega t)}, \tag{15}$$

where k is the wavenumber, ω is the frequency, and $i^2 = -1$. Substituting relations (15) into Eqs. (13) and (14) we get

$$-\hat{U}\omega^2 = -\hat{U}k^2 + a\hat{\Phi}(ik), \tag{16}$$
$$-m\hat{\Phi}\omega^2 = -c\hat{\Phi}k^2 - a\hat{U}(ik) - b\hat{\Phi}. \tag{17}$$

This can be represented in the matrix form

$$\begin{pmatrix} k^2-\omega^2 & -iak \\ iak & ck^2-m\omega^2+b \end{pmatrix} \begin{pmatrix} \hat{U} \\ \hat{\Phi} \end{pmatrix} = 0, \tag{18}$$

In order to get nontrivial solutions the determinant of this matrix must vanish, which results in

$$\omega^2 - k^2 = \frac{1}{2m}\left[(ck^2 - mk^2 + b) \pm \sqrt{(ck^2 - mk^2 + b)^2 + 4ma^2k^2}\right]. \tag{19}$$

Specifying the values of dimensionless parameters as $m = 1$, $b = 1$, $a = 0.5$ $c = 3$, we have for the microstructure model with internal variables

$$\frac{\omega^2}{k^2} - 1 = \frac{1}{2}\left[(2 + \frac{1}{k^2}) \pm \sqrt{(2 + \frac{1}{k^2})^2 + \frac{1}{k^2}}\right]. \tag{20}$$

We are interesting in the behavior of short waves, because the long wave approximation is well studied. For short waves values of the wave number are high and, therefore, $\varepsilon = 1/k^2$ is a small parameter. Then the dispersion relation is represented in the form

$$v_{ph}^2 = 1 + \frac{1}{2}\left[(2 + \varepsilon) \pm \sqrt{(2 + \varepsilon)^2 + \varepsilon}\right] \tag{21}$$

with phase velocity v_{ph}, and the corresponding dispersion curves are shown in Fig. 1. These curves represent the Mindlin microelasticity if $a = -0.5$.

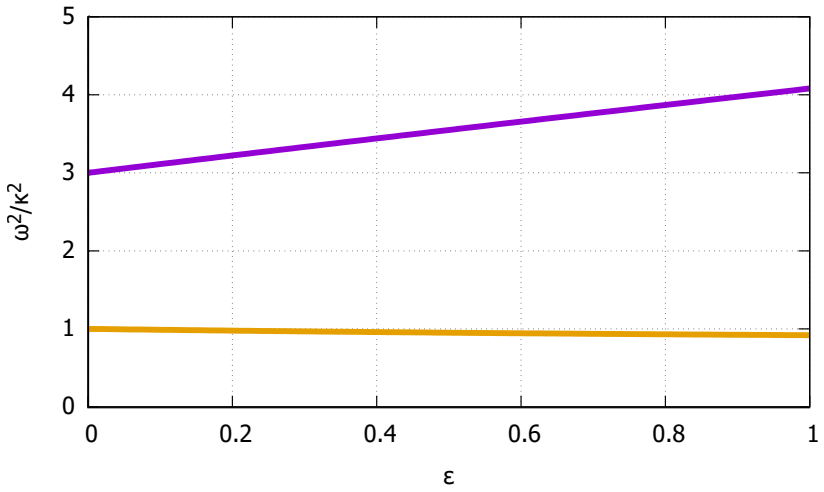

Figure 1. Dispersion curves corresponding to Eq. (21).

As it is demonstrated by direct numerical simulations [1], the Mindlin microelasticity model (as well as its extension in terms of internal variables) is unable to reproduce a pulse propagation behavior in an inhomogeneous bar if the size of inhomogeneities is comparable with the wavelength. However, the modification of the signs of material parameters resulting in equations of motion

$$U_{TT} = U_{XX} + a\Phi_X, \tag{22}$$

$$m\Phi_{TT} = c\Phi_{XX} + aU_X + b\Phi, \tag{23}$$

provides much more reliable results [3]. The corresponding dispersion relation

$$v_{ph}^2 = 1 + \frac{1}{2}\left[(2 - \varepsilon) \pm \sqrt{(2 - \varepsilon)^2 - \varepsilon}\right] \tag{24}$$

is illustrated in Fig. 2. As one can see, the dispersion curves are substantially different from those in the previous case.

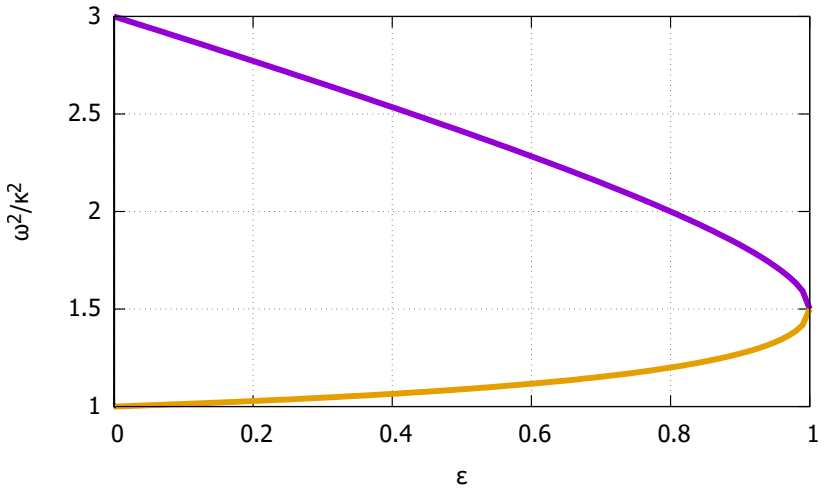

Figure 2. Dispersion curves corresponding to Eq. (24).

4 Conclusions

Analysis of the structure of micromorphic elasticity theory shows that its representation in terms of internal variables includes both the Mindlin microelasticity and relaxed micromorphic model (at least in one dimension). For short wave lengths, all these models are unable to reproduce the results direct numerical simulations of a pulse propagation in an inhomogeneous bar. The change of signs of some material parameters in the microstructure model provides more reliable results consistent with numerical results.

Acknowledgments

The work is supported by the Centre of Excellence for Nonlinear Dynamic Behaviour of Advanced Materials in Engineering CZ.02.1.01/0.0/0.0/15 003/0000493 (Excellent Research Teams) in the framework of Operational Programme Research, Development and Education, by the Grant project with Nos. 19-04956S of the Czech Science Foundation (CSF) within institutional support RVO:61388998, and by Estonian Research Council under Institutional Research Funding IUT33-24.

References

[1] Arkadi Berezovski. On the Mindlin microelasticity in one dimension. *Mechanics Research Communications* 77 (2016), pp. 60–64.

[2] Arkadi Berezovski. Internal variables associated with microstructures in solids. *Mechanics Research Communications* 93 (2018), pp. 30–34.

[3] Jüri Engelbrecht, Arkadi Berezovski, and Mihhail Berezovski. Deformation waves in microstructured materials: theory and numerics. In: *IUTAM Symposium on Recent Advances of Acoustic Waves in Solids*. Ed. by Tsung-Tsong Wu and Chien-Ching Ma. Springer. 2010, pp. 19–29.

[4] Samuel Forest. Micromorphic media. In: *Generalized Continua from the Theory to Engineering Applications*. Ed. by Holm Altenbach and Victor A. Eremeyev. Springer, 2013, pp. 249–300.

[5] Raymond David Mindlin and NN Eshel. On first strain-gradient theories in linear elasticity. *International Journal of Solids and Structures* 4 (1968), pp. 109–124.

[6] Patrizio Neff, Ionel-Dumitrel Ghiba, Angela Madeo, Luca Placidi, and Giuseppe Rosi. A unifying perspective: the relaxed linear micromorphic continuum. *Continuum Mechanics and Thermodynamics* 26 (2014), pp. 639–681.

[7] Siavouche Nemat-Nasser and Muneo Hori. *Micromechanics: Overall Properties of Heterogeneous Materials*. Elsevier, 2013.

**Proceedings of the 8th GACM Colloquium on Computational Mechanics
for Young Scientists from Academia and Industry
August 28–30, 2019 in Kassel, Germany**

A variational-based energy-momentum time integration of metamaterials in non-isothermal rotordynamical systems

Michael Groß * [1], Julian Dietzsch[1] and Chris Röbiger[1]

[1]TU Chemnitz, Professorship of applied mechanics and dynamics, Reichenhainer Straße 70, D-09126 Chemnitz, Germany.

Abstract. Textile manufacturing techniques as three-dimensional weaving of carbon yarns or the tailored fiber placement based on fixing carbon rovings on a base material are increasingly used for parts in rotordynamical systems. Examples are blades in turbine fans and pump rotors, disc brake rotors and shafts. These metamaterials allow for lower rotational masses while maintaining stiffness and improving heat conduction properties. This leads in rotordynamical systems to higher possible rotational speeds. Thereby, the direction-dependent heat conduction allows for a more efficient cooling in high temperature environments. A continuum formulation of such metamaterials has to take into account the bending stiffness of the yarns or rovings, because carbon yarns and rovings are made of thousends of carbon fibers. A standard Cauchy-continuum with a free energy based on structural tensors are not able to describe this fiber bending stiffness, because fibers are assumed as infinitely thin strings. This results in a three-point bending test of metamaterials simulated by finite elements to wrong curvature effects, in comparison to experimental data. The bending stiffness of the yarns or rovings can be taken into account by tensor invariants based on the second gradient of the deformation mapping, which leads to a generalized continuum formulation. In this paper, we consider a mixed formulation of a generalized continuum, in which the deformation gradient and the first Piola- Kirchhoff stress tensor as well as the continuum rotation vector, the angular velocity vector and the rotational momentum vector are introduced as independent fields. The corresponding weak forms arise from a principle of virtual power, which allows for energy-momentum time integrations of the considered rotordynamical systems. In this principle, the kinetic energy includes the translational energy of a standard Cauchy continuum based on the linear momentum, and the additional rotational energy with a micro-inertia tensor of a generalized continuum. This leads to two additional balance laws in comparison to a standard Cauchy continuum: the balance law of rotational momentum and the balance law of rotational energy. The exact preservation of these two balance laws along with the preservation of each balance law of a standard Cauchy continuum allows the derived energy-momentum scheme. We demonstrate the behavior of this physically-consistent simulation method by using dynamic simulations of a turbine rotor, a disc brake rotor and a rotating shaft subject to thermal and mechanical loads.

Introduction

In this paper, we show our first step, a transversely isotropic first-gradient material law in the variational setting of a generalized continuum. This assumption fits to the tailored fiber placement technique. We consider non-isothermal deformations of a transversally isotropic continuum moving in the Euclidean space $\mathbb{R}^{n_{\text{dim}}}$ with the constant ambient temperature Θ_∞. The initial configuration $\mathscr{B}_0 = \mathscr{B}_0^M \cup \mathscr{B}_0^F$ of the fiber-reinforced continuum body $\mathscr{B}$ (see Fig. 1) is defined as homogenization of the set $\mathscr{B}_0^M$ of the matrix material with the set $\mathscr{B}_0^F$ of the fiber bundels or rovings. In this way, we consider an imaginary fiber at any point $\boldsymbol{X} \in \mathscr{B}_0$, which is directed along the normalized fiber vector $\boldsymbol{a}_0$ with $\|\boldsymbol{a}_0\| = 1$. The corresponding stretched fiber vector $\boldsymbol{a} = \boldsymbol{F}\,\boldsymbol{a}_0$ in the current configuration $\mathscr{B}_t$ is given by the deformation gradient $\boldsymbol{F} := \text{Grad}[\boldsymbol{\varphi}]$ of the deformation mapping $\boldsymbol{\varphi} : \mathscr{B}_0 \to \mathscr{B}_t$. The operator Grad[•] indicates the partial derivative with respect to the material point $\boldsymbol{X} \in \mathscr{B}_0$. The deformation gradient $\boldsymbol{F}_F$ in fiber direction takes the form $\boldsymbol{F}_F := \boldsymbol{a} \otimes \boldsymbol{a}_0 = \boldsymbol{F}\,\boldsymbol{a}_0 \otimes \boldsymbol{a}_0 = \boldsymbol{F}\,\boldsymbol{A}_0$, with $\boldsymbol{A}_0 := \boldsymbol{a}_0 \otimes \boldsymbol{a}_0 = \boldsymbol{F}^{-1}\,[\boldsymbol{a} \otimes \boldsymbol{a}]\,\boldsymbol{F}^{-t} =: \boldsymbol{F}^{-1}\,\boldsymbol{A}\,\boldsymbol{F}^{-t}$. We denote by the superscript letter t the transposition of a second order tensor. The tensors $\boldsymbol{A}_0$ and $\boldsymbol{A}$ denote the material and spatial structural tensors, respectively. The deformation tensor

$$\boldsymbol{C}_F := \boldsymbol{F}_F^t\,\boldsymbol{F}_F = [\boldsymbol{F}\,\boldsymbol{a}_0 \otimes \boldsymbol{a}_0]^t\,[\boldsymbol{F}\,\boldsymbol{a}_0 \otimes \boldsymbol{a}_0] = [\boldsymbol{a}_0 \otimes \boldsymbol{a}_0]\,\boldsymbol{C}\,[\boldsymbol{a}_0 \otimes \boldsymbol{a}_0] = \boldsymbol{A}_0\,\boldsymbol{C}\,\boldsymbol{A}_0 = [\boldsymbol{C} : \boldsymbol{A}_0]\,\boldsymbol{A}_0 \tag{1}$$

*Corresponding author: michael.gross@mb.tu-chemnitz.de

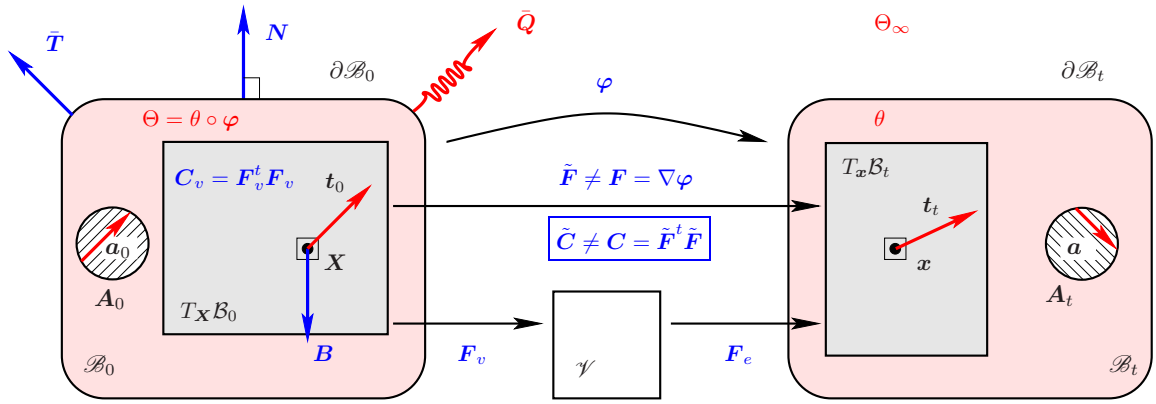

Figure 1. The initial and current configuration of a fiber-reinforced continuum with mechanical and thermal boundary as well as volume loads.

of the fibers is related to the right Cauchy-Green tensor $\boldsymbol{C} := \boldsymbol{F}^t\boldsymbol{F}$ by a projection on $\boldsymbol{A}_0$. The deformation of the isotropic matrix material complies with the multiplicative split $\boldsymbol{F} = \boldsymbol{F}_e\boldsymbol{F}_v$ of $\boldsymbol{F}$ in the viscous deformation gradient $\boldsymbol{F}_v$ and the elastic deformation gradient $\boldsymbol{F}_e$ (see Fig. 1). Here, the tangent space $\mathscr{V}$ denotes the so-called 'intermediate configuration'. Describing only isotropic viscous behaviour of the matrix material, we introduce the viscous right Cauchy-Green tensor $\boldsymbol{C}_v := \boldsymbol{F}_v^t\boldsymbol{F}_v$ as internal variable. We consider the total free energy density $\Psi(\boldsymbol{X}) := \Psi^{\mathrm{ela}}(\boldsymbol{X}) + \Psi^{\mathrm{the}}(\boldsymbol{X}) + \Psi_M^{\mathrm{vis}}(\boldsymbol{X})$ with respect to the initial configuration at any point $\boldsymbol{X} \in \mathscr{B}_0$. The elastic free energy Ψ^{ela} is given by the function

$$\hat{\Psi}^{\mathrm{ela}}(\boldsymbol{C}, C_V, C_F; \boldsymbol{A}_0) = \hat{\Psi}_M^{\mathrm{iso}}(I_1^C, I_2^C, I_3^C, I_4^C; \boldsymbol{A}_0) + \hat{\Psi}_M^{\mathrm{vol}}(C_V) + \hat{\Psi}_F^{\mathrm{ela}}(C_F) \tag{2}$$

where the semicolon in the argument separates the parameter tensor $\boldsymbol{A}_0$ acting at any $\boldsymbol{X} \in \mathscr{B}_0$ from the variables $\boldsymbol{C}$, C_V and C_F. Here, we denote by

$$I_1^C := \boldsymbol{C} : \boldsymbol{I} \qquad I_2^C := \frac{1}{2}\left[(I_1^C)^2 - \boldsymbol{C}^2 : \boldsymbol{I}\right] \qquad I_3^C := \det \boldsymbol{C} \qquad I_4^C := \boldsymbol{C} : \boldsymbol{A}_0 = \boldsymbol{C}_F : \boldsymbol{I} \tag{3}$$

the isotropic tensor invariants of the tensor pair $(\boldsymbol{C}, \boldsymbol{A}_0)$, where the tensor $\boldsymbol{I}$ designates the second-order identity tensor. The invariant $I_4^C = \boldsymbol{C} : \boldsymbol{A}_0 \equiv \boldsymbol{a}_0 \cdot \boldsymbol{C}\,\boldsymbol{a}_0 = \boldsymbol{a} \cdot \boldsymbol{a} = \|\boldsymbol{a}\|^2$ designates the squared fiber stretch λ_F^2, and the tensor invariant $C_V := [\det \boldsymbol{C}]^{\frac{1}{n_{\mathrm{dim}}}}$ the volumetric invariant of the right Cauchy-Green tensor. The thermal free energy $\Psi^{\mathrm{the}} = \hat{\Psi}^{\mathrm{the}}(\Theta, C_V, C_F)$ is defined by the function

$$\hat{\Psi}^{\mathrm{the}} := \hat{\Psi}_M^{\mathrm{cap}}(\Theta) - 2\sqrt{\tilde{C}_V^{2-n_{\mathrm{dim}}}}\,\beta_M\,[\Theta - \Theta_\infty]\,\mathrm{D}\hat{\Psi}_M^{\mathrm{vol}}(\tilde{C}_V) + \hat{\Psi}_F^{\mathrm{cap}}(\Theta) - 2\sqrt{\tilde{C}_F^{2-1}}\,\beta_F\,[\Theta - \Theta_\infty]\,\mathrm{D}\hat{\Psi}_F^{\mathrm{ela}}(\tilde{C}_F) \tag{4}$$

where the heat capacity function $\hat{\Psi}^{\mathrm{cap}}$ is separated in two parts $\hat{\Psi}_M^{\mathrm{cap}}$ and $\hat{\Psi}_F^{\mathrm{cap}}$ according to the volume fraction of matrix material and fiber material, respectively. The notation $\mathrm{D}(\bullet)$ here denotes the Fréchet derivative of a volume density with respect to its argument. The material parameter β_M and β_F are the coefficients of linear thermal expansion of the matrix material and fiber material, respectively. The field $\Theta(\boldsymbol{X})$ denotes the absolute temperature $\Theta = \theta \circ \boldsymbol{\varphi}$ of the current temperature $\theta(\boldsymbol{x})$ at a point $\boldsymbol{x} \in \mathscr{B}_t$. The viscoelastic free energy Ψ_M^{vis} of the matrix material is defined by the function $\hat{\Psi}_M^{\mathrm{vis}}(I_1^\Lambda, I_2^\Lambda, I_3^\Lambda)$ with

$$I_1^\Lambda := \boldsymbol{\Lambda} : \boldsymbol{I} \qquad I_2^\Lambda := \frac{1}{2}\left[(I_1^\Lambda)^2 - \boldsymbol{\Lambda}^2 : \boldsymbol{I}\right] \qquad I_3^\Lambda := \det \boldsymbol{\Lambda} \tag{5}$$

as invariants pertaining to the product tensor $\boldsymbol{\Lambda} := \boldsymbol{C}\boldsymbol{C}_v^{-1}$, which depends explicitly on the viscous internal variable $\boldsymbol{C}_v$. These invariants coincide with the invariants of the deformation tensor $\boldsymbol{C}_e = \boldsymbol{F}_e^t\boldsymbol{F}_e$.

In view of the introduction of a second-gradient free energy in the next steps of the project, we now introduce an independent deformation gradient $\tilde{\boldsymbol{F}}$ and right Cauchy-Green tensor $\tilde{\boldsymbol{C}}$, which is, in the discrete setting, different from $\boldsymbol{F}$ and $\boldsymbol{C}$, but related by the mixed formulation in Section 1. The deformation of the fibers is then described by the projection of the independent deformation gradient $\tilde{\boldsymbol{F}}$ on the structural tensor $\boldsymbol{A}_0$. The continuum rotation vector $\boldsymbol{\alpha}$, also introduced in Section 1, is likewise defined upon the mixed field $\tilde{\boldsymbol{F}}$. Furthermore, we introduce independent fields $\tilde{C}_F$ and $\tilde{C}_V$ for fiber and volume dilatation, because the free energy function $\hat{\Psi}_F^{\mathrm{ela}}(\tilde{C}_F)$ depends explicity on the squared fiber stretch $\tilde{C}_F$, and the free energy functions $\hat{\Psi}_M^{\mathrm{vol}}(\tilde{C}_V)$ and $\hat{\Psi}^{\mathrm{the}}(\Theta, \tilde{C}_V, \tilde{C}_F)$ also depend explicitly on the volumetric constant $\tilde{C}_V$.

1 Variational formulation

The variational formulation of the considered generalized Cauchy continuum is based on the principle of virtual power, in which the total energy balance law is considered in the functional form

$$\dot{\mathcal{H}}(\dot{\boldsymbol{\varphi}},\dot{\boldsymbol{v}},\dot{\boldsymbol{p}},\dot{\boldsymbol{\alpha}},\dot{\boldsymbol{\omega}},\dot{\boldsymbol{\pi}},\dot{\boldsymbol{C}}_v,\dot{\Theta},\dot{\eta},\dot{\tilde{\boldsymbol{F}}},\dot{\tilde{\boldsymbol{C}}},\dot{\tilde{C}}_V,\dot{\tilde{C}}_F,\tilde{\Theta},\boldsymbol{P},\boldsymbol{\tau}^t_{\mathrm{skw}},\boldsymbol{S},S_V,S_F,\boldsymbol{R},h,\lambda,\boldsymbol{Z},\hat{\boldsymbol{\omega}})=0 \tag{6}$$

where $\dot{\mathcal{H}}=\dot{\mathcal{T}}^{\mathrm{tra}}+\dot{\mathcal{T}}^{\mathrm{rot}}+\dot{\Pi}^{\mathrm{ext}}+\dot{\Pi}^{\mathrm{int}}$ denotes the time rate of the considered total energy $\mathcal{H}$, consisting of the translational and rotational kinetic energies, respectively, as well as the external and internal potential energy of the continuum body. The well-known translational kinetic power of a continuum is given by

$$\dot{\mathcal{T}}^{\mathrm{tra}}(\dot{\boldsymbol{\varphi}},\dot{\boldsymbol{v}},\dot{\boldsymbol{p}}):=\int_{\mathscr{B}_0}[\rho_0\boldsymbol{I}\,\boldsymbol{v}-\boldsymbol{p}]\cdot\dot{\boldsymbol{v}}\,\mathrm{d}V-\int_{\mathscr{B}_0}\dot{\boldsymbol{p}}\cdot[\boldsymbol{v}-\dot{\boldsymbol{\varphi}}]\mathrm{d}V+\int_{\mathscr{B}_0}\boldsymbol{p}\cdot\ddot{\boldsymbol{\varphi}}\,\mathrm{d}V \tag{7}$$

with respect to the homogenized Lagrangian mass density ρ_0 of the body in $\mathscr{B}_0$. The Lagrangian velocity field of the body is indicated by $\boldsymbol{v}$, and the conjugated Lagrangian momentum field is denoted by $\boldsymbol{p}$. In order to take into account the micro inertia of the considered heterogeneous material, we introduce

$$\dot{\mathcal{T}}^{\mathrm{rot}}(\dot{\boldsymbol{\alpha}},\dot{\boldsymbol{\omega}},\dot{\boldsymbol{\pi}}):=\int_{\mathscr{B}_0}\left[\rho_0\left[(l_F^2-l_0^2)\,\boldsymbol{A}_0+l_0^2\boldsymbol{I}\right]\boldsymbol{\omega}-\boldsymbol{\pi}\right]\cdot\dot{\boldsymbol{\omega}}\,\mathrm{d}V-\int_{\mathscr{B}_0}\dot{\boldsymbol{\pi}}\cdot[\boldsymbol{\omega}-\dot{\boldsymbol{\alpha}}]\mathrm{d}V+\int_{\mathscr{B}_0}\boldsymbol{\pi}\cdot\ddot{\boldsymbol{\alpha}}\,\mathrm{d}V \tag{8}$$

as rotational kinetic power of the continuum. Here, we denode by l_F and l_0 length scale parameters corresponding to the fiber bundels and the considered representative volume element, respectively. The Lagrangian vector field $\boldsymbol{\omega}$ denotes the Lagrangian angular velocity field, and $\boldsymbol{\pi}$ is the conjugated Lagrangian rotational momentum field. The Lagrangian vector field $\boldsymbol{\alpha}$ describes the continuum rotation, which is defined in the internal potential power functional

$$\begin{aligned}\dot{\Pi}^{\mathrm{int}}:=\;&\frac{1}{2}\int_{\mathscr{B}_0}\left\{\left[2\,\frac{\partial\hat{\Psi}_M}{\partial\tilde{\boldsymbol{C}}}+S_V\,\boldsymbol{A}^{\mathrm{vol}}+S_F\,\boldsymbol{A}_0-\boldsymbol{S}\right]:\dot{\tilde{\boldsymbol{C}}}+\left[2\,\frac{\partial\hat{\Psi}_M}{\partial\tilde{C}_V}-S_V\right]:\dot{\tilde{C}}_V\right\}\mathrm{d}V-\int_{\mathscr{B}_0}\dot{\eta}\Big[\tilde{\Theta}-\Theta\Big]\mathrm{d}V\\&+\frac{1}{2}\int_{\mathscr{B}_0}\left[2\,\frac{\partial\hat{\Psi}_F}{\partial\tilde{C}_F}-S_F\right]:\dot{\tilde{C}}_F\,\mathrm{d}V+\int_{\mathscr{B}_0}\left\{\Big[\tilde{\boldsymbol{F}}\boldsymbol{S}-\boldsymbol{P}\Big]:\dot{\tilde{\boldsymbol{F}}}+\frac{\partial\hat{\Psi}_M}{\partial\boldsymbol{C}_v}:\dot{\boldsymbol{C}}_v\right\}\mathrm{d}V+\int_{\mathscr{B}_0}\left[\eta+\frac{\partial\Psi}{\partial\Theta}\right]\dot{\Theta}\,\mathrm{d}V\\&+\int_{\mathscr{B}_0}\boldsymbol{P}:\mathrm{Grad}[\dot{\boldsymbol{\varphi}}]\,\mathrm{d}V+\int_{\mathscr{B}_0}\boldsymbol{\tau}^t_{\mathrm{skw}}:\boldsymbol{\epsilon}\cdot\left[\frac{1}{2}\,\boldsymbol{\epsilon}:\dot{\tilde{\boldsymbol{F}}}\tilde{\boldsymbol{F}}^{-1}+\dot{\boldsymbol{\alpha}}\right]\mathrm{d}V\end{aligned} \tag{9}$$

by using the third-order permutation tensor $\boldsymbol{\epsilon}$. The free energy function $\hat{\Psi}_M(\tilde{\boldsymbol{C}},\boldsymbol{C}_v,\tilde{C}_V,\Theta)$ belongs to the matrix material, and $\hat{\Psi}_F$ represents the fiber free energy. We also introduce independent (mixed) stress fields $\boldsymbol{S}$, S_V and S_F, energy-conjugated to the right Cauchy-Green tensor $\tilde{\boldsymbol{C}}$, the volumetric invariant $\tilde{C}_V$ and the squared fiber stretch $\tilde{C}_F$, respectively. Beside the absolute temperature field Θ, the thermal behaviour of the continuum is described by further mixed fields. We consider the entropy density field η as well as the assumed temperature field $\tilde{\Theta}$, which, in fact, approximate the time derivative of the thermal displacement field. Further, we denote by $\boldsymbol{P}$ the first Piola-Kirchhoff stress tensor, and the Lagrange multiplier $\boldsymbol{\tau}^t_{\mathrm{skw}}$ designates the skew-symmetric part of the Kirchhoff stress. Since we simulate continuum bodies subject to volume and boundary loads as well as apply a variational-based energy-momentum scheme, we have to consider the external power functional

$$\begin{aligned}\dot{\Pi}^{\mathrm{ext}}:=&-\int_{\mathscr{B}_0}\rho_0\boldsymbol{B}\cdot\dot{\boldsymbol{\varphi}}\,\mathrm{d}V&&-\int_{\partial_T\mathscr{B}_0}\bar{\boldsymbol{T}}\cdot\dot{\boldsymbol{\varphi}}\,\mathrm{d}A&&+\int_{\partial_Q\mathscr{B}_0}\frac{\tilde{\Theta}}{\Theta}\,\bar{Q}\,\mathrm{d}A\\&+\int_{\mathscr{B}_0}\frac{1}{\Theta}\,\mathrm{Grad}[\tilde{\Theta}]\cdot\boldsymbol{Q}\,\mathrm{d}V&&+\int_{\mathscr{B}_0}\frac{\tilde{\Theta}}{\Theta}\left(D^{\mathrm{cdu}}+D^{\mathrm{int}}\right)\mathrm{d}V&&+\int_{\mathscr{B}_0}\dot{\boldsymbol{C}}_v:\boldsymbol{\Sigma}_v\,\mathrm{d}V\\&+\int_{\partial_\Theta\mathscr{B}_0}\lambda\left[\tilde{\Theta}-\Theta_\infty\right]\mathrm{d}A&&-\int_{\partial_{\dot{\Theta}}\mathscr{B}_0}h\left[\dot{\Theta}-\dot{\tilde{\Theta}}\right]\mathrm{d}A&&-\int_{\partial_\varphi\mathscr{B}_0}\boldsymbol{R}\cdot[\dot{\boldsymbol{\varphi}}-\dot{\tilde{\boldsymbol{\varphi}}}]\,\mathrm{d}A\\&-\int_{\partial_\alpha\mathscr{B}_0}\boldsymbol{Z}\cdot[\dot{\boldsymbol{\alpha}}\;-\dot{\tilde{\boldsymbol{\alpha}}}]\,\mathrm{d}A&&-\int_{\partial_\alpha\mathscr{B}_0}\hat{\boldsymbol{\omega}}\cdot\left[\boldsymbol{\epsilon}:\boldsymbol{\tau}^t_{\mathrm{skw}}\right]\mathrm{d}A&&-\int_{\partial_W\mathscr{B}_0}\bar{\boldsymbol{W}}\cdot\dot{\boldsymbol{\alpha}}\,\mathrm{d}A\\&+\int_{\mathscr{B}_0}\frac{1}{2}\,\bar{\boldsymbol{S}}:\dot{\tilde{\boldsymbol{C}}}\,\mathrm{d}V&&+\int_{\mathscr{B}_0}\frac{1}{2}\,\bar{S}_V\,\dot{\tilde{C}}_V\,\mathrm{d}V&&+\int_{\mathscr{B}_0}\frac{1}{2}\,\bar{S}_F\,\dot{\tilde{C}}_F\,\mathrm{d}V\end{aligned} \tag{10}$$

with Dirichlet and Neumann boundaries. The stationarity condition of the virtual power principle reads

$$\delta_*\dot{\mathcal{H}}(\dot{\boldsymbol{\varphi}},\dot{\boldsymbol{v}},\dot{\boldsymbol{p}},\dot{\boldsymbol{\alpha}},\dot{\boldsymbol{\omega}},\dot{\boldsymbol{\pi}},\dot{\boldsymbol{C}}_v,\dot{\Theta},\dot{\eta},\dot{\tilde{\boldsymbol{F}}},\dot{\tilde{\boldsymbol{C}}},\dot{\tilde{C}}_V,\dot{\tilde{C}}_F,\tilde{\Theta},\boldsymbol{P},\boldsymbol{\tau}^t_{\mathrm{skw}},\boldsymbol{S},S_V,S_F,\boldsymbol{R},h,\lambda,\boldsymbol{Z},\hat{\boldsymbol{\omega}})=0 \tag{11}$$

where δ_* indicates the variation with respect to each tensor in the argument, and leads to all weak forms.

2 Numerical example

We simulate a driven rotation of a composite turbine rotor under thermal loads (see Fig. 2). The fibers in the blades lie in normal direction, and in the shaft in tangential direction. The rotation of the turbine is introduced by means of a boundary torque $\bar{\boldsymbol{W}}(t)$ on the frontside and the backside of the shaft. On the red patches, we load the plates with a periodic boundary heat flux $\bar{Q}(t)$ for cooling, and with a pressure follower load $\bar{\boldsymbol{T}}(t)$ leading to a braking rotation. The mesh is derived from Reference [1]. In Fig. 2, we show the time evolutions of a node on the drive torque boundary. The time evolution $\boldsymbol{\omega}(t)$ of the angular velocity vector reveals oscillations due to the braking pressure. The heat flux leads to an oscillating time evolution $\eta(t)$ of the entropy. The z-component of the velocity $\boldsymbol{v}(t)$ reveals also a translational motion.

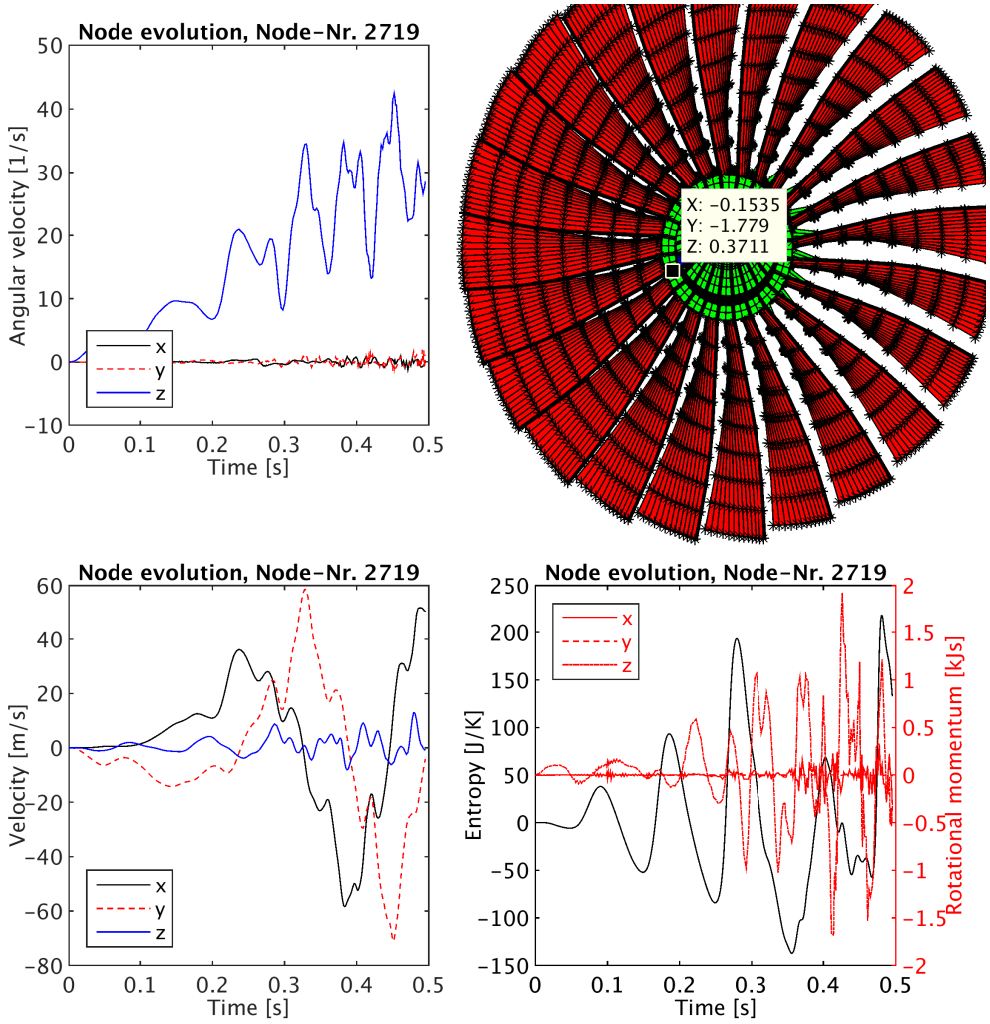

Figure 2. Time evolutions of a node on the boundary $\partial_W \mathscr{B}_0$ on the frontside of the shaft.

Acknowledgments

This research is provided by the 'Deutsche Forschungsgemeinschaft' (DFG) under the grants GR 3297/4-1 and 3297/6-1. This support is gratefully acknowledged.

References

[1] Ludovic Noels, Laurent Stainier, and Jean-Philippe Ponthot. A Consistent Dissipative Time Integration Scheme for Structural Dynamics: Application to Rotordynamics. In: *45th AIAA/ASME/ASCE/AHS/ASC Structures, Structural Dynamics & Materials Conference*. 2004, p. 1945.

**Proceedings of the 8th GACM Colloquium on Computational Mechanics
for Young Scientists from Academia and Industry
August 28–30, 2019 in Kassel, Germany**

Elastic wave propagation in periodical one-dimensional problems: Accurate finite element modelling

Radek Kolman * [1], Sang Soon Cho[2], K.C. Park[3], Arkadi Berezovski[4], José González[5], Vítězslav Adámek[6] and Pert Hora[7]

[1]Institute of Thermomechanics, Academy of Sciences of the Czech Republic, v.v.i. Dolejskova 5, Prague 8, Czech Republic

[2]Reactor Mechanical Engineering Devision, Korea Atomic Energy Research Institute, 999-111 Daedeok-Daero, Yuseong-gu, Daejeon 305-353, Korea

[3]Department of Aerospace Engineering Sciences, University of Colorado, Boulder, CO 80309-429, USA

[4]Institute of Cybernetics at Tallinn University of Technology, Akadeemia tee 21, 12618 Tallinn, Estonia

[5]Escuela Técnica Superior de Ingeniería, Universidad de Sevilla, Camino de los Descubrimientos s/n, Sevilla 41092, Spain

[6]NTIS - New Technologies for the Information Society, Faculty of Applied Sciences, University of West Bohemia, Technická 8, 301 00 Pilsen, Czech Republic

[7]Institute of Thermomechanics, v.v.i., The Czech Academy of Sciences, Veleslavínova 71/11, 301 14 Pilsen, Czech Republic

Abstract. In this contribution, we present results of novel explicit finite element approach for accurate modelling of elastic wave propagation in periodical one-dimensional layered bars. Standard approaches in explicit time integration of the finite element discretized system produce dominant spurious oscillations of stress distributions. By meaning of the local stepping process, the stress spurious oscillations are eliminated and the time scheme is suitable for accurate modelling of elastic wave propagation in heterogeneous media using the finite element method. The presented time scheme is tested in elastic wave propagation in a layered bar with two different materials.

Introduction

Elastic wave propagation in heterogeneous solids is an up-to-date open problem to study due to new growing and modern technologies for 3D printing of heterogeneous materials. Today it is possible to use 3D/4D printing technologies for manufacturing of bodies made from several materials as layered, composite or graded structures. The numerical modelling is necessary because macroscopic properties of composite materials are strongly influenced by the properties of their constituents and micro-structures. Layered periodical materials or metamaterials with auxetic behaviour represent the simplest possible pattern of composites from the theoretical point of view [3]. Their modelling as periodic structures also has a rich history, see the book of [2]. Several geometrical problems of elastic wave propagation in layered media have been studied in book of [7]. Constitutive models of effective properties for such materials are still under development using either ensemble averaging or homogenization. For short waves, it is worth to use numerical simulations for the analysis of interaction between layers and waves taking into account reflected and transmitted waves [1].

We present results of novel explicit finite element approach for accurate modelling of elastic wave propagation in periodical one-dimensional layered bars [6]. It is known that the standard approach in explicit time integration of the finite element discretized system produces spurious oscillations of stress distributions and the final stress states are numerically polluted. From that reason, we have derived and applied the modification of explicit time integration with the local stepping process based on correct local wave speed and pullback interpolation [5, 8]. With this approach, the numerical dispersion of the finite element distretization and sensitivity on time step size are suppressed.

*Corresponding author: kolman@it.cas.cz ORCID iD: 0000-0002-8167-3535

1 Time integration

We compare two explicit time schemes for finite element modelling of wave response with the finite element method: the central difference method in time [4] and local time stepping scheme [6]. The used local time stepping explicit scheme is consisted of two following computational steps based on the predictor-corrector form:

Step 1: Pull-back integration with local stepping
a) Integration by the central difference scheme with the local (elemental) critical time step size for each finite element.
b) Pull-back interpolation of local nodal displacement vector at the time t^{n+1}.
c) Assembling of local contributions of displacement vector from Step 1b.
Step 2: Push-forward integration with averaging
a) Push-forward integration by the central difference scheme with the time step size.
b) Averaging of the total displacement vectors at the time t^{n+1} form Steps 1c and 2a.
c) Evaluation of acceleration and velocity nodal vectors at the time t^{n+1}.

2 Wave propagation in a layered bar

As a comparative test, we study an problem of elastic wave propagation in a layered bar of the length $L = 2\ m$ with ten uniform layers, for detail see Fig. 1. Mechanical parameters of materials are chosen as follows: density of materials $\rho_1 = \rho_2 = 1\ kg/m^3$, Young's moduli $E_1 = 16\ Pa$ and $E_2 = 1\ Pa$. Thus wave speeds are given as $c_1 = 4\ m/s$ and $c_2 = 1\ m/s$ and acoustic impedance $Z_1 = 4\ kgm^{-2}s^{-1}$ and $Z_2 = 1\ kgm^{-2}s^{-1}$. The bar is loaded by the rectangular pulse with stress amplitude $\sigma_0 = -1\ Pa$ and with time duration $T_0 = 0.25\ s$. The final time of computations is $T_{end} = 1.2\ s$. The bar is fixed on the right hand side and the bar is at the rest at the beginning of computations.

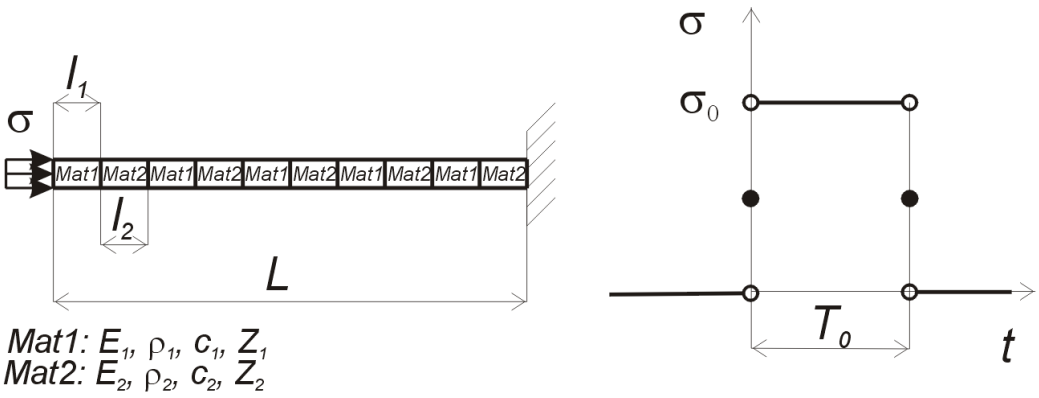

Figure 1. Formulation of wave propagation problem on a layered bar.

The stress distributions at the time 1.2 s for the both time schemes are presented in Fig 2. One can see the better stress distribution for the local time stepping than for the classical central difference method, which produces dominant spurious oscillations.

3 Conclusions

Based on the presented numerical test on wave propagation in periodical one-dimensional structure–bar, we shown accuracy of the presented approach in the finite element modelling. The results do not exhibit stress spurious oscillations against the classical explicit time integration. The local time stepping explicit scheme is a suitable and robust tool for accurate modelling of elastic wave propagation in one-dimensional

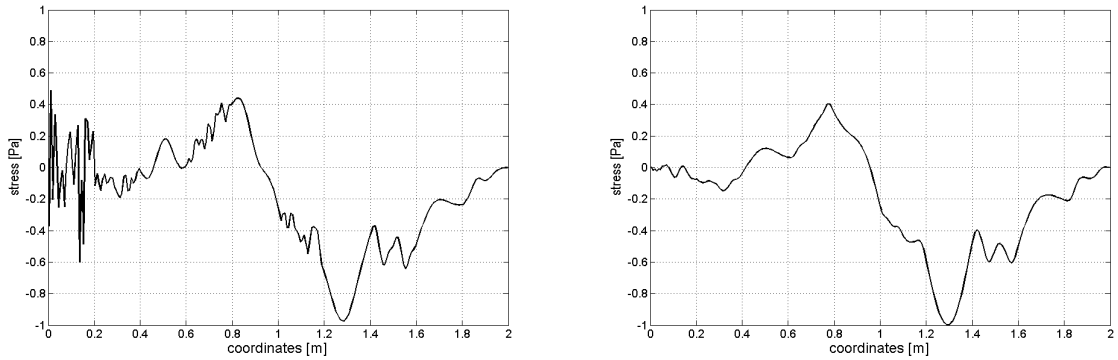

Figure 2. Spatial stress distributions in a layered bar from Fig. 1 obtained by the central difference method (on the left) and the novel local time stepping scheme (on the right).

heterogeneous cases. In future, we will pay an attention on multi-dimensional problems of elastic wave propagation tasks in heterogeneous media and solids.

Acknowledgments

The work was supported by the Grant project with No. 19-04956S of the Czech Science Foundation (CSF) within institutional support RVO: 61388998 and the Centre of Excellence for Nonlinear Dynamic Behaviour of Advanced Materials in Engineering CZ.02.1.01/0.0/0.0/15_003/0000493 (Excellent Research Teams) in the framework of Operational Programme Research, Development and Education.

References

[1] A. Berezovski, J. Engelbrecht, and G.A. Maugin. *Numerical Simulation of Waves and Fronts in Inhomogeneous Solids*. World Scientific, 2008.

[2] L. Brillouin. *Wave Propagation in Periodic Structures: Electric Filters and Crystal Lattices*. McGraw-Hill Book Company, 1946.

[3] K.F. Graff. *Wave Motion in Elastic Solids*. Clarendon Press, 1975.

[4] T.J.R Hughes. *The Finite Element Method: Linear Static and Dynamic Finite Element Analysis*. Dover Civil and Mechanical Engineering, Dover Publications., 2008.

[5] R. Kolman, S.S. Cho, and K.C. Park. Efficient implementation of an explicit partitioned shear and longitudinal wave propagation algorithm. *International Journal for Numerical Methods in Engineering* 107 (2016), pp. 543–579.

[6] R. Kolman, S.S Cho, J.G. Gonzalez, K.C Park, and A. Berezovski. *An explicit time scheme with local time stepping for one-dimensional wave propagation in a bimaterial bar*. In conference Engineering Mechanics 2017, University of technology, Institute of Solid Mechanics, Mechatronics and Biomechanics, 2017, pp. 474–477.

[7] A.H. Nayfeh. *Wave Propagation in Layered Anisotropic media*. North-Holland, 1995.

[8] K.C. Park, S.J.A Lim, and H. Huh. A method for computation of discontinuous wave propagation in heterogeneous solids: basic algorithm description and application to one-dimensional problems. *International Journal for Numerical Methods in Engineering* 91 (2012), pp. 622–643.

**Proceedings of the 8th GACM Colloquium on Computational Mechanics
for Young Scientists from Academia and Industry
August 28–30, 2019 in Kassel, Germany**

C0 continuous finite elements for gradient elasticity at finite strains

Johannes Riesselmann[1], Jonas Ketteler[2], Mira Schedensack[2] and Daniel Balzani * [1]

[1]Chair of Continuum Mechanics, Ruhr-Universität Bochum, Universitätsstraße 150, 44801 Bochum, Germany

[2]Institute for Analysis and Numerics, Westfälische Wilhelms-Universität Münster, Einsteinstraße 62, 48149 Münster, Germany

Abstract. Purely displacement based gradient elasticity formulations require C^1-continuous finite elements, for which retaining compatibility with standard software and meshing arbitrary structures are known difficulties. Another approach is to use mixed formulations instead. They have the advantage of a relaxation of continuity requirement to C^0 and making standard finite element discretizations possible. For small strains already existing mixed three-field approaches contain both displacement and displacement gradients as solution variables. In this contribution a new formulation is proposed, in which the displacements are not part of the problem anymore, but only displacement gradients, leading to a reduced number of variables to be discretized. In numerical examples the proposed formulations are compared to finite strain adaptations of existing mixed three-field approaches and unveil favorable computing time. A further reduction of variables through a penalty formulation is investigated and the ability to model size effects is shown.

1 Gradient elasticity fundamentals

Gradient elasticity formulations can be used to model specialized materials, whose elastic behavior depends on size relations between the microstructure and specimen size. Through enrichment of the internal elastic energy $W := W(\boldsymbol{F}, \nabla \boldsymbol{F})$ by the second order gradient of deformation $\nabla \boldsymbol{F}$ and additional micro-size related constitutive parameters, these so called size effects can be captured. Moreover, singularities at e.g. sharp corners of the modeled specimen, which would appear in classical elasticity formulations are avoided and corresponding numerical simulations have the advantage of remaining mesh objective. The theoretical foundation for the small strain gradient-enriched continuum theory dates back to the works of [5] and [10] and the more recent adaptation of [1]. A historical overview is given in [2] and an investigation of finite strain models can be found in [8] and [11].

The purely displacement based model problem seeks the minimizer of the potential $\Pi = \Pi^{\text{int}} + \Pi^{\text{ext}}$, where Π^{ext} is the potential of surface tractions and volume loads and

$$\Pi^{\text{int}} = \int_{\mathcal{B}} W(\boldsymbol{F}(\nabla \boldsymbol{u}), \nabla \boldsymbol{F}(\nabla \boldsymbol{u})) \, \mathrm{d}V \tag{1.1}$$

is the internal elastic potential. The solution is then sought in the Sobolev space $\boldsymbol{u} \in H^2(\mathcal{B})$ of functions, whose gradients up to second order are $L^2(\mathcal{B})$ integrable. This leads to the requirement of C^1-continuous interpolation functions, for which standard finite elements are not suitable. Isogeometric analysis e.g. as considered by [8] can satisfy the continuity requirement but has the kown difficulties when modeling complex structures and boundary conditions. Another approach is to use three-field mixed formulations instead (c.f. [9] and [12] for the small strain framework and [7] for corresponding large strain formulations). The idea is to replace $\nabla \boldsymbol{u}$ in the gradient-enriched part of W by the new independent variable $\boldsymbol{H} \in H^1(\mathcal{B})$ and enforce compatibility via the Lagrange multiplier $\boldsymbol{\lambda} \in L^2(\mathcal{B})$ such that the internal potential reads

$$\Pi^{\text{int}} = \int_{\mathcal{B}} W(\boldsymbol{F}(\nabla \boldsymbol{u}), \nabla \boldsymbol{F}(\boldsymbol{H})) + \boldsymbol{\lambda} : (\boldsymbol{H} - \nabla \boldsymbol{u}) \, \mathrm{d}V. \tag{1.2}$$

Consequently, the continuity requirement is relaxed to C^0, at the cost of having to approximate the three variables $\boldsymbol{u}, \boldsymbol{H}$ and $\boldsymbol{\lambda}$ in one BVP. Moreover, in the linear case, inf-sup stability of formulation (1.2) with

* **Corresponding author:** daniel.balzani@rub.de

respect to the standard norms is not fulfilled [7] and thus, robustness of the solution procedure in the nonlinear case is not guaranteed. In the following, an alternative C^0 continuous approach with a reduced number of solution variables is presented, which for the related biharmonic problem has already proven to be stable (c.f. [4]).

2 Curl-free mixed two-field approach

In order to reduce the number of degrees of freedom, the displacement $\boldsymbol{u}$ can be decoupled from the problem in the spirit of [4, 6]. The reformulation of (1.1) now reads

$$\Pi^{\text{int}} = \int_{\mathcal{B}} W(\boldsymbol{F}(\boldsymbol{H}), \nabla \boldsymbol{F}(\boldsymbol{H})) + \boldsymbol{\lambda} : \operatorname{rot} \boldsymbol{H} \, \mathrm{d}V, \quad \Pi^{\text{ext}} = -\int_{\mathcal{B}} \nabla \boldsymbol{g} : \boldsymbol{H} \, \mathrm{d}V \tag{2.1}$$

making $\boldsymbol{H}$ and $\boldsymbol{\lambda}$ the only solution variables, while retaining the C^0-continuity requirement. $\boldsymbol{H}$ is sought in the standard solution space $\boldsymbol{H} \in H^1(\mathcal{B})$. The nature of vanishing rotations of gradient fields for simply connected domains with boundary conditions on connected subsets of $\partial\mathcal{B}$ is employed as constraint to make sure $\boldsymbol{H}$ is indeed a gradient field. Once $\boldsymbol{H}$ is known, the displacements can be independently determined in the postprocessing step

$$\Pi^{\text{post}} = \int_{\mathcal{B}} \tfrac{1}{2} \nabla \boldsymbol{u} : \nabla \boldsymbol{u} - \nabla \boldsymbol{u} : \boldsymbol{H} \, \mathrm{d}V \Rightarrow \min_{\boldsymbol{u}}. \tag{2.2}$$

Dirichlet boundaries are taken into consideration by the relation $\boldsymbol{u} = \bar{\boldsymbol{u}} \Leftrightarrow \boldsymbol{H} \times \boldsymbol{n} = \nabla \bar{\boldsymbol{u}} \times \boldsymbol{n}$ on Γ_D, where $\boldsymbol{n}$ is the outward unit normal vector. To determine Π^{ext} of (2.1) in terms of $\boldsymbol{H}$ the preprocessing step

$$\Pi^{\text{pre}} = \int_{\mathcal{B}} \tfrac{1}{2} \nabla \boldsymbol{g} : \nabla \boldsymbol{g} - \boldsymbol{g} \cdot \boldsymbol{f} \, \mathrm{d}V - \int_{\Gamma_N} \boldsymbol{g} \cdot \boldsymbol{t} \, \mathrm{d}A \Rightarrow \min_{\boldsymbol{g}} \tag{2.3}$$

is solved analogously. In the 2D case (2.1) is equivalent to a Stokes-type problem [4] and the Lagrange multiplier is sought in the standard solution space $\boldsymbol{\lambda} \in L^2(\mathcal{B})$. Suitable corresponding finite element approximations for this are well known (see e.g. [3]) and in the following for $\boldsymbol{H}^h$ and $\boldsymbol{\lambda}^h$ the Taylor Hood type finite element discretizations P2$_{\boldsymbol{H}}$-P1$_{\boldsymbol{\lambda}}$ and Q2$_{\boldsymbol{H}}$-Q1$_{\boldsymbol{\lambda}}$ and the MINI element $P1B_{\boldsymbol{H}} - P1_{\boldsymbol{\lambda}}$ are considered. For solution spaces for the Lagrange multiplier and suitable discretizations in the 3D case the reader is referred to [4]. For the discretization $\boldsymbol{u}^h$ in (2.2) and $\boldsymbol{g}^h$ in (2.3) H^1-conforming Lagrange finite element interpolation is used.

Penalty formulation: To further reduce the number of solution variables and consequently the number of degrees of freedom a straightforward penalty approach can be applied. The integrand of the constraint term associated with the Lagrange multiplier of (2.1) is then replaced by a penalty term $\frac{\alpha}{2h}(\operatorname{rot} \boldsymbol{H})^2$ with the scalar valued penalty parameter α and the mesh size parameter h. Consequently, $\boldsymbol{H}$ is the only discretization variable in this approach. The corresponding finite elements are named P2$_{\boldsymbol{H}}$-pen for simplical meshes and Q2$_{\boldsymbol{H}}$-pen for quadrilateral and hexahedral meshes.

3 Numerical examples

In this section the proposed finite element formulations are numerically evaluated with respect to convergence behavior and numerical efficiency. For this, the gradient-enriched strain energy $W(\boldsymbol{F}, \nabla \boldsymbol{F}) = W^{\text{loc}}(\boldsymbol{F}) + W^{\text{nloc}}(\nabla \boldsymbol{F})$ is chosen, in which W^{loc} is a compressible Neo-Hooke energy function and $W^{\text{nloc}}(\nabla \boldsymbol{F}) = \frac{\mu l^2}{2} \nabla \boldsymbol{F}^2$ is a gradient enrichment term (c.f. [2, 11]) with the additional length parameter l. In what follows the elasticity constants $E = 500$ MPa, $\nu = 0.3$ and $l = 0.1$ mm are chosen.

Unit square problem with smooth solution: The first numerical example is a unit square domain $\mathcal{B} = (0,1) \times (0,1)$ mm^2, for which the displacement solution field $\boldsymbol{u} = (u_X, u_Y)^T$ with $u_Y = \beta(XY(X-1)(Y-1))^2$ and $u_X = 0$ is chosen. For this, the essential boundary conditions $\boldsymbol{u} = \boldsymbol{0}$ and $\nabla \boldsymbol{u} = \boldsymbol{0}$ on $\Gamma_D = \partial\mathcal{B}$ hold. Note, that $\beta = -50$ mm^{-8} is a scaling factor so that the order of magnitude of the displacement field is within the nonlinear elastic range. The volume load $\boldsymbol{f}$ is computed analytically via the strong form obtained by variation of (1.1) under plain strain assumption. Error measures are then constructed from the finite element solution $\boldsymbol{u}^h$ of (2.2) and $\boldsymbol{H}^h$ of (2.1) respectively. As depicted in Figure 1 a) and b) convergence is observed for all elements both in the L^2-norm of the displacement error and in

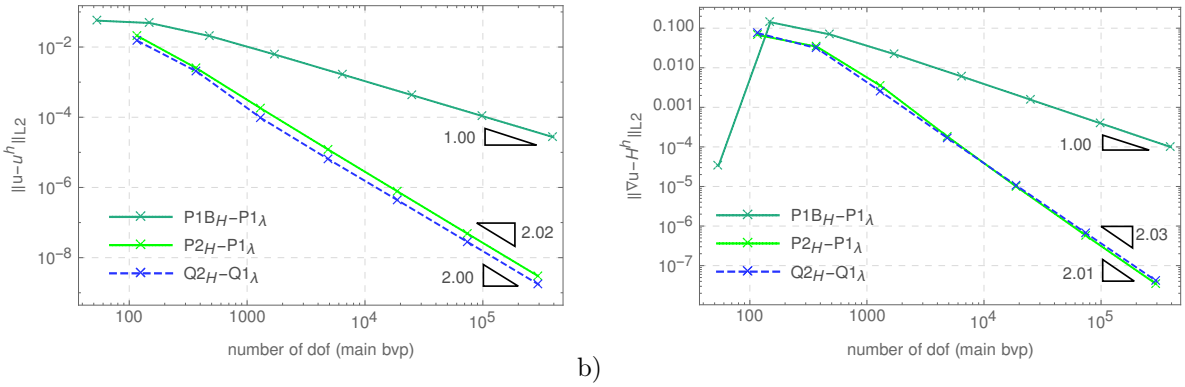

Figure 1. Unit square domain with smooth solution: a) Displacement error $\|\boldsymbol{u}^h - \boldsymbol{u}\|_{L^2(\mathcal{B})}$ and b) displacement gradient error $\|\nabla \boldsymbol{u} - \boldsymbol{H}^h\|_{L^2(\mathcal{B})}$ over numbers of degrees of freedom for uniform mesh refinement.

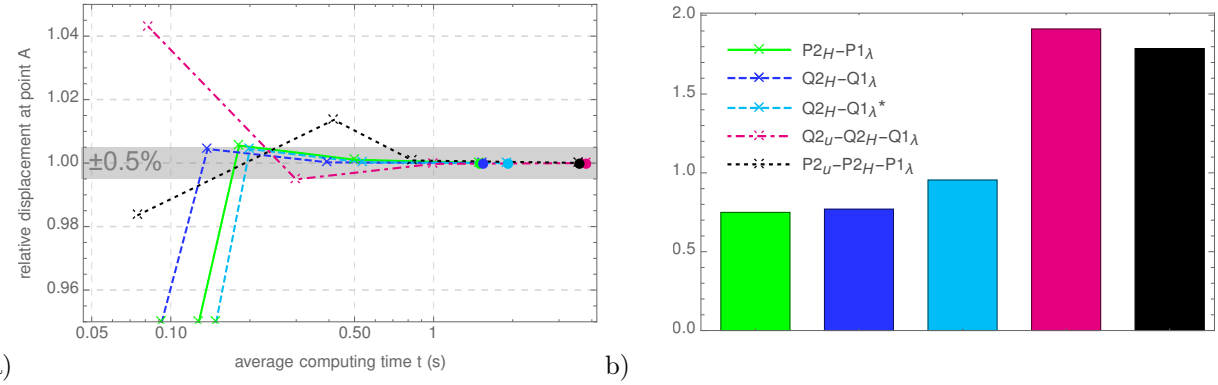

Figure 2. Comparative study on the unit square domain. Plot a) depicts the relative displacement $u_Y/u_{Y,\text{ref}}$ with $u_{Y,\text{ref}} = -0.1953$ mm at the point A$= (0.5, 0.5)$ mm. Plot b) illustrates the corresponding computing time for the converged mesh (marked with bullet points). Convergence criterion is $\Delta u_Y/u_{Y,\text{ref}} \leq 0.1\%$.

the L^2-norm of the displacement gradient error. In order to evaluate computing efficiency, the proposed P2$_{\boldsymbol{H}}$-P1$_{\boldsymbol{\lambda}}$ and Q2$_{\boldsymbol{H}}$-Q1$_{\boldsymbol{\lambda}}$ discretization is compared to the three-field formulations P2$_{\boldsymbol{u}}$-P2$_{\boldsymbol{H}}$-P1$_{\boldsymbol{\lambda}}$ and Q2$_{\boldsymbol{u}}$-Q2$_{\boldsymbol{H}}$-Q1$_{\boldsymbol{\lambda}}$ (c.f. [7]). The displacement over computing time plot for uniform mesh refinement (Figure 2) unveils a speed up factor of ≈ 2 of the proposed formulation over the three field formulations. Taking into account the additional computing time of the pre- and postprocessing step, as denoted with an asterisk for the Q2$_{\boldsymbol{H}}$-Q1$^*_{\boldsymbol{\lambda}}$ formulation unveils a relatively small increase in computing time.

Cook's problem in 3D In this numerical example, the penalty formulation is tested on the 3D Cook's problem (Figure 3 a). As the domain is clamped at $X = 0$ mm and loaded at $X = 48$ mm the Dirichlet and Neumann boundary data is given with $\boldsymbol{u}|_{\Gamma_D} = \boldsymbol{0} \Leftrightarrow (\boldsymbol{H} \times \boldsymbol{n})|_{\Gamma_D} = \boldsymbol{0}$ and $\boldsymbol{t} = (0, 0, p_0)^T$ on Γ_N. Figure 3 c) illustrates the influence of the micro-length parameter l on the stifness of the global system, since the displacement response of the gradient elasticity formulations is lower than of the classical elasticity elements P2$_{\boldsymbol{u}}$ and Q2$_{\boldsymbol{u}}$.

4 Conclusion

A C^0 continuous finite element formulation for gradient elasticity at finite strains with a reduced number of solution variables has been proposed. Numerical results in 2D show convergence and improved computing efficiency of the proposed discretization compared to the three field mixed formulations (c.f. [7]). In the 3D case the penalty approach, which further reduces the number of solution variables whilst enabling standard discretization, yields converging numerical results the ability to model size effects.

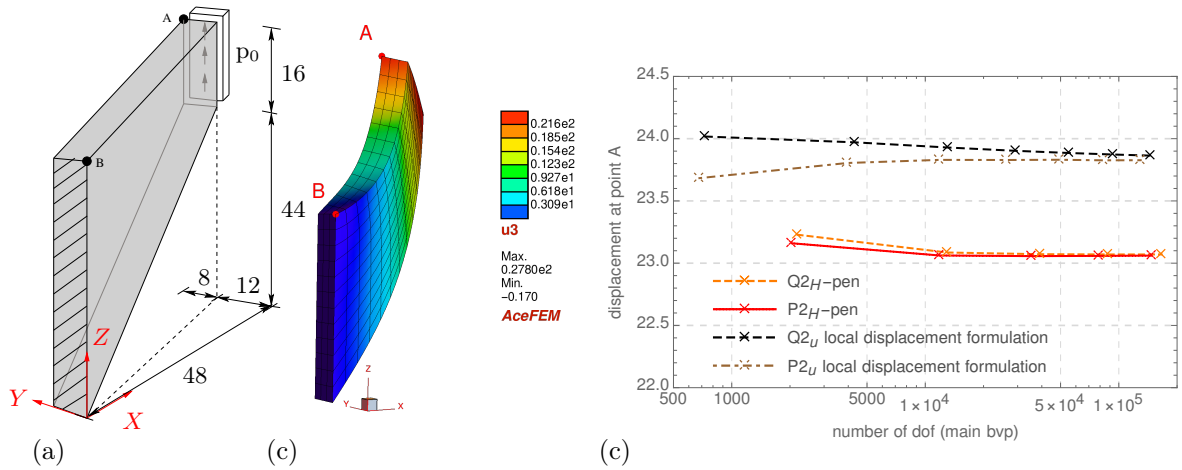

Figure 3. Displacement convergence/ size effect study on the 3D Cook's problem a) with $p_0 = 62.5$ MPa. Plot b) shows the contourplot of the u_Z displacement field. Plot c) compares the displacement at the evaluation point A=(48, 8, 60) mm over DOFs for classical displacement elements to the proposed gradient elasticity elements with length parameter $l = 3.5$ mm. The penalty parameter is $\alpha = 10^3$.

Acknowledgments

The authors greatly appreciate financial funding by the German Science Foundation (Deutsche Forschungsgemeinschaft, DFG) in the Priority Program 1748 "Reliable simulation techniques in solid mechanics. Development of non-standard discretization methods, mechanical and mathematical analysis"

References

[1] E.C. Aifantis. On the role of gradient in the localization of deformation and fracture. *Int. J. Eng. Sc.* 30.10 (1992), pp. 1279–1299.

[2] H. Askes and E.C. Aifantis. Gradient elasticity in statics and dynamics: An overview of formulation, length scale identification procedures, finite element implementations and new results. *Int. J. Solids Struct.* 48 (2011), pp. 1962–1990.

[3] D. Boffi, F. Brezzi, and M. Fortin. *Mixed Finite Element Methods and Applications*. Springer, 2013.

[4] D. Gallistl. Stable splitting of polyharmonic operators by generalized stokes systems. *Math. Comp.* 86.308 (2017), pp. 2555–2577.

[5] R. Mindlin. Micro-structure in linear elasticity. *Arch. Ration. Mech. Anal* 16 (1964), pp. 51–78.

[6] M. Ortiz and G.R. Morris. C0 finite element discretizations of Kirchhoff's equations of thin plate bending. *Int. J. Numer. Meth. Engng.* (1988).

[7] J. Riesselmann, J. Ketteler, M. Schedensack, and D. Balzani. Three-field mixed finite element formulations for gradient elasticity at finite strains. *(accepted)* (2019).

[8] S. Rudraraju, A. Van der Ven, and K. Garikipati. Three-dimensional isogeometric solutions to general boundary value problems of Toupin's gradient elasticity theory at finite strains. *Comp. Methods Appl. Mech. Engrg.* 278 (2014), pp. 705–728.

[9] J.Y. Shu, W.E. King, and N.A. Fleck. Finite Elements For Materials With Strain Gradient Effects. *Int. J. Numer. Meth. Engng.* 44 (1999), pp. 373–391.

[10] R. Toupin. Theories of elasticity with couple-stress. *Arch. Ration. Mech. Anal* 17 (1964), pp. 85–112.

[11] N. Triantafyllidis and E.C. Aifantis. A gradient approach to localization of deformation I. Hyperelastic materials. *Journal of Elasticity* 16 (1986), pp. 225–237.

[12] L. Zybell, U. Mühlich, M. Kuna, and Z.L. Zhang. A three-dimensional finite element for gradient elasticity based on a mixed-type formulation. *Computational Materials Science* 52 (2012), pp. 268–273.

**Proceedings of the 8th GACM Colloquium on Computational Mechanics
for Young Scientists from Academia and Industry
August 28–30, 2019 in Kassel, Germany**

Determining the Constitutive Parameters of a Macro-scale Second-Gradient Model for Planar Pantographic Structures by Using Optimization Algorithms

Navid Shekarchizadeh * [1] and Masoud Abedi[2]

[1]Department of Basic and Applied Sciences for Engineering, Sapienza University of Rome, Rome, Italy; International Research Center for the Mathematics and Mechanics of Complex Systems-M&MOCS, University of L'Aquila, L'Aquila, Italy

[2]Institute of Computer Science, University of Rostock, Rostock, Germany; Johann Heinrich von Thünen-Institut, Rostock, Germany

Abstract. Pantographic structures have been proposed as a group of metamaterials that show high toughness in extension. Modeling such structures is technically possible through microscopic first-order continuum theories by using a suitably small length-scale, although the computational cost would be high. The aim of this research is to estimate the constitutive parameters of a planar pantographic structure by means of an optimization process. A previously-proposed macroscopic second-gradient model which is characterized by deformation energy is used for modeling the mechanical behavior of the structure. The macroscopic model will be developed based on the results of the numerical simulations of a microscopic model. In this problem, an evolutionary multi-objective optimization algorithm is utilized which minimizes the squared error of the outputs in order to determine the parameters of the panthographic structure.

Introduction

Metamaterials are referred to a group of materials that are designed carefully to have tailored properties. Pantographic structures are an example of metamaterials that are proposed as a group of structures to have high toughness and high strength-to-weight ratio which makes them attractive for industrial and aerospace applications [4]. Figure 1 shows an example of a pantographic structure. The structure is made up of straight beams which are connected together, at their intersection points, by cylinder pivots. These pivots play a significant role in absorbing large amounts of energy by restricting the relative motion of fibers. It is possible to model pantographic structures using classical continuum mechanics, which is based on Cauchy theories, and describe the mechanical behavior in detail. However, it will not be efficient in terms of computational cost. An appropriate solution is to employ "Generalized Continuum Mechanics" in order to capture the effects of the substructure at a scale which is large enough to neglect the geometrical complexities of the micro-structure.

The goal of the present work is to identify the constitutive parameters of a macro-scale model for a planar pantographic structure in a way that the inspected properties of the structure matches well with that of the data obtained, using Cauchy model, from an exact 3D model. This model will be a tool for calculation and prediction of the mechanical behavior of the structure. As a continuation to perivous studies on numerical identifications [1, 3, 4], here, an optimization algorithm is exploited for an automated and easier parameter identification process.

Different forms of Genetic Algorithm (GA), which is among evolutionary algorithms, has been developed for dealing with optimization problems, such as Non-Dominated Sorting Genetic Algorithm (NSGA) [7] and NSGA-II [2]. The NSGA-II yields surprisingly better results compared the other two since it uses two criteria for ranking solutions: grouping the objective function values in 'Fronts' and calculating the crowding distance for values of each 'Front' [2].

In this research, we carry out the constitutive parameter identification of a planar pantographic structure in two cases. First, the optimization is done with one 'fitness' function using GA and then with two objective functions using NSGA-II.

*Corresponding author: navid.shekarchizadeh@sbai.uniroma1.it ORCID iD: https://orcid.org/0000-0002-5750-7801

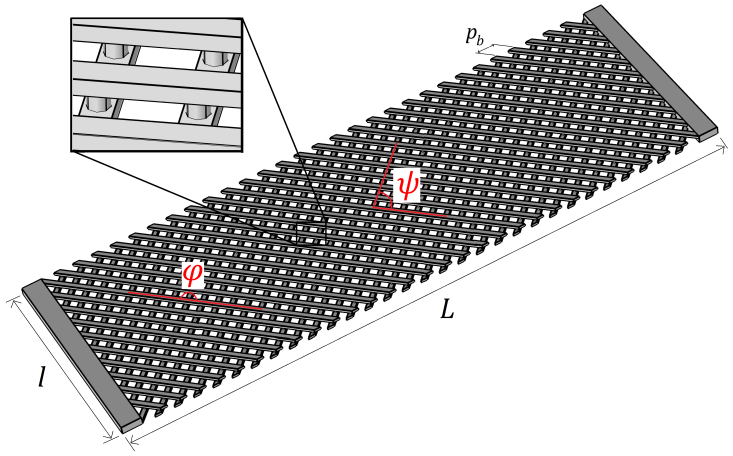

Figure 1. A pantographic structure and its geometrical parameters

1 Macro Model and Geometry

For describing the pantographic structure at macro level, the second-gradient model presented in [3] is considered here. In this model, the current position x of a material point is a function of the position $\mathbf{X}$ in the reference configuration through the map $\chi : \Omega \to \mathbf{R}^2$ where Ω is a rectangular plane region.

$$x = \chi(\mathbf{X}) = (X^\alpha + u^\alpha(X^\beta))\mathbf{D}_\alpha \tag{1}$$

The deformation gradient is $F = \nabla\chi$ and the field of unit vectors tangent to the two families of fibers is $e_\alpha = \mathbf{F}\mathbf{D}_\alpha/||\mathbf{F}\mathbf{D}_\alpha||$ where $\mathbf{D}_\alpha$ is a Lagrangean basis, $\alpha = \{1, 2\}$. The auxiliary vector field c_α is:

$$c_\alpha = \frac{\nabla\mathbf{F}|\mathbf{D}_\alpha \otimes \mathbf{D}_\alpha}{||\mathbf{F}\mathbf{D}_\alpha||} \qquad \text{where } (\nabla\mathbf{F}|\mathbf{D}_\alpha \otimes \mathbf{D}_\alpha)^\beta = \partial_\alpha F^\beta_\alpha = \partial_{\alpha\alpha}\chi^\beta \tag{2}$$

The strain measures, stretch of fibers ($\varepsilon_\alpha = \mathbf{F}|\mathbf{D}_\alpha - 1$), fiber curvature ($\kappa_\alpha = ||c_\alpha - (c_\alpha.e_\alpha)e_\alpha|| = ||(\mathbf{I} - e_\alpha \otimes e_\alpha)c_\alpha||$), and shear distortion γ ($\sin(\gamma) = e_1.e_2$) are introduced. The strain energy density that considers all the above contributions is assumed to be as follows.

$$W_M(\varepsilon_\alpha, \kappa_\alpha, \gamma) = \sum_\alpha (\frac{1}{2}K_I\varepsilon_\alpha^2 + \frac{1}{2}K_{II}\kappa_\alpha^2) + \frac{1}{2}K_p\gamma^2, \qquad K_I, K_{II}, K_p > 0, \text{ constant} \tag{3}$$

The governing equations are obtained using a variational principle:

$$\delta \int_\Omega W_M(\varepsilon_\alpha, \kappa_\alpha, \gamma)d\Omega = 0 \quad \forall\ \delta u \tag{4}$$

The pantographic structure shown in Fig. 1 is considered for modeling in this study. The geometrical parameters, shown in Fig.1, are as follows: $L = 0.2096$ m, $l = 0.06987$ m, $p_b = 4.85$ mm and the height of each beam, $h_b = 0.9$ mm, the width of each beam, $b_b = 1.6$ mm, the height of each pivot, $h_p = 1$ mm, and the diameter of each pivot $d_p = 1.2$ mm. The material used for the structure is Polyamide PA 2200 (Young Modulus = 1600 Mpa, Poisson's ratio = 0.3, and mass density = 930 kg/m^3). Bias extension tests are simulated on the structure in COMSOL Multiphysics FEM enviroment and the total stored energy and the angles ψ and φ are calculated. ψ is the angle between two beams intersecting at the center of the specimen and φ is the bending angle of the beam that meets the corner of the specimen, see Fig. 1. The reason of choosing these two angles is that ψ and φ are the representatives of the shear energy in the central region and the bending energy in the most bent region respectively [3].

2 Optimization of the Macro Model Parameters

In this section, the considered results of the macro model are fitted with the micro model results through an optimization process. The constitutive parameters of the macro model, K_I, K_{II}, and K_p, are determined by the optimization algorithm. At first, we consider the squared normalized error of the outputs

(The total stored energy and the two angles) as the 'fitness' function (f_1) and minimize it using GA. Then, we defined another objective function, which grants double significance to ψ compared to φ (Eq. (5)). This is due to the fact that the energy involved in ψ angle is mainly governed by K_p [3] and on the other hand by inspecting the energy components, we can see that the shear energy has the largest portion of the total stored energy. Therefore, if the predicted ψ has lower error, the chance of predicting more accurate energy values is higher. NSGA-II is utilized for the new optimization problem which has two objectives. For investigating the effect of defining the new objective function, NSGA-II is modeled with the same optimization algorithm parameters.

$$f_2 = 2\sum_{i}^{n}\left(\frac{\psi_i^M - \psi_i^m}{\psi_i^m}\right)^2 + \sum_{i}^{n}\left(\frac{\varphi_i^M - \varphi_i^m}{\varphi_i^m}\right)^2 \tag{5}$$

where i is the index of the i-th step loading and M and m denote the quantities from macro and micro models, respectively.

In NSGA-II, the group of objective function value(s) that dominate other values are preferred, and they are called the Pareto Front. The fronts are chosen using a matrix. The objective function values are plotted on a graph with the axes showing the first and second objective function values. The advantage of Pareto Front is that a set of optimum points can be assessed. The importance of having a set of optimum solutions is that one can choose the optimum point even in case of occurring unexpected limitations [2].

Figure 2(a) shows the Pareto Front and the Fig.2 (b) shows the number of points in Pareto Front in the ten first iterations. In complicated cases of multi-objective optimization problems, in case of applying NSGA-II, the number of points in Pareto Front fall to zero after a few iterations and then suddenly it increases as much as the number of all point. In this condition, NSGA-II acts poorly because of loss of selection pressure in objective function evaluation. For overcoming this problem and increasing the accuracy of ranking, the 'dominance' concept was replaced by 'Strictly dominance', 'Weakly dominance', and 'Indifferent' concepts through Fuzzy methods. Later, the Fuzzy-based Pareto Optimality was presented using the Left Gaussian function and the Fuzzy-Pareto-Dominance [5, 6]. Since the plot of Pareto Front is desired and the algorithm performs well in high iterations, our optimization has not encountered the above-mentioned problem. The results show that the population is not high enough to have a Pareto Front with less points than the population. On the other hand, considering the computational cost of the model, it is not efficient to increase the population.

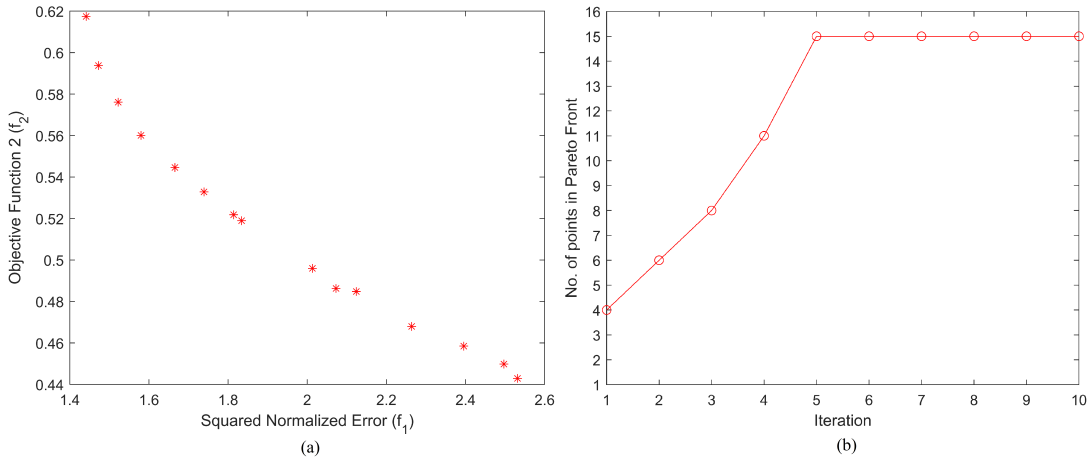

Figure 2. (a)The Pareto Front and (b)number of points in Pareto Front in every iteration

3 Results

By means of the optimization process, the constitutive parameters of the planar macro model are identified. In the first optimization, with one fitness function, the average value of the squared normalized

error of the optimum point was 1.455 and then it was slightly decreased by defining another objective function.The constitutive parameters calculated by the GA are $K_I = 6.274 \times 10^5$ (N/m), $K_{II} = 7.81 \times 10^-2$ (Nm), and $K_p = 3.684 \times 10^3$ (N/m). In NSGA-II, since it is a multi-objective optimization, a single set of parameters is not introduced as the optimum point, in other words, we have a number of optimum points in the Pareto that non of them dominate the others, therefore, we may choose any of the points with regard to the problem conditions. The values of the stored energy and the angles ψ and φ calculated by simulating a bias extension test of the pantographic structure using the planar second-gradient macro model are compared (in Fig. 3) with the values from Cauchy continuum micro model which were previously calculated in [4] for the same structure. All the calculated values show acceptable accordance except for the stored energy after 0.04m of displacement, where we see a discrepancy.

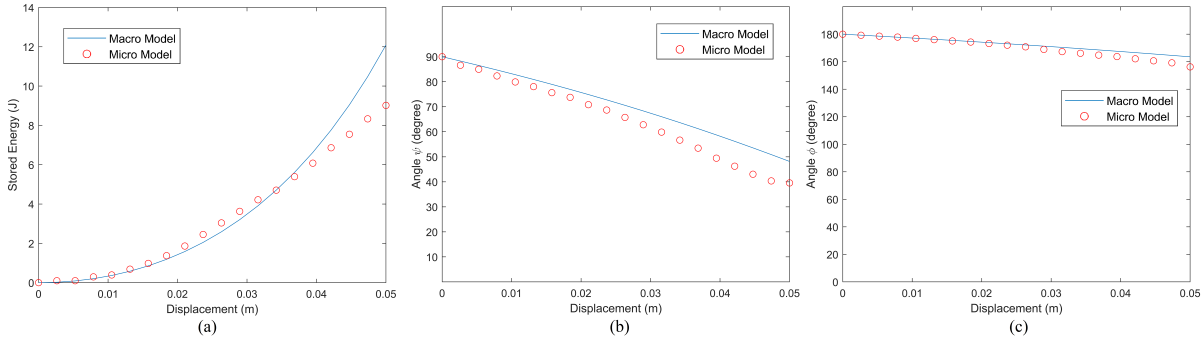

Figure 3. Comparison of the values of (a)Stored Energy, (b)The angle ψ, and (c)The angle φ from the micro[4] and macro models

4 Conclusion

In this paper, a multi-objective optimization algorithm is utilized for identifying the constitutive parameters of a second-gradient macro model for a planar pantographic structure by minimizing the error of the outputs of the model. By the virtue of the automated algorithm, the reduced-order model could be created for different structures more easily.

References

[1] Michele De Angelo, Emilio Barchiesi, Ivan Giorgio, and B. Emek Abali. Numerical identification of constitutive parameters in reduced-order bi-dimensional models for pantographic structures: application to out-of-plane buckling. *Archive of Applied Mechanics* (2019), pp. 1–26.

[2] Kalyanmoy Deb, Samir Agrawal, Amrit Pratap, and Tanaka Meyarivan. A fast elitist non-dominated sorting genetic algorithm for multi-objective optimization: NSGA-II. In: *International conference on parallel problem solving from nature*. Springer. 2000, pp. 849–858.

[3] Francesco dell'Isola, Ivan Giorgio, Marek Pawlikowski, and Nicola Luigi Rizzi. Large deformations of planar extensible beams and pantographic lattices: heuristic homogenization, experimental and numerical examples of equilibrium. *Proceedings of the Royal Society A: Mathematical, Physical and Engineering Sciences* 472.2185 (2016), p. 20150790.

[4] Ivan Giorgio. Numerical identification procedure between a micro-Cauchy model and a macro-second gradient model for planar pantographic structures. *Zeitschrift für angewandte Mathematik und Physik* 67.4 (2016), p. 95.

[5] Zhenan He, Gary G Yen, and Jun Zhang. Fuzzy-based Pareto optimality for many-objective evolutionary algorithms. *IEEE Transactions on Evolutionary Computation* 18.2 (2013), pp. 269–285.

[6] Mario Köppen, Raul Vicente-Garcia, and Bertram Nickolay. Fuzzy-pareto-dominance and its application in evolutionary multi-objective optimization. In: *International Conference on Evolutionary Multi-Criterion Optimization*. Springer. 2005, pp. 399–412.

[7] Nidamarthi Srinivas and Kalyanmoy Deb. Muiltiobjective optimization using nondominated sorting in genetic algorithms. *Evolutionary computation* 2.3 (1994), pp. 221–248.

**Proceedings of the 8th GACM Colloquium on Computational Mechanics
for Young Scientists from Academia and Industry
August 28–30, 2019 in Kassel, Germany**

Development of hybrid lattice materials using additive manufacturing

Christina Völlmecke *[1], Vivian Dreßler[1], Daniel Melzer[1], Gregor Ganzosch[2] and Anton Köllner[1]

[1]Technische Universität Berlin, School V, Institute of Mechanics, Stability and Failure of Functionally Optimized Structures Group, Einsteinufer 5, 10587 Berlin, Germany

[2]Technische Universität Berlin, School V, Institute of Mechanics, Continuum Mechanics and Material Theory group, Einsteinufer 5, 10587 Berlin, Germany

Abstract. Additive manufacturing allows slender lattice materials to be developed very easily. These slender structures are prone to buckling. By introducing pre-stressed fibres into the lattice, the buckling mode could be changed and subsequently the critical load would increase. This has been shown theoretically for unit cells (UC). Herein, the current strategies of the group for developing UCs using additive manufacturing are presented.

Introduction

In large scale civil engineering applications, steel columns are common structural elements. Slender steel columns that are additionally reinforced by pre-stressed cable stays generally exhibit an increased strength in axial compression since buckling displacement is inhibited, *e.g.* [3, 4]. So far this concept has only been applied on the large scale. Thus, the transferability of this concept to smaller length scales is to be investigated. The potential development of novel material concepts had been shown by previous analytical investigations [5]. Experimental investigations on the buckling and postbuckling behaviour of simply-supported, pre-stressed stayed columns under pure axial compression have been conducted on smaller length scales. They all displayed a reliable repeatability of the results, yielding a critical load several times higher than the bare column whilst the postbuckling characteristics remain unchanged [1, 2]. Lately, the group has been working on the development of hybrid fibre lattice materials using additive manufacturing. Therefore unit cells (UC) of the material were manufactured using two different printing technologies, namely fused deposition modelling (FDM) and stereolithography (SLA), as will be presented henceforth.

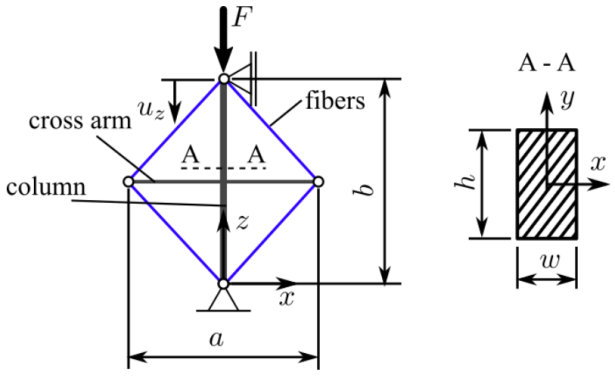

Figure 1. Schematic representation of a UC.

*Corresponding author: christina.voellmecke@tu-berlin.de

1 Manufacturing of hybrid lattice unit cells

Following up on the groups previous manufacturing approaches for pre-stressed hybrid lattice UCs (see Fig. 1) two manufacturing strategies were chosen.

Strategy A implemented the fibre directly into the printing process whilst with strategy B two parts were printed and adhesive boding of the two halves was undertaken. Both strategies were implemented using FDM (Ultimaker 3 extended) as well as SLA (Formlabs Form 2) printing.

1.1 Fibre pull-out tests

In order to gauge the bonding of the fibre with the printing material prior to manufacture of UCs, fibre pull-out tests were conducted using a microforce testing devices (MTS Tytron 250, MTS Systems Corporation, Eden Prairie, USA). A special mounting system was designed to guarantee repeatability of the tests (Fig. 2).

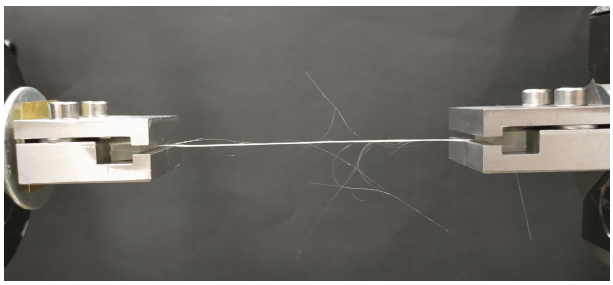

Figure 2. Fibre pull-out test.

Different filament materials were used with the FDM printer such as Polylactic Acid filament (PLA), Polymethylmethacrylat (PMMA) and Acrylnitril-Butadien-Styrol (ABS). For the SLA printed formlabs clear resin was used. As fibre materials glass, carbon and basalt were taken. Adhesive bonding was undertaken using acetone, modelling glue, super glue and epoxy resin. From the fibre pull-out tests it can at this stage be deducted that strategy A (direct implementation of the fibre) results in insufficient bonding of the fibre with the material. Using adhesive bonding of the two halves generally resulted in better bonding of the fibre but is still to be developed further in order to achieve reliable results.

1.2 Mounting device for the UC

A special mounting device was developed for the manufacturing of the UCs (Fig. 3. The device is designed such that pre-stress can be applied. Using this device a UC was successfully manufactured as can be seen in Fig. 4.

2 Conclusion

A novel approach on developing UCs for hybrid lattice materials using additive manufacture has been presented. Two strategies were pursued, namely direct integration of the fibre in the printing process or subsequent adhesive boding of two halves of the UC whilst implementing the fibre. Fibre-pull out tests revealed that both strategies cannot yet guarantee perfect bonding of the material with the fibre. Hence stresses will not to be transmitted sufficiently via the fibres. Thus, in order to implement the concept of pre-stressed cable stays already used in large scale applications on a material level, the development strategies need to be reviewed and amended.

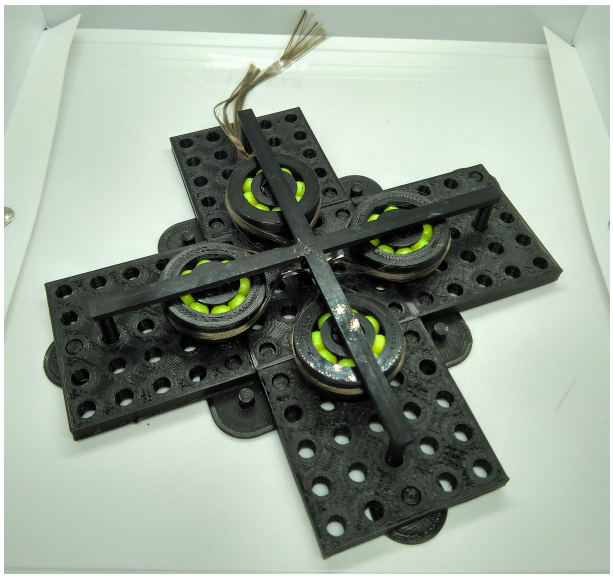

Figure 3. Mounting device for UC.

Figure 4. UC made with formlabs clear resin and basalt fibre using strategy A.

References

[1] G. Ganzosch, M. Todt, A. Köllner, and C. Völlmecke. Experimental investigations on pre-stressed stayed columns on smaller length scales. In: *Proceedings of the Eighth International Conference on Thin-walled Structures*. 2018, pp. 1–15.

[2] A. Köllner, M. Todt, G. Ganzosch, and C. Völlmecke. Experimental and numerical investigation on pre-stressed lattice structures. *Thin-Walled Structures* (under revision).

[3] D. Saito and M.A. Wadee. Post-buckling behaviour of prestressed steel stayed columns. *Engineering Structures* 30.5 (2008), pp. 1224 –1239.

[4] M.A. Wadee, L. Gardner, and T.A. Hunt. Buckling mode interaction in prestressed stayed columns. *Proceedings of the Institution of Civil Engineers - Structures and Buildings* 166.8 (2013), pp. 403–412.

[5] C. Zschernack, M. A. Wadee, and C. Völlmecke. Nonlinear buckling of fibre-reinforced unit cells of lattice materials. *Compos Struct* 136 (2016), pp. 217–228.

**Proceedings of the 8th GACM Colloquium on Computational Mechanics
for Young Scientists from Academia and Industry
August 28–30, 2019 in Kassel, Germany**

A finite strain microplane-plasticity model for concrete

Bobby Rio Indriyantho[1] and Michael Kaliske * [1]

[1]Institute for Structural Analysis, Technische Universität Dresden, 01062 Dresden, Germany

Abstract. A plasticity model is one of the powerful approaches which is essential for achieving softening response of materials, besides damage mechanics theories. Meanwhile, the microplane approach has been studied extensively and its development proved to be appropriate for modelling quasi-brittle materials, such as concrete. Numerous constitutive laws of the microplane-plasticity model have been developed in many versions for the small strain framework, and they have been utilised successfully to predict the load-displacement as well as stress-strain curves including the post-peak behaviour. However, at high hydrostatic pressure, a plastic response with very large strains or deformations may occur in concrete materials or building structures. Due to this phenomenon, the extension of the microplane-plasticity model from the small strain to the finite strain case is inevitable and it is required in order to represent the largely deformed behaviour of structures. The elastic-plastic microplane approach based on the volumetric-deviatoric decomposition employing the Drucker-Prager yield criterion extended to the finite strain regime is implemented in this present contribution. Moreover, for eliminating the pathological mesh sensitivity and obtaining a more stable finite element solution due to strain localization, the so-called implicit gradient enhancement, which is straightforward to be applied in general finite element codes, is used here. Furthermore, numerical example in quasi-static case is given and discussed to evaluate the proposed formulation. Finally, the simulated results are compared to existing experimental investigations in order to evaluate and validate the accuracy of the newly proposed model.

Introduction

A plasticity model is one of the essential approaches to solve issues regarding strain softening of materials, besides damage mechanics theories. Meanwhile, the so-called microplane model has been proven to be a powerful constitutive approach for modelling quasi-brittle materials, such as concrete, since it was firstly introduced by [2, 3]. The other microplane formulation is proposed by [7] based on the volumetric-deviatoric (V-D) split and the kinematic constraints. However, strain localization arises and the finite element solution yields unstable. In order to overcome these challenges, [8] developed an implicit gradient enhancement employing nonlocal fields which is straightforward to be implemented in general finite element codes.

Numerous versions of the microplane model for concrete have been developed and improved successfully at small strains. Nevertheless, in certain loading cases, small strain microplane models produce inaccurate results in terms of load-displacement or stress-strain curve as well as an incorrect damage visualization. At high hydrostatic pressure, the response of concrete becomes plastic and the material exhibits very large deformations with no observable cracks or damage. This experimental investigation in [4] has been confirmed in [6] and concludes that the microplane damage formulation at the small strain framework cannot yield good results for the aforementioned case. Consequently, since the microplane approach at small strains is not sufficient to accommodate very large deformations of concrete and the plastic response occurs, the use of the microplane-plasticity model at finite strains is inevitable.

The present contribution is focused on the microlane model for concrete accommodating the plastic response at very large deformations. The gradient-enhanced microplane-plasticity approach at small strains in [9] is extended to the finite strain model using the Green-Lagrange strain tensors. The aim of this work is to introduce and formulate the new extended gradient-enhanced microplane-plasticity model within the finite strain framework for concrete to obtain a reliable and accurate response in quasi-static case. Finally, the results are compared to the existing experimental data in order to evaluate the accuracy of the newly proposed model.

*Corresponding author: michael.kaliske@tu-dresden.de

1 Finite strain microplane-plasticity formulation

An additive volumetric-deviatoric split using the Green-Lagrange strain tensor $\boldsymbol{E}$ has been employed in [1, 5, 6] to extend the small strain model to the finite strain framework for concrete materials, so that it enables the elastoplastic formulation at finite strains being easy to handle, since its equations are similar to the small strain model as follows

$$E_V^e = E_V - E_V^p, \tag{1}$$
$$\boldsymbol{E}_D^e = \boldsymbol{E}_D - \boldsymbol{E}_D^p. \tag{2}$$

Hence, the microplane free-energy function with hardening H and its variable κ^{mic} is

$$\Psi^{mic}(\boldsymbol{E}^e) = \frac{1}{2}K^{mic}(E_V - E_V^p)^2 + G^{mic}(\boldsymbol{E}_D - \boldsymbol{E}_D^p)\cdot(\boldsymbol{E}_D - \boldsymbol{E}_D^p) + \frac{1}{2}H\kappa^{mic^2}. \tag{3}$$

According to [5], however, the resulting stress should be the so-called co-rotated Cauchy stress tensor $\boldsymbol{s}$ instead of the second Piola-Kirchhoff stress tensor $\boldsymbol{S}$, since the microplane orientation should rotate with the material, see [5] for details. By deriving the microplane free-energy Ψ^{mic} in the V-D split with respect to the Green-Lagrange strain tensor $\boldsymbol{E}$ and, then, integrating it over all microplanes, the homogenised co-rotated Cauchy stress tensor is

$$\boldsymbol{s} = \frac{3}{4\pi J}\int_\Omega K^{mic}(E_V - E_V^p)\,\boldsymbol{UVU}\,d\Omega + \frac{3}{4\pi J}\int_\Omega 2G^{mic}\boldsymbol{UDev}^T\cdot(\boldsymbol{E}_D - \boldsymbol{E}_D^p)\,\boldsymbol{U}\,d\Omega, \tag{4}$$

with

$$\boldsymbol{V} = \frac{1}{3}J^{\frac{2}{3}}\boldsymbol{C}^{-1}, \tag{5}$$
$$\boldsymbol{Dev} = \boldsymbol{n}\cdot\mathbb{I}^{dev} = \boldsymbol{n}\cdot\mathbb{I}^{sym} - \frac{1}{3}\boldsymbol{n}\cdot\boldsymbol{C}^{-1}\otimes\boldsymbol{C}, \tag{6}$$

where $\boldsymbol{V}$ and $\boldsymbol{Dev}$ are the volumetric and deviatoric projection tensors, respectively. Finally, the true (Cauchy) stress $\boldsymbol{\sigma}$ is obtained by

$$\boldsymbol{\sigma} = \boldsymbol{RsR}^T, \tag{7}$$

where $\boldsymbol{R}$ is the rotation tensor obtained by the polar decomposition of deformation gradient $\boldsymbol{F}$.

2 Implicit gradient enhancement and yield function

The implicit gradient enhanced method is applied by modifying the Helmholtz equation for defining nonlocal fields as follows

$$\bar{\kappa}_m - c\nabla^2\bar{\kappa}_m = \kappa_m, \tag{8}$$

with

$$\kappa_m = \max_{mic=1}^{21}\left(\kappa^{mic}\right), \tag{9}$$

where the gradient parameter c controls the interaction range of the nonlocal part and ∇^2 is the Laplace operator. Moreover, κ_m and $\bar{\kappa}_m$ are the local variable and its nonlocal counterpart, respectively. Using Eq. (9), only one of 21 microplanes is utilised to perform the regularisation as adopted from [9]. Consequently, its largest quantity is taken and updated in each time step.

By introducing the effect of the nonlocal field $\bar{\kappa}_m$ within the damage variable $\omega(\bar{\kappa}_m)$ for obtaining the softening response as implemented in [9], the modified Drucker-Prager yield function is

$$F^{mic} = \sqrt{\frac{3}{2}\boldsymbol{S}_D^{mic}\cdot\boldsymbol{S}_D^{mic}} + \alpha S_V^{mic} - (1-\omega(\bar{\kappa}_m))\left(S_0 + H\kappa^{mic}\right) \le 0, \tag{10}$$

with

$$\omega(\bar{\kappa}_m) = \alpha_p\left(1 - \exp(-\beta\bar{\kappa}_m)\right), \tag{11}$$

where α_p and β govern the maximum degradation of the yield stress and the softening branch, respectively.

3 Numerical example

A tube squash test, based on the experimental investigation in [4], can show very large strains with plastic responses in concrete at high hydrostatic pressure. Therefore, this test will be simulated using the newly proposed model and its result will be compared each other. A hollow steel tube with an inner diameter of 47.8 mm (76.2 mm outer diameter) and a height of 88.9 mm is filled by concrete and tested at the axial constant displacement rate of 0.0254 mm/s. All material parameters used here are shown in Table 1. The steel tube is modelled by common von Mises plasticity and assumed as a perfect bond between steel and concrete surface. The calibration of the empty steel tube is needed before performing the tube-squash test, see [6] for details. Afterwards, the steel-concrete tube is simulated but only one-forth of the specimen is discretised, due to the symmetry, using 4305 nodes and 2560 elements.

Table 1. Material parameter of a tube-squash test.

Parameter		Filled concrete	Steel tube
E	[MPa]	20000	200000
ν	[-]	0.2	0.3
S_0	[MPa]	30.0	-
H	[MPa]	800	500
α	[-]	0.5	-
β	[-]	500	-
α_p	[-]	0.998	-
c	[mm^2]	500	-
σ_y	[MPa]	-	360

As can be seen in Figure 1, the load-displacement curve simulated by the proposed model has a good agreement compared to the experimental result in [4]. The final axial displacement obtained by this squash test is about 31 mm or about 1/3 of the tube height. It indicates that very large strain occurs in this simulation, since the axial strain amounts approximately up to 34%.

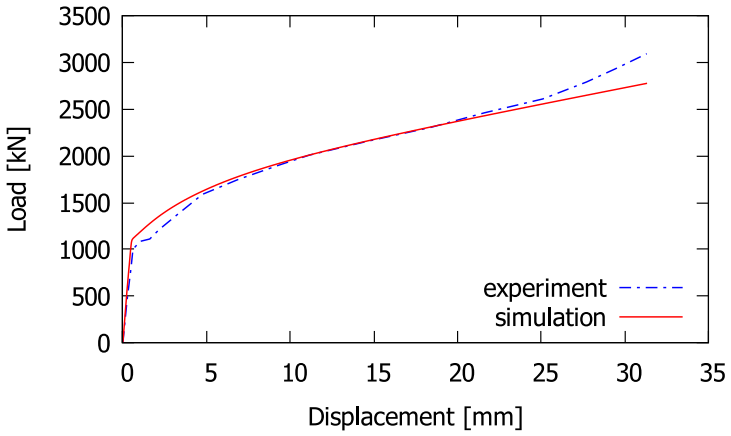

Figure 1. Comparison of load-displacement curve for experiment and simulation.

In the necessity of plastic zone visualisation, 21 microplane hardening variables κ^{mic} are homogenised and a scalar hardening measure κ^{hom} is taken into account as

$$\kappa^{hom} = \frac{\frac{3}{4\pi}\int_\Omega \kappa^{mic} d\Omega}{\frac{3}{4\pi}\int_\Omega d\Omega}. \tag{12}$$

From Figure 2(a), one can see the evolution of plastic response at different axial displacement u_z up to final time step. In this tube-squash test simulation, the filled concrete becomes plastic in the middle part of concrete. It also confirms the experimental investigations in [4] that no damage can be observed due to plastic behaviour, see Figure 2(b). By the load-displacement curve and plastic visualisation, the proposed model can predict the responses of concrete in the tube-squash test accurately.

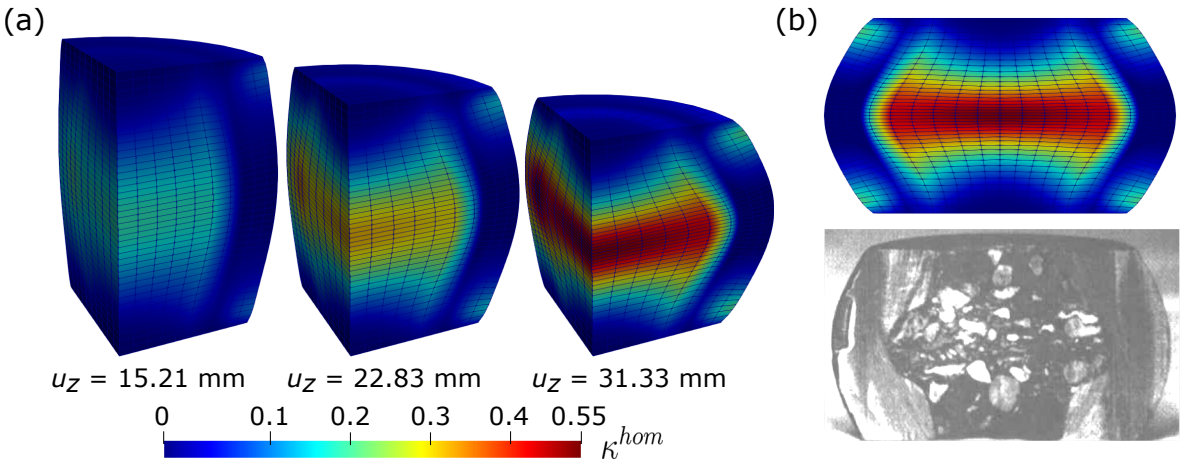

Figure 2. Simulation results: (a) evolution of plastic zone, (b) comparison between simulation and experiment.

4 Conclusions

The finite strain microplane-plasticity approach yields good results for modelling concrete at high hydrostatic pressure in a tube-squash test. The simulated result confirms the tested specimen experimentally and it can predict an accurate plastic response. Furthermore, more examples in static and dynamic cases will be performed at future work.

Acknowledgments

The authors gratefully acknowledge the financial support of Sächsiches Landesstipendium (Saxon Scholarship Program) with reference number L-201653.

References

[1] Z.P. Bažant. Finite strain generalization of small-strain constitutive relations for any finite strain tensor and additive volumetic-deviatoric split. *International Journal of Solids and Structures* 33 (1996), pp. 2887–2897.

[2] Z.P. Bažant and P.G. Gambarova. Crack shear in concrete: crack band microplane model. *Journal of Structural Engineering* 110 (1984), pp. 2015–2035.

[3] Z.P. Bažant and B.H. Oh. Microplane model for concrete for fracture analysis of concrete structures. In: *Proceedings of Symposium on the Interaction of Non-nuclear Munitions with Structures*. U.S. Air Force Academy. Colorado Springs, 1983, pp. 49–53.

[4] Z.P. Bažant, J.J.H. Kim, and M. Brocca. Finite strain tube-squash test of concrete at high pressures and shear angles up to 70 degrees. *ACI Materials Journal* 96 (1999), pp. 580–592.

[5] Z.P. Bažant, M.D. Adley, I. Carol, M. Jirásek, S.A. Akers, B. Rohani, J.D. Cargile, and F.C. Caner. Large-strain generalization of microplane model for concrete and application. *Journal of Engineering Mechanics* 126 (2000), pp. 971–980.

[6] B.R. Indriyantho, I. Zreid, and M. Kaliske. Finite strain extension of a gradient enhanced microplane damage model for concrete at static and dynamic loading. *Engineering Fracture Mechanics* (2019). DOI: `https://doi.org/10.1016/j.engfracmech.2019.106501`.

[7] M. Leukart. "Kombinierte anisotrope Schädigung und Plastizität bei kohäsiven Reibungsmaterialien". PhD thesis. Institut für Baustatik, Universität Stuttgart, 2005.

[8] R.H.J. Peerlings, R. de Borst, W.A.M. Brekelmans, and J.H.P. de Vree. Gradient enhanced damage for quasi-brittle materials. *International Journal for Numerical Methods in Engineering* 39 (1996), pp. 3391–3403.

[9] I. Zreid and M. Kaliske. An implicit gradient formulation for microplane Drucker-Prager plasticity. *International Journal of Plasticity* 83 (2016), pp. 252–272.

**Proceedings of the 8th GACM Colloquium on Computational Mechanics
for Young Scientists from Academia and Industry
August 28–30, 2019 in Kassel, Germany**

A nonlocal ductile damage model for high strength steels under dynamic multiaxial loading conditions

Marvin Nahrmann[1] and Anton Matzenmiller * [1]

[1]Institute of Mechanics, Dept. of Mechanical Engineering, University of Kassel, Mönchebergstr. 7, 34125 Kassel, Germany

Abstract. The high strength steel alloy HX340LAD (ZStE340) is investigated under quasistatic and dynamic loading conditions for different flat specimens. A thermo-viscoplastic constitutive model is applied to capture the temperature and strain rate dependent material characteristics. In order to consider the post-critical material behaviour, the model is enhanced with a nonlocal ductile damage approach. The predicted results exhibit a close agreement to the measured values leading to a successful verification of the model.

1 Introduction

Today's multi-material designs of lightweight car body structures are built upon a broad variety of different steel and aluminium alloys. The diverse material properties of these metals are tailor-made for the respective application areas. In order to ensure the occupant safety, a high tensile strength for the protection of passengers is required as well as a high ductility absorbing the crash energy in the crumpling zone by means of large plastic deformations. Microalloyed high strength steels (HSLA steels) provide a good material strength and ductility and are well suited for complex cold-formed vehicle body parts. Due to dynamic multiaxial loading conditions in the case of metal forming or vehicle crash, the finite element simulation of HSLA steel is still a sophisticated task. Particularly for high strain rates, the conversion of dissipated work into heat causes a locally significant temperature rise. Hence, a temperature and strain rate dependent constitutive model is applied for a thermo-mechanical coupled simulation. Moreover, a nonlocal ductile damage model is appended to capture the mesh independent post-critical material behaviour and enable a good prediction of the entire energy absorption potential.

2 Constitutive model for thermo-viscoplastic material behaviour

The temperature and strain rate dependent material behaviour of high strength steels is considered by the thermo-viscoplastic constitutive model comprehensively presented in [10]. The basic framework of the model is adopted from [4] and [5], whereby it is originally applied to the simultaneous hot/cold forging of metals–see [7]. In this contribution, only a moderate temperature range, from room temperature up to approximately 600 K is considered, which is sufficient to comprise the adiabatic heating for high strain rates. The constitutive equations of the thermo-viscoplasticity model are implemented as a user defined material model (*MAT_USER_DEFINED_MATERIAL_MODELS) into the commercial FE software LS-DYNA and include the temperature dependency of the YOUNG's modulus, the initial yield stress, and the nonlinear isotropic hardening.
Adiabatic heating is taken into account by the TAYLOR-QUINNEY approximation, which determines the temperature increase by means of the viscoplastic stress power and the specific heat capacity c.

$$\dot{\theta} = \frac{\gamma_{\mathrm{TQ}}}{\rho\, c}\, \mathbf{T} \cdot \dot{\mathbf{E}}_{\mathrm{vp}} \;, \quad \gamma_{\mathrm{TQ}} = 0.90 \tag{1}$$

Here, the coefficient γ_{TQ} is specified to convert 90 % of the viscoplastic work into heat. The resulting thermo-mechanical coupled problem is solved by the staggered solution scheme, whereby the thermal problem is solved with a constant displacement field and the mechanical problem with fixed temperatures, respectively.

*Corresponding author: post-structure@uni-kassel.de

3 Nonlocal ductile damage approach

The thermo-viscoplastic material model is coupled with a ductile damage approach based on continuum damage mechanics allowing the prediction of damage and failure caused by large plastic deformations. The concept of effective stresses is employed in order to obtain the CAUCHY stress tensor in the damaged (physical) space ${}^{\mathrm{a}}\mathbf{T}$ on the basis of the damage variable D and the CAUCHY stress tensor in the undamaged (effective) space $\mathbf{T}$. All internal strain variables shall be identical in both configurations, due to the strain equivalence principle–see [5]. The ductile damage growth is driven by the equivalent viscoplastic strain $\bar{\mathrm{E}}_{\mathrm{vp}}$, whereby the approach of LEMAITRE in [6] is applied, introducing the model parameter ε_{c} related to the damage initiation and ε_{f} for failure. The exponent n_{D} controls the course of the damage evolution.

$$ {}^{\mathrm{a}}\mathbf{T} = (1-D)\,\mathbf{T}\;, \quad D = \left\langle \frac{\bar{\mathrm{E}}_{\mathrm{vp}} - \varepsilon_{\mathrm{c}}}{\varepsilon_{\mathrm{f}} - \varepsilon_{\mathrm{c}}} \right\rangle^{n_{\mathrm{D}}}\;, \quad 0 \le D < 1 \tag{2} $$

The nonlocal option *MAT_NONLOCAL is inbuilt in LS-DYNA and based on the integral approach presented in [11] preventing the localisation of an arbitrary spatial field. In this contribution, the nonlocal formulation is applied to the damage variable D to maintain mesh independent outcomes–see also the investigations in [2]. Hence, the rate of the nonlocal damage variable $\dot{\bar{D}}(\mathbf{x})$ at the reference material point $\mathbf{x}$ is obtained by weighting the local damage rate $\dot{D}(\mathbf{y})$ at neighbouring points $\mathbf{y}$ over a certain region Ω of the continuum.

$$ \dot{\bar{D}}(\mathbf{x}) = \frac{1}{W(\mathbf{x})} \int_{\Omega} \dot{D}(\mathbf{y})\; w(\mathbf{x},\mathbf{y})\; \mathrm{d}\mathbf{y}\;, \quad W(\mathbf{x}) = \int_{\Omega} w(\mathbf{x},\mathbf{y})\; \mathrm{d}\mathbf{y} \tag{3} $$

For the implementation in conjunction with finite elements, the integral formulation is approximated by sums over the elements included in the integration region Ω that is determined by the characteristic length l_{c}–see Fig. 1 (left).

$$ \dot{\bar{D}}(\mathbf{x}) \approx \left[\sum_{i=1}^{N} \dot{D}_i\; w_i\; V_i\right] \left[\sum_{i=1}^{N} w_i\; V_i\right]^{-1}\;, \quad w_i = w(\mathbf{x},\mathbf{y}_i) = \left[1 + \left(\frac{\|\mathbf{x}-\mathbf{y}_i\|}{l_{\mathrm{c}}}\right)^{p}\right]^{-q} \tag{4} $$

Basically, a bell-curved function is assumed for weighting the local variable. The weighting function $w(\mathbf{x},\mathbf{y}_i)$ is evaluated at $\mathbf{y}_i$ for the elements $i = 1,\ ...,\ N$ in the integration region and is hard-coded in LS-DYNA with two model parameters, p and q, specifying its shape. Here, the values $q = 2$ and $p = 8$ are selected, leading to a broad localisation zone within the integration region. Note that this function is only valid in the integration area, so if $\|\mathbf{x}-\mathbf{y}_i\|/l_{\mathrm{c}} \le 1$–see Fig. 1 (right).
In order to enable the nonlocal formulation, the characteristic length l_{c} has to be greater than the element length in the damage zone. However, the determination of the characteristic length is still a sophisticated challenge. A measurement method for concrete is outlined in [3] on the basis of notched and unnotched tensile tests. In contrast to concrete, the material behaviour of high strength steels is much more ductile. Furthermore, it is well known that the damage and failure behaviour highly depends on the stress state–see [12]. Discussions on the internal length for ductile metals are made in [2] and [1], nevertheless, a general measurement technique has not established yet at all. In [13], the characteristic length is expected to relate to the damage mechanism. In the case of ductile metals, two different damage and failure mechanisms occur. The first is dimple rupture under hydrostatic loading, whereby internal voids are expanded and void coalescence leads to failure. The second damage mechanism is shear failure by means of void elongation within a narrow shear band. Thus, the nonlocal damage model is supposed to consider stress state dependency for the simulation of structures under multiaxial loading conditions.

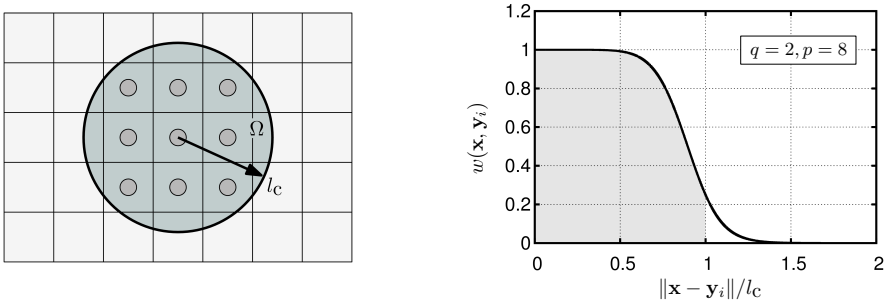

Figure 1. Integration region Ω determined by the characteristic length l_{c} (left), weighting function w (right)

4 Verification results for a high strength steel under dynamic multiaxial loading conditions

The thermo-viscoplastic material model with nonlocal ductile damage is verified for six flat specimens, made of the microalloyed high strength steel HX340LAD (ZStE340), for quasistatic (qs) as well as dynamic loading conditions under low (25 mm/s), medium (250 mm/s) and high velocities (2500 mm/s)–see Fig. 2. All model parameters of the thermo-viscoplasticity model are identified and listed in [10], whereby tensile test data from [9] and [8] as well as shear test data from [12] are employed. The parameters for the ductile damage approach and the nonlocal formulation are presented in Fig. 2 for all investigated specimens. Different damage model parameters are permitted for each specimen in the first instance, due to the absence of a stress state dependent nonlocal damage model. The characteristic length for every specimen is defined on the basis of the plastic zone prior to failure, leading to a similar extent of

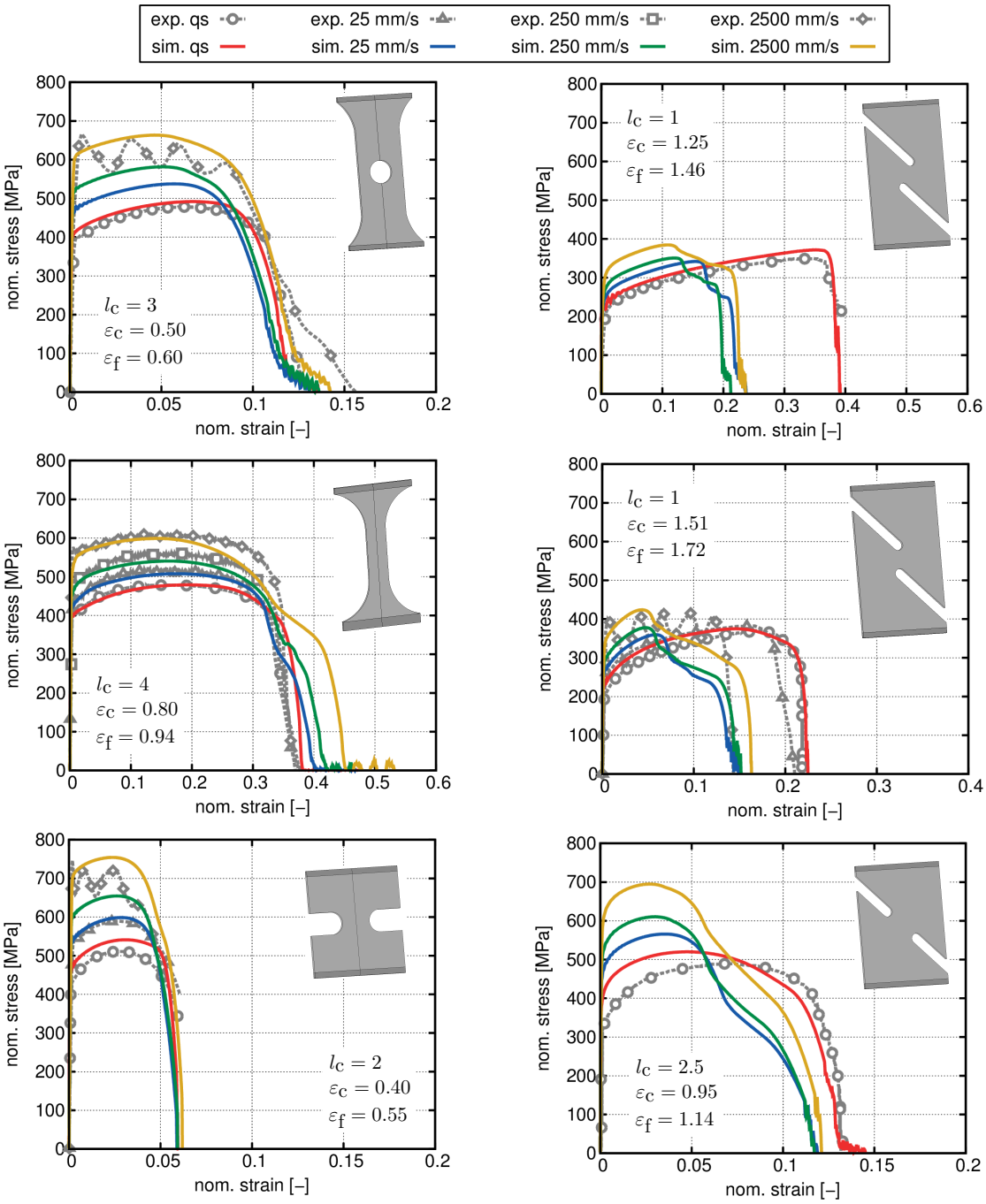

Figure 2. Simulation results compared to test data ([9],[12]) for the perforated, unnotched and notched tensile specimen (left column) as well as for the -20°, 0° and 45° shear specimen (right column)

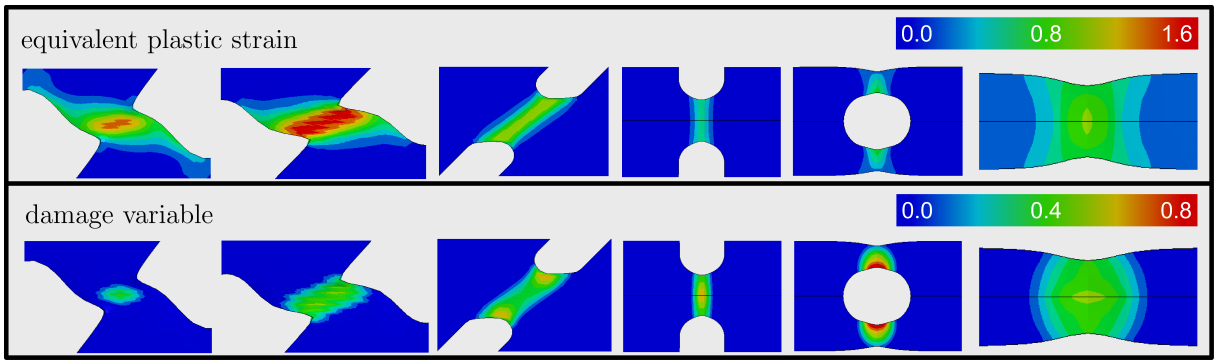

Figure 3. Spatial fields of the equivalent plastic strain and the damage variable prior to failure for the -20°, 0° and 45° shear specimen as well as for the notched, perforated and unnotched tensile specimen

high plastic deformations and damaged material–see Fig. 3. This results in noticeable different values for l_c, comparing tensile and shear test for example. The overall simulation results are in good correlation with the according test data for nearly all specimens and loading conditions. An interesting effect is the reduction of elongation for shear dominated high speed loading, recognisable in the experimental as well as in the predicted stress-strain courses–see right centred diagram in Fig. 2. A probable reason is the strong adiabatic heating in a narrow band resulting in thermal softening and premature failure.

References

[1] F. R. Ahad, K. Enakoutsa, K. N. Solanki, and D. J. Bammann. Nonlocal modeling in high-velocity impact failure of 6061-T6 aluminum. *International Journal of Plasticity* 55 (2014), pp. 108–132.

[2] F. X. C. Andrade, J. M. A. Cesar de Sa, and F. M. Andrade Pires. Assessment and comparison of non-local integral models for ductile damage. *Int J of Damage Mech* 23.2 (2014), pp. 261–296.

[3] Z. Bazant and G. Pijaudier-Cabot. Measurement of Characteristic Length of Nonlocal Continuum. *Journal of Engineering Mechanics* 115.4 (1989), pp. 755–767.

[4] C. Bröcker and A. Matzenmiller. An enhanced concept of rheological models to represent nonlinear thermoviscoplasticity and its energy storage behaviour. *Cont Mech Therm* 25 (2013), pp. 749–778.

[5] C. Bröcker and A. Matzenmiller. On the generalization of uniaxial thermoviscoplasticity with damage to finite deformations based on enhanced rheological models. *Technische Mechanik* 34 (2014), pp. 142–165.

[6] J. Lemaitre. A Continuous Damage Mechanics Model for Ductile Fracture. *Journal of Engineering Materials and Technology* 107 (1985), pp. 83–89.

[7] A. Matzenmiller and C. Bröcker. Thermo-mechanically coupled FE analysis and sensitivity study of simultaneous hot/cold forging process with local inductive heating and cooling. *International Journal of Material Forming* 5 (2012), pp. 275–300.

[8] G. Meschut and M. Gerkens. *Entwicklung einer Methode zum Nachweis der Einsetzbarkeit des Hochgeschwindigkeits-Bolzensetzen unter Berücksichtigung der Bauteileigenschaften.* Europäische Forschungsgesellschaft für Blechverarbeitung e.V., report no. 455. 2017.

[9] G. Meschut, O. Hahn, D. Hein, A. Matzenmiller, and A. Nelson. *Experimentelle und numerische Untersuchungen des Crashverhaltens hybridgefügter Verbindungen.* FOSTA report P958. 2015.

[10] M. Nahrmann and A. Matzenmiller. *Modelling and identification of coupled thermo-viscoplastic material behaviour with nonlocal ductile damage.* Proceedings of the 12. European LS-DYNA Conference, Koblenz. 2019.

[11] G. Pijaudier-Cabot and Z. Bazant. Nonlocal Damage Theory. *Journal of Engineering Mechanics* 113.10 (1987), pp. 1512–1533.

[12] A. Trondl, S. Klitschke, W. Böhme, and D.-Z. Sun. *Verformungs- und Versagensverhalten von Stählen für den Automobilbau unter crashartiger mehrachsiger Belastung.* FAT-Schriftenreihe 283. Forschungsvereinigung Automobiltechnik e.V. (FAT). 2015.

[13] V. Tvergaard and A. Needleman. Nonlocal effects on localization in a void-sheet. *International Journal of Solids and Structures* 18 (1997), pp. 2221–2238.

**Proceedings of the 8th GACM Colloquium on Computational Mechanics
for Young Scientists from Academia and Industry
August 28–30, 2019 in Kassel, Germany**

Analysis of microwire torsion using a nonlocal dislocation based plasticity formulation

Kolja Zoller * [1] and Katrin Schulz[1]

[1]Institute for Applied Materials - Computational Materials Science (IAM-CMS), Karlsruhe Institute of Technology, Kaiserstr.12, 76131 Karlsruhe, Germany

Abstract. The microstructural evolution of face-centered cubic microwires is studied using a physical motivated, homogenized continuum model of crystal plasticity. The dislocation configuration in the three-dimensional space is thereby described via a Continuum Dislocation Dynamics (CDD) theory including a dislocation source term. The resulting spatial distribution of dislocation densities and strain components are shown for a relaxation problem with torsional loading.

Introduction

Microwires under torsion show a pronounced size effect [1], whereby the consideration of single crystal allows to study the influence of strain gradients independent from grain sizes. Describing dislocation densitiy as a homogenized ensemble of dislocation lines, the CDD theory [2] is suitable for a physical consideration of such problem providing the benefits of a continuum formulation. A numerical algorithm applied to pile-ups at grain boundaries is introduced in [6]. Additional, an extension including a dislocation density production term for bending is formulated in [4] and for torsion in [7]. The connection between pile-ups and size effects is discussed in [5].

1 Dislocation density based continuum model

The considered model describes the elasto-plastic deformation behavior of face-centered cubic single crystal metals, whereby the plasticity solely results from the evolution of the dislocation microstructure characterized by CDD densities. Operating on the mesoscopic scale, the model can be divided into two coupled problems using the same length scale: The elastic problem calculating the stress field $\boldsymbol{\sigma}$ for a given plastic state and the dislocation problem describing the dislocation evolution for a given stress field resulting in plasticity via the plastic slip γ_s on all twelve slip systems $S = 12$. Each slip systems s is characterized by its plane normal $\boldsymbol{m}_s$ and the Burger's vector $\boldsymbol{b}_s = b_s \boldsymbol{d}_s$ with the length b_s and the slip direction d_s. The governing equations of both problems can be found in Tab. 1. Regarding the boundaries, it has to be remarked, that the dislocations can leave the continuum at the surfaces unhindered. The considered degrees of freedom are three nodal displacements plus four nodal dislocation density based quantities per slip system.

The curvature production term $\dot{q}_s^{prod}$ enables the model to increase the number of dislocation loops in the system. The production term is activated if the local stress exceeds a critical value and accounts for a relaxation of the local stress to its critical state. The macroscopic ideal plastic material behavior functions thereby as a upper limit for the global production rate.

Table 1. Set of governing equations in the three-dimensional space

Elastic problem		Dislocation problem	
Decomposed distorsion tensor	$\mathrm{D}\boldsymbol{u} = \boldsymbol{\beta}^{\mathrm{el}} + \boldsymbol{\beta}^{\mathrm{pl}}$	Orowan equation	$\dot{\gamma}_s = v_s b_s \rho_s$
Plastic distorsion	$\boldsymbol{\beta}^{\mathrm{pl}} = \sum_{s=1}^{S} \gamma_s \boldsymbol{M}_s$	Velocity law	$v_s = \frac{b_s}{B} \operatorname{sgn}(\tau_s^{\mathrm{eff}}) \max\left\{0, \lvert\tau_s^{\mathrm{eff}}\rvert - \tau_s^{\mathrm{y}}\right\}$
Schmid tensor	$\boldsymbol{M}_s = \boldsymbol{d}_s \otimes \boldsymbol{m}_s$	Effective stress	$\tau_s^{\mathrm{eff}} = \boldsymbol{\sigma} \cdot \boldsymbol{M}_s - \tau_s^{\mathrm{b}}$
Infinitesimal total strain	$\boldsymbol{\varepsilon} = \operatorname{sym} D\boldsymbol{u}$	Backstress	$\tau_s^{\mathrm{b}} = \frac{D\mu b_s}{\rho_s} \nabla \cdot \boldsymbol{\kappa}_s^{\perp} \quad , \quad \boldsymbol{\kappa}_s^{\perp} = \boldsymbol{\kappa}_s \times \boldsymbol{m}_s$
Stress-strain relation	$\boldsymbol{\sigma} = \mathbb{C}[\boldsymbol{\varepsilon} - \boldsymbol{\varepsilon}^{\mathrm{pl}}]$	Yield stress	$\tau_s^{\mathrm{y}}(\boldsymbol{\rho}) = a\mu b_s \sqrt{\sum_n \rho_n}$
Macroscopic balance equation	$-\operatorname{div} \boldsymbol{\sigma} = \boldsymbol{f}_{\mathcal{B}}$	Dislocation density	$\dot{\rho}_s = -\nabla \cdot \left(v_s \boldsymbol{\kappa}_s^{\perp}\right) + v_s q_s$
Dirichlet boundary conditions	$\boldsymbol{u} = \boldsymbol{u}_{\mathrm{D}}$	GND density	$\dot{\boldsymbol{\kappa}}_s = \nabla \times (\rho_s v_s \boldsymbol{m}_s)$
Neumann boundary conditions	$\boldsymbol{\sigma}\boldsymbol{n} = \boldsymbol{t}_{\mathrm{N}}$	Curvature density	$\dot{q}_s = -v_s \nabla \cdot \left(\frac{q_s}{\rho_s} \boldsymbol{\kappa}_s^{\perp}\right) + \dot{q}_s^{prod}$
			$-\frac{1}{2}\left(\left(\rho_s + \lvert\boldsymbol{\kappa}_s\rvert\right) \frac{\boldsymbol{\kappa}_s}{\lvert\boldsymbol{\kappa}_s\rvert} \otimes \frac{\boldsymbol{\kappa}_s}{\lvert\boldsymbol{\kappa}_s\rvert} + \left(\rho_s - \lvert\boldsymbol{\kappa}_s\rvert\right) \frac{\boldsymbol{\kappa}_s^{\perp}}{\lvert\boldsymbol{\kappa}_s^{\perp}\rvert} \otimes \frac{\boldsymbol{\kappa}_s^{\perp}}{\lvert\boldsymbol{\kappa}_s^{\perp}\rvert}\right) \cdot \nabla^2 v_s$
		Boundary condition	$v_s\left(\lvert\boldsymbol{n} \times \boldsymbol{m}_s\rvert \rho_s + (\boldsymbol{n} \times \boldsymbol{m}_s) \cdot \boldsymbol{\kappa}_s\right) = 0$

The used system configuration is shown in Fig. 1. A microwire with an aspect ratio of one to two is examined. The bottom is fixed and the top is subjected to a twist deformation. The surfaces on the side are traction-free. We consider an instantaneous loading with an subsequent dislocation relaxation. The resulting stress field consists mainly of two shear components with a linear distribution. Therefore, the center is stress-free and the highest stress occurs at the surface. The chosen material parameter in Tab. 2 are based on aluminium with a [0 1 0] crystal orientation. Elastic isotropy is assumed.

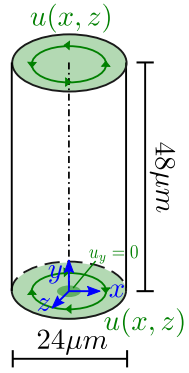

Figure 1. Geometry

Table 2. Material parameter

μ =	27	GPa
ν =	0.347	
b =	0.286	μm
B =	10^{-4}	ns GPa
D =	0.255	$\mu\mathrm{m}^{-3}$
a =	0.35	$\mu\mathrm{m}^{-2}$

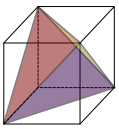

Crystal Orientation: [1 0 0]

2 Relaxation of micro-torsion

The initial condition is dislocation free and the stresses at the surface are initially twice the critical stress for the source activation. For the elastic problem a standard FEM solver with linear ansatz functions is used. The flux-based dislocation transport equations considering dislocation mean-field stresses are solved by a Runge-Kutta discontinuous Galerkin scheme with upwind flux, an implicit midpoint rule for the evolution equations and constant ansatz functions. Both solvers operate on the same mesh consisting of about 170 000 tetragonal elements. The spatial distribution over the radius of the resulting microstructure is characterized by Fig. 2 and Fig. 3.

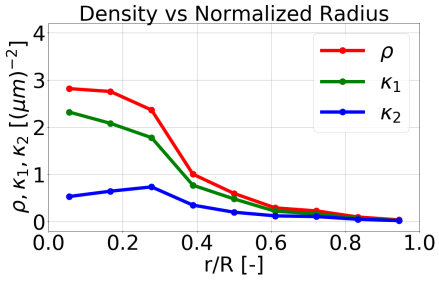

Figure 2. Resulting spatial distribution of the total dislocation density ρ as well as screw part κ_1 and edge part κ_2 of the GND density over the normalized radius with $r = \sqrt{x^2 + z^2}$ and $R = 12\,\mu m$ measured in the middle of the microwire.

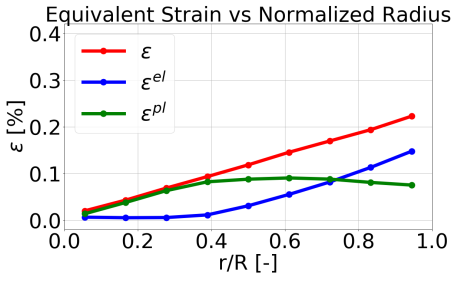

Figure 3. Resulting spatial distribution of the total strain ε and its elastic part ε^{el} and plastic part ε^{pl} over the normalized radius with $r = \sqrt{x^2 + z^2}$ and $R = 12\,\mu m$ measured in the middle of the microwire.

*Corresponding author: kolja.zoller@kit.edu

The expanding dislocation loops produced near the surface in the initial step are leaving the continuum at the surfaces and moving accordingly to the stress field towards the center forming a pile-up. Accordingly, the piled-up total dislocation density consists mainly of geometrically necessary dislocation (GND) density. Due to the orientation of the slip systems and loading case, the screw part plays with a percentage of 78.8 % of the GNDs a dominant role.

The total strain has a linear profile over the radius. The resulting plastic strain is nearly constant near the surface and decreases from a breaking point linear towards the center in the same manner as the total strain. The position of the break point correlates with the change in the dislocation density. The elastic strain and therefore the shear stress is almost zero near the center and increase linear from the break point towards the surface with the same gradient as the total strain.

3 Discussion

With the critical thickness theory (CTT) there are analytical studies on this topic [3]. When the strain reaches a critical state, the area under the elastic strain curve remains constant in the following. The qualitative distribution found by CTT is identical to the simulation results in this contribution. For the given load even the quantitative distribution is similar except for a constant higher dislocation production by a factor of one third. This is due to the three-dimensional consideration with an increasing influence over the radius since each element has the same weight but the considered area increase with the radius.

One important point is that we wouldn't expect such a torsion behavior showing the plastic plateau for a classical continuum approach. However, the flow terms of the CDD formulation enable the motion of the dislocation density produced near the surface into the center and therefore the plastification of the material with a local stress smaller than the critical value.

Acknowledgments

The financial support for this work in the context of the DFG research group FOR1650 'Dislocation based Plasticity' as well as the support by the European Social Fund and the state Baden-Wuerttemberg is gratefully acknowledged. This work was performed on the computational resource ForHLR II funded by the Ministry of Science, Research and the Arts Baden-Württemberg and DFG.

References

[1] N. A. Fleck, G. M. Muller, M. F. Ashby, and J. W. Hutchinson. Strain Gradient Plasticity: Theory and Experiment. *Acta Metallurgica et Materialia* 42(2) (1994), pp. 475–487.

[2] T. Hochrainer, S. Sandfeld, M. Zaiser, and P. Gumbsch. Continuum dislocation dynamics: towards a physical theory of crystal plasticity. *Journal of the Mechanics and Physics of Solids* 63 (2014), pp. 167–178.

[3] D. Liu, X. Zhang, Y. Li, and D. J. Dunstan. Critical thickness phenomenon in single-crystalline wires under torsion. *Acta Materialia* 150 (2018), pp. 213–223.

[4] S. Schmitt, M. Stricker, P. Gumbsch, and K. Schulz. A mechanism-based homogenization of a dislocation source model for bending. *Acta Materialia* 164 (2019), pp. 663–672.

[5] K. Schulz, M. Sudmanns, and P. Gumbsch. Dislocation-density based description of the deformation of a composite material. *Modelling and Simulation in Materials Science and Engineering* 25(6) (2017), p. 064003.

[6] K. Schulz, L. Wagner, and C. Wieners. A mesoscale continuum approach of dislocation dynamics and the approximation by a Runge-Kutta discontinuous Galerkin method. *International Journal of Plasticity* 120 (2019), pp. 248–261.

[7] K. Zoller and K. Schulz. A bottom-up continuum approach of crystal plasticity for the analysis of fcc microwires under torsion. *Proceedings in Applied Mathematics and Mechanics* PAMM28 (2019), 10.1002/pamm.201900032.

**Proceedings of the 8th GACM Colloquium on Computational Mechanics
for Young Scientists from Academia and Industry
August 28–30, 2019 in Kassel, Germany**

A phase-field model for mixed-mode fracture

Meng Fan * [1,2], Thomas Wick[2] and Yan Jin[1]

[1]State Key Laboratory of Petroleum Resources and Prospecting, China University of Petroleum, Beijing, China
[2]Institut für Angewandte Mathematik, Leibniz Universität Hannover, Welfengarten 1, 30167 Hannover, Germany

Abstract. The goal of this work is to incorporate a directional strain energy splitting method into a monolithic phase-field model for mixed-mode fracture propagation. Failure of rocks is always accompanied by the propagation of mixed-mode fractures. Some recent studies have incorporated mixed-mode fracture propagation criterion to phase-field models. But these new models have the shortcomings of being not physically sound or not numerically stable. And they are all solved with staggered scheme. In this work, an existing energy splitting method for masonry-like material is modified and incorporated into the phase-field model to account for mixed-mode fractures. A fully-monolithic scheme is used to solve the model. A primal-dual active set method, which is a semi-smooth Newton approach is utilized to treat fracture irreversibility. Mixed-mode fracture tests are carried out, and the results of the new model are compared to those of existing models.

1 Introduction

In classic fracture mechanics, three fundamental modes of fractures are defined. They are termed as tensile (mode-I), in-plane shear (mode-II) and anti-plane shear (mode-III) [2]. But the fracture we deal with in reality is mostly mixed-mode. For example, mode-I-II fracture propagation is very common in rocks under compression. A modified G-criterion for mode-I-II fracture propagation is proposed in [10]. In recent studies, this criterion is incorporated into the phase-field fracture model by splitting the crack driving energy into mode-I and mode-II parts. More specifically, the crack driving stress σ^+ is splitted into σ_I^+ and σ_{II}^+. In [13], the energy splitting method proposed in [9] is modified so that the first and second terms of σ^+ correspond to σ_I^+ and σ_{II}^+ respectively. But this method overestimates the maximum force response when mode-I loading is dominant. More physically-sound splitting methods are proposed in [12], [11] and [3], where tension-compression asymmetry normal to the fracture surface is fulfilled explicitly and the fracture surface is considered as frictionless. But in our experiments, these models are numerically unstable. In [4], a splitting method for masonry-like material is derived based on structured deformation theory under principal strain coordinates. This method has a similar formulation to [12] and [11], but is more stable. However, it only accounts for mode-I fracture. Inspired by [3], the splitting method proposed in [4] is modified in this work to account for mode-I-II fractures.

2 Governing equations for a mixed-mode phase-field fracture model

In [13], the modified G-criterion for mixed-mode fracture propagation is incorporated into the thermodynamically consistent phase-field model proposed in [9]. The formulation reads: Find displacements $u \in V$ and a phase-field variable $\varphi \in W_{in}$ such that at each incremental step:

$$\left(\left((1-\kappa)\,\varphi^2+\kappa\right)\left(\sigma_I^+(u)+\sigma_{II}^+(u)\right),e(w)\right)+\left(\sigma^-(u),e(w)\right)=0 \quad \text{for all admissible } w, \tag{1}$$

$$(1-\kappa)\left(\varphi\left(\frac{\sigma_I^+(u)}{G_{Ic}}+\frac{\sigma_{II}^+(u)}{G_{IIc}}\right):e(u),\psi\right)+\left(\frac{1}{\epsilon}(\varphi-1,\psi)+\epsilon(\nabla\varphi,\nabla\psi)\right)\geq 0 \quad \text{for all admissible } \psi. \tag{2}$$

Here, σ and e denote stress and strain respectively. ϵ is the characteristic length scale of smeared fracture. κ is a small numerical parameter to prevent singularity in Jacobian matrix. w and ψ are test functions for u and φ. G_{Ic} and G_{IIc} are mode-I and mode-II critical energy release rates. Finally, we denote L^2 scalar product with $(A,B) := (A,B)_B := \int_B A : B dx$

*Corresponding author: 2016312016@student.cup.edu.cn

3 Stress splitting for mixed-mode phase-field fracture model

In [13], σ_I^+ and σ_{II}^+ are determined as the first and second terms of the σ^+ in [9]. This splitting method can capture the wing crack geometry in uniaxial compression test by suppressing the early-stage propagation of shear cracks, but it overestimates the maximum force response under tension-dominant loading.

In [4], a splitting method is derived based on structural strain theory under principal strain coordinate. In 2D case, Let $\boldsymbol{p1}$ denotes the direction of eigenvector corresponding to the most-positive eigenvalue. And $\boldsymbol{p2}$ denotes the direction of the other eigenvector. The method can be described in the strain form:

$$e^+ = \begin{cases} \begin{pmatrix} e_{p1} & 0 \\ 0 & e_{p2} \end{pmatrix} & \text{if } e_{p2} > 0, \\ \begin{pmatrix} e_{p1} + \nu e_{p2} & 0 \\ 0 & 0 \end{pmatrix} & \text{if } e_{p2} \le 0 \text{ and } e_{p1} + \frac{\lambda}{\lambda+2\mu} e_{p2} > 0, \\ 0 & \text{if } e_{p1} + \frac{\lambda}{\lambda+2\mu} e_{p2} \le 0. \end{cases} \tag{3}$$

This splitting method can capture the tensile fracture geometry under compression loading [5]. But it does not account for mixed-mode fractures.

Therefore, we do a heuristic modification to Freddi's splitting method. More specifically, the reference frame is changed from principal strain coordinate to local crack surface coordinate. In 2D case, let $\boldsymbol{n}$ and $\boldsymbol{s}$ denote the directions normal and tangential to the crack surface. The method can be described as:

$$e_I^+ = \begin{cases} \begin{pmatrix} e_{nn} & 0 \\ 0 & e_{ss} \end{pmatrix} & \text{if } e_{nn} + \frac{\lambda}{\lambda+2\mu} e_{ss} > 0 \text{ and } e_{ss} > 0, \\ \begin{pmatrix} e_{nn} + \nu e_{ss} & 0 \\ 0 & 0 \end{pmatrix} & \text{if } e_{nn} + \frac{\lambda}{\lambda+2\mu} e_{ss} > 0 \text{ and } e_{ss} \le 0, \\ 0 & \text{if } e_{nn} + \frac{\lambda}{\lambda+2\mu} e_{ss} \le 0, \end{cases} \tag{4}$$

$$e_{II}^+ = \frac{1}{2} \begin{pmatrix} 0 & e_{ns} \\ e_{sn} & 0 \end{pmatrix}. \tag{5}$$

As for the crack surface direction, we refer to [3] to solve an additional local dissipation maximization problem. Let $\boldsymbol{\theta}$ denote the angle between $\boldsymbol{n}$ and $\boldsymbol{p1}$, we define the normalized crack driving energy as:

$$\boldsymbol{F(u,\theta)} = \left(\frac{\boldsymbol{\sigma_I^+(u,\theta)}}{\boldsymbol{G_{Ic}}} + \frac{\boldsymbol{\sigma_{II}^+(u,\theta)}}{\boldsymbol{G_{IIc}}} \right) \boldsymbol{:} \boldsymbol{e(u)} \tag{6}$$

then the normal direction of crack surface can be determined by:

$$\boldsymbol{\theta_n} = \mathrm{Arg}\{ \max_{\boldsymbol{\theta} \in [0, \frac{\pi}{2})} \boldsymbol{F(u,\theta)} \}. \tag{7}$$

After simple derivation, we can get:

$$\frac{\boldsymbol{\partial F(u,\theta)}}{\boldsymbol{\partial \theta}} = \begin{cases} \boldsymbol{\mu (e_{p1} - e_{p2})^2 \left(\frac{1}{G_{IIc}} - \frac{2}{G_{Ic}} \right) \sin 4\theta} & \text{if } e_{nn} + \frac{\lambda}{\lambda+2\mu} e_{ss} > 0 \text{ and } e_{ss} > 0, \\ \boldsymbol{\mu (e_{p1} - e_{p2})^2 \left(\frac{1}{G_{IIc}} - \frac{1}{G_{Ic}} \right) \sin 4\theta} & \\ \boldsymbol{- \frac{(\lambda + 2\mu)\left(e_{p1}^2 - e_{p2}^2 \right)}{G_{Ic}} \sin 2\theta} & \text{if } e_{nn} + \frac{\lambda}{\lambda+2\mu} e_{ss} > 0 \text{ and } e_{ss} \le 0, \\ \boldsymbol{\frac{\mu (e_{p1} - e_{p2})^2}{G_{IIc}} \sin 4\theta} & \text{if } e_{nn} + \frac{\lambda}{\lambda+2\mu} e_{ss} \le 0. \end{cases} \tag{8}$$

In all three situations, the local maximum points of $\boldsymbol{F(u,\theta)}$ are located at $\boldsymbol{\theta = 0}$ or $\boldsymbol{\theta = \frac{\pi}{4}}$ or both. Therefore, instead of implementing complicated search algorithm, we can determine the value of $\boldsymbol{\theta_n}$ by comparing $\boldsymbol{F(u,0)}$ and $\boldsymbol{F(u,\frac{\pi}{4})}$ and choose whichever maximize $\boldsymbol{F(u,\theta)}$.

4 Numerical schemes

The nonlinear quasi-monolithic displacement/phase-field system presented in the Sections 2 and 3 is solved with Newton's method and line search algorithms. The constraint minimization problem is treated with a semi-smooth Newton method (i.e., a primal-dual active set method). Both methods are combined in one single loop leading to a robust and efficient iteration scheme that is outlined in [7]. Within Newton's loop we solve the linear equation systems with GMRES solvers with a diagonal block-preconditioning AMG. The overall implementation is based on deal.II [1]; for details we refer to [6].

5 Numerical simulations

To demonstrate the capabilities of different energy splitting methods in capturing mixed-mode fracture geometry, we use the experiment in [8] as benchmark and compare the results of our method with those of Miehe's [9], Zhang's [13] and Freddi's [4] methods.

The sample is a 104 mm $\times$ 80 mm rectangle marble plate with a notch at the center. The notch is 20 mm in length and 1 mm in width and is inclined at 45° to the horizontal plane. Young's modulus $\boldsymbol{E} = 63.5$ GPa [8], Poisson's ratio $\boldsymbol{\nu} = 0.21$, and plane stress setting is used. Mode-I critical energy release rate $\boldsymbol{G_{Ic}} = 11$ J/m^2 and mode-II critical energy release rate $\boldsymbol{G_{IIc}} = 110$ J/m^2 [13]. Two uniform-refined meshes, with 7952 and 30272 cells respectively, are used in the simulation. The minimum mesh sizes $\boldsymbol{h}$ are 1.17 mm and 0.63 mm in two cases. Characteristic length $\boldsymbol{\epsilon = 2h}$. Numerical parameter $\boldsymbol{\kappa} = 10^{-10}$. Newton solver tolerance is set as 10^{-6}. The sample is subjected to displacement-controlled uniaxial compression loading at the top boundary with the time step size $\boldsymbol{\Delta t} = 10^{-3}$ s. The crack geometries using the fine mesh are shown in Figure 1. According to [8]. The crack geometry should

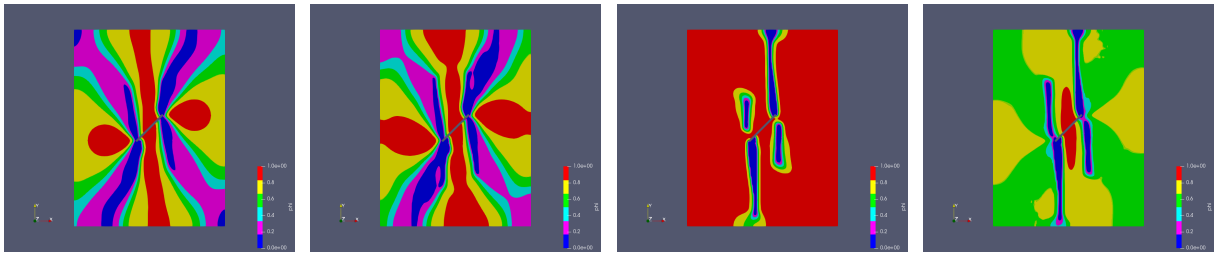

(a) Miehe's splitting method **(b)** Zhang's splitting method **(c)** Freddi's splitting method **(d)** Our new splitting method

Figure 1. Simulated crack geometries using four splitting methods.

have two features: (a) tensile fractures sub-parallel to the loading direction, which are typical mode-I fractures; (b) "X-shape" shear bands, which are typical mode-II fractures.

It is obvious that only our new splitting method can capture both features. The load-displacement curves on the upper boundary is shown in Figure 2. All four splitting methods are numerically stable in both meshes. The simulation continues until the load starts to decrease, when cracks reach the boundary. And the load-displacement curves in two meshes agree well with each other in the early stage. However, the maximum load response in the finer mesh is 25% - 30% higher than that in the coarser mesh. This phenomenon has also been observed in [14].

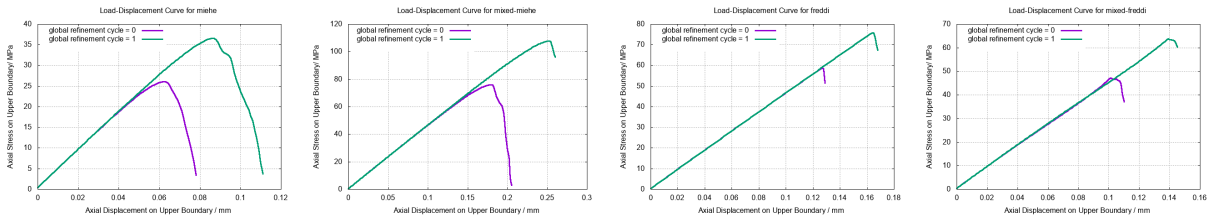

(a) Miehe's splitting method **(b)** Zhang's splitting method **(c)** Freddi's splitting method **(d)** Our new splitting method

Figure 2. Load-displacement curves using four splitting methods.

Acknowledgments

This work has been supported by the German Research Foundation, Priority Program 1748 (DFG SPP 1748) in the subproject *Structure Preserving Adaptive Enriched Galerkin Methods for Pressure-Driven 3D Fracture Phase-Field Models* with the project No. 392587580. The authors are also grateful for the financial support from the program of China Scholarships Council (No. 201806440069) and National Natural Science Foundation of China (No. 51490651).

References

[1] Daniel Arndt, Wolfgang Bangerth, Denis Davydov, Timo Heister, Luca Heltai, Martin Kronbichler, Matthias Maier, Jean-Paul Pelteret, Bruno Turcksin, and David Wells. The deal. II library, version 8.5. *Journal of Numerical Mathematics* 25.3 (2017), pp. 137–145.

[2] Barry Kean Atkinson. *Fracture mechanics of rock*. Elsevier, 2015. ISBN: 1483292746.

[3] Eric C. Bryant and WaiChing Sun. A mixed-mode phase field fracture model in anisotropic rocks with consistent kinematics. *Computer Methods in Applied Mechanics and Engineering* 342 (2018), pp. 561–584. ISSN: 00457825.

[4] Francesco Freddi and Gianni Royer-Carfagni. Regularized variational theories of fracture: A unified approach. *Journal of the Mechanics and Physics of Solids* 58.8 (2010), pp. 1154–1174. ISSN: 00225096.

[5] Francesco Freddi and Gianni Royer-Carfagni. Variational fracture mechanics to model compressive splitting of masonry-like materials. *Annals of Solid and Structural Mechanics* 2.2-4 (2011), pp. 57–67. ISSN: 1867-6936.

[6] Timo Heister and Thomas Wick. *Parallel solution, adaptivity, computational convergence, and open-source code of 2d and 3d pressurized phase-field fracture problems*.

[7] Timo Heister, Mary F. Wheeler, and Thomas Wick. A primal-dual active set method and predictor-corrector mesh adaptivity for computing fracture propagation using a phase-field approach. *Computer Methods in Applied Mechanics and Engineering* 290 (2015), pp. 466–495. ISSN: 00457825.

[8] Huang Jiefan, Chen Ganglin, Zhao Yonghong, and Wang Ren. An experimental study of the strain field development prior to failure of a marble plate under compression. *Tectonophysics* 175.1-3 (1990), pp. 269–284. ISSN: 00401951.

[9] Christian Miehe, Fabian Welschinger, and Martina Hofacker. Thermodynamically consistent phase-field models of fracture: Variational principles and multi-field FE implementations. *International Journal for Numerical Methods in Engineering* 83.10 (2010), pp. 1273–1311.

[10] B Shen and O Stephansson. Modification of the G-criterion for crack propagation subjected to compression. *Engineering Fracture Mechanics* 47.2 (1994), pp. 177–189.

[11] Christian Steinke and Michael Kaliske. A phase-field crack model based on directional stress decomposition. *Computational Mechanics* 55 (2018), p. 1017. ISSN: 0178-7675.

[12] Michael Strobl and Thomas Seelig. A novel treatment of crack boundary conditions in phase field models of fracture. *PAMM* 15.1 (2015), pp. 155–156. ISSN: 16177061.

[13] Xue Zhang, Scott W. Sloan, Chet Vignes, and Daichao Sheng. A modification of the phase-field model for mixed mode crack propagation in rock-like materials. *Computer Methods in Applied Mechanics and Engineering* 322 (2017), pp. 123–136. ISSN: 00457825.

[14] Xue Zhang, Chet Vignes, Scott W. Sloan, and Daichao Sheng. Numerical evaluation of the phase-field model for brittle fracture with emphasis on the length scale. *Computational Mechanics* 59.5 (2017), pp. 737–752. ISSN: 0178-7675.

**Proceedings of the 8th GACM Colloquium on Computational Mechanics
for Young Scientists from Academia and Industry
August 28–30, 2019 in Kassel, Germany**

Load Optimisation for Damage Reduction and Fracture Prevention

Fabian Guhr * [1] and Franz-Joseph Barthold[1]

[1]Structural Mechanics, TU Dortmund University, Dortmund, Germany

Abstract. In this paper, load optimisation is applied to air bending with the aim of reducing the damage accumulation within the critical domain of the forming process, and as such preventing fracture. A framework for load optimisation with the commercial software Abaqus is provided. Modelling the forces with polynomials and the load increments with B-splines, respectively, allows an easy implementation of load optimisation.

Introduction

The cause for macroscopic fracture is the accumulation of damage within the material. Damage is typically associated to voids and micro cracks at grain level. To prevent fracture at the macroscopic scale, damage accumulation has to be controlled and reduced.

In [6], damage was investigated for different forming processes. For example in air bending, damage can be reduced by superimposing compressive stresses in the critical area, i.e the area opposite where the tool is in contact with the sheet. Due to the high triaxiality values in the outer boundary of the sheet, i.e. a tensile dominated stress state. Damage accumulation in this region leads to the most critical point of fracture during the forming process. To circumvent failure and reduce damage accumulation, the authors of [6] developed the so-called process of *elastomer bending*. There, an elastomer cushion is placed into the die, such that the resulting compressive strains lead to a reduced damage growth by reducing the triaxiality, and thereby the stress state in the critical area.

To optimise the process numerically, the elastomer cushion, which would generate pressure forces as reaction forces, is replaced with prescribed nodal forces at the corresponding boundary. By using mathematical optimisation with the resulting external loads as the design, a new optimal load can be generated. Furthermore, by optimising the load amplitudes for the nodal loads, the load application can further be optimised to control the triaxiality during the forming process.

1 Theoretical framework

For the implementation of load optimisation, the external forces in the equilibrium condition within the finite element (FE) formulation, i.e.

$$\mathbf{R} = \mathbf{F}^{\text{int}} - \mathbf{F}^{\text{ext}} = \mathbf{K} \cdot \mathbf{u} - \lambda \mathbf{f} = \mathbf{0}, \tag{1}$$

are controlled. This leads to the following two possible adaptations:

a) load optimisation of external forces $\mathbf{f}$

b) load-path optimisation of the scaling factor for the numerical increments λ.

*Corresponding author: fabian.guhr@tu-dortmund.de ORCID iD: 0000-0002-3341-0503

The idea for optimisation of external loads (a) has been presented in [2] and [3]. There, the external loads were prescribed by a polynomial function

$$\mathbf{f} = a_n \mathbf{x}^n + a_{n-1}\mathbf{x}^{n-1} + \cdots + a_1 \mathbf{x} + a_0, \tag{2}$$

with the coefficients a_i of the polynomial as the design variables within the optimisation.

To further optimise the process beyond the concept of *elastomer bending*, the load application over time can also be optimised via the load scaling parameter λ (b). To model a more applicable and arbitrary load-path, B-splines are chosen to define the scaling parameter over the course of the forming process.

B-splines are curves generated from multiple polynomials and defined by control points $\boldsymbol{C}_i$. As such, a point $\mathbf{b}(t) = \lambda(t)$ on the B-spline at $t \in [0, 1]$ is defined as

$$\mathbf{b}(t) = \sum_{i=0}^{n} \boldsymbol{C}_i N_i^d(t), \tag{3}$$

with the basic functions N_i, the number of control points n and the degree of the curve d. Additionally, a knot vector $\mathbf{T}$ has to be defined

$$\mathbf{T} = \{t_0, t_1, \ldots, t_m\}, \tag{4}$$

with $m = d + n + 1$. In addition, the first $d + 1$ knots need to be equal to zero, as well as the last $p + 1$ to be equal to one. The remaining t_i have to fulfil the condition $t_i \leq t_{i+1}$. The basis functions N_i are

$$N_i^j(t) = \begin{cases} 1, \text{for } t \in [t_i, t_{i+1}] \\ 0, \text{else} \end{cases} \tag{5}$$

when $j = 0$. Otherwise, the basis functions result in

$$N_i^j(t) = \frac{t - t_i}{t_{i+j} - t_i} N_i^{j-1}(t) + \frac{t_{i+j+1} - t}{t_{i+j+1} - t_{i+1}} N_{i+1}^{j-1}(t), \tag{6}$$

where $j = 1, 2, \ldots, d$. Generally, the de-Boor algorithm is used for efficient calculation of the above basis functions and therefore the B-spline. For more information regarding B-splines, c.f. [1].

2 Numerical implementation

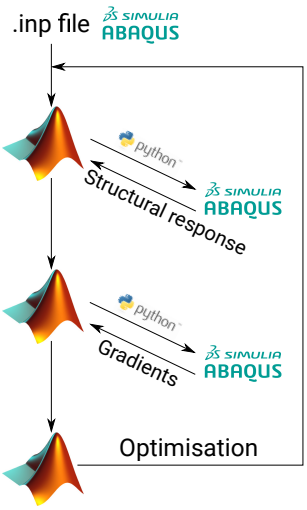

Figure 1. The overall framework for the optimisation.

The main aspect of this work is the implementation of a optimisation framework for the above case with the commercial software Abaqus in mind. The two main advantages are the direct comparibility to the results obtained in [6], as well as the contact algorithms within Abaqus, which are a necessity for the forming process at hand. For the simulation, an elasto-plastic model without damage mechanics is used. Instead, the triaxiality is used to constrain the damage growth, c.f. [4, 5].

For the framework, the python interface, which is provided by Abaqus, is used to extract the data from the output data base (odb) as well as transferring that data to Matlab for further processing. The mathematical optimisation, i.e. Sequentially Quadratic Programming (SQP), is done within Matlab. This requires the additional information of gradients for the objective function and constraints. These are generated by perturbing the design variables and calculating the numerical gradients with additional FEM simulations.

To transfer data back to the Abaqus simulations, the input file is edited with the newly generated loads or amplitude information. For the external nodal loads, this requires to define so-called *sets* within Abaqus to define the areas of interest, i.e. objective function, constraints and the area where nodal forces are applied. With this defined, the necessary information can be extracted and the exact nodal forces mapped to their respective nodes. For the load-path optimisation, tabular amplitudes are chosen. By exchanging the predefined data with the optimised B-spline data, new load-paths can be defined for the Abaqus simulation.

2.1 Optimisation problem

The main idea behind the optimisation definition is to generate a structure that is as close to the initial shape as possible. This shape is captured with the initial deformation field $\mathbf{U}^{\text{pre}}$ and compared to the current shape $\mathbf{U}(\mathbf{s})$ generated by the optimisation. To minimise the difference between those two results, the objective function $\mathfrak{J}$ is chosen to be of least square type

$$\begin{aligned} \underset{\mathbf{s}}{\text{minimise}} \quad & \mathfrak{J}(\mathbf{s}) = \|\mathbf{U}(\mathbf{s}) - \mathbf{U}^{\text{pre}}\|_2^2 \\ \text{subject to} \quad & \eta(\mathbf{s}) \leq \eta^{\max}, \end{aligned} \tag{7}$$

where $\mathbf{s}$ the vector of design variables, i.e. either the coefficients of the polynomial a_i for the load optimisation, or the vector of controls points $\mathbf{C}$ for the load-path optimisation. To reduce the damage, the triaxiality η is chosen as the constraint. The triaxiality η is defined as

$$\eta = \frac{\sigma_h}{\sigma_{vM}}, \tag{8}$$

where σ_{vM} are the von Mises stresses and

$$\sigma_h = \frac{I_1}{3} = \frac{\text{tr}(\boldsymbol{\sigma})}{3} \tag{9}$$

as the hydrostatic stresses. To constrain the triaxiality, and to compare the results to the ones obtained in [6], the critical triaxiality $\eta^{\max}$ is set to $\eta^{\max} = 0.48$.

The constraint for the optimisation problem in Eq. (7) is applied differently for the two types of optimisations at hand. In the case of external load optimisation (a), the triaxiality is only controlled at the end of the simulation and as such, the triaxiality can exceed the threshold during the simulation. To furthermore control the triaxiality during the process, the load-path optimisation (b) controls the triaxiality at each load-step during the optimisation.

3 Results

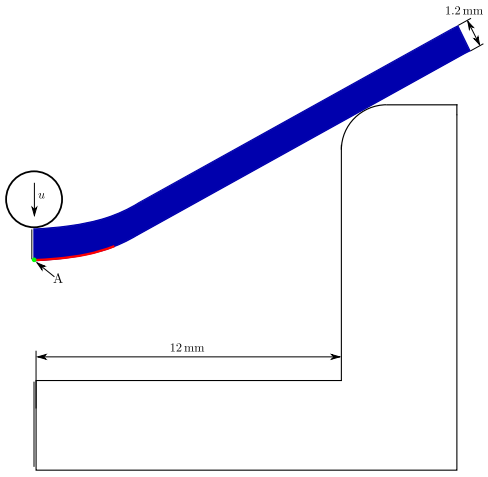

Figure 2. The simulation and optimisation setup. The deformable sheet is depicted in blue and the loads are applied at the red boundary.

The process to be optimised is depicted in Fig. 2. The red area is used to apply the necessary external forces in x- and y-direction, such that a resulting force in any of the two directions is possible. This area corresponds to the area where the elastomer cushion in [6] generates the necessary reaction forces. Node A, depicted by the small green dot, is later on used for evaluating the optimal load-path. Currently, both optimisations are done separately, as well as the load-path optimisation only supporting one node at a time.

For the external load optimisation, a small constraint is added, wherein the loads at point A shall remain perpendicular to the surface, which results in the condition

$$\mathbf{f}_x(\boldsymbol{x} = A) = 0 \rightarrow a_0^x = 0. \tag{10}$$

The results for the external load optimisation are presented in Fig. 3. The left side shows the initial, unaltered deformation and the corresponding triaxiality state. Applying the optimised loads, the triaxiality can be reduced below the threshold of $\eta^{\max}$ in a certain area around the applied forces. Compared to the results obtained in [6], the triaxiality around the area of interest shows the same characteristic triaxiality reduction.

With these optimised loads at hand, the load-path is then optimised for node A, see Fig. 2, since the triaxiality exceeds the imposed threshold due to the linear load-path during the forming process, see the blue curve in Fig. 4. Optimisation of the scaling parameter λ generates the non-linear load-path which then allows constraining the triaxiality at each time step and subsequently the critical value is never exceeded, see the red curve in Fig. 4.

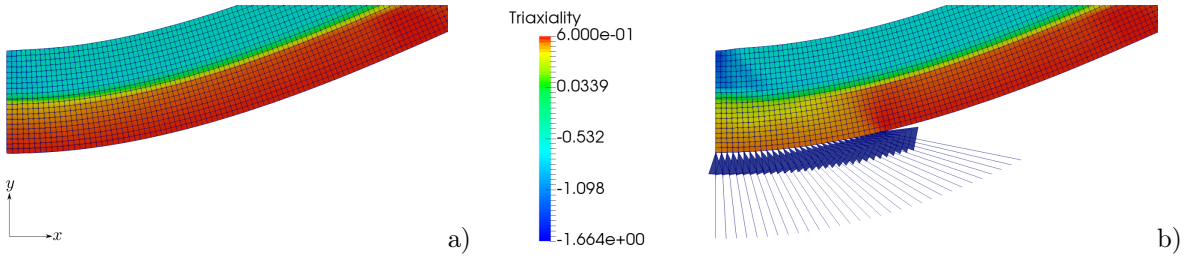

Figure 3. The triaxiality distribution in the deformed sheet. The left graph shows the initial shape with no additional loads, the right the sheet with the optimised loads.

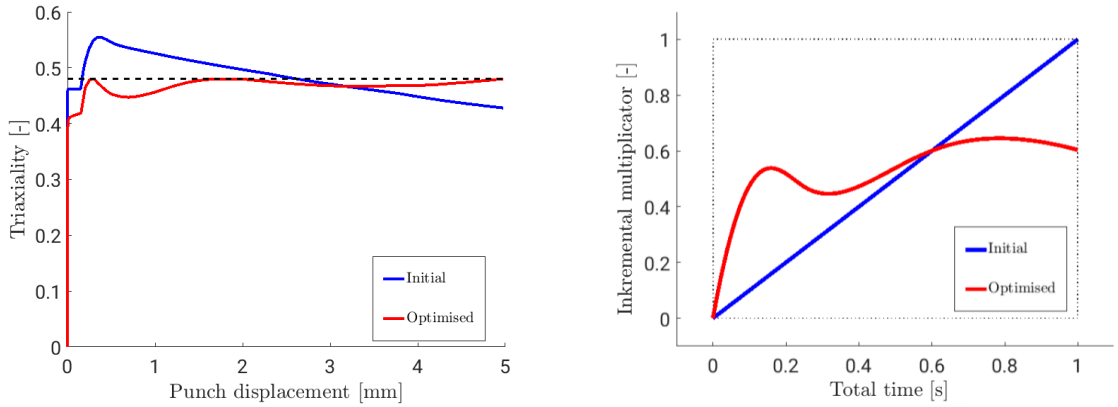

Figure 4. Results from the load-path optimisation. The triaxiality over the punch displacements on the left and the corresponding optimised load-path. The values are for node A of Fig. 2.

Acknowledgments

Funding of projects C05 within the Collaborative Research Centre TRR 188 — Projektnummer 278868966 "Damage controlled forming processes" by the Deutsche Forschungsgemeinschaft (DFG, German Research Foundation) is gratefully acknowledged.

References

[1] Gerald Farin. 8 - B-Spline Curves. In: *Curves and Surfaces for CAGD (Fifth Edition)*. Ed. by Gerald Farin. Fifth Edition. The Morgan Kaufmann Series in Computer Graphics. San Francisco: Morgan Kaufmann, 2002, pp. 119 –146.

[2] Jan Liedmann and Franz-Joseph Barthold. Sensitivity Analysis of Nonlinear Structural Response regarding Geometry and External Loads. *PAMM* 18.1 (2018), e201800135.

[3] Jan Liedmann and Franz-Joseph Barthold. Sensitvity Analysis of elastoplastic Structural Response regarding Geometry and External Loads. *Proc. ECCM6/ECFD7* (2018), pp. 1308 –1319.

[4] Rickmer Meya, Christian Löbbe, and A. Erman Tekkaya. Stress State Control by a Novel Bending Process and its Effect on Damage Evolution. *Joint MSEC-NAMRC-Manufacturing USA* 2 (2018).

[5] Christian C. Roth and Dirk Mohr. Ductile fracture experiments with locally proportional loading histories. *International Journal of Plasticity* 79 (2016), pp. 328 –354. ISSN: 0749-6419.

[6] A. Erman Tekkaya, Nooman Ben Khalifa, Oliver Hering, Rickmer Meya, Sebastian Myslicki, and Frank Walther. Forming-induced damage and its effects on product properties. *CIRP Annals* 66.1 (2017), pp. 281 –284. ISSN: 0007-8506.

**Proceedings of the 8th GACM Colloquium on Computational Mechanics
for Young Scientists from Academia and Industry
August 28–30, 2019 in Kassel, Germany**

A phase-field fracture model based on Mindlin's strain gradient theory

Resam Makvandi[1] and Daniel Juhre * [1]

[1]Institute of Mechanics, Faculty of Mechanical Engineering, Otto von Guericke University Magdeburg, Universitätsplatz 2, 39106 Magdeburg, Germany.

Abstract. The classical theory of continuum mechanics utilized in the conventional phase-field fracture models suffers from singular stress fields at the crack front. Although the so-called degradation function regularizes the problem under consideration, the singular behavior is still present in the mathematical model and therefore exerts a notable effect on the final results. Strain gradient models do not show the mentioned singular behavior. Therefore, in this contribution, the integration of these models into the phase-field modelling of fracture is proposed. It has been shown that the utilization of these models helps in mitigating the problem of stress singularities.

Introduction

The classical continuum mechanics theories are originally supposed to determine deformations in ranges from millimeter to meter, the so-called macroscopic scales. In fact, these models are approximations of physical systems neglecting the underlying microstructure [3]. For instance, the appearance of local singularities at the crack tips (or more broadly, in the presence of point and line loads) is one of the known limitations of the classical continuum mechanics theory. Generalizing these models by introducing additional kinematic terms to consider the underlying microstructure effects at macroscopic levels is one way of overcoming the already mentioned problems. Mindlin's theory of elasticity with microstructures [5] is one of the well-known works in this area. This broad-spectrum framework simplifies to strain gradient elasticity theories by introducing the relation between the micro-deformations and gradients of the macro-deformations. In gradient elasticity, the strain energy function contains both the strain terms and their gradients, which leads to stresses depending on higher-order derivatives of the displacement field. One of the motivations of proposing the gradient elasticity theory for solid mechanics is to overcome the problem of singular fields in the vicinity of crack fronts and dislocation cores [4].

1 Governing equations

In this contribution, the combination of Mindlin's based strain gradient elasticity models and phase-field fracture mechanics is proposed. In this section, we will first derive the governing equations of the gradient elasticity and then will use these equations in the phase-field modelling of fracture.

1.1 Strain gradient elasticity

In the following, only infinitesimal deformations of the continuum are assumed. Considering macroscopic and microscopic deformations, based on the theory of elasticity with microstructures [5], the strain energy density can be defined: (the contractions between tensors are defined as in [2])

$$W = \frac{1}{2}\,\boldsymbol{\varepsilon} \cdot\cdot \overset{\langle 4\rangle}{\mathbf{C}} \cdot\cdot\, \boldsymbol{\varepsilon} + \frac{1}{2}\,\boldsymbol{\gamma} \cdot\cdot \overset{\langle 4\rangle}{\mathbf{B}} \cdot\cdot\, \boldsymbol{\gamma} + \frac{1}{2}\,\boldsymbol{\kappa} \cdots \overset{\langle 6\rangle}{\mathbf{A}} \cdots \boldsymbol{\kappa} + \boldsymbol{\kappa} \cdots \overset{\langle 5\rangle}{\mathbf{D}} \cdot\cdot\, \boldsymbol{\gamma} + \boldsymbol{\varepsilon} \cdot\cdot \overset{\langle 5\rangle}{\mathbf{F}} \cdots \boldsymbol{\kappa} + \boldsymbol{\varepsilon} \cdot\cdot \overset{\langle 4\rangle}{\mathbf{G}} \cdot\cdot\, \boldsymbol{\gamma}, \tag{1}$$

*Corresponding author: daniel.juhre@ovgu.de ORCID iD: 0000-0001-8997-3818

with $\overset{\langle 6\rangle}{\mathbf{A}}$, $\overset{\langle 4\rangle}{\mathbf{B}}$, $\overset{\langle 4\rangle}{\mathbf{C}}$, $\overset{\langle 5\rangle}{\mathbf{D}}$, $\overset{\langle 5\rangle}{\mathbf{F}}$, and $\overset{\langle 4\rangle}{\mathbf{G}}$ being the constitutive tensors where the number in brackets defines the order of the tensor. In Eq. (1), $\boldsymbol{\varepsilon}$ and $\boldsymbol{\gamma}$ denote the linear strain tensor and the relative deformation, respectively, and are defined as

$$\boldsymbol{\varepsilon} := \nabla_{\mathrm{sym}}\mathbf{u} = \frac{1}{2}\left(\nabla \otimes \mathbf{u} + \mathbf{u} \otimes \nabla\right) = \frac{1}{2}\left(u_{i,j} + u_{j,i}\right) = \varepsilon_{ij}, \qquad \boldsymbol{\gamma} = \left(\nabla\mathbf{u} - \boldsymbol{\varphi}\right), \tag{2}$$

where $\mathbf{u}$ is the displacement field and $\boldsymbol{\varphi}$ represents the microscopic deformations. Moreover, we define the gradient of macroscopic deformation as

$$\boldsymbol{\kappa} := \nabla\nabla\mathbf{u} = u_{i,jk} = \kappa_{ijk}. \tag{3}$$

Assuming linear elasticity and centro-symmetric isotropic materials, Eq. (1) reduces to

$$\tilde{W} = a_1\left(\boldsymbol{\varepsilon}\cdot\cdot\mathbf{I}\right)^2 + a_2\,\boldsymbol{\varepsilon}\cdot\cdot\boldsymbol{\varepsilon} + a_3\left(\boldsymbol{\kappa}\cdot\cdot\mathbf{I}\right)\cdot\left(\boldsymbol{\kappa}\cdot\cdot\mathbf{I}\right) + a_4\,\mathbf{I}\cdot\cdot\boldsymbol{\kappa}\cdot\boldsymbol{\kappa}\cdot\cdot\mathbf{I} + a_5\left(\mathbf{I}\cdot\cdot\boldsymbol{\kappa}\right)\cdot\left(\mathbf{I}\cdot\cdot\boldsymbol{\kappa}\right) + a_6\,\boldsymbol{\kappa}\cdots\boldsymbol{\kappa} + a_7\,\boldsymbol{\kappa}\cdots\boldsymbol{\kappa}, \tag{4}$$

where $\mathbf{I}$ is the identity tensor and $a_1 \cdots a_7$ are (independent) material parameters. Equation (4) can be re-written in index notation as [6]

$$\tilde{W} = \frac{1}{2}\lambda\varepsilon_{ii}\varepsilon_{jj} + \mu\varepsilon_{ij}\varepsilon_{ij} + b_1\kappa_{iik}\kappa_{kjj} + b_2\kappa_{ijj}\kappa_{ikk} + b_3\kappa_{iik}\kappa_{jjk} + b_4\kappa_{ijk}\kappa_{ijk} + b_5\kappa_{ijk}\kappa_{kji}, \tag{5}$$

where λ and μ are the Lamé constants and $b_1 \cdots b_5$ are gradient material parameters. We define the stress $\boldsymbol{\sigma}$ (energy conjugate to $\boldsymbol{\varepsilon}$) and double stress $\boldsymbol{\tau}$ (energy conjugate to $\boldsymbol{\kappa}$) as

$$\boldsymbol{\sigma} := \frac{\partial\tilde{W}}{\partial\boldsymbol{\varepsilon}}, \qquad \sigma_{ij} := \lambda\varepsilon_{pp}\delta_{ij} + 2\mu\varepsilon_{ij} \tag{6}$$

$$\begin{aligned}\boldsymbol{\tau} := \frac{\partial\tilde{W}}{\partial\boldsymbol{\kappa}}, \qquad \tau_{ijk} = {} & \frac{1}{2}b_1\left(\delta_{jk}\,\kappa_{ppi} + 2\,\delta_{ij}\,\kappa_{kpp} + \delta_{ik}\,\kappa_{ppj}\right) + b_2\left(\delta_{jk}\,\kappa_{ipp} + \delta_{ik}\,\kappa_{jpp}\right) \\ & + 2\,b_3\,\delta_{ij}\kappa_{ppk} + 2\,b_4\,\kappa_{ijk} + b_5\left(\kappa_{kji} + \kappa_{kij}\right)\end{aligned} \tag{7}$$

To find the weak form, we now calculate the first variation of the work of the internal forces:

$$\delta\tilde{W}^{\mathrm{int}} = \int_\Omega \boldsymbol{\sigma}\cdot\cdot\,\delta\boldsymbol{\varepsilon}\,\mathrm{d}V + \int_\Omega \boldsymbol{\tau}\cdots\delta\boldsymbol{\kappa}\,\mathrm{d}V, \tag{8}$$

with $\delta\boldsymbol{\varepsilon} := \nabla_{\mathrm{sym}}(\delta\mathbf{u})$, and $\delta\boldsymbol{\kappa} := \nabla\nabla(\delta\mathbf{u})$. Applying the divergence theorem one time on the first term and two times on the second term of the the right-hand side gives us the necessary boundary terms,

$$\int_\Omega \boldsymbol{\sigma}\cdot\cdot\,\delta\boldsymbol{\varepsilon}\,\mathrm{d}V = -\int_\Omega \left(\nabla\cdot\boldsymbol{\sigma}\right)\cdot\delta\mathbf{u}\,\mathrm{d}V + \int_{\Gamma_1}\left(\boldsymbol{\sigma}\cdot\mathbf{n}\right)\cdot\delta\mathbf{u}\,\mathrm{d}A, \tag{9}$$

$$\begin{aligned}\int_\Omega \boldsymbol{\tau}\cdots\delta\boldsymbol{\kappa}\,\mathrm{d}V = {} & \int_\Omega \nabla^2\boldsymbol{\tau}\cdot\delta\mathbf{u}\,\mathrm{d}V + \int_{\Gamma_1}\Big[-\left(\nabla\cdot\boldsymbol{\tau}\right)\cdot\mathbf{n} + \nabla_s\cdot\mathbf{n}\,\boldsymbol{\tau}\cdot\cdot\,\left[\mathbf{n}\otimes\mathbf{n}\right] - \nabla_s\cdot\,\left[\boldsymbol{\tau}\cdot\mathbf{n}\right]^T\Big]\cdot\delta\mathbf{u}\,\mathrm{d}A \\ & + \int_{\Gamma_1}\left[\boldsymbol{\tau}\cdot\cdot\,\left[\mathbf{n}\otimes\mathbf{n}\right]\right]\cdot\delta\nabla_{\mathbf{n}}\mathbf{u}\,\mathrm{d}A + \int_\Xi\sum_e\left[\boldsymbol{\tau}\cdot\cdot\,\left[\mathbf{m}\otimes\mathbf{n}\right]\right]\cdot\delta\mathbf{u}\,\mathrm{d}L.\end{aligned} \tag{10}$$

In Eqs. (9) and (10), Ω represents the whole volume, Γ_1 the surface boundary and Ξ the union of the surface boundary intersection segments (a network of edges e). Moreover, $\mathbf{n}$ denotes the outer normal to the surface, $\mathbf{m}$ is the outward normal vector to Ξ and is perpendicular to $\mathbf{n}$. Finally, considering the work of the external forces and the principle of virtual work, the weak form becomes

$$\begin{aligned}&\delta\tilde{W}^{\mathrm{int}} - \delta\tilde{W}^{\mathrm{ext}} = 0, \\ &\int_\Omega \boldsymbol{\sigma}\cdot\cdot\,\delta\boldsymbol{\varepsilon}\,\mathrm{d}V + \int_\Omega \boldsymbol{\tau}\cdots\delta\boldsymbol{\kappa}\,\mathrm{d}V = \int_\Omega \mathbf{b}\cdot\delta\mathbf{u}\,\mathrm{d}V + \int_{\Gamma_1}\bar{\mathbf{t}}^1\cdot\delta\mathbf{u}\,\mathrm{d}A + \int_{\Gamma_1}\bar{\mathbf{t}}^2\cdot\delta\nabla_{\mathbf{n}}\,\mathbf{u}\,\mathrm{d}A, + \int_\Xi\bar{\mathbf{t}}^3\cdot\delta\mathbf{u}\,\mathrm{d}L.\end{aligned} \tag{11}$$

where $\mathbf{b}, \bar{\mathbf{t}}^1$, $\bar{\mathbf{t}}^2$ and $\bar{\mathbf{t}}^3$ are the vector of body forces, surface tractions, surface double tractions and edge tractions, respectively.

1.2 Strain gradient enhanced phase-field fracture model

We will consider the conventional fourth-order phase-field fracture model. The total energy of fracture can be represented by

$$\bar{W}_{\text{frac}}(\boldsymbol{\varepsilon}, \boldsymbol{\kappa}, s) = \int_\Omega \left[s^2\, \tilde{W} + \mathcal{G}_c \left(\frac{(1-s)^2}{4\epsilon} + \frac{1}{2}\epsilon |\nabla s|^2 + \frac{1}{4}\epsilon^3 \big(\Delta s\big)^2 \right) \right] \mathrm{d}V - \int_\Omega \mathbf{b} \cdot \mathbf{u}\, \mathrm{d}V, \tag{12}$$

where s is the phase-field parameter ($s = 1$ represents the intact material), $\mathcal{G}_c$ is the critical strain energy release rate, ϵ represents the length-scale parameter for the crack, and $g(s) = s^2$ is the so-called degradation function. In Eq. (12), the strain energy density of the gradient material $\tilde{W}$ (see Eqs. (4) and (5)) has replaced the classical linear elasticity strain energy density $\mathcal{W}_{\text{elas}} = \frac{1}{2}\lambda(\operatorname{tr}\boldsymbol{\varepsilon})^2 + \mu\boldsymbol{\varepsilon} \cdot\cdot\, \boldsymbol{\varepsilon}$.

Taking the first variations of Eq. (12) with respect to the displacement field and the phase-field parameter gives us the weak form of the problem at hand. Introducing the effective stresses $\boldsymbol{\sigma}_{\text{eff}} = s^2\boldsymbol{\sigma}$ and double stresses $\boldsymbol{\tau}_{\text{eff}} = s^2\boldsymbol{\tau}$, and replacing them with the stress terms in Eq. (11) gives us the weak form of the mechanical part. For the phase-field counterpart, the evolution of s is governed by

$$\frac{\partial s}{\partial t} = -M \frac{\delta \bar{W}_{\text{frac}}}{\delta s}, \tag{13}$$

where $M \geq 0$ is the mobility constant. Equation (13) leads to the weak form for the phase-field

$$\int_\Omega \left[\frac{1}{M} \left(\frac{\partial s}{\partial t} \right) \delta s + \mathcal{G}_c \left(\epsilon\, \nabla s\, \delta \nabla s + \frac{\epsilon^3}{2}\, \Delta s\, \delta \Delta s \right) + \left(2s\tilde{W} + \frac{\mathcal{G}_c (s-1)}{2\epsilon} \right) \delta s \right] \mathrm{d}V = \int_{\Gamma_2} q_n\, \delta s\, \mathrm{d}A, \tag{14}$$

where q_n is the normal flux.

2 Numerical simulations

The model derived above was implemented into the Finite Element Analysis Program (FEAP) [7] and its isogeometric analysis add-on (igaFEAP). The domain with initial and boundary conditions are shown in Fig. 1. We assume the plane strain state for all the simulations. The bottom edge of two-dimensional body is fixed in the y-direction, while movements of the right edge in the x-direction are restricted. A line displacement of magnitude 0.1 mm in the y-direction is applied to the top edge of the body in a quasi-static manner. The initial crack length is 0.25 mm and is located in the middle of the plane, starting from the left edge (see Fig. 1). The material properties used are $\lambda = 50727.5\,\text{MPa}$, $\mu = 46825.4\,\text{MPa}$, $\mathcal{G}_c = 2.0\,\frac{\text{N}}{\text{mm}}$, and $M = 2000.0\,\frac{1}{\text{MPa}\cdot\text{s}}$. For the gradient material properties, we use $b_1 = 0, b_2 = \frac{1}{2}\lambda l^2, b_3 = 0, b_4 = \frac{1}{2}\mu l^2$, and $b_5 = \frac{1}{2}\mu l^2$, where l represents the gradient length-scale parameter. This choice of gradient material parameters is identical to using the GRADELA model developed by Aifantis and co-workers [1] where the higher-order strains are defined as the gradients of the linear strain tensor. It should be noted that setting $l = 0$ recovers the classical linear elasticity theory. Furthermore, we use the isogeometric analysis and quadratic NURBS models with full integration as our model needs at least C^1-continuous elements. A mesh grid of 408×409 control points is used for the simulations shown in Fig. 2.

The results are shown in Fig. 2. The crack is expected to propagate along the path **A-A′**. The results are plotted when the maximum strain energy density in front of the crack tip reaches $x = 0.65$mm. Three different values of l are considered. Behind the crack tip, the material is broken and consequently, the existence of relatively high energy values (roughly 2.0 MPa) for the classical case (i.e. $l = 0.0$) does not have a physical meaning. The gradient theory results ($l > 0$) does not show this behavior and the strain energy density is completely zero behind the crack tip. Moreover, there is a clear difference between the classical and the gradient theories in the results depicted for the path **A-A′**. In the visualization of the phase-field parameter, a wider transition zone between the cracked and the intact material is observed for the classical theory.

Acknowledgments

The present work was financially supported by the Research Training Group 1554/2: Micro-Macro-Interactions in Structured Media and Particle Systems of the DFG (German Research Foundation). This support is gratefully acknowledged.

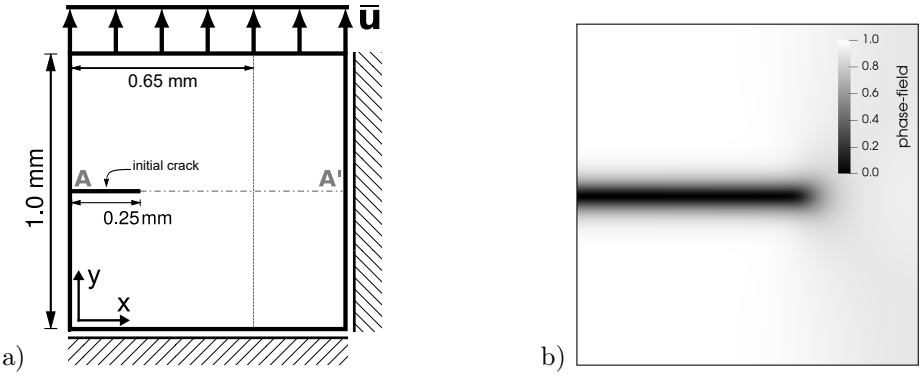

Figure 1. **a** the initial crack position (defined by the phase-field parameter, i.e. non-geometric crack), dimensions and boundary conditions of the problem, and **b** the phase-field state when the maximum strain energy density in front of the crack tip reaches $x = 0.65$mm.

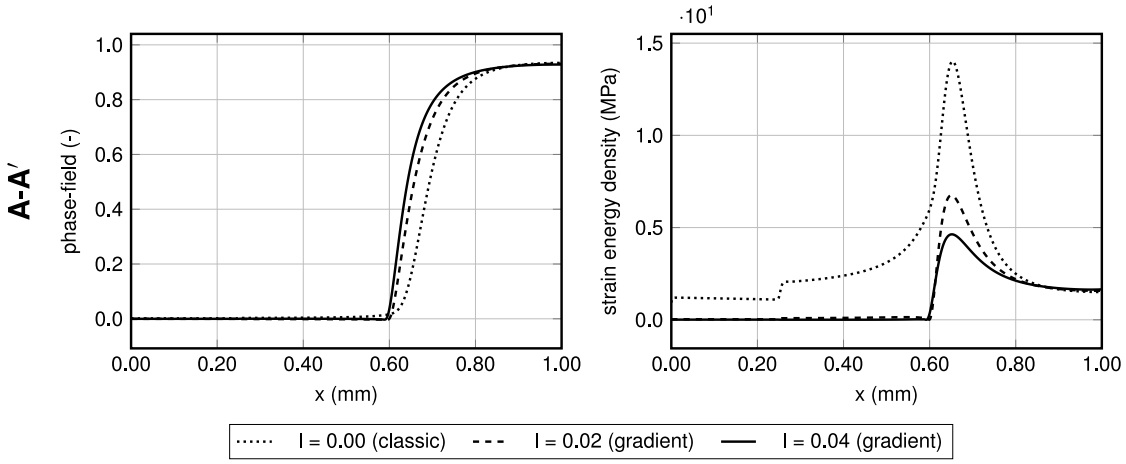

Figure 2. Results for the fourth-order formulation for different values of l and the 408×409 mesh . Distributions of the phase-field (left), and the strain energy density (right) along three different cross-sections in the plane.

References

[1] S. B. Altan and E. C. Aifantis. On the structure of the mode III crack-tip in gradient elasticity. *Scr. Metall Mater.* 26.2 (1992), pp. 319–324. ISSN: 0956716X. DOI: 10.1016/0956-716X(92)90194-J.

[2] A. Bertram. *Compendium on Gradient Materials*. 2017. DOI: 10.13140/RG.2.2.36769.51045.

[3] F. dell'Isola, P. Seppecher, and A. Della Corte. The postulations á la D'Alembert and á la Cauchy for higher gradient continuum theories are equivalent: a review of existing results. *Proceedings. Mathematical, physical, and engineering sciences* 471.2183 (2015), p. 20150415. ISSN: 1364-5021. DOI: 10.1098/rspa.2015.0415.

[4] M. Lazar, G. A. Maugin, and E. C. Aifantis. Dislocations in second strain gradient elasticity. *International Journal of Solids and Structures* 43.6 (2006), pp. 1787 –1817. ISSN: 0020-7683. DOI: 10.1016/j.ijsolstr.2005.07.005.

[5] R. D. Mindlin. Micro-structure in linear elasticity. *Arch. Ration. Mech. Anal.* 16 (1964) (1964), pp. 51–78.

[6] S.-A. Papanicolopulos and A. Zervos. Numerical solution of crack problems in gradient elasticity. *Proc. Inst. Civ. Eng.: Eng. Comput. Mech.* 163.2 (2010), pp. 73–82. DOI: 10.1680/eacm.2010.163.2.73.

[7] R. L. Taylor. *FEAP - Finite Element Analysis Program*. 2014. URL: http://projects.ce.berkeley.edu/feap/.

**Proceedings of the 8th GACM Colloquium on Computational Mechanics
for Young Scientists from Academia and Industry
August 28–30, 2019 in Kassel, Germany**

Modelling of interfacial crack propagation in strongly heterogeneous materials by using phase field method

Thanh-Tung Nguyen * [1], Julien Yvonnet[2], Danièle Waldmann[1] and Qi-Chang He[2]

[1]University of Luxembourg, Laboratory of Solid Structures, 6 Rue Richard Coudenhove-Kalergi, L-1359, Luxembourg
[2]Université Paris-Est, Laboratoire Modélisation et Simulation Multi Échelle MSME, UMR 8208 CNRS, 5 bd Descartes, F-77454 Marne-la-Vallée, France.

Abstract.

Phase field model has been proved to be a useful tool to study the fracture behaviors in heterogeneous materials. This method is able to model complex, multiple crack fronts, and branching in both 2D/3D without ad-hoc numerical treatments. In this study, a new interfacial cracking model in the phase field framework is proposed. The effects of both stiff and soft interphases on the fracture response of composite materials are considered. A dimensional-reduced model based on a rigorous asymptotic analysis is adapted to derive the null thickness imperfect interface models from an original configuration containing thin interphase. The idea of mixing the bulk and interfacial energy within the phase field framework is then used to describe the material degradation both on the interface and in bulk. Moreover, in order to ensure the physical crack propagation patterns, a unilateral contact condition is also proposed for the case of spring imperfect interface. The complex cracking phenomena on interfaces such as initiation, delamination, coalescence, deflection, as well as the competition between the interface and bulk cracking are successfully predicted by the present method. Concerning the numerical aspect, the one-pass staggered algorithm is adapted, providing an extremely robust approach to study interfacial cracking phenomena in a broad class of heterogeneous materials.

Introduction

Study of interface failure has been the topic of an intense research in the last decades. Cohesive element [11] is a powerful method to model crack propagation along interface (situation where the crack path is known). Other techniques like XFEM [4] have been also used to study interfacial cracking in bi-materials [9], where the displacement jump can be accurately reproduced through the enrichment of the displacement field with discontinuous functions. The XFEM technique has been used along with the cohesive model to simulate delamination in composite materials [10]. However, XFEM methods can hardly handle triple junctions or complex interphases, such as those in polycristals. More recently, the interfacial cracking has been studied by using the phase field model [5].

This work is dedicated to developing a phase field framework for dealing with damage of a larger class of imperfect interfaces, i.e. exhibiting either displacement jump or traction jump across an interface. In order to avoid meshing the interphase, we employ an imperfect interface model of zero thickness (with appropriate jump conditions), which is derived from a dimensional-reduced model based on a rigorous asymptotic analysis. The jump conditions depend on the ratio of the stiffness of the interphase to those of the connected materials and lead to two well-known models in the literature: *coherent imperfect interface* for very stiff interphase, and *linear spring-layer imperfect interface* for very soft interphase [12, 13]. The framework proposed in [5] is extended by including these models within the phase field framework, so as to allow interaction between the damage in the thin interphase and the bulk cracks in an efficient and robust manner.

*Corresponding author: thanh-tung.nguyen@uni.lu

1 Theoretical framework

The idea of mixing the bulk and interfacial energy within the phase field framework is used to describe the material degradation both on the interface and in bulk [5]. It implies the total energy in a standard framework of sharp discontinuity description as follows

$$E = \int_{\Omega/\Gamma_d,\Gamma_I} \psi^e \mathrm{d}\Omega + \int_{\Gamma_d} \psi^d \mathrm{d}\Gamma + \int_{\Gamma_{I,\alpha}} \psi^{ci} \mathrm{d}\Gamma + \int_{\Gamma_{I,\beta}} \psi^{si} \mathrm{d}\Gamma, \tag{1}$$

where ψ^e is the elastic energy density; ψ^d is the surface (fracture) energy density; ψ^{ci} and ψ^{si} are the densities of interfacial energy of stiff interface, and compliant interface, respectively.

We adapt here the regularized description to both crack and interface. Herein, the sharp crack is described by the smeared crack density function $\gamma_d(d, \nabla d)$, and the sharp interfaces are replaced by the smeared interfaces, i.e., $\gamma_\alpha(\alpha, \nabla\alpha)$ for stiff interphase and $\gamma_\beta(\beta, \nabla\beta)$ for compliant interphase, respectively. Furthermore, we substitute the displacement jump $[\![\mathbf{u}]\!]$ by a smeared displacement jump $\mathbf{v}(\mathbf{x})$ (see e.g. [5, 7] for more details). Then, the infinitesimal strain tensor $\boldsymbol{\varepsilon}$ in this framework can be decomposed into a part related to the bulk $\boldsymbol{\varepsilon}^e$ and a part induced by the smoothed jump at the interfaces $\tilde{\boldsymbol{\varepsilon}}$, implying $\boldsymbol{\varepsilon} = \boldsymbol{\varepsilon}^e + \tilde{\boldsymbol{\varepsilon}}$. The aforementioned energy functional can be now rewritten as

$$E = \int_\Omega \psi^e\left(\boldsymbol{\varepsilon}^e, d\right) h_{\alpha,\beta}\, \mathrm{d}\Omega + \int_\Omega g_c \gamma_d(d, \nabla d)\, \mathrm{d}\Omega + \int_\Omega \psi^{ci}(\boldsymbol{\varepsilon}^s, d)\gamma_\alpha(\alpha, \nabla\alpha)\, \mathrm{d}\Omega + \int_\Omega \psi^{si}(\mathbf{v}, d)\gamma_\beta(\beta, \nabla\beta)\, \mathrm{d}\Omega, \tag{2}$$

in which, $h_{\alpha,\beta} = (1-\alpha)(1-\beta)$ is introduced to distinguish the elastic energy of bulk phases from the one of the interfaces; g_c here denotes the fracture resistance; the tangential strain $\boldsymbol{\varepsilon}^s$ is expressed by[†]

$$\boldsymbol{\varepsilon}^s = \mathbf{T}\boldsymbol{\varepsilon}^e\mathbf{T} = \mathbf{M}_t\boldsymbol{\varepsilon}^e, \quad \text{with} \quad \mathbf{M}_t = \mathbf{T}\underline{\otimes}\mathbf{T}, \quad \text{and} \quad \mathbf{T}(\mathbf{x}) = \mathbf{I} - \mathbf{n}(\mathbf{x}) \otimes \mathbf{n}(\mathbf{x}), \tag{3}$$

where $n(\mathbf{x})$ is the unit normal vector field on the interface Γ_I, and $\mathbf{I}$ is the second order unit tensor.

The failure model for both bulk and interfacial crackings is constructed through the unilateral contact condition to maintain the physical crack propagation.

Bulk cracking

The model proposed by Miehe et al [3] with the assumption that damage induced by traction only is here used for the bulk cracking

$$\psi^e\left(\boldsymbol{\varepsilon}^e, d\right) = g(d)\ \psi^{e+}\left(\boldsymbol{\varepsilon}^e\right) + \psi^{e-}\left(\boldsymbol{\varepsilon}^e\right), \quad \text{with} \quad \psi^{e\pm}(\boldsymbol{\varepsilon}^e) = \frac{\lambda}{2}\left[\,\langle \operatorname{tr}\boldsymbol{\varepsilon}^e\rangle_\pm\,\right]^2 + \mu \operatorname{tr}\left[\,\left(\boldsymbol{\varepsilon}^{e\pm}\right)^2\,\right], \tag{4}$$

where $g(d) = (1-d)^2 + \epsilon$ (with $\epsilon \ll 1$) is the degradation function, see [1, 3]); ε^{e+} and ε^{e-} are, respectively the extensive and compressive modes of the elastic strain tensor.

Interfacial cracking: coherent imperfect interface model

The interfacial cracking of the very stiff interface is assumed to be created by the whole tangential strains, implying

$$\psi^{ci} = g(d)\psi_e^{ci} = \frac{1}{2}\boldsymbol{\varepsilon}^s : \mathbb{C}_s^{ci}(d) : \boldsymbol{\varepsilon}^s, \quad \text{and} \quad \mathbb{C}_s^{ci}(d) = g(d)\left[\lambda_s^{ci}\mathbf{T}\otimes\mathbf{T} + 2\mu_s^{ci}\mathbf{T}\underline{\otimes}\mathbf{T}\right]. \tag{5}$$

The Lamé's constants characterizing the interface, λ_s^{ci}, and μ_s^{ci} are given following [12].

Interfacial cracking: spring imperfect interface model

The interfacial cracking of the very soft interface is assumed to be created by the tangential displacement jump $\mathbf{v}_t$ and the positive part of normal displacement jump $\mathbf{v}_n^+$. This leads to a decomposition expressed by $\mathbf{v} = \mathbf{v}_n^+ + \mathbf{v}_n^- + \mathbf{v}_t$, and ψ^{si} is postulated as

$$\psi^{si} = g(d)\left(\psi_{n+}^{si} + \psi_t^{si}\right) + \psi_{n-}^{si} = \frac{1}{2}g(d)\left[\mathbf{v}_n^+ \cdot \mathbf{C}_s^{si} \cdot \mathbf{v}_n^+ + \mathbf{v}_t \cdot \mathbf{C}_s^{si} \cdot \mathbf{v}_t\right] + \frac{1}{2}\mathbf{v}_n^- \cdot \mathbf{C}_s^{si} \cdot \mathbf{v}_n^-, \tag{6}$$

[†]The tensor product operation $\mathbf{A}\underline{\otimes}\mathbf{B}$ is defined by $(\mathbf{A}\underline{\otimes}\mathbf{B})_{ijkl} = \left(A_{ik}B_{jl} + A_{il}B_{jk}\right)/2$ for any two second-order tensors $\mathbf{A}$ and $\mathbf{B}$.

with the tangential interface stiffness $\mathbf{C}_s^{si}$ being defined following [13] as $\mathbf{C}_s^{si} = \lambda_s^{si}\mathbf{n}\otimes\mathbf{n} + \mu_s^{si}(\mathbf{I} - \mathbf{n}\otimes\mathbf{n})$. The Lamé's constants characterizing the interface, λ_s^{si}, and μ_s^{si}, can be determined following [13].

The variational approach to fracture as proposed in Bourdin, Francfort and Marigo [2, 1] and developed in a convenient algorithmic setting by Miehe [3] is adopted here. It implies two problems: (i) phase field problem, corresponding to a minimization of the total energy with respect to the displacement field $\mathbf{u}$ and (ii) mechanical problem, corresponding to a minimization of the energy with respect to the scalar damage field d. The details of numerical implementation can be found in [6, 8].

2 Numerical examples: two dimensional simulation of a microstructure

A rectangular plate containing several inclusions is considered under tensile loading. The dimensions of the considered structure are $L \times B = 1 \times 1.6$ mm^2, while the inclusion diameters are taken to range from $d = 0.06$ mm to $d = 0.3$ mm. The detailed geometry and boundary conditions are provided in Fig. 1 (a).

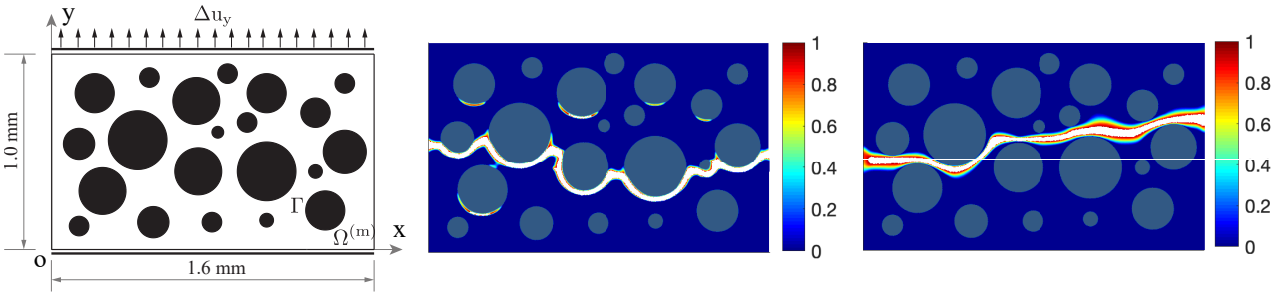

(a) Geometry/boundary conditions (b) Soft interphase (c) Stiff interphase

Figure 1. 2D simulation of a microstructure containing multiple inclusions.

Both situations of very stiff interface (CI) and very soft interface (SI) are considered. The material properties are given in the Table. 1. The tangential Lamé's constants for the interface can be determined following [12, 13] with the interphase thickness $h = 1$ µm, we obtain $\lambda_{si}^s = 105$ GPa/mm, $\mu_{si}^s = 30$ GPa/mm and $\lambda_{ci}^s = 6.857$ GPa.mm, $\mu_{ci}^s = 8$ GPa.mm.

The displacements are prescribed along the $y-$direction for upper edge ($y = B$) while the displacements along x are free. On the lower edge ($y = 0$), the displacements along y are fixed to zero, while the displacements along x are free. The monotonic displacement increments of $\Delta u_y = 2 \times 10^{-5}$ mm have been prescribed via 1000 time steps. Plane strain condition is assumed.

Table 1. Material properties of the spring/coherent interface model.

Parameter	Matrix	Inclusion	Soft interphase	Stiff interphase	Unit
λ	18	60	4.5×10^{-2}	6×10^3	GPa
μ	12	32	3×10^{-2}	4×10^3	GPa
g_c	5×10^{-4}	3×10^{-3}	$g_c^{si,n} = 3.75 \times 10^{-5}$, $g_c^{si,t} = 3.18 \times 10^{-5}$	5×10^{-3}	[kN/mm]

The obtained results of crack propagation are shown in Fig. 1(b)(c). A strong impact of interfacial properties on the fracture behavior of the heterogeneous material is obtained. We capture that the soft interface provides a major interfacial cracking mode, while the stiff interface induces a main bulk cracking behavior.

The very complex behavior of the interfacial cracking is reproduced by the present model. The competition and interaction between bulk cracking and interfacial cracking are successively simulated. More interestingly, the proposed model can predict the poorly post-cracking properties of strongly bonded interface observed in the experiment. This demonstrated the performance of the present computational framework. It then constitutes a promising tool to evaluate the mechanical performance of complex composite materials.

3 Conclusion

In this work, we introduce a robust interfacial cracking model in the phase field framework based on the mixing of bulk energy with the energy of null-thickness interface. The proposed model is able to consider the complex interfaces with various properties, i.e, very stiff interphase and very compliant interphase. We apply the present model to study the interfacial cracking in composite materials and to understand the effects of thin interphase properties on the global behavior of advanced material and structures. The new model predict very well the complex cracking phenomena on interfaces such as initiation, delamination, coalescence, and deflection.

Acknowledgments

This research is supported by the project SeRaMCo within the programme INTERREG – NWE.

References

[1] B. Bourdin, G.A. Francfort, and J.J. Marigo. "Numerical experiments in revisited brittle fracture". *Journal of the Mechanics and Physics of Solids* 48.4 (2000), pp. 797–826.

[2] G.A. Francfort and J.J. Marigo. "Revisiting brittle fracture as an energy minimization problem". *Journal of the Mechanics and Physics of Solids* 46.8 (1998), pp. 1319–1342.

[3] C. Miehe, M. Hofacker, and F. Welschinger. "A phase field model for rate-independent crack propagation: Robust algorithmic implementation based on operator splits". *Computer Methods in Applied Mechanics and Engineering* 199 (2010), pp. 2765–2778.

[4] N. Moës, J. Dolbow, and T. Belytschko. "A finite element method for crack growth without remeshing." *International Journal for Numerical Methods in Engineering.* 46(1) (1999), pp. 131–156.

[5] T.T. Nguyen et al. "A phase-field method for computational modeling of interfacial damage interacting with crack propagation in realistic microstructures obtained by microtomography". *Computer Methods in Applied Mechanics and Engineering* 312 (2016), pp. 567 –595. ISSN: 0045-7825.

[6] T.T. Nguyen et al. "A phase field method to simulate crack nucleation and propagation in strongly heterogeneous materials from direct imaging of their microstructure". *Engineering Fracture Mechanics* 139 (2015), pp. 18–39.

[7] T.T. Nguyen et al. "Multi-phase-field modeling of anisotropic crack propagation for polycrystalline materials". *Computational Mechanics* 60 (2017), pp. 289–314.

[8] T.T. Nguyen et al. "Phase field simulation of interfacial cracking in heterogeneous materials". *Submitted* (2018).

[9] N. Sukumar et al. "Partition of unity enrichment for bimaterial interface cracks". *International Journal for Numerical Methods in Engineering* 59.8 (2004), pp. 1075–1102.

[10] Y. Wang and H. Waisman. "Progressive delamination analysis of composite materials using XFEM and a discrete damage zone model". *Computational Mechanics* 55.1 (2015), pp. 1–26.

[11] X.P. Xu and A. Needleman. "Numerical simulations of fast crack growth in brittle solids". *Journal of the Mechanics and Physics of Solids* 42.9 (1994), pp. 1397–1434.

[12] J. Yvonnet, H. Le quang, and Q-C. He. "An XFEM/level set approach to modelling surface/interface effects and to computing the size-dependent effective properties of nanocomposites". *Computational Mechanics* 42.1 (2008), pp. 119–131.

[13] Q-Z. Zhu et al. "Three-dimensional numerical modelling by XFEM of spring-layer imperfect curved interfaces with applications to linearly elastic composite materials". *International Journal for Numerical Methods in Engineering* 88.4 (2011), pp. 307–328.

**Proceedings of the 8th GACM Colloquium on Computational Mechanics
for Young Scientists from Academia and Industry
August 28–30, 2019 in Kassel, Germany**

Improved Durability Prediction of Cord-rubber Composites by the Material Force Method

Carmen M. Popa, Clemens Gebhardt and Michael Kaliske *

Institute for Structural Analysis, Technische Universität Dresden, 01062 Dresden, Germany

Abstract. The research at hand deals with durability analysis of cord-reinforced elastomers using the material force concept. Different types of steel cord reinforcement are used, in order to determine the influence of the cord construction on the fracture sensitivity of the composite product. The composite is analysed using the Extended Finite Element Method to reduce the effort of the meshing process. Material forces are computed at the crack tip area and a qualitative ranking of the different reinforcement types is obtained. The results are compared to experimental investigations.

Introduction

Cord-reinforced elastomers are composite structures widely used in the production of industrial rubber products, from conveyor and power transmission belts used in industrial plants and factories, to multilayer high-pressure hoses and coated fabrics, as well as tyres, see [1]. Cord-reinforced elastomers are made of a low-modulus rubber matrix − characterised by high deformation behaviour, twisted reinforcement − with much higher strength and the adhesive film (dip), that creates a strong bond between the reinforcement and the elastomer matrix, see [2]. The operational safety of industrial products is directly influenced by the choice of reinforcement, specifically the material used, the size and configuration of each cord and density of cords in the rubber product. Ideally, the bonding between the reinforcement and the elastomer is perfect, as reinforcing cords are coated with various chemical compounds. Nevertheless, the cords are cut in order to be mounted in the respective component, which leads to a crack-prone area appearing at the end of each cord. During the lifetime of the cord-reinforced elastomer, this area has a higher probability of developing micro-cracks that lead to mechanical failure of the product. The influence of the reinforcement geometry on this behaviour is an important information for developing new types of cords and ensuring increased durability of cord-reinforced elastomers.

In this contribution, the material force method is used to analyse the influence of four different types of cord geometries on the fracture sensitivity of the composite product. For general applications of configurational forces, the books by Gurtin [4] and Maugin [6] introduce comprehensive knowledge, while general applications for a finite element implementation of material forces are presented by Müller et al. [7], Näser et al. [8] and Steinmann et al. [10].

The reinforcement model is generated by a straightforward numerical algorithm that requires a small number of input parameters to provide the geometry of the four twisted cords used in this work. In addition, the complex meshing process to match the geometry of the twisted cords, used by the Finite Element Method (FEM) is rendered unnecessary with the eXtended Finite Element Method (XFEM).

1 Theoretical framework

1.1 Constitutive material models

The elastomer matrix has a highly nonlinear stress-strain response to mechanical loading, displaying an upturn of the stress-strain diagram at large strains. The elastomer matrix of the composite is described

*Corresponding author: michael.kaliske@tu-dresden.de

by the well-known Yeoh hyperelastic constitutive model, a phenomenological formulation that appears as a practical solution to the need of characterising the elastic properties of rubber.

The role of reinforcement in most industrial rubber products is to ensure a high tensile strength-to-weight ratio, the required flexibility as well as low elongation and high mechanical impact resistance. In tyres, the reinforcement defines significantly the shape, supports loads and provides the needed rigidity of the structure for acceleration, braking or cornering. In this work, cord reinforcement is defined as long cords of twisted filaments made of steel, that provide extra strength to the rubber composites where they are embedded in. At large strain, cord materials (steel, nylon, polyester or fiberglass) exhibit nonlinear elastic behaviour, which may be described adequately by a variant of the compressible Neo-Hooke approach, according to Simo & Hughes, see [9]. The Neo-Hooke material model has the simplest formulation of a hyperelastic model and provides good results in modelling the proposed cord reinforcement material.

1.2 Modelling complex geometries

According to Khoei, see [5], the FEM is not the best choice of analysis in case of structures with discontinuities, singularities or boundary layers. The disadvantage of the method comes from the need to conform the discretisation to all the geometrical details of the modelled structure. The XFEM is a partition of unity method (PUM) that adds enrichment functions to the conventional finite element function space, in order to capture discontinuous behaviour in an internal area of a body. What makes the distinction between the XFEM and the conventional FEM is XFEM's capability of describing an internal interface without the need of conforming elements at its position, which allows the method to spare the time-consuming step of mesh generation in case of complex geometries. The following figure details how enrichement functions determine the steel material of twisted cords embedded in an elastomer sample.

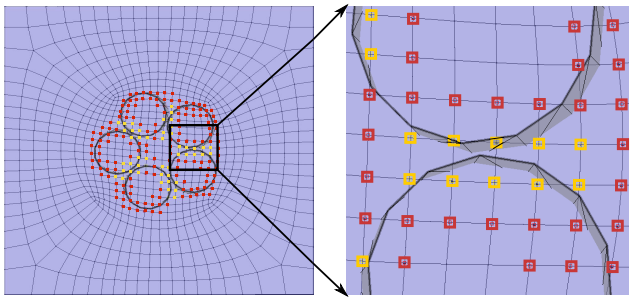

Figure 1. Enriched nodes in cord-rubber composite

The position of the cord-rubber interface is obtained through a reinforcement generating method. The numerical approach is implemented in the XFEM framework; it defines a flexible number of 2D surfaces that are extruded along a curvilinear direction which relates to the twist trajectory of the filaments. A 3D body is generated from a small number of user parameters that define the cord reinforcement. The algorithm can apply different twist trajectories to each of the specified 2D surfaces, a case mostly used in reality when modelling cord reinforcement. This proves the versatility of the numerical approach. Two of the four cord reinforcement types analysed are shown in the following figure.

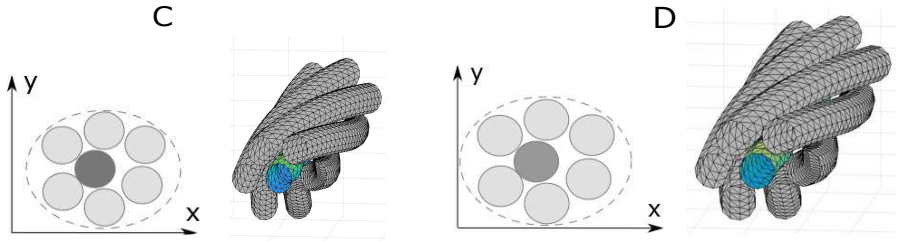

Figure 2. Cords C and D – cross-section and 3D geometries

1.3 Fracture sensitivity analysis

In case of structures with existing flaws, voids, inclusions or other singularities, fracture mechanics is an appropriate approach to determine the fracture sensitivity of the analysed structures.

In the material space, a solid is assumed to be inhomogeneous, anisotropic and possibly changing in time. Following Eshelby's thought experiment from 1951 [3], the computation of the material force on a defect p in an elastic medium can be derived by using the energy-momentum tensor. The material force, also called configurational force – the thermodynamic force that drives the change in position of the defect – is defined arbitrarily as the negative gradient of the change in energy. Material forces are a vectorial nodal output. At every nodal point of the finite elements chosen, a three-dimensional vector is plotted. Its norm represents the value of the energy release rate and its vector predicts the inverse direction of crack propagation. This is one of the main advantages the material force method has over the classical J-integral method.

2 Application

The simulation setup is chosen to replicate the initial experimental setup, where sets of four cord reinforcement samples are embedded in a rubber matrix and undergo monotonic and cyclic tensile (pull) tests. The details of the experimental setup are shown in Figure 3 and the resulting maximum displacement and force are detailed in Table 1 below.

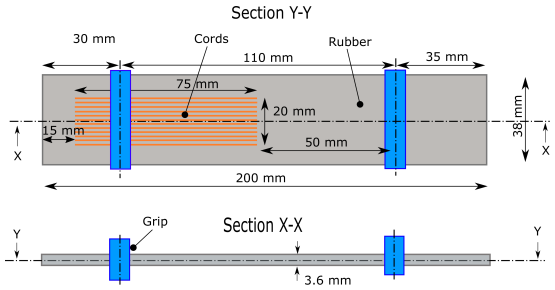

Figure 3. Experimental sample

cord	crit. force [N]	max. disp [mm]
A	1073	145
B	1013	112
C	1128	126
D	1057	109

Table 1. Force-displacement values

The modelling strategy for such large-strain static tension tests is formulated by a submodelling technique. In this work, the concept of submodelling is used to describe the crack area at the end of cord reinforcement inside the model. Static simulations are performed on samples of rubber embedding the four different types of steel cord reinforcement. The displacement values of the global sample are interpolated onto the boundary of the local model and act as input parameters for the subsequent local simulation.

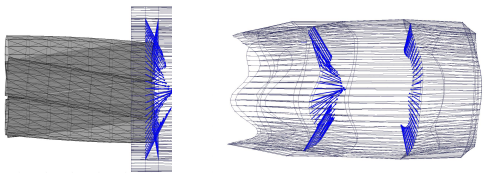

Figure 4. Material forces on crack tip area of composite element

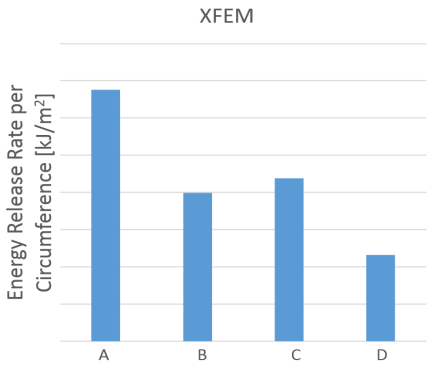

Figure 5. Energy release rate at crack tip area – XFEM comparison between four cord types

Once the local analysis is performed, the material force post-processor is applied to the crack tip area. The output of the post-processor are material force vectors, that indicate the crack propagation direction

as the opposite direction to the displayed vectors and the energy release rate. Figure 4 shows the material force vectors at the crack area for cord B and Figure 5 details the energy release rate of all four composite samples.

It can be seen that the material force vectors exhibit larger values on the left side of the crack tip area, indicating a higher sensitivity of crack initiation along the direction of the reinforcement, at a slight angle. The integration of the vectorial quantities over the crack area determines energy measures, which give information on the influence of the reinforcement type on the overall fracture behaviour of the composite.

3 Conclusion

The present work proposes a methodology for the fracture sensitivity analysis of four different cord-reinforced composites, using the XFEM combined with a cord generation technique and a post-processor based on the material force concept. Static analyses are carried out with local models, in order to determine the impact the type of cord reinforcement has on the overall fracture behaviour of the composite. The numerical results match the experiments, making the array of presented methods a good means of analysing the proposed problem.

Acknowledgments

This work has been funded by the European Social Fund (ESF) and the Free State of Saxony, which is gratefully acknowledged.

References

[1] G. Burrowes and B. Rodgers. *Reinforcing Materials in Rubber Products*. USA: Nokian Tyres, 2005.

[2] M. G. Pastore Carbone. "Investigating Mechanical Behavior of Cord-rubber Composites by Multi-Scale Experimental and Theoretical Approach". PhD thesis. Universita degli Studi di Napoli Federico II, 2011.

[3] J.D. Eshelby. The force on an elastic singularity. *Philosophical Transactions of the Royal Society of London* 244 (1951), pp. 87–112.

[4] M. E. Gurtin. *Configurational forces as basic concepts of continuum physics*. Springer, New York, USA, 2000.

[5] Amir R. Khoei. *Extended Finite Element Method. Theory and Applications*. Wiley, West Sussex, UK, 2015.

[6] G. A. Maugin. *Configurational forces: thermomechanics, physics, mathematics and numerics*. Taylor & Francis, West Sussex, UK, 2010.

[7] R. Mueller and G. A. Maugin. On material forces and finite element discretizations. *Computational Mechanics* 29 (2002), pp. 52–60.

[8] B. Naeser, M. Kaliske, and R. Mueller. Material forces for inelastic models at large strains: application to fracture mechanics. *Computational Mechanics* 40 (2007), pp. 1005–1013.

[9] J.C. Simo and T.J.R. Hughes. *Plasticity, Viscoplasticity and Viscoelasticity - Computational Aspects*. Springer, Berlin, Germany, 1992.

[10] P. Steinmann. Application of material forces to hyperelastostatic fracture mechanics. *Journal of Mechanics and Physics of Solids* 37 (2000), pp. 7371–7391.

**Proceedings of the 8th GACM Colloquium on Computational Mechanics
for Young Scientists from Academia and Industry
August 28–30, 2019 in Kassel, Germany**

Thermo-mechanical phase-field model for porous-ductile fracture

J. Schulte * [1], M. Dittmann[1], F. Aldakheel[2] and C. Hesch[1]

[1]Chair of Computational Mechanics, University of Siegen,Paul-Bonatz-Strasse 9-11, 57076 Siegen, Germany

[2]Institute of Continuum Mechanics, Leibnitz University Hannover, Appelstr. 11, 30167 Hannover, Germany

Abstract.

Phase-field methods to regularize sharp interfaces represent a well established technique nowadays. In fracture mechanics, recent works have shown the capability of the method for brittle as well as ductile problems formulated within the fully non-linear regime [4, 5].

In this contribution, we propose a novel framework to simulate porous-ductile fracture in isotropic thermo-elasto-plastic solids undergoing large deformations [3]. Therefore, a modified Gurson-Tvergaard-Needelman GTN-type plasticity model is combined with a phase-field fracture approach to account for a temperature-dependent growth of voids on micro-scale followed by crack initiation and propagation on macro-scale. The multi-physical formulation is completed by the incorporation of an energy transfer into thermal field such that on the other hand the temperature distribution depends on the evolution of the plastic strain and the crack phase-field.

Eventually, a number of numerical investigations show not only the possibilities of the approach for a multi-physical analysis of complex material behavior, but also the accordance with experimental results in terms of hardening, necking, crack initiation and propagation. Moreover, a further example based on the third Sandia Fracture Challenge is applied to demonstrate the capability of the model for the prediction of three-dimensional fracture pattern in complex geometries.

Introduction

The analysis of crack initiation and propagation in ductile materials plays an important role in predicting failure mechanisms for various engineering applications. The phase-field approach to fracture has been proven to be a very powerful technique to simulate crack phenomena in multi-physical environments [4, 5]. The goal of this work is to present a theoretical and a computationally efficient framework for ductile, porous materials undergoing thermomechanical loading conditions in order to study the influence of the growth of micro-voids, as well as the final rupture at the macro-scale [1, 2, 3].

1 Governing equations

A theory for coupled thermomechanical response at fracture undergoing large deformations is outlined in this section. The underlying, three-dimensional ($d = 3$) system leads to a multi-field setting with seven fields

$$\{\boldsymbol{\varphi}, \mathfrak{s}, \theta, \alpha, r^{\mathrm{p}}, \boldsymbol{F}^{\mathrm{p}}, f\}\,, \tag{1}$$

which are the deformation map, the crack phase-field, the absolute temperature and the four plastic fields, which are the equivalent plastic strain, its dual hardening force, the plastic deformation gradient and the void volume fraction. Here, the void volume fraction is defined as

$$f = 1 - \frac{1 - f_0}{J^{\mathrm{p}}} \tag{2}$$

*Corresponding author: jonathan.schulte@uni-siegen.de

and is assumed as a micro-mechanically motivated damage variable, related to the plastic deformation gradient through its determinant J^{p}. f_0 is the initial void volume fraction.

The deformation gradient $\boldsymbol{F} = \boldsymbol{F}^{\mathrm{e}}\,\boldsymbol{F}^{\mathrm{p}}$ and its determinant $J = J^{\mathrm{e}}\,J^{\mathrm{p}}$ are decomposed multiplicatively into elastic and plastic parts. Moreover, the fracture insensitive isochoric and volumetric parts are given by

$$\tilde{\bar{\boldsymbol{F}}}^{\mathrm{e}} = \sum_a \left[(J^{\mathrm{e}})^{-1/d}\lambda_a^{\mathrm{e}}\right]^{g(\mathfrak{s})}\,\boldsymbol{n}_a \otimes \boldsymbol{N}_a \quad \text{and} \quad \tilde{J}^{\mathrm{e}} = \begin{cases} (J^{\mathrm{e}})^{g(\mathfrak{s})} & \text{if} \quad J^{\mathrm{e}} > 1 \\ J^{\mathrm{e}} & \text{else} \end{cases}, \tag{3}$$

postulating that fracture requires a local state of tensile/shear deformation. λ_a^e are the elastic principal stretches, $g(\mathfrak{s})$ is a polynomial degradation function and $\boldsymbol{n}_a$ and $\boldsymbol{N}_a$ are the principal directions of the left and right stretch tensors.

1.1 Energetic response function

The stored energy function $\widehat{\Psi}$ for the coupled problem takes the form

$$\widehat{\Psi} = \widehat{\Psi}^{\mathrm{e}}(\boldsymbol{F}, \boldsymbol{F}^{\mathrm{p}}, \mathfrak{s}, \theta) + \widehat{\Psi}^{\theta}(\theta) + \widehat{\Psi}^{\mathrm{p}}(\alpha, \nabla\alpha, \theta) + \widehat{\Psi}^{\mathrm{f}}(\mathfrak{s}, \nabla\mathfrak{s}, \Delta\mathfrak{s}), \tag{4}$$

which reflects a coupling of gradient thermoplasticity with gradient damage mechanics. The isotropic elastic contribution is decomposed

$$\widehat{\Psi}^{\mathrm{e}} = \widehat{\Psi}^{\mathrm{e}}_{\mathrm{vol}}(\tilde{J}^{\mathrm{e}}(J, J^{\mathrm{p}}, \mathfrak{s}), \theta) + \widehat{\Psi}^{\mathrm{e}}_{\mathrm{dev}}(\tilde{\bar{\boldsymbol{F}}}^{\mathrm{e}}(\boldsymbol{F}, \boldsymbol{F}^{\mathrm{p}}, J, \mathfrak{s})), \tag{5}$$

into volumetric and deviatoric parts. As a representative constitutive law used for the numerical examples we introduce the thermomechanically extended Neo-Hookean material model

$$\widehat{\Psi}^{\mathrm{e}}_{\mathrm{vol}}(\tilde{J}^{\mathrm{e}}, \theta) = \frac{\kappa}{2}\left(\frac{(\tilde{J}^{\mathrm{e}})^2 - 1}{2} - \ln[\tilde{J}^{\mathrm{e}}]\right) - \frac{3}{2}\beta\kappa(\theta - \theta_0)\left(\tilde{J}^{\mathrm{e}} - \frac{1}{\tilde{J}^{\mathrm{e}}}\right) \tag{6}$$

and

$$\widehat{\Psi}^{\mathrm{e}}_{\mathrm{dev}}(\tilde{\bar{\boldsymbol{F}}}^{\mathrm{e}}) = \frac{\mu}{2}(\tilde{\bar{\boldsymbol{F}}}^{\mathrm{e}} : \tilde{\bar{\boldsymbol{F}}}^{\mathrm{e}} - 3). \tag{7}$$

Therein, $\mu > 0$ and $\kappa > 0$ denote the shear modulus and the bulk modulus, respectively. θ_0 is a reference temperature and β is the linear thermal expansion coefficient.

The purely thermal contribution to the stored energy (4) is assumed to have the simple form

$$\widehat{\Psi}^{\theta}(\theta) = c\left(\theta - \theta_0 - \theta\ln\left(\frac{\theta}{\theta_0}\right)\right), \tag{8}$$

where $c \geq 0$ is a constant parameter representing the specific heat capacity. Moreover, the Piola-Kirchhoff heat flux vector can be defined as

$$\boldsymbol{Q}(\boldsymbol{F}, \mathfrak{s}, \theta, \nabla\theta) := -\boldsymbol{K}(\boldsymbol{F}, \mathfrak{s}, \theta)\nabla\theta \tag{9}$$

to account for the heat transfer. This is known as Duhamel's law of heat conduction, where $\boldsymbol{K}$ is the material thermal conductivity tensor

$$\boldsymbol{K}(\boldsymbol{F}, \mathfrak{s}, \theta) := [K_0(1 - w_{\mathrm{K}}(\theta - \theta_0))(1 - \mathfrak{s}) + K^{\mathrm{conv}}\mathfrak{s}]\boldsymbol{C}^{-1}. \tag{10}$$

Note that in case of fracture, the conduction degenerates locally such that we achieve a pure convection problem and the heat transfer depends on the crack opening width. Here, we formulate the conductivity tensor $\boldsymbol{K}$ in terms of the phase-field parameter $\mathfrak{s}$. Moreover, w_{K} is a thermal softening parameter, K_0 is a conductivity parameter related to the reference temperature, K^{conv} is a convection parameter and $\boldsymbol{C} = \boldsymbol{F}^{\mathrm{T}}\boldsymbol{F}$ denotes the right Cauchy-Green tensor.

We focus on the equivalent plastic strain α and its gradient $\nabla\alpha$ with the particular form for the energetic contributions

$$\widehat{\Psi}^{\mathrm{p}}(\alpha, \nabla\alpha, \theta) = \int_0^{\alpha} \widehat{y}(\tilde{\alpha}, \theta)\,\mathrm{d}\tilde{\alpha} + y_0(\theta)\frac{l_{\mathrm{p}}^2}{2}\|\nabla\alpha\|^2\,. \tag{11}$$

Here, l_p is a plastic length scale related to a strain-gradient hardening effect and accounts for size effects to overcome the nonphysical mesh sensitivity of the localized plastic deformation in softening materials. Moreover, $\widehat{y}(\alpha,\theta)$ is a temperature dependent isotropic local hardening function obtained form experimental data.

The variational derivative of $\widehat{\Psi}^\mathrm{p}$ with respect to α yields

$$r^\mathrm{p} := \delta_\alpha \widehat{\Psi}^\mathrm{p} = \partial_\alpha \widehat{\Psi}^\mathrm{p} - \mathrm{Div}[\partial_{\nabla\alpha}\widehat{\Psi}^\mathrm{p}] \tag{12}$$

reflecting the characteristics of the gradient-extended model under consideration.

Eventually, the phase-field fracture contribution has to be formulated. Therefore, the sharp-crack surface topology Γ is replaced by a regularized functional

$$\Gamma_\mathrm{l}(\mathfrak{s}) = \int_{\mathcal{B}_0} \widehat{\gamma}(\mathfrak{s},\nabla\mathfrak{s},\Delta\mathfrak{s})\,\mathrm{d}V \quad \text{with} \quad \widehat{\gamma}(\mathfrak{s},\nabla\mathfrak{s},\Delta\mathfrak{s}) = \frac{1}{4l_\mathrm{f}}\mathfrak{s}^2 + \frac{l_\mathrm{f}}{2}\|\nabla\mathfrak{s}\|^2 + \frac{l_\mathrm{f}^3}{4}(\Delta\mathfrak{s})^2. \tag{13}$$

The functional is based on the crack surface density function $\widehat{\gamma}$ per unit volume of the solid and the fracture length scale parameter l_f that governs the regularization. Note that in the limit $l_\mathrm{f}\to 0$, the regularized crack surface functional $\Gamma_\mathrm{l}(\mathfrak{s})$ converges to the sharp crack surface Γ. For ductile fracture, we require additionally that $l_\mathrm{p} \geq l_\mathrm{f}$. For the given fracture surface functional introduced in (13), we define the critical energy required to create a diffusive fracture topology by

$$W^\mathrm{cr} = \int_{\mathcal{B}_0} \widehat{g_\mathrm{c}}(\alpha)\,\widehat{\gamma}(\mathfrak{s},\nabla\mathfrak{s},\Delta\mathfrak{s})\,\mathrm{d}V, \tag{14}$$

in terms of the Griffith-type critical energy release rate $\widehat{g_\mathrm{c}}$, which is decomposed additively into elastic and plastic contributions $\widehat{g_\mathrm{c}}(\alpha) = g_\mathrm{c,p} + g_\mathrm{c,e}\exp[-\omega_\mathrm{f}\alpha]$, using the modeling parameters $\{g_\mathrm{c,e}, g_\mathrm{c,p}, \omega_\mathrm{f}\}$. Summarized, the phase-field fracture contribution is given in terms of the crack-density function as

$$\begin{aligned}\widehat{\Psi}^\mathrm{f}(\mathfrak{s},\nabla\mathfrak{s},\Delta\mathfrak{s}) &= \widehat{g_\mathrm{c}}(\alpha)\,\widehat{\gamma}(\mathfrak{s},\nabla\mathfrak{s},\Delta\mathfrak{s}) \\ &= \frac{\widehat{g_\mathrm{c}}(\alpha)}{4l_\mathrm{f}}\mathfrak{s}^2 + \frac{\widehat{g_\mathrm{c}}(\alpha)\,l_\mathrm{f}}{2}\nabla\mathfrak{s}\cdot\nabla\mathfrak{s} + \frac{\widehat{g_\mathrm{c}}(\alpha)\,l_\mathrm{f}^3}{4}(\Delta\mathfrak{s})^2\end{aligned} \tag{15}$$

which defines the crack resistance force via the variational derivative with respect to $\mathfrak{s}$

$$r^\mathrm{f} := \delta_\mathfrak{s}\widehat{\Psi}^\mathrm{f} = \partial_\mathfrak{s}\widehat{\Psi}^\mathrm{f} - \mathrm{Div}[\partial_{\nabla\mathfrak{s}}\widehat{\Psi}^\mathrm{f}] + \Delta[\partial_{\Delta\mathfrak{s}}\widehat{\Psi}^\mathrm{f}]. \tag{16}$$

1.2 Dissipative response function

Regarding the plastic material behavior, we postulate a modified Gurson model for porous plasticity as

$$\widehat{\Phi}^\mathrm{p}(\boldsymbol{\tau}, r^\mathrm{p}) = \frac{\sigma_\mathrm{eq}^2}{r^{\mathrm{p}2}} + 2q_1 f\cosh\left[\frac{3}{2}q_2\frac{p}{r^\mathrm{p}}\right] - \left(1+(q_1 f)^2\right) \tag{17}$$

in terms of the Kirchhoff stress which is related to the Cauchy stress by $\boldsymbol{\sigma} = \boldsymbol{\tau}/J$ and the dissipative resistance force r^p. Here, $\sigma_\mathrm{eq} = \sqrt{3/2}\,\|\boldsymbol{\tau}_\mathrm{dev}/J\|$ represents the von Mises equivalent stress, whereas $p = \frac{1}{3}\mathrm{tr}[\boldsymbol{\tau}/J]$ denotes the local pressure along with the growth-based void volume fraction f and fitting parameters $q_1 \approx 1.5$ and $q_2 \approx 1.0$.

On the fracture part, we define a crack threshold function $\widehat{\Phi}^\mathrm{f}$ based on the constitutive representation

$$\widehat{\Phi}^\mathrm{f}(\mathcal{H} - r^\mathrm{f}) = \mathcal{H} - r^\mathrm{f}, \tag{18}$$

where the energetic driving force $\mathcal{H}$ is bounded by the crack resistance force r^f dual to the fracture phase-field $\mathfrak{s}$.

The associated plastic evolution equations are defined as $\boldsymbol{d}^\mathrm{p} = \lambda^\mathrm{p}\frac{\partial\widehat{\Phi}^\mathrm{p}}{\partial\boldsymbol{\tau}}$ and $\dot{\alpha} = -\lambda^\mathrm{p}\frac{\partial\widehat{\Phi}^\mathrm{p}}{\partial r^\mathrm{p}}$, whereas the evolution equation for the crack phase-field reads $\dot{\mathfrak{s}} = \lambda^\mathrm{f}\frac{\partial\widehat{\Phi}^\mathrm{f}}{\partial(\mathcal{H}-r^\mathrm{f})}$.

Eventually, we define the internal dissipation density function $\mathcal{D}_\mathrm{int} := \nu_\mathrm{p}\,\boldsymbol{\tau} : \boldsymbol{d}^\mathrm{p} + \nu_\mathrm{f}\,\mathcal{H}\dot{\mathfrak{s}}$, where ν_p is a constant dissipation factor typically chosen in the range of 85% to 95% in the context of thermoplasticity. In addition, ν_f is introduced as fracture dissipation factor based on the discussions related to an energy transfer into the thermal field in [6] and the references therein.

2 Numerical Example

To illustrate the performance and applicability of the thermo-porous ductile fracture model to complex three-dimensional geometries, a numerical example is considered in this section. Therefore, we adopt *CAD* data from the third Sandia Fracture Challenge and apply the steel like material setting given. Within the quasi-static simulation setting, the lower end of the hollow body is fixed in space while the upper end is moved upwards. No heat in- or outflow is allowed. Figure 1 shows the von Misses residual stress distribution within the deformed configuration on fully ruptured state, where the fractured regions with $g < 0.15$ are removed from the contour plot for visualization purposes.

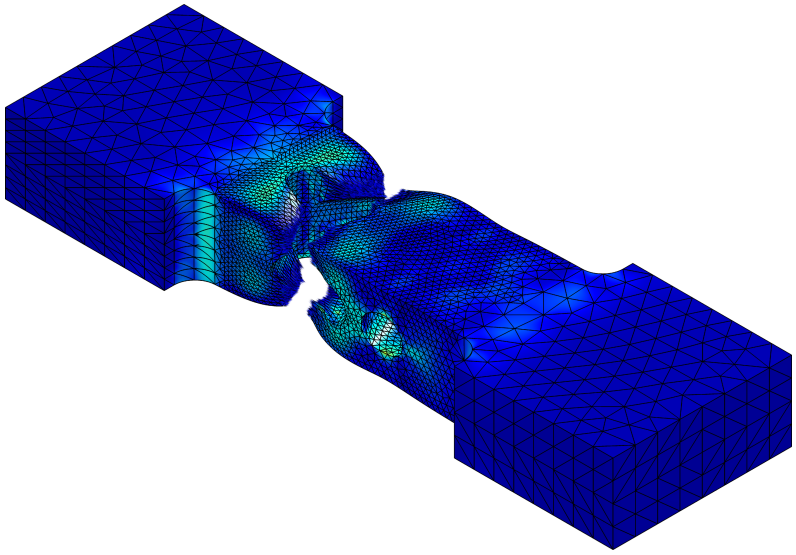

Figure 1. Third SFC. Von Mises stress distribution at fully ruptured state.

Acknowledgments

Support for the present research was provided by the Deutsche Forschungsgemeinschaft (DFG) under grant HE5943/8-1 and DI2306/1-1.

References

[1] F. Aldakheel. Micromorphic approach for gradient-extended thermo-elastic–plastic solids in the logarithmic strain space. *Continuum Mechanics and Thermodynamics* 29 (2017), 1207—1217.

[2] F. Aldakheel, P. Wriggers, and C. Miehe. A modified Gurson-type plasticity model at finite strains: formulation, numerical analysis and phase-field coupling. *Computational Mechanics* 62 (2017), 815—833.

[3] M. Dittmann, F. Aldakheel, J. Schulte, M. Krüger, P. Wriggers, and C. Hesch. Phase-field modeling of porous-ductile fracture in finite thermo-elasto-plastic solids. *submitted* (2018).

[4] M. Dittmann, F. Aldakheel, J. Schulte, P. Wriggers, and C. Hesch. Variational Phase-Field Formulation of Non-Linear Ductile Fracture. *Computer Methods in Applied Mechanics and Engineering* 342 (2018.), pp. 71–94.

[5] M. Dittmann, M. Krüger, F. Schmidt, S. Schuß, and C. Hesch. Variational modeling of thermomechanical fracture and anisotropic frictional mortar contact problems with adhesion. *Computational Mechanics* 63 (2019), pp. 571–591.

[6] J. Schulte, M. Krüger, M. Dittmann, and C. Hesch. Multi-field modeling of thermomechanical coupled fracture problems. *Proceedings in Applied Mathematics and Mechanics* (2018). DOI: 10.1002/pamm.201800348.

**Proceedings of the 8th GACM Colloquium on Computational Mechanics
for Young Scientists from Academia and Industry
August 28–30, 2019 in Kassel, Germany**

Thermo-Mechanical Coupling for Internal Thickness Extrapolation Elements

Felix Töller * [1], Stefan Löhnert[2] and Peter Wriggers[1]

[1]Institute of Continuum Mechanics, Appelstraße 11, 30167 Hannover

[2]Institute of Mechanics and Shell Structures, August-Bebel-Straße 30, 01219 Dresden

Abstract.

Internal Thickness Extrapolation (InTEx) is a new finite element technology that enables the combination of initially flat elements with bulk material models [11]. Usually flat elements like Cohesive Zone Elements use traction separation laws as bulk material models need a strain like deformation measure. Such a deformation measure cannot be determined in all directions without further assumptions by an element with an initial thickness of zero.

Tailored Forming is a manufacturing process for hybrid material components [2]. Internal Thickness Extrapolation elements can be used to model the joining zone in simulations. The forming process is usually performed at elevated temperature; often the different raw materials of the hybrid components are intended to be heated differently to obtain similar yielding properties. Hence, taking heat transfer through Internal Thickness Extrapolation elements into account is essential for the simulation of joining zones during Tailored Forming.

Introduction

Tailored Forming is a manufacturing process for hybrid material components [2], where firmly bonded hybrid work pieces are formed. The joining zone is defined as the bonded region (via intermetallic compounds and metallic bonds) and its surrounding that is directly influencing the bonding characteristics. The thickness of the joining zone is in the order of a few micrometers [11]. Modelling of the joining zone for macroscopic simulations is preferably done with initially flat elements due to its small thickness [4, 12]. Cohesive Zone Elements are initially flat and therefore often used for simulations of joining zones. Though Cohesive Zone Elements necessitate special material models, called traction separation laws. These cannot capture all relevant deformation and damaging modes during Tailored Forming. Therefore Internal Thickness Extrapolation (InTEx) elements are applied [11]. This new finite element technology allows for the combination of initially flat elements with bulk material models and thus circumvents the disadvantages of traction separation laws.

1 Internal Thickness Extrapolation

A flat element geometry is a simplification of the thin physical geometry of the joining zone. The basic idea of Internal Thickness Extrapolation is to revert this simplification to reconstruct the physical geometry of the joining zone. The thickened geometry can incorporate bulk material models. Figure 1 shows the discretised geometry and the extrapolated (InTEx) geometry; for a better visibility the discretised geometry here is not flat.

*Corresponding author: toeller@ikm.uni-hannover.de ORCID iD: 0000-0002-7457-2648

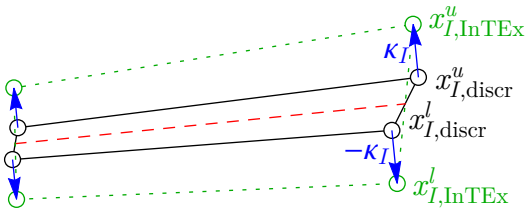

Figure 1. Discretised and extrapolated geometry in the current configuration [10]

2 Heat Transfer

The heat balance equation is [8, 13]

$$\mathrm{div}(\boldsymbol{q}) + \rho\, c_p\, \frac{\partial \Theta}{\partial t} = \overline{f} \quad . \tag{1}$$

Here no internal heat source ($\overline{f} = 0$) will be considered and the thermal state is locally assumed to be stationary ($\frac{\partial \Theta}{\partial t} = 0$). So the weak form of heat conduction is

$$\int_{\partial\Omega} \partial\Theta\, \boldsymbol{q}^T \cdot \boldsymbol{n}\, dA + \int_\Omega k \underbrace{\mathrm{grad}^T(\Theta) \cdot \mathrm{grad}(\partial\Theta)}_{=\mathrm{grad}^T(\partial\Theta)\cdot\mathrm{grad}(\Theta)} dV = 0 \quad . \tag{2}$$

The discretised form can be obtained using $\partial\Theta \approx \partial\Theta^h = N_I\, \partial\Theta_I$ and $\Theta \approx \Theta^h = N_I\, \Theta_I$ where $\sum_I$ is omitted for simplicity

$$\int_{\partial\Omega} \partial\Theta_I\, N_I\, \boldsymbol{q}^T \cdot \boldsymbol{n}\, dA + \partial\Theta_I \underbrace{\int_\Omega k\, \mathrm{grad}^T\,(N_I) \cdot \mathrm{grad}\,(N_J)\, dV}_{s_{IJ}}\, \Theta_J = 0 \quad . \tag{3}$$

So the stiffness matrix is

$$s_{IJ} = \int_\Omega k\, \mathrm{grad}^T\,(N_I) \cdot \mathrm{grad}\,(N_J)\, dV = \int_\Omega k \begin{bmatrix} N_{I,x} & N_{I,y} & N_{I,z} \end{bmatrix} \cdot \begin{bmatrix} N_{J,x} \\ N_{J,y} \\ N_{J,z} \end{bmatrix} dV = \int_\Omega k\, \boldsymbol{B}_I^T \cdot \boldsymbol{B}_J\, dV \quad . \tag{4}$$

As no internal heat source is considered, the heat flux is the residuum

$$\boldsymbol{q}^h = \boldsymbol{s} \cdot \boldsymbol{\Theta}^h \quad . \tag{5}$$

3 Numerical examples

The thermal conductivity k to be used in the joining zone has to be determined. It is assumed to depend on the damage in the joining zone. The thermal behaviour of a hybrid tube is investigated in [5] (Figure 2 left). It is intended to form a bearing bushing using the tube (Figure 2 right). For the forming process the materials are heated differently to obtain similar yielding properties; i.e. the temperature of steel (inside) has to be higher than the temperature of aluminium (outside) [3]. In the following the evolution of the temperature distribution is simulated with a special focus on the heat transfer through the joining zone. The initial temperatures are chosen according to the status "after heating" in [5] (initial in Figure 3). The transportation time (6 s from heating to the forming machine) is simulated and the temperatures are compared to the results in [5] (InTEx and Reference in Figure 3). The work piece is only press fitted and not firmly bonded which is here assumed to be equivalent to a fully damaged state ($D = 1$) of the joining zone material.

For the simulations the following material parameters are used: Steel: Thermal conductivity 42 $W/(m\,K)$ [7] and specific heat capacity 433 $kJ/(kg \cdot K)$ [7]. Aluminium: Thermal conductivity 180 $W/(m\,K)$ [9] and specific heat capacity 888 $J/(kg \cdot K)$ [1].

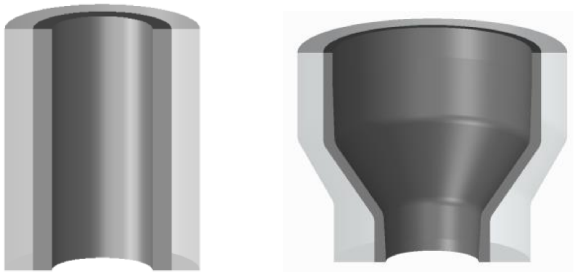

Figure 2. Semi finished work piece (left) and formed hybrid bearing bushing (right) [5]

The reference temperature distribution including the temperature jump are well reproduced by the simulations using InTEx elements (Figure 3). For the lower temperature (left in Figure 3) a thermal conductivity of $0.0105\,W/(m\,K)$ and for the higher temperatures (center and right in Figure 3) a thermal conductivity of $0.0075\,W/(m\,K)$ fit the results from [5] best.[†] The changing heat conduction is also discussed in [5] and explained by gap opening between steel and aluminium.

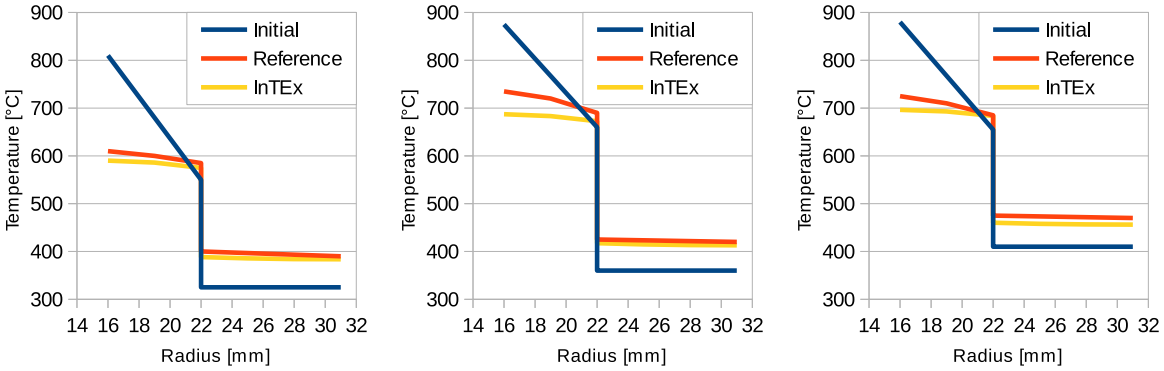

Figure 3. Initial and reference temperature distribution of a hybrid tube according to [5] and simulation results using InTEx elements for three different initial states

In a different study the thermal behaviour of a friction welded hybrid shaft is examined [6]. This is assumed to represent the undamaged ($D = 0$) state as the component is firmly bonded by the joining process. Some thermocouples are applied close ($2.5\,mm$) to the joining zone and distributed on the remaining component (TC1 ... TC6 in Figure 4). After induction heating the temperature distribution is recorded for $10\,s$. The temperature gradient around the joining zone is very low which indicates a high thermal conductivity. The global temperature distribution could be reproduced with $k = 68\,W/(m\,K)$, which represents a perfect serial connection of an equal amount of steel and aluminium (Figure 5):[‡]

$$k_{bond} = 2\frac{k_{st}\,k_{al}}{k_{st} + k_{al}} \tag{6}$$

4 Conclusion

The temperature distribution after a heating process of two different hybrid components was simulated using InTEx elements for the joining zone. The two components reflect completely firm and fully damaged joining zone material. In both cases the global temperature distribution could be well reflected; to achieve this a different thermal conductivity had to be applied which means the thermal conductivity is damage dependent.

[†]A joining zone thickness of 10 μm is used here. A different specification of the joining zone thickness (more or less adjacent material) is accompanied by a different thermal conductivity for the total joining zone material.

[‡]The measured temperature gradient could not even be reproduced with a much higher thermal conductivity. Though the value deduced here is seen as the physical limit and higher values only cause insignificant changes on the temperature gradient around the joining zone and on the global termperature distribution.

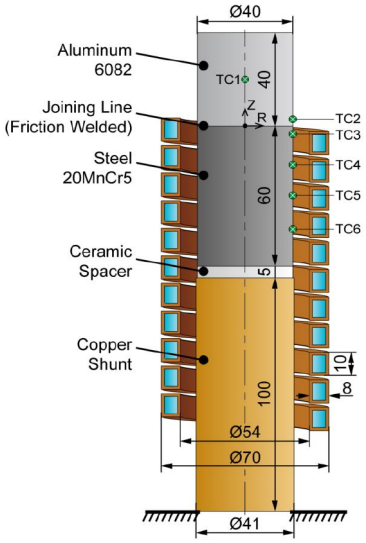

Figure 4. Hybrid shaft [6]

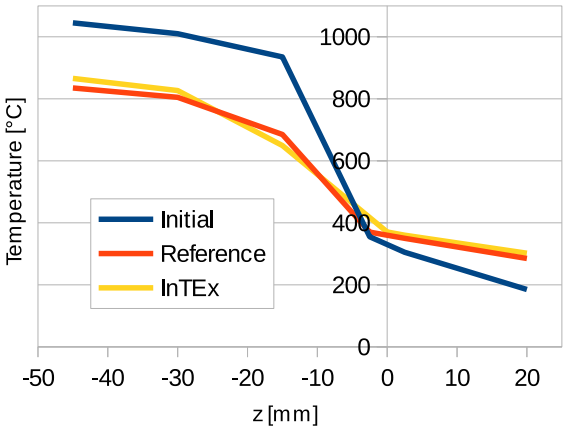

Figure 5. Initial and reference temperature distribution of a hybrid shaft according to [6] and simulation results using InTEx elements

Acknowledgments

The results presented in this paper were obtained within the Collaborative Research Centre 1153 "Process chain to produce hybrid high performance components by Tailored Forming" in the subproject C4. The authors would like to thank the German Research Foundation (DFG) for the financial and organisational support of this project.

References

[1] Joachim Ahrendts and Stephan Kabelac. F Technische Thermodynamik. In: *HÜTTE-Das Ingenieurwissen*. Springer, 2012.

[2] B.-A. Behrens, A. Huskic, C. Frischkorn, and D. Duran. Fließpressen hybrider Halbzeuge. *Werkstattstechnik online* 10-2015 (2015), pp. 704–708.

[3] B.-A. Behrens, A. Chugreev, and T. Matthias. Hybride Lagerbuchsen aus Aluminium und Stahl. *Werkstattstechnik online* 10-2018 (2018), pp. 691–697.

[4] B.-A. Behrens, B. Breidenstein, D. Duran, S. Herbst, R. Lachmayer, S. Löhnert, T. Matthias, I. Mozgova, F. Nürnberger, V. Prasanthan, et al. Simulation-Aided Process Chain Design for the Manufacturing of Hybrid Shafts. *HTM Journal of Heat Treatment and Materials* 74.2 (2019), pp. 115–135.

[5] Bernd-Arno Behrens, Robert Goldstein, and Anna Chugreeva. Thermomechanical Processing for Creating Bi-Metal Bearing Bushings. In: *Proceedings of the Thermal Processing in Motion*. 2018.

[6] Bernd-Arno Behrens, Robert Goldstein, David Guisbert, and Deniz Duran. Thermomechanical Processing of Friction Welded Steel-Aluminum Billets to Improve Joining Zone Properties (2018).

[7] Deutsche Edelstahlwerke GmbH. *Cr-Mn-legierter Einsatzstahl 20MnCr5*. 2011.

[8] K. Knothe and H. Wessels. *Finite Elemente Eine Einführung für Ingenieure*. Vol. 3. Springer, 1999.

[9] thyssenkrupp Materials (UK) Ltd. *Material Data Sheet Aluminium Alloy 6082*. 2016.

[10] F. Töller, S. Löhnert, and P. Wriggers. Internal Thickness Extrapolation. In: *Proceedings in Applied Mathematics and Mechanics*. Vol. 18. 1. Wiley Online Library, 2018.

[11] F. Töller, S. Löhnert, and P. Wriggers. Bulk material models in cohesive zone elements for simulation of joining zones. *Finite Elements in Analysis and Design* 164 (2019), pp. 42–54.

[12] F. Töller, S. Löhnert, and P. Wriggers. Modelling Tailored Forming Joining Zones with Internal Thickness Extrapolation Elements. In: *AIP Conference Proceedings*. AIP Publishing. 2019.

[13] P. Wriggers. *Finite-Elemente-Methode, Skript zur Vorlesung*.

**Proceedings of the 8th GACM Colloquium on Computational Mechanics
for Young Scientists from Academia and Industry
August 28–30, 2019 in Kassel, Germany**

On Solving Euler-Bernoulli Beams using a B-Spline based Representation for Random Variables

Christoph Eckert * [1], Michael Beer[1] and Pol Spanos[2]

[1]Institute for Risk and Reliability, Leibniz Universität Hannover, Germany
[2]L. B. Ryon Endowed Chair in Engineering, Rice University, USA

Abstract. Random quantities of stochastic systems can be approximated by the polynomial chaos representation by truncating the series expansion. Ordinarily, the basis of these series are orthogonal Hermite polynomials, which can be further extended by the Askey scheme of polynomials. In this work, B-spline basis functions, which are applied successfully in the context of isogeometric analysis, are considered for representing random variables. As an example, a simple Euler-Bernoulli beam with random beam rigidity is solved within a Galerkin framework. Further, convergence of the B-spline approach is established by numerical results which are compared with the multi-element generalized polynomial chaos. As a consequence, the B-spline representation is a generalization of the Legendre chaos and much more efficient.

Introduction

The usage of polynomial chaos (PC) representation to approximate random processes is widespread in the area of stochastic mechanics (e.g. [8, 13]). Further, the methodology has a mathematically solid framework, i.e. for any arbitrary random process with finite second-order moments the original Wiener polynomial chaos expansion [17] converges in accord with the Cameron-Martin theorem [4]. Further, the generalization of PC expansions by polynomials of the Askey scheme can be found in [19]. Afterwards, the generalized PC was further improved by [14, 15, 16] in order to captures the problems of long-term integration, large perturbation, and stochastic discontinuities. Therefore, the stochastic space is decomposed in elements and PC approximations are build within each element, which is known as the multi-element generalized polynomial chaos (ME-gPC).
In 2005, Hughes et al. [10] bridged the gap between computer aided design and engineering by introducing the methodology of isogeometric analysis (IGA), which successfully has enhanced many deterministic applications (e.g. [1, 2, 5, 6, 12]). One procedure within the IGA framework is to use non-uniform rational B-splines, which are prevalent in engineering design processes, as a basis for the analysis. In addition, it turned out that the nature of B-splines are also very beneficial in terms of analysis procedures. In this regard, it is remarkable that the notion of IGA is not widely adopted within stochastic frameworks [3, 9, 11].
In this paper, B-spline basis functions are employed in the truncated PC expansion for approximating random quantities. Further, an Euler Bernoulli beam with random flexural rigidity is solved by the B-spline representation using a stochastic Galerkin scheme and faced with the Legendre ME-gPC.

1 B-spline representation for random variables

B-spline basis functions are defined by a knot vector

$$\Xi = \{\underbrace{0,\dots,0}_{p+1},\xi_{p+2},\dots,\xi_n,\underbrace{1,\dots,1}_{p+1}\} = \{\xi_1,\dots,\xi_{n+p+1}\}, \tag{1}$$

*Corresponding author: eckert@irz.uni-hannover.de ORCID iD: 0000-0002-1266-8660

consisting of non-decreasing real numbers, where p is the polynomial order and n is the number of basis functions (e.g. [10]). The ξ_i's are called knots and define element boundaries (knot spans) if they differ. The B-spline basis functions can then be explained by the Cox-de Boor recursion formula:

$$B_{i,0}(u) := \begin{cases} 1 & \text{if} \quad \xi_i \leq u < \xi_{i+1} \\ 0 & \text{otherwise} \end{cases} \qquad \text{for } p = 0 \ , \tag{2}$$

$$B_{i,p}(u) := \frac{u - \xi_i}{\xi_{i+p} - \xi_i} B_{i,p-1}(u) + \frac{\xi_{i+p+1} - u}{\xi_{i+p+1} - \xi_{i+1}} B_{i+1,p-1}(u) \qquad \text{for } p \geq 1 \ . \tag{3}$$

Repeating inner knots in the interior of knot vectors entail in a lower continuity over knot spans, whereas single knots reveal a $\mathcal{C}^{p-1}$-continuity. This affects profoundly the number of basis functions and is indeed the main reason for the effectiveness of the subsequent method.
Next, consider an arbitrary random variable $X \in L_2(\Omega, \mathcal{F}, P)$ with finite second moment, where Ω is a sample space, $\mathcal{F}$ is an appropriate σ-field on Ω, and P is a probability measure. According to the polynomial chaos, the B-spline based approximation of X with knot vector $\Xi(p, n)$ is defined by

$$X \approx \widetilde{X} := \sum_{i=1}^{n} x_i B_{i,p}(U), \tag{4}$$

where U is uniformly distributed on $[0, 1]$. The expansion converges, because it suffices that the functions in use form a basis of the underlying Hilbert space $L_2(\Omega, \mathcal{F}, \mathcal{P})$ [8, 18]. Therefore, the coefficients x_i in Eq. (4) can be determined by solving a linear algebraic system resulting from the L_2 projection:

$$\mathbf{A}\mathbf{x} = \mathbf{b} \tag{5}$$

with

$$\mathbf{A}_{i,j} := E\left(B_{i,p}(U) B_{j,p}(U)\right) = \int_{I_U} B_{i,p}(U) B_{j,p}(U) \, dF_U = \int_0^1 B_{i,p}(u) B_{j,p}(u) \, du \tag{6}$$

$$\mathbf{b}_j := E(F_X^{-1}(U) B_{j,p}(U)) = \int_{I_U} F_X^{-1}(U) B_{j,p}(U) \, dF_U = \int_0^1 F_X^{-1}(u) B_{j,p}(u) \, du \tag{7}$$

$i, j = 1, \ldots, n$. The matrix $\mathbf{A}$ depends only on the knot vector Ξ of the B-spline basis functions, and can be stored before the analysis. Further, $\mathbf{A}$ is a band matrix with bandwidth $p + 1$.

2 Euler Bernoulli beam with random stiffness

In this section the versatility and convergence of the aforementioned approach is demonstrated by a numerical example. Specifically, the ordinary differential equation of an Euler Bernoulli beam with random stiffness is solved using a stochastic Galerkin scheme and compared to the Legendre ME-gPC by [14].

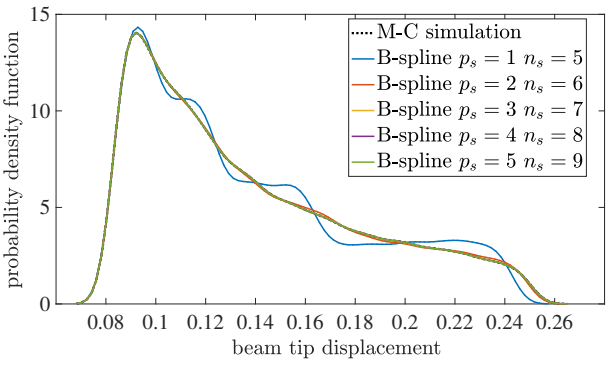

Figure 1. Solution of Eq. (12) with uniformly distributed beam rigidity $W(\theta)$ using four stochastic elements. Comparison with Monte Carlo simulations (1000 realizations).

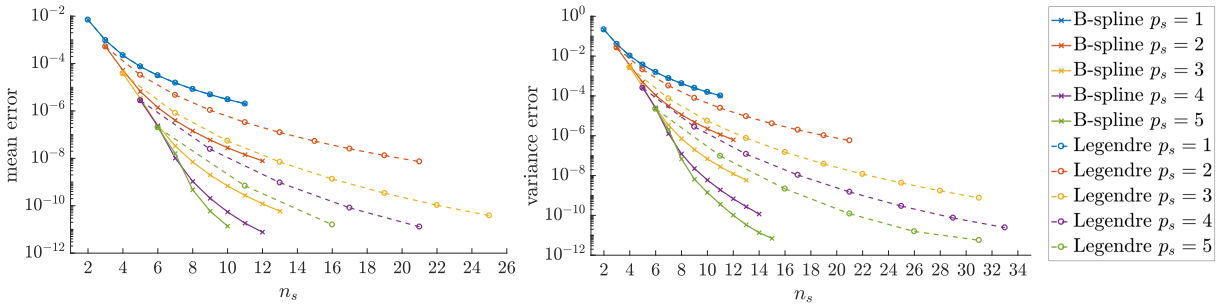

Figure 2. Comparison of mean errors (left), and variance errors (right) at the beam tip, solved by B-spline representation (solid line), and Legendre ME-gPC (dashed line) for uniformly distributed beam rigidity $W(\theta)$.

Consider the Euler Bernoulli beam of length L, clamped at $x = 0$ and subjected to a deterministic uniformly distributed load $f \equiv 1$. The governing equation is given by

$$EI \, \frac{d^4}{dx^4} u(x) = f \quad \text{with} \quad u(0) = u'(0) = 0, \tag{8}$$

where the beam rigidity $W := EI$ is assumed to be uniformly distributed in [0.5,1.5], and is specified by the modulus of elasticity E and the area moment of inertia I. In order to make Eq. (8) numerically feasible, the spatial and stochastic space of the solution and random input must be discretized. Using isogeometric subspace leads to

$$\tilde{u}(x,\theta) = \sum_{l=1}^{n_d} u_l(\theta) B^d_{l,p_d}(u(x)) = \sum_{l=1}^{n_d} \sum_{i=1}^{n_s} u_{i,l} B^s_{i,p_s}(U(\theta)) B^d_{l,p_d}(u(x)) \quad \text{, and} \tag{9}$$

$$\widetilde{W}(\theta) = \sum_{k=1}^{n_w} w_k B^w_{k,p_w}(U(\theta)), \tag{10}$$

where $u(x)$ is a linear mapping from the spatial space $[0, L]$ to the parameter space $[0, 1]$. Applying the deterministic and stochastic Galerkin procedure to Eq. (8) and using Eq. (9) and (10), yields

$$\sum_{l=1}^{n_d} \sum_{i=1}^{n_s} \sum_{k=1}^{n_w} u_{i,l} w_k E_U \left[B^s_{i,p_s}(U) B^s_{j,p_s}(U) B^w_{k,p_w}(U) \right] \int_L \frac{d^2}{dx^2} B^d_{l,p_d}(x) \, \frac{d^2}{dx^2} B^d_{m,p_d}(x) \, dx \tag{11}$$

$$= E_U \left[B^s_{j,p_s}(U) \right] \int_L f B^d_{m,p_d}(x) \, dx \qquad \begin{matrix} j = 1, \ldots, n_s \\ m = 1, \ldots, n_d \end{matrix} . \tag{12}$$

Due to the boundary conditions of Eq. (8), the first two coefficients of the vector $u_l(\theta)$ are equal to zero. Solving the reduced system, $n_d \cdot (n_s - 2)$ coefficients of $\tilde{u}(x, \theta)$ are determined, where as the control variables u_{i,n_d} with $i = 1, \ldots, n_s$ represents the stochastic beam tip deflection. Since the B-spline representation is optimal for uniform distributions [7], Eq. (10) is exact for $n_w = 2$, $w_1 = 0.5$, $w_2 = 1.5$, and knot vector $\Xi^w = \{0, 0, 1, 1\}$. In order to assess the significance of the numerical results obtained from the B-spline representation the beam problem is threated by a Monte Carlo simulation. The resulting density functions of the beam tip deflection are plotted in Fig. 1. Comparisons with different B-spline types show a satisfactory level of accuracy for $p_s \geq 2$. Further, convergence of mean, and variance of B-spline representations for the beam tip deflection are shown in Fig. 2 and juxtaposed with multi-element Legendre chaos. On the one hand, it can be concluded that the B-spline representation generalizes the multi-element Legendre chaos [7]. On the other hand, the k-refinement property of B-splines (e.g. [10]) results in higher efficiency, e.g. the B-spline representation of order $p_s = 5$ with ten stochastic elements ($n_s = 15$) results in an increased accuracy for the variance error with less than half of the number of basis functions in comparison with multi-element Legendre chaos ($n_s = 31$). This effect becomes much stronger by increasing order.

3 Conclusion

In this paper the potential of a B-spline based representation for random variables has been demonstrated. Correspondingly, the B-spline approach has been found optimal for uniform input and generalizes the

Legendre multi-element polynomial chaos of Wan and Karniadakis [14]. Further, it has been found that the smoothness property of B-spline basis functions improves significantly the efficiency when decomposing the random space, which even comes to a greater extent if the degree is increased.
As a numerical assertion, a stochastic beam problem has been investigated using Galerkin methods. Input and output of the system were represented by the new B-spline approach and a better rate of convergence has been achieved for uniform input in comparison with the multi-element Legendre chaos. Note that Wan and Karniadakis [14] have stated that the efficiency of ME-gPC is reduced significantly by the rapidly increasing number of random elements for high-dimensional problems; the results reported herein indicate that the B-spline representation may overcome this drawback of ME-gPC. The accuracy of the B-spline technique is also established by pertinent Monte Carlo simulations.

References

[1] F. Auricchio, L. Beirão da Veiga, T.J.R. Hughes, and A. Reali. Isogeometric collocation for elastostatics and explicit dynamics. *Comput Method Appl M* 249-252 (2012), pp. 2–14.

[2] Y. Bazilevs, V. M. Calo, T. J R Hughes, and Y. Zhang. Isogeometric fluid-structure interaction: Theory, algorithms, and computations. *Computational Mechanics* 43.1 (2008), pp. 3–37.

[3] G. Bhardwaj, I.V. Singh, and B.K. Mishra. Stochastic fatigue crack growth simulation of interfacial crack in bi-layered FGMs using XIGA. *Comput Method Appl M* 284 (2015), pp. 186–229.

[4] R. H. Cameron and W. T. Martin. The Orthogonal Development of Non-Linear Functionals in Series of Fourier-Hermite Functionals. *The Annals of Mathematics* 48.2 (1947), p. 385.

[5] J.A. Cottrell, A. Reali, and Y. Bazilevs. Isogeometric analysis of structural vibrations. *Comput Method Appl M* 195.41-43 (2006), pp. 5257–5296.

[6] J.A. Cottrell, J.A. Evans, S. Lipton, M.A. Scott, and T.W. Sederberg. Isogeometric analysis using T-splines. *Comput Method Appl M* 199.5-8 (2010), pp. 229–263.

[7] C. Eckert, M. Beer, and P. D. Spanos. A B-Spline based Representation for Random Variables within Stochastic Galerkin Methods (submitted for publication).

[8] R.G. Ghanem and P.D. Spanos. *Stochastic Finite Elements: A Spectral Approach.* Mineola, New York: Dover Publications, INC., 2003.

[9] T. D. Hien and H. C. Noh. Stochastic isogeometric analysis of free vibration of functionally graded plates considering material randomness. *Comput Method Appl M* 318 (2017), pp. 845–863.

[10] T. J.R. Hughes, J. A. Cottrell, and Y. Bazilevs. Isogeometric analysis: CAD, finite elements, NURBS, exact geometry and mesh refinement. *Comput Method Appl M* 194.39-41 (2005), pp. 4135–4195.

[11] K. Li, W. Gao, D. Wu, C. Song, and T. Chen. Spectral stochastic isogeometric analysis of linear elasticity. *Comput Method Appl M* 332 (2018), pp. 157–190.

[12] G. Sangalli, T.J.R. Hughes, L. Beirão da Veiga, F. Auricchio, and A. Reali. Isogeometric Collocation Methods. *Mathematical Models and Methods in Applied Sciences* 20.11 (2010), pp. 2075–2107.

[13] G. Stefanou. The stochastic finite element method: Past, present and future. *Comput Method Appl M* 198.9-12 (2009), pp. 1031–1051.

[14] X. Wan and G. E. Karniadakis. An adaptive multi-element generalized polynomial chaos method for stochastic differential equations. *Journal of Computational Physics* 209.2 (2005), pp. 617–642.

[15] X. Wan and G. E. Karniadakis. Long-term behavior of polynomial chaos in stochastic flow simulations. *Comput Method Appl M* 195.41-43 (2006), pp. 5582–5596.

[16] X. Wan and G. E. Karniadakis. Multi-Element Generalized Polynomial Chaos for Arbitrary Probability Measures. *SIAM Journal on Scientific Computing* 28.3 (2006), pp. 901–928.

[17] N. Wiener. The homogeneous chaos. *Amer. J. Math* 60.4 (1938), pp. 897–936.

[18] D. Xiu. *Numerical Methods for Stochastic Computations: A Spectral Method Approach.* Princeton: Princeton University Press, 2010.

[19] D. Xiu and G. E. Karniadakis. The Wiener–Askey Polynomial Chaos for Stochastic Differential Equations. *SIAM Journal on Scientific Computing* 24.2 (2002), pp. 619–644.

**Proceedings of the 8th GACM Colloquium on Computational Mechanics
for Young Scientists from Academia and Industry
August 28–30, 2019 in Kassel, Germany**

An Approach to Analyze the Stability of Quasiperiodic Motions with the Method of Characteristics

Robert Fiedler * [1] and Hartmut Hetzler[1]

[1]Engineering Dynamics Group, Institute of Mechanics, University of Kassel, Kassel, Germany

Abstract. The approximation of quasiperiodic motions may efficiently be realized by calculating invariant manifolds (Tori). Once a stationary solution has been determined, its stability will be of great importance. This contribution deduces a stability criterion based on the generalized Lyapunov numbers (GLNs), which can effectively be applied to quasiperiodic motions. Furthermore, the criterion is used to identify the stability of quasiperiodic motions exhibited by the forced van-der-Pol equation and compared, solely in the stable region, to an alternative, time simulation based approach.

Introduction

The investigation of quasiperiodic oscillations in engineering applications is a relatively unexplored field of research, although a well-established theoretical basis is existent in the field of mathematics. At a first glance, quasiperiodic motions might seem to be a rather artificial case. However, they turn out to be a widespread phenomenon in engineering which is produces whenever multiple mechanisms arising from different physical origins excite a dynamical system simultaneously †[2, 5]. The main challenge, when dealing with quasiperiodic motions, arises from the infinite period length, which results from an incommensurable frequency basis‡. Due to that, the use of standard methods (for periodic solutions) is usually either very disadvantageous or unsuitable, since they often aim on parameterizing the resulting motion over time. Instead of approaching the problem on one time scale, multiple cyclic time scales (torus coordinates) are introduced whereat the initial system of ordinary differential equation (dynamical system in state-space) transfers to a system of partial differential equations (invariance equations). The solution of the invariance equation is an invariant manifold (object in the state-space), which is filled densely by a quasiperiodic motion. Once calculated, the invariant manifold represents an unperturbed, stationary motion of a dynamical system. For any stationary solution informations about the stability are of great importance

The definition of orbital stability for quasiperiodic motions in the sense of Lyapunov is theoretical possible [3] but almost always not applicable when dealing with dynamical systems which cannot be solved analytically. In addition, algebraic stability criteria derived from linear maps are in the context of quasiperiodic motions not available§. This problem stems from the infinite periodic length possessed by a quasiperiodic solution in time domain. Since stability criteria are often derived from the linearized equation of motion, the exponential grow and/or decay rate result in singularities and/or infinitely large values. Nevertheless, there are methods existent which aim on approximating the Lyapunov exponents of arbitrary solutions [1]. The drawbacks, exhibited by these methods, are on the one hand the high calculation effort and on the other hand that they often base on time integrations, whereby an identification of instabilities is not possible. This contribution aims on deriving a general and time efficient approach to identify the stability of quasiperiodic motions.

*Corresponding author: robert.fiedler@uni-kassel.de

†Exceptions may be present when synchronization occurs.

‡Two incommensurable (rational independent) frequencies are for example $\omega_1 = 1$ and $\omega_2 = \pi$.

§In the context of equilibrium points or periodic solutions, the stability is usually identified by an eigenvalue analysis of the Jacobian or the Monodromy matrix, respectively.

1 Theoretical framework

The theory of quasiperiodicity is extensive and a detailed reproduction would exceed the scope of this contribution. Interested readers are e.g. referred to [3] for a comprehensive explanation of the mathematical theory. When dealing with periodic motions, a boundary value problem can be formulated to identify a solution. The main problem, when dealing with quasiperiodic motions, arises from the parameterization over time. Due to the infinite period length, the resulting boundary value problem has to be solved on an infinite, one dimensional interval $\left(t \in \left[0, \lim_{T\to\infty} T\right]\right)$. Instead of directly using the time, a parametrization over different time scales ($\theta_1 = \omega_1 t, \ldots, \theta_p = \omega_p t$) is usually used, whereby the different time scales are connected to the incommensurable frequency basis ($\omega_i,\ i = 1, \ldots p$). The resulting parametrization $\boldsymbol{\theta} = [\theta_1, \ldots, \theta_p]$ consists of cyclic coordinates (torus coordinates), whereby a parametrization over a finite, p-dimensional interval is achieved. For example, consider an dynamical system in state-space

$$\dot{\mathbf{z}} = \mathbf{f}(\mathbf{z}, \boldsymbol{\Omega} t, \gamma), \qquad \mathbf{z}(t) \in \mathbb{R}^n,\ \boldsymbol{\Omega} \in \mathbb{R}^m,\ \gamma \in \mathbb{R}, \tag{1}$$

where $\mathbf{z}$ is the state-space vector, $\boldsymbol{\Omega}$ is a vector of incommensurable forcing frequencies and γ is the bifurcation parameter. Parameterizing Eq.(1) on a torus instead over time is a change of the independent variable from t to $\boldsymbol{\theta}$[¶]: $\mathbf{z}(\Omega_1 t, \ldots \Omega_m t, \omega_{m+1} t, \ldots, \omega_p t)^{\|} = \mathbf{Z}(\theta_1, \ldots, \theta_p)$. With this one can derive the invariance equation

$$\sum_{i=1}^{m} \frac{\partial \mathbf{Z}}{\partial \theta_i} \Omega_i + \sum_{i=m+1}^{p} \frac{\partial \mathbf{Z}}{\partial \theta_i} \omega_i = \mathbf{f}(\mathbf{Z}, \tilde{\boldsymbol{\theta}}, \gamma), \qquad \tilde{\boldsymbol{\theta}} = [\theta_1, \ldots, \theta_m] \tag{2}$$

where besides the torus function $\mathbf{Z}$, the autonomous frequencies $\boldsymbol{\omega} = [\omega_{m+1}, ..., \omega_p]$ are unknown. Analogous to periodic solutions, the necessity of a phase condition is given, whereby depending on the solution strategy different approaches are possible (e.g. [4]).

1.1 Application of the method of characteristics

Since the focus of this contribution lies on the stability assessment, it is assumed that a quasiperiodic motion $\mathbf{z}_q(t)$ ($\mathbf{Z}_q(\boldsymbol{\theta}(t))$, respectively) is known. Perturbing the quasiperiodic solution ($\mathbf{z} = \mathbf{z}_q + \Delta\mathbf{z}$) and performing subsequently a Taylor-expansion, the linearized equations of motion in time domain are obtained

$$\Delta\dot{\mathbf{z}} = \mathbf{j}(t)\Delta\mathbf{z} + \mathcal{O}(\Delta\mathbf{z}^2), \qquad \mathbf{j}(t) = \left.\frac{\partial \mathbf{f}}{\partial \mathbf{z}}\right|_{\mathbf{z}_q}, \qquad \mathbf{j}(t) \in \mathbb{R}^{n\times n}, \tag{3}$$

where $\mathbf{j}$ is the Jacobian in time domain: since $\mathbf{j}$ depends on the quasiperiodic motion it is quasiperiodic, too. Converting the parametrization from time to torus domain ($[t, \mathbf{z}_q, \mathbf{j}(t)] \to [\boldsymbol{\theta}, \mathbf{Z}_q, \mathbf{J}(\boldsymbol{\theta})]$) and neglecting the higher order terms, yields a linear system of partial differential equations

$$\sum_{i=1}^{m} \frac{\partial \Delta\mathbf{Z}}{\partial \theta_i} \Omega_i + \sum_{i=m+1}^{p} \frac{\partial \Delta\mathbf{Z}}{\partial \theta_i} \omega_i = \mathbf{J}(\boldsymbol{\theta})\Delta\mathbf{Z}. \tag{4}$$

One should note, that at this point the frequencies $\omega_i,\ i = m+1, ..., p$ are known[**]. The system of linear partial differential equations (4) can be solved by using the method of characteristics, wherewith a periodic boundary value problem is converted into an initial value problem. The resulting system of ordinary differential equations reads:

$$\begin{aligned} \frac{\mathrm{d}\theta_i}{\mathrm{d}t} &= \Omega_i, \quad i = 1, \ldots, m \\ \frac{\mathrm{d}\theta_i}{\mathrm{d}t} &= \omega_i, \quad i = m+1, \ldots, p \end{aligned} \qquad \frac{\mathrm{d}\Delta\mathbf{z}}{\mathrm{d}t} = \mathbf{J}(\boldsymbol{\theta}(t))\Delta\mathbf{z}, \qquad \Delta\mathbf{z}(0, \mathbf{s}) = \Delta\mathbf{z}_0, \tag{5}$$

where $\Delta\mathbf{z}_0$ are initial values and the parametrization changes from $\boldsymbol{\theta}$ to $[t, \mathbf{s}],\ t \in \mathbb{R},\ \mathbf{s} \in \mathbb{R}^{p-1}$. The variable t corresponds to the time of the underlying dynamical system and $\mathbf{s}$ parametrizes the initial curve. Using this formulation, the evolution of a perturbed solution over time $\Delta\mathbf{z}(t)$ can be combined with the torus formulation $\mathbf{J}(\boldsymbol{\theta})$, whereby the position on the torus can always be identified by the evolution of the torus coordinates $\boldsymbol{\theta}(t)$. Through the definition of an initial curve a unique solution can be obtained.

[¶] I.e. $\mathbf{z}(t) = \mathbf{z}(\omega_1 t) = \mathbf{Z}(\theta_1)$.

[‖] Note that the first m arbitrary frequencies $\omega_i,\ i = 1, ..., m$ are substituted by the known incommensurable forcing frequencies $\boldsymbol{\Omega}$.

[**] Through the calculation of the invariant manifold by Eq.(2) and an additional phase condition (e.g [4]).

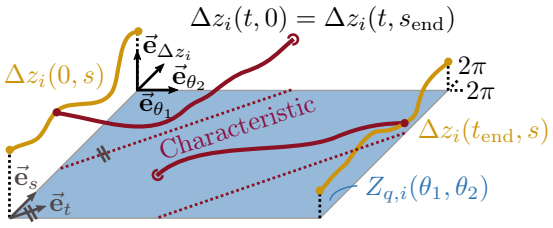

Figure 1. Schematic depiction of the approach with two torus coordinates (θ_1, θ_2). Note that only one perturbed component (Δz_i) is depicted.

Note that the choice of the initial curve is not completely arbitrary since it has to satisfy the transversality condition. Defining a set of linear independent vectors $\mathbf{\Phi} = [\Delta\mathbf{z}_1 \mid \ldots \mid \Delta\mathbf{z}_n]$ with the identity matrix as initial value $\mathbf{\Phi}(0,\mathbf{s}) = \mathbf{I}$, a normalized fundamental system is defined. Since Eq.(2) implies parallel dynamics[††] and the frequency basis $[\mathbf{\Omega}, \boldsymbol{\omega}]$ is known, the time interval $[0, t_{\text{end}}]$ on which the characteristic system has to be solved can be determined. Solving the characteristics on the defined time interval leads, due to the underlying quasiperiodic problem, to a linear map which can map arbitrary perturbations over a cyclic boundary (cf. figure 1). Choosing the initial curve orthogonal to θ_1 and solve Eq.(5) for a normalized fundamental system, a map

$$\Delta\mathbf{Z}(2\pi, \tilde{\boldsymbol{\theta}}^*) = \mathbf{\Phi}\left([2\pi, 0], [\tilde{\boldsymbol{\theta}}^*, \tilde{\boldsymbol{\theta}}]\right) \Delta\mathbf{Z}(0, \tilde{\boldsymbol{\theta}}), \quad \tilde{\boldsymbol{\theta}} = [\theta_2, ..., \theta_p] \tag{6}$$

is found, which describes the behavior of an arbitrary perturbation over the cyclic boundary. Here, $\theta_i^* = \theta_i + 2\pi\frac{\omega_i}{\omega_1}$. It is important to note, that an eigenvalue analysis of $\mathbf{\Phi}$ is not applicable, since a point on the initial curve $\Delta\mathbf{Z}(0,\mathbf{s})$ is not mapped onto itself[‡‡]

1.2 Stability criterion for quasiperiodic motions

Following, the theory of generalized Lyapunov numbers is used to deduce an applicable criterion to identify the stability of quasiperiodic motions. For a detailed view of the theory see [6, p. 56 – 69]. Since an invariant manifold possesses the particular property that orbits never leave it, solely the dynamics normal to the invariant manifold are of interest. Therefore, with the standard (Euclidean) norm, the linearized space is split

$$T\mathbb{R}^n|_{\mathcal{M}} = T\mathcal{M} \oplus \mathcal{N} \tag{7}$$

into a tangent $(T\mathcal{M})$ and normal bundle $(\mathcal{N})$. Through this splitting, the following linear operators can be constructed for the linearized flow

$$\begin{aligned} \mathbf{A}(t) \equiv \boldsymbol{\phi}(t, t_0) \quad &: \quad T_{\Delta\mathbf{z}(t_0)}\mathcal{M} \;\rightarrow\; T_{\Delta\mathbf{z}(t)}\mathcal{M} \\ \mathbf{B}(t) \equiv \mathbf{q}(t)\boldsymbol{\phi}(t, t_0) \quad &: \quad \mathcal{N}_{\Delta\mathbf{z}(t_0)} \;\rightarrow\; \mathcal{N}_{\Delta\mathbf{z}(t)}, \end{aligned} \tag{8}$$

where $\mathbf{q}(t) : T\mathbb{R}^n|_{\mathcal{M}} \rightarrow \mathcal{N}$ indicates an orthonormal projector of a vector onto the normal bundle and $\boldsymbol{\phi}$ is the fundamental solution. Both defined in time domain. By means of the linear operators, the following holds:

$$\begin{aligned} \mathbf{v}(t) &= \mathbf{A}(t)\mathbf{v}(t_0) \qquad \mathbf{v} \in T\mathcal{M} \\ \mathbf{w}(t) &= \mathbf{B}(t)\mathbf{w}(t_0) \qquad \mathbf{w} \in \mathcal{N}. \end{aligned} \tag{9}$$

Considering the linear operator of the normal space $\mathbf{B}(t)$, the first generalized Lyapunov number (GLN1) can be defined

$$\nu = \overline{\lim_{t\to\infty}} \, ||\mathbf{B}(t)||^{\frac{1}{t}}, \qquad \text{with} \qquad ||\mathbf{B}(t)|| \equiv \sup_{\mathbf{w}(t_0)\in\mathcal{N}} \frac{||\mathbf{B}(t)\mathbf{w}(t_0)||}{||\mathbf{w}(t_0)||}. \tag{10}$$

Through Eq.(6) the fundamental solution is known over a cyclic boundary. Transforming the expression of the GLN1 into torus domain $([t, \mathbf{q}(t), \boldsymbol{\phi}(t)] \rightarrow [\boldsymbol{\theta}, \mathbf{Q}(\boldsymbol{\theta}), \mathbf{\Phi}(\boldsymbol{\theta})])$ results in

$$\nu = \overline{\lim_{N\to\infty}} \left|\left| \prod_{i=1}^{N} \mathbf{Q}_i \mathbf{\Phi}_i \right|\right|^{\frac{1}{N t_{\text{end}}}} \quad \rightarrow \quad \begin{cases} < 1 & \text{stable} \\ > 1 & \text{unstable} \end{cases} \tag{11}$$

whereby an applicable and time efficient criterion for the stability of quasiperiodic motions is formulated. Note that the GLN1[§§] is independent of the splitting Eq.(7), constant on orbits and converges over time.

[††] Note that the torus coordinates are linear functions of time $\theta_i = \omega_i t$.
[‡‡] The offsets $(2\pi\frac{\omega_i}{\omega_1})$ have to be considered.
[§§] And the second generalized Lyapunov number as well.

2 Application to the forced van-der-Pol equation

In order to show the practicability of the proposed approach, it is applied to quasiperiodic solutions of the forced VAN-DER-POL equation

$$x'' + \varepsilon \left(x^2 - 1\right) x' + x = \hat{f} \cos(\Omega \tau), \tag{12}$$

where $(.)'$ is the derivation with respect to the dimensionless time τ, ε controls the nonlinearity and $\hat{f}$ and Ω are the forcing amplitude and dimensionless frequency, respectively. Following, the excitation parameters are fixed ($\hat{f} = 0.6, \Omega = 1.5$) and the bifurcation parameter is the nonlinearity ($\varepsilon \in [-1, 1]$). The quasiperiodic solutions are calculated by means of a finite difference method (FDM). The resultant quasiperiodic solution hast two base frequencies, one known non-autonomous (Ω) and one unknown autonomous (ω). In order to compare the identified stability behavior quantitatively, the LYAPUNOV exponents (LEs) are calculated with a time simulation based method [1].

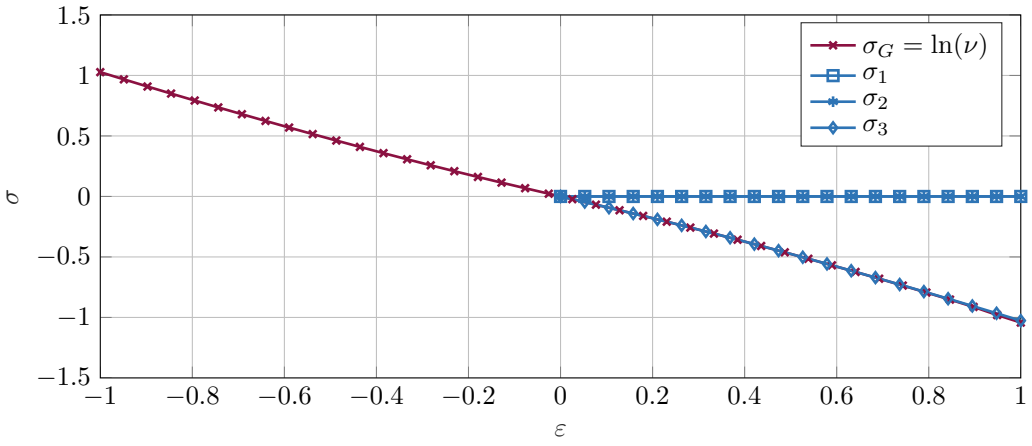

Figure 2. Comparison of LYAPUNOV exponents: Continuation ($\sigma_G = \ln(\nu)$) and time simulation ($\sigma_1, \sigma_2, \sigma_3$).

The investigation of Eq.(12) depicted in Fig.2. confirms the expected behavior. Since the autonomous state-space ($z \in \mathbb{R}^3$) is spitted into $T\mathcal{M} \in \mathbb{R}^2$ and $\mathcal{N} \in \mathbb{R}$ the normal bundle is one dimensional, whereby one LE represents its contraction/expansion rate (σ_3). Furthermore, two LEs are equal to zero, which identifies tangential directions (σ_1, σ_2). The results show, the time simulation based method can approximate the LEs until $\varepsilon = 0$. At this point the stability property changes and solely the proposed method can identify the instability of the quasiperiodic motion. Hence, the proposed method can not only predict the general stability property of invariant manifolds, in addition it does the prediction more efficient with reference to time and computational effort.

References

[1] F. Christiansen and H. H. Rugh. Computing Lyapunov spectra with continuous Gram - Schmidt orthonormalization. *Nonlinearity* 10.5 (1997), p. 1063. ISSN: 0951-7715.

[2] D. Guo, F. Chu, and D. Chen. The Unbalanced Magnetic Pull and its Effects on Vibration in a Three-Phase Generator with Eccentric Rotor. *Journal of Sound and Vibration* 254.2 (2002), pp. 297–312. ISSN: 0022460X.

[3] A. M. Samoilenko. *Elements of the Mathematical Theory of Multi-Frequency Oscillations*. Vol. 71. Mathematics and Its Applications, Soviet Series. Dordrecht: Springer, 1991. ISBN: 9789401055574. DOI: 10.1007/978-94-011-3520-7.

[4] Frank Schilder, Hinke M. Osinga, and Werner Vogt. Continuation of Quasi-periodic Invariant Tori. *SIAM Journal on Applied Dynamical Systems* 4.3 (2005), pp. 459–488. DOI: 10.1137/040611240.

[5] Sunil K. Sinha. Rotordynamic analysis of asymmetric turbofan rotor due to fan blade-loss event with contact-impact rub loads. *Journal of Sound and Vibration* 332.9 (2013), pp. 2253–2283. ISSN: 0022460X.

[6] Stephen Wiggins. Normally Hyperbolic Invariant Manifolds in Dynamical Systems. 105 (1994).

**Proceedings of the 8th GACM Colloquium on Computational Mechanics
for Young Scientists from Academia and Industry
August 28–30, 2019 in Kassel, Germany**

Initialization of the continuation of stick-slip vibrations for a two dof friction oscillator

Jonas Kappauf * [1] and Hartmut Hetzler[1]

[1]Engineering Dynamics Group, Institute of Mechanics, University of Kassel

Abstract. Within this contribution, approximation schemes for calculating periodic solutions for nonlinear self-excited systems are studied. For applying the *Harmonic Balance method* numerically, suitable initial conditions when applying Newton-like schemes are required. Hence, a procedure based on *homotopy methods* is presented for initializing the numerical calculation. In particular, a fixed-point homotopy map is constructed. This procedure is applied to calculate self-excited periodic stick-slip vibrations of a two degree of freedom friction oscillator. To this end, the influence of the harmonic order H on the homotopy path is studied and an outlook is given.

Motivation

Focussing on mechanical systems with strongly nonlinear or non-smooth forces, the initialization of numerical approximation schemes, e.g. for calculating periodic solutions, is the crucial point. As a method for approximating periodic limit cycles, that provides the ability dealing with non-smoothness in the equations of motion, the *Harmonic Balance Method* (HBM) is adressed.

For solving the resulting nonlinear algebraic HBM equation system numerically, an appropriate initial guess for the Newton-Raphson scheme is appreciated to achieve good convergence behaviour. Focussing on self-excited vibrations, usually less information may be taken from the linear system, hence the base frequency of the limit cycle is unknown. However, suitable methods, e.g. *homotopy methods* offering the ability to transform a simple or simplified version of an algebraic system, where the solution is known, to the original one. That results in a expansion of the basin of a attraction for a local solution of the HBM equations. In particular, the applicability of a fixed-point homotopy method approach is addressed to calculate periodic limit cycles of a self-excited two degree of freedom (dof) friction oscillator with velocity depending friction characteristic showing stick-slip vibrations.

1 Basic equations of the Harmonic Balance

For calculating periodic limit cycles, the *Harmonic Balance method* is a generic tool assuming the solution of a dynamical system can be expressed as a Fourier series of the form

$$\boldsymbol{x}(t) = \frac{\boldsymbol{X}_0}{2} + \mathrm{Re}\left\{\sum_{k=1}^{H} \boldsymbol{X}_k \mathrm{e}^{\,\mathrm{j}k\omega t}\right\}. \tag{1}$$

Substituting $\tau = \omega t$ and inserting eq. (1) into the equations of motion, denoted by $\boldsymbol{f}_{\mathrm{eom}}(\ddot{\boldsymbol{x}}, \dot{\boldsymbol{x}}, \boldsymbol{x}) = \boldsymbol{0}$, a Galerkin projection plus a scalar equation p_{c} leads to the set of algebraic equations

$$\boldsymbol{R}_k = \frac{1}{\pi}\int_0^{2\pi} \boldsymbol{f}_{\mathrm{eom}}(\boldsymbol{X}_i, \omega, \tau)\mathrm{e}^{\,\mathrm{j}k\tau}\mathrm{d}\tau, \quad i,k = 0,1,...,H \tag{2a}$$

$$p_{\mathrm{c}} = g(\boldsymbol{X}_i, \omega) \tag{2b}$$

*Corresponding author: kappauf@uni-kassel.de ORCID iD: 0000-0001-5142-4530

for calculating the coefficients $\boldsymbol{X}_i$ and the base frequency ω of eq. (1). Here, $\boldsymbol{R}_k$ denotes the coefficients of the residual related to the harmonic order k while p_c is the scalar phase condition, see [1].

However, the calculation of periodic limit cycles require adequate initial conditions when applying eqs. (2) to a classical NEWTON-RAPHSON scheme.

2 Homotopy methods

As mentioned above, generating initial conditions for calculating solutions in an straight-forward way, in this contribution homotopy methods are applied. Besides expanding the basin of attraction for solving the algebraic equations [2], homotopy methods are able to detect isolated solution branches. In both cases, a homotopy map $\boldsymbol{H}_\lambda$ is defined, where

$$\boldsymbol{H}_\lambda(\boldsymbol{x};\mu) = \boldsymbol{0}, \text{ for } \quad 0 < \lambda < 1 \qquad \text{and} \qquad \begin{array}{ll} \boldsymbol{H}_0(\boldsymbol{x};\mu) = \boldsymbol{G}(\boldsymbol{x};\mu) & \textit{(cheap problem)} \\ \boldsymbol{H}_1(\boldsymbol{x};\mu) = \boldsymbol{F}(\boldsymbol{x};\mu) & \textit{(expensive problem)} \end{array} \tag{3}$$

holds. For embedding the nonlinear algebraic equation systems, here eq. (2), of the form

$$\boldsymbol{F}(\boldsymbol{x};\mu) = \boldsymbol{0}, \quad \boldsymbol{x} \in \mathbb{R}^N, \quad \mu \in \mathbb{R} \tag{4}$$

into the framework of eq. (3), a convex approach is selected, where

$$\boldsymbol{H}_\lambda(\boldsymbol{x};\mu) = \lambda \boldsymbol{F}(\boldsymbol{x};\mu) + (1-\lambda)\boldsymbol{G}(\boldsymbol{x};\mu) \tag{5}$$

represents a linear superposition related to λ for fixed μ and $\boldsymbol{H}_\lambda = \boldsymbol{0}$ is assumed. Suppose $\boldsymbol{F}, \boldsymbol{G}$ are smooth functions, this map implicitly defines an smooth solution path $\boldsymbol{\gamma} = (\boldsymbol{x}^\top, \lambda)^\top$, that can be traced using path classical continuation methods, e.g. predictor-corrector schemes [1]. To ensure that $\boldsymbol{\gamma}$ is reaching a solution of eq. (4), both $\boldsymbol{\gamma}$ has finite length and the implicit function theorem holds is assumed [4]. Moreover a careful selection of $\boldsymbol{G}(\boldsymbol{x};\mu)$ increases efficiency of the method.

Within this contribution, the fixed-point homotopy is applied [3, 4], where $\boldsymbol{G}(\boldsymbol{x};\mu)$ has only one solution $\boldsymbol{x} = \boldsymbol{a}$ and is represented by

$$\boldsymbol{G}(\boldsymbol{x};\mu) = (\boldsymbol{x} - \boldsymbol{a}), \quad \boldsymbol{a} \in \mathbb{R}^N. \tag{6}$$

3 Application

Following this procedure, periodic limit cycles of a 2 dof oscillator with friction law showing in Fig. 1 are calculated. As an initial value for the homotopy map $\boldsymbol{H}_\lambda$, the solution $\boldsymbol{a}$ for an uncoupled linear system with two degrees of freedom showing purely harmonic oscillations with $\omega = 1$ at $\lambda = 0$ is given. The periodic limit cycle of the system, shown in Fig. 1 is calculated for variable harmonic order $H \in \{1, 2, 3, 4\}$ at constant belt speed $v_\mathrm{b} = 0.35$.

The homotopy maps are obtained via classical predictor-corrector scheme wit additional step size control taken from [1] and pictured in Fig. 22b. For increasing number of unknowns, the homotopy path may include more turning points. Moreover, certain areas occur, where small variation of λ leads in a large change of solution components, that results in higher computational effort. Especially $H = 4$ leads to folds in the bifurcation path near $\lambda \approx 0.78$. Zooming into that domain offers that there are more iterations of the continuation algorithm required.

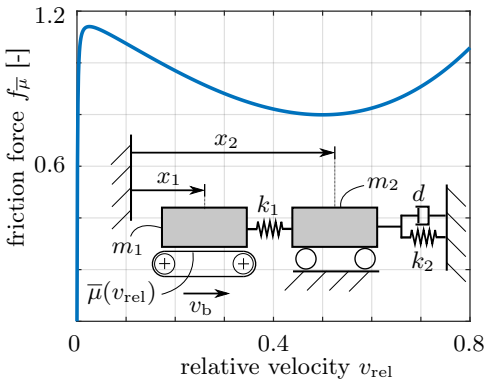

Figure 1. Friction oscillator with two degrees of freedom incl. velocity dependent friction coefficient

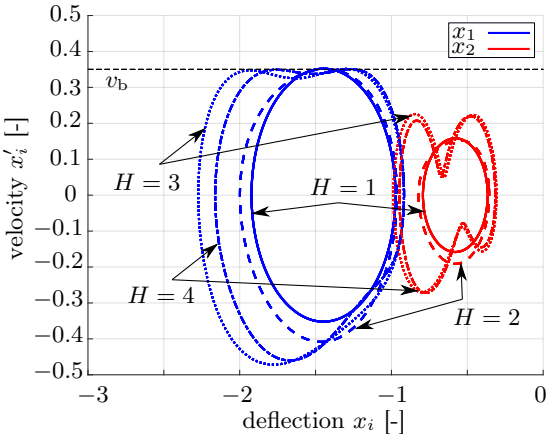

(2a) Approximated stick-slip limit cycle of the system shown in Fig. 1, where $k_1 = 1$, $k_2 = 1.5$, $\frac{m_2}{m_1} = 0.5$ and $d = 0.02$.

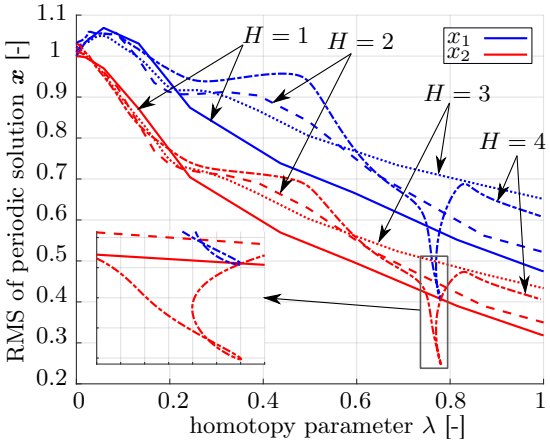

(2b) Homotopy maps of the global fixed-point homotopy for different values of H.

Nevertheless, the solution of the complex problem, namely the stick-slip limit cycle of the mechanical system, is calculated at $\lambda = 1$, however the requirements on the continuation procedure are quite challenging, especially relating to efficiency and computational effort.

4 Conclusion

This contribution aims to establish a straight forward procedure for expanding the basin of attraction for the *Harmonic Balance method* when approximating periodic limit cycles of self-excited systems. A possible convex design of a homotopy map was given and the implicit defined curve γ was traced via classical path tracking techniques. In the particular case of a two dimensional friction oscillator, solutions at a certain parameter value of the belt speed v_b were obtained. It was pointed out that for increasing number of unknowns in the nonlinear equation system, the complexity as well as the computational effort of the solution paths increase as well. In a current state of research, it is of interest to study and apply some criteria, that are already used in chemical engineering [3], to affect the shape of the homotopy path γ targeting the solution of the complex problem.

References

[1] W. Vogt B. Marx. *Dynamische Systeme: Theorie und Numerik*. Springer Verlag, 2010.

[2] J. Kappauf and H. Hetzler. Bifurcations and limit cycles due to self-excitation in nonlinear systems with joint friction: Initialization of isolated solution branches via homotopy methods. *Proceedings in Applied Mathematics & Mechanics* (2019).

[3] M. Kuno and J.D. Seader. Computing all real solutions of Systems of nonlinear equations with a Global Fixed-Point Homotopy. *I. & e. c. r.* (1988).

[4] L.T. Watson. A survey of probability-one homotopy methods for engineering optimization. *Department of Computer Science, Virginia Polytechnic Institute & State University* (1990)).

**Proceedings of the 8th GACM Colloquium on Computational Mechanics
for Young Scientists from Academia and Industry
August 28–30, 2019 in Kassel, Germany**

Thermo-hydro-mechanical modeling of liquid freezing in saturated porous media

Abdel Hassan Sweidan * [1], Yousef Heider[2] and Bernd Markert[1]

[1]Institute of General Mechanics, RWTH Aachen University, Aachen, Germany
[2]Department of Civil Engineering and Engineering Mechanics, Columbia University, New York, USA

Abstract. In the underlying research work, a thermo-hydro-mechanical (THM) finite element model is introduced to investigate the freezing-thawing process in a non-isothermal fluid-saturated porous medium. In this, a bi-phase macroscopic model considering a granular porous matrix and a fluid phase is proposed to account for the temperature development, fluid-phase transitions and volume deformations due to the ice formation based on a macroscopic phase-field-porous media approach. The theory of porous media (TPM) provides a well-founded continuum mechanical basis for the description of deformable, fluid-saturated non-isothermal porous solid aggregates. In particular, the ice and water constituents are treated as a single pore fluid and described by a unified formulation, where the phase-field method (PFM) is employed for the description of the phase transition between both components. The PFM is a diffuse interface model that relies on the specification of the free energy density function, which is the main driving force for phase transition and employs a phase-field variable to describe whether the material is ice or water. Significant virtue of the diffusive phase-field approach is that it is easy to implement and eliminates numerical challenges associated with modeling of moving sharp boundaries. Finally, a numerical example is presented to demonstrate the ability and usefulness of the model in describing the freezing process in a saturated porous solid under thermal loading.

Introduction

Freezing and thawing processes in fluid-saturated porous media are of great interest in many branches of engineering. Porous materials, like road pavements and concrete, are usually subjected to frost damage in cold regions where periodic freezing occurs. Moreover, artificial ground freezing techniques are widely used for ground-water control and temporary excavation support during tunnel construction in non-cohesive soils. Ice formation in porous media is characterized by a coupled heat and mass transport and is accompanied by ice expansion (9% volume dilation referred to the volume of liquid) and considerable deformations [1].

In order to capture such multi-physical phenomena on an engineering scale, a thermo-hydro-mechanical model consisting of a porous solid matrix and a pore-fluid phase representing solid ice and liquid water is proposed. The model is based on a coupled phase-field-porous media approach and accounts for the phase change, volume expansion and solid deformation during freezing. In this, the macroscopic theory of porous media (TPM) [6] is used for the description of the deformable, heterogeneous porous solid with the phase changing fluid constituent described by a unified formulation employing a phase-field model (PFM) [2]. The development of a thermodynamically consistent description of phase-change processes in porous media based on the necessity of satisfying the requirements of the entropy inequality of the TPM has been presented in [1]. However, the phase change process in this article is described by the mass transfer from one phase to another depending on the mass production term.

The treatment of phase change processes in a continuum description by introducing a singular front (interface) has already been tackled by many researchers [8]. Most popular interface capturing methods are the level-set, volume-of-fluid, and phase-field method (PFM). In this regard, the energy-based PFM [11] introduces a phase-field variable ϕ^F to indicate the phases of the material, e.g. $\phi^F = 0$ for the solid and $\phi^F = 1$ for the liquid states. The PFM allows for a smooth variation between these distinct values across the interface, resulting in a finite interface thickness. Such diffusive interface treatment of the freezing front can easily be implemented in finite-element codes as no explicit front tracking or application of boundary conditions at the interface is required. Therefore, we employ the PFM as an alternative method for the traditional mass transfer method that adopts the mass production term for phase change in TPM. The study combines the concepts of the TPM and the PFM for the description of the freezing process in saturated porous media, where the thermodynamic consistent constitutive

*Corresponding author: sweidan@iam.rwth-aachen.de

equations of the model together with the evolution equation of the phase-field variable are derived by exploiting the entropy inequality. Finally, a 2D numerical example is presented to demonstrate the ability of the proposed model in describing the freezing process including volume expansion in fluid-saturated porous media.

1 Theoretical framework

In the framework of the TPM [6], a continuum-mechanical description of the material φ consisting of incompressible and immiscible constituents φ^α ($\alpha = S$: solid, $\alpha = F$: fluid) is being presented. Here, the fluid occupying the pore space is the water in its ice ($\alpha = I$) or liquid ($\alpha = L$) phases. Thus, the volume fractions, the saturation condition and the density dependencies, respectively, read:

$$n^\alpha = \mathrm{d}v^\alpha/\mathrm{d}v\,, \qquad n^S + n^F = 1\,, \qquad \rho^\alpha = n^\alpha \rho^{\alpha R}\,. \tag{1}$$

Here, $\mathrm{d}v^\alpha$ and $\mathrm{d}v$ are the partial and total volume elements, and $\rho^{\alpha R}$ and ρ^α are the partial and material densities, respectively. The solid matrix is described in a Lagrangian manner via the solid displacement $\mathbf{u}_S$ and velocity $\mathbf{v}_S$, while the fluid is described by a modified Eulerian setting via the seepage velocity vector $\mathbf{w}_F = \mathbf{v}_F - \mathbf{v}_S$.

To obtain thermodynamically admissible constitutive equations for the stresses and the production terms, the entropy inequality should be fulfilled. Considering no mass transfer between the constituents, the time derivative of the saturation condition (Eq. $(1)_2$) with respect to the solid deformation is multiplied by the Lagrange multiplier Λ and added to the Clausis-Duhem in equality

$$\begin{aligned}
&\overbrace{[\mathbf{T}^S + \Lambda n^S \mathbf{I}]}^{\mathbf{T}_E^S} \cdot \mathbf{L}_S + \frac{\theta^S}{\theta^F}\overbrace{[\mathbf{T}^F + \frac{\theta^F}{\theta^S}\Lambda n^F \mathbf{I}]}^{\mathbf{T}_E^F} \cdot \mathbf{L}_F - [\overbrace{\hat{\mathbf{p}}^F - \Lambda \operatorname{grad} n^F}^{\hat{\mathbf{p}}_E^F}] \cdot \mathbf{w}_F \\
&-\rho^S (\theta^S)'_S [\eta^S + \Lambda \frac{3\,\alpha^S}{\rho^{SR}}] - \frac{\theta^S}{\theta^F}\rho^F (\theta^F)'_F [\eta^F + \Lambda \frac{\theta^F}{\theta^S}\frac{3\,\alpha^F}{\rho^{FR}}] - \frac{\theta^S}{\theta^F}\rho^F (\psi^F)'_F - \rho^S (\psi^S)'_S \\
&-\frac{1}{\theta^S}\mathbf{q}^S \cdot \operatorname{grad}\theta^S - \frac{\theta^S}{(\theta^F)^2}\mathbf{q}^F \cdot \operatorname{grad}\theta^F + \hat{\varepsilon}^F(\frac{\theta^S}{\theta^F} - 1) \geqslant 0\,,
\end{aligned} \tag{2}$$

where η^α is the constituent mass-specific entropy and θ^α is the absolute Kelvin temperature of φ^α. Λ could be identified as $\Lambda = \theta^S/\theta^F p$ for the case of non-isothermal constituents with p being the pore pressure. $\mathbf{T}^\alpha = (\mathbf{T}^\alpha)^T$ represents the symmetric partial stress tensor and $\mathbf{L}_\alpha = \operatorname{grad}\mathbf{v}_\alpha$ is the spatail velocity gradient. ε^α is the internal energy, $\mathbf{q}^\alpha$ is the heat influx and $\hat{\varepsilon}^\alpha$ is the direct energy production representing the local heat exchange between φ^α. $\hat{\mathbf{p}}^\alpha$ is the volume-specific local interaction force between φ^F and φ^S, where $\hat{\mathbf{p}}^S + \hat{\mathbf{p}}^F = \mathbf{0}$ must hold.

Employing the principle of phase separation [4], where the free energy of an individual component of the overall aggregate does only depend on its own constitutive variables as on the microscale, the *Helmholtz* free energy of the linear thermoelastic solid skeleton is written as

$$\rho_{0S}^S\,\psi^S(\theta^S, \boldsymbol{\varepsilon}_S) = \mu^S(\boldsymbol{\varepsilon}_S \cdot \boldsymbol{\varepsilon}_S) + \frac{1}{2}\lambda^S(\boldsymbol{\varepsilon}_S \cdot \mathbf{I})^2 + m^S \Delta\theta^S(\boldsymbol{\varepsilon}_S \cdot \mathbf{I}) - \rho_{0S}^S\, C_p^S \left(\theta^S \ln\frac{\theta^S}{\theta_0^S} - \Delta\theta^S\right). \tag{3}$$

Following basic papers on phase-field models for a single-phase material [10] and the arguments provided by [1, 12], the *Helmholtz* free energy for the fluid mixture φ^F including the phase change is proposed as

$$\begin{aligned}
\rho_{0F}^{FR}\psi^F(\theta^F, \phi^F, \operatorname{grad}\phi^F, \boldsymbol{\varepsilon}_F) &= \frac{1}{2}\epsilon^2 |\operatorname{grad}\phi|^2 + W g(\phi^F) + \mu^F(\boldsymbol{\varepsilon}_F \cdot \boldsymbol{\varepsilon}_F) + \frac{1}{2}\lambda^F(\boldsymbol{\varepsilon}_F \cdot \mathbf{I})^2 \\
&+ m^F \Delta\theta^F(\boldsymbol{\varepsilon}_F \cdot \mathbf{I}) - \rho_{0F}^{FR}\, C_p^F \left(\theta^F \ln\frac{\theta^F}{\theta_0^F} - \Delta\theta^F\right) - 3\left(1 - p(\phi^F)\right) k^I \alpha_p^F (\boldsymbol{\varepsilon}_F \cdot \mathbf{I}) \\
&- p(\phi^F)\rho_{0F}^{FR}\frac{L^F}{\theta_M^F}\Delta\theta_M^F - \rho_{0F}^{FR}\eta_{0I}^I \Delta\theta_M^F.
\end{aligned} \tag{4}$$

Herein, μ^α and λ^α are the *Lamé* constants, $\kappa^\alpha = 2/3\,\mu^\alpha + \lambda^\alpha$ is the compression modulus, $m^\alpha = -3\,\kappa^\alpha \alpha^F$ is the stress–temperature modulus and α_p^F is the volumetric expansion coefficient due to phase change of φ^F. C_p^α represents the specific heat capacity. L^F and η_{0I}^I are the latent heat of fusion and the reference value of the specific entropy of ice at the freezing point, respectively. $\Delta\theta^\alpha$ and $\Delta\theta_M^\alpha$ are the temperature variations compared to the reference and melting temperatures θ_0^F and θ_M^F, respectively. The subscript $\{0\,\alpha\}$ refers to quantity at time $t0$. ϵ, W are the gradient energy coefficient and energy hump parameter, respectively. The evaluation of the entropy

inequality is carried out according to the procedure of Coleman & Noll [3]. By doing so, the constitutive relations and the phase-field evolution equation are chosen as

$$\hat{\mathbf{p}}_E^F = -\frac{\mu^{FR}}{K^S}(n^F)^2\mathbf{w}_F\,, \quad \mathbf{q}^S = -\mathbf{H}^S\mathrm{grad}\,\theta^S\,, \quad \mathbf{q}^F = -\mathbf{H}^F\mathrm{grad}\,\theta^F\,, \quad \hat{\varepsilon}^F = k_{\theta V}^{FS}(\theta^S-\theta^F)\,,$$
$$(\phi^F)'_F = M\Big[\frac{\rho_{0F}^{FR}L^F}{\theta_M^F}\Delta\theta_M^F\,p'(\phi^F) - W g'(\phi^F) + \epsilon^2\,\nabla^2\phi^F\Big], \tag{5}$$

where $\mu^{FR}>0$ is the dynamic fluid viscosity and $K^S>0$ represents the isotropic intrinsic permeability of φ^S. $g(\phi^F)=(\phi^F)^2(1-\phi^F)^2$ is a double well energy function and $p(\phi^F)=(\phi^F)^3\left(6\,(\phi^F)^2-15\,\phi^F+10\right)$ is an interpolating function with $g'(\phi^F)$ and $p'(\phi^F)$ denoting their derivatives with respect to ϕ^F, respectively. The interface mobility M together with W and ϵ could be found by relating them to the material parameters and the interface width as in [2]. Moreover, to consider a change in the permeability K^S due to the deformation of φ^S, the relation provided by Markert [9] is chosen. In the sense of Fourier's law of heat conduction, $\mathbf{H}^\alpha = n^\alpha H^{\alpha R}\mathbf{I}$ represents the partial heat conductivity tensor. $k_{\theta V}^{FS}=3\,n^F/r^F k_{\theta S}^{FS}$ is a positive volume-specific heat transfer coefficient with $k_{\theta S}^{FS}$ being the heat transfer coefficient at the interface between φ^S and φ^F, r_F is the average pore channel radius and r_S is the characteristic solid particle radius.

Under small-strain conditions and based on Eq. (3), the solid effective stress reads

$$\mathbf{T}_E^S = \frac{\rho^S}{\rho_{0S}^S}[2\,\mu^S\,\boldsymbol{\varepsilon}_S^D + \kappa^S(\boldsymbol{\varepsilon}_S\cdot\mathbf{I})\mathbf{I} + m^S\,\Delta\theta^S\mathbf{I}]\,, \tag{6}$$

where $\boldsymbol{\varepsilon}_S^D$ is the deviatoric strain tensor. The dependencies of ρ^S and n^S on the solid deformation and thermal expansion can be found following the procedure provided by [5] and [7]. Based on Eq. (4), the effective fluid stress reads

$$\boldsymbol{T}_E^F = \frac{\rho^F}{\rho_{0F}^{FR}}\Big[m^F\mathbf{I}\Delta\theta^F + 2\,\mu^F\boldsymbol{\varepsilon}_F^D + \kappa^F\mathbf{I}(\boldsymbol{\varepsilon}_F\cdot\mathbf{I}) - 3\,k^F\alpha_p^F\mathbf{I}\Big] = \frac{\rho^F}{\rho_{0F}^{FR}}\Big[\phi^F\boldsymbol{T}_E^L + \big(1-\phi^F\big)\,\boldsymbol{T}_E^I\Big]\,. \tag{7}$$

In this, ϕ^F is employed to allow for a smooth variation of an arbitrary thermo-mechanical property ϱ between the liquid and frozen phases of φ^F during the phase transition, e.i. $\varrho^F=\phi^F\varrho^L+\big(1-\phi^F\big)\varrho^I$. Based on (7), the linear description of φ^F in its liquid state ($\phi^F=1$) follows by setting $\mu^L=0$. Moreover, the incompressible liquid case is obtained by letting $(\boldsymbol{\varepsilon}_L\cdot\mathbf{I})\to 0$. The case of incompressible Newtonian fluid is simply recovered by letting $\boldsymbol{T}_E^L = 2\,n^F\mu^{FR}\,\mathbf{D}_F$. For each computational cell, the displacement is obtained by integrating the velocity over time, i.e. $(\mathbf{u}_F)'_S=\mathbf{v}_F$.

The governing partial differential equations (PDEs) with primary unknowns $\{\mathbf{u}_S,\,\mathbf{v}_F,\,p,\,\theta^F,\,\theta^S,\,\phi^F\}$ are summarized as follows:

$$\begin{aligned}
&\text{Mass balance for } \varphi^F: && (\rho^F)'_F + \rho^F\,\mathrm{div}\,\mathbf{v}_F = 0\,,\\
&\text{Momentum balance for } \varphi^F: && \mathbf{0} = \mathrm{div}\,\mathbf{T}_E^F - n^F\mathrm{grad}\,p + \rho^F\mathbf{g} - \frac{(n^F)^2\mu^{FR}}{K^S}\mathbf{w}_F\,,\\
&\text{Mixture momentum balance}: && \mathbf{0} = \mathrm{div}\,\{\mathbf{T}_E^S + \mathbf{T}_E^F - \big[n^S(\frac{\theta^S}{\theta^F}-1)+1\big]\,p\,\mathbf{I}\} + [\rho^S+\rho^F]\,\mathbf{g}\,,\\
&\text{Energy balance for } \varphi^F: && \rho^F C_p^F(\theta^F)'_F + \rho^F L^F\,p'(\phi^F)(\phi^F)'_F = \mathbf{T}^F\cdot\mathbf{L}_F - \mathrm{div}\,\mathbf{q}^F + \hat{\varepsilon}^F\,,\\
&\text{Energy balance for } \varphi^S: && \rho^S C_p^S(\theta^S)'_S = \mathbf{T}^S\cdot\mathbf{L}_S - \mathrm{div}\,\mathbf{q}^S - \hat{\varepsilon}^F - \hat{\mathbf{p}}_E^F\cdot\mathbf{w}_F\,,\\
&\text{Phase-field equation}: && (\phi^F)'_F = M\Big[\frac{\rho_{0F}^{FR}L^F}{\theta_M^F}\Delta\theta_M^F\,p'(\phi^F) - W g'(\phi^F) + \epsilon^2\,\nabla^2\phi^F\Big].
\end{aligned} \tag{8}$$

In order to avoid lengthy formulation of the balance equations, we provided simplified forms through neglecting the terms that has a minor effect on the solution. This includes omitting the terms related to the thermal expansion, pressure and elastic strains in Eq. $(8)_4$. Moreover, the contribution of elastic strains was neglected in the phase-field evolution (Eq. $(8)_6$), as the primary purpose of ϕ^F is to track the interface based on the thermal driving force. To overcome stability challenges associated with the assumption of materially-incompressible fluid, a pseudo-compressibility-based scheme via Laplace of the pressure is applied in this work. When dealing with special cases where no solid deformation is considered, K_S in Eq. $(8)_2$ could be replaced by a modified version $K_\phi^S = (1-\phi^F)K_{\min}^S + \phi^F K^S$, where $K_{\min}^S \ll K^S$ is a very small positive constant. This relation is introduced to ensure that the fluid velocities reduce gradually from finite values (for $K_\phi^S = K^S$) in the liquid state of φ^F to almost zero values (for $K_\phi^S = K_{\min}^S$) in the frozen state.

2 Numerical results and discussion

In this section, a 2D numerical simulation is performed using the Finite Element Method (FEM) in order to present the application of the proposed model. The geometry and boundary conditions of the sample are shown in Fig. 1. Specifically, the model is applied to a solid specimen (cement stone) having a width $L = 0.15$ m and a height $H = 0.075$ m. All the unstressed surfaces are adiabatic to the environment. The system is initially at a temperature $\theta_0^\alpha = 293$ K with a solid volume fraction $n_{0S}^S = 0.5$. The bottom of the specimen is cooled in-line from 293 K to 253 K within 4 hours and then is held constant within 1 hour. All the four walls of the specimen are impermeable and no-slip boundary conditions are imposed ($\bar{\mathbf{v}}_F = \mathbf{0}$). The thermo-physical properties of the porous material, ice and water are adopted from [1].

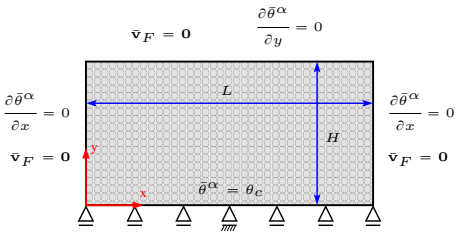

Figure 1. 2D geometry and boundary conditions

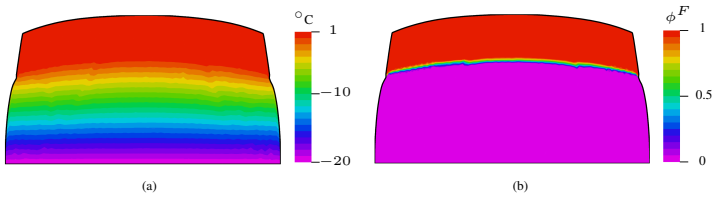

Figure 2. (a) Temperature and (b) phase-field evolution contours of the deformed porous solid at time t = 5 h

Fig. 2 shows the liquid/ice interface position and the accompanied volume deformation after 5 hours. The volume increase is mainly subject to the moving freezing front inside the porous solid, however a thermal dilatation is observed during the cooling phase in-between 293-273 K. At $\theta^F \leqslant 273$ K, the phase change from liquid to ice occurs and a significant volume deformation of the specimen due to ice freezing is observed. These results agree with the observations in [1]; however, in their work, the isothermal equilibrium model was used and the phase change process was described by the mass transfer via the mass production term. Moreover, the volume expansion due to phase change appeared to be only in the lateral direction.

3 Conclusion

In this study, a bi-phasic macroscopic model has been presented for the simulation of freezing process in liquid-saturated porous media. The model is based on a coupled phase-field-porous media approach and allows to describe the temperature distribution, freezing front propagation and volume expansion during freezing. A 2D numerical example was provided to demonstrate the ability of the proposed model in describing such process.

4 Acknowledgements

This work was funded by the Deutsche Forschungsgemeinschaft (DFG) through the project "Investigation and calculation of frost heave considering specific boundary conditions of ground freezing". The funding is herewith gratefully acknowledged.

References

[1] J. Bluhm, W.M. Bloßfeld, and T. Ricken. Energetic effects during phase transition under freezing-thawing load in porous media - a continuum multiphase description and FE-simulation. *ZAMM - J. Appl. Math. Mech. / Zeitschrift für Angew. Math. und Mech.* 94 (2014), pp. 586–608.

[2] W. J. Boettinger, J. A. Warren, C. Beckermann, and A. Karma. Phase-Field Simulation of Solidification. *Annu. Rev. Mater. Res.* 32 (2002), pp. 163–194.

[3] B.D. Coleman and W. Noll. The thermodynamics of elastic materials with heat conduction and viscosity. *Arch. Ration. Mech. Anal.* 13.1 (1963), pp. 167–178.

[4] W Ehlers. On thermodynamics of elasto-plastic porous media. *Arch. Mech.* 41.1 (1989), pp. 73–93.

[5] W. Ehlers and K. Häberle. Interfacial Mass Transfer During Gas–Liquid Phase Change in Deformable Porous Media with Heat Transfer. *Transp. Porous Media* 114.2 (2016), pp. 525–556.

[6] A.G Fallis. *Advances in Extended and Multifield Theories for Continua*. Ed. by Bernd Markert. Vol. 59. Berlin, Heidelberg: Springer, 2011, pp. 1689–1699.

[7] Y. Heider and B. Markert. A phase-field modeling approach of hydraulic fracture in saturated porous media. *Mech. Res. Commun.* 80 (2017), pp. 38–46.

[8] D. M. Anderson, G. McFadden, and A. Wheeler. Diffuse-Interface Methods in Fluid Mechanics. *Annu. Rev. Fluid Mech.* 30 (1997).

[9] B. Markert. A constitutive approach to 3-d nonlinear fluid flow through finite deformable porous continua. *Transp. Porous Media* 70 (2007), pp. 427–450.

[10] I. Steinbach. Phase-field models in materials science. *Model. Simul. Mater. Sci. Eng.* 17 (2009), p. 073001.

[11] A. H. Sweidan, Y. Heider, and B. Markert. Modeling of PCM-based enhanced latent heat storage systems using a phase-field-porous media approach. *Contin. Mech. Thermodyn.* (2019).

[12] H. Ziegler and C. Wehrli. The Derivation of Constitutive Relations from the Free Energy and the Dissipation Function. *Adv. Appl. Mech.* 25 (1987), pp. 183–238.

**Proceedings of the 8th GACM Colloquium on Computational Mechanics
for Young Scientists from Academia and Industry
August 28–30, 2019 in Kassel, Germany**

Computational modelling of creep and rate dependent strength of freezing soils

Rodolfo J. Williams M. * [1] and Günther Meschke[1]

[1]Institute for Structural Mechanics, Ruhr University Bochum, Bochum, Germany

Abstract. In this work, the rate dependent effects of freezing soils such as creep and rate-dependent strength are studied through a combination of viscoelastic and viscoplastic material models. The viscoelastic effective properties are obtained through the upscaling of the elastic and viscous properties of the ice, soil, water material phases. On the other hand, the viscoplastic component is phenomenological described with an overstress type model. The proposed strategy is validated by comparing numerical predictions to experimental results.

Introduction

The rate-dependent behavior of freezing soils is strongly related to the microstructure of the ice crystal phase, where the volumetric ice content and its cryostructure play an important role in the overall macroscopic response. Several studies have been carried out during the past decades to gain insight into the rate dependent effects such as creep, stress relaxation and rate-dependent strength behavior on the basis of experimental evidence and then formulate constitutive models for frozen soils capable of reproducing these features. Figure 1 (a) shows the three stages that can be distinguished during creep under constant stress conditions: primary, secondary and tertiary creep, which can be found on various laboratory studies. Many of these studies have provided empirical equations or phenomenological constitutive relations to describe the macroscopic behavior of the frozen soil. In this work, the extended Barcelona Basic Model (BBM) [3] with strength homogenization [5] is extended to include creep and rate dependent effects through a combination of viscoelastic and viscoplastic material models. The viscoelastic component to account for the primary creep is described by the micromechanical model presented in [2] , where the overall macroscopic response is based on the viscous behaviour of ice. On the other hand, the viscoplastic component is phenomenologically described by Duvuat and Lions overstress model [1], which allows to include viscous irreversible effects after yielding. The structure of this extended abstract is as follows: First, the rate independent constitutive model is introduced in section 1. Then, the extension of the latter model is described in section 2. Finally, for the validation of the proposed strategy, numerical predictions are compared with experimental results in section 3.

1 Rate independent constitutive model for freezing soils

1.1 Freezing state: extended Barcelona Basic Model upon strength upscaling

The framework of the extended BBM with homogenized strength properties obtained through two-step upscaling [5], is introduced in this section. The total strain $\dot{\boldsymbol{\varepsilon}}$ is defined through the additive decomposition $\dot{\boldsymbol{\varepsilon}} = \dot{\boldsymbol{\varepsilon}}^e + \dot{\boldsymbol{\varepsilon}}^p$. The stress-strain relation is assumed to be independent of the volumetric effective stress p'. For this reason, the swelling index is adopted as $\kappa = v p_{min}/k_{hom}$, with $p_{min} = 1$ kPa, $v = 1/(1-\phi)$ the specific volume and ϕ the porosity. For the determination of the homogenized bulk k_{hom} and shear μ_{hom} moduli, the Mori-Tanaka scheme for a matrix inclusion morphology is employed for the case of fully saturated frozen soil.

$$\dot{\boldsymbol{\sigma}} = \mathbb{C}^e_{hom} : \dot{\boldsymbol{\varepsilon}}^e = \mathbb{C}^{e_{hom}} : (\dot{\boldsymbol{\varepsilon}} - \dot{\boldsymbol{\varepsilon}}^p) \text{ with } \mathbb{C}^{e_{hom}} = 3k_{hom}\mathbb{I}_{vol} + 2\mu_{hom}\mathbb{I}_{dev} \tag{1}$$

*Corresponding author: rodolfo.williamsmoises@rub.mail

The temperature-dependent yield surface in the freezing state is written as

$$f[p', q, p'_o, T] = \left(\frac{q}{M^{II}_{hom}[T](p' + S^{II}_{hom}[T])} \right)^{nn} + \frac{1}{\ln[rr]} \ln \left[\frac{p' + S^{II}_{hom}[T]}{p'_{oT} + S^{II}_{hom}[T]} \right] \leq 0 \tag{2}$$

The tensile strength S_T, effective pre-consolidation pressure p'_{oT} and temperature dependent compression index λ_T are defined as:

$$S_T = \frac{c^{II}_{hom}[T]}{M^{II}_{hom}[T]}, \text{ and } p'_{oT} = \left(\frac{p'_o}{p_{atm}} \right)^{\frac{\lambda-\kappa}{\lambda_T-\kappa}} \text{ with } \lambda_T = \lambda \Big((1-r)\exp[-\beta S_f (T_f - T)] + r \Big) \tag{3}$$

2 Creep and rate dependent constitutive model for freezing soils

2.1 Viscoelastic behaviour of frozen soils

The viscous behavior of the composite is strongly dependent on the micromechanics of ice, which is described as diffusional thermal creep process, where the temperature dependent creep compliance $J^c_{dev}(t)$ is expressed by:

$$J^c_{dev}(t) = 1/\mu_c + J^v_c ln\left(1 + \frac{t}{\tau^v_c}\right) \text{ with } J^v_c(T) = \overline{J^v_c} \exp\left[-\frac{Q_i}{R}\left(\frac{1}{T} - \frac{1}{\overline{T}}\right)\right] \tag{4}$$

Figure 2 shows the influence of the liquid saturation $\chi_L = (1 + (\Delta T/\Delta T_{ch})^{\frac{1}{1-m}})^{-m}$ on the creep

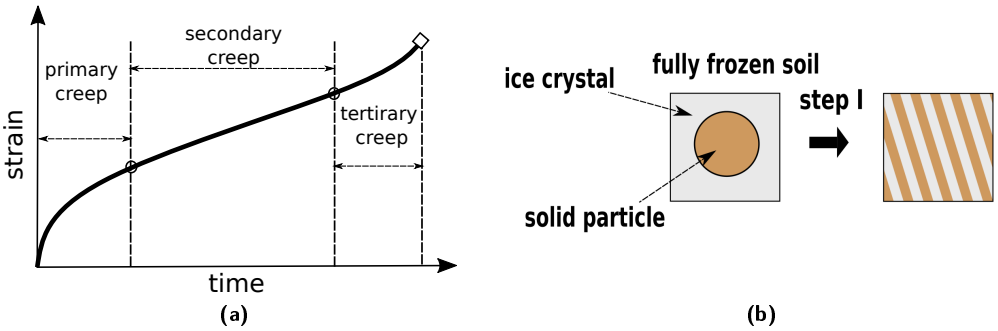

Figure 1. (a) The three creep stages: primary, secondary and tertiary creep. (b) Viscoelastic homogenization step.

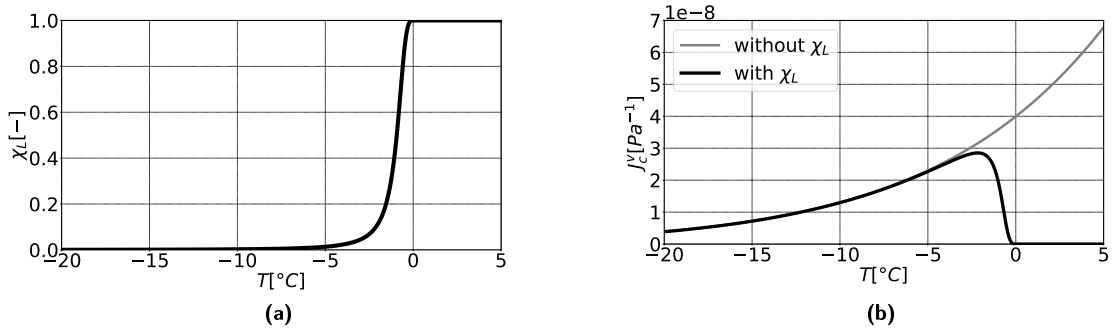

Figure 2. (a) Liquid saturation during freezing χ_L. (b) Influence of the temperature and liquid saturation on the creep compliance of the ice crystal J^c_v.

compliance of the ice crystal J^c_v. The total strain and the corresponding strain-stress relation for the viscoelastic case are defined as:

$$\dot{\boldsymbol{\varepsilon}} = \dot{\boldsymbol{\varepsilon}}^e + \dot{\boldsymbol{\varepsilon}}^{ve} \text{ and } \dot{\boldsymbol{\sigma}} = \mathbb{C}^e_{hom} : \dot{\boldsymbol{\varepsilon}}^e = \mathbb{C}^{e_{hom}} : (\dot{\boldsymbol{\varepsilon}} - \dot{\boldsymbol{\varepsilon}}^{ve}) \tag{5}$$

For the determination of the viscoelastic behavior of the frozen soils, the framework of continuum micromechanics is used. It is based on the so called correspondence principle, where the viscoelastic homogenized properties in the time domain are obtained by inverse the Laplace-Carson transformation, Figure 1 (b).

$$\frac{\partial \boldsymbol{\varepsilon}}{\partial t} = \underbrace{\mathbb{J}^{hom}_{[t-\tau]} : \frac{\partial \boldsymbol{\sigma}}{\partial t}}_{\dot{\boldsymbol{\varepsilon}}^{e}} + \underbrace{\int_{-\infty}^{t} \frac{\partial \mathbb{J}^{hom}_{[t-\tau]}}{\partial t} : \frac{\mathrm{d}\boldsymbol{\sigma}}{\mathrm{d}\tau}\mathrm{d}\tau}_{\dot{\boldsymbol{\varepsilon}}^{ve}} \tag{6}$$

$$\mathbb{J}^{hom}_{[t-\tau]} = \frac{1}{3}J^{hom}_{vol}\mathbb{I}_{vol} + \frac{1}{2}J^{hom}_{dev}\mathbb{I}_{dev} = \frac{1}{3}\frac{1}{k_{hom}}\mathbb{I}_{vol} + \frac{1}{2}\left[\frac{1}{\mu_{hom}} + (1-\chi_L)J^{v}_{hom} ln\left(1+\frac{t-\tau}{\tau^{v}_{hom}}\right)\right]\mathbb{I}_{dev} \tag{7}$$

$$\frac{\partial \mathbb{J}^{hom}_{[t-\tau]}}{\partial t} = \frac{1}{2}\frac{\partial J^{hom}_{dev}}{\partial t}[t-\tau]\mathbb{I}_{dev} = \frac{1}{2}\frac{J^{v}_{hom}}{(t-\tau+\tau^{v}_{hom})}\mathbb{I}_{dev} \tag{8}$$

2.2 Rate dependent extended Barcelona Basic Model for freezing soils incorporating viscoelastic creep

The total strain rate is defined through the additive decomposition using viscoelastic and viscoplastic strain rate components and the corresponding strain-stress relation:

$$\dot{\boldsymbol{\varepsilon}} = \dot{\boldsymbol{\varepsilon}}^{e} + \dot{\boldsymbol{\varepsilon}}^{ve} + \dot{\boldsymbol{\varepsilon}}^{vp} \text{ and } \dot{\boldsymbol{\sigma}} = \mathbb{C}^{e}_{hom} : \dot{\boldsymbol{\varepsilon}}^{e} = \mathbb{C}^{e_{hom}} : (\dot{\boldsymbol{\varepsilon}} - \dot{\boldsymbol{\varepsilon}}^{ve} - \dot{\boldsymbol{\varepsilon}}^{vp}) \tag{9}$$

In the Duvaut-Lions model the viscoplastic strain rate and the effective pre-consolidation pressure with τ_{vp} as the viscoplastic relaxation time, are formulated as:

$$\dot{\boldsymbol{\varepsilon}}^{vp} = \frac{(\mathbb{C}^{e_{hom}})^{-1} :}{\tau_{vp}} : (\boldsymbol{\sigma} - \boldsymbol{\sigma_{\infty}}) \text{ and } \dot{p'}_{o} = -\frac{1}{\tau_{vp}}(p'_{o} - p'_{o_{\infty}}) \tag{10}$$

where $\boldsymbol{\sigma_{\infty}}$ and $p'_{o_{\infty}}$ denote the stress and the effective pre-consolidation pressure obtained from the corresponding converged viscoelastic-plastic return mapping algorithm.

3 Numerical results

3.1 Uniaxial unconfined compression creep test

In this section, the proposed model is validated by numerical re-analysis of a compression creep laboratory test. The test was perfomed by Orth [4] on frozen Karlsruhe medium sand a temperature $T = -10°\mathrm{C}$. The prepared specimen had a water content of 18%. The creep test was carried out under constant temperature and constant stress σ_1. The material parameters used for the validation example are: the porosity $\phi_0 = 0.18$, bulk freezing temperature $T_f = 273$ K , freezing entropy $\Sigma_f = 1.2$ MPa , characteristic cooling $\Delta T_{ch} = 1$ °C, pore size distribution parameter $m = 0.7$, bulk modulus $k_S = 2650$ GPa $k_L = 1000$ GPa , $k_C = 917$ GPa, shear modulus $\mu_S = 37.5$ GPa, $\mu_L = 1$ MPa, $\mu_C = 3.4$ GPa. Further viscoelastic and viscoplastic parameters are listed in Table 1. Figure 3 shows the creep-induced axial strain vs time for different applied constant stresses. Good agreement between numerical and experimental results for stresses between $\sigma_1 = 3$MPa to $\sigma_1 = 6$MPa are found. However, for stress levels higher than $\sigma_1 = 6$MPa discrepancies in the results are observed.

Conclusions

The presented constitutive model has the capability of reproducing primary creep behavior based on the information of the microstructure of the frozen soil and the secondary with the help of the overstress model. Results show, however, the limitations of the model to predict tertiary creep, which might be associated with damage processes in the ice matrix. This is the topic of a current extension of the model.

Table 1. Viscoelastic and viscoplastic material properties employed in the in the numerical simulation

Material parameter	Symbol	Numerical values	Units
Creep compliance for crystal ice	J_c^v	13000	μm/m/MPa
Creep relaxation time for crystal ice	τ_c^v	1	s
Shape parameter	nn	2	–
Spacing ratio	rr	2	–
Swelling index	κ	0.0002	–
Compression index	λ	0.005	–
Parameter defining max. compressive stiffness	r	0.8	–
Parameter controlling stiffness grow rate	β	0.2	–
Preconsolidation	p'_o	1	MPa
Viscoplastic relaxation time –3 °C to –6 °C	τ_{vp}	1000	s
Viscoplastic relaxation time –7 °C to –10 °C	τ_{vp}	250	s

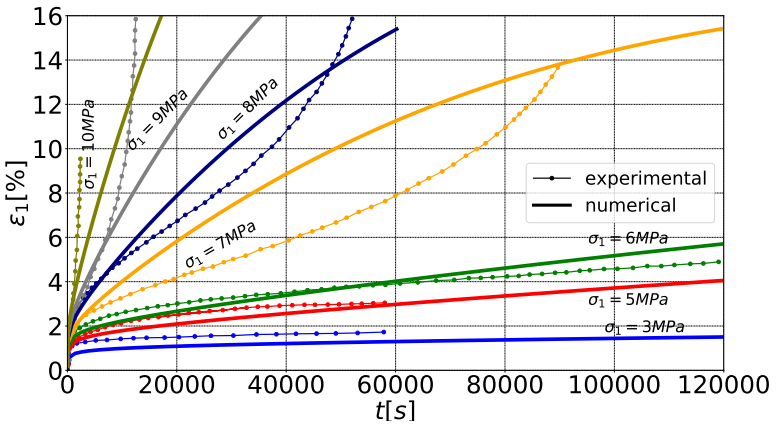

Figure 3. Evolution of axial strain of frozen sand for different prescribed constant stress levels at $T = -10$ °C.

Acknowledgments

Financial support was provided by the German Research Foundation (DFG) within the scope of Subproject C1 of the Collaborative Research Centre SFB 837.

References

[1] G. Duvaut and J.L. Lions. *Les inéquations en mécanique et en physique*. Travaux Recherches Math. Paris: Dunod, 1972. URL: http://cds.cern.ch/record/212412.

[2] R. Lackner, C. Pichler, and A. Kloiber. Artificial Ground Freezing of Fully Saturated Soil: Viscoelastic Behavior. *Journal of Engineering Mechanics* 134.1 (2008), pp. 1–11. ISSN: 0733-9399. DOI: 10.1061/(asce)0733-9399(2008)134:1(1).

[3] S. Nishimura, A. Gens, S. Olivella, and R. J. Jardine. THM-coupled finite element analysis of frozen soil: formulation and application. *Géotechnique* 59.3 (2009), pp. 159–171. ISSN: 0016-8505. DOI: 10.1680/geot.2009.59.3.159. URL: http://www.icevirtuallibrary.com/doi/10.1680/geot.2009.59.3.159.

[4] W. Orth. *Gefrorener sand als werkstoff: Elementversuche und materialmodell*. Vol. 100. Institut für Bodenmechanik und Felsmechanik der Universität Fridericiana in ..., 1986.

[5] MM. Zhou and G. Meschke. A multiscale homogenization model for strength predictions of fully and partially frozen soils. *Acta Geotechnica* 13.1 (2018), pp. 175–193. ISSN: 18611133. DOI: 10.1007/s11440-017-0538-0.

**Proceedings of the 8th GACM Colloquium on Computational Mechanics
for Young Scientists from Academia and Industry
August 28–30, 2019 in Kassel, Germany**

The FKM guidelines: Recommendations for fatigue life calculations of industrial components

Melanie Fiedler *[1] and Michael Vormwald[2]

[1]TU Dresden, Germany
[2]TU Darmstadt, Germany

Abstract. The FKM guideline „Rechnerischer Festigkeitsnachweis“ [8] is widely used in the german industry to calculate the fracture fatigue lives of components made of steel or aluminium alloy under constant or variable amplitude loadings. The guideline is based on a simple approach for Woehlercurves: constant slope and constant kink point for all kinds of ductile steels. The fatigue strength of the component can be approximated by the ultimate tensile strength and the geometrical properties of the component. No other material parameters are required. The fatigue lives for components under variable amplitude loadings can be calculated by elementary or consequent Miner rule. The elastic-plastic material behavior is neglected when using the FKM guideline also no crack growth simulation is required. In 2019 the new FKM guideline nonlinear [4] was published based on the Local Strain Approach. This new guideline considers elastic-plastic material behavior in a fatigue life calculation for crack initiation. The cyclic material behavior and the Woehlercurves for crack initiation can also be approximated by the ultimate tensile strength and the damage accumulation is also based on elementary or consequent Miner rules. In [3] the U-Concept is published, which is a new add-on to the Local Strain Approach. The U-Concept is applicable for components of steel under constant or variable amplitude loadings and transfers the advantages of the Local Strain Approach from crack initiation to fracture. This presentation gives an overview about the new add-on and presents experimental versus calculated results for a large database including more than 1500 experiments for notched components under constant amplitude loading and more than 1400 experiments under variable amplitude loading.

Introduction

The Research Associations for Mechanical Engineering (FKM) is publisher of three different guidelines for structural durability. The new FKM guideline nonlinear (FKM nonlinear, section 2) [4] for calculations with failure criteria technical crack initiation 0.25 mm $\leq a \leq$ 3 mm, the fracture mechanical guideline for crack growth simulations from crack initiation to fracture and the „Rechnerischer Festigkeitsnachweis“ (FKM linear, section 1) [8] for failure criteria fracture. The FKM linear considers elastic material behavior in the fatigue life calculation while the FKM nonlinear is able to consider elastic-plastic material behavior by using the Local Strain Approach (LSA). In section 3 the U-Concept is described, which combines the LSA with the failure criteria fracture. The results of the U-Concept in comparison to FKM linear are discussed in section 4 for constant and variable amplitude loadings for a probability of failure $P = 50\%$.

1 The FKM guideline linear

This paper considers the local stress approach proposed by the FKM guideline linear [8]. For a local stress amplitude $\sigma_a = K_t \cdot S_a$ the approach predicts the fracture fatigue life $N_{\mathrm{Calc,frac}}$ of a structure under constant amplitude loading:

$$N_{\mathrm{Calc,frac}} = N_D \cdot \begin{cases} \left(\frac{\sigma_W \cdot K_{AK,\sigma}/K_{WK,\sigma}}{\sigma_a}\right)^k & \text{for } \sigma_a > \sigma_W \cdot K_{AK,\sigma}/K_{WK,\sigma} \\ \infty & \text{for } \sigma_a \leq \sigma_W \cdot K_{AK,\sigma}/K_{WK,\sigma} \end{cases} \tag{1}$$

with the fatigue limit $N_D = 10^6$ and the slope $k = 5$ for steel, the endurance strength of the material σ_W, the mean stress effect factor $K_{AK,\sigma}$ and the component factor $K_{WK,\sigma}$.

*Corresponding author: melanie_fiedler@tu-dresden.de ORCID iD: ORCID (optional)

The endurance strength σ_W for tension/compression can be approximated by the ultimate tensile strength R_m using $\sigma_W = f_{W,\sigma} \cdot R_m$ with the tension-compression-factor $f_{W,\sigma} = [0.4; 0.45]$ for steel structures.
For structures under variable amplitude loading the FKM guideline linear uses the elementary or consequent miner rule for damage accumulation. For damage sum $D = 1$ the approach of the linear guideline tends to overestimate the fracture fatigue live of a component under variable amplitude loading in comparison to experimental results, see [5]. Based on an approach by [5], effective damage sums $0.3 \leq D_{\text{eff}} \leq 1$ have to be taken into account during the calculation to guaranty conservative calculated fatigue lives.

2 The FKM guideline nonlinear

The FKM guideline nonlinear [4] is based on the Local Strain Approach (LSA) and is able to consider elastic-plastic material behavior during the fatigue life calculation for crack initiation. Based on an elastic FE-calculation, elastic-plastic material behavior can be assumed by the flow curve approach by Neuber [7] or by Seeger and Beste [10]. The elastic-plastic material behavior is described by the cyclic stabilized Ramberg-Osgood-equation:

$$\varepsilon_a = \frac{\sigma_a}{E} + \left(\frac{\sigma_a}{K'}\right)^{1/n'} \tag{2}$$

The material parameters E, K' and n' can be approximated by the FKM method [13] based on the ultimate tensile strength R_m and the material group. The local stress strain path is simulated with a Hysteresis Counting Method (HCM) [1], which combines the rainflow counting method with the elastic plastic material behavior and is able to consider Masing's law and the three memory effects. The guideline considers two damage parameters. Damage parameter P_{RAM} which is based on P_{SWT} [11] and P_{RAJ} based on P_J by [12]. Both damage parameters are able to consider mean stress effects, P_{RAJ} is also able to take sequence effects into account. The damage parameter Woehlercurves for crack initiation can be approximated by

$$N_{\text{Calc,CI}} = 10^3 \cdot \begin{cases} (P_{\text{RAM}}/P_{\text{RAM,Z}})^{1/d_1} & \text{for } P_{\text{RAM}} > P_{\text{RAM,Z}} \\ (P_{\text{RAM}}/P_{\text{RAM,Z}})^{1/d_2} & \text{for } P_{\text{RAM}} \leq P_{\text{RAM,Z}} \end{cases} \tag{3}$$

and

$$N_{\text{Calc,CI}} = \begin{cases} (P_{\text{RAJ}}/P_{\text{RAJ,Z}})^{1/d} & \text{for } P_{\text{RAJ}} > P_{\text{RAJ,D}} \\ \infty & \text{for } P_{\text{RAJ}} \leq P_{\text{RAJ,D}} \end{cases} \tag{4}$$

with grid points $P_{\text{RAM,Z}}$ and $P_{\text{RAJ,Z}}$, fatigue strength $P_{\text{RAJ,D}}$ and slopes d, d_1, d_2 which are approximated by the ultimate tensile strength R_m, the material group, [13], and the component factors f_{RAM} and f_{RAJ}, [4]. The damage accumulation for variable amplitude loadings is also based on elementary or consequent Miner rules, see [4].

3 The U-Concept

The U-Concept (UC) by [3] is a simple add-on to the LSA in order to calculate technical fracture fatigue lives $N_{\text{Calc,frac}}$ for non-welded structures of steel based on elastic-plastic material behavior. The UC contains different approaches for damage parameters P_{RAM} and P_{RAJ}. The approaches $P_{\text{RAM,KP}}$ and $P_{\text{RAJ,KP}}$ propose a constant shift of the damage parameter Woehlercurves from crack initiation to fracture. The shift factor f depends on the ultimate tensile strength R_m, the plastic load factor K_p and the nominal stress ratio R, see [3].

$$N_{\text{Calc,frac}} = f(R_m, K_p, R) \cdot N_{\text{Calc,CI}} \tag{5}$$

The approach $P_{\text{RAJ,U}}$ considers the different slopes of crack initiation and fracture Woehlercurves which can be observed in experiments, [9]. The shift function f_U depends on the elastic-plastic calculated stress amplitude σ_a and mean stress σ_m of the closed hysteresis loop as well as the ultimate tensile strength R_m, the plastic load factor K_p and the nominal stress ratio R, [3].

$$N_{\text{Calc,frac}} = f_U(\sigma_a, \sigma_m, R_m, K_p, R) \cdot N_{\text{Calc,CI}} \tag{6}$$

The UC considers the effective damage sum approach by [5] in combination with a method correction factor f_{meth} to $D_{\text{eff,NL}} = f_{\text{meth}} \cdot D_{\text{eff}}$ with $f_{\text{meth}} = 1$ for FKM linear. The damage accumulation for variable amplitude loadings is also based on elementary or consequent Miner rules.

4 Results

The experiments of this section are mostly taken out of the database DaBef, [2]. The structural database consists of experimental results for notched specimens under constant or variable amplitude loadings for steel, cast steel and aluminum alloy. For constant amplitude loadings, the database was extended by the sources [6, 9].

4.1 Constant amplitude loadings

In figure 1 results for notched specimens under constant amplitude loadings are shown. On the left side, the results of the U-Concept with approach $P_{\mathrm{RAJ,U}}$ are compared to the experimental results, on the right side, the results for FKM linear are plotted against the experimental fatigue lives. The U-Concept shows a smaller scatter of the quotient $q_N = N_{\mathrm{Exp,frac}}/N_{\mathrm{Calc,frac}}$ than the approach by FKM linear.

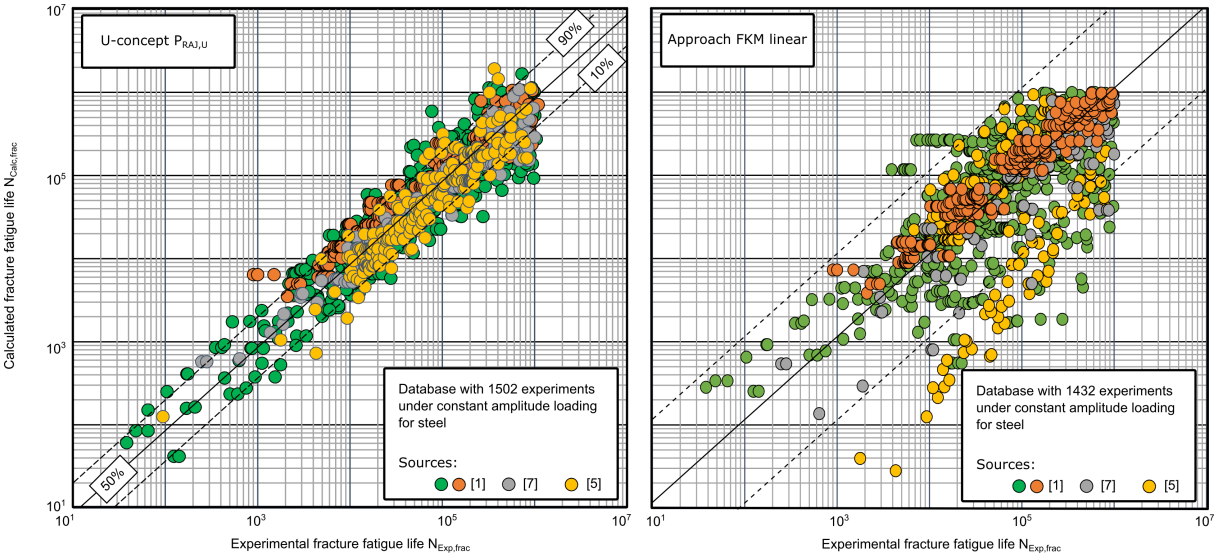

Figure 1. Comparison of experiments for notched specimens under constant amplitude loading with calculated fracture fatigue lives with approaches FKM linear (right) and U-Concept $P_{\mathrm{RAJ,U}}$ (left) with $P = 50\%$, [3]

4.2 Variable amplitude loadings

Figure 2 (left) shows a comparison between the experimental results by [6] for specimens under variable amplitude loading (bending, $\bar{R} = -1$) with calculated results. The loading sequence is normal distributed and the calculated results are neither calculated with the approaches of the U-Concept ($P_{\mathrm{RAM,KP}}$, $P_{\mathrm{RAJ,KP}}$ and $P_{\mathrm{RAJ,U}}$) or with the approach of the FKM linear for a probability of $P = 50\%$. In combination with the consequent miner rule the approaches $P_{\mathrm{RAJ,KP}}$ and $P_{\mathrm{RAJ,U}}$ show the best match with the progression of the experimental results. Figure 2 (right) shows the results of the quotient of experimental to calculated fatigue lives $q_N = N_{\mathrm{Exp,frac}}/N_{\mathrm{Calc,frac}}$ for all concepts. The 1413 experiments and the variable amplitude loading sequences were taken out of the database DaBef, [2].

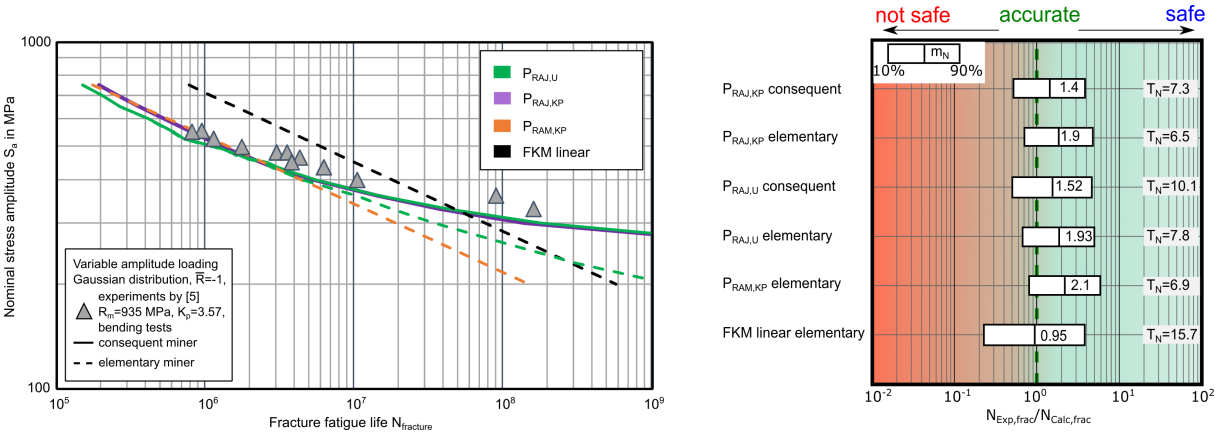

Figure 2. (left) Comparison of experiments by [6] with calculated, fracture fatigue live curves for the different concepts with $P = 50\%$ and $D = D_{\mathrm{eff,NL}}$, [3]; (right) Comparison of the accuracy of the different approaches with 1413 experiments [2] of specimens under variable amplitude loading for life quotient $q_N = N_{\mathrm{Exp,frac}}/N_{\mathrm{Calc,frac}}$ and $D = D_{\mathrm{eff,NL}}$, [3]. The accuracy is described by mean value m_N and life variance T_N, assuming a logarithmic normal distribution.

References

[1] U. Clormann. "Örtliche Beanspruchungen von Schweißverbindungen als Grundlage des Schwingfestigkeitsnachweises". Dissertation. Darmstadt: TU Darmstadt, 1986.

[2] F. Ellmer, K. Hinkelmann, K.-G. Eulitz, and Esderts A. *Datenbank und Auswertesystem Betriebsfestigkeit*. FKM-report No. 313. 2011.

[3] M. Fiedler. "Das U-Konzept - Technische Bruchlebensdauern auf Basis des Örtlichen Konzepts". Dissertation. Darmstadt: TU Darmstadt, submitted 2019, unpublished.

[4] M. Fiedler, M. Wächter, I. Varfolomeev, M. Vormwald, and A. Esderts. *Richtlinie nichtlinear - Rechnerischer Festigkeitsnachweis unter expliziter Erfassung nichtlinearen Werkstoffverformungsverhaltens*. VDMA Verlag, Frankfurt am Main, 2019.

[5] K. Hinkelmann. "Korrekturfunktionen zur Verbesserung der rechnerischen Lebensdauerabschätzung bei schwingender Beanspruchung". Dissertation. TU Clausthal, Clausthal-Zellerfeld, 2012.

[6] M. Hück and J. Bergmann. *Bewertung der Schwingfestigkeit der mikrolegierten Stähle 27 Mn VS 6 und 38 Mn VS 5 - Teil II*. FKM-report No. 122. 1992.

[7] H. Neuber. Theory of Stress Concentration for Shear-Strained Prismatical Bodies with Arbitrary Nonlinear Stress-Strain Law. *Trans. ASME, J. Appl. Mech.* 28 (1961), 544–550.

[8] R. Rennert, E. Kullig, M. Vormwald, A. Esderts, and D. Siegele. *Rechnerischer Festigkeitsnachweis für Maschinenbauteile aus Stahl, Eisenguss- und Aluminiumwerkstoffen*. VDMA-Verlag, Frankfurt am Main, 6. revised ed., 2012.

[9] H. Saal. *Einfluß von Formzahl und Spannungsverhältnis auf die Zeit- und Dauerfestigkeit und Rißfortschreitungen bei Flachstäben aus St52, Report 17*. Veröffentlichung des Instituts für Statik und Stahlbau der Technischen Hochschule Darmstadt, 1971.

[10] T. Seeger and A. Beste. Zur Weiterentwicklung von Näherungsformeln für die Berechnung von Kerbbeanspruchungen im elastisch-plastischen Bereich. *Bruchvorgänge und Schadensanalyse* (1977). Ed. by Bruchvorgänge und Schadensanalyse, 1–56.

[11] R.N. Smith, P. Watson, and T.H. Topper. A stress-strain function for the fatigue of metals. *Journal of Materials* 5 (1970), pp. 767–778.

[12] M. Vormwald. *Anrißlebensdauervorhersage auf der Basis der Schwingbruchmechanik kurzer Risse*. Veröffentlichung des Instituts für Stahlbau und Werkstoffmechanik der TH-Darmstadt, Vol. 47, 1989.

[13] M. Wächter. "Zur Ermittlung von zyklischen Werkstoffkennwerten und Schädigungsparameterwöhlerlinien". Dissertation. Clausthal-Zellerfeld: TU Clausthal, 2016.

**Proceedings of the 8th GACM Colloquium on Computational Mechanics
for Young Scientists from Academia and Industry
August 28–30, 2019 in Kassel, Germany**

An Approach to Characterize Fatigue Crack growth by Material Forces

Jad Khodor[1] and Michael Kaliske * [1]

[1]Institute of Structural Analysis, Technische Universität Dresden, 01062 Dresden, Germany

Abstract. A new approach is proposed to model fatigue crack growth using material forces based on the degradation of the fracture toughness. The variable used in the degradation function is the accumulated norm of the material force acting on the crack tip. A non-local accumulation is performed in order to avoid mesh dependency.

Introduction

Nowadays, many structures are subjected to cyclic loading, where the maximum value of the load could be much smaller than the ultimate design load. Although the applied load is smaller than the ultimate one, some structures fail after a certain number of cycles. In the framework of fracture mechanics the crack propagation can be divided into three main stages. In the first stage there will be nucleation of micro-cracks that merge together to form a macro-crack. The second stage, describes the stable propagation of the macro-crack, whereas in the third stage the crack propagates in an unstable manner. The pioneering law in describing the second stage is known as PARIS' law [5] that correlates the stress intensity factor to the rate of crack length per cycle. However, the use of the stress intensity factor is only limited to cases where the theory of linear elastic fracture mechanics (LEFM) is governing. In the work of [2], the cyclic J-integral ΔJ is introduced for gross plasticity to overcome the limitation of the stress intensity factor. In this paper, a new approach to characterize fatigue crack growth using material forces or configurational forces will be presented.

1 Material Forces

Configurational forces or material forces are non-NEWTONIAN forces which act on an inhomogeneity within a body. This inhomogeneity can be an inclusion or a crack tip. The material force that acts on the crack tip is considered as the crack driving force. The direction of the material force vector at the crack tip can be used to determine the crack propagation direction, whereas its norm can be used to calculate the energy release rate. The material force can be computed using ESHELBY's thought experiment [3]. ESHELBY considered an inclusion within a homogeneous elastic body. The body is subjected to traction forces as shown in Figure 1. He studied the energy variation due to an infinitesimal displacement $\delta \boldsymbol{X}$ of the surface P to the new position P'. The energy variation is defined as the dot product between the material force acting on the inclusion and the infinitesimal displacement and can be written as

$$\delta\psi = \boldsymbol{F} \cdot \delta \boldsymbol{X}, \tag{1}$$

where $\boldsymbol{F}$ is the material force that is defined as

$$\boldsymbol{F} = -\int_P [\psi \boldsymbol{I} - \nabla_{\boldsymbol{X}} \boldsymbol{u}^t \boldsymbol{\sigma}] \boldsymbol{n} dS, \tag{2}$$

where ψ is the strain energy, $\boldsymbol{I}$ is the second order identity tensor, $\boldsymbol{\sigma}$ is the CAUCHY stress tensor and $\nabla_{\boldsymbol{X}} \boldsymbol{u}$ is the gradient of the displacement field. For a small strain linear elastic material, the ESHELBY

*Corresponding author: Michael.kaliske@tu-dresden.de

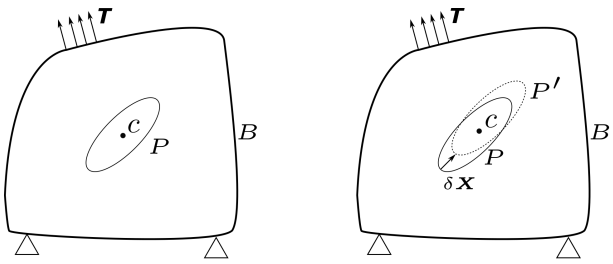

Figure 1. ESHELBY's thought experiment

stress tensor is defined as $\boldsymbol{\Sigma} = \psi \boldsymbol{I} - \nabla_{\boldsymbol{X}} \boldsymbol{u}^t \boldsymbol{\sigma}$. In case of finite strains, the ESHELBY stress tensor is defined as $\boldsymbol{\Sigma} = \psi \boldsymbol{I} - \boldsymbol{F}^t \boldsymbol{P}$, where $\boldsymbol{F}$ and $\boldsymbol{P}$ are the deformation gradient and the PIOLA-KICHHOFF stress tensor, respectively.

2 Fatigue Crack Growth Using Material Forces

2.1 Fracture Toughness Degradation

In the work of [1], a degradation function has been introduced to reduce the fracture toughness using the phase-field method. The accumulated variable used in the degradation function was the active part of the strain energy density. In this study, the norm of the material force at the crack tip will be accumulated. The degradation function is defined as

$$0 \leq f(\overline{\gamma}(t)) \leq 1, \tag{3}$$

$$f(\overline{\gamma}(t)) = \begin{cases} 1 & \text{if } \overline{\gamma}(t) \leq \gamma_0 \\ (\frac{2\gamma_0}{\overline{\gamma}(t)+\gamma_0})^2 & \text{if } \overline{\gamma}(t) \geq \gamma_0 \end{cases}, \tag{4}$$

where $\overline{\gamma}(t)$ is the accumulated variable and γ_0 is a material parameter. The degradation variable is accumulated as

$$\overline{\gamma}(t) = \int_0^t H(\gamma\dot{\gamma})|\dot{\gamma}| d\tau, \tag{5}$$

where $H(\gamma\dot{\gamma})$ is the HEAVISIDE function and $\gamma = \left\| \boldsymbol{F}^{\text{crack}} \right\|$ is the norm of the material force acting on the crack tip. The numerical accumulation of the material force norm is obtained as

$$\overline{\gamma}_{n+1} = \overline{\gamma}_n + \Delta\overline{\gamma}, \tag{6}$$

$$\Delta\overline{\gamma} = |\gamma_{n+1} - \gamma_n| \, H(\frac{\gamma_{n+1} - \gamma_n}{\Delta t}). \tag{7}$$

GRIFFITH [4] states that the condition for crack propagation is defined as

$$G - G_c = 0, \tag{8}$$

where G and G_c are the potential energy release rate and the fracture toughness, respectively. In case of fatigue crack propagation, the fracture toughness is degraded and therefore Eq. (8) can be written as

$$G - f(\overline{\gamma}(t)) G_c = 0. \tag{9}$$

2.2 Non-Local Accumulation of The Degradation Variable

In order to avoid mesh dependency of the degradation function, the accumulation should be achieved in a non-local way. $\Delta\alpha_{\text{cracktip}}$ and $\Delta\alpha_{\text{node}}$ represent the accumulation increment at the crack tip node and at a node next to the crack tip, respectively. The non-local accumulation over the nodes surrounding the crack tip is defined as

$$\Delta\overline{\alpha}_{\text{node}} = \Delta\overline{\alpha}_{\text{cracktip}} \times e^{-\frac{\left\| \boldsymbol{x}_{\text{cracktip}} - \boldsymbol{x}_{\text{node}} \right\|^2}{2l_c^2}}, \tag{10}$$

where l_c is a length scale parameter, $\boldsymbol{x}_{\text{cracktip}}$ and $\boldsymbol{x}_{\text{node}}$ are the position vectors of crack tip node and the surrounding node, respectively.

3 Numerical Example

The validation of this approach is achieved by applying a cyclic load on a tensile test specimen with an initial crack length $a_0 = 0.2$mm. The dimensions and the boundary conditions of the specimen are shown in Figure 2. The specimen is subjected to prescribed displacements at the boundaries with a maximum value $u_{\max} = 0.2$ mm and loading ratio $R = \frac{u_{\min}}{u_{\max}} = 0$. A linear elastic isotropic material, which uses a YOUNG's modulus $E = 10$GPa and a POISSON's ratio $\nu = 0.25$, has been utilized in this simulation.

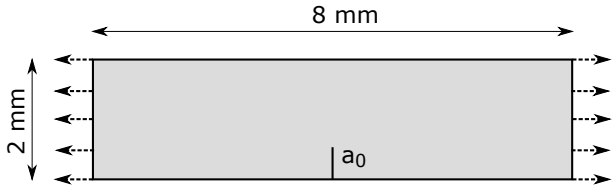

Figure 2. Tensile test specimen

The fracture parameters used are $G_c = 150\text{N mm}^{-1}$, $\gamma_0 = 3000\text{N mm}^{-1}$ and $l_c = 0.2$mm. The simulation is performed with 2-D 4 node quadrilateral elements at plane strain conditions. The results obtained from the simulation are the number of cycles and material force norms corresponding to each crack length. Using these data the crack increment per cycle can be plotted against the material force norm as represented in Figure 3.

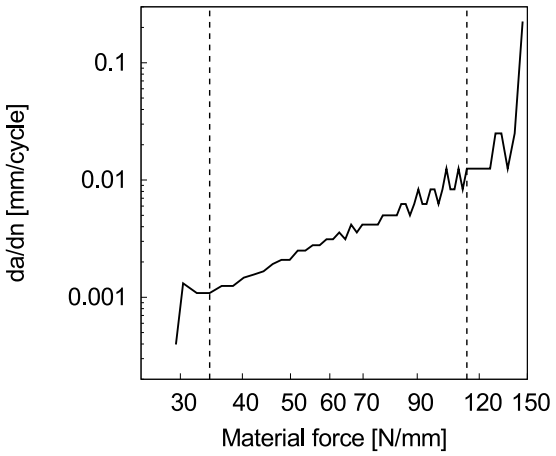

Figure 3. Double logarithmic plot of the crack increment per cycle and the material force norm at the crack tip (small strains)

It can be seen from Figure 3 that the three stages of fatigue crack growth are depicted by the proposed approach, the PARIS' parameters can be obtained from the second stage that is located between the two dotted lines. The relation between the crack increment per cycle and the material force norm is $\frac{da}{dn} = 10^{-6} \left\| \boldsymbol{F}^{\text{crack}} \right\|^{1.89}$. The idea behind using material forces is to overcome the limitations of the stress intensity factor. In case of straight crack propagation, the material force norm is equal to the J-integral. In this example, the crack propagates straightly without kinking. Therefore, the relation between the stress intensity factor and material force norm is defined as

$$\left\| \boldsymbol{F}^{\text{crack}} \right\| = \frac{K^2}{E'}, \tag{11}$$

where K is the stress intensity factor, $E' = E$ and $E' = \frac{E}{1-\nu^2}$ for plane stress and plane strain conditions, respectively. A NEO-HOOKEAN material model is used to validate the approach in case of finite strain theory, which has the following energy function

$$\psi = \frac{1}{2}(K_0 - \frac{2}{3}G)(J-1)^2 + \frac{1}{2}G(I_c - 3 - 2ln(J)), \tag{12}$$

where J is the determinant of the deformation gradient and $I_c = tr(\boldsymbol{F}^t\boldsymbol{F})$. The parameters K_0 and G are computed using E and ν, where

$$K_0 = \frac{E}{3(1-2\nu)}, \tag{13}$$

$$G = \frac{E}{2(1+\nu)}. \tag{14}$$

The same values for E and ν are used for the hyperelastic case. The plot of the crack increment per cycle and the material force norm is shown in Figure 4.

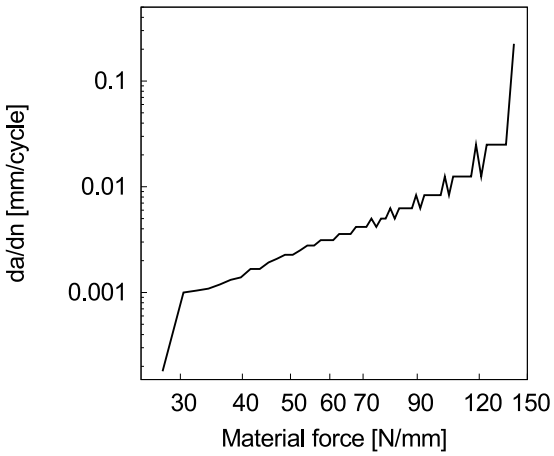

Figure 4. Double logarithmic plot of the crack increment per cycle and the material force norm at the crack tip (finite strains)

It can be seen from Figure 4 that the three stages of fatigue crack growth are depicted for the finite strain theory case. The relation between the crack increment per cycle and the material force norm is $\frac{da}{dn} = 5 \times 10^{-7} \left\| \boldsymbol{F}^{\text{crack}} \right\|^{2.13}$.

4 Conclusion

The proposed approach is able to depict the three stages of fatigue crack propagation. The newly introduced material parameters l_c and γ_0 can be calibrated with some experiments in order to get the same Paris's parameters, as of the experiments. The use of material forces in fatigue crack growth helps in overcoming the limitations of the stress intensity factor.

Acknowledgments

The authors of this work gratefully acknowledge ANSYS Inc., Canonsburg for their financial support.

References

[1] P. Carrara, M. Ambati, R. Alessi, and L. De Lorenzis. A Novel Framework to Model The Fatigue Behavior of Brittle Materials Based on a Variational Phase-Field Approach (2018).

[2] N. Dowling and J. Begley. Fatigue Crack Growth During Gross Plasticity and the J-Integral. *ASTM STP 590* (1976), pp. 82–103.

[3] J.D. Eshelby. The Force on an Elastic Singularity. *Philosophical Transactions of the Royal Society of London* 244 (1951), pp. 87–112.

[4] A. Griffith. The Phenomena of Rupture and Flow in Solids. *Philosophical Transactions of the Royal Society of London, Series A* 221 (1920), pp. 163–198.

[5] P. Paris and F. Erdogan. A Critical Analysis of Crack Propagation Laws. *Journal of Basic Engineering* 85 (1963), pp. 528–533.

**Proceedings of the 8th GACM Colloquium on Computational Mechanics
for Young Scientists from Academia and Industry
August 28–30, 2019 in Kassel, Germany**

Extension of the notch strain concept to transient cyclic material behaviour and residual stresses

David Kühne * [1], Martha Seiler[2], Franz Ellmer[1], Peter Hantschke[1] and Markus Kästner[2]

[1]Structural Durability Group, TU Dresden, Dresden, Germany
[2]Chair of Computational and Experimental Solid Mechanics, TU Dresden, Dresden, Germany

Abstract. A number of different forming processes result in significant residual stresses within the produced components, which lead to changes of their fatigue life properties. Furthermore materials are able to change their cyclic hardening behaviour during fatigue life which can also result in residual stresses. While state-of-the-art fatigue concepts (e.g. the notch strain concept) assume stabilized cyclic material behaviour throughout the entire fatigue life of the component, this assumption is not adequate for residual stress- and cyclic hardening afflicted components. Hence, a generalization to transient cyclic material behaviour with an asymmetry in tension and compression is introduced. To consider the load sequence order for variable amplitude load series on the fatigue life, the hysteresis counting method (HCM) is used. The damaging effect of each half-hysteresis is evaluated by a damage parameter according to Smith-Watson-Topper based on a strain Wöhler curve which represents the second set of input data. The fatigue concept is applied to the analysis of residual stress afflicted components.

Introduction

Forming processes generally lead to residual stresses. Compressive residual stresses can have a beneficial impact on the fatigue life of components while tensile residual stresses cause a shortening in fatigue life. Reiß and Merklein et al. [2, 11] demonstrated that different forming processes induce residual stresses into a component, which have a significant impact on its fatigue life. The Mechanical fatigue describes the process of crack initiation from the undamaged material on during the occurence of cyclic loads. From this point, stabilized crack growth occurs until a critical crack length is reached and the residual crack initiates. The fatigue life is defined here as the number of cycles until the crack initiates. This process is characterized by microscopic dislocation movements and discontinuities at the crystall grain scale. These phenomena can be summarized to an elastic-plastic-material behaviour on the macroscopic scale. The most common material concept considering fatigue is the notch strain concept. In general it assumes unchanging cyclic material behaviour throughout the entire fatigue life of the component. This assumption is not adequate for transient and residual stress afflicted material behaviour. As will be demonstrated later, residual stresses in combination with transient material behaviour behaviour have a considerable influence on the fatigue life. Therefore we extend the standard notch strain concept to a transient approach. The extended fatigue concept is depicted in Fig. 1. The circled numbers ◯ denotes the different features of the concept, described in the section below.

1 Theoretical framework

1.1 Standard Notch Strain Concept

The notch strain concept [9] is a material-based concept which retraces a representative local stress-strain path and calculates the damage associated with it. The local stress strain path generally depends on the notch geometry, the elasto-plastic material parameters and the external load-time sequence. It is reduced to a series of reversal points. Thus, the external load data for the fatigue-analysis is a sequence

*Corresponding author: david.kuehne@tu-dresden.com

of elastically calculated stresses at the considered material point over the loading path. The state of the art here is to convert the linear elastically calculated strain states using the Neuber rule ⑥ [7].

As an input for the revaluation serves the sequence of elastic stresses and strains, which is derived by scaling the stress-strain state of one elastic baseline simulation ② to all reversal points of the loading path ④. Result of the revaluation is an elasto-plastic stress-strain path from which hystereses can be identified. The shape of the initial stress-strain path is determined by the cyclic stress strain curve (CSSC) described by the Ramberg-Osgood Equation [10], where the elastic stress-strain state σ_{el}, $\varepsilon_{\mathrm{el}}$ is revaluated to elasto-plastic stress and strain amplitudes σ_{a}, ε_{a}

$$\varepsilon_{\mathrm{a}} = \varepsilon_{\mathrm{a,el}} + \varepsilon_{\mathrm{a,pl}} = \frac{\sigma_{\mathrm{a}}}{E} + \left(\frac{\sigma_{\mathrm{a}}}{K'}\right)^{1/n'}, \qquad (1)$$

$$\Delta\varepsilon = \frac{\Delta\sigma}{E} + 2\left(\frac{\Delta\sigma}{2K'}\right)^{1/n'}. \qquad (2)$$

Here, K' and n' are material constants to describe hardening behaviour. The CSSC can be obtained from either constant amplitude tests (CA-Tests) or incremental step tests (IST). Although the stress-strain path changes with increasing damage, it is common practise to use the stabilized CSSC which manifests after 50 percent of fatigue life. On top of that, the CSSC is usually symmetrised, neglecting the different behaviour in tension and compression.

The Masing behaviour [5] considers the hysteresis shape which corresponds to the CSSC scaled by the factor two in the direction of stress- and strain. Hereby, the stress and strain path is described by relative values $\Delta\sigma$, $\Delta\varepsilon$ with regard to the reversal points. The loading path is processed step by step and can thus take into account effects of the chronological loading order. To consider variable load amplitudes or random loads, the hysteresis counting method (HCM) [1] is used to determine the memory behaviour. The fatigue strength of the material is represented by the strain-life curve ⑤. It relates the total strain amplitude ε_{a} with the endurable number of load cycles N and is described using the Manson-Coffin-Morrow approach [4]

$$\varepsilon_{\mathrm{a}} = \varepsilon_{\mathrm{a,el}} + \varepsilon_{\mathrm{a,pl}} = \frac{\sigma'_{\mathrm{f}}}{E} \cdot (2N)^b + \varepsilon'_{\mathrm{f}} \cdot (2N)^c \qquad (3)$$

with the parameters σ'_{f}, b determining the contribution of the elastic strain and $\varepsilon'_{\mathrm{f}}$, c the one of the plastic strain part. The damaging effect of each hysteresis including its mean stress value is evaluated by a damage parameter $P_{\mathrm{SWT}} = \sqrt{(\sigma_a + \sigma_m) \cdot \varepsilon_a \cdot E}$ (P-value), e.g. according to Smith-Watson-Topper [12]. With the P-value ⑧ the strain-life curve is converted into a damage-life curve, which provides the number of load cycles N, that the material could theoretically endure, if it was loaded with hystereses with that specific P-value only. According to the linear damage accumulation hypothesis [6, 8] the total damage

$$D = \sum_{i=1}^{n} \frac{1}{N_i} \qquad (4)$$

can be summed up from all n hystereses with the damage contributions $1/N_i$. The total damage characterises the resistance of the component against the applied load: if D reaches 1, failure occurs theoretically, i.e. a crack initiation can be observed. With this criterion, the life time can be predicted from the given load sequence ④.

1.2 Extension of the Fatigue Concept

As described in the publication [3] the Notch Strain Concept is extended to asymmetric and transient cyclic material behaviour. For the asymmetric behaviour the material law (CSSC) in the standard notch strain concept must distinguish between tensile and compressive stresses. Therefore, an asymmetric stress-strain relationship is introduced by applying different cyclic hardening parameters K'_+ and K'_- and n'_+ and n'_- for tensile and compressive stresses, which must be related to the damage variable D to describe the transient behaviour over the course of fatigue life ③

$$K' \rightarrow \begin{cases} K'_+(D) & \sigma \geq 0 \\ K'_-(D) & \sigma < 0 \end{cases} \qquad n' \rightarrow \begin{cases} n'_+(D) & \sigma \geq 0 \\ n'_-(D) & \sigma < 0 \end{cases}. \qquad (5)$$

Hence, the Ramberg-Osgood (1) equation including Masing behaviour (2) can be rewritten as

$$\Delta\varepsilon_{\pm}(\Delta\sigma,\gamma) = \mathrm{sign}(\Delta\sigma)\left(\frac{|\Delta\sigma|}{E} + \gamma_{\pm}\left(\frac{|\Delta\sigma|}{K'_{\pm}(D)}\right)^{1/n'_{\pm}(D)}\right). \tag{6}$$

For an asymmetric stress-strain relationship, the hysteresis curve must be adjusted with the parameter γ to fit the experimental CSSC. Therefore, the parameters γ_+ and γ_- are introduced to describe the asymmetric reloading curves for tension and compression.

Due to the symmetrized CSSC Masing behaviour can be assumed. Thus the absolute value of hysteresis paths despite loading and unloading paths are equal and hysteresis are compulsory closed at their initial point. While in the non-transient approach no hysteresis shift occurs, the transient approach (7) causes a shift in stress- or strain-direction. To consider residual stresses (1), the initial point of the stress strain path is shifted along the initial CSSC. Thus the the first point of the stress-strain-path starts at σ_m with the related ε_m wich is associated to the CSSC. Throughout the shift, the hysteresis closure no longer necessarily takes place at the starting point of the hysteresis and the determination of the damage is not trivial anymore. Hence the evaluation with the damage parameter is no longer performed for closed hystereses but for half hystereses (9) . Hence, the linear damage accumulation hypothesis, with $0.5/N_i$ being the damage contribution of one half hysteresis, is modified to

$$D = \sum_{i=1}^{n} \frac{0.5}{N_i}. \tag{7}$$

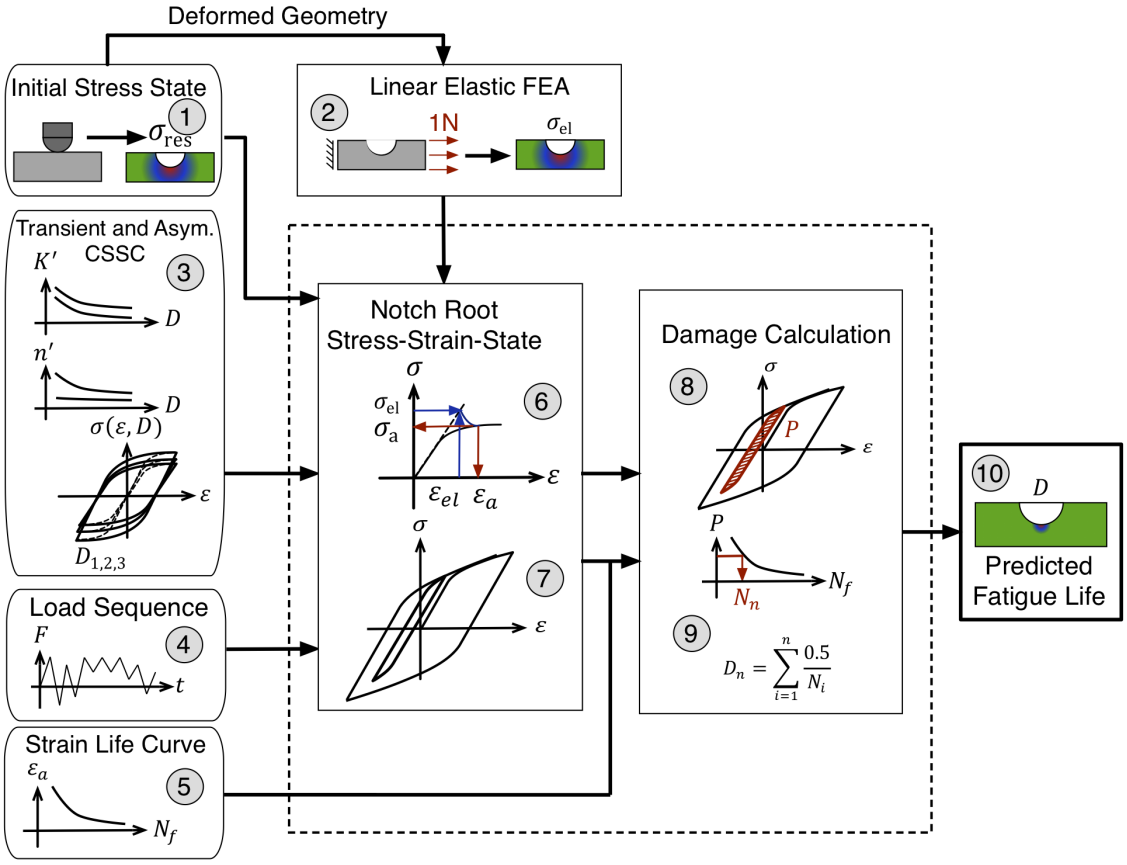

Figure 1. Scheme of the extended notch strain concept.

2 Demonstration Example

The concept has been validated and applied to analyse the general influence of residual stresses on the transient cyclic behaviour. To do so, moderate residual stresses $\sigma_{\mathrm{res}} \in \{-300, 300\}$ MPa are included

in the analysis as mean stress σ_m. The superimposed residual stresses shift, the hysteresis curves to different stress levels. Higher stresses lead to a faster damage accumulation and, as a consequence of the asymmetric transient cyclic behaviour, the hystereses become tilted with increasing fatigue damage. In the next step, the influence of the transient behaviour of the CSSC on fatigue life ⑩ is analysed in terms of the cyclic hardening parameter K' for different residual stresses. Fig. 2 depicts three different cyclic characteristics, K'_{+1} as it was fitted to the experimental data, obtained from an Incremental Step Test with an unnotched specimen and additionally two functions K'_{+2} and K'_{+3} with less pronounced cyclic softening, for comparison. Furthermore, the estimated fatigue life N_f for the three transient K' in dependence of the residual stresses is also shown. Moreover, a constant $K' = K'_{+1}(D = 0.5)$, which allows for a comparison with the standard concept, is considered. Remarkable is the deviation of the fatigue lifes at very high compressive residual stresses. It follows that the progression of the cyclic material parameters in combination is especially relevant for fatigue life in case of compressive residual stresses.

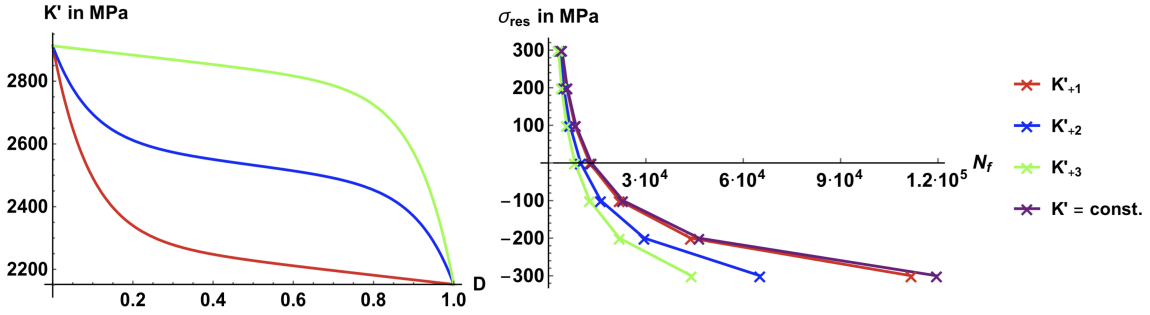

Figure 2. Comparison of the fatige life for different residual stresses, calculated for a strain amplitude of $\varepsilon_a = 0.5\%$ with the standard notch strain concept and the extended one.

References

[1] U.H. Clormann and T. Seeger. *Rainflow-HCM: ein Hysteresisschleifen-Zählalgorithmus auf werkstoffmechanischer Grundlage*. Fachgebiet Werkstoffmechanik, Technische Hochschule Darmstadt.

[2] Influence of machining process on residual stresses in the surface of cemented carbides. *Procedia Engineering* 19 (2011). 1st CIRP Conference on Surface Integrity (CSI), pp. 252 –257.

[3] D. Kühne, C. Guilleaume, M. Seiler, P. Hantschke, F. Ellmer, T. Linse, A. Brosius, and M. Kästner. Fatigue analysis of rolled components considering transient cyclic material behaviour and residual stresses. *Production Engineering* 13.2 (2019), pp. 189–200.

[4] SS Manson. Fatigue: a complex subject—some simple approximations. *Experimental mechanics* 5.7 (1965), pp. 193–226.

[5] G. Masing and W. Mauksch. *Eigenspannungen und Verfestigung des plastisch gedehnten und gestauchten Messings*. Berlin, Heidelberg: Springer Berlin Heidelberg, 1925, pp. 244–256.

[6] M. A. Miner. *Cumulative damage in fatigue.* Journal of applied mechanics. Band 12, Nr. 3, S. 159–164. Journal of applied mechanics., 1945.

[7] H. Neuber. Theory of stress concentration for shear-strained prismatical bodies with arbitrary nonlinear stress-strain law. *Journal of applied mechanics* 28.4 (1961), pp. 544–550.

[8] A. Palmgren. *Die Lebensdauer von Kugellagern.* Zeitschrift des Vereins Deutscher Ingenieure. Band 68, Nr. 14, 1924, S. 339–341. Zeitschrift des Vereins Deutscher Ingenieure., 1924.

[9] D. Radaj, C. M. Sonsino, and W. Fricke. *Fatigue assessment of welded joints by local approaches*. Woodhead publishing, 2006.

[10] W. Ramberg and W. R. Osgood. Description of stress-strain curves by three parameters (1943).

[11] A. Reiss, U. Engel, and M. Merklein. Investigation on the Influence of Manufacturing Parameters on the Fatigue Strength of Components. In: *The Current State-of-the-Art on Material Forming*. Vol. 554. Key Engineering Materials. Trans Tech Publications Ltd, July 2013, pp. 280–286.

[12] K.N. Smith, T.H. Topper, and P. Watson. *A Stress-strain Function for the Fatigue of Metals*.

**Proceedings of the 8th GACM Colloquium on Computational Mechanics
for Young Scientists from Academia and Industry
August 28–30, 2019 in Kassel, Germany**

Transferability concepts of Fatigue Strength for high purity copper components in electrical engines

Stefan Pruy[1], Markus Kästner[2] and Peter Hantschke[2]

[1]ZF Friedrichshafen AG, Germany
[2]TU Dresden, Germany

Abstract.

The fatigue strength of high purity copper components in electrical engines is influenced by the manufacturing process and the geometrical properties of the notches. A test setup on an electrodynamic shaker allows to get component specific S-N curves. The manufacturing influence can either be evaluated by hardness measurements or a process simulation, which is described for a forming process in this study. A comparison of common methods for the geometrical transferability shows the untypical behaviour of high purity copper. Neither the relative stress gradient nor the high stress volume indicate a correlation to the fatigue strength for the given specimens.

Introduction

The electrification of the powertrain in vehicle construction leads to new requirements for the operationally stable and reliable design of components and assemblies. For a valid design process according to vibrational and time dependent temperature loads a customized fatigue life evaluation is required. This is especially important for the materials used in mechatronic assemblies as they typically react sensitive to environmental and operational loads. Within the scope of this study, the influences on the fatigue strength of high purity copper components are identified. A concept for the transferability of the fatigue strength which considers the manufacturing process and the geometrical influence on the notch stresses is proposed.

1 Influences on the fatigue strength

Influences on the fatigue strength for electrical connectors can be divided into two parts: the manufacturing processes and the geometrical influences which are coupled with the load situation.

1.1 Manufacturing processes

To produce economical and reliable busbars with high efficiency, high-purity copper sheets or wires commonly serve as raw materials. The following manufacturing processes are typical and influence the fatigue strength:

- **Rolling:** Rolling of the raw copper material allows to produce a specific sheet thickness and strength properties.
- **Stamping and cutting:** Stamping and cutting allows to get specific semi-finished parts out of the metal sheets or wires.

- **Forming and bending:** Forming and bending processes are commonly used to get spacial components out of copper sheets. Areas which have a high deformation ratio are further strengthened due to plastic hardening.
- **Welding and soldering:** Manufacturing operations such as welding and soldering can be used to get a non-removable metallurgically-bonded connection of different stamping-bending parts.

Instead of assuming an isotropic and location-independent material behaviour throughout the electrical part, the history of all relevant processes needs to be considered.

1.2 Geometrical influences

Aside of the manufacturing processes there are several geometrical influences on the fatigue properties caused by the load situation. This could be either by a modal resonance of the whole assembly or a forced displacement due to connected parts. In any case the notch stress situation influences the impact of cyclic stresses and the resulting damage accumulation. Geometrical effects due to a specific load configuration can be handled by different concepts:

- **Relative stress gradient:** The relative stress gradient χ^* is a parameter to estimate a supporting effect of the structure. [2]
- **High stress volume:** Another concept to consider the geometrical effect of notch stresses is the high stress volume according to a specific value e.g. V_{90}. The assumption refers to the statistical probability of defects like pores and cavities in a material volume.

For conventional construction materials like steel and aluminium alloys these two concepts can be used to describe the transferability of the geometrical influencing factors. In the FKM-Guideline [1] it is recommended to consider a supportive factor according to Stieler which is described by the relative stress gradient χ^*. Another transferability option is the material mechanics supportive factor which includes a statistic supportive factor based on the high stress notch area A_{90}. Wagener tries to find a transferability concept for high-copper alloys based on the high stress volume for standard and small specimens like solder connections in electronics. [3]

2 Test rig setup

To receive valid information on the fatigue strength a test setup is proposed which allows to stress the components by a constant deflection.

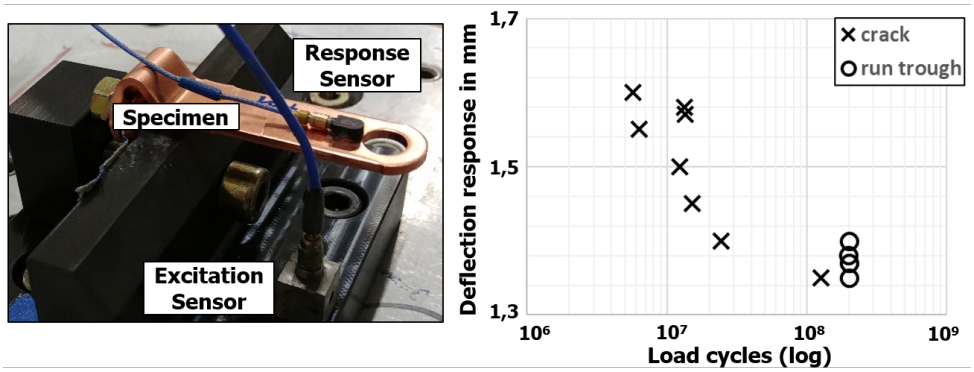

Figure 1: Test rig setup for resonance specific S-N curves and test results

The moment of crack initiation can be identified by a drop of the stiffness which influences the natural frequency of the test specimen. A variation of the load levels and a statistical evaluation

allows the derivation of component specific S-N curves. The number of load cycles within the fatigue relevant area reaches high values up to $N = 10^8$ load cycles, which is to be expected of a cubic face-centered metal such as copper.

Figure 1 shows the test rig setup on an electrodynamic vibration table and the excitation and response sensor on the specimen. Each specimen is tested until mechanical failure (drop of stiffness) or until a specific number of cycles (run through). With this information a displacement-controlled S-N curve based on the pearl string method can be derived.

3 Simulations

To examine the transferability of fatigue strength values, the detailed load and stress situation of the component test as well as the relevant manufacturing processes have to be calculated.

3.1 Load cases

Due to the small size of the specimen and the restricted access to the crack initiation area, neither strain gauge nor measurement peaks can be applied. To get the local stress and strain values in the notch, an FE-based calculation will transfer the applied load to the local stress values. According to the notch stress concept for lifetime estimation, the transfer function will be linear. This allows to calculate a notch stress S-N curve based on the vibration dwell testing with constant deflection.

3.2 Manufacturing processes

It can be shown that the manufacturing processes such as rolling, stamping and forming influence both the geometrical properties and the local strength. The simulation of the two-step manufacturing process forming for the treated part shows two relevant areas with high forming ratios. This results in local cold work hardening and residual stresses. To validate the process simulation a hardness measurement on the specimen was made along the inner surface of the bending area. A comparison between the local hardness and the local yield strength shows good correlation for the process simulation and the real manufactured part.

The next step would be to consider the local material properties for cyclic loads and fatigue as the failure criterion. Thus, the local distribution of the static strength due to cord work hardening and residual stresses can be used.

4 Transferability of fatigue strength

The influence of the real notch geometry can be shown by a comparison of the calculated and tested crack initiation area. Using a measured 3D-surface geometry of the specimen and a thus optimized FE-Mesh, the high stress area fits much better with the tested damage pattern.

4.1 Manufacturing processes

The manufacturing processes are considered by using either the measured local hardness or the local yield strength according to a forming process simulation. Even if it was possible to get a good prediction of the local hardness and yield strength, the fatigue strength cannot be predicted clearly. The transferability of fatigue parameters is only possible for similar products and processes, depending on the manufacturing history and the load during lifetime.

4.2 Geometrical influences

The geometrical influences can be evaluated by the relative stress gradient χ^* or the high stress volume V_{90}. Aside from the difficulty to separate the basic effects, the results of this research show no obvious correlation between notch parameters and fatigue strength for high purity copper components. Independent of the considered notch parameters the fatigue strength scatters between a specific notch stress value of approximately $\sigma_{W,a} = 126\ MPa$ for $N = 3 \cdot 10^7$ load cycles for different specimens.

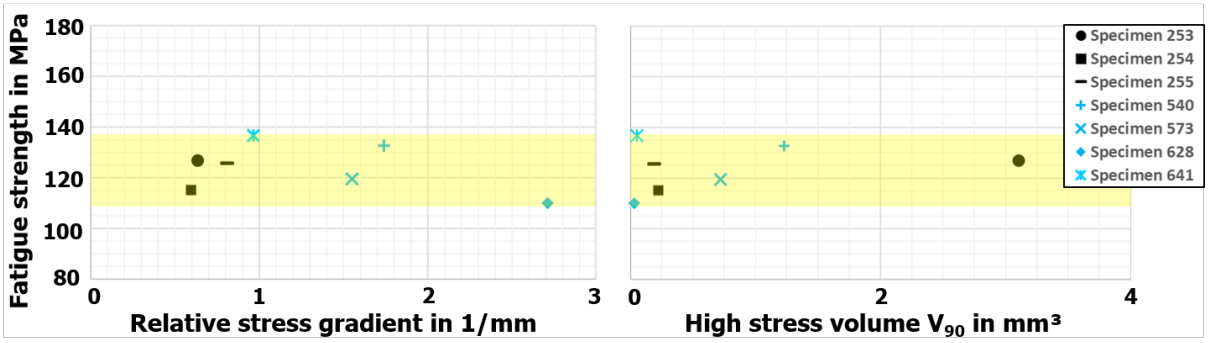

Figure 2: Application of the common transferability concepts for metals on the test results (black: milled specimen, blue: stamping-bending specimen)

Whereas typical components based on steel and aluminium alloys have a well known dependency of the relative stress gradient or the high stress volume, the tested specimen in this research show no significant dependency. For the high-purity copper which is the focus of this research no transferability of the geometrical notch effects can be detected according to conventional methods. This is in accordance to the results of Wagener. [3]

5 Outlook

In this research it is shown that the manufacturing process has a significant influence both on the load distribution and on the fatigue strength. Due to locally different material properties the failure criterion can only be predicted properly based on the process simulation. Geometrical properties for the notch stress concepts have a minor influence on the fatigue strength and thus the transferability. Whenever the manufacturing process has a major impact on the cold work hardening or a thermal process leads to annealing or recrystallization the geometrical transferability can be neglected.
Aside from these high-frequency vibrational loads, transient and stationary temperature loads need to be considered. According to the behaviour of the static strength of the copper material, a significant influence of the ambient temperature on the cyclic strength is to be expected.

References

[1] Forschungskuratorium Maschinenbau (FKM). FKM-Richtlinie - Rechnerischer Festigkeitsnachweis für Maschinenbauteile. 6. überarbeitete Ausgabe (2012).

[2] Erwin Haibach. *Betriebsfestigkeit - Verfahren und Daten zur Bauteilberechnung*. Wiesbaden: Springer, 2006.

[3] R. Wagener, M. Scurria, T. Kimpel, M. Haouel, H. Kaufmann, and T. Melz. Schwingfestigkeitsverhalten von Kupfer-Legierungen für die Anwendung in mobilen Steuergeräten. *METALL* 70. Jahrgang 11/2016 (2016), pp. 458 –461.

**Proceedings of the 8th GACM Colloquium on Computational Mechanics
for Young Scientists from Academia and Industry
August 28–30, 2019 in Kassel, Germany**

Simulation of Fatigue with Cyclic Cohesive Zone Models

Stephan Roth * [1], Meinhard Kuna[1] and Björn Kiefer[1]

[1]TU Bergakademie Freiberg, Institute of Mechanics and Fluid Dynamics, Lampadiusstraße 4, 09596 Freiberg, Germany

Abstract. Cyclic cohesive zone models offer the ability for a unique modeling of fatigue since they comprise both toughness-based and strength-based fatigue criteria. This way, S–N-curves (Wöhler) and fatigue crack growth rate curves (Paris) can be predicted with numerical cycle-by-cycle simulations.

In particular, this study addresses the formation and propagation of fatigue cracks in elastic-plastic material. The capabilities of cyclic cohesive zone models to account for load sequence effects are presented by means of an illustrative example of a semi-infinite crack under K-controlled loading with a single overload. The interaction between the damage process zone within the cohesive zone and the plastic zone inside the bulk material is demonstrated.

1 Cyclic cohesive zone model

The cyclic cohesive zone model (CCZM) applied here to simulate fatigue crack growth (FCG) is briefly presented in this section [4]. The traction–separation relation of the model is fully described by a cohesive (state) potential, which is formulated in terms of the normalized effective separation $\lambda = |\vec{s}|\,/s_0$ and a *fundamental damage variable*, $0 \leq \overline{D} \leq \infty$, namely

$$\Gamma\big(\lambda,\, \overline{D}\big) = \frac{1}{F}\left[\mathrm{e} - [1+\lambda F]\exp(1-\lambda F)\right] \ . \tag{1}$$

Here $F\big(\overline{D}\big)$ represents an auxiliary function which includes the dependency on damage. The coordinates of the traction vector $\vec{t}$ are calculated by $t_i/t_0 = \partial\Gamma/\partial\big(s_i/s_0\big)$. Since $\vec{t}$ and $\vec{s}$ are collinear to ensure rotational equilibrium, the separation law at a particular given damage state can be expressed by

$$\tau\big(\lambda,\, \overline{D}\big) = \lambda F \exp(1-\lambda F) \ , \tag{2}$$

with $\tau = |\vec{t}|\,/t_0$ being the normalized effective traction. The parameters cohesive strength t_0 and cohesive length s_0 mark the maximum of the traction–separation envelope (TSE)

$$\tau^{\mathrm{TSE}}(\lambda) = \begin{cases} \tau\big(\lambda,\, \overline{D}=1\big) & ,\ \forall\ \lambda < 1 \\ \tau\big(\lambda,\, \overline{D}=\lambda\big) & ,\ \forall\ \lambda \geq 1 \end{cases} \ , \tag{3}$$

which is shown in Fig. 1 (in normalized space), where also some non-linear unloading paths for several damage states are depicted. The area under the TSE represents the normalized fracture energy density Γ_0, which in general depends on the shape of the TSE.

Damage initiation and accumulation are controlled by the evolution equation

$$\dot{\overline{D}} = \left[\frac{\lambda}{\overline{D}}\right]^{\varrho} \langle\dot{\lambda}\rangle\ \mathrm{H}(\lambda - \lambda^{\mathrm{e}}) \ , \tag{4}$$

with the damage exponent ϱ and a state-dependent endurance limit $\lambda^{\mathrm{e}}\big(\overline{D}; \tau_0^{\mathrm{e}}, \alpha\big)$ defined by the normalized initial endurance limit τ_0^{e} and the endurance exponent α. A load scenario illustrating the damage evolution

*Corresponding author: stephan.roth@imfd.tu-freiberg.de ORCID iD: 0000-0003-4827-1195

is shown in Fig. **??**. Further details about the CCZM and its implementation in an ABAQUS user element subroutine are given in [1, 4].

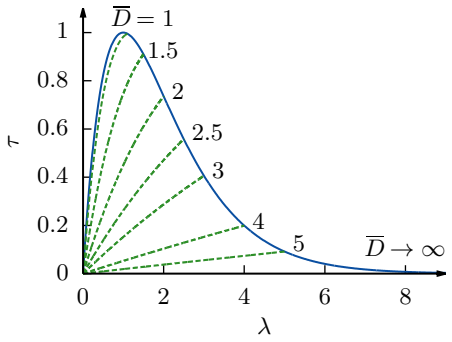

Figure 1. Monotonic envelope and non-linear unloading paths for several damage states $\overline{D}$={1, 1.1, 1.5, 2, 2.5, 3, 4, 5, 6} (taken from [4])

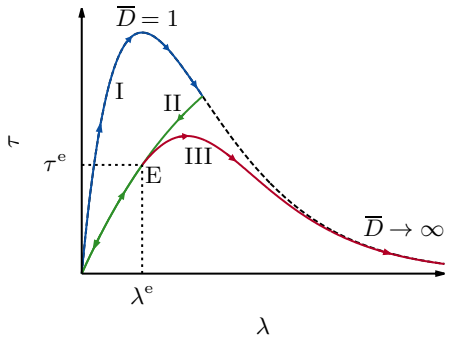

Figure 2. Initial loading (I), unloading (II), and reloading (III) paths of the CCZM (endurance limit E); dashed: monotonic envelope (taken from [4])

2 Application of the CCZM to problems of fatigue

The CCZM presented above has been applied to several problems of fatigue. Since the cohesive model comprises both strength and toughness type characteristics represented by, e.g., the material parameters t_0 and Γ_0, uniaxial fatigue tests and FCG have been simulated and analyzed using the CCZM, see [2, 4]. It turns out that the particular constitution of the cohesive model—consisting of a potential-based TSE and an independent damage evolution equation with a damage-dependent endurance limit—additionally allows to describe the size-dependent macroscopic fatigue failure mode, i.e. a unique modeling of fatigue where the pure failure modes "uniform debonding" and "fatigue crack growth" represent the material response for negligible and infinite characteristic length scales, respectively. Consequently, corresponding limit curves separating fatigue from endurable behavior and static failure in a KITAGAWA-TAKAHASHI-Diagram (KTD) or a Cyclic Failure Assessment Diagram (CFAD) can be predicted, see Fig. **??** and **??**. Note that these limit curves depend on the parameters of the elastic bulk material *and* the parameters of the CCZM, compare [3].

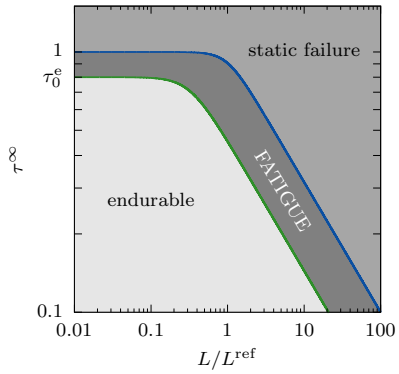

Figure 3. KTD with failure limit curves predicted by the CCZM (taken from [3])

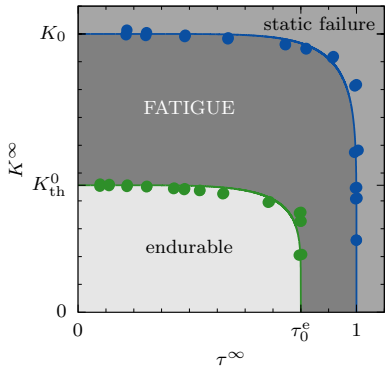

Figure 4. CFAD with failure limit curves predicted by the CCZM (taken from [3])

3 Combination of CCZM with elastic-plastic bulk material

In all previous studies, the CCZM has been utilized in combination with linear-elastic bulk material, using the basic assumption that all inelastic processes are covered by the cohesive behavior. Now, the interplay of the cohesive model with surrounding elastic-plastic material is analyzed. The boundary layer

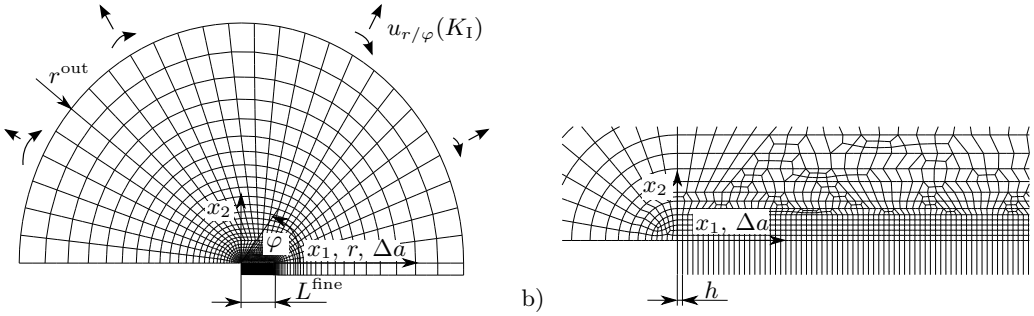

Figure 5. a) Crack model with K_I-controlled displacement boundary conditions; b) detailed mesh within the finely meshed region $0 \leq x_1 \leq L^\mathrm{fine}$ (taken from [4])

model of a semi-infinite crack under plane strain conditions subjected to Mode-I loading is considered, see Fig. **??**. More details can be found in [4]. In the vicinity of the crack tip, J_2-plasticity with non-linear isotropic hardening according to the power-law

$$\frac{\sigma_\mathrm{y}}{\sigma_\mathrm{y0}} = \left[\frac{\sigma_\mathrm{y}}{\sigma_\mathrm{y0}} + \frac{E}{\sigma_\mathrm{y0}}\varepsilon_\mathrm{eq}\right]^n \,, \tag{5}$$

with yield stress σ_y, initial yield stress σ_y0, YOUNG's modulus E, equivalent plastic strain ε_eq, and hardening exponent n is applied. The chosen geometric and constitutive parameters are summarized in Tab. **??**:

Table 1. Parameters of the cohesive crack model: geometry, material, loading

r^out/s_0	L^fine/s_0	h/s_0	E/σ_y0	ν	σ_y0	n	t_0/σ_y0	s_0	Γ_0	ϱ	τ_0^e	α	$\Delta K/K_0$	R
10^8	$20 - 10^4$	0.5	340	0.3	1	0.1	3.4	1	2.7	1	0.2	2	0.6	0

For a given load ratio $R = K_\mathrm{I}^\mathrm{min}/K_\mathrm{I}^\mathrm{max} = 0$, FCG rate curves were computed based on simulations with a maximum stress intensity factor varying in a range of $0.15 \leq K_\mathrm{I}^\mathrm{max}/K_0 \leq 1.2$ with $K_0 = \sqrt{E\, t_0 s_0 \Gamma_0 / [1-\nu^2]}$ and $\Delta K = K_\mathrm{I}^\mathrm{max}$. In order to demonstrate the influence of plasticity, a reference FCG rate curve for a ratio $t_0/\sigma_\mathrm{y0} = 0.5$ representing linear elasticity was generated. The normalized FCG rate curves are depicted in Fig. **??**. For the given set of material parameters, both curves coincide in the near-threshold and PARIS regions up to $\Delta K \approx 0.5 K_0$. With further increase of the load level, considerable cyclic plastic deformation and thus dissipation occurs leading to a deviation of the FCG rate curves. While the elastic curve approaches static failure at $\Delta K = K_0$, FCG also occurs at higher load levels in case of plastic bulk material.

Significant differences also appear when the FCG behavior is observed after single overloads. Here, as illustrated in Fig. **??**, an overload of $\Delta K = 0.9 K_0$ is applied after steady-state FCG has been established, i.e. after 50 load cycles ($N = 50$), at a basic load level of $\Delta K = 0.6 K_0$. At steady-state, the FCG rates for elastic and elastic-plastic material behavior are nearly the same, compare Fig. **??**. Also, the magnitudes of the crack length jumps in consequence of the overload do not differ. After the single overload, when the basic cyclic load level $\Delta K = 0.6 K_0$ is again applied, the elastic model quickly returns to the former FCG rate, thus predicting an acceleration of FCG. In contrast, the plastic model shows a pronounced crack retardation before the steady-state is reached again. To explain this effect, the distributions of equivalent plastic strain (in the bulk material) and damage (in the cohesive zone) is visualized in Fig. **??**–**??** at i) $N = 1$ (primary plastic zone, PPZ), ii) $N = 50$ (steady-state), iii) $N = 51$ (overload), iv) $N = 85$ (crack retardation), and v) $N = 101$ (return to steady-state). After leaving the primary plastic zone, the steady-state is characterized by a constant FCG rate accompanied by a growth of the cyclic plastic zone (CPZ) around the fatigue crack tip. The overload causes a sudden crack jump and an enlargement of the plastic zone. This region has to be crossed subsequently by the FCG crack inducing the observed crack retardation. Once the region affected by the overload is left, the FCG crack returns to the steady-state.

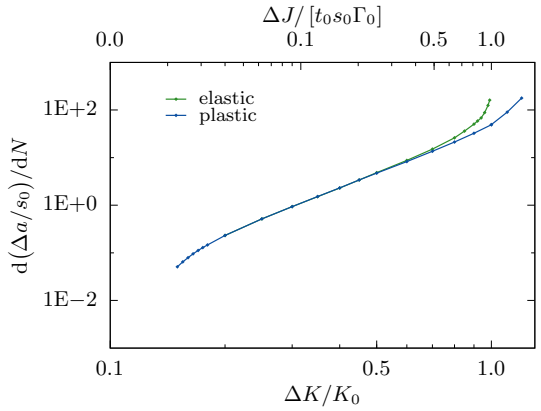

Figure 6. FCG rate curves for elastic and plastic ($t_0/\sigma_{y0} = 3.4$) bulk material

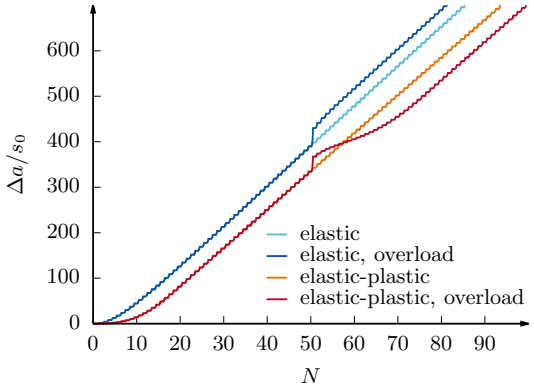

Figure 7. Fatigue crack extension $\Delta a(N)$ with and without single overload at $N = 51$

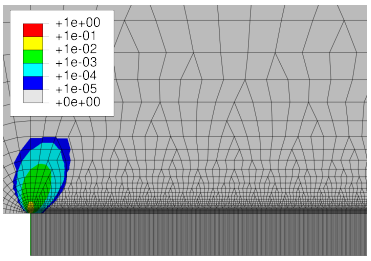

Figure 8. PPZ: $N = 1$

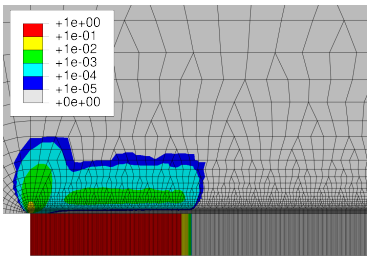

Figure 9. Steady-state: $N = 50$

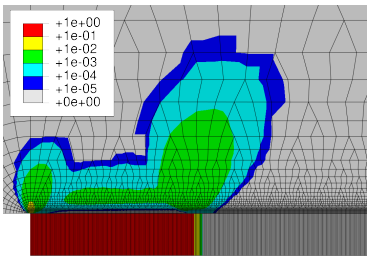

Figure 10. Overload: $N = 51$

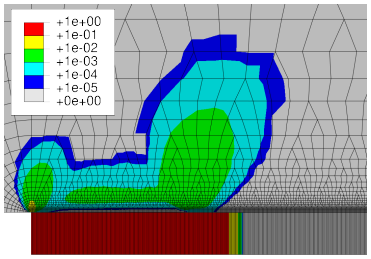

Figure 11. Crack retardation: $N = 85$

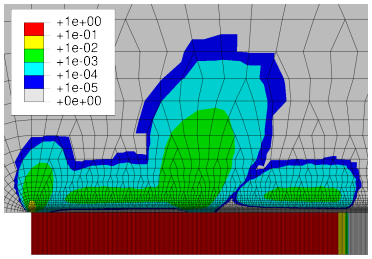

Figure 12. Return to steady-state: $N = 101$

4 Summary

In this study, the combination of a plastic bulk material and a CCZM to simulate FCG was investigated. For a representative ratio t_0/σ_{y0}, the FCG rate curve was computed and compared with the elastic curve. The typical behavior of crack propagation in the near-threshold and Paris-regions is reflected. As expected, due to plastic dissipation, static failure occurs at considerably higher load levels. The application of a single overload causes crack retardation, which also matches experimental observations.

References

[1] S. Roth. "Entwicklung und Implementierung zyklischer Kohäsivzonenmodelle zur Simulation von Werkstoffermüdung". Dissertation. TU Bergakademie Freiberg, 2016.

[2] S. Roth and B. Kiefer. Simulation of fatigue crack growth with a cyclic cohesive zone model using a phase field description. In: *DVM-Bericht 251*. DVM. 2019, pp. 159–168.

[3] S. Roth and M. Kuna. Prediction of size-dependent fatigue failure modes by means of a cyclic cohesive zone model. *Int. J. Fatigue* 100.1 (2017), pp. 58–67.

[4] S. Roth, G. Hütter, and M. Kuna. Simulation of fatigue crack growth with a cyclic cohesive zone model. *Int. J. Fract.* 188.1 (2014), pp. 23–45.

**Proceedings of the 8th GACM Colloquium on Computational Mechanics
for Young Scientists from Academia and Industry
August 28–30, 2019 in Kassel, Germany**

Efficient phase-field modelling of fatigue in ductile materials

Martha Seiler * [1], Thomas Linse[1], Peter Hantschke[2] and Markus Kästner[1]

[1]Chair of Computational and Experimental Solid Mechanics, TU Dresden, 01062 Dresden, Germany
[2]Structural Durability Group, TU Dresden, 01062 Dresden, Germany

Abstract. Fatigue loads come along with high numbers of load cycles which makes the simulation of fatigue fracture computationally very demanding. We present a numerically efficient method which avoids resolving the loading path and instead requires only one increment per load cycle at most. We combine the phase-field method for fracture with a classic fatigue concept. A local lifetime variable is obtained, which we use to modify the material resistance incrementally in order to consider the progressive weakening of the material. Focussing on ductile material behaviour, we make use of an elasto-plastic revaluation technique instead of a full plastic material model. The model allows to describe fatigue crack initiation as well as propagation and reproduces Paris behaviour.

Introduction

Fatigue fracture is one of the most common causes of failure in structures, while still being insufficiently predictable. Fatigue life is divided in a crack initiation and a crack propagation stage. Stable cyclic crack propagation can be described by the Paris-Erdogan law [5]: It links the cyclic crack propagation rate $\mathrm{d}a/\mathrm{d}N$ to the range of stress intensity factor ΔK by the power law $\mathrm{d}a/\mathrm{d}N = C\Delta K^m$ with material parameters C and m. For the numerical simulation of crack propagation, the phase-field method is a very promising approach, being able to model both crack initiation and propagation in a straightforward manner [3]. Carrara et al. [1] applied the method to fatigue fracture in *brittle* materials, decreasing the crack resistance due to repetitive loading. Analogously, we introduce a model for *ductile* materials such as metals. It is also based on the reduction of the fracture toughness, but considers that fatigue crack propagation in ductile materials is caused by cyclic plasticity.

1 Model framework

The model is based on the phase-field formulation for brittle fracture introduced by Miehe et al. [3]. In order to describe the crack topology, an additional phase-field variable $d \in [0, 1]$ is introduced, smoothly bridging the fully intact ($d = 0$) and fully damaged ($d = 1$) state. The degradation function $g(d) = (1 - d)^2$ couples the mechanical field $\boldsymbol{u}$ and the phase-field d, degrading the stress $\boldsymbol{\sigma} = g(d)\,\partial\psi^{\mathrm{e}}/\partial\boldsymbol{\varepsilon}$. Approximating the crack geometry by regularizing the phase-field with the length scale parameter ℓ, the regularized energy functional can be written as

$$\Pi_\ell = \int_\Omega g(d)\,\psi^{\mathrm{e}}(\boldsymbol{\varepsilon})\,\mathrm{d}V + \int_\Omega \alpha(D)\,\mathcal{G}_{\mathrm{c}}\frac{1}{2\ell}(d^2 + \ell^2|\nabla d|^2)\,\mathrm{d}V. \tag{1}$$

The standard phase-field formulation is thereby extended to fatigue by introducing a scalar reduction function $\alpha(D) \in [\alpha_0, 1]$ with $0 < \alpha_0 < 1$. It reduces the fracture toughness $\mathcal{G}_{\mathrm{c}}$ locally in order to model the progressive material weakening. This reduction function depends on a lifetime variable D. For $D = 0$ a material point has experienced no fatigue loads at all, while $D = 1$ means it has undergone all load cycles it can possibly bear before loosing its integrity.

*Corresponding author: martha.seiler@tu-dresden.de

On this basis the function

$$\alpha(D) = (1 - \alpha_0)(1 - D)^{\xi} + \alpha_0 \tag{2}$$

with the parameters α_0 and ξ is proposed. The governing equations for the coupled problem

$$\vec{0} = \nabla \cdot \boldsymbol{\sigma} \qquad \alpha(D)\, d - \nabla\alpha(D) \cdot \ell^2 \nabla d - \alpha(D)\, \ell^2 \Delta d = (1 - d)\, \psi^{\mathrm{e}}(\boldsymbol{\varepsilon}) 2\ell / \mathcal{G}_{\mathrm{c}} \tag{3}$$

are complemented with boundary conditions $\boldsymbol{n} \cdot \boldsymbol{\sigma} = \tilde{\boldsymbol{t}}$, $\boldsymbol{u} = \tilde{\boldsymbol{u}}$ and $\boldsymbol{n} \cdot \nabla d = 0$. We set the irreversibility condition $\dot{d} \geq 0$. For a discussion of the influence of irreversibility see Linse et al. [2].

The lifetime variable D is determined with the notch strain concept [6], which is in its original sense a common scheme for service life prediction of components. Stresses and strains derived from the solution of the displacement field $\boldsymbol{u}$ are revaluated to virtual elasto-plastic values following Neuber's rule[4]. Hence, no plastic material model is needed, which significantly reduces computational time. With the revaluated stress and strains, the damage parameter P_{SWT} [7] is determined, which is associated with the area inside the stress-strain hysteresis curve. It only depends on the stress and strain amplitudes σ_{a} and ε_{a} and the mean stress σ_{m}. Hence, for alternating loads one elastic simulation per load cycle at amplitude load is sufficient in order to determine its damaging effect. With the damage parameter the lifetime contribution ΔD_i of a load cycle can be determined from strain Wöhler curves, which are derived from standardised cyclic experiments.

2 Numerical examples

The method is tested with a compact tension (CT) test. The specimen is loaded with a constant force amplitude of $\tilde{F} = 4.9$ N and no mean load. The model parameters are chosen to $E = 210$ GPa, $\nu = 0.3$ and $\mathcal{G}_{\mathrm{c}} = 2.7$ N/mm, $\alpha_0 = 0.05$ and $\xi = 1$. The set-up as well as evolution of the phase-field and the lifetime variable are displayed in Fig. 1. Starting from the notch, a zone of $D = 1$ forms progressively. This area can be associated with the plastic zone, since D is computed from the damage parameter P_{SWT}, which is again associated with the area inside a stress-strain hysteresis – a measure for dissipation.

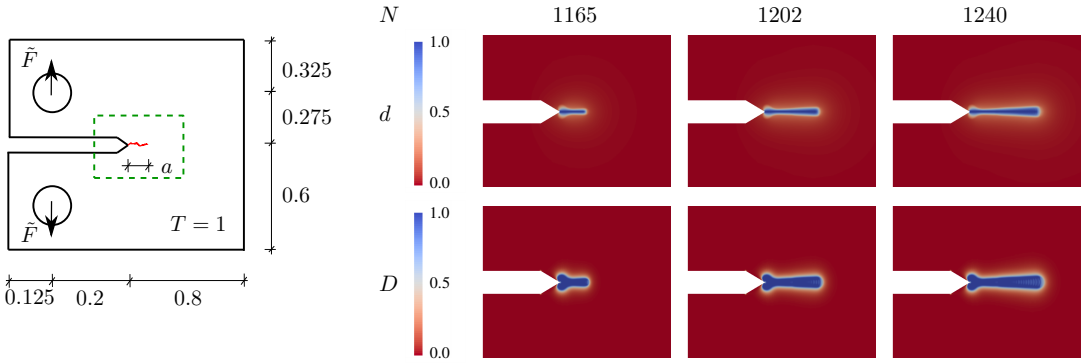

Figure 1. Compact tension test. All dimensions in mm. Development of phase-field variable d and lifetime variable D for load cycles N.

The resulting crack propagation curves for varying $\tilde{F}$ are displayed in Fig. 2, showing a crack initiation as well as a propagation stage. The Paris plot in Fig. 3a shows that the method can repoduce Paris behaviour: The Paris parameters C and m, fitted to the stable crack propagation stage, are independent of the load. Being material parameters, they are influenced by material properties instead, as Fig. 3b shows by varying the hardening modulus K' of the cyclic stress-strain curve.

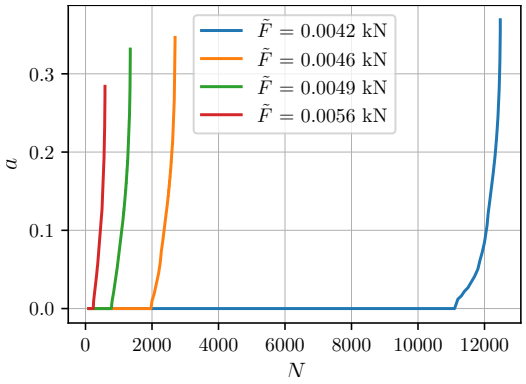

Figure 2. Cyclic crack propagation in CT specimen. N - cycle number, a - crack length, $\tilde{F}$ - force amplitude.

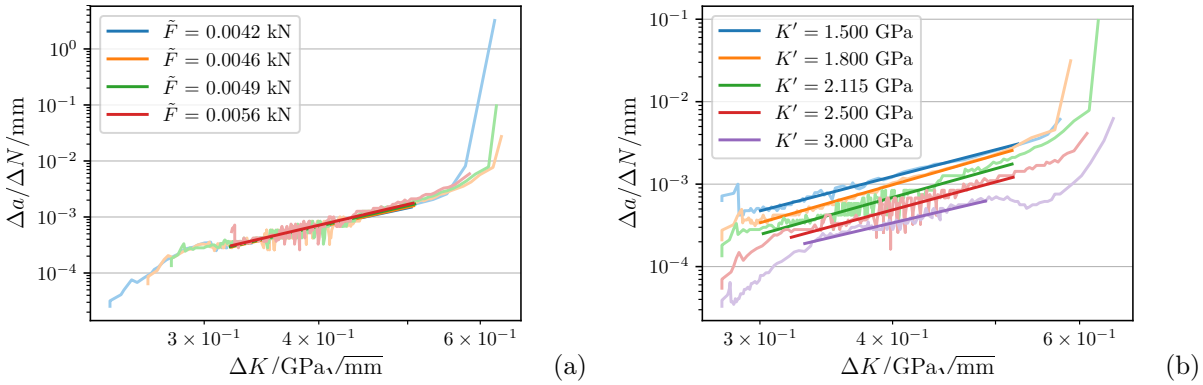

Figure 3. Paris plot of cyclic crack propagation in CT specimen. $\Delta a/\Delta N$ - crack propagation rate, ΔK - stress intensity factor range, $\tilde{F}$ - force amplitude, K' - material parameter of the cyclic stress-strain curve.

Acknowledgments

This work was supported by the German Research Foundation DFG within the Priority Programme 2013 *Targeted Use of Forming Induced Residual Stresses in Metal Components* grant number KA 3309/7-1.

References

[1] P. Carrara, M. Ambati, R. Alessi, and L. De Lorenzis. A novel framework to model the fatigue behavior of brittle materials based on a variational phase-field approach (2018). arXiv: 1811.02244.

[2] T. Linse, P. Hennig, M. Kästner, and R. de Borst. A convergence study of phase-field models for brittle fracture. *Engineering Fracture Mechanics* 184.Supplement C (2017), pp. 307 –318.

[3] C. Miehe, F. Welschinger, and M. Hofacker. Thermodynamically consistent phase-field models of fracture: Variational principles and multi-field FE implementations. *International Journal for Numerical Methods in Engineering* 83.10 (2010), pp. 1273–1311.

[4] H. Neuber. Theory of Stress Concentration for Shear-Strained Prismatical Bodies With Arbitrary Nonlinear Stress-Strain Law. *Journal of Applied Mechanics* 28.4 (1961), pp. 544 –550.

[5] P. Paris and F. Erdogan. A Critical Analysis of Crack Propagation Laws. *Journal of Basic Engineering* 85.4 (1963), p. 528.

[6] T Seeger. Grundlagen für Betriebsfestigkeitsnachweise. *Fundamentals for Service Fatigue-Strength Assessments),"Stahlbau Handbuch (Handbook of Structural Engineering), Stahlbau-Verlags-gesellschaft, Cologne* 1 (1996), pp. 5–123.

[7] K. N. Smith, T. Topper, and P. Watson. A stress-strain function for the fatigue of metals. *Journal of Materials* 5 (1970), pp. 767–778.

**Proceedings of the 8th GACM Colloquium on Computational Mechanics
for Young Scientists from Academia and Industry
August 28–30, 2019 in Kassel, Germany**

High-order cycle jump integration of a concrete fatigue damage model

Thomas Titscher * [1], Jörg F. Unger[1] and Javier Oliver[2]

[1]Federal Institute for Materials Research and Testing (BAM)

[2]International Center for Numerical Methods in Engineering (CIMNE), Technical Univ. of Catalonia (BarcelonaTech)

Abstract. Fatigue models that accurately resolve the complex three-dimensional failure mechanisms of concrete are numerically expensive. Especially the calibration of fatigue parameters to existing Wöhler lines requires solving for thousands or millions of cycles and a naive cycle-by-cycle integration is not feasible. The proposed adaptive cycle jump methods provide a remedy to this challenge. They greatly reduce the numerical effort of fatigue simulations and provide the basis for a development of those models.

1 Introduction

Optimizing and maximizing the structures performance under fatigue load has the potential of saving resources and energy. Especially for concrete, this requires precise models to handle the complexity of the material. A common approach for the lifetime estimation are Wöhler lines that relate an external cyclic load to the number of loading cycles a test specimen endures. An elastic simulation of the structure identifies the highest stresses and the corresponding lifetime estimation is read from the Wöhler lines. It is challenging to relate the test specimen results to a structural level, because they are influenced by numerous factors, e.g. loading frequency, environmental conditions, size effects, stress redistributions and multiphysics effects. This results in enormous experimental efforts to create Wöhler curves for all combinations of effects.

A more general approach that is commonly used in low cycle fatigue[3] is the cycle-by-cycle integration. A single load cycle is divided into several load steps and the structures equilibrium state is computed for each of those cycles. That approach does not rely on experimental Wöhler lines as an input to the material law, but has two main challenges that will be addressed in the following work. First, sophisticated fatigue models are needed that accumulate a failure defining variable in each cycle. Second, the high numerical effort has to be reduced. Compared to the Wöhler approach, however, this has additional benefits. It allows modeling of stress redistributions over the lifetime, it is independent of the load shape and it can lead to deeper understanding of the processes that lead to fatigue failure.

The changing state of a material is described by the change of its history variables κ. For cyclic loading, this change $\Delta\kappa$ is small in a single cycle. But over the lifetime of the material, it changes significantly and may lead to material failure. This scale separation gives rise to the vivid idea of cycle jump where the small change over one cycle is extrapolated.

This idea can be generalized to an explicit ordinary differential equation that relates the *global* change of the history variables over the lifetime with the *local* change over one cycle. It reads

$$\frac{\mathrm{d}\kappa}{\mathrm{d}N} = \Delta\kappa(\kappa, N), \tag{1}$$

where N denotes the cycle number. Its left-hand side can be approximated with suitable, well-known integration schemes and results in cycle jump methods. The evaluation of the right-hand side typically involves the solution of a finite element model that is capable of reproducing the material behavior. Both problems are now disconnected and can be evaluated and assessed separately.

*Corresponding author: thomas.titscher@bam.de ORCID iD: 0000-0001-9470-281X

2 Adaptive cycle jump methods

The first order Euler forward discretization of the left-hand side in Eq. (1) corresponds to the direct cycle jump method[1] and is illustrated in Fig. 1. Higher-order methods like the midpoint rule[6] or a fourth order Runge-Kutta method[2] provide more accurate approximations at the cost of more evaluations of the right-hand side.

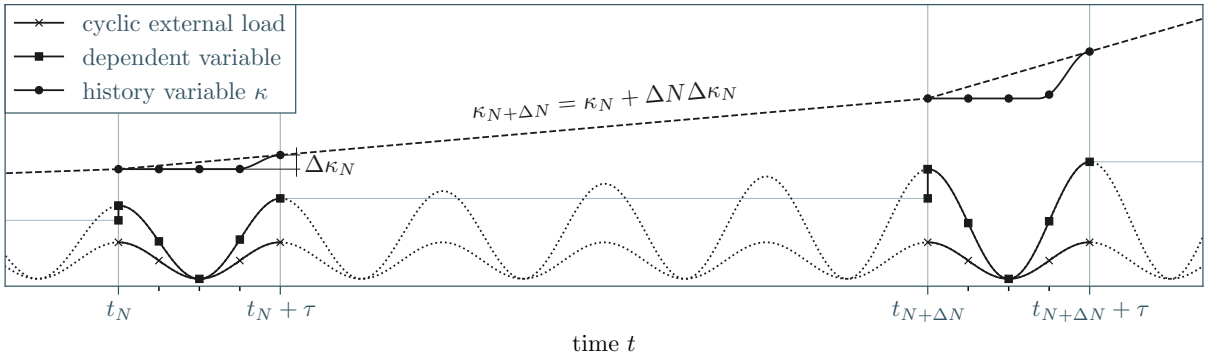

Figure 1. Direct cycle jump method based on an Euler forward approximation of the history variables.

In the first part of the lifetime, the structures state is dominated by static effects and changes rapidly. This requires small jump lengths or even a direct numerical simulation (DNS) of those cycles to minimize the error of the cycle jump approximation. In the next region of steady material degradation, the jump length can be increased. Material failure then happens rapidly and, again, requires small step sizes. So efficient implementations have to provide a measure to adapt the jump length.

For this purpose, the adaptive Runge-Kutta schemes Bogacki-Shampine(3(2)) and Dormand-Prince(5(4)) are explored. They provide an algorithm to adaptively determine the step size (jump length). In the case of Dormand-Prince(5(4)), both a fourth and a fifth order approximation is provided in each step. The difference of both approximations is compared to a prescribed tolerance δ to a) decide to accept or decline the fifth order step and b) determine the next jump length.

3 Fatigue extension of the implicit gradient-enhanced damage model

In this work, the material behavior is described by the implicit gradient-enhanced damage model by Peerlings et al.[5]. It consists of the momentum balance equation

$$\nabla \cdot \boldsymbol{\sigma} = \nabla \cdot [(1-\omega)\boldsymbol{C} : \boldsymbol{\varepsilon}] = \mathbf{0} \tag{2}$$

with the second order strain and stress tensors $\boldsymbol{\varepsilon}$ and $\boldsymbol{\sigma}$, respectively, the fourth order elasticity tensor $\boldsymbol{C}$ and the isotropic damage variable $\omega \in [0, 1)$. Damage is driven by the scalar strain-like history variable κ that only grows on the damage surface

$$g(\kappa) = \bar{\varepsilon} - \kappa = 0, \tag{3}$$

which is described by the Karush–Kuhn–Tucker conditions

$$\dot{\kappa} \geq 0, \quad g \leq 0, \quad g\dot{\kappa} = 0. \tag{4}$$

In Eq. (3), $\bar{\varepsilon}$ are the nonlocal strains that are related to a local strain norm ε_{eq} via the screened Poisson equation

$$\bar{\varepsilon} - l^2 \nabla^2 \bar{\varepsilon} = \varepsilon_{\text{eq}}(\boldsymbol{\varepsilon}). \tag{5}$$

It limits the curvature of the nonlocal strains $\bar{\varepsilon}$ depending on the length parameter l and, thus, regularizes the model.

Equation (4) for static material failure is extended to fatigue failure by allowing the growth of κ *below* the damage surface[4]

$$\dot{\kappa} = \begin{cases} \dot{\varepsilon}_{\text{eq}} & \text{if } g = 0 \\ \langle \dot{\bar{\varepsilon}} \rangle_+ f(\kappa, \bar{\varepsilon}) & \text{if } g < 0. \end{cases} \tag{6}$$

The Macaulay brackets denoted by $\langle \ \rangle_+$ correspond to the ramp function and prohibit a damage accumulation in unloading conditions and the fatigue function f controls the actual fatigue behavior.

4 Results

The model is exposed to cyclic loading to investigate the fatigue properties. Both displacement and force controlled simulations are performed in a one-dimensional uniaxial setting to evaluate the fatigue function f. Basic expected fatigue behavior like the lifetime decrease for increased loading amplitudes is recovered. A compact tension specimen under cyclic loading shows the stress redistribution over the specimen's lifetime. The material at the notch tip cannot withstand the initial stress concentration. Damage occurs and deflects the stresses to a slightly larger region. This process continues and widens the notch tip.

Both experiments are also integrated with the cycle jump methods, which drastically reduces the number of cycle evaluations (the main numerical effort) to about 1-2% of the direct simulation. The accuracy of this approximation varies both in terms of resolving a reference solution after a given number of cycles and in resolving the failure point. The first case can be efficiently solved with cycle jump methods and a fixed jump length. Here, second order method clearly outperform first order methods. The benefit of the forth order methods, however, is ambiguous. They require a longer jump length to reach comparable computational efficiency which can lead to significant deviations from the solution in the early fatigue life. The second case of resolving material failure practically requires adaptive cycle jump methods as the final number of cycles is unknown. Here, the accuracy of the commonly used Dormand-Prince(5(4)) method is similar to the numerically cheaper Bogacki-Shampine(3(2)) method.

The Bogacki-Shampine method is then used to simulate Wöhler lines of three-dimensional cylinder specimen under cyclic loading. Different combinations of fatigue parameters either shift the resulting Wöhler line or modify its slope and allow the calibration to experimental data.

References

[1] D Cojocaru and AM Karlsson. A simple numerical method of cycle jumps for cyclically loaded structures. *International Journal of fatigue* 28.12 (2006), pp. 1677–1689.

[2] VM Kindrachuk and JF Unger. A Fourier transformation-based temporal integration scheme for viscoplastic solids subjected to fatigue deterioration. *International Journal of Fatigue* 100 (2017), pp. 215–228.

[3] M Kuna and S Roth. General remarks on cyclic cohesive zone models. *International Journal of Fracture* 196.1-2 (2015), pp. 147–167.

[4] JJ Marigo. Modelling of brittle and fatigue damage for elastic material by growth of microvoids. *Engineering Fracture Mechanics* 21.4 (1985), pp. 861–874.

[5] RHJ Peerlings, R De Borst, WAM Brekelmans, and JHP De Vree. Gradient enhanced damage for quasi-brittle materials. *International Journal for Numerical Methods in Engineering* 39.19 (1996), pp. 3391–3403.

[6] RHJ Peerlings, WAM Brekelmans, R de Borst, and MGD Geers. Gradient-enhanced damage modelling of high-cycle fatigue. *International Journal for Numerical Methods in Engineering* 49.12 (2000), pp. 1547–1569.

**Proceedings of the 8th GACM Colloquium on Computational Mechanics
for Young Scientists from Academia and Industry
August 28–30, 2019 in Kassel, Germany**

Mixed finite element formulations and energy-momentum time integrators for thermo-mechanically coupled fiber-reinforced continua

Dietzsch, J.[1], Groß, M.[2] and Flessing, L.[3]

[1] Technische Universität Chemnitz, Professorship of applied mechanics and dynamics, Reichenhainer Straße 70, D-09126 Chemnitz, julian.dietzsch@mb.tu-chemnitz.de

[2] michael.gross@mb.tu-chemnitz.de

[3] tmd@mb.tu-chemnitz.de

Abstract. Fiber-reinforced materials in lightweight structures and their accurate dynamic simulation play an even increasingly significant role today. These materials are used for example in aircraft, automobiles and wind turbines. The low density and the high modulus of elasticity play a major role, but also the thermal properties should not be neglected. First of all, the thermal expansion of the matrix part and the ability to conduct the heat in a directional way with the fibers. For these materials, volumetric locking effects of an incompressible matrix material as well as locking effects due to stiff fibers can occur. On the one hand, there are combinations of well known mixed elements with an independent approximation of the volumetric dilation of the deformation gradient and an independent approximation of the right Cauchy green tensor for the anisotropic part of the strain energy function to reduce these effects. On the other hand, we have developed mixed elements where fields for the fourth and fifth invariants are added, as well as a version with the corresponding tensor fields. For long-term simulations it is necessary to use higher order time integrators to perform an accurate dynamic simulation. Galerkin-based time integrators offer a good option for this application. To eliminate a huge energy error these have to be extended to an energy-momentum time integration scheme. It is logical to combine these methods and thus combine the advantages of these methods. We formulate the mixed elements using Hu-Washizu functionals and combine this with the mixed principle of virtual power. By adding an thermo-mechanical coupling part in the strain energy and introducing the fourier heat conduction we obtain a thermo-mechanical formulation for the different mixed elements and a higher order Galerkin-based time integrator. Dirichlet boundary conditions in the form of Lagrange multiplier methods as well as Neumann boundary conditions in the mechanical and thermal context are also provided. In addition, we extend the continuum so that we can model different fiber families and the directional heat conduction of the fibers. As numerical examples serves cook's cantilever beam as well as a rotating heat pipe. We primarily analyze the spatial and time convergence, the conservation properties as well as the effect of the heat conduction of the fibers.

1 Introduction

As continuum model, we consider an anisotropic material with n_{F} fiber directions $\mathbf{a}_0^i$ moving in the Euclidean space $\mathbb{R}^{n_{\mathrm{dim}}}$ with the constant ambient temperature Θ_∞. The strain energy function of the material with a thermo-viscoelastic matrix and thermoelastic fibers is given by

$$\Psi(\boldsymbol{C}, \boldsymbol{C}_v, \Theta) = \Psi_{\mathrm{M}}(\boldsymbol{C}, \boldsymbol{C}_v, \Theta) + \sum_{i=1}^{n_{\mathrm{F}}} \Psi_{\mathrm{F}_i}(\boldsymbol{C}, \Theta, \boldsymbol{M}_i), \tag{1}$$

which is split into a single matrix part Ψ_{M} and multiple n_{F} fiber parts Ψ_{F_i}. Here, $\boldsymbol{M}_i = \boldsymbol{a}_0^i \otimes \boldsymbol{a}_0^i$ define the structural tensor, $\boldsymbol{C} = \boldsymbol{F}^T\boldsymbol{F}$ define the right Cauchy-Green tensor, $\boldsymbol{C}_v$ define the viscous right Cauchy-Green tensor and Θ define the absolute temperature. With the volumen dilatation $J = \det[\boldsymbol{F}] = \sqrt{\det[\boldsymbol{C}]}$, we assume the specific dependencies:

$$\Psi_{\mathrm{M}}(\boldsymbol{C}, \boldsymbol{C}_v, \Theta) = \Psi_{\mathrm{M}}^{\mathrm{iso}}(\boldsymbol{C}, \mathrm{cof}[\boldsymbol{C}], J) + \Psi_{\mathrm{M}}^{\mathrm{vol}}(J) + \Psi_{\mathrm{M}}^{\mathrm{cap}}(\Theta) + \Psi_{\mathrm{M}}^{\mathrm{coup}}(\Theta, J) + \Psi_{\mathrm{M}}^{\mathrm{vis}}(\boldsymbol{\Lambda}) \tag{2}$$

$$\Psi_{\mathrm{F}_i}(\boldsymbol{C}, \Theta, \boldsymbol{M}_i) = \Psi_{\mathrm{F}_i}^{\mathrm{ela}}(\boldsymbol{C}, \mathrm{cof}[\boldsymbol{C}], J, \boldsymbol{M}_i) + \Psi_{\mathrm{F}_i}^{\mathrm{cap}}(\Theta) + \Psi_{\mathrm{F}_i}^{\mathrm{coup}}(\Theta, \boldsymbol{C}, \boldsymbol{M}_i) \tag{3}$$

The elastic part of the matrix function Ψ_{M} is split into an isochoric part Ψ_{M}^{iso} and a volumetric part

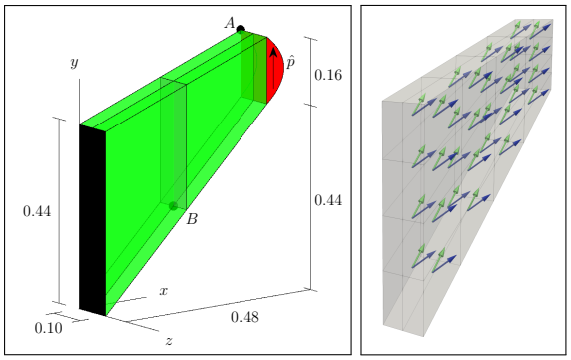

$\epsilon_1 = 0.1e6$	$V_{\text{dev}} = 0.1e4$	$k_{\text{F}_1} = 0.1$
$\epsilon_2 = 0.1e6$	$V_{\text{vol}} = 0.2e4$	$\beta_{F_1} = 1e-10$
$\epsilon_3 = 1.8e6$	$\epsilon_6 = 10e6$	$c^0_{\text{F}_1} = 1500$
$\epsilon_4 = 100e6$	$\epsilon_7 = 4$	$c^1_{\text{F}_1} = 0.003$
$\epsilon_5 = 4$	$\epsilon_8 = 4$	$k_{\text{F}_2} = 50$
$\epsilon^{\text{vis}}_1 = 0.1e5$	$\epsilon_9 = 1$	$\beta_{\text{F}_2} = 1e-10$
$\epsilon^{\text{vis}}_2 = 0.1e5$	$\epsilon_{10} = 0.1e6$	$c^0_{\text{F}_2} = 3000$
$\epsilon^{\text{vis}}_3 = 1.8e5$	$k_{\text{M}} = 0.1$	$c^1_{\text{F}_2} = 0.006$
$\epsilon^{\text{vis}}_4 = 100e5$	$\beta_{\text{M}} = 1e-10$	$\Theta_\infty = 300$
$\epsilon^{\text{vis}}_5 = 4$	$c^0_{\text{M}} = 1500$	$\hat{p} = 1.5e6$
$\rho_0 = 1000$	$c^1_{\text{M}} = 0.003$	
$h_n = 0.005$	$T = 1.5$	$TOL = 1e-4$

Figure 1. Geometry, configuration, simulation parameters and fiber directions $(\mathbf{a}^1_0)^T = [1\ 1\ 1]$ (blue) and $(\mathbf{a}^2_0)^T = [1\ 1\ 0]$ (green) of cooks cantilever beam.

Ψ^{vol}_{M}. We subdivided the thermo-elastic free energy of the matrix into a heat capacity part Ψ^{cap}_{M} and the part of the thermo-mechanical coupling effect, which takes the form

$$\Psi^{\text{coup}}_{\text{M}}(\Theta, J) = -2n_{\text{dim}}\beta_{\text{M}}(\Theta - \Theta_\infty)J\frac{\partial\Psi^{\text{vol}}_{\text{M}}(J)}{\partial J}, \tag{4}$$

where β_{M} ist the coefficient of linear thermal expansion for the matrix. The function $\Psi^{\text{vis}}_{\text{M}}$ is the viscoelastic free energy function of the matrix material, with $\boldsymbol{\Lambda} = \boldsymbol{C}\boldsymbol{C}_v^{-1}$. The thermal part of the fiber free energy is separated in the same manner. We consider a heat capacity function $\Psi^{cap}_{\text{F}_i}$ and the function of the thermo-mechanical coupling

$$\Psi^{\text{coup}}_{\text{F}_i}(\Theta, \boldsymbol{C}, \boldsymbol{M}_i) = -2\beta_{\text{F}_i}(\Theta - \Theta_\infty)\sqrt{I^i_4}\frac{\partial\Psi^{\text{ela}}_{\text{F}_i}(I^i_4, \dots)}{\partial I^i_4}, \tag{5}$$

with the coefficients of linear thermal expansion β_{F_i} and the fourth invariant $I^i_4(\boldsymbol{C}, \boldsymbol{M}_i) = \text{tr}[\boldsymbol{C}\boldsymbol{M}_i]$.

As shown in Reference [1], using the CoCoA element prevents looking in an efficient manner. This finite element formulation is based on a Hu-Washizu functional. The complete functional of the internal energy is given by

$$\begin{aligned}\Pi^{\text{int}} = &\int_{\mathcal{B}_0}\Psi\text{d}V + \int_{\mathcal{B}_0}\eta\ (\Theta - \tilde{\Theta})\text{d}V + \int_{\mathcal{B}_0}\boldsymbol{B} : (\text{cof}[\boldsymbol{C}(\boldsymbol{q})] - \boldsymbol{H})\text{d}V + \int_{\mathcal{B}_0}\tilde{p}\ (J(\boldsymbol{q}) - \tilde{J})\text{d}V \\ &+ \int_{\mathcal{B}_0}\frac{1}{2}\boldsymbol{S}_A : (\boldsymbol{C}(\boldsymbol{q}) - \boldsymbol{C}_A)\text{d}V + \int_{\mathcal{B}_0}\boldsymbol{B}_A : (\text{cof}[\boldsymbol{C}(\boldsymbol{q})] - \boldsymbol{H}_A)\text{d}V + \int_{\mathcal{B}_0}\tilde{p}_A(J(\boldsymbol{q}) - \tilde{J}_A)\text{d}V\end{aligned} \tag{6}$$

With independent variables for the assumed temperature field $\tilde{\Theta}$, for the volumetric dilatation $\tilde{J}$ (see Reference [5]), $\boldsymbol{H}$ for the cofactor of $\boldsymbol{C}$ (see Reference [3]) , for the anisotropic parts Ψ_{F_i} of the material formulation $\boldsymbol{C}_A$(see Reference [4]) and $\boldsymbol{H}_A$ and $\tilde{J}_A$ (see Reference [1]). Notable Lagrange multipliers are $\tilde{p}$ wich plays the role of the hydrostatic pressure, $\boldsymbol{S}_A$ as anisotropic part of the stress tensor and the entropy density field η. Thus the dependencies in the strain energy function change as follows:

$$\Psi_{\text{M}} = \Psi^{\text{iso}}_{\text{M}}(\boldsymbol{C}, \boldsymbol{H}, \tilde{J}) + \Psi^{\text{vol}}_{\text{M}}(\tilde{J}) + \Psi^{\text{cap}}_{\text{M}}(\Theta) + \Psi^{\text{coup}}_{\text{M}}(\Theta, \tilde{J}) + \Psi^{\text{vis}}_{\text{M}}(\boldsymbol{\Lambda}) \tag{7}$$

$$\Psi_{\text{F}_i} = \Psi^{\text{ela}}_{\text{F}_i}(\boldsymbol{C}_A, \boldsymbol{H}_A, \tilde{J}_A, \boldsymbol{M}_i) + \Psi^{\text{cap}}_{\text{F}_i}(\Theta) + \Psi^{\text{coup}}_{\text{F}_i}(\Theta, \boldsymbol{C}_A, \boldsymbol{M}_i) \tag{8}$$

In order to obtain the weak form, we use the mixed principle of virtual power, as shown in Reference [2]. The basis is the total energy balance

$$\dot{T}(\dot{\boldsymbol{q}}, \dot{\boldsymbol{v}}, \dot{\boldsymbol{p}}) + \dot{\Pi}^{\text{ext}}(\dot{\boldsymbol{q}}, \boldsymbol{\lambda}, \dot{\boldsymbol{C}}_v, \tilde{\Theta}) + \dot{\Pi}^{\text{int}}(\dot{\boldsymbol{q}}, \dot{\boldsymbol{C}}_v, \dot{\Theta}, \dot{\eta}, \tilde{\Theta}, \tilde{p}, \dot{\tilde{J}}, \boldsymbol{B}, \dot{\boldsymbol{H}}, \boldsymbol{S}_A, \dot{\boldsymbol{C}}_A, \boldsymbol{B}_A, \dot{\boldsymbol{H}}_A, \tilde{p}_A, \dot{J}_A) = 0 \tag{9}$$

where the time derivative of the kinetic energy

$$\dot{T}(\dot{\boldsymbol{q}}, \dot{\boldsymbol{v}}, \dot{\boldsymbol{p}}) = \int_{\mathcal{B}_0}(\rho_0\boldsymbol{v} - \boldsymbol{p}) \cdot \dot{\boldsymbol{v}}\text{d}V + \int_{\mathcal{B}_0}\dot{\boldsymbol{p}} \cdot (\dot{\boldsymbol{q}} - \boldsymbol{v})\text{d}V + \int_{\mathcal{B}_0}\boldsymbol{p} \cdot \ddot{\boldsymbol{q}}\text{d}V \tag{10}$$

is defined by the velocity $\boldsymbol{v}$, the linear momentum $\boldsymbol{p}$ and the mass density ρ_0. As external power functional, we assume

$$\dot{\Pi}^{\text{ext}}(\dot{\boldsymbol{q}}, \boldsymbol{\lambda}, \dot{\boldsymbol{C}}_v, \tilde{\Theta}) = -\int_{\partial\mathcal{B}_0} \boldsymbol{t}\cdot\dot{\boldsymbol{q}}\mathrm{d}A - \int_{\partial\mathcal{B}_0} \boldsymbol{\lambda}\cdot(\dot{\boldsymbol{q}} - \dot{\boldsymbol{q}}^{\text{ref}})\mathrm{d}A + \int_{\mathcal{B}_0} \nabla\left(\frac{\tilde{\Theta}}{\Theta}\right)\cdot\boldsymbol{Q}\mathrm{d}V$$
$$+ \int_{\mathcal{B}_0} \frac{\tilde{\Theta}}{\Theta} D^{\text{int}}\mathrm{d}V + \int_{\mathcal{B}_0} \dot{\boldsymbol{C}}_v : \mathbb{V}(\boldsymbol{C}_v) : \dot{\boldsymbol{C}}_v\mathrm{d}V \qquad \boldsymbol{Q} = -\left[\sum_{i=1}^{n_{\text{F}}} J\frac{k_{\text{F}_i} - k_{\text{M}}}{\boldsymbol{C} : \boldsymbol{M}_i}\boldsymbol{M}_i + kJ\boldsymbol{C}^{-1}\right]\nabla\Theta \quad (11)$$

Here, $\boldsymbol{Q}$ denotes the Piola heat flux vector derived from Duhamel's law (see Reference [2]). Where k_{M} and k_{F_i} denotes the material conductivity coefficients for matrix and fibers. The field $\dot{\boldsymbol{q}}^{\text{ref}}$ denotes the time evolution of the Dirichlet boundary displacement vector with the corresponding Lagrange multiplier $\boldsymbol{\lambda}$. And $\boldsymbol{t}$ denotes the traction load for the Neumann boundary condition. The non-negative internal viscous dissipation D^{int} and positive-definite viscosity tensor $\mathbb{V}$ ist given by

$$D^{\text{int}} = \dot{\boldsymbol{C}}_v : \mathbb{V}(\boldsymbol{C}_v) : \dot{\boldsymbol{C}}_v \qquad \mathbb{V}(\boldsymbol{C}_v) = \frac{1}{4}\left(V_{\text{vol}} - \frac{V_{\text{dev}}}{n_{\text{dim}}}\right)\boldsymbol{C}_v^{-1}\otimes\boldsymbol{C}_v^{-1} + \frac{V_{\text{dev}}}{4}\mathbb{I}_{\text{s}} : \boldsymbol{C}_v^{-1}\otimes\boldsymbol{C}_v^{-1}, \quad (12)$$

with the fourth-order symmetric projection tensor $\mathbb{I}_{\text{s}}$ and the material paramenters V_{dev} and V_{vol} which represent the volumetric and deviatoric viscosity constants, respectively. By variation with respect to the variables in the argument from Eqn. (9) (as shown in Reference [2]) we obtain the weak forms. Thereby all quantities are approximated with Lagrangian shape functions in space (see Reference [2]) and time (see Reference [2]). Each integral that exist are solved with the corresponding Gaussian quadrature rule. The internal variable $\boldsymbol{C}_v$ is determined on the element using the Newton-Raphson method, but not at each spatial quadrature point by using spatial finite element shape functions. After eliminating $\boldsymbol{p}$ and η, we condense out the resulting formulation at the element level to a displacement and temperature formulation (see Reference [3]). Therefore, all mixed fields except $\boldsymbol{q}$ and Θ are discontinuous at the boundaries of spatial elements.

2 Numerical Example

As numerical example serves the well-known Cook's cantilever beam with a quadratic distribution of an in-plane load on the Neumann boundary. Two different fibers are used for this example. On the one side a fiber (F_1,$(\mathbf{a}_0^1)^T = [1\ 1\ 1]$) for mechanical reinforcement of the matrix, but with an equally low thermal conductivity. On the other side, a fiber (F_2,$(\mathbf{a}_0^2)^T = [1\ 1\ 0]$) with a very high thermal conductivity, but a low stiffness. The energy functions are given by

$$\Psi_{\text{M}}^{\text{iso}} = \frac{\epsilon_1}{2}(\text{tr}[\boldsymbol{C}])^2 + \frac{\epsilon_2}{2}(\text{tr}[\text{cof}[\boldsymbol{C}]])^2 - \epsilon_3\ln(J) \quad \Psi_{\text{M}}^{\text{vol}} = \frac{\epsilon_4}{2}(J^{\epsilon_5} + J^{-\epsilon_5} - 2)$$
$$\Psi_{\text{M}}^{\text{vis}} = \frac{\epsilon_1^{\text{vis}}}{2}(\text{tr}[\boldsymbol{C}])^2 + \frac{\epsilon_2^{\text{vis}}}{2}(\text{tr}[\text{cof}[\boldsymbol{C}]])^2 - \epsilon_3^{\text{vis}}\ln(J) + \frac{\epsilon_4^{\text{vis}}}{2}(J^{\epsilon_5^{\text{vis}}} + J^{-\epsilon_5^{\text{vis}}} - 2)$$
$$\Psi_{\text{F}_1}^{\text{ela}} = \epsilon_6\left(\frac{1}{\epsilon_7+1}(\text{tr}[\boldsymbol{C}\boldsymbol{M}_1])^{\epsilon_7+1} + \frac{1}{\epsilon_8+1}(\text{tr}[\text{cof}[\boldsymbol{C}]\boldsymbol{M}_1])^{\epsilon_8+1} + \frac{1}{\epsilon_9}\det[\boldsymbol{C}]^{-\epsilon_9}\right)$$
$$\Psi_{\text{F}_2}^{\text{ela}} = \frac{\epsilon_{10}}{2}(\text{tr}[\boldsymbol{C}\boldsymbol{M}_2] - 1)^2 \quad \Psi_X^{cap} = c_X^0(1 - \Theta_\infty c_X^1)(\Theta - \Theta_\infty - \Theta\ln\frac{\Theta}{\Theta_\infty}) - \frac{1}{2}c_X^0 c_X^1(\Theta - \Theta_\infty)^2$$

and the prescribed simulation parameters, geometry, configuration and fiber directions are shown in Fig. 1. We use the CoCoA210000 element, with an quadratic approximation of $\boldsymbol{q}$ and a linear approximation of $\boldsymbol{H}$. All other quantities are approximated constant. This selection is based on the results of Reference [1], where this element showed an excellent convergence rate. In the first step we only use F_1. The result can be found in part 1 and 2 of Fig. 2. First we see the asymmetric bending caused by the fiber as well as the typical stress curve (tensile and compressive stress, neutral fiber). Together with the small number of elements, the excellent convergence rate of the mixed elements is once again clearly shown. Regarding the temperature distribution we can see that in some areas, as a result of the dissipation of the viscous part, the temperature increases. If we now add the second fiber, these temperature increases are distributed according to the fiber direction.

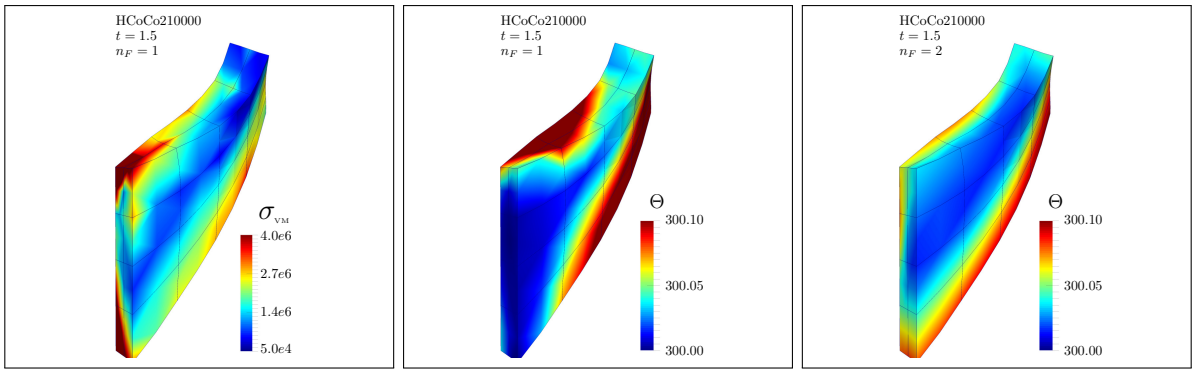

Figure 2. Deformed configuration $\mathcal{B}_t$ and v. Mises equivalent stress σ_{VM} and the absolute temperature θ for the parameters shown in Fig 1 and fibers F_1 and F_2 for $t = 1.2$. Cook's cantilever beam with $n_{el} = 32$ spatial finite elements.

3 Conclusions

We were able to show that the extension to an thermo-viscoelastic material formulation, do not affect the excellent convergence rates of the mixed elements. This saves computational time, which is especially advantageous with regard to the local iteration of the viscous internal variable. In the next step, we extend the fiber part by a viscous component and we extend this formulation to an energy conserving time integrator.

Acknowledgments

The authors thank the 'Deutsche Forschungsgesellschaft (DFG)' for financial support of this work under the grant GR 3297/4-1 and Matthias Bartelt (GR 3297/2-2) for providing the program code and help with its implementation.

References

[1] Julian Dietzsch, Michael Groß, and Lars Flessing. THERMO-MECHANICAL COUPLING IN FIBER-REINFORCED CONTINUA: MIXED FINITE ELEMENT FORMULATIONS AND ENERGY-MOMENTUM TIME INTEGRATION. In: *VIII International Conference on Computational Methods for Coupled Problems in Science and Engineering*. Sitges (Barcelona), Spain, June 2019.

[2] Michael Groß, Julian Dietzsch, and Matthias Bartelt. Variational-based higher-order accurate energy–momentum schemes for thermo-viscoelastic fiber-reinforced continua. *Computer Methods in Applied Mechanics and Engineering* 336 (2018), pp. 353 –418. ISSN: 0045-7825. DOI: https://doi.org/10.1016/j.cma.2018.03.019. URL: http://www.sciencedirect.com/science/article/pii/S0045782518301440.

[3] Jörg Schröder, Peter Wriggers, and Daniel Balzani. A new mixed finite element based on different approximations of the minors of deformation tensors. *Computer Methods in Applied Mechanics and Engineering* 200.49 (2011), pp. 3583 –3600. ISSN: 0045-7825. DOI: https://doi.org/10.1016/j.cma.2011.08.009. URL: http://www.sciencedirect.com/science/article/pii/S0045782511002647.

[4] Jörg Schröder, Nils Viebahn, Daniel Balzani, and Peter Wriggers. A novel mixed finite element for finite anisotropic elasticity; the SKA-element Simplified Kinematics for Anisotropy. *Computer Methods in Applied Mechanics and Engineering* 310 (2016), pp. 475 –494. ISSN: 0045-7825. DOI: https://doi.org/10.1016/j.cma.2016.06.029. URL: http://www.sciencedirect.com/science/article/pii/S0045782516306478.

[5] J.C. Simo, R.L. Taylor, and K.S. Pister. Variational and projection methods for the volume constraint in finite deformation elasto-plasticity. *Computer Methods in Applied Mechanics and Engineering* 51.1 (1985), pp. 177 –208. ISSN: 0045-7825. DOI: https://doi.org/10.1016/0045-7825(85)90033-7. URL: http://www.sciencedirect.com/science/article/pii/0045782585900337.

**Proceedings of the 8th GACM Colloquium on Computational Mechanics
for Young Scientists from Academia and Industry
August 28–30, 2019 in Kassel, Germany**

Application of diagonally implicit Runge Kutta methods to structural dynamics problems

Matthias Grafenhorst*[1] and Stefan Hartmann[1]

[1]Institute of Applied Mechanics, Clausthal University of Technology, Clausthal-Zellerfeld, Germany

Abstract. The most important class of one-step procedures for the numerical integration of nonlinear stiff ordinary differential equations and differential-algebraic equations are implicit Runge-Kutta methods which are characterized by pronounced stability and accuracy properties. The focus of this contribution is on the application of diagonally implicit Runge-Kutta (DIRK) methods. In the case of quasi-static problems, it was shown in [4, 9] that DIRK-methods are highly accurate and stable. In this presentation, DIRK-methods are applied to structural dynamics problems within the context of the method of vertical lines. As already mentioned in first investigations of linear structural dynamics, see [8], some stiffly accurate DIRK-methods have better accuracy and stability properties as the HHT-α method, see [6]. However, these methods do not achieve the same accuracy as in the case of quasi-static problems. In dynamics, order reduction phenomena can be observed when applying DIRK-methods, which will be demonstrated by simple one-dimensional examples.

Introduction

In this contribution, we show the applicability of diagonally implicit Runge-Kutta schemes (DIRK) for the time discretization of structural dynamic problems.

1 Space and time discretization

The balance of linear momentum and constitutive models of evolutionary-type lead to an initial boundary-value problem. The problem is solved by consistent application of the method of vertical lines. In the first step, the space discretization using standard finite elements is carried out yielding either an ODE-system of second order for the discretized equation of motion or a system of differential-algebraic equations (DAE-system) if constraints are also considered. In the case of inelastic materials, a further part in form of an ODE-system of first order results from the evolution equations of the internal variables which have to be evaluated at all spatial integration points. In the subsequent step, the time discretization is carried out. Here, higher-order accurate DIRK-methods are the method of choice. For the application of the DIRK-approach on the semi-discretized ODE-system of second order, it must first be transformed into an ODE-system of first order by exploiting the trivial relationship $\dot{\boldsymbol{u}}(t) = \boldsymbol{v}(t) \in \mathbb{R}^{n_{\mathrm{uu}}}$. The semi-discretized ODE-system of first order $\boldsymbol{F}(t, \boldsymbol{y}(t), \dot{\boldsymbol{y}}(t)) \in \mathbb{R}^m$ of the dimension $m = 2n_{\mathrm{uu}} + n_{\mathrm{Q}}$ is defined by

$$\boldsymbol{F}(t, \boldsymbol{y}(t), \dot{\boldsymbol{y}}(t)) = \begin{Bmatrix} \boldsymbol{M}\dot{\boldsymbol{v}}(t) + \boldsymbol{g}_{\mathrm{u}}(\boldsymbol{u}, \boldsymbol{q}, t) + \overline{\boldsymbol{M}}\,\ddot{\overline{\boldsymbol{u}}}(t) \\ \dot{\boldsymbol{u}}(t) - \boldsymbol{v}(t) \\ \dot{\boldsymbol{q}}(t) - \boldsymbol{r}_{\mathrm{Q}}(\boldsymbol{u}, \boldsymbol{q}, t) \end{Bmatrix} = \boldsymbol{0}, \quad \boldsymbol{y}(t) = \begin{Bmatrix} \boldsymbol{v}(t) \\ \boldsymbol{u}(t) \\ \boldsymbol{q}(t) \end{Bmatrix} \in \mathbb{R}^m, \quad \boldsymbol{y}(t_0) = \begin{Bmatrix} \boldsymbol{v}_0 \\ \boldsymbol{u}_0 \\ \boldsymbol{q}_0 \end{Bmatrix}, \quad (1)$$

with the unknown nodal displacements $\boldsymbol{u}(t) \in \mathbb{R}^{n_{\mathrm{uu}}}$, the unknown nodal velocities $\boldsymbol{v}(t) \in \mathbb{R}^{n_{\mathrm{uu}}}$, the known nodal displacements $\overline{\boldsymbol{u}}(t) \in \mathbb{R}^{n_{\mathrm{up}}}$, which are prescribed by appropriate Dirichlet boundary conditions, and the internal variables $\boldsymbol{q}(t) \in \mathbb{R}^{n_{\mathrm{Q}}}$, which describe the history dependence of the material behavior. Applying the DIRK-approach, see [2, 3], to the ODE-system (1) yields in each stage a system of non-linear equations

$$\begin{Bmatrix} \boldsymbol{G}_{\mathrm{u}}(\boldsymbol{U}_{ni}, \boldsymbol{Q}_{ni}) \\ \boldsymbol{L}(\boldsymbol{U}_{ni}, \boldsymbol{Q}_{ni}) \end{Bmatrix} = \begin{Bmatrix} \boldsymbol{M}\,\dfrac{\boldsymbol{U}_{ni} - \hat{\boldsymbol{U}}^{\mathrm{S}}_{ni}}{\Delta t_n^2 \bar{a}_{ii}} + \boldsymbol{g}_{\mathrm{u}}(\boldsymbol{U}_{ni}, \boldsymbol{Q}_{ni}, T_{ni}) + \overline{\boldsymbol{M}}\ddot{\overline{\boldsymbol{u}}}(T_{ni}) \\ \dfrac{\boldsymbol{Q}_{ni} - \boldsymbol{Q}^{\mathrm{S}}_{ni}}{\Delta t_n a_{ii}} - \boldsymbol{r}_{\mathrm{Q}}(\boldsymbol{U}_{ni}, \boldsymbol{Q}_{ni}, T_{ni}) \end{Bmatrix} = \boldsymbol{0} \quad \in \mathbb{R}^{n_{\mathrm{uu}}+n_{\mathrm{Q}}}. \quad (2)$$

*Corresponding author: matthias.grafenhorst@tu-clausthal.de

The stage i, $i = 1, \ldots, s$, is evaluated at the stage time $T_{ni} = t_n + c_i \Delta t_n$. The system of non-linear equations (2) depends on the stage values $\boldsymbol{U}_{ni} \in \mathbb{R}^{n_{\mathrm{uu}}}$, $\boldsymbol{Q}_{ni} \in \mathbb{R}^{n_{\mathrm{Q}}}$, the time step-size Δt_n, the algorithmic parameters a_{ij}, $\bar{a}_{ij} = \sum_{k=1}^{s} a_{ik} a_{kj}$ and c_i of the implicit s-stage Runge-Kutta method. The starting vectors $\hat{\boldsymbol{U}}_{ni}^{\mathrm{S}} = \boldsymbol{u}_n + c_i \Delta t_n \boldsymbol{v}_n + \Delta t_n^2 \sum_{j=1}^{i-1} \bar{a}_{ij} \boldsymbol{A}_{nj}$ and $\boldsymbol{Q}_{ni}^{\mathrm{S}} = \boldsymbol{q}_n + \Delta t_n \sum_{j=1}^{i-1} a_{ij} \dot{\boldsymbol{Q}}_{nj}$ depend on the known quantities $\boldsymbol{u}_n \in \mathbb{R}^{n_{\mathrm{uu}}}$, $\boldsymbol{v}_n \in \mathbb{R}^{n_{\mathrm{uu}}}$ and $\boldsymbol{q}_n \in \mathbb{R}^{n_{\mathrm{Q}}}$ at time t_n and the known stage derivatives $\boldsymbol{A}_{ni} = (\boldsymbol{U}_{ni} - \hat{\boldsymbol{U}}_{ni}^{\mathrm{S}})/(\Delta t_n^2 \bar{a}_{ii})$, $\dot{\boldsymbol{Q}}_{ni} = (\boldsymbol{Q}_{ni} - \boldsymbol{Q}_{ni}^{\mathrm{S}})/(\Delta t_n a_{ii})$ of the previous stages. After solving (2) for each stage i, $i = 1, \ldots, s$, the approximations at time t_{n+1} are computed by

$$\boldsymbol{u}_{n+1} = \boldsymbol{u}_n + \Delta t_n \boldsymbol{v}_n + \Delta t_n^2 \sum_{i=1}^{s} \bar{b}_i \boldsymbol{A}_{ni}, \quad \boldsymbol{v}_{n+1} = \boldsymbol{v}_n + \Delta t_n \sum_{i=1}^{s} b_i \boldsymbol{A}_{ni}, \quad \boldsymbol{q}_{n+1} = \boldsymbol{q}_n + \Delta t_n \sum_{i=1}^{s} b_i \dot{\boldsymbol{Q}}_{ni}, \quad (3)$$

with weighting factors b_i, $\bar{b}_i = \sum_{j=1}^{s} b_j a_{ji}$. Owing to the fact that stiffly accurate, diagonally implicit Runge–Kutta methods of higher-order are used, where the conditions $a_{sj} = b_j$ as well $\bar{a}_{sj} = \bar{b}_j$ are implied, the last calculation step (3) can be omitted. In particular, the stiff accuracy property ensures $\boldsymbol{u}_{n+1} = \boldsymbol{U}_{ns}$, $\boldsymbol{v}_{n+1} = \boldsymbol{V}_{ns}$, $\boldsymbol{q}_{n+1} = \boldsymbol{Q}_{ns}$.

2 Numerical results

In this section, we analyze the continuum oscillations in a one-dimensional elastic rod, see Fig. 1a, and in a one-dimensional non-linear viscoelastic rod, see Fig. 1b. For both geometrically linear problems, the

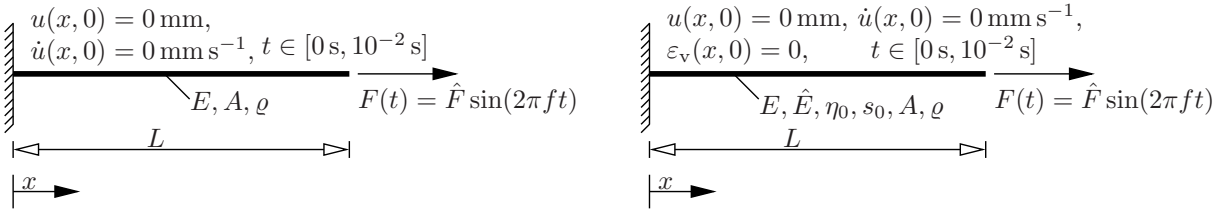

(a) Linear elastic rod **(b)** Non-linear viscoelastic rod

Figure 1. One-dimensional simulation model: fixed boundary condition ($u(0,t) = 0\,\mathrm{mm}$) on the left and an applied external force $F(t)$ on the right

load is applied at the free end as a sinusoidal force $F(t) = \hat{F}\sin(2\pi f t)$, with the amplitude $\hat{F} = 10^5\,\mathrm{N}$ and the excitation frequency $f = 10^2\,\mathrm{Hz}$. The left end of the rod is clamped. The treatment of the first initial boundary value problem, see Fig. 1a, which is subjected to the specific initial conditions $u(x,0) = 0\,\mathrm{mm}$ and $\dot{u}(x,0) = 0\,\mathrm{mm\,s^{-1}}$ and the boundary conditions $u(0,t) = 0\,\mathrm{mm}$ and $\partial u(L,t)/\partial x = \hat{\varepsilon}\sin(\Omega t)$, $\hat{\varepsilon} = \hat{F}/(EA)$, requires the solution of the wave equation $\partial^2 u(x,t)/\partial t^2 = c^2 \partial^2 u(x,t)/\partial x^2$, with the longitudinal wave speed $c = \sqrt{E/\varrho}$. For a specific computation, we have chosen a parameter set of $E = 2.1 \times 10^5\,\mathrm{N\,mm^{-2}}$, $A = 2 \times 10^3\,\mathrm{mm^2}$, $L = 10^3\,\mathrm{mm}$, $\varrho = 8 \times 10^{-9}\,\mathrm{t\,mm^{-3}}$, where E denotes the Young's modulus, A the cross-sectional area, L the rod length and ϱ the mass density. For the illustrated linear elastodynamic problem, the integration methods detailed in Table 1 are analyzed in view of their

Table 1. Applied stiffly accurate DIRK-methods

abbreviation	**method**	**order** p	**stages** s
BE	Backward-Euler	1	1
Alex2/Ell	Alexander/Ellsiepen	2	2
CAA	trapezoidal rule or CAA	2	2
Alex3/Cash	Alexander/Cash	3	3

expected and achieved temporal convergence order for the longitudinal displacement field $u(x,t)$ and the longitudinal velocity field $v(x,t) = \dot{u}(x,t)$, see Fig. 2. The basis for the calculation of the global error measures $\mathbf{err}_{\boldsymbol{u}}$ and $\mathbf{err}_{\boldsymbol{v}}$ is formed by the analytical reference solution

$$u(x,t) = \frac{2\hat{\varepsilon}}{L}\left(\sum_{n=1}^{\infty} \frac{(-1)^n}{k_n^2}\left(\frac{\omega_n \Omega}{\omega_n^2 - \Omega^2}\sin(\omega_n t) - \frac{\Omega^2}{\omega_n^2 - \Omega^2}\sin(\Omega t)\right)\sin(k_n x)\right) + x\hat{\varepsilon}\sin(\Omega t), \quad (4)$$

with $k_n = \pi/(2L)(2n-1)$, $\omega_n = c\,k_n$ and $\Omega = 2\pi f$. The approach adopted here for setting up these reference solution is based on the strategies outlined in [7] and uses the concept of separation of variables for solving the hyperbolic partial differential equation. The temporal convergence behavior of the

DIRK-methods is compared with another time integration class, namely the generalized-α methods (abbreviation: Gen-α, order: $p = 2$) with the algorithmic parameterization defined in terms of the desired amount of high-frequency dissipation and expressed by means of the spectral radius $\rho_\infty = 0.8$, and is depicted in Fig. 2. For more details to the Generalized-α method, we refer to [3] and the literature cited therein. The space discretization of the rod using standard finite elements is carried out with $n^{\mathrm{e}} = 10^4$ three-node line Q2-elements (quadratic line elements). For modeling the inertia properties of the rod, we use a consistent mass matrix. In Fig. 2a, we report comparable to problems in plasticity, see [1], an

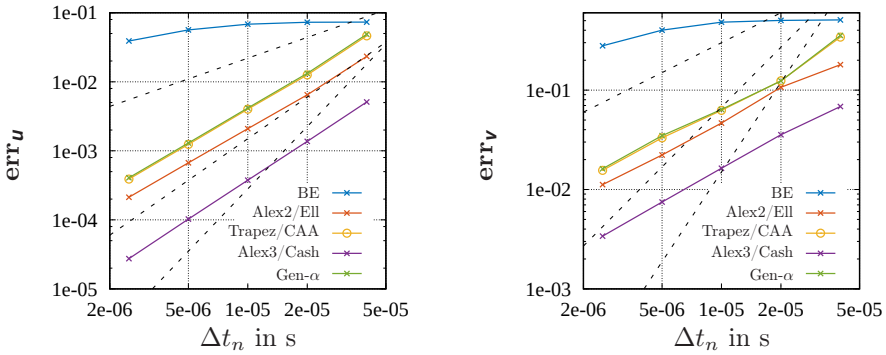

(a) Global error of the displacement field **(b)** Global error of the velocity field

Figure 2. Convergence analysis for the linear elastic rod - Global error $\mathbf{err}_{\boldsymbol{u}}$ and $\mathbf{err}_{\boldsymbol{v}}$ vs. step-size Δt_n

order reduction where the third order of the Alex3/Cash method is not attained. As seen in Fig. 2b, where the global error for the velocity field is depicted, further unsatisfactory tendencies are observed. Here, the higher-order convergence is not obtained and is limited to one. As a possible explanation, we assume that the hyperbolic solution characteristics inherent to the wave equation leads to a significant degeneration of the temporal convergence behavior.

The modeling of the non-linear viscoelastic rod as shown in Fig. 1b utilizes the three-parameter model of small strain viscoelasticity incorporating non-linear rate-dependence, see [5]. This step transforms the initial boundary-value problem to be solved into the form $\partial N(x,t)/\partial x = \varrho A \partial^2 u(x,t)/\partial t^2$, $N = \sigma A$, $\sigma = E\varepsilon + \hat{E}(\varepsilon - \varepsilon_{\mathrm{v}})$, $\varepsilon = \partial u/\partial x$, $\dot{\varepsilon}_{\mathrm{v}} = \hat{E}/\eta(\varepsilon - \varepsilon_{\mathrm{v}})$, $\eta = \eta_0 e^{-s_0|\sigma - E\varepsilon|}$ where the same initial- and boundary conditions for the longitudinal displacement and velocity field are taken as in the linear elastic case. The internal variables in this constitutive model is the viscous strain field $\varepsilon_{\mathrm{v}}(x,t)$, whose initial condition is given by $\varepsilon_{\mathrm{v}}(x,0) = 0$. For a complete problem description, the material parameter set will be extended by the material parameters $\hat{E} = E = 2.1 \times 10^5\,\mathrm{N\,mm^{-2}}$, $\eta_0 = 13\,\mathrm{N\,s\,mm^{-2}}$ and $s_0 = 1.1\,\mathrm{MPa^{-1}}$, associated with the overstress part of the constitutive model. Due the non-linear rate-dependence of the applied constitutive model induced by the non-linear viscosity function $\eta(\varepsilon, \varepsilon_{\mathrm{v}})$, there exists no analytical solution in contrast to the previously discussed elastodynamic problem. In order to compute the global error measures $\mathbf{err}_{\boldsymbol{u}}$, $\mathbf{err}_{\boldsymbol{v}}$ and $\mathbf{err}_{\boldsymbol{q}}$, we conduct a high-precision reference solution employing Alex3/Cash method with a constant step-size of $\Delta t_n = 10^{-6}\,\mathrm{s}$. The results of the temporal convergence study are shown in Fig. 3. The presence of a physical damping mechanism inherently anchored in the material model leads obviously – in comparison to the order investigations in Fig. 2 – to an improved temporal convergence behavior. A more descriptive interpretation of the statements made in this section are provided by Fig. 4, in which the structural responses of the elastic and viscoelastic calculation models are compared. From Fig. 4a, it is clear that the oscillation behavior of the linear-elastic rod is more pronounced. On the other hand, for the viscoelastic rod, as a result of the viscous damping properties of the material, almost all high-frequency components are filtered out, see Fig. 4b.

In the case of quasi-static problems, it was shown in [4, 9] that classical stiffly accurate DIRK-schemes are highly accurate and stable. These numerical observations will be reviewed for the one-dimensional physically non-linear example discussed here. For this purpose, only the inertia properties of the non-linear viscoelastic rod are switched off so that an elliptic boundary-value problem must be solved within the context of the method of vertical lines. The results of the temporal convergence study for the quasi-static case are shown in Fig. 5 and are in perfect agreement with the theory.

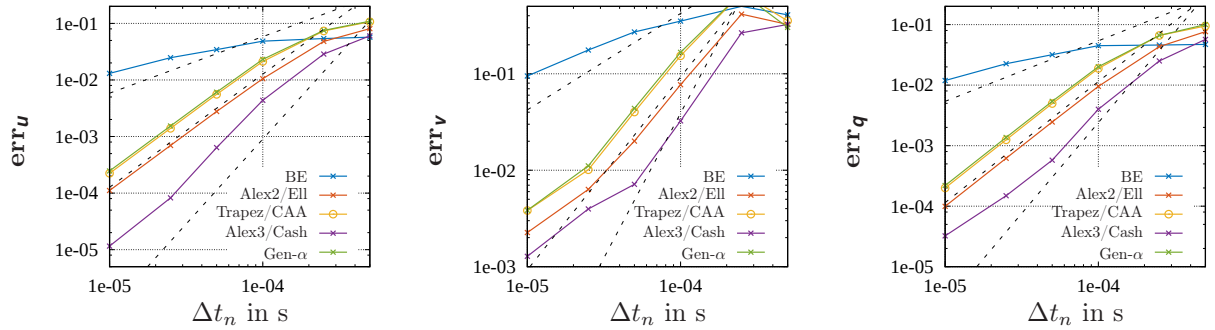

(a) Global error of the displacement field

(b) Global error of the velocity field

(c) Global error of the internal variables

Figure 3. Convergence analysis for the non-linear viscoelastic rod - Global error $\mathbf{err_u}$, $\mathbf{err_v}$ and $\mathbf{err_q}$ vs. step-size Δt_n

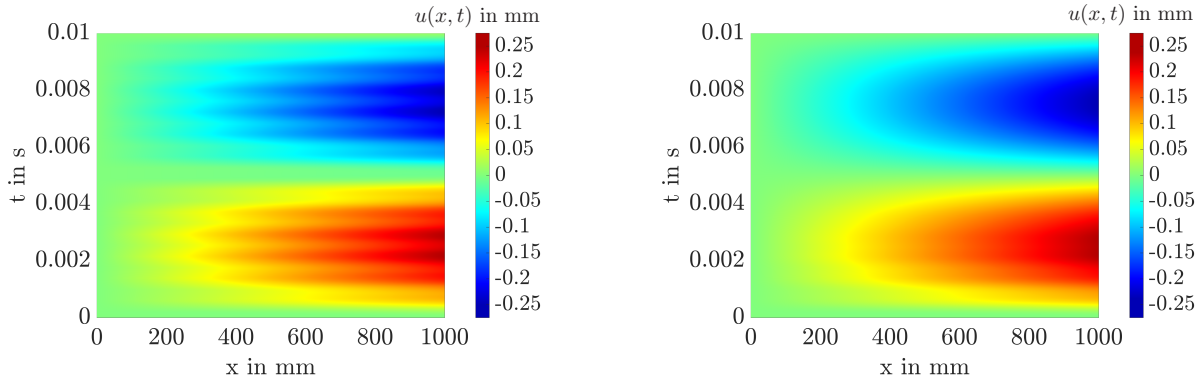

(a) Space-Time-Displacement diagram for the linear elastic rod: analytical solution, see Eq. (4)

(b) Space-Time-Displacement diagram for the non-linear viscoelastic rod: numerical reference solution

Figure 4. Comparison of the oscillation behavior between linear elastic and non-linear viscoelastic system

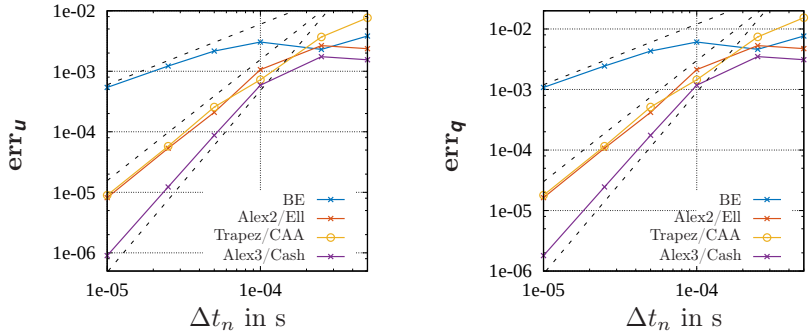

(a) Global error of the displacement field

(b) Global error of the internal variables

Figure 5. Convergence analysis for the non-linear viscoelastic rod for the quasi-static problem - Global error $\mathbf{err_u}$ and $\mathbf{err_q}$ vs. step-size Δt_n

3 Conclusions

In this contribution, the accuracy of higher-order DIRK-methods was analyzed with the help of a one-dimensional wave propagation example. It is shown that the higher-order accuracy of DIRK-methods, as proposed in [4, 9] for the quasi-static case, is not one-to-one transferable into the regime of structural dynamics. Undesirable side effects in the area of structural dynamics occur for DIRK-integrators in the form of order reduction phenomena, which reduce the performance of the analyzed time integration methods.

References

[1] P. Ellsiepen and S. Hartmann. Remarks on the Interpretation of Current Non-linear Finite-Element-Analyses as Differential-Algebraic Equations. *International Journal for Numerical Methods in Engineering* 51 (2001), pp. 679–707.

[2] Matthias Grafenhorst. "Zeitadaptive Finite-Elemente-Berechnungen thermomechanisch gekoppelter Problemstellungen sowie Mortarkontakt". PhD thesis. Clausthal-Zellerfeld: Institute of Applied Mechanics, Clausthal University of Technology, 2018.

[3] Matthias Grafenhorst, Joachim Rang, and Stefan Hartmann. Time-adaptive finite element simulations of dynamical problems for temperature-dependent materials. *Journal of Mechanics of Materials and Structures* 12.1 (2017), pp. 57–91.

[4] S. Hartmann. Computation in finite strain viscoelasticity: finite elements based on the interpretation as differential-algebraic equations. *Computer Methods in Applied Mechanics and Engineering* 191.13-14 (2002), pp. 1439–1470.

[5] S. Hartmann. A remark on the application of the Newton-Raphson method in non-linear finite element analysis. *Computational Mechanics* 36.2 (2005), pp. 100–116.

[6] Hans M. Hilber, Thomas J. R. Hughes, and Robert L. Taylor. Improved numerical dissipation for time integration algorithms in structural dynamics. *Earthquake Engineering and Structural Dynamics* 5.3 (1977), pp. 283–292.

[7] Kurt Meyberg and Peter Vachenauer. *Höhere Mathematik 2: Differentialgleichungen, Funktionentheorie, Fourier-Analysis, Variationsrechnung*. 4th ed. Springer-Lehrbuch. Berlin, Heidelberg: Springer Berlin Heidelberg, 2001.

[8] B. Owren and H. H. Simonsen. Alternative integration methods for problems in structural dynamics. *Computer Methods in Applied Mechanics and Engineering* 122.1-2 (1995), pp. 1–10.

[9] Steffen Rothe, Ahmad-Wahadj Hamkar, Karsten J. Quint, and Stefan Hartmann. Comparison of diagonal-implicit, linear-implicit and half-explicit Runge–Kutta methods in non-linear finite element analyses. *Archive of Applied Mechanics* 82.8 (2012), pp. 1057–1074.

**Proceedings of the 8th GACM Colloquium on Computational Mechanics
for Young Scientists from Academia and Industry
August 28–30, 2019 in Kassel, Germany**

A higher-order energy-momentum scheme for a non-isothermal two-phase dissipation model of fibrous composites

Michael Groß * [1], Julian Dietzsch[1] and Chris Röbiger[1]

[1]TU Chemnitz, Professorship of applied mechanics and dynamics, Reichenhainer Straße 70, D-09126 Chemnitz, Germany.

Abstract. Fiber-reinforced plastics are made of an isotropic polymer matrix reinforced with inorganic or organic fibers. These composites become more and more important in light-weight structures. The major contribution to the internal dissipation in these fibrous composites is due to the isotropic matrix material. However, internal dissipation in the fibers has to be taken into account if Carbon or Kevlar fibers, respectively, are applied, or by using organic fibers, which are applied in the automotive industry, for example. The presented two-phase dissipation model is based on the multiplicative split of the deformation gradient of the composite in an elastic and viscous deformation gradient, as well as on the multiplicative split of the fiber deformation gradient in an elastic and viscous fiber deformation gradient. The corresponding viscous evolution equations are derived by a principle of virtual power together with further mechanical and thermal time evolution equations of a dynamic continuous problem. For instance, in the internal power, we consider free energy functions depending on matrix and fiber invariants. In the external power, the non-negative internal dissipation with respect to a positive-definite matrix viscosity tensor and a positive fiber viscosity parameter, respectively, are introduced. The internal power also includes mixed fields for the thermo-elastic matrix and fiber behaviour. In this way, we obtain a mixed stress-strain formulation, which also avoids locking behavior due to the stiff fibers embedded in the incompressible matrix material. Algorithmic terms in the virtual external power provide the energy-momentum scheme of this two-phase dissipation model. We demonstrate the independent dissipative material behaviour due to the matrix and the fibers in dynamic numerical examples with different mechanical and thermal boundary conditions.

Introduction

The derivation of a viscoelastic material model for fibers from a three-dimensional constitutive model for isotropic materials is successful (see Reference [3]). Therefore, we derive from the constitutive model of the matrix material in Reference [1] a new fiber viscoelasticity formulation. In Reference [1], the formulation is based on the well-known multiplicative split of the deformation gradient in a viscous and an elastic product tensor. Considering also deformations of fibers, we thus assume the product structure $\boldsymbol{F}_F = \boldsymbol{F}_F^e \boldsymbol{F}_F^v$ of the fiber deformation gradient $\boldsymbol{F}_F := \boldsymbol{a}_t \otimes \boldsymbol{a}_0$ with the elastic fiber deformation gradient $\boldsymbol{F}_F^e := \boldsymbol{a}_t \otimes \bar{\boldsymbol{a}}$ and the viscous fiber deformation gradient $\boldsymbol{F}_F^v := \bar{\boldsymbol{a}} \otimes \boldsymbol{a}_0$. These second-order tensors are defined by the stretched fiber direction vector $\boldsymbol{a}_t$ in the tangent space $T_x\mathscr{B}_t$ at the current configuration $\mathscr{B}_t$, the fiber direction vector $\bar{\boldsymbol{a}}$ in the linear space $\mathscr{V}_F$ ('intermediate fiber configuration') and the unit direction vector $\boldsymbol{a}_0$ with $\|\boldsymbol{a}_0\| = 1$ in the tangent space $T_X\mathscr{B}_0$ at the initial configuration $\mathscr{B}_0$ (see Fig. 1). The symbol $\otimes$ denotes a dyadic tensor product. In principle, we assume a generalized Maxwell element with an elastic and a viscoelastic branch, but considering large deformations, we define the fiber free energy $\Psi_F = \Psi_F^{\text{ela}} + \Psi_F^{\text{vis}}$. The elastic free energy $\Psi_F^{\text{ela}} := \hat{\Psi}_F^{\text{ela}}(\tilde{C}_F)$ depends on the squared fiber stretch

$$\tilde{C}_F := \boldsymbol{a}_t \cdot \boldsymbol{a}_t = \boldsymbol{a}_0 \boldsymbol{F}^T \cdot \boldsymbol{F}\boldsymbol{a}_0 = \boldsymbol{C} : \boldsymbol{a}_0 \otimes \boldsymbol{a}_0 = \boldsymbol{C} : \boldsymbol{A}_0 = \boldsymbol{C}_F : \boldsymbol{I} \tag{1}$$

with the structural tensor $\boldsymbol{A}_0 := \boldsymbol{a}_0 \otimes \boldsymbol{a}_0$, the right Cauchy-Green tensor $\boldsymbol{C} := \boldsymbol{F}^T\boldsymbol{F}$, the unity metric tensor $\boldsymbol{I}$ in $\mathscr{B}_0$, and the right Cauchy-Green tensor $\boldsymbol{C}_F := \boldsymbol{F}_F^T\boldsymbol{F}_F = [\boldsymbol{C} : \boldsymbol{A}_0]\,\boldsymbol{A}_0$ of the fibers. Note that the superscript letter 'T' denotes the transposition of a second-order tensor. The elastic fiber stretch

$$C_F^e := \boldsymbol{C}_F^e : \bar{\boldsymbol{I}} = [\boldsymbol{F}_F^e]^T\,\boldsymbol{F}_F^e : \bar{\boldsymbol{I}} = [\boldsymbol{F}_F^v]^{-T}\,\boldsymbol{F}^T\boldsymbol{F}\,[\boldsymbol{F}_F^v]^{-1} : \bar{\boldsymbol{I}} = [\boldsymbol{F}_F^v]^{-T}\,\boldsymbol{C}\,[\boldsymbol{F}_F^v]^{-1} : \bar{\boldsymbol{I}} \tag{2}$$

*Corresponding author: michael.gross@mb.tu-chemnitz.de

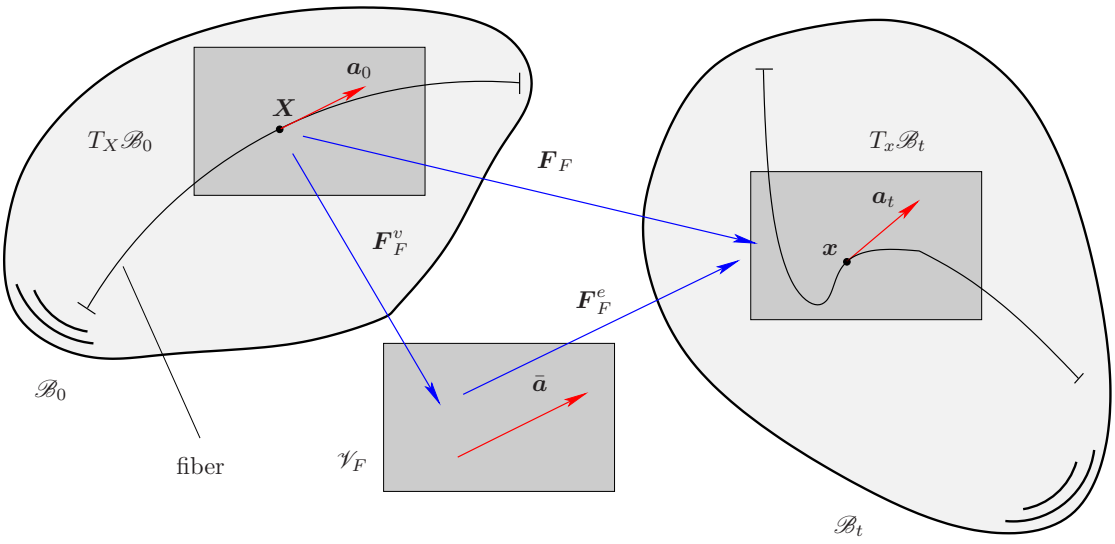

Figure 1. Fiber configurations with tangent spaces.

determines the viscoelastic free energy, where $\bar{\boldsymbol{I}}$ designates the unity metric tensor of the linear space $\mathscr{V}_F$. Tensor algebraic manipulations then leads to the relation $C_F^e = \boldsymbol{C}^T : [\boldsymbol{F}_F^v]^{-1}\,[\boldsymbol{F}_F^v]^{-T} = \boldsymbol{C}\,[\boldsymbol{C}_F^v]^{-1} : \boldsymbol{I}$, where the second-order tensor $\boldsymbol{C}_F^v$ denotes the viscous right Cauchy-Green tensor

$$\boldsymbol{C}_F^v = [\boldsymbol{F}_F^v]^T\,\boldsymbol{F}_F^v = [\boldsymbol{a}_0 \otimes \bar{\boldsymbol{a}}] \cdot [\bar{\boldsymbol{a}} \otimes \boldsymbol{a}_0] = [\bar{\boldsymbol{a}} \cdot \bar{\boldsymbol{a}}]\,\boldsymbol{A}_0 =: C_F^v\,\boldsymbol{A}_0 \tag{3}$$

The scalar-valued field C_F^v denotes the new viscous internal variable of the fibers, and the inverse of the viscous right Cauchy-Green tensor of the fiber family is defined by $[\boldsymbol{C}_F^v]^{-1} := [\boldsymbol{F}_F^v]^{-1}\,[\boldsymbol{F}_F^v]^{-T}$, where the inverse $[\boldsymbol{F}_F^v]^{-1}$ satisfies the relation $\boldsymbol{a}_0 = [\boldsymbol{F}_F^v]^{-1}\,\bar{\boldsymbol{a}} =: \bar{\lambda}_F\,[\boldsymbol{a}_0 \otimes \bar{\boldsymbol{a}}] \cdot \bar{\boldsymbol{a}} = \bar{\lambda}_F\,[\bar{\boldsymbol{a}} \cdot \bar{\boldsymbol{a}}]\,\boldsymbol{a}_0 = \bar{\lambda}_F\,C_F^v\,\boldsymbol{a}_0$. Thus, the multiplier $\bar{\lambda}_F$ denotes the inverse of the viscous internal variable, and the inverse of the viscous right Cauchy-Green tensor takes the form $(C_F^v)^2\,[\boldsymbol{C}_F^v]^{-1} = [\boldsymbol{a}_0 \otimes \bar{\boldsymbol{a}}] \cdot [\bar{\boldsymbol{a}} \otimes \boldsymbol{a}_0] = [\boldsymbol{a}_0 \otimes \boldsymbol{a}_0]\,C_F^v = C_F^v\,\boldsymbol{A}_0$. Hence,

$$C_F^e = \boldsymbol{C}\,\frac{1}{C_F^v}\,\boldsymbol{A}_0 : \boldsymbol{I} = [\boldsymbol{C} : \boldsymbol{A}_0]\,\frac{1}{C_F^v} = \frac{\tilde{C}_F}{C_F^v} \tag{4}$$

is the relation for the elastic fiber stretch. In this way, we obtain the viscous free energy function $\Psi_F^{\mathrm{vis}} := \hat{\Psi}_F^{\mathrm{vis}}(C_F^e) = \hat{\Psi}_F^{\mathrm{ela}}(\tilde{C}_F[C_F^v]^{-1})$, which means we apply the same free energy function as in the elastic branch, but with a different argument and generally different material constants. According to the Clausius-Plank inequality and the definition of the entropy, the viscous internal dissipation in the fibers takes the form

$$D_F^{\mathrm{int}} := \frac{1}{2}\,S_F\,\dot{\tilde{C}}_F - \dot{\Psi}_F^{\mathrm{ela}} - \dot{\Psi}_F^{\mathrm{vis}} = \tilde{C}_F\,S_F\,\frac{\dot{\tilde{C}}_F}{2\,\tilde{C}_F} - \dot{\Psi}_F^{\mathrm{ela}} - \dot{\Psi}_F^{\mathrm{vis}} = M_F\,L_F - \dot{\Psi}_F^{\mathrm{ela}} - \dot{\Psi}_F^{\mathrm{vis}} \geqslant 0 \tag{5}$$

where we introduced the Mandel-like fiber stress $M_F := \tilde{C}_F\,S_F$, which is energy-conjugated to the fiber strain rate L_F. The time rate of the free energy pertaining to the elastic branch then takes the form

$$\dot{\Psi}_F^{\mathrm{ela}} = 2\,\frac{\partial \Psi_F^{\mathrm{ela}}}{\partial \tilde{C}_F}\,\frac{\dot{\tilde{C}}_F}{2} = 2\,\tilde{C}_F\,\frac{\partial \Psi_F^{\mathrm{ela}}}{\partial \tilde{C}_F}\,L_F =: M_F^{\mathrm{ela}}\,L_F \tag{6}$$

and the time rate of the free energy associated with the viscoelastic branch reads

$$\dot{\Psi}_F^{\mathrm{vis}} = \frac{\partial \Psi_F^{\mathrm{vis}}}{\partial C_F^e}\,\dot{C}_F^e = 2\,C_F^e\,\frac{\partial \Psi_F^{\mathrm{vis}}}{\partial C_F^e}\left[\frac{\dot{\tilde{C}}_F}{2\,C_F} - \frac{\dot{C}_F^v}{2\,C_F^v}\right] =: M_F^{\mathrm{vis}}\,[L_F - L_F^v] \tag{7}$$

Thus, the viscous dissipation in the fibers are given by $D_F^{\mathrm{int}} := \left[M_F - M_F^{\mathrm{ela}} - M_F^{\mathrm{vis}}\right] L_F + M_F^{\mathrm{vis}}\,L_F^v \geqslant 0$. The Clausius-Plank inequality is then fulfilled by setting $M_F := M_F^{\mathrm{ela}} + M_F^{\mathrm{vis}}$, and by defining the viscous evolution equation

$$\boxed{M_F^{\mathrm{vis}} \doteq \Sigma_F^v} \tag{8}$$

with $\Sigma_F^v := V_F\,L_F^v$ as viscous driving force associated with the viscosity constant $V_F > 0$.

1 Higher-order energy-momentum time integration

The energy-momentum time integration of the viscous fiber evolution equation requires that the relation

$$\Psi^{\mathrm{vis}}_{F_{t_{n+1}}} - \Psi^{\mathrm{vis}}_{F_{t_n}} = \int_{t_n}^{t_{n+1}} \dot{\Psi}^{\mathrm{vis}}_F \,\mathrm{d}t \equiv \int_0^1 \overset{\circ}{\Psi}{}^{\mathrm{vis}}_F \,\mathrm{d}\alpha \tag{9}$$

is exactly satisfied on each time step $[t_n, t_{n+1}]$, or on the normalized time interval $[0,1]$, respectively (cp. Reference [1]). Here, we indicate by a superimposed $\circ$ the derivative with respect to $\alpha \in [0,1]$. We satisfy this constraint by means of a new algorithmic Mandel stress $\bar{M}^v_F$. Note that in Reference [1], the energy-momentum time integration of the viscous free energy of the matrix material is only based on the algorithmic elastic Mandel stress, which modifies the equations of motion only. This leads in the isothermal case to an unmodified viscous evolution equation of the matrix material. Motivated by Reference [2], in which the viscous evolution equation is modified by a discrete derivative, we here modify also the viscous Mandel stress of the fibers. In this way, the equations of motion as well as the viscous evolution equation are modified. Note also that, in contrast to Reference [2], the modification in this paper is higher-order accurate. We determine the algorithmic Mandel stress $\bar{M}^v_F$ by using a separate constrained variational problem with the Lagrange functional

$$\mathcal{F}^v_F(\bar{M}^v_F, \mu^v_F) := \mu^v_F \,\mathcal{G}^v_F(\bar{M}^v_F) + \int_0^1 F^v_F(\bar{M}^v_F)\,\mathrm{d}\alpha \tag{10}$$

with the Lagrange multiplier μ^v_F as well as a function and functional, respectively, defined by

$$F^v_F(\bar{M}^v_F) := \frac{(\bar{M}^v_F)^2}{2} \qquad \text{and} \qquad \mathcal{G}^v_F(\bar{M}^v_F) := \Psi^{\mathrm{vis}}_{F_{t_{n+1}}} - \Psi^{\mathrm{vis}}_{F_{t_n}} - \int_0^1 G^v_F(\bar{M}^v_F)\,\mathrm{d}\alpha \tag{11}$$

with respect to the constraint function

$$G^v_F(\bar{M}^v_F) := \left[M^{\mathrm{vis}}_F + \bar{M}^v_F\right]\left[L_F - L^v_F\right] \tag{12}$$

The minimization of the Lagrange functional $\mathcal{F}$ leads to the Euler-Lagrange equations

$$\frac{\delta \mathcal{F}^v_F}{\delta \bar{M}^v_F} \equiv \int_0^1 \bar{M}^v_F\,\delta\bar{M}^v_F\,\mathrm{d}\alpha - \mu^v_F \int_0^1 \left[L_F - L^v_F\right]\delta\bar{M}^v_F\,\mathrm{d}\alpha = 0 \qquad \frac{\delta \mathcal{F}^v_F}{\delta \mu^v_F} \equiv \mathcal{G}^v_F = 0 \tag{13}$$

which, in turn, lead to the algorithmic Mandel stress $\bar{M}^v_F := \mu^v_F\left[L_F - L^v_F\right]$ with the Lagrange multiplier

$$\mu^v_F := \frac{\Psi^{\mathrm{vis}}_{F_{t_{n+1}}} - \Psi^{\mathrm{vis}}_{F_{t_n}} - \displaystyle\int_0^1 M^{\mathrm{vis}}_F\left[L_F - L^v_F\right]\mathrm{d}\alpha}{\displaystyle\int_0^1 \left[L_F - L^v_F\right]^2 \mathrm{d}\alpha} \tag{14}$$

According to Reference [1], we apply a mixed finite element formulation which leads to an independent fiber stress S_F. The corresponding fiber stress equation then includes the algorithmic viscous Mandel stress, so that we arrive at the space-time weak form

$$\int_{t_{n+1}}^{t_n}\int_{\mathscr{B}_0} \delta\dot{\tilde{C}}_F \left[2\,\frac{\partial \Psi_F}{\partial \tilde{C}_F} + \bar{S}_F + \frac{\bar{M}^v_F}{\tilde{C}_F} - S_F\right]\mathrm{d}V\,\mathrm{d}t = 0 \tag{15}$$

where the algorithmic fiber stress $\bar{S}_F$ fulfills the gradient theorem (cp. Eq. (9)) with respect to Ψ^{ela}_F. This fiber stress then determines the stress power in the equation of motion. Further, we obtain the weak form of the new viscous evolution equation of the fibers, given by

$$\int_{t_{n+1}}^{t_n}\int_{\mathscr{B}_0} \delta\dot{C}^v_F \left[-Y_F - \frac{\bar{M}^v_F}{2\,C^v_F} + \frac{V_F}{2\,C^v_F}\,L^v_F\right]\mathrm{d}V\,\mathrm{d}t = 0 \tag{16}$$

Note that a further advantage of the existence of the additional algorithmic stress $\bar{M}^v_F$ besides the algorithmic stress $\bar{S}_F$ is, that each free energy part of the fiber family possesses its own algorithmic modification. Hence, neglecting one part of the fiber free energy allows for the neglection of the corresponding algorithmic stress term. This simultaneous modification of the equation of motion and the viscous evolution equation of the fibers by means of the same algorithmic stress term leads to the same stable time integration as in Reference [2], but now also in the case of higher order accuracy in time.

2 Numerical example

We consider a displacement controlled tensile test of a tension bar. The fibers lie along the bar axis. On the top (blue patches in Fig. 2, left) and at the bottom, we fix the temperature and horizontal positions, but move in vertical direction. We apply symmetry boundary conditions in the x-z- and y-z-plain (green patches in Fig. 2, left). The initial conditions are homogenous. In Fig. 2, right, we show the fiber stress.

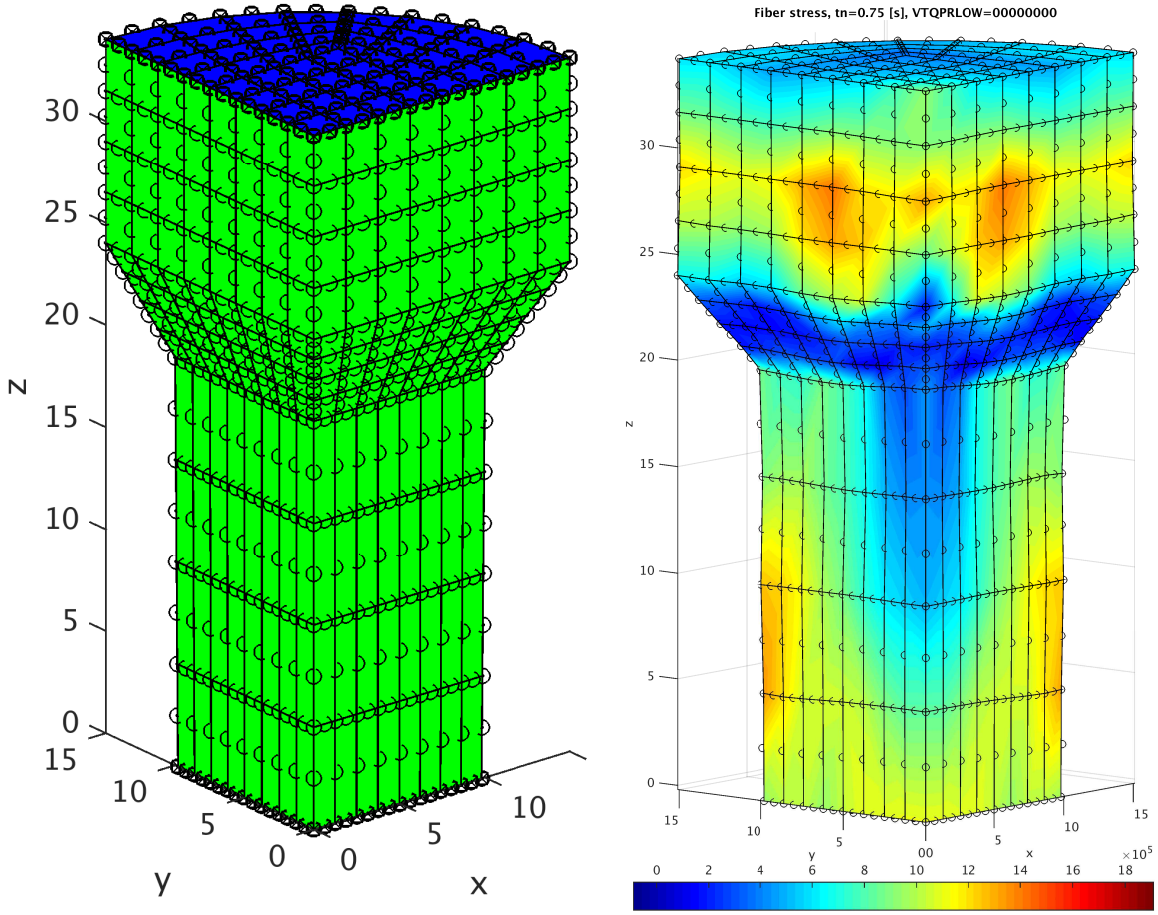

Figure 2. Left: Boundary conditions of the tension bar. Right: Fiber stress at $t_n = 0.75\,\mathrm{s}$ (maximum load time).

Acknowledgments

This research is provided by the 'Deutsche Forschungsgemeinschaft' (DFG) under the grants GR 3297/4-1 and 3297/6-1. This support is gratefully acknowledged.

References

[1] Michael Groß and Julian Dietzsch. Variational-based locking-free energy–momentum schemes of higher-order for thermo-viscoelastic fiber-reinforced continua. *Computer Methods in Applied Mechanics and Engineering* 343 (2019), pp. 631–671.

[2] Michael Groß, Matthias Bartelt, and Peter Betsch. Structure-preserving time integration of non-isothermal finite viscoelastic continua related to variational formulations of continuum dynamics. *Computational Mechanics* 62.2 (2018), pp. 123–150.

[3] Boumediene Nedjar. An anisotropic viscoelastic fibre–matrix model at finite strains: continuum formulation and computational aspects. *Computer Methods in Applied Mechanics and Engineering* 196.9-12 (2007), pp. 1745–1756.

**Proceedings of the 8th GACM Colloquium on Computational Mechanics
for Young Scientists from Academia and Industry
August 28–30, 2019 in Kassel, Germany**

Implicit Runge-Kutta Schemes and Galerkin Methods Similarities and Differences

Bettina Schröder * [1] and Detlef Kuhl[1]

[1]Institute of Mechanics and Dynamics, University of Kassel, Mönchebergstraße 7, 34109 Kassel

Abstract. In the present paper the numerical realization of linear elastodynamics is depicted, focussing on the usage of higher order accurate time discretization schemes. Thereby, an implicit Runge-Kutta Radau IIA scheme and a continuous Galerkin method are compared, depicting their similarities and differences.

Introduction

Social as well as economic conditions, together with an increasing environmental conscience lead to aspirations for high performance products manufactured by resource efficient production strategies. One example of the latter is the creation of functionally graded structures out of mono-materials by using an integrated thermomechanical forming process, cf. [9]. For a proper predictability of the structures' properties using simulation techniques, appropriate material models as well as adequate numerical schemes have to be exploited. In this context the application of higher order accurate time integration schemes plays an important role. In the following an implicit Runge-Kutta Radau IIA scheme and a continuous Galerkin method are analyzed, whereby linear elasticity is taken as a model problem for simplicity.

1 Fundamental Equation for Linear Elastodynamics

In order to derive the fundamental equation for elastodynamics, the principle of Jourdain is used, cf. [6]. Therefore, in a first step, the balance of energy of a continuum mechanical body $\mathcal{B}$ with domain Ω and surface Γ

$$P(\dot{\boldsymbol{u}}) = \dot{K} + \dot{E} + P^* = 0, \tag{1}$$

is formulated. It consists of the rate of the kinetic energy $\dot{K}$, the rate of the internal energy $\dot{E}$ and the power due to external forces P^* defined as:

$$\dot{K} = \int_\Omega \rho_0 \ddot{\boldsymbol{u}} \cdot \dot{\boldsymbol{u}}\, dV, \qquad \dot{E} = \int_\Omega \dot{\boldsymbol{\varepsilon}} : \mathbb{C}_\mathrm{e} : \boldsymbol{\varepsilon}\, dV, \qquad P^* = -\int_\Omega \rho_0 \dot{\boldsymbol{u}} \cdot \boldsymbol{f}\, dV - \int_\Gamma \dot{\boldsymbol{u}} \cdot \boldsymbol{t}^*\, dA. \tag{2}$$

Therein, the expression ρ_0 refers to the body's density, the variable $\boldsymbol{f}$ to the applied mass forces and $\boldsymbol{t}^*$ to the external Cauchy stress vector. The displacement field is indicated by $\boldsymbol{u}$, while $\dot{\boldsymbol{u}}$ as well as $\ddot{\boldsymbol{u}}$ are the corresponding first and second time derivatives. The associated strain tensor and its rate are denoted by $\boldsymbol{\varepsilon}$ and $\dot{\boldsymbol{\varepsilon}}$. The quantity $\mathbb{C}_\mathrm{e}$ refers to the elastic constitutive tensor. Additionally, appropriate initial conditions $\boldsymbol{u}_0 = \boldsymbol{u}(t_0)$ as well as $\dot{\boldsymbol{u}}_0 = \dot{\boldsymbol{u}}(t_0)$ are chosen.

In a second step, it is assumed that the total power P of a system reaches a stationary point, cf. [1, 8], demanding that

$$0 \in \partial P_{\dot{\boldsymbol{u}}}\,(\dot{\boldsymbol{u}}) \tag{3}$$

holds, where $\partial_{(\bullet)}$ represents the subdifferential with regard to the respective quantity, cf. [7, 10].

*Corresponding author: schroederbettina@uni-kassel.de, kuhl@uni-kassel.de

Evaluating Eq. (3) yields the weak form of elastodynamics

$$\int_{\Omega} \rho_0 \delta\dot{\boldsymbol{u}} \cdot \ddot{\boldsymbol{u}}\, dV + \int_{\Omega} \delta\dot{\boldsymbol{\varepsilon}} : \mathbb{C}_{\mathrm{e}} : \boldsymbol{\varepsilon}\, dV - \int_{\Omega} \rho_0 \delta\dot{\boldsymbol{u}} \cdot \boldsymbol{f}\, dV - \int_{\Gamma_{t^*}} \delta\dot{\boldsymbol{u}} \cdot \boldsymbol{t}^*\, dA = 0. \tag{4}$$

2 Numerical Realization of Linear Elasticity

In order to solve Eq. (4) for a general continuum mechanical body, numerical schemes are adapted. First of all Eq. (4) is discretized in space using the finite element method. Therefore, the body's domain Ω is divided in *NE* subdomains assuming that on each element Eq. (4) has to be fulfilled. Furthermore, the geometry, the primary variable $\boldsymbol{u}$, its time derivatives and the virtual displacement rate $\delta\dot{\boldsymbol{u}}$ as well as the corresponding gradients are approximated by nodal values and LAGRANGE shape functions. Inserting these approximations in Eq. (4), evaluating the appearing integrals by a GAUSS-LEGENDRE quadrature, assembling all element equations and applying the fundamental lemma of variational calculus, results in the equation of motion

$$\mathbf{M}\ddot{\mathbf{u}} + \mathbf{K}\mathbf{u} = \mathbf{R}^*, \qquad \text{with} \qquad \mathbf{u}_0 = \mathbf{u}(t_0), \qquad \dot{\mathbf{u}}_0 = \dot{\mathbf{u}}(t_0) \tag{5}$$

on structural level. Therein, $\mathbf{M}$ indicates the mass matrix, $\mathbf{K}$ the stiffness matrix and $\mathbf{R}^*$ the vector of external loads, cf. [11].

To determine the unknown displacement field, a relation between the accelerations $\ddot{\mathbf{u}}$ and the displacements $\mathbf{u}$ has to be established, before the emanating linear system of equations can be solved. This can be done exploiting distinct time integration schemes. Therefore, Eq. (5) is rewritten in a system of first order equations in time

$$\bar{\mathbf{M}}\dot{\mathbf{w}} + \bar{\mathbf{K}}\mathbf{w} = \bar{\mathbf{R}}^*, \qquad \text{with} \qquad \mathbf{w}_0 = \mathbf{w}(t_0) \tag{6}$$

where

$$\bar{\mathbf{M}} = \begin{bmatrix} \mathbf{M} & \mathbf{0} \\ \mathbf{0} & \mathbf{I} \end{bmatrix}, \qquad \bar{\mathbf{K}} = \begin{bmatrix} \mathbf{0} & \mathbf{K} \\ -\mathbf{I} & \mathbf{0} \end{bmatrix}, \qquad \mathbf{w} = \begin{bmatrix} \mathbf{v} \\ \mathbf{u} \end{bmatrix}, \qquad \bar{\mathbf{R}}^* = \begin{bmatrix} \mathbf{R}^* \\ \mathbf{0} \end{bmatrix} \tag{7}$$

holds with the identity matrix $\mathbf{I}$. Additionally, the time period of interest $[0, T]$ is divided into a number of *NT* time steps $[t_n, t_{n+1}]$ with step size Δt.

2.1 Stiffly Accurate Fully Implicit Runge-Kutta Schemes

One method to discretize Eq. (6) in time is to use stiffly accurate fully implicit RUNGE-KUTTA schemes. In this context, Eq. (6) is evaluated only at discrete points in time t_{ni}, so called stages which are determined by

$$t_{ni} = t_n + c_i \Delta t, \tag{8}$$

with the coefficients $c_i \in [0, 1]$ and $i = 1, ..., s$, where s embodies the maximum number of stages. The link between the primary variable vector $\mathbf{w}$ and its time derivative is established by exploiting the fundamental theorem of calculus as well as by approximating the appearing integrals using the particular quadrature rules

$$\mathbf{w}_{n+1} = \mathbf{w}_n + \Delta t \sum_{i=1}^{s} b_i\, \dot{\mathbf{w}}_{ni}, \qquad \mathbf{w}_{ni} = \mathbf{w}_n + \Delta t \sum_{j=1}^{s} a_{ij}\, \dot{\mathbf{w}}_{nj}, \tag{9}$$

with weighting coefficients b_i and a_{ij}, cf. [3]. The indices represent the points in time, where the respective quantity is calculated, e.g. $\mathbf{w}_{ni} = \mathbf{w}(t_{ni})$. To provide a better overview of the chosen quadrature parameters, they are conventionally sorted into a BUTCHER tableau, see Fig. 1. In what follows, only the two stage RADAU IIA scheme of Fig. 1(b) will be considered. This method is, due to the property $a_{2i} = b_i$, stiffly accurate so that the last stage is identical to the end of the time step $t_{ns} = t_{n+1}$ and Eq. $(9)_1$ is superfluous. Moreover, its matrix $\mathbf{A}$, see Fig. 1(c), can be inverted. Hence, Eq. $(9)_2$ can be reformulated and inserted in Eq. (6) leading to

$$\left[\frac{1}{\Delta t}\bar{\mathbf{M}}_{\mathrm{t}}\mathbf{A}_{\mathrm{t}}^{-1} + \bar{\mathbf{K}}_{\mathrm{t}}\right] \mathbf{w}_{\mathrm{t}} = \bar{\mathbf{R}}_{\mathrm{t}}^* + \frac{1}{\Delta t}\bar{\mathbf{M}}_{\mathrm{t}}\mathbf{A}_{\mathrm{t}}^{-1}\mathbf{w}_{\mathrm{t},n}, \tag{10}$$

(a)

$$\begin{array}{c|ccc} c_1 & a_{11} & \cdots & a_{1s} \\ \vdots & \vdots & \ddots & \vdots \\ c_s & a_{s1} & \cdots & a_{ss} \\ \hline & b_1 & \cdots & b_s \end{array}$$

(b)

$$\begin{array}{c|cc} \frac{1}{3} & \frac{5}{12} & -\frac{1}{12} \\ 1 & \frac{3}{4} & \frac{1}{4} \\ \hline & \frac{3}{4} & \frac{1}{4} \end{array}$$

(c)

$$\begin{array}{c|c} \mathbf{c} & \mathbf{A} \\ \hline & \mathbf{b}^{\mathrm{T}} \end{array}$$

Figure 1. (a) Implicit RUNGE KUTTA method, (b) RADAU IIA scheme, (c) Short notation of the BUTCHER tableau

whereby $\mathbf{w}_{\mathrm{t}} = [\mathbf{w}_{n1}, \mathbf{w}_{n2}]$ represents the aggregated stage values and $\mathbf{w}_{\mathrm{t},n}$ includes two copies of $\mathbf{w}_n$. $\bar{\mathbf{M}}_{\mathrm{t}}$ as well as $\bar{\mathbf{K}}_{\mathrm{t}}$ are the augmentations of the mass and the stiffness matrix. The variable $\bar{\mathbf{R}}_{\mathrm{t}}^*$ refers to the extended external load vector. Analogously, $\mathbf{A}_{\mathrm{t}}$ is a proper extension of the coefficient matrix $\mathbf{A}$ taking into account the problem's number of degrees of freedom or rather the size of $\mathbf{w}_n$. For the proposed RADAU IIA scheme Eq. (10) transfers into

$$\begin{bmatrix} \frac{3}{2\Delta t}\bar{\mathbf{M}}_{n1} + \bar{\mathbf{K}}_{n1} & \frac{1}{2\Delta t}\bar{\mathbf{M}}_{n1} \\ \frac{-9}{2\Delta t}\bar{\mathbf{M}}_{n2} & \frac{5}{2\Delta t}\bar{\mathbf{M}}_{n2} + \bar{\mathbf{K}}_{n2} \end{bmatrix} \begin{bmatrix} \mathbf{w}_{n1} \\ \mathbf{w}_{n2} \end{bmatrix} = \begin{bmatrix} \bar{\mathbf{R}}_{n1}^* \\ \bar{\mathbf{R}}_{n2}^* \end{bmatrix} + \frac{\mathbf{w}_n}{\Delta t} \begin{bmatrix} 2\bar{\mathbf{M}}_{n1} \\ -2\bar{\mathbf{M}}_{n2} \end{bmatrix} \tag{11}$$

and the unknown field variables can be determined by solving the linear system of equations.

2.2 Continuous Galerkin Methods

An alternative way to discretize Eq. (6) in time is to use continuous GALERKIN methods. The idea behind these schemes is, to apply the finite element method to the time domain, cf. [2]. Thus, Eq. (6) is multiplied with a test function $\delta\mathbf{t}$ and integrated over the time domain to yield the weak form

$$\int_{-1}^{1} \delta\mathbf{t} \left[\bar{\mathbf{M}}\dot{\mathbf{w}} + \bar{\mathbf{K}}\mathbf{w} - \bar{\mathbf{R}}^*\right] \, J_{\mathrm{t}} \, d\xi_{\mathrm{t}} = 0. \tag{12}$$

The integral therein is linked to a standard time element based on natural coordinates $\xi_{\mathrm{t}} \in [-1, 1]$, exploiting

$$t^n = \frac{\Delta t}{2}\xi_{\mathrm{t}} + \frac{t_n + t_{n+1}}{2}. \tag{13}$$

The term $J_{\mathrm{t}} = \Delta t/2$ denotes the JACOBIAN in time. To solve the weak form Eq. (12) in time the primary variable and its time derivative are approximated employing nodal values and LAGRANGE shape functions $N_{\mathrm{t}}^i(\xi_{\mathrm{t}})$ of polynomial degree p_{t} with $i \in [1, p_{\mathrm{t}}+1]$. The test function is approximated employing LAGRANGE shape functions $\bar{N}_{\mathrm{t}}^i(\xi_{\mathrm{t}})$ of polynomial degree $\bar{p}_{\mathrm{t}}$ with $i \in [1, \bar{p}_{\mathrm{t}} + 1]$

$$\mathbf{w} \approx \sum_{i=1}^{p_{\mathrm{t}}+1} \mathbf{w}^i N_{\mathrm{t}}^i(\xi_{\mathrm{t}}), \qquad \dot{\mathbf{w}} \approx \sum_{i=1}^{p_{\mathrm{t}}+1} \mathbf{w}^i \dot{N}_{\mathrm{t}}^i(\xi_{\mathrm{t}}), \qquad \delta\mathbf{t} \approx \sum_{i=1}^{\bar{p}_{\mathrm{t}}+1} \delta\mathbf{t}^i \bar{N}_{\mathrm{t}}^i(\xi_{\mathrm{t}}). \tag{14}$$

Additionally, the integral in Eq. (12) is determined using a quadrature rule with NG_{t} quadrature points and weighting coefficients, so that at the end a linear system has to be solved. In the following special choices for the shape functions and the quadrature rule will be depicted in detail. The idea is to elect $p_{\mathrm{t}} = NG_{\mathrm{t}} = \bar{p}_{\mathrm{t}} + 1 = 2$, to consider a RADAU quadrature rule with quadrature points $\bar{\boldsymbol{\xi}}_{\mathrm{t}} = [-1/3 \; 1]$ as well as with weighting coefficients $[3/2 \; 1/2]$, to designate the RADAU quadrature points as supporting points for the LAGRANGE shape functions $\bar{N}_{\mathrm{t}}^i(\xi_{\mathrm{t}})$ and to choose $\boldsymbol{\xi}_{\mathrm{t}} = [-1 \; \bar{\boldsymbol{\xi}}_{\mathrm{t}}]$ as supporting points for the LAGRANGE shape functions $N_{\mathrm{t}}^i(\xi_{\mathrm{t}})$. With the interpolatory property of the LAGRANGE shape functions, cf. [4], the following results are obtained

$$\begin{array}{llllllll} \bar{N}_{\mathrm{t}}^1(-1/3) = 1 & \bar{N}_{\mathrm{t}}^2(-1/3) = 0 & \bar{N}_{\mathrm{t}}^1(1) = 0 & \bar{N}_{\mathrm{t}}^2(1) = 1 \\ N_{\mathrm{t}}^1(-1/3) = 0 & N_{\mathrm{t}}^2(-1/3) = 1 & N_{\mathrm{t}}^3(-1/3) = 0 & \\ N_{\mathrm{t}}^1(1) = 0 & N_{\mathrm{t}}^2(1) = 0 & N_{\mathrm{t}}^3(1) = 1. & \end{array} \tag{15}$$

The evaluations of the shape functions' derivatives result in

$$\begin{array}{lllllllll} \dot{N}_{\mathrm{t}}^1(-1/3) & = & -\dfrac{2}{\Delta t} & \dot{N}_{\mathrm{t}}^2(-1/3) & = & \dfrac{6}{4\Delta t} & \dot{N}_{\mathrm{t}}^3(-1/3) & = & \dfrac{2}{4\Delta t} \\ \dot{N}_{\mathrm{t}}^1(1) & = & \dfrac{2}{\Delta t} & \dot{N}_{\mathrm{t}}^2(1) & = & -\dfrac{18}{4\Delta t} & \dot{N}_{\mathrm{t}}^3(1) & = & \dfrac{10}{4\Delta t}. \end{array} \tag{16}$$

Inserting Eq. (14), Eq. (15) and Eq. (16) into Eq. (12) leads to

$$\begin{bmatrix} \frac{3}{4}\bar{\mathbf{M}}(-1/3) + \bar{\mathbf{K}}(-1/3)\frac{\Delta t}{2} & \frac{1}{4}\bar{\mathbf{M}}(-1/3) \\ \frac{-9}{4}\bar{\mathbf{M}}(1) & \frac{5}{4}\bar{\mathbf{M}}(1) + \bar{\mathbf{K}}(1)\frac{\Delta t}{2} \end{bmatrix} \begin{bmatrix} \mathbf{w}^2 \\ \mathbf{w}^3 \end{bmatrix} = \begin{bmatrix} \frac{\Delta t}{2}\bar{\mathbf{R}}^*(-1/3) \\ \frac{\Delta t}{2}\bar{\mathbf{R}}^*(1) \end{bmatrix} + \mathbf{w}^1 \begin{bmatrix} \bar{\mathbf{M}}(-1/3) \\ -\bar{\mathbf{M}}(1) \end{bmatrix} \tag{17}$$

and the unknown field variables can be determined by solving the linear system of equations. Comparing Eq. (17) to Eq. (11) shows that both forms are identical if Eq. (17) is multiplied by $2/\Delta t$ and if $t^n(-1/3) = t_{n1}$ as well as $t^n(1) = t_{n2}$ are taken into account. Hence, in the case of linear elasticity the fully implicit RUNGE-KUTTA scheme can be interpreted as a special continuous GALERKIN method, although the derivation strategy is a different one.

3 Conclusion and Outlook

In the present paper, the fundamental equation of linear elastodynamics is derived and its numerical realization is demonstrated. The focus is laid on the time discretization, using a two stage implicit RADAU IIA scheme as well es a continuous GALERKIN method with RADAU quadrature rule and LAGRANGE shape functions. It could be shown, that in contrast to [5], both time integrators yield, in the case of linear elastodynamics, the same system of linear equations and, hence, can be considered as identical. Nevertheless, the methods' derivation strategies are different, except that both use quadrature rules for approximating integrals.

Open questions, however, are whether this behavior can be transferred to the nonlinear case and if the identity between implicit RADAU IIA and continuous GALERKIN schemes can be shown for higher stage orders as well. A further issue, which has to be clarified is - what are the consequences, if systems of second order in time are treated directly without reduction to first order systems.

References

[1] P. Germain. The method of virtual power in continuum mechanics. Part 2: Microstructure. *SIAM Journal on Applied Mathematics* 25 (1973), pp. 556–576.

[2] T. Gleim and D. Kuhl. Higher order accurate discontinuous and continuous p-Galerkin methods for linear elastodynamics. *Zeitschrift für angewandte Mathematik und Mechanik* 93 (2013), pp. 177–194.

[3] E. Hairer and G. Wanner. *Solving Ordinary Differential Equations II*. Springer-Verlag, 2002.

[4] T. J. R. Hughes. *The Finite Element Method. Linear Static and Dynamic Finite Element Analysis*. Dover Publications, INC., 2000.

[5] B. L. Hulme. Discrete Galerkin and Related One-Step Methods for Ordinary Differential Equations. *Mathematics of Computation* 26 (1972), pp. 881–891.

[6] P. E. B. Jourdain. Note on an Analogue of Gauß' Principle of Least Constraints. *Quarterly Journal of Pure and Applied Mathematics* 40 (1909), pp. 153–157.

[7] R. T. Rockafellar. *Convex Analysis*. Princeton University Press, 1970.

[8] B. Schröder and D. Kuhl. Small strain plasticity: classical versus multifield formulation. *Archive of Applied Mechanics* 85 (2015), pp. 1127–1145.

[9] K. Steinhoff, U. Weidig, and N. Saba. Investigation of Plastic Forming Under the Influence of Locally and Temporally Variable Temperature and Stress States. In: *Functionally Graded Materials in Industrial Mass Production*. Ed. by K. Steinhoff, H.J. Maier, and D. Biermann. Auerbach: Verlag Wissenschaftliche Scripten, 2009.

[10] E. Zeidler. *Nonlinear Functional Analysis and its Applications III*. Springer Verlag, 1985.

[11] O. C. Zienkiewicz and R. L. Taylor. *The Finite Element Method*. Butterworth Heinemann, 2000.

**Proceedings of the 8th GACM Colloquium on Computational Mechanics
for Young Scientists from Academia and Industry
August 28–30, 2019 in Kassel, Germany**

Higher order reciprocal mass matrices via heuristic customization

Anton Tkachuk * [1]

[1] Institute for Structural mechanics, University of Stuttgart, Pfaffenwaldring 7, 70550 Stuttgart, Germany

Abstract. Customization of finite elements for low dispersion error through grid dispersion analysis requires a symbolic expansion of a determinant of a representative dynamic stiffness matrix. Such an expansion turns out to be a bottleneck for many practical cases with the size of the representative matrix greater than eight or ten even if the modern computer algebra systems are applied. In this contribution, we propose an alternative approach for low-dispersion customization that avoids explicit determinant expansion. This approach reduces the customization problem to a series of quadratic programming problems and consists of two main steps. First, the customization problem is reformulated as a rank minimization problem for the representative dynamic stiffness matrix evaluated at several discrete pairs of wavenumbers and frequencies. Second, the rank minimization problem is solved approximately via log-det heuristics. An example for customization of reciprocal mass matrices verifies the proposed approach.

Introduction

Several formulations of reciprocal mass matrices are proposed recently in [2, 3, 6, 8] and they contain naturally few free real-valued parameters. These free parameters are chosen to meet various performance goals for transient structural problems, like low dispersion error at acoustic branches and higher critical time step. The process of such parameter selection is called customization.The former goal is usually achieved through Grid Dispersion Analysis (GDA), i.e. obtaining relation between angular frequency and wavevector for a propagating wave in a given discretization. Necessary conditions for low dispersion error are imposed on the coefficients of Taylor expansion of the dispersion relation yielding a set of algebraic equations with respect to the free parameters. These favorable values of the free parameters increase the convergence order beyond the expected performance of the consistent mass matrix and it leads to so-called high order reciprocal mass matrices, see examples [6, 8] . Unfortunately, symbolic evaluation of the dispersion relation is not always possible because of a determinant of the representative dynamic stiffness matrix should be expanded symbolically in an intermediate step of GDA. Such a symbolic expansion is not tractable for many practical cases with the size of the representative matrix larger than eight or ten even if the modern computer algebra systems are applied. Therefore, an alternative approach is sought that avoids explicit expansion of the determinant.

A conceptually new way for dispersion customization is based on enforcing not full rank of the representative dynamic stiffness matrix instead of setting its determinant to zero [7]. Symbolic rank evaluation is still a hard problem. Therefore, it is solved for the matrix evaluated at few pairs of angular frequency and wavevector. The latter problem belongs to a class of well-studied affine rank minimization problems (ARMP) [1, 4] and it is solved numerically by log-det heuristic [1]. Affinity means that the underlying representative dynamic stiffness matrix linearly depends on the free parameters, which is the case for mentioned above formulations of reciprocal mass matrix.

1 Theoretical framework

Consider a representative dynamic stiffness matrix (RDSM)

$$\mathbf{K}_{\mathrm{dyn,rep}}(\mathbf{s},\omega,\mathbf{k}) = \mathbf{Q}\mathbf{C}^{\circ}(\mathbf{s})\mathbf{K}\mathbf{S}(\mathbf{k}) - \omega^2\mathbf{I}_{\mathrm{rep}} \tag{1}$$

*Corresponding author: tkachuk@ibb.uni-stuttgart.de ORCID iD: 0000-0001-8572-8532

for a given representative patch with dimension n_{rep}, wave vector $\mathbf{k}$ and angular frequency ω. $\mathbf{I}_{\text{rep}}$ denotes an identity matrix of size n_{rep} . RDSM depends on the stiffness matrix $\mathbf{K}$, a reciprocal mass matrix $\mathbf{C}^{\circ}$, filtering matrix $\mathbf{Q}$ and a shift matrix $\mathbf{S}(\mathbf{k})$ as shown in [7]. The latter two matrices describe topology and periodicity of the representative patch.

The proposed problem statement avoids explicit symbolic determinant expansion of RDSM. Instead it assumes some knowledge about the branches of the dispersion relation of the continuous model that should be accurately modeled. We select n_w frequency-wavevector pairs $(\omega_j, \mathbf{k}_j)$ $j = \overline{1, n_w}$ that satisfy the continuum dispersion relations and enforce the singularity of the matrix in Eq. (1) at these pairs in form

$$\operatorname{rank}\left(\mathbf{K}_{\text{dyn,rep}}(\mathbf{s}, \omega_j, \mathbf{k}_j)\right) < n_{\text{rep}}, \qquad j = \overline{1, n_w}. \tag{2}$$

Checking all n_w inequalities is still a hard problem. Instead a good solution is sought that minimizes the sum of the ranks of RDSM for all pairs j. Such a sum now defines the objective of the customization. The optimization problem has constraints on the plausible values for the free parameters. A convex subset $\mathbf{s} \in \mathcal{K}$ arises naturally in the construction of the reciprocal mass matrices, where all customization parameters are non-negative and the sum of them is less than one due to positive definiteness restriction on RMM suggested in [5, 8]. Having the objective function and constraints at hand, the problem statement can be given.

Problem statement. Given a set of pairs frequency, wavevector $(\omega_j, \mathbf{k}_j)$ with $j = \overline{1, n_w}$ and a representative dynamic stiffness matrix with dimension n_{rep} that linearly depend on a set of free parameters $\mathbf{s} = [s_j]$ with $j = \overline{1, n_p}$. Find the values of the free parameters $\mathbf{s}^*$ from a convex subset $\mathcal{K}$ such that

$$\mathbf{s}^* = \arg\min_{\mathbf{s} \in \mathcal{K}} \left[\operatorname{rank} \operatorname*{diag}_{j=\overline{1,n_w}} \left(\mathbf{K}_{\text{dyn,rep}}(\mathbf{s}, \omega_j, \mathbf{k}_j)\right) \right]. \tag{3}$$

Here, an operator diag denotes a constructor of a block diagonal matrix from a list of rectangular matrices.

The stated above ARMP is solved approximately by log-det heuristic [1]. A substantial difference to the original method is due complex entries of the RDSM matrices. The original rank minimization algorithm is valid for a real semi-definite matrices. To bring our problem to an appropriate shape, a matrix $\mathbf{X}$ is introduced with

$$\mathbf{X} = \operatorname*{diag}_{j=\overline{1,n_w}} \left(\mathbf{K}^{\text{H}}_{\text{rep,dyn}}(\mathbf{s}, \omega_j, \mathbf{k}_j)\mathbf{K}_{\text{rep,dyn}}(\mathbf{s}, \omega_j, \mathbf{k}_j)\right) \tag{4}$$

with superscript $\square^{\text{H}}$ being Hermitian transpose. The resultant matrix is a Hermitian positive semi-definite matrix, which is sufficient for the original log-det heuristics [1]. The rank of matrix $\mathbf{X}$ coincides with the objective function in Eq. (3), but dependency on the free parameters is quadratic. Now, a rank minimization problem is formulated for matrix $\mathbf{X}$ with

$$\mathbf{s}^* = \arg\min_{\mathbf{s} \in \mathcal{K}} \left(\operatorname{rank}(\mathbf{X})\right) \tag{5}$$

Rather than solving rank minimization problem, a log-det smooth surrogate for $\operatorname{rank}(\mathbf{X})$ is used

$$\mathbf{s}^* = \arg\min_{\mathbf{s} \in \mathcal{K}} \left(\log\det\left(\mathbf{X} + \delta\mathbf{I}\right)\right), \tag{6}$$

where $\delta > 0$ is a small regularization constant. Despite complex entries of the matrix $\mathbf{X}$, the determinant of Hermitian positive definite matrix $(\mathbf{X}+\delta\mathbf{I})$ is real and positive. Here, we follow the paper [1] and reduce the optimization to a series of quadratic programming problems. A Taylor expansion of the objective function in the vicinity of current value $\mathbf{X}_k$ is carried out

$$\log\det(\mathbf{X} + \delta\mathbf{I}) \approx \log\det(\mathbf{X}_k + \delta\mathbf{I}) + \operatorname{trace}\left(\mathbf{W}_k(\mathbf{X} - \mathbf{X}_k)\right), \tag{7}$$

where $\mathbf{W}_k = (\mathbf{X}_k + \delta\mathbf{I})^{-1}$ is a weighting matrix and it is computed numerically. The first term in the linearization does not influence extremum and it is never computed. The second term is quadratic with function with respect to customization parameters $\mathbf{s}$ and it is minimized using standard quadratic programming algorithm on a convex set $\mathcal{K}$. This brings us to the customization algorithm described in Figure 1.

1. Given regularization parameter $\delta > 0$, tolerance $\epsilon > 0$ and number of iteration maxiter
2. Initialize counter $k = 0$ and free parameters $\mathbf{s}_0 \in \mathcal{K}$,
3. Compute $\mathbf{X}_0 = \mathbf{X}(\mathbf{s}_0)$
4. Repeat until $k <$ maxiter
5. Compute weighting $\mathbf{W}_k = (\mathbf{X}_k + \delta\mathbf{I})^{-1}$
6. Solve QP: $\mathbf{s}_{k+1} = \arg\min_{\mathbf{s}\in\mathcal{K}} \operatorname{trace}(\mathbf{W}_k(\mathbf{X} - \mathbf{X}_k))$
7. Compute $\mathbf{X}_{k+1} = \mathbf{X}(\mathbf{s}_{k+1})$
8. If $||\mathbf{s}_{k+1} - \mathbf{s}_k||_2 < \epsilon$ then break;
9. Goto 4.

Figure 1. Algorithm for customization based on log-det heuristic proposed in [1].

2 Example

An example for the proposed customization approach is presented for a 6-node triangular acoustic element in 2D. Only uniform hexagonal mesh with element size h with a uniform isotropic material (phase velocity $c_0 = 1$, $\rho = 1.0$ and $K_{\text{bulk}} = 1.0$) is considered. An implementation of the proposed algorithm in computer algebra system *Maple* is used for all examples. Accuracy of the computations is controlled by assigning a value to the environment variable *Digits* to 40. Quadratic problems within algorithm are solved by a procedure *Minimize* of the package *Optimization*. We use the default options of the procedure.

This element has two free parameters for the reciprocal mass matrix $\mathbf{s} = [C_{21}, C_{22}]$ within a convex set $\mathcal{K} := \{C_{21} \geq 0;\, C_{22} \geq 0;\, 1 - C_{21} - C_{22} \geq 0\}$. GDA predicts an optimal low-frequency accuracy in case of hexagonal meshes for values $\mathbf{s}^* = [0.36, 0.41]$. These values provide fourth order of accuracy with small constants at sixth order error term in the acoustic branch. This case studies an over-determined set ($n_w > n_s$) with of four frequency-wavevectors pairs

$$h\mathbf{k}_1 = [0.1, 0], \quad h\mathbf{k}_2 = [0.2, 0], \quad h\mathbf{k}_3 = [0.05\sqrt{3}, 0.05], \quad h\mathbf{k}_4 = [0.1\sqrt{3}, 0.1], \quad \omega_j = \quad c_0|\mathbf{k}_j|, \tag{8}$$

with wavevectors along $x-$axis and in the direction tilted by 30° to $x-$axis. The size of the representative patch n_{rep} is four. Thus, the dimension of the matrix $\mathbf{X}$ is 16. We use a tolerance $\epsilon = 10^{-13}$, regularization $\delta = 3 \cdot 10^{-24}$, 101 iterations and initialization of customization parameters $\mathbf{s}_0 = [0.34, 0.45]$ in this case. The algorithm converges within eleven iterations to a solution

$$C_{21}^* = 0.3599102881, \qquad C_{22}^* = 0.4334932521 \tag{9}$$

with the lowest eigenvalues of RDSM below 10^{-15}.

3 Conclusions

A novel method for customization of reciprocal mass matrices is presented that avoids symbolic expansion of the determinant of the representative dynamic stiffness matrix. The customization problem is recast into a rank minimization problem for the representative dynamic stiffness matrix at discrete frequency-wavenumber pairs. The rank minimization problem is consequently solved via det-log heuristic [1]. The log-det heuristic provides a smooth surrogate function of the matrix rank whose minimum can be find by nonlinear programing algorithms. Here, this minimum is found by sequence of quadratic programming solves as suggested in [1]. An example verifies applicability of the approach to a customization of a 6-node triangular acoustic element in 2D.

Acknowledgments

The work of the author was supported by the Deutsche Forschungsgemeinschaft (DFG - German Research Foundation) Projektnummer 326748051 (TK 63/1-1).

References

[1] Maryam Fazel, Haitham Hindi, and Stephen P Boyd. Log-det heuristic for matrix rank minimization with applications to Hankel and Euclidean distance matrices. *Proceedings of the 2003 American Control Conference.* 3 (2003), pp. 2156–2162.

[2] José A González, R Kolman, SS Cho, CA Felippa, and KC Park. Inverse Mass Matrix via the Method of Localized Lagrange Multipliers. *International Journal for Numerical Methods in Engineering* (2017), pp. 1–24.

[3] Jose A. Gonzalez, Jan Kopačka, Radek Kolman, S. S. Cho, and K. C. Park. Inverse Mass Matrix for Isogeometric Explicit Transient Analysis via the Method of Localized Lagrange Multipliers. *International Journal for Numerical Methods in Engineering* 117 (2019), pp. 939–966.

[4] Karthik Mohan and Maryam Fazel. Iterative reweighted algorithms for matrix rank minimization. *Journal of Machine Learning Research* 13.Nov (2012), pp. 3441–3473.

[5] Anne-Kathrin Schaeuble. "Variationally Consistent Inertia Templates for Speed-up and Customization in Explicit Dynamics". PhD thesis. Stuttgart: Institut für Baustatik und Baudynamik der Universität Stuttgart, 2019.

[6] Anne-Kathrin Schaeuble, Anton Tkachuk, and Manfred Bischoff. Variationally consistent inertia templates for B-Spline and NURBS-based FEM: Inertia scaling and customization. *Computer Methods in Applied Mechanics and Engineering* 326 (2017), pp. 596–621.

[7] A Tkachuk. Customization of reciprocal mass matrices via log-det heuristic (submitted). *International Journal for Numerical Methods in Engineering* (2019).

[8] A. Tkachuk and M. Bischoff. Direct and sparse construction of consistent inverse mass matrices: general variational formulation and application to selective mass scaling. *International Journal for Numerical Methods in Engineering* 101.6 (2015), pp. 435–469.

**Proceedings of the 8th GACM Colloquium on Computational Mechanics
for Young Scientists from Academia and Industry
August 28–30, 2019 in Kassel, Germany**

Modeling the thermomechanical behavior of strain-induced crystallization in unfilled polymers

Serhat Aygün * and Sandra Klinge

Institute of Mechanics, TU Dortmund University, Leonhard-Euler-Strasse 5, 44227 Dortmund, Germany

Abstract. The crystallization in certain polymers, such as natural rubber, is a phenomenon manifesting itself as the natural reinforcement caused by high deformation. Starting from crystallization nuclei, polymer chains leave their natural entangled structure, stretch out, fold back and stack to regions with a regular structure. This property of polymers must be taken into consideration when planning manufacturing processes, since it significantly influences mechanical and thermal properties of the final product. In the present contribution, the described material behavior is simulated by a coupled thermomechanical model. The micromechanical continuum model, involving the degree of network regularity as an internal variable, has the following features: First, the thermodynamically consistent framework enables us to simulate the reduction of the crystallinity degree during the unloading phase by proposing a dissipation potential and by assuming a specific coupling condition between the inelastic deformations and the network regularity. Secondly, possible material microstructures are reconstructed on the basis of experimental data, and the evolution of the network regularity under the cyclic tensile load is visualized. In addition to the purely mechanical framework, the heat conduction equation is solved in order to simulate the temperature evolution. The resulting, thermomechanically coupled system of equations is solved in a monolithic way. Finally, selected examples for unfilled natural rubber compare the numerically simulated effective material response with the experimental data.

Introduction

The phenomenon of strain-induced crystallization (SIC) in polymers is characterized by the fact that, under the influence of high strains, polymer chains partially form a regular structure that resembles a crystalline pattern. Under the increasing strain, the evolution of the microstructure causes the strengthening of material and changes the reaction to the macroscopic mechanical and thermal influences. Experimental data for cyclic uniaxial tests show that the stress response builds a hysteresis which indicates that the process has a dissipative character. Moreover, the results show that crystallization starts at a stretch of about 430%. At the stretch of 600% the crystallinity degree reaches 15%. The higher values of crystallinity can be achieved if the higher stretches are applied. However, additional inelastic processes occur simultaneously to the SIC in that case. It is also worth mentioning that heat produced by the formation of crystalline regions leads to an increase in temperature, whereas the regression of crystalline regions during the unloading phase yields a temperature decrease. Accordingly, the temperature diagram has an analogous form to the diagram of crystallinity degree as shown in [2].

Most of the models focusing on the mechanical modeling of polymers use the Langevin expression for the free energy as a basis [3, 6]. However, the model presented here treats a polymer affected by the strain induced crystallization as a heterogeneous medium consisting of regions with a different degree of network regularity. The model proposed is thermodynamically consistent. It is based on the Arruda-Boyce assumption for the Helmholtz free energy and on the assumption for the dissipation potential [1]. The free energy primarily includes terms due to elastic deformation and temperature. The external variables are temperature and deformation, whereas the inelastic deformations and degree of the network regularity are internal variables. Their evolution equations are derived according to the minimum principle of the dissipation potential [4]. In addition to the balance of linear momentum describing the mechanical part, the heat equation is used to simulate the temperature response due to the crystallization.

*Corresponding author: serhat.ayguen@tu-dortmund.de

1 Micromechanical modeling of SIC in polymers

The theory of finite deformations is the suitable framework for the simulation of polymers. Typical of this theory, the modeling of dissipative processes requires a multiplicative decomposition of the deformation gradient into an elastic part and an inelastic part $\boldsymbol{F} = \boldsymbol{F}^{\mathrm{e}} \cdot \boldsymbol{F}^{\mathrm{c}}$. In our case, $\boldsymbol{F}^{\mathrm{c}}$ represents the deformations caused by the crystallization. However, the multiplicative decomposition alone is not enough to describe the phenomena such as the formation and growth of crystalline regions. For this purpose, an internal variable is introduced denoting the regularity of the polymer chain network χ. This variable takes values from range [0,1], where 0 corresponds to a totally amorphous polymer and 1 to completely crystalline regions. The minimum principle of the dissipation potential is pursued in order to derive the evolution laws obeying the second thermodynamic law. According to this theory, the Lagrange function involves the elastic power and dissipation potential $L = \dot{\Psi} + \Delta$. In this work, the Helmholtz energy $\Psi(\boldsymbol{F}^{\mathrm{e}}, \Theta) = \Psi^{\mathrm{e}}(\boldsymbol{F}^{\mathrm{e}}) + \Psi^{\Theta}(\Theta)$ consists of an elastic part depending on elastic deformations and a purely temperature dependent part, where Θ is the temperature. We assume the free energy of an Arruda-Boyce material for the elastic part with a split into a volumetric and a deviatoric contribution

$$\begin{aligned} &\Psi^{\mathrm{e}}(\boldsymbol{F}^{\mathrm{e}}) = \Psi^{\mathrm{e}}(J^{\mathrm{e}}, \boldsymbol{C}^{\mathrm{e}}) = K\,U(J^{\mathrm{e}}) + \frac{\bar{\mu}}{2}\left[\left(\bar{I}_1 - 3\right) + \frac{m}{10}\left(\bar{I}_1^2 - 9\right) + \frac{11\,m^2}{525}\left(\bar{I}_1^3 - 27\right)\right] , \\ &U(J^{\mathrm{e}}) = \frac{1}{4}\left((J^{\mathrm{e}})^2 - 1 - 2\ln(J^{\mathrm{e}})\right) \;, \quad \bar{I}_1 = J^{e^{-\frac{2}{3}}}\mathrm{tr}(\boldsymbol{C}^{\mathrm{e}}) \;, \quad \bar{\mu} = \frac{\mu}{1 + \frac{3}{5}m + \frac{99}{175}m^2} \;, \quad m = \frac{1}{\lambda_m^2} \;. \end{aligned} \tag{1}$$

In the chosen constitutive law, $\boldsymbol{C}^{\mathrm{e}} = (\boldsymbol{F}^{\mathrm{e}})^T \cdot \boldsymbol{F}^{\mathrm{e}}$ represents the elastic right Cauchy-Green deformation tensor, $J^{\mathrm{e}} = \det(\boldsymbol{F}^{\mathrm{e}})$ is the elastic Jacobian, K is the bulk modulus, μ denotes the shear modulus and λ_m is the limiting network stretch. We furthermore assume the dissipation potential and the evolution law for variable B

$$\Delta = (A + B)\,|\dot{\chi}| \;, \quad \dot{B} = \frac{c}{f(\chi)}\mathrm{sgn}\left(\dot{\overline{\|\boldsymbol{M}^{\mathrm{dev}}\|}}\right)|\dot{\chi}| \;, \quad \boldsymbol{M}^{\mathrm{dev}} = \boldsymbol{M} - \frac{\mathrm{tr}(\boldsymbol{M})}{3}\boldsymbol{I} \;, \tag{2}$$

where the material constant A is the crystallization limit, being a threshold for the start of the regularity evolution and B determines its evolution depending on the stress state. Symbol $\boldsymbol{M}^{\mathrm{dev}}$ denotes the deviatoric part of the Mandel stress tensor $\boldsymbol{M} = \boldsymbol{F}^{\mathrm{e}T} \cdot \partial\Psi/\partial\boldsymbol{F}^{\mathrm{e}}$. In the present model, the regularity evolution is favored in regions with a high value of the regularity degree which is achieved by introducing function $f(\chi)$. Finally, the evolution of the $\boldsymbol{F}^{\mathrm{c}}$ is coupled with the evolution of regularity χ through the relationship for velocity gradient $\boldsymbol{L}^{\mathrm{c}}$

$$\boldsymbol{L}^{\mathrm{c}} = \dot{\boldsymbol{F}}^{\mathrm{c}} \cdot \boldsymbol{F}^{\mathrm{c}\,-1} = k\,\dot{\chi}\,\mathrm{sgn}\left(\dot{\overline{\|\boldsymbol{M}^{\mathrm{dev}}\|}}\right)\frac{\boldsymbol{M}^{\mathrm{dev}}}{\|\boldsymbol{M}^{\mathrm{dev}}\|} \;, \tag{3}$$

where k is a positive proportionality constant. The particularity of the assumption (3) is the introduction of the signum function depending on the evolution of the Mandel stress tensor. This enables the regularity to increase during the loading phase and to subsequently decrease during the unloading phase.

2 Thermodynamic consistency and thermal modeling of SIC

The study of thermal effects starts with the consideration of the dissipation inequality which is expressed by using the Clausius-Duhem formalism

$$D = -\dot{\Psi} - \eta\,\dot{\Theta} + \frac{1}{\rho_0}\boldsymbol{P} : \dot{\boldsymbol{F}} - \frac{1}{\rho_0\,\Theta}\boldsymbol{q}_0 \cdot \nabla_{\boldsymbol{X}}\Theta \geq 0 \;. \tag{4}$$

This formulation of the second thermodynamic law depends on the density in reference configuration (ρ_0), the first Piola-Kirchhoff stress tensor ($\boldsymbol{P}$), the entropy (η) and the heat flux vector ($\boldsymbol{q}_0$). The time derivative of the free energy now reads

$$\dot{\Psi} = \frac{\partial\Psi}{\partial\boldsymbol{F}^{\mathrm{e}}} : \dot{\boldsymbol{F}}^{\mathrm{e}} + \frac{\partial\Psi}{\partial\Theta}\dot{\Theta} \;, \quad \dot{\boldsymbol{F}}^{\mathrm{e}} = \dot{\boldsymbol{F}} \cdot \boldsymbol{F}^{\mathrm{c}\,-1} - \boldsymbol{F}^{\mathrm{e}} \cdot \dot{\boldsymbol{F}}^{\mathrm{c}} \cdot \boldsymbol{F}^{\mathrm{c}\,-1} \;, \tag{5}$$

such that Eq. (4) is reformulated as

$$D = \left(\frac{1}{\rho_0}\boldsymbol{P} - \frac{\partial\Psi}{\partial\boldsymbol{F}^{\mathrm{e}}} \cdot \boldsymbol{F}^{\mathrm{c}\,-T}\right) : \dot{\boldsymbol{F}} + \boldsymbol{M} : \boldsymbol{L}^{\mathrm{c}} - \left(\frac{\partial\Psi}{\partial\Theta} + \eta\right)\dot{\Theta} - \frac{1}{\rho_0\,\Theta}\boldsymbol{q}_0 \cdot \nabla_{\boldsymbol{X}}\Theta \geq 0 \;. \tag{6}$$

Inequality (6) yields two consequences: Firstly, the constitutive laws for the the first Piola-Kirchhoff stress tensor $\boldsymbol{P} = \rho_0\, \partial\Psi/\partial\boldsymbol{F}^{\mathrm{e}} \cdot \boldsymbol{F}^{\mathrm{c}-T}$ and the entropy $\eta = -\partial\Psi/\partial\Theta$ are obtained by assuming that each expression in parentheses is equal to zero. Secondly, the dissipation includes a term due to the crystalization (D_{SIC}) and a term due to heat conduction (D_{cond}). As usual, the positivity of each term is required separately:

$$D_{\mathrm{SIC}} + D_{\mathrm{cond}} \geq 0\ , \quad D_{\mathrm{SIC}} = \boldsymbol{M} : \boldsymbol{L}^{\mathrm{c}} = q_\chi\, \dot{\chi} \geq 0\ , \quad D_{\mathrm{cond}} = -\frac{1}{\rho_0\, \Theta} \boldsymbol{q}_0 \cdot \nabla_{\boldsymbol{X}} \Theta \geq 0\ . \tag{7}$$

Dissipation D_{SIC} implies that the regularity evolution and the corresponding thermodynamic driving force (q_χ) have the same sign, whereas the classic Fourier's conduction law is introduced as a solution of inequality (7 c). The thermal problem is described by the local form for the balance of energy

$$\dot{\Psi} + \eta\, \dot{\Theta} + \Theta\, \dot{\eta} + \frac{1}{\rho_0} \mathrm{Div}(\boldsymbol{q}_0) = \frac{1}{\rho_0} \boldsymbol{P} \colon \dot{\boldsymbol{F}} + r_\Theta\ , \quad \dot{\eta} = -\frac{\partial^2 \Psi}{\partial \Theta^2} \dot{\Theta}\ , \tag{8}$$

where r_Θ is the heat source. Finally, the insertion of Eq. (5) into Eq. (8) yields the heat conduction equation

$$c_d\, \dot{\Theta} + \frac{1}{\rho_0} \mathrm{Div}(\boldsymbol{q}_0) = r_\Theta + q_\chi\, \dot{\chi}\ , \quad c_d = -\Theta \frac{\partial^2 \Psi}{\partial \Theta^2}\ , \tag{9}$$

determining the temperature change caused by the SIC. At this stage, our model assumes the heat capacity (c_d) to be constant during the process.

3 Numerical example

The material model for SIC is implemented into the FE program FEAP [7]. In order to illustrate its application, a uniaxial tensile test for a square sample with the dimensions 100×100 nm is chosen. The lower and the upper boundaries are constrained and a gradually increasing displacement within the range [0, 250 mm] is applied at each of these boundaries in the normal direction. Thereafter, the specimen is gradually unloaded. The total loading time amounts to 10 s and the time increment is $\Delta t = 1\mathrm{e}{-3}$ s. The regularity of the polymer network in the starting configuration has random initial values within the range [0, 1e−3], which simulates the nuclei of the crystalline regions (Fig. 1 a). During the loading phase the regularity increases and its growth is favored in regions with the higher initial values. This is achieved by introducing function $f(\chi)$ in the evolution of B (Eq. (2 b)). Figure 1 b shows the state of the network regularity in the final loading step. At this stage, the crystallinity degree is about 18 %. Subsequently, the crystalline regions decrease with a lower rate during the unloading phase (results not shown here). Finally, the material becomes entirely amorphous.

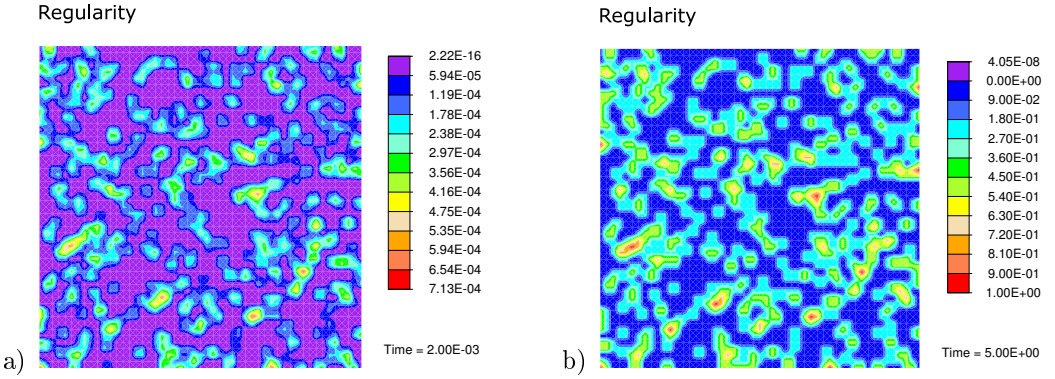

Figure 1. **a**) The initial microstructure with a random distribution of the regularity. **b**) Distribution of the regularity in the final loading step. The applied material parameters are: $K = 5\mathrm{e}8$ Pa, $\mu = 4\mathrm{e}5$ Pa, $\lambda_m = 3$, $k = 7\mathrm{e}{-2}$, $A = 1\mathrm{e}6$ Pa, $c = 2\mathrm{e}5$ Pa and $c_d = 2.2\mathrm{e}5$ J/(kg K).

The temperature distributions during the loading phase at a stretch of $\lambda = 5$ and in the last loading step at a stretch of $\lambda = 6$ are shown in Fig. 2. The temperature development behaves similarly to the regularity evolution: The highest temperature occurs in the completely crystallized regions, whereas the temperature in the amorphous regions hardly changes during the process.

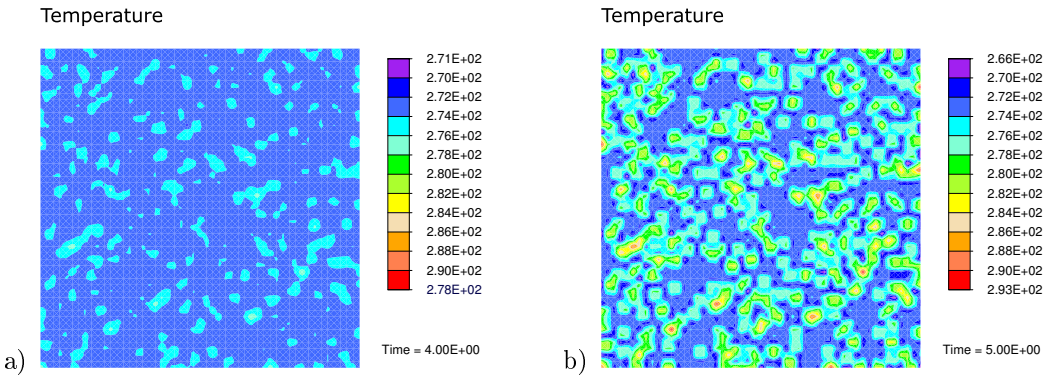

Figure 2. **a**) Temperature distribution (in Kelvin) during loading at a stretch of $\lambda = 5$. **b**) Temperature distribution (in Kelvin) in the final loading step. The applied material parameters are the same as in Fig. 1.

4 Conclusions

The present work shows a thermodynamically consistent model based on the assumptions for the free energy and dissipation potential. The main advantages of the approach are: i) It enables the simulation of the formation and development of crystalline regions during loading and degradation of crystalline regions during unloading. ii) The microstructure evolution is visualized, which is not possible with experimental techniques. iii) The heat production due to the SIC and the related temperature change can be observed. iv) The model is applicable for implementation within the multiscale concept [5] in order to study the influence of crystalline regions on the effective material behavior of polymers. The proposed model is suitable for further extensions and offers a good basis for simulating effects, such as damage, crack propagation and coupling with plastic deformations. In all these cases, a comparison with additional experimental results would be necessary for a reliable determination of material parameters.

Acknowledgments

The authors, S. Aygün and S. Klinge, gratefully acknowledge the financial support of the German Research Foundation (DFG), research grant No. 324689375.

References

[1] S. Aygün and S. Klinge. Study of the microstructure evolution caused by the strain-induced crystallization in polymers. *PAMM* 18 (2018), e201800224.

[2] N. Candau, R. Laghmach, L. Chazeau, J.-M. Chenal, C. Gauthier, T. Biben, and E. Munch. Influence of strain rate and temperature on the onset of strain induced crystallization in natural rubber. *Eur. Polym. J.* 64 (2015), pp. 244–252.

[3] R. Dargazany, V. N. Khiêm, E. A. Poshtan, and M. Itskov. Constitutive modeling of strain-induced crystallization in filled rubbers. *Phys. Rev. E* 89 (2014), p. 022604.

[4] K. Hackl and F. D. Fischer. On the relation between the principle of maximum dissipation and inelastic evolution given by dissipation potentials. *Proc. R. Soc. A* 464 (2008), pp. 117–132.

[5] S. Klinge and K. Hackl. Application of the multiscale FEM to the modeling of nonlinear composites with a random microstructure. *Int. J. Multiscale Com.* 10 (2012), pp. 213–227.

[6] S. J. Mistry and S. Govindjee. A micro-mechanically based continuum model for strain-induced crystallization in natural rubber. *Int. J. Solids Struct.* 51 (2014), pp. 530–539.

[7] O. C. Zienkiewicz, R. L. Taylor, and J. Z. Zhu. *The Finite Element Method: Its Basis and Fundamentals, 7th edition.* Elsevier Science, Butterworth-Heinemann, 2013.

**Proceedings of the 8th GACM Colloquium on Computational Mechanics
for Young Scientists from Academia and Industry
August 28–30, 2019 in Kassel, Germany**

Crystallization of semi-crystalline polymers simulated with a cellular automaton

Tobias Daniel Horn * [1], Hans Wulf[1] and Jörn Ihlemann[1]

[1]Chair of Solid Mechanics, Chemnitz University of Technology, Reichenhainer Str. 70, D-09126 Chemnitz, Germany

Abstract. During crystallization of semi-crystalline polymers from melt, structures evolve at different scales. When crystallized from viscous melts or solutions at moderate undercooling, the polymer forms lamellae by chain folding at the nanometer scale. These lamellae grow predominantly in radial direction and branch irregularly by non-crystallographic branching. By this, spherulites are formed at the micrometer scale.
In this contribution, a simulation model based on a concept of isothermal crystallization of semi-crystalline polymers is derived. To this end, the polymer chains are divided into four different categories concerning their mobility. For these categories, different rules for diffusion and conversion are defined, which cover the physical processes the chains experience during crystallization. With these rules, the crystallization of the polymer to lamellae is modeled. The simulation is realized by using a cellular automaton, which is a natural choice to model growth processes due to its local character.

Introduction

Crystallization in polymer systems, which transfers the entangled melt into a semi-crystalline state, is a process of primary importance and has been studied since long time. Over the years various conceptual models have been proposed [1].

In the multistage model, Strobl [2, 3] categorize the crystallization process into three different phases: the amorphous phase, the mesomorphic layers and the crystal. In the amorphous phase the polymer chains form irregular and entangled coils with a high inner mobility. During crystallization the polymer chains rearrange and form ordered regions called lamellae, where the polymer chains are both aligned and folded. Here, the chains are fixed due to physical bonds. However, crystallization is not a discrete process. In front of the lamellae (in the growing direction) the amorphous phase rearrange and a thin layer with a mesomorphic inner structure forms between the crystal front and the melt. Within this phase the polymer chains still have an enhanced inner mobility, but the structure of the crystalline phase is already formed.

1 Simulation Model

The crystallization of semi-crystalline polymers is simulated by using a cellular automaton. Therefore, at each cell of the automaton the polymer is differentiated into four phases. For this the mobility of the chains is taking into consideration. In the *amorphous phase* the polymer chains have a high inner mobility. In front of the lamellae the polymer chains rearrange, physical bonds are evolved and the mobility of the chains is restricted. According to the multistage model in this phase the polymer crystallizes under formation of blocks. Hence, the phase is called *blocked phase*. In the *crystalline phase* there are a maximum of physical bonds and for this the mobility of the polymer chains is limited to a minimum. Furthermore, due to chain folding there is another phase at the lateral side of the lamellae, where at least one part of the polymer chain is restricted in his mobility (because the chain end is integrated in the blocked phase or the crystal phase). Therefore the phase is called the *trapped phase*. The phases are visualized in figure 1. As e.g. shown in figure 1 c) a polymer chain can belong to more than one phase.

*Corresponding author: tobias.horn@mb.tu-chemnitz.de ORCID iD: 0000-0002-7396-9563

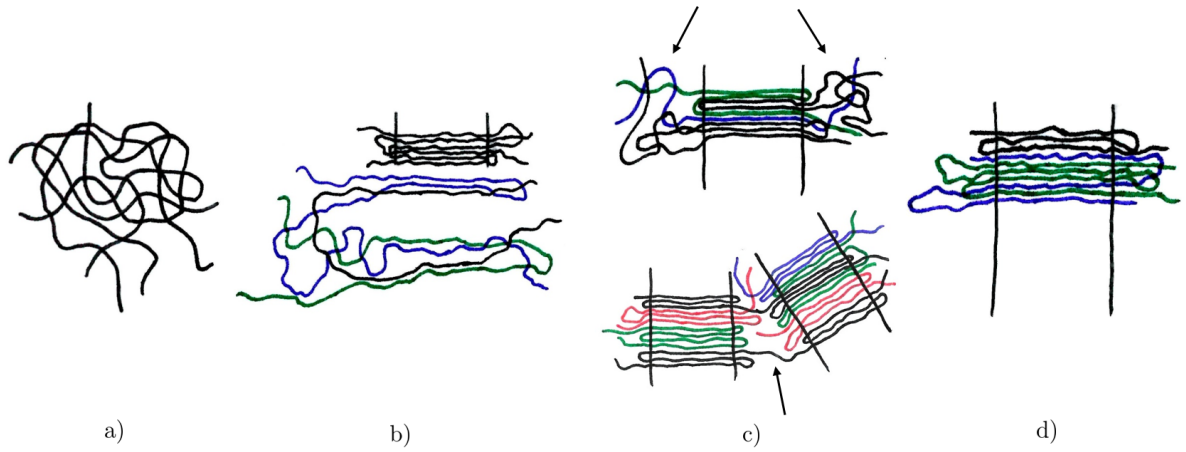

Figure 1. Model concept of the four phases in the polymer during crystallization. In the figures the polymer chains within these phases are visualized. Figure a) shows the amorphous phase, b) the blocked phase, c) the trapped phase (marked with arrows) next to the crystalline phase, which is also shown in d).

The mobility of the phases is modeled by using Fick's second law of diffusion (anisotropic and for multicomponent systems). Due to their low mobility, in the blocked phase and the crystalline phase the diffusion is suppressed. The remaining dimensionless diffusion coefficients are defined at every cell of the automaton by using the two parameters $\bar{D}_a$ and $\bar{D}_t$

$$\begin{bmatrix} D_a & D_{at} \\ D_{ta} & D_t \end{bmatrix} = \begin{bmatrix} \bar{D}_a & \bar{D}_a\bar{D}_t \\ \bar{D}_a\bar{D}_t & \bar{D}_t \end{bmatrix} (1-\rho)\,, \tag{1}$$

where ρ is the local density.

During crystallization the chains convert from the amorphous phase to the other phases. This is realized by a Markov chain as shown in figure 2. The related transition matrix is given in equation (2). The matrix elements are locally defined at every cell of the cellular automaton and depend on the state of the Moore region around the cell.

$$[M] = \begin{bmatrix} M_{aa} & M_{ab} & M_{at} & 0 \\ M_{ba} & M_{bb} & 0 & M_{bc} \\ M_{ta} & 0 & M_{tt} & 0 \\ 0 & 0 & 0 & M_{cc} \end{bmatrix} \tag{2}$$

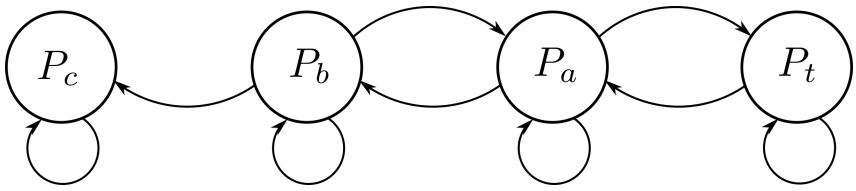

Figure 2. Markov chain with all possible conversions in one time step. P_a, P_b, P_t and P_c are the percentages of the several phases of the polymer at one cell of the cellular automaton.

2 Simulation Results

With these rules for the cellular automaton the crystallization is simulated. Here, the thickness of the lamellae h_L is a model parameter and the growing direction $\alpha = 25°$ is set as a constant parameter. For this simulation with 200 time steps and a cellular automaton with 3600 cells the calculation time was $15s$.

In figure 3 the distribution of the crystalline phase is shown at the cells of the cellular automaton. Therein, the gray vertical and horizontal lines mark the borders of the cells. Grayscale is used to indicate the

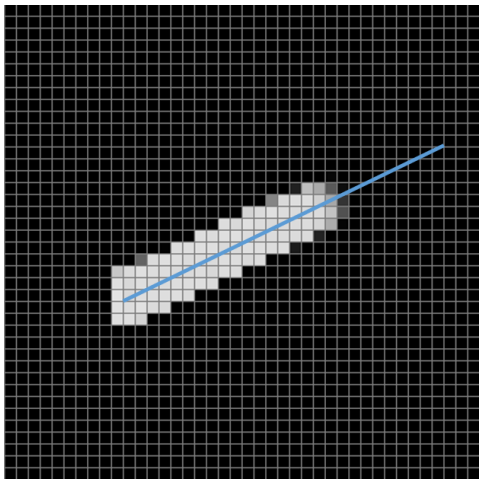

Figure 3. Distribution of the crystalline phase after 200 time steps. At the grayscale black indicates $P_c = 0$ and white $P_c = 1$. The marked path is for the evaluation in figure 4

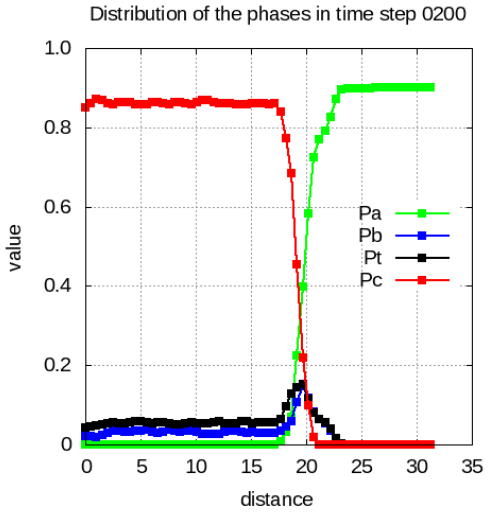

Figure 4. Distribution of the several phases on the path marked in figure 3 after 200 time steps

distribution of the crystalline phase, where black indicates $P_c = 0$ and white $P_c = 1$. In figure 4 the distribution of the several phases in the crystal, at the front of the crystal and in the amorphous phase is shown. At the front of the crystal, the amorphous phase is converted into the blocked phase and the trapped phase, as claimed in section 1. In the crystal the amorphous phase is not present, but still the blocked and trapped phases. They are interpreted as crystal defects.

3 Conclusion

Based on the multistage model of Strobl [2, 3] the crystallization process is modeled by using a cellular automaton at the scale of the lamellae. The basic principles of the simulation model was presented and the result of an easy simulation of the crystallization of a single lamellae was shown.

Acknowledgments

The authors gratefully acknowledge the German Research Foundation (Deutsche Forschungsgemeinschaft, DFG) for supporting this work.

References

[1] Joseph D Menczel. The rigid amorphous fraction in semicrystalline macromolecules. *Journal of thermal analysis and calorimetry* 106.1 (2011), pp. 7–24.

[2] G Strobl. A thermodynamic multiphase scheme treating polymer crystallization and melting. *The European Physical Journal E* 18.3 (2005), pp. 295–309.

[3] Gert R Strobl. *The physics of polymers*. Springer, 2007.

**Proceedings of the 8th GACM Colloquium on Computational Mechanics
for Young Scientists from Academia and Industry
August 28–30, 2019 in Kassel, Germany**

Towards thermo-viscoelastic experimental characterisation and numerical modelling of VHB polymer

Mokarram Hossain*[1] and Zisheng Liao[2]

[1]Zienkiewicz Centre for Computational Engineering, Swansea University, UK
[2]School of Civil Engineering and Transportation, South China University of Technology, China

Abstract. In this study, we have presented a wide variety of temperature experiments of a commercially available VHB polymer ranging from -30°C to 80°C at various strain rates and stretch levels under homogeneous deformation and temperature fields. The study demonstrates a pronounced influence of the temperature field on mechanical responses of the VHB polymer. After a wide range of experiments, we have proposed a finite-strain thermo-viscoelastic constitutive model where a non-linear evolution law is devised based on the classical concept of multiplicative decomposition of the deformation gradient. Then, decoupled one-dimensional equations are fitted to identify relevant material parameters appearing in the model. The thermo-viscoelastic model validation shows its excellent capability to predict the experimental results.

1 Introduction

The so-called Very High Bond (VHB in short) becomes an ideal polymer for producing prototypes of electric field-responsive functional materials, e.g., actuators in soft robotics, stretch sensors in wearable devices, and energy harvesters from ambient motions. The commercially available polymer comes up with several thicknesses. For this study, we have selected VHB 4905 thanks to its wide use as a common material for dielectric elastomers. The acrylic-based polymer is highly deformable, extremely viscoelastic, and highly sensitive to temperature fluctuations. Hence, in order to understand its mechanical and electro-mechanical behaviours, extensive experiments need to be conducted to demonstrate temperature dependencies in addition to rate-dependences. The aims of the current work are twofolds. On the one hand, a complete thermo-viscoelastic mechanical characterization of VHB 4905 is presented considering some standard experiments suitable for viscoelastic polymers at large strains, e.g. loading-unloading cyclic tests, quasi-static tests at very slow strain rates, single-step relaxation tests, and multi-step relaxation tests under homogeneous thermo-mechanical loads. On the other hand, a thermodynamically consistent phenomenologically-motivated geometrically non-linear thermo-viscoelastic material model is developed for VHB polymers. At this stage, all experiments are performed under a homogeneous deformation, both mechanical and thermal loads. Hence, the three-dimensional thermo-viscoelastic model is decoupled to a set of one-dimensional equations. After that, all relevant parameters appearing in the model are identified by a simultaneous optimisation routine. Once all necessary material parameters are identified, the model fits well with the data that are not included during the identification process, see [1, 2].

2 Experimental study

In order to characterize viscoelastic behaviours of the VHB polymer, at first cyclic experiments are carried out with regard to different deformations, strain rates, and temperatures. In these experiments, we adopt three different deformation levels, i.e., 100%, 200%, and 300%, three different strain rates, i.e., 0.1 /s, 0.05 /s and 0.03 /s, and eight different temperature profiles, i.e. 80°C, 60°C, 40°C, 20°C, 0°C, -20°C, -30°C and -40°C. Results are presented in Figs 1 and 2. In Fig 1, temperature-dependent results are presented ranging from -20°C to + 60°C temperatures while experiments are conducted at a strain rate of 0.1/s with deformations of 300%. These graphs indicate that at all tested temperatures, a larger deformation

*Corresponding author: mokarram.hossain@swansea.ac.uk ORCID iD: ORCID:https://orcid.org/0000-0002-4616-1104

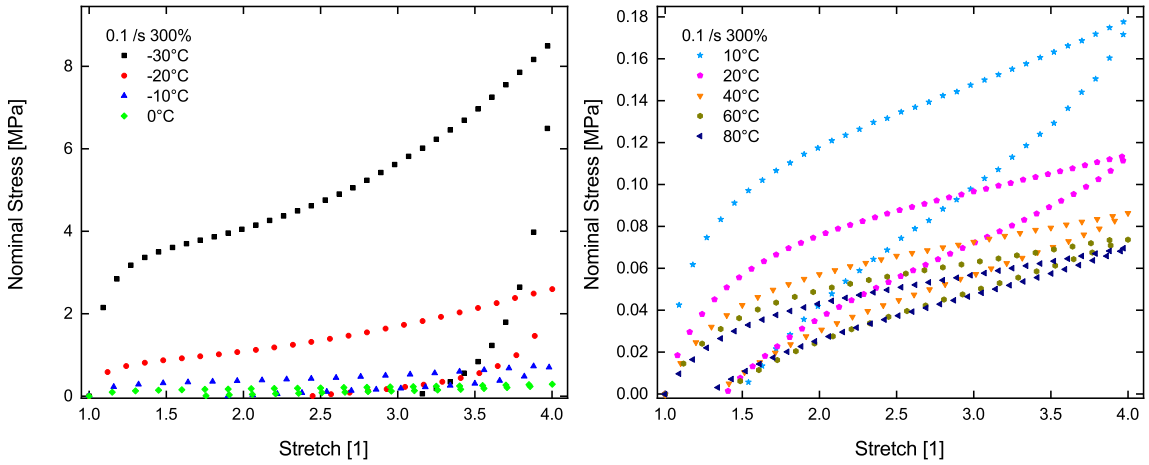

Figure 1. Temperature-dependent stress responses under a wide range of temperature profile where experiments are conducted at 300% deformation and 0.1 /s strain rate, (Left) below 0°C, (Right) above 0°C. All results clearly reveal that the temperature field has a major role in changing mechanical stress responses of VHB

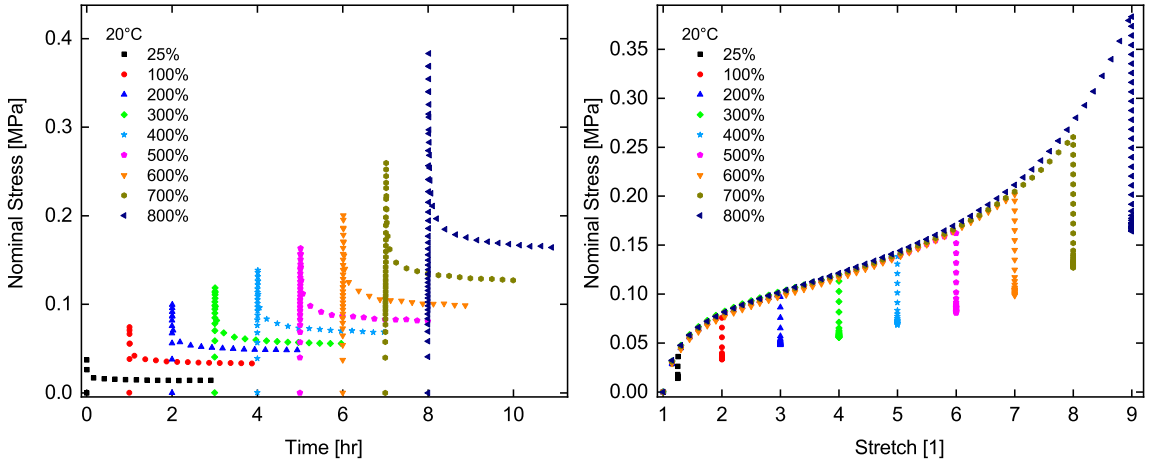

Figure 2. (Left) Single step relaxation test results from 25% to 800% deformations. (Right) Stress-strain curves of multi-step tests depicting the amount of stress relaxations during the holding times

results in a bigger hysteresis with a larger residual strain. Moreover, it is clear that the nonlinearity of the stress-stretch response is getting stronger from a higher to a lower temperature at the same strain. These results also demonstrate that the VHB 4905 becomes less dissipative with an increasing positive temperature.

Single-step relaxation experiments are performed on tensile specimens from 100% to 800% deformations with an internal of 100% deformations. For a better demonstration purpose, the stress history curves are shifted along the time axis to avoid overlapping of the curves, as is shown in Fig 2(left). From the results, it can be observed that with the time evolving, the stress attenuates to an equilibrium level. However, at a larger strain, it takes a longer time to relax. This implies that at a larger deformation level, more relaxation time is required to obtain an equilibrium stress. Another way to identify the equilibrium stress of a polymeric material is the multi-step relaxation tests. Similar to the single step relaxation experiments, the specimen is stretched to a certain strain level and is allowed to relax for a three-hour period before the specimen is re-loaded to the next strain level instead of being unloaded. In this case, a multi-step relaxation experiment is carried out at an interval of 100%, 300%, 500% , and 700%. As is shown in Fig 2(right) the single step relaxation tests and the corresponding steps of the multi-step relaxation tests share similar relaxation history curves with very close relaxed stresses (equilibrium stresses).

3 Numerical modelling

In uniaxial tests, the specimen is elongated only in one direction, i.e., $\lambda_1 = \lambda$ while the other two directions are free to move. From the incompressibility condition at fixed temperature, i.e., $\det\boldsymbol{F} = \det\bar{\boldsymbol{F}} = \det\boldsymbol{F}_v = \det\boldsymbol{F}_\Theta = 1$, i.e., $\lambda_1\lambda_2\lambda_3 = 1$ and the assumption of symmetry the complementary principal stretches follow as $\lambda_2 = \lambda_3 = \lambda^{-1/2}$. Therefore, the complete deformation gradient reads $\boldsymbol{F} = \{\lambda; \lambda^{-1/2}; \lambda^{-1/2}\}$. Note that since the elongation is only in one direction, the specimen will contract in the transversal directions and due to the stress-free boundary conditions, both Piola stresses P_2 and P_3 are zero and only the Piola stress P_1 needs to be determined. The elastic part of the Piola stress is obtained:

$$P^e = \left[\frac{\Theta}{\Theta_0} + g^e(\Theta)\right]\left[2a + 8b[2\lambda^{-1} + \lambda^2]^3 + c[1 + 2\lambda^3]^{-\frac{1}{2}}\right]\left[\lambda - \lambda^{-2}\right] \tag{1}$$

for details, see [1, 3, 4]. Note that since we have observed negligible influence of the temperature on the equilibrium response during our study, $g^e(\Theta) = 1 - \frac{\Theta}{\Theta_0}$ is taken here. Now, the viscous part of the stress for a single Maxwell element is formulated :

$$\begin{aligned} P^v &= \left[\frac{\Theta}{\Theta_0} + g_1^v(\Theta)\right]\sum_{j=1}^{2} P^{v,j} + \left[\frac{\Theta}{\Theta_0} + g_2^v(\Theta)\right]\sum_{j=3}^{5} P^{v,j} \\ &= \left[\frac{\Theta}{\Theta_0} + g_1^v(\Theta)\right]\sum_{j=1}^{2} 6c_4^j\left[\frac{\lambda^2}{[\lambda_v^j]^2} + \frac{2\lambda_v^j}{\lambda} - 3\right]^2\left[\frac{\lambda}{[\lambda_v^j]^2} - \frac{\lambda_v^j}{\lambda^2}\right] \\ &+ \left[\frac{\Theta}{\Theta_0} + g_2^v(\Theta)\right]\sum_{j=3}^{5} 2c_5^j\left[\frac{\lambda}{[\lambda_v^j]^2} - \frac{\lambda_v^j}{\lambda^2}\right], \end{aligned} \tag{2}$$

where λ_v^2 is the principal stretch of the internal variable. Similar to the one-dimensional formulation of the total stress, the first evolution law is derived:

$$\dot{\overline{\lambda_v^j}} = \frac{4}{\tau_1^j}\left[\frac{\lambda^2}{[\lambda_v^j]^2} + \frac{2\lambda_v^j}{\lambda} - 3\right]^2\left[\frac{\lambda^2}{\lambda_v^j} - \frac{[\lambda_v^j]^2}{\lambda}\right], \qquad j = 1, 2 \tag{3}$$

and the one-dimensional form of the second evolution equation is

$$\dot{\overline{\lambda_v^j}} = \frac{4}{3\tau_2^j}\left[\frac{\lambda^2}{\lambda_v^j} - \frac{[\lambda_v^j]^2}{\lambda}\right], \qquad j = 3 \cdots 5. \tag{4}$$

Now both the scalar-valued differential equations need to be discretized by a suitable integration scheme. Discretizing by the unconditionally stable implicit Euler-backward integration scheme, the differential equation for the internal variable λ_v^j for a single Maxwell element yields

$$\begin{aligned} \lambda_v^j &= \lambda_v^{j,n} + \frac{4\Delta t}{3\tau_2^j}\left[\frac{\lambda^2}{\lambda_v^j} - \frac{[\lambda_v^j]^2}{\lambda}\right], \\ f(\lambda_v^j) &= \lambda_v^j - \lambda_v^{n,j} - \frac{4\Delta t}{3\tau_2^j}\left[\frac{\lambda^2}{\lambda_v^j} - \frac{[\lambda_v^j]^2}{\lambda}\right] \end{aligned} \tag{5}$$

where $[\bullet]^k = [\bullet](t_k)$ and $\Delta t = t_{n+1} - t_n$. For the sake of brevity, the index for the current value (t_{n+1}) of the stretch λ_v^j has been dropped in Eqn (5). Eqn (5) is non-linear in terms of λ_v^j. Therefore, a Newton-type iterative scheme is required to find the current value of λ_v^j that need to be inserted in Eqn (2) to obtain the updated value of the total Piola stress, $P(t) = P^e + P^v(t)$.

4 Model validation

For the identification of hyperelastic material parameters appearing in a model, three main procedures have been discussed in the literature, see [2]. The first option is to perform single-step relaxation experiments at various strain levels. When a test specimen is held at a certain strain, the stress will gradually

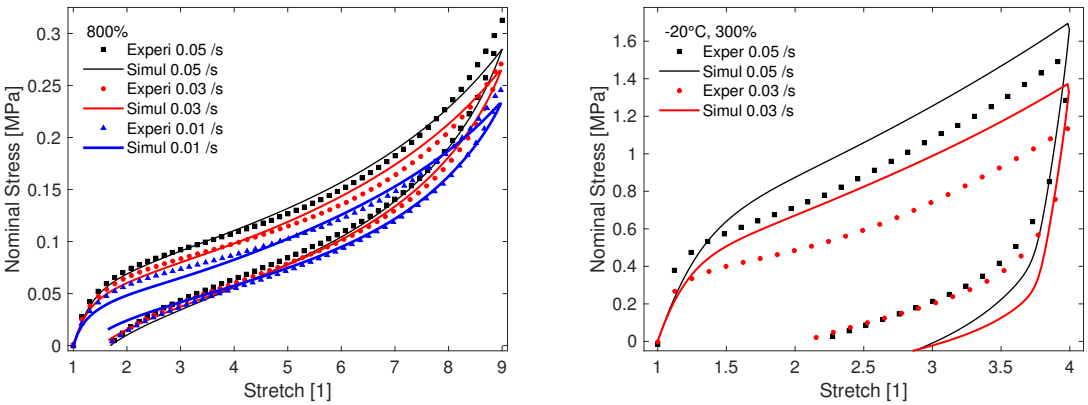

Figure 3. Viscoelastic parameter identification: Three different strain rates are used to identify viscous parameters while hyperelastic parameters identified earlier are kept frozen. Total five Maxwell elements, each having two material parameters, are well enough to capture the strain rate-dependent data up to 800% deformations. (Right) Model performance is validated by other strain rate dependent tests

reduce and will asymptotically reach an equilibrium stress state, which can be considered as the relaxed and basic elastic stress at the corresponding strain. The next step is to identify the viscoelastic parameters. With the hyperelastic parameter, the equilibrium stress can be calculated, and the over-stress modulus and over-stress relaxation spectrum are yet to be identified in order to obtain the viscous over-stress. Since viscoelasticity is the strain rate dependent behavior, we identify the parameters using three sets of data at 800% strain and at different strain rates, which are 0.01 /s, 0.03 /s, and 0.05 /s, simultaneously. Note that during the identification process, we find that five sets of Maxwell elements can capture the viscoelastic behavior with a fair accuracy while more elements could not improve the results significantly, cf Fig 3 (left). During the viscoelastic parameter identification, hyperelastic parameters are kept fixed. With the identified parameters, both strain rate dependences and large strain nonlinearities are captured successfully, see Fig 3(right).

5 Conclusion

In this contribution, a detail thermo-viscoelastic experimental characterizations of a widely-used VHB polymer is presented. All experiments were performed in a purposively-built temperature chamber that can operate under a wide span of temperature ranging from -50°to 150°C. In order to quantify viscoelastic behaviours of the polymer, all classical experimentations, i.e., quasi-static tests at very low strain rates, single-step and multi-step relaxation tests, loading-unloading cyclic tests were conducted at different strain rates and at different temperature profiles. Exploring the experimental data obtained in the current study, a thermodynamically consistent phenomenologically motivated thermo-viscoelastic material model at finite strain is proposed. Once, a complete set of viscoelastic parameters are identified, we use them to validate other sets of data that are not utilised in any identification process. All validation examples show an excellent agreement between model and experimental data.

References

[1] Z. Liao, M. Hossain, X. Yao, M. Mehnert, P. Steinmann, *On thermo-viscoelastic experimental characterisations and numerical modelling of VHB polymer*, In Review, 2019

[2] M. Hossain, D. K. Vu, P. Steinmann, *Experimental study and numerical modelling of VHB 4910 polymer*, Computational Materials Science, 59:65-74, 2012

[3] P. Steinmann, M. Hossain and G. Possart, *Hyperelastic models for rubber-like materials: Consistent tangent operators and suitability of Treloar's data*, Arch. of Appl. Mech., 82(9):1183-1217, 2012

[4] M. Hossain, P. Steinmann, *More hyperelastic models for rubber-like materials: Consistent tangent operator and comparative study*, Journal of Mechanical Behaviour of Materials, 22(1-2):27-50, 2013

**Proceedings of the 8th GACM Colloquium on Computational Mechanics
for Young Scientists from Academia and Industry
August 28–30, 2019 in Kassel, Germany**

A Macroscopic Model for Magnetorheological Elastomers based on Microscopic Simulations

Karl A. Kalina *[1], Philipp Metsch[1], Jörg Brummmund[1] and Markus Kästner[1,2]

[1]Chair of Computational and Experimental Solid Mechanics, TU Dresden, 01062 Dresden, Germany.
[2]Dresden Center for Computational Materials Science (DCMS), TU Dresden, 01062 Dresden, Germany.

Abstract. Herein, the parametrization of a macro-model for magneto-rheological elastomers based on microscopic simulations is presented. Within a computational homogenization, the effective response of the composite system is calculated and the data are used for parameter identification. The merit of this strategy is the adjustment of the model independent of any macroscopic sample geometry. With the developed model, the magnetostrictive behavior of a macroscopic sample is simulated.

Introduction

Magnetorheological elastomers (MREs) are a class of active composites which consist of a polymer matrix filled with micron-sized magnetizable particles. Thus, the effective stiffness or the shape of a specimen can be controlled with an external magnetic field.

Continuum based strategies regarding the modeling of MREs can be divided into microscopic [5, 6, 9, 10] and macroscopic [1, 2, 3, 4] approaches. In the former, the heterogeneous microstructure is explicitly resolved and it is possible to predict the effective behavior of the composite. However, the disadvantage of microscopic continuum models is the computationally expensive numerical solution. In contrast to that, macroscopic models, which consider the MRE as a homogeneous continuum, enable the efficient simulation of real structures. Since such models are phenomenologically motivated, the model parameters have to be determined which is done by using experimental results so far, e. g. [2, 3]. Due to the inhomogeneous fields inside the MRE sample [7, 8], this procedure however requires several simplifying assumptions.

In this contribution a macroscopic model for MREs is identified from data generated by a microscopic model combined with a computational homogenization approach. This strategy enables to identify the parameters independent of any sample geometry.

1 Theoretical framework

The presented approach is based on a general continuum formulation of the coupled magneto-mechanical boundary value problem [5, 6, 7, 10] which is valid on the micro- as well as the macroscale. To link these two scales, a suitable homogenization scheme is applied [9, 10].

1.1 Microscopic Simulations

For the description of the macroscopic MRE-behavior in the isotropic case, a random microstructure has to be taken into account. In order to ensure a statistical representation, the number of embedded particles is chosen to $N = 300$, where representative volume elements (RVEs) with the characteristic values $\phi = \{10, 15, 20, 25, 30, 35, 40\}\,\%$ are generated. To estimate mean values as well as confidence

*Corresponding author: karl.kalina@tu-dresden.de

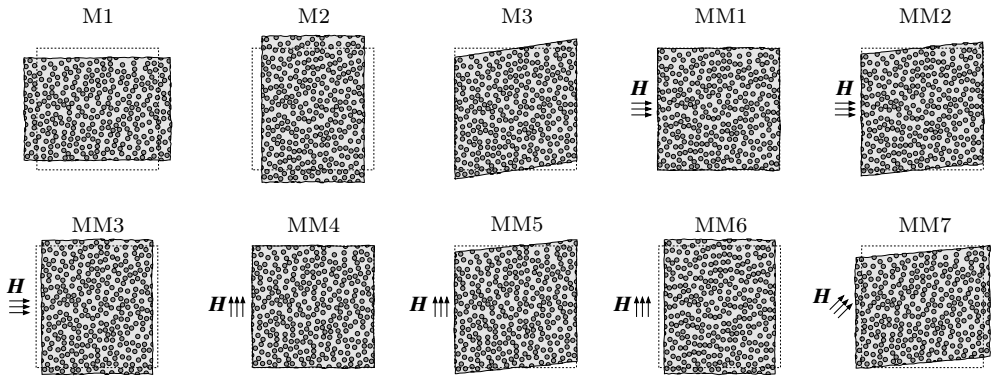

Figure 1. Schematic illustration of the simulated purely mechanical load cases M1 – M3 and coupled magneto-mechanical load cases MM1 – MM7 for an RVE with $\phi = 30\,\%$. The effective deformation and the magnetic field are applied simultaneously within the homogenization. The maximum applied effective stretch and shear deformation are chosen to $\lambda = 1.15$ and $\gamma = 0.15$ for the mechanical load cases. In the coupled cases, the values $|\boldsymbol{H}| = 230\,\mathrm{kA\,m^{-1}}$, $\lambda = 1.1$ and $\gamma = 0.1$ are applied.

intervals for the effective magneto-mechanical response, five different microstructures are considered for each particle-volume fraction.

All RVEs are analyzed by means of three pure mechanical load cases (M1 – M3) and seven coupled magneto-mechanical load cases (MM1 – MM7) in the linear magnetic regime, see Fig. 1. Within the microscopic simulations, the constitutive models presented in [5, 10] are used. All performed simulations are realized for the plane strain case.

1.2 Macroscopic Model

In order to enable a separate description of deviatoric and volumetric parts of the MRE behavior, the deformation gradient $\boldsymbol{F}$ is divided into isochoric $\bar{\boldsymbol{F}} = J^{-1/3}\boldsymbol{F}$ and volumetric contributions according to the Flory-split, where $J = \det \boldsymbol{F}$ denotes the Jacobi determinant. Due to the assumed isotropy, the MREs effective response can be described in terms of the six invariants

$$\bar{I}_1 = \operatorname{tr} \bar{\boldsymbol{C}}\ ,\ \bar{I}_2 = \frac{1}{2}(\operatorname{tr}^2 \bar{\boldsymbol{C}} - \operatorname{tr} \bar{\boldsymbol{C}}^2)\ ,\ I_3 = J^2\ ,\ I_4 = |\boldsymbol{H}|^2\ ,\ \bar{I}_5 = \boldsymbol{H}\cdot\bar{\boldsymbol{C}}\cdot\boldsymbol{H} \text{ and } \bar{I}_6 = \boldsymbol{H}\cdot\bar{\boldsymbol{C}}^{-1}\cdot\boldsymbol{H}\ . \quad (1)$$

Therein, $\boldsymbol{C}$ and $\boldsymbol{H}$ denote the right Cauchy-Green deformation tensor and the Lagrangian magnetic field, respectively. For a separate discussion, the amended free energy function

$$\Omega = \Omega^{\mathrm{mech}}(\boldsymbol{C}) + \Omega^{\mathrm{coup}}(\boldsymbol{C},\boldsymbol{H}) + \Omega^{\mathrm{mag}}(\boldsymbol{H}) + \Omega^{\mathrm{free}}(\boldsymbol{C},\boldsymbol{H}) \quad (2)$$

is split into mechanic, coupling, magnetic and free space part, where the latter is the Lagrangian counterpart of the magnetic free field energy and is independent of any material properties. With that, the ansatz

$$\Omega = \frac{1}{2}\Big[C(\bar{I}_1 - 3) + K(I_3 - 1)\Big] + \mu_0\Big[\alpha_1\bar{I}_5 + \alpha_2\bar{I}_6 + \alpha_3(I_3 - 1)\bar{I}_6\Big] + \frac{\mu_0\beta}{2}I_4 - \frac{\mu_0}{2}J\boldsymbol{C}^{-1} : (\boldsymbol{H}\otimes\boldsymbol{H}) \quad (3)$$

is chosen for the macro-model, where μ_0 is the permeability of vacuum.

1.3 Parameter Identification

To ensure a high accuracy of the model, it should describe the effective magnetization $\boldsymbol{m}$ as well as the total and mechanical stress tensors $\boldsymbol{\sigma}^{\mathrm{tot}}$ and $\boldsymbol{\sigma}$. The material parameter sets $\underline{\kappa} = \{\underline{\kappa}^{\mathrm{mech}}, \underline{\kappa}^{\mathrm{coup}}, \underline{\kappa}^{\mathrm{mag}}\}$

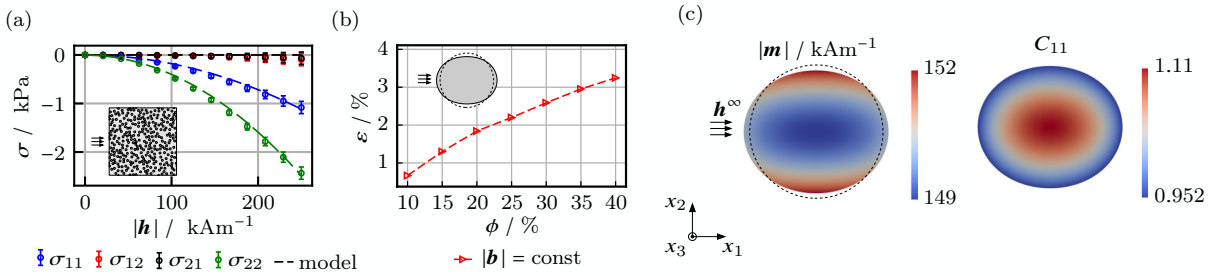

Figure 2. Simulation of MREs: (a) average of the homogenized mechanical stress with 95 % error bound and fitted model for load case MM1 with $\phi = 20\,\%$, (b) overall magnetostrictive strain $\varepsilon = \Delta l/l_0$ in dependence of ϕ and (c) local magnetization $|\boldsymbol{m}|$ and deformation field C_{11} within a deformed circular MRE sample with $\phi = 30\,\%$. The undeformed configuration is marked with dashed lines and the depiction of the deformed configuration is scaled with the factor five.

are determined within a stepwise algorithm which results in three linear optimization schemes. Finally, to achieve a good approximation of all considered fields, the inherently nonlinear step

$$\{\underline{\kappa}^{\mathrm{coup}}, \underline{\kappa}^{\mathrm{mag}}\} = \arg\left\{ \min_{\underline{\kappa}^{\mathrm{coup}}\,\underline{\kappa}^{\mathrm{mag}}} \sum_{i=1}^{N} \left(W_i^{\sigma} \left\| \boldsymbol{\sigma}(\boldsymbol{F}_i, \boldsymbol{H}_i, \underline{\kappa}) - \boldsymbol{\sigma}_i \right\|^2 \ldots \right.\right.$$
$$\left.\left. \ldots + W_i^{m} \left| \boldsymbol{m}(\boldsymbol{F}_i, \boldsymbol{H}_i, \underline{\kappa}^{\mathrm{coup}}, \underline{\kappa}^{\mathrm{mag}}) - \boldsymbol{m}_i \right|^2 \right) \right\} \tag{4}$$

is realized, where the parameters determined in the previous steps are used as initial values. W_i^m and W_i^σ denote weighting factors for the single error sums which are determined as the inverse of the maximum value of σ_{kl} and m_k for each load case, respectively.

2 Results

The fitting procedure is applied to the homogenized data of the load cases M1–M3 as well as MM1–MM3, where Fig. 1(a) exemplarily depicts $\boldsymbol{\sigma}$ for MM1 with a volume fraction of $\phi = 20\,\%$. The model deviations of the load cases which where not used within the parameter identification procedure are in a similar range as the fitted ones. Thus, the quality of the developed model could be validated.

Finally a circular MRE sample within a surrounding free space is simulated, where special attention is drawn to the magnetostriction [8, 9], i. e. the elongation or contraction in an external field $\boldsymbol{h}^{\infty}$. As shown in Fig. 1(c), the induced magnetization within the sample is almost homogeneous, whereas the deformation field is strongly inhomogeneous. In case of a rectangular shaped sample, this effect intensifies [7, 8]. This demonstrates again, that the parameter identification for macroscopic MRE models from experimental results requires several assumptions in the fitting process.

If the underlying particle volume fraction of the MRE is varied, a degressive curve for the overall magnetostrictive strain $\varepsilon = \Delta l/l_0$ is observed if the applied local induction $\boldsymbol{b}$ is set constant, see Fig. 1(b). Altogether, the predicted elongation of the sample in the direction of the external field is in qualitative accordance with experiments for isotropic MREs.

Acknowledgments

The present study is funded by the German Research Foundation, Priority Programme 1681 grant KA 3309/2-3. This support is gratefully acknowledged.

References

[1] B.E. Abali and A.F. Queiruga. Theory and computation of electromagnetic fields and thermomechanical structure interaction for systems undergoing large deformations. *Journal of Computational Physics* 394 (2019), pp. 200 –231.

[2] R. Bustamante, A. Dorfmann, and R.W. Ogden. Numerical solution of finite geometry boundary-value problems in nonlinear magnetoelasticity. *International Journal of Solids and Structures* 48.6 (2011), pp. 874 –883.

[3] K. Danas, S. V. Kankanala, and N. Triantafyllidis. Experiments and modeling of iron-particle-filled magnetorheological elastomers. *Journal of the Mechanics and Physics of Solids* 60.1 (2012), pp. 120–138.

[4] K. Haldar, B. Kiefer, and A. Menzel. Finite element simulation of rate-dependent magneto-active polymer response. *Smart Materials and Structures* 25.10 (2016), p. 104003.

[5] K. A. Kalina, P. Metsch, and M. Kästner. Microscale modeling and simulation of magnetorheological elastomers at finite strains: A study on the influence of mechanical preloads. *International Journal of Solids and Structures* 102–103 (2016), pp. 286 –296.

[6] K. A. Kalina, J. Brummund, Metsch P., M. Kästner, D. Yu. Borin, J. M. Linke, and S. Odenbach. Modeling of magnetic hystereses in soft MREs filled with NdFeB particles. *Smart Materials and Structures* 26 (2017), pp. 105019 –105031.

[7] K. A. Kalina, P. Metsch, J. Brummund, and M. Kästner. Development of a Macro-Model for Magnetorheological Elastomers based on Microscopic Simulations. *International Journal of Soldis and Structures* (submitted 2019).

[8] M.-A. Keip and M. Rambausek. Computational and analytical investigations of shape effects in the experimental characterization of magnetorheological elastomers. *International Journal of Solids and Structures* 121 (2017), pp. 1 –20.

[9] P. Metsch, K. A. Kalina, Christian Spieler, and M. Kästner. A numerical study on magnetostrictive phenomena in magnetorheological elastomers. *Computational Materials Science* 124 (2016), pp. 364 –374.

[10] P. Metsch, K. A. Kalina, J. Brummund, and M. Kästner. Two- and three-dimensional modeling approaches in magneto-mechanics: a quantitative comparison. *Archive of Applied Mechanics* 89 (2018), pp. 47–62.

**Proceedings of the 8th GACM Colloquium on Computational Mechanics
for Young Scientists from Academia and Industry
August 28–30, 2019 in Kassel, Germany**

Experimental Characterization, Modeling and FE-Simulation of Curing Phenomena in an Elastomeric Adhesive

Ralf Landgraf * [1] and Jörn Ihlemann[1]

[1]Chair of Solid Mechanics, Chemnitz University of Technology, Chemnitz, Germany

Abstract.

This contribution deals with the curing process of a PU based adhesive. The basic experimental methods and corresponding modeling approaches are introduced. Moreover, an application of the resulting curing model to the simulation of the production process of piezo-metal compounds by finite element simulations is shown.

Introduction

The crosslinking (or curing) process of a PU based adhesive is considered. The raw material is a one-component paste with enclosed encapsulated isocyanate. The curing process is initiated by raising the temperature above $90°C$. Once the curing process has started, the material cures to a solid within few minutes and the final material exhibits rubber-like material behavior.

Aiming for the simulation of the material behavior, both experimental characterization methods and phenomenological modeling approaches were applied, which is shown in Section 1. Moreover, an exemplifying finite element simulation provided in Section 2 will highlight the capability of the modeling approach.

1 Experimental characterization and material modeling

1.1 Progress of the chemical curing process

Differential scanning calorimetry (DSC) measurements were applied to characterize the chemical crosslinking process (see [4]). Thereby, the rate of the specific reaction enthalpy $\dot{h}$ was measured during isothermal curing experiments at temperatures θ_{iso}. Additionally, the ultimate specific heat reaction h_{ult}, i.e. the maximum reaction enthalpy that the material releases within a complete curing reaction, was experimentally determined. These values were employed to define the degree of cure $q \in [0,1]$ by its rate

$$\dot{q} = \frac{\dot{h}(\theta_{iso})}{h_{ult}} \tag{1}$$

Next, a phenomenological curing model was formulated. It is based on the Kamal and Sourour autocatalytic reaction model [3] in combination with Fournier's diffusion factor $f_D(q, q_{end}(\theta))$ [2]:

$$\dot{q} = \Big(K_1(\theta) + K_2(\theta)\, q^{\alpha}\Big)\Big(1-q\Big)^{\beta}\; f_D(q, q_{end}(\theta)) \;, \quad q_{end}(\theta) = \frac{k_1}{1+\exp\big[-k_2\,(\theta-\theta_{ref})\big]} - k_3 \;. \tag{2}$$

The factors $K_1(\theta)$ and $K_2(\theta)$ are temperature-dependent functions that show Arrhenius behavior. For the maximum attainable degree of cure at certain temperatures $q_{end}(\theta)$, the ansatz $(2)_2$ was chosen. The curing model includes the material parameters α, β, k_1, k_3, k_3 as well as further parameters inside the Arrhenius functions and Fournier's diffusion factor. A summary of the identification procedure, where the

*Corresponding author: ralf.landgraf@mb.tu-chemnitz.de ORCID iD: 0000-0001-7715-5674

model (2) is adapted to the experimental data (1), and a list of the identified parameters can be found in [4]. The resulting behavior of the model is exemplified in Fig. 1 (left) for different curing temperatures. Therein, it can be seen that curing only takes place at temperatures above 90°C.

1.2 Heat expansion and chemical shrinkage

Volume changes due to varying temperatures and chemical crosslinking were analyzed by a test setup based on Archimedes' principle (for details, see [8]). However, instead of using long term measurements (as applied in [8]), only specific states were analyzed for the current material due to its specific curing characteristics (very fast curing at temperatures above 90°C). The tested sequence includes measurements of the uncured material ($q = 0$) at temperatures of 25° C, 50° C and 75° C. Next, the material was cured at 95° C and the mass density of the fully cured material was measured. Finally, a sequence of decreasing test temperatures was applied to identify the mass density of the fully cured materials ($q = 1$). The resulting mass densities of two different specimens are depicted in Fig. 1 (right). Moreover, the results of a fully cured test specimen (experiment 3) are included as well.

Fig. 1 (right) reveals decreasing mass densities for increasing temperatures (heat expansion). Moreover, the mass density decreases during the phase change from liquid to solid state, which is in contrast to the well-known chemical shrinkage during curing. The increasing volume during the curing process could be attributed to the formation of pores. The temperature and curing dependent mass density is modeled as follows:

$$\varrho(\theta, q) = \frac{\widetilde{\varrho}}{\varphi(\theta, q)} \ , \quad \varphi(\theta, q) = \exp\Big[\alpha_\theta(\theta - \widetilde{\theta}) + \beta_q\, q\Big] \ , \ \alpha_\theta = 4.21 \cdot 10^4\,\mathrm{K}^{-1} \ , \ \beta_q = 6.06 \cdot 10^{-2} \ . \tag{3}$$

Therein, $\widetilde{\varrho} = 1515\,\frac{\mathrm{kg}}{\mathrm{m}^3}$ is the reference mass density, which was measured at the reference temperature $\widetilde{\theta} = 25°\mathrm{C}$ and the reference degree of cure $\widetilde{q} = 0$. The function $\varphi(\theta, q)$ is the thermochemical volume ratio, for which a phenomenological ansatz was chosen. The ansatz includes the heat expansion coefficient α_θ and the chemical expansion coefficient β_q. The corresponding parameter values for the investigated adhesive are given in Eq. (3).

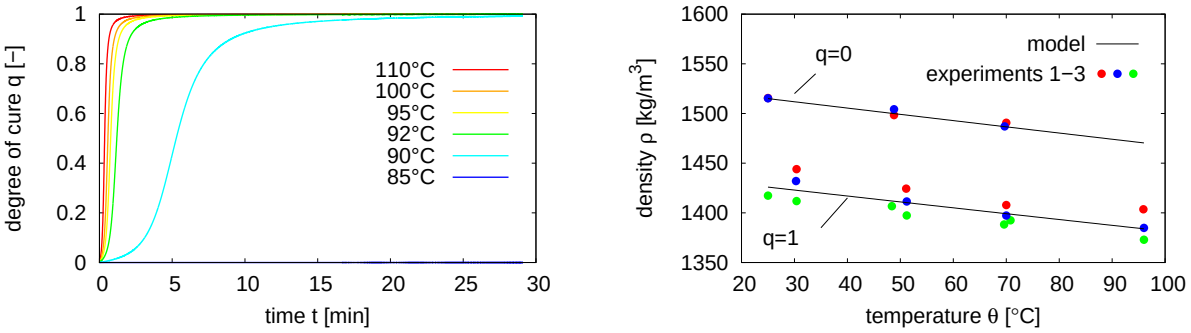

Figure 1. Simulation of the evolution of the degree of cure q for different constant temperatures (left), and results of mass density measurements (right).

1.3 Mechanical behavior

In a first step, the mechanical behavior was characterized by uniaxial tension tests on fully cured specimens. The resulting stress-strain curves of loading/unloading cycles with increasing amplitudes revealed typical phenomena of rubber-like materials (see Fig. 2, left). Because of this, the Model of Rubber Phenomenology (MORPH, see [1]) was adapted to the experimental data by the help of a parameter identification procedure (see [4]). Thereby, the eight included material parameters $\widetilde{p}_1 - \widetilde{p}_8$ were identified with respect to a reference temperature $\widetilde{\theta} = 25°\mathrm{C}$ and a reference degree of cure $\widetilde{q} = 1$. Fig. 2 (left) depicts the comparison of a tensile test and the corresponding simulation of the mechanical behavior with the MORPH model. Therein, a good accordance between experiments and simulation can be observed.

Next, the MORPH model was extended by temperature and degree of cure effects. Thereby, the reference material parameters were replaced by the parameter functions:

$$p_i(\theta, q) = \widetilde{p}_i \cdot f_q(q) \cdot f_\theta(\theta) \ , \quad i = 1 \dots 8 \ , \tag{4}$$

where $f_q(q)$ is a factor depending on the degree of cure. This function was adapted to measurements of increasing storage moduli, which were obtained by rheometer tests on the adhesive during its curing process. In addition, $f_\theta(\theta)$ is a temperature dependent function that was adapted to temperature ramp experiments on the cured material within dynamical mechanical analyses (DMA). An example of the evolution of the stress-strain curves within a curing process is given in Fig. 2 (right). Therein, the increasing stiffness and the inelastic material behavior can be observed. More details on the modeling approach can be found in [4].

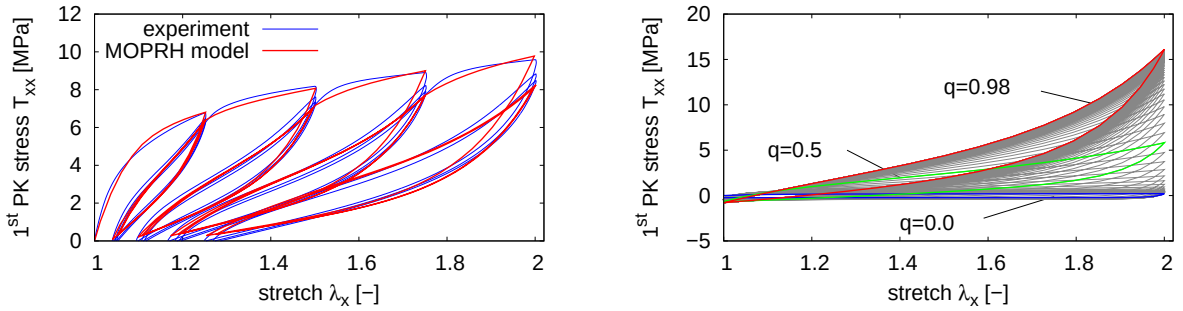

Figure 2. MORPH model: adaption to uniaxial tension tests (left) and simulation of evolving stress-strain behavior within a curing process (right).

2 Finite element simulations

The model outlined in Section 1 was implemented into the commercial finite element software ANSYS (see [6] and [5]) to simulate the production process of smart sheet metal compounds with included sensor and actuator functionality. Such a piezo-metal compound (PMC) consists of two metal sheets that are connected by an initially liquid adhesive layer. Moreover, a sensor/actuator (like macro-fiber-composites) is embedded inside the adhesive layer (see Fig. 3, left). The production of a 3D-curved PMC consists of three different steps according to Fig. 3. First, a local heating/cooling step causes the outer regions of the adhesive layer to cure while the inner adhesive region remains in liquid state. Next, the pre-cured compound is formed to its final state. The liquid adhesive core thereby protects the sensor/actuator and the cured outer adhesive region prevents the liquid adhesive core to leak. In the final step, the adhesive core of the formed PMC is cured to obtain a complete closure of the compound.

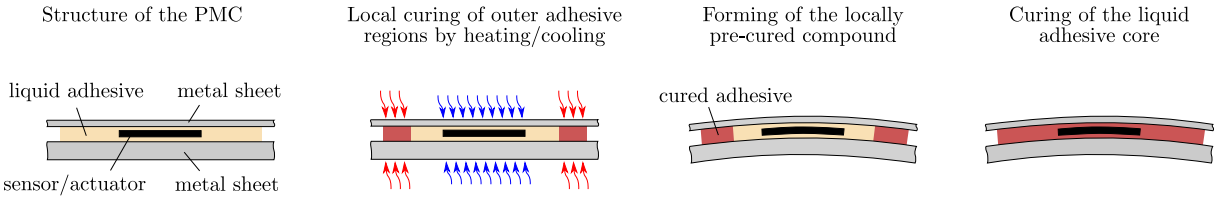

Figure 3. Structure and three basic steps for the production of PMCs.

The steps for the production of PMCs were analyzed by finite element simulations. First, the local heating/cooling step on flat PMCs was investigated by pure thermal FE simulations. Thereby, heating/cooling was induced by convection boundary conditions on the metal sheets. The arising temperature distribution within the adhesive layer results in local curing (see Fig. 4, left). More precisely, only regions are cured, where the temperature rises above 90°C, i.e. in the outer regions near the heating units. Instead, the adhesive core remains liquid ($q = 0$). More results on this production step are reported in [5].

Next, the geometry and the material properties of the cured adhesive were passed to project partners, who simulated the forming of the PMC to a 3D-curved shape.[†] Fig. 4 (middle) depicts the von Mises equivalent

[†]Simulations were conducted by S. Hensel (SFB/TR39, subproject B1) using the FE software LS-DYNA.

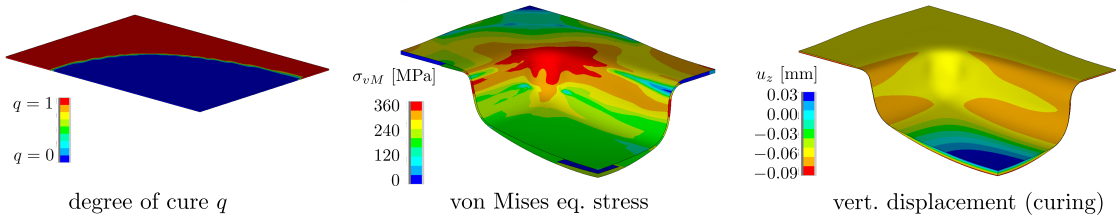

degree of cure q | von Mises eq. stress | vert. displacement (curing)

Figure 4. Finite element simulation of the production process of PMCs: local heating/cooling (left), forming (middle), and final curing (right).

stress field in all solid parts (metal sheets, sensor, and cured adhesive). It can be seen that only low stresses act on the sensor/actuator due to the floating support of the liquid adhesive. The final geometry was then passed back to simulate the remaining curing process. Due to the complete and homogeneous heating of the PMC, mechanical finite element simulations with prescribed temperatures were applied to investigate the effect of volume changes and increasing stiffness. The results are exemplified by Fig. 4 (right), where vertical displacements are depicted that appear due to the curing process. It can be observed that the previously liquid core increases its volume due to the curing process.

Summary

A combined approach for the experimental characterization and phenomenological modeling of curing processes in a PU based adhesive has been presented. Moreover, an exemplifying application of the curing model within finite element simulations has been given. The general approach can also be applied to different polymers and technical processes, see for example [6] and [7].

Acknowledgments

This research was funded by the German Research Foundation (DFG) within the Collaborative Research Center SFB/TR39 “PT-PIESA”.

References

[1] D. Besdo and J. Ihlemann. A phenomenological constitutive model for rubberlike materials and its numerical applications. *International Journal of plasticity* 19.7 (2003), pp. 1019–1036.

[2] J. Fournier, G. Williams, C. Duch, and G. A. Aldridge. Changes in molecular dynamics during bulk polymerization of an epoxide-amine system as studied by dielectric relaxation spectroscopy. *Macromolecules* 29.22 (1996), pp. 7097–7107.

[3] M. R. Kamal and S. Sourour. Kinetics and thermal characterization of thermoset cure. *Polymer Engineering & Science* 13.1 (1973), pp. 59–64.

[4] R. Landgraf and J. Ihlemann. Application and extension of the MORPH model to represent curing phenomena in a PU based adhesive. In: *Constitutive Models for Rubber X*. Ed. by A. Lion and M. Johlitz. London: Taylor & Francis Group, 2017, pp. 137–143.

[5] R. Landgraf and J. Ihlemann. Thermally Controlled Adhesive Curing during the Production of Piezo-Metal-Compounds: Finite Element Modeling and Analyses. *Advanced Engineering Materials* 20 (2018). DOI: doi:10.1002/adem.201800411.

[6] R. Landgraf, M. Rudolph, R. Scherzer, and J. Ihlemann. Modelling and simulation of adhesive curing processes in bonded piezo metal composites. *Computational Mechanics* 54.2 (2014), pp. 547–565.

[7] R. Landgraf, J. Ihlemann, S. Kolmeder, A. Lion, H. Lebsack, and C. Kober. Modelling and simulation of acrylic bone cement injection and curing within the framework of vertebroplasty. *ZAMM-Journal of Applied Mathematics and Mechanics* 95.12 (2015), pp. 1530–1547.

[8] M. Rudolph, M. Stockmann, R. Landgraf, and J. Ihlemann. Experimental determination and modelling of volume shrinkage in curing thermosets. *arXiv Preprint arXiv:404.0310* (2014).

**Proceedings of the 8th GACM Colloquium on Computational Mechanics
for Young Scientists from Academia and Industry
August 28–30, 2019 in Kassel, Germany**

Modeling the Chemo-Thermo-Mechanical Material Behavior of an Epoxy Resin System

Chris Leistner *[1] and Stefan Hartmann[1]

[1]Institute of Applied Mechanics, Clausthal University of Technology, Adolph-Roemer-Straße 2a, 38678 Clausthal-Zellerfeld, Germany

Abstract. Epoxy resin systems frequently are applied in fiber composite materials for lightweight constructions. During the production process, the epoxy resin system must be cured by an exothermic chemical reaction, which leads to an inhomogeneous temperature distribution in the part and further affects the curing kinetics. Especially for thick-walled structures, combustion might occur during curing. Furthermore, chemical and thermal shrinkage yield residual stresses, warpage or cracks. The goal is to describe these properties of the material by a material model. The rate-type constitutive equations for the mechanical and the curing part are implemented into an implicit finite element program, where high-order and time-adaptive time integration are required to predict precisely the maximum temperature and residual stresses within a part.

Introduction

In this contribution, the thermo-mechanical properties of a pure epoxy resin system are experimentally investigated and modeled. Regarding further information of the chemo-thermal investigation of the particular epoxy resin system, we refer to [3]. In [4] the volumetric thermal and chemical deformation according to the curing reaction is investigated. Such deformation causes mechanical strains and residual stresses, which are constituted within a viscoplasticity model. The viscous effects are based on a Prony series of Maxwell elements combined with a hysteretic part using an endochronic model. Of course, the temperature- and cure-dependent quantities required in the heat equation are provided as well. A particular focus lies on the challenging parameter identification regarding a unique set of parameters. Apart from experimental investigations and modeling, the numerical treatment is discussed.

1 Experiments

Tensile tests with dogbone-like specimens of the cured epoxy resin system were carried out as part of the material investigation. Strain-controlled long-term relaxation tests and multi-step relaxation tests at four different temperatures serve to separate the state of equilibrium. The basic procedure is similar to the investigations in [2]. Fig. 1a clearly shows that the material has pronounced relaxation times. In order to reduce the testing time, the holding time of the multi-step relaxation tests is set to 6 h. Since the material cannot totally relax within short time, the equilibrium point must be estimated, where we choose an exponential function using the courses of the long-term relaxation tests, see Fig. 1b.

2 Material Modeling

The rheological model depicted in Fig. 2 serves to represent the material behavior. The strains are additively decomposed into a thermo-chemical and a mechanical part, where the mechanical part consists of elastic and a viscous strains:

$$\mathbf{E} = \mathbf{E}_{\Theta \mathrm{c}} + \mathbf{E}_{\mathrm{M}} \quad \text{and} \quad \mathbf{E}_{\mathrm{M}} = \mathbf{E}_{\mathrm{e}i} + \mathbf{E}_{\mathrm{v}i} \tag{1}$$

*Corresponding author: chris.leistner@tu-clausthal.de

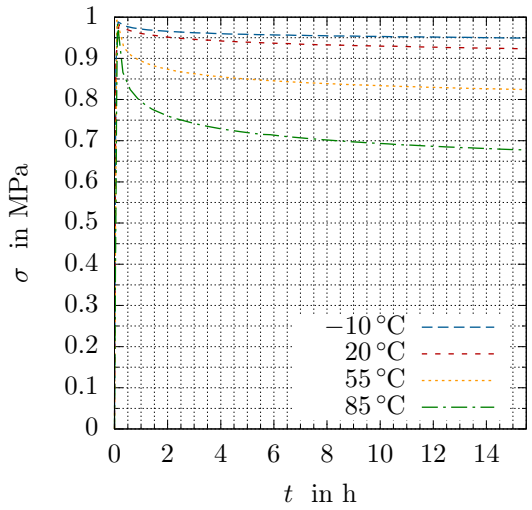

(a) Long time relaxation

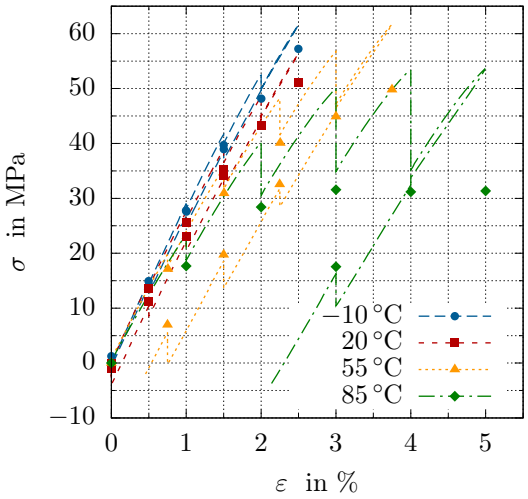

(b) Multi-step relaxation (the markers define estimated equilibrium points of relaxation)

Figure 1. Tensile tests at four different temperatures

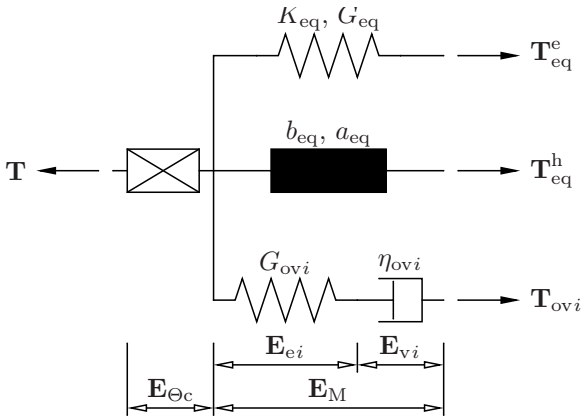

Figure 2. Rheological model

Furthermore, the additive decomposition of the stress state

$$\mathbf{T} = \mathbf{T}^{\mathrm{e}}_{\mathrm{eq}} + \mathbf{T}^{\mathrm{h}}_{\mathrm{eq}} + \mathbf{T}_{\mathrm{ov}i} \tag{2}$$

is proposed as depicted in Fig. 2, where $\mathbf{T}_{\mathrm{ov}i}$ indicates a sum of Maxwell elements. The stress can be represented formally as a split into spherical and deviatoric quantities, whereby the spherical stress consists of a purely elastic equilibrium stress $\mathbf{T}^{\mathrm{e}}_{\mathrm{eq}}$ and the deviatoric stress is decomposed into

$$\mathbf{T}^{\mathrm{D}} = \mathbf{T}^{\mathrm{e}\ \mathrm{D}}_{\mathrm{eq}} + \mathbf{T}^{\mathrm{h}\ \mathrm{D}}_{\mathrm{eq}} + \mathbf{T}_{\mathrm{ov}i}{}^{\mathrm{D}}. \tag{3}$$

Thus, the total stress power reads

$$\mathbf{T}\cdot\dot{\mathbf{E}} = -p\mathbf{I}\cdot\dot{\mathbf{E}} + \mathbf{T}^{\mathrm{D}}\cdot\dot{\mathbf{E}} = -p\dot{\varepsilon}_{\mathrm{vol}} + \left(\mathbf{T}^{\mathrm{e}\ \mathrm{D}}_{\mathrm{eq}} + \mathbf{T}^{\mathrm{h}\ \mathrm{D}}_{\mathrm{eq}}\right)\cdot\dot{\mathbf{E}}_{\mathrm{M}} + \mathbf{T}_{\mathrm{ov}i}{}^{\mathrm{D}}\cdot\left(\dot{\mathbf{E}}_{\mathrm{e}} + \dot{\mathbf{E}}_{\mathrm{v}}\right) + \mathbf{T}^{\mathrm{D}}\cdot\dot{\mathbf{E}}_{\Theta\mathrm{c}}. \tag{4}$$

Due to advantages in constitutive modeling of caloric processes and volumetric expansions, we define a hybrid free energy, which was introduced in [5]

$$\varphi = \psi + \frac{1}{\rho}p\varepsilon_{\mathrm{vol}}. \tag{5}$$

Under consideration of the hybrid free energy, the Clausius-Duhem inequality reads

$$\delta = -\dot{\varphi} - \frac{1}{\rho}\varepsilon_{\mathrm{vol}}\dot{p} + \frac{1}{\rho}\mathbf{T}^{\mathrm{D}}\cdot\dot{\mathbf{E}} - s\dot{\Theta} - \frac{1}{\rho\Theta}\vec{q}\cdot\vec{g} \geq 0 \quad \text{with} \quad \vec{g} = \operatorname{grad}\Theta, \tag{6}$$

where the hybrid free energy can generally be defined by introducing the primary variables

$$\varphi(t) = \tilde{\varphi}(p, \mathbf{E}_\mathrm{M}, \mathbf{E}_\mathrm{e}, \mathbf{Y}, \Theta, c) = \hat{\varphi}(p, \Theta, c) + \bar{\varphi}(\mathbf{E}_\mathrm{M}, \mathbf{E}_\mathrm{e}, \mathbf{Y}, \Theta, c). \tag{7}$$

Apart from the stress power Eq. (4), the general time derivative of the hybrid free energy Eq. (7) can be inserted into the Clausius-Duhem inequality, which must be fulfilled for arbitrary values of the time derivatives of the primary variables in order to satisfy thermodynamic consistency

$$\begin{aligned}\rho\delta = &\left(\varepsilon_\mathrm{vol} - \rho\frac{\partial\tilde{\varphi}}{\partial p}\right)\dot{p} + \left(\mathbf{T}_\mathrm{eq}^{\mathrm{e}\ \mathrm{D}} - \rho\frac{\partial\tilde{\varphi}}{\partial\mathbf{E}_\mathrm{M}}\right)\cdot\dot{\mathbf{E}}_\mathrm{M} + \mathbf{T}_\mathrm{eq}^{\mathrm{h}\ \mathrm{D}}\cdot\dot{\mathbf{E}}_\mathrm{M} - \rho\frac{\partial\tilde{\varphi}}{\partial\mathbf{Y}}\cdot\dot{\mathbf{Y}} \\ &+ \left(\mathbf{T}_\mathrm{ov}^\mathrm{D} - \rho\frac{\partial\tilde{\varphi}}{\partial\mathbf{E}_\mathrm{e}}\right)\cdot\dot{\mathbf{E}}_\mathrm{e} + \mathbf{T}_\mathrm{ov}^\mathrm{D}\cdot\dot{\mathbf{E}}_\mathrm{v} + \mathbf{T}^\mathrm{D}\cdot\dot{\mathbf{E}}_{\Theta\mathrm{c}} - \rho\frac{\partial\tilde{\varphi}}{\partial c}\dot{c} - \rho\left(s + \frac{\partial\tilde{\varphi}}{\partial\Theta}\right)\dot{\Theta} - \frac{1}{\Theta}\vec{q}\cdot\vec{g} \geq 0.\end{aligned} \tag{8}$$

Evaluation of Eq. (8) leads to the constitutive equations listed in Tab. 1. The corresponding material

Table 1. Constitutive equations

Volumetric strains

$$\varepsilon_\mathrm{vol} = 3\left({J_{\Theta\mathrm{c}}}^{1/3} - 1\right) - \frac{1}{K_\mathrm{eq}}p \quad \text{with} \quad J_{\Theta\mathrm{c}} = 1 + \alpha_\Theta\vartheta - \alpha_\mathrm{c}c - \alpha_{\Theta\mathrm{c}}\vartheta c \tag{9}$$

Elastic equilibrium stress (spherical)

$$\mathbf{T}_\mathrm{eq}^{\mathrm{e}\ \mathrm{V}} = K_\mathrm{eq}(\operatorname{tr}\mathbf{E}_\mathrm{M})\mathbf{I} \tag{10}$$

Elastic equilibrium stress (deviatoric)

$$\mathbf{T}_\mathrm{eq}^{\mathrm{e}\ \mathrm{D}} = 2G_\mathrm{eq}(s_\mathrm{M}, \Theta)\mathbf{E}_\mathrm{M}^\mathrm{D} \quad \text{with} \quad G_\mathrm{eq}(s_\mathrm{M}, \Theta) = \frac{\alpha_{\mathrm{eq}1}M_1(\Theta)}{\alpha_{\mathrm{eq}2}M_1(\Theta) + s_\mathrm{M}}, \quad s_\mathrm{M} = \sqrt{\mathbf{E}_\mathrm{M}^\mathrm{D}\cdot\mathbf{E}_\mathrm{M}^\mathrm{D}} \tag{11}$$

Hysteretic equilibrium stress (deviatoric)

$$\dot{\mathbf{T}}_\mathrm{eq}^{\mathrm{h}\ \mathrm{D}} = a_\mathrm{eq}M_2(\Theta)\dot{\mathbf{E}}_\mathrm{M}^\mathrm{D} - b_\mathrm{eq}\dot{\hat{s}}_\mathrm{M}\mathbf{T}_\mathrm{eq}^{\mathrm{h}\ \mathrm{D}}, \quad \dot{\hat{s}}_\mathrm{M} = \sqrt{\dot{\mathbf{E}}_\mathrm{M}^\mathrm{D}\cdot\dot{\mathbf{E}}_\mathrm{M}^\mathrm{D}} \tag{12}$$

Overstress (deviatoric)

$$\dot{\mathbf{T}}_{\mathrm{ov}i}{}^\mathrm{D} = 2G_{\mathrm{ov}i}\dot{\mathbf{E}}_\mathrm{M}^\mathrm{D} - \frac{2G_{\mathrm{ov}i}}{\eta_{\mathrm{ov}i}}\mathbf{T}_{\mathrm{ov}i}{}^\mathrm{D} \tag{13}$$

Curing kinetics

$$\begin{aligned}\dot{c} = f_\mathrm{k}(\Theta, c)f_\mathrm{d}(\Theta, c) \qquad &\text{with} \quad f_\mathrm{k}(\Theta, c) = k(\Theta)\left(g + (1-g)\,c - c^2\right)^n \\ &\text{and} \quad f_\mathrm{d}(\Theta, c) = \frac{1}{2}\left(1 - \tanh\left(b\left(\Theta_\mathrm{G}(c) - \Theta\right)\right)\right)\end{aligned} \tag{14}$$

Temperature shift functions

$$M_1(\Theta) = \frac{1}{2}\left(1 - \tanh\left(\frac{\Theta - p_{\Theta 1}}{p_{\Theta 2}}\right)\right) \quad \text{and} \quad M_2(\Theta) = \frac{1}{2}\left(1 - \tanh\left(\frac{\Theta_\mathrm{G}(c) - \Theta}{p_{\Theta 3}}\right)\right) \tag{15}$$

parameters are identified by step-wise procedures in order to obtain a unique set of parameters.

3 Simulation

As a numerical example a plate with a hole of pure epoxy resin system is considered, which cures within a cavity at a fixed outer temperature Θ_s. The dimensions and boundary conditions are depicted in Fig. 3a. Quadratic hexahedral elements are applied with a concentration at the outer surfaces. In order

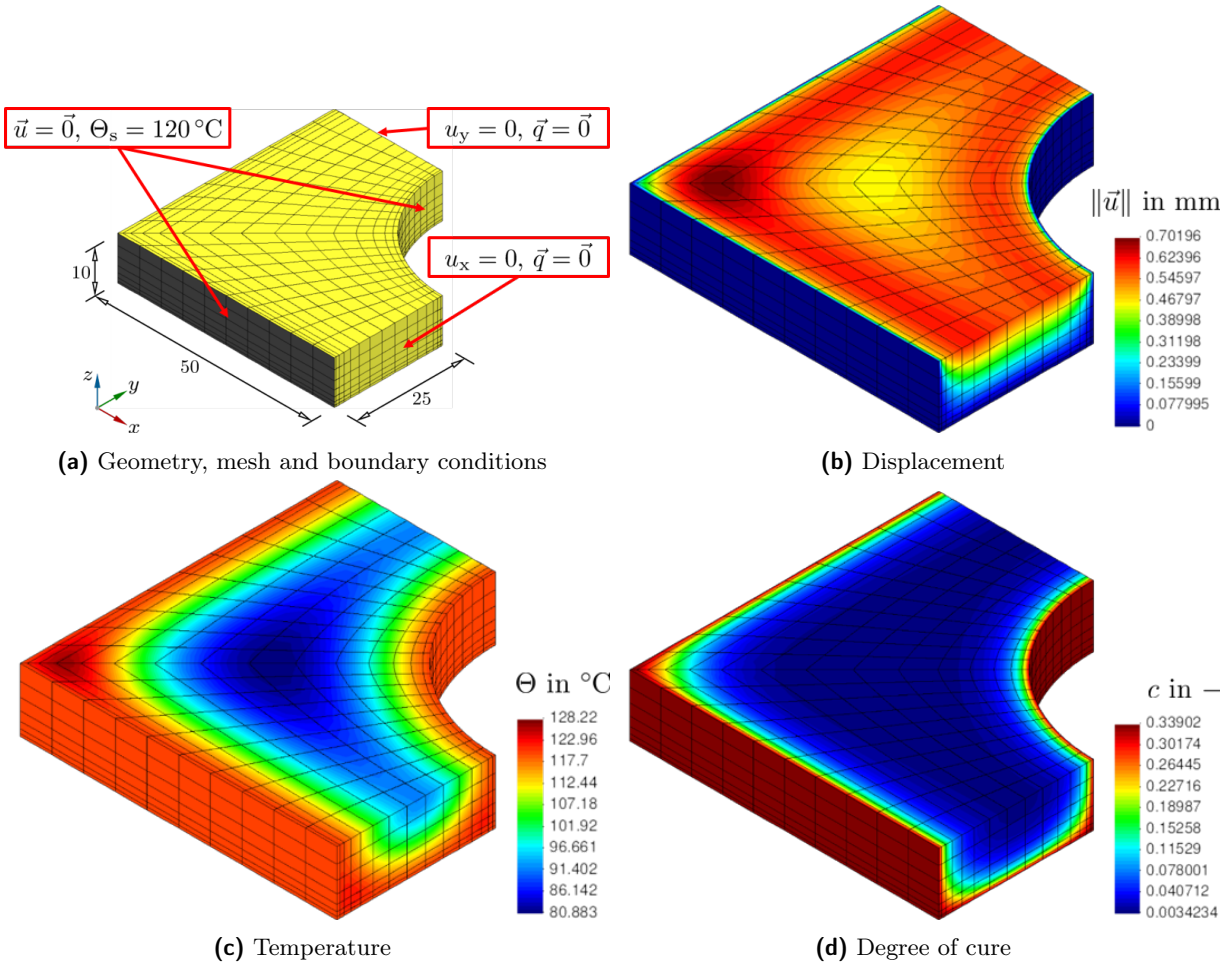

(a) Geometry, mesh and boundary conditions

(b) Displacement

(c) Temperature

(d) Degree of cure

Figure 3. Simulation example at $t = 350\,\mathrm{s}$

to solve the illustrated problem, we apply diagonally implicit Runge-Kutta (DIRK) methods extended by time-adaptivity based on [1] and the works cited therein. The resulting distributions of displacement, temperature and degree of cure at $t = 350\,\mathrm{s}$ are represented in Figs. 3b to 3d.

References

[1] P. Ellsiepen and S. Hartmann. Remarks on the interpretation of current non-linear finite element analyses as differential-algebraic equations. *International Journal for Numerical Methods in Engineering* 51 (2001), pp. 679–707.

[2] S. Hartmann. A thermomechanically consistent constitutive model for polyoxymethylene. *Archive of Applied Mechanics* 76.5-6 (2006), pp. 349–366.

[3] C. Leistner, S. Hartmann, D. Abliz, and G. Ziegmann. Modeling and simulation of the curing process of epoxy resins using finite elements. *accepted for publication, Continuum Mechanics and Thermodynamics* (2018), pp. 1–24.

[4] C. Leistner, S. Hartmann, J. Wittrock, and K. Bode. Shrinkage behavior of Araldite epoxy resin using Archimedes' principle. *Polymer Testing* 67 (2018), pp. 409–416.

[5] A. Lion, B. Dippel, and C. Liebl. Thermomechanical material modelling based on a hybrid free energy density depending on pressure, isochoric deformation and temperature. *International Journal of Solids and Structures* 51.3 (2014), pp. 729–739.

**Proceedings of the 8th GACM Colloquium on Computational Mechanics
for Young Scientists from Academia and Industry
August 28–30, 2019 in Kassel, Germany**

Modelling and simulation approaches for the numerical analysis of UV curing polymers used in additive manufacturing

T. Rehbein * [1], A. Lion[1] and M. Johlitz[1]

[1]Instute of Mechanics, Faculty of Aerospace Engineering, Bundeswehr University Munich

Abstract. This contribution focuses on the experimental characterisation and modelling of the crosslinking of UV curing polymers used in additive manufacturing processes such as digital light processing and stereolithography. First photocalorimetric measurements with varying temperature and light intensity are shown. From the exothermic specific heat flows measured during the crosslinking reaction, the degree of cure can be determined for each experimental scenario. It is shown that the test temperature and light intensity have a significant influence on the crosslinking reaction. A first modelling approach for the description of the crosslinking reaction is presented. Moreover, parameter identification and validation of the proposed model are conducted.

Introduction

Additive manufacturing (AM) is an innovative technology to create three dimensional objects with complex geometry. Although the technology has been used in industrial applications for decades, reliable and experimentally validated models for the design of printed components are still missing. Especially the material modelling and finite element analysis of UV curing polymers (so-called photopolymers) used in processes such as digital light processing and stereolithography are challenging tasks. For this purpose, the crosslinking reaction in the additive manufacturing process must be described correctly by a phenomenological model and adapted to experimental data.
The crosslinking of photopolymers is initiated by the absorption of a light source. Besides that, the process depends strongly on the ambient temperature: a higher ambient temperature leads to faster crosslinking whereby the same applies to an increasing light intensity. Calorimetric measurements with the aid of an additional light source have proved useful for the experimental investigation of the crosslinking reaction of photopolymers [2].
Since the degree of cure directly influences the mechanical, thermal and chemical properties of photopolymers, a validated material model for the degree of cure is essential for finite element analysis of additive manufacturing processes.

Experimental characterisation

In order to understand and investigate the crosslinking process of commercial photopolymers used in additive manufacturing processes, differential photocalorimetry (DPC) measurements are conducted using the TA Instruments DSC Q2000 with an additional light source (OmniCure® S2000). The light source contains a high pressure 200 W mercury lamp with an spectral output of 320 to 500 nm.
To investigate the crosslinking reaction, the DSC measures the specific heat flow $\dot{h}$ between a sample in a pan and an empty reference pan during the crosslinking reaction. The following relationship is used to convert the specific heat flow into the degree of cure:

$$q\left(t\right) = \frac{\int_0^t \dot{h}\left(\tilde{t}\right) \mathrm{d}\tilde{t}}{h_{\mathrm{tot}}} \tag{1}$$

*Corresponding author: rehbein@unibw.de

Due to the normalisation to the maximum specific heat h_{tot} during the crosslinking reaction, the degree of cure assumes values between 0 and 1.
The commercial photopolymer LOCTITE® 3D 3830 was used for the photocalorimetric measurements. It is an acrylic compound for prototype development with low elongation at break, high tensile strength and low chemical shrinkage. During the photocalorimetry measurement, following steps are performed subsequently for the determination of the specific heat flow $\dot{h}\left(\tilde{t}\right)$ in eq. (1):

1. Equilibration of the measurement cell at a specific temperature ($-10°\mathrm{C}\ldots 50°\mathrm{C}$).
2. Isothermal phase of 60 s.
3. Irradiation of the specimen for 300 s at constant light intensity (5 mW/cm^2 and 10 mW/cm^2).
4. Isothermal phase of 60 s.

After finishing step four, the whole procedure is repeated with the cured specimen generating the baseline. The baseline is subtracted from the heat flow signal of the first measurement to consider only the heat flow of the crosslinking reaction. Otherwise, the light energy input would be taken into account.
In order to determine the maximum specific heat h_{tot} during the crosslinking reaction, an additional measurement at non-isothermal temperature is performed. During 300 s irradiation, the temperature is increased from 20 °C to 70 °C at 5 °C/min leading to a maximum specific heat of $h_{\mathrm{tot}} = 319.73$ J/g which is taken as reference value for the conversion of the specific heat during crosslinking reaction into degree of cure for all measurements. The specific heat flows after substraction of the baseline of all

Table 1. Maximum attainable degree of cure $q_{\max}$ of all measurements

	−10 °C	0 °C	10 °C	20 °C	30 °C	40 °C	50 °C
5 mW/cm^2	0.469	0.619	0.675	0.775	0.851	0.904	0.947
10 mW/cm^2	0.593	0.685	0.775	0.845	0.907	0.949	0.997

measurements are shown in fig. 1. It can be clearly seen that the crosslinking reaction proceeds very quickly and that the specific heat flows have reached their maximum value after only a few seconds. Additionally, it is obvious that a higher light intensity leads to higher maximum values in the heat flows and that a higher temperature accelerates the reaction. Moreover, complete curing is not achieved at low temperatures and light intensities and the crosslinking reaction is stopped prematurely, cf. fig. 2. The maximum attainable degrees of cure $q_{\max}$ for all measurements are listed in table 1. It can be seen that an almost fully cured material is achieved at a temperature of 50 °C, regardless of the light intensity. This result must definitely be taken into account when formulating the material model for the degree of cure.

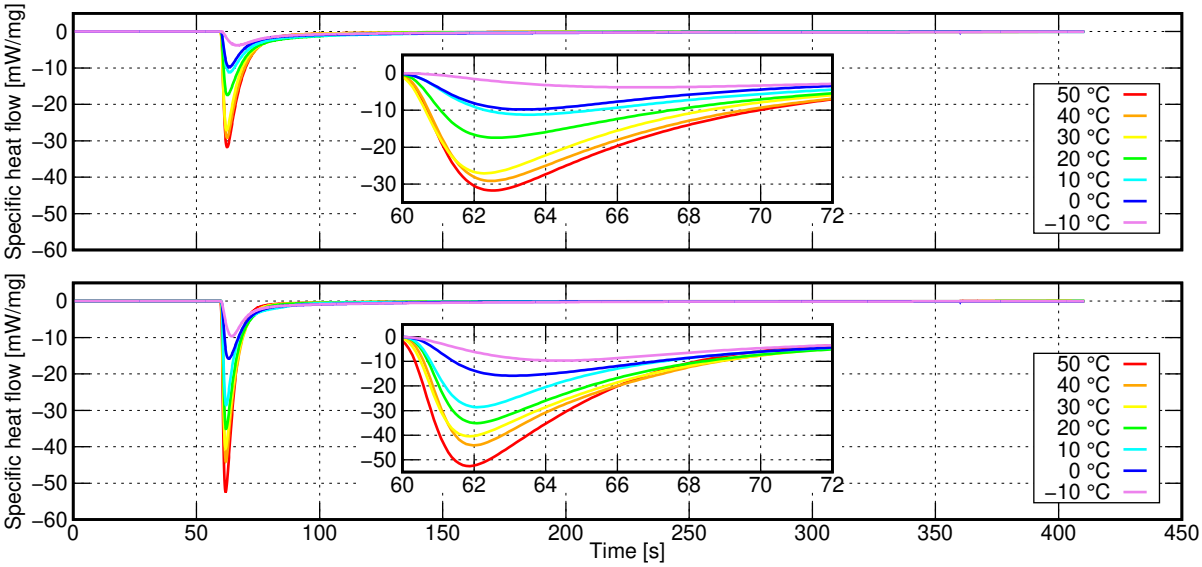

Figure 1. Measured specific heat flows after substraction of the baseline. Top: light intensity $\mathcal{I} = 5$ mW/cm^2, bottom: light intensity $\mathcal{I} = 10$ mW/cm^2.

Modelling of the degree of cure

The differential equation for the degree of cure q depends on time, light intensity $\mathcal{I}(z(t),t)$ and temperature T. Following the work of Kamal [3], an autocatalytic model of $(m+n)$th order incorporating the maximum attainable degree of cure $q_{\max}$ is applied for the degree of cure q:

$$\dot{q} = \left(k_1\left(\mathcal{I}(z(t),t),T\right) + k_2\left(\mathcal{I}(z(t),t),T\right)q^m\right)\left(q_{\max}-q\right)^n \quad . \tag{2}$$

Here, $\mathcal{I}(z(t),t)$ denotes the time- and location-dependent light intensity. The light intensity must depend on the vertical location $z(t)$ since it evolves during the printing process. The maximum attainable degree of cure acts as a limit value. The constants

$$k_i\left(\mathcal{I}(z(t),t),T\right) = k_{0i}(T)\left(\frac{\mathcal{I}(z(t),t)}{\mathcal{I}_{\text{ref}}}\right)^b \tag{3}$$

with the Arrhenius type equations

$$k_{0i}(T) = A_i \exp\left(-\frac{E_i}{RT}\right) \tag{4}$$

are based on the proposal by Maffezzoli and Terzi [5] depending on light intensity $\mathcal{I}(z(t),t)$ and temperature T. If no light source is present, i.e. $\mathcal{I}(z(t),t)=0$, the crosslinking reaction is stopped. A_i and E_i are pre-exponential factors and activation energies, respectively. R denotes the universal gas constant. The additional parameter b is introduced for a better representation of experimental data. Furthermore, the auxiliary variable $\mathcal{I}_{\text{ref}} = 1\ \text{mW/cm}^2$ is used to convert the light intensity into a unitless value.

Parameter identification and validation

The parameters in eq. (2) are identified using the commerical optimisation program LS-OPT® in combination with MATLAB®'s `ode45` solver. LS-OPT® uses the sequential response surface method for optimisation. For further informations see [6].
The parameter identification depends strongly on the initial values. The parameters listed in table 2 represent the first result of the parameter identification which identified the equation for the degree of cure on the measurement results. For simplification, the particular maximum attainable degree of cure was specified as a parameter in order to achieve a better agreement with the measurement results. Fig. 2 shows the simulations of the degree of cure compared to all measurements according to eqs. (1) and (2) with identified model parameters.

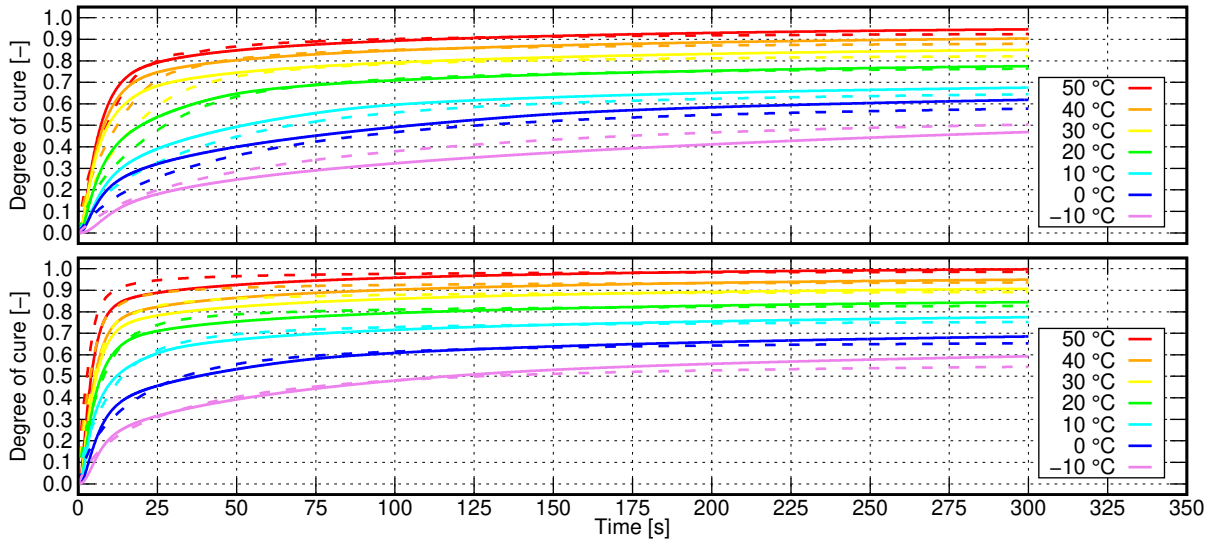

Figure 2. Measurement (—) and simulation (- -) of the degree of cure q with identified model parameters. Top: light intensity $\mathcal{I} = 5\ \text{mW/cm}^2$, bottom: light intensity $\mathcal{I} = 10\ \text{mW/cm}^2$.

Table 2. Identified model parameters for the description of the crosslinking reaction

A_1	A_2	E_1	E_2	R	m	n	b
1/s	1/s	J/mol	J/mol	J/(mol K)	-	-	-
0.6606	0.8744	9794	1001	8.314	4.554	2.996	1.365

Summary and outlook

First measurements for the experimental characterisation of the crosslinking reaction of photopolymers used in additive manufacturing processes are presented in this contribution. It is shown that temperature and light intensity have a significant influence on the crosslinking reaction.
A differential equation incorporating the maximum attainable degree of cure $q_{\max}$ is proposed for the phenomenological description of the degree of cure. Parameter identification using commercial optimisation tools is carried out. The validation shows a good agreement between measurements and simulations. Forthcoming considerations include the correct description of the maximum attainable degree of cure as a function of temperature and light intensity:

$$q_{\max} = f\left(T, \mathcal{I}\right) \tag{5}$$

Kolmeder et al., for example, have already carried out work for this purpose [4]. Since the glass transition temperature of acrylic photopolymers strongly depends on the degree of cure, conventional DSC measurements must be performed after irradiation to determine the glass transition temperature for distinct degrees of cure. Subsequently, DiBenedetto's proposal [1] can also be used to establish a relationship between the maximum attainable degree of cure and the glass transition temperature.

Acknowledgement

The authors would like to thank the German Research Foundation (DFG) and Agence nationale de la recherche (ANR) for the financial support of the project "Constitutive modeling of UV-curing printed polymer composites".

References

[1] A. T. Di Benedetto. Prediction of the Glass Transition Temperature of Polymers: A Model Based on the Principle of Corresponding States. *Journal of Polymer Science: Part B: Polymer Physics* 25 (1987), pp. 1949–1969.

[2] G. W. H. Höhne, W. F. Hemminger, and H.-J. Flammersheim. *Differential Scanning Calorimetry*. Springer-Verlag Berlin Heidelberg, 2003.

[3] M. R. Kamal. Thermoset Characterization for Moldability Analysis. *Polymer Engineering and Science* 14.3 (1974), pp. 231–239.

[4] S. Kolmeder, A. Lion, R. Landgraf, and J. Ihlemann. Thermophysical properties and material modelling of acrylic bone cements used in vertebroplasty. *Journal of Thermal Analysis and Calorimetry* 105 (2011), pp. 705–718.

[5] A. Maffezzoli and R. Terzi. Effect of irraditation intensity on the isothermal photopolymerization kinetics of acrylic resins for stereolithography. *Thermochimica Acta* 321 (1998), pp. 111–121.

[6] N. Stander, W. Roux, A. Basudhar, T. Eggleston, T. Goel, and K. Craig. *LS-OPT® User's Manual*. Livermore Software Technology Corporation. 2015.

**Proceedings of the 8th GACM Colloquium on Computational Mechanics
for Young Scientists from Academia and Industry
August 28–30, 2019 in Kassel, Germany**

Simulation of delamination in ferromagnetic-ferroelectric laminate composites

Alexander Schlosser * [1] and Andreas Ricoeur[1]

[1]University of Kassel

Abstract. A cohesive zone model for magnetoelectromechanical loadings is presented and the influence of Maxwell stresses on the fracture behavior is investigated taking the example of a bimaterial DCB-specimen. Furthermore, the influence of delamination in magnetoelectric laminates on their functional coupling properties is shown.

1 Introduction

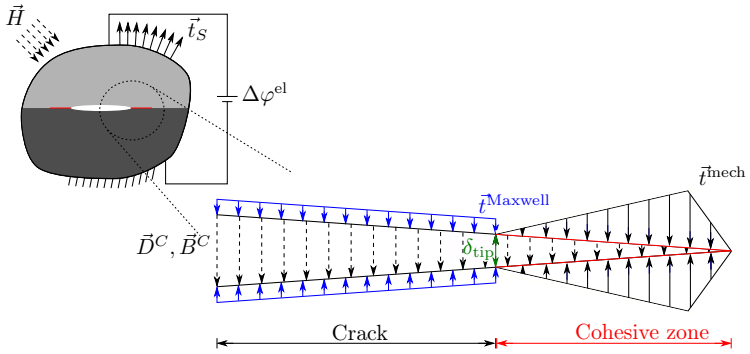

Figure 1. Interface crack under magnetoelectromechanical loading and a cohesive model

The efficiency in converting magnetic into electric energy and vice versa makes magnetoelectric (ME) composites promising candidates for many technical applications. The ferroelectric matrix as well as the magnetostrictive inclusions of particle composites and the layers of laminates are mostly ceramics or other brittle materials, thus being prone to cracking. Independent from the kind of composite the transmission of stresses via the interfaces between the constituents plays the key role in the functionality of ME composites. Therefore, the investigation of delamination processes is of great interest for the prediction of durability and coupling factors. In order to investigate delamination processes in ME composites, cohesive elements are being developed and applied in combination with ME finite elements described in [1] and [2]. Those cohesive elements must be able to describe delamination fracture processes under magnetoelectromechanical loadings as seen in Figure 1.

2 Theoretical framework

2.1 Magnetoelectroelastic behavior during delamination

The ME cohesive element is based on a potential

$$\Psi = \Psi^{\mathrm{mech}} - \frac{1}{2}\left(\overline{\kappa}\frac{(\Delta\varphi^{\mathrm{el}})^2}{\delta_n + \Delta_0} + \overline{\mu}\frac{(\Delta\varphi^{\mathrm{mag}})^2}{\delta_n + \Delta_0}\right) - \overline{e}_i\delta_i\Delta\varphi^{\mathrm{el}} - \overline{q}_i\delta_i\Delta\varphi^{\mathrm{mag}}, \tag{1}$$

*Corresponding author: alexander.schlosser@uni-kassel.de

where δ_i, $\Delta\varphi^{\mathrm{el}}$ and $\Delta\varphi^{\mathrm{mag}}$ are the discontinuities of the displacement, the electric potential and the magnetic potential at the interface. δ_n, in particular, denotes the normal displacement jump. Here $\overline{\mu}$ and $\overline{\kappa}$ are the magnetic and electric permeabilities, respectively. The vectors $\overline{q}_i$ and $\overline{e}_i$ represent piezomagnetic and -electric behaviors of the interface. The mechanical contribution Ψ^{mech} can be adapted to any mechanical behavior of choice. In the following, a mechanical potential in the form of $\Psi^{\mathrm{mech}} = \overline{c}_{ij}\delta_i\delta_j$ is used, where $\overline{c}_{ij}$ is the cohesive stiffness tensor. The constitutive equations of the interface result from the derivative of Eq. (1) with respect to the related independent variables. This leads to a composition of five contributions to the restraining stress vector:

$$t_i = \frac{\partial\Psi}{\partial\delta_i} = \overline{c}_{ij}\delta_j + \frac{1}{2}\Big(\overline{\kappa}\Big(\frac{\Delta\varphi^{\mathrm{el}}}{\delta_n+\Delta_0}\Big)^2 + \overline{\mu}\Big(\frac{\Delta\varphi^{\mathrm{mag}}}{\delta_n+\Delta_0}\Big)^2\Big)n_i - \overline{q}_i\Delta\varphi^{\mathrm{mag}} - \overline{e}_i\Delta\varphi^{\mathrm{el}}. \tag{2}$$

The first contribution is the classical mechanical one resulting from the chosen traction-separation-law (TSL). The second and third parts are the contributions of the electric and magnetic fields to the Maxwell-stresses, followed by the linear piezomagnetic and -electric stress contributions. The derivations with respect to the magnetic and electric potential jumps lead to the cohesive constitutive equations for the magnetic surface normal $B_i n_i$ and the electric surface charge ω_{S}:

$$\begin{aligned} B_i n_i &= -\frac{\partial\Psi}{\partial\Delta\varphi^{\mathrm{mag}}} = \overline{\mu}\frac{\Delta\varphi^{\mathrm{mag}}}{\delta_n+\Delta_0} + \overline{q}_i\delta_i \\ &\text{and} \\ D_i n_i &= -\omega_{\mathrm{S}} = -\frac{\partial\Psi}{\partial\Delta\varphi^{\mathrm{el}}} = \overline{\kappa}\frac{\Delta\varphi^{\mathrm{el}}}{\delta_n+\Delta_0} + \overline{e}_i\delta_i. \end{aligned} \tag{3}$$

The first terms in the Eqs.(3) are an extended capacitor analogy, originally introduced in [3]. The extension is on the one hand composed of a small constant Δ_0 which is mainly incorporated to avoid division by zero during numerical simulations. On the other hand, it is a dependency of the permeabilities on the damage state of the interface (see below). The second terms, in turn, are the contributions of piezomagnetic and - electric effects. All above mentioned material constants depend on a damage variable f which is driven by the chosen TSL. This variable leads to a decrease of all material properties during the fracture or delamination process, respectively. The properties $\overline{c}_{ij}, \overline{e}_i$ and $\overline{q}_i$ decrease to zero when the surface is completely damaged. Following [4], the permeabilities $\overline{\mu}$ and $\overline{\kappa}$ decrease to the properties of a chosen medium (e.g. air) filling the emerging crack.

3 Results

3.1 Fracture behavior under mode I/II/IV/V loading

A composite of one layer $BaTiO_3$ (upper half) and one layer $CoFe_2O_4$ (lower half) is investigated. Both materials exhibit linear behavior and are perfectly poled in x_2-direction meaning that no switching processes occur. Cohesive zone elements with the above described behavior are implemented between the two layers. The piezoelectric and -magnetic properties of the cohesive zone are both neglected. The permeabilities, including κ_{Bulk} nad μ_{Bulk}, are defined as averages between the upper and lower layer. Two test cases have been simulated. In both cases first an electric field and a crack mouth opening displacement u_{COD} are applied creating a Mode I/II/IV/V-loading. The Mode-II contribution arises from the asymmetry of the specimen in combination with the piezoelectric effect. In the first set of simulations the opening displacement was increased until the crack had grown through the whole specimen. In the second case, a constant displacement is applied in a way that the crack only partly propagates through the specimen. Figure 3 (Left) shows load-displacement-curves for different electric loadings ranging from

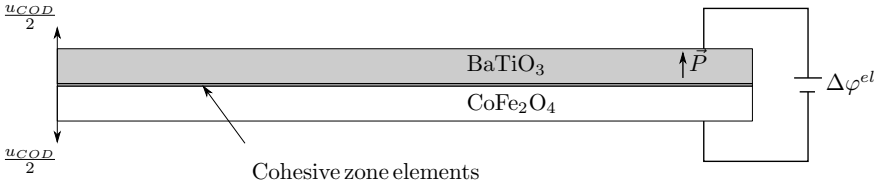

Figure 2. Two-layer-composite made of $BaTiO_3$ and $CoFe_2O_4$ and electromechanical loading

-1000 to 1000 V/mm. For positive signs, the electric field is parallel to the poling direction and for negative ones it is antiparallel. One can clearly see a significant nonlinear influence of the electric field

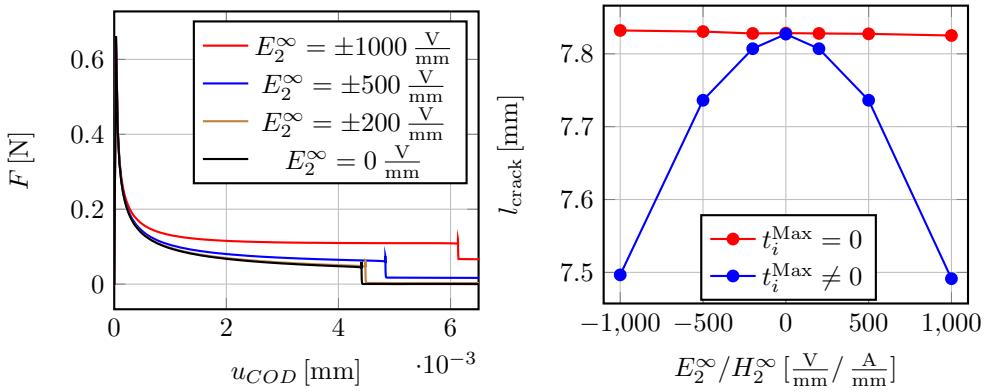

Figure 3. Left:load-displacement curves of the DCB-specimen with linearly increased opening displacements and different electric fields. Right: crack lengths for a constant opening displacement $u_{COD} = 1.0 \cdot 10^{-3}$ mm and different electric fields simulated with and without Maxwell stresses.

on the fracture behavior and at the same time an independece on the sign of the electric field. This leads to the conclusion that, lacking piezoelectric properties of the cohesive or fracture process zone, the only relevant influence of the electric load on the fracture behavior comes from the Maxwell stresses which are proportional to the square of the electric field in the crack. The same conclusion can be drawn from the results shown in the right plot of Figure 3. Here, the crack lengths for a constant opening displacement $u_{COD} = 1.0 \cdot 10^{-3}$ mm and various electric fields simulated with and without Maxwell stresses are shown. The crack lengths show a quadratic dependence on the electric field due to the Maxwell stresses. The results without Maxwell stresses show a small ($\ll 1\%$) dependency on the electric field which is caused by the piezoelectric and -magnetic behaviors of the bulk materials.

3.2 Influence of interface cracks on ME coupling

As a second test specimen a three-layered composite in L-L configuration (both constituents are polarized/magnetized along the long edge of the laminate) was created. It also consists of $CoFe_2O_4$ and $BaTiO_3$ with linear piezomagnetic and -electric behaviors. It is loaded with a magnetic field antiparallel to the magnetization vector. Figure 4 shows the shear and normal stress distributions along a perfect interface (no cohesive elements) under a large magnetic loading of $H_1 = -1000$ A/mm. The stress distribution is quite similar to one known from the free-edge effect (see [5]) and probably also mathematically singular at the free edges. To investigate the influence of interface cracks on the ME coupling coefficient $g_{11} = \frac{E_1}{H_1}$, cohesive elements are placed along the interfaces. In order to mimic semipermeable cracks, the damage variable f was locally set to $f = 1$. Figure 5 shows the results of these simulations for different

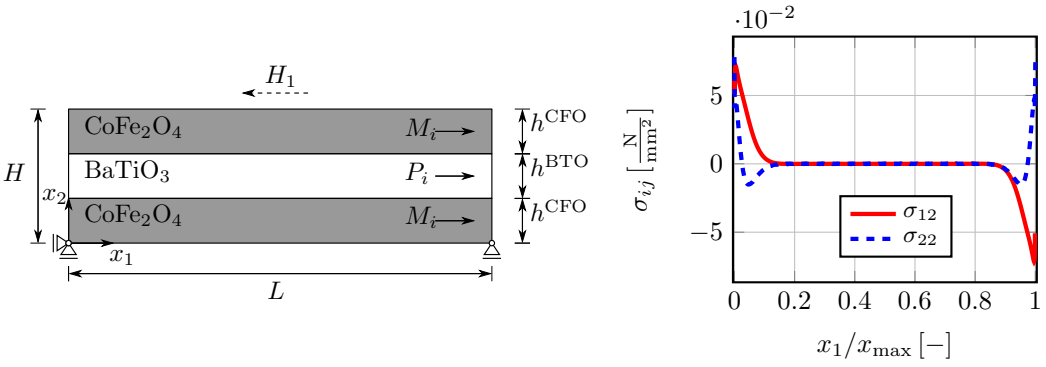

Figure 4. Left: three layered ME composite. $H = 1$ mm, $L = 10$ mm, $\frac{h^{\mathrm{BTO}}}{H} = 0.5$. Right: shear and normal stresses along the interface

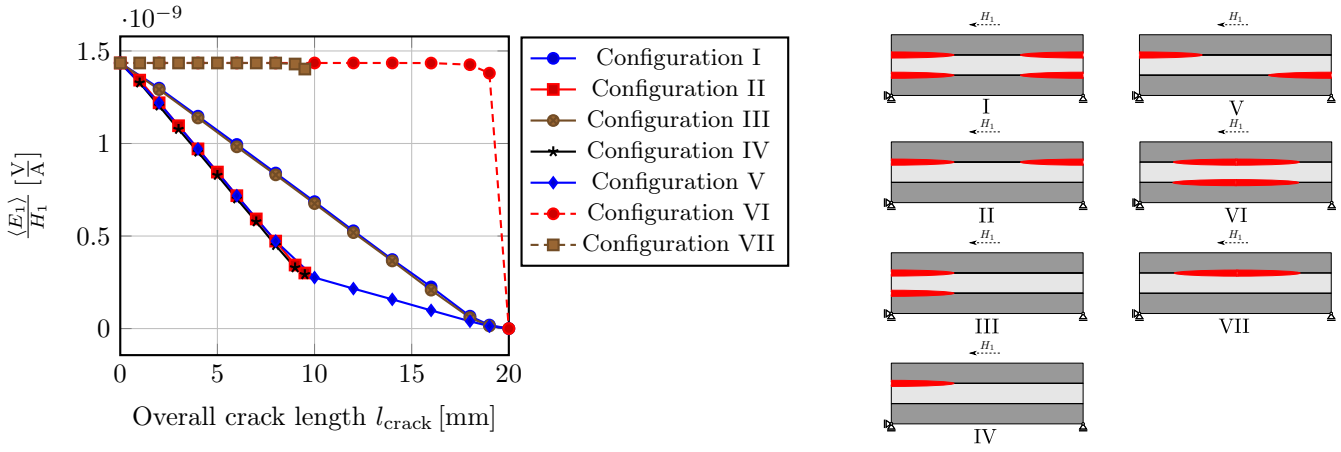

Figure 5. Influence of crack lengths of different crack configurations on the ME coupling

crack configurations under a minor load of $H_1 = 1$ A/mm to avoid crack growth. The coupling coefficient decreases linearly with increasing crack lengths for the configurations I-IV and bilinearly for configuration V. In case of inner cracks, the coupling coefficient is only significantly effected for $l_{\text{crack}} \approx L$.

4 Conclusion

A cohesive zone element for delamination under magnetoelectromechanical loading has been developed and implemented in the commercial FE software ABAQUS. The influence of Maxwell stresses on the fracture behavior under mode I/II/IV/V loading has been shown at a bimaterial DCB-specimen. Furthermore the influence of delamination on the MEcoupling of a three-layered laminate in L-L-configuration has been investigated.

References

[1] Artjom Avakian and Andreas Ricoeur. Constitutive modeling of nonlinear reversible and irreversible ferromagnetic behaviors and application to multiferroic composites. *Journal of Intelligent Material Systems and Structures* 27.18 (2016), pp. 2536–2554.

[2] Artjom Avakian, Roman Gellmann, and Andreas Ricoeur. Nonlinear modeling and finite element simulation of magnetoelectric coupling and residual stress in multiferroic composites. *Acta Mechanica* 226.8 (2015), pp. 2789–2806.

[3] Tian-Hu Hao and Zi-Yuan Shen. A new electric boundary condition of electric fracture mechanics and its applications. *Engineering Fracture Mechanics* 47.6 (1994), pp. 793–802.

[4] Sergii Kozinov, Meinhard Kuna, and Stephan Roth. A cohesive zone model for the electromechanical damage of piezoelectric/ferroelectric materials. *Smart Materials and Structures* 23.5 (2014), p. 055024.

[5] Christian Mittelstedt and Wilfried Becker. Interlaminar stress concentrations in layered structures: Part I-a selective literature survey on the free-edge effect since 1967. *Journal of Composite Materials* 38.12 (2004), pp. 1037–1062.

**Proceedings of the 8th GACM Colloquium on Computational Mechanics
for Young Scientists from Academia and Industry
August 28–30, 2019 in Kassel, Germany**

Simulation and Modeling of Stator Elastomers in Positive Displacement Motors

Alexander Schöne * [1], Ralf Landgraf[1] and Jörn Ihlemann[1]

[1]Chair of Solid Mechanics, Chemnitz University of Technology, Chemnitz, Germany

Abstract.

Positive Displacement Motors contain an elastomer lining. During operation, the rubber is not only exposed to mechanical loads, but also to volume changing effects. This loading leads to failure of the elastomer lining and thus to failure of the whole motor. Consequently, it is necessary to consider the mentioned effects within numerical simulations of the motor, which is possible by a corresponding extension of a material model for the simulation of rubber like behavior. Obtained results show a significant influence of the volume changing effects on the stresses and strains in the elastomer.

Introduction

Positive displacement motors (PDMs) are the most important drives for drilling operations in the oil and gas industry. They deliver a high power density and are suitable for directional drilling [4]. Furthermore, they are very economical and flexible in comparison to other types of downhole power units. The power section of a PDM consists of a steel rotor and a contoured stator with an elastomer lining. Rotor and stator have a different number of helical lobes, so that cavities between the two parts arise. Due to the high pressure of the drilling fluid inside the drillstring, the cavities inside the power section move, which leads to a rotation of the rotor inside the stator. Thus, the hydraulic energy of the fluid is converted into mechanical energy of the rotating rotor, which drives the drill bit [1].

The purpose of the elastomer lining is to seal the cavities from each other and to ensure a tolerance regarding manufacturing inaccuracies. So it is of essential relevance for the whole power section. Moreover, most failures of PDMs are due to failures of the stator elastomer. The rubber is not only exposed to the mechanical loading due to the rotation of the rotor, but also to different volume changing effects. Beside high temperature changes and huge hydrostatic pressures, also interactions with the drilling fluid and additives contained therein cause significant volume changes. In order to model the resulting stresses and strains inside the elastomer properly, it is necessary to take these effects into account.

1 Setup of the FE-model

In order to simulate the power section of a PDM with the use of the finite element method (FEM), an appropriate model is required. This model should consider all important geometric and load information and it should deliver highly resolved results in a reasonable amount of calculating time. One way to achieve both of these contrary aspects is to simulate just a small part of the power section, which has to be representative for the geometry and the load of the whole power section. Therefore, it is called a representative model section (RMS).

The entire geometry would be received by a regular repetition of the RMS along the motor axis. To take this repeatable structure of the sector into account, periodic boundary conditions (PBCs) are used. They create couplings between the displacements of corresponding nodes on associated end faces by applying

*Corresponding author: alexander.schoene@mb.tu-chemnitz.de

coupling equations [3]. Thus it is guaranteed, that neither penetrations nor gaps occur between the corresponding faces of adjacent RMSs.

Figure 1 depicts an RMS, which has been used for the simulation of the power section during operation. The outer component in light gray is the contoured steel stator. On its inside is the elastomer lining of even thickness (dark gray). The middle part is the steel rotor, which can rotate around the stator axis and its own axis. It can be seen, that the rubber lining is meshed much finer than the other components. The PBCs are applied on the front faces of all three parts and the corresponding faces at the back of the RMS, which are not visible in the picture.

2 Material modeling

2.1 Modeling of inelastic rubber materials with the MORPH material model

For modeling the behavior of the polymer, the MORPH (**Mo**del of **R**ubber **Ph**enomenology) material model is used [2, 5]. It is a constitutive model to consider typical effects of filled rubber materials undergoing large deformations, like nonlinearity, hysteresis and Mullins effects. The MORPH model includes eight independent parameters $p_1 - p_8$.

The equations for the MORPH are given in the box below. The total Cauchy stress $\underline{\underline{\sigma}}$ is composed of a Neo-Hookean like component, which depends on the material function α and the left Cauchy-Green tensor $\underline{\underline{b}}$, an additional stress $\underline{\underline{\sigma}}^A$, and a hydrostatic part including the hydrostatic pressure p and the unit tensor $\underline{\underline{I}}$, where $()'$ denotes the deviatoric part. The additional stress is constituted by an ordinary differential equation using the Zaremba-Jaumann derivative $\overset{*}{\underline{\underline{\sigma}}}^A$. It depends on the material function β, the Tresca invariant of the Zaremba-Jaumann rate of the Cauchy-Green tensor $\overset{*}{b}_T$ and the limiting stress $\underline{\underline{\sigma}}^L$. The latter is calculated by an exponential tensor function and includes a further material function γ. Moreover, the factor b_T^S describes the maximum Tresca invariant of the Cauchy-Green tensor in the time span $[0, t]$. It takes the pre-stretch into account and thus is a measure for the softening. To use the MORPH for a specific material, the eight material parameters $p_1 - p_8$ have to be identified by appropriate experiments.

$$\underline{\underline{\sigma}} = \left(2\alpha \underline{\underline{b}} + \underline{\underline{\sigma}}^A\right)' - p\underline{\underline{I}} \qquad \overset{*}{\underline{\underline{\sigma}}}^A = \beta \overset{*}{b}_T \left(\underline{\underline{\sigma}}^L - \underline{\underline{\sigma}}^A\right) \qquad \underline{\underline{\sigma}}^L = \gamma \exp\left(\left(p_7 \frac{\overset{*}{\underline{\underline{b}}}}{\overset{*}{b}_T} \frac{b_T}{b_T^S}\right)\right) + p_8 \frac{\overset{*}{\underline{\underline{b}}}}{\overset{*}{b}_T}$$

$$b_T = \max\left[|b_I - b_J| \,;\, I, J = 1, 2, 3\right] \qquad b_T^S = \max\left[b_T\left(\tau\right) \,;\, 0 \le \tau \le t\right]$$

$$\alpha = p_1 + \frac{p_2}{\sqrt{1 + \left(p_3 b_T^S\right)^2}} \qquad \beta = \frac{p_4}{\sqrt{1 + \left(p_3 b_T^S\right)^2}} \qquad \gamma = p_5 b_T^S \left(1 - \frac{p_6}{\sqrt{{p_6}^2 + \left(b_T^S\right)^2}}\right)$$

For the usage of the MORPH material model in the context of an FE-simulation within the commercial software ABAQUS, an appropriate implementation is required. Therefore, the available user interface UMAT (User subroutine to define a material's mechanical behavior) is used. The basis for the implementation of the MORPH material model is the strain rate tensor $\underline{\underline{D}}$. In comparison to an implementation based on the deformation gradient $\underline{\underline{F}}$, the usage of $\underline{\underline{D}}$ has the advantage of more stability and an extended load range can be simulated.

2.2 Extension of MORPH with respect to volume changing effects

Because the implementation is based on the strain rate tensor, the extension for volume changing effects uses the additive decomposition of the strain rate tensor. The modeled effects are chemical shrinkage during the vulcanization process, thermal expansion due to temperature changes and swelling as a result of the exposure of the stator elastomer to drilling fluids.

The modeling of volume changes is done by the introduction of a function φ, which represents the volume ratio of corresponding deformations. The formulation of the deformation gradient due to volume changes reads

$$\underline{\underline{F}}_{\varphi} = \varphi^{1/3} \underline{\underline{I}} \,. \tag{1}$$

With the help of the relation between deformation gradient and strain rate tensor in the form

$$\underline{\underline{D}}_{\varphi} = \left(\dot{\underline{\underline{F}}}_{\varphi} \cdot \underline{\underline{F}}_{\varphi}^{-1} \right)^{S} , \tag{2}$$

the equivalent formulation for the strain rate tensor is given by

$$\underline{\underline{D}}_{\varphi} = \frac{1}{3} \frac{\dot{\varphi}}{\varphi} \underline{\underline{I}} \,. \tag{3}$$

Taking into account the dependency of function φ from the temperature θ, the swelling variable $q \in [0,1]$ and the shrinkage variable $s \in [0,1]$, equation (3) becomes:

$$\underline{\underline{D}}_{\varphi} = \frac{1}{3} \frac{1}{\varphi} \left(\frac{\partial \varphi}{\partial \theta} \dot{\theta} + \frac{\partial \varphi}{\partial q} \dot{q} + \frac{\partial \varphi}{\partial s} \dot{s} \right) \underline{\underline{I}} \,. \tag{4}$$

To evaluate this equation, it is necessary to formulate a specific ansatz for the function φ, which considers the three volume changing effects. Each of these aspects uses an exponential approach to calculate the associated volume changes:

$$\varphi_{\theta}(\theta) = \exp\left(\alpha_T \left(\theta - \theta_{ref}\right)\right) \qquad \varphi_Q(q) = \exp\left(\alpha_Q \left(q - q_{ref}\right)\right) \qquad \varphi_S(s) = \exp\left(\alpha_S \left(s - s_{ref}\right)\right) . \tag{5}$$

Within these equations, the different α-parameters represent constant volumetric expansion coefficients, while θ_{ref}, q_{ref} and s_{ref} are the reference values for temperature, swelling and shrinkage, respectively. To consider all three effects in one simulation, different ways of connecting them and taking interactions between them into account are thinkable. By now they have been treated as independent, but couplings could easily be added.

On the basis of an implementation of the presented equations it is possible to simulate the volume changing effects of rubber linings in PDMs.

3 Numerical results

The numerical simulations of the RMS shown in figure 1 have been carried out with the commercial FE-software ABAQUS. At this point, a short overview about the general behavior of the elastomer inside the power section will be provided based on the obtained simulation results.

The investigation of strains and stresses inside the rubber lining show repetitive distributions following the movement of the rotating rotor in the stator. As expected, the hydrostatic pressure forms a maximum line along the contact area between rotor and stator. Instead, the distribution of the von Mises stress behaves significantly different, which is shown in figure 2. The picture displays a contour plot of the stresses in the elastomer. Rotor and contoured stator, which have also been modeled, are not shown in this picture.

It is clearly visible, that not one single maximum line occurs, but a combination of two maximum lines separated by a minimum line. The reason for this behavior is, that rubber materials prefer shape changes in comparison to volume changes. Consequently, the elastomer moves away from the direct contact zone with the rotor. This explains the characteristic distribution of the von Mises stress, which takes the deviatoric stresses into account. The minimum line in the middle of the two maximum lines is due to nearly pure volumetric deformations in this area. So in total, with each rotation of the rotor, every material point inside the elastomer undergoes a combination of a shape change, followed by a volume change and a second shape change.

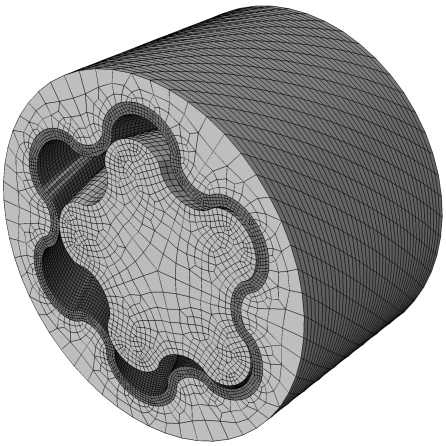

Figure 1. Meshed RMS for the simulation of the drilling process

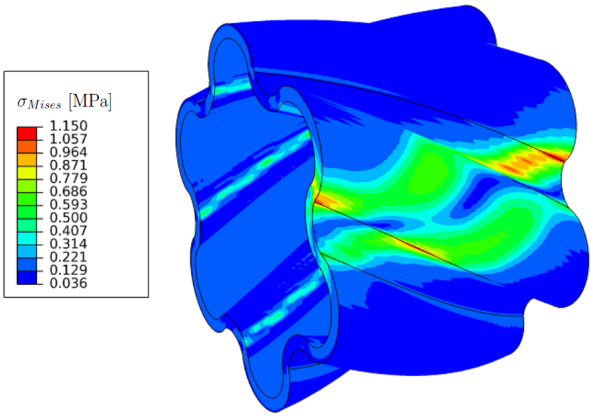

Figure 2. Distribution of von Mises stress in the elastomer during operation

The described distribution occurs also if the volume changing effects are neglected in the simulation, but the absolute values of stresses and strains are substantially smaller. So it is necessary to consider the volumetric effect, to get realistic results for the mechanical load of the elastomer.

To understand the influence of different material properties, parameter variations have been carried out. They show that the bulk modulus as well as the investigated volumetric expansion coefficients have a strong impact on the resulting deformations, strains and stresses. So even little changes of those material parameters lead to a significant change of the results, which demonstrates the importance of taking these effects into account. Furthermore, the dependency of the results on the material parameters offers the opportunity to influence the internal loads in the stator elastomer and thus its fatigue life.

Conclusions

The MORPH material model has been extended to take volume changing effects of the elastomer in PDMs into account. The results of numerical simulations show very characteristic stress and strain distributions, because rubber materials prefer shape changes compared to volume changes. In general, it is important to consider the volume effects, because they have a significant influence on the mechanical load and thus on the fatigue life of the stator elastomer. In future work, experiments should be performed to understand the interactions between the described effects. Moreover, the vulcanization process could be regarded in more detail, like given in [5]. In drilling mode, further aspects, like hysteresis heating and the resulting thermal expansion, should be investigated. Finally, the model should be extended to take the external loads in downhole operation into account, that have a big influence on the power section behavior.

References

[1] S. BA, M. Pushkarev, A. Kolyshkin, L. Song, L. L. Yin, et al. Positive Displacement Motor Modeling: Skyrocketing the Way We Design, Select, and Operate Mud Motors. In: *Abu Dhabi International Petroleum Exhibition & Conference*. Society of Petroleum Engineers. 2016.

[2] D. Besdo and J. Ihlemann. A phenomenological constitutive model for rubberlike materials and its numerical applications. *International Journal of plasticity* 19.7 (2003), pp. 1019–1036.

[3] N. Goldberg, H. Donner, and J. Ihlemann. Evaluation of hyperelastic models for unidirectional short fibre reinforced materials using a representative volume element with refined boundary conditions. *TECHNISCHE MECHANIK* 35.2 (2015), pp. 80–99.

[4] T. Jaeger and J. L. Herlitzius. *Navi-Drill Motor Handbook*. Baker Hughes Incorporated, 2016.

[5] R. Landgraf and J. Ihlemann. Application and extension of the MORPH model to represent curing phenomena in a PU based adhesive. In: *Constitutive Models for Rubber X*. CRC Press, 2017, pp. 137–143.

**Proceedings of the 8th GACM Colloquium on Computational Mechanics
for Young Scientists from Academia and Industry
August 28–30, 2019 in Kassel, Germany**

Transient dissipation heating in polycrystalline ferroelectrics accounting for mutual nonlinear couplings

Andreas Warkentin * [1] and Andreas Ricoeur[1]

[1]Institute of Mechanics, Chair of Engineering Mechanics/ Continuum Mechanics, University of Kassel, Moenchebergstraße 7, 34125 Kassel, Germany

Abstract. This research is on irreversible domain wall motion, leading to a transient change in temperature of the material, the so–called self–heating, if materials are subjected to high frequencies and large electrical loads with insufficient heat dissipation. This work shows both the theoretical fundamentals and results of the temperature change in ferroelectric materials assuming transient heating, as well as theoretical fundamentals and results assuming an adiabatic process compared to experimental findings. Predictions concerning polycrystalline material behavior are made by the condensed method.

Introduction

Ferroelectric materials, such as lead zirconate titanate (PZT) or barium titanate (BT) are technically attractive ceramics because of their special properties. They are often used for actuators or sensors in the precision range. Problems arise due to irreversible domain wall motion leading to self–heating associated with changes in the material properties, thermal stresses and sometimes even phase transformations, whereupon the devices finally are inoperative. In low Curie temperature materials, such as BT, even depolarization is possible.
In order to be able to make predictions about the functionality in ferroelectric materials as a result of temperature changes, it is necessary to be able to calculate the temperature change in ferroelectrics due to irreversible domain–switching processes. For this purpose, the so–called condensed method (CM) is extended by nonlinear bilateral caloric–electromechanical couplings, whereby the temperature change in ferroelectric materials can be calculated based on a single polycrystalline material point representing the entire material. The CM has been developed to simulate e.g. hysteresis loops and residual stresses for polycrystalline materials without spatial discretization of the grain structure. It is suitable and efficient for the implementation of different constitutive behaviors, considering interactions between grains or different components of a material compound with low computational complexity and high numerical stability [2].
In addition, a comparison of the results by this work and those of the FEM according to [4] is presented. For further verification, the theoretical results from the CM and FEM are compared to experimental results from [1].

1 Basic equations

In addition to the nonlinear constitutive equations of a thermoelectromechanical problem

$$\sigma_{ij} = C_{ijkl}\left(\varepsilon_{kl} - \varepsilon_{kl}^{\mathrm{irr}}\right) - e_{lij}E_l - \beta_{ij}\theta\,, \tag{1}$$

$$D_i = e_{ikl}\left(\varepsilon_{kl} - \varepsilon_{kl}^{\mathrm{irr}}\right) + \kappa_{ij}E_j + k_i\theta + P_i^{\mathrm{irr}}\,, \tag{2}$$

$$s = \beta_{ij}\left(\varepsilon_{ij} - \varepsilon_{ij}^{\mathrm{irr}}\right) + k_iE_i + \gamma\theta\,, \tag{3}$$

*Corresponding author: warkentin@uni-kassel.de ORCID iD: 0000-0001-5277-6327

where σ_{ij} describes the mechanical stress, D_i the electric displacement and s the specific entropy, and the electromechanical balance laws $\sigma_{ij,j} = 0$ and $D_{i,i} = 0$, an energy balance is required to compute the distribution of temperature change due to irreversible domain wall motions. The rate–dependent formulation emanates from the local form of the first law of thermodynamics and the GIBB's fundamental equation of the chosen thermodynamical potential [4]:

$$-\dot{q}^A_{j,j} + \dot{\omega}^{\mathrm{diss}} = T\dot{s}\,. \tag{4}$$

Here, $\dot{q}^{\mathrm{A}}_j$ is the surface heat flux and $\dot{\omega}^{\mathrm{diss}}$ is the dissipative power. Note, while T is the absolute thermodynamic temperature of the material

$$\theta = T - T_0 \tag{5}$$

denotes a temperature change. Inserting Eq. (3), in a rate dependent formulation, the energy balance Eq. (4) results in:

$$-\dot{q}^A_{j,j} + \dot{\omega}^{\mathrm{diss}} = T\left(\beta_{ij}\left(\dot{\varepsilon}_{ij} - \dot{\varepsilon}^{\mathrm{irr}}_{ij}\right) + k_i\dot{E}_i + \gamma\dot{\theta}\right)\,. \tag{6}$$

Summarizing the irreversibilities to $\dot{\chi} = \dot{\omega}^{\mathrm{diss}} + \beta_{ij}\dot{\varepsilon}^{\mathrm{irr}}_{ij}$ and neglecting reversible contributions to heating or cooling in terms of the pyroelectric coefficient k_i and the linear contribution of the thermal stress coefficients β_{ij} yields

$$-\dot{q}^A_{j,j} + \dot{\chi} = T\gamma\dot{\theta}\,. \tag{7}$$

The more general integral form of Eq. (7) is

$$\int_{\Omega_2}\dot{\theta}\gamma T\,\mathrm{d}V = \int_{\Omega_1}\dot{\chi}\,\mathrm{d}V - \int_{\partial\Omega}\dot{q}_i n_i\,\mathrm{d}A_S\,, \tag{8}$$

where Ω_1 (region of the heat source) and Ω_2 (volume around the heat source) are the considered areas and $\partial\Omega$ is the surface of Ω_2.

1.1 Transient heating assuming a homogeneus temperature distribution and an adibatic behaviour

Inserting FOURIER's law of heat conduction into $\dot{q}^A_{j,j}$ (note that the tensor of heat conduction λ_{ij} is assumed to be homogeneous in the body) in Eq. (7) and assuming a homogeneous distribution of temperature change $\overline{\theta}$ in a material point, the gradient $\overline{\theta}_{,i}$ and thus the derivative $\overline{\theta}_{,ij}$ disappear. This simplifies the energy balance presuming an adiabatic behavior and it remains

$$\dot{\theta}\gamma T = \dot{\chi}\,. \tag{9}$$

The solution of this differential equation in terms of to θ, using Eq. (5) resolved to T, is obtained as follows:

$$\int_{\theta_0}^{\theta_1}\gamma(T_0+\theta)\mathrm{d}\theta = \int_{\chi_0}^{\chi_1}\mathrm{d}\chi = \Delta\chi \quad\Rightarrow\quad \theta_1 = \frac{\Delta\chi}{\gamma\left(T_0 + \frac{1}{2}\left(\theta_1+\theta_0\right)\right)} + \theta_0\,. \tag{10}$$

In Eq. (10), θ_1 and θ_0 are identified as temperature changes of the current and previous load steps and $\Delta\chi$ as the associated dissipation. Inserting the leading order terms of the dissipative power $\dot{\omega}^{\mathrm{diss}}$, further assuming $\theta_1 \approx \theta_0$ to obtain an explicit representation of the temperature from Eq. (10) and rewriting the energy balance within the context of the CM [2, 3], the macroscopic multi–grain formulation of an i–th time step is obtained as

$$\overline{\theta}_{\mathrm{i}} = \left(\langle\sigma_{ij}\Delta\varepsilon^{\mathrm{irr}}_{ij}\rangle + \overline{E}_i\langle\Delta P^{\mathrm{irr}}_i\rangle + T\langle\beta_{ij}\Delta\varepsilon^{\mathrm{irr}}_{ij}\rangle\right)\frac{1}{T\langle\gamma\rangle} + \overline{\theta}_{\mathrm{i}-1}\,, \tag{11}$$

where angled brackets denote quantities averaged over M grains of a representative volume element (RVE), i.e. $\langle\xi\rangle := \frac{1}{M}\sum_{m=1}^{M}\xi^m\,,\ \forall m \in M$ and bars denote homogeneous quantities with the context of a generalized VOIGT approximation.

1.2 Transient heating with heat dissipation

In order to describe the transient heating, the heat flux $\dot{q}_\mathrm{S} = \Theta\alpha$ with $\Theta = T_\mathrm{S} - T_\infty$ has to be taken into account. Inserting the heat flux relation into Eq. (8) by using the identity $\dot{q}_i^\mathrm{A} n_i = \dot{q}_\mathrm{S}$ the differential equation is obtained as

$$\dot{\theta} \; + \frac{\alpha A_S}{T\{\gamma_i V_i\}}\theta = \dot{\chi}\frac{V_{\Omega_1}}{T\{\gamma_i V_i\}} \; , \tag{12}$$

where the abbreviation $\sum_{i=1}^{v} \gamma_i V_i =: \{\gamma_i V_i\}$ has been introduced with v as the number of all volumes with dissmilar thermal properties. A further reduction with $\alpha A_S/(T\{\gamma_i V_i\}) =: \tilde{\kappa}$ and $V_{\Omega_1}/(T\{\gamma_i V_i\}) =: \tilde{\beta}$ provides

$$\dot{\theta} \; + \tilde{\kappa}\theta = \tilde{\beta}\dot{\chi} \; . \tag{13}$$

The solution of the differential equation within the context of the CM [2, 3] provides the macroscopic multi–grain formulation

$$\overline{\theta}(t) = \langle\dot{\chi}\rangle f^\mathrm{g}(t) = \langle\dot{\chi}\rangle\frac{V_{\Omega_1}}{\alpha A_S}\left(1 - \mathrm{e}^{-\tilde{\kappa}t}\right) \; , \tag{14}$$

where $f^\mathrm{g}(t)$ is a geometry– and time–dependent function, not depending on the calculations from the CM.

2 Results

Fig. 1 shows the electromechanical loading schemes for the numerical examples which are shown in Fig. 2. Starting from Eq. (11), Fig. 2 shows the results for the temperature development vs. load cycles compared to the experimental results and those of the FEM.

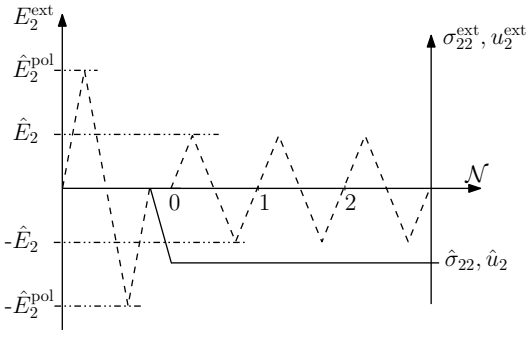

Figure 1. Electromechanical loading schemes for the numerical examples

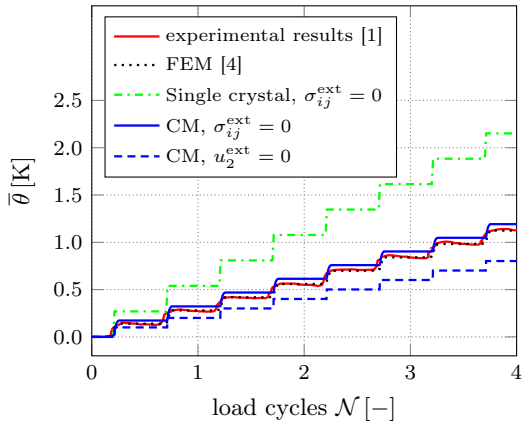

Figure 2. Temperature development $\overline{\theta}$ for polycrystal and single crystal polarized with $\hat{E}_2^\mathrm{pol} = 2\,E_C$ and loaded with $\hat{E}_2 = 1.2\,E_C$ vs. electric load cycles $\mathcal{N}$ for different loading conditions.

The result from the simulation of a polycrystal, solid blue line, according to Eq. (11) is in very good agreement with the experimental result [1] and those obtained by the FEM [4]. Due to the lack of residual inter–grain stresses, the heating of a single crystal is larger than that of a polycrystal. On the other hand, the temperature development is reduced by using displacement boundary conditions according to $u_2^\mathrm{ext} = 0$, since it leads to increased external stresses. Based on the assumptions of the results shown in Fig. 2, a stationary state is not attained, resulting in a monotonously increasing heating. Taking into account temperature–dependent material parameters, the temperature change in the material approaches zero with increasing heating and disappears when reaching the Curie temperature.
Calculated from Eq. (14), Fig. 4 shows the transient heating due to irreversible domain wall motions of

the sample shown in Fig. 3 induced by bipolar electrical load cycles with $\hat{E}_2 = 1.2\, E_C$. A stationary state is attained depending on the geometry, the external electrical load and the frequency. Experiments are work in progress and seem to confirm the shown results according to Fig. 4.

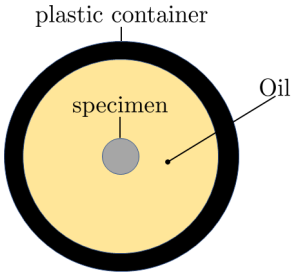

Figure 3. Experimental setup

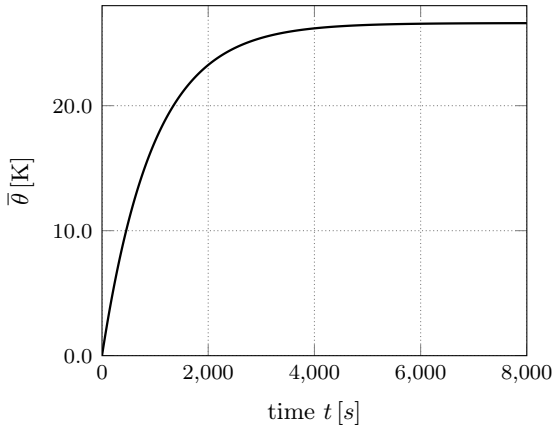

Figure 4. Temperature development $\overline{\theta}$ for a polycrystal. The material has been poled with $\hat{E}_2^{\mathrm{pol}} = 4.28\, E_{\mathrm{C}}$ and cyclically loaded with $\hat{E}_2 = 1.2\, E_{\mathrm{C}}$. The load conditions according to Fig. 1 with $\hat{\sigma}_{22} = \hat{u}_2 = 0$ were applyed

3 Conclusion

The results presented in this work show, that the extended CM is able to predict the temperature evolution as a result of irreversible domain wall motion. The deviation between CM, experiment and FEM for a larger number of load cycles is caused by the adiabatic boundary conditions. Taking into account heat dissipation as well as temperature–dependent material parameters, a stationary state is finally attained.

References

[1] H.-S Chen and Y.-M Pei. Rate Dependent Heat Generation in Single Cycle of Domain Switching of Lead Zirconate Titanate via In-Situ Spontaneous Temperture Measurment. *Applied Physics Letters* 102 (2013).

[2] A. Ricoeur and S. Lange. A Condensed Microelectromechanical Approach for Modeling Tetragonal Ferroelectrics. *International Journal of Solids and Structures* 54 (2015), pp. 100–110.

[3] A. Ricoeur and S. Lange. Constitutive Modeling of Polycrystalline Multiconstituent and Multiphase Ferroic Materials Based on a Condensed Approach. *Archive of Applied Mechanics* 89 (2019).

[4] Marius Wingen and Andreas Ricoeur. Caloric Aspects of Nonlinear Ferroelectric Constitutive Behavior: Modeling and Simulation. *Continuum Mechanics and Thermodynamics* 31 (2019), pp. 549–568.

**Proceedings of the 8th GACM Colloquium on Computational Mechanics
for Young Scientists from Academia and Industry
August 28–30, 2019 in Kassel, Germany**

Numerical treatment of material parameter identification using finite elements

Rose Rogin Gilbert *[1] and Stefan Hartmann[1]

[1]Institute of Applied Mechanics, Clausthal University of Technology, Germany

Abstract. In solid mechanics, different properties of materials are characterized by different constitutive models, particularly models of evolutionary-type. The material parameters in these constitutive models are calibrated to experimental data to predict the material behavior within the range of application and is called material parameter identification, see [2, 5]. Different types of experiments are performed in order to uniquely identify the material parameters. Reaction forces from the force gauges as well as surface strains or displacements using Digital Image Correlation (DIC) methods are most widely used experimental data. The sensitivities of the material parameters are provided to the least-square solver to identify the material parameters. There are different methods to obtain these material parameter sensitivites. External Numerical Differentiation (END) is the most commonly used method to calculate these sensitivities, see, for the terminology [10]. However, for a complex constitutive model with inhomogeneous deformation having large number of parameters, the computational time is high when using END. To circumvent this disadvantage, Internal Numerical Differentiation (IND) is performed which reduces the computational time. Even though the computational time is reduced, there are additional storage requirements that need to be fulfilled when performing IND method.

Introduction

There are many materials having different properties and behaviors, which are characterized in solid mechanics by constitutive models. These constitutive models have material parameters, which have to be calibrated to experimental data in order to predict the material behavior within the range of application. This calibration is called *material parameter identification* or briefly *parameter identification*, see [2, 5].

Depending on the homogeneity of the deformation, the procedure of material parameter identification varies. If the deformation is inhomogeneous, the entire boundary-value problem need to be solved, commonly by using finite element method. The material parameter identification for inelastic materials using finite elements were discussed in [1, 7, 8]. To identify the material parameters, the sensitivities due to parameter variations needs to be calculated. The most common method to calculate these sensitivites is external numerical differentiation, see, for the terminology, [10]. However, for a constitutive model with inhomogeneous deformation having large number of parameters, the computational cost is high. To circumvent this drawback, internal numerical differentiation is performed, which reduces the computational time by a considerable amount.

Problem statement

The most commonly used basis for parameter identification process is a least-square formulation. The simulated results $\boldsymbol{s} \in \mathbb{R}^{n_s^e}$ (n_s^e is the number of simulated data) from the finite-element program are compared with the experimental data $\boldsymbol{d} \in \mathbb{R}^{n_d^e}$ (n_d^e is the number of experimental data from one or more experiments). The residual vector, $\tilde{\boldsymbol{r}}(\boldsymbol{\kappa}) = \boldsymbol{W}\{\boldsymbol{s}(\boldsymbol{\kappa}) - \boldsymbol{d}\}$, describes the difference between the experimental and the simulated data. In order to consider the different order of physical values (forces, displacements), weighting matrices $\boldsymbol{W}$ are introduced. The so-called *objective function*, $f(\boldsymbol{\kappa}) = \frac{1}{2}\tilde{\boldsymbol{r}}^T(\boldsymbol{\kappa})\tilde{\boldsymbol{r}}(\boldsymbol{\kappa})$, is then minimized in a least-square sense using methods outlined in [3]. The displacements from the experiments are obtained by using Digital Image Correlation (DIC), which are then projected onto the FEM surface data to obtain the displacements at each evaluation points. The forces are obtained from force gauges of the

*Corresponding author: rose.rogin.gilbert@tu-clausthal.de

testing machnine. A trust-region reflective algorithm, provided by Matlab routine `lsqnonlin.m`, is used to solve the problem. A necessary condition for a minimum at $\boldsymbol{\kappa} = \boldsymbol{\kappa}^*$ requires the derivative to be zero

$$\boldsymbol{F}(\boldsymbol{\kappa}^*) = \left.\frac{\mathrm{d}f}{\mathrm{d}\boldsymbol{\kappa}}\right|_{\boldsymbol{\kappa}=\boldsymbol{\kappa}^*} = \boldsymbol{D}^T(\boldsymbol{\kappa}^*)\left\{\boldsymbol{s}(\boldsymbol{\kappa}^*) - \boldsymbol{d}\right\} = \boldsymbol{0}, \tag{1}$$

with $\boldsymbol{D}(\boldsymbol{\kappa}) := \mathrm{d}\tilde{\boldsymbol{r}}(\boldsymbol{\kappa})/\mathrm{d}\boldsymbol{\kappa} = \mathrm{d}\boldsymbol{s}(\boldsymbol{\kappa})/\mathrm{d}\boldsymbol{\kappa}$, $\boldsymbol{D} \in \mathbb{R}^{n_\mathrm{D} \times n_\kappa}$. $\boldsymbol{D}(\boldsymbol{\kappa})$ represent the sensitivites and are calculated either by external differentiation or internal differentiation.

External Numerical Differentiation

It is more common to apply external differentiation schemes to approximate the sensitivites by

$$\frac{\mathrm{d}\tilde{\boldsymbol{u}}_{n+1}}{\mathrm{d}\boldsymbol{\kappa}} \approx \sum_{i=1}^{n_\mathrm{D}} \sum_{j=1}^{n_\kappa} \frac{\tilde{\boldsymbol{u}}_{n+1}(\boldsymbol{\kappa} + \Delta\kappa_j \overline{\boldsymbol{e}}_j) - \tilde{\boldsymbol{u}}_{n+1}(\boldsymbol{\kappa})}{\Delta\kappa_j} \boldsymbol{e}_i \overline{\boldsymbol{e}}_j^T, \tag{2}$$

with the "unit vectors" $\boldsymbol{e}_i \in \mathbb{R}^{n_\mathrm{D}}$ (all entries are zero except for one having a 1 in row i) and $\overline{\boldsymbol{e}}_j \in \mathbb{R}^{n_\kappa}$. Here, the entire finite element program has to be run $(n_\kappa + 1)$-times, for each iteration of the least-square solver. For each iteration, the material parameters are perturbed in order to obtain the sensitivites using a forward difference scheme. Therefore, the computational cost to calculate the sensitivities using external numerical differentiation is very high when the number of parameters to be identified are high. If high accuracy requirements are necessary, the external numerical differentiation might lead to an insufficient iteration scheme to obtain a local minimum.

Internal Numerical Differentiation

In the case of internal numerical differentiation, the entire time integration step is assumed to be dependent on the parameters $\boldsymbol{\kappa}$. For pure hyperelatic constitutive models, the computation of the sensitivities is simple and can be easily implemented, see for example [9],

$$\boldsymbol{g}(t, \boldsymbol{u}(\boldsymbol{\kappa}), \boldsymbol{\kappa}) = \boldsymbol{0} \rightsquigarrow \frac{\partial \boldsymbol{g}}{\partial \boldsymbol{u}} \frac{\mathrm{d}\boldsymbol{u}}{\mathrm{d}\boldsymbol{\kappa}} = -\frac{\partial \boldsymbol{g}}{\partial \boldsymbol{\kappa}} \rightsquigarrow \boldsymbol{D}_\mathrm{u} = \frac{\mathrm{d}\boldsymbol{u}}{\mathrm{d}\boldsymbol{\kappa}}. \tag{3}$$

Once the equilibrium conditions, $\boldsymbol{g} = \boldsymbol{0}$, are satisfied after each load step t_n, the sensitivities $\boldsymbol{D}_\mathrm{u}|_{t_n}$ have to be computed and stored. The quantity $\dfrac{\partial \boldsymbol{g}}{\partial \boldsymbol{\kappa}}$ can be obtained by using the code generating software Acegen [6].

However, for constitutive models of rate-type (viscoelastic, viscoplastic) the internal numerical differentiation is more complicated. The sensitivities are calculated based on Multilevel-Newton algorithm and are provided from the finite element program itself. Following spatial discretization, a system of differential-algebraic equations (DAE)

$$\begin{aligned} \boldsymbol{g}(t, \boldsymbol{u}(\boldsymbol{\kappa}), \boldsymbol{q}(\boldsymbol{\kappa}), \boldsymbol{\kappa}) &= \boldsymbol{0}, \\ \dot{\boldsymbol{q}}(t, \boldsymbol{\kappa}) &= \boldsymbol{r}(t, \boldsymbol{u}(\boldsymbol{\kappa}), \boldsymbol{q}(\boldsymbol{\kappa}), \boldsymbol{\kappa}) \end{aligned} \tag{4}$$

are obtained. Applying classical Backward-Euler method to the DAE-system leads to

$$\begin{aligned} \boldsymbol{g}(t_{n+1}, \boldsymbol{u}_{n+1}(\boldsymbol{\kappa}), \boldsymbol{q}_{n+1}(\boldsymbol{\kappa}), \boldsymbol{\kappa}) &= \boldsymbol{0}, \\ \boldsymbol{I}(t_{n+1}, \boldsymbol{u}_{n+1}(\boldsymbol{\kappa}), \boldsymbol{q}_{n+1}(\boldsymbol{\kappa}), \boldsymbol{q}_n(\boldsymbol{\kappa}), \boldsymbol{\kappa}) &= \boldsymbol{0}, \end{aligned} \tag{5}$$

with the integration step for the internal variables

$$\boldsymbol{I}\big(t_{n+1}, \boldsymbol{u}_{n+1}(\boldsymbol{\kappa}), \boldsymbol{q}_{n+1}(\boldsymbol{\kappa}), \boldsymbol{q}_n(\boldsymbol{\kappa}), \boldsymbol{\kappa}\big) = \boldsymbol{q}_{n+1}(\boldsymbol{\kappa}) - \boldsymbol{q}_n(\boldsymbol{\kappa}) - \Delta t_n \boldsymbol{r}\big(t_{n+1}, \boldsymbol{u}_{n+1}(\boldsymbol{\kappa}), \boldsymbol{q}_{n+1}(\boldsymbol{\kappa}), \boldsymbol{\kappa}\big). \tag{6}$$

For convenience, the following abbreviations

$$\boldsymbol{G}_\mathrm{u} = \frac{\partial \boldsymbol{g}}{\partial \boldsymbol{u}}, \quad \boldsymbol{G}_\mathrm{q} = \frac{\partial \boldsymbol{g}}{\partial \boldsymbol{q}}, \quad \boldsymbol{G}_\kappa = \frac{\partial \boldsymbol{g}}{\partial \boldsymbol{\kappa}}, \quad \boldsymbol{L}_\mathrm{u} = \frac{\partial \boldsymbol{I}}{\partial \boldsymbol{u}}, \quad \boldsymbol{L}_\mathrm{q} = \frac{\partial \boldsymbol{I}}{\partial \boldsymbol{q}}, \quad \boldsymbol{L}_\kappa = \frac{\partial \boldsymbol{I}}{\partial \boldsymbol{\kappa}}. \tag{7}$$

are introduced. The derivative of the (5) with respect to the parameters $\boldsymbol{\kappa}$, which are the sensitivities, at time t_{n+1} yields

$$\begin{aligned} \boldsymbol{G}_{\mathrm{u}n+1}\boldsymbol{D}_{\mathrm{u}n+1} + \boldsymbol{G}_{\mathrm{q}n+1}\boldsymbol{D}_{\mathrm{q}n+1} + \boldsymbol{G}_{\kappa n+1} &= \boldsymbol{0} \\ \boldsymbol{L}_{\mathrm{u}n+1}\boldsymbol{D}_{\mathrm{u}n+1} + \boldsymbol{L}_{\mathrm{q}n+1}\boldsymbol{D}_{\mathrm{q}n+1} + \boldsymbol{L}_{\mathrm{q}n}\boldsymbol{D}_{\mathrm{q}n} + \boldsymbol{L}_{\kappa n+1} &= \boldsymbol{0}. \end{aligned} \tag{8}$$

Following some rearrangements, as shown in [4], $(8)_2$ leads to

$$\boldsymbol{D}_{\mathrm{q}n+1} = -\boldsymbol{L}_{\mathrm{q}n+1}^{-1}\left[\boldsymbol{L}_{\mathrm{u}n+1}\boldsymbol{D}_{\mathrm{u}n+1} - \boldsymbol{L}_{\mathrm{q}n}\boldsymbol{D}_{\mathrm{q}n} + \boldsymbol{L}_{\kappa n+1}\right]. \tag{9}$$

This is then inserted into $(8)_1$ to obtain

$$\left[\boldsymbol{G}_{\mathrm{u}n+1} - \boldsymbol{G}_{\mathrm{q}n+1}\boldsymbol{L}_{\mathrm{q}n+1}^{-1}\boldsymbol{L}_{\mathrm{u}n+1}\right]\boldsymbol{D}_{\mathrm{u}n+1} = -\boldsymbol{G}_{\kappa n+1} + \boldsymbol{G}_{\mathrm{q}n+1}\boldsymbol{L}_{\mathrm{q}n+1}^{-1}\left[-\boldsymbol{D}_{\mathrm{q}n} + \boldsymbol{L}_{\kappa n+1}\right]. \tag{10}$$

The coefficient matrix on the left-hand side is exactly the tangential stiffness matrix of the equilibrium iteration from the MLNA. The coefficient $\boldsymbol{L}_{\mathrm{q}n+1}^{-1}\left[-\boldsymbol{D}_{\mathrm{q}n} + \boldsymbol{L}_{\kappa n+1}\right] = \boldsymbol{D}_{\mathrm{q}n+1}$ is the result of the linear system, which has to be solved on Gauss-point level and has to be stored for the next time-step, in which they represent the quantity $\boldsymbol{D}_{\mathrm{q}n}$ for the next time-step. The total amount of storage is $n_{\mathrm{el}} \times n_{\mathrm{GP}}^{e} \times n_{\mathrm{q}} \times n_{\kappa}$ where n_{el} is the number of elements, n_{GP}^{e} the number of Gauss-points in each element, and n_{q} the number of internal variables.

These calculated sensitivities are then provided to the Matlab routine `lsqnonlin.m` to identify the material parameters. Since the sensivities are calculated internally using Acegen, the entire finite element program has to be run only once per iteration of the least-square solver. This reduces the computational cost considerably. However, there are additional storage requirements that needs to be fulfilled.

Conclusion

The basic concepts of material parameter identification along with different methods to obtain the sensitivites are detailed in this short communication. Two methods, namely external numerical differentiation and internal numerical differentiation, to obtain the sensitivities are explained. END is the most common method which is time consuming but easily implemented. IND on the other hand is a complicated method but faster than END. The main drawback of the IND is the additional storage requirements. A clear algorithmic structure is provided which can be extended according to different requirements.

References

[1] K. Andresen, S. Dannemeyer, H. Friebe, R. Mahnken, R. Ritter, and E. Stein. Parameteridentifikation für ein plastisches Stoffgesetz mit FE-Methoden und Rasterverfahren. *Bauingenieur* 71 (1996), pp. 21–31.

[2] J. V. Beck and K. J. Arnold. *Parameter estimation in engineering science*. 1st. New York: John Wiley & Sons, 1977.

[3] J. E. Dennis and R. B. Schnabel. *Numerical methods for unconstrained optimization and nonlinear equations*. Vol. 16. Classics in Applied Mathematics. Philadelphia: SIAM Society for Industrial and Applied Mathematics, 1996.

[4] S. Hartmann. A remark on material parameter identification using finite elements based on constitutive models of evolutionary-type. *Computer Assisted Methods in Engineering and Science* Vol. 24, no. 2 (2017), pp. 113–126.

[5] S. Hartmann and R. R. Gilbert. Identifiability of material parameters in solid mechanics. *Archive of Applied Mechanics* 88.1 (2018), pp. 3–26.

[6] J. Korelc. Multi-language and multi-environment generation of nonlinear finite element codes. *Engineering with Computers* 18.4 (2002), pp. 312–327.

[7] R. Mahnken and E. Stein. A unified approach for parameter identification of inelastic material models in the frame of the finite element method. *Computer Methods in Applied Mechanics and Engineering* 136 (1996), pp. 225–258.

[8] R. Mahnken and E. Stein. Parameter identification for finite deformation elasto-plasticity in principal directions. *Computer Methods in Applied Mechanics and Engineering* 147 (1997), pp. 17–39.

[9] G. Scheday. "Theorie und Numerik der Parameteridentifikation von Materialmodellen der finiten Elastizität und Inelastizität auf der Grundlage optischer Feldmessmethoden". PhD-thesis, Report No. I-11 (2003). Institute of Mechanics: University of Stuttgart (Germany), 2003.

[10] K. Schittkowski. *Numerical data fitting in dynamical systems*. Dordrecht: Kluwer Academic Publ., 2002.

**Proceedings of the 8th GACM Colloquium on Computational Mechanics
for Young Scientists from Academia and Industry
August 28–30, 2019 in Kassel, Germany**

Parameter identification for constitutive models of textile composite materials using digital image correlation

Justin Felix Hofmann*[1], Claudia von Boyneburgk[2], Sophie Tunger[1], Hans-Peter Heim[2] and Detlef Kuhl[1]

[1]Institute of Mechanics and Dynamics, University of Kassel

[2]Institute of Material Engineering, Polymer Engineering, University of Kassel

Abstract. This contribution focuses on a composite material consisting of multiple woven layers made of continuous wooden strips (salix americana) embedded in a polymer matrix (polypropylene). To asses the suitability of the material in an architectural context, a finite element simulation of potential use-cases is carried out. The simulation is based on a constitutive model assuming homogenous orthotropic elastic behaviour and will be expanded to include multiscale modelling as well as nonlinearity in future research.

The non-isotropic behaviour as well as the heterogeneous structure of the material lead to a significant inhomogeneity of the resulting stress and strain distributions during experiments, especially in off-axis configurations. This can't be sufficiently captured using traditional measurement techniques. However, the advances in full-field measurement techniques enable us to capture this behaviour in sufficiently large regions of the specimen.

Experimental results of uniaxial on- and off-axis tensile tests using digital image correlation are shown and used for the identification of the material parameters of the given model. Two different identification processes and their transferability to more complex material models are discussed.

Motivation

Standardized testing methods for the determination of elastic material parameters often focus on isotropic mechanical behavior. They require specific specimen geometries to generate homogeneous strain states during testing, which in turn require only a small number of local measurements to be fully captured. However, nonisotropic, as well as inhomogeneous materials demand more sophisticated measurement techniques, which in turn require more complex processing. The parameter identification methods presented here are based on finite element model updating and process full-field displacement measurements gained during experiments. Rectangular specimens (Fig. 2) were tested in on and off-axis configurations in a quasi static uniaxial tensile test (Fig. 1). However, the methods could be applied to other specimen geometries and forms of testing as well.

The methods are applied to a composite material based on woven fabrics made from continuous wooden fibers and thin polypropylene films. It is expected that the material behavior is orthotropic.

1 Experiment

To enable independent stress-strain states during the tests, the specimens were cut from the base material at different angles (0°/45°/90°) with respect to the warp direction of the textile layers. Pictures of the specimens surfaces were taken at regular intervals during the experiments using a two-camera setup and converted into displacement data $\boldsymbol{u}^{exp}$ using digital image correlation. The transformation between camera and specimen coordinate systems was acquired during a calibration step. Corresponding force measurements were taken using a load cell.

The experimental results have demonstrated highly inhomogeneous displacement fields (Fig. 4) due to the inhomogeneity of the composite.

*Corresponding author: hofmann@uni-kassel.de

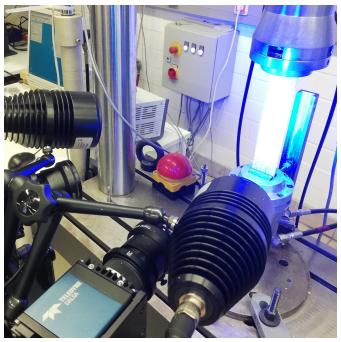

Figure 1. Uniaxial tensile tests

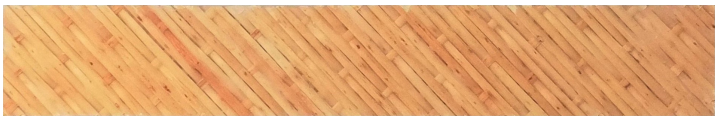

Figure 2. 45°-specimen

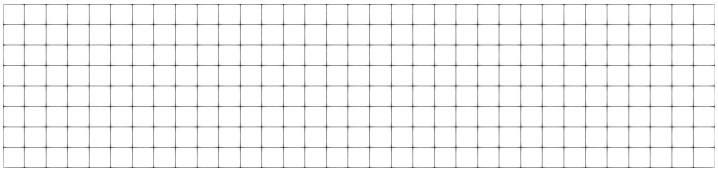

Figure 3. Finite element mesh

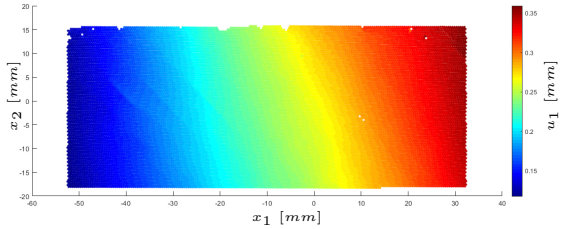

Figure 4. Displacement field (45°-specimen)

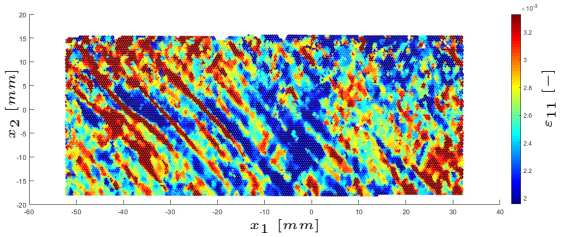

Figure 5. Strain field (45°-specimen)

2 Finite element model

A static finite element model reproducing the test setup was created separately for each specimen and load step. Each model includes the specimen geometry (width, thickness, effective length between clamps), the orientation of the material with regard to the specimen coordinate system, as well as the boundary conditions applied during the campaign (clamps, force). The specimens were discretized using a finite element mesh consisting of bilinear quadrilateral elements (Fig. 3). The initial material parameters $\boldsymbol{p}_0$ for an orthotropic linear elastic material model were chosen arbitrarily.

3 Parameter identification

Two parameter identification algorithms were implemented and the results were compared. The first algorithm is based on [1], the second is a modified version of this method. Both follow the idea of finite element model updating (Fig. 6 and Fig 7). Experimental and numerical results are compared on the strain level using error function

$$e(\boldsymbol{p}) = \sum_{i=1}^{M} \frac{\sum_{j=N_{i-1}+1}^{N_i} |\boldsymbol{\varepsilon}_j^{num}(\boldsymbol{p}) - \boldsymbol{\varepsilon}_j^{exp}|^2}{\sum_{j=N_{i-1}+1}^{N_i} |\boldsymbol{\varepsilon}_j^{exp}|^2}$$

where $\boldsymbol{\varepsilon}_j^{num}$ and $\boldsymbol{\varepsilon}_j^{exp}$ are pairs of spatially corresponding strains, which are grouped into M subsets (one for each specimen and load step). The error is subsequently minimized using the gradient descent method to find a set of optimal material parameters. The difference of both versions is in the computation of the strain field $\boldsymbol{\varepsilon}^{exp}$ from $\boldsymbol{u}^{exp}$, which occurs prior to solving the inverse optimization problem.

The first algorithm utilizes the finite element mesh of the corresponding finite element simulation to approximate experimental strain data at the gauss points of each element containing sufficient corresponding measurements by solving a local element-wise optimization problem described in [1]. The quality of the strain computation is therefor dependent on the chosen finite element mesh and spatial discretization of the finite element model is limited by the resolution of the measured displacement field.

The second algorithm generates strain data independently of the finite element simulation. Delaunay triangulation is applied to each set of measuring points, to generate a mesh consisting of triangular

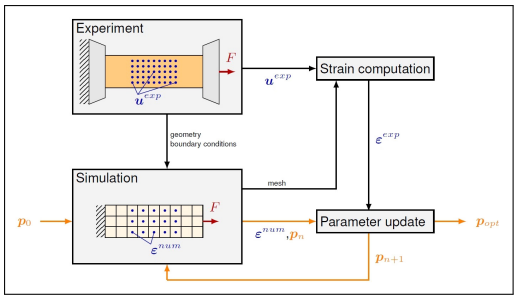

Figure 6. Algorithm of [1]

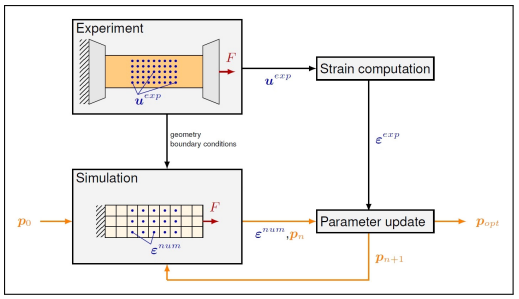

Figure 7. Modified algorithm

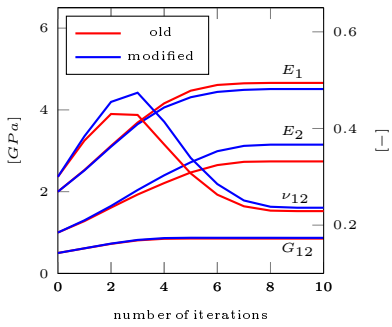

Figure 8. Model parameters

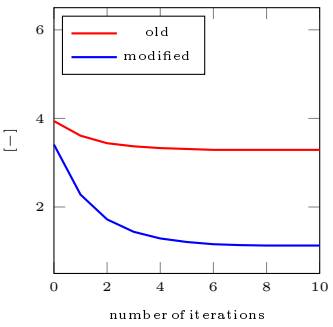

Figure 9. Error function

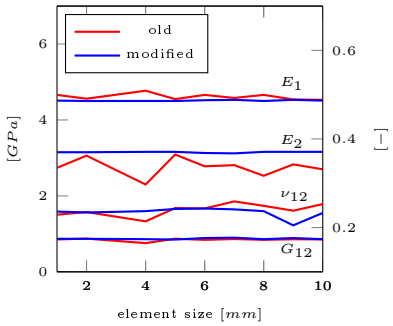

Figure 10. Converged solutions for various element sizes

elements with known node displacements $\boldsymbol{u}^{exp}$. Strain data $\boldsymbol{\varepsilon}^{exp}$ is subsequently calculated at the gauss point of each element (Fig. 5).

Both algorithms were tested for different starting values and element sizes. Given reasonable starting values, both algorithms fully converged after approximately 10 iterations (Fig. 8 and 9). The converged solutions were independent of the starting values. While the first algorithm required much less computation time, it showed a much higher dependency on the chosen finite element size, compared to the modified version (Fig. 10).

4 Conclusion and outlook

Two versions of an inverse method for the identification of the elastic material parameters of orthotropic materials have been presented. The methods are based on finite element model updating. Displacement measurements taken during tensile tests were compared to the results of a finite element simulation using a strain based error function, which is subsequently minimized via the gradient descent method. It could be shown that the methods converge against solutions for the orthotropic material parameters, which are in agreement with the expected range of values, based on previously determined material parameters of the individual material components and the theory of mixtures of composites. The solutions are independent of the chosen starting values. However, the first algorithm showed a high dependency on spatial discretization.

The experimental results show a strong material inhomogeneity, which can't be reproduced by the material model used in this work. Consequently, the parameter identification method will be applied to multiscale modeling in future research.

References

[1] D. Lecompte, H. Sol, J.Vantomme, and A. M. Habraken. Identification of Elastic Orthotropic Material Parameters Based on ESPI Measurements. *SEM annual conference and exposition on experimentaland applied mechanics* (2005).

**Proceedings of the 8th GACM Colloquium on Computational Mechanics
for Young Scientists from Academia and Industry
August 28–30, 2019 in Kassel, Germany**

Monitoring of multiaxial failure surfaces and the evolution of deformation bands in PVC foams using 3D digital image correlation

Anne Jung * [1], Francesca Concas[1] and Stefan Diebels[1]

[1]Chair of Applied Mechanics, Saarland University, Saarbrücken, Germany

Abstract. Cellular materials such as foams are biomimetic structures used for lightweight constructions and for energy absorption. Closed-cell polyvinylchloride (PVC) foams are among the most used core materials for sandwich composites. Therefore, a deep knowledge of their multiaxial behaviour is fundamental for application of this material. The present contribution focuses on the evolution of failure surfaces and the elucidation of the local deformation mechanism under multiaxial loading. Uniaxial,pure torsion as well as torsion experiments with superimposed uniaxial loads combined with 3D digital image correlation are performed.

1 Introduction

Cellular materials are built according to the blueprint of nature as lightweight construction materials with porous structure. Open-cell foams are inspired by bones, while closed-cell foams mimic the structure of wood or cork [1]. Although metal foams offer advantages concerning ductility and energy absorption capacity, they lack in terms of corrosion and elasticity. In contrast, polymer foams can be used advantageously due to their lightweight construction properties and flexibility. However, they lack in terms of stiffness and thermal stability. Usually, foams are processed in the form of sandwich structures with foam core. Closed-cell polyvinylchloride (PVC) foams are among the most used core materials for sandwich composites. Applications are in ship building as well as in aerospace industry and for wind turbine blades [1]. In all of these applications, multiaxial loading is of utmost importance. Hence, the investigation of failure surfaces under multiaxial loading is needed for the secure design of components made of closed-cell PVC foams. However, up to now, experimental investigations on cellular materials under multiaxial loading are very limited due to the challenging and complex nature of the experiments.
The present contribution deals with the experimental multiaxial characterisation of a closed-cell PVC foam and the probing of the corresponding failure surfaces. The local deformation mechanisms were studied by 3D digital image correlation (DIC) using an eight camera system.

2 Material and Methods

Closed-cell PVC foams were purchased from Diab International (Laholm, Sweden). Especially plates of Divinycell® HP100 with a density of 100 g/cm^3 were studied. Cylindrical dog-bone specimens with a height to diameter ratio of 2:1 were cut from in-plane direction of the plates. More details on the specimen preparation can be found in Concas et al. [3].
Multiaxial experiments under different loading conditions are needed for probing of the failure surface. Therefore, uniaxial compression and tension experiments, torsion experiments and torsion experiments with superimposed constant uniaxial tensile or compression loads were performed using an Instron ElectroPuls® E10000 universal testing machine (Instron Ltd., Pfungstadt, Germany). A 360° DIC analysis was carried out to elucidate the local deformation mechanism under multiaxial loading. Therefore, an eight camera system and the commercial DIC software Istra4D® (Dantec Dynamics Ltd., Slovkunde, Denmark) were used. A detailed description of the procedure for the experimental probing of failure surfaces for foams can be found in previous works [3, 5, 6].

*Corresponding author: anne.jung@mx.uni-saarland.de

3 Results and Discussion

Figure 1 presents the experimentally probed failure surface for the Divinycell® HP100 foams in the hydrostatic plane, which is formed in the stress space by the hydrostatic axis and the deviatoric axis. The hydrostatic axis is defined by the first principal invariant I_1 of the stress tensor. The deviatoric axis describes pure shear states and is defined by the square root of the negative second deviatoric invariant J_2 of the stress tensor. The resulting asymmetric closed failure surface is shifted along the hydrostatic axis to the tensile part and has its maximum under combined tension-torsion loading. Pure tensile failure stresses are higher than pure compression failure stresses. The closed shape of the failure surface accounts for the compressibility of the foam.
A single-surface yield criterion to reliably describe such asymmetric failure surfaces is the yield criterion according to Bier et al. [2], which was introduced for multiaxial yielding of compacted powder. However, the fit in **Figure 1** shows the good approximation of the failure surface by this criterion for the investigated Divinycell® HP100 foams. The corresponding material parameters can be identified by inverse calculations [4].

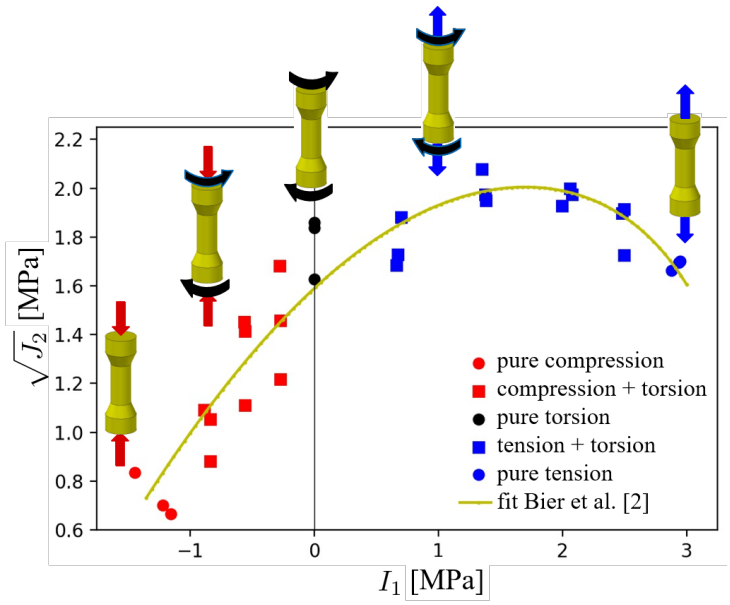

Figure 1. Failure surface of a closed-cell Divinycell® HP100 foam.

The DIC analysis of the individual experiments outlined buckling during the plateau phase under compression loading making a further investigation of the mechanical properties difficult. Uniaxial tensile loading results in a concentrated failure by a crack perpendicular to the loading direction. Failure under torsion results in crack with a 45° angle to the loading direction. The torsion experiments with superimposed uniaxial loading result in localisation bands in two diametrically opposite regions of the specimen, where the highest strain gradients occur at the beginning of fracture. The corresponding DIC analysis can be found by Concas et al. [3].

4 Conclusion

The present contribution dealt with the experimental probing of a failure surface for closed-cell PVC foams and the monitoring of the local deformation using 3D DIC. An asymmetric, closed failure surface shifted to higher tensile failure stresses was received. It outlined the importance of multiaxial experiments for the reliable design of components made of such foams. The 360° DIC provided important and interesting insights in the local deformation mechanisms and the evolution of strain fields during uniaxial and multiaxial loading.

References

[1] M. F. Ashby. The mechanical properties of cellular solids. *Metallurgical Transactions A* 14.9 (1983), pp. 1755–1769.

[2] W. Bier and S. Hartmann. A finite strain constitutive model for metal powder compaction using a unique and convex single surface yield function. *European Journal of Mechanics-A/Solids* 25.6 (2006), pp. 1009–1030.

[3] F. Concas, S. Diebels, and A. Jung. Multiaxial failure surface of PVC foams and monitoring of deformation bands by three-dimensional digital image correlation. *Journal of the Mechanics and Physics of Solids* 130 (2019), pp. 195–215.

[4] S Heinze, T Bleistein, A Düster, S Diebels, and A Jung. Experimental and numerical investigation of single pores for identification of effective metal foams properties. *ZAMM-Journal of Applied Mathematics and Mechanics/Zeitschrift für Angewandte Mathematik und Mechanik* 98.5 (2018), pp. 682–695.

[5] A Jung and S Diebels. Microstructural characterisation and experimental determination of a multiaxial yield surface for open-cell aluminium foams. *Materials & Design* 131 (2017), pp. 252–264.

[6] A Jung and S Diebels. Yield surfaces for solid foams: A review on experimental characterization and modeling. *GAMM-Mitteilungen* 41.2 (2018), e201800002.

**Proceedings of the 8th GACM Colloquium on Computational Mechanics
for Young Scientists from Academia and Industry
August 28–30, 2019 in Kassel, Germany**

Full-field strain measurements on single struts of a Ni/PU hybrid foam

Martin Reis*[1], Stefan Diebels[1] and Anne Jung[1]

[1]Chair of Applied Mechanics, Saarland University, Saarbrücken, Germany

Abstract. Ni/PU hybrid foams are an example of open-cell hybrid foams. They are based on a polyurethane (PU) foam template coated with nanocrystalline nickel (Ni). Due to their coating they show quite impressive energy absorption capacity at low weights. Due to this fact, they have a high potential as energy absorbers. The deformation in the macroscale results from single strut deformation in the microscale. Therefore, the study of each size scale is necessary to get a full understanding of the material. In the present contribution, tensile tests on individual struts of a Ni/PU hybrid foam are presented and evaluated using a homogenised geometrical model of each strut. To proof the reliability of the homogenised models and to analyse the coating thickness, micro sections of five individual struts are carried out. The micro sections show a clear difference in coating thickness but almost no scattering of the cross sectional area for the PU core. This strengthened the use of a homogenised geometrical model.

1 Introduction

Foams are bio-inspired structures, which can be divided into closed-cell foams, comparable to the inner structure of cork, and open-cell foams, inspired by trabecular bones. In the present work, open-cell foams are of interest. Thereby, the macroscopic structure consists of single pores on the mesoscale and single struts on the microscale. Through the open structure, these materials allow to be coated by an electrodeposition process with different kinds of metals. Therefore, an open porous template, such as aluminium or the cheaper PU, is needed. In the case of PU, an additional electric conductive coating is necessary to enable the electrodeposition process. Coated foams are classified as hybrid foams. The material behaviour of hybrid foams is dominated by the material behaviour of the coating material. Coating a PU foam with Ni immensely increases the energy absorption capacity of the structure. Comparing a Ni/PU hybrid foam with a pure aluminium foam shows that the energy absorption to weight ratio strongly increases and the production costs decrease. Among others, both characteristics determine the material to be an ideal lightweight structure with high potential for the use in the automotive sector and for aerospace applications. Before it can be used in a real-world application, further investigations of the material behaviour are necessary. Due to the micro structure, the material behaviour of the macroscopic foam is composed of the behaviour of the pores and struts. Thus, realistic models require information from all scales. In addition, the fine grain structure and different orientations of the grains in the coating affect the material parameters of the Ni coating which differ from the material parameters of the bulk material. Therefore, experimental investigations on single pores and struts are needed. The small dimensions of the struts with a length of about 2 mm and a width of about 0.4 mm combined with the irregular surface only allow using digital image correlation (DIC) to evaluate strains on the specimen's surface. Due to the inhomogeneous coating thickness and the variable strut geometry, the experimental results include large scattering. A realistic stiffness can be determined by transferring the force-displacement-data to a stress-strain-curve using the cross sectional area in the crack area and the initial length of the struts. To avoid any additional uncertainties produced by the experimental set-up, high measurement accuracy is important. Therefore, the DIC noise is minimised with a pre-test routine and the noise level is determined for each experiment. This contribution presents results from tensile tests on single struts and optical analysis of micro sections on single struts.

*Corresponding author: martin.reis@uni-saarland.de

2 Material and Methods

The following microscale experiments are performed with a custom-build testing device [**jung2015**]. The used stepper motor in combination with the high precision screw drive allows a stroke resolution of 1 μm and a force up to 6 kN with a repeatability of 0.02 μm, controlled with a custom software based on LabVIEW^{TM}. Besides the controlling, the software records the forces and captures the images for the DIC measurements. Due to the complex and individual structure of each strut, the specific geometry of each strut is needed to calculated the stress. For this task, another custom-build device is used. The set-up rotates a single strut in 24 steps ones around its longitudinal axis and acquires an image in each step. This process is repeated for a second translation angle of the camera. Below the sample a pattern allows to identify the rotation angle of the specimen. The information on the rotation of the pattern combined with the edges and shadows of the sample found in each image allow to generate a 3D geometric model using the commercial software 3DSOM^{TM}. The resolution of this process is comparable with the accuracy of a model received from computed tomography [**bleistein2019**]. Starting with this model, the initial cross sectional area at the crack position can be measured. Therefore, the model is distinguished in a stack of approximately 1,000 images. In this stack, the position of the crack is found and the cross sectional area is measured for 11 images close to the crack position. Here the mean area is calculated as fracture area. The initial area and the force allow to calculate the engineering stress during the experiment. Even using a commercial software to perform a DIC measurement, many factors, as for examples lighting, environment and subset size, have an influence on measurement noise. To achieve a high quality measurement it is necessary to estimate the error and to reduce it to a minimum. For this purpose, a simple three-step routine was evolved [**reis2019**]. In the first step, a series of images from a static specimen is taken. For this series the DIC measured displacement, which equals the noise of this experiment, is evaluated. The value is reduced to a minimum changing lighting settings, reducing environmental influences and finding the optimal evaluation settings in the DIC software. These hardware and software settings are validated in the second step with the measurement of a rigid body motion and the comparison to the machine stroke. In the third step, a calibration target found by Patterson et al. [**patterson2007**], adapted to the small dimensions of the present sample, was used. Due to its three-point bending structure, it links the force measured by a force to the DIC measured displacement using the Euler-Bernoulli beam theory. Both validation steps show, that the best settings in step 1 are the best settings for the following measurements. 20 images are taken without any movement to quantify the DIC noise for each test. A 9 MPx CCD camera (Manta G917B, Allied Vision Technology GmbH, Stadtroda, Germany) in combination with a telecentric lens (DTCM16.6-110, vico imaging, Guangdong, China) is used for imaging. The camera lens combination has a field of view of 12.8 $\times$ 10 mm^2 with a pixel edge length of 3.69 μm. Because of the coating process, the coating thickness locally varies in the macroscopic foam sample. Since the individual struts are extracted from all over the foam sample, their coating thickness varies as well. To measure the specific coating thickness, micro sections of five exemplary struts are done. Therefore, the struts are moulded upright in a slip-free casting compound (Technovit 4002IQ, Kulzer GmbH, Hanau, Germany) and polished with sandpaper (P1200, P2500) to generate a micro section approximated every 50 μm in axial direction of the strut reaching up to 40 images. Due to processing reasons, only 33 micro sections could be made. The images were captured with a light microscope (Axio Imager 2, Carl Zeiss Microscopy GmbH, Jena, Germany) using a lens with a magnification of $\times$10 (EC "Epiplan-Neofluar" 10x/0,25 HD DIC M27, Carl Zeiss Microscopy GmbH, Jena, Germany). For all struts in all images, the coating thickness was measured at six points (**Figure 2** (a)). Additionally, the area of the inner PU core (**Figure 2** (b)) was estimated using Heron's formula (1) to calculate the surface area of a triangle.

$$A = \sqrt{s(s-a)(s-b)(s-c)} \tag{1}$$

$$\text{with} \quad s = \frac{a+b+c}{2} \quad \text{and} \quad a, b, c : \text{triangle side lengths}$$

3 Results and Discussion

The deformation of the strut in the tensile test starts with a homogeneous strain distribution over the complete strut during the linear elastic deformation (**Figure 1** ① and ②). With damage initialisation, first deformation bands occur (**Figure 1** ③ and ④) and grow until the sample fractures (**Figure1** ⑤ and ⑥). Thereby, the orientations of the deformation bands show every case between pure tension and shear deformation.

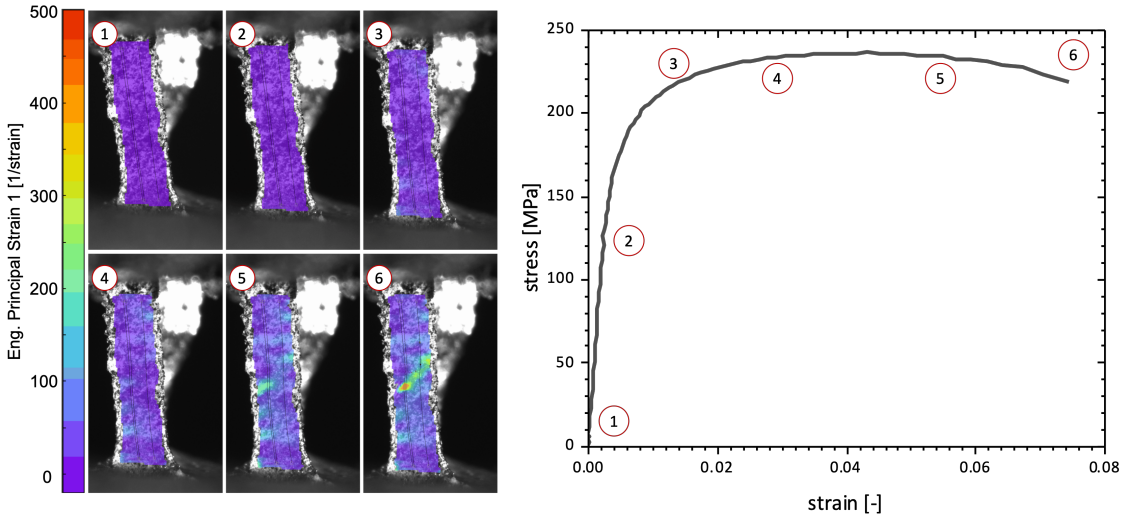

Figure 1. Full-field strain measurement using DIC on an individual strut during tensile testing at six different deformation steps (left) and stress-strain-diagram with highlighted deformation steps ①-⑥ (right)

The varying deformation behaviour could have different reasons. Due to the complex structure of the struts, a perfect alignment in the device is not always possible. The error in the alignment changes the experimental mode from pure tensile loading to bending the strut followed by a tensile load. Thereby, the bending results in a local elevation of the load followed by an inhomogeneous failure. A second reason can be found within the coating of the struts. The coating thickness varies around the strut, as well as it contains defects which reduce the stability. Defects in the coating could only be located using an in-situ CT scan, which is not available for the investigated struts. Therefore, a huge number of experiments is needed to estimate homogeneous material parameters to map the real behaviour of the individual struts. The scattering in stiffness for eight struts (TS1-TS8) can be found in Table 1. No clear distribution function can be extracted, more experiments are needed to analyse the scattering of the material parameters and to estimate a distribution function of the material parameters.

Table 1. Stiffness during linear elastic deformation for eight struts

	TS1	TS2	TS3	TS4	TS5	TS6	TS7	TS8
stiffness [GPa]	31.766	27.873	52.672	40.766	42.184	48.385	68.414	24.249

For performing the micro sections, five struts (UD1-UD5) are chosen. During the investigation of the coating thickness, a huge scattering can be found. For the five struts, the coating thickness scatters from 20.96 $\pm$ 2.66 μm to 80.97 $\pm$ 10.22 μm. Whereas the cross sectional area of the PU core area stays constant for all struts in all measurements (**Figure 2**). Hence, the outer dimensions of the strut in the photogrammetric model allow to estimate the coating thickness.

4 Conclusion

Regarding the micro sections of struts it has been shown that the PU template foam has constant strut cross sectional area for the different struts. Therefore, a good estimation of the coating thickness can

**Proceedings of the 8th GACM Colloquium on Computational Mechanics
for Young Scientists from Academia and Industry
August 28–30, 2019 in Kassel, Germany**

A Lie group generalization of the RATTLE scheme applied to nonholonomic constraints

Stefan Hante *

Institute of Mathematics
Martin Luther University Halle-Wittenberg
06099 Halle (Saale), Germany

Abstract. We present an integration scheme which generalizes the well-known RATTLE scheme in two respects: First, we will use a nonlinear configuration space with Lie group structure using a Lie algebra approach. Second, we will extend the scheme to nonholonomic constraints in Pfaffian form. By using the approach of variational integrators, we obtain a scheme which simultaneously supports holonomic and nonholonomic constraints. We performed numerical experiments on the rolling disk problem, where the disk is considered a rigid body with configuration space similar to SE(3). We will show test results and conclude that nonholonomic constraints such as rolling or sliding contact can be incorporated in multibody simulation environments, where it is infeasible to choose the best suited coordinates for each body by hand.

Introduction

When simulating large multi-body systems, it is impractical to choose minimal coordinates for each body by hand. Rather, it is convenient to use standardized coordinates for position and orientation for all bodies and introduce joints and restrictions by constraint equations. It is well-known that representing orientation by a set of three rotation angles can lead to singularities if large rotations are present. Thus, one has to use a non-linear configuration space for orientation. Fortunately, such non-linear configuration spaces often possess Lie group structure. This can be used to construct integration schemes that automatically preserve the structure of the non-linear configuration space. Here, we use the Lie algebra approach [2] to construct a variational integrator [7], which works on a Lie group. The nonholonomic RATTLie scheme is derived in order to solve equations of motion of mechanical systems with simultaneous holonomic and nonholonomic constraints. A nonholonomic RATTLE scheme was already introduced in [4], which inspired this nonholonomic RATTLie scheme.

1 Lie group structured configuration spaces, variational principles and nonholonomic contraints

We consider a system with an n-dimensional configuration space G. We suppose G has a (matrix) Lie group structure $(G, \circ)$, where $\circ$ is the Lie group operation $\circ\colon G \times G \to G$. Let $e \in G$ be the identity element. We call the tangent space T_eG the Lie algebra of G. Since tangent spaces are linear, we can identify T_eG with $\mathbb{R}^n$ by an isomorphism $\widetilde{\bullet}\colon \mathbb{R}^n \to T_eG$. We define the hat operator $\widehat{\bullet}\colon \mathbb{R}^n \to \mathbb{R}^{n\times n}$ by $\widetilde{\widehat{\boldsymbol{a}} \cdot \boldsymbol{b}} = [\widetilde{\boldsymbol{a}}, \widetilde{\boldsymbol{b}}]$, where $[\bullet, \bullet]$ is the Lie bracket of the Lie algebra.

The main idea of the Lie algebra approach [2] is to describe all derivatives $\dot{q}(t) \in T_{q(t)}G$ for a function $q(t) \in G$ by velocity vectors $\boldsymbol{v}(t) \in \mathbb{R}^n$ and the kinematic equation

$$\dot{q}(t) = dL_{q(t)}(e)\, \widetilde{\boldsymbol{v}(t)}, \tag{1}$$

*Corresponding author: stefan.hante@mathematik.uni-halle.de

where dL_q is the differential of the left multiplication $L_q\colon Q \mapsto q \circ Q$. The exponential function $\exp\colon T_eG \to G$ is defined by the evolution of (1) with constant velocity vector $\boldsymbol{w}$:

$$\exp(t\widetilde{\boldsymbol{w}}) = q(t) \qquad \Leftrightarrow \qquad \dot{q}(t) = dL_{q(t)}(e)\ \widetilde{\boldsymbol{w}}, \quad q(0) = e.$$

The tangent operator $\mathbf{T}\colon \mathbb{R}^n \to \mathbb{R}^{n\times n}$ characterizes the derivative of the exponential function:

$$\frac{d}{dt}\exp(\widetilde{\boldsymbol{v}}) = dL_{\exp(\widetilde{\boldsymbol{v}})}(e)\ \widetilde{\mathbf{T}(\boldsymbol{v})\cdot\dot{\boldsymbol{v}}}, \qquad \big(\boldsymbol{v} = \boldsymbol{v}(t),\ \dot{\boldsymbol{v}} = \dot{\boldsymbol{v}}(t)\big).$$

The derivative with respect to an element of the Lie group G can be expressed in our framework using the differential operator $\mathbf{D}$ defined by

$$\mathbf{D}f(g)\cdot\boldsymbol{w} = df(g)\ dL_g(e)\ \widetilde{\boldsymbol{w}}, \qquad \big(g \in G,\ \boldsymbol{w} \in \mathbb{R}^n,\ \mathbf{D}f(g) \in \mathbb{R}^{\dim(\operatorname{im} f)\times n}\big).$$

For Lie groups which typically appear in multi-body dynamics (such as products and semidirect products of $\mathbb{R}^3$, unit quaternions $\mathbb{S}^3$, etc.) these Lie group functions exp, $\mathbf{T}$, $\widetilde{\bullet}$, $\widehat{\bullet}$, etc. can be expressed in closed form and are easy to compute.

We will consider a constrained mechanical system with Lie group structured configuration space $G \ni q(t)$, kinetic energy $\mathcal{T}\big(\boldsymbol{v}(t)\big) = \frac{1}{2}\big(\boldsymbol{v}(t)\big)^T\cdot\mathbf{M}\cdot\boldsymbol{v}(t)$ and potential energy $\mathcal{U}\big(q(t)\big)$, where $q(t)$ and $\boldsymbol{v}(t)$ are related through the kinematic equation (1) and $\mathbf{M}$ is a constant, symmetric and positive definite mass matrix. We assume the mathematical system is constrained by holonomic constraints $\boldsymbol{\Phi}\big(q(t)\big) = \mathbf{0}$ as well as by nonholonomic constraints in Pfaffian form $\mathbf{B}\big(q(t)\big)\cdot\boldsymbol{v}(t) = \mathbf{0}$ with $\boldsymbol{\Phi}(q) \in \mathbb{R}^{m_1}$ and $\mathbf{B}(q) \in \mathbb{R}^{m_2\times n}$. We use the Lagrange-d'Alembert principle with an augmented Lagrangian for the holonomic constraints and arrive at the constrained variational principle

$$0 = \delta\int_0^T \mathcal{T}\big(\boldsymbol{v}(t)\big) - \mathcal{U}\big(q(t)\big) - \big(\boldsymbol{\lambda}(t)\big)^T\cdot\boldsymbol{\Phi}\big(q(t)\big)\ dt, \tag{2}$$

where the variation vanishes at the endpoints and fulfills the nonholonomic constraints:

$$\delta q(t) = dL_{q(t)}(e)\ \widetilde{\boldsymbol{\delta q}(t)}, \qquad \mathbf{0} = \boldsymbol{\delta q}(0) = \boldsymbol{\delta q}(T), \qquad \mathbf{B}\big(q(t)\big)\cdot\boldsymbol{\delta q}(t) = \mathbf{0}. \tag{3}$$

The usual approach for Hamilton's principle on Lie groups [3] together with the approach for the nonholonomic Lagrange-d'Alembert principle [6] and the kinematic equation (1) yields the equations of motion

$$\mathbf{M}\cdot\dot{\boldsymbol{v}} = \widehat{\boldsymbol{v}}^T\cdot\mathbf{M}\cdot\boldsymbol{v} - \big(\mathbf{D}\mathcal{U}(q)\big)^T - \big(\mathbf{D}\boldsymbol{\Phi}(q)\big)^T\cdot\boldsymbol{\lambda} - \big(\mathbf{B}(q)\big)^T\cdot\boldsymbol{\mu}, \tag{4a}$$

$$\mathbf{0} = \boldsymbol{\Phi}(q), \tag{4b}$$

$$\mathbf{0} = \mathbf{B}(q)\cdot\boldsymbol{v}, \tag{4c}$$

where $\boldsymbol{\mu}(t) \in \mathbb{R}^{m_2}$ are additional Lagrange multipliers associated with the nonholonomic constraints.

2 The nonholonomic RATTLie time integration scheme

In order to construct the nonholonomic RATTLie time integration scheme, we use the approach of variational integrators [7] and start with the variational principle (2). We replace $q(t)$ by a discretized version $q^d(t)$ defined by

$$q^d(t) = q_{k-1}\circ\exp\Big(\frac{t-t_{k-1}}{h}\widetilde{\boldsymbol{v}_{k-1/2}}\Big), \qquad t \in [t_{k-1}, t_k),$$

where $t_k = t_0 + kh$ are equidistant grid points with step size $h = T/N$. The $\boldsymbol{v}_{k-1/2}$ are defined in such a way that q^d is continuous. The function q^d is differentiable for $t \in (t_{k-1}, t_k)$ with constant velocity vector $\boldsymbol{v}_{k-1/2}$. Furthermore, we replace $\boldsymbol{\lambda}(t)$ by a discretized version $\boldsymbol{\lambda}^d(t)$ that we allow to be discontinuous at t_k and define $\boldsymbol{\lambda}_k^{\pm} = \lim_{\tau\to t_k\pm 0}\boldsymbol{\lambda}^d(\tau)$. By splitting the integral into several integrals over (t_{k-1}, t_k), evaluating the integral over the kinetic energy and approximating the remaining integrals with the trapezoidal rule, we arrive at the discrete variational principle $0 = \delta\sum_{k=1}^N L^d(q_{k-1}, q_k, \boldsymbol{\lambda}_k^+, \boldsymbol{\lambda}_k^-)$ with variations that fulfill a discretized version of (3) and with the discrete augmented Lagrangian

$$L^d(q_{k-1}, q_k, \boldsymbol{\lambda}_k^+, \boldsymbol{\lambda}_k^-) = \frac{h}{2}\boldsymbol{v}_{k-1/2}^T\cdot\mathbf{M}\cdot\boldsymbol{v}_{k-1/2} - \frac{h}{2}\mathcal{U}(q_{k-1}) - \frac{h}{2}\mathcal{U}(q_k) - \frac{h}{2}\big(\boldsymbol{\Phi}(q_{n-1})\big)^T\cdot\boldsymbol{\lambda}_{n-1}^+ - \frac{h}{2}\big(\boldsymbol{\Phi}(q_n)\big)^T\cdot\boldsymbol{\lambda}_n^-.$$

The discrete variational principle leads to a form of discrete Euler-Lagrange equations:

$$h\boldsymbol{\mu}_k^T \cdot \mathbf{B}(q_k) = \mathbf{D}_2 L^d(q_{k-1}, q_k, \boldsymbol{\lambda}_k^+, \boldsymbol{\lambda}_k^-) + \mathbf{D}_1 L^d(q_k, q_{k+1}, \boldsymbol{\lambda}_{k+1}^+, \boldsymbol{\lambda}_{k+1}^-),$$
$$\mathbf{0} = d_3 L^d(q_{k-1}, q_k, \boldsymbol{\lambda}_k^+, \boldsymbol{\lambda}_k^-), \qquad \mathbf{0} = d_4 L^d(q_{k-1}, q_k, \boldsymbol{\lambda}_k^+, \boldsymbol{\lambda}_k^-).$$

The term $h\boldsymbol{\mu}_k^T \cdot \mathbf{B}(q_k)$ results from the fact that we only consider variations that satisfy the nonholonomic constraint. We will apply a discrete Legendre transformation, where we write the impulses as $\mathbf{M} \cdot \boldsymbol{v}_k$, where $\boldsymbol{v}_k$ is the velocity vector. The equations $\mathbf{0} = d_3 L^d$ and $\mathbf{0} = d_4 L^d$ are both equal to the constraint equations $\mathbf{0} = \boldsymbol{\Phi}$, so we replace one of them by the hidden constraints $\mathbf{D}\boldsymbol{\Phi}(q) \cdot \boldsymbol{v} = \mathbf{0}$, which we obtain by differentiating the constraint equation (4b). Plugging everything together, we arrive at the nonholonomic RATTLie integration scheme:

$$\begin{aligned}
q_k &= q_{k-1} \circ \exp(h\widetilde{\boldsymbol{v}_{k-1/2}}),\\
\mathbf{M} \cdot \boldsymbol{v}_{k-1} &= \mathbf{T}^{-T}(-h\boldsymbol{v}_{k-1/2}) \cdot \mathbf{M} \cdot \boldsymbol{v}_{k-1/2} - \frac{h}{2}\boldsymbol{f}_{k-1} + \frac{h}{2}\big(\mathbf{D}\boldsymbol{\Phi}(q_{k-1})\big)^T \cdot \boldsymbol{\lambda}_{k-1}^+ + \frac{h}{2}\big(\mathbf{B}(q_{k-1})\big)^T \cdot \boldsymbol{\mu}_{k-1},\\
\mathbf{0} &= \boldsymbol{\Phi}(q_k),\\
\mathbf{M} \cdot \boldsymbol{v}_k &= \mathbf{T}^{-T}(h\boldsymbol{v}_{k-1/2}) \cdot \mathbf{M} \cdot \boldsymbol{v}_{k-1/2} + \frac{h}{2}\boldsymbol{f}_k - \frac{h}{2}\big(\mathbf{D}\boldsymbol{\Phi}(q_k)\big)^T \cdot \boldsymbol{\lambda}_k^- - \frac{h}{2}\big(\mathbf{B}^T(q_k)\big)^T \cdot \boldsymbol{\mu}_k,\\
\mathbf{0} &= \mathbf{D}\boldsymbol{\Phi}(q_k) \cdot \boldsymbol{v}_k, \qquad \mathbf{0} = \mathbf{B}(q_k) \cdot \boldsymbol{v}_k.
\end{aligned}$$

Here, $\boldsymbol{f}_k = \big(\mathbf{D}\mathcal{U}(q_k)\big)^T + \boldsymbol{F}(t_k, q_k)$ is the sum of external, conservative and nonconservative forces. The Lagrange multipliers $\boldsymbol{\lambda}_k = (\boldsymbol{\lambda}_k^+ + \boldsymbol{\lambda}_k^-)/2$ and $\boldsymbol{\mu}_k$ become unstable for fine step sizes h, so we have to calculate corrected Lagrange multipliers by solving

$$\begin{bmatrix} \mathbf{M} & \big(\mathbf{D}\boldsymbol{\Phi}(q_k)\big)^T & \big(\mathbf{B}(q_k)\big)^T \\ \mathbf{D}\boldsymbol{\Phi}(q_k) & \mathbf{0} & \mathbf{0} \\ \mathbf{B}(q_k) & \mathbf{0} & \mathbf{0} \end{bmatrix} \cdot \begin{bmatrix} \dot{\boldsymbol{v}}_k^{\mathrm{corr}} \\ \boldsymbol{\lambda}_k^{\mathrm{corr}} \\ \boldsymbol{\mu}_k^{\mathrm{corr}} \end{bmatrix} = \begin{bmatrix} \widehat{\boldsymbol{v}_k}^T \cdot \mathbf{M} \cdot \boldsymbol{v}_k + \boldsymbol{f}_k \\ \dfrac{\mathbf{D}\boldsymbol{\Phi}(q_{k-1}) - \mathbf{D}\boldsymbol{\Phi}(q_{k+1})}{2h} \cdot \boldsymbol{v}_k \\ \dfrac{\mathbf{B}(q_{k-1}) - \mathbf{B}(q_{k+1})}{2h} \cdot \boldsymbol{v}_k \end{bmatrix}.$$

3 The rolling disk

We consider an infinitely thin disk of radius 1 which rolls without slip on the plane $P_{1,2} = \{\boldsymbol{x} \in \mathbb{R}^3 \colon [0,0,1] \cdot \boldsymbol{x} = 0\}$. We chose $\mathbb{S}^3 \times \mathbb{R}^3 \ni (p, \boldsymbol{x})$ as configuration space, where $\boldsymbol{x}$ is the position of the disk's center point and p is the disk's orientation as a unit quaternion. We want to describe both velocity $\boldsymbol{U}$ and angular velocity $\boldsymbol{\Omega}$ with respect to the body-fixed frame. Therefore, the configuration space gets the structure of the semidirect product Lie group $(\mathbb{S}^3 \ltimes \mathbb{R}^3, \circ)$, similar to $SE(3)$. For the orientation $p = [1,0,0,0]^T$, the disk is supposed to lie flat in the plane $P_{1,2}$. Now we can calculate the lowest point of the disk $\boldsymbol{y}_L(p)$ with orientation $p = [p_0, p_1, p_2, p_3]^T \in \mathbb{S}^3$ with respect to the body-fixed frame:

$$\boldsymbol{y}_L(p) = \big[p_0 p_2 - p_1 p_3,\ p_2 p_3 - p_0 p_1,\ 0\big]^T / \sqrt{(p_1^2 + p_2^2)(p_0^2 + p_3^2)}.$$

In order for the disk to roll on the plane $P_{1,2}$ it has to hold $x_3 = -2\sqrt{(p_1^2 + p_2^2)(p_0^2 + p_3^2)}$ where $\boldsymbol{x} = [x_1, x_2, x_3]^T$. Since the disk should roll without slip, the overall velocity of the contact point has to vanish. From this, it follows $\mathbf{C}(p, \boldsymbol{x}) \cdot [\boldsymbol{\Omega}^T, \boldsymbol{U}^T]^T = \mathbf{0}$ with $\mathbf{C}(p, \boldsymbol{x}) = \big[x_3 \operatorname{skw}\big(\boldsymbol{y}_L(p)\big), x_3 \mathbf{I}_3\big]$. If we reformulate this constraint with respect to the inertial frame by applying the unit quaternion p to each column of $\mathbf{C}(p, \boldsymbol{x})$, we get

$$\mathbf{0} = \begin{bmatrix} \mathbf{B}(p, \boldsymbol{x}) \\ \mathbf{D}\boldsymbol{\Phi}(p, \boldsymbol{x}) \end{bmatrix} \cdot \begin{bmatrix} \boldsymbol{\Omega} \\ \boldsymbol{U} \end{bmatrix},$$

where $\boldsymbol{\Phi}(p, \boldsymbol{x}) = x_3^2/2 - 2(p_1^2 + p_2^2)(p_0^2 + p_3^2)$. We can see that one condition is integrable and defines a holonomic constraint, while the other two are not integrable and define two nonholonomic constraints. Plugging everything together, we obtain the disk's equations of motion (4) with $q = (p, \boldsymbol{x})$, $\boldsymbol{v} = [\boldsymbol{\Omega}^T, \boldsymbol{U}^T]^T$, $\mathbf{M} = \operatorname{blkdiag}(\mathbf{J}, m\mathbf{I}_3)$ and $\mathcal{U}(q) = -m\boldsymbol{\gamma}^T \cdot \boldsymbol{x}$, where $\boldsymbol{\gamma} \in \mathbb{R}^3$ is the gravitational acceleration and $\mathbf{J}$ is the inertia tensor of the disk with respect to the body-fixed frame. Due to the choice of the configuration space and its Lie group structure, the inertia tensor $\mathbf{J}$ and the mass matrix $\mathbf{M}$ are constant diagonal matrices.

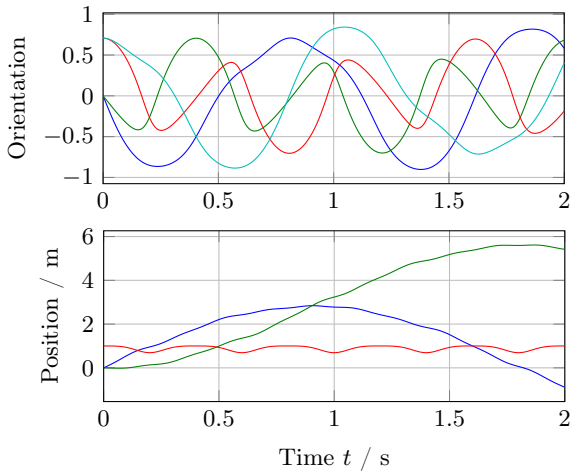

Figure 1. Orientation and position of the disk over time for $h \approx 10^{-6}\,\mathrm{s}$

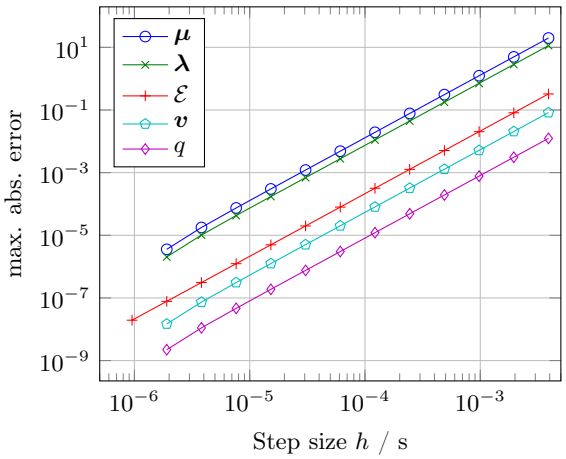

Figure 2. Maxima of absolute errors in configuration, velocity, Lagrange multipliers and mechanical energy $\mathcal{E}$ over step size h

4 Numerical tests

In order to test the nonholonomic RATTLie integration scheme, we have simulated the rolling disk with mass $m = 15\,\mathrm{kg}$, inertia tensor $\mathbf{J} = m\,\mathrm{diag}(0.25\,\mathrm{m}^2, 0.25\,\mathrm{m}^2, 0.5\,\mathrm{m}^2)$ and gravity $\boldsymbol{\gamma} = [0, 0, -9.81\,\mathrm{m/s}^2]^T$ from $t_0 = 0\,\mathrm{s}$ to $T = 2\,\mathrm{s}$. We chose the consistent initial values $p = \left[0, 0, \sqrt{1/2}, \sqrt{1/2}\right]^T$ and $x = [0\,\mathrm{m}, 0\,\mathrm{m}, 1\,\mathrm{m}]^T$. The initial angular velocity was chosen to be $\boldsymbol{\Omega} = [0\,\mathrm{s}^{-1}, 15\,\mathrm{s}^{-1}, 5\,\mathrm{s}^{-1}]^T$ and the initial velocity $\boldsymbol{U}$ was chosen to be consistent. We have shown the evolution of orientation and position of the disk in Figure 1.

In Figure 2, we have plotted the maxima of the absolute errors in the configuration q, velocity $\boldsymbol{v}$, Lagrange multipliers $\boldsymbol{\lambda}$ and $\boldsymbol{\mu}$ as well as in the mechanical energy $\mathcal{E} = \mathcal{T} + \mathcal{U}$ over the step size in double logarithmic scale. We have calculated the errors with respect to a numeric solution obtained by applying the same integration scheme with very fine step size $h = 2^{-20}\mathrm{s} \approx 10^{-6}\,\mathrm{s}$. We can see that if we scale the step size h by a factor c, we can expect that the errors will be scaled by a factor c^2. This suggests that the scheme is, like the original RATTLE [1], an integration scheme of second order [5]. As we expect from a variational integrator [7], the nonholonomic RATTLie scheme does not show a systematic drift in mechanical energy.

References

[1] H. C. Andersen. Rattle: A "velocity" version of the shake algorithm for molecular dynamics calculations. *Journal of Computational Physics* 52.1 (1983), pp. 24–34.

[2] M. Arnold, A. Cardona, and O. Brüls. A Lie algebra approach to Lie group time integration of constrained systems. In: *Structure-Preserving Integrators in Nonlinear Structural Dynamics and Flexible Multibody Dynamics*. Ed. by P. Betsch. Springer, 2016, pp. 91–158.

[3] O. Brüls, M. Arnold, and A. Cardona. Two Lie group formulations for dynamic multibody systems with large rotations. In: *Proceedings of IDETC/MSNDC 2011, ASME 2011 International Design Engineering Technical Conferences*. Washington, USA, 2011.

[4] S.J. Ferraro, D. Iglesias-Ponte, and D.M. de Diego. Numerical and geometric aspects of the nonholonomic SHAKE and RATTLE methods. *Discrete Contin. Dyn. Syst* (2009), pp. 220–229.

[5] E. Hairer and G. Wanner. *Solving Ordinary Differential Equations II. Stiff and Differential-Algebraic Problems*. 2nd ed. Springer-Verlag Berlin Heidelberg, 2002.

[6] W.S. Koon and J.E. Marsden. The Hamiltonian and Lagrangian approaches to the dynamics of nonholonomic systems. *Reports on Mathematical Physics* 40.1 (1997), pp. 21–62.

[7] J.E. Marsden and M. West. Discrete mechanics and variational integrators. *Acta Numerica* 10 (2001), pp. 357–514.

Proceedings of the 8th GACM Colloquium on Computational Mechanics
for Young Scientists from Academia and Industry
August 28–30, 2019 in Kassel, Germany

A Brief Survey on Non-standard Constraints: Simulation and Optimal Control

Dominik Kern * [1] and Ulrich J. Römer[2]

[1]TU Chemnitz, Germany
[2]Karlsruhe Institute of Technology (KIT), Germany

Abstract. In terms of simulation and control holonomic constraints are well documented and thus termed standard. As non-standard constraints, we understand non-holonomic and unilateral constraints. We limit this survey to mechanical systems with a finite number of degrees of freedom. The long-term behavior of non-holonomic integrators as compared to structure-preserving integrators for holonomically constrained systems is briefly discussed. Some recent research regarding the treatment of unilaterally constrained systems by event-driven or time-stepping schemes for time integration and in the context of optimal control problems is outlined.

1 Introduction

Many technical systems are modeled as multibody systems which are comprised of rigid or elastic bodies, joints, and force elements or forcing. We restrict the discussion to discrete systems, meaning elastic bodies are presumed to be discretized by shape functions or finite elements and the system is represented by a finite number of degrees of freedom. Joints are the typical pictorialization of constraints; for example they constrain a body to move only along or around a certain axis. Generally, constraints may either account for kinematic restrictions of a body, such as with redundant coordinates, or for interactions between bodies and the environment. Such interactions may be described by an equation, such as a pivot, or by an inequation, such as a non-penetration condition.

Without any claim for completeness, we report about some active research related to simulation and control. We adopt the common classification of constraints into: holonomic or non-holonomic (e. g. massless rigid connectors or rolling without sliding), scleronomic or rheonomic (e. g. static or moving environment), and unilateral or bilateral (e. g. limiters or bearings). Bilateral holonomic, particularly holonomic-scleronomic, constraints are the simplest type of constraints and their treatment has been well studied and is covered in many textbooks [12, 32]. Therefore, we refer to them as *standard*. There are some ongoing discussions regarding the remaining constraint types, non-holonomic and unilateral, which is why we refer to them as *non-standard*.

2 Non-holonomic constraints

We need to recall the definition of a holonomic constraint to give meaning to the term *non-holonomic*. Having a multibody system with generalized coordinates $\mathbf{q}$ in mind, a holonomic-scleronomic constraint is given by an algebraic equation $\Psi(\mathbf{q}) = 0$ on position level, whereas a holonomic-rheonomic constraint would explicitly depend on time t. For further details on non-holonomic systems we refer to the classical textbook of Neimark & Fufaev [25] and more recently Rabier & Rheinboldt and Bloch [5, 26]. A popular formulation for the numerical solution of holonomically constrained systems was proposed by Gear, Gupta and Leimkuhler [11]

*Corresponding author: dominik.kern@mb.tu-chemnitz.de ORCID iD: 0000-0002-1958-2982

$$\dot{\mathbf{q}} = \mathbf{v} - \mathbf{G}^{\mathsf{T}}(\mathbf{q})\boldsymbol{\eta} \,, \tag{1a}$$

$$\mathbf{M}(\mathbf{q})\dot{\mathbf{v}} = \mathbf{f}(\mathbf{q}, \mathbf{v}) - \mathbf{G}^{\mathsf{T}}(\mathbf{q})\boldsymbol{\lambda} \,, \tag{1b}$$

$$\boldsymbol{\Psi}(\mathbf{q}) = \mathbf{0} \,, \tag{1c}$$

$$\mathbf{G}(\mathbf{q})\mathbf{v} = \mathbf{0} \,, \tag{1d}$$

with mass matrix $\mathbf{M}(\mathbf{q})$, generalized forces $\mathbf{f}$, Lagrange multipliers $\boldsymbol{\lambda}$ and $\boldsymbol{\eta}$, and $\mathbf{G} = \partial\boldsymbol{\Psi}/\partial\mathbf{q}$. It enforces the constraints on both, position and velocity level, and is also referred to as stabilized index-2 formulation. A combination of differential and algebraic equations like in the example given by eq. (1) is called *differential algebraic equation (DAE)* or *descriptor system*.

Non-holonomic constraints are usually understood as equations between differentials of d$\mathbf{q}$ that cannot be integrated to an equation on position level. A general criteria for non-integrability gives the Frobenius-Theorem [14]. In mechanical systems, where most constraints appear as linear forms $\mathbf{A}(\mathbf{q})\dot{\mathbf{q}} = \mathbf{0}$, there is a simple necessary condition. For a non-holonomic constraint the derivative of the corresponding row in $\mathbf{A}$ must be a non-symmetric matrix.

From the point of view of numerics, the inclusion of non-holonomic constraints into eq. (1) is straightforward: they are added to the holonomic constraints on velocity level. This formulation works well for moderate time spans. The robustness and the excellent long-time behavior of structure-preserving integrators for unconstrained and holonomically constrained systems [13] suggest taking advantage of the geometrical properties of non-holonomic systems. However, non-holonomic systems do not, in general, preserve a symplectic structure. There is the open question whether energy conservation is the only geometric property of non-holonomic systems. Consequently, an energy-consistent scheme has already been proposed [4] to include both, holonomic and non-holonomic constraints. Recent research indicates that the good long-term behavior of current non-holonomic integrators is due to the special properties of popular benchmark systems and does not hold in general [22].

Lie-group methods [8, 24] and their successful application for the description of large rotations are not considered further, since there is no hope to identify a Lie-group for any possible constraint.

The consideration of non-holonomic constraints in optimal control problems is also more challenging than for holonomic ones. We restrict the discussion to feed-forward control, meaning we calculate a nominal trajectory that is optimal in the sense of a given cost functional. These are constrained optimizations, because the equations of motion, or more generally the system dynamics, are imposed as constraints on the optimal control problem. For a general discussion, we refer to the comprehensive textbook [12] and take a glance at concepts motivated by structure preservation. Both, the discretization-based approach *Discrete Mechanics and Optimal Control of Constrained systems (DMOCC)* [19] and the functional-based approach [15], are designed for holonomic constraints. Nevertheless, both allow different time discretizations than variational integrators. Consequently, it will be interesting to find out how an energy-consistent time discretization like the one proposed by Betsch [4] performs in this context.

3 Unilateral constraints

While bilateral constraints describe relationships between some or all state variables via equations, *unilateral constraints* introduce one-sided limits on the admissible domain which result in inequations $\phi(\mathbf{q}) \geq \mathbf{0}$ or inclusions. Consequently, solutions may be non-smooth or even discontinuous. In mechanics, typical origins of unilateral constraints are collisions and friction. Several approaches exist to describe such systems, we refer to [6, 17] for further details. Numerical methods for approximate solutions have to deal with the (piecewise) non-smooth dynamics and follow one of two basic philosophies: event-driven or time-stepping, cf. figure 1. *Event-driven schemes* rely on algorithms for ODEs or DAEs to solve the smooth

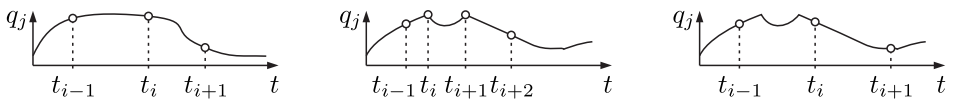

Figure 1. Numerical approximation of time behavior of state q_j: **left** smooth solution (variable time step); **middle** non-smooth solution with event-driven approach (variable time step); **right** non-smooth solution with time-stepping scheme (fixed time step).

parts of the solution trajectory [3], discrete events where inequalities become active are determined iteratively [29], a discrete state update is evaluated and the smooth solver is restarted. *Time-stepping schemes* approximate the solution trajectory at fixed time steps where constraints are satisfied exactly (subject only to numerical precision), but might be (slightly) violated in between [1, 6]. Event-driven schemes are standard in most commercial software tools, since high-order methods can be used for the smooth parts of the solution and good performance is achieved if there is a moderate number of events. They perform badly if there is a high number of events or even accumulation points (Zeno behavior), since this leads to very small time steps and the algorithm gets stuck. Furthermore, existence and uniqueness of a solution of the ODE or DAE after an event is not guaranteed (cf. the Painlevé paradox) [31]. Time-stepping schemes overcome these problems by "averaging" over the influence of all events during fixed time steps [23]. Velocity jumps due to collisions are treated by a coefficient of restitution which acts as though all collisions within a time step occur simultaneously [30]. They can be formulated as implicit time integration methods which require the solution of a linear or nonlinear complementary problem at every time step [2].

In terms of structure-preservation, event-driven collision integrators follow naturally from Hamilton's principle, when the collision time is an additional variable [9]. Note, that this use of Hamilton's principle in equality form [9] does not allow trajectories to approach or to exit motions along the admissible set boundary, i.e. contacts being opened or closed. In addition, the adjusted time steps may slightly violate the conservation properties of variational integrators and thus accumulate errors. The extension of classical analytical mechanics to perfect unilateral constraints, with possible persistent contact, requires a reformulation of the variational principles of mechanics in terms of variational inequalities [18]. It is thus natural to consider a nonsmooth, discrete Variational Principle for inequality constrained systems [16]. Since variational integrators are formulated in terms of momenta and avoid direct computation of forces they are a convenient choice for time-stepping schemes. There is ongoing research in the development of higher order methods to increase time step size and performance [28]. In the context of transient simulations, the competition between event-driven and time-stepping schemes is not decided yet and maybe never will.

For the optimal control problem (feed-forward), we distinguish two cases: firstly one only requires compliance with the unilateral constraints, secondly there are collisions with the admissible boundary set. The first case, pure compliance with unilateral constraints such as actuator saturation, is comparatively simple and commonly accounted for by the Karush-Kuhn-Tucker conditions [7]. The second case, when the events of interaction with the boundary of the admissible domain become subject of the optimization, requires more sophistication since then the related dynamics are non-smooth and the events, their number and their states, are additional unknown variables. As an example, consider a pendulum-on-cart-system where the cart moves between two limiters and the collisions with these boundaries are to be utilized for a swing-up of the pendulum. Since classical control theory presumes smooth dynamics, the direct approach, not to say brute-force, splits this problem into two layers. The inner layer finds the optimal solution between two collisions. The earlier collision is given by a fixed post-collision state and the later one by a fixed pre-collision state, defining already the subsequent post-collision state. The outer layer is used to find the optimal collision times and states [10]. A further outer layer may optimize the contact mode sequence, which is an integer programming problem growing exponentially with the number of contact constraints. Alternatively, time transformations [27] or contact-implicit trajectory optimization [21] can be used to avoid this mixed integer optimal control problem. We further mention that there is a close relation to the theory of switched systems [20].

References

[1] V. Acary and B. Brogliato. *Numerical methods for nonsmooth dynamical systems: applications in mechanics and electronics*. Berlin: Springer, 2008.

[2] M. Anitescu. Optimization-based simulation of nonsmooth rigid multibody dynamics. *Math Program* 105.1 (2006), pp. 113–143.

[3] M. Arnold and K. Frischmuth. Solving problems with unilateral constraints by DAE methods. *Math Comput Simulat* 47.1 (1998), pp. 47–67.

[4] P. Betsch. A Unified Approach to the Energy-Consistent Numerical Integration of Nonholonomic Mechanical Systems and Flexible Multibody Dynamics. *GAMM-Mitteilungen* 27.1 (2004), pp. 66–87.

[5] A. M. Bloch. Nonholonomic mechanics. In: *Nonholonomic mechanics and control*. Vol. 24. New York: Springer, 2003, pp. 207–276.

[6] B. Brogliato. *Nonsmooth Mechanics*. 2nd ed. London: Springer, 1999.

[7] R. Cottle and C. E. Lemke. *Nonlinear programming*. Vol. 9. SIAM-AMS Proceedings. American Mathematical Soc., 1976.

[8] P. E. Crouch and R. Grossman. Numerical integration of ordinary differential equations on manifolds. *J Nonlinear Sci* 3.1 (1993), pp. 1–33.

[9] R. C. Fetecau, J. E. Marsden, M. Ortiz, and M. West. Nonsmooth Lagrangian mechanics and variational collision integrators. *SIAM J Appl Dyn Syst* 2.3 (2003), pp. 381–416.

[10] K. Flaßkamp and S. Ober-Blöbaum. Variational formulation and optimal control of hybrid Lagrangian systems. In: *P Int Conf HSCC*. ACM. 2011, pp. 241–250.

[11] C. W. Gear, B. Leimkuhler, and G. K. Gupta. Automatic integration of Euler-Lagrange equations with constraints. *J Comput Appl Math* 12 (1985), pp. 77–90.

[12] M. Gerdts. *Optimal control of ODEs and DAEs*. Berlin: De Gruyter, 2011.

[13] E. Hairer, C. Lubich, and G. Wanner. *Geometric numerical integration: structure-preserving algorithms for ordinary differential equations*. Berlin: Springer, 2006.

[14] T. Hawkins. Frobenius, Cartan, and the problem of Pfaff. *Arch Hist Exact Sci* 59.4 (2005), pp. 381–436.

[15] E. R. Johnson and T. D. Murphey. Scalable variational integrators for constrained mechanical systems in generalized coordinates. *IEEE T Robot* 25.6 (2009), pp. 1249–1261.

[16] D. M. Kaufman and D. K. Pai. Geometric numerical integration of inequality constrained, nonsmooth Hamiltonian systems. *SIAM J Sci Comput* 34.5 (2012), A2670–A2703.

[17] J. Kleinert and B. Simeon. Differential-algebraic equations and beyond: from smooth to nonsmooth constrained dynamical systems. *arXiv:1811.07658 (preprint)* (2018).

[18] R. I. Leine, U. Aeberhard, and C. Glocker. Hamilton's principle as variational inequality for mechanical systems with impact. *J Nonlin Sci* 19.6 (2009), p. 633.

[19] S. Leyendecker, S. Ober-Blöbaum, J. E. Marsden, and M. Ortiz. Discrete mechanics and optimal control for constrained systems. *Optim Contr Appl Met* 31.6 (2010), pp. 505–528.

[20] D. Liberzon. *Switching in systems and control*. Boston: Birkhäuser, 2003.

[21] Z. Manchester, N. Doshi, R. J Wood, and S. Kuindersma. Contact-implicit trajectory optimization using variational integrators. *Int J Rob Res* (2019).

[22] K. Modin and O. Verdier. What makes nonholonomic integrators work? *arXiv:1707.04514 (preprint)* (2019).

[23] J. J. Moreau. Unilateral contact and dry friction in finite freedom dynamics. In: *Nonsmooth Mechanics and Applications*. Vienna: Springer, 1988, pp. 1–82.

[24] H. Munthe-Kaas. Runge-Kutta methods on Lie groups. *BIT* 38.1 (1998), pp. 92–111.

[25] J. I. Neimark and N. A. Fufaev. *Dynamics of nonholonomic systems*. American Mathematical Society, 2004.

[26] P. J. Rabier and W. C. Rheinboldt. *Nonholonomic Motion of Rigid Mechanical Systems from a DAE Viewpoint*. Philadelphia: SIAM, 2000.

[27] M. Ringkamp, S. Ober-Blöbaum, and S. Leyendecker. On the time transformation of mixed integer optimal control problems using a consistent fixed integer control function. *Math Program* 161.1-2 (2017), pp. 551–581.

[28] T. Schindler and V. Acary. Timestepping schemes for nonsmooth dynamics based on discontinuous Galerkin methods: definition and outlook. *Math Comput Simulat* 95 (2014), pp. 180–199.

[29] L. F. Shampine and S. Thompson. Event location for ordinary differential equations. *Comput Math Appl* 39.5-6 (2000), pp. 43–54.

[30] B. Smith, D. M. Kaufman, E. Vouga, R. Tamstorf, and E. Grinspun. Reflections on simultaneous impact. *ACM T Graphic* 31.4 (2012), pp. 1–12.

[31] D. E. Stewart. Rigid-body dynamics with friction and impact. *SIAM Rev* 42.1 (2000), pp. 3–39.

[32] G. Wanner and E. Hairer. *Solving ordinary differential equations II*. Berlin: Springer, 1996.

**Proceedings of the 8th GACM Colloquium on Computational Mechanics
for Young Scientists from Academia and Industry
August 28–30, 2019 in Kassel, Germany**

Comparison of timestepping schemes for non-smooth mechanics using orbital convergence

Paschkowski, Manuela * [1] and Arnold, Martin[1]

[1]Martin Luther University Halle-Wittenberg, Institute of Mathematics, 06099 Halle (Saale), Germany

Abstract. The dynamics of mechanical systems with non-smooth forces like friction, contacts and impacts can be simulated by differential equations in combination with inequality constraints. However a constraint gets active, parts of the solutions characterising the velocity of the system deal with jumps, with discontinuity points. Timestepping schemes are well-known possibilities to integrate such dynamical systems numerically. Their advantage is the avoided event detection such that a large number of discontinuity points – especially accumulation points of velocity jumps – can be handled with higher computational efficiency. These schemes are always of integration order one with respect to discrete L^p-norms. Hence, this classical tool can not be used to compare different algorithms. A more reasonable tool to compare the approximation accuracy is the concept of orbital convergence. This new concept is studied for time-independent systems with invariant limit cycles using an experimental convergence analysis.

1 Non-Smooth Mechanics

In the following, the motion of a multibody system connected to joints or other mechanical elements like springs or dampers is of interest. The generalised coordinates are represented by $q : I \subset \mathbb{R} \to \mathbb{R}^n$ and the velocity by $\mathrm{d}q =: v : I \to \mathbb{R}^n$. The degree of freedom of the motion can be reduced by involving interaction forces like contacts or impacts effecting on the multibody system in form of additional inequalities

$$g(q(t)) \geq 0, t \in I, \qquad g : \mathbb{R}^n \to \mathbb{R}^m.$$

There are critical points $t \in I$ where a positive constraint becomes zero. In these points summarised in

$$T^* := \{t \in I : \exists\ \delta > 0, i = 1, \ldots, m \text{ s.t. } g_i(q(\tau)) > 0, \forall \tau \in [t-\delta, t), g_i(q(t)) = 0\}$$

v can be discontinuous and q non-differentiable. Combining classical variational principles with Lagrange multiplier methods, the equations of motion of non-smooth mechanical problems have the form

$$M(q(t))\mathrm{d}v(t) = f(q(t), v(t))\mathrm{d}t + G(q)^T(\lambda(t)\mathrm{d}t + \Lambda(t)\mathrm{d}\eta), \tag{1}$$

$$0 \leq \lambda(t) \perp g(q) \geq 0, \tag{2}$$

$$0 \leq \Lambda(t) \perp G(q)(v^+ + \epsilon v^-) \geq 0, \tag{3}$$

$$\eta = \sum_{s \in T^*(q(t))} \delta_s \tag{4}$$

where M is the mass matrix, $G = \partial g / \partial q$ the constraint matrix, f the vector of the external forces, λ the Lagrange multipliers representing the contact forces, Λ the Lagrange multipliers representing the impact forces, $\epsilon \in [0, 1]$ the resolution number, $\mathrm{d}t$ the Lebesgue measure and δ_s the Dirac measure in time point s. The formulation $0 \leq a \perp b \geq 0$ is equivalent to $a, b \geq 0, a^T b = 0$ and is called complementarity problem.

A simple non-smooth mechanical system is the impact oscillator [2] in Figure 1 which motion is influenced by a periodic force p and an obstacle in position σ. Of course, the oscillator can not penetrate the obstacle. The inequality $g(q) = \sigma - q \geq 0$ symbolises this condition. Everytime the oscillator and the obstacle get in contact ($g(q) = 0$), an impact can be observed. This means, q gets non-differentiable and v discontinuous (see Figure 2). The force λ induces that the inequality constraint is fulfilled for all following time points and the impact force Λ represents the impact intensity.

*Corresponding author: manuela.paschkowski@mathematik.uni-halle.de

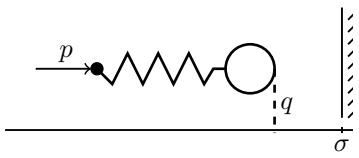

Figure 1. Impact oscillator.

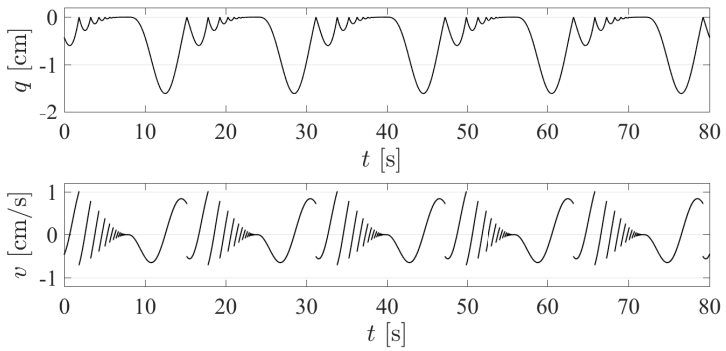

Figure 2. Impact oscillator: Trajectories ($\sigma = 0, p = \sin(\pi t/8), \epsilon = 0.6$).

2 Non-Smooth Timestepping Schemes

There are two main groups of numerical methods to solve (1)-(4). The *event-driven* ones identify impact points $t \in T^*$ exact. Those methods are very accurate when dealing with few critical points, but get inconsistent when the number increases or even an accumulation point of jumps can be observe like for the impact oscillator. For this situation, the *timestepping schemes* have been developed. They define a partition of the time interval $t_0 < t_1 < \ldots < t_N = T$ with step sizes $h_i := t_i - t_{i-1}$ which is never changed during the whole integration process and therefore independent of the location of impacts. In t_i approximations $q_i \approx q(t_i), v_i \approx v(t_i)$ are calculated in different ways. The first timestepping scheme was developed in [3], uses the explicit Euler method between impacts and does not distinguish between contact forces λ and impact forces Λ (see Algorithm 1).

Algorithm 1 Explicit Moreau-Jean timestepping scheme [3]

Require: time interval $[t_0, T]$, initial values $q_0 = q(0), v_0 = v(0), i = 0$, step size $h = T/N$
1: **procedure** MoreauJean(T, N, q_0, v_0, δ_1)
2: **while** $t_{i+1} < T$ **do**
3: $q_{i+1} = q_i - hv_i$
4: $M(q_i)(v_{i+1} - v_i) = h(f(q_i, v_i) + G(q_i)^T\Lambda)$ ▷ Solve lines 6 and 7 simultaneously
5: $0 \le \Lambda \perp G_{J^1(q_{i+1})}(q_i)(v_{i+1} + \epsilon v_i) \ge 0$
6: $t = t + h,\ i = i + 1$
7: **end while**
8: **return** q, v
9: **end procedure**

Algorithm 2 Forecasting trapezoidal rule [4]

Require: time interval $[t_0, T]$, initial values $q_0 = q(0), v_0 = v(0), i = 0$, step size $h = T/N$
1: **procedure** TrapezoidalRule(T, N, q_0, v_0, δ_1)
2: **while** $t_{i+1} < T$ **do**
3: $M(q_i)(v_{i,1} - v_i) = h(f(q_i, v_i) + G^T(q_i)\lambda_i)$
4: $0 \le \lambda_i \perp g(q_i) \ge 0$
5: $q_{i+1} = q_i + h(v_i + v_{i,1})/2$
6: $M(q_{i+1})(v_{i+1} - v_{i,1}) = h\left((f(q_i, v_i) + G^T(q_i)\lambda_i) + (f(q_{i+1}, v_{i,1}) + G^T(q_{i+1})\lambda_{i_1})\right)/2 + G^T(q_i)\Lambda_i$
7: $0 \le \lambda_{i_1} \perp g(q_{i+1}) \ge 0$
8: $0 \le \Lambda_i \perp G(q_i)(v_{i+1} + \epsilon v_{i,1}) \ge 0$
9: $t_{i+1} = t_i + h,\ i = i + 1$
10: **end while**
11: **return** q, v
12: **end procedure**

Because the classical timestepping scheme in Algorithm 1 has only order of convergence one, in literature a lot of numerical possibilities are studied to increase the accuracy or order. Different strategies are extrapolation or step-size adaptation or retrospective bisections [1, 5]. They often deal with instabilities and

an inconsistent treatment of the non-smooth phases and are not satisfactory understood and analysed. Based on this uncertain understanding of higher-order methods, in [4] a whole set of methods for the consistent numerical treatment of (1)-(4) and their accuracy enhancement is developed based on discontinuous Galerkin methods. These methods are special mortar methods which use discontinuous ansatz and test functions in any situation not just if the situation demands it. One method of this algorithm family is the forecasting trapezoidal rule in Algorithm 2. In smooth phases it uses the trapezoidal rule of integration order two and distinguish between contact and impact forces.

3 Orbital Convergence and Test Implementations

Let (q, v) be the solution of (1)-(4) and $(q_i^h), (v_i^h) \in \mathbb{R}^n$ numerical approximations in $t_0, t_1, t_2, \ldots, t_N \subset I$ with constant step size $h > 0$. The global discretisation errors of a numerical scheme in t_k are defined as $e_k^q := q(t_k) - q_k^h, e_k^v := v(t_k) - v_k^h$. Let $e^q = (e_0^q, \ldots, e_N^q)^\top, e^v = (e_0^v, \ldots, e_N^v)^\top$ and $\|.\|_{N+1}$ be a norm depending on the dimension $N+1$ of e. A numerical scheme is called convergent of order p if $\|e\|_{N+1} \in \mathcal{O}(h^p)$. The approximation accuracy increases if p increases. Here, the L^1-norm is used

$$\|e\|_{N+1,1} := \frac{1}{N+1} \sum_{k=0}^{N} \|e_k\|_2 \,.$$

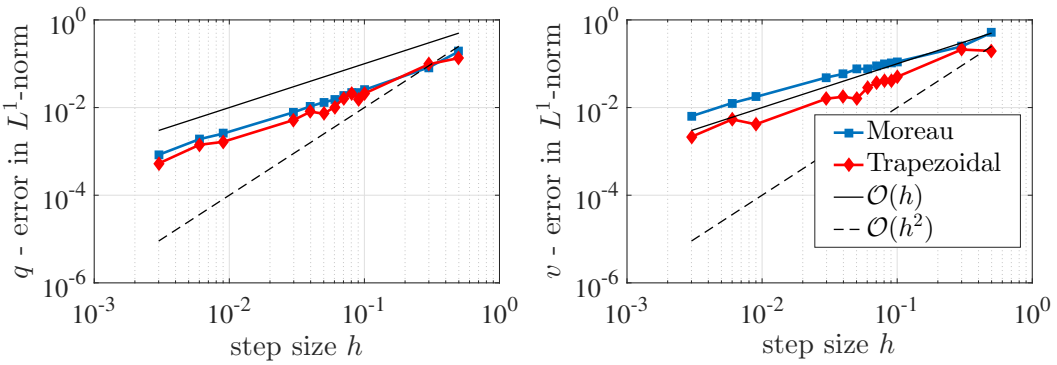

Figure 3. Classical convergence order for the impact oscillator.

In Figure 3, convergence order one for Algorithm 1 and 2 can be observed for the impact oscillator. It makes no difference that Algorithm 2 uses a higher ordered method between impacts and a consistent treatment of non-smooth forces. An increased computational effort for a better approximation of the solution in the smooth phases is *not reflected* in the order of convergence at all. If one does not identify the critical points in a certain accuracy like it would be typically for event-driven schemes, it may happen that they are *not noticed in the right time step*. Figure 4 highlights visually the described phenomenon. If there is a jump in the solution and it is noticed regardless of the step size first in the next time step, the error remains almost constant. In such a point , the error is about as large as the jump. It may even happen that a jump is registered at the correct interval with step size h and with $h/2$ not.

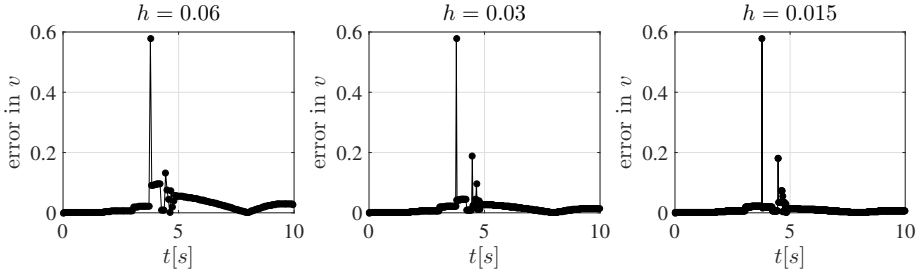

Figure 4. Absolute error in v: Impact oscillator.

In order to be able to compare different numerical methods, one needs *another tool* to judge their approximation quality. There are applications with a higher relevance of a good numerical approximation

of the *whole solution set* than of the approximation in *certain time points*. Noteworthy are invariant limit cycles such as equilibrium points or periodic solutions. Therefore, the approximation quality of the whole solution set, so-called orbits is now considered. It is important to mention, however, that the concept is only plausible for applications with *invariant limit cycles*. Let $x(t) = (q(t), v(t))$ be the solution of (1)-(4) with initial value $x(t_0) = x_0$. Then we call the set $\Gamma(x_0, I) = \{x(t), t \in I\}$ *orbit* in x_0 of I. The discrete set $\Gamma^h(I) = \left\{x_i^h = (q_i^h, v_i^h), i = 0, 1, \ldots, N\right\}$ is called *numerical orbit* of I. A numerical scheme has *orbital convergence order* p if $\rho\left(\gamma^h(I), \gamma(x_0, I)\right) \in \mathcal{O}(h^p)$ where

$$\rho(A, B) := \sup_{a \in A} \inf_{b \in B} \|a - b\|, A \subset \mathbb{R}^m, B \in \mathbb{R}^n$$

is the one-sided Hausdorff-distance. In Figure 5, the orbit of the impact oscillator is plotted in black. For both Algorithms 1 and 2, the numerical orbits for four different step sizes is added pointwise. They approximate well the exact orbit; the ones belonging to Algorithm 2 better. Next, the numerical orbits representing different step sizes are compared with the continuous one using the one-sided Hausdorff distance. Figure 6 shows that we can observe orbital convergence order one for the Moreau-Jean scheme and order two for the trapezoidal rule like we expect it.

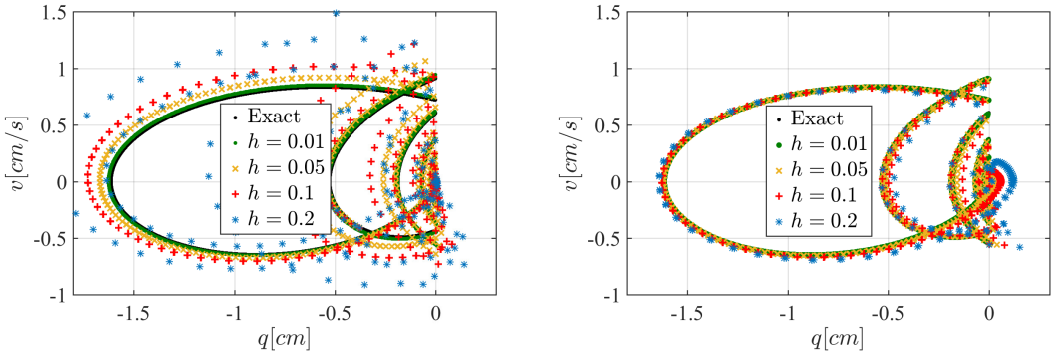

(a) Moreau-Jean scheme (b) Trapezoidal rule

Figure 5. Impact oscillator orbits.

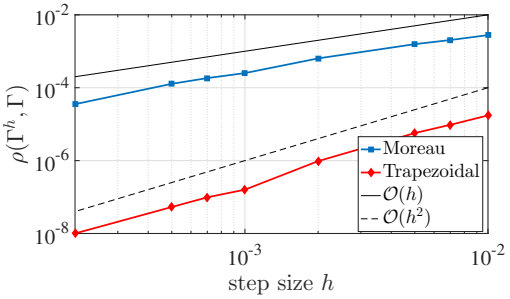

Figure 6. Orbital convergence: Impact oscillator

References

[1] V. Acary. Higher order event capturing time-stepping schemes for nonsmooth multibody systems with unilateral constraints and impacts. *Applied Numerical Mathematics* 62.10 (2012), pp. 1259–1275.

[2] C. Budd, F. Dux, and A. Cliffe. The effect of frequency and clearance variations on single-degree-of-freedom impact oscillators. *Journal of sound and vibration* 184(3) (1995), pp. 475–502.

[3] M. Jean and J.J. Moreau. Dynamics in the presence of unilateral contacts and dry friction: a numerical approach. In: *Unilateral Problems in Structural Analysis 2*. Springer, 1987, pp. 151–196.

[4] T. Schindler and V. Acary. Timestepping schemes for nonsmooth dynamics based on discontinuous Galerkin methods: definition and outlook. *Mathematics and Computers in Simulation* 95 (2014), pp. 180–199.

[5] C.W. Studer. "Augmented time-stepping integration of non-smooth dynamical systems". PhD thesis. ETH Zurich, 2008.

**Proceedings of the 8th GACM Colloquium on Computational Mechanics
for Young Scientists from Academia and Industry
August 28–30, 2019 in Kassel, Germany**

Investigation of the fractal properties of aerogels by diffusion-limited aggregation models

Rasul Abdusalamov * [1], Mikhail Itskov[1], Barbara Milow[2], Gudrun Reichenauer[3] and Ameya Rege † [2]

[1]Department of Continuum Mechanics, RWTH Aachen University, Aachen, Germany

[2]Institute of Materials Research, German Aerospace Center, Cologne, Germany

[3]Division Energy Efficiency, Bavarian Center for Applied Energy Research, Würzburg, Germany

Abstract. Aerogels are highly porous materials characterized by low thermal conductivities and sound velocities. Most aerogels exhibit fractal morphology which strongly influences their mechanical properties. Diffusion-limited aggregation (DLA) and diffusion-limited cluster aggregation (DLCA) models [7] best describe the properties of silica aerogels [3, 6]. In our work, these models are implemented to characterize the fractal features and mechanical properties of silica aerogels. To this end, the model results are first validated by comparison with the fractal exponents derived from experimental small angle X-ray scattering (SAXS) data. Furthermore, the application of such aggregation models to describe the mechanical properties of these aerogels is studied by importing the generated structure into a finite element analysis (FEA) tool.

Introduction

Silica aerogels belong to a class of highly open porous materials, those that are synthesized by the sol-gel process. This process involves the assembly of smaller particles leading to the formation of clusters and aggregates eventually forming a (percolating) backbone. Several studies in the literature have focused on the thermal properties of silica aerogels given their super-insulating features. Due to their application spectrum, there has also been a rise in investigations on their structural features and mechanical properties. Modeling and simulations have proven to be a very useful tool in understanding these properties in many colloidal-like materials including silica aerogels. In this context, molecular dynamics simulations [8] and coarse-grained modeling [2, 6] have been well exploited tools.

In this paper, an aggregation-based model approach is presented. Hasmy et al. [3, 4] investigated various aggregation-based algorithms and concluded that diffusion-limited aggregation-based models best describe silica aerogel microstructures. Since then, several studies have implemented such aggregation-based models to describe the structural features of silica aerogels. In this work, highly porous structures were formed, which were subsequently compared to experimental data from small angle X-ray scattering (SAXS) measurements. As a result of the measurement, the mass fractal behavior is determined. Furthermore, a representative volume element (RVE) was generated using the modeled structures to perform a finite element (FE) simulation. Periodic boundary conditions (PBCs) were applied to the RVE. The aim of the FE simulation was to investigate the bulk mechanical properties of the structures created by means of the aggregation algorithm and compare them to experimental values of silica aerogels at given porosity.

1 Generation of models using DLA and DLCA

DLA models were initially introduced in the 1980s by Witten and Sander [10]. In this case, the Brownian motion of particles in the form of random walks is modeled on a regular cubic lattice. A total of N_{W} particles, often referred to as walkers, are initialized with an arbitrary position within this domain. These particles then move in all directions according to the random walk process. In addition to the walkers,

*Corresponding author: abdusalamov@km.rwth-aachen.de ORCID iD: 0000-0003-4988-4794
†Corresponding author: ameya.rege@dlr.de ORCID iD: 0000-0001-9564-5482

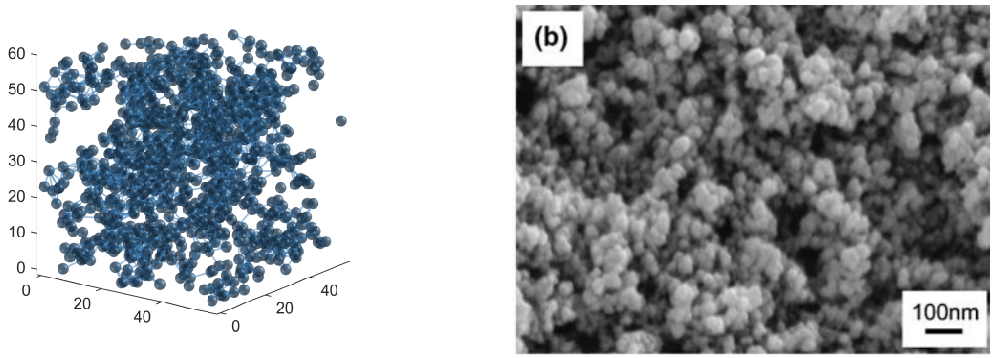

Figure 1. (a) Model silica aerogel aggregates generated by DLCA, (b) scanning electron microscopy image of silica aerogel showing the aggregated morphology mimicked by DLCA (Reprinted by permission from Springer Nature Customer Service Centre GmbH: [5], ©Springer Science+Business Media, LLC 2008).

N_S seeds are initialized. These are also located at random positions in the cube. If a walker is located within a critical radius from the seed, it will be diffused to it. Progressively, a tree of seeds similar to a cluster-like structure emerges. The DLA model is extended if the seeds move in addition to the walkers. The so extended model is known as diffusion-limited cluster-cluster aggregation model (DLCA). Furthermore, the different trees of the seeds can be linked to each other. Therefore, they also must be within a critical radius. For the seeds as well as for the walkers, the width of the jumps can be specified for the random walk in addition to this critical radius. In this work, the particles move on lattice points, although this is also possible continuously. In addition, rotations of the clusters can also be implemented, but are not considered in this work. According to Botet and Jullien [1], this does not affect the fractal properties of the resulting clusters. In our case, a periodic structure is required, therefore the seeds as well as the walkers are allowed to move beyond the cube borders and enter on the opposite side. The code for the DLCA models was implemented in MATLAB. Such a generated structure can be compared with scanning electron microscopy (SEM) images showing real aerogel microstructures (see Figure 1).

2 Correlation of clusters to experimental SAXS measurements

In order to validate the correlation of the models to the experimental results, the mass fractal behavior of the models must be determined. Accordingly, the structure generation is first briefly summarized. If a cubic box with the side length L is considered and N_W walkers are located in this region, the dimensionless concentration or the volume fraction c can be determined. Assuming that the particles have a spherical shape, c can be expressed by:

$$c = \frac{V_{\text{particles}}}{L^3} \quad \text{with} \quad V_{\text{particles}} = N_W \cdot \frac{4\pi}{3} R^3 \ . \tag{1}$$

The edge length of the cube was $L = 57\,\text{nm}$ and in total 1137 seeds were created. For the spherical particles, a diameter ($2R = 3\,\text{nm}$) was chosen based on the experimentally evaluated silica aerogel particle size. The evaluated $c = 0.0868$, where the porosity $\phi = (1 - c)$, which corresponds to 91.32%.

Figure 2a shows the experimental small angle scattering curve for a silica aerogel with a porosity of about 92%. The above calculated ϕ is then in good correlation to the porosity of the silica aerogel as determined from experiments. In the double-log plot of scattered intensity vs. scattering vector, the curve is characterized by two regimes where the intensity is scaling with q: The q^{-d_f} dependence at low q-values indicates the scattering from clusters within the aerogel with a mass fractal dimension of d_f, which can directly be deduced from the slope in the double-log plot. At high q values, I scales with q^{-4} indicating scattering from the particles forming the aggregates. The point where the two slopes are intersecting can be converted in the characteristic particle size d [9].

To determine the mass fractal dimensions, the change of density as a function of distance r from a reference point inside the aggregate was used. Accordingly, the mass m is expressed as

$$m \propto r^{d_f}. \tag{2}$$

where $0 < d_f < 3$ is the fractal dimension of the aggregate.

The correlation of m versus r is presented in Figure 2b with $d_f = 2.42$ is obtained. This is in agreement with the experimental SAXS data, where the fractal dimension of $d_f = 2.32 \pm 0.05$ was obtained.

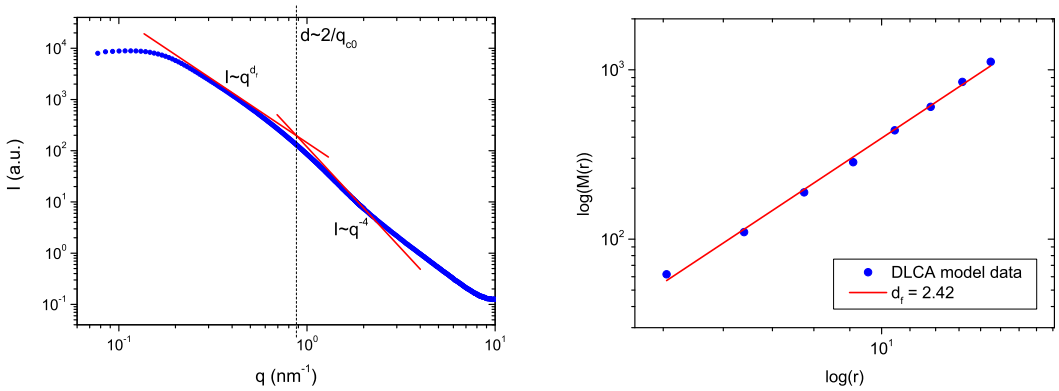

Figure 2. (a) Log-log plot of scattered intensity versus scattering vector as measured by SAXS, (b) visualization of the mass $m(r)$ contained in concentric spheres with radius r plotted over r. The exponent of the generated fit is the fractal dimension d_f. In our case, $d_f = 2.42$.

3 Finite element simulation

For the FE simulations, the structures generated in MATLAB were exported to LS-DYNA in the form of nodes and elements. Here, the nodes represent the aerogel particle centers while the bonds between the particles are modeled as beam elements with a circular cross-section. Beam elements were chosen such that it accounts for the three modes of deformation that a bond undergoes: bending, torsion and tension/compression. In addition, a frictional contact between the elements is defined. Since the structure is completely periodic, the PBCs can be directly applied to the symmetry nodes. All nodes on the upper and lower borders as well as the right and left borders are linked together. Hereby, the translational and rotational degrees of freedom are coupled in the plane. With the help of dummy nodes, the desired strains can be controlled. The resulting deformations for a 2-d structure can be seen in Figure 3, where a compression of 10% is applied.

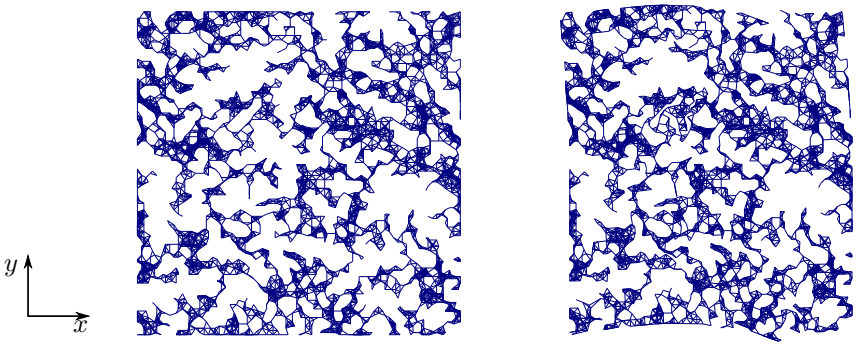

Figure 3. FE simulation of 10% compression applied to the generated 2-d aerogel structure (RVE).

4 Summary

In this paper, an aggregation-based model approach to characterize the fractal features and mechanical properties of silica aerogels is presented. The mass fractal behavior is in agreement with typical values derived from experimental small angle X-ray scattering data. For the study of their mechanical properties, a finite element simulation of a 2-d aerogel structure is performed. As an outlook, 3-d silica aerogel structures will be created and simulated to investigate their structural features and mechanical properties.

References

[1] R. Botet and R. Jullien. A theory of aggregating systems of particles : the clustering of clusters process. *Annales de Physique* 13.3 (1988), pp. 153–221.

[2] L. D Gelb. Simulating silica aerogels with a coarse-grained flexible model and langevin dynamics. *The Journal of Physical Chemistry C* 111.43 (2007), pp. 15792–15802.

[3] A. Hasmy and E. Anglaret. Small-angle neutron-scattering investigation of long-range correlations in silica aerogels: Simulations and experiments. *Physical Review B* 50.9 (1994).

[4] A. Hasmy, M. Foret, J. Pelous, and R. Jullien. Small-angle neutron-scattering investigation of short-range correlations in fractal aerogels: Simulations and experiments. *Physical Review B* 48.13 (1993), p. 9345.

[5] C. E. Kim, J. S. Yoon, and H. J. Hwang. Synthesis of nanoporous silica aerogel by ambient pressure drying. *Journal of Sol-Gel Science and Technology* 49.1 (2008), p. 47.

[6] H-S. Ma, A. P. Roberts, J-H. Prévost, R. Jullien, and G. W. Scherer. Mechanical structure–property relationship of aerogels. *Journal of Non-Crystalline Solids* 277.2-3 (2000), pp. 127–141.

[7] P. Meakin. Formation of fractal clusters and networks by irreversible diffusion-limited aggregation. *Physical Review Letters* 51.13 (1983), pp. 1119–1122.

[8] S. P. Patil, A. Rege, Sagardas, M. Itskov, and B. Markert. Mechanics of Nanostructured Porous Silica Aerogel Resulting from Molecular Dynamics Simulations. *The Journal of Physical Chemistry B* 121.22 (2017), pp. 5660–5668.

[9] G. Reichenauer. Structural Characterization of Aerogels. In: *Aerogels Handbook Advances in Sol-Gel Derived Materials and Technologies*. Ed. by M. A. Aegerter, N. Leventis, and M. M. Koebel. Springer Science & Business Media, Mar. 2011, pp. 449–498. ISBN: 978-1-4419-7477-8. DOI: 10.1007/978-1-4419-7589-8_21.

[10] T. A. Witten and L. M. Sander. Diffusion-limited aggregation. *Chemistry Letters* 27.9 (1983), pp. 1211–1214.

**Proceedings of the 8th GACM Colloquium on Computational Mechanics
for Young Scientists from Academia and Industry
August 28–30, 2019 in Kassel, Germany**

Simulation of Dual-Phase Steel Microstructures Using Optimized Arrangements of Finite Cells

Yannick F. Fangye, Niklas Miska and Daniel Balzani *

Ruhr-Universität Bochum, Lehrstuhl für Kontinuumsmechanik, Universitätstraße 150, 44801 Bochum, Germany

Abstract. In this contribution, the finite cell method is applied for the simulation of the microstructure of dual-phase steel. As the geometry is typically given as voxel data, an alternative approach for the subcell decomposition is presented, which exploits such data structures. The efficiency and accuracy of this new approach is compared to the classical octree decompostion in two examples.

Introduction

The microstructure of dual-phase (DP) steel consists of a ferrite matrix with martensite inclusions. For numerical simulations, this microstructure must be efficiently discretized. To this end, in [1, 2] statistically similar RVEs (SSRVEs) were constructed, which have a lower complexity compared to the real microstructure but still exhibit a similar mechanical behavior. The finite cell method (FCM) [3, 6] facilitates the use of a regular finite element mesh and includes the microscopic material decomposition in terms of subcells for integration purposes only. This approach is especially favorable for microstructures given as voxel-based data, since the voxels can directly be considered to construct the integration mesh.

1 An optimal subcell decomposition for voxel-based geometry data

The FCM transfers the geometry representation from the finite element mesh to the integration level. It is based on the use of a regular FE grid mesh with a decomposed integration, for which elements with more than one material phases are subdivided into subcells. Each subcell consist then of a single phase. Then, the integration of an element is given as

$$\boldsymbol{k}^{\mathrm{e}} = \sum_{c=1}^{n_c} \boldsymbol{k}^{\mathrm{c}} = \sum_{c=1}^{n_c} \int_{\mathcal{B}_{\mathrm{c}}} \boldsymbol{B}^{\mathrm{T}}(\boldsymbol{\xi}(\boldsymbol{r}))\mathbb{C}_{\mathrm{c}}\boldsymbol{B}(\boldsymbol{\xi}(\boldsymbol{r}))\det \boldsymbol{J}_e \det \boldsymbol{J}_c \, dV, \tag{1}$$

where $\boldsymbol{k}^{\mathrm{c}}$ denotes the stiffness matrix contribution of a single subcell and n_c the number of subcells in the element. The jacobian matrices $\boldsymbol{J}_e$ and $\boldsymbol{J}_c$ are respectively related to the mapping functions between the local element ($\boldsymbol{\xi}$) and the global coordinate system as well as the subcell ($\boldsymbol{r}$) and the element coordinate system.

In [3], a classic octree algorithm is used to construct the subcells, where the domain of interest is recursively subdivided into eight equal regions. Thereby the phase fraction of the different materials varies depending on the subdivision level. For voxel-based data, we propose to construct subcells that exactly capture the material boundaries to overcome this issue (see also [5]). For this purpose a loop over all spatial directions is carried out, wherein the voxels with the same material are successively merged in order to build the largest possible subcells. To this end, all possible variations of orders of directions are evaluated and the one with the least number of subcells is considered. In Fig. 1a an example of a simple voxel-based geometry is shown, which is discretized using four finite elements. The resulting subcells for both decomposition approaches, the octree split and the proposed algorithm, are depicted in Fig. 1b and Fig. 1c respectively. For the octree decomposition, a relatively high subdivision level and therefore a high

*Corresponding author: daniel.balzani@rub.de

number of subcells is required to exactly capture the material boundaries. This may induce considerable assembling effort. In contrast to that, the proposed approach constructs subcells that exactly coincide with the borders of the voxels with considerably less subcells. However, it is possible that very narrow subcells arise from this. Thus, the impact of these irregular subcells on the integration is investigated in the following section. For this purpose, we introduce the subcell irregularity, defined as the ratio of the longest to the smallest subcell edge, as characterizing measure.

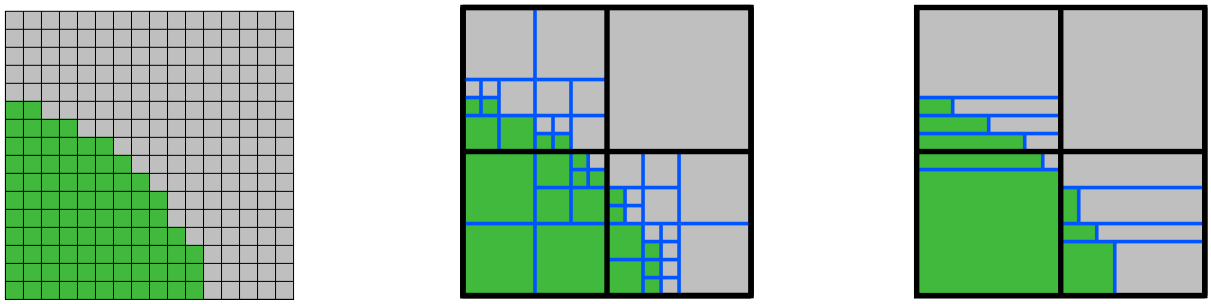

a) b) c)

Figure 1. Illustration of **a** the considered voxel-based geometry, **b** resulting subcells from the octree method and **c** resultings subcells from the proposed optimal decomposition.

2 Numericals examples

In the first example the proposed subcell decomposition approach is compared with the octree method in the context of the FCM. We consider a uniaxial tension test of a cube which is discretized with only one 27-noded hexahedral finite element. The cube consists of 24 voxels in each spatial direction, in which a martensite phase, described by an 11×11×11 voxel sized subcube, is positioned. The remaining voxels belong to the ferrite phase. For the individual phases a finite J_2 plasticity model (with isotropic hardening) following [4] is used. The corresponding integration meshes are shown in Fig. 2a for the octree method of level six with 5923 subcells and Fig. 2b for the proposed approach with only four subcells. The results of the simulations for both approaches are depicted in Fig. 2c and Fig. 2d. It is observed

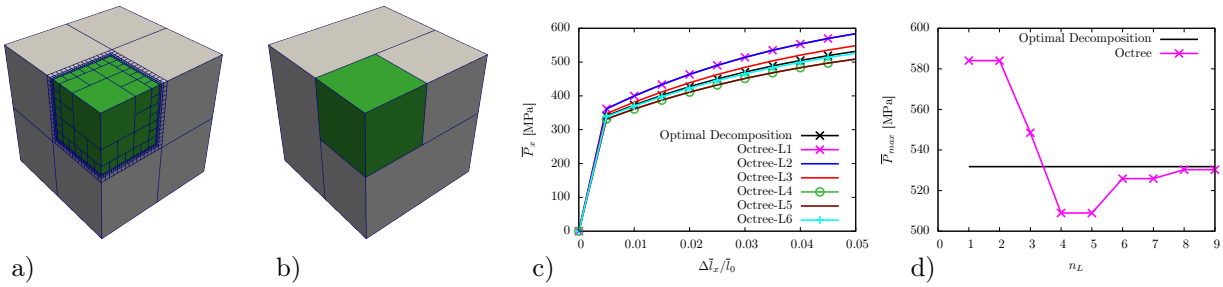

a) b) c) d)

Figure 2. **a** Subcells for the octree of level six (5923), **b** subcells for the optimal decomposition approach, **c** homogenized first Piola–Kirchhof stresses vs. relative elongation and **d** maximal macroscopic stress vs. subdivision level for the octree method.

that the choice of the appropriate octree level is not straightforward although the results of the octree split tend to the one of the optimal decomposition approach with increasing number of subcells.

For the next example, a more complicated microstructure is used, namely the SSVRE from [2]. Based on a geometry representation with a resolution of 60×60×60 voxels, a mesh of 12×12×12 hexahedral finite elements with cubic shape functions is considered. In addition to the previously introduced integration methods, some variations of them are examined. In order to reduce the number of subcells arising from the octree (T) decomposition within an element, the resulting subcells are, if possible, subsequently merged (octree-merged (T-M) approach). As mentioned in Sec. 1, the optimal decomposition (OD) may generate very narrow subcells. To avoid this, the octree-optimal decomposition (T-OD) method is introduced, where the OD is performed within the finest octree level. The T-OD-M approach is similar to the T-OD method and tries to merge all subcells arising from the T-OD split within an element. Fig. 3a shows the subcells for the optimal decomposition approach. In Fig. 3b it is shown that the macroscopic

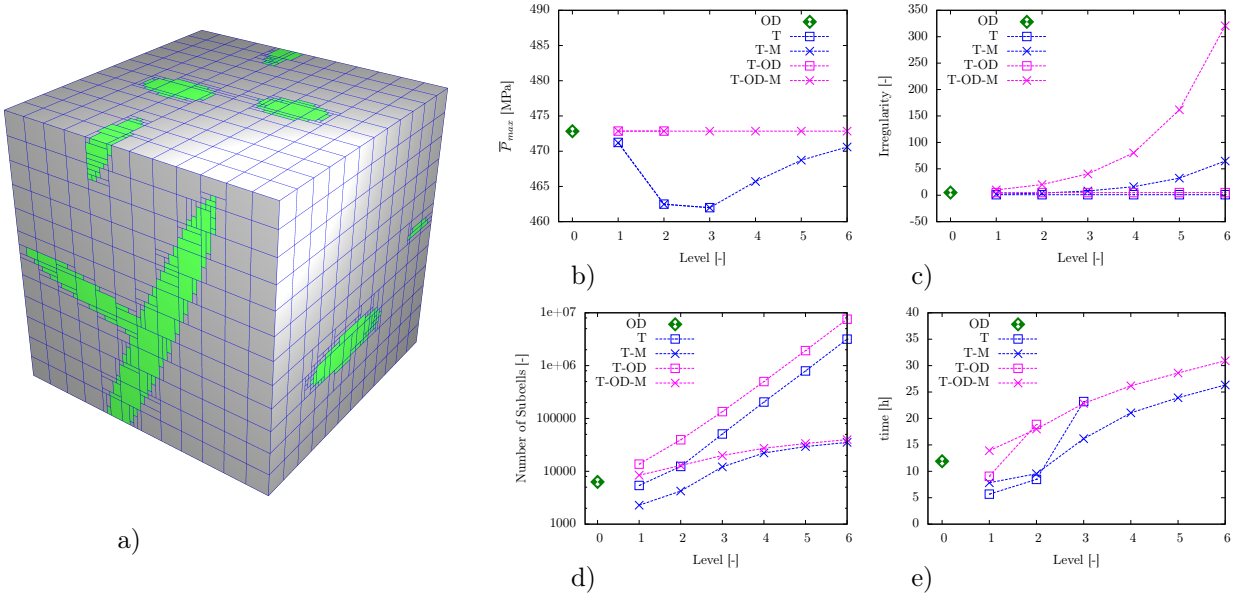

Figure 3. **a** Subcells for the optimal decomposition approach, **b** maximal macroscopic stress, **c** irregularity, **d** number of subcells and **e** computing time.

material responses of methods T and T-M are similar, since they have the same material boundaries and only differ in the number of subcells and therefore consequently in the computing time as it can be seen in Fig. 3d and Fig. 3e. Between T-OD and T-OD-M a similar behavior to T and T-M can be observed. While the stress for T and T-M is changing depending on the subdivision level of the subcell and tend with increasing subdivision level to the value of OD, the one of T-OD and T-OD-M remains constant and has the same value as that for OD. The main advantage of the (-M) approaches is a reduction in the number of subcells as compared to the preceding approaches. However, also an increase of the irregularity of the subcells can be observed for the (-M) methods with increasing subdivision level, as depicted in Fig. 3c. In summary, the optimal decomposition method provides the best compromise in terms of accuracy, computing time and irregularity.

Acknowledgments

The authors greatly appreciate financial funding by the German Science Foundation (Deutsche Forschungsgemeinschaft, DFG) as part of the priority program 1648, project BA2823/11-2.

References

[1] D. Balzani, L. Scheunemann, and D. Brands. Construction of two- and three-dimensional statistically similar RVEs for coupled micro-macro simulations. *Computational Mechanics* 54 (2014), pp. 1269–1284.

[2] D. Brands, D. Balzani, L. Scheunemann, J. Schröder, H. Richter, and D. Raabe. Computational modeling of dual-phase steels based on representative three-dimensional microstructures obtained from EBSD data. *Archive of Applied Mechanics* 86 (2016), pp. 575–598.

[3] A. Düster, J. Parvizian, Z. Yang, and E. Rank. The finite cell method for three-dimensional problems of solid mechanics. *Computer Methods in Applied Mechanics and Engineering* 197 (2008), pp. 3768–3782.

[4] S Klinkel. "Theorie und Numerik eines Volumen-Schalen-Elementes bei finiten elastischen und plastischen Verzerrungen". PhD thesis. Universitat Fridericiana zu Karlsruhe, 2000.

[5] N. Miska and D. Balzani. Quantification of uncertain macroscopic material properties resulting from variations of microstructure morphology based on statistically similar volume elements: application to dual-phase steel microstructures. *Computational Mechanics* (2019).

[6] D. Schillinger and M. Ruess. The Finite Cell Method: A Review in the Context of Higher-Order Structural Analysis of CAD and Image-Based Geometric Models. *Archive of Computational Methods in Engineering* 22 (2015), pp. 391–455.

**Proceedings of the 8th GACM Colloquium on Computational Mechanics
for Young Scientists from Academia and Industry
August 28–30, 2019 in Kassel, Germany**

Modeling interpenetrating metal matrix composites using a fast Fourier transform formulation

Dominik Horny * [1] and Katrin Schulz[1]

[1]Institute for Applied Materials - Computational Materials Science (IAM-CMS), Karlsruhe Institute of Technology, Kaiserstr.12, 76131 Karlsruhe, Germany

Abstract. Just recently, a novel interpenetrating composite has been experimentally generated based on highly porous ceramic foam preform. The heterogeneous microstructure of this interpenetrating Metal matrix composite (MMC) is modeled in order to investigate the deformation behavior and basic failure mechanisms. We use a fast Fourier transform (FFT) formulation to simulate high resolution grids of the delicate microstructre with reasonable computational effort. Subjected to external loading, we investigate the mechanical behavior of the material and the interactions on the microscale. Homogenized properties are derived from the simulations and compared to experimental investigations of the material.

Introduction

Metal matrix composites with an interpenetrating microstructure made from Al_2O_3 ceramic foam infiltrated with AlSi12 cast alloy have been investigated. This class of materials is very promising since it perfectly combines both good mechanical and thermal properties and has a notable lightweight potential as well. Therefore, it can be used in the mobile sector e.g. to increase the efficiency of combustion engines, thus reduce CO_2-emissions [4]. The Simulation with a high resolution grid and a reasonable computing time requires more efficient methods than the commonly used finite Element method (FEM) due to the complex and highly heterogeneous microstructure [8]. Here, the fast Fourier transform (FFT) method provides an efficient tool to analyze the complex materials interaction [3]. We present a formulation based on the spectral spectral solver framework of DAMASK (Düsseldorf Advanced Material Simulation Kit) [5] to perform the FFT-based microstructure simulations and discuss the results with respect to the homogeneous representation by an representative volume element (RVE) approach.

1 Fast Fourier transform based modeling

In order to describe the change of material point positions $\mathbf{x}$ in the reference configuration to $\mathbf{y}$ in a deformed configuration due to external load, a deformation map $\boldsymbol{\chi}(\mathbf{x})$ is introduced. This deformation map can be expressed as the sum of a homogeneous deformation gradient $\overline{\mathbf{F}}$ and a superimposed deformation fluctuation field $\tilde{\mathbf{w}}$ with $\boldsymbol{\chi}(\mathbf{x}) = \overline{\mathbf{F}}\mathbf{x} + \tilde{\mathbf{w}}$ where the periodicity condition is constrained by $\tilde{\mathbf{w}}^- = \tilde{\mathbf{w}}^+$ on corresponding surfaces. Since the total deformation gradient is given by $\mathbf{F} = \mathrm{Grad}\boldsymbol{\chi}$ it can also be decomposed into homogeneous $\overline{\mathbf{F}}$ and fluctuating part $\tilde{\mathbf{F}}$ reading $\mathbf{F} = \overline{\mathbf{F}} + \tilde{\mathbf{F}}$.
The material response to external load is given by an energy density functional $\mathcal{W}$: $\mathbf{P}(\mathbf{x}) = \delta\mathcal{W}/\delta\mathbf{F}(\mathbf{x})$. The direct variational formulation of the static equilibrium is obtained by minimizing $\mathcal{W}$ over all deformation fields and can be expressed in real and Fourier space as $\min_{\boldsymbol{\chi}} \mathcal{W} = \mathrm{Div}\,\mathbf{P}(\mathbf{x}) = \mathcal{F}^{-1}[\mathbf{P}(\mathbf{k})i\mathbf{k}] = \mathbf{0}$, with the frequency vector in Fourier space $\mathbf{k}$ and the Fourier transform operator $\mathcal{F}$. It is equivalent to finding the root of the residual body force field $\mathcal{R}[\boldsymbol{\chi}(\mathbf{k})] = \mathbf{P}(\mathbf{k})i\mathbf{k} = \mathbf{0}$ with the preconditioning operator $\mathcal{R}$. Since this is an ill-conditioned PDE, a reference problem with a homogeneous linear reference material is introduced. The well-conditioned PDE then reads

$$\mathcal{R}_{\mathrm{direct}}[\mathbf{F}(\mathbf{k})] := \Gamma(\mathbf{k})\mathbf{P}(\mathbf{k}) = \mathbf{0} \tag{1}$$

*Corresponding author: dominik.horny@kit.edu

with the Gamma operator Γ. More detailed explanation can be found in [3]. Discretizing the direct variational formulation of the static equilibrium with a collocation-based approach at the grid points leads to the so called "basic"-scheme:

$$\mathcal{R}_{\text{basic}}[\mathbf{F}(\mathbf{x})] := \mathcal{F}^{-1}\left[\begin{cases}\Gamma(\mathbf{k})\mathbf{P}(\mathbf{k}) & \text{if } \mathbf{k} \neq \mathbf{0} \\ \Delta\mathbf{F}_{BC} & \text{if } \mathbf{k} = \mathbf{0}\end{cases}\right]. \tag{2}$$

The equation system (2) can be solved iteratively by e.g. non-linear GMRES solver or other non-linear numerical solvers provided by PETSc library. The convergence criterion for the solution is defined by the root mean square (RMS) of the divergence of stress introducing the equilibrium tolerance ε_{eq} and the unit of length m:

$$\varepsilon_{\text{eq}} \times \text{m} \geq \frac{\text{RMS}(\text{Div}\mathbf{P}(\mathbf{x}))}{\|\overline{\mathbf{P}}\|_2}. \tag{3}$$

For a more detailed explanation see references [3, 5, 6].

2 Effective elastic properties

We investigate a binarized micro computer tomography (μ-CT) reconstruction of an Al_2O_3 foam specimen with an edge length of around 1.9 mm (see Fig.1). The determined microstructural characteristics of the foam are given in Tab.1.

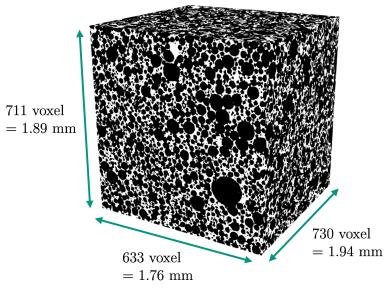

Figure 1. μ-CT scan of the Al_2O_3 foam. white = ceramic, black = pore

Table 1. Microstructural characteristics

voxel size =	2.66^3	μm^3
porosity =	69.6	%
mean pore radius =	14.39	μm
median pore radius =	10.01	μm

We choose different sizes of representative volume elements (RVEs) with edge lengths from 10-100 voxel at 15 randomly chosen point inside the specimen to investigate the mechanical properties of the foam and the MMC. The raw materials properties as well as properties of the ceramic foam and the MMC were determined experimentally and are listed in Tab.2.

Table 2. Experimentally determined material properties

Material	E [GPa]	μ
Al_2O_3	350	0.23
AlSi12	77.8	0.32
foam	31	0.29
MMC	127	0.27

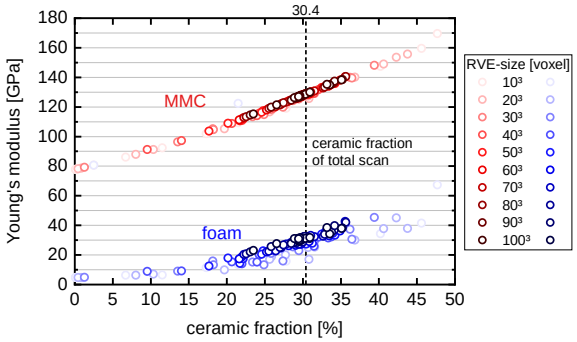

Figure 2. Simulation Results of RVE study on Effective Young's modulus.

For each RVE, six independent load cases (pressure in x-, y- and z-direction as well as shear in xy-, xz- and yz-direction) were applied to determine the stiffness tensor $\mathbb{C}$ of the foam/MMC. Then, the Effective Properties of $\mathbb{C}$ have been derived as described in [7]. The results of a comparison of the effective Young's modulus dependent on the ceramic volume fraction measured for the RVEs, respectively, is shown in Fig.2.

3 Damage behavior

Stress distributions resulting from the elastic simulations of the MMC exemplify that stress peaks occur especially in very thin ceramic rods. It is reasonable to assume that damage will first occur at these points of stress concentration. Therefore, we analyze the damage behavior for a simplified benchmark structure of a single ceramic rod embedded into an aluminum matrix, see Fig3.

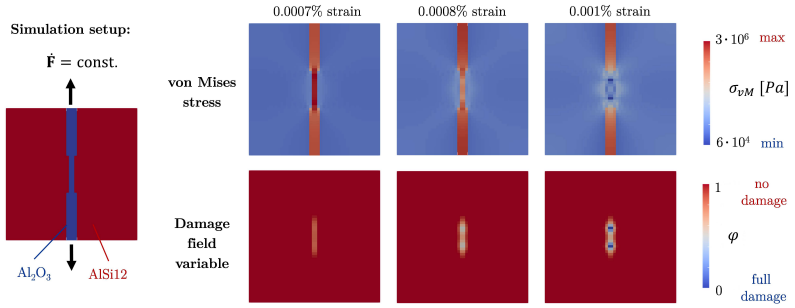

Figure 3. Phase field damage evolution of an Al_2O_3 rod embedded in AlSi12 under tensile load.

The damage and its evolution is prescribed by a phase field damage model introducing the scalar non-local phase field damage variable φ varying between $\varphi = 1$ (undamaged) and $\varphi = 0$ (fully damaged). The damage evolution is formulated by the classical Ginzburg-Landau equation [1] as a relaxation of the overall free energy:

$$\dot{\varphi} = -\mathrm{M}\left[2\varphi\mathbf{SE} - \frac{\mathcal{G}}{\mathrm{l}_0} - \nabla\mathcal{G}\mathrm{l}_0\nabla\varphi\right] \tag{4}$$

Here M is the damage mobility, $\mathbf{S}$ the 2$^{\text{nd}}$ Piola Kirchhoff stress, $\mathbf{E}$ the Green-Lagrange strain, $\mathcal{G}$ the fracture surface energy and l_0 the characteristic length. A brittle damage is used which is driven by the release of stored elastic energy $\psi_{\text{el}} = \frac{1}{2}\,\varphi^2\mathbf{S}\cdot\mathbf{E}$ which has to overcome the surface tension resistance $\psi_{\text{surf}} = \frac{1}{2}\,\mathcal{G}\mathrm{l}_0|\nabla\varphi|^2 + \frac{\mathcal{G}}{\mathrm{l}_0}(1-\varphi)$ as described in detail in [2] and [5].

4 Discussion

Comparing the effective elastic properties given in Fig.2 and Tab.2 shows very good agreement of the simulation results and the experimental values. Evaluating the FFT modeling techniques for the highly heterogeneous MMC microstructures obtained by μ-CT scans, we derive reasonable elastic material properties and a robust as well as efficient computational method. Furthermore, the dominating role of the ceramic fraction on the effective properties and the minor influence of the RVE-size itself could be shown during the analysis. In conclusion a small RVE with the same ceramic fraction as the entire material is sufficient to extract effective elastic Properties of the MMC. However, this holds true just to a limited extent for the ceramic foam structure.
Damage was modeled for a benchmark problem and the evolution from undamaged to fully damaged material has been shown as a first evaluation of a phase field approach coupled with the FFT formulation. In further steps, the knowledge gained from this test structure will be used to model damage in the significantly more complex interpenetrating microstructures.

Acknowledgments

The financial support for this work in the context of the DFG research project SCHU 3074/1 as well as the support by the European Social Fund and the State Baden-Württemberg is gratefully acknowledged.

References

[1] S. M. Allen and J. W. Cahn. A microscopic theory for antiphase boundary motion and its application to antiphase domain coarsening. *Acta Metallurgica* 27 (1979), pp. 1085–1095.

[2] M. Diehl, M. Wicke, F. Roters, P. Shanthraj, A. Brueckner-Foit, and D. Raabe. Coupled Crystal Plasticity–Phase Field Fracture Simulation Study on Damage Evolution Around a Void: Pore Shape Versus Crystallographic Orientation. *Jom* 69 (2017), pp. 872–878.

[3] P. Eisenlohr, M. Diehl, R. A. Lebensohn, and F. Roters. A spectral method solution to crystal elasto-viscoplasticity at finite strains. *International Journal of Plasticity* 46 (2013), pp. 37–53.

[4] Daniel B. Miracle. Metal matrix composites - From science to technological significance. *Composites Science and Technology* 65 (2005), pp. 2526–2540.

[5] F. Roters, M. Diehl, P. Shanthraj, P. Eisenlohr, C. Reuber, S. L. Wong, T. Maiti, A. Ebrahimi, T. Hochrainer, H. O. Fabritius, S. Nikolov, M. Friák, N. Fujita, N. Grilli, K. G. F. Janssens, N. Jia, P. J. J. Kok, D. Ma, F. Meier, E. Werner, M. Stricker, D. Weygand, and D. Raabe. DAMASK – The Düsseldorf Advanced Material Simulation Kit for modeling multi-physics crystal plasticity, thermal, and damage phenomena from the single crystal up to the component scale. *Computational Materials Science* 158 (2019), pp. 420–478.

[6] P. Shanthraj, M. Diehl, P. Eisenlohr, F. Roters, and D. Raabe. Spectral Solvers for Crystal Plasticity and Multi-physics Simulations. In: *Handbook of Mechanics of Materials*. Ed. by C. H. Hsueh and et.al. Singapore: Springer, 2019, pp. 1–25.

[7] C. Soyarslan, S. Bargmann, M. Pradas, and J. Weissmüller. 3D stochastic bicontinuous microstructures: Generation, topology and elasticity - Supplementary. *Acta Materialia* 149 (2018), pp. 326–340.

[8] J. Zeman, T. W. J. de Geus, J. Vondřejc, R. H. J. Peerlings, and M. G. D. Geers. A finite element perspective on nonlinear FFT-based micromechanical simulations. *International Journal for Numerical Methods in Engineering* 111 (2017), pp. 903–926.

**Proceedings of the 8th GACM Colloquium on Computational Mechanics
for Young Scientists from Academia and Industry
August 28–30, 2019 in Kassel, Germany**

Can the constituent stress-strain laws of composite materials be determined uniquely from integral measurements?

Fabian Sewerin *

Institute of Solid Mechanics, Technische Universität Braunschweig, Langer Kamp 8, 38106 Braunschweig

Abstract.

Naturally occurring composite materials can serve as a blueprint for engineering materials. However, the transfer of design principles is often complicated by the absence of detailed information on the material behaviour of the individual constituents. Conversely, progress in imaging and non-destructive measurement techniques has rendered the intra-sample arrangement of constituents accessible. In this contribution, we enquire whether it is possible to conclude on the stress-strain laws of constituent materials based on force-strain measurements on a composite sample whose geometrical structure is known. Since *a priori* intuition about the functional forms of these stress-strain laws can be difficult to acquire, a discretization in terms of global shape functions is explored. Starting from a candidate set of standard material tests, we propose the adoption of a criterion for local qualitative identifiability that is based on the sensitivity matrix of model predictions. Apart from an initial estimate, the analysis for local identifiability does not involve any experimental data and may hence be used in the design process for an experimental campaign. As an example, we analyze combinations of uni- and equibiaxial tension tests on a hyperelastic composite sheet for identifiability. The force-strain response of the sheet is almost completely controlled by the volume ratio of two constituents.

Introduction

Composite materials are made from several constituents that are arranged and interconnected in a particular way. In engineering applications, composites are commonly designed with the objective to unify the material properties of disparate constituents and create a hybrid that is more amenable to the intended deployment than the constituents alone. Conversely, natural composite materials such as skeletal muscle tissue or plant parenchyma can serve as a blueprint for artificially engineered composites. However, in many cases, our understanding of the material behaviour of the natural constituents is limited and experimental efforts to elucidate the mechanisms by which natural composites absorb and redistribute mechanical loads have been challenging. For example, the isolation of individual constituents without impairment can be extremely difficult if the geometrical arrangement of the constituents is intricate or covers several length scales. At the same time, Oskay and Fish [2] argue that the material behaviour of pure constituents in bulk may differ from the material behaviour a constituent exerts as part of a composite, for example, on account of interfacial effects [3]. On the other hand, the geometrical arrangement of constituents within a composite material can often be reconstructed with the aid of non-destructive measurement techniques. By consequence, we are led to ask whether the material behaviour of the constituents inside a composite sample can be inferred from standard material tests given records of the geometrical intra-sample arrangement. Assuming that the model description is exact and measurement errors are absent, this question falls into the realm of qualitative identifiability [4].

In practice, constitutive laws such as stress-strain relations are frequently determined by estimating a functional form and, subsequently, identifying the free parameters using a least-squares optimization based on experimental measurements and corresponding model predictions. However, in the absence of experimental measurements on the material response of isolated constituents, it may be difficult to gain or substantiate an *a priori* intuition about the functional forms of the stress-strain relations. In order to mitigate this lack of intuition, we explore the direct discretization of a stress-strain relation in terms of

*Corresponding author: f.sewerin@tu-braunschweig.de ORCID iD: 0000-0001-6588-7739

global shape functions here. Although this idea affords generality in the inference of unknown functions, it implicitly involves an assumption on the class of materials that dictates the physical nature of the unknown functions, for example, a strain energy density governing a hyperelastic constituent.

In view of practical deployment, we adopt a sensitivity-based criterion for local identifiability. It is argued that this criterion may be checked iteratively in the course of a Gauss-Newton scheme for estimating the coefficients of the representation in terms of global shape functions. The Gauss-Newton sequence requires an initial estimate for the coefficients and we provide evidence indicating that local identifiability is maintained throughout the scheme if it holds for the initial estimate. Based on a library of candidate material tests, those combinations which render the material model locally identifiable are determined. As an example, we consider a composite sheet made from a regular arrangement of two hyperelastic constituents. The material behaviour of the sheet is mainly influenced by the volume ratio of both constituents and, only to a negligible extent, by the particular intra-sample constituent distribution. Considering uniaxial and equibiaxial tension tests as candidate material tests, the local identifiability analysis indicates that a minimum experimental campaign may involve both material tests and two samples with different constituent volume ratios.

Parameter identification and local identifiability

Since our focus lies on standard material tests, we restrict the consideration to tests i which yield integral forces $F_i = \hat{F}_i(\varepsilon)$ over a prescribed engineering strain range $\varepsilon \in \mathcal{E}_i$. Concomitantly, suppose that a physical model is available which returns a force-engineering strain relation $F_i = F_i(\varepsilon; \mathbf{w})$, $\varepsilon \in \mathcal{E}_i$, for given material parameters $\mathbf{w}$. These parameters are commonly determined as solution of the following least squares problem

$$\sum_i \int_{\mathcal{E}_i} \left(F_i(\varepsilon; \mathbf{w}) - \hat{F}_i(\varepsilon) \right)^2 d\varepsilon = \underset{\mathbf{w}}{\text{Min}}! \tag{1}$$

In a Gauss-Newton scheme to solve the necessary conditions of optimality for Eq. (1), an estimate $\mathbf{w}_n$, $n = 0, 1, \ldots$, is updated iteratively by an increment $\beta_{n+1}\Delta\mathbf{w}_{n+1}$ with

$$\mathbf{G}(\mathbf{w}_n)\Delta\mathbf{w}_{n+1} = -\mathbf{r}(\mathbf{w}_n), \tag{2}$$

where $\mathbf{r}(\mathbf{w})$ represents the gradient with respect to $\mathbf{w}$ of the objective function in Eq. (1) and the left hand side $\mathbf{G}(\mathbf{w})$ is given by

$$\mathbf{G}(\mathbf{w}) = \sum_i \int_{\mathcal{E}_i} \frac{\partial F_i(\varepsilon; \mathbf{w})}{\partial \mathbf{w}} \left(\frac{\partial F_i(\varepsilon; \mathbf{w})}{\partial \mathbf{w}} \right)^T d\varepsilon. \tag{3}$$

If we conceive of the vector $\partial F_i(\varepsilon; \mathbf{w})/\partial \mathbf{w}$ for given ε as an observation, then $\mathbf{G}(\mathbf{w})$ corresponds to the autocorrelation matrix of observations over the range $\varepsilon \in \mathcal{E}_i$. In fact, application of a quadrature approximation to Eq. (3) with weights γ_j and quadrature points ε_j shows that $\mathbf{G}(\mathbf{w})$ can be related to a snapshot matrix $\mathbf{X}(\mathbf{w})$ whose dominant modes are frequently analyzed with the aid of a singular value decomposition (SVD).

$$\mathbf{G}(\mathbf{w}) = \mathbf{X}(\mathbf{w})\mathbf{X}(\mathbf{w})^T \tag{4}$$

$$\mathbf{X}(\mathbf{w}) = \left(\sqrt{\gamma_1} \frac{\partial F_1(\varepsilon_1; \mathbf{w})}{\partial \mathbf{w}}, \sqrt{\gamma_2} \frac{\partial F_1(\varepsilon_2; \mathbf{w})}{\partial \mathbf{w}}, \ldots \right) \tag{5}$$

The transpose of $\mathbf{X}(\mathbf{w})$ coincides with the sensitivity matrix of the predicted force-engineering strain curves $(\sqrt{\gamma_1}F_1(\varepsilon_1; \mathbf{w}), \sqrt{\gamma_2}F_1(\varepsilon_2; \mathbf{w}), \ldots)$ sampled at the quadrature points and scaled by the square roots of the corresponding weights.

A necessary condition for the Gauss-Newton scheme to converge is that the left hand side matrix $\mathbf{G}(\mathbf{w})$ is regular at all points $\mathbf{w}_n$ visited along the iteration sequence. By Eq. (4), this implies that the rank of $\mathbf{X}(\mathbf{w}_n)$ coincides with the number of material parameters in $\mathbf{w}$. For practical purposes, we adopt the criterion that the normalized smallest eigenvalue of $\mathbf{G}(\mathbf{w})$ exceeds a small tolerance ϵ,

$$\bar{\lambda}_{\min} = \frac{\min\{\lambda_1, \lambda_2, \ldots\}}{\sum_i \lambda_i} > \epsilon, \tag{6}$$

where the eigenvalues $\lambda_i = \sigma_i^2$ are computed as the squares of the singular values of $\mathbf{X}(\mathbf{w})$. Since the sensitivity matrix $\mathbf{X}(\mathbf{w})^T$ does not involve any experimental measurements (Eq. (5)), the regularity of $\mathbf{G}(\mathbf{w})$ at the initial estimate $\mathbf{w}_0$ can be assessed before material tests are undertaken. This attains even more significance as we observed, for all examples considered and synthetic measurements, that regularity at subsequent iterates $\mathbf{w}_n$, $n = 1, 2, \ldots$, never ceased as long as $\mathbf{G}(\mathbf{w})$ was regular at $\mathbf{w}_0$. Commensurately, Vajda et al. [4] pointed out that if the rank of $\mathbf{X}(\mathbf{w}_0)$ coincides with the number of unknown parameters in $\mathbf{w}_0$, then the model for $F_i(\varepsilon_j; \mathbf{w})$ is locally identifiable at $\mathbf{w}_0$.

This suggests that a subset of material tests for which $F_i(\varepsilon_j; \mathbf{w})$ is locally identifiable can be determined out of a library of candidate tests by selecting an initial estimate $\mathbf{w}_0$ and assessing the information content of $\mathbf{X}(\mathbf{w}_0)$ with the aid of the SVD-based criterion in Eq. (6).

A hyperelastic composite sheet

In order to corroborate the viability of the rationale developed above, we exemplarily consider a thin composite sheet made from two hyperelastic constituents that are arranged in a grid-like pattern (Figure 1(a)). The composite sheet can be subjected to simple and equibiaxial tension tests [1] that yield records of the horizontal and/or vertical forces over the applied engineering strain. On an integral basis, the material is controlled by the volume ratio $\alpha \in [0, 1]$ of both constituents. By varying the spatial distribution of the constituent patches while keeping α constant, we observed that the force-engineering strain curves in either material test are almost exclusively controlled by the volume ratio α and to a negligible extent influenced by the particular spatial arrangement. In this analysis, the first constituent was taken as Neo-Hookean, while the second one was endowed with an exponential strain energy density.

In the Introduction, we argued that estimates of the functional forms of the strain energy densities $W_1(I_1, I_3)$ and $W_2(I_1, I_3)$ characterizing the constituents may not always be available. In order to analyze local identifiability despite this lack of information, $W_1(I_1, I_3)$ and $W_2(I_1, I_3)$ are approximated in terms of global shape functions $H_i(I_1, I_3)$, $i = 1, \ldots, n_H$,

$$W_j^h(I_1, I_3) = \sum_{i=1}^{n_H} w_i^{(j)} H_i(I_1, I_3), \quad j = 1, 2. \tag{7}$$

Here, I_1 and I_3 denote the first and third invariants, respectively, of the right Cauchy-Green deformation tensor and, for simplicity, the strain energy densities are assumed to be independent of the second invariant I_2. The shape functions can be chosen almost arbitrarily, albeit subject to a linear independence condition on the subset of I_1-I_3-space which is expected to be accessed in the course of the material tests. Furthermore, we choose the shape functions in such a way that the strain energy densities W_j^h as well as the second Piola-Kirchhoff stresses $\mathbf{S}_j^h$ vanish in an unstretched reference configuration. As starting point for a local identifiability analysis, the parameters $w_i^{(j)}$ are set to

$$w_1^{(j)} = 200\,\mathrm{N/m^2} \quad \text{and} \quad w_i^{(j)} = 0 \quad \text{for} \quad i = 2, \ldots, n_H = 5, \quad j = 1, 2 \tag{8}$$

such that, for the present choice of shape functions (not listed), both $W_1^h(I_1, I_3)$ and $W_2^h(I_1, I_3)$ coincide and are given by a Neo-Hookean material with moduli $\mu = 200\,\mathrm{N/m^2}$ and $\lambda = 0\,\mathrm{N/m^2}$.

Figure 1(b) depicts a heatmap of the smallest normalized eigenvalue $\bar{\lambda}_{\min}$ of $\mathbf{G}(\mathbf{w})$ for combinations of uniaxial and equibiaxial tension tests on two composite samples with volume ratios α_1 and α_2. If the threshold ϵ in Eq. (6) is chosen slightly larger than the computing precision, for example, $\epsilon = 10^{-14}$, then it appears that the material law in Eq. (7) is locally identifiable for any (α_1, α_2) pair. Beyond this positive conclusion, Figure 1(b) also provides some insight into the relative information content of different combinations of material tests. For example, $\bar{\lambda}_{\min}$ increases with the difference between α_1 and α_2, indicating that the conditioning of $\mathbf{G}(\mathbf{w})$ improves as the samples are more dissimilar. Further analyses on our part indicate that, in the present example, at least four material tests which differ either in terms of the sample constitution α or the type of test (uniaxial or equibiaxial) are required for local identifiability and that the addition of a fifth test does not improve upon the best conditioning in Figure 1(b) for $\alpha_1 = 1$ and $\alpha_2 = 0$. At the same time, not all combinations of four, five or six material tests result in local identifiability.

For those combinations of material tests for which local identifiability was ascertained in Figure 1(b), we further quantified the reidentification accuracy assuming that the true constituents possess a Neo-Hookean and an exponential strain energy density, respectively (not shown).

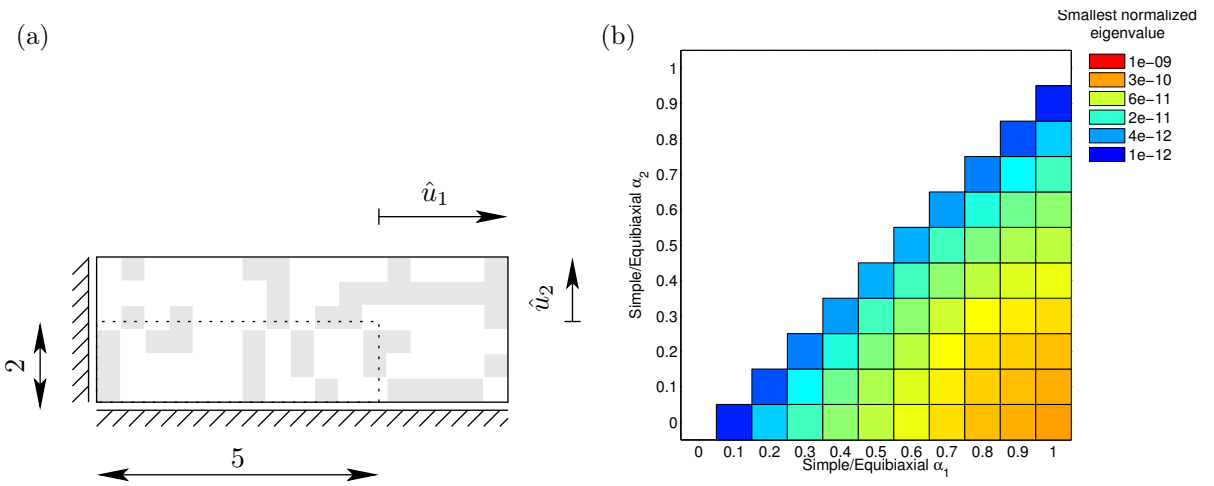

Figure 1. (a) Schematic illustration of a composite sheet made from patches of two different hyperelastic constituents in equibiaxial tension. The dotted lines indicate the unstretched reference configuration. (b) Heatmap of the smallest normalized eigenvalue $\bar{\lambda}_{\min}$ for an experimental campaign involving one uniaxial and one equibiaxial tension test on composite samples with two different volume ratios $\alpha_1 \neq \alpha_2$.

Conclusions

In order to support elucidating the material behaviour of constituents in composite materials, we addressed the question as to whether the constituent strain energy densities of hyperelastic composites can be inferred from integral force-engineering strain measurements if information on the intra-sample geometry is available. In the absence of *a priori* intuition about the functional form of these strain energy densities, a direct discretization in terms of global shape functions was explored. Slightly reinterpreting the governing question, we proposed to consider a library of candidate material tests and select those combinations for which the sensitivity matrix of model predictions with respect to the material parameters obeys a rank criterion. Apart from an initial estimate of the parameters, this criterion does not yet involve any experimental data and may be employed to rationalize an experimental campaign encompassing a minimum of material tests. The sensitivity-based criterion for local identifiability can also be deployed iteratively in the course of a Gauss-Newton scheme for solving the parameter estimation problem, but we observed that local identifiability at the initial estimate was sufficient to maintain identifiability along the Gauss-Newton sequence.

Acknowledgments

I gratefully acknowledge Abimathi Siva Subramanian who assisted me in setting up the test case reported here during a DAAD WISE internship in summer 2018.

References

[1] R. W. Ogden, G. Saccomandi, and I. Sgura. Fitting hyperelastic models to experimental data. *Computational Mechanics* 34.6 (2004), pp. 484–502.

[2] C. Oskay and J. Fish. On calibration and validation of eigendeformation-based multiscale models for failure analysis of heterogeneous systems. *Computational Mechanics* 42.2 (2008), pp. 181–195.

[3] U. Schmidt, J. Mergheim, and P. Steinmann. Multiscale parameter identification. *International Journal for Multiscale Computational Engineering* 10.4 (2012), pp. 327–342.

[4] S. Vajda, H. Rabitz, E. Walter, and Y. Lecourtier. Qualitative and quantitative identifiability analysis of nonlinear chemical kinetic models. *Chemical Engineering Communications* 83.1 (1989), pp. 191–219.

**Proceedings of the 8th GACM Colloquium on Computational Mechanics
for Young Scientists from Academia and Industry
August 28–30, 2019 in Kassel, Germany**

Numerical thermo-elasto-plastic analysis of residual stresses on different scales during cooling of hot formed parts

S. Uebing * [1], L. Scheunemann[1], D. Brands[1] and J. Schröder[1]

[1]Insitute of Mechanics, Civil Engineering, University Duisburg-Essen, Universitätsstr. 15, 45141 Essen, Germany

Abstract. The targeted application of residual stress states is an important tool in order to improve component properties such as strength or durability. Therefore, in current research more and more attention is paid to the numerical analysis on different scales, i.e. macroscale, mesoscale and microscale. Initiated by the hot forming process of a cylindrical specimen, a microscopic phase transformation occurs which is directly linked to the evolution of mesoscopic strains and related residual stresses. Hence, in this contribution two models are built, one describing macroscopic stresses due to cooling and one describing the individual steps from transformation to residual stress state on the lower scales.

Introduction

The experimental and numerical investigation of hot bulk forming processes is a useful tool to improve the component properties, e.g. extension of lifetime. Hot forming processes offer the opportunity to adjust some process parameters, i.e. deformation state, temperature profile or cooling media, in order to influence the distribution of residual stresses. Therefore, underlying experiments and related macroscopic numerical simulations of a hot formed cylindrical specimen made of Cr-alloyed steel 1.3505 (DIN 100Cr6) are done at the Institute of Forming Technology and Machines (IFUM) at Leibniz University (LU) Hannover. Detailed information regarding the procedure as well as resulting macroscopic residual stress states can be found in [1]. Following [3], those stresses can be characterized as residual stresses of first type. Residual stresses of second and third type refer to the lower scales, i.e. polycrystal and grain level. They are a consequence of the phase transformation occuring on the microscale during cooling from an initially stress-free austenitic material. To gain a more detailed understanding of the link between production process and the final component's properties, two computations are presented. First, the cooling of a slice, representing a part of the cylindrical specimen is investigated with regard to evolving macroscopic stresses. Additionally, an isothermal combination of Multi-Phase Field and Finite Element simulations is used to analyze the influence of phase transformation regarding micro- and mesoscopic residual stresses.

1 Cooling of a slice

A thermo-elasto-plastic Finite Element simulation is used to model the cooling process of the experimentally investigated cylindrical specimen. This specimen has an eccentric hole to evoke a heterogeneous distribution of the temperature during cooling. The cooling induces shrinking of the geometry, such that the associated thermally induced strains are coupled to the mechanical strains, which are decomposed into elastic and plastic strains. For the computation, an elasto-plastic material law with a von Mises yield criterion and exponential hardening is used, following [5],

$$y(\theta) = y_0(\theta) + (y_\infty(\theta) - y_0(\theta))(1 - \exp(-\delta\epsilon)) + h\epsilon\,. \tag{1}$$

Therein, θ denotes the temperature, y_0 the initial yield strength, y_∞ the limiting yield strength, δ the exponential hardening parameter, h the linear hardening parameter and ϵ the internal variable, which resembles plastic effects. The boundary value problem bases on a slice of the cylindrical specimen.

*Corresponding author: sonja.uebing@uni-due.de

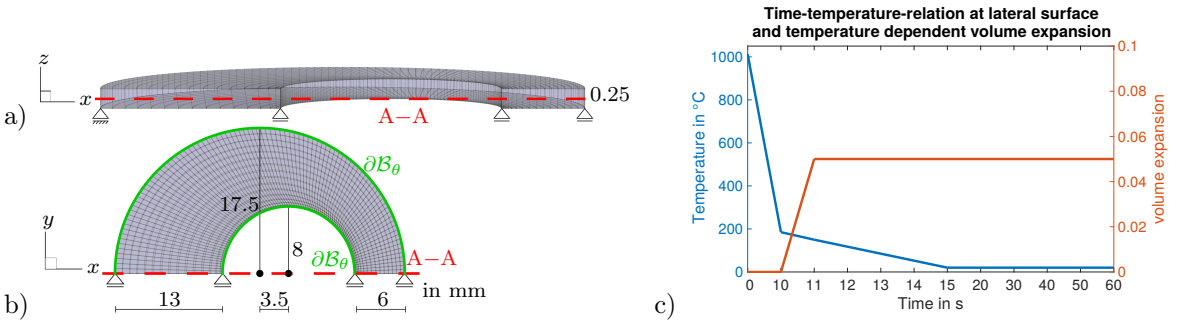

Figure 1. a) and b): dimensions and boundary conditions for the slice using symmetry conditions. A−A illustrates the investigated line. c) The slice is cooled over the lateral surface $\partial\mathcal{B}_\theta$) from 1012.45 °C down to room temperature 20 °C in 15 seconds and a volume expansion of 5% is applied.

Due to symmetry conditions, only one half of the slice is modeled, see Figure 1a,b, which illustrate the dimensions and boundary conditions of the slice. Starting at an initial temperature of $\theta_0 = 1012.45\,°\mathrm{C}$ and a pure austenitic material (austenitic volume fraction $\varphi = 1$), the lateral surface is cooled down to room temperature of $\theta = 20\,°\mathrm{C}$, see Figure 1c. Between $\theta = 185\,°\mathrm{C}$ and $\theta = 150\,°\mathrm{C}$ the phase transformation is considered by the material changing linearly to 87% martensite and 13% retained austenite ($\varphi = 0.13$). Simultaneously, a volumetric jump of 5% is applied incrementally to represent the lattice shearing in a simplified manner, see Figure 1c. On that account, the volumetric strain ε^*_{vol} is applied on the principal diagonal of the strain tensor, i.e.

$$\varepsilon^*_{vol} = \frac{0.05}{(185\,°\mathrm{C} - 150\,°\mathrm{C})}(185\,°\mathrm{C} - \theta), \qquad \operatorname{diag}\boldsymbol{\varepsilon} \Leftarrow \operatorname{diag}\boldsymbol{\varepsilon} - \frac{1}{3}\varepsilon^*_{vol}\mathbf{1}\,. \tag{2}$$

For both materials, namely austenite and martensite, the temperature dependent material parameters are calculated using Table 1 and the functions

$$f_1 = \varphi(a_1 + a_2\,\theta)a_3 + (1-\varphi)(a_4 + a_5\,\theta)a_6\,, \qquad f_2 = \varphi\,a_1\exp(a_2\,\theta)a_3 + (1-\varphi)a_4\exp(a_5\,\theta)a_6\,. \tag{3}$$

Table 1. Material parameters w.r.t. temperature θ and austenitic volume fraction φ: bulk modulus κ, shear modulus μ, initial yield strength y_0, limiting yield stress y_∞, exponential hardening δ, linear hardening h, thermal conductivity aa, specific heat capacity cc, thermal expansion coefficient α_T.

parameter	unit	$f_\bullet$	a_1	a_2	a_3	a_4	a_5	a_6
κ	MPa	f_1	1.01	$-1.851\,10^{-4}$	160287	1.015	$-1.766\,10^{-4}$	166349
μ	MPa	f_1	1.024	$-4.814\,10^{-4}$	76700	1.025	$-3.789\,10^{-4}$	80977
y_0	MPa	f_2	1.044	$-1.475\,10^{-3}$	420	1.028	$-9.932\,10^{-4}$	3050
y_∞	MPa	f_2	1.044	$-7.172\,10^{-4}$	780	1.026	$-7.437\,10^{-4}$	3420
δ	–	f_1	35	0	1	20	0	1
h	MPa	f_1	520	0	1	500	0	1
aa	N/(mm K)	f_1	0.966	$6.868\,10^{-4}$	$1.758\,10^{-2}$	1.016	$8.024\,10^{-5}$	$3.721\,10^{-2}$
cc	J/(mm^3 K)	f_1	0.986	$3.862\,10^{-4}$	$3.692\,10^{-3}$	0.946	$9.550\,10^{-4}$	$3.548\,10^{-3}$
α_T	1/C	f_1	0.998	$-9.180\,10^{-5}$	$2.361\,10^{-5}$	0.986	$2.889\,10^{-4}$	$1.228\,10^{-5}$

When the temperature at the lateral surface, see Figure 1b, reaches 185 °C (computation time $t = 10\,\mathrm{s}$), the phase transformation starts. Up to now, no stresses occur on the investigated line, outlined in Figure 1b as A−A with $y = 0\,\mathrm{mm}$ and $z = 0.125\,\mathrm{mm}$, cf. Figure 2a. One second later, i.e. $t = 11\,\mathrm{s}$, high compressive stress values arise near the boundary, cf. Figure 2b. The material core of the cylinder is still warmer than the transformation start temperature of 185 °C, such that no transformation has started. At $t = 15\,\mathrm{s}$, the temperature at the lateral surface reaches room temperature. Now, the material core transforms from austenite to martensite and the volumetric jump is applied. Thus, high compressive stresses in this domain cause tensile stresses in the outer regions, in which the phase transformation is already completed, see Figure 2c.

In comparison to Figure 1d, in which the results of the work at the IFUM, LU Hannover, are shown, it is to be noticed, that the magnitude of the computed stresses highly differs. This has to be investigated in detail such that the results from both approaches can be fitted accordingly. But qualitatively both numerical investigations coincide such that tensile stresses occur at the outer boundary after the complete cooling. Within the scope of the work to improve the component's properties, e.g. compressive stresses in the outer region, some adjustments to the process parameters should be done, e.g. modifying the cooling route.

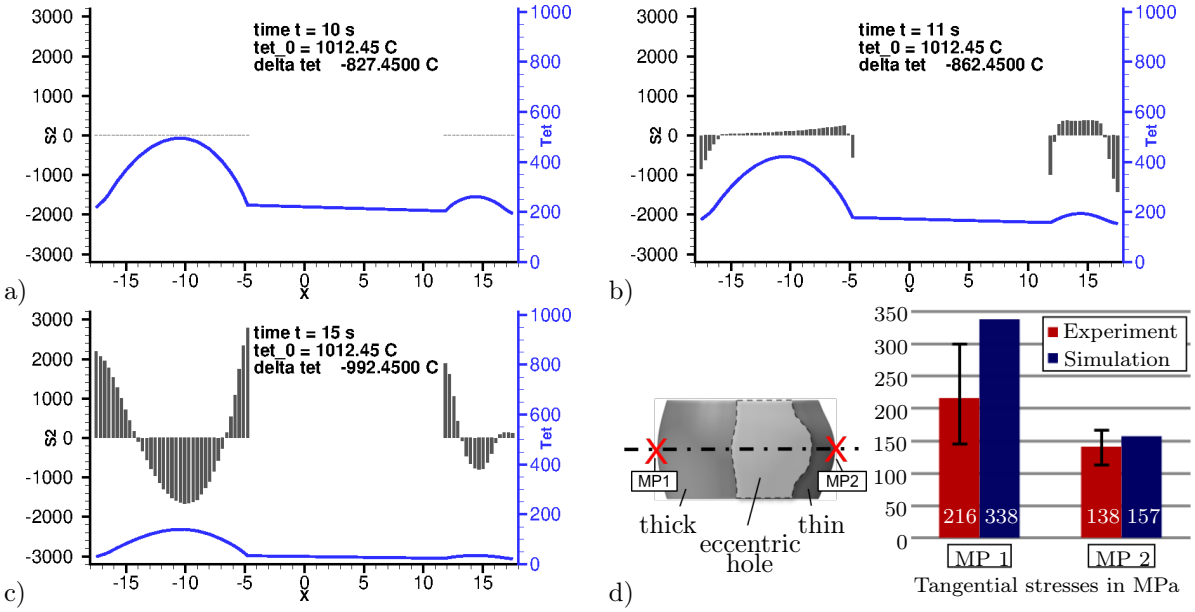

Figure 2. Tangential stresses in MPa and temperature in °C a) after 10 s, temperature at lateral surface $\theta = 185\,°\mathrm{C}$, b) after 11 s, temperature at lateral surface $\theta = 150\,°\mathrm{C}$, c) after 15 s, temperature at lateral surface $\theta = 20\,°\mathrm{C}$ and d) tangential stresses in outer regions computed and measured by IFUM, LU Hannover.

2 Phase transformation on meso- and microscale

The numerical analysis of the slice only considers microscopic effects such as the phase transformation in an approximate manner. Hence, the aim is to model the diffusionless phase transformation from austenite to martensite occuring during cooling. Therefore, a combined model, firstly proposed in [1], of an elastic Multi-Phase Field (MPF) model, see [6], and a two-scale Finite Element simulation, cf. e.g. [4], is chosen. The MPF model is applied to describe the lattice shearing from face-centered cubic austentitic unit cells to body-centered tetragonal martensitic unit cells. In order to describe the martensitic lattice on the microscale three variants I, II and III are taken into account which are linked to eigenstrains and represented by the so-called Bain groups, cf. [2], see Figure 3a. When applying a partial rank-one homogenization scheme, martensitic grains containing only two of three variants are obtained, see Figure 3b.

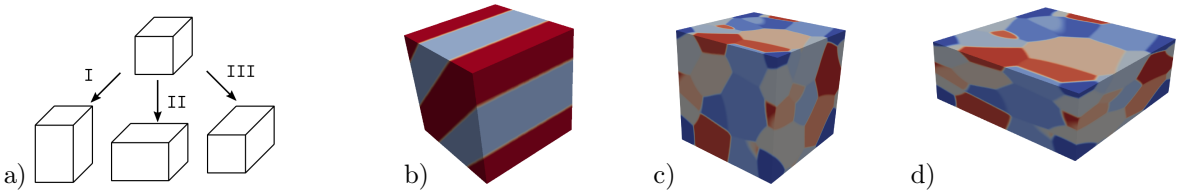

Figure 3. a) Considered martensitic variants, b) microscopic laminate structure of one martensite grain, c) initial and d) deformed mesoscopic polycrystal

To transfer the results to the mesoscale, another MPF simulation is used based on normal grain growth. It configures an austenitic polycrystal, see Figure 3c, with a certain number of austenitic grains. The polycrystalline structure is firstly deformed, see Figure 3d, and afterwards cooled down to room temperature. During cooling the phase transformation from austenite to martensite occurs when reaching the martensite start temperature defined as 185° C. The phase transfomation follows the principle of minimizing the elastic energy in the system. Finally, depending on macroscopic, experimental results, the polycrystal consists of approximately 87% martensite and 13% retained austenite.

With this information at hand, a two-scale Finite Element simulation [4] is done which takes into account plastic effects and computes residual stresses of second type. More details are given in [1]. In absence of outer forces, the resulting stresses can be interpreted as residual stresses rather than mechanical stresses. The radial, tangential and axial stresses, denoted by σ_r, σ_φ, σ_z, respectively as well as the equivalent

plastic strains ε^p_{eq} and the von Mises stresses σ_{vM} are shown in Figure 4, of which the tangential stresses are most important for the investigation of durability for instance.

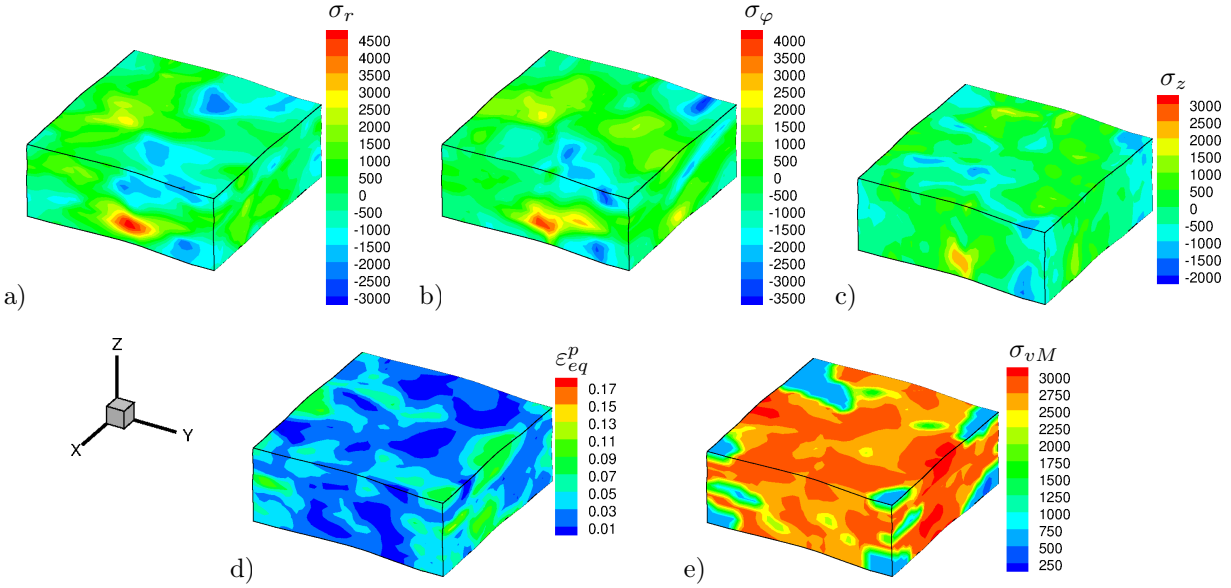

Figure 4. Results: a) radial stresses σ_r in MPa, b) tangential stresses σ_φ in MPa, c) axial stresses σ_z in MPa, d) equivalent plastic strains ε^p_{eq} and e) von Mises stresses σ_{vM} in MPa

3 Conclusion and outlook

In this work, the numerical analysis of a slice of cylindrical specimen, which was cooled from 1000 °C to 20 °C was presented. Therefore, a macroscopic and a micro-and mescoscopic model were applied in order to compute residual stresses. The numerical simulations show qualitatively similar results comparing to the experimental investigations. To obtain a more quantitative accordance, the coupling of the different scales must be enhanced.

Acknowledgments

Thank you to: DFG - 374871564 (BE 1691/223-1, BR 5278/3-1, SCHR 570/33-1) for funding; Prof. Dr.-Ing. B.-A. Behrens, Dipl.-Ing. A. Chugreev and C. Kock (IFUM, LU Hannover), Prof. Dr. I. Steinbach and Dr. O. Shchyglo (ICAMS, RU Bochum) and Dr.-Ing. R. Niekamp and M. Sarhil (U Duisburg-Essen) for their scientific collaboration and support.

References

[1] B.-A. Behrens, J. Schröder, D. Brands, L. Scheunemann, R. Niekamp, M. Sarhil, S. Uebing, and C. Kock. Experimental and Numerical Investigations of the Development of Residual Stresses in Thermo-Mechanically Processed Cr-Alloyed Steel 1.3505. *Metals* 9.4 (2019), 480 (28 pages).

[2] K. Bhattacharya. *microstructure of martensite: why it forms and how it gives rise to the shape-memory effect*. Oxford: Oxford University Press, 2003.

[3] E. Macherauch, H. Wohlfahrt, and U. Wolfstied. *Härterei-Technische Mittelungen - Zeitschrift für Werkstoffe, Wärmebehandlung, Fertigung* 28.3 (1973), pp. 201–211.

[4] J. Schröder. A numerical two-scale homogenization scheme: the FE^2-method. In: *Plasticity and Beyond - Microstructures, Crystal-Plasticity and Phase Transitions (CISM Lecture Notes 550, Eds. J. Schröder, K. Hackl)*. Springer, 2014, pp. 1–64.

[5] J.C. Simo and C. Miehe. Associative coupled thermoplasticity at finite strains: Formulation, numerical analysis and implementation. *Computer Methods in Applied Mechanics and Engineering* 98 (1992), pp. 41–104.

[6] I. Steinbach. Phase-field models in materials science. *Modelling and Simulation in Materials Science and Engineering* 17 (2009), 073001 (31 pages).

**Proceedings of the 8th GACM Colloquium on Computational Mechanics
for Young Scientists from Academia and Industry
August 28–30, 2019 in Kassel, Germany**

A Weak Dirichlet-Neumann Partitioned Algorithm for 1-Dimensional Structures Embedded in a 3-Dimensional Fluid

Nora Hagmeyer*[1], Matthias Mayr[1] and Alexander Popp[1]

[1]Institute for Mathematics and Computer-Based Simulation, University of the Bundeswehr Munich, Germany

Abstract. Modeling of slender bodies via 1-dimensional beam theories can greatly increase the efficiency of numerical simulations and lead to rather well-posed formulations. Especially the application of so-called geometrically exact beam theories as standalone models can yield precise solutions at only a fraction of the computational cost of full 3-dimensional solid models. Harnessing the efficiency of these theories in mixed-dimensional multi-physics simulations necessitates the development of efficient and stable load and motion transfer schemes as well as constraint enforcement techniques for unavoidably non-matching meshes. This contribution primarily addresses these challenges in the context of Fluid-Structure Interaction (FSI). In order to couple a 1-dimensional structure model with the full 3-dimensional continuum theory of a surrounding Newtonian incompressible fluid, a weak Dirichlet-Neumann coupling algorithm is proposed and applied to numerical test problems. The focus lies on the transfer schemes and constraint enforcement techniques employed to couple the 1-dimensional beam formulations and 3-dimensional fluid flow and their limitations.

Reduced Dimensional Structure Models

The interaction of rod-like structures with fluid flow plays an important role in a broad spectrum of applications varying from biomechanical materials to industrial processes. In order to ensure a well-posed formulation as well as an efficient usage of resources, applications can often gain from using 1-dimensional beam theory to model the slender bodies as compared to a full 3-dimensional formulation.

In our case, the slender continua are modeled using geometrically nonlinear semi-induced beam theories like the theories of Euler-Bernoulli and Kirchhoff, which consistently derive the kinematic relations from the 3D continuum theory under some simplifying assumptions. On the other hand, the constitutive equations are directly postulated in 1D and conserve essential mechanical principles such as equilibrium of forces. For the numerical simulations using the Finite Element Method (FEM), the beams are discretized using a C^1 continuous centerline interpolation with Hermite polynomials, allowing for a smooth approximation of the beam geometry even for coarse meshes [**Meier2014**].

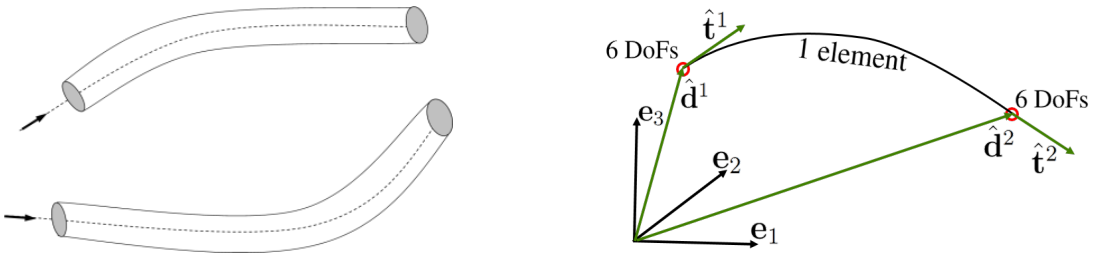

(a) Depiction of the centerline in a beam with circular cross section

(b) Visualization of a Hermite beam centerline interpolation

Figure 1. Coarse interpolation of a slender body with 1D beam elements using 3rd order Hermite shape functions for the centerline interpolation

*Corresponding author: nora.hagmeyer@unibw.de

Immersed Boundary Method

In terms of numerical modeling for the considered Fluid-Beam Interaction problem (FBI), the Finite Element Method (FEM) applied to the incompressible isothermal Navier-Stokes equations as well as the beam models is used in conjunction with an Immersed Boundary type approach. The Immersed Boundary Method (IBM) was first introduced by Peskin in [**Peskin2002**] for the simulation of heart valves. These types of methods have been the topic of ongoing research in recent years, in particular because of their robustness in the presence of large displacements.

In Immersed Boundary type Methods, the boundary of the immersed solid is not resolved by the fluid mesh, but a (volume) coupling of the fluid to the solid is implemented via a transfer of quantities, usually load and kinematic values, between the two physics-specific meshes. The flexibility of this approach in terms of the relation of the two meshes to each other makes it suitable for the application to mixed-dimensional Fluid-Structure Interaction (FSI) problems.

A Weak Dirichlet-Neumann Partitioned Algorithm

In [**Peskin2002**], Peskin proposed a Neumann-Dirichlet type formulation in the sense that the fluid velocity was transfered to the structure mesh in order to enforce the kinematic coupling, and vice versa a force was transfered from the structure mesh and applied to the fluid. This builds a contrast to Dirichlet-Neumann partitioned algorithms classically used in full-dimensional FSI simulation because of their convergence properties. Reasons for this choice presumably include the problem of prescribing velocity values within the incompressible fluid while still staying divergence-free in a weak sense. In addition, when using simple linear material laws in the structure model, the fact that the fluid velocity already completely determines the structure movement in each point makes it possible to condense the structure equations, and to only supply the resulting interaction force to the fluid equation, thus avoiding additional costly solution steps.

Nevertheless, we propose a Dirichlet-Neumann type partitioned algorithm that enforces the Dirichlet conditions on the fluid in a weak sense. This allows to fulfill the divergence condition in the vicinity of the embedded structure weakly and to treat occurring instabilities in a natural way using established coupling techniques. Similar Dirichlet-Neumann type algorithms have already been proposed for Lagrange Multiplier based Mortar Finite Element surface coupling in contact mechanics in [**dirichletneumannconvergence**] as well as in classical ALE-based Fluid-Structure Interaction in [**Kloppel2012**]. Both works propose enforcing the Dirichlet condition, which is the non-penetration condition in contact mechanics and the geometric continuity condition in FSI respectively, in a weak sense, while also using the Lagrange multiplier to transfer the resulting interaction force to the Neumann partition.

Constraint Enforcement Technique

There exists a multitude of techniques for the weak enforcement of Dirichlet conditions roughly separated into the categories of Penalty Methods and Lagrange Multiplier based approaches, among them Nitsche's Method and stabilized Lagrange Multiplier approaches. Differing existentially in their derivation from the weak from, members of these two categories display very different properties.

Within this work, a Penalty Method is employed to weakly enforce the kinematic coupling condition on the Dirichlet partition, meaning that the following penalty term is added to the weak form of the Navier-Stokes equations:

$$\int_{\Gamma_i} \epsilon \left(v^f - \bar{v}^b\right) \cdot u^f \, \mathrm{d}\Gamma,$$

with the unknown fluid velocity v^f, the projection of the beam velocity $\bar{v}^b$ in the fluid function space, the fluid test function u^f, the penalty parameter ϵ, and the FBI interface Γ_i. Besides the penalty method's simplicity, further advantages include its robustness, which comes with the price of never fulfilling the enforced condition exactly for finite penalty parameters ϵ as well as the non-trivial choice of such a problem-appropriate ϵ. Figure 2 depicts this fact for a rigid beam in a fluid channel.

Load and Motion Transfer Scheme

In order to obtain the projection of the beam velocity $\bar{v}^b$, representing the weakly enforced Dirichlet condition, into the fluid function space a projection operator has to be defined. In the discrete problem, this corresponds to a mapping operator of the beam velocity to the fluid mesh. Within this contribution a Gauss-Point-to-Segment type approach, commonly employed in contact mechanics to transfer the quantities of interest between the meshes, is applied to numerical examples showing the suitability of the proposed method as well as its modeling limitations.

Figure 2. Fluid velocity in x-direction around a beam immersed in a fluid channel

**Proceedings of the 8th GACM Colloquium on Computational Mechanics
for Young Scientists from Academia and Industry
August 28–30, 2019 in Kassel, Germany**

Spline-Based Finite Element Method for Exact Geometric Interface Representation

Michel Make * [1], Norbert Hosters[1] and Marek Behr[1]

[1]Chair for Computational Analysis of Technical Systems (CATS), RWTH Aachen University, Germany

Abstract. Computer-Aided Design (CAD) tools are commonly used for the design of many engineering applications. These tools often utilize Non-Uniform Rational B-Splines (NURBS) to represent geometries. Isogeometric analysis (IGA) [3], allows us to directly use NURBS for numerical analysis. Analyzing fluid flows, however, involves complex three-dimensional flow domains. Parametrizing such volumetric domains using NURBS can be challenging and is still an ongoing topic in the IGA community.

With the recently developed NURBS-enhanced finite element method (NEFEM) [4, 5], the favorable geometric characteristics of NURBS are utilized within a standard finite element method. This is achieved by enhancing the elements touching the boundary by using the NURBS geometry itself. In the current work, the NEFEM for a three-dimensional space-time formulation suitable for fluid-structure interaction simulations is discussed. Furthermore, the method is demonstrated by means of a benchmark problems.

Introduction

In many engineering applications involving fluid-structure interaction (FSI) phenomena, accurate geometry representation is crucial. Computer-Aided Design (CAD) tools, due to their capabilities, are commonly used in the early design stage of such applications. Such tools often rely on Non-Uniform Rational B-Splines (NURBS) to represent geometries. The mathematical properties of NURBS make them well suited to accurately describe complex shapes. The introduction of isogeometric analysis (IGA) in [3], made it possible to directly exploit these favorable geometric properties for numerical analysis. Analyzing fluid flows, however, often involves three-dimensional volume domains. Parametrizing such domains using closed volume splines can be a challenge and is still an ongoing topic of research in the IGA community.

To circumvent the need for volume splines, an alternative approach is proposed in [4], which is further developed to incorporate space-time finite elements and free-surface flows in [5]. The method suggests the use of standard finite elements in the interior of the computational domain, and supplement these with the so-called NURBS-enhanced finite elements along the domain boundaries. These NURBS-enhanced finite elements (NEFEM) use a NURBS description of the domain boundary in order to integrate the exact geometry into the finite element method. By doing so, the error caused by discretizing a computational domain by means of, e.g., an elementwise linear approximation is avoided (see Figure 1).

1 3D NURBS-Enhanced Finite Elements

Similar to its two-dimensional counterpart [2], for the 3D NURBS-enhanced elements, a non-linear mapping – termed Tetrahedron-Hexahedron-Tetrahedron (THT) mapping – from physical elements to the reference element is used to incorporate the NURBS definition.

The THT-mapping is based on the idea to construct shape functions by degeneration [2]. First, a simple mapping from a hexahedron to a tetrahedron is defined by coalescing nodes and adding together their corresponding shape functions [6].

*Corresponding author: make@cats.rwth-aachen.de ORCID iD: 0000-0001-9504-955X

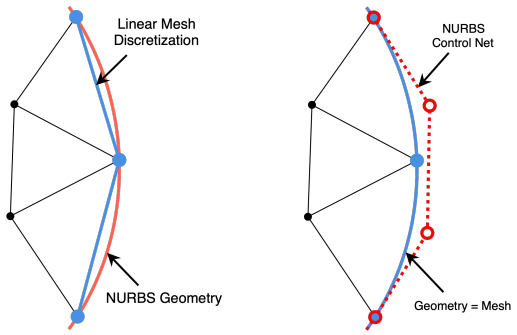

Figure 1. Standard FE and NEFEM mesh boundary.

To obtain the NEFEM, the mapping is first used to map a global tetrahedron element to a reference hexahedron element. Using the inverse mapping, this hexahedron is then mapped to the well-known reference tetrahedron (see Figure 2).

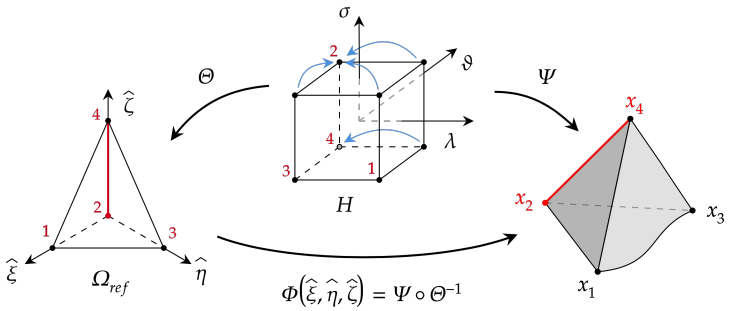

Figure 2. Tetrahedron-Hexahedron-Tetrahedron (THT) mapping.

The THT-mapping can now be used to define the shape functions and quadrature point distribution on the elements which have a common face or edge with the NURBS boundary (see Figure 3). Note that two different mappings need to be defined for the edge and face elements.

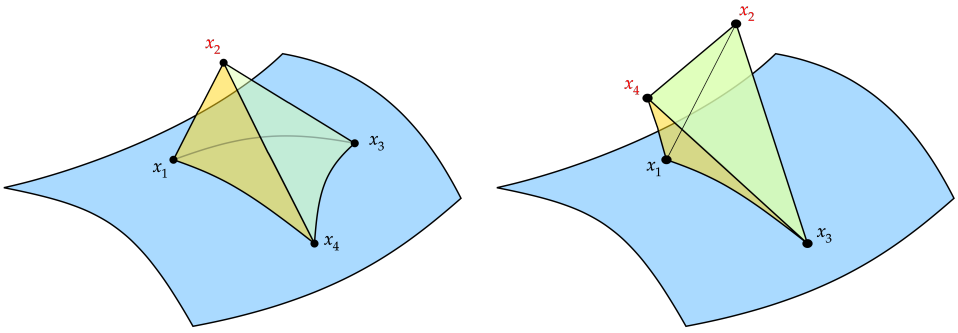

a) Element with NURBS face. **b)** Element with NURBS edge.

Figure 3. Different NEFEM element configurations.

The mapping for the face element shown in Figure 3a can be defined as follows:

$$\Phi_{face}(\hat{\xi},\hat{\eta},\hat{\zeta}) = (\hat{\xi}+\hat{\eta}+\hat{\zeta})\vec{C}\left(\frac{\vec{\Theta}_1\hat{\xi}+\vec{\Theta}_3\hat{\eta}+\vec{\Theta}_4\hat{\zeta}}{\hat{\xi}+\hat{\eta}+\hat{\zeta}}\right)+(1-\hat{\xi}-\hat{\eta}-\hat{\zeta})\vec{x}_2. \tag{1}$$

Here, $\hat{\xi},\hat{\eta}$ and $\hat{\zeta}$ represent the reference coordinates on the reference tetrahedron, $\vec{\Theta}_i$ the parametric

coordinates of the element nodes along the NURBS and $\vec{x}_i$ the global coordinates of the element nodes. Note that the element node numbering in Equation (1) corresponds to that used in Figure 3.

Analogous to the method discussed in [2], the mappings used in this work can be extended for space-time finite elements. This is done by defining a linear combination of of the upper and lower time level of a space-time slab.

2 Domain Volume Computation

An accurate representation of the computational domain can significantly affect simulations involving FSI phenomena, especially when closed domains are to be considered. This has been demonstrated previously for two-dimensional problems in [1].

To show the benefit of the presented method, the volume of a domain with curved boundaries is studied. In this case a cuboid is considered, from which a 120 degree segment is subtracted. The resulting volume consists of five plane faces and one curved face, which can be represented by a NURBS surface exactly (see also Figure 1).

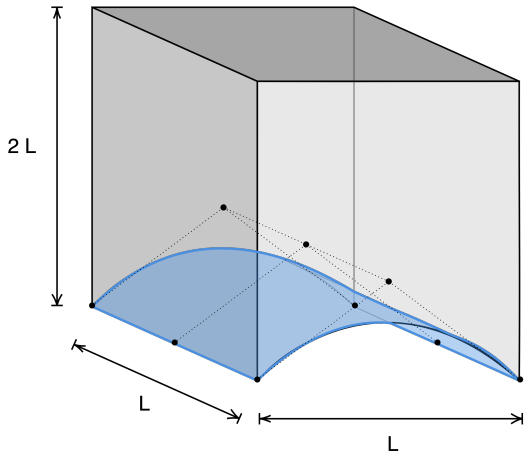

Figure 4. Computational domain with curved face represented by a NURBS surface.

The volume of the domain is computed using both standard finite elements (SFEM) and NEFEM. For NEFEM, the curved surface is represented by a second order NURBS surface with a control net as shown in Figure 1. The absolute error between the exact volume and that computed using SFEM and NEFEM elements is shown in Figure 5 and Table 1. The exact volume of the domain is defined by $V_{excact} = L^3(2 - \frac{\pi}{9} - \frac{1}{\sqrt{48}})$.

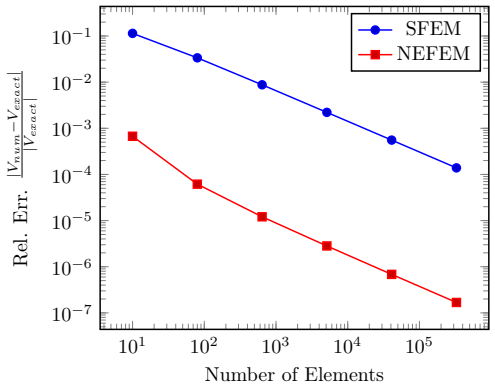

Figure 5. Relative volume error for SFEM and NEFEM.

Table 1. Grid refinement and relative error in volume computation.

Grid	Elements	Relative error	
		SFEM	NEFEM
0	10	0.1140e+00	6.7198e−04
1	80	0.0336e+00	6.1552e−05
2	640	0.0087e+00	1.2086e−05
3	5,120	0.0022e+00	2.8218e−06
4	40,960	5.5479e−04	6.8374e−07
5	327,680	1.3878e−04	1.6825e−07

In Figure 5 and Table 1, it can be seen that the NEFEM formulation allows for an accurate volume computation with a relatively coarse mesh. The computed error for NEFEM, relative to the exact volume, is roughly four orders of magnitude smaller than that of the standard finite elements.

Acknowledgments

This work is partially made possible through the DAAD with funds from the Federal Ministry of Education and Research (BMBF)

References

[1] N. Hosters. "Spline-based methods for fluid-structure interaction". Dissertation. Aachen: RWTH Aachen University, 2018. DOI: 10.18154/RWTH-2018-223770.

[2] N. Hosters, J. Helmig, A. Stavrev, M. Behr, and S. Elgeti. Fluid–structure interaction with NURBS-based coupling. *Computer Methods in Applied Mechanics and Engineering* 332 (2018), pp. 520 –539. ISSN: 0045-7825. DOI: https://doi.org/10.1016/j.cma.2018.01.003.

[3] T.J.R. Hughes, J.A. Cottrell, and Y. Bazilevs. Isogeometric analysis: CAD, finite elements, NURBS, exact geometry and mesh refinement. en. *Computer Methods in Applied Mechanics and Engineering* 194.39-41 (Oct. 2005), pp. 4135–4195. ISSN: 00457825. DOI: 10.1016/j.cma.2004.10.008.

[4] R. Sevilla, S. Fernández-Méndez, and A. Huerta. NURBS-Enhanced Finite Element Method (NEFEM). en. *Archives of Computational Methods in Engineering* 18.4 (Nov. 2011), p. 441. ISSN: 1134-3060, 1886-1784. DOI: 10.1007/s11831-011-9066-5.

[5] A Stavrev, P. Knechtges, S Elgeti, and A. Huerta. Space-time NURBS-enhanced finite elements for free-surface flows in 2D. *International Journal for Numerical Methods in Fluids* 81.7 (2016), pp. 426–450.

[6] O. C. Zienkiewicz, R. L. Taylor, and J. Z. Zhu. *The finite element method: its basis and fundamentals*. Elsevier, 2005.

**Proceedings of the 8th GACM Colloquium on Computational Mechanics
for Young Scientists from Academia and Industry
August 28–30, 2019 in Kassel, Germany**

An interface element formulation for frictionless normal contact between rough surfaces

Jacopo Bonari [*1], Maria Rosaria Marulli[1], Nora Hagmeyer[2], Matthias Mayr[2], Alexander Popp[2] and Marco Paggi[1]

[1]IMT School for Advanced Studies Lucca

[2]Institute for Mathematics and Computer-Based Simulation, University of the Bundeswehr Munich

Abstract. A new multi-scale finite element formulation for contact mechanics between nominally smooth but microscopically rough surfaces is proposed. The approach integrates the finite element method (FEM) for modelling interface interactions at the macro-scale with a boundary element method for the solution of the contact problem at the micro-scale.

Introduction

This contribution presents a novel finite element formulation for solving the problem of frictionless normal contact between two bodies across a rough interface using a multi-scale approach. The method combines a new interface finite element for modelling the surfaces interactions at the macro-scale with the boundary element method (BEM) for the solution of the contact problem at the micro-scale.

The standard procedure for solving contact mechanics problem with roughness using the finite element method (FEM) is limited by the issue of requiring an accurate representation of roughness. The proposed variational approach overcomes this difficulty, treating the interface as nominally smooth at the macro-level and embedding, at the micro-level, the actual rough topology, avoiding any assumption on the surface height distribution, as previously done in other multi-scale frameworks [4].

1 Variational formulation

Let two elastic bodies occupy the domains $\Omega_i \in \mathbb{R}^2$ $(i = 1, 2)$ in the not deformed configuration defined by the reference system Oxz, Fig. 1. The two domains are separated by an interface Γ defined by the opposite boundaries Γ_i $(i = 1, 2)$ of the two bodies, viz. $\Gamma = \bigcup_{i=1,2} \Gamma_i$, where contact takes place. The whole boundary of the i-th body, $\partial\Omega_i$, is therefore divided into three parts: the classic Dirichlet and Neumann boundaries, where displacements and tractions respectively are imposed, named as $\partial\Omega_i^D$ and $\partial\Omega_i^N$ and the interface Γ_i where specific boundary conditions have to be imposed in order to model contact. We assume that Γ_i is nominally smooth but microscopically rough, resulting, in the not deformed state, in two distinct but coincident curves. For each of the two bodies a displacement field $\mathbf{u}_i = (u_i, v_i)^{\mathrm{T}}$ is defined, while at the interface the configuration of the system is described by the gap field across the interface $\mathbf{g} = (g_{\mathrm{t}}, g_{\mathrm{n}})^{\mathrm{T}}$, defined as the projection of the relative displacement $\mathbf{u}_1 - \mathbf{u}_2$ onto the normal and tangential direction of the interface defined by the unit normal and tangent vector $\mathbf{n}$ and $\mathbf{t}$. Neglecting body forces, the strong form of equilibrium for each body reads:

$$\nabla \cdot \boldsymbol{\sigma}_i = \mathbf{0} \ \text{ in } \Omega_i, \tag{1a}$$

$$\mathbf{u}_i = \hat{\mathbf{u}} \ \text{ on } \partial\Omega_i^D, \tag{1b}$$

$$\boldsymbol{\sigma}_i \cdot \mathbf{n} = \mathbf{T} \ \text{ on } \partial\Omega_i^N, \tag{1c}$$

$$g_{\mathrm{n}} \geq 0, \ p_{\mathrm{n}} \geq 0 \ \text{ on } \Gamma. \tag{1d}$$

*Corresponding author: jacopo.bonari@imtlucca.it

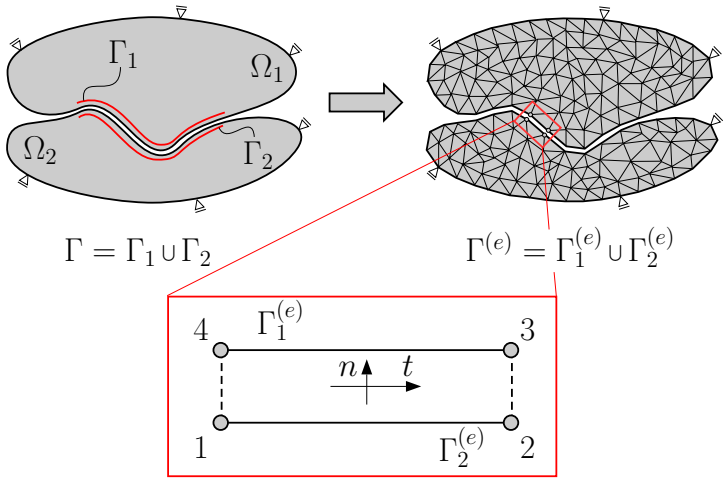

Figure 1. Domains Ω_i $(i = 1, 2)$, their Dirichlet $(\partial\Omega_i^D)$ and Neumann $(\partial\Omega_i^N)$ boundaries, and the contact interface $\Gamma = \Gamma_1 \bigcup \Gamma_2$, together with the proposed interface discretization.

where $\hat{\mathbf{u}}$ denotes the imposed displacement, and $\mathbf{T}$ the applied traction vector. The nominal pressure p_n, is given by the micro-scale contact interactions predicted by the BEM, and can be qualitatively expressed by:

$$p_\mathrm{n}(g_\mathrm{n}) = \begin{cases} p_\mathrm{n} & \text{if } g_\mathrm{n} > 0, \\ 0, & \text{if } g_\mathrm{n} \leq 0. \end{cases} \tag{2}$$

2 Finite element discretization of the interface at the macro-scale

At the macro-scale, a four nodes zero thickness linear interface element is used for modelling surface interactions. Its kinematics is borrowed from the formulation of interface elements used in non-linear fracture mechanics for cohesive crack growth [2]. The integral expressions for the stiffness operator and the residual vector are approximated via a Gaussian integration, and the values of the contact pressure are evaluated by solving, for each Gauss point, the contact problem between an elastic half plane and a rough surface, exploiting the BEM. To evaluate the normal gap g_n at any point inside the interface element, the nodal displacement vector $\mathbf{d} = (u_1, v_1, \ldots, u_4, v_4)^\mathrm{T}$ must be introduced, collecting the displacements u and v of the four nodes. The relative displacement $\mathbf{g}$ for the nodes 1-4 and 2-3 is given by:

$$\mathbf{g} = -\mathbf{QNLd}, \tag{3}$$

where $\mathbf{L}$ maps the relative displacements, $\mathbf{N}$ interpolates them via linear shape functions over the length of the element and $\mathbf{Q}$ rotates the reference system from the global to the local one. The integral expressions for the stiffness operator and the residual vector are evaluated via a Gaussian quadrature and read:

$$\mathbf{R}_e^{(k)} = -\det J \sum_{i=1}^{2} w_i \mathbf{L}^\mathrm{T}\mathbf{N}^\mathrm{T}\mathbf{Q}^\mathrm{T}\mathbf{p}(x_{\mathrm{g}i}), \qquad \mathbf{K}_e^{(k)} = \det J \sum_{i=1}^{2} w_i \mathbf{L}^\mathrm{T}\mathbf{N}^\mathrm{T}\mathbf{Q}^\mathrm{T}\mathbb{C}(x_{\mathrm{g}i})\mathbf{QNL}, \tag{4}$$

where $w_i = 1$ is the weight, $x_{\mathrm{g}1,2} = \mp 1/\sqrt{3}$ are the positions of the two Gauss Points along the element, $\mathbf{p} = (0, p_\mathrm{n})^\mathrm{T}$ is the interface pressure and $\mathbb{C}$ is the linearised interface constitutive matrix:

$$\mathbb{C} = \begin{bmatrix} 0 & 0 \\ 0 & \dfrac{\partial p_\mathrm{n}}{\partial g_\mathrm{n}} \end{bmatrix} \tag{5}$$

3 Boundary element method for micro-scale interactions

At this stage, the value of p_n at each Gauss Point is computed by solving the normal contact problem of a rigid rough surface indenting an elastic half-plane. The normal displacement at a point of the half-plane

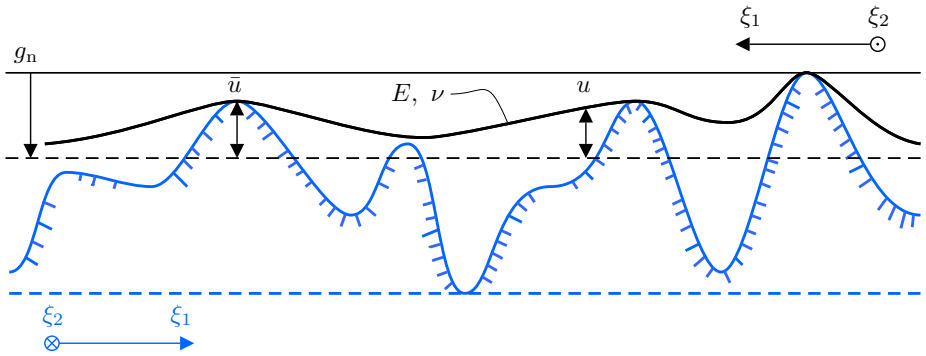

Figure 2. Illustration of the contact problem between a rigid rough surface, solid blue line, and an elastic half plane, for a given far field displacement g_n. The rigid body motion of the half plane is indicated by the dashed black lines, while its deformed boundary by the solid black one.

characterized by a position vector $\boldsymbol{\xi}$ is related to the pressure $p(\boldsymbol{\eta})$ exerted at other points by the following relations:

$$u(\boldsymbol{\xi}) = \int_S H(\boldsymbol{\xi}, \boldsymbol{\eta}) p(\boldsymbol{\eta})\, \mathrm{d}\boldsymbol{\eta}, \tag{6}$$

where $H(\boldsymbol{\xi}, \boldsymbol{\eta})$ is the Green function, representing the displacement at point $u(\boldsymbol{\xi})$ caused by a surface pressure $p(\boldsymbol{\eta})$. For a given far-field displacement g_n, Eq. (6) must be satisfied, together with the unilateral contact constraint [1]:

$$w(\boldsymbol{\xi}, g_\mathrm{n}) \geq 0, \tag{7a}$$
$$p(\boldsymbol{\xi}) \geq 0, \tag{7b}$$
$$w(\boldsymbol{\xi}, g_\mathrm{n}) p(\boldsymbol{\xi}) = 0, \tag{7c}$$

where $w(\boldsymbol{\xi}, g_\mathrm{n}) = u(\boldsymbol{\xi}) - \overline{u}(\boldsymbol{\xi}, g_\mathrm{n})$ and $\overline{u}(\boldsymbol{\xi}, g_\mathrm{n})$ denotes the indentation of the half-space at the points in contact, as shown in Fig. 2. The normal pressure p_n is obtained dividing the total reaction force P by the nominal surface area of the indenter.

4 Multi-scale coupling

Two main different approaches have been explored for performing the coupling between the micro- and the macro-scale. In the first one, which is referred to as FEM-BEM semi-analytical (FBEM-SAN), the normal contact problem at the micro-scale is solved off-line according to BEM, for a sequence of different far-field displacements. The solution of the problem in terms of predicted average contact pressure vs. the imposed far-field displacement is finally fitted with a power-law continuous function of the type:

$$p_\mathrm{n}(g_\mathrm{n}) = a g_\mathrm{n}^b, \tag{8}$$

which provides a closed-form expression for $p_\mathrm{n}(g_\mathrm{n})$ [3]. Its derivative, $\partial p_\mathrm{n}/\partial g_\mathrm{n}$, entering the linearised interface stiffness matrix $\mathbb{C}$, is also available in closed-form. In the second, a full integration of FEM and BEM is proposed and labelled FEM BEM Quasi-Newton (FBEM-QN). The interface finite element has been coded as a user element for the software FEAP, exploiting a Newton-Raphson solution scheme. At each time step and for each Gauss point, the contact pressure $p_\mathrm{n}(g_\mathrm{n})$ and the contact stiffness $\partial p_\mathrm{n}/\partial g_\mathrm{n}$ are computed by calling twice the subroutine based on BEM: the first time p_n is evaluated, the second one a perturbation is applied to compute the normal contact stiffness via a finite difference approximation:

$$\frac{\partial p_\mathrm{n}}{\partial g_\mathrm{n}} \simeq \frac{p_{\mathrm{n},k+1} - p_{\mathrm{n},k}}{g_{\mathrm{n},k+1} - g_{\mathrm{n},k}} \tag{9}$$

where $g_{\mathrm{n,k}}$ is the far-field displacement of the macro-scale model for the current k-th Newton-Raphson iteration, and $g_{\mathrm{n,k+1}} = g_{\mathrm{n,k}} + \Delta g_{\mathrm{n,k}}$ is a small perturbation of its value, for which the pressure values $p_{\mathrm{n,k}}$ and $p_{\mathrm{n,k+1}}$ are computed by BEM.

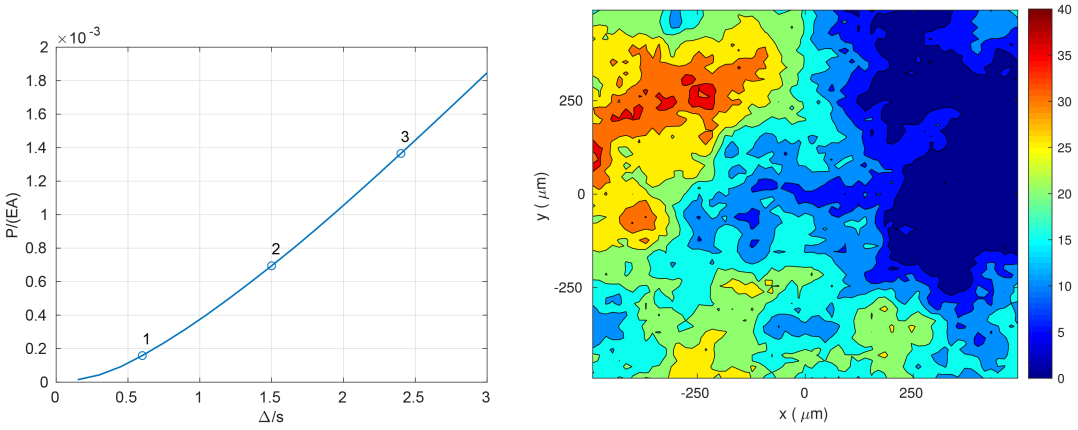

(a) Dimensionless overall reaction force against imposed displacement.

(b) Point 3, $A/A_{\mathrm{n}} = 3.12\%$.

Figure 3. Evolution of the free volume of the real geometry at the micro-scale.

5 Results

The results of a benchmark test involving two stacked blocks in contact, whose interface is discretized by a single interface finite element are shown in Fig. 3 for a given imposed displacement Δ/s linearly increasing between 0 and 3, being s the variance of the height distribution of the rough surface. The scale separation is guaranteed by a ratio between the rigid indenter at the micro-scale and the interface element size at the macro-scale of 0.1. In the contour plot, the ratio between the real contact area A and the nominal one A_{n} is provided. The dark blue islands show the contact area while the deepest valley still not in contact are marked in red.

Acknowledgments

The authors would like to acknowledge funding from the MIUR-DAAD Joint Mobility Program 2017 to the project "Multi-scale modelling of friction for large scale engineering problems". The project has been granted by the Italian Ministry of Education, University and Research (MIUR) and by the Deutscher Akademischer Austausch Dienst (DAAD) through funds of the German Federal Ministry of Education and research (BMBF).

References

[1] A. Bemporad and M. Paggi. Optimization algorithms for the solution of the frictionless normal contact between rough surfaces. *International Journal of Solids and Structures* 69-70 (June 2015). DOI: 10.1016/j.ijsolstr.2015.06.005.

[2] P. Wriggers M. Paggi. A nonlocal cohesive zone model for finite thickness interfaces–Part II: FE implementation and application to polycrystalline materials. *Computational Materials Science* 50.5 (2011), pp. 1634–1643.

[3] M. Paggi and J. R. Barber. Contact conductance of rough surfaces composed of modified RMD patches. *International Journal of Heat and Mass Transfer* 54 (2011), pp. 4664–4672. DOI: 10.1016/j.ijheatmasstransfer.2011.06.011.

[4] G. Zavarise, P. Wriggers, E. Stein, and B.A. Schrefler. Real contact mechanisms and finite element formulation–a coupled thermomechanical approach. *International Journal for Numerical Methods in Engineering* 35 (1992), pp. 767–785.

**Proceedings of the 8th GACM Colloquium on Computational Mechanics
for Young Scientists from Academia and Industry
August 28–30, 2019 in Kassel, Germany**

Multiscale Rubber Friction Homogenization on Rough Surfaces

Felix Hartung[1] and Michael Kaliske * [1]

[1]Institute for Structural Analysis, Technische Universität Dresden, 01062 Dresden

Abstract.

This paper introduces a multiscale approach for friction that considers friction on different length scale. On each scale, a friction homogenization procedure generates the friction feature for the next coarser scale so that a macroscopic friction coefficient is accumulated out of the micro- and mesoscopic friction behavior. Within the multiscale approach, adhesion implemented as non-linear traction-separation law is assumed to act only on microscopic length scales. By using the finite element method (FEM), the sensitivity of the influencing factors, for instance slip velocity and contact pressure, may be investigated. A numerical validation of this approach proves the validity of the homogenization method with respect to the distance of adjacent length scales.

Introduction

Friction, defined as force resisting the relative motion of solid surfaces, fluid layers and material elements sliding against each other, is a complex phenomenon and has a significant importance in daily life. One challenging field of research is associated with tire industry, because tire-pavement interaction affects every driving maneuver. Hence, the substrate structure is characterized by many asperities, it is important to understand the physical background of sliding on different length scales. Friction in general consists of different contributions - hysteresis friction, adhesion, viscous friction and interlocking effects. Both, hysteresis friction due to internal dissipation of the viscoelastic material and adhesion in consequence of molecular bonding to the surface represent the main friction parts. Adhesion as well as hysteresis friction strongly depend on e.g. contact pressure, sliding velocity and temperature conditions. The analytical approaches for multiscale friction of Persson (see among others [1]) and Klüppel/Heinrich (e.g. [2]) are common and show suitable results compared to friction measurements. Numerical models like the multiscale approaches [3], [4] and [5], which base for instance on the finite element method (FEM), give the opportunity to consider additional multi-physical phenomena.

1 Multiscale Approach

1.1 Scale Identification

Due to the different asperities of a rough surface, e.g. asphalt pavement, it is necessary to consider the entire frequency spectrum or length scales. With several surface characterization methods, like the height difference correlation function (see [3] and [5]), the power spectral density function (see [4]) and bandpass filters (see [6]), the frequency spectrum is classified in specific frequency clusters. In contrast to the height difference correlation and power spectral density function, bandpass filters provide the decomposed surface textures for each length scale directly.

*Corresponding author: michael.kaliske@tu-dresden.de

1.2 Adhesion Model

Adhesion describes mainly the molecular bonds between two different surfaces and gives an important contribution to rubber friction. Adhesion behavior can be modeled for instance by a non-linear traction-separation-law with the adhesional stress vector

$$\boldsymbol{\sigma} = (1 - D) \cdot K \cdot \boldsymbol{\delta} \,, \tag{1}$$

that is a function of the relative separation vector $\boldsymbol{\delta}$ between two contact points in normal and two tangential directions, the initial adhesional stiffness K and the damage function

$$D = \frac{G}{G_{tot}} = \frac{1}{G_{tot}} \int_0^{\delta_{max}} \hat{\sigma} \, d\delta \,. \tag{2}$$

In Eq. (2), G and G_{tot} represent the current and total fractal energy, $\delta_{max} = \max(\|\boldsymbol{\delta}\|)$ is the largest separation and $\hat{\sigma} = \|\boldsymbol{\sigma}\|$ stands for the absolute adhesion stress. The adhesion model distinguishes between normal (no contact) and tangential ($\sigma_N = 0$) adhesion. A patch test is shown in Fig. 1a in which a cube with edge length of 1 mm is pressed by $1\,\mathrm{N/mm^2}$ on a rigid surface. Then the upper nodes (5-8) are displaced 0.1 mm along the x-axis (step I). In the next step (II), the same nodes are moved back to the original position. Finally, the upper nodes are lifted 0.1 mm along the z-axis (step III). The time duration of each step is one second. The Coulomb friction coefficient of the rigid surface is 0.5, $K = 100\,\mathrm{N/mm^3}$ and $G_{tot} = 0.01\,\mathrm{N/mm}$.

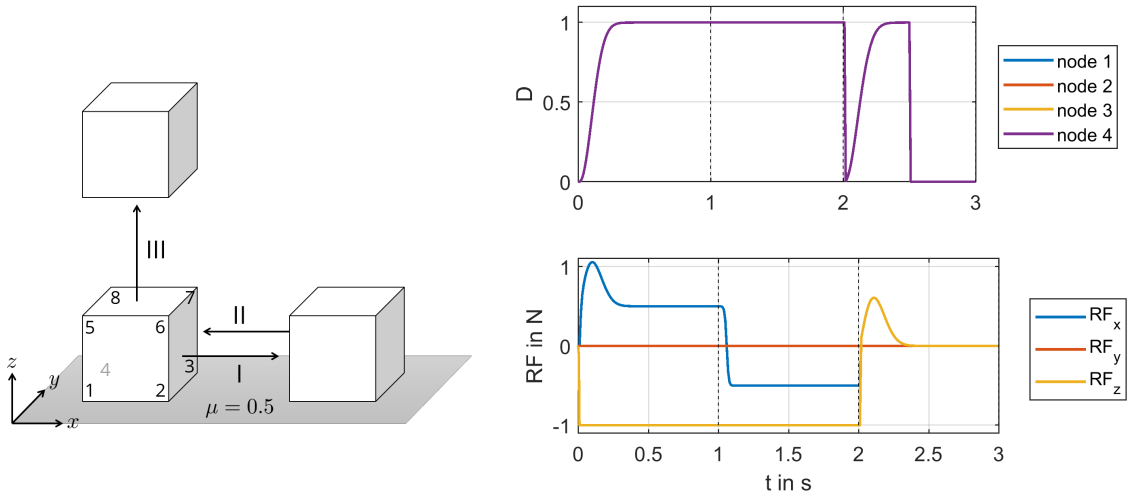

(a) Patch test for adhesion model **(b)** Damage values and reaction forces during patch test

Figure 1. Patch test of adhesion model

Fig. 1b shows the damage evolution of all bottom nodes (1-4) and the resulting reaction forces. At the beginning of step I, both tangential adhesion and friction are acting together until the total fracture energy is reached. In step II, only friction remains, by changing the sign. At the beginning of step III, friction vanishes, because of missing contact, and the adhesion model is switching from tangential to normal adhesion. After the damage value is equal one, no stress in normal direction is transferred, the contact points are released and the damage is reseted to zero to ensure repeated contacts.

1.3 Friction Homogenization

Within the multiscale approach, friction features as result of the deformation of dissipative material as well as adhesion are homogenized on each scale to form a friction law for the next coarser scale. For this purpose, FEM simulations are performed on block level. During every simulation, a rubber block is pressed on a periodic rigid surface that is generated by the scale identification algorithm. Then, the block is sliding over the rough rigid surface with a constant velocity. The ratio of the total horizontal and

vertical reaction forces forms the friction coefficient $\mu(t)$ as a function of time. The time homogenization algorithm of the friction coefficient

$$\mu_{hom} = \frac{1}{t_{tot} - t_{st}} \int_{t_{st}}^{t_{tot}} \mu(t)\, dt \tag{3}$$

only takes the steady state part starting at $t = t_{st}$ into account. In Fig. 2a, t_{st} is reached after six periods. The friction law for the next upper scale is computed by piecewise cubic spline interpolation

$$\mu_{spl}(p, v) = \sum_{i=1}^{n_p} \sum_{j=1}^{n_v} c_{i,j} \cdot (p - \xi_p)^{n_p - i} \cdot (v - \xi_v)^{n_v - j} \tag{4}$$

with $n_p = n_v = 4$, the breakpoints ξ_p and ξ_v (load and velocity conditions in each block simulation) and the spline coefficients $c_{i,j}$. Fig. 2b shows the homogenized friction coefficients at breakpoints ξ_p and ξ_v as well as the spline evaluation (friction map). It has to be ensured that the friction map consists of an

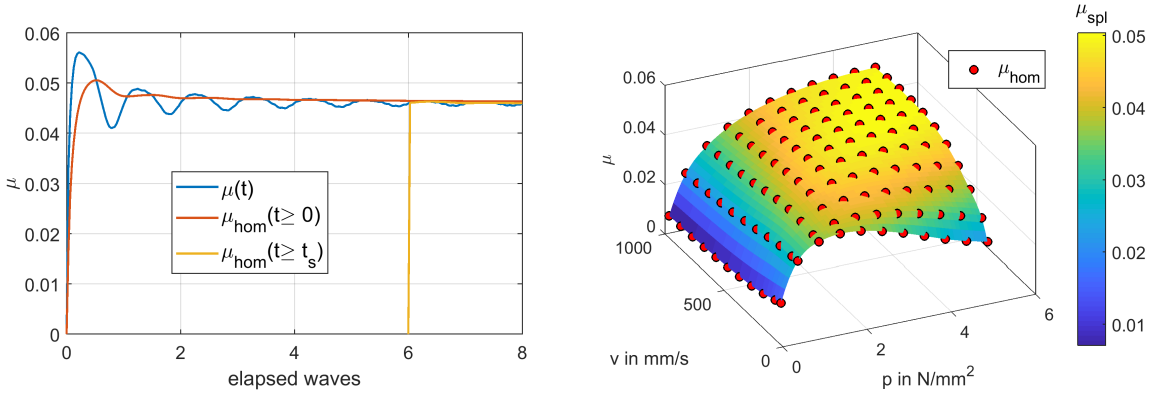

(a) Homogenization of friction coefficient

(b) Friction map created by spline interpolation

Figure 2. Homogenization and friction map

adequate range of pressure and velocity breakpoints so that no friction coefficients outside the fitted map are used during the block simulations on the next coarser length scale. On the microscopic length scale (finest scale), only adhesion is applied as friction law. The computational costs strongly depend on the scale identification algorithm, which influences the mesh generation of the rubber blocks on each length scale. Once the parameters K and G_{tot} are identified, the substrate is recorded in sufficient detail and the rubber material is characterized, this multiscale approach can compute macroscopic friction coefficients (adhesion plus hysteresis friction) as a function of macroscopic pressure and sliding velocity.

2 Numerical Validation of the Multiscale Approach

The multiscale approach is numerically validated by an simple 2D academic example using two different scales represented by sine waves (see also [4]). The macroscopic wave is described by $z_2(x) = 0.075\,\text{mm} \sin(2\,\pi/5\,\text{mm}\, x)$ with a wave length of 5 mm. In contrast to [4], three different microscopic scales $z_{1,I}$, $z_{1,II}$ and $z_{1,III}$ with wave lengths of 0.5 mm, 0.2 mm and 0.1 mm and a ratio between amplitude and wave length of 0.02 are investigated. Figs. 3a, 3b and 3c display the macroscopic friction coefficients of the full models with $z_i(x) = z_{1,i}(x) + z_2(x)$ and $i = I, II, III$ in comparison to the resulting friction coefficients of the macroscopic scale with and without microscopic friction. The macroscopic load and slip velocity are $1\,\text{N/mm}^2$ and $500\,\text{mm/s}$. The material properties as well as the mesh sizes are mainly taken from [4]. Adhesion is neglected in this example. Even for this simple example, the multiscale approach reduces the computational time by 86.76 % using $z_{1,I}$, 97.28 % using $z_{1,II}$ and 99.50 % using $z_{1,III}$ (assumption: all microscale simulation run in parallel) in comparison to the full model simulations. The numerical validation example shows that the quality of the homogenization method depends on the distance between adjacent scales. This should be considered within the scale identification to ensure the validity of the multiscale approach.

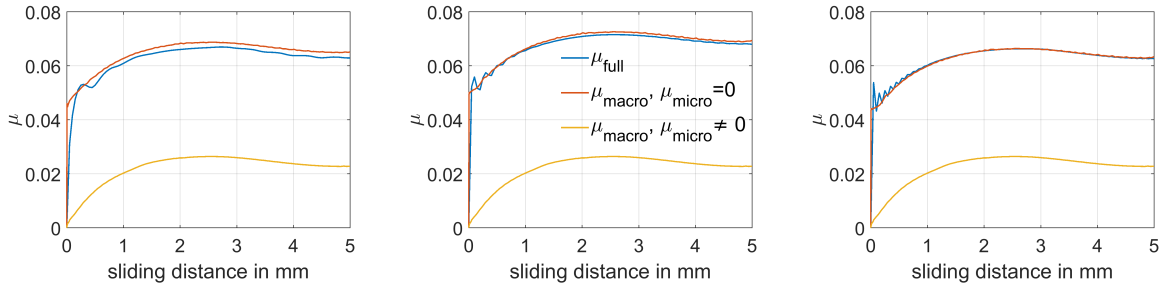

(a) microscopic scale $z_{1,I}$ **(b)** microscopic scale $z_{1,II}$ **(c)** microscopic scale $z_{1,III}$

Figure 3. Numerical validation of the multiscale approach using three different microscopic scales

3 Conclusion

The introduced multiscale approach can consider friction as result of deformation of dissipative materials (hysteresis friction) as well as adhesion on different length scales. By homogenization of friction features on each scale, a friction law as function of pressure and sliding velocity is obtained via piecewise cubic spline interpolation for the corresponding coarser length scale. Note that the scale identification algorithm has to ensure an adequate distance between adjacent length scales to guarantee the validity of the multiscale homogenization procedure as explained in Section 2.

Acknowledgments

The financial support of the German Research Foundation (DFG) of Research Unit FOR 2089 under grant KA 1163/30 is gratefully acknowledged.

References

[1] B.N.J. Persson. Contact mechanics for randomly rough surfaces. *Surface Science Reports* 61 (2006), pp. 201–227. DOI: 10.1016/j.surfrep.2006.04.001.

[2] A. Le Gal and M. Klüppel. Investigation and modelling of rubber stationary friction on rough surfaces. *Journal of Physics: Condensed Matter* 20 (2007), p. 015007. DOI: 10.1088/0953-8984/20/01/015007.

[3] P. Wriggers and J. Reinelt. Multi-scale approach for frictional contact of elastomers on rough rigid surfaces. *Computer Methods in Applied Mechanics and Engineering* 198 (2009), pp. 1996–2008. DOI: 10.1016/j.cma.2008.12.021.

[4] P. Wagner, P. Wriggers, C. Klapproth, C. Prange, and B. Wies. Multiscale FEM approach for hysteresis friction of rubber on rough surfaces. *Computer Methods in Applied Mechanics and Engineering* 296 (2015), pp. 150–168. DOI: 10.1016/j.cma.2015.08.003.

[5] K. Falk, R. Lang, and M. Kaliske. Multiscale Simulation to Determine Rubber Friction on Asphalt Surfaces. *Tire Science and Technology* 44 (2016), pp. 226–247. DOI: 10.2346/tire.16.440401.

[6] P. Wagner, P. Wriggers, L. Veltmaat, H. Clasen, C. Prange, and B. Wies. Numerical multiscale modelling and experimental validation of low speed rubber friction on rough road surfaces including hysteretic and adhesive effects. *Tribology International* 111 (2017), pp. 243–253. DOI: 10.1016/j.triboint.2017.03.015.

**Proceedings of the 8th GACM Colloquium on Computational Mechanics
for Young Scientists from Academia and Industry
August 28–30, 2019 in Kassel, Germany**

An unbiased self-contact formulation for explicit FEA stabilized by the bipenalty method

Ján Kopačka*[1], Dušan Gabriel[1] and Radek Kolman[1]

[1]Institute of Thermomechanics of the Czech Academy of Sciences,Dolejškova 1402/5, 182 00 Praha 8, Czech Republic

Abstract. In the explicit finite element analysis (FEA), contact boundary conditions are often enforced by the penalty method. However, it is well known that the penalty parameter negatively affects the size of the critical time step of the explicit time integration scheme. A remedy to this issue could provide the bipenalty method. Recently, promising results for 1D contact-impact problems have confirmed this idea. Therefore, further development and testing for higher spatial dimensions followed. The objective of this contribution is to present the energy conservation properties of the bipenalty method and thus to prove the suitability of this approach for solving the explicit FEA contact-impact problems. To this end, a symmetry preserving contact algorithm has been modified to consider self-contact. Several numerical examples will be presented to demonstrate the performance of the proposed contact algorithm.

Introduction

Computational analysis of fast contact-impact problems, such as drop tests of mobile or other devices, crashworthiness of vehicles, or bird aircraft strike hazard is most often performed by the explicit finite element method. Contact constraints are usually enforced by a contact-impact algorithm based on the penalty method. The advantage of this approach is a simple implementation with the possibility of parallelization. The disadvantage is then only the conditional stability of explicit time integration, which dictates the maximum size of the time step. Moreover, the penalty method used to enforce the contact constraints deteriorates the stability of the explicit time integration by increasing the maximum natural frequency of the system. It is evident from the physical interpretation of the penalty parameter, which can be understood as a spring that acts in the normal direction at the contact interface when penetration occurs. The size of penetration is inversely proportional to the stiffness of the penalty spring. The higher the stiffness of the spring, the smaller the penetration. Theoretically, zero penetration can be obtained for infinitely high stiffness. In numerical practice, however, the infinite value cannot be approached. The high value of the penalty parameter leads to the poor conditionality of the linear system of equations for implicit methods. For explicit calculation, it increases the maximum eigenfrequency of the system and thus reduces the critical time step.

An alternative that eliminates the described difficulties in explicit dynamics is the so-called bipenalty method [1]. The main idea is to penalize not only potential energy but also kinetic energ. It leads not only to the introduction of the stiffness penalty but also the mass penalty parameter. By tuning their mutual ratio, it is possible to influence whether and how much the maximum natural frequency will increase. Such a ratio of penalty parameters corresponds to the non-penalized system is called a critical penalty ratio [4]. The bipenalty method was extended to systems with an arbitrary set of multipoint constraints [5]. A detailed one-dimensional study of stability and reflection-transmission properties of the bipenalty method in contact-impact problems was performed in [6]. The bipenalty method thus appears to be a valuable improvement to the standard penalties method.

In this paper, the bipenalty method will be combined with a symmetry-preserving contact formulation [3] and used to solve a multidimensional impact problem. The potential of the proposed unbiased contact-impact formulation to address self-contact tasks will be emphasized.

*Corresponding author: kopacka@it.cas.cz ORCID iD: 0000-0002-2975-8347

1 Contact formulation

The basis for the discretization of a problem described by partial differential equations by the finite element method is its formulation in a weak sense. The description of the contact formulation, therefore, begins with a weak form of the balance of linear momentum which can be formulated as follows: in every time instance, t, find the displacement field, $\boldsymbol{u}$, from some suitably chosen function space, $\mathcal{U}$, which for all test functions, $\delta\boldsymbol{v}$, from the selected test functions space, $\mathcal{V}$, satisfies

$$\sum_{s=1}^{2}\left\{\int_{\Omega_0^{(s)}}\delta\boldsymbol{v}^{(s)}\cdot\rho\ddot{\boldsymbol{u}}^{(s)}\,\mathrm{d}V+\int_{\Omega_0^{(s)}}\nabla\delta\boldsymbol{v}^{(s)}:\boldsymbol{P}^{(s)}\,\mathrm{d}V-\int_{\Gamma_\mathrm{c}^{(s)}}\delta\boldsymbol{v}^{(s)}\cdot\boldsymbol{T}_\mathrm{c}^{(s)}\,\mathrm{d}S\right.$$
$$\left.-\int_{\Gamma_\mathrm{D}^{(s)}}\delta\boldsymbol{v}^{(s)}\cdot\boldsymbol{T}^{(s)}\,\mathrm{d}S-\int_{\partial\Omega_0^{(s)}}\delta\boldsymbol{v}^{(s)}\cdot\boldsymbol{b}^{(s)}\,\mathrm{d}V\right\}=0 \tag{1}$$

where Ω_0 is the domain representing the initial configuration, ρ is the density, $\boldsymbol{u}$ is the displacement field, $\boldsymbol{P}$ it the first Piola-Kirchhoff stress tensor, $\boldsymbol{T}$ is the Piola traction vector, $\boldsymbol{T}_\mathrm{c}$ is the Piola contact traction vector, and $\boldsymbol{b}$ is the vector of volume forces. Further, $\Gamma_\mathrm{c}^{(s)}$ and $\Gamma_\mathrm{N}^{(s)}$ denote contact and Neumann boundary, respectively. Superimposed dots indicate time derivatives. The upper index, s, in round brackets denotes the index of body.

In what follows, the attention will be paid only to the contact term which expresses the virtual power of the contact forces

$$\delta\mathrm{P}_\mathrm{cont}:=-\int_{\Gamma_\mathrm{c}}\delta\boldsymbol{v}\cdot\boldsymbol{T}_\mathrm{c}\,\mathrm{d}S \tag{2}$$

where $\Gamma_\mathrm{c}=\bigcup_s\Gamma_\mathrm{c}^{(s)}$. One may notice that this term has the same structure as the Neumann boundary condition. However, there is one difference, neither the contact traction vector nor the contact boundary is known in advance and as such are part of the solution. It leads to an optimization constrained problem. The penalty method transforms this constrained optimization problem into a series of unconstrained ones by penalizing the constraints, which at the end leads to the regularization of the contact traction vector. In particular case of bipenalty method, the contact traction vector has the form

$$\boldsymbol{T}_\mathrm{c}=\left(\epsilon_\mathrm{s}\left\langle g_\mathrm{N}\right\rangle+\epsilon_\mathrm{m}H\left(g_\mathrm{N}\right)\ddot{g}_\mathrm{N}\right)\boldsymbol{n} \tag{3}$$

Notice that for the sake of simplicity of the presentation, only frictionless case is considered. Here, ϵ_s and ϵ_m are the stiffness and mass penalty parameters, respectively, $\boldsymbol{n}$ is the normal vector, $H(\bullet)$ is the Heaviside step function, and $\langle\bullet\rangle:=(\bullet+|\bullet|)/2$ are the Macaulay brackets representing the ramp function, which return zero if the operand is negative and the operand itself otherwise. Finally, g_N is the normal gap function defined as $g_\mathrm{N}:=-\left(\boldsymbol{x}_\mathrm{m}-\boldsymbol{x}\right)\cdot\boldsymbol{n}$, which for a point $\boldsymbol{x}$ returns the signed distance from the closest point $\boldsymbol{x}_\mathrm{m}$ in the direction of $\boldsymbol{n}$.

1.1 Spatial discretization

The spatial discretization is performed with the aid of the finite element method. Standard procedures lead to the system of an ordinary differential equation (ODE) in time

$$\left[\mathbf{M}+\mathbf{M}_\mathrm{cont}\right]\ddot{\mathbf{d}}(t)+\mathbf{F}_\mathrm{inter}\left(\mathbf{d}(t)\right)+\mathbf{F}_\mathrm{cont}\left(\mathbf{d}(t)\right)-\mathbf{F}_\mathrm{extern}(t)=\mathbf{0} \tag{4}$$

where $\mathbf{M}$ is the mass matrix, $\mathbf{M}_\mathrm{cont}$ is the mass matrix due to contact inertia, $\mathbf{d}$ is the vector of equivalent nodal displacements, and $\mathbf{F}_\mathrm{inter}$, $\mathbf{F}_\mathrm{extern}$, $\mathbf{F}_\mathrm{cont}$ are the internal, external, contact equivalent nodal forces, respectively. Again, at this place, the attention will be paid only to the contact terms. They are assembled from the local counterparts

$$\mathbf{F}_\mathrm{cont}^e=-\int_{\Gamma_\mathrm{c}^e}\epsilon_\mathrm{m}\left\langle g_\mathrm{N}\right\rangle\mathbf{G}_\mathrm{N}\,\mathrm{d}S \tag{5}$$

$$\mathbf{M}^e_{\text{cont}} = \int_{\Gamma^e_c} \epsilon_{\text{m}} H\left(g_{\text{N}}\right) \mathbf{G}_{\text{N}} \left[\begin{array}{cc} \mathbf{G}^{\text{T}}_{\text{Nm}} & -\mathbf{G}^{\text{T}}_{\text{N}} \end{array} \right] \text{d}S \tag{6}$$

where $\mathbf{G}_{\text{N}} := \mathbf{N}\mathbf{n}$ and $\mathbf{G}_{\text{Nm}} := \mathbf{N}_{\text{m}}\mathbf{n}$. Here, matrices $\mathbf{N}$ and $\mathbf{N}_{\text{m}}$ consist of shape functions, N_a, evaluated at the integration points and their closest point projections, $\boldsymbol{x}_{\text{m}}$, respectively. In particular $\mathbf{N} := \left[\begin{array}{ccc} N_1\mathbf{I}_{n_{\text{sd}}} & \cdots & N_{n_{\text{nod}}}\mathbf{I}_{n_{\text{sd}}} \end{array} \right]^{\text{T}}$, where n_{nod} is the number of nodal points of the element, n_{sd} indicates number of spatial dimensions, and $\mathbf{I}_{n_{\text{sd}}}$ is the n_{sd}-dimensional identity matrix.

1.2 Time discretization

The purpose of the time discretization is to transform the ODE system (4) into the system of algebraic equations by means of an integration scheme. In this work, the central difference method (CDM) is employed. Its integration scheme is: Assume that the displacement vector $\mathbf{d}^n$ at time step t^n and half-step velocity vector $\mathbf{v}^{n-1/2}$ are known. Then one can calculate the acceleration

$$\mathbf{a}^n = \left(\mathbf{M} + \mathbf{M}_{\text{cont}}\right)^{-1} \left\{\mathbf{F}_{\text{inter}}\left(\mathbf{d}^n\right) + \mathbf{F}_{\text{cont}}\left(\mathbf{d}^n\right) - \mathbf{F}_{\text{extern}}(t^n)\right\} \tag{7}$$

and update the velocity and displacement.

$$\mathbf{v}^{n+1/2} = \mathbf{v}^{n-1/2} + \Delta t \mathbf{a}^n, \qquad \mathbf{d}^{n+1} = \mathbf{d}^n + \Delta t \mathbf{v}^{n+1/2} \tag{8}$$

As already mentioned, this time integration scheme is conditionally stable. The stability analysis implies the condition on the stable time step

$$\Delta t \leq \frac{2}{\omega_{\max}} \tag{9}$$

where $\omega_{\max}$ is the maximal angular eigenfrequency of the system.

2 Numerical example

The performance of the method will be presented by means of a numerical example of longitudinal impact of two thick plates [2]. The geometry setting of the problem are depicted in Figure 1. The dimensions are $2d = 5\,\text{mm}$, and $l = 2.5\,\text{mm}$. The linear elasticity is considered with material parameters: $E = 2.1e5\,\text{MPa}$, $\nu = 0.3$, and $\rho = 7800\,\text{kg/m}^3$. The inital velocity is $v_0 = 1\,\text{m/s}$ and the stiffness penalty parametr was set to $\epsilon_{\text{s}} = 1e16\,\text{MPa/m}$.

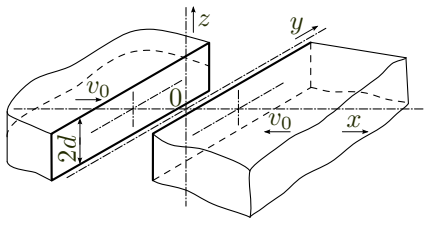

Figure 1. Longitudinal impact of two thick plates: geometry setting.

Figure 2 shows the dimensionless stress component, $\sigma^*_{\text{X}} = c_1\sigma_{\text{X}}/(\Lambda v_0)$, in the direction of the impact axis at dimensionless time $t^* = c_1 t/d = 0.56$, where $c_1 = \sqrt{(\Lambda + 2\mu)/\rho}$ is the speed of the longitudinal wave, and Λ, μ are Lamé's constants. In the left part of Figure 2, one can see the convergence of the solution with the mesh refinement for the time integration with the critical time step. It can be seen that while the standard penalty method would diverge, the bipenalty method is stable. In the right part of Figure 2, one can see the convergence of the solution with the refinement of the time step. One can also notice the well-known fact that the oscillations caused by the spatial dispersion of the FEM mesh are minimal for integration with the critical time step. Provided that the linear elements with the lumped mass matrix are used.

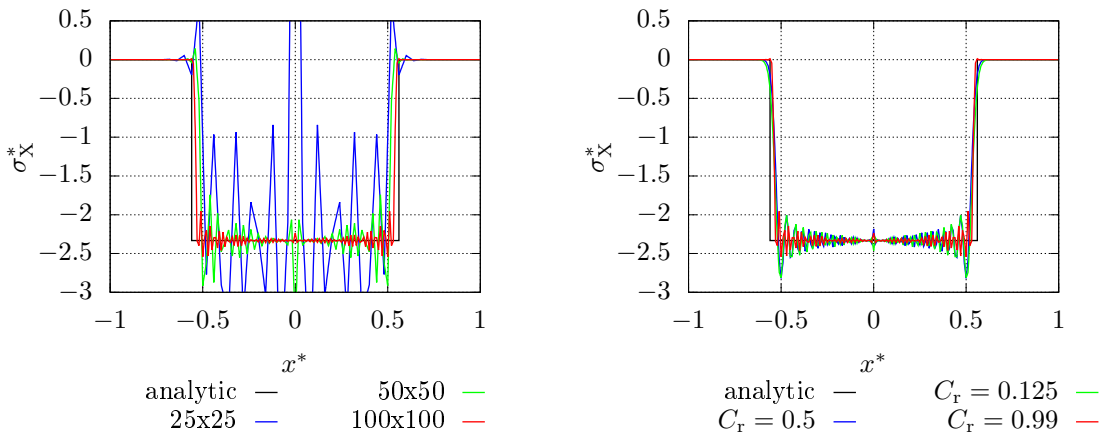

Figure 2. The spatial (left) and temporal (right) convergence of the dimensionless stress component in the direction of the impact axis.

3 Conclusions

In this paper, a symmetry-preserving contact formulation suitable for self-contact problems was presented. Contact constraints were enforced by the bipenalty method, and the central difference method was used for time integration. A numerical example of the longitudinal impact of two thick plates was considered. It was shown that by using the bipenalty method, it is possible to stably integrate even with a critical time step corresponding to a non-penalized system.

Acknowledgments

The work of Radek Kolman and Ján Kopačka was supported by the grant project No. 19-04956S of the Czech Science Foundation (CSF) within institutional support RVO:61388998 and the work of all three authors was supported by the Centre of Excellence for Nonlinear Dynamic Behaviour of Advanced Materials in Engineering CZ.02.1.01/0.0/0.0/15_003/0000493 (Excellent Research Teams) in the framework of Operational Programme Research, Development and Education.

References

[1] Harm Askes, Miguel Caramés-Saddler, and Antonio Rodríguez-Ferran. Bipenalty method for time domain computational dynamics. *Proceedings of the Royal Society A* 466 (2010), pp. 1389–1408. DOI: 10.1098/rspa.2009.0350.

[2] Rudolf Brepta and František Valeš. Longitudinal impact of bodies. *Acta technica ČSAV* 5 (1987), pp. 575–602.

[3] Dušan Gabriel, Jiří Plešek, and Miran Ulbin. Symmetry preserving algorithm for large displacement frictionless contact by the pre-discretization penalty method. *International Journal for Numerical Methods in Engineering* 61.15 (2004), pp. 2615–2638. ISSN: 00295981. DOI: 10.1002/nme.1173.

[4] Jack Hetherington, Antonio Rodríguez-Ferran, and Harm Askes. A new bipenalty formulation for ensuring time step stability in time domain computational dynamics. *International Journal for Numerical Methods in Engineering* 90 (2012), pp. 269–286. DOI: 10.1002/nme.3314.

[5] Jack Hetherington, Antonio Rodríguez-Ferran, and Harm Askes. The bipenalty method for arbitrary multipoint constraints. *International Journal for Numerical Methods in Engineering* 93 (2013), pp. 465–482. DOI: 10.1002/nme.4389.

[6] Ján Kopačka, Anton Tkachuk, Dušan Gabriel, Radek Kolman, Manfred Bischoff, and Jiří Plešek. On stability and reflection-transmission analysis of the bipenalty method in contact-impact problems: A one-dimensional, homogeneous case study. *International Journal for Numerical Methods in Engineering* 113.10 (2018), pp. 1607–1629. ISSN: 00295981. DOI: 10.1002/nme.5712. URL: http://doi.wiley.com/10.1002/nme.5712.

**Proceedings of the 8th GACM Colloquium on Computational Mechanics
for Young Scientists from Academia and Industry
August 28–30, 2019 in Kassel, Germany**

Extended Mortar Methods for Isogeometric Analysis

Melanie Krüger* [1] and Christian Hesch[1]

[1]Chair of Computational Mechanics, University of Siegen

Abstract. In the present contribution, we first introduce a framework for large deformation porous-ductile fracture in thermo-elasto-plastic solids based on a modified Gurson-Tvergaard-Needelmann type plasticity model. Since higher-order phase-field models require at least C^1 continuity, NURBS based shape functions are applied for the spatial discretization. Due to the tensor-product structure of the underlying spline bases, severe restrictions in the geometry lead to a multi-patch environment. In this context, we introduce a novel methodology, to enforce interface conditions preserving higher-order continuity across the in general non-conform interface, stated as extended Mortar method.

Introduction

The analysis of crack initiation and propagation in ductile materials plays an important role in predicting failure mechanisms for various engineering applications. A large number of phenomenological and micromechanical approaches exists in literature for the modeling of ductile fracture. Gurson developed a macroscopic yield surface by homogenization of a porous RVE with assumed rigid plastic flow, that degrades with increasing void fraction. This approach has been further modified by Tvergaard and Needlemann to account for damage growth, nucleation and coalescence effects. Here, we further extend the coupled problem towards finite strain thermo-porous-plasticity based on the phase-field approach. Therefore, a multiplicative triple split of the deformation gradient, previously introduced in Dittmann et al. [1], is presented along with a higher-order phase-field formulation and a gradient.

A primal approach in terms of constrained basis functions reflecting weakly continuity up to maximal regularity for multi-patch geometries without crosspoints has been introduced in [2, 6] for problems in structural mechanics such as linear elasticity and plate models. This formulation allows in a natural way for a primal-dual reformulation in terms of a Lagrange multiplier. For this specific condition, we will demonstrate different approaches to enforce the constraints, either using a basis modification approach, a null-space reduction scheme as well as the explicit usage of Lagrange multipliers. Afterwards, we demonstrate how to deal with crosspoints in such multi-patch geometries, see [3]. This modification is constructed in such a way, that we decouple the Lagrange multipliers at the crosspoint to avoid a global coupling condition across all interfaces. Moreover, we recast the underlying B-Splines such that they preserve the higher-order best approximation property across the interface and the crosspoint. Eventually, we present actual developments in the context of Mortar methodology applied to contact problems. Therefore, detailed investigation on thermomechanical porous ductile fracture problems will demonstrate the general applicability, accuracy and capability of the proposed approach, see [5].

1 Governing equations

In this section, we summarize the fundamental equations of the thermo-elasto-plastic solid including porous ductile fracture. The underlying, three-dimensional ($d = 3$) system leads to a multi-field setting with seven fields

$$\{\boldsymbol{\varphi}, \mathfrak{s}, \theta, \alpha, r^{\mathrm{p}}, \boldsymbol{F}^{\mathrm{p}}, f\}\,, \tag{1}$$

*Corresponding author: melanie.krueger@uni-siegen.de

which are the deformation map, the crack phase-field, the absolute temperature and the four plastic fields, which are the equivalent plastic strain, its dual hardening force, the plastic deformation gradient and the void volume fraction. Here, the void volume fraction is defined as

$$f = 1 - \frac{1 - f_0}{J^{\mathrm{p}}} \tag{2}$$

and is assumed as a micro-mechanically motivated damage variable, related to the plastic deformation gradient through its determinant J^{p}. f_0 is the initial void volume fraction. The theory of Griffith for brittle fracture [4] has to be modified to account for ductile behavior, i.e. the critical local fracture energy density is defined as $g_{\mathrm{c}} := g_{\mathrm{c}}(\alpha)$. To implement the theory within a finite element framework, we define a regularized crack surface functional, for the modeling of the crack, which regularizes the sharp crack interface Γ_0^{f} with a specific regularization profile γ

$$\int_{\Gamma_0^{\mathrm{f}}} g_{\mathrm{c}}(\alpha)\,\mathrm{d}\Gamma \approx \int_{\mathcal{B}_0} g_{\mathrm{c}}(\alpha)\,\gamma(\mathfrak{s}, \nabla\mathfrak{s}, \Delta\mathfrak{s})\,\mathrm{d}V = \int_{\mathcal{B}_0} \Psi^{\mathrm{f}}(\mathfrak{s}, \nabla\mathfrak{s}, \Delta\mathfrak{s}, \alpha)\,\mathrm{d}V\,. \tag{3}$$

This regularization yields the crack-density function Ψ^{f}. The deformation gradient $\boldsymbol{F} = \boldsymbol{F}^{\mathrm{e}}\,\boldsymbol{F}^{\mathrm{p}}$ and its determinant $J = J^{\mathrm{e}}\,J^{\mathrm{p}}$ are decomposed multiplicatively into elastic and plastic parts. Moreover, the fracture insensitive isochoric and volumetric parts are given by

$$\tilde{\bar{\boldsymbol{F}}}^{\mathrm{e}} = \sum_a \left[(J^{\mathrm{e}})^{-1/d}\lambda_a^{\mathrm{e}}\right]^{g(\mathfrak{s})} \boldsymbol{n}_a \otimes \boldsymbol{N}_a \quad \text{and} \quad \tilde{J}^{\mathrm{e}} = \begin{cases} (J^{\mathrm{e}})^{g(\mathfrak{s})} & \text{if} \quad J^{\mathrm{e}} > 1 \\ J^{\mathrm{e}} & \text{else} \end{cases}, \tag{4}$$

postulating that fracture requires a local state of tensile/shear deformation. λ_a^e are the elastic principal stretches, $g(\mathfrak{s})$ is a polynomial degradation function and $\boldsymbol{n}_a$ and $\boldsymbol{N}_a$ are the principal directions of the left and right stretch tensors.

The whole energy density with elastic, thermal, plastic and fracture contributions reads

$$\Psi := \Psi^{\mathrm{e}}(\boldsymbol{F}, \boldsymbol{F}^{\mathrm{p}}, \mathfrak{s}, \theta) + \Psi^{\theta}(\theta) + \Psi^{\mathrm{p}}(\alpha, \nabla\alpha, \theta) + \Psi^{\mathrm{f}}(\mathfrak{s}, \nabla\mathfrak{s}, \Delta\mathfrak{s}, \alpha)\,, \tag{5}$$

where the different dependencies are indicated.

Concerning the plastic material behavior, we postulate a modified Gurson model for porous plasticity in terms of the Kirchhoff stresses $\boldsymbol{\tau}$ and the dissipative resistance force r^{p}

$$\Phi^{\mathrm{p}}(\boldsymbol{\tau}, r^{\mathrm{p}}) = \frac{\sigma_{\mathrm{eq}}^2}{{r^{\mathrm{p}}}^2} + 2\,q_1\,f\cosh\left(\frac{3}{2}\,q_2\,\frac{p}{r^{\mathrm{p}}}\right) - \left(1 + [q_1\,f]^2\right) \tag{6}$$

Here, the von Mises equivalent stress is represented by $\sigma_{\mathrm{eq}} = \sqrt{3/2}\,\|\boldsymbol{\tau}_{\mathrm{dev}}/J\|$ and the local pressure by $p = \frac{1}{3}\mathrm{tr}[\boldsymbol{\tau}/J]$. Moreover, q_1 and q_2 are fitting parameters.

For the heat transfer, Duhamel's law of heat conduction is used and modified by the crack phase-field. Here, the material thermal conductivity tensor is given by

$$\boldsymbol{K}(\boldsymbol{F}, \mathfrak{s}, \theta) := \left\{K_0\left[1 - w_{\mathrm{K}}\,(\theta - \theta_0)\right](1 - \mathfrak{s}) + K^{\mathrm{conv}}\,\mathfrak{s}\right\}\boldsymbol{C}^{-1}\,. \tag{7}$$

In case of fracture, we achieve a pure convection problem and the heat transfer depends on the crack opening width. w_{K} is a thermal softening parameter, K_0 is a conductivity parameter related to the reference temperature, K^{conv} is a convection parameter and $\boldsymbol{C} = \boldsymbol{F}^{\mathrm{T}}\boldsymbol{F}$ denotes the right Cauchy-Green tensor.

2 Discretization in space

Concerning the spatial discretization, displacement based finite element methods are applied subdividing the domain $\mathcal{B}_0$ into a finite set of non-overlapping elements $e \in \mathbb{E}$, such that

$$\mathcal{B}_0 \approx \mathcal{B}_0^{\mathrm{h}} = \bigcup_{e \in \mathbb{E}} \mathcal{B}_0^e\,. \tag{8}$$

Since the two fields of the plastic deformation gradient and the void volume fraction are locally solved, we have five fields for the spatial approximation. These fields are approximated differently. The approximations of the solution field of $\{\boldsymbol{\varphi},\, \mathfrak{s},\, \theta\}$ and their variations read

$$(\bullet)^{\mathrm{h}} = \sum_{A\in\mathcal{I}} R^A (\bullet)_A, \quad \delta(\bullet)^{\mathrm{h}} = \sum_{A\in\mathcal{I}} R^A \delta(\bullet)_A\,, \tag{9}$$

Therein, we use the same spline based approximations for all three fields, where the global shape functions $R^A : \mathcal{B}_0 \to \mathbb{R}$ are associated with control points $A \in \mathcal{I} = \{1, \ldots, \mathfrak{N}\}$. With regard to the continuity requirement of $\mathfrak{s}^{\mathrm{h}}, \delta\mathfrak{s}^{\mathrm{h}} \in \mathcal{H}^2(\mathcal{B}_0)$, we make use of quadratic NURBS based shape functions

$$R^A := R^{\boldsymbol{i}}(\boldsymbol{\xi}) = \frac{\prod_{a=1}^{d} B^{i_a}(\xi^a)\, w_{\boldsymbol{i}}}{\sum_{\boldsymbol{j}} \prod_{a=1}^{d} B^{j_a}(\xi^a)\, w_{\boldsymbol{j}}}\,, \tag{10}$$

where B^{i_a} are univariate non-rational B-Splines and $w_{\boldsymbol{j}}$ are corresponding NURBS weights. Note that different shape functions are used for $\{\alpha,\, r^{\mathrm{p}}\}$ to avoid stability issues, see [1] for details.

3 Extended mortar method

Concerning a general multi-patch situation with non-conformingly discretized subdomains $i \in \{1, \ldots, N\}$, the C^n coupling conditions read

$$\mathcal{L}(u_{\mathrm{h}}^{(i)} - u_{\mathrm{h}}^{(j)}) = \mathbf{0} \quad \text{on} \quad \partial\mathcal{B}_{\mathrm{h}}^{(i,j)} \quad \text{with} \quad i \neq j, \tag{11}$$

where $\partial\mathcal{B}_{\mathrm{h}}^{(i,j)} = \partial\mathcal{B}_{\mathrm{h}}^{(i)} \cap \partial\mathcal{B}_{\mathrm{h}}^{(j)}$ denotes the common interface of two subdomains and the linear operator $\mathcal{L}$ represents the respective coupling conditions[†]. Now, to enforce these conditions we construct a saddle point system by introducing a Lagrange multiplier field on the finer resolved subdomain as

$$\lambda_{\mathrm{h}}^{(i)} = \sum_{A=1}^{\bar{\mathfrak{n}}^{(i)}} R^{A,(i)}(\bar{\boldsymbol{\xi}}^{(i)})\, \lambda_A^{(i)}, \tag{12}$$

where $R^{A,(i)}(\bar{\boldsymbol{\xi}}^{(i)})$ are the B-spline based shape functions of the corresponding subdomain evaluated at the interface $\partial\mathcal{B}_{\mathrm{h}}^{(i,j)}$. Here the number $\bar{\mathfrak{n}}^{(i)}$ of involved Lagrange multipliers depends not only on the mesh of the slave side but also on the order of the applied continuity. Applying a classical mortar approach for the implementation of C^0 continuity, the mortar constraint for node $A = 1, \ldots, \bar{\mathfrak{n}}^{(i)}$ at the interface $\partial\mathcal{B}_{\mathrm{h}}^{(i,j)}$ reads as

$$\Phi_0^{A,(i,j)} := h_A^{2\,(1-m)} \int_{\partial\mathcal{B}_{\mathrm{h}}^{(i,j)}} \left(R^{A,(i)}(\bar{\boldsymbol{\xi}}^{(i)})\, R^{B,(i)}(\bar{\boldsymbol{\xi}}^{(i)})\, u_B^{(i)} - R^{A,(i)}(\bar{\boldsymbol{\xi}}^{(i)})\, R^{C,(j)}(\bar{\boldsymbol{\xi}}^{(j)})\, u_C^{(j)} \right) \mathrm{d}\Gamma, \tag{13}$$

which we enforce such that $\Phi_0^{A,(i,j)} = 0$. Here, $2\,m$ is the order of the considered differential equation, i.e., for a second order elliptic equation $m = 1$ the scaling factor is equal to one. The parametric B-spline coordinates $\bar{\boldsymbol{\xi}}^{(j)}$ are determined by a projection defined for a given $\bar{\boldsymbol{\xi}}^{(i)}$ as minimization problem

$$\|\bar{\boldsymbol{X}}_{\mathrm{h}}^{(i)}(\boldsymbol{\xi}^{(i)}) - \bar{\boldsymbol{X}}_{\mathrm{h}}^{(j)}(\boldsymbol{\xi}^{(j)})\| = \min_{\boldsymbol{\xi}\in\partial\bar{\mathcal{B}}_{\mathrm{h}}^{(j)}} \|\bar{\boldsymbol{X}}_{\mathrm{h}}^{(i)}(\boldsymbol{\xi}^{(i)}) - \bar{\boldsymbol{X}}_{\mathrm{h}}^{(j)}(\boldsymbol{\xi})\|, \tag{14}$$

where $\bar{\boldsymbol{X}}_{\mathrm{h}}^{(i)}$ and $\bar{\boldsymbol{X}}_{\mathrm{h}}^{(j)}$ represent the isoparametric geometry representation of the interface. It is obvious that only basis functions having a non-zero trace enter.

[†]E.g. $\mathcal{L}u = u$ for a C^0 coupling, $\mathcal{L}u = [u, u_{,1}, u_{,2}]^\top$ for a C^1 coupling and $\mathcal{L}u = [u, u_{,1}, u_{,2}, u_{,11}, u_{,22}, u_{,12}]^\top$ for a C^2 coupling of two-dimensional subdomains. Here and in the following $(\cdot)_{,i}$ denotes the first partial derivative with respect the ith-direction of the physical space and $(\cdot)_{,ij}$ denotes the corresponding second partial derivative.

Next, for an extension of the mortar approach to preserve C^1 continuity across the interface the mortar constraint at node A can be written as

$$\Phi_1^{A,(i,j)} := \Phi_0^{A,(i,j)} + h_A^{2(2-m)} \sum_{k=1}^{d} \int_{\partial \mathcal{B}_{\mathrm{h}}^{(i,j)}} \Big(R_{,k}^{A,(i)}(\bar{\boldsymbol{\xi}}^{(i)})\, R_{,k}^{B,(i)}(\bar{\boldsymbol{\xi}}^{(i)})\, u_B^{(i)} - R_{,k}^{A,(i)}(\bar{\boldsymbol{\xi}}^{(i)})\, R_{,k}^{C,(j)}(\bar{\boldsymbol{\xi}}^{(j)})\, u_C^{(j)} \Big) \mathrm{d}\Gamma \tag{15}$$

again enforced such that $\Phi_1^{A,(i,j)} = 0$. Here the scaling factor is equal to one for a fourth order equation whereas the mesh size parameter h_A has a negative power for sixth-order equations and a positive power for second order equations. To guarantee C^2-continuity weakly, we require for each node A

$$\Phi_2^{A,(i,j)} := \Phi_0^{A,(i,j)} + \Phi_1^{A,(i,j)} + h_A^{2(3-m)} \sum_{\substack{k,l=1 \\ k \geq l}}^{d} \int_{\partial \mathcal{B}_{\mathrm{h}}^{(i,j)}} \Big(R_{,kl}^{A,(i)}(\bar{\boldsymbol{\xi}}^{(i)})\, R_{,kl}^{B,(i)}(\bar{\boldsymbol{\xi}}^{(i)})\, u_B^{(i)} - R_{,kl}^{A,(i)}(\bar{\boldsymbol{\xi}}^{(i)})\, R_{,kl}^{C,(j)}(\bar{\boldsymbol{\xi}}^{(j)})\, u_C^{(j)} \Big)\, \mathrm{d}\Gamma, \tag{16}$$

where we enforce $\Phi_2^{A,(i,j)} = 0$. For sixth-order equations the weak C^2-continuity is mandatory. In theory there is no limitation of this approach and it can be naturally extended to C^n-continuity, $n > 2$.

4 Contact mechanics

Assuming two bodies in a contact situation, the boundaries are no longer predetermined as usual for domain decomposition problems. Moreover, the Lagrange multiplier field represents the Piola traction $\boldsymbol{t}^{(i)}$ associated with the contact surface $\partial \mathcal{B}_0^{(i),\mathrm{c}}$. In order to take different physical mechanisms in normal and tangential direction into account, the Piola traction is decomposed as follows

$$\boldsymbol{t}^{(1)} = -t_{\mathrm{N}}\, \boldsymbol{n} - \boldsymbol{t}_{\mathrm{T}} \qquad \text{with} \qquad \boldsymbol{t}_{\mathrm{T}} \cdot \boldsymbol{n}, \tag{17}$$

where $\boldsymbol{n} = \boldsymbol{n}^{(2)}$ denotes the current outward normal vector on $\partial \mathcal{B}^{(2),\mathrm{c}}$. Accordingly, we define the local normal and tangential gap functions (g_{N}, $\boldsymbol{g}_{\mathrm{T}}$), noting that we enforce only C^0 continuity in normal direction.

Acknowledgments

Support for this research was provided by the German Research Foundation (DFG) under grant HE5943/8-1 and DI 2306/1-1

References

[1] M. Dittmann, F. Aldakheel, J. Schulte, P. Wriggers, and C. Hesch. Variational Phase-Field Formulation of Non-Linear Ductile Fracture. *Comput. Methods Appl. Mech. Engrg.* 342 (2018), pp. 71–94.

[2] M. Dittmann, S. Schuß, B. Wohlmuth, and C. Hesch. Weak C^n coupling for multi-patch isogeometric analysis in solid mechanics. *Int. J. Numer. Methods Eng.* (2019). DOI: 10.1002/nme.6032.

[3] M. Dittmann, S. Schuß, B. Wohlmuth, and C. Hesch. Crosspoint modification for multi-patch isogeometric analysis. *Comput. Methods Appl. Mech. Engrg.* (submitted 2019).

[4] A.A. Griffith. The phenomena of rupture and flow in solids. *Philosophical Transactions of the Royal Society London* 221 (1921), pp. 163–198.

[5] M. Krüger, M. Dittmann, F. Aldakheel, A. Härtel, P. Wriggers, and C. Hesch. Porous-ductile fracture in thermo-elasto-plastic solids with contact applications. *Computational Mechanics* (submitted 2019).

[6] S. Schuß, M. Dittmann, B. Wohlmuth, S. Klinkel, and C. Hesch. Multi-patch isogeometric analysis for Kirchhoff-Love shell elements. *Comput. Methods Appl. Mech. Engrg.* 349 (2019), pp. 91–116.

**Proceedings of the 8th GACM Colloquium on Computational Mechanics
for Young Scientists from Academia and Industry
August 28–30, 2019 in Kassel, Germany**

Solving computational contact problems efficiently at large scale

Matthias Mayr * [1] and Alexander Popp[1]

[1]Institute for Mathematics and Computer-Based Simulation, University of the Bundeswehr Munich

Abstract. We present computational kernels and solution strategies for an efficient treatment of mortar terms in the context of fully tied or unilateral contact mechanics problems. In particular, we propose approaches to perform domain decompositions of mortar interface discretizations and discuss their implications on computational cost and parallel scalability. We present strong and weak scaling results for mortar-related costs in fully tied contact scenarios and exercise the interface domain decomposition capabilities in the context of unilateral contact problems.

Introduction

Mortar finite element methods are used in a variety of interface problems, e.g. in fully tied or unilateral contact, fluid flow, fluid-structure interaction, or electrochemistry [1, 2, 4, 5]. They allow for non-matching interface meshes and enable a variationally consistent imposition of interface constraints. However, they come at high numerical costs, which are in particular related to the numerical integration to form the mortar projection operators and to incorporate mortar terms into the linear system. Also, the resulting linear system requires specialized preconditioning techniques [6]. Here, we fully focus on the parallel implementation and domain decomposition for an efficient evaluation of all mortar-related terms [3].

Problem description and finite element discretization

Two solid bodies $\Omega^{(1)}$ and $\Omega^{(2)}$ with unknown displacement fields $\underline{\mathbf{u}}^{(i)}, i \in \{1,2\}$ and governed by the laws of nonlinear elasticity interact with each other at the interface Γ_*. At this interface, a kinematic constraint $\underline{\mathbf{g}}(\underline{\mathbf{u}}^{(1)}, \underline{\mathbf{u}}^{(2)})$ is imposed using a Lagrange multiplier field $\underline{\boldsymbol{\lambda}}$. Assuming suitable solution and test spaces, the weak form of the coupled problem is given as

$$\sum_{i=1}^{2} \delta \mathcal{W}^{(i)} + \int_{\Gamma_*} \underline{\boldsymbol{\lambda}}\, \delta \underline{\mathbf{g}} \, \mathrm{d}\Gamma + \int_{\Gamma_*} \delta \underline{\boldsymbol{\lambda}}\, \underline{\mathbf{g}} \, \mathrm{d}\Gamma = 0.$$

Therein, the first term denotes the weak form of the PDE governing the domain $\Omega^{(i)}, i \in \{1,2\}$, the second term represents the interface traction contribution, while the third term expresses the kinematic coupling constraint at the interface Γ_*.

Using shape functions N to discretize the displacement fields $\underline{\mathbf{u}}^{(i)}, i \in \{1,2\}$ and shape functions $\boldsymbol{\Phi}$ to discretize the Lagrange multiplier field $\underline{\boldsymbol{\lambda}}$, the mortar coupling matrices $\mathcal{D}$ and $\mathcal{M}$ are then assembled

*Corresponding author: matthias.mayr@unibw.de ORCID iD: 0000-0002-2780-1233

from the nodal contributions

$$\int_{\Gamma_*} \underline{\boldsymbol{\lambda}}\, \delta\underline{\mathbf{g}}\, \mathrm{d}\Gamma \approx \sum_{j=1}^{m^{(1)}} \sum_{k=1}^{n^{(1)}} \boldsymbol{\lambda}_j^{\mathrm{T}} \overbrace{\left[\int_{\Gamma_{*,\mathrm{h}}^{(1)}} \Phi_j \frac{\partial \mathbf{g}}{\partial \mathbf{u}^{(1)}} \left(\mathbf{u}^{(1)}, \mathbf{u}^{(2)} \right) N_k^{(1)} \, \mathrm{d}\Gamma \right]}^{\mathfrak{D}[j,k]} \delta \mathbf{u}_k^{(1)} - \sum_{j=1}^{m^{(1)}} \sum_{\ell=1}^{n^{(2)}} \boldsymbol{\lambda}_j^{\mathrm{T}} \underbrace{\left[\int_{\Gamma_{*,\mathrm{h}}^{(1)}} \Phi_j \frac{\partial \mathbf{g}}{\partial \mathbf{u}^{(2)}} \left(\mathbf{u}^{(1)}, \mathbf{u}^{(2)} \right) \left(N_\ell^{(2)} \circ \chi_{\mathrm{h}} \right) \mathrm{d}\Gamma \right]}_{\mathfrak{M}[j,\ell]} \delta \mathbf{u}_\ell^{(2)}. \tag{1}$$

Scalable evaluation of mortar matrices

Evaluating (1) is numerically expensive, especially since it requires projections of meshes and data between the master and slave interface. To leverage the parallelism capabilities of modern computing hardware, both domains $\Omega^{(i)}, i \in \{1, 2\}$ are decomposed into subdomains $\Omega^{(m)}, m \in \{0, \ldots, n^{\mathrm{proc}} - 1\}$. Then, each subdomain is assigned to a parallel process m. To enable an efficient evaluation of the mortar integrals (1), *independent* domain decompositions (DDs) are performed for the slave and master side of the mortar interface, respectively. An exemplary DD for a two-dimensional problem run on four MPI ranks is shown in Figure 1. Now, all processes $m \in \{0, \ldots, n^{\mathrm{proc}} - 1\}$ contribute their share to the

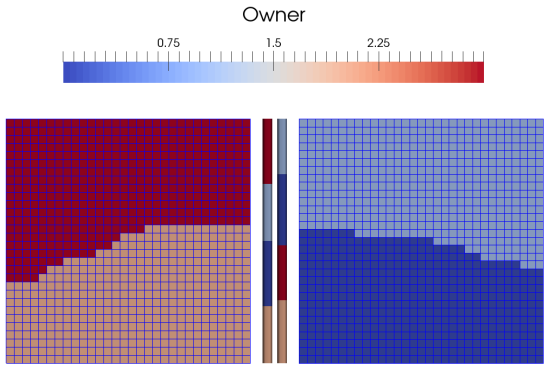

Figure 1. Example of independent volume and interface domain decompositions for optimal parallel processing. Coloring reflects the assignment of a subdomain to a parallel process.

evaluation of (1), yielding speed-up of the entire mortar evaluation process. This process is often referred to as *load balancing*.

Numerical results for the meshtying of two solid blocks

Strong and weak scaling studies for the time to evaluate (1) have been performed. For strong scaling, the problem size is fixed, while the number of subdomains and parallel resources is increased, hoping for an equivalent reduction in computational time. For weak scaling, the problem size is increased at the same rate as the number of parallel processes, such that the work load per process is kept constant.

Figure 2 reports strong and weak scaling results for the meshtying of two 3D solid cubes. Optimal strong and weak scaling can only be achieved, if the interface DD is independent from the underlying volume DD.

Numerical results for the contact of a rolling cylinder

The cost of mortar integration is even more dominant in contact problems, since the mortar terms have to be evaluated in every nonlinear iteration. Due to changes in the topology (either by rotation of a body

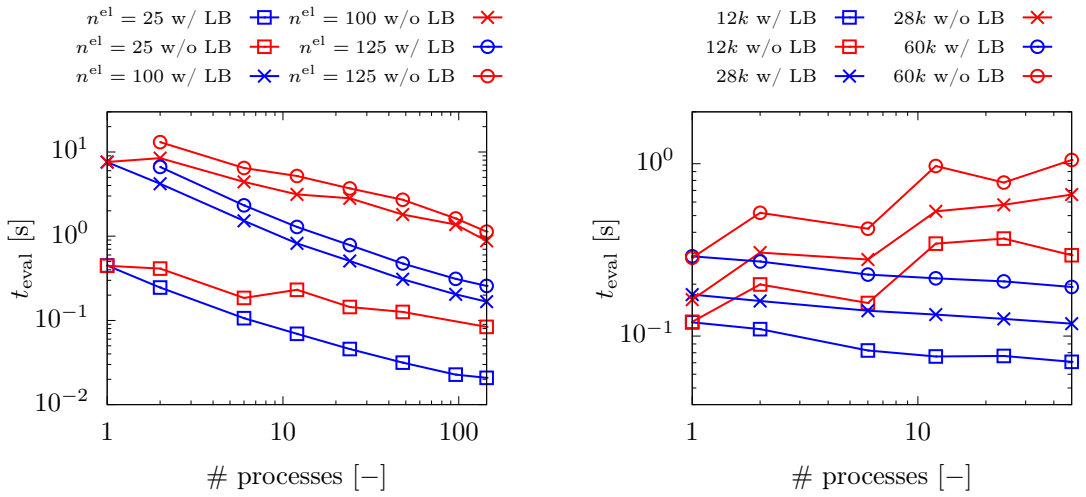

(a) Strong scaling with n^{el} elements along an edge

(b) Weak scaling with $12k/28k/60k$ unknows per process

Figure 2. Scaling results for meshtying of two 3D solid cubes: strong and weak scaling can only be achieved, if the interface DD ("w/ LB") is independent from the underlying volume DD ("w/o LB").

or by large sliding), the interface DDs depend on the current configuration. Thus, updating the interface DDs is crucial for the overall efficiency of the contact solver.

We study three scenarios:

- **Static LB:** Perform an initial load-balancing as in the meshtying case.
- **Static Contact-LB:** Perform an initial load-balancing, but take contact search results into account.
- **Dynamic Contact-LB:** Monitor the load-balancing throughout the simulation and update the interface DD if necessary while taking the contact search results into account.

Timing results for the mortar evaluation are reported in Figure 3. The work is only distributed equally to all processes when using dynamic contact-specific load balancing. It also delivers the fastest mortar evaluation throughout the entire simulation. A snapshot indicating volume and interface DDs for the dynamic contact-specific load balancing is shown in Figure 4.

References

[1] A. Ehrl, A. Popp, V. Gravemeier, and W. A. Wall. A dual mortar approach for mesh tying within a variational multiscale method for incompressible flow. *Int. J. Numer. Meth. Fl.* 76.1 (2014), pp. 1–27.

[2] R. Fang, P. Farah, A. Popp, and W. A. Wall. A monolithic, mortar-based interface coupling and solution scheme for finite element simulations of lithium-ion cells. *Int. J. Numer. Meth. Eng.* 114.13 (2018), pp. 1411–1437.

[3] M. Mayr and A. Popp. "Scalable computational kernels for mortar coupling of interface problems". in preparation.

[4] M. Mayr, T. Klöppel, W. A. Wall, and M. W. Gee. A Temporal Consistent Monolithic Approach to Fluid–Structure Interaction Enabling Single Field Predictors. *SIAM J. Sci. Comput.* 37.1 (2015), B30–B59.

[5] A. Popp, M. Gitterle, M. W. Gee, and W. A. Wall. A dual mortar approach for 3D finite deformation contact with consistent linearization. *Int. J. Numer. Meth. Eng.* 83.11 (2010), pp. 1428–1465.

[6] T. A. Wiesner, A. Popp, M. W. Gee, and W. A. Wall. Algebraic multigrid methods for dual mortar finite element formulations in contact mechanics. *Int. J. Numer. Meth. Eng.* 114.4 (2018), pp. 399–430.

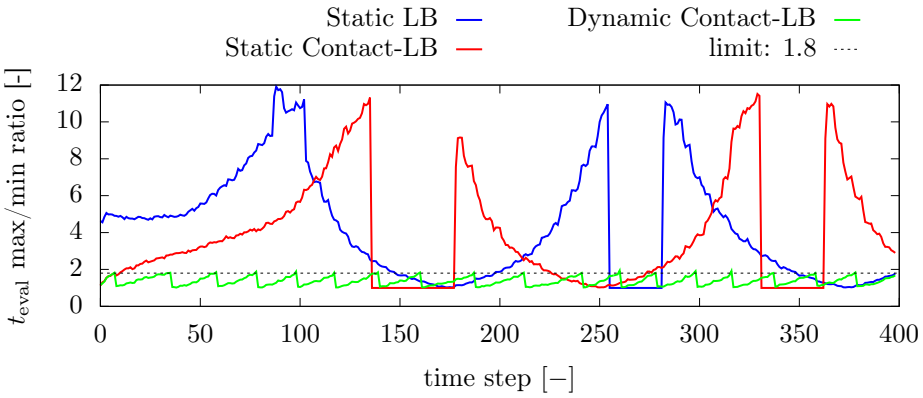

(a) Parallel unbalance

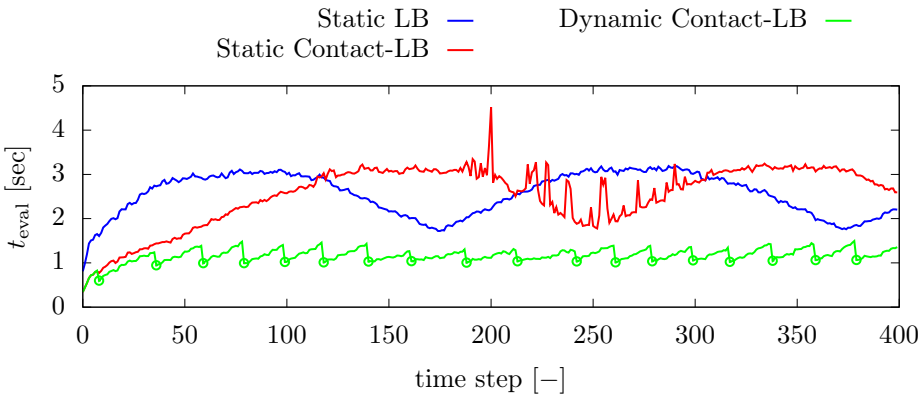

(b) Contact evaluation time

Figure 3. Contact of a rolling cylinder: efficiency of various load rebalancing schemes.

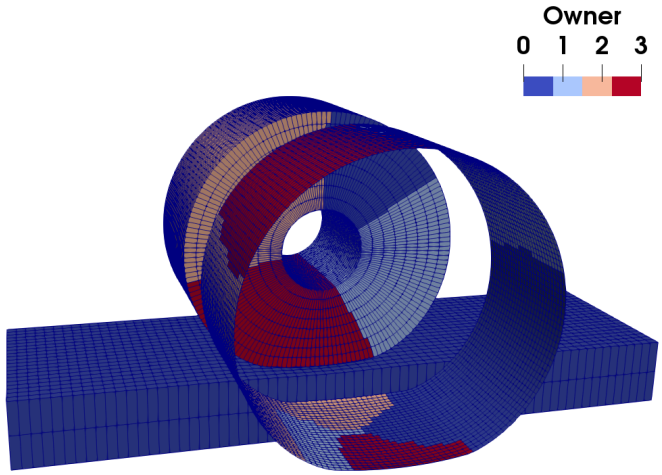

Figure 4. Contact of a rolling cylinder: snapshot illustrating volume and interface DDs using dynamic contact-specific load balancing.

**Proceedings of the 8th GACM Colloquium on Computational Mechanics
for Young Scientists from Academia and Industry
August 28–30, 2019 in Kassel, Germany**

Isogeometric Dual Mortar Methods for Computational Contact and Interface Mechanics

Alexander Popp * [1], Linus Wunderlich[2], Alexander Seitz[3] and Barbara Wohlmuth[4]

[1]Institute for Mathematics and Computer-Based Simulation, University of the Bundeswehr Munich, Germany
[2]School of Mathematical Sciences, Queen Mary University of London, U.K.
[3]Institute for Computational Mechanics, Technical University of Munich, Germany
[4]Institute for Numerical Mathematics, Technical University of Munich, Germany

Abstract. Compared to classical Lagrange polynomials in finite element analysis (FEA), isogeometric analysis (IGA) offers higher inter-element continuity and a smooth surface representation, which makes the application to computational contact mechanics particularly appealing. In addition to contact analysis, so-called weak patch-coupling is an important feature for practical applications of IGA. Within isogeometric methods, the computational domain is usually divided into several spline patches and the solution is approximated by spline functions on each patch. Within this contribution, a new class of mortar methods with dual Lagrange multiplier bases is transferred from the FEA to the IGA universe and for the first time combines the efficiency of dual mortar methods with the beneficial IGA inherent concept of a smooth geometry. The newly developed schemes are applied to both patch-coupling and unilateral contact problems. Spatial convergence orders for the discretization error are studied numerically by applying uniform mesh refinement.

Isogeometric analysis

Robust and accurate contact discretizations for nonlinear finite element analysis have been an active field of research in the past decade, and a new class of formulations has emerged with the introduction of isogeometric analysis (IGA) [1]. IGA is intended to bridge the gap between computer aided design (CAD) and finite element analysis (FEA) by using the smooth non-uniform rational B-splines (NURBS) or T-splines common in CAD also as a basis for the numerical analysis. This promises some advantages over classical Lagrange polynomials for FEA such as a possibly higher accuracy per degree of freedom and, more importantly, a higher inter-element continuity. While finite elements based on Lagrange polynomials are limited to C^0 inter-element continuity independent of the polynomial order p, NURBS can be constructed with a maximum of C^{p-1} continuity. This high continuity results, amongst others, in a smooth surface representation, which makes the application to computational contact mechanics particularly appealing. In addition to contact analysis, so-called weak patch-coupling is an important feature for practical applications of IGA. Within isogeometric methods, the computational domain is usually divided into several spline patches and the solution is approximated by spline functions on each patch. Typically, multivariate splines are defined based on a tensor-product structure, and a flexible coupling between the individual patches is extremely important to gain some flexibility of the local meshes (e.g. in order to meet different local mesh resolution requirements without graded meshes).

Mortar methods

Over the last two decades, mortar methods have emerged as one the most promising and mathematically well-founded concepts to deal with non-conforming mesh- or patch-coupling and nonlinear frictional contact problems in the context of classical FEA [3]. Consequently, there have been numerous efforts to transfer the advantages of mortar methods to the IGA universe [2]. However, these efforts have so far been limited to the class of so-called standard mortar methods, which simply construct a stable discrete Lagrange multiplier basis using the trace space of the underlying mesh. While admittedly effective and

*Corresponding author: alexander.popp@unibw.de ORCID iD: 0000-0002-8820-466X

rather straightforward to transfer from the FEA to the IGA case, standard mortar methods cause high computational costs due to the resulting indefinite equation systems of saddle point type. To propose an alternative approximation of the Lagrange multipliers, so-called dual mortar methods were originally introduced in the context of FEA domain decomposition [5] and later extended to finite deformation contact analysis [3]. In contrast to standard mortar methods, the use of a dual Lagrange multiplier basis yields a localization of the interface constraints due to the so-called biorthogonality property of the dual shape functions. The aim of this work is to transfer this concept from finite elements to IGA, thus for the first time combining the efficiency of dual mortar methods with the beneficial IGA inherent concept of a smooth geometry. The newly developed isogeometric dual mortar method is applied to both patch-coupling (i.e. domain decomposition) and contact problems. In both applications, spatial convergence orders for the discretization error are studied numerically by applying uniform mesh refinement.

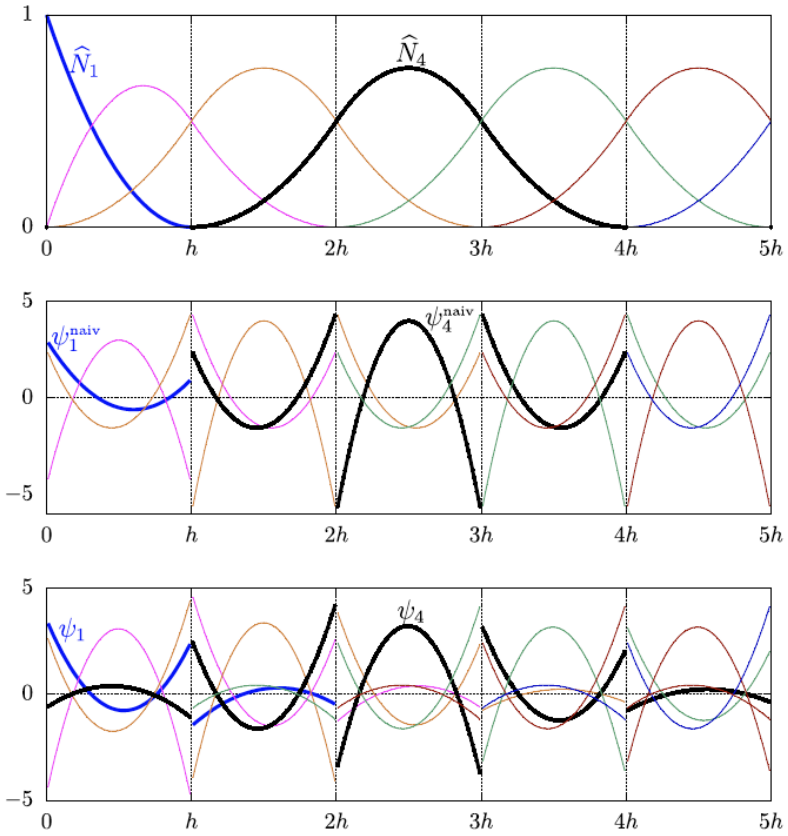

Figure 1. Primal (top), naive dual (middle) and optimal dual (bottom) basis functions shown on the first five elements of a quadratic spline patch. The first and fourth basis functions are highlighted in bold.

A simple but non-optimal biorthogonal basis

As a first step, a rather straightforward and naive extension of dual mortar methods from FEA to IGA is investigated: the dual basis functions in this first version have the same support as their primal counterparts, fulfil a partition of unity and are constructed via element-wise linear combinations of the primal basis functions [4]. Consequently, the global approximation order is limited to one in the L^2-norm, independent of the local approximation. Therefore, since the dual NURBS do not possess the optimal reproduction order, optimal convergence rates cannot be guaranteed theoretically. However, for contact problems the solution is typically in $H^t(\Omega(i))^3$ with $t < 5/2$, such that a priori estimates are already limited by the regularity of the solution. It can be quite easily shown that the naive version of dual mortar methods in IGA still yields optimal a priori estimates for the discrete contact problem. With regard to NURBS patch-coupling, however, the naive version lacks the optimal approximation order such that convergence of order $\mathcal{O}(h^p)$ in the H^1-norm cannot be guaranteed, but only $\mathcal{O}(h^{3/2})$ can be achieved. Extensive numerical tests and mesh refinement studies for both patch-coupling and finite deformation contact within IGA have been carried out to confirm these theoretical findings in practice.

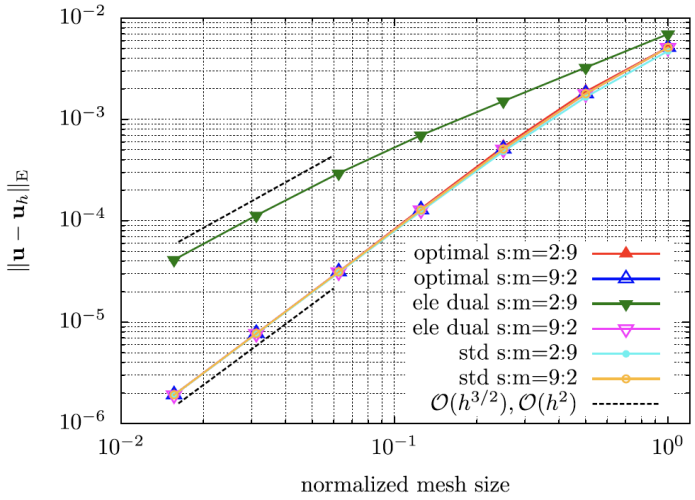

Figure 2. Exemplary convergence results for weak patch-coupling with quadratic NURBS: Comparison of the naive biorthogonal basis ('ele dual'), optimal biorthogonal basis and standard Lagrange multipliers.

An optimal locally supported biorthogonal basis

To obtain optimal results with dual mortar methods in IGA also for the patch-coupling case, a new set of biorthogonal splines is proposed as a second step [6]. The underlying idea comes from the fact that patch-coupling optimality could be recovered for FEA by extending the support of the dual basis functions. An extension of this approach to B-splines and especially its general implementation has still been an open question until very recently. Here, we can finally present a new construction of local dual basis functions with optimal approximation properties based on an extended support as suggested in the finite element context. For the first time, this scheme allows to combine the two crucial features of local support of the dual basis and optimal approximation properties. We first present the univariate construction (i.e. 1D interfaces), which has an inherent cross-point modification. The multivariate construction (i.e. 2D interfaces) is then based on a tensor product approach for weighted integrals, whereby the important properties are inherited from the univariate case. Numerical results include finite deformations in 3D to confirm the optimal convergence properties in practice. They also demonstrate the suitability and efficiency of the method for large-scale applications.

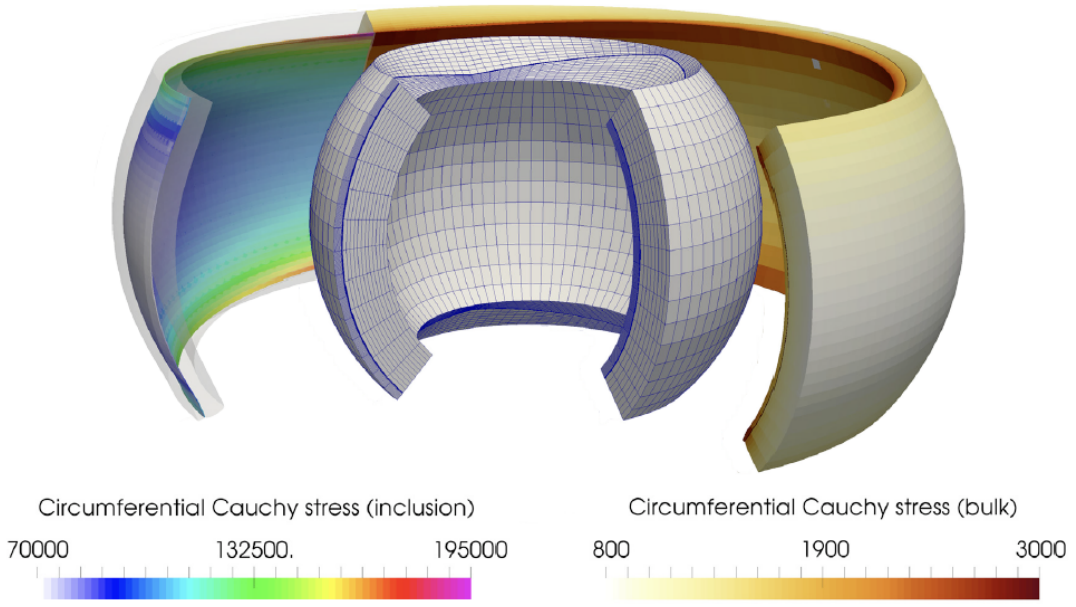

Figure 3. Exemplary contact problem with complex curved interface in 3D.

References

[1] J.A. Cottrell, A. Reali, Y. Bazilevs, and T.J.R. Hughes. Isogeometric analysis of structural vibrations. *Computer Methods in Applied Mechanics and Engineering* 195.41–43 (2006), pp. 5257 –5296.

[2] L. De Lorenzis, P. Wriggers, and T.J.R. Hughes. Isogeometric contact: a review. *GAMM-Mitteilungen* 37.1 (2014), pp. 85–123.

[3] A. Popp and P. Wriggers, eds. *Contact Modeling for Solids and Particles*. Vol. 585. CISM International Centre for Mechanical Sciences. Springer International Publishing, 2018.

[4] A. Seitz, P. Farah, J. Kremheller, B. Wohlmuth, W.A. Wall, and A. Popp. Isogeometric dual mortar methods for computational contact mechanics. *Computer Methods in Applied Mechanics and Engineering* 301 (2016), pp. 259–280.

[5] B. Wohlmuth. A mortar finite element method using dual spaces for the Lagrange multiplier. *SIAM Journal on Numerical Analysis* 38 (2000), pp. 989–1012.

[6] L. Wunderlich, A. Seitz, M.D. Alaydin, B. Wohlmuth, and A. Popp. Biorthogonal splines for optimal weak patch-coupling in isogeometric analysis with applications to finite deformation elasticity. *Computer Methods in Applied Mechanics and Engineering* 346 (2019), pp. 197–215.

**Proceedings of the 8th GACM Colloquium on Computational Mechanics
for Young Scientists from Academia and Industry
August 28–30, 2019 in Kassel, Germany**

A residual-type a posteriori estimator for the adaptive discretization in space and time of a viscoelastic contact problem.

Mirjam Walloth * [1]

[1]Fachbereich Mathematik, TU Darmstadt, Germany

Abstract. We present a residual-type a posteriori estimator for the linear viscoelastic Signorini contact problem. The estimator constitutes global upper and lower bounds with respect to an error notion which measures the error in the displacements, the velocities and a suitable approximation of the contact forces. For the spatial error at each discrete time step local lower bounds are given in terms of the spatial estimator contributions. As the estimator splits in temporal and spatial contributions it can be used for the adaptation of the time step and the mesh size.

Introduction

As a contribution to the efficient numerical simulation of viscoelastic contact problems we present an a posteriori error estimator.

We consider the linear viscoelastic Signorini contact problem as a model problem. The linear viscoelastic material obeys the Kelvin-Voigt model. Viscoelasticity means that the material behavior shows both elastic and viscous features and thus the stress tensor depends on the displacements as well as the velocities. Examples of viscoelastic materials are biological tissue as cartilage, bones and tendons. The resulting quasi-static contact problem gives rise to a time-dependent variational inequality.

Due to the constraints contact problems are non-smooth problems and thus the numerical simulation to reach a certain accuracy is usually very expensive. Therefore, the adaptive numerical simulation based on a posteriori estimators is in great demand.

A popular estimator for linear elliptic problems, which appears attractive in view of its simplicity and generality is standard residual estimation, see e.g. [5]. The estimator contributions are explicitly computable from the given data and the discrete finite element solution.

In this talk we present a residual-type a posteriori error estimator for the time-dependent variational inequality of the linear viscoelastic Signorini contact problem [6]. To the best of our knowledge that is the first residual-type estimator for this kind of contact problem without a regularization of the non-penetration condition. For a normal compliance viscoelastic contact problem we refer to [1].

We consider an error measure representing the error in the displacements, velocities and constraining forces. The presented estimator constitutes a global in space and time upper bound and a global in space and local in time lower bound of this error measure. Further, the spatial estimator contributions constitute local lower bounds for the spatial error at each discrete time point. The details of the proofs of efficiency and reliability are shown in [6].

The estimator splits in temporal and spatial contributions which can be used for the adaptation of the time step as well as the mesh size. The estimator reduces to a standard residual estimator in the absence of contact. The estimator contributions addressing the non-linearity are related to the contact stresses and the complementarity condition with respect to the solution in two subsequent discrete time points. Due to the fact that we exploit the local structure we avoid any spatial estimator contributions related

*Corresponding author: walloth@mathematik.tu-darmstadt.de

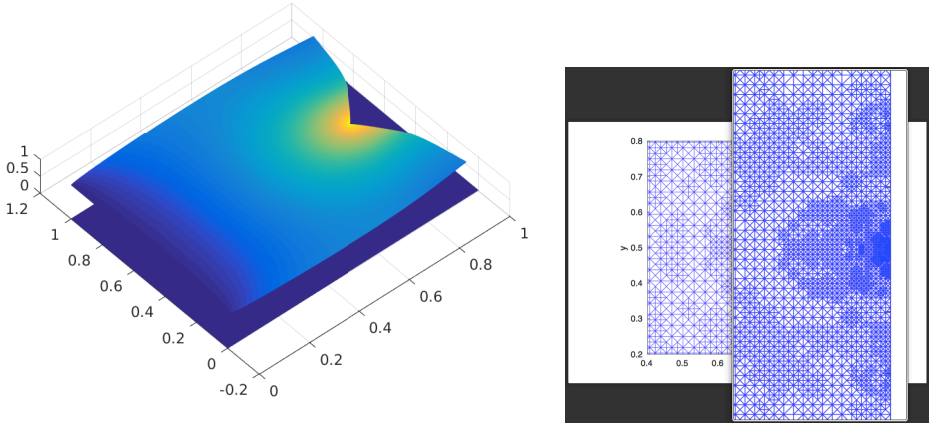

(a) deformation **(b)** mesh

Figure 1. Deformation and zoom in adaptively refined mesh

to the non-linearity in areas where the bodies are fully in contact in the surrounding of a node, so-called full-contact areas. In consequence, the estimator perceives that at the boundary which is in full-contact adaptive mesh refinement cannot improve the solution.

Finally, numerical examples confirm our theoretical results, see e.g. Figure 1. We present the convergence rate of the estimator compared to uniform refinement. Further, the adaptively refined meshes at each discrete time point and the adaptation of the time step size are shown.

1 Linear viscoelastic Signorini contact problem

We consider the contact between a linear viscoelastic body Ω and a rigid obstacle. The displacements and velocities are denoted by $\boldsymbol{u}$ and $\dot{\boldsymbol{u}}$. The stress tensor obeys the following constitutive law $\boldsymbol{\sigma} := \boldsymbol{\mathcal{A}}\boldsymbol{\epsilon}(\dot{\boldsymbol{u}}) + \boldsymbol{\mathcal{B}}\boldsymbol{\epsilon}(\boldsymbol{u})$ where $\boldsymbol{\mathcal{A}}$ is the viscosity tensor and $\boldsymbol{\mathcal{B}}$ is the elasticity tensor and $\boldsymbol{\epsilon}$ is the linearized strain tensor. The time interval is denoted by I. Consistent to the linearized material, a linearized non-penetration condition is considered. The linearized non-penetration condition is enforced by imposing the constraints $u_\nu \leq g$ for a given gap function g and a given direction of constraints $\boldsymbol{\nu}$ on the potential contact boundary Γ_C. The Dirichlet and the Neumann boundary are denoted by Γ_D, Γ_N.

The complete problem formulation of the quasi-static contact problem is given by

Problem 1. *Find a displacement field* $\boldsymbol{u} : \Omega \times \bar{I} \to \mathbb{R}^d$ *with* $\boldsymbol{u}(0) = \boldsymbol{u}^0$ *such that*

$$\begin{aligned}
-\mathrm{div}\boldsymbol{\sigma}(\boldsymbol{u}) &= \boldsymbol{f} \quad \text{in} \quad \Omega \times I \\
\hat{\boldsymbol{\sigma}}(\boldsymbol{u}) &= \boldsymbol{\pi} \quad \text{on} \quad \Gamma_N \times I \\
\boldsymbol{u} &= \boldsymbol{u}_D \quad \text{on} \quad \Gamma_D \times I \\
u_\nu &\leq g \quad \text{on} \quad \Gamma_C \times I \\
\hat{\sigma}_\nu &\leq 0 \quad \text{on} \quad \Gamma_C \times I \\
(u_\nu - g) \cdot \hat{\sigma}_\nu &= 0 \quad \text{on} \quad \Gamma_C \times I \\
\hat{\boldsymbol{\sigma}}_{\tan} &= \boldsymbol{0} \quad \text{on} \quad \Gamma_C \times I
\end{aligned}$$

with $\hat{\boldsymbol{\sigma}} := \boldsymbol{\sigma}(\boldsymbol{u})\boldsymbol{n}$ where $\boldsymbol{n}$ is the unit outward normal, $\hat{\sigma}_\nu := \hat{\boldsymbol{\sigma}} \cdot \boldsymbol{\nu}$ and $\hat{\boldsymbol{\sigma}}_{\tan} := \hat{\boldsymbol{\sigma}}(\boldsymbol{u}) - \hat{\sigma}_\nu \boldsymbol{\nu}$.

1.1 Fully-discrete formulation

For the discretization in time we use the implicit Euler scheme and for the discretization in space we use linear finite elements on a shape-regular mesh $\mathfrak{M}$ with simplicial elements $\mathfrak{e}$. At each discrete time t^n the fully discrete solution is denoted by $\boldsymbol{u}_{\mathfrak{m}}^n$, the forces by $\boldsymbol{f}^n = \boldsymbol{f}(t^n)$, $\boldsymbol{\pi}^n = \boldsymbol{\pi}(t^n)$ and the gap function by $g_{\mathfrak{m}}^n = g_{\mathfrak{m}}(t^n)$. The space of linear finite elements in time step n is given by $\boldsymbol{\mathcal{H}}_{\mathfrak{m}} := \{\boldsymbol{v}_{\mathfrak{m}} \in \boldsymbol{\mathcal{C}}^0(\Omega) \mid \forall \mathfrak{e} \in$

$\mathfrak{M},\ \boldsymbol{v}_{\mathfrak{m},\mathfrak{e}} \in \boldsymbol{\mathcal{P}}_1(\mathfrak{e})$ and $\boldsymbol{v}_\mathfrak{m} = \boldsymbol{u}_D^n$ on $\Gamma_D\}$ where we assume $\boldsymbol{u}_D$ to be continuous and piecewise linear in space and time. The admissible set is given by $\boldsymbol{\mathcal{K}}_\mathfrak{m}^n := \{\boldsymbol{v}_\mathfrak{m} \in \boldsymbol{\mathcal{H}}_\mathfrak{m} \mid v_{\mathfrak{m},1} \leq g_\mathfrak{m}^n \text{ on } \Gamma_C\}$ where from now on for the ease of presentation we choose the coordinate system such that $\boldsymbol{\nu} = \boldsymbol{e}_1$.

For each time interval $(t^{n-1}, t^n]$ we define the time step size $\tau^n := t^n - t^{n-1}$ and the linearly interpolated solution $\boldsymbol{u}_\mathfrak{m}^\tau := \frac{t^n - t}{\tau^n}\boldsymbol{u}_\mathfrak{m}^{n-1} + \left(1 - \frac{t^n - t}{\tau^n}\right)\boldsymbol{u}_\mathfrak{m}^n$ and its derivative $\dot{\boldsymbol{u}}_\mathfrak{m}^\tau := \delta\boldsymbol{u}_\mathfrak{m}^n := \frac{\boldsymbol{u}_\mathfrak{m}^n - \boldsymbol{u}_\mathfrak{m}^{n-1}}{\tau^n}$. The fully discrete problem is given by

Problem 2 (Discrete variational inequality)**.** *For each time step $n = 1, \dots, N$ find $\boldsymbol{u}_\mathfrak{m}^n \in \boldsymbol{\mathcal{K}}_\mathfrak{m}^n$ fulfilling*

$$\langle \boldsymbol{\mathcal{A}}\boldsymbol{\epsilon}(\delta\boldsymbol{u}_\mathfrak{m}^n), \boldsymbol{\epsilon}(\boldsymbol{v}_\mathfrak{m}) - \boldsymbol{\epsilon}(\boldsymbol{u}_\mathfrak{m}^n)\rangle + \langle \boldsymbol{\mathcal{B}}\boldsymbol{\epsilon}(\boldsymbol{u}_\mathfrak{m}^n), \boldsymbol{\epsilon}(\boldsymbol{v}_\mathfrak{m}) - \boldsymbol{\epsilon}(\boldsymbol{u}_\mathfrak{m}^n)\rangle \geq \langle \boldsymbol{f}^n, \boldsymbol{v}_\mathfrak{m} - \boldsymbol{u}_\mathfrak{m}^n\rangle + \langle \boldsymbol{\pi}^n, \boldsymbol{v}_\mathfrak{m} - \boldsymbol{u}_\mathfrak{m}^n\rangle_{\Gamma_N}, \quad \forall \boldsymbol{v}_\mathfrak{m} \in \boldsymbol{\mathcal{K}}_\mathfrak{m}^n.$$

2 Residual-type a posteriori error estimator

The works [2, 4] reveal that sharp a posteriori estimators for obstacle and contact problems can be derived by involving the error in the contact forces in the error measure. Here, the contact force density in the continuous setting is given by $\langle \boldsymbol{\lambda}, \boldsymbol{\varphi}\rangle_{-1,1} := \langle \boldsymbol{f}, \boldsymbol{\varphi}\rangle + \langle \boldsymbol{\pi}, \boldsymbol{\varphi}\rangle_{\Gamma_N} - \langle \boldsymbol{\mathcal{A}}\boldsymbol{\epsilon}(\dot{\boldsymbol{u}}), \boldsymbol{\epsilon}(\boldsymbol{\varphi})\rangle - \langle \boldsymbol{\mathcal{B}}\boldsymbol{\epsilon}(\boldsymbol{u}), \boldsymbol{\epsilon}(\boldsymbol{\varphi})\rangle$. To compare the discrete contact force density $\langle \boldsymbol{\lambda}_\mathfrak{m}^n, \boldsymbol{\varphi}_\mathfrak{m}\rangle_{-1,1} := \langle \boldsymbol{f}^n, \boldsymbol{\varphi}_\mathfrak{m}\rangle + \langle \boldsymbol{\pi}^n, \boldsymbol{\varphi}_\mathfrak{m}\rangle_{\Gamma_N} - \langle \boldsymbol{\mathcal{A}}\boldsymbol{\epsilon}(\delta\boldsymbol{u}_\mathfrak{m}^n), \boldsymbol{\epsilon}(\boldsymbol{\varphi}_\mathfrak{m})\rangle - \langle \boldsymbol{\mathcal{B}}\boldsymbol{\epsilon}(\boldsymbol{u}_\mathfrak{m}^n), \boldsymbol{\epsilon}(\boldsymbol{\varphi}_\mathfrak{m})\rangle$ to $\boldsymbol{\lambda}$ we need to extend it to a functional on $\boldsymbol{H}^1$. Therefore, we define $\left\langle \tilde{\boldsymbol{\lambda}}_\mathfrak{m}^\tau, \boldsymbol{\varphi}\right\rangle_{-1,1} = \left\langle \tilde{\boldsymbol{\lambda}}_\mathfrak{m}^n, \boldsymbol{\varphi}\right\rangle_{-1,1}$ on $(t^{n-1}, t^n]$ with

$$\begin{aligned}\left\langle \tilde{\boldsymbol{\lambda}}_\mathfrak{m}^n, \boldsymbol{\varphi}\right\rangle_{-1,1} := &\sum_{p \in \mathfrak{N}_\mathfrak{m}^{\mathrm{sC}}} s_p^n c_p(\varphi_1) \int_{\widehat{\gamma}_{p,C}} \phi_p \\ &+ \sum_{p \in \mathfrak{N}_\mathfrak{m}^{\mathrm{fC}}} \left(s_p^n c_p(\varphi_1) \int_{\widehat{\gamma}_{p,C}} \phi_p - \int_{\widehat{\gamma}_{p,C}} \hat{\sigma}_1(\boldsymbol{u}_\mathfrak{m}^n)(\varphi_1 - c_p(\varphi_1))\phi_p \right) \end{aligned} \tag{1}$$

where $c_p(\varphi_1)$ are weighted mean values, $s_p^n := \frac{\left\langle \lambda_{\mathfrak{m},1}^n, \phi_p\right\rangle_{-1,1}}{\int_{\gamma_{p,C}} \phi_p}$ and $\widehat{\gamma}_{p,C}$ is the union of all boundary sides connected with $\boldsymbol{p}$ in time steps n and $n-1$, compare [6, Section 2.4]. We distinguish between full-contact nodes $\boldsymbol{p} \in \mathfrak{N}_\mathfrak{m}^{\mathrm{fC}}$, fulfilling $u_{\mathfrak{m},1}^n = g_\mathfrak{m}^n$, $u_{\mathfrak{m},1}^{n-1} = g_\mathfrak{m}^{n-1}$ and $\hat{\sigma}_1 \leq 0$ on $\widehat{\gamma}_{p,C}$ and the remaining actual contact nodes, called semi-contact nodes $\boldsymbol{p} \in \mathfrak{N}_\mathfrak{m}^{\mathrm{sC}}$.

We note that compared to the work [3] on parabolic obstacle problems, the definition of full-contact depending on the solutions at the discrete times t^n and t^{n-1} enables to show lower bounds of η_6, η_7.

We define the global error measure on a time interval I which considers the error in the displacements, the velocities as well as in the contact force density by

$$\begin{aligned}&\mathrm{ErrMeasG}(\boldsymbol{u}_\mathfrak{m}^\tau, \dot{\boldsymbol{u}}_\mathfrak{m}^\tau, \tilde{\boldsymbol{\lambda}}_\mathfrak{m}^\tau, I) := \\ &\left(\int_I \left(\sup_{\varphi \in \mathcal{H}_0} \left(\frac{\langle \boldsymbol{\mathcal{A}}\boldsymbol{\epsilon}(\dot{\boldsymbol{u}} - \dot{\boldsymbol{u}}_\mathfrak{m}^\tau), \boldsymbol{\epsilon}(\boldsymbol{\varphi})\rangle + \left\langle \boldsymbol{\lambda} - \tilde{\boldsymbol{\lambda}}_\mathfrak{m}^\tau, \boldsymbol{\varphi}\right\rangle_{-1,1}}{\|\nabla\boldsymbol{\varphi}\|} \right) \right)^2 \right. \\ &\left. + \|\boldsymbol{\epsilon}(\boldsymbol{u} - \boldsymbol{u}_\mathfrak{m}^\tau)\|_{L^2(I, L^2_\mathcal{B})}^2 + \|\boldsymbol{\epsilon}(\boldsymbol{u} - \boldsymbol{u}_\mathfrak{m}^\tau)(T)\|_{L^2_\mathcal{A}}^2 \right)^{\frac{1}{2}}, \end{aligned} \tag{2}$$

where $\|\cdot\|_{L^2_\mathcal{A}} := \langle \boldsymbol{\mathcal{A}}(\cdot), (\cdot)\rangle$, $\|\cdot\|_{L^2_\mathcal{B}} := \langle \boldsymbol{\mathcal{B}}(\cdot), (\cdot)\rangle$ are the norms induced by the bilinear forms.

Further, we define the local spatial error measure at each time t^n

$$\begin{aligned}&\mathrm{ErrMeasL}_p(\boldsymbol{u}_\mathfrak{m}^n, \dot{\boldsymbol{u}}_\mathfrak{m}^\tau, \tilde{\boldsymbol{\lambda}}_\mathfrak{m}^n) := \\ &\left(\left(\sup_{\varphi \in \mathcal{H}_0(\omega_p)} \left(\frac{\langle \boldsymbol{\mathcal{A}}\boldsymbol{\epsilon}(\dot{\boldsymbol{u}} - \dot{\boldsymbol{u}}_\mathfrak{m}^\tau), \boldsymbol{\epsilon}(\boldsymbol{\varphi})\rangle + \left\langle \boldsymbol{\lambda} - \tilde{\boldsymbol{\lambda}}_\mathfrak{m}^n, \boldsymbol{\varphi}\right\rangle_{-1,1}}{\|\nabla\boldsymbol{\varphi}\|_{\omega_p}} \right) \right)^2 + \|\boldsymbol{\epsilon}(\boldsymbol{u} - \boldsymbol{u}_\mathfrak{m}^n)\|_{L^2_\mathcal{B}(\omega_p)}^2 \right)^{\frac{1}{2}}. \end{aligned} \tag{3}$$

The error estimator which we define in the following constitutes global upper and lower bounds with respect to the global error measure (2) and local lower bounds with respect to the local spatial error measure (3) at each time t^n. The estimator

$$\eta := \left(\sum_n (\eta^n)^2\right)^{\frac{1}{2}} := \left(\sum_n (\eta_\tau^n)^2 + \tau^n (\eta_{\mathfrak{m}}^n)^2\right)^{\frac{1}{2}}$$

consists of the temporal estimator $\eta_\tau^n := \sqrt{\frac{\tau^n}{3}} \|\boldsymbol{\epsilon}(\boldsymbol{u}_{\mathfrak{m}}^n - \boldsymbol{u}_{\mathfrak{m}}^{n-1})\|_{L^2_{\mathcal{B}}}$ and the spatial estimator $\eta_{\mathfrak{m}}^n := \sqrt{\sum_{k=1}^7 (\eta_k^n)^2}$ which has the following different contributions

$$\begin{aligned}
\eta_1^n &:= \left(\sum_{p\in\mathfrak{N}_{\mathfrak{m}}} (\eta_{1,p}^n)^2\right)^{\frac{1}{2}}, & \eta_{1,p}^n &:= h_p \|\boldsymbol{f}^n\|_{\widehat{\omega}_p} \\
\eta_2^n &:= \left(\sum_{p\in\mathfrak{N}_{\mathfrak{m}}} (\eta_{2,p}^n)^2\right)^{\frac{1}{2}}, & \eta_{2,p}^n &:= h_p^{\frac{1}{2}} \|\boldsymbol{J}^I(\boldsymbol{u}_{\mathfrak{m}}^n)\|_{\widehat{\gamma}_{p,I}} \\
\eta_3^n &:= \left(\sum_{p\in\mathfrak{N}_{\mathfrak{m}}^{\bar{N}}} (\eta_{3,p}^n)^2\right)^{\frac{1}{2}}, & \eta_{3,p}^n &:= h_p^{\frac{1}{2}} \left\|\boldsymbol{J}^N(\boldsymbol{u}_{\mathfrak{m}}^n)\right\|_{\widehat{\gamma}_{p,N}} \\
\eta_4^n &:= \left(\sum_{p\in\mathfrak{N}_{\mathfrak{m}}^C} (\eta_{4,p}^n)^2\right)^{\frac{1}{2}}, & \eta_{4,p}^n &:= h_p^{\frac{1}{2}} \|\boldsymbol{J}^C_{\tan}(\boldsymbol{u}_{\mathfrak{m}}^n)\|_{\widehat{\gamma}_{p,C}} \\
\eta_5^n &:= \left(\sum_{p\in\mathfrak{N}_{\mathfrak{m}}^C\setminus\mathfrak{N}_{\mathfrak{m}}^{\mathrm{fC}}} (\eta_{5,p}^n)^2\right)^{\frac{1}{2}}, & \eta_{5,p}^n &:= h_p^{\frac{1}{2}} \|\hat{\sigma}_1(\boldsymbol{u}_{\mathfrak{m}}^n)\|_{\widehat{\gamma}_{p,C}} \\
\eta_6^n &:= \left(\sum_{p\in\mathfrak{N}_{\mathfrak{m}}^{\mathrm{sC}}} (\eta_{6,p}^n)^2\right)^{\frac{1}{2}}, & \eta_{6,p}^n &:= \left(s_p^n \tfrac{1}{2} \textstyle\int_{b_p} (g_{\mathfrak{m}}^n - u_{\mathfrak{m},1}^n)\phi_p\right)^{\frac{1}{2}} \\
\eta_7^n &:= \left(\sum_{p\in\mathfrak{N}_{\mathfrak{m}}^{\mathrm{sC}}} (\eta_{7,p}^n)^2\right)^{\frac{1}{2}}, & \eta_{7,p}^n &:= \left(s_p^n \tfrac{1}{2} \textstyle\int_{b_p} (g_{\mathfrak{m}}^{n-1} - u_{\mathfrak{m},1}^{n-1})\phi_p\right)^{\frac{1}{2}}
\end{aligned}$$

where h_p is the diameter of $\widehat{\omega}_p$ and $b_p \subsetneq \widehat{\omega}_p$. Here, the set of all nodes is denoted by $\mathfrak{N}_{\mathfrak{m}}$, the subset of all nodes belonging to Γ_C is given by $\mathfrak{N}_{\mathfrak{m}}^C$ and the subset of all nodes belonging to $\bar{\Gamma}_N$ is given by $\mathfrak{N}_{\mathfrak{m}}^{\bar{N}}$. Further, $\boldsymbol{J}^I(\boldsymbol{u}_{\mathfrak{m}}^n) := (\boldsymbol{\sigma}(\boldsymbol{u}_{\mathfrak{m}}^n)|_{\mathfrak{e}_1} - \boldsymbol{\sigma}(\boldsymbol{u}_{\mathfrak{m}}^n)|_{\mathfrak{e}_2}) \cdot \boldsymbol{n}$ are the jump terms where $\mathfrak{e}_1$, $\mathfrak{e}_2$ are two elements sharing a side and $\boldsymbol{J}^N(\boldsymbol{u}_{\mathfrak{m}}^n) := \boldsymbol{\pi} - \hat{\boldsymbol{\sigma}}(\boldsymbol{u}_{\mathfrak{m}}^n)$ and $\boldsymbol{J}^C_{\tan}(\boldsymbol{u}_{\mathfrak{m}}^n) := -\hat{\boldsymbol{\sigma}}_{\tan}(\boldsymbol{u}_{\mathfrak{m}}^n)$.

If $g \neq g_{\mathfrak{m}}$ we get further estimator contributions, see [6, Section 3.2].

References

[1] J. R. Fernández and R. Martínez. A normal compliance contact problem in viscoelasticity: An a posteriori error analysis and computational experiments. *J. Comput. Appl. Math.* 235.12 (2011), pp. 3599–3614.

[2] Rolf Krause, Andreas Veeser, and Mirjam Walloth. An efficient and reliable residual-type a posteriori error estimator for the Signorini problem. *Numer. Math.* 130.1 (2015), pp. 151–197.

[3] Kyoung-Sook Moon, Ricardo H. Nochetto, Tobias von Petersdorff, and Chen-song Zhang. A posteriori error analysis for parabolic variational inequalities. *M2AN Math. Model. Numer. Anal.* 41.3 (2007), pp. 485–511.

[4] Andreas Veeser. Efficient and reliable a posteriori error estimators for elliptic obstacle problems. *SIAM J. Numer. Anal.* 39.1 (2001), pp. 146–167.

[5] Rüdiger Verfürth. *A posteriori error estimation techniques for finite element methods.* Numerical Mathematics and Scientific Computation. Oxford University Press, Oxford, 2013.

[6] Mirjam Walloth. Residual-type a posteriori error estimator for a quasi-static Signorini contact problem. *IMA J. Numer. Anal.* (2019). DOI: 10.1093/imanum/drz023.

**Proceedings of the 8th GACM Colloquium on Computational Mechanics
for Young Scientists from Academia and Industry
August 28–30, 2019 in Kassel, Germany**

Molecular Interactions of Slender Fibers Modeled as Cosserat Continua

Maximilian J. Grill *, Wolfgang A. Wall † and Christoph Meier ‡

Institute for Computational Mechanics, Technical University of Munich, Boltzmannstr. 15, 85748 Garching b. München, Germany

Abstract. This contribution presents a 3D beam-to-beam interaction model for molecular interactions between curved slender fibers undergoing large deformations recently proposed by the authors. A direct evaluation of the total interaction potential for general 3D bodies requires the integration of contributions from molecule or charge distributions over the volumes of the interaction partners, leading to a 6D integral (two nested 3D integrals) that has to be solved numerically. The novel strategy presented here proposes to formulate reduced section-to-section interaction laws for the resultant interaction potential between a pair of cross-sections of two slender fibers such that only two 1D integrals along the fibers' length directions have to be solved numerically. This section-to-section interaction potential (SSIP) approach yields a significant gain in efficiency, which is essential to enable the simulation of relevant time and length scales for many practical applications.

1 Introduction

Motivated by the abundance and manifoldness of slender fibrous species (e.g. collagen, DNA, cellulose) and their interactions in biological nano- and micro-scale systems, we propose a set of novel numerical methods to model different kinds of molecular interactions between such fibers. Due to the focus on macroscopic applications, most existing methods consider fiber interactions in form of mechanical contact, interpreted as a non-penetration constraint (see e.g. [3, 6, 10]). On the scale of nano- and micrometers, however, other molecular interactions such as electrostatics or van der Waals adhesion are no less crucial for the system behavior and for instance even outweigh the effect of gravity by orders of magnitude. Therefore, the development of accurate as well as efficient numerical methods is of utmost importance to enable the simulation of the large and complex assemblies, e.g., networks, bundles or membranes, that fibers typically form in biological systems. The long-term and higher-level goal of our research is to shed light on some of the many yet poorly understood mechanisms and processes in the human body that are governed by such fibrous structures. To give but one example, recent experiments with single collagen fibrils suggest that molecular interactions between their constituting parts, which are again fiber-like collagen molecules, contribute significantly to the overall mechanical response and might be exploited as a mechanism to tune their structural stiffness [1]. The development of a computational model for collagen fibrils in order to foster the in-depth understanding of their self-assembly and mechanics is one of the biophysical applications we are currently pursuing in interdisciplinary collaborations.

2 The section-section interaction potential (SSIP) approach

Our approaches are based on the first principles of molecular interactions, which are formulated as point pairwise interaction potentials $\Phi(r)$ and typically follow a power law in the separation r of the point-like, fundamental interaction partners, e.g. molecules or point charges. Understanding two deformable 3D bodies as continua composed of these fundamental interaction partners, the total interaction potential

*Corresponding author: grill@lnm.mw.tum.de ORCID iD: 0000-0003-1680-0259
†Corresponding author: wall@lnm.mw.tum.de ORCID iD: 0000-0001-7419-3384
‡Corresponding author: meier@lnm.mw.tum.de ORCID iD: 0000-0002-3501-1696

requires the numerical evaluation of two nested 3D, i.e., a 6D integral over the contributions of all individual point pairs [2, 8].

$$\Pi_{\mathrm{ia}} = \iint_{V_1,V_2} \rho_1(\mathbf{x}_1)\rho_2(\mathbf{x}_2)\,\Phi(r)\,\mathrm{d}V_2\mathrm{d}V_1 \tag{1}$$

Unfortunately, these high-dimensional integrals come at a tremendous computational cost, which renders the direct methods unfeasible if large fiber systems are considered. Thus, the slenderness of the fibers is fully exploited by employing a mechanical description as 1D Cosserat continua widely known from the so-called geometrically exact beam theory. In terms of the sought-after fiber-fiber interaction potential, this results in our novel, so-called section-section interaction potential (SSIP) approach [4], where the contributions of all pairs of beam cross-sections $\tilde{\tilde{\pi}}$ are cumulated in two nested 1D integrals along the centerline curves $\boldsymbol{r}_i$ of both interacting fibers $i = \{1, 2\}$.

$$\Pi_{\mathrm{ia}} = \iint_{l_1,l_2} \underbrace{\iint_{A_1,A_2} \rho_1(\boldsymbol{x}_1)\rho_2(\boldsymbol{x}_2)\,\Phi(r)\,\mathrm{d}A_2\mathrm{d}A_1}_{\text{SSIP law } \tilde{\tilde{\pi}}(\boldsymbol{r}_{1-2},\boldsymbol{\psi}_{1-2})}\ \mathrm{d}s_2\mathrm{d}s_1. \tag{2}$$

In this way, the need for numerical integration is reduced from 6D to 2D, which (in our considered examples) saves a factor of $10^4 - 10^6$ of integration point evaluations. The SSIP approach, which has exemplarily been derived for the cases of Coulombic, van der Waals and repulsive steric interactions, thus yields a significant gain in efficiency, which only enables the simulation of relevant time and length scales in the applications described above.

3 Numerical examples

3.1 Peeling and pull-off behavior of adhesive elastic fibers

The numerical example illustrated below has been studied in [5] and considers the separation of two adhesive elastic fibers starting from contact along their entire length to fully separated fibers. Figure 1 shows the problem setup and resulting force-displacement curve.

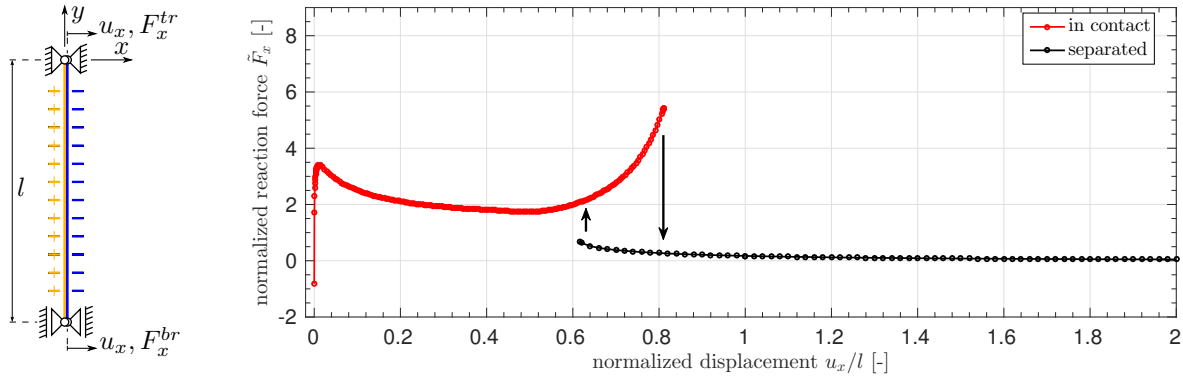

Figure 1. Numerical peeling and pull-off experiment with two adhesive elastic fibers. Problem setup (left) and resulting quasi-static force-displacement curve (right). Force values to be interpreted as multiple of a reference point load that causes a deflection of $l/4$ if applied at the fiber midpoint. Figure taken from [5].

3.2 Two oppositely charged fibers dynamically snap into contact

The numerical example illustrated below has been studied in [4] and considers two initially straight, crossed fibers, which snap into contact due to the electrostatic attraction of their opposite surface charges. Figure 2 shows the resulting sequence of simulation snapshots where electrostatic forces on both fibers are shown in green.

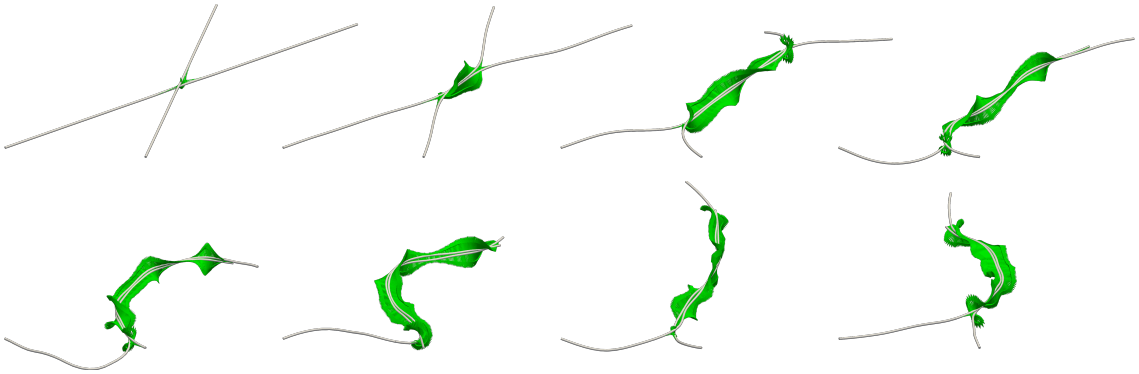

Figure 2. Sequence of simulation snapshots (left to right, top to bottom). Adhesive electrostatic forces acting on both fibers shown in green. Figure taken from [4].

4 Generalization

Interestingly, it will be shown that the section constitutive laws and objective deformation measures of the geometrically exact beam theory according to Simo [9] and Reissner [7] can be considered as a special case of the SSIP formulation in its most general form. In this special case, both interacting cross-sections (and thus all molecular interaction partners) are parts of one and the same beam. In fact, this result is not surprising since a body's macroscale constitutive behavior eventually follows from microscale interactions between its constituting molecules or atoms.

References

[1] Orestis G Andriotis, Sylvia Desissaire, and Philipp J Thurner. Collagen Fibrils: Nature's Highly Tunable Nonlinear Springs. *ACS Nano* 12.4 (2018), pp. 3671–3680.

[2] C Argento, A Jagota, and W C Carter. Surface formulation for molecular interactions of macroscopic bodies. *Journal of the Mechanics and Physics of Solids* 45.7 (1997), pp. 1161–1183.

[3] D Durville. Contact-friction modeling within elastic beam assemblies: an application to knot tightening. *Computational Mechanics* 49.6 (2012), pp. 687–707.

[4] Maximilian J. Grill, Wolfgang A. Wall, and Christoph Meier. A Computational Model for Molecular Interactions Between Curved Slender Fibers Underging Large 3D Deformations With a Focus on Electrostatic, van der Waals and Repulsive Steric Forces. *In preparation* ().

[5] Maximilian J. Grill, Christoph Meier, and Wolfgang A. Wall. Simulation of the Peeling and Pull-off Behavior of Adhesive Elastic Fibers. *In preparation* ().

[6] Christoph Meier, Wolfgang A. Wall, and Alexander Popp. A unified approach for beam-to-beam contact. *Computer Methods in Applied Mechanics and Engineering* 315 (2017), pp. 972–1010.

[7] E Reissner. On finite deformations of space-curved beams. *Zeitschrift für Angewandte Mathematik und Physik (ZAMP)* 32.6 (1981), pp. 734–744.

[8] Roger A. Sauer and Laura De Lorenzis. A computational contact formulation based on surface potentials. *Computer Methods in Applied Mechanics and Engineering* 253 (2013), pp. 369–395.

[9] J C Simo. A Finite Strain Beam Formulation. The Three-Dimensional Dynamic Problem. Part I. *Computer Methods in Applied Mechanics and Engineering* 49 (1985), pp. 55–70.

[10] P. Wriggers and G Zavarise. On contact between three-dimensional beams undergoing large deflections. *Communications in Numerical Methods in Engineering* 13.6 (1997), pp. 429–438.

**Proceedings of the 8th GACM Colloquium on Computational Mechanics
for Young Scientists from Academia and Industry
August 28–30, 2019 in Kassel, Germany**

An isogeometric scaled boundary shell formulation for thin-walled structures

Markus Klassen * [1] and Sven Klinkel[1]

[1]RWTH Aachen University

Abstract. The present work aims at a numerical implementation of a shell formulation which is capable to model extremely thin structures such as electroactive paper. To this end, the scale boundary concept is used for the description of the shell kinematics. This concept leads to a separation of the shell deformation in an in-plane and thickness direction. The separation is applicable to the discretization of the shell geometry as well as to the solution method for both directions. By this means, the scaling parameter is associated with the thickness of the shell. Furthermore, the formulation allows for a full 3D description of the constitutive law of the shell material. In this contribution, the in-plane direction is treated numerically by isogeometric analysis. This means that the in-plane geometry is discretized by NURBS functions which allow for a higher continuity between the isogemetric elements. For the thickness direction of the shell, two alternatives are proposed. The first option is given by a semi-analytical approach in which the displacement field along the thickness of the shell is approximated by an analytical solution. Under the assumption of linear elastic material behavior, the integration constants of the analytical ansatz are obtained by the boundary conditions of the top and bottom surface of the shell. The second option is proposed by the use of a collocation method along the scaling (thickness) direction. This approach can be regarded as a mixed numerical implementation with different methods on the in-plane and thickness direction. Due to the geometric simplicity of the shell thickness, B-Spline functions are considered for the numerical ansatz. The work presents the fundamental concept of the scaled boundary method for shells. Details for an isogeometric discretization on the in-plane direction are offered as well as the methodology for the two proposed shell thickness approaches. Subsequently, numerical examples are provided in order to reveal the capabilities of the proposed methods. Therefore, the obtained solutions are compared with analytical solutions as well as with standard finite element results.

1 Scaled boundary kinematics

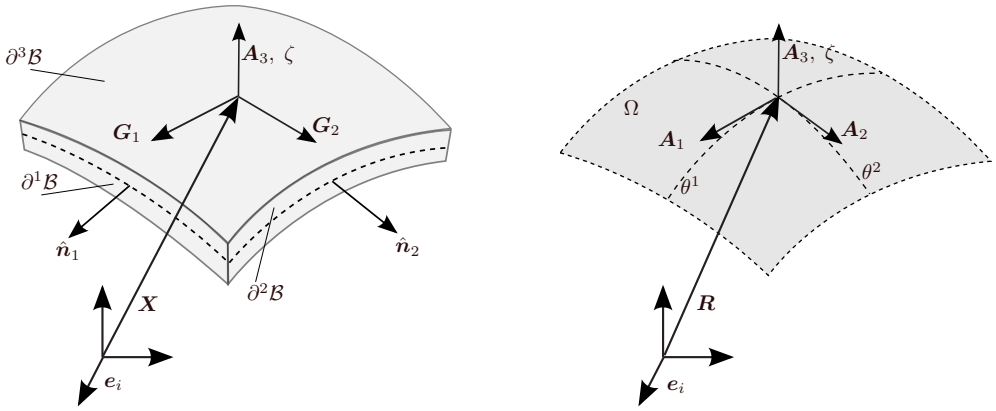

Figure 1. Left: the shell body $\mathcal{B}$ determined by the boundary surfaces $\partial^i\mathcal{B}$, right: the reference surface of the shell with convective coordinates θ^α

The geometry of the shell body $\mathcal{B}$ is given by a curvilinear coordinate system θ^α, $\theta^3 = \zeta$ in which the Greek indexes take the values of 1,2 while ζ is regarded as the thickness parameter which also corresponds to the scaling parameter, see Fig. 1. A point on the reference surface Ω (mid surface) is defined by the

*Corresponding author: klassen@lbb.rwth-aachen.de

position vector $\boldsymbol{R}(\theta^\alpha)$. Thus, by means of the scaled boundary geometry description, the position vector of a point in the shell body $\mathcal{B}$ is provided according to,

$$\boldsymbol{X}(\theta^\alpha, \zeta) = \boldsymbol{R}(\theta^\alpha) + \zeta \boldsymbol{A}_3(\theta^\alpha), \tag{1}$$

in which $\boldsymbol{A}_3$ is the normal vector to the reference surface Ω. The co-variant tangent vectors are obtained by the parametric derivatives of the position vector. Thus,

$$\boldsymbol{G}_\alpha = \boldsymbol{R}_{,\alpha} + \zeta \boldsymbol{A}_{3,\alpha}\,, \quad \boldsymbol{G}_3 = \boldsymbol{A}_3 \quad \text{in } \mathcal{B}. \tag{2}$$

For the computation of the gradient and divergence of tensorial quantities in matrix notation by means of the scaled boundary kinematics, the L-operator is introduced according to

$$\mathbf{L}(\dots) = \underbrace{\begin{bmatrix} \boldsymbol{G}^\alpha \cdot \boldsymbol{e}_1 & 0 & 0 \\ 0 & \boldsymbol{G}^\alpha \cdot \boldsymbol{e}_2 & 0 \\ 0 & 0 & \boldsymbol{G}^\alpha \cdot \boldsymbol{e}_3 \\ \boldsymbol{G}^\alpha \cdot \boldsymbol{e}_2 & \boldsymbol{G}^\alpha \cdot \boldsymbol{e}_1 & 0 \\ \boldsymbol{G}^\alpha \cdot \boldsymbol{e}_3 & 0 & \boldsymbol{G}^\alpha \cdot \boldsymbol{e}_1 \\ 0 & \boldsymbol{G}^\alpha \cdot \boldsymbol{e}_3 & \boldsymbol{G}^\alpha \cdot \boldsymbol{e}_2 \end{bmatrix}}_{\boldsymbol{b}_\alpha} \frac{\partial \dots}{\partial \theta^\alpha} + \underbrace{\begin{bmatrix} \boldsymbol{A}_3 \cdot \boldsymbol{e}_1 & 0 & 0 \\ 0 & \boldsymbol{A}_3 \cdot \boldsymbol{e}_2 & 0 \\ 0 & 0 & \boldsymbol{A}_3 \cdot \boldsymbol{e}_3 \\ \boldsymbol{A}_3 \cdot \boldsymbol{e}_2 & \boldsymbol{A}_3 \cdot \boldsymbol{e}_1 & 0 \\ \boldsymbol{A}_3 \cdot \boldsymbol{e}_3 & 0 & \boldsymbol{A}_3 \cdot \boldsymbol{e}_1 \\ 0 & \boldsymbol{A}_3 \cdot \boldsymbol{e}_3 & \boldsymbol{A}_3 \cdot \boldsymbol{e}_2 \end{bmatrix}}_{\boldsymbol{b}_3} \frac{\partial \dots}{\partial \zeta}. \tag{3}$$

It should be noted, that the matrices $\boldsymbol{b}_\alpha$ are defined by the contra-variant tangent vectors $\boldsymbol{G}^\alpha$ and the orthonormal Cartesian basis vectors $\boldsymbol{e}_i$. Under this perspective, the strain tensor is obtained in matrix notation for the scaled boundary kinematics through the application of the L-operator on the displacement vector $\boldsymbol{u}$,

$$\boldsymbol{\varepsilon} = \mathbf{L}\boldsymbol{u} = \boldsymbol{b}_\alpha \boldsymbol{u}_{,\alpha} + \boldsymbol{b}_3 \boldsymbol{u}_{,\zeta}\,. \tag{4}$$

2 Governing equations

The equilibrium state of the shell body $\mathcal{B}$ is defined by the local balance of linear momentum and the Neumann traction on the boundary of the shell $\partial_t \mathcal{B}$. Therefore, the equilibrium is modeled by the governing field equations

$$\mathbf{L}^T \boldsymbol{\sigma} + \rho \boldsymbol{b} = \mathbf{0} \qquad \text{in } \mathcal{B}, \tag{5}$$

$$\boldsymbol{n}_i^T \boldsymbol{\sigma} = \bar{\boldsymbol{t}} \qquad \text{on } \partial_t^i \mathcal{B}. \tag{6}$$

For the numerical solution of the boundary value problem, the displacement $\boldsymbol{u}$ and virtual displacement $\delta\boldsymbol{u}$ are discretized for the in-plane directions by means of the introduced scaled boundary concept,

$$\boldsymbol{u}(\theta^\alpha, \zeta) = \boldsymbol{N}(\theta^\alpha)\hat{\boldsymbol{u}}(\zeta), \quad \delta\boldsymbol{u}(\theta^\alpha, \zeta) = \boldsymbol{N}(\theta^\alpha)\,\delta\hat{\boldsymbol{u}}(\zeta). \tag{7}$$

It should be noted, that the field vectors are approximated by form functions $\boldsymbol{N}(\theta^\alpha)$ which are defined on the reference surface Ω of the shell. The discretization in scaling (thickness) direction $\hat{\boldsymbol{u}}(\zeta)$, $\delta\hat{\boldsymbol{u}}(\zeta)$ is not defined yet, since two approaches are to be compared in this contribution. For this reason, the field equation in scaling direction needs to derived by taking the discretization on the in-plane direction into account. This is performed through the application of the principle of virtual work on eqns. (5) and (6) and subsequent partial integration. Furthermore, a linear elastic constitutive law is assumed in the present contribution. Substituting the discretizations (7) in the derivation process leads to the balance equations for the scaling direction which are obtained as,

$$\boldsymbol{E}_0 \hat{\boldsymbol{u}}_{,\zeta\zeta} + (\boldsymbol{E}_1 - \boldsymbol{E}_1^T - \bar{\boldsymbol{E}}_1^T)\hat{\boldsymbol{u}}_{,\zeta} - (\boldsymbol{E}_2 + \bar{\boldsymbol{E}}_2)\hat{\boldsymbol{u}} + \boldsymbol{F}_b = \mathbf{0}, \tag{8}$$

$$(\boldsymbol{E}_0 \hat{\boldsymbol{u}}_{,\zeta} + \boldsymbol{E}_1 \hat{\boldsymbol{u}} - \boldsymbol{F}_\zeta)\Big|_{\partial^3 \mathcal{B}} = \mathbf{0}. \tag{9}$$

It is observed, that the differential equations are functions of the scaling parameter ζ. The coefficients are obtained by the integration over the reference surface Ω and are defined as follows:

$$\boldsymbol{E}_0 = \int_{\theta^1}\int_{\theta^2} \boldsymbol{B}_3^T \mathbb{C} \boldsymbol{B}_3 J \,\mathrm{d}\theta^1 \,\mathrm{d}\theta^2, \quad \boldsymbol{E}_1 = \int_{\theta^1}\int_{\theta^2} \boldsymbol{B}_3^T \mathbb{C} \boldsymbol{B}_{12} J \,\mathrm{d}\theta^1 \,\mathrm{d}\theta^2, \quad \bar{\boldsymbol{E}}_1 = \int_{\theta^1}\int_{\theta^2} \boldsymbol{B}_3^T \mathbb{C} \bar{\boldsymbol{B}}_{12} J \,\mathrm{d}\theta^1 \,\mathrm{d}\theta^2, \tag{10}$$

$$\boldsymbol{E}_2 = \int_{\theta^1}\int_{\theta^2} \boldsymbol{B}_{12}^T \mathbb{C} \boldsymbol{B}_{12} J \,\mathrm{d}\theta^1 \,\mathrm{d}\theta^2, \quad \bar{\boldsymbol{E}}_2 = \int_{\theta^1}\int_{\theta^2} \bar{\boldsymbol{B}}_{12}^T \mathbb{C} \boldsymbol{B}_{12} J \,\mathrm{d}\theta^1 \,\mathrm{d}\theta^2. \tag{11}$$

The $\mathbb{C}$ matrix denotes the elasticity tensor for a 3D linear elastic constitutive law and J stands for the determinant of the Jacobian. The B-matrices are obtained in dependency of the in-plane shape functions $\boldsymbol{N}(\theta^\alpha)$ and the matrices introduced with the L-operator,

$$\boldsymbol{B}_3^T = \boldsymbol{N}^T \boldsymbol{b}_3^T, \qquad \boldsymbol{B}_{12}^T = \boldsymbol{N}^T{}_{,\alpha}\, \boldsymbol{b}_\alpha^T, \qquad \bar{\boldsymbol{B}}_{12}^T = \boldsymbol{N}^T \boldsymbol{b}_\alpha^T{}_{,\alpha}\,. \tag{12}$$

The shell reference surface Ω is provided by CAD data. By means of isogeometric analysis, the discretization of the solution field on the in-plane direction, see (7), is performed with NURBS functions. Regarding the scaling direction, two approaches are considered.

3 Methodology in scaling direction

In order to complete the element formulation, two methods are proposed for the solution of the thickness direction of the shell. The first method consists in a semi-analytical formulation in which the thickness displacement distribution is described by an exponential function. The second approach is a numerical one which is defined by the collocation method which solves the governing equations at the collocation points.

3.1 Semi-analytical method

A semi-analytical shell element formulation is obtained by providing the analytical solution for eqns. (8) and (9). To this end, the mentioned equations are rearranged into a system of first order differential equations. In addition, a dual vector field is introduced as the main unknown. It consists of the displacement field $\hat{\boldsymbol{u}}(\zeta)$ and the traction force $\boldsymbol{F}_\zeta(\zeta)$ in scaling direction. Consequently, the system of equations can be expressed as a homogeneous first order differential equation in which the matrix exponential function is the general solution. The matrix exponential function is computed by a Taylor series. The consideration of the traction boundary conditions $\boldsymbol{F}_\zeta(\zeta)$ at the top and bottom surface of the shell body allows for the elimination of the integration constants in the general solution. Thus, the relation between $\boldsymbol{F}_\zeta(\zeta)$ and $\hat{\boldsymbol{u}}(\zeta)$ is obtained, which defines the shell element stiffness matrix, see [1]. Each element node is defined by 6 degrees of freedom in which three correspond to the displacement of the shell bottom and three to the shell top.

3.2 Collocation Method

In the collocation method, the field eqns. (8) and (9) are evaluated at so called collocation points along the scaling direction. For this purpose, the displacement field $\hat{\boldsymbol{u}}(\zeta)$ is discretized by a linear combination of B-Spline functions which is then substituted in the mentioned equations. The order of the B-Spline functions is defined by the number of collocation points according to $p = n_{cp} - 1$ in which n_{cp} is the number of collocation points. The coordinates of the collocation points are defined in dependency of the B-Spline knot vector by means of the Greenville abscissae. By the evaluation of eqns. (8) and (9), a linear system of equations is obtained which defines the stiffness matrix of the shell element. In contrast to the semi-analytical shell element, the number of degrees of freedom per node depends on the number of collocations points in which three degrees of freedom are assigned to each collocation point.

4 Numerical results

The objective of the numerical example is to provide a first implementation test of the proposed isogeometric shell formulation with the analytical and collocation method for the thickness direction. To this end, the proposed methods are compared with the implementation of a standard solid finite element and a scaled boundary method in which the thickness direction is solved by a weak formulation. For the sake of simplicity, a plate geometry as depicted in Fig. 2 is studied. The dimensions of the plate are defined by $w = l = 1$ and the thickness is considered as a variable parameter for the study. A linear elastic constitutive law is defined for the material behavior with $E = 1000$ and $\nu = 0.3$. Furthermore, a traction of $T_x = 4$ is applied as a boundary condition as shown in Fig. 2. It is important to note, that the traction boundary condition is only applied to the degrees of freedom which correspond to the top

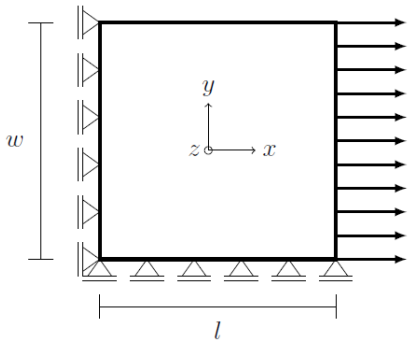

Figure 2. Setting.

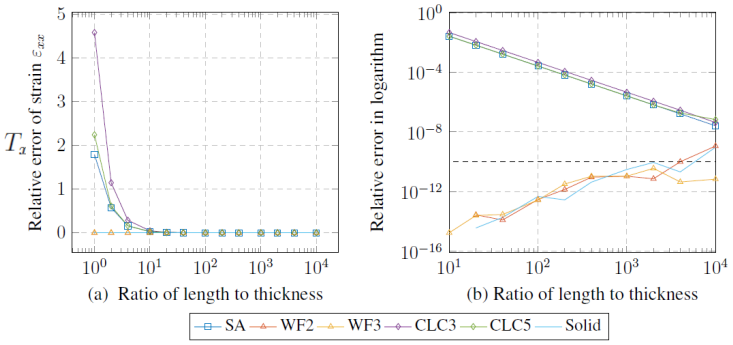

Figure 3. Results

and bottom surface of the plate. The reason is given by the limitation of the semi-analytical element which only allows for top and bottom degrees of freedom. In order to evaluate the numerical results, a relative error is defined for the study. It consists of the relative difference between the strain in traction direction of the numerical results and the strain obtained according to Hooke's law for a linear elastic material. At this point it should be noted, that the analytical strain obtained by Hook's law assumes a homogeneous traction distribution over the thickness of the plate. Since the traction forces are applied as singular loads on the top and bottom surface of the plate in the proposed methods, an inward buckling of the cross section is predicted. This buckling effect is more pronounced for thick plates and vanishes with decreasing plate thickness.

The discretization of the plate is performed on the in-plane direction with linear NURBS which corresponds to a standard finite element implementation with linear Lagrange polynomials. In scaling direction, four different strategies are considered. The first one considers the semi-analytical (SA) method while the second one consists in the collocation method with 3 (CLC3) and 5 (CLC5) collocation points. In both strategies, the traction forces are only applied on the top and bottom degrees of freedom which allows for the cross sectional buckling. In the third case, solid elements (Solid) with linear Lagrange interpolation are considered while the fourth method is defined by a weak formulation with two and three nodes over the plate thickness with linear (WF2) and quadratic (WF3) interpolation. In the latter strategies, the application of the traction force is applied by means of a constant distribution over the thickness which does not allow for a cross sectional buckling.

The relative error in dependency of the length to thickness ratio is depicted in Fig. 3. It can be observed, that the semi-analytical (SA) and the collocation method (CLC3, CLC5) converge to the analytical solution with a decreasing plate thickness. This effect is due to the traction boundary conditions which allow for a cross sectional buckling. For the cases of a large plate thickness, the buckling leads to a larger deformation than the one predicted by Hooke's law for constant traction over the thickness. Furthermore, it is observed that the proposed methods agree very well. In the simulations with a constant traction over the thickness (Solid, WF2 and WF3), the relative error increases unsteadily as the plate thickness decreases. This observation speaks for a lower capability of the latter methods to handle elements with a large length to thickness ratio.

Acknowledgments

The authors thank the German research foundation (DFG) for the funding of the project KL 1345/15-1.

References

[1] H. Man, C. Song, W. Gao, and F. Tin-Loi. A unified 3D-based technique for plate bending analysis using scaled boundary finite element method. *Int. J. Numer. Meth. Engng* 91 (2012), pp. 491–515.

**Proceedings of the 8th GACM Colloquium on Computational Mechanics
for Young Scientists from Academia and Industry
August 28–30, 2019 in Kassel, Germany**

Free Material Optimization of Multilayer Composite Materials

Simon Loske *[1] and Franz-Joseph Barthold[1]

[1]Structural Mechanics, TU Dortmund, Dortmund, Germany

Abstract. The use of composite materials in various types of devices has increased steadily in the past decades. Hence, it is worth investigating into the structural behaviour of these materials. The optimization of stacking sequences in multilayer composite materials opens a large field of improvements in industrial applications of composite materials. The center of investigation is set on fiber reinforced laminate plies, which are examined in the case of linear anisotropic theory of elasticity. One very auspicious way for optimization of these laminates is the implementation of Free Material Optimization (FMO). In these optimization procedures, arbitrary values of parameters of the elasticity matrix are obtained under constraints that only require the elasticity matrix to be symmetric and positive semidefinite. Also, the trace of the elasticity matrix is restricted to prevent the total stiffness of the material from becoming unnaturally large. Sensitivity information is obtained by the variational approach for sensitivity analysis [1], which represents the most efficient known way of computing sensitivity information.

Introduction

The most important application area of FMO is thin walled structures like laminates of very high strength fiber materials, often used in aerospace or wind energy applications. The fundamental idea of FMO is the optimization of a material tensor, which can vary in each single Gaussian point of the design domain. There is only one major restriction to the optimization, which is that the material tensor has to be positive semidefinite. The obtained values of the material tensor are characterizing the distribution of material density and local material properties in an indirect way. The most promising approach with the idea of FMO lies in patch field analysis, which identifies larger areas in the structure with insignificantly changing stress fields. Due to the restriction on the material tensor to be positive semidefinite, the obtained problem is a nonlinear semidefinite optimization problem [3]. With that requirement, the Method of Moving Asymptotes (MMA) [2] seems to be an appropriate alternative to the nonlinear semidefinite optimization algorithms. Controlling the eigenvalues of the material tensors to be strictly positive values fulfills the controlling of positive semidefiniteness.

1 FMO Problem Formulation

The examined optimization problem is limited to two-dimensional linear elasticity, so that stresses can only occur in the plane. Assuming a two-dimensional material law reduces the number of independent material parameters in each Gaussian point from a total number of 21 (symmetric three-dimensional material) to a number of only 6 independent parameters

$$\hat{\boldsymbol{E}} = \begin{bmatrix} E_1 & E_3 & E_5 \\ E_3 & E_2 & E_6 \\ E_5 & E_6 & E_4 \end{bmatrix}, \qquad \text{with} \quad \hat{\boldsymbol{E}} = \hat{\boldsymbol{E}}^T \succcurlyeq 0. \tag{1}$$

In the FMO approach the material parameters are usually not restricted by physical properties. It is convenient to restrict the design domain by boxed constraints that are calibrated by reasonable values which are known from the typical physical behavior of materials like Young's modulus or Poisson's ratio.

*Corresponding author: simon.loske@tu-dortmund.de

However, there are no restrictions to the relation between different parameters, which are part of the material tensor, so that they can vary completely independently from each other. That leads to the fact that, normally, no material exists that can exactly fulfill all the optimized material parameters. This is not a big problem if the focus is put on multilayer materials. In this case, the material tensor of a laminate is the result of preintegration of material properties in each single layer over the whole thickness.

The weak form of static equilibrium can be obtained by

$$\boldsymbol{R}(\boldsymbol{u},\boldsymbol{v}) = \int_\Omega \hat{\boldsymbol{\sigma}}(\boldsymbol{u},\boldsymbol{s}) : \hat{\varepsilon}(\boldsymbol{v})\,\mathrm{d}\Omega - \int_\Omega \boldsymbol{b}\cdot\boldsymbol{v}\,\mathrm{d}\Omega - \int_\Gamma \bar{\boldsymbol{t}}\cdot\boldsymbol{v}\,\mathrm{d}\Gamma. \tag{2}$$

With this weak form, the pseudoload matrix, which is essential for the optimization can be calculated by variation. In this weak form only the term of stresses is dependent on the design variables

$$\boldsymbol{P} = \frac{\partial \boldsymbol{R}}{\partial \boldsymbol{s}} = \int_\Omega \frac{\partial \hat{\boldsymbol{\sigma}}(\boldsymbol{u},\boldsymbol{s})}{\partial \boldsymbol{s}} : \hat{\varepsilon}(\boldsymbol{v})\,\mathrm{d}\Omega = \int_\Omega \frac{\partial \hat{\boldsymbol{E}}}{\partial \boldsymbol{s}}\,\hat{\varepsilon}(\boldsymbol{u}) : \hat{\varepsilon}(\boldsymbol{v})\,\mathrm{d}\Omega. \tag{3}$$

The optimization problem is the minimization of compliance,that is, the maximization of global stiffness. The compliance C and its gradient with respect to changes in design can be calculated from known quantities

$$C(\boldsymbol{s}) = -2\,\Pi(\boldsymbol{s}) = \boldsymbol{u}^T\boldsymbol{f}, \qquad \nabla_s C(\boldsymbol{s}) = \frac{\partial C(\boldsymbol{s})}{\partial \boldsymbol{s}} = -2\frac{\partial \Pi(\boldsymbol{s})}{\partial \boldsymbol{s}} = -\boldsymbol{u}^T\boldsymbol{P}. \tag{4}$$

This leads to the optimization problem with control of eigenvalues and density

$$\begin{aligned} &\text{minimize } C(\boldsymbol{s}),\\ s_i^l \le s_i \le\ & s_i^u, \qquad i = 1,...,6,\\ -\lambda_j \le\ & 0, \qquad j = 1,...,3,\\ \rho^l \le t\sum_{j=1}^{3}\lambda_j \le\ & \rho^u. \end{aligned} \tag{5}$$

2 Numerical Example With Patch Analysis

To show that the optimization scheme is working precisely, a numerical example is consulted. Therefore, a cantilever beam is chosen, which is clamped on one edge and loaded on the other. For the initial design and the affecting force, the following values are assumed

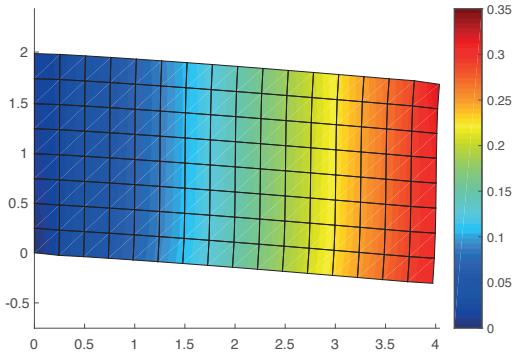

Figure 1. Initial deformation of structure

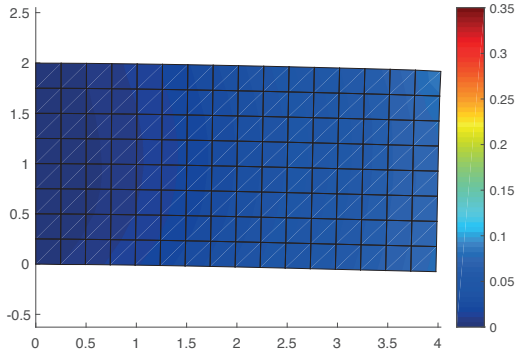

Figure 2. Optimized deformation of structure

$$\hat{\boldsymbol{E}} = \begin{bmatrix} 50000 & 1000 & 1000 \\ 1000 & 50000 & 1000 \\ 1000 & 1000 & 1000 \end{bmatrix}, \qquad t = 0.1, \qquad F = 10,$$

$$1000 \leq E_i \leq 100000, \qquad 300 \leq t \sum_{j=1}^{3} \lambda_j \leq 12000. \tag{6}$$

Fig. 1 and Fig. 2 show the significant change in compliance through the process.

In the patch analysis the whole structure is divided into a fixed number of patches, in which the materials parameters are the same for all elements belonging to this patch. This reduces the number of design parameters to a much lower number, depending on the number of assumed patches. Thereby the size of patches is the same for all of them and they are disposed in a structured mesh (cf. Fig. 3).

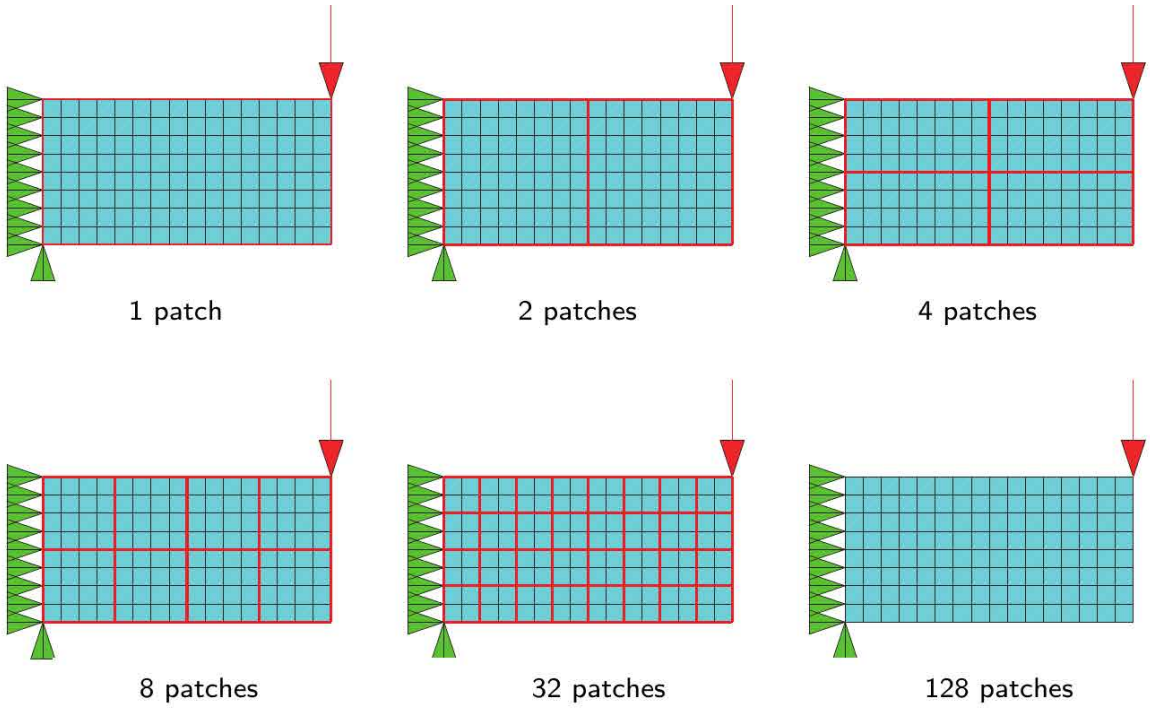

Figure 3. Subdivision of area in different number of patches, with equal material properties

Table 1. Results in compliance, number of iterations and computing time with respect to number of patches

Number of patches	Compliance	Number of iterations	Computing time in s
1	0.9687	153	47
2	0.9653	157	60
4	0.9563	178	67
8	0.8854	217	84
32	0.8471	414	162
128	0.8392	630	7462

In Tab. 1 it is shown that for a low number of patches the number of finite elements is the same for all models. The total number of design variables can be preserved by the number of patches and 6 design variables per patch. The number of necessary iteration and the computing time does not change

significantly. Also, the compliance is decreasing slowly. For a very high number of patches, the number of iteration and most strikingly the computing times are increased significantly.

Acknowledgments

The founding of this project by the German Research Foundation (DFG) and the provision of the MMA algorithm by Krister Svanberg [2] is kindly acknowledged.

References

[1] N. Gerzen, F. J. Barthold, S. Klinkel, W. Wagner, and D. Materna. Variational sensitivity analysis of a nonlinear solid shell element. *International Journal for Numerical Methods in Engineering* 96.1 (2013), pp. 29–42. DOI: 10.1002/nme.4545. URL: https://doi.org/10.1002%2Fnme.4545.

[2] Krister Svanberg. The method of moving asymptotes—a new method for structural optimization. *International Journal for Numerical Methods in Engineering* 24.2 (1987), pp. 359–373. DOI: 10.1002/nme.1620240207. URL: https://doi.org/10.1002%2Fnme.1620240207.

[3] Alemseged Gebrehiwot Weldeyesus and Mathias Stolpe. Free material optimization for laminated plates and shells. *Structural and Multidisciplinary Optimization* 53.6 (2016), pp. 1335–1347. DOI: 10.1007/s00158-016-1416-3. URL: https://doi.org/10.1007%2Fs00158-016-1416-3.

**Proceedings of the 8th GACM Colloquium on Computational Mechanics
for Young Scientists from Academia and Industry
August 28–30, 2019 in Kassel, Germany**

Mesh Tying and Contact Algorithms for Nonlinear Beam-to-Solid Interactions

Ivo Steinbrecher * [1] and Alexander Popp[1]

[1]Institute for Mathematics and Computer-Based Simulation, University of the Bundeswehr Munich (UniBw M), Germany

Abstract. The interaction of Rod- or Beam-like structures with 3-dimensional continua (solids) can be found in a variety of different physical problems, e.g. fiber-reinforced materials. In many cases a complete 3-dimensional model of the beams is numerically expensive and leads to a considerable modeling effort. A homogenization of the composite material on the other hand, comes with limitations when detailed information about the interaction between beams and solid is desired. This work introduces a beam-to-solid volume coupling method, based on classical mortar methods, which allows for the efficient coupling of 1-dimensional beams models to 3-dimensional solids, while still being able to preserve their complex effect on the overall response of the coupled structure.

Introduction

From a mechanical point of view, rod- or beam-like structures can be represented by a 1-dimensional continuum, described by a centerline and – depending on the kinematic assumptions of the employed beam theory – up to three rotations of the beam cross-section. This leads to a reduced set of governing equations compared to a full 3-dimensional continuum, thus allowing for an efficient numerical analysis of such structures.

Going beyond purely beam-based structures, many applications also require accurate models for the fully nonlinear interaction between beams and solid bodies. Beam-to-solid interaction can be divided into three elementary cases: beam-to-volume coupling, beam-to-surface coupling and beam-to-surface contact. In the presented case of beam-to-volume coupling, a beam is embedded inside a solid volume, and the beam is tied to the solid. For the numerical simulations, we utilize the finite element method (FEM) to discretize both the beams and solids [2, 5]. The constraints are discretized with mortar coupling methods, which have become state-of-the-art in the coupling of non matching rids on deformable solids [3, 4].

1 Problem formulation

We consider a 3D finite deformation beam-to-solid volume coupling problem as shown in Figure 1. The principle of virtual (PVW) work serves as basis for the employed finite element method. Contributions to the total virtual work of the system can be split up into solid, beam and coupling terms, whereat the beam and solid terms are independent the coupling constraint. Therefore well established formulations for the solid as well as the beam can be used without modification. Obviously, this introduces a modeling error, since we assume overlapping material points, but nonetheless this allows for an efficient and simple model of the solid, while still being able to account for complex nonlinear effects due to the embedded beams.

The beam-to-solid coupling constraints are formulated on the beam surface Γ^B in the reference configuration and read

$$\underline{\boldsymbol{u}}^B - \underline{\boldsymbol{u}}^S = \underline{\mathbf{0}} \quad \text{on} \quad \Gamma^B. \tag{1}$$

The mortar method is employed to discretize the coupling, introducing a Lagrange multiplier vector field $\underline{\boldsymbol{\lambda}}$ defined on Γ^B, which can be interpreted as the negative interface tractions acting on the beam surface.

*Corresponding author: ivo.steinbrecher@unibw.de

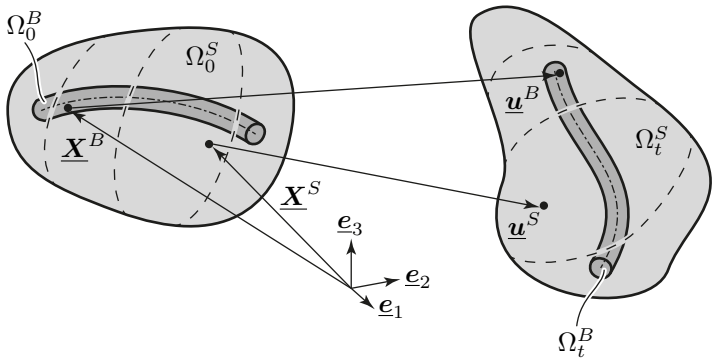

Figure 1. Notation of the finite deformation beam-to-solid volume coupling problem.

Contributions to the total virtual work are the virtual work of the coupling tractions and the variational form of the coupling constraints

$$-\delta W_c^f = \int_{\Gamma^B} \underline{\boldsymbol{\lambda}} \left(\delta \underline{\boldsymbol{u}}^B - \delta \underline{\boldsymbol{u}}^S\right) \mathrm{d}A_0 \,, \qquad \delta W_\lambda^f = \int_{\Gamma^B} \delta \underline{\boldsymbol{\lambda}} \left(\underline{\boldsymbol{u}}^B - \underline{\boldsymbol{u}}^S\right) \mathrm{d}A_0 \,. \tag{2}$$

These integrals are evaluated on the coupling surface Γ^B which results in computationally expensive numerical integration. If the cross-section radius of the beams is small compared to the other dimensions of the beam-to-solid volume coupling problem, we can approximate those surface integrals as line integrals along the beam centerline

$$\delta W_c^f \approx \int_L \underline{\boldsymbol{\lambda}} \left(\delta \underline{\boldsymbol{u}}^B - \delta \underline{\boldsymbol{u}}^S\right) ds \; = \delta W_c, \qquad \delta W_\lambda^f \approx \int_L \delta \underline{\boldsymbol{\lambda}} \left(\underline{\boldsymbol{u}}^B - \underline{\boldsymbol{u}}^S\right) ds \; = \delta W_\lambda. \tag{3}$$

This approximation changes the coupling applied on the physical beam-to-solid volume coupling model. The full surface integrals represent a surface-to-volume coupling, while the approximated line integrals model a line-to-volume (1D-3D) coupling. This is a significant change in the mathematical description of the mechanical model, which has implications on the coupling of beam cross-section rotations. The coupling terms are now exclusively formulated along the beam centerline, which uncouples the cross-section rotations from the solid deformations.

2 Spatial discretization and numerical integration

A finite element discretization is employed to approximate the continuous fields for position, displacement and Lagrange multipliers, as well as their variations. The discretization introduces discrete values for the field functions and interpolates them with corresponding shape functions,

$$\underline{\boldsymbol{u}}_h^S = \sum_{k=1}^{n_S} N_k \boldsymbol{d}^S, \qquad \underline{\boldsymbol{u}}_h^B = \sum_{k=1}^{n_B} H_k \boldsymbol{d}^B, \qquad \underline{\boldsymbol{\lambda}}^h = \sum_{k=1}^{n_\lambda} \Phi_k \boldsymbol{\lambda}. \tag{4}$$

For the interpolation of the Lagrange multipliers standard linear Lagrangian shape functions are employed. Inserting the finite element discretization into the virtual work of the coupling terms leads to the discretized coupling interactions

$$-\delta W_{c,h} = \delta \boldsymbol{d}^{B\,\mathrm{T}} \boldsymbol{D}^{\mathrm{T}} \boldsymbol{\lambda} - \delta \boldsymbol{d}^{S\,\mathrm{T}} \boldsymbol{M}^{\mathrm{T}} \boldsymbol{\lambda} \tag{5}$$

$$\delta W_{\lambda,h} = \delta \boldsymbol{\lambda}^{\mathrm{T}} \boldsymbol{D} \boldsymbol{d}^B - \delta \boldsymbol{\lambda}^{\mathrm{T}} \boldsymbol{M} \boldsymbol{d}^S, \tag{6}$$

where $\boldsymbol{D}$ and $\boldsymbol{M}$ are the so called mortar coupling matrices defined as

$$\boldsymbol{D}[j,k] = \int_L \Phi_j H_k ds \, \boldsymbol{I}, \qquad \boldsymbol{M}[j,k] = \int_L \Phi_j \left(N_k \circ \chi_h\right) ds \, \boldsymbol{I}. \tag{7}$$

All integrals are evaluated on the beam centerline, therefore a projection of the solid shape functions onto the beam centerline is required, which is denoted with the nonlinear mapping operation $N_k \circ \chi_h$. Accurate

numerical integration is fundamental to fulfill basic consistency tests for beam-to-solid volume coupling. Figure 2 illustrates the two different types of numerical integration schemes used to evaluate the coupling terms. Element-based integration uses a fixed number of Gauss–Legendre integration points per beam element, only if a beam sticks out of the solid domain (strong discontinuity), the integration domain is adapted. Segment-based integration on the other hand also splits the integration domain at points where the beam crosses between two solid elements (weak discontinuity). A comprehensive comparison between the different numerical integration schemes in the context of 3-dimensional mortar coupling can be found in [1].

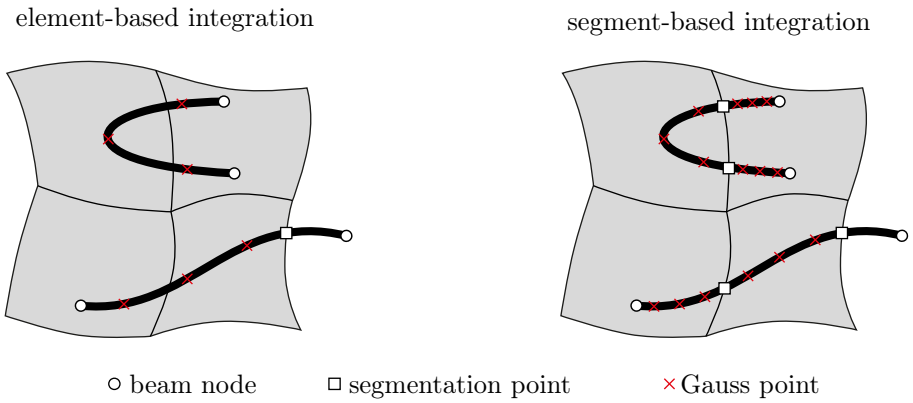

Figure 2. Illustration of element-based (left) and segment-based (right) integration.

The mortar coupling constraints are enforced via the penalty method, resulting in the following global quasi-static equilibrium equations

$$\begin{bmatrix} \boldsymbol{K}_{SS} + \epsilon \boldsymbol{M}^{\mathrm{T}} \boldsymbol{M} & -\epsilon \boldsymbol{M}^{\mathrm{T}} \boldsymbol{D} \\ -\epsilon \boldsymbol{D}^{\mathrm{T}} \boldsymbol{M} & \boldsymbol{K}_{BB} + \epsilon \boldsymbol{D}^{\mathrm{T}} \boldsymbol{D} \end{bmatrix} \begin{bmatrix} \boldsymbol{d}^S \\ \boldsymbol{d}^B \end{bmatrix} = \begin{bmatrix} \boldsymbol{r}^S \\ \boldsymbol{r}^B \end{bmatrix}, \tag{8}$$

where ϵ is the penalty parameter.

3 Examples

Figure 3 shows the patch test setup used to verify the consistency of the beam-to-solid volume coupling method, as well as the results obtained with different numerical integration schemes for the coupling terms. It is clear that segment based integration gives better results than the element based integration, i.e. a lower integration error.

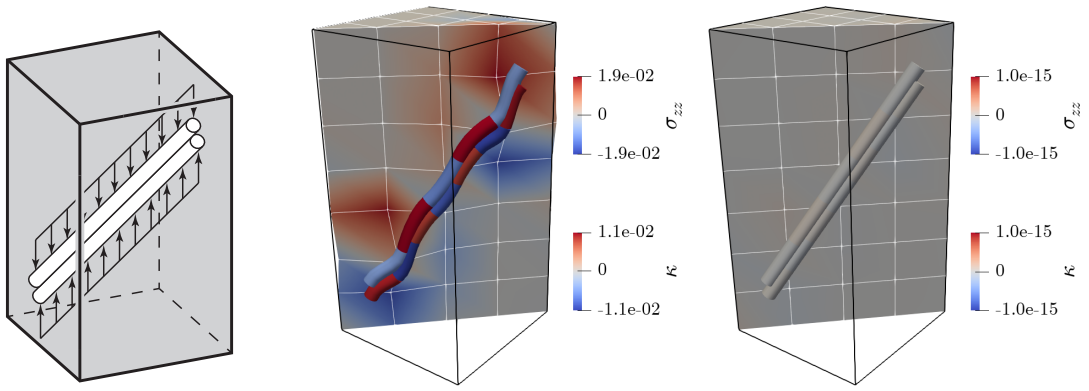

Figure 3. Patch test with overlapping straight beams – problem setup (left), element-based integration (middle) and segment-based integration (right). The Cauchy stress σ_{zz} is shown in the solid and the curvature κ at the middle of each beam element. Displacements of beams and solid are scaled with a factor of 100.

The spatial convergence of the beam-to-solid volume coupling method is shown in Figure 4. One can see that for a certain element size the approximation of the coupling terms as line integrals results in a non

converging behavior. At this point the solid element size is in the same range as the beam cross-section dimensions and the line integral approximation does not accurately describe the coupling terms.

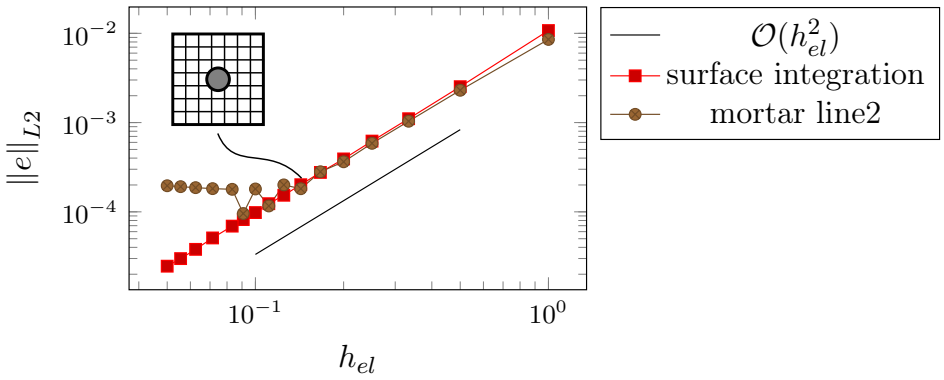

Figure 4. Spatial convergence behavior of the displacement error $\|e\|_{L2}$ – the solid mesh with the beam cross-section is shown for the mesh configuration where the convergence of the centerline coupling stops.

To demonstrate the applicability of the beam-to-solid volume coupling method to problems with fiber-reinforced materials, Figure 5 shows a composite plate with an unsymmetrical layer setup, where the fibers are modeled using beam elements and the matrix is modeled with solid-shell elements. In the right part of Figure 5 the coupling tractions between the fibers and the matrix are shown.

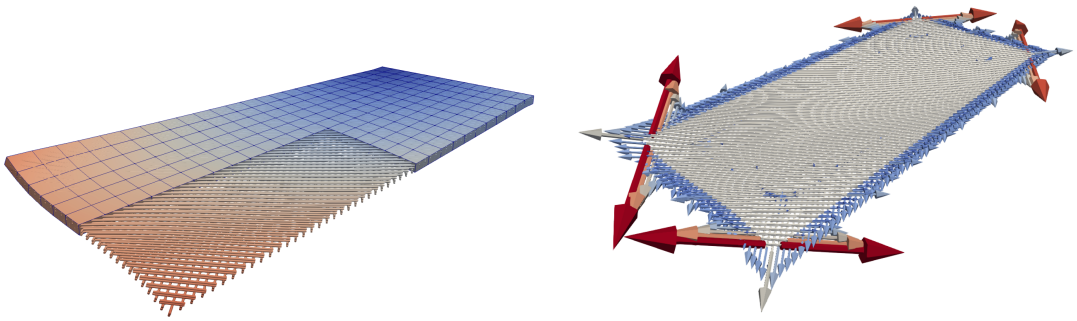

Figure 5. Composite plate, fibers modeled with beam elements – deformed structure (left), coupling tractions between the beams and the matrix (right).

References

[1] P. Farah, A. Popp, and W. A. Wall. Segment-Based vs. Element-Based Integration for Mortar Methods in Computational Contact Mechanics. *Computational Mechanics* 55.1 (2015), pp. 209–228.

[2] C. Meier, A. Popp, and W. A. Wall. Geometrically Exact Finite Element Formulations for Slender Beams: Kirchhoff–Love Theory Versus Simo–Reissner Theory. *Archives of Computational Methods in Engineering* 26.1 (2017), pp. 163–243.

[3] A. Popp and P. Wriggers. *Contact Modeling for Solids and Particles*. Springer, 2018.

[4] M. A. Puso. A 3D Mortar Method for Solid Mechanics. *International Journal for Numerical Methods in Engineering* 59.3 (2004), pp. 315–336.

[5] P. Wriggers. *Nonlinear Finite Element Methods*. Springer-Verlag Berlin Heidelberg, 2008.

**Proceedings of the 8th GACM Colloquium on Computational Mechanics
for Young Scientists from Academia and Industry
August 28–30, 2019 in Kassel, Germany**

Analysis of support conditions applying coupling-based deformation modes in Generalised Beam Theory (GBT)

Fabiola Tartaglione * [1], Marcelo J. Bianco[1], Abinet K. Habtemariam[1], Volkmar Zabel[1] and Carsten Könke[1]

[1]Institute of Structural Mechanics. Bauhaus-Universität Weimar, Germany

Abstract.

Thin-walled structures are generally subjected to mechanical effects such as cross-sectional ovalisation and warping. Existing approaches to study their mechanical behaviour require computationally intensive shell element models. The Generalised Beam Theory (GBT) is a numerical method that has an excellent performance for analysing local and global stability of thin-walled structures, overcoming the computational efforts demanded by shell element models. While conventional GBT analysis has made substantial progress, the coupling of GBT deformation modes due to partial support conditions has not been addressed yet. This research focuses on the implementation of multi-freedom constraints in linear GBT for modelling the existing coupling between deformation modes due to stiff or flexible spring support conditions. The applicability of the proposed method is verified through numerical simulations of an above-ground pipeline system with various partial support conditions and compared with Kirchoff-Love and Reissner-Midlin shell models. The results demonstrated accurate predictions in the displacement and stress fields using the GBT coupling analysis. It is also concluded that increasing the number of participating deformation modes in the GBT analysis revealed a higher correlation of the results with respect to the shell FEM solutions.

Keywords: above-ground pipeline systems, generalised beam theory, master-slave method, coupling deformation modes, exact finite element formulation, partial supports.

Introduction

Above-ground pipelines are thin-walled structural systems that are generally analysed using shell elements. Nevertheless, the use of these elements would result in large computational cost due to the large amount of degrees of freedom (DOF) needed. The detailed mechanics that must be described requires also rigorous and precise treatment. Therefore, a remarkable alternative for modelling above-ground pipelines is the Generalised Beam Theory (GBT).

GBT is a state-of-the-art approach which analyses local and global stability behaviour of thin-walled members by incorporating 2D aspects of shell theories into the classical beam theory, providing the faculty to describe distortion and shear deformation [6]. Although the theory provides accurate results by itself [2, 4, 6], further developments in terms of the coupling between deformation modes have not been addressed yet.

Typically, boundary conditions in GBT application are assumed orthogonal for several engineering problems. However, non-standard support conditions can no longer sustain this major assumption, as the boundary conditions act as a coupler factor among the traditional uncoupled GBT modes. Non-standard boundary conditions of above-ground pipelines, namely partial supports over the perimeter of the cross-section, lead to coupling of GBT deformation modes.

In this work, the implementation of multi-freedom constraints (MFC) in linear GBT is carried out to model the existing coupling between deformation modes due to partial localised stiff or flexible spring support conditions. GBT elements are implemented based on an exact finite GBT element formulation [1], while MFC are based on the master-slave method, which serves as a coupling relation between all GBT deformation modes. The applicability of the coupling method is verified through numerical simulations of an above-ground pipeline system with various partial support conditions and compared with Kirchoff-Love and Reissner-Midlin shell models.

*Corresponding author: fabiola.tartaglione@uni-weimar.de ORCID iD: https://orcid.org/0000-0001-6566-4682

1 GBT analysis

GBT is a numerical method introduced by Schardt [5] that adds to the kinematics of Vlasov the distortion of the cross-section by means of expressing the deformation of the member as the superposition of a series of cross-sectional modes. Hence, GBT equations are decoupled with respect to normal stresses and transverse stresses [4]. GBT's main feature is the cross-section analysis, which is based on the geometry and mechanical properties of the cross-section. The analysis leads to n natural orthogonal deformation mode shapes, where lower modes (i=1,2,3) represent the rigid body modes, i.e. elongation and bending in both transverse directions; and higher modes (i>3) describe the cross-section distortions and ovalisations. The analysis for a circular hollow sections (CHS) is defined by orthogonal deformation modes (see Figure 1a) based on Fourier series [5]. The displacement field is described for the centre line of the cross-section at each angular position θ as:

$$u\left(x,\theta\right)=\sum_{i=1}^{n}{}^{i}u\left(\theta\right){}^{i}V_{,x}\left(x\right)\qquad v\left(x,\theta\right)=\sum_{i=1}^{n}{}^{i}v\left(\theta\right){}^{i}V\left(x\right)\qquad w\left(x,\theta\right)=\sum_{i=1}^{n}{}^{i}w\left(\theta\right){}^{i}V\left(x\right)\tag{1}$$

where u, v and w are the displacements in longitudinal, transverse tangential and transverse perpendicular directions, respectively; while ${}^{i}V(x)$ is the amplification function along the beam length for each GBT deformation mode i. In the longitudinal displacement u, the first derivative ${}^{i}V_{,x}(x)$ grants the possibility to describe zero-shear deformations.

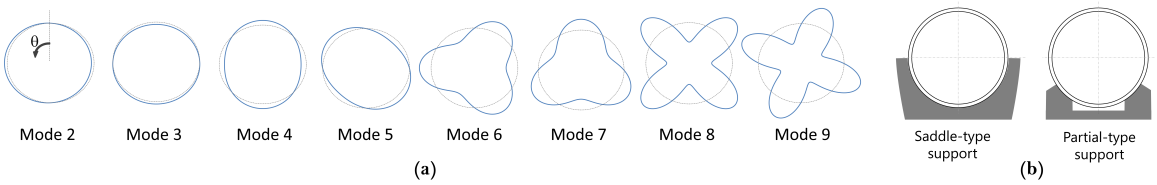

Figure 1. (a) Cross-section deformation mode shapes according to GBT.
(b) Partial supports types for above-ground pipeline systems.

2 Coupling-based deformation modes in GBT

One of GBT's main assumptions is the orthogonality between modal displacements and stress fields. Thus, the final GBT equations are decoupled with respect to normal stresses and transverse stresses [3]. Although typical boundary conditions - Dirichlet or Neumann types - are assumed to be orthogonal in GBT, non-standard support conditions such as the partial nodal supports in Figure 3b, suggest a factorisation between the conventional GBT deformation modes. Hence, the final displacement state of a cross-section is a relation between the rigid-body modes and the ovalisation modes, which is found at each support node. The MFC is carried out by means of the master-slave method, which consists in defining the master and slave DOF. The slave DOF are then explicitly eliminated. For the implementation of the method, the boundary condition can be expressed as:

$${}^{sp}\delta w\left(\bar{\theta}\right)=\sum_{i=1}^{n}{}^{i}w\left(\bar{\theta}\right){}^{i}V\left(x=x_{sp}\right)\tag{2}$$

where ${}^{sp}w$ is the unknown spring displacement located at $\bar{\theta}$. This displacement shall be equal to the summation of all GBT participating modes, which are affected by the amplification function at the longitudinal position of the support x_{sp}. From this expression a coupling vector is obtained, which is represented by the slave mode as function of the remaining deformation modes. Therewith, the modified displacement can be determined and transformed into the actual displacement. A scheme of this procedure is presented in Figure 2.

Two general conditions arise in the analysis: (i) each spring support leads to one coupling equation which require at least two GBT deformation modes to be coupled; as a consequence, (ii) GBT deformation

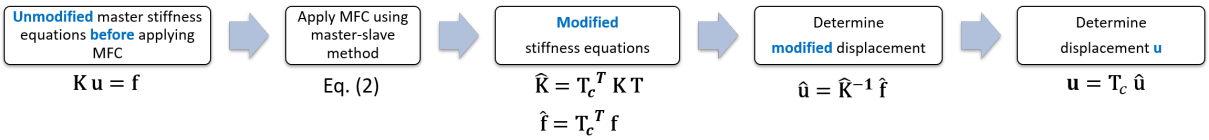

Figure 2. Scheme of multi-freedom constraints (MFC) application.

modes with and without external loads have a contribution to the total beam stiffness. In order to satisfy the conditions, for n coupling springs, the number of GBT modes to consider shall be $n+1$. Additionally, due to symmetric load conditions as illustrated in Figure 3b, the actual presence of locking effect can be avoided by considering only half of the total of spring equations for the complete cross-section analysis.

3 Numerical example

The coupling method is verified through a symmetric 4-span above-ground pipeline system. The partial nodal supports shown in Figure 3b have been defined -in structural terms - as elastic translational springs with a stiffness of 500N/mm. The pipeline system is subjected to self-weight and a linear projected surface load due to gas weight. The material properties are Young's modulus $E = 2.1 \cdot 10^5$ MPa and Poisson's ratio ν=0.3.

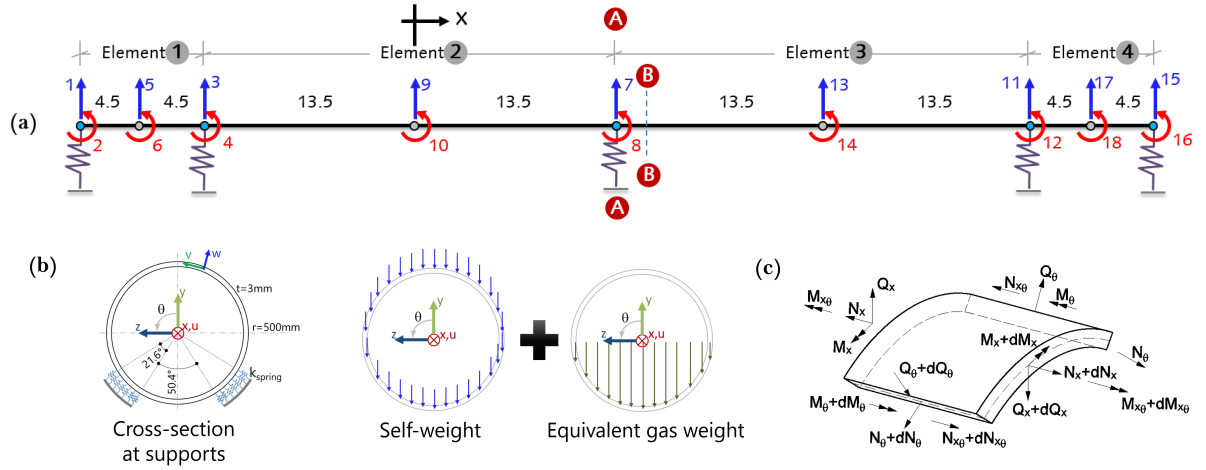

Figure 3. (a) Longitudinal discretisation in GBT ; (b) Cross-section and external forces ; (c) Internal forces orientation

The cross-section deformation and internal forces obtained from GBT and FEM shell analysis for section A-A are presented in Figure 4 and 5. Considering 7 coupling equations, the number of GBT modes to analyse is then $n = 8$. Two analyses in GBT for this case were conducted. The first analysis involves only conventional deformation modes, while in the second analysis 28 modes including the extension mode ($i = 1$) are assessed. As far as shell analysis is regarded, linear Kirchoff-Love and Reissner-Midlin shell elements in Ansys® were considered.

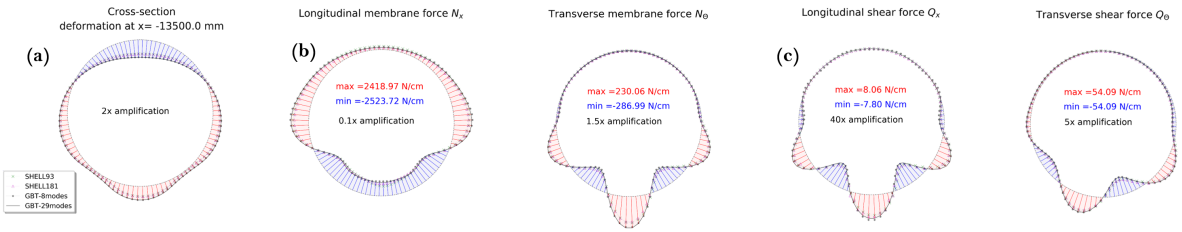

Figure 4. (a) Cross-section deformation ; Longitudinal and transverse (b)membrane forces (c) plate forces

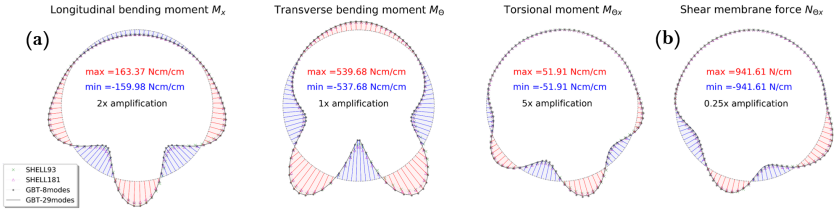

Figure 5. (a) Longitudinal, transverse and torsion moments; (b) Shear membrane force

Regarding the numerical performance, the required amount of DOF in the GBT analysis was around 544, compared to the nearly 1.44 Million DOF required in the shell analysis. This comparison evidences one of the most remarkable aspects from GBT analysis. Results from GBT regarding the displacement field at support nodes in section A-A showed an excellent agreement with shell element models. Also, when more than the minimum required GBT modes were taken into account, the correlation between GBT and shells tended to increase. In the stress field, results from both analyses showcased a disruption, which can be associated to the implementation of non-standard support conditions. Therewith, results of internal forces illustrated in Figure 4 correspond to a cross-section B-B, which is at 0.5m distant from section A-A that presented consistent results for both analyses. The results obtained in GBT have also shown a high correlation with respect to shell analysis. As seen in the displacement field, correlation between models increases when more GBT deformations modes are included.

4 Conclusions

In this work, the implementation of MFC in linear GBT to model the coupling between deformation modes due to non-standard support conditions has been conducted. The Master-Slave method has been used due to its straightforward implementation. With the application of this coupling method, main assumptions from conventional GBT have been changed. Therewith, the new linear equation system must be solved considering that the coupling equations generated due to boundary conditions requires a minimum amount of deformation modes. Consequently, all deformation modes - with and without external loads - are coupled and contribute to the internal stress energy. Results have demonstrated that GBT presents an outstanding numerical performance with respect to shell analysis. Moreover, an excellent correlation between shell models and GBT has been obtained for both displacement and stress fields for several cases. A difference between results can be diminished if more GBT deformation modes are included in the GBT analysis for non-standard support conditions.

Acknowledgments

This work was carried out under the Horizon 2020 MSCA-RISE-2015 project No. 691213 entitled “Exchange Risk”.

References

[1] M.J. Bianco, C. Könke, A.K. Habtemariam, and V. Zabel. Exact finite element formulation in generalized beam theory. *International Journal Advanced Structural Engineering* (2018), 295—323.

[2] D. Camotim, N. Silvestre, C. Basaglia, and R. Bebiano. GBT-based buckling analysis of thin-walled members with non-standard support conditions. *Thin-Walled Structures* 46 (2008), pp. 800–815.

[3] J. Jönsson and M.J. Andreassen. Distortional eigenmodes and homogeneous solutions for semi-discretized thin-walled beams. *Thin-Walled Structures* 49 (2011), pp. 691–707.

[4] J. Jönsson and M.J. Andreassen. Distortional solutions for loaded semi-discretized thin-walled beams. *Thin-Walled Structures* 50 (2012), pp. 116–127.

[5] Richard Schardt. *Verllgemeinerte Technische Biegetheorie*. Springer-Vertrag, 1989.

[6] N. Silvestre and D. Camotim. Influence of shear deformation on the local and global buckling behaviour of composite thin-walled members. In: *Proceedings of the 4th International Conference on Thin-Walled Structures*. Ed. by J. Loughlan. IOP Publishing Ltd, 2003, pp. 659–668.

**Proceedings of the 8th GACM Colloquium on Computational Mechanics
for Young Scientists from Academia and Industry
August 28–30, 2019 in Kassel, Germany**

Multirate GARK schemes for the simulation of fluid-structure interaction: Linear stability and the geometric conservation law

Sascha Bremicker-Trübelhorn*[1] and Sigrun Ortleb[1]

[1]University of Kassel, Department of Mathematics, Heinrich-Plett-Str. 40, 34132 Kassel, Germany

Abstract. A novel loosely coupled partitioned approach to the simulation of mechanical fluid-structure interaction (FSI) problems based on step size-adaptive multirate GARK schemes (MGARK) and discontinuous Galerkin schemes (DG) is presented. We use mixed implicit-explicit (IMEX) GARK schemes of orders up to three for the temporal integration of the DG-discretized partitioned fluid-structure system and apply these GARK schemes in a multirate fashion to respect the different time scales of the involved subsystems. An efficient coupling between the subsystems is realized by using a compound step-based coupling strategy that preserves the order of the base RK schemes. The linear stability properties of the overall temporal integration scheme are investigated and it is shown how the geometric conservation law (GCL) can be respected by calculating the velocities of the moving mesh points in an appropriate way. Additionally, we consider the relation between geometrical conservation and the ability of the scheme to preserve its order obtained on a fixed mesh also in the presence of arbitrary mesh motion. The feasibility and efficiency of our approach is investigated by applying it to a two-dimensional test case of inviscid compressible flow around an oscillating airfoil.

Introduction

Coupled systems as in the context of fluid-structure interaction (FSI) often consist of subsystems with significantly different time scales. These subsystems may also deviate considerably in terms of their stiffness. It is reasonable to allow each subsystem of the coupled problem to advance with its preassigned time integration scheme which is adapted to its stiffness and time scales. In addition, it is sensible to evaluate slow components less often than fast ones. In [1, 2] the authors have shown how the class of multirate generalized-structure additively partitioned Runge-Kutta schemes [3]—the multirate generalization of the class of GARK schemes [6]—can be used to do so, and successfully applied it in a novel step size-adaptive fashion to the 1D piston problem, a classical test problem of mechanical FSI.

This paper shows the feasibility of this approach for the application to a more complex 2D problem of mechanical FSI and is structured as follows: First, in Sec. 1 we briefly describe the considered test case and its spatial discretization. In Sec. 2 we sketch our multirate time integration approach and investigate its linear stability properties. Sec. 3 gives insight on how to respect the geometric conservation law (GCL) within our 2D-DG-MGARK approach and on the relation of GCL-compliance and the preservation of our scheme's temporal order of convergence in the presence of mesh motion. The numerical results obtained from applying our scheme to the described test case of FSI are shown in Sec. 4. The paper finishes with a summary of our conclusions in Sec. 5.

1 Test case of fluid-structure interaction and its spatial discretization

We consider an oscillating NACA0012 airfoil with two degrees of freedom—which are rotation and vertical displacement—that is exposed to transonic compressible fluid flow with a Mach number of 0.8. This problem has already been used in the past to study the performance of multirate IMEX procedures [5]. The fluid flow is considered to be inviscid and is therefore modeled with the compressible Euler equations. The airfoil is modeled as an harmonic oscillator driven by the external forces lift and torque, that are exerted by the fluid surrounding it.

*Corresponding author: struebel@mathematik.uni-kassel.de

The 2D fluid equations are spatially discretized within the arbitrary Lagrangian-Eulerian (ALE) framework using a discontinuous Galerkin (DG) approach on a triangle mesh comprising 9050 triangular cells. In order to take into account the mesh motion as a result of the deformation of the spatial fluid domain due to the structure's movement, radial basis function interpolation is used to determine the inner mesh nodes with respect to the current state of the structure system.

2 Multirate generalized-structure additively partitioned Runge-Kutta schemes

We regard the problem described in Sec. 1 as a partitioned system of first-order ordinary differential equations, which comprises two components: the DG-discretized fluid component and the structure component, which corresponds to the oscillating airfoil. Due to its generally shorter time scales, the fluid subsystem is considered as the fast component and is advanced with several small and generally adaptive so-called micro steps h_λ, while at the same time the slow component (i. e. the structure) is advanced with only one large so-called macro step H. Let N denote the ratio of micro steps per macro step, which is allowed to change from one macro step to the next due to the adaptivity of the step sizes. With $m_\lambda = H/h_\lambda$ $(\lambda = 1, \dots, N)$ the generalized Butcher table of our scheme reads

$$
\begin{array}{c|c}
\boldsymbol{A}^{\{1,1\}} & \boldsymbol{A}^{\{1,2\}} \\
\hline
\boldsymbol{A}^{\{2,1\}} & \boldsymbol{A}^{\{2,2\}} \\
\hline
\boldsymbol{b}^{\{1\}\mathsf{T}} & \boldsymbol{b}^{\{2\}\mathsf{T}}
\end{array}
=
\begin{array}{cccc|c}
m_1\boldsymbol{A}^{\{\mathfrak{f},\mathfrak{f}\}} & & & & \boldsymbol{A}^{\{\mathfrak{f},\mathfrak{s},1\}} \\
m_1\mathbf{1}\boldsymbol{b}^{\{\mathfrak{f}\}\mathsf{T}} & m_2\boldsymbol{A}^{\{\mathfrak{f},\mathfrak{f}\}} & & & \boldsymbol{A}^{\{\mathfrak{f},\mathfrak{s},2\}} \\
\vdots & \vdots & \ddots & & \vdots \\
m_1\mathbf{1}\boldsymbol{b}^{\{\mathfrak{f}\}\mathsf{T}} & m_2\mathbf{1}\boldsymbol{b}^{\{\mathfrak{f}\}\mathsf{T}} & \cdots & m_N\boldsymbol{A}^{\{\mathfrak{f},\mathfrak{f}\}} & \boldsymbol{A}^{\{\mathfrak{f},\mathfrak{s},N\}} \\
\hline
m_1\boldsymbol{A}^{\{\mathfrak{s},\mathfrak{f},1\}} & \mathbf{0} & \cdots & \mathbf{0} & \boldsymbol{A}^{\{\mathfrak{s},\mathfrak{s}\}} \\
\hline
m_1\boldsymbol{b}^{\{\mathfrak{f}\}\mathsf{T}} & m_2\boldsymbol{b}^{\{\mathfrak{f}\}\mathsf{T}} & \cdots & m_N\boldsymbol{b}^{\{\mathfrak{f}\}\mathsf{T}} & \boldsymbol{b}^{\{\mathfrak{s}\}\mathsf{T}}
\end{array}
\,.
$$

Since only the very first micro step is coupled to the macro step, all further coupling coefficients of the fluid-to-structure-coupling part of the Butcher table are set to zero. We chose explicit RK base schemes $(\boldsymbol{A}^{\{\mathfrak{f},\mathfrak{f}\}}, \boldsymbol{b}^{\{\mathfrak{f}\}})$ for the integration of the fluid subsystem and implicit RK base schemes $(\boldsymbol{A}^{\{\mathfrak{s},\mathfrak{s}\}}, \boldsymbol{b}^{\{\mathfrak{s}\}})$ for the integration of the structure subsystem. Further details on our order-preserving fully explicit coupling strategies and on the applied IMEX base schemes can be found in [2].

2.1 Linear stability

We studied the linear stability properties of our schemes using the two-times component partitioned test equation $\boldsymbol{u}'(t) = \boldsymbol{E}\boldsymbol{u}(t)$, with $\boldsymbol{u}\colon \mathbb{R}_{\geq 0} \to \mathbb{R}^2$, $\boldsymbol{E} \in \mathbb{R}^{2\times 2}$. Let H denote the macro step size and $\boldsymbol{Z} = H\boldsymbol{E}$. We computed the amplification matrix resulting from applying our micro step size-adaptive MGARK scheme to the test equation and showed that its eigenvalues can be expressed in terms of the three quantities

$$
\xi = \frac{z_{1,1}}{1 - z_{1,1}}, \qquad \eta = \frac{z_{1,2}z_{2,1}}{2z_{1,1}z_{2,2} - z_{1,2}z_{2,1}} \qquad \text{and} \qquad \kappa = \frac{z_{2,2}}{z_{1,1}},
$$

which correspond to the admissibly macro step size, strength and orientation of the coupling, and the stiffness ratio of the subsystems, respectively. We showed that in the case of the invertibility of the matrices $\boldsymbol{I} - z_{1,1}\boldsymbol{A}^{\{1,1\}}$ and $\boldsymbol{I} - z_{2,2}\boldsymbol{A}^{\{2,2\}} - z_{1,2}z_{2,1}\boldsymbol{A}^{\{2,1\}}(\boldsymbol{I} - z_{1,1}\boldsymbol{A}^{\{1,1\}})^{-1}\boldsymbol{A}^{\{1,2\}}$ the subset

$$
\left\{ \boldsymbol{Z} \in \mathbb{R}^{2\times 2} \;\middle|\; z_{1,1}, z_{2,2} < 0 \;\wedge\; \tfrac{z_{1,2}z_{2,1}}{z_{1,1}z_{2,2}} \neq 2 \;\wedge\; \forall \lambda \in \sigma(\boldsymbol{Z}) : \mathrm{Re}(\lambda) < 0 \right\} \cap S
$$

of the whole stability region S can be expressed in terms of $(\xi, \eta, \kappa) \in (-1, 0) \times (-1, 1) \times (0, \infty)$, which on the one hand provides a more compact representation of that region and on the other hand reduces its dependence from four variables to three. By numerically determining this stability region's subset in terms of ξ, η and κ for the developed MGARK schemes of orders up to three and a varying ratio of micro steps per macro step, we found that our first order scheme has a large stability region even in the case of high step size rates N and turned out to be well-suited for the application to stiff problems. However, in the case of high stiffness the third order method suffers from a severe loss of stability under increasing N, which makes it less suited for the efficient application within our multirate framework.

3 The geometric conservation law

For numerical simulations involving the movement of the spatial mesh, special attention on geometrical conservation has to be paid. The usage of the ALE-formulation for the spatial discretization of the fluid equations led to a modification of the convective flux tensor depending on the velocities of the moving mesh nodes. Our schemes satisfy the geometric conservation law (GCL)—i. e. they exactly preserve any initially uniform flow—by the careful construction of these mesh velocities within every RK-stage of every micro step of the fast fluid RK-integration in a suitable way. To do so, we extended an approach derived in [4] to the application to our 2D-DG-MGARK schemes. The approach is based on a space-time DG-discretization of the fluid equations, which is known to automatically satisfy the GCL, and a linear and continuous finite element ansatz for the mesh velocity. The equations for the mesh velocity obtained within this space-time DG-formulation are then translated into the DG-MGARK context.

We verified the GCL-compliance of our schemes of orders up to three both analytically and numerically, using an artificial mesh motion on a 2D test grid. It was observed that a naive choice of the mesh velocity by using its analytical values obtained by differentiating the artificial mesh motion equations led to a violation of the GCL. Nevertheless, the GCL-compliant choice of the mesh velocity led to a loss of the temporal order of convergence for the third order MGARK scheme in the case of simulations with a non-uniform initial condition. Since this loss of order was not observed with the naive and non-GCL-compliant choice of the mesh velocity for this kind of simulations, we conclude that GCL-compliance is neither a sufficient nor necessary condition for a numerical scheme to preserve its order of convergence obtained on a fixed mesh also in the presence of arbitrary mesh motion.

4 Numerical results for the considered test case

The results shown in Fig. 1 were obtained by applying the GCL-compliant DG-MGARK schemes of orders one and two to the test case described in Sec. 1, using constant step sizes and various ratios N of micro steps per macro step. In each case the spatial order of the DG-approximation is chosen to match the temporal order of the respective MGARK scheme. The reference solution was computed with a monolithic all-explicit RK procedure of the respective order of convergence for the integration of the overall FSI system using a suitable small uniform time step size.

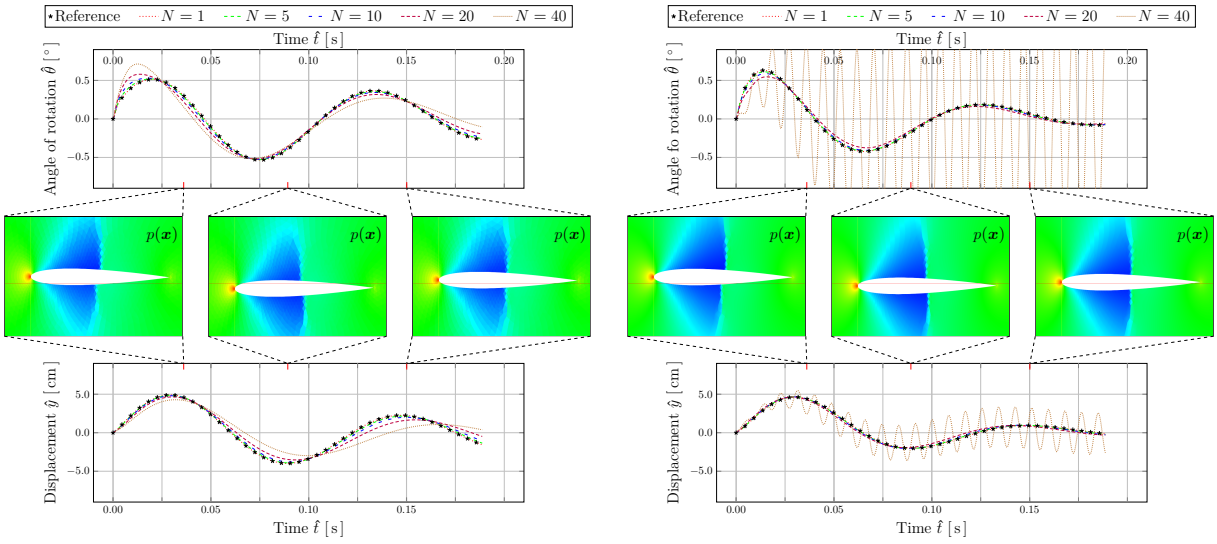

Figure 1. Evolution of the angle of rotation $\hat{\theta}$ and of the vertical displacement $\hat{y}$ of the NACA0012 airfoil for different step size rates N. The fluid pressure p in the environment of the airfoil is shown at three selected points in time. Left: First-order simulation. Right: Second-order simulation.

For step size ratios up to $N = 20$, the results obtained with the first-order scheme are close to or very close to the reference solution. Only the case $N = 40$ shows clearly recognizable deviations from the reference in terms of the amplitude and frequency of the observed oscillation. The second-order scheme shows very similar behavior with regard to the quality of the results obtained for up to and including

$N = 20$. The results for the case $N = 40$, however, show a superposition of the actual oscillation with a higher frequency and unphysical disturbance. This loss of stability observed for higher ratios of step sizes becomes even more severe for the third-order scheme (not shown in the figure), in case of which the simulations with $N \geq 20$ diverged after a short time and $N = 5$ resp. $N = 10$ produced slight resp. strong deviations from the reference oscillation.

Therefore, the first- and second-order scheme proved to be well suited for the application within the described multirate context in case of not too large step size ratios, whereas the third-order scheme turned out to be less suited for this kind of application.

5 Conclusion

This paper focused on the linear stability properties and the compliance with the geometric conservation law of our loosely coupled step size-adaptive multirate partitioned mixed implicit-explicit approach [1, 2] to the simulation of mechanical fluid-structure interaction. We showed the feasibility of combining DG-based high-order spatial discretization with high-order MGARK-based temporal discretization schemes and successfully applied our scheme to the simulation of 2D transonic compressible flow around an oscillating airfoil. The GCL-compliance of the scheme is assured by the careful construction of suitable mesh velocities within every RK-stage of every micro step of the fluid RK-integration. Both the linear stability analysis and the numerical results showed that the first- and second order schemes are well suited for the application within the considered multirate context, whereas the third-order scheme suffers from severe stability issues. Future research might therefore focus on the construction of a more robust and stable third-order DG-MGARK scheme.

References

[1] S. Bremicker-Trübelhorn and S. Ortleb. Time-adaptive multirate generalized-structure additively partitioned Runge-Kutta schemes for mechanical fluid-structure interaction. *PAMM* 16.1 (2016), pp. 869–870. DOI: 10.1002/pamm.201610423.

[2] S. Bremicker-Trübelhorn and S. Ortleb. On Multirate GARK Schemes with Adaptive Micro Step Sizes for Fluid–Structure Interaction: Order Conditions and Preservation of the Geometric Conservation Law. *Aerospace* 4.1 (2017). DOI: 10.3390/aerospace4010008.

[3] M. Günther and A. Sandu. *Multirate generalized additive Runge Kutta methods.* Technical Report CSL-TR-6/2013. Computational Science Laboratory, 2013. arXiv: 1310.6055.

[4] D. J. Mavriplis and C. R. Nastase. On the geometric conservation law for high-order discontinuous Galerkin discretizations on dynamically deforming meshes. *J. Comp. Phys.* 230.11 (2011), pp. 4285–4300. DOI: 10.1016/j.jcp.2011.01.022.

[5] S. Piperno. Explicit/implicit fluid/structure staggered procedures with a structural predictor and fluid subcycling for 2D inviscid aeroelastic simulations. *International Journal for Numerical Methods in Fluids* 25 (1997), pp. 1207–1226.

[6] A. Sandu and M. Günther. A Generalized-Structure Approach to Additive Runge-Kutta Methods. *SIAM J. Numer. Anal.* 53.1 (2015), pp. 17–42.

**Proceedings of the 8th GACM Colloquium on Computational Mechanics
for Young Scientists from Academia and Industry
August 28–30, 2019 in Kassel, Germany**

Stability Analysis of IMEX-DG-Schemes for Advection-Diffusion with Focus on the Diffusion Treatment

Sigrun Ortleb

FB Mathematik und Naturwissenschaften, Universität Kassel; ortleb@mathematik.uni-kassel.de

Abstract. This talk describes a fully discrete L^2-stability analysis for linear 1D advection-diffusion problems, discretized in space by the DG scheme based on the (σ, μ)-family of diffusion discretizations and implicit-explicit Runge-Kutta schemes in time. Advection terms are discretized explicitly in time while diffusion terms are solved implicitly. Conditions on the parameters σ and μ are derived which guarantee L^2-stability for time steps $\Delta t = \mathcal{O}(d/a^2)$, where a and d denote the advection and diffusion coefficient, respectively, i.e. the allowable time step size does not decrease under grid refinement. These conditions are fulfilled in particular by the BR2 scheme as well as the recent $(\frac{1}{4}, \frac{9}{4})$-recovery scheme. However, the BR1 scheme and the Baumann-Oden method do not possess a similar stablility property which is also confirmed by numerical experiments.

Introduction

In computational fluid dynamics, advection-diffusion problems usually arise when the time evolution of chemical substances or biological species in a flowing medium is described. Furthermore, the flow of viscous fluids itself, modelled by the compressible or incompressible Navier-Stokes equations contains both convective and viscous terms which have different characteristics when discretized in space. In particular, the resulting systems of ordinary differential equations become increasingly stiff under grid refinement due to the presence of the diffusion terms. Explicit time integration then leads to severe time step restrictions which reduce the time step with the square of the grid size. Purely implicit time discretization requires the solution of large non-linear systems of equations. This has lead to the development of implicit-explicit (IMEX) methods to be applied to advection-diffusion type problems. Hereby, a common approach is to discretize advection terms explicitly while the diffusion terms are treated implicitly. While this approach alleviates the severe time step restriction caused by the diffusion terms, a CFL-type time step restriction may still have to be fulfilled due to the explicit treatment of the advection terms, scaling the time step with the grid size. However, for some combinations of space and time discretization schemes, the time step does not have to be reduced under grid refinement. This favourable stability property has already been shown in the literature for specifically designed IMEX methods and Fourier spatial discretization, where the time step solely depends on the advection and diffusion coefficients. A similar unconditional stability result has recently been proven by Wang et al. [2] in the context of spatial discretization by the local discontinuous Galerkin (LDG) method. Since Wang et al. consider a specific diffusion discretization, the question arises if this favourable property is also inherent to more general DG methods. In this talk, conditions on the parameters of a larger family of DG diffusion schemes are derived which allow for this type of unconditional stability. It turns out that these parameter restrictions are neither fulfilled by the simple first approach of Bassi and Rebay nor by the classical Baumann-Oden scheme, hence these schemes do not allow for a grid-independent time step choice. However, both the second approach of Bassi and Rebay with an adjusted penalty constant and the more recent recovery scheme by van Leer and Nomura fulfill the presented conditions.

1 The IMEX-DG scheme for 1D linear advection-diffusion

We consider the linear advection-diffusion equation

$$U_t + aU_x = dU_{xx}, \qquad (x,t) \in Q = \Omega \times (0,T),\ \Omega = (x_a, x_b) \tag{1}$$

with diffusion coefficient $d > 0$ and advective velocity $a > 0$, supplemented by the periodic initial condition $U(x,0) = U_0(x)$ in $L^2(\Omega)$ and periodic boundary conditions. The domain Ω is partitioned into cells $I_j = (x_{j-\frac{1}{2}}, x_{j+\frac{1}{2}})$, $j = 1, \dots, K$ with $x_{\frac{1}{2}} = x_a$, $x_{K+\frac{1}{2}} = x_b$. Here, we consider uniform grids with cell length $x_{j+\frac{1}{2}} - x_{j-\frac{1}{2}} = \Delta x$. The basis functions and test functions used to define the DG scheme are taken from the finite element space

$$V_h = \{v \in L^2(\Omega) \mid v|_{I_j} \in \mathcal{P}_N(I_j)\, \forall j = 1, \dots, K\}, \tag{2}$$

where $\mathcal{P}_N(I_j)$ denotes the space of polynomial functions on I_j of degree at most N. As usual in DG schemes, the functions in V_h may be discontinuous across element boundaries. At each element boundary, the left-hand side and right-hand side values of a piece-wise continuous function v are denoted by v^- and v^+, respectively. Periodicity is realized by setting $v^-_{\frac{1}{2}} = v^-_{K+\frac{1}{2}}$ and $v^+_{K+\frac{1}{2}} = v^+_{\frac{1}{2}}$. The corresponding jump at element interfaces is denoted by $[v] = v^+ - v^-$ and the arithmetic mean is given by $\{v\} = \frac{1}{2}(v^+ + v^-)$.

The semi-discrete DG scheme for (1) is defined as the solution $u(t) \in V_h$ of the variational formulation

$$(u_t, v)_j = a\mathcal{H}_j(u,v) + d\mathcal{L}_j(u,v), \qquad \forall t > 0, v \in V_h, \tag{3}$$

where $(\cdot,\cdot)_j$ denotes the usual inner product in $L^2(I_j)$ and the advective and diffusive fluxes are discretized by the upwind numerical flux for advection resulting in

$$\mathcal{H}_j(u,v) = (u, v_x)_j - u^-_{j+\frac{1}{2}} v^-_{j+\frac{1}{2}} + u^-_{j-\frac{1}{2}} v^+_{j-\frac{1}{2}}, \tag{4}$$

and the (σ,μ)-family for diffusion also considered in [1], i.e.

$$\begin{aligned} \mathcal{L}_j(u,v) = &-(u_x, v_x)_j + \{u_x\}_{j+\frac{1}{2}} v^-_{j+\frac{1}{2}} - \{u_x\}_{j-\frac{1}{2}} v^+_{j-\frac{1}{2}} \\ &+ \frac{\sigma}{2}\left(\left(v^-_x[u]\right)\Big|_{j+\frac{1}{2}} + \left(v^+_x[u]\right)\Big|_{j-\frac{1}{2}} \right) + \frac{\mu}{\Delta x}\left(\left([u]v^-\right)\Big|_{j+\frac{1}{2}} - \left([u]v^+\right)\Big|_{j-\frac{1}{2}} \right). \end{aligned} \tag{5}$$

The DG diffusion discretization is hence specified by the two parameters $\sigma, \mu \in \mathbb{R}$.

Now, implicit time discretization for the diffusion term and explicit time discretization for advection yields fully discrete IMEX-DG schemes. For time stepping, two time integration methods are considered. First order IMEX time integration yields the fully discrete scheme

$$(u^{n+1}, v)_j = (u^n, v)_j + \Delta t\, a\mathcal{H}_j(u^n, v) + \Delta t\, d\mathcal{L}_j(u^{n+1}, v), \qquad \forall v \in V_h, \tag{6}$$

where u^n, u^{n+1} denote the approximations at times t^n and $t^{n+1} = t^n + \Delta t$, while by second order IMEX time integration using an intermediate stage $u^{(n,1)}$ we obtain

$$\begin{aligned} (u^{(n,1)}, v)_j &= (u^n, v)_j + \Delta t \left(\gamma a\mathcal{H}_j(u^n, v) + \gamma d\mathcal{L}_j(u^{(n,1)}, v) \right), \\ (u^{n+1}, v)_j &= (u^n, v)_j + \Delta t \left(\delta a\mathcal{H}_j(u^n, v) + (1-\delta) a\mathcal{H}_j\left(u^{(n,1)}, v\right) \right) \\ &\quad + \Delta t \left((1-\gamma) d\mathcal{L}_j(u^{(n,1)}, v) + \gamma d\mathcal{L}_j(u^{n+1}, v) \right), \qquad \forall v \in V_h, \end{aligned} \tag{7}$$

where γ, δ are given by $\gamma = 1 - \frac{\sqrt{2}}{2}$ and $\delta = 1 - \frac{1}{2\gamma}$.

2 Theoretical stability results for IMEX-DG schemes with (σ,μ)-diffusion discretization

For the above schemes, we may show that the admissible time step guaranteeing L^2-stability is independent of the mesh width. More precisely, the following results can be proven.

Theorem 2.1 *Let $N \in \mathbb{N}_0$ denote the polynomial degree of the DG approximation space V_h defined in (2). Let $\sigma, \mu \in \mathbb{R}$ fulfill the condition*

$$\tilde{\mu} := \frac{(1-\sigma)^2}{4\omega_0} < \mu,$$

where ω_0 denotes the first weight of the Gauss-Lobatto quadrature with $N+1$ nodes. Then, the IMEX-DG scheme (6) with the (σ,μ)-diffusion operator $\mathcal{L}_j$ defined in (5) fulfills $\|u^{n+1}\| \le \|u^n\|$ if the time step is bounded by

$$\Delta t \le \frac{d}{a^2 C},$$

where the constant C is set to $C = \max\{\frac{\nu}{\mu}, 1\}$, if $\sigma = 1$, and to $C = \frac{\nu+\mu}{\mu-\tilde{\mu}}$, if $\sigma \neq 1$.

Theorem 2.2 *Let $N \in \mathbb{N}_0$ denote the polynomial degree of the DG approximation space V_h defined in (2). Let $\sigma, \mu \in \mathbb{R}$ fulfill the condition*

$$\tilde{\mu} := \frac{\left(|1-\sigma| + |1+\sigma| \frac{\beta_2}{\sqrt{\beta_1 \beta_3}}\right)^2}{4\omega_0} < \mu \,,$$

where ω_0 denotes the first weight of the Gauss-Lobatto quadrature with $N+1$ nodes and $\beta_1, \beta_2, \beta_3$ are defined by $\beta_1 = \frac{\theta(2\gamma-1)+1}{6}$, $\beta_2 = \frac{1+\theta-\gamma(3+\theta)}{4}$, $\beta_3 = \frac{\gamma(1+\theta)}{6}$, for $\theta \in [0, 0.7]$ suitably chosen. Then, the IMEX-DG scheme (7) with the (σ, μ)-diffusion operator $\mathcal{L}_j$ defined in (5) fulfills $\|u^{n+1}\| \leq \|u^n\|$ if the time step is bounded by the condition

$$\Delta t \frac{a^2}{d} \leq \frac{1}{C} \min \left\{ \left(\frac{\alpha_1^2}{\beta_1} + \frac{2\alpha_2^2}{\beta_3} \right)^{-1}, \frac{\theta \beta_3}{2\alpha_3^2} \right\}, \quad C = \frac{\nu + \mu}{\mu - \tilde{\mu}} \,,$$

with $\alpha_1, \alpha_2, \alpha_3$ given by $\alpha_1 = \frac{1-\theta+(1+\theta)\gamma}{2}$, $\alpha_2 = \frac{\theta+1}{2}$, $\alpha_3 = \frac{\theta+1}{2}(1-\gamma)$.

3 Numerical results

In this section, we compare the stability of IMEX-DG schemes with respect to the discretization of the diffusion terms. We consider the exact solution $U(x,t) = e^{-dt}\sin(x-at)$ to equation (1) in the interval $(x_a, x_b) = (-\pi, \pi)$. The advection-diffusion problem is discretized in space by the second order nodal DG scheme on Gauss-Lobatto nodes, hence the polynomial degree is $N = 1$. As in the theoretical investigation, advection terms are discretized by upwind fluxes and diffusion terms are discretized either by the LDG scheme or by various members of the (σ, μ)-family. First and second order IMEX schemes are considered for time integration.

From the theoretical analysis, we expect the schemes to be stable for time steps $\Delta t \leq \frac{\tau d}{a^2}$, where τ is some constant independent of grid refinement. Tables 1 and 2 show the analysis of the maximum stable time step for different advection and diffusion parameters a and d, where we vary the number of cells K and compute the numerical solution until the final time $T = 1000$. The maximum stable time step Δt_{max} is determined as the maximum time step for which the L^2-norm of the numerical solution is non-increasing and the corresponding values of $\tau = \frac{a^2}{d}\Delta t_{max}$ are listed. As predicted by the theoretical analysis, the BR1 and Baumann-Oden(BO) scheme do not admit grid-independent time step sizes. Here, we clearly observe the behavior $\tau = \mathcal{O}(\Delta x)$ for the admissible time step, analogous to the time step restrictions for explicitly discretized advection equations. For second order IMEX time integration, further variants of σ and μ have been tested. Here, except for the BR1 and BO scheme, the values of τ nearly coincide for moderate sizes of the diffusion coefficient (Table 1). In addition, first order IMEX time integration yields no restriction on the time step at all for this particular test case. For small sizes of the diffusion coefficient (Table 2), the first order IMEX scheme yields nearly constant maximum time steps for LDG, BR2 and the recovery scheme, whereas for second order IMEX time integration, on coarse grids, the allowable time step size scales with the grid size. In this respect, those members of the (σ, μ)-family with a large value of μ admit much larger time steps. On fine grids, the allowable time step sizes almost coincide again, except for the BR1 and BO discretizations.

References

[1] B. van Leer, M. Lo, R. Gitik, and S. Nomura. A venerable family of discontinuous Galerkin schemes for diffusion revisited. In: *Adaptive High-Order Methods in Computational Fluid Dynamics*. Ed. by Z. J. Wang. World Scientific, 2011, pp. 185–201.

[2] H. Wang, C.-W. Shu, and Q. Zhang. Stability and Error Estimates of Local Discontinuous Galerkin Methods with Implicit-Explicit Time-Marching for Advection-Diffusion Problems. *SIAM J. Numer. Anal.* 53.1 (2015), pp. 206–227.

First order IMEX time integration					
K	LDG	Recovery	BR1	BR2	BO
20	+	+	3.36e-01	+	3.85e-01
40	+	+	1.62e-01	+	1.74e-01
80	+	+	7.94e-02	+	8.25e-02
160	+	+	3.92e-02	+	3.98e-02
320	+	+	1.96e-02	+	1.96e-02
640	+	+	9.26e-03	+	9.87e-03
Second order IMEX time integration					
K	LDG	Recovery	BR1	BR2	BO
20	2.42	2.42	3.23e-01	2.45	4.50e-01
40	2.41	2.41	1.57e-01	2.42	2.35e-01
80	2.41	2.41	7.91e-02	2.41	8.89e-02
160	2.41	2.41	3.03e-02	2.41	4.01e-02
320	2.41	2.41	1.08e-02	2.41	2.05e-02
640	2.41	2.41	9.26e-03	2.41	9.87e-03
K	$\sigma=-1$ $\mu=10$	$\sigma=-1$ $\mu=1.5$	$\sigma=0.25$ $\mu=0.5$	$\sigma=0.25$ $\mu=1$	$\sigma=0.25$ $\mu=10$
20	2.45	7.52e-01	2.34	2.39	2.45
40	2.42	2.42	2.39	2.40	2.42
80	2.41	2.41	2.40	2.41	2.41
160	2.41	2.41	2.41	2.41	2.41
320	2.41	2.41	2.41	2.41	2.41
640	2.41	2.41	2.41	2.41	2.41

Table 1. Values of $\tau = \frac{a^2}{d}\Delta t_{max}$, where Δt_{max} is the maximum time step to ensure a non-increasing L^2-norm for $d = 0.1, a = 0.1$. An entry of "+" means that for this test case, the scheme is unconditionally stable independent of the time step.

First order IMEX time integration					
K	LDG	Recovery	BR1	BR2	BO
20	2.15	2.09	2.20	2.15	2.05
40	2.03	2.02	2.04	2.03	2.00
80	2.01	2.01	1.57	2.01	1.66
160	2.01	2.01	7.86e-01	2.01	1.09
320	2.01	2.01	3.93e-01	2.01	4.73e-01
640	2.01	2.01	1.96e-01	2.01	2.16e-01
Second order IMEX time integration					
K	LDG	Recovery	BR1	BR2	BO
20	6.63	6.82	6.30	6.87	6.42
40	3.45	3.78	3.15	3.80	3.21
80	1.96	2.53	1.57	2.73	1.66
160	1.40	1.77	7.82e-01	2.17	9.03e-01
320	1.50	1.48	3.92e-01	1.70	5.01e-01
640	1.42	1.42	1.96e-01	1.50	2.84e-01
K	$\sigma=-1$ $\mu=10$	$\sigma=-1$ $\mu=1.5$	$\sigma=0.25$ $\mu=0.5$	$\sigma=0.25$ $\mu=1$	$\sigma=0.25$ $\mu=10$
20	1.05e+01	6.46	6.45	6.53	1.01e+01
40	6.22	3.30	3.24	3.35	5.95
80	3.80	1.75	1.69	1.88	3.62
160	2.39	1.01	1.01	1.32	2.28
320	1.75	6.93e-01	9.38e-01	1.24	1.69
640	1.50	1.49	1.25	1.34	1.48

Table 2. Values of $\tau = \frac{a^2}{d}\Delta t_{max}$, where Δt_{max} is the maximum time step to ensure a non-increasing L^2-norm for $d = 0.01, a = 0.2$.

**Proceedings of the 8th GACM Colloquium on Computational Mechanics
for Young Scientists from Academia and Industry
August 28–30, 2019 in Kassel, Germany**

Comparison of exponential-explicit (EXPEX) schemes in the domain-based implicit-explicit (IMEX) setting with IMEX-RK schemes for CFD applications

Veronika Straub * [1] and Sigrun Ortleb[1]

[1]Department of Mathematics, University of Kassel, Heinrich-Plett-Str. 40, 34132 Kassel, Germany

Abstract. Computational Fluid Dynamics (CFD) problems typically require meshes, which have a low percentage of very small cells. For sufficiently high grid-induced stiffness, meaning having a high ratio between the largest and the smallest cell sizes, purely implicit or purely explicit schemes may become inefficient due to the large nonlinear and linear systems needed for implicit solvers, respectively the small timestep sizes dictated by the smallest cell size needed for stable explicit time integration. Domain-based implicit-explicit (IMEX) schemes turned out to outperform conventional schemes in such cases, as shown by Kanevsky, Carpenter et. al. for IMEX-Runge-Kutta (IMEX-RK) schemes. We utilize the class of exponential integrators called EPIRK in that domain-based IMEX-setting, resulting in schemes which we denoted as IMEX-sEPIRK. Due to the formally explicit nature of the applied exponential integrators, we rename those schemes to exponential-explicit (EXPEX) schemes. Here, we compare a first and two third order versions of it to the domain-based IMEX-Runge-Kutta (IMEX-RK) schemes as well as to purely eplicit, implicit and exponential methods on a 2D laminar flow in a nozzle. The EXPEX schemes prove to be competetive and even superior to other schemes.

Introduction

In CFD the inviscid flow can be modeled by the Euler-equations, which are a nonlinear system of hyperbolic PDE's. The test case, we focus at is the flow in a twodimensional nozzle. The spatial domain Ω is subdivided into elements $\tau \in T_h = \{\tau_i\}_i$ with $\Omega = \dot{\cup}_i^K \tau_i$, on which the PDE-system is discretized in space by a Disconinuous Galerkin scheme resulting in the autonomuous, semidiscrete System of ODE's with given initial and boundary data:

$$\frac{\mathrm{d}}{\mathrm{d}t}\mathrm{U}(t) = \mathrm{F}(\mathrm{U}(t)), \quad \mathrm{U} : \mathbb{R} \to \mathbb{R}^N,\ \mathrm{F} : \mathbb{R}^N \to \mathbb{R}^N,\ t \in [t_0, T]. \tag{1}$$

The idea of domain-based IMEX schemes is to split the computational domain Ω into two regions $\Omega = \Omega_{\mathrm{im}} \dot{\cup} \Omega_{\mathrm{ex}}$ such that the implicit region Ω_{im} contains the smallest elements and the explicit region the remaining. The right-hand side (abbreviated by rhs in the following) F is also split into two parts $\mathrm{F} = \mathrm{F}^E + \mathrm{F}^I$ by assigning all terms linked to the explicit region to F^E and the others to F^I. Now, explicit time stepping is applied to F^E and an implicit (or just A- and unconditionally CFL-stable) scheme to F^I with the purpose to overcome the strict CFL-condition for explicit schemes, which dictates the maximal stable timestep size dependent on the smallest cell size in the computational domain. Since Ω_{ex} does not include the smallest elements of Ω any more, larger global timesteps can be chosen for both schemes, since the implicit scheme does not underly a CFL-condition.

Our aim is to apply the exponential schemes of EPIRK type [7] in the implicit domain, since they turned out to be more efficient than typical implicit schemes for large stiff problems [4]. We showed that they are also unconditionally CFL-stable though their explicit nature and analyzed the linear stability and conservation properties in [6]. In [5] we have shown that the intuitive coupling of EPIRK and ERK schemes is limited to first order of convergence and presented the IMEX-sEPIRK schemes as a remedy to achieve arbitrary high order schemes. Since the EPIRK schemes are explicit by definition, but are used for the implicit part of the domain-based IMEX splitting, we rename the IMEX-sEPIRK schemes

*Corresponding author: vstraub@mathematik.uni-kassel.de ORCID iD: ORCID (optional)

to EXPEX (exponential-explicit) schemes. Nevertheless, we proceed to catogorize them in the class of IMEX schemes, as they are applied in the domain-based IMEX-setting.

While our previous proceedings contributions concentrated on the theoretical analysis of the EXPEX schemes, here we focus on numerical investigations and oppose them to four different types of schemes: IMEX-RK, purely implicit, purely explicit and exponential schemes. Before that, we explain how we devided Ω in Ω_{ex} and Ω_{im} and demonstrate the relevance of a clever IMEX decomposition.

Numerical investigations

To examine the efficiency of the EXPEX schemes, a test case with high grid-induced stiffness in two dimensions is taken as in [2]: The two-dimensional flow in a nozzle. This is a classical steady-state problem for inviscid flow, where the analytical solution at the centerline $y = 0$ is known. Due to symmetry of the geometry, the computational grid contains only the upper half, having the centerline of the nozzle at the bottom of the grid ($y = 0$) with a symmetry condition as boundary condition. We choose inlet and outlet data as in chapter 4.3.1 in [2], for which the flow results in a stationary normal shock located at $x \approx 7.5623$ after $t > 20$. To obtain a precise solution at the centerline of the shock position, the grid is locally refined at that point $P_{\text{shock}} = (0,\ 7.5623)$. We designed a grid with an in-house tool for grid generation (see Fig. 2a).

Our strategy to split the domain into an implicit and explicit region by utilizing a scale parameter a is given in Algorithm 1. The large task lies in determining a reasonable percentage of implicit cells, i.e. finding a suitable parameter a. This effects the efficiency of the IMEX scheme to a high degree, since too many implicit cells, on the one hand, result in larger nonlinear systems and too many explicit cells, on the other hand, shrink the maximal stable timestep size. An intelligent IMEX decomposition strategy is not published so far and our approach to find such an algorithm is currently in process. Therefore, we temporary use the following experimental approach for our test case: We first analyze the behaviour of the IMEX schemes for diverse percentages of implicit cells, starting from 0% up to $\approx 99\%$ with CFL adaptivity and a fixed CFL number of 0.1 until the end time $t = 1$. To this end, we plot work-precision diagrams, in which we connect the points for all the different percentages of implicit cells in ascending order for each of the IMEX schemes. The work is measured in terms of scaled right-hand side evaluations: The number of F^E-evaluations multiplied by the percentage of explicit cells plus the number of F^I-evaluations multiplied by the percentage of implicit cells, since the work for the evaluation of the entries of F^E resp. F^I scales with those percentages. The precision is determined by a reference solution for a very small timestep size. The results are shown in Fig. 1.

Determine $\tau_{\max} = \max_{\tau\in\Omega} |\tau|$;
Determine $\tau_{\min} = \min_{\tau\in\Omega} |\tau|$;
$\tau_{\text{mid}} := \frac{\tau_{\min}+\tau_{\max}}{2}$;
for $\tau \in \Omega$ **do**
  if $|\tau| \leq a * \tau_{mid}$ **then**
    $\tau \in \Omega_{\text{im}}$;
  else
    $\tau \in \Omega_{\text{ex}}$;
  end
end

Algorithm 1: IMEX decomposition strategy

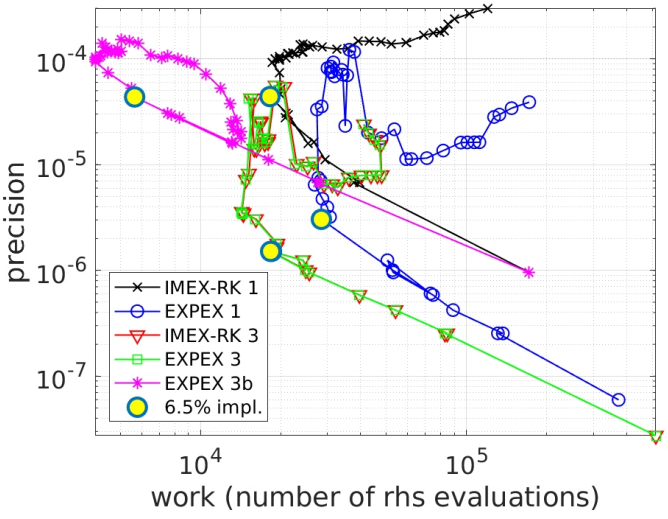

Figure 1. Results for different IMEX decompositions: 0% until $\approx$ 99% of impl. cells are connected in ascending order by a line for each scheme. The first point of the curve (0% of impl. cells) is that with the highest precision of the respective scheme.

We see that fully explicit or mostly implicit schemes are expensive: The first and the last point of the curve tend to the maximal computational cost. The minimum of the computational work is achieved at a still appropriate precision. Since that minimum varies for each of the IMEX scheme, we choose the value 4.5e-02 for a resulting in 6.5% of implicit cells, for which the distance to the minimal point is relatively close for all schemes, but gives a higher precision at a quite similar cost. We highlighted our choice of a with a filled yellow circle in Fig. 1.

We define the grid-induced stiffness similar to [2] by $S = \frac{\min_{\tau\in\Omega_{\text{ex}}} |\tau|}{\min_{\tau\in\Omega_{\text{im}}} |\tau|}$ with $|\tau|$ being the area of the element τ. The grid-induced stiffness S for the parameter $a = 4.5\text{e-}02$ results in 591.55. The visualization of the IMEX regions can be found in Fig. 2.

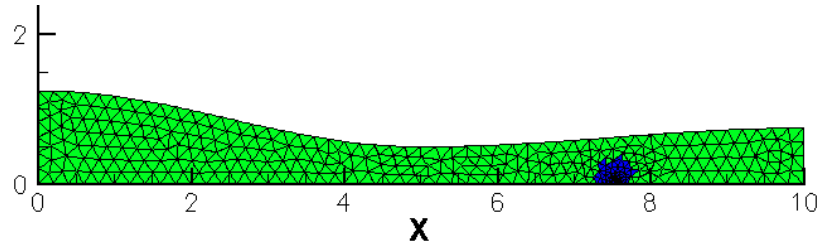

a) Decomposition into an explicit region (green) and an implicit region (blue).

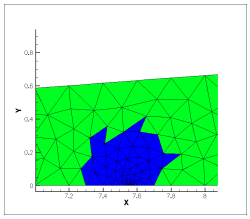

b) Zoom of the implicit region.

Figure 2. IMEX region for $a = 4.5\text{e-}01$ resulting in 6.5% of implicit cells.

We perform computations until $t = 5$ with CFL-adaptive timestep sizes for CFL-numbers in [4.88e-05, 6.55e+03] starting from the largest one halfening it until the smallest one. It is known that (semi-)explicit schemes become stable for CFL-numbers around 1 and implicit schemes are theoretically stable for arbitrary large CFL-numbers, but the internal solvers for the nonlinear and linear systems or the matrix exponential approximations begin to be unstable for too large timestep sizes. In the following Table 1 we summarize the time integration schemes that are compared and their experimentally maximal stable CFL-number.

Name	Description of the scheme	$\text{CFL}_{\text{stable}}$
IMEX-RK 1	1st order IMEX-RK: Coupling of the implicit and explicit Euler methods	4.00e-01
EXPEX 1	1st order EXPEX method, denoted as IMEX-EPIRK 1 in [5]	8.00e-01
IMEX-RK 3	3rd order IMEX-RK method, denoted as ARK3(2)4L[2]SA in [3]	8.00e-01
EXPEX 3	3rd order EXPEX method, denoted as IMEX-sEPIRK3 in [5]	8.00e-01
EXPEX 3b	3rd order EXPEX method, denoted as IMEX-sEPIRK3b in [5]	8.00e-01
expl. Eul.	the explicit Euler method	1.60e+00
expl. 2nd	a 2nd order explicit RK method	1.60e+00
expl. 3rd	a 3rd order explicit RK method	1.60e+00
expon. Eul.	a 2nd order exponential integrator, called Epi2 in [4]	1.64e+03
EPIRK4SC	a 4th order, stiffly accurate exponential integrator [4]	8.19e+02
EPIRK5C	a 5th order exponential integrator [4]	1.64e+03
EPIRK5SC	a 5th order, stiffly accurate exponential integrator [4]	8.19e+02
impl. Eul.	the implicit Euler method	>6.55e+03
ESDIRK3	a 3rd order explicit step singly diagonal RK scheme, see i.e. [1]	3.28e+03

Table 1. Considered time stepping schemes of different types: IMEX, explicit, exponential and implicit. Their experimentally maximal stable CFL-number $\text{CFL}_{\text{stable}}$ is listed as well.

The results are shown in Fig. 3. First, we verify the order of convergence in Fig. 3a: All schemes achieve the expected slopes until machine precision interrupts. The higher order exponential schemes hit that ground already for large timestep sizes ($\approx$ 3e-03), since the subsequent point with the same slope would be beyond machine precision. Moreover, we see the large difference in the maximal stable time-step sizes for the different types of schemes: implicit or exponential, IMEX and explicit. Even though the maximal stable CFL-number for the IMEX-schemes is a bit below the one of the explicit schemes in that testcase

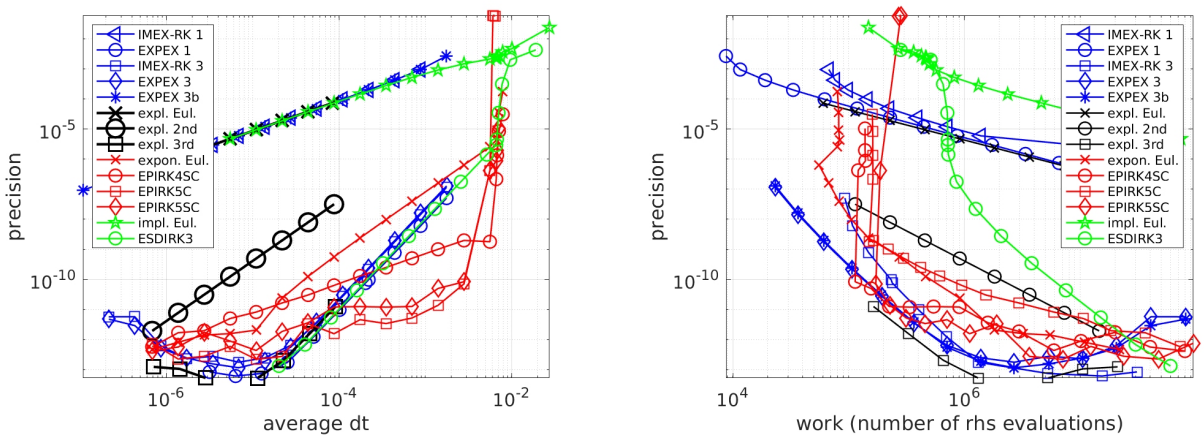

Figure 3. Results of the computations of the Nozzle flow test case until t=5. For orientation the graphs of the IMEX schemes are in blue, of the explicit schemes in black, of the exponential schemes in red and of the implicit schemes in green.

(see Tab. 1), the maximal stable timestep size can be chosen 50 times larger than for explicit schemes, since the smallest element in the CFL-condition is much larger for IMEX-schemes.

The work-precision diagram confirms the efficiency advantage of the IMEX schemes compared to non-IMEX schemes in that the same precision can be achieved at a similar or lower cost. The novel EXPEX schemes beat the IMEX-RK schemes with factors of up to 2.5 for the 3rd order schemes and a factor of up to 6 for the 1st order schemes. Furthermore, the high efficiency of the exponential integrators is demonstrated impressively, verifying that they are the key to efficiency in the EXPEX schemes, while implicit RK schemes are the most inefficient in our setting.

Acknowledgments

We thank the German Research Foundation DFG for its financial support within the project GZ: ME 1889/7-1, by which we could employ the student assistant Georgios Tsompanidis, who did the testing and we thank Mayya Tokman for providing online the code package EPIC with the exponential integrators.

References

[1] P. Birken. *Numerical Methods for the Unsteady Compressible Navier-Stokes Equations*. Habilitation Thesis. University of Kassel, 2012.

[2] Alex Kanevsky, Mark H. Carpenter, David Gottlieb, and Jan S. Hesthaven. Application of implicit-explicit high order Runge-Kutta methods to discontinuous-Galerkin schemes. *J. Comput. Phys.* 225.2 (2007).

[3] Christopher A. Kennedy and Mark H. Carpenter. Additive Runge-Kutta Schemes for Convection-Diffusion-Reaction Equations. *Applied Numerical Mathematics* 44.1-2 (2003).

[4] J. Loffeld and M. Tokman. Comparative performance of exponential, implicit, and explicit integrators for stiff systems of ODEs. *J. Comput. Appl. Math.* 241 (2013).

[5] Veronika Straub, Sigrun Ortleb, Philipp Birken, and Andreas Meister. Adopting (s)EPIRK schemes in a domain-based IMEX setting. *AIP Conference Proceedings* 1863 (2017).

[6] Veronika Straub, Sigrun Ortleb, Philipp Birken, and Andreas Meister. On Stability and Conservation Properties of (s)EPIRK Integrators in the Context of Discretized PDEs. In: *Theory, Numerics and Applications of Hyperbolic Problems II*. Ed. by Christian Klingenberg and Michael Westdickenberg. Vol. 237. Springer International Publishing, 2018.

[7] M. Tokman. A new class of exponential propagation iterative methods of Runge-Kutta type (EPIRK). *J. Comput. Phys.* 230.24 (2011).

**Proceedings of the 8th GACM Colloquium on Computational Mechanics
for Young Scientists from Academia and Industry
August 28–30, 2019 in Kassel, Germany**

High order IMEX splitting methods for low Mach number flows

Jonas Zeifang * [1]

[1]IAG, University of Stuttgart, Pfaffenwaldring 21, D-70569 Stuttgart

Abstract. Flows at low Mach numbers require the use of specially designed numerical schemes. In this talk two approaches for the efficient treatment of low Mach number flows for different applications will be presented. First, the so-called RS-IMEX splitting for the Euler equations, introduced in [2], is recalled. It relies on the incompressible limit equations and requires a specific modification of the Euler equations to prevent the eigenvalues of the explicit system from becoming complex. This splitting is combined with a high order discontinuous Galerkin method in space and an IMEX-Runge-Kutta method in time. For solving the arising linear system, a matrix-free GMRES method is equipped. Several testcases will show the influence of the modification and the performance of the developed method. Second, approaches on how to enable matrix-free fully implicit simulations of low Mach number flows in a multiphase setting and how to increase their efficiency are addressed.

Introduction

Considering the Euler equations of fluid dynamics different types of characteristic waves are present - fast pressure waves and convection. For low Mach number flows, the ratio of the convective velocity and the velocity of the pressure waves is very low, leading to a stiff system. Especially, when simulating multiphase flows often situations occur where the flow field is characterized by low Mach numbers. Frequently used explicit time integration schemes require the temporal resolution of all waves necessitating very small timesteps as the CFL condition

$$\Delta t = \mathrm{CFL} \cdot \frac{\Delta x}{\max|\lambda|}, \quad \mathrm{CFL} < 1,$$

has to be fulfilled. For the one dimensional Euler equations the eigenvalues λ are given by

$$\lambda_{1,3} = u \pm c, \quad \lambda_2 = u,$$

Hence, they are computationally inefficient for the simulation of low Mach number flows where $u \ll c$. Implicit schemes have the advantage of allowing much larger timesteps but require the solution of large non-linear systems and introduce very much numerical viscosity. IMEX schemes combine both approaches enabling an efficient treatment of low Mach number flows.
In [2] we have introduced the so-called RS-IMEX splitting for the Euler equations which allows the splitting of the equations in a Mach number dependent and independent part. It offers one possibility of encountering the problems arising from the stiff system.
When simulating multiphase flows, solving the equation system becomes numerically even more challenging as very large density rations are present and more complex equations of state have to be used. Here we will present the influence of the design of the matrix-free method on the efficiency of the scheme.

*Corresponding author: jonas.zeifang@iag.uni-stuttgart.de

1 RS-IMEX splitting for the Euler equations

The RS-IMEX splitting for the Euler equations has been introduced in [2] and will be recalled shortly. We consider the non-dimensional Euler equations

$$\partial_t \underbrace{\begin{pmatrix} \rho \\ \rho \boldsymbol{u} \\ E \end{pmatrix}}_{=:\boldsymbol{w}} + \nabla \cdot \underbrace{\begin{pmatrix} \rho \boldsymbol{u} \\ \rho \boldsymbol{u} \otimes \boldsymbol{u} + \frac{p}{\varepsilon^2} Id \\ \boldsymbol{u}\,(E+p) \end{pmatrix}}_{=:\boldsymbol{f}(\boldsymbol{w})} = 0,$$

where ρ denotes density, $\boldsymbol{u}$ velocity, E energy density and the pressure is computed via the equation of state for a perfect gas. The RS-IMEX splitting defines the fluxes $\widetilde{\boldsymbol{f}}$ and $\widehat{\boldsymbol{f}}$ as

$$\widetilde{\boldsymbol{f}}(\boldsymbol{w}) := \boldsymbol{f}(\boldsymbol{w}_{\text{ref}}) + \nabla_{\boldsymbol{w}} \boldsymbol{f}(\boldsymbol{w}_{\text{ref}})(\boldsymbol{w} - \boldsymbol{w}_{\text{ref}}) \qquad \text{and} \qquad \widehat{\boldsymbol{f}}(\boldsymbol{w}) := \boldsymbol{f}(\boldsymbol{w}) - \widetilde{\boldsymbol{f}}(\boldsymbol{w}).$$

for a given reference solution $\boldsymbol{w}_{\text{ref}}$. The choice of this splitting would result in potentially complex eigenvalues of the Jacobian of $\widehat{\boldsymbol{f}}$. Hence, $\widehat{\boldsymbol{f}}$ is redefined as

$$\widehat{\boldsymbol{f}}(\boldsymbol{w}) = \boldsymbol{f}(\boldsymbol{w}) - \widetilde{\boldsymbol{f}}(\boldsymbol{w}) - \begin{pmatrix} 0 \\ -\frac{\gamma-1}{2}\rho \|\boldsymbol{u}_{\text{ref}} - \boldsymbol{u}\|^2 \cdot \boldsymbol{I} \\ \frac{\varepsilon^2(\gamma-1)}{2}\rho \left[(\|\boldsymbol{u}_{\text{ref}}\|_2^2 - \|\boldsymbol{u}\|_2^2)(\boldsymbol{u} - \boldsymbol{u}_{\text{ref}}) - \|\boldsymbol{u} - \boldsymbol{u}_{\text{ref}}\|_2^2 \boldsymbol{u}_{\text{ref}} \right] \end{pmatrix},$$

violating $\widehat{\boldsymbol{f}} + \widetilde{\boldsymbol{f}} = \boldsymbol{f}$, and introducing a modeling error to with respect to the Euler equations. If now $\boldsymbol{u}_{\text{ref}}$ is chosen as the incompressible velocity field for the same initial conditions, the size of the modeling error lies in $\mathcal{O}(\varepsilon^2)$. The eigenvalues of the flux Jacobians are now real and for $\widehat{\boldsymbol{f}}$ even independent of the reference Mach number ε. Hence, an IMEX time discretization treating $\widehat{\boldsymbol{f}}$ explicitly and $\widetilde{\boldsymbol{f}}$ implicitly allows the choice of the time step independent on the Mach number. In this talk we will present results of combining the RS-IMEX splitting with a high order IMEX Runge-Kutta scheme in time and a high order discontinuous Galerkin method in space.

2 A Jacobian-free method for multiphase simulations

Simulating flows where liquids are concerned necessitates the use of non ideal gas equation of states. The simplest variant is the stiffened gas equation of state

$$p = (\gamma - 1)\left(E - \frac{1}{2}\rho \|\boldsymbol{u}\|_2^2 - \rho q\right) - \gamma p_\infty,$$

where q and p_∞ are material dependent parameters. Other options such as the use of tabulated equation of states require the use of dimensional quantities for the simulation. This results in very large absolute values e.g. for the energy density, leading to problems with machine accuracy especially when using implicit time discretization with a Jacobian-free approach. The implicit time discretization relies on the solution of a non-linear equation system. This can be solved with a Newton-GMRES method based on the approximate evaluation of the product of the Jacobian of the spatial discretization with the solution vector of Newton's method $\Delta \boldsymbol{w}$

$$\frac{\partial \widetilde{\boldsymbol{R}}(\boldsymbol{w})}{\partial \boldsymbol{w}} \Delta \boldsymbol{w} \approx \frac{\widetilde{\boldsymbol{R}}(\boldsymbol{w} + \Delta_{FD}\Delta \boldsymbol{w}) - \widetilde{\boldsymbol{R}}(\boldsymbol{w})}{\Delta_{FD}}, \tag{1}$$

with $\widetilde{\boldsymbol{R}}$ denoting the spatial operator of the implicitly treated system and Δ_{FD} being a design parameter. The choice of Δ_{FD} has to be a trade off between truncation error of the finite difference (Eq. (1)) and round off errors caused by limited machine accuracy. Here, we will present the influence of the choice of Δ_{FD} which can exemplary be found in [1] and cast into the form

$$\Delta_{FD} = \frac{\sqrt{\varepsilon_{\text{machine}}}}{\|\Delta \boldsymbol{w}\|_2} \varepsilon_{scale},$$

on the accuracy of the Jacobian vector product (Eq. (1)). Another approach to increase the accuracy of the matrix-free method is to decrease the truncation error using a second order finite difference

$$\frac{\partial \widetilde{\boldsymbol{R}}(\boldsymbol{w})}{\partial \boldsymbol{w}} \Delta \boldsymbol{w} \approx \frac{\widetilde{\boldsymbol{R}}(\boldsymbol{w} + \Delta_{FD\mathcal{O}2} \Delta \boldsymbol{w}) - \widetilde{\boldsymbol{R}}(\boldsymbol{w} - \Delta_{FD\mathcal{O}2} \Delta \boldsymbol{w})}{2\Delta_{FD\mathcal{O}2}}.$$

In this talk it will be shown that for realistic multiphase settings the use of a second order finite difference is necessary. Moreover the choice of Δ_{FD} has a significant influence on the efficiency of the scheme.

Acknowledgments

This work has been supported by the German Research Foundation (DFG) through the International Research Training Group GRK 2160/1: Droplet Interaction Technologies. The support and computing time provided by the High Performance Computing Center Stuttgart (HLRS) through the *hpcdg* project is acknowledged.

References

[1] D. A. Knoll and D. E. Keyes. Jacobian-free Newton–Krylov methods: A survey of approaches and applications. *Journal of Computational Physics* 193 (2004), pp. 357–397.

[2] J. Zeifang, J. Schütz, K. Kaiser, A. Beck, M. Lukáčová-Medvid'ová, and S. Noelle. A novel full-Euler low Mach number IMEX splitting. *Accepted by Communications in Computational Physics* (2019).

**Proceedings of the 8th GACM Colloquium on Computational Mechanics
for Young Scientists from Academia and Industry
August 28–30, 2019 in Kassel, Germany**

Computation of the Stability Limit of Nonlinear Bladerow Flutter with a Fully Coupled Frequency Domain FSI Solver

Christian Berthold[1], Johann Gross[2], Christian Frey[1] and Malte Krack[2]

[1]Institute of Propulsion Technology, German Aerospace Center, Linder Höhe, 51147 Cologne, Germany , christian.berthold@dlr.de
[2]Institute of Aircraft Propulsion Systems, University of Stuttgart, Pfaffenwaldring 6, 70569 Stuttgart, Germany

Abstract. To guarantee a safe operation of turbomachinery components engineers need to consider the aeroelastic behavior of the mechanical design. Due to increasing demands with respect to efficiency and fuel consumption components need to be further optimized. However conventional computational analysis methods for aeroelasticity which are commonly used in industry during the design phase have uncertainties since they are often based on linearization or neglect interactions between physical nonlinear effects in the solid and fluid domain. Thus large safety margins for conventional methods need to be considered resulting in restrictive design guidelines. Furthermore the nonlinear behavior of blade vibrations and the interaction with the surrounding nonlinear flow is only rarely analyzed and therefore not yet fully understood. Time accurate methods can deliver higher accuracy but the computational costs are prohibitive for the industrial design process. In this study a fully coupled fluid-structure interaction (FSI) solver in the frequency domain is presented to provide a computationally efficient simulation tool which is able to consider nonlinear solid and fluid effects of blade limit cycle oscillations (LCOs) in turbo engines. It can compute stable LCOs as well as unstable LCOs (stability limit) which can occur e.g. due to dry nonlinear friction in shrouded blades and is based on the Harmonic Balance method. The fourier components of the blade vibration and the frequency are passed to the flow solver and the aerodynamic forces are returned to the strucure solver. Because the frequency of self excited vibrations is not known a priori the FSI solver considers the frequency as part of the sought solution. Furthermore a linearization of the aerodynamic forces inside the structure solver is introduced to improve the convergence of the coupled solver and countermeasures are implemented to prevent the solver from converging to the trivial solution (zero amplitude). To further reduce the computational costs the structural model is reduced with the Craig-Bampton approach. During the reduction the degrees of freedom in the solid contact regions of the bladerow are retained to model dry friction. To initialize the solver the energy method is extended to approximately determine the nonlinear behavior with a one-way coupling approach. The novel method is applied to a bladerow which is aerodynamically stable for small vibration amplitudes. With increasing amplitude the modeshape as well as the frequency change due to nonlinear friction in the joints of the shrouded rotor. This has an effect on the aerodynamic response and for large amplitudes the oscillations are aerodynamically unstable. The coupled solver is able to determine the limit of stability and the frequency of the coupled problem while conventional energy methods are not able to detect a stability boundary at all.

Introduction

An important topic within aeroelasticity are self-excited vibrations of turbomachinery blades leading to limit cycle oscillations (LCOs) [3]. The conventional design approach is to discard all designs which exhibit flutter. However, as fluttering blades often vibrate at small amplitudes, this approach may be too restrictive. On the other hand an aerodynamically stable bladerow could become unstable for large amplitudes due to nonlinear effects which also cannot be predicted with conventional design methods [7] since the conventional energy method is based on the linearization of the coupled system for small vibrations.
In structural dynamics, nonlinear effects can occur due to nonlinear physical phenomena in mechanical joints located e.g. in the shroud, blade root or by the use of underplatform dampers [5]. With increasing amplitudes the contact conditions may change from fully sticking to a sliding motion which in turn result in a change of shape and frequency of the structural eigenmode. On the aerodynamic side it is well-known that the aerodynamic response depends strongly on the vibrational frequency and on the modeshape [3]. Available time integration simulation methods are computationally to expensive [2]. Frequency domain methods such as the harmonic balance (HB) method are popular in both physical domains due to low

simulation costs. Current frequency domain approaches are usually one-way coupled methods. It is therefore desirable to have a computationally efficient two-way coupled FSI solver for the analysis of flutter induced LCOs. In this study a method which enables a two-way coupled analysis of LCOs due to flutter with the use of the HB method is presented. The refined energy method [3] is used to validate the coupled solver and also to supply a good initialization to the coupled FSI solver. In the following a hat indicates complex Fourier coefficents.

1 Benchmark model and single-domain solvers

The low pressure turbine testcase (see Fig. 1) is kindly provided by MTU Aero Engines AG. The contact areas are modeled with nodal contact elements and are located in the shroud. For details on this modeling approach, see [5]. The full bladed disk is assumed as rotationally periodic system. To increase the

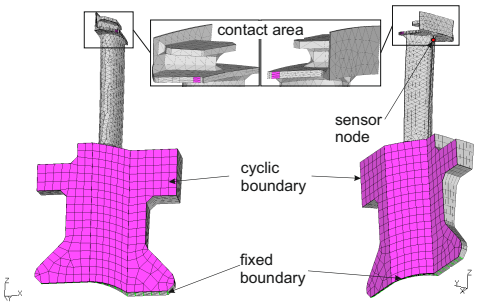

Figure 1. Structural FE model of the bladed disk [3]

computational efficiency the full FEM model which models the dynamic force equilibrium is reduced with the Craig-Bampton substructuring technique [4]. The reduced order model (ROM) is transformed into the frequency domain with the HB technique [5]. The solution (i.e. the displacements of the structure $\boldsymbol{u}^{\mathrm{s}}(t)$) is approximated with a truncated fourier series $\boldsymbol{u}^{\mathrm{s}}(t) \approx \Re\left\{\sum_{k=0}^{K} e^{ik\omega t}\hat{\boldsymbol{u}}_k^{\mathrm{s}}\right\}$ which is solved for a given harmonic aerodynamic force $\hat{\boldsymbol{f}}^{\mathrm{a}}(\hat{\boldsymbol{u}}^{\mathrm{f}}, \omega)$. The conservative flow variables $\boldsymbol{u}^{\mathrm{f}} = [\rho,\, \rho u,\, \rho v,\, \rho w,\, \rho E]^T$ (mass, x-, y-, z-momentum and energy) of the URANS equations are solved together with a k-ω turbulence model. After applying the FV method to each cell the flow equations are subsequently transformed into the frequency domain [1] analogous to the structural model. Both systems of equations denoted by $\boldsymbol{R}^{\mathrm{f}}(\hat{\boldsymbol{u}}^{\mathrm{f}}, \omega, \hat{\boldsymbol{\chi}}) = 0$ (solved with TRACE) and $\boldsymbol{R}^{s}(\hat{\boldsymbol{u}}^{\mathrm{s}}, \omega, \hat{\boldsymbol{f}}^{\mathrm{a}}) = 0$ (solved with NLvib) are coupled through the aerodynamic force $\hat{\boldsymbol{f}}^{\mathrm{a}}(\hat{\boldsymbol{u}}^{\mathrm{f}}, \omega)$ and the FV mesh motion $\hat{\boldsymbol{\chi}}(\hat{\boldsymbol{u}}^{\mathrm{s}})$ due to the motion of the structure.

2 Coupled solver

The coupled FSI solver [3] consists of the fluid and structure HB solvers and exchanges the Fourier components of the solution (see Fig. 2). The vibrational frequency is considered as a part of the solution since for self excited vibrations the exact frequency is usually not known a priori. The structural solver has the tendency to converge to the trivial solution (static equilibrium). As countermeasure the fundamental harmonic $\hat{\boldsymbol{u}}_1^{\mathrm{s}}$ is prevented from converging to zero by setting the real part of a selected generalized coordinate $\hat{u}_j^{\mathrm{s}} = \boldsymbol{e}_j^T \hat{\boldsymbol{u}}_1^{\mathrm{s}}$ constant as depicted in Fig. 3 (see [3] for details). The imaginary part is still part of the solution and thus there is an implicit phase constraint which would otherwise be arbitrary in the autonomous case. Since the coupled system is self-excited it is of autonomous nature and the coupled frequency is part of the solution. Furthermore only by considering the frequency as unknown, the structural algebraic system of equations is not overdetermined. The phase constraint applied to the structural solver in conjunction with passing the updated frequency to the flow solver will enable the FSI solver to determine the frequency during the coupling iterations.
Within the structural solver the aerodynamic force $\hat{\boldsymbol{f}}^{\mathrm{a}}$ can be linearized (which corresponds to the conventional energy method) to speed up the overall convergence of the FSI solver. This is motivated by obeservations that show, that often the aerodynamic damping coefficient does not depend significantly on the vibration amplitude [6]. For details on the linearization see [3].

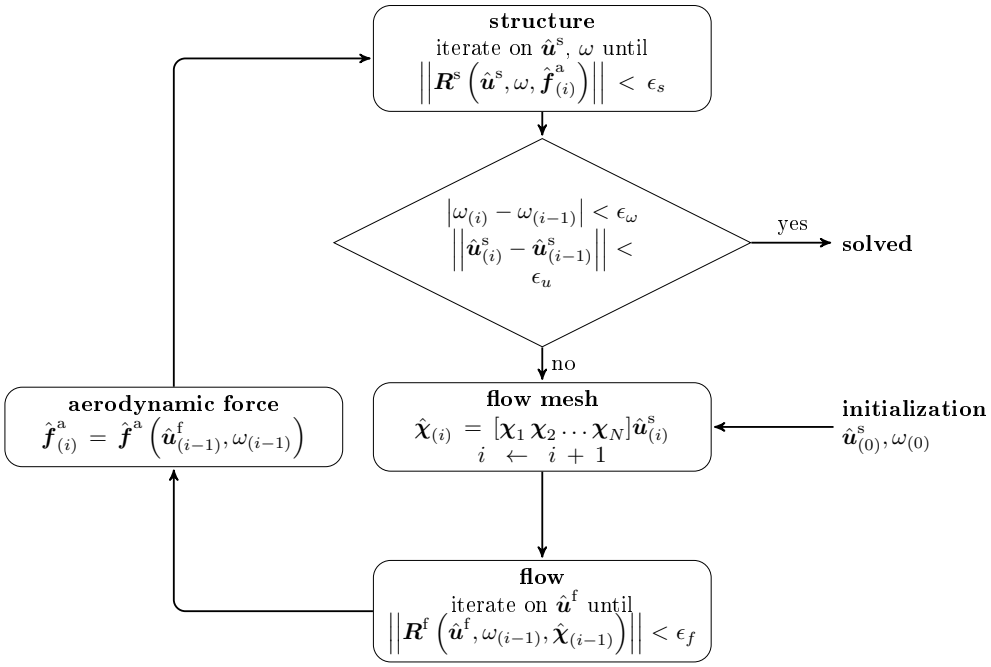

Figure 2. The algorithm scheme for the FSI frequency domain solver. [3]

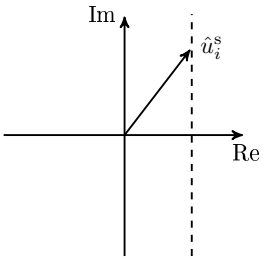

Figure 3. Avoidance of trivial solution.

3 Testcase Results

The testcase configuration is aerodynamically stable for small vibrational amplitudes and unstable for larger amplitudes due to a change of modeshape and eigenfrequency. Thus the coupled FSI solver is used to determine the stability limit amplitude. The ND -4 is selected for the investigation of the coupled nonlinear vibrational behavior. One harmonic in the structure model and the fundamental and the second harmonic in the fluid model are considered. The convergence of the first four iterations of the coupled FSI solver are shown in Fig. 4(a) and the convergence of $\hat{u}^{\mathrm{s}}_j$ is shown in Fig. 4(b). The chosen linearization approach for the aerodynamic force performed in a robust way for this testcase configuration. The vibrational frequency of the refined energy method ($\approx$418 Hz) and the FSI solver solution are significantly different from the in-vacuum frequency of the linearized eigenmode (519.661 Hz). The results of the refined energy method and the FSI solver agree very well and the deviations of frequency and $\hat{u}^{\mathrm{s}}_j$ are 0.149 % and 2.137 % respectively. The mode shapes of the FSI solver solution and the refined energy method are very similar. The coupled solver requires 83.5 hours on 10 cores.

4 Conclusions

The good agreements between the solutions of the novel FSI solver and the refined energy method verify the implementation of the coupled solver and show its value for future investigations. The testcase configuration demonstrated the occurence of nonlinear instability of the coupled problem due to nonlinear friction in the structure. Only the novel frequency domain methods are capable of detecting the instability and also predict the stability boundarys while the conventional energy method predicts a stable

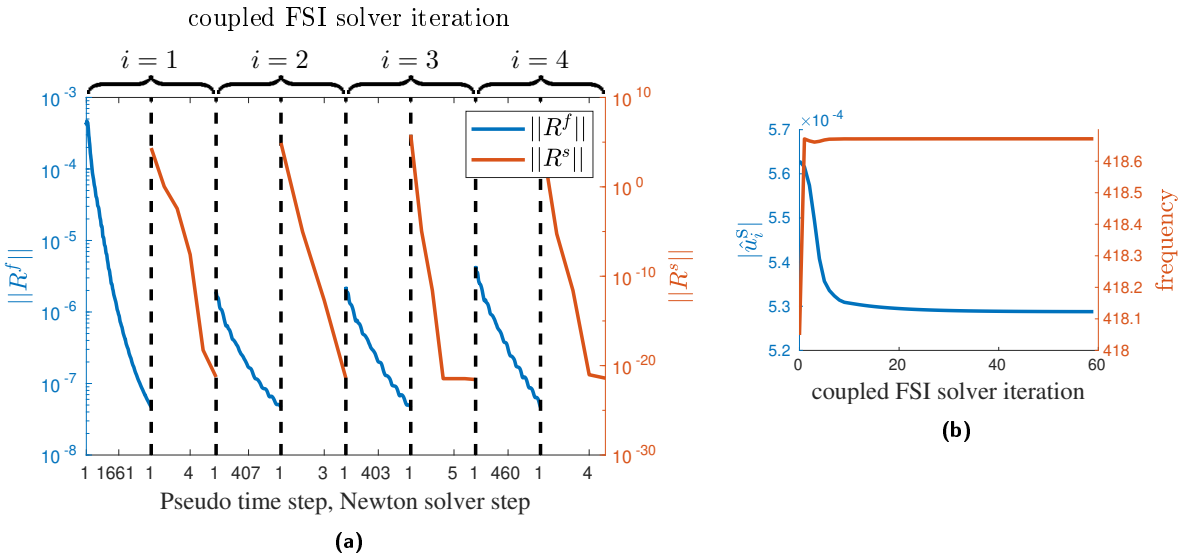

Figure 4. ND -4: (a) Convergence of the FSI solver for the unstable LCO; (b) Convergence of the dominant DOF for the unstable LCO. [3]

vibration. Further improvement of the coupled frequency domain FSI solver needs to be done regarding the initialization to circumvent the use of the refined energy method completely.

Acknowledgments

The research project (FVV no. 6001308, DFG no. FR 3970/1-1) was performed by the Institute of Propulsion Technology (ILA) at the German Aerospace Center and by the Institute of Aircraft Propulsion Systems (ILA) at University of Stuttgart. The authors greatfully acknowledge the support received from the FVV (Research Association for Combustion Engines eV) and the DFG (German Research Foundation).

References

[1] G. Ashcroft, C. Frey, and H.-P. Kersken, eds. *On the development of a harmonic balance method for aeroelastic analysis.* 2014.

[2] Christian Berthold, Christian Frey, Guido Dhondt, and Harald Schönenborn. FULLY COUPLED AEROELASTIC SIMULATIONS OF LIMIT CYCLE OSCILLATIONS IN THE TIME DOMAIN. In: *Proceedings of the 15th ISUAAAT.* 2018. URL: https://elib.dlr.de/127137/.

[3] Christian Berthold, Johan Gross, Malte Krack, and Christian Frey. Computation of the Stability Limit of Nonlinear Bladerow Flutter with a Fully Coupled Frequency Domain FSI Solver. *Journal of Fluids and Structures (Status: Submitted)* (2019).

[4] R. R. Craig and M. C.C. Bampton. Coupling of Substructures for Dynamic Analysis. *AIAA Journal* 6.7 (1968), pp. 1313–1319.

[5] Malte Krack, Loic Salles, and Fabrice Thouverez. Vibration prediction of bladed disks coupled by friction joints. *Archives of Computational Methods in Engineering* 24.3 (2017), pp. 589–636.

[6] Charles E. Seeley, Christian Wakelam, Xuefeng Zhang, Douglas Hofer, and Wei-Min Ren. Investigations of Flutter and Aero Damping of a Turbine Blade: Part 1 - Experimental Characterization. In: *ASME Turbo Expo 2016: Turbomachinery Technical Conference and Exposition.* 49842. 2016, V07BT34A024–. DOI: 10.1115/GT2016-57930. URL: http://dx.doi.org/10.1115/GT2016-57930.

[7] X Wu, M Vahdati, C Schipani, and M Imregun. Analysis of Low-Pressure Turbine Flutter for Different Shroud Interfaces. In: *ASME Turbo Expo 2007: Power for Land, Sea, and Air.* American Society of Mechanical Engineers. 2007, pp. 629–636.

**Proceedings of the 8th GACM Colloquium on Computational Mechanics
for Young Scientists from Academia and Industry
August 28–30, 2019 in Kassel, Germany**

Adaptive Multilevel Optimization of Fluid-Structure Interaction Problems

Johanna K. Biehl[1] and Stefan Ulbrich[1]

[1]FB Mathematik, AG Optimierung, TU Darmstadt

Abstract. We present an effective way to control fluid-structure interaction problems in a two dimensional setting, where the fluid is modeled with the Navier–Stokes equations and the structure is hyperelastic. To this end, we first introduce the model and the coupling conditions used. Then, a weak formulation is derived, which is the basis for a monolithic finite element discretization in space and a Crank-Nicolson scheme in time. Since the discretization results in a problem which is costly and time consuming to solve, for an effective optimization, we want to reduce the computational time. Therefore, we introduce a reduced order model based on proper orthogonal decomposition. The stability of solutions of the resulting reduced saddle point problem is ensured with help of supremizers, which guarantee that the inf-sup condition is satisfied. For the optimization we then introduce an adjoint based adaptive multilevel SQP method. Here, the accuracy of the finite element model is further ensured by adaptive grid refinement strategies which result from residual based a posteriori error estimators.

Introduction

The interaction between fluids and structures is a widespread problem in many applications, as for example in medicine and civil engineering. We present a multilevel SQP method to control these kind of problems. We consider a two dimensional setting, where the fluid is modeled as a Newtonian fluid by the Navier–Stokes equations and the structure is hyperelastic, e.g., a Saint Venant–Kirchhoff material. We first introduce the model from which we derive a weak formulation. This is the basis for a monolithic finite element discretization in space and a Crank-Nicolson scheme in time. This discretization results in a high dimensional, highly nonlinear problem. For an effective optimization, we therefore want to reduce the computational cost. This is done by introducing a reduced order model based on the discrete proper orthogonal decomposition technique. The resulting system is a saddle point problem and is extended by supremizers to ensure the stability of solutions by guaranteeing that the *inf-sup* condition is satisfied. For the optimization an adjoint based adaptive multilevel sequential quadratic programming method is used. The basic idea is to compute the optimization steps on the reduced order model and control their accuracy on the finite element level. We further ensure the accuracy of the finite element model by adaptive grid refinement strategies, which result from residual based a posteriori error estimators. Finally, the presented method is applied to the Benchmark problem proposed by Turek and Hron in [7].

1 Problem modelling

The fluid is considered to be Newtonian and, as already mentioned, modeled by the Navier–Stokes equations, consisting of mass and momentum conservation equations. These equations depend on the pressure p and the velocity v of the flow. This flow interacts with the hyperelastic structure, given by the momentum conservation, e.g., the nonlinear elasticity equation, which is solved for the deformation u. To overcome the difficulty that usually fluids are modeled in a Eulerian and solids in a Lagrangian setting, an Arbitrary Lagrangian Eulerian (ALE) formulation is used. This can be done in two ways, either all terms are transformed onto the reference domain or the fluid is modeled on the deformed domain. Here, we concentrate on the first option and denote with a hat symbol whenever a function or variable is defined on the reference configuration.

As interaction conditions on the interface we impose the continuity of velocities $\partial_t u = v$ and the action equals reaction condition for the normal stresses. We further choose a suitable do-nothing boundary condition for the flow on the outflow boundary and no-slip conditions, a Dirichlet inflow condition and no-slip conditions on the remaining boundaries.

For the boundary of the solid which is not part of the interface we impose homogeneous Dirichlet boundary conditions. All together this gives the following initial value problem for a time interval $T := [0, t_{end}]$.

Problem 1 *Find $\hat{u}\colon \hat{\Omega}_s \times T \to \mathbb{R}^2$, $\hat{v}\colon \hat{\Omega}_f \times T \to \mathbb{R}^2$ and $p\colon \hat{\Omega}_f \times T \to \mathbb{R}$, such that for suitable initial data $\hat{u}(\hat{x}, 0) = \hat{u}_0(\hat{x})$ in $\hat{\Omega}_s$ and $\hat{v}(\hat{x}, 0) = \hat{v}_0(\hat{x})$ in $\hat{\Omega}_f$ it holds:*

$$\begin{aligned} \rho_s \partial_{tt}^2 \hat{u} - \widehat{\operatorname{div}}\,(\hat{J}\hat{\sigma}_s \hat{F}^{-T}) &= \rho_s \hat{f}_s, \\ \hat{J}\rho_f \partial_t \hat{v} + \hat{J}\rho_f (\hat{F}^{-1}(\hat{v} - \partial_t \hat{\mathcal{T}}) \cdot \widehat{\nabla})\hat{v} - \widehat{\operatorname{div}}\,(\hat{J}\hat{\sigma}_f \hat{F}^{-T}) &= \hat{J}\rho_f \hat{f}_f, \\ \widehat{\operatorname{div}}\,(\hat{J}\hat{F}^{-1}\hat{v}) &= 0, \end{aligned}$$

with constant densities ρ_s, ρ_f, interaction conditions

$$\begin{aligned} \hat{J}\hat{\sigma}_s \hat{F}^{-T}\hat{n}_s = \hat{J}\hat{\sigma}_f \hat{F}^{-T}\hat{n}_f, \quad &on \quad \hat{\Gamma}_I \times T, \\ \partial_t \hat{u} = \hat{v}, \quad &on \quad \hat{\Gamma}_I \times T, \end{aligned}$$

and boundary conditions

$$\begin{aligned} \hat{v} = \hat{v}^{in} \quad &on \quad \hat{\Gamma}_{in}^D \times T, \\ \hat{v} = 0 \quad &on \quad \hat{\Gamma}_f^D \times T, \\ \rho_f \nu_f \hat{\nabla}\hat{v}\hat{F}^{-1} \cdot \hat{n} - \hat{p}\hat{I} = 0 \quad &on \quad \hat{\Gamma}_N^{out} \times T, \\ \hat{u} = 0 \quad &on \quad \hat{\Gamma}_s^D \times T. \end{aligned}$$

The stress tensors are given by

$$\begin{aligned} \hat{\sigma}_s &= \hat{J}^{-1}\hat{F}(\lambda \operatorname{tr}(\hat{E})I + 2\mu\hat{E})\hat{F}^T, \\ \hat{\sigma}_f &= -\hat{p}\hat{I} + \rho_f \nu_f (\hat{\nabla}\hat{v}\hat{F}^{-1} + \hat{F}^{-T}\hat{\nabla}\hat{v}^T). \end{aligned}$$

Here, $\hat{\mathcal{T}}$, the ALE transformation, is a diffeomorphism extending the deformation $\hat{\mathcal{T}}_L := \hat{x} + \hat{u}(\hat{x}, t)$, $\hat{F}$ is the so-called deformation gradient and $\hat{J}$ its determinant. Further, $\hat{E}$ denotes the Green–Lagrange strain tensor. The densities are given by the constants ρ_f and ρ_s and the material is defined by using the Lamé constants μ and λ.

The basis for the discretization is a weak formulation of the problem. This is derived by multiplying the equations with suitable test functions and integrating over the domain. Then, by integration by parts, we can shift some derivatives onto the test functions. The so derived weak system is then discretized by a finite element approach in space and a Crank-Nicolson scheme in time, following [3].

2 Reduced order model

To reduce the costs of the computation, we use model order reduction, more specifically, the proper orthogonal decomposition method. The basic idea of this method is to approximate the state by approximating the space spanned by a given number of time snapshots. This method has already been successfully used for a variety of optimal control problems, see, e.g., [2, 5].

As the finite element discretization, also the reduction for fluid structure interaction problems results in a saddle point problem. Existence and stability of a solution for such problems can be ensured with *Brezzi's Splitting Theorem*. This means we have to make sure that the *inf-sup* condition holds true for the derived reduced model. This does not need to be the case for the standard choice of the POD basis. Thus, we follow the proposal of Rozza and Veroy in [6] and enrich the POD basis.

Since in general we are looking at optimization problems and calculate the derivative of the cost function by using adjoint calculation, we also reduce the space of the adjoint states.

3 Optimization

For the optimization we use a multilevel sequential quadratic programming method, with adaptive mesh refinement. The method is based on the works of Ziems, Ulbrich and Bott in [8, 9] and [1].

Therefore, we need to control the finite element error as well as the error occuring through the model order reduction. For the finite element error, we derive an estimator which is close to the one in [4] for the time independent Navier–Stokes equations. We further control the error introduced by the time discretization by a suitable routine. The idea of the second error estimator is to evaluate the finite element system with the solutions of the reduced order model. This gives reasonable estimates, see [1].

4 Application

The setting of the Benchmark problem and the notation is shown in Figure 1. The structure with domain $\hat{\Omega}_s$ is attached to a fixed cylinder in a two dimensional channel flow $\hat{\Omega}_f$, with interface $\hat{\Gamma}_I$, inflow boundary $\hat{\Gamma}^D_{in}$, and outflow boundary $\hat{\Gamma}^N_{out}$.

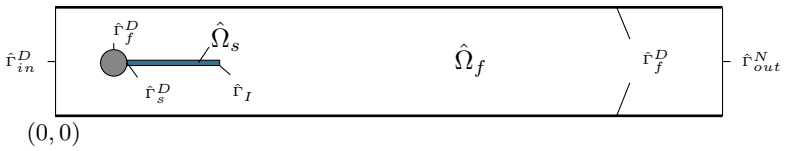

Figure 1. Benchmark problem.

The implementation of the finite element model is in good agreement to the in the benchmark proposed values. For the test of the optimization algorithm we first have to introduce a control z and a suitable control space $\mathcal{Z}$ as well as a cost functional J. For the control we choose a body force acting on a given subdomain of the fluid $\hat{\Omega}_f$, for which we introduce box constraints. As an example for a cost functional, we choose the lift forces acting on the interface and cylinder.

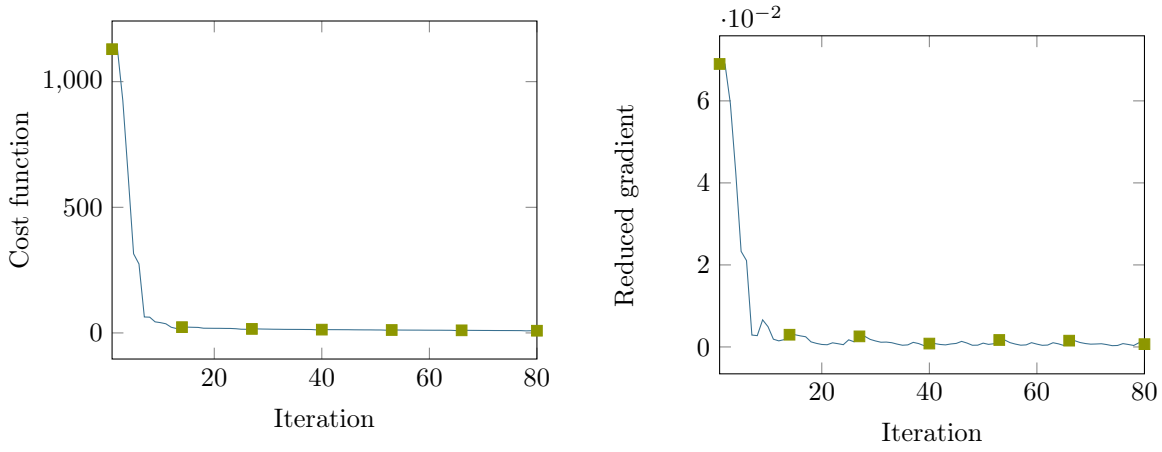

Figure 2. Development of cost function and reduced gradient

In Figure 2, we see the development of the cost function and the reduced gradient over the iterations of the multilevel SQP method. The squares always denote a finite element evaluation. All other steps are computed on a reduced order model. The original and optimized lift forces are shown in Figure 3.

Acknowledgments

This work is supported by the 'Excellence Initiative' of the German Federal and State Governments and the Graduate School of Computational Engineering at Technische Universität Darmstadt.

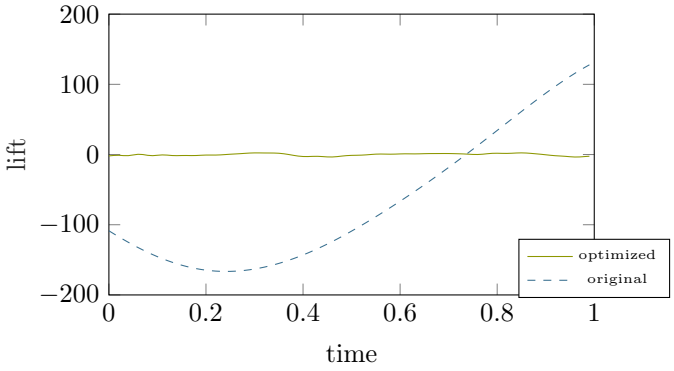

Figure 3. Original and reduced lift forces

References

[1] S. Bott. "Adaptive SQP method with reduced order models for optimal control problems with constraints on the state applied to the Navier–Stokes Equations". PhD thesis. Technischen Universität Darmstadt, 2016.

[2] K. Gubisch and S. Volkwein. Proper orthogonal decomposition for linear–quadraticuadratic optimal control (2013).

[3] Jaroslav Hron and Stefan Turek. A monolithic FEM/multigrid solver for an ALE formulation of fluid-structure interaction with applications in biomechanics. English. In: *Fluid-structure interaction. Modelling, simulation, optimisation. Proceedings of the workshop, Hohenwart, Germany, October 2005*. Berlin: Springer, 2006, pp. 146–170. ISBN: 3-540-34595-7/pbk.

[4] Volker John. Residual a posteriori error estimates for two-level finite element methods for the Navier-Stokes equations. English. *Appl. Numer. Math.* 37.4 (2001), pp. 503–518. ISSN: 0168-9274. DOI: 10.1016/S0168-9274(00)00058-1.

[5] K. Kunisch and S. Volkwein. Proper orthogonal decomposition methods for a general equation in fluid dynamics. *SIAM J. Numer. Anal.* 40.2 (2002), pp. 492–515. DOI: 10.1137/S0036142900382612. URL: http://dx.doi.org/10.1137/S0036142900382612.

[6] Gianluigi Rozza and Karen Veroy. On the stability of the reduced basis method for Stokes equations in parametrized domains. English. *Comput. Methods Appl. Mech. Eng.* 196.7 (2007), pp. 1244–1260. ISSN: 0045-7825. DOI: 10.1016/j.cma.2006.09.005.

[7] Stefan Turek and Jaroslav Hron. Proposal for numerical benchmarking of fluid-structure interaction between an elastic object and laminar incompressible flow. English. In: *Fluid-Structure Interaction*. Vol. 53. Lecture Notes in Computational Science and Engineering. Springer Berlin Heidelberg, 2006, pp. 371–385. ISBN: 978-3-540-34595-4. DOI: 10.1007/3-540-34596-5_15. URL: http://dx.doi.org/10.1007/3-540-34596-5_15.

[8] Stefan Ulbrich and Jan Carsten Ziems. Adaptive multilevel trust-region methods for time-dependent PDE-constrained optimization. English. *Port. Math. (N.S.)* 74.1 (2017), pp. 37–67. ISSN: 0032-5155; 1662-2758/e.

[9] C. Ziems. "Adaptive multilevel SQP–methods for PDE–constrained optimization". PhD thesis. Technischen Universität Darmstadt, 2010.

**Proceedings of the 8th GACM Colloquium on Computational Mechanics
for Young Scientists from Academia and Industry
August 28–30, 2019 in Kassel, Germany**

Finite element modelling of ultrasonic guided waves propagation in the fluid-composite structure interaction

Bhuiyan Shameem Mahmood Ebna Hai * [1] and Markus Bause[1]

[1]Numerical Mathematics, Faculty of Mechanical Engineering, Helmut Schmidt University, Hamburg, Germany.

Abstract. This work proposes a concept of coupling the ultrasonic guided waves (UGWs) propagation with the fluid-composite structure interaction, where the composite elastic structure consists of at least two layers. This coupled multiphysics model tracks the UGWs propagation through the fluid, composite/multilayer structure, and their interface as a part of the structural health monitoring (SHM) system. The model includes a monolithically coupled system of acoustic and elastic wave equations. The solid part comprises the Saint-Venant Kirchhoff (STVK) and neo-Hookean (INH) material model. The coupling between the two solid layers as well as between the multilayer structure and fluid inclusion is achieved via the geometric, kinematic, dynamic, interface regularity and boundary conditions. To ensure that the multilayer structure and fluid domains are conforming, we use the Arbitrary Lagrangian-Eulerian (ALE) technique. The numerical solution approach is based on the combination of Finite Element and Finite Difference methods. We follow the Rothe method, in which discretization in time is followed by space discretization, solving the resulting problem according to the monolithic approach. Discretization in space is done via a Finite Element method. An application example discussed here offers computational support for the off-line (or passive) SHM systems for a composite/multilayer material and lightweight structure.

Rationale

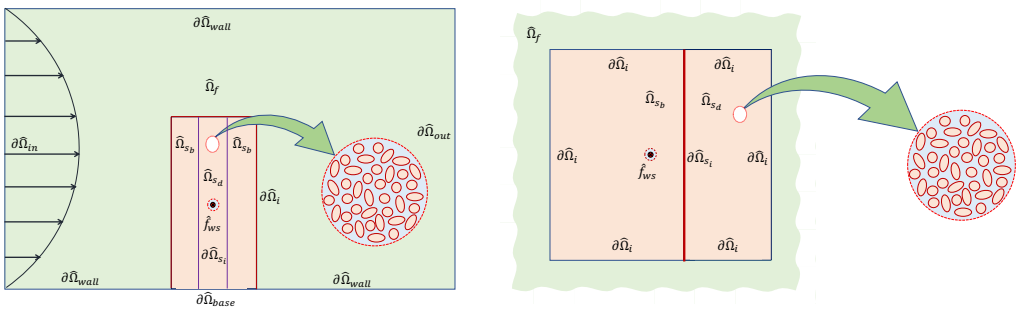

Figure 1. Configuration of 2D solid plate with a disc-shaped burst signal $\hat{f}_{ws}$: (a) a elastic body with three layers under fluid flow, and (b) a composite solid plate with two butt-joint solids.

While structural damage can be a continuously process that spreads during the operation of the object, a complete failure is usually a sudden event. As history shows, the consequences can be catastrophic. Therefore, it is of utmost importance to predict and ultimately avoid the occurrence of such events. It is precisely the motivation behind the design of an online SHM system. In addition, ideally, concerns for safety should not put a properly functioning structure out-of-service. Thereby, online SHM system is also a matter of cost-effectiveness. Furthermore, the online SHM system should be able to facilitate an operation during the unexpected or expected external forcing. For example, during such extreme events as earthquake, explosion, storm, collision, etc. an online SHM system can be used to detect, evaluate the extent of the damage, and decide whether the use of the mechanical structure is safe. The eXtended fluid-structure interaction (eXFSI) model constitutes a first step towards the computational support for

*Corresponding author: ebnahaib@hsu-hh.de ORCID iD: 0000-0002-7747-5536

the online SHM system and finds it's use in a wide range of applications [**1**, **2**, **3**, **4**, **5**, **6**, **7**, **8**]. This work contributes to the emerging strand of literature focusing on computational techniques, supporting the SHM system design.

To start with, we specify the computational domain. Let us consider, the given test configuration $\hat{\Omega}$ at time $t = 0$, $t \in I$, and $T > 0$, be composed of two time-dependent subdomains: solid domain $\hat{\Omega}_s = \hat{\Omega}_{s_b} \cup \hat{\Omega}_{s_d}$, and fluid domain $\hat{\Omega}_f$. Here, $\hat{\Omega} = \hat{\Omega}_s \cup \hat{\Omega}_f$, and $\hat{\Omega}_s \cap \hat{\Omega}_f = \emptyset$ (cf. Figure 1). The reference (or initial) domain $\hat{\Omega}$ has a Lipschitz boundary $\partial\hat{\Omega} \subset \mathbb{R}^{d-1}$, which is subdivided into four parts as follows: $\partial\hat{\Omega} = \partial\hat{\Omega}_{in} \cup \partial\hat{\Omega}_{wall} \cup \partial\hat{\Omega}_{base} \cup \partial\hat{\Omega}_{out}$, where for the displacements and velocities $\partial\hat{\Omega}_{wall}$, $\partial\hat{\Omega}_{in}$, and $\partial\hat{\Omega}_{base}$ are consider as Dirichlet boundaries, and $\partial\hat{\Omega}_{out}$ denotes as the fluid outflow Neumann boundary. The common fluid-solid interface $\partial\hat{\Omega}_i \subset \mathbb{R}^{d-1}$ and solid-solid interface $\partial\hat{\Omega}_{s_i} \subset \mathbb{R}^{d-1}$ are given by $\partial\Omega_i = \overline{\hat{\Omega}_f} \cap \overline{\hat{\Omega}_s}$ and $\partial\Omega_{s_i} = \overline{\hat{\Omega}_{s_b}} \cap \overline{\hat{\Omega}_{s_d}}$, respectively. Since we are using a variational monolithic coupling method, the displacements and velocity spaces are extended to the entire domain $\hat{\Omega}$. For the eXFSI problem, we work with the following spaces:

$$\hat{L}_{\hat{\Omega}_X} := L^2(\hat{\Omega}_X), \quad \hat{L}^0_{\hat{\Omega}_X} := L^2(\hat{\Omega}_X)/\mathbb{R}, \quad \hat{V}_{\hat{\Omega}_X} := H^1(\hat{\Omega}_X), \quad \hat{V}^0_{\hat{\Omega}_X} := H^1_0(\hat{\Omega}_X).$$

Here, $X = \{s, f\}$ is a set of suffixes, where "f" stands for the fluid and "s" stands for the solid. For convenience, we omit the explicit time-dependence term when indicating the time-dependent domains i.e. $\Omega := \Omega(t)$. Last, but not least, for the current domains Ω, Ω_f and Ω_s, we can denote the corresponding spaces without the 'hat' ($\hat{}$) notation. Next, we introduce the FSI problem that is fully coupled with the WpFSI problem [**9**] – eXtended fluid-structure interaction (eXFSI) problem. Accordingly, we combine the following models: (i) nonlinear fluid-structure interaction in the ALE framework, including the incompressible Navier-Stokes in the ALE framework, elastodynamics in Lagrangian framework, and the biharmonic mesh moving model; and (ii) nonlinear wave propagation (WpFSI) problem in the ALE framework. The latter is a coupled problem of the time-harmonic elastic wave propagation with a signal force in the ALE framework and acoustic wave propagation in the ALE framework [**9**]. The novelties of the present work include: formulation of a coupled wave propagation problem in the ALE framework, coupling it to the FSI model, where the solid part comprises the STVK and INH material model. Next, the model is used to analyse the implications of FSI for the wave propagation on solid-solid interface.

The eXFSI problem

Let us consider, $\hat{v}^D$ and $\hat{u}^D$ are suitable extensions of Dirichlet inflow data. Find the global velocity $\hat{v} \in \{\hat{v}^D + \hat{V}^0_{\hat{\Omega}}\}$, displacement $\hat{u} \in \{\hat{u}^D + \hat{V}^0_{\hat{\Omega}}\}$, auxiliary variable $\hat{\xi} \in \hat{V}_{\hat{\Omega}}$, pressure $\hat{p} \in \hat{L}^0_{\hat{\Omega}}$, wave displacement $\hat{u}_w \in \hat{V}^0_{\hat{\Omega}}$, wave velocity $\hat{v}_w \in \hat{L}_{\hat{\Omega}}$, and wave pressure $\hat{p}_w \in \hat{L}^0_{\hat{\Omega}}$, such that the initial conditions $\hat{v}(0) = \hat{v}^0$, $\hat{u}(0) = \hat{u}^0$, $\hat{u}_w(0) = \hat{u}^0_w$, and $\partial_t \hat{u}_w(0) = \hat{v}^0_w$ are satisfied, and for almost all time $t \in I$ it holds that:

$$\text{FSI part} \begin{cases} (\hat{J}\hat{\rho}_f \partial_t \hat{v}, \hat{\phi}^v)_{\hat{\Omega}_f} - \langle \hat{J}\hat{g}_f F^{-T}, \hat{\phi}^v \rangle_{\partial\hat{\Omega}_N} & \\ +(\hat{J}\hat{\rho}_f (\hat{F}^{-1}(\hat{v} - w) \cdot \hat{\nabla})\hat{v}, \hat{\phi}^v)_{\hat{\Omega}_f} & \\ +(\hat{J}\hat{\sigma}_f \hat{F}^{-T}, \hat{\nabla}\hat{\phi}^v)_{\hat{\Omega}_f} + (\hat{\rho}_s \partial_t \hat{v}, \hat{\phi}^v)_{\hat{\Omega}_s} & \\ +(\hat{J}\hat{\sigma}_s \hat{F}^{-T}, \hat{\nabla}\hat{\phi}^v)_{\hat{\Omega}_s} & = 0 \quad \forall \hat{\phi}^v \in \hat{V}^0_{\hat{\Omega}}, \\ (\alpha_u \hat{\xi}, \hat{\phi}^\xi)_{\hat{\Omega}_f} - (\alpha_u \hat{\nabla}\hat{u}, \hat{\nabla}\hat{\phi}^\xi)_{\hat{\Omega}_f} & \\ +(\alpha_u \hat{\xi}, \hat{\phi}^\xi)_{\hat{\Omega}_s} - (\alpha_u \hat{\nabla}\hat{u}, \hat{\nabla}\hat{\phi}^\xi)_{\hat{\Omega}_s} & = 0 \quad \forall \hat{\phi}^\xi \in \hat{V}_{\hat{\Omega}}, \\ (\hat{\rho}_s(\partial_t \hat{u} - \hat{v}), \hat{\phi}^u)_{\hat{\Omega}_s} + (\alpha_u \hat{\nabla}\hat{\xi}, \hat{\nabla}\hat{\phi}^u)_{\hat{\Omega}_f} & = 0 \quad \forall \hat{\phi}^u \in \hat{V}^0_{\hat{\Omega}}, \\ (\hat{\text{div}}(\hat{J}\hat{F}^{-1}\hat{v}), \hat{\phi}^p)_{\hat{\Omega}_f} + (\hat{p}_s, \hat{\phi}^p)_{\hat{\Omega}_s} & = 0 \quad \forall \hat{\phi}^p \in \hat{L}^0_{\hat{\Omega}}, \ \text{(STVK)} \\ (\hat{\text{div}}(\hat{J}\hat{F}^{-1}\hat{v}), \hat{\phi}^p)_{\hat{\Omega}_f} + (\det \hat{F} - 1, \hat{\phi}^p)_{\hat{\Omega}_s} & = 0 \quad \forall \hat{\phi}^p \in \hat{L}^0_{\hat{\Omega}}, \ \text{(INH)} \end{cases}$$

$$\text{WpFSI part} \begin{cases} (\hat{\rho}_s \partial_t \hat{u}_w, \hat{\phi}^{u_w})_{\hat{\Omega}_s} - (\hat{\rho}_s \hat{v}_w, \hat{\phi}^{u_w})_{\hat{\Omega}_s} & \\ +(\hat{J}\hat{\rho}_f \partial_t \hat{u}_w, \hat{\phi}^{u_w})_{\hat{\Omega}_f} - (\hat{J}\hat{\rho}_f \hat{v}_w, \hat{\phi}^{u_w})_{\hat{\Omega}_f} & \\ -(\hat{J}\hat{\rho}_f (\hat{F}^{-1}\hat{w} \cdot \hat{\nabla})\hat{u}_w, \hat{\phi}^{u_w})_{\hat{\Omega}_f} & = 0 \quad \forall \hat{\phi}^{u_w} \in \hat{L}_{\hat{\Omega}}, \\ (\hat{\rho}_s \partial_t \hat{v}_w, \hat{\phi}^{v_w})_{\hat{\Omega}_s} + (\hat{J}\hat{\sigma}_{ws} \hat{F}^{-T}, \hat{\nabla}\hat{\phi}^{v_w})_{\hat{\Omega}_s} & \\ -(\hat{J}\hat{f}_{ws}, \hat{\phi}^{v_w})_{\hat{\Omega}_s} + (\hat{J}\hat{\rho}_f \partial_t \hat{v}_w, \hat{\phi}^{v_w})_{\hat{\Omega}_f} & \\ -(\hat{J}\hat{\rho}_f (\hat{F}^{-1}\hat{w} \cdot \hat{\nabla})\hat{v}_w, \hat{\phi}^{v_w})_{\hat{\Omega}_f} & \\ +(c^2 \hat{J}\hat{\rho}_f (\hat{\nabla}\hat{u}_w \hat{F}^{-1})\hat{F}^{-T}, \hat{\nabla}\hat{\phi}^{v_w})_{\hat{\Omega}_f} & = 0 \quad \forall \hat{\phi}^{v_w} \in \hat{V}^0_{\hat{\Omega}}, \\ \underbrace{(\hat{p}_{w_s}, \hat{\phi}^{p_w})_{\hat{\Omega}_s}}_{\text{STVK}} + \underbrace{(\det \hat{F} - 1, \hat{\phi}^{p_w})_{\hat{\Omega}_s}}_{\text{INH}} & = 0 \quad \forall \hat{\phi}^{p_w} \in \hat{L}^0_{\hat{\Omega}}, \end{cases}$$

with the linearized stress tensor given by

$$
\begin{aligned}
\hat{\sigma}_f &= -\hat{p}_f\,\mathrm{I} + \hat{\rho}_f \nu_f (\hat{\nabla}\hat{v}_f \hat{F}^{-1} + \hat{F}^{-T}\hat{\nabla}\hat{v}_f^T),\\
\hat{\sigma}_s &= \begin{cases} \hat{J}^{-1}\hat{F}\left(2\mu_s \hat{E}_s + \lambda_s \operatorname{tr}(\hat{E}_s)\,\mathrm{I}\right)\hat{F}^T & \text{(STVK)},\\ \hat{p}_s\,\mathrm{I} + \mu_s(\hat{F}\hat{F}^T - \mathrm{I}) & \text{(INH)}, \end{cases}\\
\hat{E}_s &= \frac{1}{2}\left(\hat{\nabla}\hat{u}_s\hat{F}^{-1} + \hat{F}^{-T}\hat{\nabla}\hat{u}_s^T\right),\\
\hat{\sigma}_{ws} &= \begin{cases} \hat{J}^{-1}\hat{F}\left(2\mu_s \hat{E}_{ws} + \lambda_s \operatorname{tr}(\hat{E}_{ws})\,\mathrm{I}\right)\hat{F}^T & \text{(STVK)},\\ \hat{p}_{w_s}\,\mathrm{I} + \mu_s(\hat{F}\hat{F}^T - \mathrm{I}) & \text{(INH)}, \end{cases}\\
\hat{E}_{ws} &= \frac{1}{2}\left(\hat{\nabla}\hat{u}_{ws}\hat{F}^{-1} + \hat{F}^{-T}\hat{\nabla}\hat{u}_{ws}^T\right).
\end{aligned}
$$

where a deformation gradient is given by $\hat{F} = I + \hat{\nabla}\hat{u}_s$ and, in turn, the deformation determinant $\hat{J}$ is a function of $\hat{F}$. The value of $\hat{w}$ is determined from the FSI problem. Furthermore, a correction term for the 'do-nothing' outflow condition is given by $\hat{g}_f = -\hat{\rho}_f \nu_f \hat{F}^{-T}\hat{\nabla}\hat{v}_f^T\,\hat{\mathrm{n}}_\mathrm{f}$ on $\partial\hat{\Omega}_{out}$. The ultimate goal of tests conducted in this work is to track the wave propagation in solid-solid interface. In particular, we consider the wave propagation problem in the deformable elastic structure with two butt-joint solids, where the solid part constitutes the STVK compressible material. In this proceedings, we consider the ideal case, where the structure remains in its initial position and the acting force, i.e. the FSI effect, is negligible. Thereby, there is no solid mesh deformation due to the additional force. We apply the Rothe method for the problem discretization. The temporal discretization is performed by using the finite difference scheme, and for the spatial discretization we refer to a standard Galerkin finite element approach. This nonlinear problem is solved using a Newton-like method. Worth noting, we refer to the direct solver UMFPACK [**10**] for solution of the linear equation systems at each Newton step. The implementation is accomplished via the software library package DOpELib [**11**].

Numerical simulation

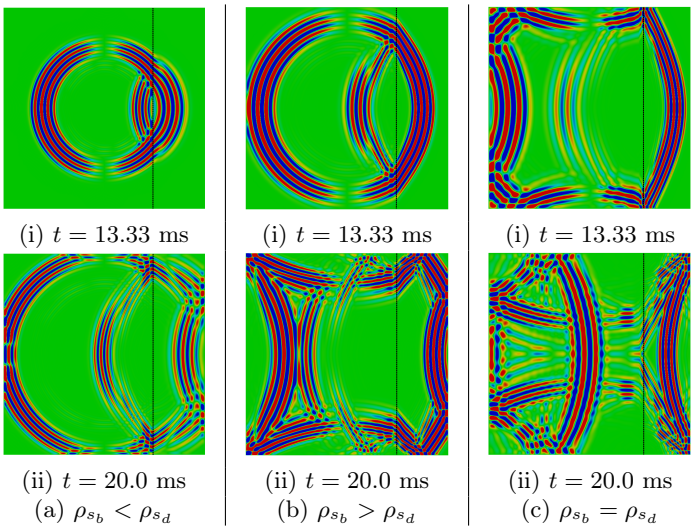

Figure 2. The displacement field component $\hat{u}_{x_1}$ in a solid plate with two butt-joint solids.

Let us consider an elastic base plate with two butt-joint solid domains (cf. Figure-1(b)). We use the non-vanishing disc-shaped piezoelectric actuator $\hat{f}_{ws}(\hat{x}, t)$ with a radius $\hat{r}_{f_{ws}}$ of 7.5 mm, which is located at the geometric centre $(0, 0)$ of the solid plate. The actuator is used for the excitation of a burst Lamb wave package. Here, for the numerical simulation tests, we consider a five-cycle Lamb wave package, which has two main displacement field components $\hat{u}_{x_1}$ and $\hat{u}_{x_2}$ in the plane. The non-vanishing burst signal force is given in [**1**, **2**, **3**, **4**] where the signal frequency (f_c) is 1000 Hz, and for the numerical simulation test, a five-cycle Lamb wave package ($n_s = 5$) is used. It has two UGWs displacement field components $\hat{u}_{x_1}$ and $\hat{u}_{x_2}$ in the plane. Figure-2 illustrates the displacement component $\hat{u}_{x_1}$ of a five cycle Lamb wave burst signal for various relations between the density of a base solid plate and the density of a secondary solid

domain. Due to the different propagation rate, the UGWs passes through the secondary solid domain at a different time and with a different wavelength [**1**, **2**, **3**, **4**, **5**]. In addition, as the wave propagates from the base domain to the secondary domain through the common solid-solid interface, strong reflections occur. We demonstrate that this result is robust with respect to alternative material specifications, which induce differences only in terms of speed of propagation and the amount of reflections.

Remarks

In the present work, we propose a coupled multiphysics model which supports the design of the SHM system. We demonstrate the alterations to the wave propagation pattern for alternative media. Specifically, we mimic the alternative configuration of a butt-joint solid plates to explore the wave propagation behaviour on the solid-solid interface. We show that our proposed model successfully depicts the differences in the reflectivity between two solids and thereby is in agreement with the fundamental theory. The simulation results clearly show the successful identification of the location of the solid-solid common interface. In the present work we limit our focus on the STVK solid-solid butt-joint edge. Yet, one can extend the numerical simulation results to identification of the structural damage, for which the fluid inclusion can be considered [**1**, **3**, **4**]. More complete simulation results will be available in the extended version of this proceeding. Noteworthy, the WpFSI model serves as a first step towards the implementation of a machine learning approach to SHM system design.

References

[1] Ebna Hai, B. S. M. 2017. "Finite Element Approximation of Ultrasonic Wave Propagation under Fluid-Structure Interaction for Structural Health Monitoring Systems", Doctoral dissertation, Helmut Schmidt University, Hamburg, Germany.

[2] Ebna Hai, B. S. M., and M. Bause. 2019. "Numerical study and comparison of alternative time discretization schemes for an ultrasonic guided wave propagation problem coupled with fluid–structure interaction". *Comput Math Appl*.

[3] Ebna Hai, B. S. M., and M. Bause. 2019. "Modeling Concept and Numerical Simulation of Ultrasonic Waves Propagation in a Moving Fluid-Structure Domain based on a Monolithic Approach". *Appl Math Model*.

[4] Ebna Hai, B. S. M., and M. Bause. 2018. "Finite Element Approximation of Fluid-Structure Interaction (FSI) Problem with Coupled Wave Propagation". *PAMM*, vol. 17, pp. 511–512.

[5] Ebna Hai, B. S. M., and M. Bause. 2017. "Mathematical Modelling and Numerical Simulation of the online Structural Health Monitoring System". In F.-K. Chang and F. Kopsaftopoulos (eds.), *Structural Health Monitoring 2017*, vol. 1, pp. 580–587.

[6] Ebna Hai, B. S. M., and M. Bause. 2018. "Numerical Modeling and Approximation of the Coupling Lamb Wave Propagation With Fluid-Structure Interaction Problem". *In proceedings of: the ASME 2018 International Mechanical Engineering Congress & Exposition*, Pittsburgh, USA, vol. 9.

[7] Ebna Hai, B. S. M., M. Bause, and P. A. Kuberry. 2016. "Finite Element Approximation of the eXtended Fluid-Structure Interaction (eXFSI) Problem". *In proceedings of: the ASME 2016 Fluids Engineering Division Summer Meeting*, Washington, D.C., USA, vol. 1A.

[8] Ebna Hai, B. S. M., and M. Bause. 2018. "Mathematical Modelling of Structural Health Monitoring Systems: Coupling Fluid-Structure Interaction with Wave Propagation". *In proceedings of: the ECCOMAS ECCM-ECFD 2018*, Glasgow, UK, pp. 394–404.

[9] Ebna Hai, B. S. M., and M. Bause. 2019. "Modeling and Simulation of Ultrasonic Guided Waves Propagation in the Fluid-Structure Domain by a Monolithic Approach". *J Fluid Struct*, vol. 88, pp. 100-121.

[10] Davis, T. A. and I. S. Duff. 2007. "An unsymmetric-pattern multifrontal method for sparse LU factorization". *SIAM Journal on Matrix Analysis and Applications*, vol. 18, pp. 140–158.

[11] C. Goll, T. Wick. and W. Wollner. 2017. "DOpElib: Differential Equations and Optimization Environment". *Archive of Numerical Software*, vol. 5, pp. 1–14.

**Proceedings of the 8th GACM Colloquium on Computational Mechanics
for Young Scientists from Academia and Industry
August 28–30, 2019 in Kassel, Germany**

An efficient implementation of gradient-enhanced crystal plasticity models

V. Fohrmeister * and J. Mosler

Institute of Mechanics, TU Dortmund University, Germany

Abstract. For the physically sound simulation of forming processes and a prediction of evolving textures, micromechanically motivated crystal-plasticity models are frequently applied. If these models are enhanced with gradients of the plastic deformations, they can capture hardening due to geometrically necessary dislocations. This is, for instance, important for the consideration of the Hall-Petch relation. However and in line with the underlying local crystal plasticity model, a straightforward implementation of rate-independent models leads to a complex and potentially ill-posed system of inequalities at the global finite elment level (see, e.g., [6]). In order to eliminate this problem, the inequalities corresponding to the loading/unloading conditions are rewritten by means of equivalent nonlinear complementarity conditions (NCP) equations, cf. [8]. Furthermore and in order to reduce the implementational effort, the micromorphic approach [1] is adapted.

1 Local Crystal-Plasticity – Variational formulation

1.1 Fundamentals

The framework is based on the multiplicative split of the deformation gradient

$$\boldsymbol{F} = \boldsymbol{1} + \nabla \boldsymbol{u} = \boldsymbol{F}^{\mathrm{e}} \cdot \boldsymbol{F}^{\mathrm{p}} \tag{1}$$

into incompatible elastic and plastic components $\boldsymbol{F}^{\mathrm{e}}$ and $\boldsymbol{F}^{\mathrm{p}}$. With free Helmholtz energy $\Psi = \hat{\Psi}(\boldsymbol{F}^{\mathrm{e}}, \boldsymbol{\alpha})$, where $\boldsymbol{\alpha}$ are internal variables describing the hardening within each slip system, we can define the Mandel stress and the corresponding thermodynamic driving forces to $\boldsymbol{\alpha}$ as

$$\boldsymbol{\Sigma} := -\partial_{\boldsymbol{F}^{\mathrm{p}}} \Psi \cdot [\boldsymbol{F}^{\mathrm{p}}]^{\mathrm{T}} \text{ and } \boldsymbol{Q} := -\partial_{\boldsymbol{\alpha}} \Psi \,. \tag{2}$$

By using these definitions and in line with the well-known Schmid-law, a yield criterion for every slip-system (i) of type

$$\phi^{(i)} = \left| \boldsymbol{M}^{(i)} \cdot \boldsymbol{\Sigma} \cdot \boldsymbol{N}^{(i)} \right| - \left[Q_0^{(i)} + Q^{(i)} \right] . \tag{3}$$

is used. Here, $\boldsymbol{M}^{(i)}$ and $\boldsymbol{N}^{(i)}$ are orthonormal vectors defining the slip direction and slip plane, respectively. $Q_0^{(i)}$ denotes the initial yield limit. These yield functions define an outer bound for the space of admissible stresses

$$\mathbb{E} := \left\{ (\boldsymbol{\Sigma}, \boldsymbol{Q}) \in \mathbb{R}^{(3\times 3)+n_{\mathrm{sys}}} \mid \phi^{(i)}(\boldsymbol{\Sigma}, Q^{(i)}) \leq 0 \quad \forall i \right\} . \tag{4}$$

Utilising the postulate of maximum dissipation, the evolution equations for the internal variables result in

$$\dot{\boldsymbol{F}}^{\mathrm{p}} \cdot [\boldsymbol{F}^{\mathrm{p}}]^{-1} = \sum_{i=1}^{n_{\mathrm{sys}}} \dot{\gamma}^{(i)} \, \boldsymbol{M}^{(i)} \otimes \boldsymbol{N}^{(i)} \text{ with } \dot{\gamma}^{(i)} = \operatorname{sign}\left(\boldsymbol{\Sigma} : \left[\boldsymbol{M}^{(i)} \otimes \boldsymbol{N}^{(i)} \right] \right) \lambda^{(i)} \,, \tag{5}$$

$$\dot{\boldsymbol{\alpha}} = -\boldsymbol{\lambda} \,, \tag{6}$$

where $\lambda^{(i)}$ denotes the plastic multiplier of the i-th slip system. The internal dissipation corresponding to this model is $\mathcal{D}_{\mathrm{int}} = \sum_{i=1}^{n_{\mathrm{sys}}} Q^{(i)} \, \lambda^{(i)}$.

*Corresponding author: volker.fohrmeister@tu-dortmund.de ORCID iD: 0000-0001-8467-9863

1.2 Variational formulation

For the isothermal setting, and in line with e.g. [7], rate potential

$$\dot{\mathcal{I}} := \int_\Omega \left[\dot{\Psi} + \mathcal{D}_{\text{int}} \right] \mathrm{d}V + \mathcal{P}_{\text{ext}} \tag{7}$$

is introduced. Here, $\mathcal{P}_{\text{ext}}$ is the powers associated with external forces acting on the body Ω. The integral term is referred to as the stress power and can be expressed as $\boldsymbol{P} : \dot{\boldsymbol{F}}$ for the local formulation with $\boldsymbol{P} = \partial_{\boldsymbol{F}} \Psi$ being the first Piola stress conjugated to $\boldsymbol{F}$. The underlying equations of the physical problem now follow directly by the stationary conditions with respect to the velocity $\dot{\boldsymbol{u}}$ and the plastic multipliers $\boldsymbol{\lambda}$, e.g.

$$\delta_{\dot{\boldsymbol{u}}} \dot{\mathcal{I}} = \int_\Omega \boldsymbol{P} : \delta \dot{\boldsymbol{F}} \, \mathrm{d}V + \delta_{\dot{\boldsymbol{u}}} \mathcal{P}_{\text{ext}} = 0 \qquad \text{and} \qquad \delta_{\lambda^{(i)}} \dot{\mathcal{I}} = -\phi^{(i)} \geq 0 \,. \tag{8}$$

While the first equation corresponds to the balance of linear momentum, the second one assures admissibility of the stresses, see Eq. (4).

1.3 Implementation based on a nonlinear complementary problem

After applying a backward-Euler time integration to the aforementioned equations, the optimality w.r.t. the time integrated plastic multipliers $\Delta\boldsymbol{\lambda} := \int_{t_n}^{t_{n+1}} \boldsymbol{\lambda} \, \mathrm{d}t$ can be expressed in terms of a set of Karush-Kuhn-Tucker conditions

$$\partial_{\Delta\lambda^{(i)}} \mathcal{I} \geq 0 \;\wedge\; \Delta\lambda^{(i)} \geq 0 \;\wedge\; \partial_{\Delta\lambda^{(i)}} \mathcal{I} \, \Delta\lambda^{(i)} = 0 \quad \forall i \,. \tag{9}$$

For numerical reasons, these inequalities are rewritten into an equivalent nonlinear complementary problem of type

$$\tilde{\phi}^{(i)} := \sqrt{[\partial_{\Delta\lambda^{(i)}} \mathcal{I}^{(i)}]^2 + [\Delta\lambda^{(i)}]^2 + 2\,\delta^2} - \partial_{\Delta\lambda^{(i)}} \mathcal{I}^{(i)} - \Delta\lambda^{(i)} \stackrel{!}{=} 0 \quad \forall i \,, \tag{10}$$

i.e., the NCP functions according to Fischer and Burmeister are employed, see [4, 8]. Here, small perturbation parameter δ circumvents the singularity of Eq. (10) in its origin, albeit approximating the original problem, see[2] for further information.

2 Gradient enhancement

For the incorporation of size effects into the presented crystal plasticity model, the model is enhanced by non-local contributions of the free energy. To be more precise, and following the idea of so-called *micromorphic models*, as presented e.g. in [1], a macroscopic field $\boldsymbol{\varphi}^{\text{p}}$ is introduced and coupled to the internal variable $\boldsymbol{\alpha}$ using penalty like energy $\Psi^{\text{intr}}(\boldsymbol{\varphi}^{\text{p}}, \boldsymbol{\alpha})$. Now, gradient dependent energies $\Psi^{\text{glob}}(\nabla\boldsymbol{\varphi}^{\text{p}})$ can be introduced into the model, without the need for modifying the underlying local constitutive update significantly.

3 Implementation based on Hyper-Dual Step Differentiation

For an efficient implementation of the aforementioned optimization problem, a Newton-type iteration scheme is employed. In order to compute the required first and second derivatives, an automatic derivation scheme based on so called *hyper-dual numbers* is elaborated, see [3, 5, 9]. In analogy to standard complex numbers, this algebra contains non-real, so called *dual*, components ϵ_j with the properties $\epsilon_k \, \epsilon_j = \epsilon_j \, \epsilon_k$ and $\epsilon_j^2 = 0$. Analysing the Taylor-series of an arbitrary function $f(x)$, one can show that the first and second derivatives of this function can be extracted by

$$\left.\frac{\mathrm{d}\, f}{\mathrm{d}\, x}\right|_{x_0} = \frac{\mathfrak{D}_1 \, f(x_0 + a\,\epsilon_1)}{a} \,, \qquad \left.\frac{\mathrm{d}^2 f}{\mathrm{d}\, x^2}\right|_{x_0} = \frac{\mathfrak{D}_{12} \, f(x_0 + a\,\epsilon_1 + b\,\epsilon_2)}{a\,b} \,.$$

$\mathfrak{D}_1(\bullet)$ here extracts the coordinate in ϵ_1 direction and $\mathfrak{D}_{12}(\bullet)$ extracts the coordinate of the mixed direction $\epsilon_1\,\epsilon_2$, analogously. In contrast to other numerical schemes, the obtained derivatives are exact.

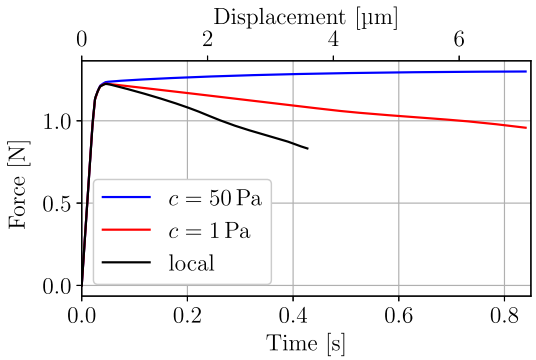

(a) Load-displacement curve of a tensile test with local and non-local material behaviour.

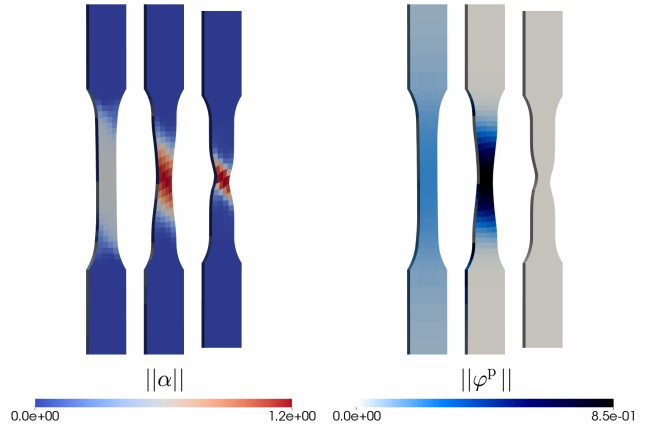

(b) Deformed configuration and distribution of $\|\boldsymbol{\alpha}\|$ (left) and $\|\boldsymbol{\varphi}^{\mathrm{P}}\|$ (right). The plots correspont to the final state of deformation. The three computations correspond to $c = 1\,\mathrm{Pa}$, $c = 50\,\mathrm{Pa}$ and $c = 0$.

Figure 1. Simulation of a tensile test of a single-crystal specimen.

4 Numerical Example

Simulations have been carried out with a single-crystal tensile specimen with length 96 µm and width 10 µm. The crystal orientation is not aligned with the specimen axes. For the elastic energy, a Neo-Hooke model is used, while the coupling and penalizing energy contributions have been assumed quadratically. Ideal plasticity is considered.
One can clearly see the performance of the non-local model in Figure 1. The local simulation stops prematurely due to convergence difficulties, while the non-local simulations are able to show the interaction between geometrical softening and gradient-induced hardening.

Acknowledgement

Financial support from the German Research Foundation (DFG) via SFB/TR TRR 188 (project number 278868966), project C04, is gratefully acknowledged.

References

[1] O. Aslan, N.M. Cordero, A. Gaubert, and S. Forest. Micromorphic approach to single crystal plasticity and damage. *International Journal of Engineering Science* 49.12 (2011), pp. 1311–1325. DOI: 10.1016/j.ijengsci.2011.03.008.

[2] Thorsten Bartel, Robin Schulte, Andreas Menzel, Björn Kiefer, and Bob Svendsen. Investigations on enhanced Fischer–Burmeister NCP functions: application to a rate-dependent model for ferroelectrics. *Archive of Applied Mechanics* (Sept. 2018). DOI: 10.1007/s00419-0181466-7.

[3] J. A. Fike and J. J. Alonso. Automatic Differentiation Through the Use of Hyper-Dual Numbers for Second Derivatives. In: *Recent Advances in Algorithmic Differentiation*. Ed. by S. Forth, P. Hovland, E. Phipps, J. Utke, A. Walther, T. J. Barth, M. Griebel, D. E. Keyes, R. M. Nieminen, D. Roose, and T. Schlick. Vol. 87. Lecture Notes in Computational Science and Engineering. Springer Berlin Heidelberg, 2012, pp. 163–173. ISBN: 978-3-642-30023-3. DOI: 10.1007/978-3-642-30023-3_15.

[4] A. Fischer. A special newton-type optimization method. *Optimization* 24.3-4 (1992), pp. 269–284. DOI: 10.1080/02331939208843795. URL: https://doi.org/10.1080/02331939208843795.

[5] Volker Fohrmeister, Alexander Bartels, and Jörn Mosler. Variational updates for thermomechanically coupled gradient-enhanced elastoplasticity – Implementation based on hyper-dual numbers. *Computer Methods in Applied Mechanics and Engineering* 339 (2018), pp. 239–261. ISSN: 0045-7825. DOI: 10.1016/j.cma.2018.04.047. URL: http://www.sciencedirect.com/science/article/pii/S0045782518302329.

[6] Christian Miehe and Jörg Schröder. A comparative study of stress update algorithms for rate-independent and rate-dependent crystal plasticity. *International Journal for Numerical Methods in Engineering* 50.2 (2001), pp. 273–298. DOI: 10.1002/1097-0207(20010120)50:2<273::AID-NME17>3.0.CO;2-Q.

[7] J. Mosler and O.T. Bruhns. On the implementation of rate-independent standard dissipative solids at finite strain – Variational constitutive updates. *Computer Methods in Applied Mechanics and Engineering* 199.9-12 (Jan. 2010), pp. 417–429. ISSN: 0045-7825. DOI: 10.1016/j.cma.2009.07.006.

[8] Martin Schmidt-Baldassari. Numerical concepts for rate-independent single crystal plasticity. *Computer Methods in Applied Mechanics and Engineering* 192.11–12 (2003), pp. 1261–1280. ISSN: 0045-7825. DOI: 10.1016/S0045-7825(02)00563-7. URL: http://www.sciencedirect.com/science/article/pii/S0045782502005637.

[9] Masato Tanaka, Daniel Balzani, and Jörg Schröder. Implementation of incremental variational formulations based on the numerical calculation of derivatives using hyper dual numbers. *Computer Methods in Applied Mechanics and Engineering* 301 (2016), pp. 216–241. ISSN: 0045-7825. DOI: 10.1016/j.cma.2015.12.010. URL: http://www.sciencedirect.com/science/article/pii/S0045782515004156.

**Proceedings of the 8th GACM Colloquium on Computational Mechanics
for Young Scientists from Academia and Industry
August 28–30, 2019 in Kassel, Germany**

A thermomechanical finite element based framework for phase transitions in laser based additive manufacturing processes

Isabelle Guschke * [1], Thorsten Bartel[1] and Andreas Menzel[1,2]

[1]Institute of Mechanics, TU Dortmund University, Dortmund, Germany
[2]Division of Solid Mechanics, Lund University, Lund, Sweden

Abstract.

Additive manufacturing describes a unique processing technology, where a part is manufactured layer by layer in contrast to traditional material removal or casting technologies. Within the laser based additive manufacturing processes, the metallic particles of a powder layer are molten by a laser beam. The industry has a high interest in additive manufacturing processes, as custom-made light-weight parts can be produced for a reasonable price. The influence of process parameters and predictability of the outcome are in so far still challenging, as complex thermal and mechanical phenomena arise during the production cycle, whereby the effects especially of high temperature gradients and phase transformations are difficult to predict. Thus, simulations incorporating advanced material models are necessary to gain a better understanding of the process. In this contribution, a physically well-motivated material model based on the minimisation of the free energy is established for improved predictions of the effective material properties of the additively manufactured workpiece. A thermomechanically fully coupled finite element based framework is employed to solve the balance of linear momentum and the energy equation. With this at hand, it is possible to develop a more sophisticated material model to gain a better understanding of the laser based additive manufacturing processes.

1 Thermomechanical framework

For the simulation of the additive manufacturing process, a fully coupled thermomechanical model is used to capture the temperature evolution and the process-induced eigenstresses. The finite element simulation is based on the balance of linear momentum and on the energy equation

$$\nabla \cdot \boldsymbol{\sigma} + \boldsymbol{b} = \boldsymbol{0} \quad \text{and} \tag{1}$$

$$-\nabla \cdot \boldsymbol{q} + r + \mathcal{D}_{\text{mech}} + \theta\, \partial_\theta [\, \boldsymbol{\sigma} : \dot{\boldsymbol{\varepsilon}} - \mathcal{D}_{\text{mech}} \,] - \widetilde{c}\, \dot{\theta} = 0 \,, \tag{2}$$

respectively. In these equations, $\boldsymbol{\sigma}$ represents the stress tensor, $\boldsymbol{b}$ is the body force, $\boldsymbol{q}$ describes the heat flux vector, r is the externally supplied heat, $\mathcal{D}_{\text{mech}}$ symbolises the mechanical dissipation, θ denotes the temperature and $\widetilde{c} := -\,\theta\, \partial^2_{\theta\theta} \psi$ defines the effective specific heat capacity based on the specific energy ψ. For the time being, the linearised strain measure $\boldsymbol{\varepsilon}$ is considered appropriate.

2 Constitutive framework

The following model is adopted from phase transformations in shape memory alloys, see e.g. [1]. In contrast to common models in additive manufacturing, i.e. [5], the underlying material model is based on the definition of energy densities for each state of the material, i.e. the powder, molten and re-solidified material. The goal is to develop a more advanced model which is based on constitutive relations for each of the considered phases of the material rather than on the use of temperature dependent material parameters.

*Corresponding author: isabelle.guschke@tu-dortmund.de ORCID iD: https://orcid.org/0000-0002-9841-6623

The composition of the material in terms of precise values for the phase fractions is obtained via energy minimisation of the overall averaged mass specific energy density, i.e.

$$\psi' = \frac{1}{m} \int \sum_{i=1}^{n_{\mathrm{ph}}} \psi_i' \, \mathrm{d}m_i = \sum_{i=1}^{n_{\mathrm{ph}}} \zeta_i \, \psi_i' = \sum_{i=1}^{n_{\mathrm{ph}}} \frac{\rho_i \, \xi_i \, V}{m} \, \psi_i' = \frac{V}{m} \sum_{i=1}^{n_{\mathrm{ph}}} \xi_i \, \psi_i \,, \tag{3}$$

where the mass specific energy of each phase is introduced as ψ_i' and the volume specific energy as ψ_i for all phases n_{ph}. The specific energies consist of a mechanical and a caloric part. The respective mass fractions are denoted as ζ_i and the volume fractions as ξ_i. Furthermore, m defines the mass and V denotes the initial volume.

It is assumed that the strain states in each phase $\boldsymbol{\varepsilon}_i$ may differ from each other, additively decompose into elastic and inelastic parts and will minimise the energy, such that

$$\boldsymbol{\varepsilon}_i = \arg\min \, \psi' \quad \text{subject to} \quad \boldsymbol{r}_{\boldsymbol{\varepsilon}} = \textstyle\sum_{i=1}^{n_{\mathrm{ph}}} \zeta_i \, \boldsymbol{\varepsilon}_i - \boldsymbol{\varepsilon} = \boldsymbol{0} \,. \tag{4}$$

Accordingly, the mass fractions ζ_i are determined via the minimisation while taking into account the physical restrictions

$$\zeta_i = \arg\min \, \psi' \quad \text{subject to} \quad 0 \leq \zeta_i \leq 1 \quad \text{and} \quad \textstyle\sum_{i=1}^{n_{\mathrm{ph}}} \zeta_i = 1 \,. \tag{5}$$

An additional constraint $\dot{\zeta}_{\mathrm{pow}} \leq 0$ needs to be taken into account for the case of powder bed additive manufacturing, as the rate of the powder fraction $\dot{\zeta}_{\mathrm{pow}}$ cannot increase. Taking (4) and (5) into account, the resulting effective energy obtained by the minimisation

$$\psi^{\mathrm{rel}} = \min_{\boldsymbol{\varepsilon}_i, \zeta_i} \{\psi'\} \tag{6}$$

yields the relaxed energy density of the problem which is identical to the convex hull due to (4). The effective stress $\boldsymbol{\sigma}$ can be calculated for the coupled thermomechanical problem as follows

$$\boldsymbol{\sigma} = \frac{\partial \psi}{\partial \boldsymbol{\varepsilon}} \,. \tag{7}$$

3 Representative examples

The energy densities of the phases determine the respective constitutive behaviour, whereas contributions are chosen as

$$\begin{aligned} \psi_{\mathrm{pow}} &:= \tfrac{1}{2} \, \boldsymbol{\varepsilon}_{\mathrm{pow}} : \mathbf{E}_{\mathrm{pow}} : \boldsymbol{\varepsilon}_{\mathrm{pow}} - c_{\mathrm{pow}} \, \theta \ln \theta + L_{\mathrm{pow}} \, \frac{\theta - \theta^{\mathrm{ref}}}{\theta^{\mathrm{ref}}} \\ \psi_{\mathrm{mel}} &:= \tfrac{1}{2} \, \left[\boldsymbol{\varepsilon}_{\mathrm{mel}} - \boldsymbol{\varepsilon}_{\mathrm{mel}}^{\mathrm{irr}}\right] : \mathbf{E}_{\mathrm{mel}} : \left[\boldsymbol{\varepsilon}_{\mathrm{mel}} - \boldsymbol{\varepsilon}_{\mathrm{mel}}^{\mathrm{irr}}\right] - c_{\mathrm{mel}} \, \theta \ln \theta \\ \psi_{\mathrm{sol}} &:= \tfrac{1}{2} \, \left[\boldsymbol{\varepsilon}_{\mathrm{sol}} - \boldsymbol{\varepsilon}_{\mathrm{sol}}^{\mathrm{irr}}\right] : \mathbf{E}_{\mathrm{sol}} : \left[\boldsymbol{\varepsilon}_{\mathrm{sol}} - \boldsymbol{\varepsilon}_{\mathrm{sol}}^{\mathrm{irr}}\right] - c_{\mathrm{sol}} \, \theta \ln \theta + L_{\mathrm{sol}} \, \frac{\theta - \theta^{\mathrm{ref}}}{\theta^{\mathrm{ref}}} \end{aligned} \tag{8}$$

for the powder, molten pool and re-solidified phase, respectively. In these equations, $\mathbf{E}_i$ defines the respective fourth-order isotropic elasticity tensor, $\boldsymbol{\varepsilon}_i^{\mathrm{irr}}$ is the irreversible strain of the respective phase, c_i denotes the specific heat capacity and L represents the latent heat contribution with reference temperature θ^{ref}. Dissipative effects due to the irreversible behaviour of the molten and solid phase are captured within $\mathcal{D}_{\mathrm{mech}}$.

For the molten phase and the solid phase, transformation strains $\boldsymbol{\varepsilon}_i^{\mathrm{trans}}$ are taken into account to capture the volume changes of the material during phase transitions due to the different mass densities. In addition, a viscoelastic strain $\boldsymbol{\varepsilon}_{\mathrm{mel}}^{\mathrm{vis}}$ is introduced to include the fluid-like behaviour of the molten pool in the material model. In contrast, plastic deformation $\boldsymbol{\varepsilon}_{\mathrm{sol}}^{\mathrm{pl}}$ is used to capture the irreversible behaviour of the solid phase. Furthermore, thermal strains $\boldsymbol{\varepsilon}_{\mathrm{sol}}^{\mathrm{th}}$ using a linear heat expansion model are considered in the re-solidified phase. At a material point level, a representative boundary value problem based on titanium aluminium alloy $\mathrm{Ti_6Al_4V}$ is implemented, see Figure 1 hereto. The following results are gained while using slightly different densities.

As a first approach, equal densities in all phases are assumed so that conservation of mass is fulfilled a priori, even if volume fractions are used as the conserved quantity, cf. [3]. For equal densities, the result

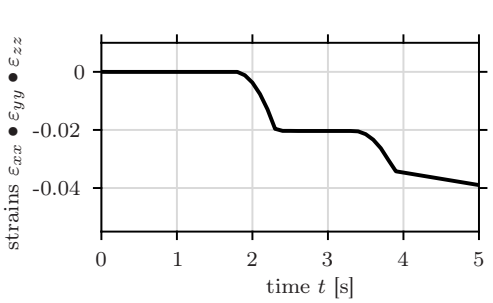

(a) Evolution of normal strain components.

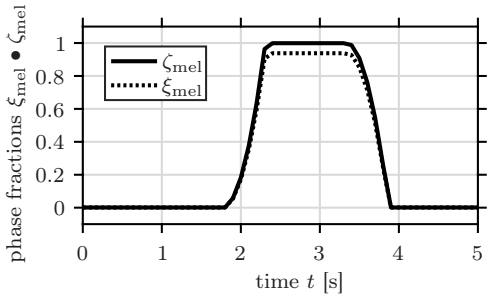

(b) Evolution of volume and mass fraction of molten phase.

Figure 1. The temperature is prescribed at material point level. First, the temperature linearly increases from $\theta = 1200$ K to $\theta = 2200$ K and then decreases back to $\theta = 1200$ K again, while zero Neumann boundary conditions are assumed. The resulting strain evolution can be seen in Figure (a), where the severe changes occur due to the transformation strains. The linear evolution of strains after the full transformation into the re-solidified phase is due to the linear heat expansion model. In Figure (b), the evolution of the mass fractions, respectively volume fractions of the molten phase is shown, particularly showing the difference between these two quantities.

of the convex hull defined by ψ^{rel} coincides with the ansatz by the Reuss bound, where constant stress states are assumed in each phase. For this case, the overall mass and volume specific energy density coincide and the volume fractions match the mass fractions. Thus, no transformation strains $\boldsymbol{\varepsilon}_i^{\text{trans}}$ are necessary. However, already for slight differences in the densities as they are applicable for the additive manufacturing process, the sum of the volume fractions no longer equals one. These differences shall be discussed in the following.

A small scale boundary value problem for a titanium aluminium alloy Ti_6Al_4V is implemented into the commercial finite element software Abaqus to demonstrate the capacity of the constitutive model. Here, the fully coupled thermal stress analysis is used which is based on the weak forms of (1) and (2). The previously discussed constitutive material model is then implemented as a user material in the subroutine `UMAT`. The related inequality constraints are solved by a regularised Fischer-Burmeister NCP approach, see i.e. [2]. With this at hand, the temperature-induced change of the material's composition is obtained. The resulting mass and volume fractions are saved as internal state variables. In order to finalise the overall material model, further homogenisation assumptions are applied to define the averaged heat conductivity. A classic isotropic Fourier ansatz is adopted for the heat conduction model, and the effective specific heat capacity is implemented in the subroutine `UMATHT`. For further information on the implementation of a user material into Abaqus, see i.e. [6].

Additional challenges are related to the finite element based modelling of the manufacturing process itself, e.g. in terms of a suitable modelling of the layer build-up and the adequate modelling of the laser beam impact, as well as to choosing correct thermal and mechanical boundary conditions. The model of the laser beam itself is implemented in the subroutine `DFLUX`, where the temperature field arises due to a moving volumetric heat source, as introduced in [4] and applied to the simulation of selective laser melting processes in, e.g. [3]. The resulting temperature and mass fraction evolution are shown for the case of equal densities in Figure 2.

4 Conclusion

A thermomechancially fully coupled model is developed in this work for the simulation of laser based additive manufacturing processes. A physically well-motivated material model based on the minimisation of the free energy is established, where the different states of the material, namely powder, molten, and re-solidified, are captured as single phases weighted by respective mass or volume fractions. Some numerical examples for a small scale problem are used to illustrate capabilities of the overall framework.

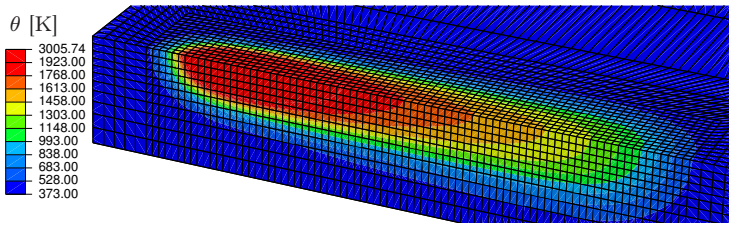

(a) Temperature distribution θ.

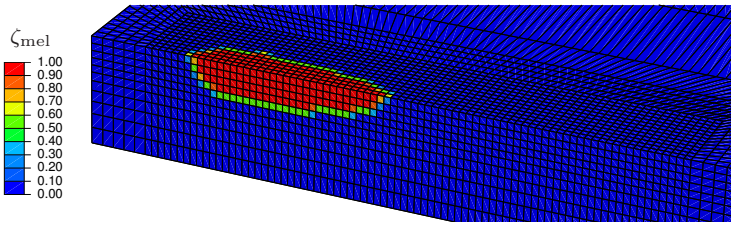

(b) Evolution of mass fraction ζ_{mel} for the molten phase for equal densities.

Figure 2. A representative example is used to demonstrate the additive manufacturing process using equal densities for all phases. These plots show in Figure (a) the temperature distribution and in Figure (b) the mass fraction of the molten pool ζ_{mel} at an identical time step induced by the moving volumetric heat source modelling the laser beam impact.

References

[1] T. Bartel and K. Hackl. A micromechanical model for martensitic phase-transformations in shape-memory alloys based on energy-relaxation. *Zeitschrift für Angewandte Mathematik und Mechanik* 89.10 (2009), pp. 792–809. DOI: 10.1002/zamm.200900244.

[2] T. Bartel, R. Schulte, A. Menzel, B. Kiefer, and B. Svendsen. Investigations on enhanced Fischer-Burmeister NCP functions: application to a rate-dependent model for ferroelectrics. *Archive of Applied Mechanics* 89.6 (2019), pp. 995–1010. DOI: 10.1007/s00419-018-1466-7.

[3] T. Bartel, I. Guschke, and A. Menzel. Towards the simulation of Selective Laser Melting processes via phase transformation models. *Computers & Mathematics with Application* (available online 2018). DOI: 10.1016/j.camwa.2018.08.032.

[4] J. Goldak, A. Chakravarti, and M. Bibby. A New Finite Element Model for Welding Heat Sources. *Metallurgical Transactions B* 15 (1984), pp. 299–305. DOI: 10.1007/BF02667333.

[5] D. Riedlbauer, P. Steinmann, and J. Mergheim. Thermomechanical finite element simulations of selective electron beam melting process: Performance considerations. *Computational Mechanics* 54 (2014), pp. 109–122. DOI: 10.1007/s00466-014-1026-0.

[6] Dassault Systèmes. *Abaqus Analysis User's Manual v2016*. 2015.

**Proceedings of the 8th GACM Colloquium on Computational Mechanics
for Young Scientists from Academia and Industry
August 28–30, 2019 in Kassel, Germany**

A Sliding Interface Approach with Application to Twin-Screw Extruders

Jan Helmig * [1] and Stefanie Elgeti[1]

[1]Chair for Computational Analysis of Technical Systems (CATS), RWTH Aachen University, Germany

Abstract.

Co-rotating twin-screw extruders are important processing devices within the plastics-producing industry. The utilized screw elements are conveying and kneading elements. For conveying elements the geometry can be considered smooth in longitudinal direction. In contrast, kneading elements feature discontinuities in longitudinal direction. Within this work we present a finite-element framework to solve the flow of plastic melt inside extruders. For such simulations the methods presented in [2, 3] allow to use boundary-conforming meshes for conveying elements. However, kneading elements with their discontinuities in longitudinal direction remain out of scope. Thus, we introduce a sliding interface approach based on Nitsche's method [5] combined with a multimesh technique [4] that couples the solution fields of the individual meshes at the interface. In contrast to standard fictitious domain methods, cut cells only have to be computed in 2D which avoids difficulties with degenerated polygons. We show the potential of the method for a testcase that computes the flow of plastic melt in a realistic extruder section.

Introduction

Co-rotating twin-screw extruders are important processing devices within the plastic-producing industry: Reasons are their versatile modes of usage in processing, mixing, and reaction. The utilized screw elements can be roughly classified into either conveying and kneading elements, Fig. 1(a). The design of conveying elements is based on a sweep of a 2D cross section, see Fig. 1(b). The geometry can be considered smooth in longitudinal direction. Instead, kneading elements feature geometrical discontinuities in longitudinal direction, see Fig. 1(a).

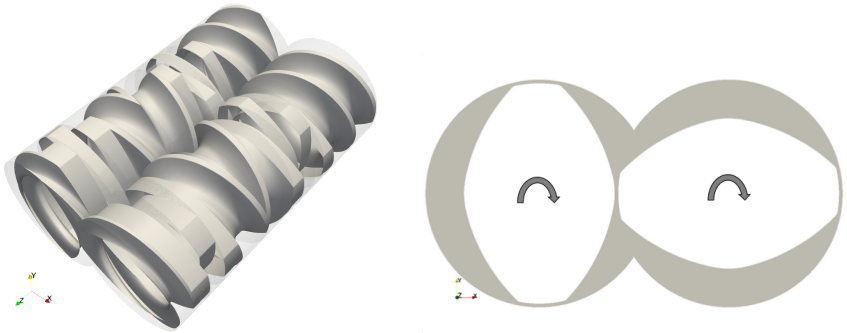

(a) 3D extruder section including kneading and conveying elements.

(b) 2D extruder cross section.

Figure 1. Sketch of a twin-screw extruder.

Flow simulations of plastic melts inside twin-screw extruders pose exeptional difficulties. This is due to the constantly rotating screws in combination with small gap sizes. Furthermore, modeling the plastic melt is a multi-physics problem: The melt is heated up due to shearing, which then in turn influences the material properties of the melt. Thus, the flow equations have to be coupled to the heat equation. In

*Corresponding author: helmig@cats.rwth-aachen.de

terms of numerical approach, we aim at using a boundary-conforming finite-element method within this work.

Boundary-conforming meshes have two major advantages: (1) It is straightforward to strongly impose the kinematics of the screw, and (2) it is easy to construct high-quality boundary-layer meshes. The challenge arises when those meshes need to be deformed; especially without re-meshing. A suitable deformation method – the Snapping Reference Mesh Update Method (SRMUM) – has been presented in [2]. It already enables the simulation of unsteady flow inside convex-shaped conveying elements. A method also amenable to concave shapes has been presented in [3]. It extends the idea of SRMUM with a spline-parameterization of the geometry. Still, kneading elements with their discontinuity in longitudinal direction remain out of scope. The methods described are able to generate and update high-quality boundary-conforming meshes for each individual continuous part of a kneading block. However, these individual meshes do not match at the interface.

The major part of this work aims to couple the individual meshes at their interfaces. We present a sliding interface approach that is inspired by [1, 5]. It allows to couple two meshes at an interface, composed of parts of the mesh boundary surfaces. Breaking down the coupling to a surface is advantageous since this simplifies the computation of the combined interface triangulation, cut cells, and avoids difficulties with degenerated polygons.

1 Theoretical framework

1.1 Governing equations and general solution method

The behavior of plastic melt inside an extruder is modeled as the flow of a viscous incompressible temperature-dependent fluid. It is governed by the incompressible Navier-Stokes equations. We consider Newtonian as well as Generalized-Newtonian models for the constitutive equation. For Generalized-Newtonian models the viscosity of the plastic melt is not constant anymore. It depends on shear rate and temperature and thus enables to account for shear-thinning effects. We employ a semi-discrete finite element method in order to solve the governing equations. We use first order interpolation for all degrees of freedom. Thus, we have to stabilize our equations using a Galerkin-Least-Squares approach. Furthermore, the rotation of the screws results in a constant movement of the computational domain and thus, the mesh. In order to account for that movement we employ the Arbitrary-Lagrangian-Eulerian (ALE) approach. Additionally, we decouple the temperature equation from equations governing conservation of mass and momentum. Still, the flow and temperature field are coupled strongly using a fixed-point iteration.

1.2 Sliding interface approach

Within this section, we will introduce the most important ideas of the sliding interface approach that can be used to couple the solution fields of two boundary-conforming meshes at a common interface Γ^{ff}. We refer to this method as sliding interface since the meshes are allowed to move/rotate and thus slide over each other. A sketch of Γ^{ff} for an exemplary composition of two kneading elements is given in Fig. 2. In Fig. 2(a) the cross sections of the two individual boundary-conforming meshes are given as well as the interface itself in Fig. 2(b). The interface Γ^{ff} can be seen as $\Gamma^{ff} = \Gamma^{red} \cap \Gamma^{blue}$. In the general case we consider $\Gamma^{ff} = \Gamma^1 \cap \Gamma^2$.

The motivation of the method was given in [1], where rotating domains are coupled with steady ones based on a common spline interface. In the following we will neglect the temperature for simplicity. However, the concept for the sliding interface approach for the temperature field works in the same way as for the flow field. We refer to the combined discrete stabilized variational formulation for both individual meshes without the coupling terms as $B(\{\boldsymbol{v}_h, q_h\}, \{\boldsymbol{u}_h, p_h\})$, where $\boldsymbol{u}_h$, p_h are the discrete velocity and pressure fields and $\boldsymbol{v}_h$, q_h the corresponding test functions. In order to account for the coupling we add Nitsche coupling terms at the common interface and obtain the combined discrete variational formulation:

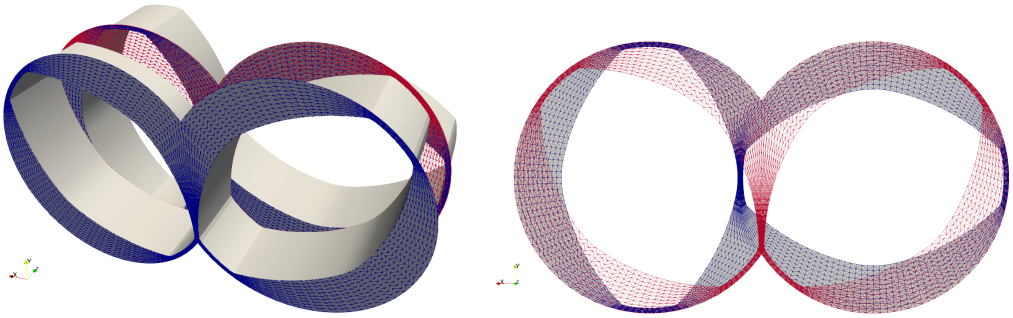

(a) 3D view of the interface.

(b) 2D cross section. Γ^{ff} is composed of the two interfaces Γ^{red} and Γ^{blue}.

Figure 2. Example kneading element.

$$
\begin{aligned}
B^{Nitsche}(\{\boldsymbol{v}_h, q_h\}, \{\boldsymbol{u}_h, p_h\}) &= B(\{\boldsymbol{v}_h, q_h\}, \{\boldsymbol{u}_h, p_h\}) \\
+ \langle [\![\boldsymbol{v}_h]\!] \cdot \boldsymbol{n}, \{p_h\} \rangle_{\Gamma^{ff}} - \langle [\![\boldsymbol{v}_h]\!], \{2\eta\boldsymbol{\varepsilon}(\boldsymbol{u}_h) \cdot \boldsymbol{n}\} \rangle_{\Gamma^{ff}} - \langle \{q_h\}, [\![\boldsymbol{u}_h]\!] \cdot \boldsymbol{n} \rangle_{\Gamma^{ff}} - \langle \{2\eta\boldsymbol{\varepsilon}(\boldsymbol{v}_h) \cdot \boldsymbol{n}\}, [\![\boldsymbol{u}_h]\!] \rangle_{\Gamma^{ff}} \\
+ \langle \gamma\eta / h_n [\![\boldsymbol{v}_h]\!], [\![\boldsymbol{u}_h]\!] \rangle_{\Gamma^{ff}} - \langle \rho(\boldsymbol{u}_h \cdot \boldsymbol{n})\{\boldsymbol{v}_h\}_m, [\![\boldsymbol{u}_h]\!] \rangle_{\Gamma^{ff}} + \frac{1}{2} \langle \rho \, |\boldsymbol{u}_h \cdot \boldsymbol{n}| \, [\![\boldsymbol{v}_h]\!], [\![\boldsymbol{u}_h]\!] \rangle_{\Gamma^{ff}} = 0.
\end{aligned} \tag{1}
$$

The terms in the second and third line of Eq.(1) weakly enforce the continuity of velocities and tractions on the interface [5]. The third last term penalizes the discrete version. In order to evaluate the integrals introduced, it is necessary to compute all cuts of the two discretizations at the interface. We subdivide the resulting cut elements into triangles to define quadrature rules.

So far, the presented approach neglected possible movements/obstacles at the interface. Looking at Fig. 2(b) we want ensure that e.g. flow in normal direction at Γ^{red} is only allowed on Γ^{ff}. Furthermore, for $\Gamma^{red} \setminus \Gamma^{ff}$ we attempt to apply a no-slip condition on the neighbouring screw. We enforce this condition $\boldsymbol{g}$, weakly. This is done by enhancing $B^{Nitsche}(\{\boldsymbol{v}_h, q_h\}, \{\boldsymbol{u}_h, p_h\})$:

$$
\begin{aligned}
B^{SlidInt}(\{\boldsymbol{v}_h, q_h\}, \{\boldsymbol{u}_h, p_h\}) &= B^{Nitsche}(\{\boldsymbol{v}_h, q_h\}, \{\boldsymbol{u}_h, p_h\}) \\
&+ \sum_{i=1}^{2} \Big[\; (\boldsymbol{v}_h \cdot \boldsymbol{n}, p_h)_{\Gamma^i \setminus \Gamma^{ff}} - (\boldsymbol{v}_h, 2\eta\boldsymbol{\varepsilon}(\boldsymbol{u}_h) \cdot \boldsymbol{n})_{\Gamma^i \setminus \Gamma^{ff}} \\
- (q_h, (\boldsymbol{u}_h - \boldsymbol{g}) \cdot \boldsymbol{n})_{\Gamma^i \setminus \Gamma^{ff}} - (2\eta\boldsymbol{\varepsilon}(\boldsymbol{v}_h) \cdot \boldsymbol{n}, (\boldsymbol{u}_h - \boldsymbol{g}))_{\Gamma^i \setminus \Gamma^{ff}} + (\gamma\eta / h_n \boldsymbol{v}_h, (\boldsymbol{u}_h - \boldsymbol{g})_{\Gamma^i \setminus \Gamma^{ff}} \Big] &= 0.
\end{aligned} \tag{2}
$$

One open question is how to determine $\Gamma^i \setminus \Gamma^{ff}$. The construction requires that we detect all elements that are not cut or only partly cut. This might result into cut polygons that are not necessarily convex. In order to avoid this extra computational effort, we use the multimesh concept introduced in [4]. The idea is to apply the extra terms added in Eq.(2) on Γ^i and subtract them on Γ^{ff} by using negative quadrature weights.

2 Numerical examples

In a first step, the presented sliding interface approach has been used to compute the flow of Newtonian fluids inside a simplified kneading block with only two kneading elements for a single-screw extruder. The computational domain is given in Fig. 3(a). Fig. 3(b) shows the velocity distribution in axial direction for the two non-matching interfaces. The validity of the weak imposition of boundary conditions is clearly visible since the axial velocity is zero in that part of each interface that is attached to the opposite screw. Furthermore, the velocities match at both interfaces. This clearly indicates that the method correctly couples the flow throughout the non-matching interface.

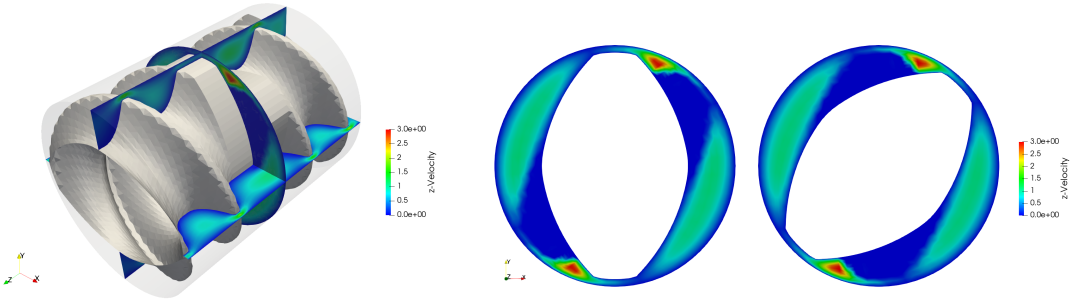

(a) 3D flow results.

(b) z-velocity distribution at the non-matching interface.

Figure 3. Single-screw extruder with one kneading section.

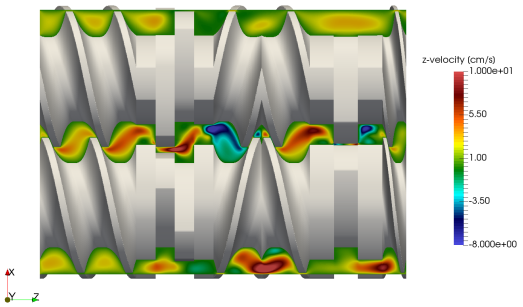

Figure 4. z-velocity distribution inside a twin-screw extruder section including conveying and kneading elements.

In the following, we use the presented method to compute the flow of a shear-thinning fluid inside a realistic twin-screw extruder section. It consists of forward and backward conveying as well as kneading elements. Fig. 4 shows the axial velocity on a slice in the xz-plane. The transition between non-matching meshes is very smooth.

3 Conclusion

We have presented a sliding interface approach that enables to couple two boundary-conforming meshes at a common moving interface. It is based on Nitsche's method combined with a multimesh approach. This simplifies the computation of cut cells at the interface. We show flow results of plastic melts inside single- and twin-screw extruders that demonstrate the validity of the proposed method.

References

[1] Yuri Bazilevs and Tom Hughes. NURBS-based isogeometric analysis for the computation of flows about rotating components. *Computational Mechanics* 43.1 (2008), pp. 143–150.

[2] Jan Helmig, Marek Behr, and Stefanie Elgeti. Boundary-Conforming Finite Element Methods for Twin-Screw Extruders: Unsteady - Temperature-Dependent - Non-Newtonian Simulations. *Computers & Fluids* (2019).

[3] Jochen Hinz, Jan Helmig, Matthias Möller, and Stefanie Elgeti. Boundary-Conforming Finite Element Methods for Twin-Screw Extruders using Spline-Based Parameterization Techniques. *arXiv preprint arXiv:1905.11829* (2019).

[4] August Johansson, Benjamin Kehlet, Mats G Larson, and Anders Logg. Multimesh finite element methods: Solving PDEs on multiple intersecting meshes. *Computer Methods in Applied Mechanics and Engineering* 343 (2019), pp. 672–689.

[5] Andre Massing, Benedikt Schott, and Wolfgang A Wall. A stabilized Nitsche cut finite element method for the Oseen problem. *Computer Methods in Applied Mechanics and Engineering* 328 (2018), pp. 262–300.

**Proceedings of the 8th GACM Colloquium on Computational Mechanics
for Young Scientists from Academia and Industry
August 28–30, 2019 in Kassel, Germany**

Partitioned coupling of fluid-structure interaction for the simulation of floating wind turbines

Jorrid Lund*[1], Bjarne Wiegard[1], Lars Radtke[1], Marcel König[1] and Alexander Düster[1]

[1]Numerical Structural Analysis with Application in Ship Technology (M-10), Hamburg University of Technology, Am Schwarzenberg-Campus 4c, 21073 Hamburg, Germany

Abstract. Fluid-structure interaction problems appear in many different fields of application. An interesting and highly topical field is offshore renewable energy. An increasing energy demand, limited fossil energy sources and the climate change in combination with limited suitable and available space ashore lead to an increased relevance of offshore renewable energy. A promising offshore renewable energy concept is the use of floating wind turbines.

For the simulation of floating wind turbines, the necessary and computationally expensive fluid-structure interaction coupling has to be combined with large domains, highly nonlinear and dynamic structural behavior and complex flow situations. This requires new and innovative techniques in the solution process.

In this work, the partitioned solution utilizing existing field solvers is suitable for this type of problem due to the availability of well-developed fluid and structural solvers.

To manage the partitioned coupling, the in-house C++ library *comana* is employed. This coupling framework is employed to control the iterative solution process and to perform the necessary exchange of surface quantities on the interface between the fluid and structural field of the fluid-structure interaction problem. Through this, *comana* enables the computation of complex strongly coupled fluid-structure interaction problems within a reasonable amount of time. Despite the necessary changes for the partitioned coupling, the modifications to the existing specialized high-fidelity fluid and structural solvers are minimized to maintain their sophisticated solution techniques.

The partitioned coupling procedure is described and simulation results are presented.

Different measures to accelerate, stabilize and improve the solution of this fluid-structure interaction problem are demonstrated. Among these measures are the prediction and the convergence acceleration in the implicit coupling of the fluid and structural field solvers.

In the scope of a future research project, the presented method will be applied to develop the simulation of a point wave energy absorber used for the conversion of wave energy into electric energy.

Introduction

The partitioned coupling strategy is a powerful solution approach for many fluid-structure interaction (FSI)-problems. Due to the partitioned approach, existing specialized field solvers can be used to solve FSI-problems only with the exchange of surface quantities in a fast and efficient way. Among the many applications of this approach are offshore renewable energies of which the most prominent technology are offshore wind turbine plants. Wind blows stronger and more continuously offshore, which is an important advantage of offshore wind energy turbine plants especially with respect to power grid stability in face of the transition to renewable energies. Even though offshore wind energy has many advantages over traditional onshore wind energy plants, it also poses serious challenges. For large water depths, offshore wind energy turbine plants with a foundation in the seafloor are not cost-effective. For these water depths, floating wind turbines are more suitable and economic. The construction and design of floating wind turbines, however, poses serious challenges since the forces on the structure, which are affected by the dynamic motion and structural deformations, are hard to determine with uncoupled structural or fluid simulations. A coupled simulation nevertheless requires well developed solvers able to cover the different physical effects that have to be taken into account for such a complex simulation.

*Corresponding author: Jorrid.Lund@tuhh.de ORCID iD: 0000-0003-4537-8720

1 Partitioned solution approach for FSI-problems

For the solution of FSI-problems, fluid and structural equations, which are dependent on each other, have to be solved in a coupled approach. For this, it is possible to solve both subproblems by coupling them in a partitioned (segregated) or in an monolithic (integrated) way [5, p.3252].

To solve the fluid and structural equations in an integrated way, the monolithic approach requires the development of solvers appropriate to the given FSI-problem. Integrated FSI solvers are more robust, but require the labor-intensive development of a dedicated solver for the problem at hand [2, p.140]. They are not easily modifiable in the selection of the discrete equations that describe the structural or fluid problem [3, p. 1119]. Partitioned solution procedures on the other hand allow for an independent and flexible modelling to select the most appropriate techniques for the solution of the structural or fluid side. This enables the usage of highly specialized solvers for both subproblems in a black-box manner, where only the surface quantities have to be exchanged [3, p. 1120].

The in-house software library *comana* has been developed to control this iterative exchange of quantities in multi-physic problems [7].

To compute the displacements and velocities of a solid body under external loads, the finite-element-method (FEM) is among the most popular discretization schemes. For the computation of the flow field in a moving domain, finite-volume-method (FVM) and boundary-element-method (BEM) are widely used methods to compute the pressure and velocity inside the fluid domain.

In order to couple the FEM with the BEM or FVM to account for FSI, the displacements $\vec{d}$ calculated by the structural solver S_s are interpolated to the nodes on the boundary of the fluid solver such that the fluid mesh can be deformed according to the movement of the structure.

The fluid solver F_s can then compute tractions $\vec{t_i} = F_s(\vec{d_i})$ on the interface between the fluid and structural side in the deformed domain. These tractions can be applied to the structure as external loads to compute new displacements $\vec{d}_{i+1} = S_s(\vec{t_i})$.

This procedure can be seen as a fixed-point iteration since the quantity (in this case displacements) that is computed is the same that enters the procedure:

$$\vec{d}_{i+1} = S_s(F_s(\vec{d_i})) \tag{1}$$

The procedure described by equation (1) is repeated until the displacement increment between two subsequential iterations reaches a predefined tolerance. The converged displacements are taken as the solution for the current time step and the structural and fluid solvers are advanced in time such that the procedure can be repeated for the next time step.

In order to speed up and stabilize the fixed-point iteration (1), different measures can be taken.

The prediction of the displacements at the beginning of a time step is used to provide a good initial guess for the displacements entering the fixed-point iteration. A polynomial of order p depending on time t can be constructed based on the previous $m = p + 1$ time steps by requiring that the polynomial is equal to the displacements at the previous m time steps.

$$\tilde{d}(t_j) = \sum_{i=0}^{p} a_i t_j^i \qquad \text{for } j = -1, ..., -m \tag{2}$$

The resulting system of equations (2) can be used to determine the parameters a_i. With these parameters a_i the prediction of the displacements for the current time step $\tilde{d}(t_0)$ can be computed based on the previous time steps. The dependence on the previous time steps is constant in the case of a constant time step size.

While the prediction operates on the solution of previous time steps, the results within the implicit iterations of one time step can also be improved based on the solution of previous iterations in the same time step. To accelerate and stabilize fixed-point iterations, a variety of methods exist. The simplest method is the constant relaxation which just multiplies a constant factor to the increment between two iterations. For FSI-problems, advanced methods like Aitken or quasi-Newton methods are

more suitable. Among quasi-Newton methods, the quasi-Newton least square method has shown good convergence behaviour for many FSI-problems [9][4].

2 Floating wind turbine

To demonstrate the benefits of the simulation of FSI using partitioned coupling, complex real world problems like the simulation of a floating wind turbine is well suited. The floating wind turbine presented here was developed within the joint research program 'Hydrodynamic and Structural Optimization of a Semi-submersible Offshore Wind Turbine'. The related FSI simulations were carried out in the subproject 'Fluid-Structure Interaction and Optimization of a Floating Wind Turbine'.

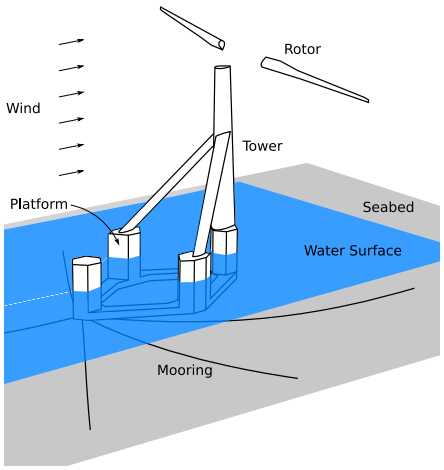

Figure 1. Schematic overview [6, p. 219]

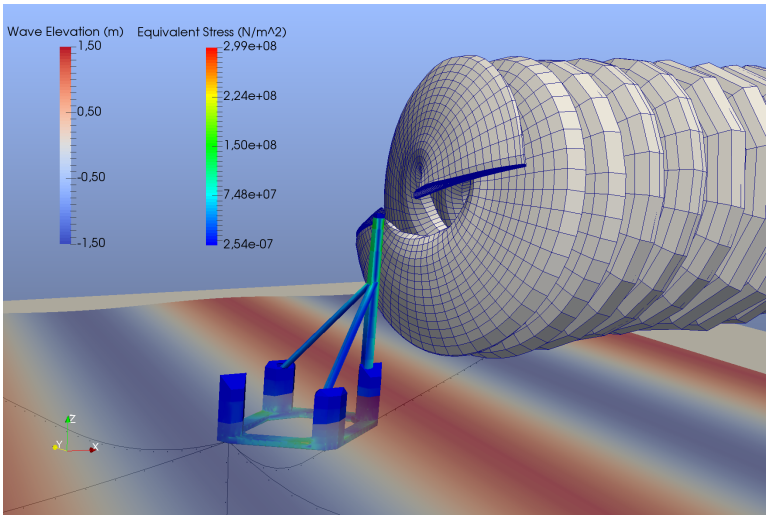

Figure 2. Stresses inside the structure and elevation of the water surface

In Figure 1 an overview of the floating wind turbine is given. This floating wind turbine consists of a platform to lift and stabilize the whole structure and a tower on which the rotor is mounted. To prevent drifting, the platform is anchored in the seabed such that it is self-aligning in the wind [10].

The deformation of the platform, the tower and the rotor is simulated with FEM using the commercial software package ANSYS [1]. The fluid simulation is performed using the boundary element method implemented in the in-house software *pan*MARE [8]. *comana* [7] is used to control the iterative solution procedure and exchange tractions and displacements between ANSYS and *pan*MARE.

In Figure 2 the result of a coupled FSI simulation is shown. Not only the forces on the tower and rotor due to the wind but also the effects of the ocean current and waves is taken into account. Suitable techniques like sub-structuring with large rotations [10] available in the structural solver can be used without modifying the partitioned coupling procedure.

The partitioned simulation allows for the evaluation of deformations and stresses at all points in the structure in every time step taking the important dynamic and nonlinear effects into account. Not only the structural integrity of the platform but also the orientation of the platform in the wind and waves can be evaluated.

3 Conclusion and outlook

The partitioned approach turned out to be suitable for FSI simulations. In a recent research project, the motion and the structural behaviour of a floating wind turbine was successfully investigated. A precise stress analysis is possible and effects of the structural deformation on the motion behaviour can be evaluated [10].

Even though the simulation of the floating wind turbine showed good results, the boundary element method can not fully account for the flow separation and turbulence in the wake of the rotors. To

increase the solution accuracy, the region where turbulence effects and flow separation occur can be modelled by the FVM, which is more accurate but at the same time computationally more expensive. The FVM can be applied to the wake region of the rotor while the outer region which exhibits non of these effects could be modelled with BEM.

The techniques which have been applied to the floating wind turbine can also be transferred to other floating offshore plants. An example for such an application is the point wave energy converter. The approach is promising for every type of floating structures which is subjected to external forces.

Acknowledgments

The research regarding the floating wind turbine was funded by the Federal Ministry for Economic Affairs and Energy of Germany (BMWi) in the joint project HyStOH (project number 03SX409C).

References

[1] *ANSYS Academic Research Mechanical, Release 18.2*. Southpointe: ANSYS, Inc., 2017.

[2] Yuri Bazilevs, Kenji Takizawa, and Tayfun E. Tezduyar. *Computational fluid-structure interaction : methods and applications*. 2013. ISBN: 9780470978771.

[3] Hans-Joachim Bungartz, Florian Lindner, Miriam Mehl, and Benjamin Uekermann. A plug-and-play coupling approach for parallel multi-field simulations. *Computational Mechanics* 55.6 (2015), pp. 1119–1129.

[4] Joris Degroote, Klaus-Jürgen Bathe, and Jan Vierendeels. Performance of a new partitioned procedure versus a monolithic procedure in fluid-structure interaction. *Computers and Structures* 87 (2009), pp. 793–801.

[5] Carlos Felippa, Kwang-Chun Park, and Charbel Farhat. Partitioned analysis of coupled mechanical. *Computer Methods in Applied Mechanics and Engsystemsineering* 190.24 (2001), pp. 3247–3270.

[6] Marcel König. "Partitioned Solution Strategies for Strongly-Coupled Fluid-Structure Interaction Problems in Maritime Applications". PhD thesis. Hamburg University of Technology, 2018.

[7] Marcel König, Lars Radtke, and Alexander Düster. A flexible C++ framework for the partitioned solution of strongly coupled multifield problems. *Computers & Mathematics with Applications* (2016).

[8] Stefan Netzband, Christian Schulz, and Moustafa Abdel-Maksoud. A fully coupled simulation method for floating offshore wind turbine dynamics using a boundary element method in the time domain. In: *10th International Workshop on Ship and Marine Hydrodynamics IWSH 2017*. 2017.

[9] Lars Radtke, Marcel König, and Alexander Düster. Convergence acceleration for partitioned simulations of the fluid-structure interaction in arteries. *Computational Mechanics* 57 (2016), pp. 901–920.

[10] Bjarne Wiegard, Lars Radtke, Marcel König, Moustafa Abdel-Maksoud, and Alexander Düster. Simulation of the Fluid-Structure Interaction of a Floating Wind Turbine. *Ships and Offshore Structures* (2019).

**Proceedings of the 8th GACM Colloquium on Computational Mechanics
for Young Scientists from Academia and Industry
August 28–30, 2019 in Kassel, Germany**

Particle Finite Element Simulation for Additive Manufacturing Processes of Fresh Concrete

Janis Reinold * [1], Jithender Jaswant Timothy[1] and Günther Meschke[1]

[1]Institute for Structural Mechanics, Ruhr-University Bochum

Abstract. In this work a computational model based on the Particle Finite Element Method for the simulation of extrusion-based additive manufacturing of fresh concrete is presented. The constitutive law is based on a Bingham model, which is approximated by a classical elasto-viscoplastic Perzyna model in a rate form. A mixed velocity-pressure formulation in an updated Lagrangian framework is chosen to solve the system of equations. Model capabilities are demonstrated using two numerical test cases.

Introduction

Additive manufacturing techniques so far have found application predominantly in the manufacture of high-end components in the bio-medical and aeronautical industry mainly due to the high costs of the materials used and the specialized technology associated with the technique. Recently there is growing interest in the development of this technology for large scale fabrication of concrete structures [1]. The most common approach is based on layered extrusion of fresh mortar or concrete, that allows for automated construction of concrete structures and components. Due to process or machine parameters and the time dependent nature of (fresh) concrete, the final properties of printed components are much more dependent on the 'casting' process, than in conventional casting of concrete. Therefore, numerical models can help to understand the complex interactions of various parameters in additive manufacturing processes of fresh concrete. To this end, a numerical framework based on the Particle Finite Element Method (PFEM) is developed for the simulation of extrusion-based additive manufacturing processes of fresh concrete. Flow of homogenized fresh concrete is generally based on the Bingham model, which is a non-Newtonian yield stress fluid. Hence, a certain yield stress must be exceeded to initiate viscous flow. In many engineering problems the material response before yielding is neglected and assumed to be rigid, which is retained by regularized models and a large viscosity before yielding. These models have the advantage that no internal variable must be stored. However, a drawback of these methods is, that the stresses of the material at 'rest' are deduced from the material that never really comes to rest. Therefore, the Bingham model is modeled with a classical elasto-viscoplastic model, so that the viscoplastic contribution is approximated with an overstress function. In contrast to regularized rigid-viscoplastic Bingham models, stresses of material at rest can be assessed more accurately, which is relevant for the characterisation of initial stress states of printed components in additive manufacturing processes of fresh concrete.

1 Theoretical framework

1.1 Constitutive law

In order to describe the flow of homogenized fresh concrete, the constitutive law is based on a Bingham model, which is approximated by a classical elasto-viscoplastic Perzyna formulation [4]. The elastic parts of the strains are assumed small in comparison to the plastic deformations. Under these assumptions, the material model is given in a hypoelastic rate form and the deformation rate tensor $\boldsymbol{d}$ is additively split

*Corresponding author: janis.reinold@rub.de

into elastic and plastic parts as $\boldsymbol{d} = \boldsymbol{d}_e + \boldsymbol{d}_p$ with $\boldsymbol{d}_e$ and $\boldsymbol{d}_p$ denoting the elastic and plastic deformation rates, respectively. The objective Jaumann stress rate of the Kirchhoff stresses is given as

$$\boldsymbol{\tau}^{\nabla J} = \boldsymbol{C} : (\boldsymbol{d} - \boldsymbol{d}_e) \tag{1}$$

with the the elasticity tensor $\boldsymbol{C} = 2\mu(\mathbf{I} - \frac{1}{3}\boldsymbol{I} \otimes \boldsymbol{I}) + \kappa \boldsymbol{I} \otimes \boldsymbol{I}$ where μ denotes the shear modulus, κ the bulk modulus, $I_{ij} = \delta_{ij}$ the second order identity tensor and $\mathrm{I}_{ijkl} = (\delta_{ik}\delta_{jl} + \delta_{il}\delta_{kj})/2$ the fourth order symmetric identitiy tensor. In comparison to Bingham models based on regularized formulations, a fixed yield function need to be satisfied as

$$\Phi(\boldsymbol{\tau}) = q(\boldsymbol{\tau}) - \sigma_0 \tag{2}$$

with $q(\boldsymbol{\tau}) = \sqrt{\frac{3}{2}\mathrm{dev}[\boldsymbol{\tau}] : \mathrm{dev}[\boldsymbol{\tau}]}$ denoting the equivalent stress and σ_0 the yield stress. As a standard procedure from computational plasticity, the plastic flow rule [5] is defined by

$$\boldsymbol{d}_p = \dot{\gamma} \frac{\partial \Phi}{\partial \boldsymbol{\tau}} \tag{3}$$

in which $\dot{\gamma}$ is the plastic multiplier, that must obey the standard Kuhn-Tucker loading/ unloading conditions for classical rate-independent plasticity $\Phi(\boldsymbol{\tau}) \leq 0$, $\dot{\gamma} \geq 0$ and $\Phi(\boldsymbol{\tau})\dot{\gamma} = 0$ along with the consistency condition $\dot{\gamma}\dot{\Phi}(\boldsymbol{\tau}) = 0$. The Bingham model is obtained by a Perzyna formulation [4] of the plastic multiplier with an overstress function equal to the yield function as

$$\dot{\gamma} = \frac{< q(\boldsymbol{\tau}) - \sigma_0 >}{\eta} \tag{4}$$

where η is a viscosity parameter, which is related to the fluid viscosity μ as $\eta = 3\mu$ and "$< . >$" are the McCauley brackets given as

$$< f(\boldsymbol{\tau}) >= \begin{cases} f(\boldsymbol{\tau}) & \text{if} \quad f(\boldsymbol{\tau}) \geq 0, \\ 0 & \text{if} \quad f(\boldsymbol{\tau}) < 0. \end{cases} \tag{5}$$

1.2 Governing equations

The local form of the balance of momentum for homogenized fresh concrete, covering the domain Ω in the time interval $(0, T)$, becomes

$$\rho \frac{D\boldsymbol{v}}{Dt} = \nabla \cdot \boldsymbol{\sigma} + \boldsymbol{b} \quad \text{in } \Omega \ \times \ (0, T) \tag{6}$$

where ρ denotes the density, $\boldsymbol{v}$ the velocity, $\boldsymbol{\sigma}$ the Cauchy stress tensor $\boldsymbol{b}$ the body forces. The boundary conditions on the Neumann boundary $\partial\Omega_N$ are $\boldsymbol{\sigma}(\boldsymbol{x}, t)\boldsymbol{n} = \boldsymbol{t}^p(\boldsymbol{x}, t)$ with the normal vector $\boldsymbol{n}$ and the prescribed tractions $\boldsymbol{t}^p(\boldsymbol{x}, t)$. The boundary conditions on the Dirichlet boundary $\partial\Omega_D$ are $\boldsymbol{v}(\boldsymbol{x}, t) = \boldsymbol{v}^p(\boldsymbol{x}, t)$ with the prescribed velocities $\boldsymbol{v}^p(\boldsymbol{x}, t)$. Due to the form of the underlying plasticity model, situations may appear, where the material response is nearly incompressible. Hence, locking phenomena might occur with a pure velocity formulation. Therefore, the mean stress is separated from the stress field and discretized over an additional equilibrium equation, the balance of mass. The balance of mass is defined by

$$\nabla \cdot \boldsymbol{v} = \frac{1}{\kappa} \frac{Dp}{Dt} \quad \text{in } \Omega \ \times \ (0, T) \tag{7}$$

with the mean stress or pressure p and the bulk modulus κ. Consequently, the bulk modulus κ is also separated from the elasticity tensor and objective stress integration is just performed on the deviatoric parts of the stress tensor.

2 Numerical framework and the particle finite element method

The governing equations (6) and (7) are solved using the Particle Finite Element Method (PFEM) [2]. In PFEM the underlying weak form is discretized by means of standard finite elements in an updated Lagrangian formulation. The computational domain is frequently re-meshed to avoid element distortion. Hence, fast remeshing is essential and is achieved by using triangular and tetrahedral elements in two or three dimensions, respectively. The remeshing algorithm consists of two steps: First a standard Delaunay

triangulation of a point cloud is formed and second, in order to describe the free surface of the domain, elements with a circumcircle or circumsphere larger than a threshold value α are removed from the mesh. This procedure is called the α-shape method.
In the context of this work, the mixed velocity-pressure formulation is discretized by linear finite elements and the formulation is stabilized by a direct pressure stabilization.

3 Numerical application: Dam break test

The flow behavior of the proposed numerical model is compared with the flow of a regularized Bingham model [3] using a typical dam break test. See Figure 1a) for the geometry of the problem. The material and simulation parameters are the plastic viscosity $\mu = 5$ Pa $\cdot$ s, the dynamic yield stress $\mu = 300$ Pa, the density $\rho = 2000$ kg/m^3 and the time step size $\Delta t = 2 \cdot 10^{-5}$ s. The study is performed with three different element sizes $h = 0.01,\ 0.005,\ 0.0025$. Finally, the free surface of the material for the finest element size is given for different time instances in Figure 1b). As can be observed, the time dependent flow behavior is almost identical to the one obtained from a regularized Bingham model. Similar observations can be made from the evolution of the current material front position over time, see Figure 1c). Furthermore, as can be observed from Figure 1c), the flow of the material stops at around 0.6 s.

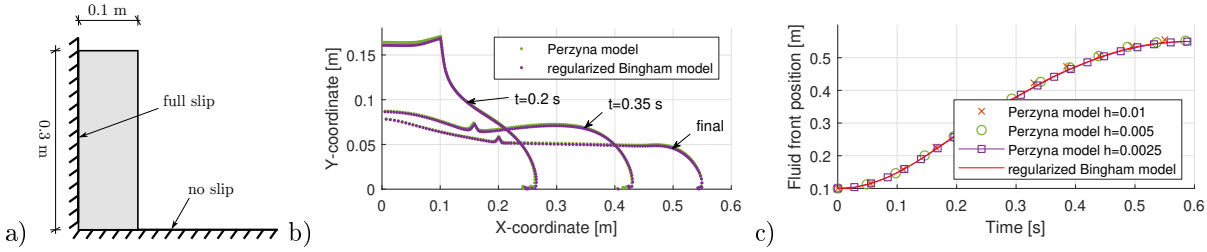

Figure 1. a) Geometry of the dam break test b) Shape of the material for different time instances of the dam break test c) Fluid front position over time diagram for the dam break test

4 Numerical application: 3D-concrete-printing

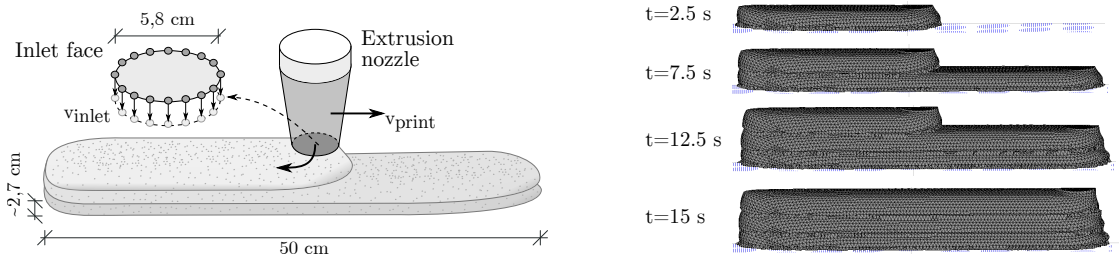

Figure 2. a) Geometry of the extrusion-based additive manufacturing of concrete scenario b) Printed shapes of the extrusion-based additive manufacturing test case scenario for different time instances with $\tau_0^s = 1$ kPa

In this scenario of 3D-concrete-printing, three layers of 50 cm length and 2.7 cm height are numerically printed, see Figure 2a). The simulation is conducted in 3D by using symmetry along the printing direction. The presented results focus on the shape of the concrete after leaving the extrusion nozzle and on pressure acting on lower layers, which is generated by the extrusion of the material. Due to a short process time of a few seconds, the influence of time dependent material behavior (structural build-up) is neglected in this analysis. The flow rate of the extruded concrete at the nozzle outlet is assumed to be constant over the cross section. Hence, the interaction between processes in the machine and the resulting flow rates is not considered. Therefore, the inlet flow from the extrusion nozzle is approximated with a velocity inlet, see Figure 2a). The material and simulation parameters are viscosity $\mu = 15$ Pa·s, dynamic yield stress $\tau_0 = 0.75$ kPa, density $\rho = 2000$ kg/m^3, Young's modulus $E = 0.1$ MPa, Poisson's ratio $\nu = 0.3$, printing velocity $v_{print} = 0.1$ m/s, flow rate $v_{inlet} = 0.09744$ m/s, nozzle-separation distance $\Delta z_{nozzle} = 2.7$ cm, $\Delta t = 0.5 \cdot 10^{-4}$ s and $t_{max} = 15$ s. For reflecting different states of structuration, the static yield stress

of already printed layers is set to a value of $\tau_0^s = 1$, 1.5 and 2 kPa. This yield stress is responsible to prevent the material from collapse in the printing process.
The numerically printed shapes of the test case scenario of extrusion-based additive manufacturing of fresh concrete with a static yield stress $\tau_0^s = 1$ kPa for different time instances are depicted in Figure 2b). In Figure 3a) the outline of the cross section of each additively manufactured concrete layer are shown. The results are given for the time instances when the first layer ($t = 5$ s), the second ($t = 10$ s) and third layer ($t = 15$ s) is printed. As can be observed, there is a significant squeezing of lower layers in the manufacturing process, when material is extruded on top of already printed layers. Fresh concrete slightly flows in the direction perpendicular to the printing direction. These observations are underlined by the results depicted in Figure 3b), where the yielded (red) and unyielded (blue) regions of the manufacturing process for the time instance $t = 12.5$ s are given. Figure 3b) reveals that the equivalent stress exceeds the yield stress in a certain region below the extrusion nozzle of lower layers. Hence, the material is not strong enough to bear the pressure generated from the inlet flow. By changing the static yield stress to values of $\tau_0^s = 1.5$ and 2 kPa for reflecting different states of structural build-up and a certain waiting time between each layer, lower layers become strong enough to carry the load from the inlet flow, see Figure 3b).

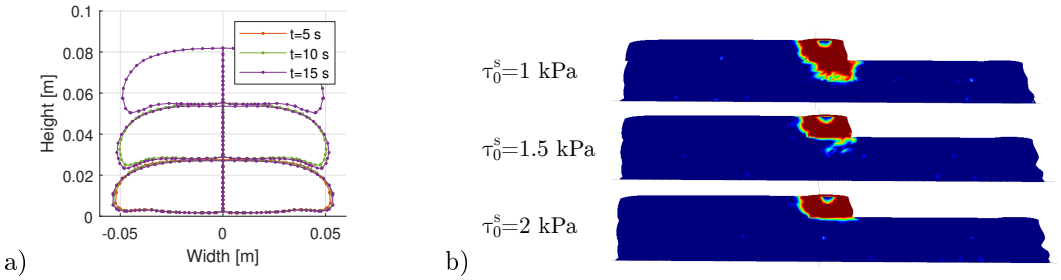

Figure 3. a) Outline of the cross section of the additively manufactured concrete layers for different time instances $t = 5$ s (first layer printed), $t = 10$ s (second layer printed), $t = 15$ s (third layer printed) with $\tau_0^s = 1$ kPa b) Yielded (red) and unyielded (blue) regions for different static yield stresses for t=12.5 s (view on the symmetry line)

5 Conclusions

A computational model based on the Particle Finite Element Method for the simulation of extrusion processes of 3D-concrete-printing techniques is presented. The constitutive law is based on a Bingham model, which is approximated with a classical elasto-viscoplastic formulation. Results show that the flow behavior of this model is almost identical to the flow behavior of models with a regularized Bingham model. Furthermore, robustness of the proposed model is shown in a numerical test case scenario of extrusion processes in additive manufacturing of fresh concrete. Simulations of a 3D-printing process show that in addition to the self weight of upper layers, the extrusion process itself generates a pressure on lower layers, that temporarily also need to be carried by these layers. If the static yield stress of these layers is not large enough, the yield stress is exceeded and lower layers are squeezed, which results in unintended displacements that might adversely influence the integrity of the printed layers during the additive manufacturing process.

References

[1] S. Lim, R.A. Buswell, T.T. Le, S.A. Austin, A.G.F. Gibb, and T. Thorpe. Developments in construction-scale additive manufacturing processes. *Automation in Construction* 21 (2012), pp. 262 –268.

[2] Eugenio Oñate, Sergio R Idelsohn, Facundo Del Pin, and Romain Aubry. The particle finite element method: an overview. *International Journal of Computational Methods* 1.02 (2004), pp. 267–307.

[3] T.C. Papanastasiou. Flows of Materials with Yield. *Journal of Rheology* 31.5 (1987), pp. 385–404.

[4] P. Perzyna. Fundamental problems in viscoplasticity. In: *Advances in Applied Mechanics*. Ed. by G. Kuerti. 9. Academic Press, New York, 1966, pp. 244–368.

[5] J.C. Simo and T.J.R. Hughes. *Computational Inelasticity*. Berlin: Springer, 1998.

**Proceedings of the 8th GACM Colloquium on Computational Mechanics
for Young Scientists from Academia and Industry
August 28–30, 2019 in Kassel, Germany**

Optimisation of Diffusion Driven Degradation Processes

Navina Waschinsky * [1], Franz-Joseph Barthold[1] and Andreas Menzel[2,3]

[1]Structural Mechanics, TU Dortmund, Dortmund, Germany
[2]Institute of Mechanics, TU Dortmund, Dortmund, Germany
[3]Division of Solid Mechanics, Lund University, Sweden

Abstract. It is known that nature always strives for optimal processes in order to prevent early damage or failure, for example bones which regulate the tissue in high stress areas or the optimal shape of trees. Many materials in nature are highly complex as they are designed for long duration. Taking the nature itself as a role model means taking its complexity into account, especially when considering materials which suffer from chemical attacks and the degradation of materials. From this point of view, we create an algorithm which considers degradation processes triggered by chemical substances which depend on diffusion conditions in a finite element (FE) framework. In addition, we perform design optimisation with stress restrictions by taking evolutionary processes as a role model. In this paper a biological inspired algorithm which considers degradation processes triggered by chemical substances is presented. We create a coupled diffusion and growth/degradation approach with a permeable structure allowing a gradient-based flow of concentrations. The continuum describes a one-phase approach with continuum modeling of a growth/degradation process. With a thermodynamically consistent evaluation we formulate the govering equations, including stress, particle diffusion and chemical reactions.

Introduction

This paper focuses on the general outline of the algorithm combining a specific structural coupled problem to an optimisation framework. In detail, we deal with the coupling of diffusion and growth/degradation processes embedded in a design optimisation algorithm.

In the following we present the evaluation of the structural analysis leading to a fully coupled diffusion and growth/degradation material. We outline the kinematic approach of isotropic growth combined with the constitutive evaluation of the chemical particles which are the trigger for mass growth or degradation. Furthermore, we present the thermodynamically consistent evaluation of the govering equations, including mechanical stress, particle diffusion and chemical reactions. The structural analysis is implemented in a Fortran code, which is embedded in a Matlab framework. The advantages of the power of Matlab allow the application of a Matlab optimisation toolbox within a finite element method (FEM) formulation. We outline the general optimisation algorithm referring to a simple example.

1 Structural Analysis

1.1 Kinematics

The kinematic concept enables the description of all tangent operations in the continuum mechanical concept, for further information see [1, 2, 3]. Figure 1 gives a short overview of the assumptions. We introduce the coordinates in the reference configuration X_i, in the actual configuration x_i, in the growth space $\widehat{\mathrm{X}}_\mathrm{i}$ and in the parameter space Θ_i, namely the convective coordinates. Furthermore, we apply mappings between the configurations for geometry κ, for motion μ and for growth γ. Partial derivatives of the mappings with respect to the respective local coordinates result in the convective tangent vectors $\mathbf{G}_\mathrm{i}$, $\mathbf{g}_\mathrm{i}$ and $\widehat{\mathbf{G}}_\mathrm{i}$. The gradients of the mappings between the parameter space and the introduced configurations lead to the local, fundamental gradients $\mathbf{K}$, $\mathbf{M}$ and $\mathbf{T}$.

*Corresponding author: navina.waschinsky@tu-dortmund.de ORCID iD: 0000-0002-4319-7988

These gradients are important two-point tensors providing transformations between objects related to the respective configurations. The commonly used deformation gradient $\mathbf{F}$ is related to the reference and actual configuration. Thus, Lagrangian mapping from the reference configuration to the actual configuration φ_t can be described by the composition $\varphi_t := \mu \circ \kappa^{-1}$. In analogy to growth in a living structure we refer to a volumetric growth approach. We apply a multiplicative decomposition of the deformation gradient $\mathbf{F}$ into an elastic part $\mathbf{F}^e$ and a growth part $\mathbf{F}^g$ as introduced in [4, 6, 8]. Following Lubarda and Hoger [7], we apply an isotropic ansatz for the growth part of the deformation gradient with the stretch ratio ν

$$\begin{aligned} \mathbf{F} &= \mathbf{F}^e\,\mathbf{F}^g \\ \mathbf{F}^g &= \nu\,\mathbf{1}_{\widehat{\mathbf{X}}}. \end{aligned} \tag{1}$$

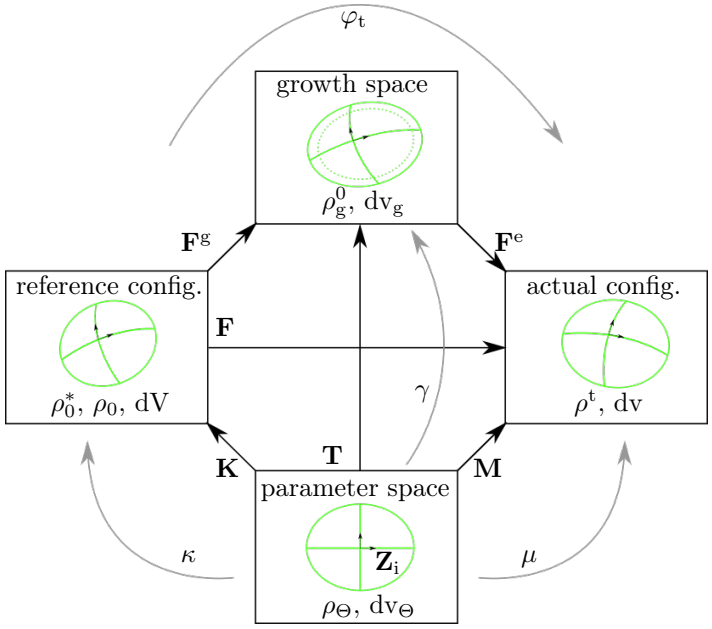

Figure 1. Kinematic concept

Mass exchange is realized by a mass source/sink term R_0 in the reference configuration which leads to time dependent update of the initial mass density ρ_0^* to the resulting mass density ρ_0, i.e.

$$\rho_0 = \rho_0^* \pm \int_{t_0}^{t} R_0\,dt. \tag{2}$$

1.2 Constitutive Framework

As postulated in the second law of thermodynamics, a system's entropy never decreases. On this basis, we shortly present a thermodynamically consistent evaluation of the coupled chemical and mechanical problem motivated by the outline of Hu and Shen in [5]. The evaluation yields the mechanical stresses and the description of the chemical diffusion. We apply the fundamental Gibbs equation for reversible processes with chemical impact as follows

$$\rho_t \epsilon' = \theta\, s' + \mathbf{T} : \mathbf{D} + \mu_\gamma\, c'_\gamma, \tag{3}$$

wherein ϵ is the internal energy, θ is the temperature, s is the entropy, $\mathbf{T}$ is the Cauchy stress tensor in the actual configuration, $\mathbf{D}$ is the velocity gradient, μ_γ are the chemical potentials and c_γ are the concentrations. With the local form of the balance equation of energy, the time derivative of the total entropy results in

$$s' = \frac{1}{\theta}\,[\,\mu_\gamma\, c_\gamma\, \mathrm{div}\,\mathbf{x}'_\gamma - \epsilon\,\frac{R_0}{J}]. \tag{4}$$

Herein, $\mathbf{x}'_\gamma$ is the velocity vector of the concentrations evaluated by the balance of mass of the concentrations with $c'_\gamma = -\,c_\gamma\,\mathrm{div}\,\mathbf{x}'_\gamma$. As presented in Hu and Shen [5], the internal dissipation energy in the medium is transformed to the dissipation heat and produces the irreversible entropy. With this, the total entropy can be decomposed in a reversible and in an irreversible part $s' = s'^{(r)} + s'^{(i)}$. We evaluate the reversible part of the entropy

$$s'^{(r)} = -\,\frac{\epsilon\, R_0}{\theta\, J} + \mathrm{div}[\frac{\mu_\gamma\, c_\gamma\, \mathbf{x}'_\gamma}{\theta}], \tag{5}$$

wherein the irreversible part of the entropy can be calculated by $s'^{(i)} = s' - s'^{(r)}$, i. e.

$$s'^{(i)} = \frac{1}{\theta}\,[-\,\mathbf{x}'_\gamma \cdot \mathrm{grad}\,(c_\gamma\, \mu_\gamma)]. \tag{6}$$

We use the Legendre transformation to obtain the Helmholtz function $\psi = \epsilon - \theta\,\mathrm{s}$. With the evaluation of the local energy balance and the entropy, we identify the time derivative of the Helmholtz function under isothermal conditions, namely

$$\psi' = -\,\epsilon\,\frac{\mathrm{R}_0}{\rho_\mathrm{t}\,\mathrm{J}} + \frac{1}{\rho_\mathrm{t}}\,(\mathbf{D} : \mathbf{T}) + \frac{\epsilon\,\mathrm{R}_0}{\mathrm{J}} + \mu_\gamma\,\mathrm{c}'_\gamma + \mathbf{x}'_\gamma \cdot \mathrm{grad}\,(\mathrm{c}_\gamma\,\mu_\gamma). \tag{7}$$

Furthermore, we separate the elastic and dissipative part of the Helmholtz energy function as follows

$$\begin{aligned} &\text{elastic part} \quad : \quad \psi'^{\mathrm{el}} := \frac{1}{\rho_\mathrm{t}}\,(\mathbf{D} : \mathbf{T}) + \mu_\gamma\,\mathrm{c}'_\gamma \\ &\text{dissipative part} \quad : \quad \psi'^{\mathrm{dis}} := \mathbf{x}'_\gamma \cdot \mathrm{grad}(\,\mathrm{c}_\gamma\,\mu_\gamma). \end{aligned} \tag{8}$$

We can decompose the ansatz for the Helmholtz function in a mechanical, applying the neo-Hookean hyperelastic model ψ^{Neo}, and a chemical part ψ^{Chem}. To ensure the entropy inequality, we evaluate the following equations for the stress $\mathbf{T}$, the chemical potential μ_γ and the velocity of the concentrations $\mathbf{x}'_\gamma$

$$\begin{aligned} \mathbf{T} &= 2\,\rho_\mathrm{t}\,\mathbf{F}\,\frac{\delta\psi^{\mathrm{Neo}}}{\delta\,\mathbf{C}}\,\mathbf{F}^{\mathrm{T}} \\ \mu_\gamma &= \frac{\partial\psi^{\mathrm{Chem}}}{\partial \mathrm{c}_\gamma} \\ \mathbf{x}'_\gamma &= -\mathrm{D}\,\mathrm{grad}(\mathrm{c}_\gamma), \end{aligned} \tag{9}$$

wherein D is the diffusion coefficient.

1.3 Numerical Solution

The previously introduced material formulation for the coupled diffusion and growth/degradation model leads to a reduction of the unknown quantities and to a set of coupled differential equations. A numerical approximation, the FEM, is applied for further procedures. In order to close the system of partial differential equations, the unknown quantities are solved by the choice of governing equations. This approach is used to solve the set of degrees of freedom, including the displacement $\mathbf{u}$ and the concentration c_γ evaluated with the balance of momentum and the balance of mass for concentrations. The weak forms together with $\mathbf{T} = \frac{1}{\mathrm{J}}\,\mathbf{P}\,\mathbf{F}^{\mathrm{T}}$ results in

$$\begin{aligned} \int_{\mathrm{B}_0} \mathbf{P} : \mathrm{Grad}\,(\delta\mathbf{u})\;\mathrm{dV} &= \int_{\partial\mathrm{B}_0} \mathbf{t}\cdot\delta\mathbf{u}\;\mathrm{dA} \\ \int_{\mathrm{B}_0} \mathrm{c}'_\gamma\,\delta\mathrm{c}_\gamma - \mathbf{x}'_\gamma \cdot \mathrm{grad}\,(\,\delta\mathrm{c}_\gamma)\;\mathrm{dV} &= \int_{\partial\mathrm{B}_0} \mathbf{x}'_\gamma \cdot \mathbf{n}\,\delta\mathrm{c}_\gamma\;\mathrm{dA}. \end{aligned} \tag{10}$$

2 Structural Optimisation

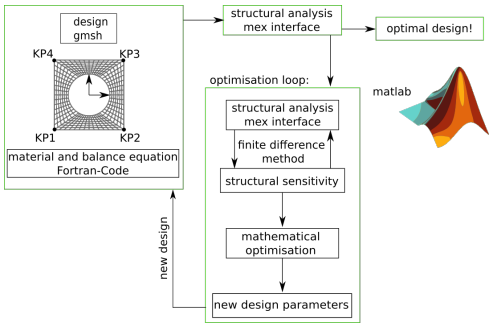

Figure 2. Algorithmic concept

Figure 2 gives an overview of the optimisation algorithm. The entire program runs in a Matlab framework, which includes a connection to the open software gmsh for mesh creation on the one hand, and an interface to a Fortran code using MEX-file interfaces on the other. So, the model presented here is embedded as a Fortran code using MEX-file interfaces. We apply Matlab to access the integrated optimisation toolboxes. Purpose of the optimisation problem is a computational design framework accompanied by von Mises stress and design restrictions. In this example we focus on a simple example, namely a structure with a hole. For the optimisation of the initial problem, an objective function, design parameters and side conditions are required. In this example, the objective function J(s) is the area of the structure aiming a reduction of material using the parameters of the hole as the design parameters.

3 Numerical Example

We consider a structure with a hole, which is attacked by chemical concentrations from the left side. The impact of the concentrations, results in degradation of the material. Figure 3 shows the time depending development of the degradation gradient $\mathbf{F}^{\mathrm{g}}$ triggered by the concentrations. The optimisation algorithm enables a design reduction, thus holding the side conditions.

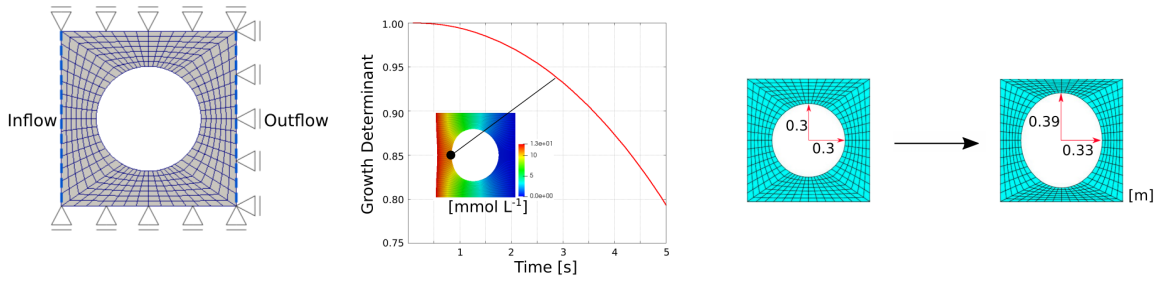

Figure 3. Left: Boundary condition of the concentration and displacement. Middle: Contour plot, showing the distribution of the concentration in the last time step and the impact on $\mathbf{F}^{\mathrm{g}}$ in the marked point. Right: Optimised design with a material reduction of 17.38%.

References

[1] F.-J. Barthold. *Zur Kontinuumsmechanik inverser Geometrieprobleme*. TU Braunschweig, 2002.

[2] F.-J. Barthold. Remarks on variational shape sensitivity analysis based on local coordinates. *Engineering Analysis with Boundary Elements* 32 (2008), pp. 971–985.

[3] F.-J. Barthold, N. Gerzen, W. Kijanski, and D. Materna. Efficient Variational Design Sensitivity Analysis. In: *Mathematical Modeling and Optimization of Complex Structures*. Springer International Publishing, 2016, pp. 229–257.

[4] G. Himpel, E. Kuhl, A. Menzel, and P. Steinmann. Computational modelling of isotropic multiplicative growth. *Computer Modeling in Engineering & Sciences* 8 (2005), pp. 119–134.

[5] S. Hu and S. Shen. Non-equilibrium thermodynamics and variational principles for fully coupled thermal–mechanical–chemical processes. *Acta Mechanica* 224 (2013), pp. 2895–2910.

[6] D. Kuhl, F. Bangert, and G. Meschke. Coupled chemo-mechanical deterioration of cementitious materials. Part I: Modeling. *International Journal of Solids and Structures* 41 (2004), pp. 15–40.

[7] V. A. Lubarda and A. Hoger. On the mechanics of solids with a growing mass. *International Journal of Solids and Structures* 39 (2002), pp. 4627–4664.

[8] A. Menzel and E. Kuhl. Frontiers in growth and remodeling. *Mechanics Research Communications* 42 (2012), pp. 1–14.

**Proceedings of the 8th GACM Colloquium on Computational Mechanics
for Young Scientists from Academia and Industry
August 28–30, 2019 in Kassel, Germany**

Acoustic-structure interaction in the Scaled Boundary Finite Element Method for prismatic geometries

Paul Wasmer * [1], Jannis Bulling[1], Hauke Gravenkamp[2] and Jens Prager[1]

[1]Bundesanstalt für Materialforschung und -prüfung
[2]University of Duisburg-Essen, Germany

Abstract. Due to the short wavelength compared to the dimensions of the structure, the simulation of ultrasonic waves is still a challenging task. A numerical method wellisuited for this purpose is the semi-analytical Scaled Boundary Finite Element Method (SBFEM). When applying this method, only the boundary of a computational domain is discretized using finite elements, while the interior is described by an analytical ansatz. Hence, the number of degrees of freedom is reduced significantly compared to the classical Finite Element Method (FEM). In recent years, a particular formulation of the SBFEM for the simulation of ultrasonic guided waves was developed. The method constitutes an efficient algorithm for prismatic structures of arbitrary length, such as plates, pipes, or beams. Wave propagation phenomena in such structures can be modeled for isotropic and anisotropic inhomogeneous waveguides. Even though the method is an efficient tool for the simulation of guided waves in solid media, a reliable model for the simulation of acoustic wave propagation in fluids as well as acoustic-structure interaction in terms of SBFEM is still missing. In principle, the fluid can be described by a displacement-based formulation and thus be implemented in existing SBFEM algorithms for solid bodies. However, due to the discretization with classical finite elements, spurious modes occur, which cannot be separated from the physical modes straightforwardly. The spurious modes can be suppressed using a penalty parameter. Although very accurate results were achieved for some problems, this procedure has been proven unreliable for certain cases. For this reason, we propose a different approach in this contribution. We employ a pressure model to simulate the acoustic behavior of fluids. The implementation of the pressure model results in a higher effort due to the necessity of incorporating coupling terms, but it presents a stable alternative without spurious modes. The accuracy of the method is demonstrated in comparison with results obtained using the FEM.

Introduction

Prismatic geometries, e.g. plates or pipes, act as waveguides for ultrasonic acoustic waves. In waveguides waves can travel long distances without decaying. The physical behavior in waveguides is very complex as the ultrasonic waves show strongly dispersive behavior. An efficient numerical tool to simulate ultrasonic guided waves is therefore essential to investigate the physical behavior. Besides other numerical methods, the Finite Element Method (FEM) can be used to simulate wave propagation. However, due to the short wavelengths at ultrasonic frequencies, a very fine mesh is required. Thus, FE models result in large numerical systems and hence, long computation times. An efficient alternative is given by the Scaled Boundary Finite Element Method (SBFEM) [4]. In the SBFEM, a semi-analytical method, only the boundary of the computational domain is discretized with finite elements and hence, the number of degrees of freedom is reduced compared to the FEM. The physical behavior in the interior of a computational domain is described analytically. A special formulation of the SBFEM for prismatic geometries, e.g. plates and pipes, was developed by Gravenkamp et al. [1, 2, 3].
The method can be used to simulate wave behavior in isotropic and anisotropic inhomogeneous solid waveguides. However, a stable method for the simulation of acoustic behavior in fluids and the simulation of acoustic-structure interaction is still missing. In a first attempt, a displacement-based formulation was used to describe the fluid. Due to the discretization by finite elements, this approach results in spurious modes, a phenomenon widely reported in the literature. The spurious modes can be suppressed by applying a penalty parameter [5]. However, this method does not work reliably for all cases.

*Corresponding author: paul.wasmer@bam.de

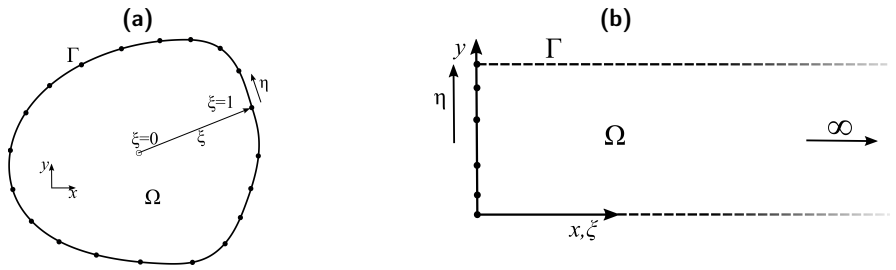

Figure 1. a) 2D domain discretized with the SBFEM; b) prismatic semi-infinite 2D geometry discretized with the SBFEM

A pressure model constitute a more natural and straightforward approach to describe the acoustic behavior of a fluid. For the application of fluid-structure interaction, this method results in a higher implementation effort compared to the displacement-based approach, as coupling terms between the acoustic and the structural domain are needed. However, to the best knowledge of the authors, no numerical instabilities are reported in the literature. Thus, we employ the pressure model in the SBFEM for the computation of dispersion curves. To show the accuracy of the method, results are compared to those obtained using the finite element software COMSOL Multiphysics.

1 Theoretical framework

The SBFEM relies on a coordinate transformation. In general, the Cartesian coordinates are mapped onto the so-called SBFEM coordinates, η and ξ. η is the local coordinate of the finite elements on the boundary (see Fig. 1a). ξ is the scaling direction pointing from the so-called "scaling center" to the boundary. In the case of prismatic geometries the scaling center is placed at $x = -\infty$. It follows that ξ is equivalent to the Cartesian x coordinate. It therefore only becomes necessary to discretize the boundary along the y direction. By applying the coordinate transformation, the partial differential equation is transformed into an ordinary differential equation. In the case of prismatic geometries, a linear ordinary differential equation is obtained.

1.1 Acoustic-structure interaction

The algorithm to describe acoustic wave behavior in solids can be found in [1, 3] and is therefore not repeated here. The acoustic behavior of a fluid using pressure as the primary variable is described by the Helmholtz equation

$$\mathrm{K}\Delta p - \rho_\mathrm{f}\ddot{p} = 0\,, \tag{1}$$

where K is the bulk modulus and ρ_f the density of the fluid. The divergence of the pressure in 2D is given by

$$\nabla p = \mathbf{D_1}\mathbf{p_n}_{,x}(x) + \mathbf{D_2}\mathbf{p_n}(x) \tag{2}$$

where $\mathbf{p_n}(x)$ is a vector containing the nodal pressure values and $\mathbf{D_1}$ and $\mathbf{D_2}$ are given by

$$\mathbf{D_1} = \begin{bmatrix}1 & 0\end{bmatrix}^\intercal \mathbf{N_p} \qquad \mathbf{D_2} = \frac{1}{y_{,\eta}}\begin{bmatrix}0 & 1\end{bmatrix}^\intercal \mathbf{N}_{\mathbf{p},\eta}\,. \tag{3}$$

$\mathbf{N_p}$ is a vector containing the shape functions. Through applying the coordinate transformation to SBFEM coordinates and performing some computation steps (equivalent to the computation steps for solid found in [1]), the SBFEM equation in the frequency domain is obtained

$$\mathbf{E_{0p}}\mathbf{p_n}_{,xx}(x) - \mathbf{E_{2p}}\mathbf{p_n}(x) - \omega^2\mathbf{M_{0p}}\mathbf{p_n} = 0\,. \tag{4}$$

$\mathbf{E_{0p}}$, $\mathbf{E_{2p}}$ and $\mathbf{M_{0p}}$ are coefficient matrices integrated over the discretized boundary

$$\mathbf{E_{0p}} = \int \mathbf{D_1}^\intercal \mathrm{K}\mathbf{D_1}|\mathbf{J}|\mathrm{d}\Gamma_1\,, \quad \mathbf{E_{2p}} = \int \mathbf{D_2}^\intercal \mathrm{K}\mathbf{D_2}|\mathbf{J}|\mathrm{d}\Gamma_1\,, \quad \mathbf{M_{0p}} = \int \mathbf{N_p}^\intercal \rho_\mathrm{f}\mathbf{N_p}|\mathbf{J}|\mathrm{d}\Gamma_1\,. \tag{5}$$

The boundary condition between fluid and solid in the frequency domain is given by

$$\mathrm{K}\frac{\partial p}{\partial n} = \omega^2 \rho_\mathrm{f} \mathbf{n}^\intercal \mathbf{u}\,, \tag{6}$$

where $\mathbf{n}$ is the normal vector pointing from the fluid domain into the solid domain. For the SBFEM, this results in the following equation system

$$\begin{bmatrix} \mathbf{E_{0s}} & \mathbf{0} \\ \mathbf{0} & \mathbf{E_{0p}} \end{bmatrix} \begin{bmatrix} \mathbf{u_n}_{,xx} \\ \mathbf{p_n}_{,xx} \end{bmatrix} + \begin{bmatrix} \mathbf{E_{1s}}^\intercal - \mathbf{E_{1s}} & \mathbf{0} \\ \mathbf{0} & \mathbf{0} \end{bmatrix} \begin{bmatrix} \mathbf{u_n}_{,x} \\ \mathbf{p_n}_{,x} \end{bmatrix} - \tag{7}$$

$$\begin{bmatrix} \mathbf{E_{2s}} & \mathbf{Q} \\ \mathbf{0} & \mathbf{E_{2p}} \end{bmatrix} \begin{bmatrix} \mathbf{u_n} \\ \mathbf{p_n} \end{bmatrix} + \omega^2 \begin{bmatrix} \mathbf{M_{0s}} & \mathbf{0} \\ -\rho_\mathrm{f} \mathrm{K} \mathbf{Q}^\intercal & \mathbf{M_{0p}} \end{bmatrix} \begin{bmatrix} \mathbf{u_n} \\ \mathbf{p_n} \end{bmatrix} = \mathbf{0}\,, \tag{8}$$

where $\mathbf{E_{0s}}, \mathbf{E_{1s}}, \mathbf{E_{2s}}$ and $\mathbf{M_{0s}}$ are the coefficient matrices of the solid domain. A detailed description of their computation can be found in [1]. The vector $\mathbf{u_n}$ contains the nodal displacements. In 2D the coupling matrix is reduced to

$$\mathbf{Q} = \int \mathbf{N}^\intercal \mathbf{n} \mathbf{N_p} \mathrm{d}\Gamma_2 = \mathbf{1} \tag{9}$$

where $\mathbf{N}$ are the shape functions of the solid element and Γ_2 the discretized boundary between solid and fluid. The dispersion behavior is obtained by solving the eigenvalue problem (8). We apply the algorithm proposed in [1].

2 Examples

To demonstrate the accuracy of the method, two examples are presented. In the first example the dispersion curves of two aluminium plates with a thin liquid layer in between are calculated (see Fig. 2a). Both plates have a thickness of h = 5 mm. The liquid layer in between has a height of d = 1 mm. Both plates are made from aluminium (E = 70 GPa, $\nu = 0.33$, $\rho = 2700\,\frac{\mathrm{kg}}{\mathrm{m}^3}$). As liquid water (K = 2.19 GPa and $\rho_\mathrm{f} = 1000\,\frac{\mathrm{kg}}{\mathrm{m}^3}$) is used. The dispersion behavior of the phase velocity is shown in Fig. fig:twoPlatesResults. The results are in perfect agreement with dispersion curves computed with COMSOL Multiphysics.

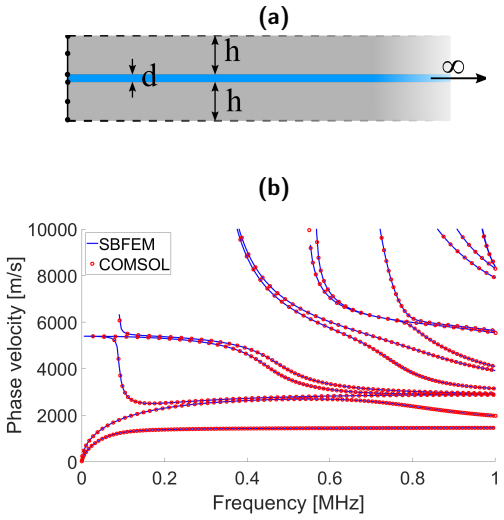

Figure 2. Dispersion behavior of plate with a fluid layer in between. a) simulated geometry b) phase velocity over frequency.

In a second example, the dispersion behavior of a fluid-filled pipe is computed. The pipe is made of steel ($\rho = 7850\,\frac{\mathrm{kg}}{\mathrm{m}^3}$, $\nu = 0.3$ and E = 200 GPa) with an inner radius of $r = 5$ mm and a wall thickness of $h = 1$ mm (see Fig. 3a). The inside is filled with water ($\rho_\mathrm{f} = 1000\,\frac{\mathrm{kg}}{\mathrm{m}^3}$ and K = 2.19 GPa). Here, an axisymmetric model is used, where in the SBFEM only one radius of the pipes has to be discretized with

one-dimensional finite elements [2]. Hence, very short computation times are achieved. In Fig. 3b the dispersion behavior is displayed. The results of SBFEM are compared to results from COMSOL Multiphysics. The results from both methods are in excellent agreement. By comparing the computational times on the same machine (Intel Xeon X650, 96 GB RAM) for both methods the efficiency of SBFEM becomes obvious: The implemted SBFEM algorithm takes 36 s, whereas FEM is much more expensive. COMSOL Multiphysics runs 7 min 30 s to produce the shown results.

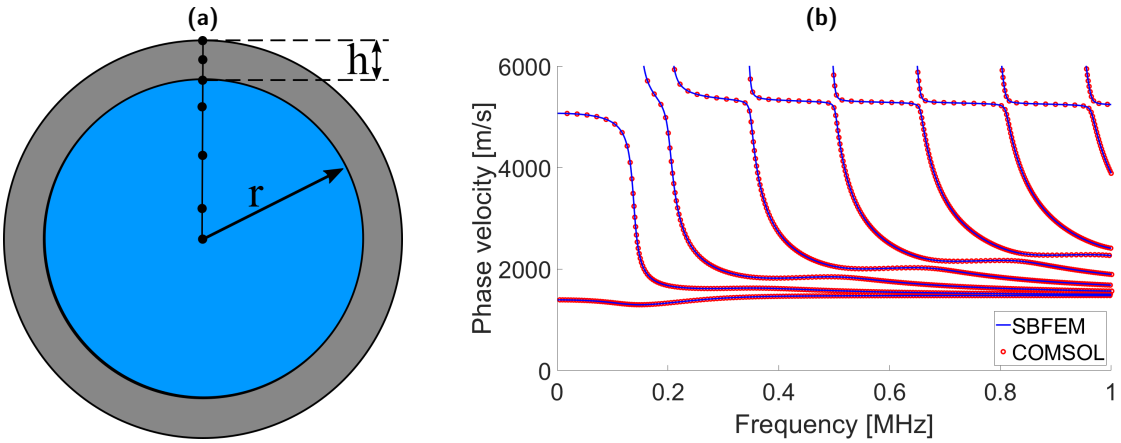

References

[1] H. Gravenkamp, C. Song, and J. Prager. A numerical approach for the computation of dispersion relations for plate structures using the scaled boundary finite element method. *Journal of Sound and Vibration* 311 (11 2012), pp. 2543–2557.

[2] H. Gravenkamp, C. Birk, and C. Song. The computation of dispersion relations for axisymmetric waveguides using the Scaled Boundary Finite Element Method. *Ultrasonics* 54 (2014), pp. 1373–1385.

[3] H. Gravenkamp, C. Birk, and C. Song. Simulation of elastic guided waves interactiong with defects in arbitrarily long structures using the scaled boundary finite element method. *Journal of Computational Physics* 295 (2015), pp. 438–455.

[4] C. Song. The scaled boundary finite element method in structural dynamics. *International Jounral for Numerical Methods in Engineering* 77 (2009), pp. 1139–1171.

[5] P. Wasmer, F. Krome, J. Bulling, and J. Prager. Prismatic semi-analytical elements for the simulation of linear elastic problems in structures with piecewise uniform cross section. *PAMM* 18 (2017), e201800139.

**Proceedings of the 8th GACM Colloquium on Computational Mechanics
for Young Scientists from Academia and Industry
August 28–30, 2019 in Kassel, Germany**

Modelling the Soil-Water Interaction at Fluid-Infiltrated Roads under Loading of Steady State Rolling Tires

Ines Wollny * [1], WaiChing Sun[2] and Michael Kaliske[1]

[1]Institute for Structural Analysis, Technische Universiät Dresden, 01062 Dresden, Germany
[2]Department of Civil Engineering and Engineering Mechanics, Columbia University, 4709 New York, NY, USA

Abstract. In case of tires driving over a fluid-infiltrated subsoil like off-road on soils or on porous and permeable pavements, the interaction between the solid and the fluid constituent inside the underground affects the tire-subsoil interaction. This hydro-mechanical coupling effect is captured via poro-elasticity theory. In order to achieve a numerically efficient description of the tire rolling over the fluid-infiltrated subsoil, the poromechanical balance equations are formulated in an arbitrary Lagrangian Eulerian (ALE) frame and account for finite deformation. The solution of the poromechanical ALE model of the fluid-infiltrated subsoil via a finite element (FE) formulation is performed by an operator split scheme. Thereby, different split assumptions (drained, undrained, semi-drained) are investigated for the solid step. This staggered solid-fluid iteration is embedded into a coupled tire-subsoil interaction model, which is solved via a sequential iteration scheme as well. The whole tire-soil-water interaction is, then, solved within a hierarchical operator split scheme.

1 Poromechanical ALE formulation

In case of fluid-infiltrated porous media, fluid constituents (e.g. water and air) are present in addition to the solid constituent. In the poromechanics, these phases are not treated separately but as multi-phase continua. A fully saturated soil is considered as two-phase (solid-water) continuum while an unsaturated soil is modelled as a three-phase continuum (solid-water-air) with the corresponding volume fractions $\phi^\alpha = v_\alpha / v$ of the constituents $\alpha = \mathrm{s}, \mathrm{w}, \mathrm{a}$, which is defined by the current volume v_α of the constituent in proportion to the current volume $v = \sum_\alpha v_\alpha$ of the total mixture. In contrast to a single-phase continua that undergoes compatible deformation, the fluid and solid constituents of a fluid-infiltrated porous medium may move at different trajectories, see Fig. 1. Thus, a controlled mass of solid constituents may contain fluid in the deformed void space that was not necessarily present in the void space of the solid skeleton in the reference configuration.

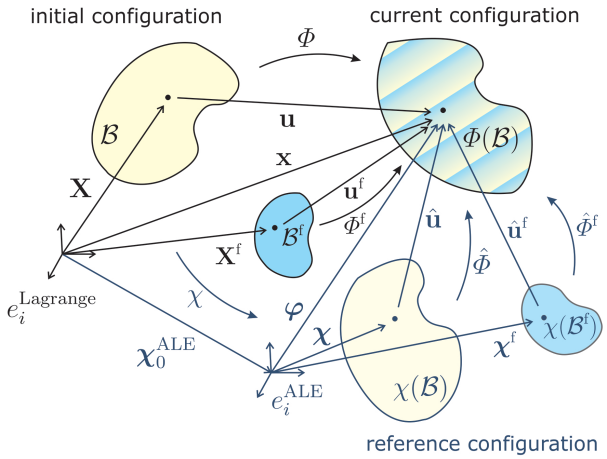

Figure 1. Poromechanical ALE kinematics for a two-phase continuum

*Corresponding author: ines.wollny@tu-dresden.de

The solid and the fluid constituents occupy the combined space $\Phi(\mathcal{B})$ in the current configuration. In the initial configuration $\mathcal{B}$ contains the solid phase and $\mathcal{B}^{\mathrm{f}}$ contains the pore fluid. For the arbitrary Lagrangian Eulerian (ALE) formulation, an additional reference configuration is introduced, where the solid phase is in space $\chi(\mathcal{B})$ and the fluid phase is described by $\chi(\mathcal{B}^{\mathrm{f}})$. Thereby, the mapping from the initial to the reference configuration is a rigid body motion. Then, the current position $\boldsymbol{x}$ of a point P at time t of combined solid and fluid can be expressed in terms of the initial solid position $\boldsymbol{X}$ or in terms of the initial fluid position $\boldsymbol{X}^{\mathrm{f}}$ by

$$\boldsymbol{x} = \Phi\left(\boldsymbol{X}, t\right) = \hat{\Phi}\left(\chi\left(\boldsymbol{X}, t\right)\right) = \Phi^{\mathrm{f}}\left(\boldsymbol{X}^{\mathrm{f}}, t\right) = \hat{\Phi}^{\mathrm{f}}\left(\chi\left(\boldsymbol{X}^{\mathrm{f}}, t\right)\right). \tag{1}$$

By introducing, further, a moving reference coordinate system e_i^{ALE} in the ALE frame, the current position of a point P might be expressed in several ways by

$$\boldsymbol{x} = \boldsymbol{X} + \boldsymbol{u} = \boldsymbol{X}^{\mathrm{f}} + \boldsymbol{u}^{\mathrm{f}} = \boldsymbol{\chi}_{\mathbf{o}}^{\mathrm{ALE}} + \boldsymbol{\varphi} = \boldsymbol{\chi}_{\mathbf{o}}^{\mathrm{ALE}} + \boldsymbol{\chi} + \hat{\boldsymbol{u}} = \boldsymbol{\chi}_{\mathbf{o}}^{\mathrm{ALE}} + \boldsymbol{\chi}^{\mathrm{f}} + \hat{\boldsymbol{u}}^{\mathrm{f}}. \tag{2}$$

In the treated case of fluid-infiltrated roads under rolling tire load, the introduced reference frame moves with the tire through the space. In case of steady state rolling tires and a subsoil, which is homogeneous in driving direction, the deformation state of the tire and the subsoil with respect to the introduced moving reference frame becomes time-independent. This feature enables a numerically efficient description of the tire-subsoil interaction. It is worth noting that treating the tire-soil interaction with respect to the introduced moving coordinate system leads to a flow of the material particles through the reference configuration. The deformation gradient can be expressed as

$$\underline{\boldsymbol{F}} = \frac{\partial \boldsymbol{x}}{\partial \boldsymbol{X}} = \frac{\partial \boldsymbol{\varphi}}{\partial \boldsymbol{X}} = \frac{\partial \boldsymbol{\varphi}}{\partial \boldsymbol{\chi}} \cdot \frac{\partial \boldsymbol{\chi}}{\partial \boldsymbol{X}} = \hat{\underline{\boldsymbol{F}}} \cdot \underline{\boldsymbol{R}}, \tag{3}$$

where $\hat{\underline{\boldsymbol{F}}}$ is the deformation gradient with respect to the reference configuration and $\underline{\boldsymbol{R}}$ contains the rigid body rotations from the initial to the reference configuration with $\det \underline{\boldsymbol{R}} = 1$.

The total Cauchy stress of the mixture is obtained by summing up all partial stress tensors of the constituents $\underline{\boldsymbol{\sigma}} = \sum_\alpha \underline{\boldsymbol{\sigma}}^\alpha$. Postulating that only volumetric stresses act on the water and the air constituent, their partial stress tensors read

$$\underline{\boldsymbol{\sigma}}^\alpha = -\phi^\alpha p_\alpha \underline{\boldsymbol{I}}, \quad \alpha = \mathrm{w},\, \mathrm{a} \tag{4}$$

with the macroscopic pore pressure p_α. The effective stress $\underline{\boldsymbol{\sigma}}'$ that is energy-conjugate to the rate of deformation of the solid matrix is obtained by

$$\underline{\boldsymbol{\sigma}}' = \underline{\boldsymbol{\sigma}} + B\left(S_{\mathrm{w}} p_{\mathrm{w}} + (1 - S_{\mathrm{w}}) p_{\mathrm{a}}\right) \underline{\boldsymbol{I}} \tag{5}$$

with the Biot's coefficient B and the degree of saturation $S_{\mathrm{w}} = \phi^{\mathrm{w}}/(1 - \phi^{\mathrm{s}})$. Please note that the fully saturated case is obtained for $S_{\mathrm{w}} = 1$. Subsequently, it is assumed that the air pressure is negligible $p_{\mathrm{a}} = 0$.

The continuum mechanical description and the corresponding balance principles for the multi-phase continua are derived based on the solid trajectory and the solid deformation mapping with respect to the reference configuration. The balance of linear momentum, which is the base for the solid step in the later described staggered solution, with respect to the reference configuration reads

$$\hat{\rho}\, \dot{\boldsymbol{v}} = \mathrm{Div}\, \hat{\underline{\boldsymbol{P}}} + \hat{\rho}\, \boldsymbol{b}. \tag{6}$$

Thereby, $\hat{\rho}$ is the density in the reference frame, volume loads are represented by $\boldsymbol{b}$, the divergence is $\mathrm{Div}\, \underline{\boldsymbol{A}} = \partial A_{ab}/\partial \chi_b$ and $\dot{\boldsymbol{v}}$ is the time derivative of the solid material velocity $\boldsymbol{v}\left(\boldsymbol{x}, t\right)$. The first Piola-Kirchhoff stress tensor with respect to to reference frame is obtained from $\hat{\underline{\boldsymbol{P}}} = J \underline{\boldsymbol{\sigma}} \cdot \hat{\underline{\boldsymbol{F}}}^{-T}$.

The balance of the pore water mass content in the solid skeleton, which is the base for the fluid step in the later described staggered solution, with respect to the reference frame is

$$\dot{M}^{\mathrm{w}} + \mathrm{Div}\, \hat{\boldsymbol{\omega}} = 0. \tag{7}$$

Thereby, $M^{\mathrm{w}} = J \phi^{\mathrm{w}} \rho_{\mathrm{w}}$ is the water mass content and $\hat{\boldsymbol{\omega}} = J \hat{\underline{\boldsymbol{F}}}^{-1} \cdot \boldsymbol{\omega}$ is the relative mass flow with respect to the reference frame based on the Eulerian relative mass flow $\boldsymbol{\omega} = \phi^{\mathrm{w}} \rho_{\mathrm{w}} (\boldsymbol{v}^{\mathrm{w}} - \boldsymbol{v})$, which is assumed to be Darcian. The corresponding finite element (FE) equations of the balance equations are obtained by applying Galerkin's method, including the constitutive relations, linearization and discretization, compare [2] for the fully saturated case.

2 Sequential solid-fluid solver

The mass balance equation as well as the balance of linear momentum depend both on the current deformation state $\boldsymbol{\varphi}$ and the pore water pressure p_{w}. To solve this coupled system of equations, a staggered solution procedure is applied.

The staggered solid-fluid-iteration starts with a solid step by evaluating the balance of linear momentum (Eq. (6)) to update the current deformation state $\boldsymbol{\varphi}$. Thereby three different split assumptions are studied for the solid step. In case of a drained split, the fluid mass content might change (drainage) while the pore water second Piola-Kirchhoff stress tensor $\hat{\underline{\boldsymbol{S}}}_{\mathrm{w}} = -JBS_{\mathrm{w}}p_{\mathrm{w}}\hat{\underline{\boldsymbol{F}}}^{-1} \cdot \hat{\underline{\boldsymbol{F}}}^{-T}$ remains constant during the solid step. At an undrained split, it is assumed that the pore water mass content does not change during the solid step. This condition is obtained by prescribing $\mathrm{Div}\,\hat{\boldsymbol{\omega}} = 0$, which finally leads to a prediction of the updated pore water pressure $p^{\star}$. The drained split assumption neglects the stiffness stemming from the presence of the pore water during the solid step and leads, thus, to an overestimation of the solid deformations that might cause oscillating or non-converging solid-fluid-iterations. In contrast, the undrained split assumption overestimates the stiffness stemming from the presence of the pore water during the solid step and leads, thus, to an underestimation of the solid deformations that might cause slowly converging solid-fluid-iterations. Therefore, a semi-drained split is studied as third case that is obtained by a modification of the undrained pore water predictor.

After the solid step, the pore water pressure p_{w} is updated by evaluating the mass balance equation (Eq. (7)). During the fluid step, the solid deformation is fixed. If the residual of the balance of linear momentum using the updated pore water pressure p_{w} is smaller than a prescribed tolerance, the solid-fluid-iteration is terminated. Otherwise, it restarts with a new solid step.

3 Coupled tire-soil-water interaction

To enable a realistic representation of tires rolling over a fully/partially saturated soft subground (soil), the developed poromechanical ALE formulation is implemented into the coupled tire-pavement computation scheme presented in [1]. Since, the tire and the pavement are simulated in different FE codes, this tire-pavement computation is organized by a program interface as staggered iteration between the FE ALE tire model and the FE ALE pavement model. The implementation of the staggered solid-fluid iteration scheme for the poromechanical ALE formulation into the staggered tire-pavement computation scheme demands for a hierarchical solution strategy, see Fig. 2, where the tire-pavement or rather the tire-soil iteration is the outer iteration loop, while the solid-fluid interaction is solved during an inner iteration loop at the pavement or soil computation.

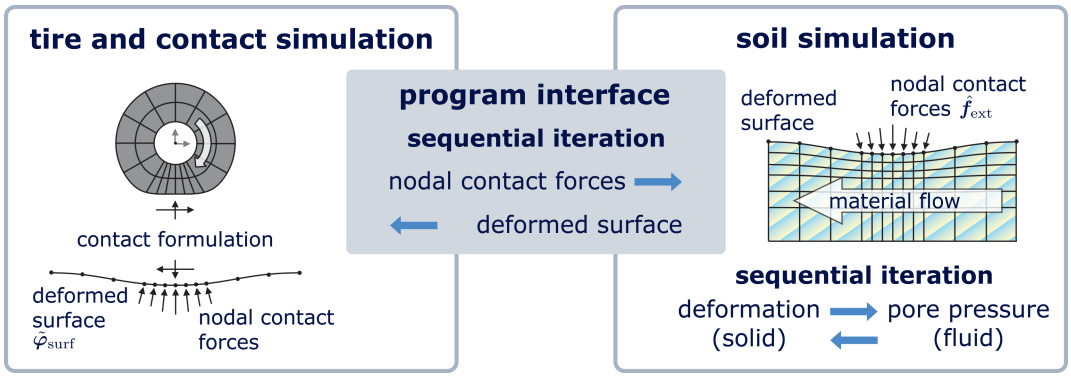

Figure 2. Hierarchical sequential coupling procedure for tire-soil interaction

This staggered tire-soil iteration scheme is applied, subsequently, for the computation of a hyperelastic truck tire loaded by 2 tons ($\hat{=}$19.62 kN) that is rolling over a fully saturated soil subground at different driving velocities. The solid soil material is represented by the hyperelastic Neo-Hookean model. The applied material parameters of the fully saturated soil are given in Tab. 1. As boundary conditions for the discretized FE model of the soil segment, all displacements at the bottom as well as the normal displacements at the lateral surfaces are fixed. Further, the pore pressure is zero at the whole top surface, while all other boundaries are undrained.

Table 1. Material parameters of fully saturated soil

solid	$\mu\,[\mathrm{kN/m^2}]$	$K\,[\mathrm{kN/m^2}]$	$K_\mathrm{s}\,[\mathrm{kN/m^2}]$	$B\,[-]$
	22 500	40 000	$4 \cdot 10^8$	1
fluid	$k\,[\mathrm{m^4/kNs}]$	$\hat{\phi}^\mathrm{w}\,[-]$	$K_\mathrm{w}\,[\mathrm{kN/m^2}]$	
	$3.06 \cdot 10^{-6}$	0.3	80 000	

The resulting distribution of the pore water pressure in the soil is shown in Figure 3 for two different speeds. As expected, the pore pressures are higher at larger speed, since the time for drainage is shorter in this case. Fig. 4 illustrates, additionally, the resulting surface displacements of the saturated soil along the driving lane for the two different speeds as well as for the interaction of the tire with a dry soil (without p_w). The displacements are largest in the dry case, since the solid phase has to carry the whole tire load. In case of the fully saturated soil, the pore water pressure increases at increasing speed. Thus, the solid effective stress and the solid displacements decrease at increasing speed.

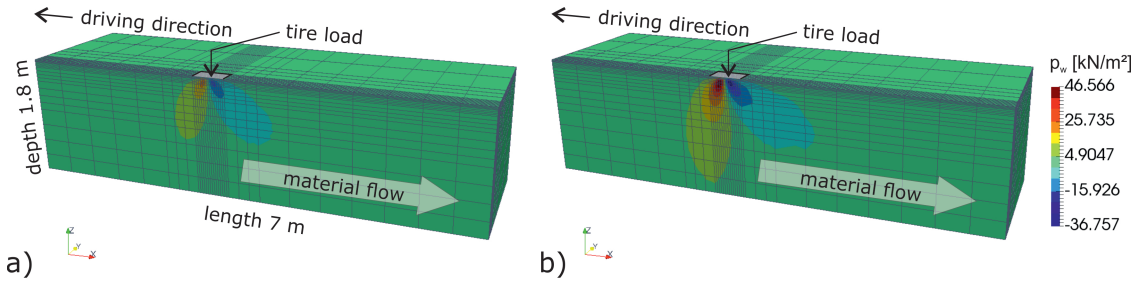

Figure 3. Pore water pressure in plane along driving lane for guiding velocity of a) $w_1 = 0.5\,\mathrm{m/s}$, b) $w_1 = 1\,\mathrm{m/s}$

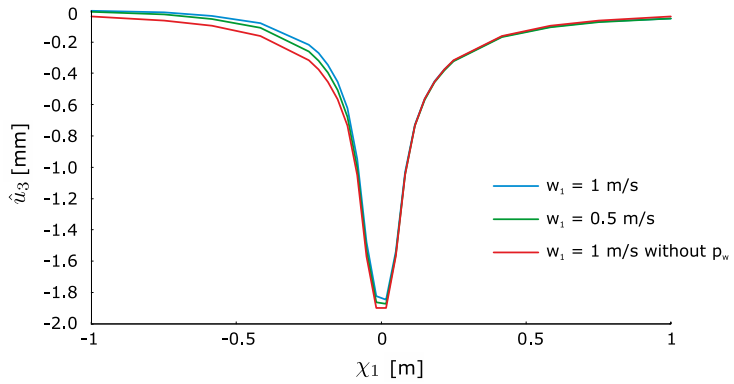

Figure 4. Vertical displacements of the surface along the driving lane for the three computation cases

Acknowledgments

The financial support of the German Research Foundation (DFG) of Research Unit FOR 2089 under grant KA 1163/30 is gratefully acknowledged.

References

[1] M. Kaliske, I. Wollny, R. Behnke, and C. Zopf. Holistic Analysis of the Coupled Vehicle-Tire-Pavement System for the Design of Durable Pavements. *Tire Science and Technology* 43 (2015), pp. 86–116.

[2] I. Wollny, W. Sun, and M. Kaliske. A hierarchical sequential ALE poromechanics model for tire-soil-water interaction on fluid-infiltrated roads. *International Journal for Numerical Methods in Engineering* 112 (2017), pp. 909–938.

Proceedings of the 8th GACM Colloquium on Computational Mechanics for Young Scientists from Academia and Industry August 28–30, 2019 in Kassel, Germany

Constitutive modelling of carbon fibre reinforced polymers for adhesively bonded cfrp-steel joints

Michael Donhauser[1] and Anton Matzenmiller*,[1]

[1]Institute of Mechanics, Dept. of Mechanical Engineering, University of Kassel, Mönchebergstr. 7, 34125 Kassel, Germany

Abstract. This contribution comprises the constitutive modelling and finite element failure analysis of adhesively bonded cfrp-steel joints under quasi-static loading with the focus on the modelling of the cfrp. A transversely isotropic material model is utilised for the elastic-brittle behaviour of the cfrp, where a nonlinear ansatz takes the axial shear behaviour into account. The inter-fibre failure and postcritical behaviour of the cfrp are modelled by Puck's failure criterion and a failure mode based anisotropic damage approach. Delamination is considered by means of an interface model with a bilinear traction-separation-law. The adhesive layer is characterised by the so-called Toughened-Adhesive-Polymer (TAPO) model, for elasto-plasticity and isotropic damage. An elasto-plastic material model is used for the steel components. For four of the six test cases, the numerical validation results under quasi-static loading show a good agreement with the test data.

1 Introduction

Today, material compounds with enhanced mechanical properties are made of carbon fibre reinforced polymers (cfrp) and steel components by means of adhesive joining. In order to optimise the structural strength of the material compound with the finite element method, material models must be used that capture the elastic and failure behaviour of each individual material accurately. Especially, the failure modelling of cfrp is a challenging task due to the complex failure mechanisms and the interaction of different failure modes causing ultimate fracture. In [6], material models, which are implemented in the commercial FE-software LS-DYNA, are used to perform FE-simulations for cfrp and adhesive-cfrp-steel joints that exhibit a simple stress state. The lack of capturing the nonlinear axial shear behaviour as well as the postcritical behaviour after a first ply failure, leads to improvable results. Therefore, in [7], a detailed model for the cfrp is developed, which captures the nonlinear axial shear behaviour, the intralaminar failure due to fibre and inter-fibre breakage, the postcritical behaviour after a first ply failure and the interlaminar failure i. e. delamination. The constitutive model of the cfrp is presented in this contribution.

2 Constitutive Modelling

2.1 Carbon Fibre Reinforced Polymer

The elastic material behaviour of the unidirectional layer (ud-layer), depicted in Fig. 1, is described by the transverse isotropic model. The model is formulated in the material coordinate system (x_1, x_2, x_3), where x_1 denotes the fibre direction. For the normal strain the strain-stress relation reads as

$$\begin{Bmatrix} \varepsilon_{11} \\ \varepsilon_{22} \\ \varepsilon_{33} \end{Bmatrix} = \begin{bmatrix} \frac{1}{E_1} & -\frac{\nu_{12}}{E_1} & -\frac{\nu_{12}}{E_1} \\ & \frac{1}{E_2} & -\frac{\nu_{23}}{E_2} \\ \text{sym.} & & \frac{1}{E_2} \end{bmatrix} \begin{Bmatrix} \sigma_{11} \\ \sigma_{22} \\ \sigma_{33} \end{Bmatrix} , \tag{1}$$

whereby E_1 is the Young's modulus in fibre direction, E_2 perpendicular to the fibre direction and ν_{12} is the Poisson's ratio in the coordinate direction x_1x_2. The transverse shear behaviour is described with the transverse shear modulus G_{23} by the linear ansatz:

$$\tau_{23} = G_{23}\gamma_{23} \quad \text{with} \quad G_{23} = \frac{E_2}{2(1+\nu_{23})} , \tag{2}$$

*Corresponding author: e-mail post-structure@uni-kassel.de, phone +49 (0)561 804 2043, fax +49 (0)561 804 2720

and the axial shear behaviour by the nonlinear ansatz with the model parameters c_0-c_3:

$$\tau_{1j}(\gamma_{1j}) = c_0 \tanh(c_1\ \gamma_{1j}) + c_2 \tanh(c_3\ \gamma_{1j}) \quad j = 2,3 \quad . \tag{3}$$

Failure model The intralaminar failure of the cfrp is divided into inter-fibre and fibre failure. In PUCK's exposure criterion, the normal stress σ_n and shear stress τ_{nt} and τ_{n1} acting on the potential fracture plane, which is inclined about the fracture angle θ_{fp} (see Fig. 1), are used to describe the inter-fibre failure in an ud-layer. For tensile loading ($\sigma_n \geq 0$) the exposure criterion reads as

$$f_E^+(\theta_{fp}) = \sqrt{\left(\frac{1}{R_\perp^{+A}} - \frac{p_{\perp\psi}^+(\theta_{fp})}{R_{\perp\psi}^A(\theta_{fp})}\right)^2 \sigma_n^2(\theta_{fp}) + \left(\frac{\tau_{nt}(\theta_{fp})}{R_{\perp\perp}^A}\right)^2 + \left(\frac{\tau_{n1}(\theta_{fp})}{R_{\perp\parallel}^A}\right)^2} + \frac{p_{\perp\psi}^+(\theta_{fp})}{R_{\perp\psi}^A(\theta_{fp})}\sigma_n(\theta_{fp}) = 1 \tag{4}$$

and for compressive loading ($\sigma_n < 0$) as

$$f_E^-(\theta_{fp}) = \sqrt{\left(\frac{\tau_{nt}(\theta_{fp})}{R_{\perp\perp}^A}\right)^2 + \left(\frac{\tau_{n1}(\theta_{fp})}{R_{\perp\parallel}^A}\right)^2 + \left(\frac{p_{\perp\psi}^-(\theta_{fp})}{R_{\perp\psi}^A(\theta_{fp})}\sigma_n(\theta_{fp})\right)^2} + \frac{p_{\perp\psi}^-(\theta_{fp})}{R_{\perp\psi}^A(\theta_{fp})}\sigma_n(\theta_{fp}) = 1\ . \tag{5}$$

In Eqs. (4)-(5) all quantities R^A are fracture resistances acting on the action plane A and all $p^\pm$ are slope parameters of failure envelopes, see [8] for details. The fracture stresses are functions of the global stress state and the fracture angle θ_{fp}:

$$\sigma_n(\theta_{fp}) = c^2\sigma_{22} + s^2\sigma_{33} + 2cs\tau_{23}, \quad \tau_{nt}(\theta_{fp}) = -sc\sigma_{22} + sc\sigma_{33} + (c^2 - s^2)\tau_{23}, \quad \tau_{n1}(\theta_{fp}) = c\tau_{12} + s\tau_{13} \tag{6}$$

with $c = \cos(\theta_{fp})$ and $s = \sin(\theta_{fp})$. The fibre stress σ_{11} does not influence the inter-fibre failure and is therefore neglected in Eq. (6). In order to evaluate the exposure criterion, it is always necessary to determine the fracture angle θ_{fp} for a given stress state $(\sigma_{22}, \sigma_{33}, \tau_{12}, \tau_{23}, \tau_{13})$. The fracture angle is defined as that one, for which the exposure criterion reaches the maximum value. Hence, for tension ("+") or compression ("-") we solve the corresponding nonlinear scalar equation

$$\frac{\partial f_E^\pm(\theta_{fp})}{\partial \theta_{fp}} = 0 \qquad \text{with} \qquad \theta_{fp} \in [-90°, 90°] \tag{7}$$

using Newton's method. The obtained fracture angle from (7) and corresponding stress state from (6) are used to evaluate the exposure criterion (4) or (5), while an inter-fibre failure occurs if $f_E^\pm \geq 1$.

The fibre failure under tensile loading is taken into account by the maximum stress criterion

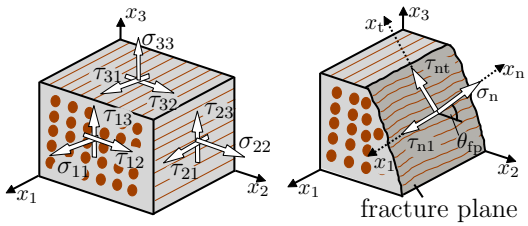

Figure 1. Ud-layer with stress state on fracture plane

$$f_{fb} = \frac{\sigma_{11}}{R_\parallel} = 1 \quad \text{with} \quad R_\parallel : \text{tensile fibre strength}\ . \tag{8}$$

Post-critical behaviour In a multidirectional laminate, first ply failure due to an inter-fibre breakage does not lead to abrupt loss of load-bearing. The load-bearing capacity is still remaining, but with a reduced laminate stiffness. In this contribution, a failure mode based anisotropic damage approach with six damage variables is applied to capture the stiffness reduction according to [4]. A 3×3 damage operator with the damage variables ω_{11}, ω_{22} and ω_{33} arranged along the major diagonal, is introduced and applied to Eq. (1) in order to obtain the compliance relationship in terms of the damage variables:

$$\begin{Bmatrix} \varepsilon_{11} \\ \varepsilon_{22} \\ \varepsilon_{33} \end{Bmatrix} = \begin{bmatrix} \frac{1}{(1-\omega_{11})E_1} & -\frac{\nu_{12}}{E_1} & -\frac{\nu_{13}}{E_1} \\ & \frac{1}{(1-\omega_{22})E_2} & -\frac{\nu_{23}}{E_2} \\ \text{sym.} & & \frac{1}{(1-\omega_{33})E_3} \end{bmatrix} \begin{Bmatrix} \sigma_{11} \\ \sigma_{22} \\ \sigma_{33} \end{Bmatrix}\ . \tag{9}$$

The proposed method of [5] is applied to the components of the minor diagonal in Eq. (9) to retain the symmetry of the compliance matrix. In case of damage, the linear and nonlinear ansatz of the shear behaviour in Eq. (2) and (3) reads as:

$$\tau_{23} = (1-\omega_{23})G_{23}\gamma_{23}\ , \qquad \tau_{1j} = (1-\omega_{1j})(c_0 \tanh(c_1\ \gamma_{1j}) + c_2 \tanh(c_3\ \gamma_{1j})) \quad j = 2,3 \quad . \tag{10}$$

The Eqs. (4),(5) and (8) are used to define the loading functions

$$f_2^\pm = f_E^\pm - r_2^\pm = 0 \quad \text{and} \quad f_1 = f_{fb} - r_1 = 0 \tag{11}$$

with the variable thresholds

$$r_2^{\pm} = \max\Big[1, \max_{-\infty<\tau<t}\big(f_{\mathrm{E}}^{\pm}\big)\Big] \quad \text{and} \quad r_1 = \max\Big[1, \max_{-\infty<\tau<t}\big(f_{\mathrm{fb}}\big)\Big] \tag{12}$$

due to inter-fibre and fibre failure, respectively. For $f_2^{\pm} < 0$ and $f_1 < 0$ there is no damage evolution, thus $r_2^{\pm} = 1$ and $r_1 = 1$. With the damage growth functions for the corresponding failure mode

$$\phi_2^{\pm} = 1 - \exp\left[\frac{1-(r_2^{\pm})^{m_2}}{m_2}\right] \quad \text{and} \quad \phi_1 = 1 - \exp\left[\frac{1-(r_1)^{m_1}}{m_1}\right] \tag{13}$$

the damage evolution is defined as

$$\boldsymbol{\omega} = \phi_1 \mathbf{l} + \phi_2 \mathbf{q} \tag{14}$$

with $\boldsymbol{\omega} = [\omega_{11}, \omega_{22}, \omega_{33}, \omega_{12}, \omega_{23}, \omega_{13}]^{\mathsf{T}}$, $\mathbf{l} = [1, l_{22}, l_{33}, l_{12}, l_{23}, l_{13}]^{\mathsf{T}}$ and $\mathbf{q} = [0, q_{22}, q_{33}, q_{12}, q_{23}, q_{13}]^{\mathsf{T}}$. In Eq. (13), the quantities m_2 and m_1 denote the strain softening parameters. The components of $\mathbf{l}$ and $\mathbf{q}$ in Eq. (14) are parameters, which enable the coupling of the individual damage variables. In brittle multidirectional laminates, which are considered in this contribution, abrupt and ultimate failure occurs, when the fibre failure criterion in Eq. (8) is reached, thus ϕ_1 in Eq. (14) is zero. The presented constitutive equations for the cfrp are implemented as a user defined material model in LS-DYNA.

Delamination In order to describe the delamination process, interface elements are used in combination with the interface model Cohesive-Mixed-Mode (*Mat_138) from LS-DYNA, which includes a bilinear traction-separation-law and a quadratic mixed mode criterion according to [3]. The model parameters are identified from test data of fracture mechanical DCB- and ENF-specimens.

2.2 Adhesive Layer and Steel Components

The adhesive layer is characterised by the so-called TAPO-model, which is an elasto-plastic model with damage. More details about this material model can be found in [1] and [2].
The material behaviour of the steel is described by the simple model Piecewise-Linear-Plasticity (*Mat_24) from LS-DYNA together with stress-strain test data of the steel at hand. The element deletion method is applied, when the equivalent strain reaches the defined failure value.

3 Validation

The FE-simulation and failure analysis is carried out for the so-called thin shear specimen, depicted in Fig. 2. The specimen consists of a steel adherend and a quasi-isotropic laminate, which are bonded together by the adhesive layer. The quasi-isotropic laminate has 13 plies and an overall thickness of 2 mm. The thin shear specimen is tested for three adhesive thicknesses (d_{k}=0.3, 1 and 2 mm) and two laminate orientation (0° and 90°) in order to investigate their influence on the failure behaviour. For the laminate orientation of 0° the layup configuration is [0°,90°,+45°,-45°,0°,90°,+45°,90°, 0°,-45°,+45°,90°,0°], whereby the fibre direction of the top layer, which is attached to the adhesive, coincides with the loading direction, see Fig 2. In the case of the 90° orientation, the fibres in the top layer are arranged perpendicular to the loading direction leading to the layup configuration [90°,0°,-45°,+45°,90°,0°,-45°,0°,90°,+45°,-45°,0°,90°]. Each of the thirteen single layers is discretised by a three-dimensional solid element in the FE-model, where interface elements are placed between adjacent layers to take delamination into consideration. In the FE-simulation, failure can occur in the adhesive layer, the steel component or in the laminate in form of a fibre breakage, an inter-fibre fracture or a delamination. The material parameters are identified from test data of individual specimens of each material. The identification procedure and all identified parameters are documented in [7] in detail. In Fig. 3, the numerical and experimental results are shown for a quasi-static loading ($v = 1\,\mathrm{mm/min}$). In four of six test cases the numerically obtained stress-strain-curves correspond well with the experiments, see Fig. 3 a, b, d, f. The structural strength is slightly and the failure strain strongly underestimated for the both other cases (Fig. 3 c, e). For the laminate orientation of 90° in the test and in the simulation, failure occurs always

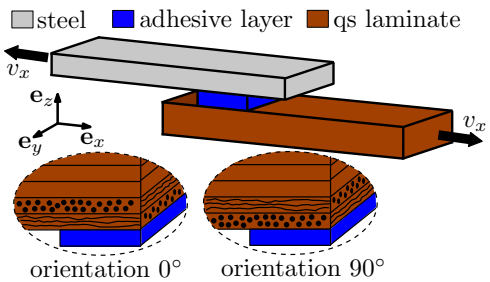

Figure 2. Sketch of thin shear specimen with different laminate orientations

in the laminate due to delamination between the first and second ply caused by an preceding inter-fibre breakage in the top layer, see Fig 3 for instance. In the test, failure in the adhesive layer occurs for the laminate orientation of 0° and the adhesive thickness of $d_k = 0.3$ and 1 mm. The FE-calculation predicts the correct failure mode for the thinner adhesive layer. The test results of the specimen with $d_k = 2$ mm and laminate orientation 0° shows mixed failure in the adhesive layer and laminate, where the simulation predicts only failure in the laminate. The validation results under quasi-static loading show that with the presented method four of the six force-displacement-curves with the corresponding failure mode are reproduced well. In both other cases (Fig. 3 c, e), the deviation in the force-displacement-curves is caused by premature delamination in the FE-simulation, which will be part of forthcoming investigations.

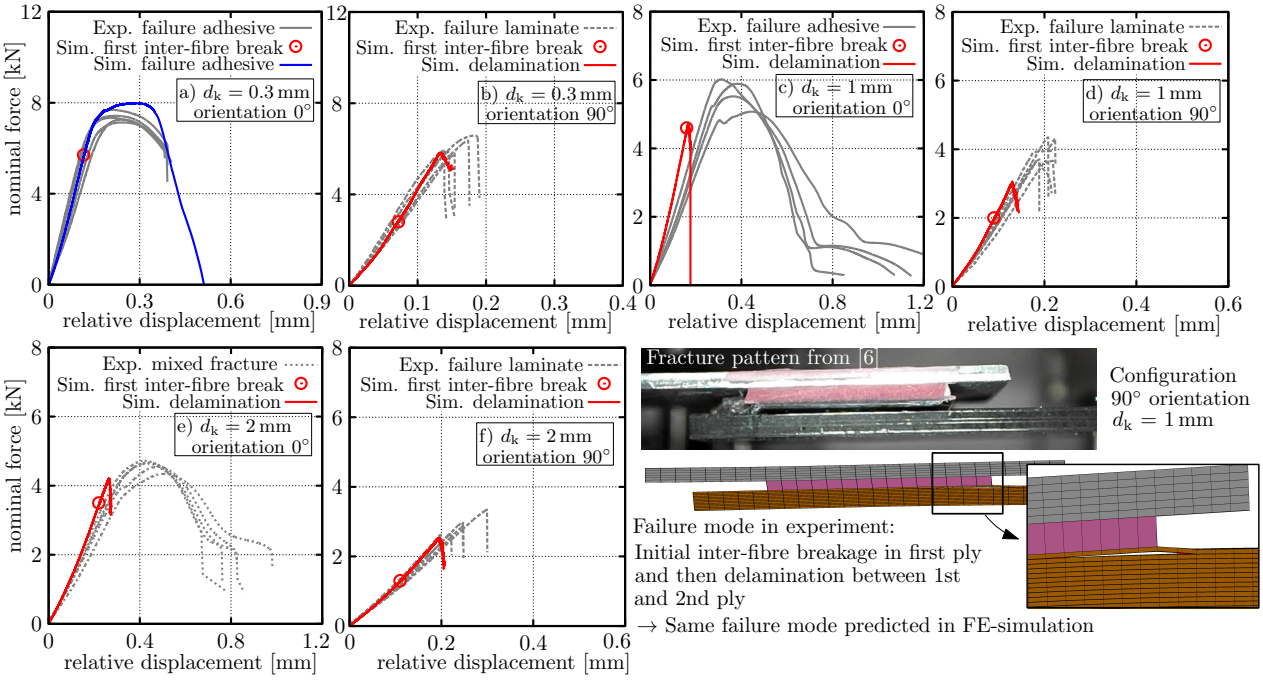

Figure 3. Validation results of adhesively bonded thin shear specimen with steel adherend and quasi-isotropic laminate

References

[1] W. Böhme, M. Brede, F. Burbulla, C. Fehrenbach, O. Hesebeck, S. Kilchert, J. Lienhard, R. Mahnken, S. Marzi, A. Matzenmiller, Michael May, D. Memhard, N. Nörenberg, L. Reissig, and H. Voß. *Robustheit und Zuverlässigkeit der Berechnungsmethoden von Klebverbindungen mit hochfesten Stahlblechen unter Crashbedingungen.* Abschlussbericht, FOSTA-Forschungsvereinigung. 2013.

[2] M. Brede, F. J. Heise, M. Schlimmer, A. Matzenmiller, R. Mahnken, O. Hahn, K. Dilger, P. Gumbsch, K. Thoma, and O. D. Hennemann. *Methodenentwicklung zur Berechnung von höherfesten Stahlklebverbindungen des Fahrzeugbaus unter Crashbelastung.* Abschlussbericht, FOSTA-Forschungsvereinigung. 2008.

[3] Pedro P Camanho and Carlos G Dávila. Mixed-mode decohesion finite elements for the simulation of delamination in composite materials (2002).

[4] M. Chatiri and A. Matzenmiller. A Damage-Mode Based Three Dimensional Constitutive Model for Fibre-Reinforced Composites. *CMC: Computers, Materials & Continua* 35.3 (2013), pp. 255–283.

[5] A. Matzenmiller, J. Lubliner, and R. L. Taylor. A constitutive model for anisotropic damage in fiber-composites. *Mechanics of materials* 20.2 (1995), pp. 125–152.

[6] G. Meschut, M. Wünsche, A Matzenmiller, and M. Schmerbauch. *Beanspruchungs- und fertigungsgerechtes Kleben von Faserverbundkunststoffen im Multi-Material-Design.* Abschlussbericht, Foschungsvereinigung Stahlanwendung FOSTA. 2015.

[7] G. Meschut, K. Henkel, A Matzenmiller, and M. Donhauser. *Experimentelle und numerische Untersuchungen zum Versagensverhalten von kalt ausgehärteten Stahl-FVK-Klebverbindungen unter schlagartiger Belastung.* Abschlussbericht, Forschungsvereinigung DECHEMA. 2018.

[8] A. Puck. *Festigkeitsanalyse von Faser-Matrix-Laminaten: Modelle für die Praxis.* Hanser, 1996.

Proceedings of the 8th GACM Colloquium on Computational Mechanics for Young Scientists from Academia and Industry August 28–30, 2019 in Kassel, Germany

Crack patterns at bi-material joints: An asymptotic coupled stress and energy approach

Julian Felger *[1] and Wifried Becker[1]

[1]Technische Universität Darmstadt

Abstract. The effective strength of bi-material joints depends significantly on the elastic material properties of the constituents as well as on geometrical parameters such as the orientation of the material interface. In this work, a scarf joint specimen made of a polymer foam and aluminum is investigated using a four-point bending specimen test with variable scarf angle. The critical load at failure is determined employing a coupled stress and energy criterion relying on the concept of finite fracture mechanics where joint failure is defined as spontaneous crack formation. Since a variety of potential crack configurations is admissible, an efficient asymptotic model is employed reducing numerical effort significantly. Failure predictions according to the asymptotic approach are compared to numerical reference data and experimental findings from literature.

Introduction

The use of lightweight design concepts employing composite materials such as sandwich structures and adhesively bonded joints are frequently used in modern engineering structures. The material mismatch, however, induces highly localised stress concentrations triggering crack initiation and subsequent catastrophic failure of the structure. Hence, a detailed analysis of such stress raisers combined with a physically sound failure criterion is required to reliably assess the structural integrity. Stress-based approaches evaluate a stress criterion in a certain distance from the stress concentration [23] whereas classical fracture mechanics approaches presume the existence of an inherent flaw [20]. These criteria, however, rely on an empirical length which depends on material as well as on geometrical parameters of the structure. In case of sharp notches or multi-material junctions failure criteria based on a critical value of the generalised stress intensity factor (GSIF) have been applied [13]. This approach displays the drawback that the critical GSIF does not represent a material property but depends on the structure's geometry, for instance the notch opening-angle [2] or the interface orientation in scarf joints [12].

In the present work, crack nucleation in a bi-material scarf joint is investigated employing a coupled stress and energy criterion proposed by Leguillon [9]. The coupled criterion states that an energy as well as a stress criterion must be fulfilled simultaneously forming a necessary and sufficient condition for fracture. Following the concept of finite fracture mechanics for brittle failure as introduced by Hashin [7], the process of crack initiation is modelled as an instantaneous formation of a finite sized crack. In contrast to classical linear-elastic fracture mechanics, the finite crack length Δa enters the problem as a new unknown. Employing the coupled criterion allows for calculating the a-priori unknown finite crack length Δa as well as the load at crack onset. Only material strength and fracture toughness as fundamental material quantities enter the coupled criterion and no empirical length parameter is required. The coupled criterion has been applied for strength predictions of numerous situations such as sharp V-notches [24], rounded notches [11], open-hole plates [3, 4, 16, 22], adhesively bonded joints [6, 18] and has been used to predict the nucleation of anticracks to model snow slab avalanche [15]. A review of finite fracture mechanics can be found in [21]. In the present case of a bi-material scarf joint, multiple competing crack configurations exist. Since all admissible crack configurations have to be considered, a high numerical effort is needed in order to evaluate the coupled criterion. Thus, an asymptotic approach is followed combining the method of complex potentials with the method of matched asymptotic expansions [8, 10]. This ultimately forms a semi-analytical framework allowing for efficiently model crack formation triggered by the singularity at the bi-material notch. The resulting predictions of failure load, location of crack

*Corresponding author: felger@fsm.tu-darmstadt.de ORCID iD: ORCID (optional)

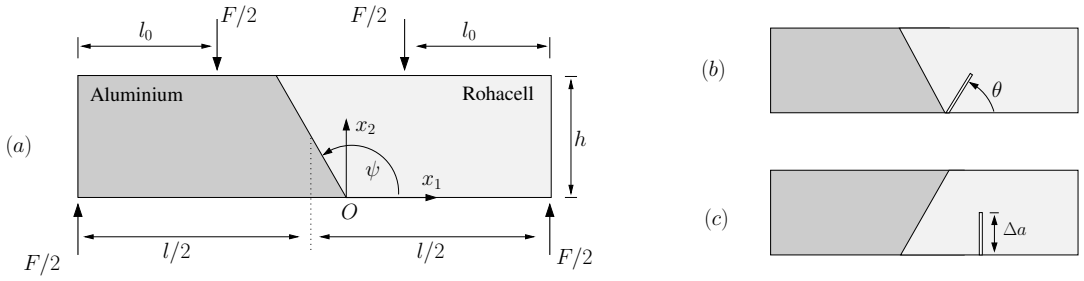

Figure 1. Bi-material scarf joint under four-point bending loading with an aluminum adherend on the left hand side and a Rohacell adherend on the right hand side as used in [14]. (a) Uncracked scarf joint configuration with interface angle ψ, height $h = 40$mm, thickness $t = 40$mm and lengths $l_0 = 150$mm, $l = 445$mm. (b) Notch induced failure mode. (c) Bending failure mode.

onset and angle of crack initiation are discussed in detail and compared to experimental findings from literature [14].

1 Failure model: the coupled stress and energy criterion

Consider a bi-material scarf joint under four-point bending loading as depicted in Fig. 1(a). The joint consists of a Rohacell 51 foam (material data according to [1]) and an aluminium adherend ($E_{\mathrm{A}} = 70$ GPa, $\nu_{\mathrm{A}} = 0.3$). Only cohesive failure of Rohacell is considered. The elastic contrast between both adherends induces mathematical singular stresses at the bi-material point O. Hence, it is assumed that cracks might emanate from O as show in Fig. 1(b). However, the constraint imposed by a small interface angle may also lead to crack initiation at a certain distance from the bi-material point as depicted in Fig. 1(c). The situation which ultimately occurs is related to the smallest failure load F_{f} and will be determined by the underlying failure model. The coupled criterion requires a stress criterion to be fulfilled along the potential crack path Γ_{C}. As stress criterion, a quadratic interaction law of the form

$$f = \sqrt{\left(\frac{\sigma_{nn}}{\sigma_{\mathrm{c}}}\right)^2 + \left(\frac{\tau_{nt}}{\tau_{\mathrm{c}}}\right)^2} \geq 1, \quad \text{along} \quad \Gamma_{\mathrm{C}}, \tag{1}$$

is employed accounting for mixed-mode conditions. In addition, an energetic criterion must be satisfied for crack onset to occur. The energy criterion is based on the energy balance and may be written as

$$-\frac{\Delta\Pi}{\Delta a} = \bar{\mathcal{G}} \geq \mathcal{G}_{\mathrm{c}}. \tag{2}$$

Here, $\bar{\mathcal{G}}$ is denoted as incremental energy release rate. The resulting failure load F_{f} is defined as the minimum load F such that both criteria are fulfilled simultaneously:

$$F_{\mathrm{f}} = \min_{\Delta a,\theta,F} \left\{ F \;\middle|\; f\left(\sigma_{ij}\right) \geq 1 \text{ along } \Gamma_{\mathrm{C}} \quad \text{and} \quad \bar{\mathcal{G}} \geq \mathcal{G}_{\mathrm{c}} \right\}. \tag{3}$$

Solving Eq. (3) finally yields the failure load F_{f}, the crack length Δa and the crack initiation angle θ.

2 Asymptotic expansion of stresses and incremental energy release rate

The stress field in the vicinity of the notch-tip can be expressed in form of a coordinate expansion with respect the distance r:

$$\boldsymbol{\sigma}(r,\phi) = K_1 r^{\lambda_1 - 1}\boldsymbol{\sigma}_1(\phi) + K_2 r^{\lambda_2 - 1}\boldsymbol{\sigma}_2(\phi) + \overline{K}_2 r^{\overline{\lambda}_2 - 1}\overline{\boldsymbol{\sigma}}_2(\varphi) + o(r^{\mathrm{Re}[\lambda_2 - 1]}), \quad \text{as} \quad r \to 0. \tag{4}$$

Here, λ_i are characteristic exponents defining the behaviour of the stresses in radial direction, $\boldsymbol{\sigma}_i(\phi)$ are eigenfunctions depending only on the circumferential coordinate, K_i represent the generalised stress intensity factors (GSIFs) and $\overline{(\cdot)}$ is the complex conjugate of a quantity. The exponents λ_i as well as the eigenfunctions are determined analytically using the complex potential method and GSIFs are calculated by means of a path independent integral, see [5, 10, 17] for more details. Assuming the crack length

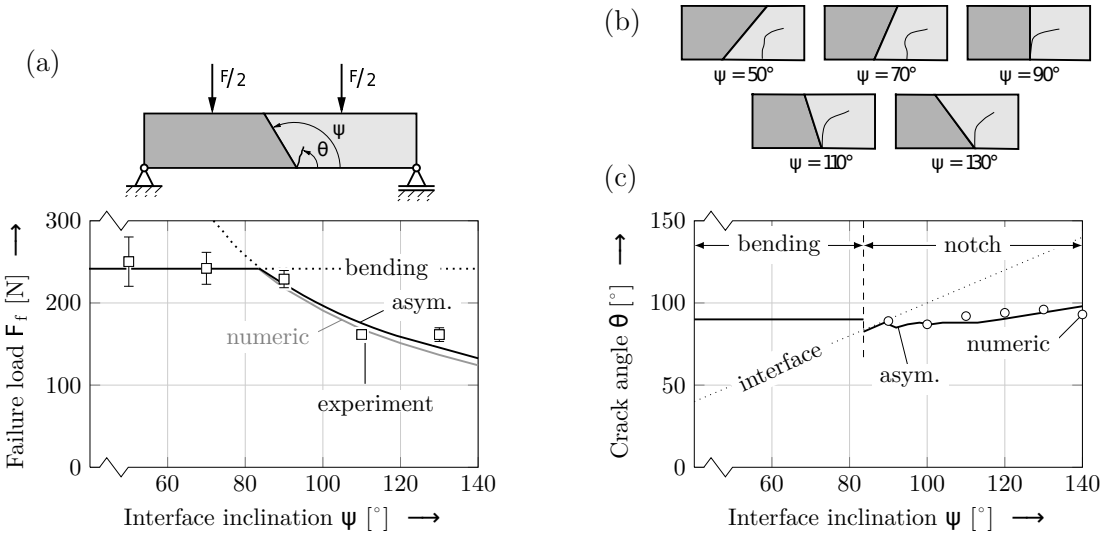

Figure 2. Failure of Aluminum-Rohacell scarfed joints with respect the scarf angle ψ. (a) Comparison between predicted failure loads F_f according to the asymptotic approach and numerical reference data as well as experimental data. (b) Schematic of experimentally observed crack paths according to [14]. (c) Predicted the crack initiation angles θ.

Δa to be small compared to a characteristic structural length, that is the beams' height h, the crack length can be understood as a small perturbation parameter. Using the method of matched asymptotic expansions allows for deriving a series expansion of the incremental energy release rate for small values of crack length, cf. [5, 8]:

$$\bar{\mathcal{G}} = K_1^2 \Delta a^{2\lambda_1 - 1} A_{11} + 4\mathrm{Re}\left[K_1 K_2 A_{12} \Delta a^{\lambda_1 + \lambda_2 - 1}\right] + o\left(\Delta a^{\lambda_1 + \lambda_2 - 1}\right), \quad \text{as} \quad \Delta a \to 0. \tag{5}$$

The numerical scaling coefficients A_{ij} depend on the interface angle ψ and are computed numerically, cf. [5]. Note that only two finite element analyses for each interface angle are necessary to determine the quantities K_1, K_2, A_{11}, A_{21}. In contrast, following a purely numerical approach numerous finite element analyses of the cracked configuration must be carried out to calculate the incremental energy release in terms of the unknown crack length. The derived expansions in Eq. (4) and Eq. (5) serve as a basis to efficiently solve the optimisation problem in Eq. (3). Note, that the second-order terms in the asymptotic expansion of stresses and energy, respectively, must be taken into account in the present case to yield an adequate approximation and accurate failure predictions.

3 Results and discussion

The failure load F_f of the scarf joint specimen under four-point bending loading is depicted in Fig 2(a) with respect to the interface inclination defined by the angle ψ. For an interface inclination exceeding 85°, the initiating cracks emanate from the bi-material notch. In this region, failure loads depend significantly on the interface orientation and the joint strength decreases with increasing values of ψ. The asymptotic approach yields accurate predictions compared to the experimental results with a maximum relative error of 9%. Moreover, the relative error between asymptotics and a purely numerical reference solution is smaller than 6.6%. According to the predictions, cracks tend to initiate perpendicularly to the joints edge which is reflected by the experiments, cf. 2(b) and 2(c). Reducing the interface angle below 85° leads to a transition from notch induced failure to a bending failure mode. Here, cracks initiate vertically in a certain distance away from the notch tip and failure loads are only hardly sensitive to ψ. To tackle the problem of bending failure using the coupled criterion, the stress distribution is modelled according to the elementary Euler–Bernoulli beam theory and the corresponding incremental energy release rate can be calculated by means of an empirical relation given in [19].

4 Conclusion

In this work, failure of a bi-material scarf joint under four-point bending has been investigated by means of a coupled stress and energy criterion. Depending on the material interface orientation, two distinct failure mechanisms have been observed, that is, notch induced failure and bending failure, respectively. Bending failure is characterised by crack onset within the Rohacell foam in a certain distance from the bi-material notch and failure loads are independent of the interface orientation. In contrast, for sufficiently large interface angles, crack nucleation is induced by the singular stress field at the notch tip and the effective joint's strength depends significantly on the interface orientation. For notch induced failure, the use of asymptotics enabled an efficient solution of the optimization problem and has led to a significant reduction of computational effort compared to a fully numerical treatment. Taking higher order terms into account, accurate predictions of experimentally observed failure loads have been achieved with a relative error smaller than 7%.

References

[1] M. Burman. PhD thesis. KTH, Stockholm, 1998.

[2] M. L. Dunn, W. Suwito, and S. Cunningham. *International Journal of Solids and Structures* 34.29 (1997), pp. 3873–3883.

[3] J. Felger, N. Stein, and W. Becker. *Engineering Fracture Mechanics* 182 (2017), pp. 621–634.

[4] J. Felger, N. Stein, and W. Becker. *International Journal of Solids and Structures* 122 (2017), pp. 14–24.

[5] J. Felger, P.L. Rosendahl, D. Leguillon, and W. Becker. *International Journal of Solids and Structures* 164 (2019), pp. 191–201.

[6] J. Felger, N. Stein, C. Frey, and W. Becker. *Composite Structures* 208 (2019), pp. 546–556.

[7] Z. Hashin. *Journal of the Mechanics and Physics of Solids* 44.7 (1996), pp. 1129–1145.

[8] D Leguillon. *European Journal of Mechanics-A/Solids* 12.1 (1993), pp. 33–51.

[9] D. Leguillon. *European Journal of Mechanics-A/Solids* 21.1 (2002), pp. 61–72.

[10] D. Leguillon and E. Sanchez-Palencia. John Wiley & Sons, Inc., 1987.

[11] D. Leguillon and Z. Yosibash. *International Journal of Fracture* 122.1-2 (2003), pp. 1–21.

[12] Z. Qian and A.R. Akisanya. *Acta Materialia* 46.14 (1998), pp. 4895–4904.

[13] E.D. Reedy and T.R. Guess. *International Journal of Solids and Structures* 30.21 (1993), pp. 2929–2936.

[14] S. Ribeiro-Ayeh and S. Hallström. *Engineering Fracture Mechanics* 70.12 (2003), pp. 1491–1507.

[15] P. L. Rosendahl and P. Weißgraeber. *The Cryosphere Discussions* (2019).

[16] P. L. Rosendahl, P. Weißgraeber, N. Stein, and W. Becker. *International Journal of Solids and Structures* 113 (2017), pp. 10–23.

[17] G.B. Sinclair, M. Okajima, and J.H. Griffin. *International Journal for Numerical Methods in Engineering* 20.6 (1984), pp. 999–1008.

[18] N. Stein, P. Weißgraeber, and W. Becker. *Composite Structures* 133 (2015), pp. 707–718.

[19] H. Tada, P. Paris, and G. Irwin. *New York: ASME Press* 2 (2000).

[20] M.E. Waddoups, J.R. Eisenmann, and B.E. Kaminski. *Journal of Composite Materials* 5.4 (1971), pp. 446–454.

[21] P. Weißgraeber, D. Leguillon, and W. Becker. *Archive of Applied Mechanics* 86.1 (2016), pp. 375–401.

[22] P. Weißgraeber, J. Felger, D. Geipel, and W. Becker. *European Journal of Mechanics-A/Solids* 55 (2016), pp. 192–198.

[23] J.M. Whitney and R.J. Nuismer. *Journal of Composite Materials* 8.3 (1974), pp. 253–265.

[24] Z. Yosibash, E. Priel, and D. Leguillon. *International Journal of Fracture* 141.1-2 (2006), pp. 291–312.

Proceedings of the 8th GACM Colloquium on Computational Mechanics for Young Scientists from Academia and Industry August 28–30, 2019 in Kassel, Germany

Hyperelastic adhesive joints: from crack nucleation to ultimate failure

Philipp L. Rosendahl * [1], Yves Staudt[2], Alexandra P. Schneider[1], Jens Schneider[3] and Wilfried Becker[1]

[1]Technische Universität Darmstadt, Fachgebiet Strukturmechanik, Franziska-Braun-Str. 7, 64287 Darmstadt

[2]Ingenieurbüro Bräuer und Späh, Ludwig-Beck-Str. 8, 68163 Mannheim

[3]Technische Universität Darmstadt, Institute of Structural Mechanics and Design, Franziska-Braun-Str. 3, 64287 Darmstadt

Abstract. The present analysis proposes a mixed-mode failure model for crack initiation in nonlinear elastic materials. Characterized in independent experiments, the model is used to determine critical loads of hyperelastic adhesive bonds in both shear and tension dominated configurations. For any of the examined adhesive joint configurations the model predicts and explains size effects and agrees well with experimental findings. The present work demonstrates how a physical understanding of the failure processes in complex materials allows for predicting crack nucleation and the derivation of simple engineering tools.

Introduction

The unique molecular structure of silicones provides mechanical properties which render them excellent structural adhesives. However, at bi-material corners between adherends and adhesive stress singularities owing to geometrical and material discontinuities are present. In order to capture crack onset at these singularities, classical approaches such as stress-based criteria or fracture mechanics can only be applied using an additional length parameter.

In fact, many modern theories of fracture involve a material length scale, i.e., a parameter with the dimensions of a length. Among these nonlocal approaches there are stress-based methods such as point method (PM) and line method (LM) where stresses are evaluated either in a point-wise manner in a certain distance from a stress concentration [14] or averaged over a specific length [13]. Nonlocal approaches using fracture mechanics are the imaginary crack method (ICM) which examines the energy release rate at the tip of an assumed pre-existing crack [24] and the finite crack extension method (FCE) which averages the energy release rate over a finite crack extension [6]. Strain energy density (SED) methods either evaluate SED along rays from the crack tip [20] or averaged in a finite sized domain [8].

Different nonlocal approaches were successfully applied to hyperelastic materials. Clift et al. [3] evaluate stress criteria in relatively coarsely discretized finite element analyses (FEAs) of silicone bonds. When a fixed discretization is used in FEAs, the element size appears as a characteristic length scale implicitly. Ayatollahi at al. [1] are more specific in their use of a critical distance in rubbers. They evaluate an effective stretch criterion in a certain distance from notches and obtain good agreements with experiments. Berto [2] averages strain energy density (SED) in a finite volume around V-notches to predict crack initiation. Miehe and Schänzel [12] predict crack initiation in hyperelastic materials using the regularized phase-field approach. The models are able to describe experimental findings on hyperelastic materials adequately. Yet, the length parameter involved in all of the above approaches is not known a priori and lacks definite physical meaning. Pipes et al. [15], for instance, find a dependence of the critical distance on geometrical features which, hence, cannot be regarded a material constant.

Assuming the sudden nucleation of a finite sized crack introduces a length scale with clear physical meaning – the finite size of the initiated crack. In order to determine the finite crack size Leguillon [9] proposed requiring the simultaneous satisfaction of both a stress and an energy criterion as necessary and sufficient

*Corresponding author: rosendahl@fsm.tu-darmstadt.de ORCID iD: 0000-0002-6587-875X

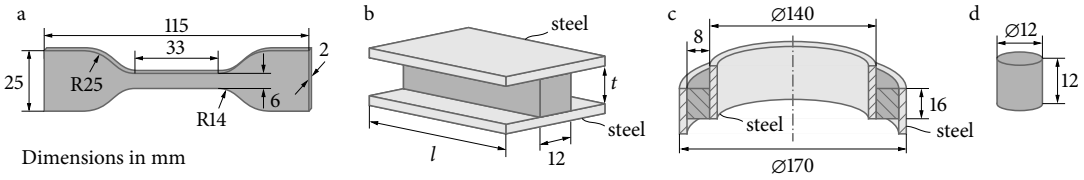

Figure 1. DOWSIL^{TM} 993 specimens used in the present work. a) Dumbbell specimen for uniaxial tests according to ASTM Standard D412-16, b) H-shaped specimen with adhesive thickness t and bond length l for simple shear and normal plate separation tests according to ETAG 002, c) tubular lap joint specimen for unnotched circular shear tests and d) cylindrical specimen for uniaxial compression tests according to ISO 7743. Please refer to Staudt at al. [21] for details on specimen manufacturing.

condition for crack nucleation. This so-called coupled stress and energy criterion provides excellent predictions for mixed-mode failure [5, 23], adhesive joint failure [7, 22], the formation of crack patterns [16], the failure of structures with elliptical open-holes [4, 25] and it can be linked to micromechanical material properties [11]. A comprehensive review is given by Weißgraeber et al. [26].

Common to all of the above finite fracture mechanics (FFM) studies are the assumptions of brittleness and linear-elastic material behavior. However, the physical background of the coupled criterion allows for a generalization of the method. For instance, Leguillon and Yosibash [10] revisit the assumption of brittleness and develop a theoretical FFM framework for quasi-brittle materials. The present work elaborates the question of material behavior. It proposes a formulation of finite fracture mechanics for hyperelastic materials. It uses the example of structural silicone adhesives. Yet, the presented methodology is applicable to crack initiation from stress concentrations in any nonlinear elastic material.

1 Failure model for brittle crack nucleation in hyperelastic materials

Consider DOWSIL^{TM} (a nearly incompressible hyperelastic two-component room temperature curing silicone) as an exemplary material. Despite large deformations prior to failure, no significant inelastic deformations are present and DOWSIL^{TM} 993 can be considered brittle. Fracture surfaces of a fully fractured specimen align perfectly because only the formation of the fracture surface dissipates energy.

Using the specimens shown in Figure 1, Staudt et al. [21] characterize the constitutive behavior of DOWSIL^{TM} 993 and Rosendahl et al. [17] develop a strain-based mixed-mode failure criterion for the hyperelastic bulk material. Independent fracture toughness measurements by Rosendahl et al. [18] together with this bulk material failure criterion allow for the derivation of a coupled strain and energy failure model for corner-induced crack nucleation in notched specimens as proposed by Rosendahl et al. [19].

The criterion assumes the instantaneous formation of a finite sized crack at a critical load. It requires the simultaneous satisfaction of two necessary conditions: The structure must be overloaded in a finite domain and the energy release of a finite crack must suffice. The energy condition requires the incremental energy release rate $\overline{\mathcal{G}}$ to exceed the material's fracture toughness

$$\overline{\mathcal{G}}(\Delta A) = -\frac{\Delta \Pi}{\Delta A} \geq \mathcal{G}_{\mathrm{c}}, \tag{1}$$

where $\Delta\Pi$ is the change in total potential energy of the structure with a crack increment of size ΔA. The nonlinear elastic adhesive is assumed overloaded when an equivalent strain averaged over the entire potential crack surface $\overline{\varepsilon}_{\mathrm{eq}}(\Delta A)$ exceeds a critical threshold

$$\overline{\varepsilon}_{\mathrm{eq}}(\Delta A) = \frac{1}{\Delta A} \int_{\Delta A} \varepsilon_{\mathrm{eq}}(\mathbf{x}) \mathrm{d}A \ \geq \ \varepsilon_{\mathrm{c}}. \tag{2}$$

The equivalent strain function $\varepsilon_{\mathrm{eq}}$ must be capable of describing bulk material failure under complex loads at any given location $\mathbf{x}$. Using the second and third invariants $II'_{\boldsymbol{\varepsilon}}$ and $III'_{\boldsymbol{\varepsilon}}$ of the deviator of the

spatial Hencky strain tensor $\boldsymbol{\varepsilon}^{\dagger}$, we obtain an equivalent strain function with the required properties:

$$\varepsilon_{\mathrm{eq}}(\mathbf{x}) = \sqrt{2\mathit{II}'_{\boldsymbol{\varepsilon}}(\mathbf{x})}\cos\left[\beta\frac{\pi}{6} - \frac{1}{3}\arccos\left(\alpha\,\frac{3\sqrt{3}}{2}\,\frac{\mathit{III}'_{\boldsymbol{\varepsilon}}(\mathbf{x})}{\mathit{II}'_{\boldsymbol{\varepsilon}}(\mathbf{x})^{3/2}}\right)\right], \tag{3}$$

where α and β are shape parameters. For plane problems with through-thickness cracks and out-of-plane width w we obtain $\Delta A = w\Delta a$ and the coupled criterion reads

$$\overline{\varepsilon}_{\mathrm{eq}}(\Delta a) \geq \varepsilon_{\mathrm{c}} \quad \wedge \quad \overline{\mathcal{G}}(\Delta a) \geq \mathcal{G}_{\mathrm{c}}. \tag{4}$$

Rosendahl et al. [17] report $\alpha = 0.86, \beta = 1.12$ and $\varepsilon_{\mathrm{c}} = 1.47 \pm 0.10$ for DOWSIL$^{\mathrm{TM}}$ 993. Fracture toughness measurements by Rosendahl et al. [18] yield $\mathcal{G}_{\mathrm{c}} = 4.22 \pm 0.60\,\mathrm{N/mm}$.

2 Prediction of structural failure

In order to validate the failure model, we tested 77 H-shaped DOWSIL$^{\mathrm{TM}}$ 993 specimens under simple shear loading, performed normal plate separation tests of 7 H-shaped specimens and circular shear tests of 4 tubular lap joints. Exemplary results are shown in Figure 2.

Figures 2a and b compare predictions of the FFM failure model to measured failure loads of simple shear specimens of out-of-plane width $w = 12\,\mathrm{mm}$ and lengths $l = 50\,\mathrm{mm}$ and $l = 100\,\mathrm{mm}$, respectively. Experimental data is indicated as mean and standard deviation. FFM failure loads τ_{f} and initial crack lengths Δa are evaluated using mean fracture properties. In order to account for the uncertainty of fracture properties, failure load predictions are given with shaded 95% confidence intervals. Overall a good agreement between model and experiments is observed despite significant scatter in both experimental data and fracture properties. While failure loads are slightly overestimated, all trends are captured correctly. Confidence intervals of the predictions overlap with experimental standard deviations in any case. The experiments show the adhesive thickness effect, i.e., a reduction of the effective joint strength with increasing adhesive thickness t. The effect originates from an increasing energy release rate with increasing adhesive thickness which dominates the crack initiation process. Because the coupled strain and energy criterion accounts for the energy balance, the effect is reproduced well.

Figures 2c and d show the results of normal plate separation test of H-shaped specimens and circular shear tests of notched tubular lap joints, respectively. We used H-shaped specimens with adhesive thickness $t = 12\,\mathrm{mm}$, length $l = 50\,\mathrm{mm}$ and width $w = 12\,\mathrm{mm}$ and tubular lap joint specimens with two 3 mm notches, adhesive thickness $t = 8\,\mathrm{mm}$, width $w = 16\,\mathrm{mm}$ and inner diameter $\oslash 140\,\mathrm{mm}$. For the plate separation test, FFM predictions are slightly conservative. However, as observed in Figures 2a and b, they agree with experimental standard deviations within their confidence intervals. The circular shear case shows similar results as the simple shear setup. While in Figures 2c and d, only one geometry of each adhesive joint is tested, FFM again predicts the adhesive thickness effect which is expected to occur in the present test configurations as well.

References

[1] M. R. Ayatollahi, M. Heydari-Meybodi, M. Dehghany, and F. Berto. *Adv. Eng. Mater.* 18.8 (2016), pp. 1364–1370.

[2] F. Berto. *Theor. Appl. Fract. Mech.* 76 (2015), pp. 17–26.

[3] C. D. Clift, L. D. Carbary, P. Hutley, and J. H. Kimberlain. *J. Facade Des. Eng.* 2.3–4 (2014), pp. 137–161.

[4] J. Felger, N. Stein, and W. Becker. *Eng. Fract. Mech.* 182 (2017), pp. 621–634.

[5] J. Felger, P. L. Rosendahl, D. Leguillon, and W. Becker. *Int. J. Solids Struct.* 164 (2019), pp. 191–201.

[6] Z. Hashin. *J. Mech. Phys. Solids* 44.7 (1996), pp. 1129–1145.

[7] S. Hell, P. Weißgraeber, J. Felger, and W. Becker. *Eng. Fract. Mech.* 117 (2014), pp. 112–126.

[8] P. Lazzarin and R. Zambardi. *Int. J. Fract.* 112.3 (2001), pp. 275–298.

[9] D. Leguillon. *Eur. J. Mech. – A/Solids* 21.1 (2002), pp. 61–72.

[10] D. Leguillon and Z. Yosibash. *Int. J. Solids Struct.* 122-123 (2017), pp. 1–13.

[†]The spatial logarithmic Hencky strain tensor reads $\boldsymbol{\varepsilon} = \ln\sqrt{\mathbf{F}\mathbf{F}^{\top}}$ where $\mathbf{F}$ is the deformation gradient. Its deviator tensor is obtained from $\operatorname{dev}\boldsymbol{\varepsilon} = (\operatorname{tr}\boldsymbol{\varepsilon})\mathbf{I}/3$ where $\mathbf{I}$ is the identity matrix. In terms of principal strains $(\varepsilon_{\mathrm{I}}, \varepsilon_{\mathrm{II}}, \varepsilon_{\mathrm{III}})$, the second and third deviatoric invariants read $\mathit{II}'_{\boldsymbol{\varepsilon}} = \left((\varepsilon_{\mathrm{I}} - \varepsilon_{\mathrm{II}})^2 + (\varepsilon_{\mathrm{II}} - \varepsilon_{\mathrm{III}})^2 + (\varepsilon_{\mathrm{III}} - \varepsilon_{\mathrm{I}})^2\right)/6$ and $\mathit{III}'_{\boldsymbol{\varepsilon}} = (\varepsilon_{\mathrm{I}} + \varepsilon_{\mathrm{II}} - 2\varepsilon_{\mathrm{III}})(2\varepsilon_{\mathrm{I}} - \varepsilon_{\mathrm{II}} - \varepsilon_{\mathrm{III}})(\varepsilon_{\mathrm{I}} - 2\varepsilon_{\mathrm{II}} + \varepsilon_{\mathrm{III}})/27$, respectively.

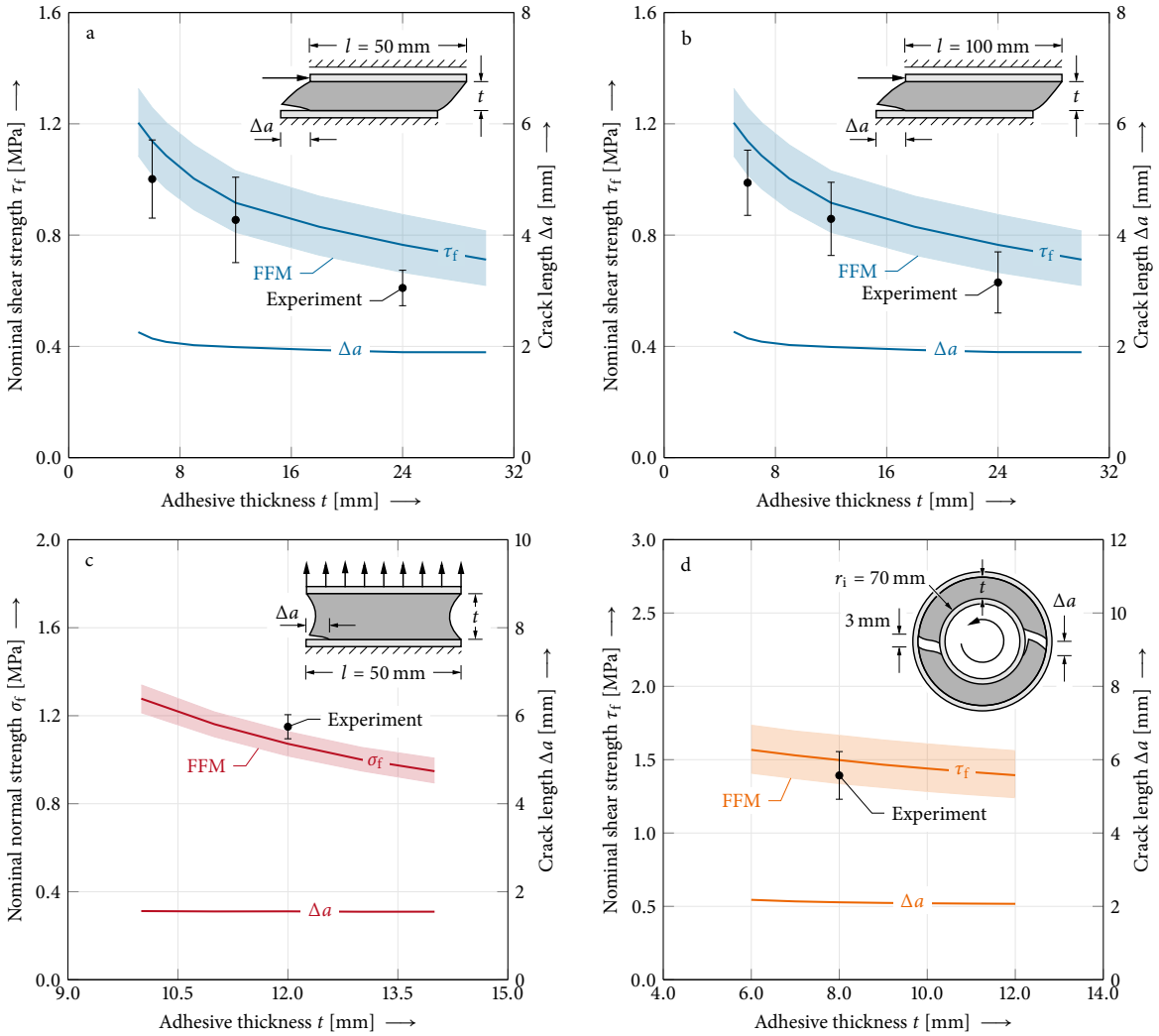

Figure 2. Finite fracture mechanics (FFM) failure load predictions in comparison to experiments. a) Simple shear test with overlap length $l = 50\,\text{mm}$, b) simple shear test with $l = 100\,\text{mm}$, c) normal plate separation test and d) notched tubular lap shear test. Experimental data is indicated as mean and standard deviation. FFM failure loads $(\sigma_\text{f}, \tau_\text{f})$ are computed using mean fracture properties and are given with shaded 95% confidence intervals accounting for uncertainty of the fracture properties. Reported finite crack lengths Δa correspond to mean fracture property predictions.

[11] D. Leguillon, E. Martin, O. Ševeček, and R. Bermejo. *Int. J. Fract.* 212.1 (2018), pp. 89–103.

[12] C. Miehe and L.-M. Schänzel. *J. Mech. Phys. Solids* 65 (2014), pp. 93–113.

[13] H. Neuber. *Forsch. auf dem Gebiete des Ingenieurwesens* 7.6 (1936), pp. 271–274.

[14] R. E. Peterson. In: *Stephen Timoshenko Anniv. Vol.* New York: Macmillan, 1938, pp. 179–183.

[15] R. B. Pipes, R. C. Wetherhold, and J. W. Gillespie. *J. Compos. Mater.* 13.2 (1979), pp. 148–160.

[16] P. L. Rosendahl, P. Weißgraeber, N. Stein, and W. Becker. *Int. J. Solids Struct.* 113-114 (2017), pp. 10–23.

[17] P. L. Rosendahl, M. Drass, J. Felger, J. Schneider, and W. Becker. *Int. J. Solids Struct.* 166 (2019), pp. 32–46.

[18] P. L. Rosendahl, Y. Staudt, C. Odenbreit, J. Schneider, and W. Becker. *Int. J. Adhes. Adhes.* 91 (2019), pp. 64–71.

[19] P. L. Rosendahl, Y. Staudt, A. P. Schneider, J. Schneider, and W. Becker. *Mater. Des.* Under Review (2019).

[20] G. C. Sih. *Int. J. Fract.* 10.3 (1974), pp. 305–321.

[21] Y. Staudt, C. Odenbreit, and J. Schneider. *Int. J. Adhes. Adhes.* 82 (2018), pp. 126–138.

[22] N. Stein, P. Weißgraeber, and W. Becker. *Compos. Struct.* 133 (2015), pp. 707–718.

[23] A. Talmon l'Armée, S. Hell, P. L. Rosendahl, J. Felger, and W. Becker. *Eng. Fract. Mech.* 186 (2017), pp. 283–299.

[24] M. E. Waddoups, J. R. Eisenmann, and B. E. Kaminski. *J. Compos. Mater.* 5.4 (1971), pp. 446–454.

[25] P. Weißgraeber, J. Felger, D. Geipel, and W. Becker. *Eur. J. Mech. - A/Solids* 55 (2015), pp. 192–198.

[26] P. Weißgraeber, D. Leguillon, and W. Becker. *Arch. Appl. Mech.* 86.1-2 (2016), pp. 375–401.

Proceedings of the 8th GACM Colloquium on Computational Mechanics for Young Scientists from Academia and Industry August 28–30, 2019 in Kassel, Germany

J-integral and mixed-mode cohesive zones

Johannes Scheel * [1] and Andreas Ricoeur[1]

[1]University of Kassel, Institute of Mechanics, D-34125 Kassel, Mönchebergstraße 7, Germany

Abstract. The J-integral is a powerful and accurate means for characterizing crack tip loadings and was independently introduced by Rice [4] and Cherepanov [2]. The calculation of both matrix and interface crack tip loadings is possible, commonly implementing line or equivalent domain integrals. The crack tip opening displacement, as fracture mechanics loading quantity of cohesive zone models, on the other hand, was related to the J-integral by Rice [4], however just for the pure mode I loading case. In this work, mixed-mode loading conditions are considered, resulting in a generalization of the single mode I relation. The J_1 coordinate of the generalized relation is verified analytically, considering a Dugdale-Barenblatt crack model under mixed-mode loading.

Introduction

The crack tip loading quantities of linear elastic fracture mechanics are all related to one another. The J-integral, however, was originally only related to the crack tip opening displacement for the single mode I loading scenario by Rice [4]. Scheel and Ricoeur [5] showed in their analysis of a matrix crack in the vicinity of a cohesive interface crack, that in the J-integral vector formulation of the matrix crack, the cohesive crack tip loading in terms of a J-integral vector can be derived exhibiting two non-zero coordinates, being the mixed-mode generalization of Rice's original relation [4]. The generalization of the J_1 coordinate is straightforward and uniquely related to the normal and tangential crack tip opening displacements, whereas the second coordinate depends on the solution of the boundary value problem and requires an integration along the cohesive crack faces. The generalized relation is verified using the Griffith crack model. For the Griffith crack, the J-integral is easily calculated with the stress intensity factors for single and mixed mode loading and is the reference value. Introducing a cohesive zone in front of the crack tip, in a Dugdale-Barenblatt crack model [1, 3], the cohesive crack tip loading can also be calculated for mixed mode loading scenarios using the derived generalized relation. For a ratio of applied stress to yield stress tending to zero, the length of the cohesive zone also approaches zero. The small scale yielding approximation is then becoming accurate, so that the J-integral calculated for the Dugdale-Barenblatt crack model with the generalized relation approaches the reference value. This verification is restricted to the J_1 coordinate in this work.

1 The J-integral vector of a mixed-mode loaded cohesive zone

The generalized relation for a mixed mode loaded cohesive crack given by Scheel and Ricoeur [5], shows the relation between J-integral and crack tip opening displacements in the first coordinate of the vector and the dependence on the boundary value problem in the second coordinate:

$$\begin{aligned} J_k = &\left(\int_0^{\delta_2^t} t_2(\delta_2) d\delta_2 + \int_0^{\delta_1^t} t_1(\delta_1) d\delta_1 \right) \vec{e_1} \\ &+ \left(\int_0^{\Delta l} \frac{1}{2} (\sigma_{11}^+ \varepsilon_{11}^+ - \sigma_{11}^- \varepsilon_{11}^- + \sigma_{22}(\varepsilon_{22}^- - \varepsilon_{22}^+) + 2\sigma_{12}(\Omega_{12}^- - \Omega_{12}^+)) dx_1 \right) \vec{e_2}. \end{aligned} \tag{1}$$

*Corresponding author: j.scheel@uni-kassel.de ORCID iD: https://orcid.org/0000-0003-4400-0283

Here, $\delta_i^t = \delta_{1/2}^t$ describe the opening separations at the physical crack tip and it is assumed that the tractions t_i are only functions of the mode-associated separations δ_i. The integration contour has been shrunk to the cohesive surfaces of a straight cohesive crack [4], with a cohesive zone length of Δl and the superscripts $+/-$ indicate affiliations of the quantities to the upper $(+)$ or lower $(-)$ fictitious crack face. The tangential strain $\varepsilon_{11}^{+/-}$ is not continuous and thus has to remain separated, while the tractions are continuous, i.e. $t_i^+ = -t_i^-$. This formulation involves the jumps of normal strain $\varepsilon_{22}^{+/-}$ and rotation $\Omega_{12}^{+/-}$ over the cohesive crack faces, with

$$\Omega_{ij} = \frac{1}{2}(u_{i,j} - u_{j,i}), \tag{2}$$

where $u_{i,j}$ is the displacement gradient.

2 Verification of the first coordinate J_1

For the verification of the first coordinate of the generalized relation of Eq. (1), it is assumed that the cohesive laws for mode I and II are equal, that the constitutive behavior is equal to perfect plasticity and that the cohesive zone is equally mode I and mode II loaded. For the calculation of the first coordinate of the J-integral vector of Eq. (1) the crack tip opening displacements are needed, but in order to calculate them the length of the cohesive zone needs to be calculated first. With the assumptions made, it is calculated exploiting the condition that there is no stress singularity at the fictitious crack tip, yielding

$$\Delta l = a \left[\sec\left(\frac{\pi \sigma^\infty}{2\sigma_0} \right) - 1 \right], \tag{3}$$

where a is the Griffith crack length, σ^∞ is the applied stress and σ_0 is the yield stress. The crack tip opening displacements then can be calculated as

$$\delta_i^t = 8 \frac{\sigma_0 a}{\pi E'} \ln\left(\frac{a + \Delta l}{a} \right), \tag{4}$$

where $E' = E$ is the Young's modulus for plane stress and for plane strain $E' = E/(1-\nu^2)$, with ν as Poisson's ratio ans E as Young's modulus. The J_1 coordinate for the Dugdale-Barenblatt crack model, in the following denoted as J_1^{coh}, is calculated inserting Eqs. (4) and (3) into the first coordinate of Eq. (1), yielding

$$J_1^{coh} = 16 \left(\sigma_0^2 \ln\left(\sec\left[\frac{\pi \sigma^\infty}{2\sigma_0} \right] \right) \right). \tag{5}$$

The J_1 coordinate of the Griffith crack, in the following denoted as J_1^{LEFM}, can be calculated with the stress intensity factors by the established relation,

$$J_1^{LEFM} = \frac{K_I^2 + K_{II}^2}{E'} = \frac{2(\sigma^\infty)^2 \pi a}{E'}. \tag{6}$$

The ratio of the two calculated values is plotted in Figure 1 versus the ratio of applied stress to yield stress. The ratio of the Dugdale-Barenblatt crack length $(a + \Delta l)$ to the Griffith crack length a is depicted there too. It is clearly visible that for a stress ratio going to zero, the calculated coordinates J_1^{coh} and J_1^{LEFM} as well as the Griffith and the Dugdale-Barenblatt crack lengths become equal. A very small cohesive zone size complies with the small scale yielding approximation, therefore J_1^{coh} being equal to J_1^{LEFM} for that condition, verifies the first coordinate J_1^{coh} of the generalized relation of Eq. (1).

3 Conclusion

The J-integral vector of a mixed mode loaded cohesive zone derived by Scheel and Ricoeur [5], being the generalization of the scalar formulation derived by Rice [4], is picked up in this work. The second coordinate of the vector is not as straightforwardly derived as the first. In contrast to the first coordinate, the second requires the solution of the boundary value problem, whereas the first coordinate has a direct relation to the cohesive laws and the crack tip opening displacements. The first coordinate is verified in

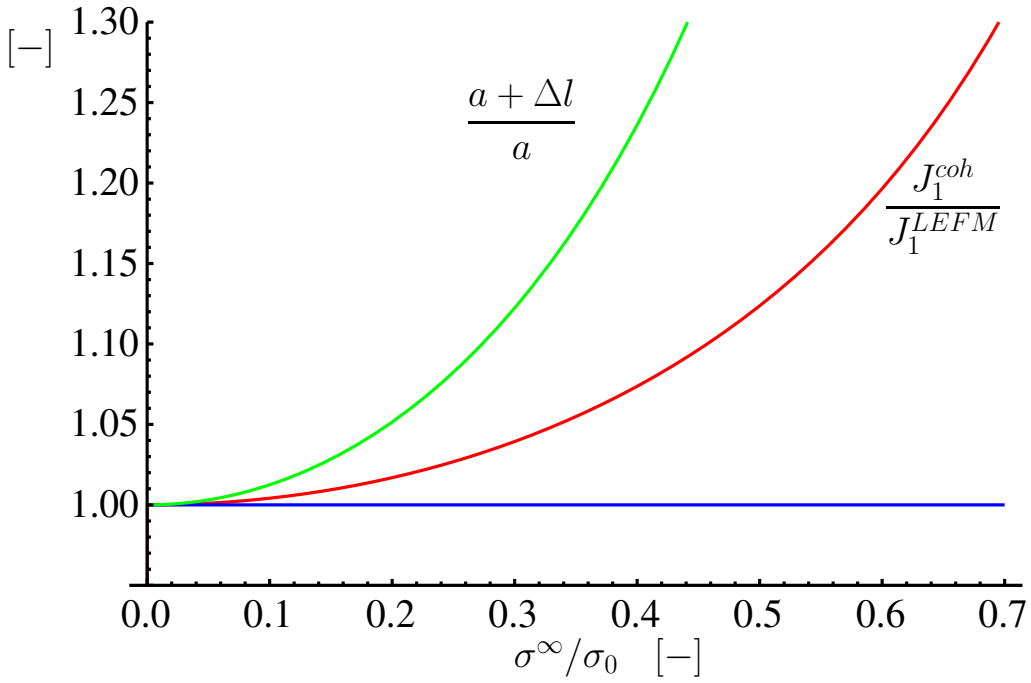

Figure 1. Ratio of the calculated J_1 coordinates and ratio of the Dugdale-Barenblatt crack length to the Griffith crack length, plotted vs. the ratio of applied stress to yield stress

this work at a Griffith crack model. The J-integral classically calculated with the stress intensity factors for the Griffith crack is accurate with the condition of small scale yielding and acts as reference. For a Dugdale-Barenblatt crack with a cohesive zone length tending to zero, this condition is also valid and in the limiting case the model becomes equal to the Griffith crack model. It is shown, that the J_1 coordinate calculated for the Dugdale-Barenblatt crack with the generalized relation, equals the J_1 coordinate of the Griffith crack for the small scale yielding approximation, finally confirming the generalized relation for the first coordinate. The verification of the second coordinate is in progress.

References

[1] G. I. Barenblatt. The mathematical theory of equilibrium cracks in brittle fracture. *Advances in applied mechanics* 7 (1962), pp. 55–129.

[2] G. P. Cherepanov. Crack propagation in continuous media (translation from russian). *Journal of Applied Mathematics and Mechanics* 31 (1967), pp. 503–512.

[3] D. S. Dugdale. Yielding of steel sheets containing slits. *Journal of the Mechanics and Physics of Solids* 8 (1960), pp. 100–104.

[4] J. R. Rice. A path independent integral and the approximate analysis of strain concentration by notches and cracks. *Journal of Applied Mechanics* 35 (1968), pp. 379–386.

[5] J. Scheel and A. Ricoeur. A comprehensive interpretation of the J-integral for cohesive interface cracks and interactions with matrix cracks. *Theoretical and Applied Fracture Mechanics* 100 (2019), pp. 281–288.

Proceedings of the 8th GACM Colloquium on Computational Mechanics for Young Scientists from Academia and Industry August 28–30, 2019 in Kassel, Germany

Finite element model to describe crack deflection and constrained micro-cracking

Markus Tauscher * [1], Martin Pletz[1], Florain Arbeiter[2] and Clara Schuecker[1]

[1]Designing Plastics and Composite Materials, Department of Polymer Engineering and Science, Montanuniversitaet Leoben, Austria

[2]Materials Science and Testing of Polymers, Department of Polymer Engineering and Science, Montanuniversitaet Leoben, Austria

Abstract. An incremental finite element model is presented that predicts the growth of a crack through a 2D structure containing round pores. The crack is deflected due to the influence of the pores on the strain field and might grow into a pore. Furthermore, the initiation of cracks from the pore surfaces is modelled with a combined stress-energy criterion. The model contributes to the understanding of toughening mechanisms in heterogeneous materials. It is capable of showing the influence of the pore content, the pore arrangement and pore shape on the resistance to crack propagation.

1 Introduction

In some heterogeneous materials, exceptionally high strength and toughness values are observed. It is well known that the strength and toughness is not only determined by the properties of the constituents, but also by the arrangement of the inclusions in the matrix. For an existing crack, effects like fiber bridging, crack deflection, residual stresses and constrained micro-cracking can reduce the crack's driving forces and thus increase the composites toughness. Through this crack-arresting effect, hierarchical materials can also be less sensitive to existing cracks, making them more damage tolerant. Hierarchical materials, as found in nature, can feature such toughening mechanisms on different length scales [5]. Typical examples for such hierarchical structures are nacre, bone, and wood. Using those mechanisms for engineering materials seems very promising, but is often limited by the capabilities of the manufacturing processes. In recent years, however, production technologies have been rapidly evolving and make it possible to manufacture more complex structured compounds at reasonable costs.
Many groups of engineers work on understanding those toughening mechanisms in natural materials [3] and using such mechanisms to develop engineering materials with improved strength and toughness [4] by means of testing, modelling and manufacturing.
In this work, a numerical model to predict crack deflection and constrained microcracking in inhomogeneous materials is developed. By doing so, both crack propagation and initiation must be accounted for. While crack propagation in brittle bulk materials is well established (Griffith–Irvine), some novel concepts such as the Finite Fracture Mechanics (FFM) concept [2, 4] can predict crack initiation. This concept is based on coupling a stress and an energy criterion, which both have to be fulfilled for a crack to initiate. Here, a Finite Element (FE) model for a Compact Tension (CT) specimen with an initial crack and several inclusions is used. These inclusions can deflect, trap or initiate the crack. As a first step towards describing some of these toughening mechanisms, circular voids are considered rather than inclusions to avoid competing fracture mechanisms like delamination and other effects of the interface. Such specimen can easily be manufactured through 3D printing, which is currently under way.

2 Finite element model setup

The FE model represents a CT specimen that is used for testing fracture toughness and is set up in the finite element code ABAQUS [1]. Figure 1a shows the model's geometry and the applied boundary

*Corresponding author: markus.tauscher@unileoben.ac.at

conditions. The surfaces of the two left holes are kinematically coupled to reference points, where a displacement load u is applied. Those reference points are constrained in the horizontal direction but free to rotate.

The model is set up with linear geometry and uses quadratic plane stress elements with reduced integration. The material used in the numerical analysis is polylactic acid (PLA), which is quite common in 3D printing. The selected PLA features a Young's modulus of 3.4 GPa, a Poisson's ratio of 0.37 and a fracture toughness K_{Ic} of 4.5 MPa$\sqrt{\text{m}}$. Typical strength values of PLA are about 40 MPa. For plane stress, the fracture energy G_c is obtained as $K_c^2/E = 5.96$ mJ/mm^2. The analysis assumes the material to behave in a brittle manner, which is valid for PLA if the temperatures are low and the loading rate is high. Between the crack faces, no contact is defined because in the first simple configuration, no closed and compressed cracks occur.

At the beginning of the analysis, there is an initial crack with a length of 10 mm in the center of the specimen. This is the primary crack. During loading, additional secondary cracks can initiate from the pores. The displacement load is applied in steps of Δu of 0.2 mm. In each increment of the modelling scheme, see Figure 1b, the FE model containing all existing cracks is run and crack initiation from the pores is checked. In the next step, the primary crack and all initiated cracks are checked for crack propagation. If crack growth is predicted for those cracks, the cracks are extended and the loop starts again. Once no cracks initiate and no cracks grow in one increment, the displacement load is increased by Δu and crack initiation and crack growth is checked for this increased load similar as for the previous displacement.

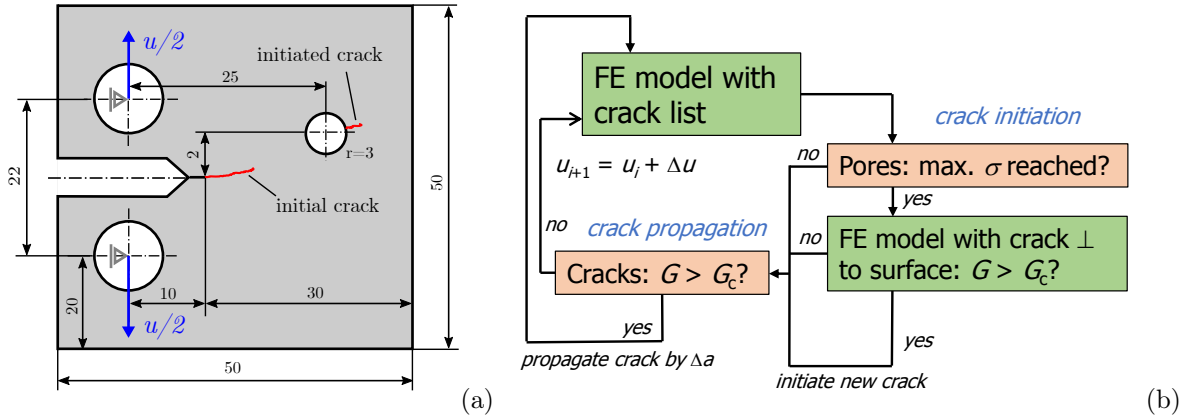

Figure 1. Geometry (dimensions in mm) and loads applied on the CT specimen model (a) and work flow of the incremental modelling method (b).

2.1 Crack initiation from pores

The crack increment Δa is taken as a suitable value that can yield a sufficiently fine discretization of the crack growth. For crack initiation, the maximum principal stress is evaluated at a normal distance Δa from the pore surface, and the position of highest stress along the circumference of the pore is taken as the critical location. If this stress is higher than the material's strength, a crack of the length Δa is initiated at that location normal to the surface. Then, it is checked whether the J-integral of this crack is above the material's fracture energy. This is a simplified formulation of the combined stress/energy criterion for crack initiation, where both energy release rate and stress are evaluated at different positions starting from the surface, and the crack initiation with different crack lengths can be predicted. It should be noted that the strength used in the FFM stress criterion is not the actual strength of the material but has to be calibrated. In this study, it was assumed to be 100 MPa, but will be calibrated when first test results are available.

2.2 Crack growth

In each iteration, the J-integral of the cracks is evaluated and used for assessing the crack's growth by comparing it to the fracture energy G_c. The maximum tangential stress criterion as implemented in ABAQUS [1] is used to obtain the direction of crack propagation, as done in a similar analysis in [6].

When a crack tip comes close to a pore surface such that the normal distance is less than the value of Δa, the crack is extended into the pore. In the future, more sophisticated concepts for predicting crack growth such as the configurational force concept will be studied.

3 First model results

The modelling scheme is used for a CT specimen with and without a pore. The crack length increment Δa is chosen as 0.04 mm. For the model that contains a pore, there is a vertical offset of the pore from the crack plane, as indicated in Figure 1a. Figure 2 shows contour plots of the maximum principal stresses in the CT specimen as the crack grows. The instants of the contour plots are taken for a horizontal length of the crack a_x of 17.6 mm, 22.3 mm and 31.6 mm in Figure 2a, b and c, respectively. There is a distinct deflection of the crack from its initial plane as it grows towards the pore. When the crack grows into the pore, it is arrested and has to initiate again. Note the reduced level of maximum stress when the crack has grown into the pore in Figure 2b.

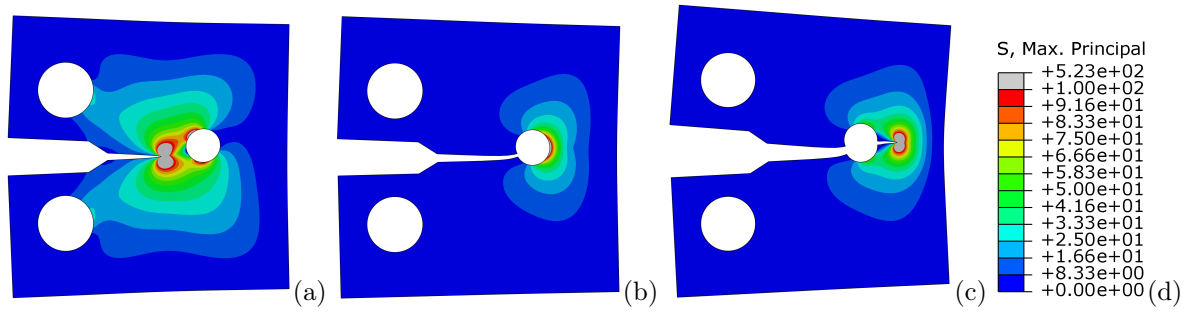

Figure 2. Contour plots of the maximum principal stresses in the model with a crack length of a) 17.6 mm, b) 22.3 mm and 31.6 mm. The legend of the contour plots (in MPa) is given in (d).

To assess the influence of the pore on the crack's propagation, Figure 3 plots the horizontal crack length a_x over the applied displacement load u. For the CT specimen without a pore, the initial crack starts to grow at a value of u=0.6 mm and leads to a gradual failure of the specimen. The specimen with pore has an earlier growth of the initial crack (at a displacement u of 1 mm, the crack already runs into the pore), but then stops and has to re-initiate at the pore, which it does at a value of u=2.2 mm. Apart from the region with a displacement load u of 1 mm to 2.2 mm, there are only slight differences between the two curves.

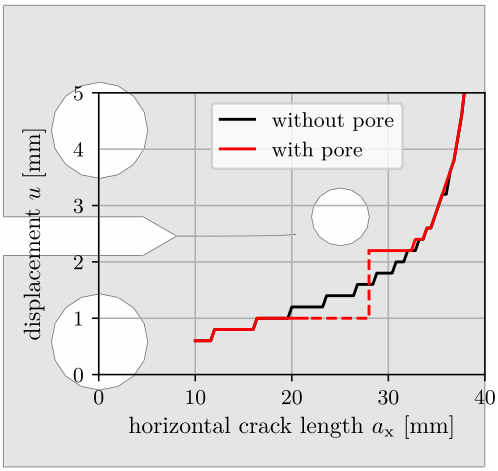

Figure 3. Comparison of model results between a CT specimen without and with pore in terms of load/displacement u vs. horizontal crack length a_x. There is an influence of the pore in the region of the pore: Towards the pore, the crack grows earlier, and then, a higher u value than in the model without pore is needed for a further crack extension.

4 Conclusions

The shown modelling procedure is capable to predict the influence of a pore on the crack propagation in a CT specimen. The crack is deflected by the pore and has to re-initiate after growing into the pore. For the selected geometry and material parameters, the overall course of the crack length – displacement curve is similar for the models with and without pore. In the future, the modelling approach can be extended towards more sophisticated methods for crack growth and crack initiation.
For the validation, CT specimens will be 3D-printed and tested. During testing, strains and crack paths are captured by Digital Image Correlation and can be compared directly to the results of the model for each load step. The validated model can help to understand crack deflection and constrained microcracking to identify key parameters and design rules. Furthermore, the model can be extended to multiphase compounds, where interface failure will play a role.

References

[1] Abaqus. *ABAQUS Theory Guide, 6.14*. Providence, RI, USA: Dassault Systèmes, 2014.

[2] Pietro Cornetti, Nicola Pugno, Alberto Carpinteri, and David Taylor. Finite fracture mechanics: A coupled stress and energy failure criterion. *Engineering Fracture Mechanics* 73.14 (Sept. 2006), pp. 2021–2033. ISSN: 00137944. DOI: 10.1016/j.engfracmech.2006.03.010.

[3] Zian Jia and Lifeng Wang. 3D printing of biomimetic composites with improved fracture toughness. *Acta Materialia* 173 (July 2019), pp. 61–73. ISSN: 13596454. DOI: 10.1016/j.actamat.2019.04.052.

[4] D. Leguillon, E. Martin, O. Ševeček, and R. Bermejo. Application of the coupled stress-energy criterion to predict the fracture behaviour of layered ceramics designed with internal compressive stresses. *European Journal of Mechanics - A/Solids* 54 (Nov. 2015), pp. 94–104. ISSN: 09977538. DOI: 10.1016/j.euromechsol.2015.06.008.

[5] Flavia Libonati and Markus J. Buehler. Advanced Structural Materials by Bioinspiration: Advanced Structural Materials by Bioinspiration. *Advanced Engineering Materials* 19.5 (May 2017), p. 1600787. ISSN: 14381656. DOI: 10.1002/adem.201600787.

[6] Z. Majer, M. Pletz, C. Krautgasser, L. Náhlík, P. Hutař, and R. Bermejo. Numerical Analysis of Sub-critical Crack Growth in Particulate Ceramic Composites. *Procedia Materials Science* 3 (2014), pp. 2071–2076. ISSN: 22118128. DOI: 10.1016/j.mspro.2014.06.335.

Proceedings of the 8th GACM Colloquium on Computational Mechanics for Young Scientists from Academia and Industry August 28–30, 2019 in Kassel, Germany

Stress Control on Interfaces Using Shape Optimisation

Felix Wohlgemuth *[1] and Franz-Joseph Barthold[1]

[1]Structural Mechanics, TU Dortmund University, Dortmund, Germany

Abstract. The stress field information states a main point of interest, when regarding structural optimisation of bimaterial structures. The introduction of stress criteria along the volume is crucial in the development of new designs. In the case of bimaterials the stress field in particular along the interface deserves additional attention e.g. to prevent delamination. Tracing the interface through shape optimisation in CAD-based methods is rather expensive due to the high cost in remeshing techniques. Therefore, level set methods with fixed background meshes are used as in [5].

In this work an approach for controlling strains and stresses on the interface in a framework of shape optimisation is introduced. The geometry description is managed by parametrised level set functions and a sub-meshing technique is coupled with the extended finite element method. The parametrisation with superellipses allows to reduce the number of design variables to a minimum of six variables per introduced ellipse while holding up a sufficient precision in the geometry description, c.f. [4]. Moreover, it simplifies the shape derivatives as it provides an implicit description for the moving interfaces. The sub-meshing technique makes it possible to keep existing strategies from homogeneous structures and to transform them on a discontinuous material using enriched shape functions provided by the standard extended finite element method, c.f. [1]. Shape sensitivities are evaluated on the sub-elements and extrapolated to the interface introducing pseudo nodes. The sensitivity information of the stress field among these pseudo nodes can be used in the framework of stress minimisation as well as for a side condition in a volume minimisation setup.

Introduction

In many cases the interface between different materials is the weak point of a structure. Stress-induced phenomena like plasticity or delamination occur in particular there. Thus, an investigation of the stress field along the interface is of special interest for the engineer. And a main goal in the development of new designs is to control the stress state at the material discontinuity. This work will focus on the restriction of stresses with the tools of structural optimisation. The concept is to change the shape and size of the interface in order to find the optimal stress state. For this a modified extended finite element formulation is used for both the structural and the sensitivity analysis.

1 A Modified XFEM Approach

Discontinuous material behaviour in the framework of standard finite element methods requires a meshing of the structure following the material interface. With a moving discontinuity, remeshing in every optimisation step would be needed. Therefore, an alternative approach is used.
The extended finite element method (XFEM) was developped to represent discontinuities in the field quantities with a fixed mesh, c.f. [3]. The unsteady behaviour within the element is modelled by enhancing the shape functions with a part that represents the particular behaviour

$$u^h(\mathbf{x}) = \sum_{i \in I} N_i(\mathbf{x})\, u_i + \sum_{j=1}^{N} \sum_{i \in I_j^*} N_i^*(\mathbf{x})\, \psi^j(\mathbf{x})\, a_i^j \,. \tag{1}$$

In this work a modified approach is used, which divides the cut element into sub elements alining with the interface within the element. Those uncut sub elements are treated as standard finite elements. The field quantities of the sub nodes which emerge during the sub meshing are then extrapolated to the global

*Corresponding author: felix.wohlgemuth@tu-dortmund.de

nodes. The stresses are evaluated on the gaussian points in the sub elements and weighed onto the sub nodes using the sub element area. Along the intersection points of the interface with the element edges, pseudo nodes are introduced. The stresses along the interface can then be computed as

$$\sigma_{int} = \frac{\sum \sigma_{ip} \mathrm{d}A_{ip}}{\sum \mathrm{d}A_{ip}}, \tag{2}$$

where the integration point stresses (σ_{ip}) are calculated with standard finite element techniques within one sub element and the desired interface stresses (σ_{int}) are merged from these.

2 Structural Optimisation

In this work, two different concepts for the stress control are introduced. On the one hand we use the stress as the objective function and aim to minimise the interface stresses themselves while holding up to a prescribed volume of the structure. For this approach we need to measure the stresses along the interface in order to reduce the cost of the optimisation algorithm. This is done by the p-norm. On the other hand the stresses are constraint through upper (or lower) bounds while the volume is minimised.

$$\begin{aligned} &\min_{\mathbf{s}\in\mathbb{D}} V(\mathbf{s}), \\ &\text{s.t. } \sigma(\mathbf{s}) \leq \sigma_{\max} \end{aligned} \tag{3}$$

$$\begin{aligned} &\min_{\mathbf{s}\in\mathbb{D}} J(\mathbf{s}), \quad \text{with } J(\mathbf{s}) = \left[\int_{\partial\Omega} \sigma(\mathbf{s})^p \, \mathrm{d}x(\mathbf{s})\right]^{1/p}, \\ &\text{s.t. } V_{\text{incl}}(\mathbf{s}) \leq V_{\max} \end{aligned} \tag{4}$$

For both of these concepts the sensitivities of the stresses with respect to changes in the design, i.e. the shape and size of the interface are required. We keep in mind that the design of the interface is defined by a superellipse, providing six parameters which are our design variables $\mathbf{s}$. The sensitivity is now given by the total variation of the integration point stresses with respect to the design

$$\begin{aligned} \delta_s \sigma_{\text{ip}} &= \delta_{\mathbf{u}_{ej}} \sigma_{\text{ip}} \frac{\partial \mathbf{u}_{ej}}{\partial \bar{\mathbf{u}}} \frac{\mathrm{d}\bar{\mathbf{u}}}{\mathrm{d}\mathbf{s}} + \delta_{\mathbf{x}_{ej}} \sigma_{\text{ip}} \frac{\partial \mathbf{x}_{ej}}{\partial \mathbf{s}} \\ &= \mathbf{A}_u \mathbf{T}\mathbf{S} + \mathbf{A}_x \mathbf{W} = [\mathbf{A}_u, \ \mathbf{A}_x] \begin{bmatrix} \mathbf{T}\,\mathbf{S} \\ \mathbf{W} \end{bmatrix}. \end{aligned} \tag{5}$$

It is noted that the variation is split up to a sub elemental part including the variation of stresses with respect to sub nodal quantities ($\mathbf{A}_u, \mathbf{A}_x$) and a mapping part for the displacements ($\mathbf{T}\,\mathbf{S}$) and the coordinates ($\mathbf{W}$), see [6] aswell. This seperation makes it possible to use existing techniques for the sensitivity analysis on sub element level, for example the variational approach from [2], which states the main benefit of this approach in contrast to other XFEM-based optimisation techniques.

References

[1] Franz-Joseph Barthold and Daniel Materna. A modified extended finite element method approach for design sensitivity analysis. *International Journal for Numerical Methods in Engineering* 104.3 (2015). nme.4930, pp. 209–234.

[2] Franz-Joseph Barthold, Nikolai Gerzen, Wojciech Kijanski, and Daniel Materna. Efficient Variational Design Sensitivity Analysis. In: *Mathematical Modeling and Optimization of Complex Structures*. Ed. by Pekka Neittaanmäki, Sergey Repin, and Tero Tuovinen. Cham: Springer International Publishing, 2016, pp. 229–257.

[3] Nicolas Moës, John Dolbow, and Ted Belytschko. A finite element method for crack growth without remeshing. *International Journal for Numerical Methods in Engineering* 46.1 (1999), pp. 131–150.

[4] Lise Noël, Laurent Van Miegroet, and Pierre Duysinx. Analytical sensitivity analysis using the extended finite element method in shape optimization of bimaterial structures. *International Journal for Numerical Methods in Engineering* 107.8 (2016). nme.5181, pp. 669–695.

[5] Stanley Osher and James A. Sethian. Fronts propagating with curvature dependent speed: algorithms based on Hamilton–Jacobi formulations. *Journal of Computational Physics* (1988), pp. 12–49.

[6] Felix Wohlgemuth and Franz-Joseph Barthold. Structural Optimisation Using Parametrised Level Set Methods and Extended Finite Element Method. *PAMM* 18.1 (2018), e201800367.

**Proceedings of the 8th GACM Colloquium on Computational Mechanics
for Young Scientists from Academia and Industry
August 28–30, 2019 in Kassel, Germany**

Fragment Detection Algorithm for Postprocessing High Velocity Impact and Natural Fragmentation

Marvin Becker * [1,2], Marina Seidl[1], Miriam Mehl[2] and Mhamed Souli[3]

[1]ISL (Institute of Saint Louis), 5 Rue de General Cassagnou, BP 70034, 68300 Saint-Louis - France

[2]University of Stuttgart, Universitätsstr. 38, 70569 Stuttgart - Germany

[3]Lille 1 University, Cité Scientifique, 59650 Villeneuve d'Ascq - France

Abstract. Post-processing software like Paraview and LS-Prepost are valuable tools for the visualization of simulation output. However, when fracture occurs it is not possible to distinguish separated parts in the output. In particular, for evaluating the mass or average velocity of fragments the manual workaround is time-consuming and error-prone.
There is only little literature available on this particular application, but the problem can be abstracted from graph theory. If the nodal positions of the particles are known, a suitable criterion determining the graph connectivity is needed. An algorithm from literature is used to determine the connectivity graph and thus the fragments. As the number of nodes in a three-dimensional simulation is very large an efficient algorithm and a fast implementation is indispensable. A further technical challenge is the incorporation of the fragment information back into the visualization data.
The algorithm is applied to two applications. First, a high-velocity impact of a steel cylinder with round shaped nose is investigated. Second, the natural fragmentation of a steel cylinder shell under blast is visualized with the tool. Besides the fragment visualization, a statistical investigation of the fragments shows the versatility of this code. Experimental results of the two applications have been conducted in the laboratories of ISL (Institute of Saint-Louis) for validation purposes. Thus, the approach gives the possibility to quickly evaluate if the numerical prediction and the experimental results coincides based on the statistical information of the fragments. The temporal crack evolution or formation of fragments can only be investigated using the numerical results processed with this methodology.

Introduction

Numerical simulations are used in structural analysis to investigate damage and fracture. In some applications, like durability studies or crash tests, the interest is restricted to the binary information if the specimen stays intact. However, for other applications the fracture behavior itself needs to be examined explicitly. For the development of advanced protective structures, a predictive model, which describes the fracture behavior of a ballistic threat properly, is important. To validate such a numerical model, an academic example with similar properties is the natural fragmentation of a cylinder shell under blast. These two examples are investigated with the new fragment detection approach in this abstract. The field of applications where researchers are interested in the emerging fragments is much broader, as the following example from aerospace engineering shows: During the takeoff and touchdown of an airplane the blades of the turbine engine can fracture if the local loads on them are too high. It is important that these fragments do not exceed a certain size and velocity, such that they do not harm the engine [5].

To include a tracking of fragments in the post processing requires a change of the data structure and is thus not available in most of the post processors - for instance, not in those used by the authors. To overcome this shortcoming, two different approaches to detect fragments in particle simulations based on the nodal positions are presented in the following. This extended abstract summerizes the underlying theory and algorithmic aspect, and shows an extract of results visualized with the software MegaMol, developed at the VISUS (University of Stuttgart) [6].

*Corresponding author: marvin.becker@isl.eu

1 Theory

From a mathematical point of view, fragment identification can be considered as a question in graph theory. Starting with an arbitrary set of particles (nodes), connections (edges) are created between nodes which are close enough to each other, resulting in an undirected graph. The fragments are then defined as the connected components of this graph. This section summarizes the two approaches used to identify fragments based on a point cloud in three dimensions.

1.1 Problem Description

Let S be a set of points in $\mathbb{R}^3 \times \mathbb{R}$, then two particles $x_i \in S$ and $x_j \in S$ are referred to as neighbors at time t_0 if and only if

$$||x_i(t_0) - x_j(t_0)|| < \varepsilon, \tag{1}$$

where $||\cdot||$ denotes the Euclidean norm and ε is the threshold distance. The particles are called connected neighbors if and only if they are neighbors at all times t:

$$||x_i(t) - x_j(t)|| < \varepsilon \qquad \forall t. \tag{2}$$

A fragment is the recursive set of connected neighbors. Let X_i be the set of points belonging to a fragment which contains the start point x_i, and $cn(x_j)$ be the function which returns the connected neighbors of an arbitrary point x_j. Then, the function determining all points can be expressed in pseudo-code as follows:

def add_frag(X_i, x_i) :
  $X_i = \{X_i, \quad cn(x_i) \backslash X_i\}$
  $X_i = \text{add\_frag}(X_i, x_j) \quad \forall x_j \in \{cn(x_i) \backslash X_i\}\}$
  return X_i

$X_i = \text{add\_frag}(x_i, x_i)$

1.2 Classical Approach

The classical approach solves the problem described in the previous section straight forward. First, the neighbors of all particles are determined: This can be done with different algorithms: Comparing all particle with each other gives a complexity of $O(n^2)$. One possibility to reduce the best-case complexity to $O(n)$, is to discretize the particle domain with voxels and check for neighbors only in neighboring voxels. If the particle distribution is very sparse, such a discretization can be very memory consuming, or again, result in a worst-case complexity of $O(n^2)$. Instead, a more advanced discretization of voxels is needed, which is beyond the scope of this work, and thus, an alternative approach is suggested: If the neighbor list is generated for the initial time-step, the particles are densely packed, much less memory is required, and best-case complexity can be ensured. Zhang, even circumvents generating the neighbor list at all, whilst using initial particle positions based on a FEM mesh where the neighbors are given by the structured mesh [9]. It has been shown that such a particle distribution is inferior for its uniformity [1]. Thus, this approach is not applied, and instead the neighbor list is generated for the initial time step to allow a more general particle distribution. The neighbor list, or graph connectivity, is then updated for the following time-steps and connections which do not exist further are deleted.
Finally, the connected components of the resulting undirected graph are identified using either breadth-first search or depth-first search, which are both linear in time.

1.3 Machine Learning Approach

Another possibility to determine fragments from a set of points is using unsupervised machine learning. Density-based spatial clustering of applications with noise (DBSCAN) is a data clustering algorithm introduced by Ester et al. [4]. The algorithm is calibrated with two parameters: the *minpts* value defines the amount of connections required to belong to a cluster of points, and the *eps* value determines whether or not two points are connected. A development of this algorithm is HDBSCAN, where the H stands for hierarchical. This modification determines the fitting parameters automatically: Different values of *eps* are used and the result is integrated to give the best stability over *eps*.

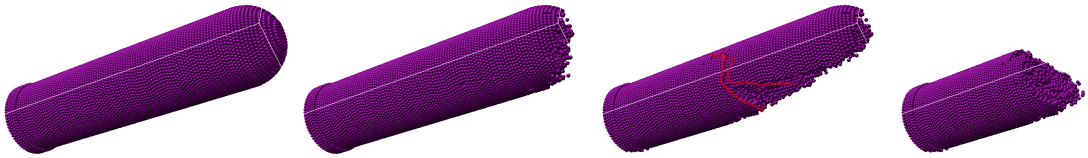

(a) t=0 μs. **(b)** t=40 μs. **(c)** t=80 μs. **(d)** t=120 μs.

Figure 1. Visualization of high-velocity impact (800 m/s, 30° NATO obliquity). The largest fragment is visualized in the initial position at four different time steps. In particular, the crack formation can be identified with this visualization technique (highlighted in red).

2 Results

This section shows the possibilities which emerge when applying one of the proposed techniques to post process the simulation output. Two different applications are investigated: The first application is an oblique high-velocity impact of a steel cylinder with round-shaped nose. Here, the aim is to process the largest fragment, to compare it to experimental data. The second application is the natural fragmentation of a cylinder ring subjected to blast. For this application, a statistic evaluation of the fragment-size-distribution is required for the validation of the numerical method.

2.1 High-Velocity Impact

During a high-velocity impact large pressure, strain rate and stresses emerge [7]. Depending on the impact scenario - impact velocity, obliquity angle, yaw of the impactor, and the involved materials - the material fails, leading to fracture or partial fragmentation of the impactor[8]. Especially for the case of oblique impact, the bending results in localized stresses and provokes such mechanisms. From an experimental point of view, recovering the largest fragment can be realized easily and is therefore well suited for a comparison. The mass, shape, and velocity of this fragment are properties which can be tested during the experiment. Having identified the fragments in the numerical simulation provides all these properties automatically to quickly evaluate parameter studies in a consistent manor.
Figure 1 shows the largest fragment of an oblique impact at different time steps. Besides the properties which are tested post-impact, the crack evolution can be observed in the time series of the images.

2.2 Natural Fragmentation of Cylinder Shells

The second example where the interest lies in an evaluation of fragment size, fragment velocity, and a visualization of crack patterns is the natural fragmentation of explosively driven cylinder rings [3]. While the fragment-size-distribution can be tested a posteriori in the experiment, the physical mechanisms can only be revealed with numerical simulation: because of the large deformations of the fragments during the ring expansion, the ring can not be reconstructed. To argue that the simulation is reproducing the experimental behavior well, the fragment-size-distribution can be compared as a measure of accuracy. Since there is no direct post processing option for this task, the proposed algorithm fills the gap to get the distribution and visualize the crack patterns (compare Figure 2 and 3). The particle visualization software MegaMol [6], is used for the three-dimensional visualization of particles.

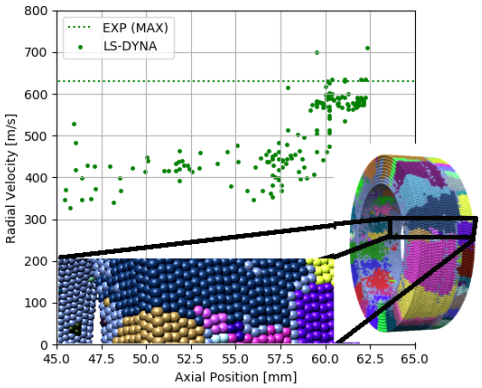

Figure 2. Evaluation of the fragment velocity over the initial axial position and comparison to the experiment. Each scatter point visualizes one fragment. [2].

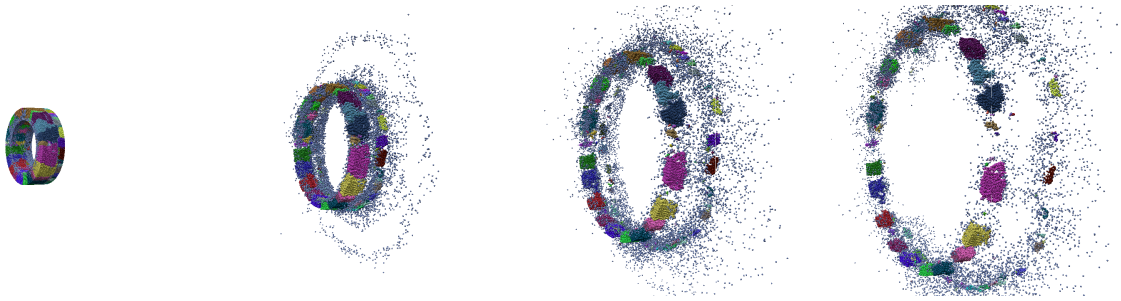

(a) t=0 μs. **(b)** t=50 μs. **(c)** t=100 μs. **(d)** t=150 μs.

Figure 3. Visualization of natural fragmentation with MegaMol. Each color represents a different fragment. Due to a large amount of fragments similar colors might appear.

3 Outlook

Hitherto, the detection and visualization of the fragments is implemented in a standalone application. The aim is to exchange this knowledge with the developers of post processors like LS-Prepost, to see this being developed for a wider audience.

Acknowledgments

The authors acknowledge the contribution of the VISUS department at University Stuttgart for setting up MegaMol, the Institute of Saint-Louis (ISL) for funding the PhD, and the Universities of Lille and Stuttgart for supervising the PhD.

References

[1] Marvin Becker, Marina Seidl, Miriam Mehl, and Mhamed Souli. A Study on Initial Conditions in Smooth Particle Hydrdynamics Modelling of High-Velocity Impact. In: *2018 Nordic LS-DYNA User Conference*. 2018.

[2] Marvin Becker, Tom De Vuyst, Marina Seidl, Miriam Mehl, and Mhamed Souli. Numerical And Experimental Evaluation of Natural FragmFragment of Explosively Driven Cylinder Rings‘. *Procedings of Light Weight Armor Group 2019 (tbp)* (2019).

[3] Tom De Vuyst, Rade Vignjevic, James C Campbell, Andreas Klavzar, and Marina Seidl. A Study of the effect of aspect ratio on fragmentation of explosively driven cylinders. *Procedia Engineering* 204 (2017), pp. 194–201.

[4] Martin Ester, Hans-Peter Kriegl, Joerg Sander, and Xiaowei Xu. A density-based algorithm for discovering clusters in large spatial databases with noise. *Prodeedings of the Second International Conference on Knowledge Discovery and Data Mining (KDD-96)* (1996).

[5] Norbert Faderl, G Guetter, Th Wolf, C Doenlen, and S Gaisser. *Modellversuche zur Simulation des Impakts von Turbinensplittern aus der Nickel-Basis-Legierung Inco 718 auf strukturierte Triebwerksteile*. Tech. rep. French-German Research Institute Saint-Louis (ISL), 2008.

[6] Sebastian Grottel, Michael Krone, Christoph Muller, Guido Reina, and Thomas Ertl. MegaMol - A Prototyping Framework for Particle-Based Vizualization. *IEEE Transactions on Visualization* (2015).

[7] Zvi Rosenberg and Erez Dekel. *Terminal ballistics*. Springer, 2012.

[8] Marina Seidl, Thomas Wolf, and Rainer Nuesing. Numerical investigations on ricochet of a spin-stabilised projectile on differently shaped target surfaces. In: *30th ISB, Long Beach*. 2017.

[9] Xiaotian Zhang, Jia Guanghui, and Hai Huang. Fragment identification and statistics method of hypervelocity impact SPH simulation. *Chinese Journal of Aeronautics* 24.1 (2011), pp. 18–24.

**Proceedings of the 8th GACM Colloquium on Computational Mechanics
for Young Scientists from Academia and Industry
August 28–30, 2019 in Kassel, Germany**

Multiphase-field Simulation Study of Brittle Anisotropic Crack Propagation in Sandstones

Michael Späth * †1, Nishant Prajapati†1, Christoph Herrmann†1, Daniel Schneider[1,2], Michael Selzer[1,2] and Britta Nestler[1,2]

[1]Institute of Applied Materials (IAM-CMS), Karlsruhe Institute of Technology (KIT), Straße am Forum 7, 76131 Karlsruhe, Germany

[2]Institute of Digital Materials Science (IDM), Karlsruhe University of Applied Sciences, Moltkestrasse 30, 76133 Karlsruhe, Germany

Abstract. This work outlines a computational framework to model anisotropic transgranular and intergranular fracture propagation in sandstones at microscopic length scale using a multiphase-field. We incorporate an anisotropic crack resistance formulation to account for the variations in the fracture toughness of quartz along different crystallographic directions. Moreover, in order to model the intergranular fracturing, a reduced interfacial crack resistance formulation is utilised. We demonstrate the capabilities of the model through the representative numerical example.

Introduction

Fractures are ubiquitous in rocks such as sandstone and originate due to a wide range of mechanical loading conditions. At microscale, quartzarenite sandstone primarily consists of quartz grains with different crystallographic orientations. The intergranular pore space is filled with quartz cements that are deposited in optical continuity with the grains. Experiments [1] report that the fracture toughness of prismatic quartz varies with the crystallographic direction, giving rise to preferential direction of crack growth inside each grain. Furthermore, when the tip of a propagating fracture reaches a grain boundary, depending upon the resistance offered in that region, intergranular, transgranular or mixed fracturing might occur. All these anisotropies at grain scale, along with the loading conditions, control the crack path and account for complex fracture geometries at microscales. These microcracks influence the physical properties of rocks, like strength and permeability, and act as a nucleation site for marcofractures. Therefore, a deep understanding of the formation and growth of microfractures is imperative.
Computational modeling of fracturing in geological materials has emerged as a field of intense research in the past decades. Different numerical methods were used to investigate crack formation in geological structures [8, 9, 10]. In this work, we present a multiphase-field simulation study of microfracturing in sandstone, which takes an anistropic fracture toughness and lower crack resistance along the grain boundaries into account. The present model builts upon the framework of Schneider et al. [6] and ensures that the mechanical jump conditions of the solid phases are fulfilled [5].

1 Mulitphase-field model for crack propagation

We consider a computational domain consisting of N solid phases and a crack phase. Each phase is represented by an order parameter $\phi_\alpha(\mathbf{x}, t)$, $\alpha \in [1, \ldots, N, c]$, which describes the volume fraction of a particular phase at position $\mathbf{x}$ and time t. The transition region between different phases is described by a diffuse interface in which the order parameter $\phi_\alpha(\mathbf{x}, t)$ varies continuously from 1 inside the phase α to 0 outside. The crack phase, represented by ϕ_c, describes the material degradation, where $\phi_c = 1$ represents a fully damaged and $\phi_c = 0$ a fully intact material. At each point in the computational domain, the

*Corresponding author: michael.spaeth@kit.edu
†Authors contributed equally

summation constraint of all occurring phase-fields $\sum_{\alpha}^{N} \phi_\alpha = 1 - \phi_c$ is fulfilled. All the phase-fields are collected in a phase-field vector $\boldsymbol{\phi}(\boldsymbol{x}, t) = \{\phi_1(\mathbf{x}, t), \dots \phi_N(\mathbf{x}, t), \phi_c(\mathbf{x}, t)\} = \{\boldsymbol{\phi}_\mathrm{s}, \phi_\mathrm{c}\}$.
Based on the theory of Griffith [2], a total free energy functional $\mathcal{F}$ to describe crack propagation in a multiphase system of volume V is applied

$$\mathcal{F}(\boldsymbol{\phi}, \nabla\phi_c, \boldsymbol{\varepsilon}_\mathrm{el}) = \int_V \underbrace{\frac{G_\mathrm{c}(\boldsymbol{\phi}, \nabla\phi_c)}{2}\left[\frac{1}{\epsilon}\omega_\mathrm{c}(\phi_c) + \epsilon|\nabla\phi_c|^2\right] + f_\mathrm{el}(\boldsymbol{\varepsilon}_\mathrm{el}, \boldsymbol{\phi})}_{f(\boldsymbol{\phi}, \nabla\phi_c, \boldsymbol{\varepsilon}_\mathrm{el})} \,\mathrm{d}V. \tag{1}$$

The effective crack resistance is denoted by $G_\mathrm{c}(\boldsymbol{\phi}, \nabla\phi_c)$ and $f_\mathrm{el}(\boldsymbol{\varepsilon}_\mathrm{el}, \boldsymbol{\phi})$ represents the effective strain energy density. $\nabla\phi_c$ is the gradient of crack phase-field ϕ_c and $\boldsymbol{\varepsilon}_\mathrm{el}$ is the elastic strain tensor according to the infinitesimal strain assumption. The crack resistance maps the energy of a crack in a regularised manner by using a one-side well-potential $\omega_\mathrm{c}(\phi_c) = \phi_c^2$ and a gradient term $|\nabla\phi_c|^2$. The length scale parameter ϵ controls the crack interface width. The evolution of the crack phase-field is described in terms of a variational derivative of the free energy functional which is given as

$$\frac{\partial\phi_c(\mathbf{x}, t)}{\partial t} = -M\frac{1}{\epsilon}\frac{\delta\mathcal{F}(\boldsymbol{\phi}, \nabla\phi_c, \boldsymbol{\varepsilon}_\mathrm{el})}{\delta\phi_c} = -M\frac{1}{\epsilon}\left(\frac{\partial f(\boldsymbol{\phi}, \nabla\phi_c, \boldsymbol{\varepsilon}_\mathrm{el})}{\partial\phi_c} - \nabla\cdot\left(\frac{\partial f(\boldsymbol{\phi}, \nabla\phi_c, \boldsymbol{\varepsilon}_\mathrm{el})}{\partial\nabla\phi_c}\right)\right), \tag{2}$$

where M is the mobility. With the interpolation function of solid phases $h_\mathrm{s}^\alpha(\boldsymbol{\phi}) = \phi_\alpha / \sum_\beta^N \phi_\beta$ the evolution of solid phases reads

$$\frac{\partial\phi_\alpha}{\partial t} = -h_\mathrm{s}^\alpha(\boldsymbol{\phi})\frac{\partial\phi_c}{\partial t} \qquad \text{for} \quad \alpha = 1, .., N. \tag{3}$$

This multiphase-field model for crack formation can be extended to different applications by modifying the crack resistance or strain energy density. For modeling crack propagation in brittle geological materials a formulation for an anisotropic crack resistance is introduced in [4], where the crack resistance can be modified along the c- and a-axis of arbitrary orientated crystals. Moreover for modeling intergranular fracturing an interfacial crack resistance is presented. The crack resistance along grain boundaries can be adapted with a third order polynomial function. An extension to elasto-plastic crack propagation in geological materials with Drucker Prager plasticity is presented in [7]. Furthermore the presented muliphase-field model is extended in [3] for ductile fracturing in metals and is applied to a cast-iron microstructure.
The static impulse balance $\boldsymbol{\nabla}\cdot\bar{\boldsymbol{\sigma}} = \mathbf{0}$ is solved for the displacement field with the degraded volume-averaged stresses

$$\bar{\boldsymbol{\sigma}} = (1-\phi_c)^2\sum_{\alpha=1}^{N}\boldsymbol{\sigma}^\alpha \quad \text{with} \quad \boldsymbol{\sigma}^\alpha = \frac{\partial}{\partial\boldsymbol{\varepsilon}_\mathrm{el}^\alpha}\left(\frac{1}{2}\boldsymbol{\varepsilon}_\mathrm{el}^\alpha\cdot\boldsymbol{\mathcal{C}}^\alpha[\boldsymbol{\varepsilon}_\mathrm{el}^\alpha]\right) = \boldsymbol{\mathcal{C}}^\alpha[\boldsymbol{\varepsilon}_\mathrm{el}^\alpha], \tag{4}$$

where $\boldsymbol{\sigma}^\alpha$ is the phase-inherent stress tensor, $\boldsymbol{\mathcal{C}}^\alpha$ is the phase-inherent stiffness tensor, and $\boldsymbol{\varepsilon}_\mathrm{el}^\alpha$ is the phase-inherent elastic strain tensor. In multiphase regions the mechanical jump conditions are fulfilled for the solid phases [5].

2 Numerical example

The capabilities of the presented model are demonstrated in a multiphase system containing quartz grains. The simulation setup, the boundary conditions, and the crystallographic orientation of the grains are depicted in Figure 1 a). In Figure 1 b) the crack resistance field is illustrated. The crack resistance along the a-axis is reduced based on the experimental values of the fracture toughness [1]. Furthermore the crack resistance between grain boundaries is decreased. Schematically, the interfacial crack resistance along the line (I-II) and the anisotropic crack resistance at the crack tip is visualised. Figure 1 c) depicts the simulated crack path exhibiting both anisotropic transgranular and intergranular fracturing, resulting in an irregular crack geometry.

Acknowledgments

The research has been supported by the German Research foundation (DFG) through the project NE 822/34-1. Furthermore the authors thank the Helmholtz Association for the financial support through the program “Renewable Energies (RE)”, efficient use of geothermal energy 35.14.01.

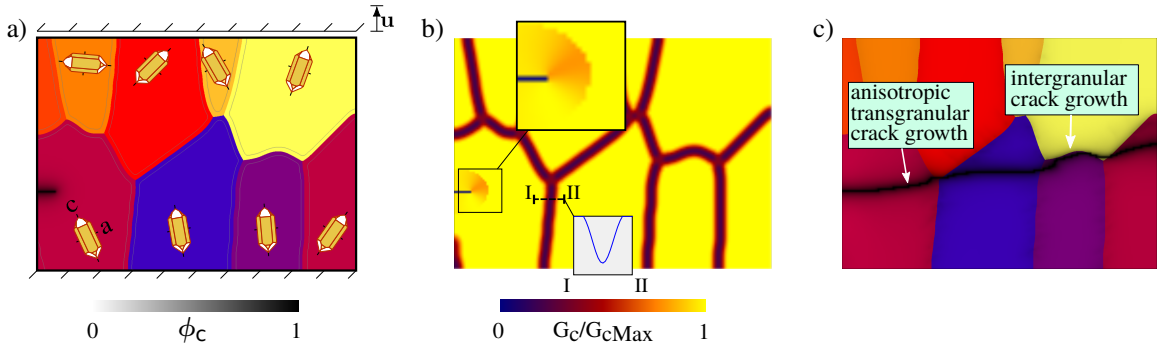

Figure 1. Crack propagation in a multigrain system, analogous to quartz sandstone. a) Simulation setup illustrating a microstructure with quartz grains along with applied boundary conditions and a pre-existing crack. The crystallographic orientation of different grains is depicted schematically within each grain. b) Crack resistance field at the beginning of the simulation. The anisotropic crack resistance at the crack tip and the interfacial crack resistance along path (I-II) is highlighted. c) Fully fractured specimen.

References

[1] Colin C Ferguson, Geoffrey E Lloyd, and Robert J Knipe. Fracture mechanics and deformation processes in natural quartz: a combined Vickers indentation, SEM, and TEM study. *Canadian Journal of Earth Sciences* 24.3 (1987), pp. 544–555.

[2] Alan Arnold Griffith. VI. The phenomena of rupture and flow in solids. *Philosophical transactions of the royal society of london. Series A, containing papers of a mathematical or physical character* 221.582-593 (1921), pp. 163–198.

[3] Christoph Herrmann, Daniel Schneider, Ephraim Schoff, Felix Schwab, and Britta Nestler. Multiphase-field model for the simulation of brittle and ductile crack propagation in grey cast iron microstructures (in preparation).

[4] Nishant Prajapati, Christoph Herrmann, Michael Späth, Daniel Schneider, Michael Selzer, and Britta Nestler. Brittle Anisotropic Fracture Propagation in Quartz Sandstone: Insights from Phase-field Simulations (in preparation).

[5] Daniel Schneider, Oleg Tschukin, Abhik Choudhury, Michael Selzer, Thomas Böhlke, and Britta Nestler. Phase-field elasticity model based on mechanical jump conditions. *Computational Mechanics* 55.5 (2015), pp. 887–901.

[6] Daniel Schneider, Ephraim Schoof, Yunfei Huang, Michael Selzer, and Britta Nestler. Phase-field modeling of crack propagation in multiphase systems. *Computer Methods in Applied Mechanics and Engineering* 312 (2016), pp. 186–195.

[7] Michael Späth, Christoph Herrmann, Nishant Prajapati, Daniel Schneider, Felix Schwab, Michael Selzer, and Britta Nestler. Multiphase-field modelling of crack propagation in geological materials with Drucker Prager plasticity (in preparation).

[8] Simon Virgo, Steffen Abe, and Janos L Urai. Extension fracture propagation in rocks with veins: Insight into the crack-seal process using Discrete Element Method modeling. *Journal of Geophysical Research: Solid Earth* 118.10 (2013), pp. 5236–5251.

[9] XiaoLong Wang, Fang Shi, Chuang Liu, DeTang Lu, He Liu, and HengAn Wu. Extended finite element simulation of fracture network propagation in formation containing frictional and cemented natural fractures. *Journal of Natural Gas Science and Engineering* 50 (2018), pp. 309–324.

[10] Xi Zhang and Robert G Jeffrey. Role of overpressurized fluid and fluid-driven fractures in forming fracture networks. *Journal of Geochemical Exploration* 144 (2014), pp. 194–207.

**Proceedings of the 8th GACM Colloquium on Computational Mechanics
for Young Scientists from Academia and Industry
August 28–30, 2019 in Kassel, Germany**

User-defined material subroutines for FEM calculations based on automatic differentiation of strain energy functions

Markus Hillgaertner * [1], Theron Guo[1] and Mikhail Itskov[1]

[1]Department of Continuum Mechanics, RWTH Aachen University, Kackertstr. 9, 52072 Aachen, Germany

Abstract. The implementation of material models into the implicit finite element method (FEM) codes requires the calculation of a fourth order tangent tensor. In hyperelastic models this tensor can be obtained from the second derivative of the strain energy function with respect to the deformation gradient. Deriving and implementing this derivative manually can be tedious and error prone.

This contribution presents an easy-to-use alternative based on automatic differentiation (AD) capable of efficiently evaluating accurate derivatives [3, 6]. This technique is applied to automatically derive a user-defined material subroutine (UMAT) for implicit FEM analysis of a hyperelastic anisotropic model of arterial layers [1] in ABAQUS. Additionally, a pseudo-elastic model for the Mullins effect in filled rubber [7] is implemented to evaluate the applicability of the discussed approach in cases where the material model exhibits inelastic behavior described by internal variables.

1 Introduction

The implementation of material models into implicit finite element method (FEM) codes requires the calculation of a fourth order tangent tensor. In constitutive models given in terms of a strain energy function, this tensor can be obtained from the second derivative of tis function with respect to the deformation gradient. The manual derivation and implementation of this derivative can be tedious and error prone. In order to automatize this process, automatic differentiation of code can be a suitable tool to create user defined material models without the need of manual differentiation. While the concept has been used in the FEM context before [i.e. 10], we focus on its applicability inside the framework of commercial FEM programs like ABAQUS.

2 Materials and methods

2.1 Constitutive modeling

Let us consider a material model using a multiplicative split of the deformation gradient $\mathbf{F}$ into an isochoric (volume preserving) part $\bar{\mathbf{F}}$ and a volumetric (volume changing) part $\hat{\mathbf{F}}$ as

$$\mathbf{F} = \hat{\mathbf{F}}\bar{\mathbf{F}}, \qquad J = \det \mathbf{F}, \qquad \hat{\mathbf{F}} = J^{1/3}\mathbf{I}, \qquad \bar{\mathbf{F}} = J^{-1/3}\mathbf{F}, \qquad \det \bar{\mathbf{F}} = 1. \tag{1}$$

Accordingly, the right Cauchy-Green tensor $\mathbf{C}$ and its isochoric part $\bar{\mathbf{C}}$ take the form

$$\mathbf{C} = \mathbf{F}^{\mathrm{T}}\mathbf{F}, \qquad \bar{\mathbf{C}} = \bar{\mathbf{F}}^{\mathrm{T}}\bar{\mathbf{F}} = J^{-2/3}\mathbf{C}, \tag{2}$$

which leads to the invariants of $\bar{\mathbf{C}}$ as

$$\bar{\mathrm{I}} = \mathrm{I}_{\bar{\mathbf{C}}} = \operatorname{tr} \bar{\mathbf{C}}, \qquad \bar{\mathrm{II}} = \mathrm{II}_{\bar{\mathbf{C}}} = \frac{1}{2}\left[(\operatorname{tr} \bar{\mathbf{C}})^2 - \operatorname{tr}\left(\bar{\mathbf{C}}^2\right)\right], \qquad \bar{\mathrm{III}} = \mathrm{III}_{\bar{\mathbf{C}}} = \det \bar{\mathbf{C}}. \tag{3}$$

*Corresponding author: hillgaertner@km.rwth-aachen.de ORCID iD: 0000-0001-7974-2055

In terms of a strain energy function Ψ the first and second Piola-Kirchhoff stress tensors $\mathbf{P}$ and $\mathbf{S}$, and the Cauchy stress tensor $\boldsymbol{\sigma}$ can be expressed as

$$\mathbf{P} = \frac{\partial \Psi}{\partial \mathbf{F}}, \qquad \mathbf{S} = 2\frac{\partial \Psi}{\partial \mathbf{C}}, \qquad \boldsymbol{\sigma} = \frac{1}{J}\mathbf{P}\mathbf{F}^{\mathrm{T}} = \frac{1}{J}\frac{\partial \Psi}{\partial \mathbf{F}}\mathbf{F}^{\mathrm{T}}. \tag{4}$$

In order to obtain convergence during a FEM iteration step, the calculation of a tangent tensor is necessary. A variety of different tangent tensors exist:

The material tangent tensor (or Lagrangian tangent tensor) is given as the derivative of the second Piola-Kirchhoff stress tensor $\mathbf{S}$ with respect to the Green-Lagrange strain $\mathbf{E}$, which is its work conjugate strain [4, 8]

$$\mathbb{C} = \frac{\partial \mathbf{S}}{\partial \mathbf{E}} = 2\frac{\partial \mathbf{S}}{\partial \mathbf{C}} = 4\frac{\partial^2 \Psi}{\partial \mathbf{C} \partial \mathbf{C}}. \tag{5}$$

The spatial tangent tensor $\mathbb{c}$ (or Eulerian tangent tensor) can be obtained from $\mathbb{C}$ using a push-forward operation given as

$$\mathbb{c}_{ijkl} = \frac{1}{J}\mathbb{C}_{IJKL}\mathbf{F}_{iI}\mathbf{F}_{jJ}\mathbf{F}_{kK}\mathbf{F}_{lL}. \tag{6}$$

In addition to the tangent tensors in the spatial or material formulation, one can define a mixed tangent tensor using the first Piola-Kirchhoff stress $\mathbf{P}$ as [4]

$$\mathbb{A} = \frac{\partial \mathbf{P}}{\partial \mathbf{F}} = \frac{\partial^2 \Psi}{\partial \mathbf{F} \partial \mathbf{F}}. \tag{7}$$

$\mathbb{A}$ is particularly useful in the context of automatic differentiation, as it utilizes the strain energy function of interest Ψ and the deformation gradient $\mathbf{F}$, which is the primary input in a user-defined subroutine for a user material in the FE framework. The spatial tangent tensor $\mathbb{c}$ can be directly calculated for a given $\mathbb{A}$.

Differentiating Ψ with respect to the deformation gradient $\mathbf{F}$ is general, as it includes material models based on the right Cauchy-Green tensor $\mathbf{C} = \mathbf{F}^{\mathrm{T}}\mathbf{F}$ or its invariants without additional effort. In less general cases derivatives directly with respect to $\mathbf{C}$ or its invariants can be numerically favorable. In this case, less general user subroutines such as UHYPER can be more suitable.

2.2 Automatic differentiation

The desired first (stress) and second (tangent) derivatives of the strain energy can be obtained in many ways: While a handcoded analytical derivative is exact and often the numerically fastest method, creating this code is time consuming and error prone. Subsequent minor changes in Ψ can lead to a huge amount of outdated code, which needs to be updated manually. Alternatively, finite differentiation can be utilized. This procedure, while easy to implement, only provides approximated results and often requires an extensive amount of computational time. Automatic differentiation on the other hand guarantees exact results at a computational effort. [5]

We choose the tangent mode of automatic differentiation, which applies the chain rule in forward direction. To this end, Tapenade [3] is utilized twice: Once in order to obtain $\mathbf{P} = \frac{\partial \Psi}{\partial \mathbf{F}}$ and once again to obtain $\mathbb{A} = \frac{\partial^2 \Psi}{\partial \mathbf{F} \partial \mathbf{F}} = \frac{\partial \mathbf{P}}{\partial \mathbf{F}}$. The specific stress and tangent tensors, required by the chosen FEM programm can now be obtained based on $\mathbf{P}$ and $\mathbb{A}$.

2.3 Implementation into an Abaqus/Standard user-defined material subroutine (UMAT)

The minimally required outputs of a UMAT subroutine in Abaqus/Standard are `STRESS` (Cauchy stress $\boldsymbol{\sigma}$) and the Jacobian matrix of the constitutive model `DDSDDE` ($\mathbb{c}^{\mathrm{Abaqus}}$). This tangent required by the UMAT relates the volume-normalized Jaumann rate of the Kirchhoff stress to the symmetric rate of deformation tensor [4, 8] and is given by

$$\mathbb{c}^{\mathrm{Abaqus}} = \mathbb{c} + \mathbb{c}', \tag{8}$$

where the fourth order tensor $\mathbb{c}'$ can be expressed by Equation (6) as [4, 8]

$$\mathbb{c}'_{ijkl} = \frac{1}{2}\left(\delta_{ik}\boldsymbol{\sigma}_{jl} + \delta_{il}\boldsymbol{\sigma}_{jk} + \delta_{jk}\boldsymbol{\sigma}_{il} + \delta_{jl}\boldsymbol{\sigma}_{ik}\right), \tag{9}$$

which possesses major and minor symmetries. δ_{ij} denotes the Kronecker delta defined as

$$\delta_{ij} = \begin{cases} 1 & \text{for } i = j \\ 0 & \text{for } i \neq j. \end{cases} \tag{10}$$

While $\mathbb{c}$ needs to be calculated for each material model, the implementation of $\mathbb{c}'$ is independent of the chosen material description.

3 Numerical examples

In this study, three different material models have been implemented into UMATs: The neo-Hookean strain energy (subsection 3.1) as the simplest case of an isotropic elastic model, the Ogden-Roxburgh model (subsection 3.2) as extension of the neo-Hookean strain energy function to include the Mullins effect and a model of arterial layers incorporating anisotropy (subsection 3.3). The models have been implemented in terms of strain energy functions and the corresponding derivatives for the stress and the tangent have been obtained using automatic differentiation.

3.1 Neo-Hookean strain energy

The neo-Hookean [9] hyperelastic material model can be represented as a strain energy function

$$\Psi_{\mathrm{NH}}(\bar{\mathrm{I}}, J) = C_{10}(\bar{\mathrm{I}} - 3) + U(J) \tag{11}$$

where C_{10} denotes a material constant and $U(J)$ enforces near-incompressibility [2].

3.2 Ogden-Roxburgh pseudo-elastic model

The Ogden-Roxburgh model [7] extends the neo-Hookean strain energy function, given in equation (11), to include the Mullins effect. This is achieved by scaling the elastic Cauchy stress $\boldsymbol{\sigma}_0$ with a softening function $\eta(\Psi, \Psi_{max})$, which depends on the current strain energy Ψ and the maximum strain energy Ψ_{max} in the load history. Accordingly,

$$\boldsymbol{\sigma}_{OR} = \eta(\Psi, \Psi_{\mathrm{max}})\boldsymbol{\sigma}_0. \tag{12}$$

This pseudo-elastic model utilizes an internal variable, implemented as solution-dependent state variable `STATEV`, which needs to be correctly used and properly updated in the automatically differentiated subroutine.

3.3 Fiber reinforced hyperelastic model

A simple hyperelastic model of arterial layers [1] utilizes the neo-Hookean strain energy presented in subsection 3.1 for the fiber-reinforced ground substance. The n fiber families are modeled using

$$\Psi_i^{\mathrm{f}}(\bar{\mathbf{C}}) = \frac{k_1}{2k_2}\left[\exp\left(k_2\left[\bar{E}_i(\bar{\mathbf{C}})\right]^2\right) - 1\right], \qquad i = 1, ..., n, \tag{13}$$

where k_1 and k_2 denote material parameters and $\bar{E}_i$ represent strain-like quantities in the preferred directions of fibers (please refer to [1] for details). The complete strain energy for the composite can be given as

$$\Psi_{\mathrm{G}}(\bar{\mathbf{F}}) = \Psi_{\mathrm{NH}}(\bar{\mathrm{I}}, J) + \sum_{i=1}^{n} \Psi_i^{\mathrm{f}}(\bar{\mathbf{C}}), \qquad \bar{I} = \bar{I}(\bar{\mathbf{C}}), \qquad \bar{\mathbf{C}} = \bar{\mathbf{C}}(\bar{\mathbf{F}}), \qquad J = J(\bar{\mathbf{F}}). \tag{14}$$

4 Results and conclusion

All three investigated models have been successfully implemented in terms of the corresponding strain energy Ψ and then derived automatically in order to create fully functional UMAT subroutines. Since the applied automatic differentiation procedure grants exact derivatives, the results and convergence behavior did not differ significantly from the manually programmed ones.

While the analysis of computational times for the different examples is still in progress, the difference in implementation time in comparison to manual programming is enormous. Once a template is created, a strain energy function can be automatically turned into a subroutine without manual differentiation. This advantage in the implementation can save a considerable amount of time during the development and testing phases of new constitutive models.

References

[1] Thomas Christian Gasser, Ray W. Ogden, and Gerhard A. Holzapfel. Hyperelastic modelling of arterial layers with distributed collagen fibre orientations. *Journal of the Royal Society, Interface* 3.6 (2006), pp. 15–35.

[2] Stefan Hartmann and Patrizio Neff. Polyconvexity of generalized polynomial-type hyperelastic strain energy functions for near-incompressibility. *International Journal of Solids and Structures* 40.11 (2003), pp. 2767–2791.

[3] Laurent Hascoet and Valérie Pascual. The Tapenade automatic differentiation tool: Principles, model, and specification. *ACM Transactions on Mathematical Software* 39.3 (2013), pp. 1–43.

[4] Maria A. Holland. *The Hitchhiker's Guide to Abaqus*. 2017.

[5] Charles C. Margossian. A Review of automatic differentiation and its efficient implementation. January (2018), pp. 1–19.

[6] Uwe Naumann. *The Art of differentiating computer programs: an introduction to algorithmic differentiation*. Society for Industrial and Applied Mathematics, 2012. ISBN: 161197206X.

[7] Ray W. Ogden and David George Roxburgh. A pseudo–elastic model for the Mullins effect in filled rubber. *Proceedings of the Royal Society of London. Series A: Mathematical, Physical and Engineering Sciences* 455.1988 (1999), pp. 2861–2877.

[8] V. Prot and B. Skallerud. Nonlinear solid finite element analysis of mitral valves with heterogeneous leaflet layers. *Computational Mechanics* 43.3 (2009), pp. 353–368.

[9] R. S. Rivlin. Large Elastic Deformations of Isotropic Materials. IV. Further Developments of the General Theory. *Philosophical Transactions of the Royal Society A: Mathematical, Physical and Engineering Sciences* 241.835 (1948), pp. 379–397.

[10] Florian Zwicke, Philipp Knechtges, Marek Behr, and Stefanie Elgeti. Automatic implementation of material laws: Jacobian calculation in a finite element code with TAPENADE. *Computers & Mathematics with Applications* 72.11 (2016), pp. 2808–2822.

**Proceedings of the 8th GACM Colloquium on Computational Mechanics
for Young Scientists from Academia and Industry
August 28–30, 2019 in Kassel, Germany**

Nonlinear fibre distribution in a finite element model of a human left ventricle for sparse and non-constant data sets

David Holz * [1], Minh Tuan Doung[1,3], Myoungsic Kim[1], Muhannad Alkassar[2], Sven Dittrich[2] and Sigrid Leyendecker[1]

[1]Chair of Applied Dynamics, University of Erlangen-Nuremberg

[2]Pediatric Cardiology, University of Erlangen-Nuremberg

[3]School of Mechanical Engineering, Hanoi University of Science and Technology

Abstract. The morphology of the cardiac tissue is one of the most important characteristics to ensure a proper and choreographed contraction and thus the overall pump function of the heart. The morphology, especially the characteristic fibre structure of the heart, substantially influences the electrical and mechanical function. Thus, the correct representation of the specific fibre orientation is fundamental for all computational models in cardiac research. Often, there is a lack in experimental data or DT-MRI and thus rule-based schemes have to be applied in order to capture the realistic and patient specific fibre orientation as accurate as possible. For this purpose, we propose a finite element based nonlinear fibre interpolation scheme.

Introduction

The specific morphology and especially the fibre orienation of the cardiac tissue is the basis for the characteristic motion and pump function of the heart. Thus, it is fundamental in cardiac modelling to realistically represent the fibre orientation since it substantially influences the mechanical and electrophysiological properties. The fibre orientation of the cardiac tissue can be measured e.g. using DT-MRI or histology. However, in the case that no patient-specific fibre orientation is known or only sparse data from clinical measurements is available, rule-based models are applied. Under these circumstances, it is assumed that the fibre angles are measured at discrete points of the heart, often on the endo- and epicardium (e.g. from simplified reference measurements on the surface rather than in the volume or layers). Additional information about the transmural change in fibre angle are obtained e.g. from histology slides. Here, however, we assume that a nonlinear function representing the transmural change in fibre angle is given, see Figure 1.

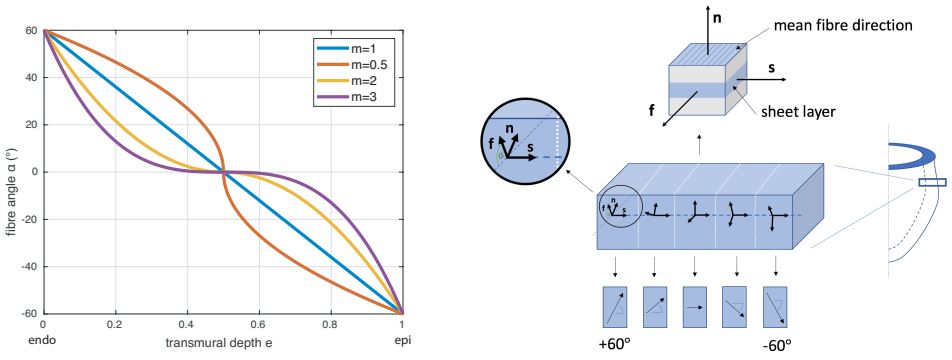

Figure 1. Left: transmural fibre angle $\alpha(e) = R * sgn(1-2e)|1-2e|^m$ depending on the transmural depth $e \in [0,1]$, R =60° represents the maximum fibre angle, $m \in \mathbb{N}$ is to be chosen in accordance with clinical measurements, see [1]. Right: characteristic morphology of the cardiac tissue with the transmurally varying fibre direction $\boldsymbol{f}$, sheet direction $\boldsymbol{s}$ and normal direction $\boldsymbol{n}$.

*Corresponding author: david.holz@fau.de ORCID iD: https://orcid.org/0000-0003-4838-718X

Based on the approach by Wong [3], we propose a finite element-based approach to assign the smooth nonlinear fibre distribution in a human left ventricle. Therefore, we solve an anisotropic Laplace equation, with a scalar-valued unknown, representing a specific vector component of the fibre direction $\boldsymbol{f} \in \mathbb{R}^3$. We show that the proposed interpolation scheme is capable of creating a smooth nonlinear interpolation for a geometrically complex patient-specific left ventricle obtained from high-resolution MRI at the Universitätsklinikum Erlangen-Nürnberg. Often sparse and insufficient data sets are available as boundary conditions for the Laplace problem. Analytical or least squares approaches can usually not be used or only under certain restrictions. However, also in this case, the proposed method provides an easy and robust way to create a smooth nonlinear fibre distribution with acceptable errors in fibre angle.

1 Theoretical framework

We solve an anisotropic Laplace-equation for each vector component f_i with $i = x, y, z$ of the fibre vector f.

$$\nabla \cdot (\boldsymbol{\lambda} \nabla f_i) = 0 \qquad \text{in } \mathcal{E} \tag{1}$$

with given Dirichlet and Neumann boundary conditions (b.c.)

$$f_i = \bar{f}_i \qquad \text{on } \partial\mathcal{E}, \tag{2}$$

The partial differential Equation (1) is transformed into its weak form and integrated over the domain, being discretised with linear tetrahedral elements. We define the Dirichlet b.c. as well as the element specific diffusion coefficient $\lambda_{i,n}$ in the sequel.

1.1 Dirichlet boundary conditions

To define the Dirichlet boundary conditions, we assign the given (in an ideal case measured) fibre orientation (more specifically absolute values of vector components) to local coordinate frames on the nodes of the finite element mesh on the boundary, see Figure 2. Here, we assume that the fibre orientation on the entire endo- and epicardium is given, being +60° and -60° with respect to the circumferential direction, respectively.

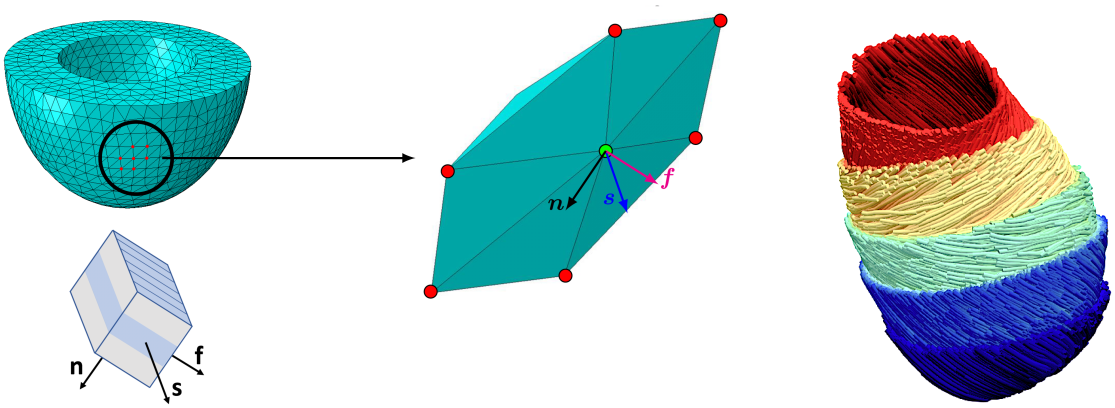

Figure 2. Left: characteristic microstructure of the cardiac tissue represented by local coordinate frames at each finite elemet node. Following [2], the cardiac tissue is characterized by an orthotropic structure consisting of the fibre direction $\boldsymbol{f}$, sheet direction $\boldsymbol{s}$ and normal direction $\boldsymbol{n}$. Right: visualisation of the fibre orientation in layers of the heart. The red colour represents the positive angle of +60° on the endocardium, the blue colour represents the negative angle of -60° on the epicardium with respect to the circumferential direction.

For more detailed information about the definition of the local coordinate system, see [3].

1.2 Diffusion coefficient

To assign the element and component specific diffusion coefficient $\lambda_{i,n}$, where $i = x, y, z$ and n accounts for the specific element, we consider the influence of the following three factors: vector component interpolation (1), area dependency (2) and nonlinear fibre distribution (3).

(1) vector component interpolation

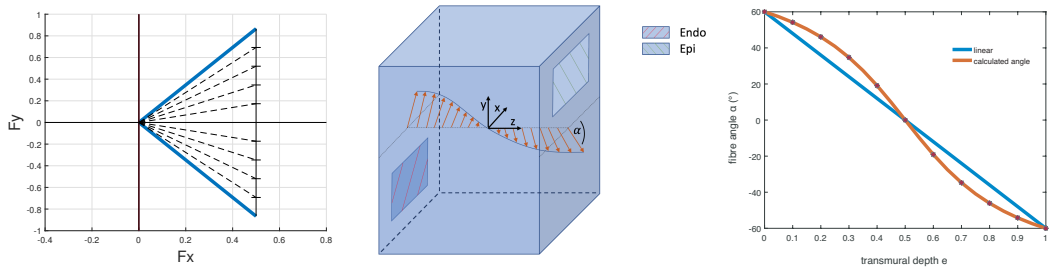

Figure 3. Vector component interpolation for a simple cube with $\alpha = +60°$ on endo- and $\alpha = -60°$ on epicardium (left) leads to a nonlinear angle interpolation (right), even though the prescribed transmural fibre angle $\alpha(e)$ is linear ($m = 1$). Based on the spherical linear interpolation, we propose Equation (3) to take into account the nonlinear change of the vector components, where e_n is is the transmural depth of the specific element n, $A_{i,n}$ and $C_{i,n}$ are the vector components of the tangent vectors (of the fibre direction $\boldsymbol{f}$) on the endo- and epicardium and B defines the angle spanned by $\boldsymbol{A}_n$ and $\boldsymbol{C}_n$.

$$\lambda_{i,n}^{(1)} = \frac{1}{|w_{i,n}|} \quad \text{with} \quad w_{i,n}(e_n, A_{i,n}, C_{i,n}) = \frac{(A_{i,n} \cdot sin((1-e_n) \cdot B) + C_{i,n} \cdot sin(e_n \cdot B)}{sin(B)} \tag{3}$$

(2) area dependency

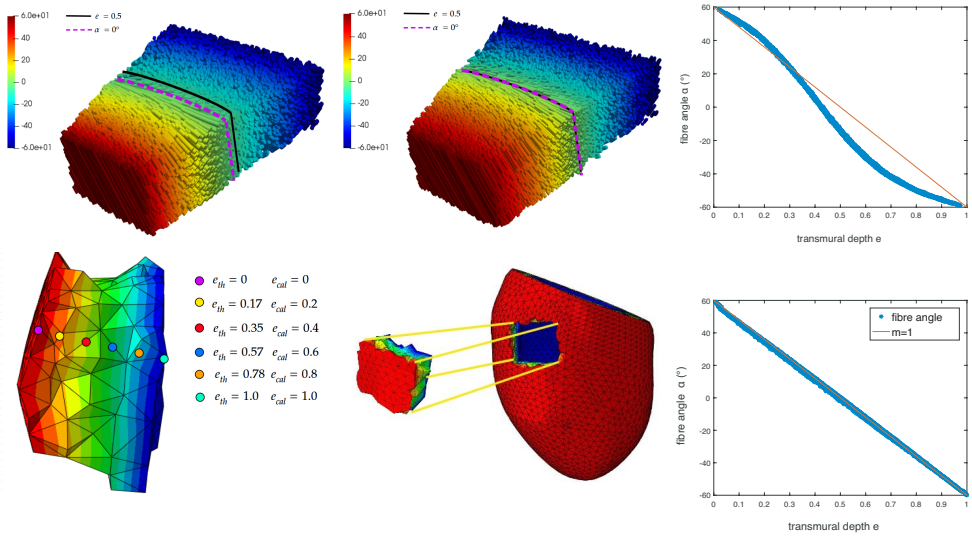

Figure 4. Top left: transmural fibre angle α without accounting for the different area on the endo-and epicardium (shift of $0°$ line to endo; $e < 0.5$). Top center: transmural fibre angle α taking into account the area change ($\alpha = 0°$ at $e = 0.5$). Top right: fibre angle α over the transmural depth e without accounting for the area. Bottom - left and center: comparison of the transmural depth computed by a diffusion problem with a constant isotropic diffusion coefficient (Dirichlet b.c.: 0 on endo and 1 on epi; e_{th} is the transmural depth for each element) and the transmural depth e_{cal} calculated by following the steepest descent of the diffusion field for an MRI-based left ventricle. Bottom - right: linear angle interpolation following the proposed Equation (4) to account for the local area change in the LV.

$$\lambda_n^{(2)} = \left(\frac{e_{n_{cal}}}{e_{n_{th}}}\right)^2 \tag{4}$$

(3) nonlinear fibre distribution

The nonlinear fibre interpolation is also influenced by the derivative of the predefined function $\alpha(e_n)$.

$$\lambda_n^{(3)} = \frac{1}{T'(e_n)} \tag{5}$$

Thus, the total description of the elementwise and vector component dependent diffusion coefficient $\lambda_{i,n}^{(tot)}$ reads

$$\lambda_{i,n}^{(tot)} = \lambda_{i,n}^{(1)} \cdot \lambda_n^{(2)} \cdot \lambda_n^{(3)}. \tag{6}$$

2 Results

In Figure 5 (left), the nonlinear fibre distribution with $m = 3$ for a left ventricle is shown. The proposed method creates a smoothly varying interpolation with acceptable errors in angle interpolation.

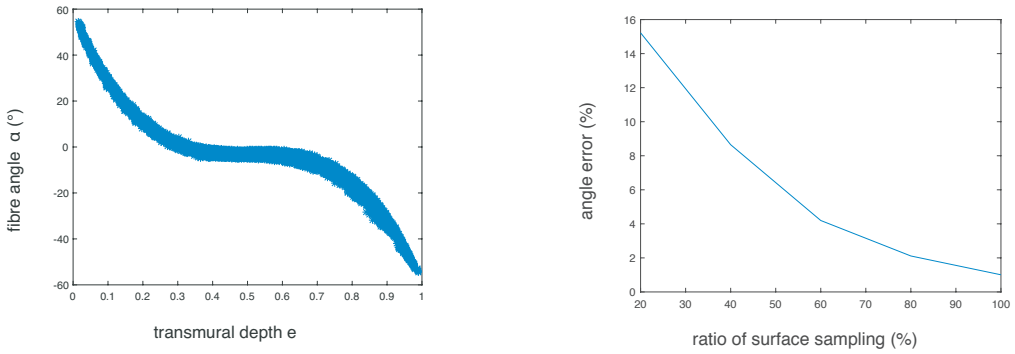

Figure 5. Left: fibre angle α over the transmural depth for each element (fibre vectors in the apex area reassigned). Right: sensitivity analysis shows that even for a reduced set of Dirichlet boundary conditions (up to 20%), the method provides results with acceptable errors (max. error approx. 15°).

Figure 5 (right) shows that even in the case of sparse data, represented by a reduced set of Dirichlet boundary conditions (up to 20%), the method provides results with acceptable errors (max. error approx. 15°).

In this work, we show that the proposed method is capable of creating a smooth nonlinear fibre interpolation. The method is easy to apply, robust and even employable in the case of sparse data. Further, the method can be extended to also take into account non-constant fibre angles on the endo- and epicardium.

Acknowledgments

The authors thank the Klaus Tschira Stiftung grant 00.289.2016 for funding support

References

[1] V. Carapella, R. Bordas, P. Pathmanathan, M. Lohezic, J. Schneider, P. Kohl, K. Burrage, and V. Grau. Quantitative Study of the Effect of Tissue Microstructure on Contraction in a Computational Model of Rat Left Ventricle. *PLOS ONE* 9 (2014), pp. 1–12.

[2] G. A. Holzapfel and R. W. Ogden. Constitutive modelling of passive myocardium: a structurally based framework for material characterization. *Royal Society of London Philosophical Transactions A: Mathematical, Physical and Engineering Sciences* 367 (2009), pp. 3445–3475.

[3] J. Wong and E. Kuhl. Generating fibre orientation maps in human heart models using Poisson interpolation. *Computer methods in biomechanics and biomedical engineering* 17 (2014), pp. 1217–1226.

**Proceedings of the 8th GACM Colloquium on Computational Mechanics
for Young Scientists from Academia and Industry
August 28–30, 2019 in Kassel, Germany**

A Frictional and Adhesive Contact Model for Debonding of the Bone-Implant interface Based on State Variable Friction Laws

Katharina Immel * [1,2], Thang X. Duong[1], Vu-Hieu Nguyen[2], Guillaume Haïat[2] and Roger A. Sauer[1]

[1]Aachen Institute for Advanced Study in Computational Engineering Science (AICES), RWTH Aachen University, Templergraben 55, 52056 Aachen, Germany

[2]CNRS, Laboratoire Modélisation et Simulation Multi Echelle, MSME UMR 8208 CNRS, 61 Avenue du Général de Gaulle, 94010 Créteil Cedex, France

Abstract. Implant loosening is one of the major problems of cementless orthopedic and dental implants. However, the underlying phenomena of osseointegration, especially regarding frictional and adhesive effects at the interface and their influence on long term stability, remain poorly understood. Most numerical studies so far assume either a fully bonded interface, frictionless contact or pure Coulomb's friction. While this assumption might be valid for the prediction of initial stability, the prediction of failure of osseointegrated implants requires the inclusion of more complex frictional and adhesive effects. Here, a macroscopic contact formulation is proposed based on state variable friction laws [5] that can model debonding at the bone-implant interface. For each element on the contact surface, the tangential contact stress depends on the normal contact pressure, the sliding rate, and the current state of the element (fully bonded, debonding or fully sliding) with respect to its sliding history and initial bonding state. This model leads to different contact laws for every state, for example, a frictional adhesion model [4] for fully bonded elements and pure Coulomb's friction for fully sliding once. This contact formulation is embedded in a finite element contact framework [2], including a NURBS-enrichment approach for three-dimensional contact elements [1] for an efficient contact treatment. It is validated by comparing the numerical results with experimental data [3] and used to model the torsional debonding of osseointegrated implants. The results show good agreement with experimental data and provide estimates for the material properties of the bone-implant interface, such as the shear modulus, Young's modulus, and friction coefficient. Furthermore, it allows the analysis of the debonding behavior, for example, in terms of maximum bearing loads and stresses, and crack propagation, that are difficult to measure in vivo or in vitro.

Introduction

Cementless, endosseous implants are widely used in orthopedic and oral surgery. These implants achieve primary stability during surgery by mechanical interlocking, while long term stability is achieved by bone growing around and into the porous or rough surface of the implant, a process called *osseointegration*. However, failures still occur and may cause the debonding of the bone-implant interface, which in turn leads to a revision of the implant. It remains difficult to predict implant failure since the underlying osseointegration phenomena, especially in terms of friction and adhesion, and their influence on the primary and secondary stability of the implant, is still poorly understood. We therefore propose a contact formulation that can model the debonding behavior of osseointegrated implants.

1 Theoretical framework

Given two 3D bodies $\mathcal{B}_1$ and $\mathcal{B}_2$ and their contact surface $\partial_c\mathcal{B}$, the contact traction $\boldsymbol{t}_c$ can be decomposed into a normal and tangential component, i.e. $\boldsymbol{t}_c = \boldsymbol{t}_n - \boldsymbol{t}_t$. The magnitude of the normal traction is equal to the normal contact pressure, i.e.

$$\|\boldsymbol{t}_n\| = p, \tag{1}$$

*Corresponding author: immel@aices.rwth-aachen.de

and is always compressive if no adhesion is present. For frictional contact, the tangential traction is determined by the behavior during sticking and sliding. The distinction between these two states is based on a slip criterion of the form

$$f_\mathrm{s} \begin{cases} < 0, & \text{for sticking,} \\ = 0, & \text{for sliding.} \end{cases} \tag{2}$$

It can be formulated as

$$f_\mathrm{s} = \|\boldsymbol{t}_\mathrm{t}\| - t_\mathrm{t}^{\max}, \quad \|\boldsymbol{t}_\mathrm{t}\| \leq t_\mathrm{t}^{\max}, \tag{3}$$

where $t_\mathrm{t}^{\max} > 0$ is the maximal tangential contact traction. For sticking, the tangential traction is defined by the constraint that no relative tangential motion occurs, while for sliding, the tangential traction is defined by a sliding law. Most numerical analyses of implant stability only consider either fully bonded contact, frictionless contact or pure Coulomb's friction, according to

$$\boldsymbol{t}_\mathrm{t} = -\mu\, p\, \frac{\dot{\boldsymbol{g}}_\mathrm{s}}{\|\dot{\boldsymbol{g}}_\mathrm{s}\|}, \tag{4}$$

where μ is a constant friction coefficient, p is the normal contact pressure, and $\dot{\boldsymbol{g}}_\mathrm{s}$ denotes the sliding rate. Such an approach may be a valid assumption for the assessment of initial stability, where no adhesive forces are expected. However, to predict the failure of osseointegrated implants, adhesive and frictional effects need to be taken into account. One approach to account for the change of contact behavior due to different states of the interface are *state variable* friction laws, introduced by Rice and Ruina [5]. In general, these laws assume that at any given time, the frictional stress of a point $\boldsymbol{x}$ on the contact surface depends on the normal pressure, the sliding rate $\dot{g}_\mathrm{s} = \|\dot{\boldsymbol{g}}_\mathrm{s}\|$ and a state variable S, i.e.

$$\boldsymbol{t}_\mathrm{t} = \boldsymbol{t}_\mathrm{t}(p, \dot{g}_\mathrm{s}, S). \tag{5}$$

Although these laws are mainly applied in geology and geophysics, the state variable S can be interpreted as the current bonding state of a certain point $\boldsymbol{x}$ on the bone-implant interface $\partial_\mathrm{c}\mathcal{B}$. Here, S is modeled as a smooth step function from 1 to 0 and depends on the total displacement of the contact surface. This definition can be used to model macroscopic frictional and adhesive phenomena at the interface, e.g.

- adhesive contact while bonded ($S > 0$),
- debonding due to displacement ($0 < S < 1$),
- frictional sliding when fully debonded ($S = 0$).

The corresponding current state then determines the appropriate contact law. An example is using the frictional adhesion model of Mergel et al. [4] for fully bonded and Coulomb's law for debonded points. Adhesion in normal direction can be modeled, e.g. by an exponential cohesive zone model [7] or van der Waals adhesion [4]. This contact formulation is implemented into an existing finite element (FE) contact formulation, based on Duong and Sauer [2] and Sauer and De Lorenzis [6]. It uses an efficient contact enrichment approach based on Non-Uniform Rational B-Splines (NURBS) basis functions for the contact elements and Lagrangian basis functions for the bulk, see Corbett and Sauer [1].

2 Application

This contact model is used to simulate mode III debonding of three-dimensional, osseointegrated implants, based on experimental data from Mathieu et al. [3]. The problem setup is illustrated in Figure 2. The implant is meshed with 72 linear Lagrangian bulk elements and 36 quadratic NURBS-enriched contact elements, while the bone block is meshed with 648 bulk elements and 324 contact elements. The mesh and the contact surface of the implant are depicted in Figure 1. The lower surface of the bone block is fixed in all directions, while the sides are fixed in their corresponding normal direction. The bone material parameters are $G_\mathrm{b} = 8$ GPa, $E_\mathrm{b} = 21$ GPa, $\nu_\mathrm{b} = 0.3$, for the shear modulus, Young's modulus, and Poisson ration, respectively. The friction coefficients and the average contact pressure are $\mu_1 = 0.4$, $\mu_2 = 0.55$ and $\bar{p} = 3.1$ MPa, and are determined by a parameter fitting. The cylindrical titanium implant (Ti-6Al-4V) is rotated by 10° around its central axis with a constant load step size of 0.01°/s. In the following we analyze the resulting torque M_t as a function of the imposed rotation angle θ.

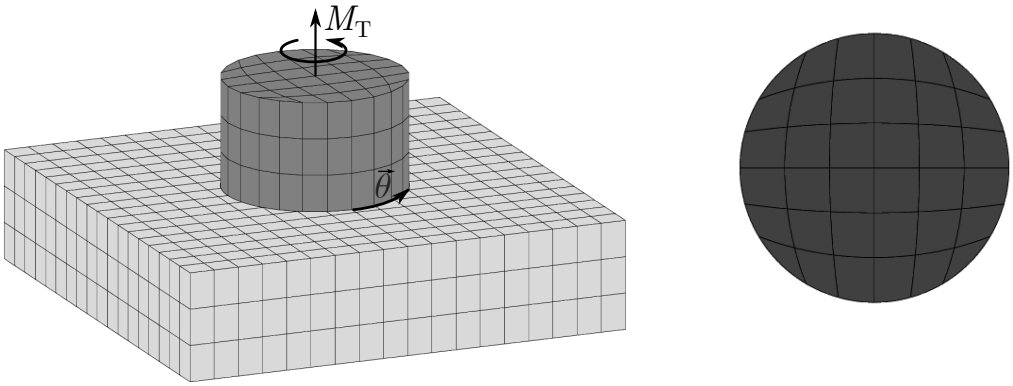

Figure 1. NURBS-enriched finite element mesh. Left: complete geometry. Right: Enlargement of the contact surface of the implant.

Figure 2 shows the torque-per-angle curve for one sample obtained by the experiments and the analytical model of Mathieu et al. [3] compared to the FE results of the present contact model. It can be seen that our proposed model results in an overall better fit of the experimental measurements than the analytical model. The analytical model was fit to match the peak and the decrease in torque, which resulted in a mean relative error of 11.26 %. The proposed contact model can reproduce more characteristics of the torque curve, such as the initial slope, the peak, the softening, and the torque for complete debonding, which leads to a mean relative error of 2.15 %.

Some minor deviations from the experimental results can be seen for $\theta > 2.4°$ where the decrease of the torque is not exactly matched. A different transition function for S may allow for a closer fit there. Another deviation can be seen in between 0.2° and 1.8° where the FE solution shows an idealized peak. Mathieu et al. [3] showed that part of the limitations of their model lies in the assumption of a fully bonded interface at the beginning of the experiment. A visual analysis of the implants' surfaces after debonding indicated that most likely, full osseointegration was not achieved. This resulted in regions where no bone tissue was initially attached to the implant surface and thus no adhesive or frictional effects can take place there. As the peak in the torque-per-angle curve represent the part of the deformation where adhesive forces are expected to have a large influence, considering an interface that is only partially bonded in the beginning might improve the numerical results there.

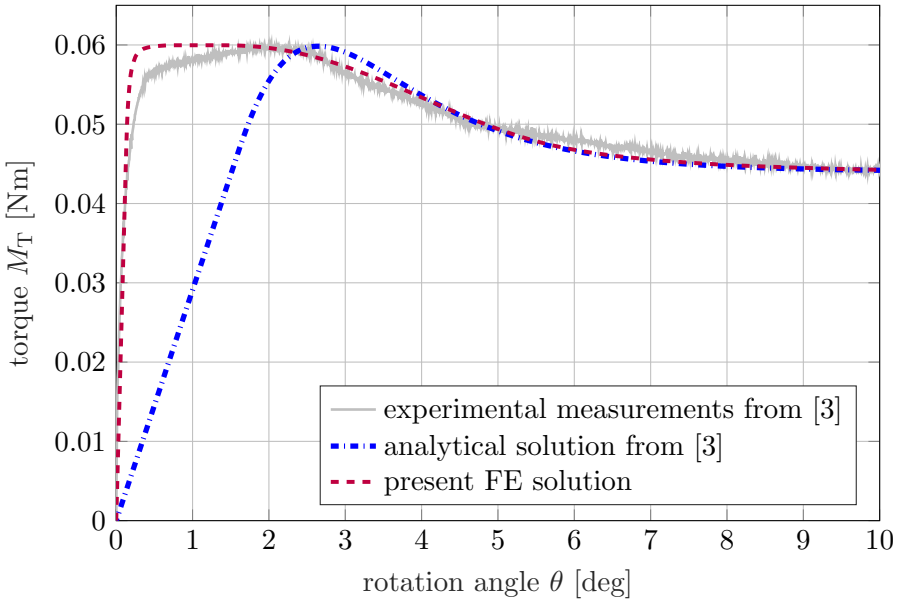

Figure 2. Mode III debonding of an implant. Variation of the torque M_T as a function of the imposed rotation angle θ.

3 Conclusion

This work presents a frictional and adhesive contact model, based on a state variable friction law and its application to the debonding of osseointegrated implants. A numerical solution with the new friction model is applied to the mode III debonding of a coin-shaped implant and the results are compared to experimental and analytical results from the works of Mathieu et al. [3]. Overall it is shown, that assuming a smooth transition from an unbroken to a broken state, characterized by a decreasing friction coefficient during the debonding process, leads to good agreement with experimental data. It also provides good estimates for the interface properties, such as the shear modulus, Young's modulus, and friction coefficient. Furthermore, it enables the analysis of the debonding behavior, e.g. in terms of maximum bearing loads and stresses and crack propagation. An extension to partial osseointegration, rough surfaces, as well as realistic implant geometries, will be considered in future works.

Acknowledgments

This work has received funding from the European Research Council (ERC) under the European Union's Horizon 2020 research and innovation program (grant agreement No 682001, project ERC Consolidator Grant 2015 BoneImplant) and the Jülich Aachen Research Alliance Center for Simulation and Data Science (JARA-CSD) School for Simulation and Data Science (SSD).

References

[1] Callum J. Corbett and Roger A. Sauer. Three-dimensional isogeometrically enriched finite elements for frictional contact and mixed-mode debonding. *Computer Methods in Applied Mechanics and Engineering* **284** (2015), pp. 781–806.

[2] Thang X. Duong and Roger A. Sauer. A concise frictional contact formulation based on surface potentials and isogeometric discretization. *Computational Mechanics* (2018), pp. 1–20. DOI: https://doi.org/10.1007/s00466-019-01689-0.

[3] Vincent Mathieu, Romain Vayron, Etienne Barthel, Davy Dalmas, Emmanuel Soffer, Fani Anagnostou, and Guillaume Haïat. Mode III cleavage of a coin–shaped titanium implant in bone: Effect of friction and crack propagation. *Journal of the Mechanical Behavior of Biomedical Materials* **8**.1 (2012), pp. 194–203.

[4] Janine C. Mergel, Riad Sahli, Julien Scheibert, and Roger A. Sauer. Continuum contact models for coupled adhesion and friction. *The Journal of Adhesion* (2018), pp. 1–33. DOI: 10.1080/00218464.2018.1479258.

[5] James R. Rice and Andy L. Ruina. Stability of steady frictional slipping. *Journal of Applied Mechanics* **50**.2 (1983), pp. 343–349.

[6] Roger A. Sauer. Local finite element enrichment strategies for 2D contact computations and a corresponding post-processing scheme. *Computational Mechanics* **52**.2 (2013), pp. 301–319.

[7] Roger A. Sauer and Laura De Lorenzis. A computational contact formulation based on surface potentials. *Computer Methods in Applied Mechanics and Engineering* **253** (2013), pp. 369–395.

**Proceedings of the 8th GACM Colloquium on Computational Mechanics
for Young Scientists from Academia and Industry
August 28–30, 2019 in Kassel, Germany**

Finite element technologies for stent simulations

Kiran Manjunatha *[1], Jan Frischkorn[2] and Stefanie Reese[1]

[1]Institute of Applied Mechanics, RWTH Aachen University, Mies-van-der-Rohe Str. 1, D-52074 Aachen, Germany
[2]Volkswagen AG, Wolfsburg

Abstract. Solid-beam formulation (Q1STb) is a finite element technology developed with the aim of conducting accurate simulations of beam-like structures (e.g. stents) with minimal element count. The reduced integration solid element formulation (Q1SP) with hourglass stabilization is an efficient and locking-free alternative for standard brick elements and can handle incompressibility as well as a wider range of aspect ratios. The scope of this work is to investigate the usage of a combination of both the aforementioned formulations in analyzing drug-eluting stents. It will be shown that this strategy is viable and efficient in comparison to the element formulations cuurently available in commercial finite element softwares.

Introduction

Stents are medical devices inserted into blood vessels to treat atherosclerosis and hence recover blood flow to normality, and also to stabilize aneurysms. Most commercial stent configurations comprise of filigree constructions which render the three-dimensional finite element stenting simulations computationally expensive. Significant expenses can be attributed to the following factors: Accurate resolution of local phenomena (e.g. plasticity, phase transformations, damage etc.) requires multiple elements across the cross-section of the stent struts. Also, to restrict the element aspect ratios within reasonable bounds, dense discretizations in the longitudinal direction of stent struts are expected. Additionally, modeling material nonlinearities, large deformations and contact incur significant computational costs. Lastly, the presence of multiple layers within the stent cross-sections (e.g. drug-eluting polymer layer, gold reinforcement layer for welds etc.) exacerbates the cost of high-fidelity simulations.

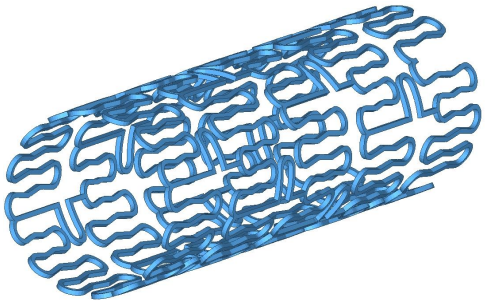

Figure 1. Coronary stent

In the context of drug-eluting stents, development of a robust and computationally efficient strategy for high-fidelity simulations is a challenging task. As a first step in this regard, we investigate the use of a combination of two advanced finite element formulations for efficiently modeling the mechanics of stent deployment. The solid-beam formulation [1] is utilized to model the metallic core. A reduced integration solid element formulation with hourglass stabilization [2] is utilized to model the drug-eluting polymer layer.

*Corresponding author: kiran.manjunatha@ifam.rwth-aachen.de

1 Finite element technologies

1.1 Solid-beam formulation (Q1STb)

The short-hand notation Q1STb denotes a formulation based on the classical "Q1" element, "ST" indicating "stabilization based on Taylor expansion " and the "b" indicating the (solid-)beam type of element within the so-called Q1STx family of elements. A brief outline of the formulation in its current state is provided below.

The foundation of the formulation is a mixed variational principle based on the Hu-Washizu three-field functional with the displacement, the stress and the strain field being treated as primary unknowns. Curvature thickness locking and significant portion of transverse shear locking are alleviated using the assumed natural strain (ANS) method. Poisson thickness locking, which occurs due to the ANS-modified transverse normal strains, and transverse shear locking in the beam plane are cured using the enhanced assumed strain (EAS) method. Volumetric locking is partially treated by the EAS method.The reduced integration concept, within which the formulation is embedded, helps eliminate volumetric locking completely. Full integration is performed on the transverse plane at the center of the beam axis and reduced integration is carried with respect to the beam axis. Efficient analytical integration of hourglass parts of the stiffness matrix as well as the internal force vector is achieved by (a) approximating the inverse Jacobian via a Taylor series expansion with respect to the element center. (b) reducing the number of terms within the polynomial approximations of the Green-Lagrange strain and the B-operator via Taylor series expansions with respect to the element center. (c) a Taylor series expansion of the second Piola-Kirchhoff stress with respect to the transverse plane at the center of the beam axis. The adaptive hourglass material tangent is defined by means of the deviatoric part of the linear elasticity matrix containing an effective shear modulus term which can be interpreted as an average secant stiffness at the quadrature points. The reader is directed to [1] and [4] for implementation details.

1.2 Reduced integration solid element formulation with hourglass stabilization (Q1SP)

The short-hand notation Q1SP denotes a formulation based on the classical "Q1" element, "S" indicating a "stabilized" element and "P" indicating the assumption of an equivalent "parallelepiped". The formulation is based on the non-linear Hu-Washizu principle and the stabilization concept considers the full tangent (except in compression) as opposed to the earlier works wherein the geometrical stiffness was neglected to ensure stability. Volumetric and shear locking are alleviated by introducing a modified stabilization stiffness contribution which involves the assumption of an equivalent parallelepiped and the enrichment of strains using the enhanced strain method introduced in [5] and [6]. The stabilization factors in the large deformation regime are computed by arriving at an expression analogous to the linear elasticity case. The reader is directed to [2] for implementation details.

No special considerations are necessary for coupling the two formulations since they behave as solid elements in this context. Also, the coupled setup can handle double-sided contacts which are often encountered in stent simulations.

2 Numerical investigations

Based on the results presented in [3] , a critical section of the drug-eluting stent (Fig. 1), which repeats itself throughout the structure, is chosen for our investigations. Cross-section with just the metal core as well as that including the polymer layer are investigated under the boundary conditions shown below.

The parameters $R = 0.2$ mm, $\theta = 8.5°$, $h = 0.0675$ mm for both type of cross-sections. For the bare-metal strut, $l = 0.912$ mm and for the multi-layered strut, $l = 0.92$ mm. Within the cross-sections, $ts = 0.8$ mm and $tp = 0.08$ mm.

The sum of reaction forces at the point of application of displacement $D = 0.25$ mm is investigated and presented.

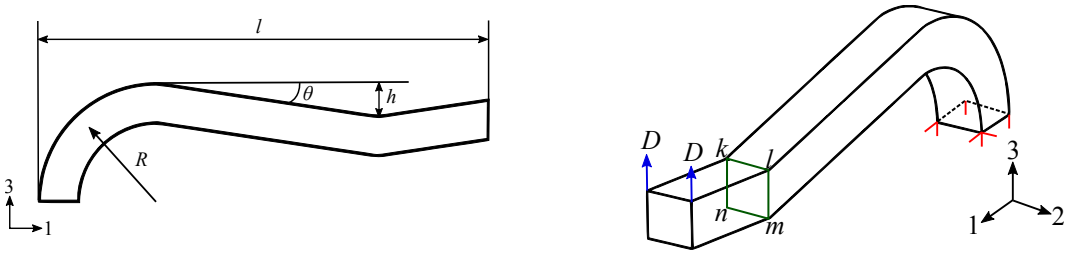

(a) geometry **(b)** boundary conditions

Figure 2. Stent strut

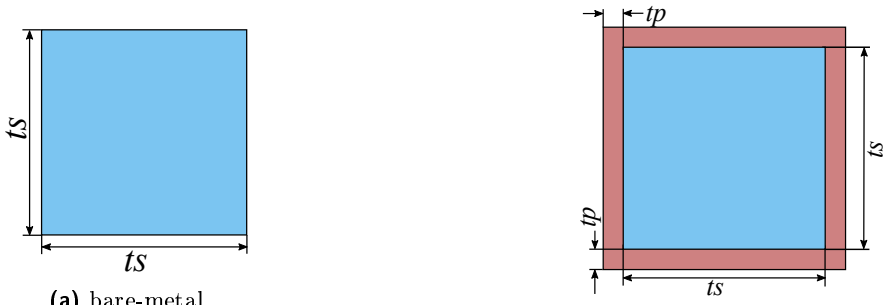

(a) bare-metal **(b)** multi-layer

Figure 3. Strut cross-sections $(k-l-m-n)$

Table 1. Material parameters

Layer	Material model	E	ν	σ_y	H
Metal core	elasto-plasticity with linear isotropic hardening	200 GPa	0.3	370 MPa	7 GPa
Polymer	Neo-Hooke	1 GPa	0.49	-	-

Abbreviations: NQT = number of quadrature points on the trasnverse plane at the center of beam axis, NEL = number of elements longitudinally along the radius, NET = number of elements across the thickness.

First, the bare-metal stent strut is analyzed with one element across the thickness for varying NEL and NQT. Further, by fixing NEL and NQT, the effect of varying NET is analyzed and compared to the results using C3D8I elements within ABAQUS. The sum of reaction forces F is normalized using the value obtained by using a fine discretization of 8 C3D8I elements across the thickness. Finally, results for the multi-layered strut using Q1STb and Q1SP are compared with the value obtained using a discretization of 8 C3D8I elements across the thickness in the metal layer and 2 C3D8R elements across the thickness in the polymer layer. For the multi-layered cross-section, the polymer layer is discretized with just one element across the thickness when using Q1SP.

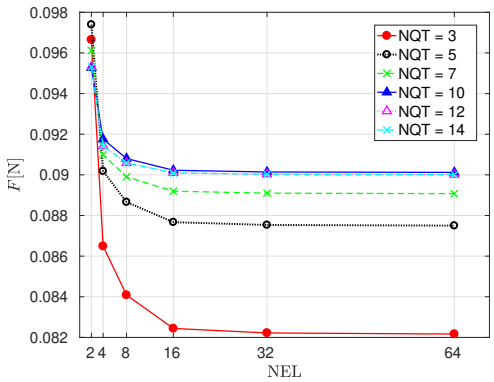

Figure 4. NEL and NQT convergence

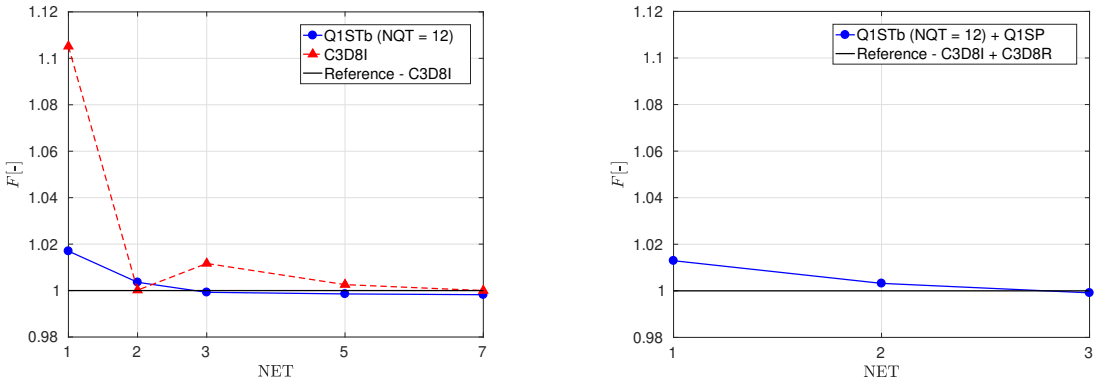

(a) bare-metal **(b)** multi-layer

Figure 5. *NET* convergence

3 Conclusions

It is observed that with just one element across both the layers, results comparable to those using fine discretizations of the strut with C3D8I and C3D8R elements are obtained. Hence, usage of Q1STb and Q1SP formulations for stent deployment analyses is a viable and an efficient choice.

Acknowledgments

Financial support of the project 395712048 by the German Science Foundation (DFG) is gratefully acknowledged.

References

[1] J. Frischkorn and S. Reese. A solid-beam finite element and non-linear constitutive modelling. *Comput. Methods Appl. Mech. Engrg.* 265 (2013), pp. 195–212.

[2] S. Reese, P. Wriggers, and B.D. Reddy. A new locking-free brick element technique for large deformation problems in elasticity. *Computers and Structures* 75 (2000), pp. 291–304.

[3] A Schiavone, T Y Qiu, and L G Zhao. Crimping and deployment of metallic and polymeric stents - finite element modelling. *Vessel Plus 2017 Jan 19.[Online First]* (2019).

[4] M. Schwarze and S. Reese. A reduced integration solid-shell finite element based on the EAS and the ANS concept—Large deformation problems. *Int. J. Numer. Meth. Engng* 85 (2011), pp. 289–329.

[5] J. C. Simo and F. Armero. Geometrically non-linear enhanced strain mixed methods and the method of incompatible modes. *Int. J. Numer. Meth. Engng* 33 (1990), pp. 1413–1449.

[6] J. C. Simo and M. S. Rifai. A class of mixed assumed strain methods and the method of incompatible modes. *Int. J. Numer. Meth. Engng* 29 (1990), pp. 1595–1638.

**Proceedings of the 8th GACM Colloquium on Computational Mechanics
for Young Scientists from Academia and Industry
August 28–30, 2019 in Kassel, Germany**

Numerical simulation of the viral entry into a cell by receptor driven endocytosis

T. Wiegold*[1], S. Klinge[1], R. P. Gilbert[2] and G. A. Holzapfel[3,4]

[1]TU Dortmund University, Institute of Mechanics, Leonhard-Euler-Str. 5, 44227 Dortmund, Germany

[2]University of Delaware, Department of Mathematical Sciences, 312 Ewing Hall, Newark, Delaware 19716, USA

[3]Graz University of Technology, Institute of Biomechanics, Stremayrgasse 16/2, 8010 Graz, Austria

[4]Norwegian University of Science and Technology (NTNU), Department of Structural Engineering, 7491 Trondheim, Norway

Abstract. The present contribution deals with the viral entry into a cell dictated by the change of the receptor density. While the receptors of the virus are considered to be fixed on the surface, the ones of the cell are mobile over the membrane. Upon contact, a locally increased receptor density of the cell is required, which causes the receptors to diffuse towards the virus. In the contact (adhesion) zone the membrane inflicts and forms an envelope around the virus. The vesicle created in this process imports its cargo into the cell. The described problem is simulated based on the assumption that the differential equation typical of the heat transport together with two boundary conditions is suitable to describe the diffusion of receptors. The differential equation is accompanied by two boundary conditions. The first condition considers the balance of fluxes on the adhesion front, where the amount of receptors required for advancement has to be equal to the amount provided by the cell. At the front, the velocity is supposed to be proportional to the gradient of the chemical potential. The second condition considers the energetic aspects of the process. Here, contributions due to the binding of receptors, the free energy of the membrane, its curvature and the kinetic energy due to the motion of the front are taken into account. The resulting moving boundary problem consisting of the differential equation and the two boundary conditions is well posed. The finite difference method as a direct numerical method for the solution of the differential equation is used to solve the underlying system. Numerical examples investigate the influence of the mobility of receptors as well as of different starting configurations in the cells and virus receptor distribution on the endocytosis process.

Introduction

One of the main mechanisms used by viruses in order to enter a cell is receptor driven endocytosis [**gibbons2010**]. During this process the virus connects its receptors to the receptors of the cell. This causes the cell membrane to bend and to build a vesicle around the virus. The process is characterized by the ability of the receptors of the cell to move freely within its membrane, while the receptors of the virus are fixed and occur with a much higher density. Upon contact, the virus dictates the required receptor density for bonding, thus causing the receptors of the cell to move towards the contact area. As a consequence, the contact area grows while the local receptor density of the cell changes, resulting in a moving boundary problem.

1 Endocytosis as a moving boundary problem

At the beginning of the process a virus connects to the cell and splits the cell membrane into two areas separated by an adhesion front. These two areas are characterized by the distribution of the receptor density $\xi(x,t)$. In the contact area the cell receptor density matches the constant receptor density of the virus $\xi(x,t) = \xi_{\mathrm{eq}}$. In the area in front of the adhesion zone the density is a function of position and time $\xi(x,t)$ with its minimum at the adhesion front, where $\xi(x,t) = \xi_{+}$. Since the cell size is orders of magnitudes larger than the virus size, the density profile remains unchanged far away from the contact

*Corresponding author: tillmann.wiegold@tu-dortmund.de

area $\lim_{x\to\infty} \xi(x,t) = \xi_0$. The motion of the receptors on the cell surface is based on the diffusion differential equation depending on the mobility m, i.e.

$$\frac{\partial \xi}{\partial t} = m \frac{\partial^2 \xi}{\partial x^2}. \tag{1}$$

A solution of this partial differential equation requires additional boundary conditions. The conservation of binders is considered first. It states that the amount of receptors required for the advancement of the adhesion front has to be equal to the amount of receptors provided by the flux. Following Fick's first law, the diffusion equation leads to the first boundary condition

$$(\xi_{\mathrm{eq}} - \xi_+)\, v_+ - m \left[\frac{\partial \xi}{\partial x}\right]_+ = 0, \tag{2}$$

which depends on quantities related to the adhesion front [**freund2004**]. Here, v_+ denotes the velocity of the front. For the second boundary condition an approach considering the energetic aspects of the front motion is chosen [**wiegold2019**]. The front movement, represented by the kinetic energy $E_{\mathrm{kin}} = \frac{1}{2}\, k\, T\, \xi_{\mathrm{eq}}\, v_+^2$ is caused by the difference in the energy in front of and behind the front, each consisting of several contributions denoted by superscript "$-$" behind the front and superscript "$+$" in front of the front. Thus,

$$E_{\mathrm{b}}^- + E_{\mathrm{e}}^- + E_{\kappa}^- - E_{\mathrm{e}}^+ + E_{\mathrm{v}}^+ = E_{\mathrm{kin}}. \tag{3}$$

Behind the front, $E_{\mathrm{b}}^- = -k\, T\, C_{\mathrm{b}}\, \xi_{\mathrm{eq}}$ denotes a reduction in the free energy due to the binding of receptors, with k being the Boltzmann constant, T the absolute temperature and C_{b} a reduction factor. The term $E_{\mathrm{e}}^- = k\, T\, \xi_{\mathrm{eq}} \ln\left(\frac{\xi_{\mathrm{eq}}}{\xi_0}\right)$ represents the energy associated with the entropy of receptors. Here, the initial binder density ξ_0 is adopted as a reference value. The term $E_{\kappa}^- = \frac{1}{2}\, k\, T B\, \kappa^2$ represents the energy related with bending, where κ is the curvature of the membrane and where B is the bending stiffness. In front of the front $E_{\mathrm{e}}^+ = k\, T\, \xi_+ \ln\left(\frac{\xi_+}{\xi_0}\right)$ represents the energy associated with the entropy of receptors. The term $E_{\mathrm{v}}^+ = \frac{1}{2}\, k\, T\, \xi_+\, v_{\mathrm{r}}^2$ represents the kinetic energy of the receptors in front of the front moving towards the adhesion area, with v_{r} being their corresponding velocity. Finally, the second boundary condition is expressed in terms of the receptor density $\xi(x,t)$ and the front velocity v_+ by

$$\left[-\xi_{\mathrm{eq}}\, C_{\mathrm{b}} + \xi_{\mathrm{eq}} \ln\left(\frac{\xi_{\mathrm{eq}}}{\xi_0}\right) + \frac{1}{2} B \kappa^2\right] - \left[\xi_+ \ln\left(\frac{\xi_+}{\xi_0}\right) + \frac{1}{2}\, k\, T\, \xi_+\, v_{\mathrm{r}}^2\right] = \left[\frac{1}{2}\, \xi_{\mathrm{eq}}\, v_+^2\right]. \tag{4}$$

The corresponding non-linear system of equations is implemented by using the finite difference method and is solved numerically by a Newton Raphson scheme.

2 Cooperativity

As soon as receptors of two opposing surfaces create bonds they will smooth out the membranes such that they become more conform to each other [**weikl2009**]. This makes it easier for additional receptors to create bonds and strengthens the adhesion between the two surfaces. This effect during the edocytosis process is called cooperativity. The cooperativity reduces the total amount of required receptor bonds in order to connect the virus with the cell according to

$$\xi_{\mathrm{eq\_req}} = c\left(\frac{\kappa}{k_{\mathrm{B}} T}\right) l_{\mathrm{we}}^2 K_{\mathrm{pl}}^2 [\xi_{\mathrm{eq}}]^2 [\xi_0]^2. \tag{5}$$

Here, $\xi_{\mathrm{eq\_req}}$ is the required amount of receptors that need to bind, c is a dimensionless prefactor, l_{we} is the interaction range between two opposing receptors and K_{pl} is the two dimensional equilibrium constant.

3 Numerical results

The chosen numerical example models the uptake of a spherical virus. The evolution of the receptor profile of the cell as well as the motion of the adhesion front are shown in Fig. 1. At the beginning of the process the receptor density at the front experiences a strong decrease and reaches $\approx 50\%$ of its initial value after 300 time steps. This decrease weakens as the time progresses. During the whole process the adhesion front advances continuously, while its velocity decreases towards a limit value. The numerical

results are strongly influenced by the mobility parameter m which measures how fast the cell can provide receptors to the adhesion zone. Further important factors are the initial receptor density of the virus as well as of the cell [**wiegold2019**].

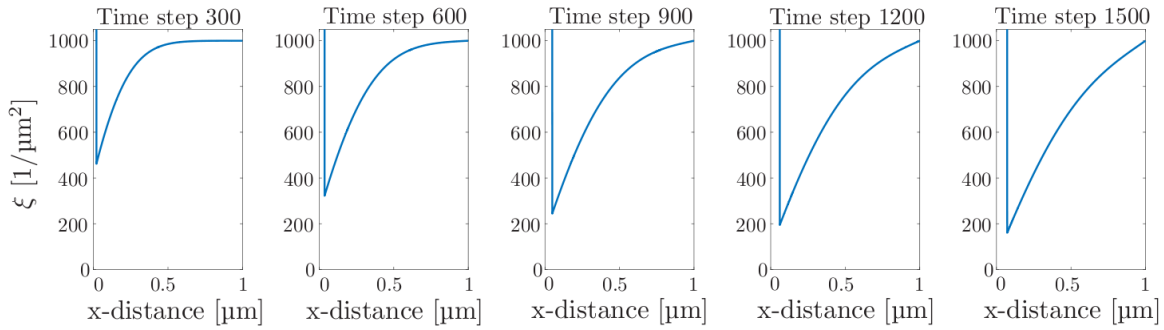

Figure 1. Receptor density over the cell surface for the time steps 0 - 1500. Chosen process parameters are $m = 1\mu m^2/s$, $C_b = 5$, $B = 30$, $\xi_{eq} = 4800\ 1/\mu m^2$, $\xi_+ = 1000\ 1/\mu m^2$, virus diameter $D = 0.05\mu m$.

Cooperativity is incorporated into the simulations by considering a patch of receptors with a distinct interaction range surrounded by receptors with a different interaction range. The two considered interaction ranges are $l_{we} = 1.2$ nm in the inner patch, which leads to a required receptor density of $\xi_{eq\_req} = 3262\ 1/\mu m^2$ and $l_{we} = 1$ nm for the surrounding receptors, which leads to a required receptor density of $\xi_{eq\_req} = 2265\ 1/\mu m^2$. The results of the simulations for the described setup are shown in Fig. 2. The top row shows the density profile over the cell membrane for different time steps up to the state when the whole virus entered the cell. The velocity of the front, the position of the front and the receptor density at the front are presented in the bottom row of Fig. 2.

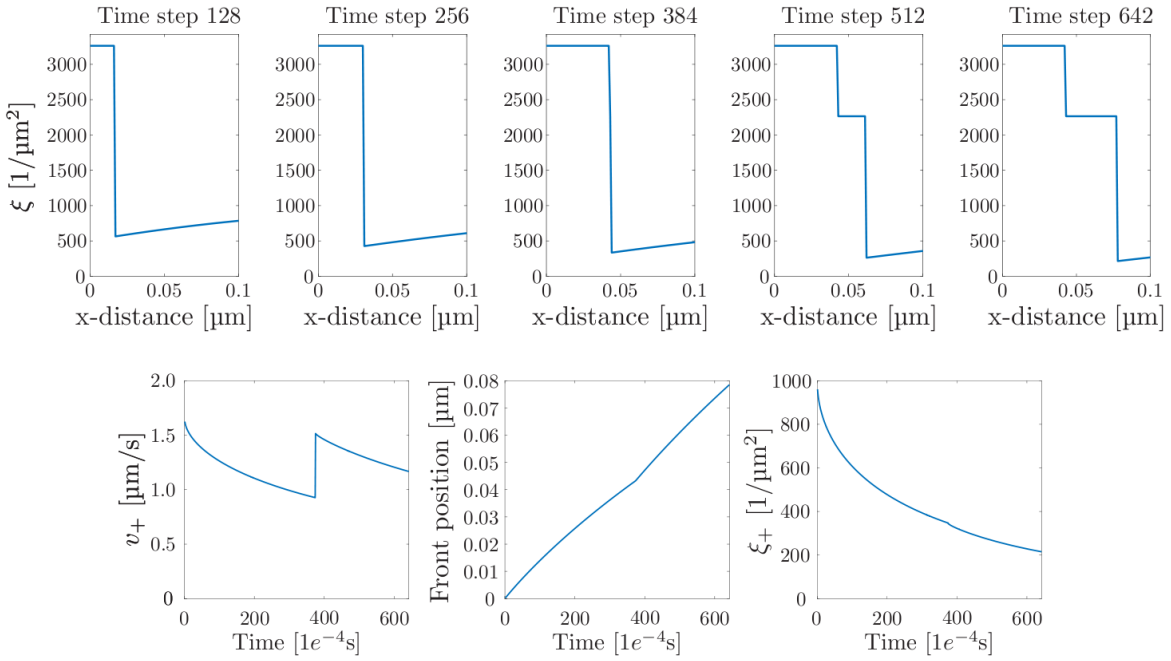

Figure 2. The required density is calculated taking into account the cooperativity. Chosen process parameters are the same as in Fig. 1. Additionally $\xi_{eq\_req} = 3262\ 1/\mu m^2$ in the inner patch and $\xi_{eq\_req} = 2265\ 1/\mu m^2$ in the surrounding area. The upper row shows the receptor density over the cell surface for different time steps. The bottom row shows the velocity of the front, position of the front and receptor density at the front over time.

The different patches are clearly differentiated in the diagrams by either a jump or a kink in the corresponding diagrams. The velocity is most affected by the change of the required density. In the area with a smaller interaction range less receptors are required, which significantly increases the velocity of the process.

4 Conclusions

The present study focuses on the simulation of the influence of the binder mobility in the viral entry driven by receptor diffusion. The process is described by a diffusion differential equation accompanied by two boundary conditions. The two boundary conditions describe the flux balance and the energy balance at the adhesion front. The proposed moving boundary problem enables an efficient numerical simulation of the process and provides the basis for the consideration of additional relevant aspects like cooperativity. Bending of the cell in front of the adhesion front and an alternative expression for bending lipid bilayers are envisaged as topics of the future work.

Acknowledgments

We gratefully acknowledge the financial support of the German Research Foundation (DFG), research grant No. 385960030, and the Austrian Science Fund (FWF), research grant No. I 3431-N32.

**Proceedings of the 8th GACM Colloquium on Computational Mechanics
for Young Scientists from Academia and Industry
August 28–30, 2019 in Kassel, Germany**

Optimization-based comparison of different anisotropic models for growth and remodeling in arterial walls

Anna Zahn and Daniel Balzani *

Chair of Continuum Mechanics, Department of Civil and Environmental Engineering,
Ruhr-Universität Bochum, Universitätsstraße 150, 44801 Bochum, Germany

Abstract. The simulation of growth and remodeling processes is an elegant way to obtain approximations for residual stresses and fiber orientations in arterial walls. In order to enable a comparison of different model variants within a framework of combined growth and remodeling, and to assess the assumptions on the underlying fundamental mechanisms, a method based on the optimization of model parameters is developed. The minimization of a mechanobiologically motivated objective function permits to evaluate the approaches with respect to their ability of effectively reducing stress peaks and stress inhomogeneities in the arterial wall.

Introduction

Unfortunately, residual stresses and fiber orientations in arterial walls can currently hardly be measured in vivo. However, they considerably affect the mechanical behavior of arterial tissues and have thus to be known in order to perform reliable patient-specific numerical simulations. By modeling the adaptation processes of arteries to their mechanobiological environment, an approximation of residual stresses and fiber orientations can be obtained automatically as a result of arterial growth and fiber reorientation. The combined framework for stress-driven growth and remodeling presented in [8] provides a set of variable formulations, which are based on different hypotheses on the mechanobiological mechanism of stress reduction. In order to identify the most probable of these mechanisms, a quantitative comparison of the model variants has to be enabled. To this aim, the growth parameters are computed by minimizing an objective function, which is formulated such that its minimum reflects the energetically most efficient reduction of stress peaks and inhomogeneities in the arterial wall. In Section 1, a summary of the general framework is given. Section 2 focuses on the optimization-based comparison of model variants within this framework and gives numerical results. The contribution ends with a short conclusion.

1 General growth and remodeling framework

Following Rodriguez et al. [7], the deformation gradient $\boldsymbol{F} = \boldsymbol{F}_\mathrm{e}\boldsymbol{F}_\mathrm{g}$ is multiplicately decomposed into a growth part $\boldsymbol{F}_\mathrm{g}$, which is associated to a stress-free volume change by factor $J_\mathrm{g} = \det[\boldsymbol{F}_\mathrm{g}]$, and an elastic part $\boldsymbol{F}_\mathrm{e}$. With regard to the orthotropic behavior of soft biological tissues, the growth tensor itself is decomposed according to $\boldsymbol{F}_\mathrm{g} = \boldsymbol{F}_\mathrm{g}^{(3)}\boldsymbol{F}_\mathrm{g}^{(2)}\boldsymbol{F}_\mathrm{g}^{(1)}$ into three parts, which are related to a set of perpendicular directions $\boldsymbol{A}_\mathrm{g}^{(a)}$ $(a = 1, 2, 3)$ and to the internal variables $\vartheta^{(a)}$, which determine the amount of growth associated to these directions. Based on the assumption that adaptation processes in soft biological tissues are stress-driven [3], the elastic part of the Mandel stress tensor $\boldsymbol{C}_\mathrm{e}\boldsymbol{S}_\mathrm{e} =: \boldsymbol{\Sigma}_\mathrm{e}$ with $\boldsymbol{C}_\mathrm{e} = \boldsymbol{F}_\mathrm{g}^{-T}\boldsymbol{C}\boldsymbol{F}_\mathrm{g}^{-1}$ and $\boldsymbol{S}_\mathrm{e} = 2\,\partial\psi/\partial\boldsymbol{C}_\mathrm{e}$ is chosen as driving quantity for growth and remodeling as suggested by Himpel et al. [5]. The directions $\boldsymbol{A}_\mathrm{g}^{(a)}$ are then computed as principal directions of $\boldsymbol{\Sigma}_\mathrm{e}$ and growth related to those directions is assumed to reduce the associated principal stresses. The growth factors $\vartheta^{(a)}$ are defined by a coupled set of evolution equations $\dot{\vartheta}^{(a)} = k_\vartheta^{(a)}(\vartheta^{(a)})\,\phi^{(a)}(\boldsymbol{\Sigma}_\mathrm{e})$, involving a growth driving quantity $\phi^{(a)}$ formulated in terms of $\boldsymbol{\Sigma}_\mathrm{e}$ and a growth function $k_\vartheta^{(a)}$ taken from Lubarda & Hoger [6]. This function assures that the growth factors $\vartheta^{(a)}$ are within a range of $[\vartheta_{(a)}^-, \vartheta_{(a)}^+]$ with $\vartheta_{(a)}^- < 1$ and $\vartheta_{(a)}^+ > 1$.

*Corresponding author: daniel.balzani@ruhr-uni-bochum.de

A polyconvex material model for fiber-reinforced materials is used to describe the basic material behavior [1]. Each of the two included fiber families is assumed to continously reorient in response to local demands. The target fiber orientation vectors are defined based on the principal directions and eigenvalues of the stress tensor $\boldsymbol{\Sigma}_\mathrm{e}$ in analogy to the approach of Hariton et al. [4]. The reorientation is regulated by the angles $\eta^{(1)}$ and $\eta^{(2)}$ between the existing and the target fiber vectors, which are supposed to evolve towards zero over time as described by the evolution equation $\dot{\eta}^{(a)} = k_\eta(\eta^{(a)})$. The remodeling velocity is controlled by the parameters of the remodeling function $k_\eta(\eta^{(a)}) = -k_\eta^+ \ln(m_\eta^+|\eta^{(a)}| + 1)$, cf. [8].

Based on hypotheses on the mechanical mechanism of stress reduction, different types of the multiplicative parts of the growth tensor and the associated driving forces are imaginable. Here, the growth tensors

$$\boldsymbol{F}_\mathrm{g}^{(a)} = \vartheta^{(a)}\boldsymbol{I} \qquad \text{for isotropic growth,} \tag{1a}$$

$$\boldsymbol{F}_\mathrm{g}^{(a)} = \vartheta^{(a)}\boldsymbol{I} + \left(1-\vartheta^{(a)}\right)\boldsymbol{A}_\mathrm{g}^{(a)} \otimes \boldsymbol{A}_\mathrm{g}^{(a)} \qquad \text{for growth perpendicular to } \boldsymbol{A}_\mathrm{g}^{(a)} \text{ and} \tag{1b}$$

$$\boldsymbol{F}_\mathrm{g}^{(a)} = \boldsymbol{I} + \left(\vartheta^{(a)}-1\right)\boldsymbol{A}_\mathrm{g}^{(a)} \otimes \boldsymbol{A}_\mathrm{g}^{(a)} \qquad \text{for growth in the direction of } \boldsymbol{A}_\mathrm{g}^{(a)} \tag{1c}$$

are considered. Whereas isotropic growth is supposed to be least realistic, an increase of the cross section as well as growth in the direction of the stress might be adequate. A set of driving forces is given by

$$\phi^{(a)}(\boldsymbol{\Sigma}_\mathrm{e}) = \boldsymbol{\Sigma}_\mathrm{e} : \boldsymbol{I}, \tag{2a}$$

$$\phi^{(a)}(\boldsymbol{\Sigma}_\mathrm{e}) = \boldsymbol{\Sigma}_\mathrm{e} : \boldsymbol{M}_\mathrm{g}^{(a)} \qquad \text{with} \quad \boldsymbol{M}_\mathrm{g}^{(\bullet)} = \boldsymbol{A}_\mathrm{g}^{(\bullet)} \otimes \boldsymbol{A}_\mathrm{g}^{(\bullet)}, \tag{2b}$$

$$\phi^{(a)}(\boldsymbol{\Sigma}_\mathrm{e}) = \langle \boldsymbol{\Sigma}_\mathrm{e} : \boldsymbol{M}_\mathrm{g}^{(a)} \rangle \qquad \text{and} \tag{2c}$$

$$\phi^{(a)}(\boldsymbol{\Sigma}_\mathrm{e}) = \begin{cases} \frac{1}{2}\boldsymbol{\Sigma}_\mathrm{e} : \left(\boldsymbol{M}_\mathrm{g}^{(\mathrm{I})} + \boldsymbol{M}_\mathrm{g}^{(\mathrm{II})}\right) & \text{for} \quad \Sigma_\mathrm{e}^\mathrm{I} > 0, \quad \Sigma_\mathrm{e}^\mathrm{II} > 0 \\ \boldsymbol{\Sigma}_\mathrm{e} : \boldsymbol{M}_\mathrm{g}^{(\mathrm{I})} & \text{for} \quad \Sigma_\mathrm{e}^\mathrm{I} > 0, \quad \Sigma_\mathrm{e}^\mathrm{II} \leq 0 \end{cases}, \tag{2d}$$

where the indices I/II point out that the $1^{\mathrm{st}}/2^{\mathrm{nd}}$ principal directions of $\boldsymbol{\Sigma}_\mathrm{e}$ are referred to, and $\Sigma_\mathrm{e}^\mathrm{I}/\Sigma_\mathrm{e}^\mathrm{II}$ are the eigenvalues of $\boldsymbol{\Sigma}_\mathrm{e}$. Besides the isotropic stress measure in Eq. (2a), a projection of $\boldsymbol{\Sigma}_\mathrm{e}$ in the direction of $\boldsymbol{A}_\mathrm{g}$ is considered in Eq. (2b). The case that only tensile values of these stresses provoke growth is reflected in Eq. (2c). Eq. (2d) represents the average stress state within the plane spanned by the fibers.

2 Optimization-based comparison of model variants

With the aim of finding combinations of model components which are suited best to improve the load-bearing behavior, a quantitative comparison of model variants has to be enabled. To this end, the growth and remodeling parameters have to be set specifically for each model variant, such that the best possible particular behavior can be achieved. This is done by minimizing a biologically motivated objective function, which then also serves as comparative value between the model variants. Most of the parameters mainly affect the temporal behavior but rarely the state of steady growth. The optimization is therefore restricted to the limiting values $\vartheta_{(a)}^+$ for positive growth – all other parameters are throughout set as specified in Tab. 1. As stated in [8], the ratio of internal pressure and axial strain is an additional important factor affecting the resulting stresses. To accommodate this, the level of the axial displacement is either considered as optimization variable as well or an averaging over different levels is performed.

2.1 Objective function

Provided that a steady growth state under constant load is reached, the value of the objective function $f_\mathrm{obj} = \sum \omega_i\, q_i$ serves as comparative measure between different model variants. The arguments

$$q_1 = \frac{\max\limits_r |\sigma_\varphi|}{\tilde{\sigma}_\mathrm{peak}}, \qquad q_2 = \frac{\max\limits_r |\sigma_z|}{\tilde{\sigma}_\mathrm{peak}}, \qquad q_3 = \frac{\operatorname{mean}\limits_r |\sigma_\varphi - \sigma_z|}{\left|\operatorname{mean}\limits_r \sigma_\varphi\right|},$$

$$q_4 = \frac{\max\limits_r |\sigma_\varphi| - \left|\operatorname{mean}\limits_r \sigma_\varphi\right|}{\tilde{\sigma}_\mathrm{diff}}, \qquad q_5 = \frac{\max\limits_r |\sigma_z| - \left|\operatorname{mean}\limits_r \sigma_z\right|}{\tilde{\sigma}_\mathrm{diff}}, \qquad q_6 = \left|\operatorname{mean}\limits_r J_\mathrm{g} - 1\right|$$

denote optimization objectives which are claimed to be minimal in a state of steady growth. The operator "mean" denotes the volume average of a quantity over the radial direction r, and the stresses $\tilde{\sigma}_\mathrm{peak} =$

100 kPa and $\tilde{\sigma}_{\mathrm{diff}} = 50\,\mathrm{kPa}$ are introduced as normalizing values. All expressions are normalized such that they are unitless and of same order of magnitude. Their mechanobiological motivation is, that the aim of efficient adaptation processes is a reduction of stress peaks (q_1, q_2), differences (q_3) and gradients (q_4, q_5) at a low level of energetic costs, i. e. a low volume change induced by growth (q_6). Assuming that all objectives are equally important, all weighting factors ω_i are set to $\omega_i = 1$.

2.2 Exemplary results

A series of model variants assuming the same combination of growth tensor and driving force for each of the three directions $\boldsymbol{A}_{\mathrm{g}}^{(a)}$ is analyzed and compared to isotropic growth. Exploiting the rotational symmetry of idealized arterial segments, all simulations are reduced to the radial dimension using rotationally symmetric 1D finite elements. The initial fiber angles are set to $\pm 30°$ and the internal pressure to $p = 120\,\mathrm{mmHg}$. A prescribed axial displacement u_z is either chosen among 0 %, 10 % or 20 % of the initial length or determined by optimization. All other, unvaried parameters are listed in Tab. 1.

Table 1. Parameters of the material model [1], adjusted to human media in [2], parameters of the remodeling function k_η and unvaried parameters of the growth function $k_\vartheta^{(a)}$, set equally for all directions.

c_1	ϵ_1	ϵ_2	α_1	α_2	k_η^+	m_η^+	k_ϑ^+	m_ϑ^+	ϑ^-	k_ϑ^-	m_ϑ^-
17.5 kPa	499.8 kPa	2.4	30 001.9 kPa	5.1	$0.6\,\mathrm{s}^{-1}$	5.0	$1.0\,\mathrm{s}^{-1}$	3.0	0.95	$1.0\,\mathrm{s}^{-1}$	3.0

Table 2. Type of growth tensor $\boldsymbol{F}_{\mathrm{g}}^{(a)}$

1	isotropic growth	Eq. (1a)
2	growth perpendicular to $\boldsymbol{A}_{\mathrm{g}}^{(a)}$	Eq. (1b)
4	growth in direction of $\boldsymbol{A}_{\mathrm{g}}^{(a)}$	Eq. (1c)

Table 3. Type of driving force $\phi^{(a)}(\boldsymbol{\Sigma}_{\mathrm{e}})$

2	isotropic	Eq. (2a)
4	stress in the direction of $\boldsymbol{A}_{\mathrm{g}}^{(a)}$	Eq. (2b)
5	stress within the plane of the fibers	Eq. (2d)
6	tensile stress in the direction of $\boldsymbol{A}_{\mathrm{g}}^{(a)}$	Eq. (2c)

For the relative comparison of the different approaches, a performance measure $P = -(f_{\mathrm{obj}} - f_{\mathrm{obj}}^{\mathrm{ref}})/f_{\mathrm{obj}}^{\mathrm{ref}}$ is defined, which represents the improvement of each approach with respect to the reference case where no growth and remodeling are included. This reference value $f_{\mathrm{obj}}^{\mathrm{ref}}$ depends on the height of the axial displacement, see Fig. 1d. Positive values of P are associated with model variants which indeed lead to improvements in the mechanobiological state: the higher P, the stronger are the improvements.

The optimization results are given in Fig. 1a–c. The denotations on the horizontal axis consist of up to three pairs of numbers for each approach, which are associated to the type of growth tensor and driving force for the three directions. Tab. 2–3 explain those numbers and refer to the correspondent equations. In Fig. 1a, the performance measure obtained when optimizing growth parameters $\vartheta_{(a)}^+$ and axial loading u_z is illustrated. This optimization scenario reveals the best possible performance of the models. All considered approaches lead to an improvement compared to the reference case, and most anisotropic approaches perform better than isotropic growth (denoted by "12"). However, the axial load might vary naturally within a physiological range, such that Fig. 1a alone is not sufficient for an assessment. If a single set of growth parameters is identified for an averaged value of the objective function using $u_z \in [0\,\%, 10\,\%, 20\,\%]$, the results shown in Fig. 1b are obtained. They represent the mean model performance and are in most cases significantly lower than in Fig. 1a. In Fig. 1c, the sensibility of the approaches with respect to the axial displacement is shown. Here, the parameters are optimized for each load level separately, which explains the higher performance measures compared to Fig. 1b.

Conclusion

A method for the comparison of different approaches within an existing framework of combined growth and fiber reorientation in arterial walls has been proposed. It relies on the evaluation of a mechanobiologically motivated objective function at steady growth state and should in principle enable a comparative assessment of the fundamental assumptions on which the individual model variants are founded.

With regard to the numerical results presented here, it is obviously not possible to draw a clear conclusion concerning the most probable growth mechanism so far. High performance measures for the average

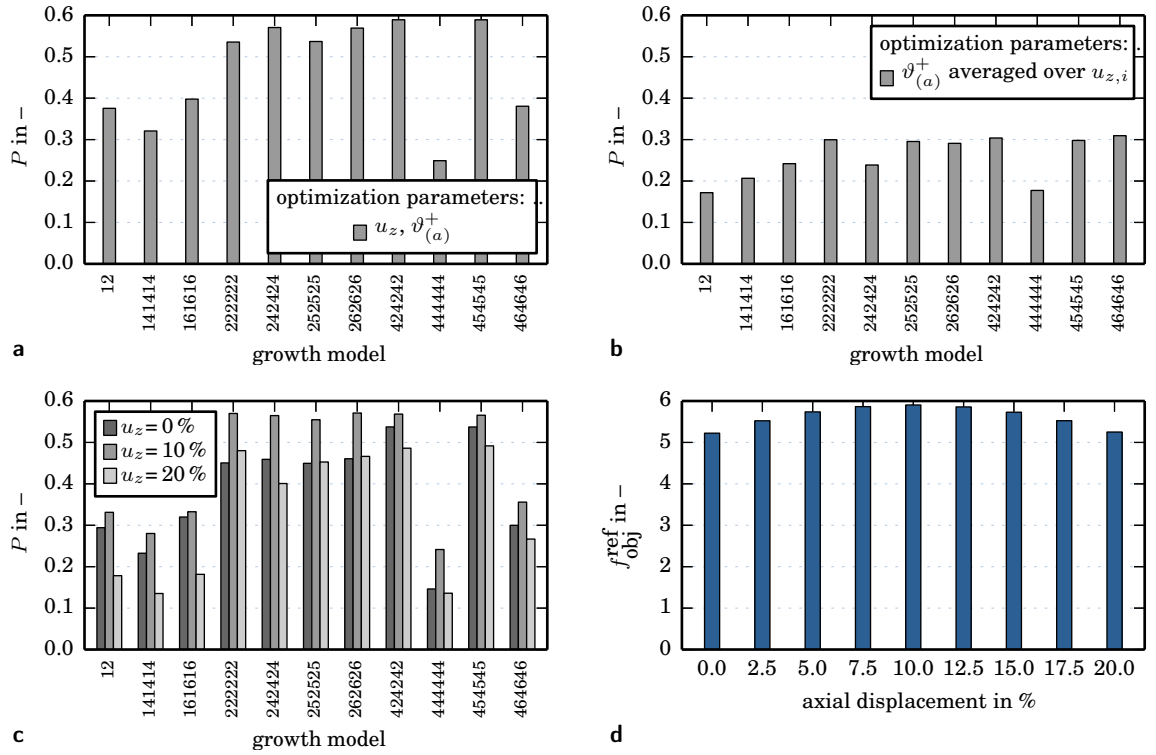

Figure 1. Performance measure P for optimization of a subset of different approaches with respect to a) the best model performance, b) the average model performance and c) the best model performance for a given axial loading. Subfigure d shows the reference values of the objective function.

model performance are obtained for non-isotropic growth tensors in combination with all driving forces except the one given in Eq. (2b). To get more insight into the results, the robustness of the individual approaches is worth to be considered in further examinations. If this is still not sufficient to obtain a clearer statement, it might on the one hand be necessary to vary the weighting factors for the arguments of the objective function or to take further important effects like smooth muscle activity into account. On the other hand, it might be a hint on faulty model assumptions, for example the one that all adaptation processes are stress-driven.

Acknowledgments

The authors thank the DFG (German Science Foundation) for funding in the project BA 2823/13-2.

References

[1] D. Balzani, P. Neff, J. Schröder, and G. A. Holzapfel. *Int. J. Solids Struct.* 43 (2006), pp. 6052–6070.

[2] D. Brands, A. Klawonn, O. Rheinbach, and J. Schröder. *Comput. Methods Biomech. Biomed. Engin.* 11 (2008), pp. 569–583.

[3] E. Comellas, A. Carriero, M. Giorgi, A. Pereira, and S. J. Shefelbine. Modeling the Influence of Mechanics on Biological Growth. In: *Numerical Methods and Advanced Simulation in Biomechanics and Biological Processes*. Ed. by M. Cerrolaza, S. J. Shefelbine, and D. Garzón-Alvarado. Elsevier, 2018. Chap. 2, pp. 17–35.

[4] I. Hariton, G. deBotton, T. C. Gasser, and G. A. Holzapfel. *Biomech. Model. Mechan.* 6 (2007), pp. 163–175.

[5] G. Himpel, E. Kuhl, A. Menzel, and P. Steinmann. *Comput. Model. Eng. Sci.* 8 (2005), pp. 119–134.

[6] V. A. Lubarda and A. Hoger. *Int. J. Solids Struct.* 39 (2002), pp. 4627–4664.

[7] E. K. Rodriguez, A. Hoger, and A. D. McCulloch. *J. Biomech.* 27 (1994), pp. 455–467.

[8] A. Zahn and D. Balzani. *Z. Angew. Math. Mech.* 98 (2018), pp. 2072–2100.

**Proceedings of the 8th GACM Colloquium on Computational Mechanics
for Young Scientists from Academia and Industry
August 28–30, 2019 in Kassel, Germany**

Application of Voronoi tessellations to model cellular aerogels

Rajesh Chandrasekaran * [1], Markus Hillgärtner[1], Barbara Milow[2], Ameya Rege[2] and Mikhail Itskov[1]

[1]Department of Continuum Mechanics, RWTH Aachen University, Aachen, Germany
[2]Institute of Materials Research, German Aerospace Center, Cologne, Germany

Abstract. Many aerogels are characterized by a fibrillar morphology. Recently proposed constitutive models have shown good predictive capabilities in describing the mechanical behavior of such aerogels. On the one hand, these models account for the cellular nature and adhere to the cell-size distributions, while on the other hand they are based on the assumption of the network made up of idealized square-shaped cells. The heterogeneous cellular morphology of aerogels can computationally be described by a Voronoi tessellation-based approach. Accordingly, the random cell shapes within the network are accounted for by means of the pore-size distribution data obtained from experiments. To this end, 2-d and 3-d periodic representative volume elements (RVEs) are generated from the cellular structure obtained using Voronoi tessellations and simulated under compression using finite element analysis.

Introduction

Aerogels exhibit unique physical properties such as high porosity, high specific surface area, low thermal conductivity and low density. Aerogels are synthesized by sol-gel processing from molecular precursors [3]. Amongst many kinds of aerogels, polysaccharide-based ones are characterized by a fibrillar morphology with the cellular-like microstructure. The microstructure of biopolymers can be tailored by means of different material sources, extracting and processing methods, and also by synthesis and drying routes [10]. For example, the density and pore size distribution of biopolymer aerogels are observed to depend on the biopolymer concentration. Accordingly, the mechanical properties can be directly evaluated based on synthesis parameters.

The mechanical and structural properties of biopolymer aerogels have recently been studied. Rege et al. [7] developed a micromechanically motivated constitutive model to describe the mechanical behavior of biopolymer aerogels. The model formulations were based on the assumption that the aerogel network consists of continuously distributed idealized square shaped microcells. Recently, the model was further improved and generalized to describe the mechanical behavior and properties of other biopolymer aerogels, like pectin and k-carrageenan [8]. Although this constitutive model demonstrated good agreement with experimental data, the assumption of the square shaped microcells remains an idealization. The shape of microcells throughout the aerogel network is highly randomized and not restricted to quadrangle. In order to create a more realistic geometry, a Voronoi tesselation-based approach can be applied. One of the advantage of this approach is that, it not only accounts for the randomized cell size distribution, but also for the randomised cell shapes.

In this contribution, a recently reported model [9] characterizing biopolymer aerogel morphologies by means of a Voronoi tessellation-based algorithm is presented and extended. The Voronoi geometry is designed to fit the obtained pore size distribution data from experimental nitrogen sorption tests. The homogenized macroscopic response of the model was simulated using the concept of representative volume element (RVE) employed in combination with periodic boundary conditions (PBCs). The 2-d model is extended to 3-d in order to obtain realistic microstructures.

*Corresponding author: chandrasekaran@km.rwth-aachen.de

1 Methods

1.1 Voronoi tessellation of aerogels

A Voronoi tessellation technique decomposes the entire domain in m-dimensional space into n distinct regions with random set of points [1]. Each region R_i $(i = 1, 2, ..., n)$ forms a Voronoi cell containing exactly one generating point, known as seed S_i $(i = 1, 2, ..., n)$. For each seed S_i there exist a region consisting of all points closer to that particular seed S_i than to any other seed S_j $(j = 1, 2, ..., n,\ i \neq j)$. Based on the Euclidean metric $(||\bullet||_2)$, the i-th Voronoi cell generated from n seeds can be expressed as

$$R_i = \left\{ x \in \mathbb{R}^m \,\middle|\, ||x - S_i||_2 \leq ||x - S_j||_2 \right\} \quad \forall\, j = 1, 2, ..., n \ : j \neq i, \tag{1}$$

where x represents the position of any point in m-dimensional space. In 2-d space $(m = 2)$, the tessellation results in n Voronoi cells in the shape of convex polygon. Each vertex of i-th cell is equidistant from two nearest seeds. In the present approach, the Voronoi structure was generated in MATLAB [6], which utilizes the open source software Qhull [2] to create 2-d Voronoi tessellations. In order to create a periodic cellular microstructure, the Voronoi seeds were repeated in a 3×3 pattern. To obtain a geometry resembling microstructure of aerogels, the Voronoi seeds were chosen in accordance with the measured cell size distributions resulting from the experimental data (available in [9]).

1.2 Finite element modelling

From the Voronoi structures generated in MATLAB for three different cell size distribution of aerogels, square shaped RVEs of the dimension 250nm x 250nm were created. Each RVE has a fully periodic cellular pattern in order to apply PBCs. Furthermore, the edges of the Voronoi cells are represented as FE beam elements with a cross section reproducing the cell wall fibres in the biopolymer aerogel network. To this end, the edges of the polygonal cells were imported into LS-DYNA as beam elements with circular cross section. The Belytschko beam element formulation was used [4]. A linear elastic material model (*MAT_ELASTIC) with Young's modulus of 12 GPa was defined to each of the beam elements. A global contact using *CONTACT_AUTOMATIC_GENERAL with 0.1 friction coefficient was defined to the entire RVE. This contact formulation is suitable for beam-to-beam contacts [5]. The Voronoi geometry constituting of LS-DYNA beam elements representing the microstructure of the aerogel with a cellulose concentration of 5 wt.% is shown in Fig. 1a.

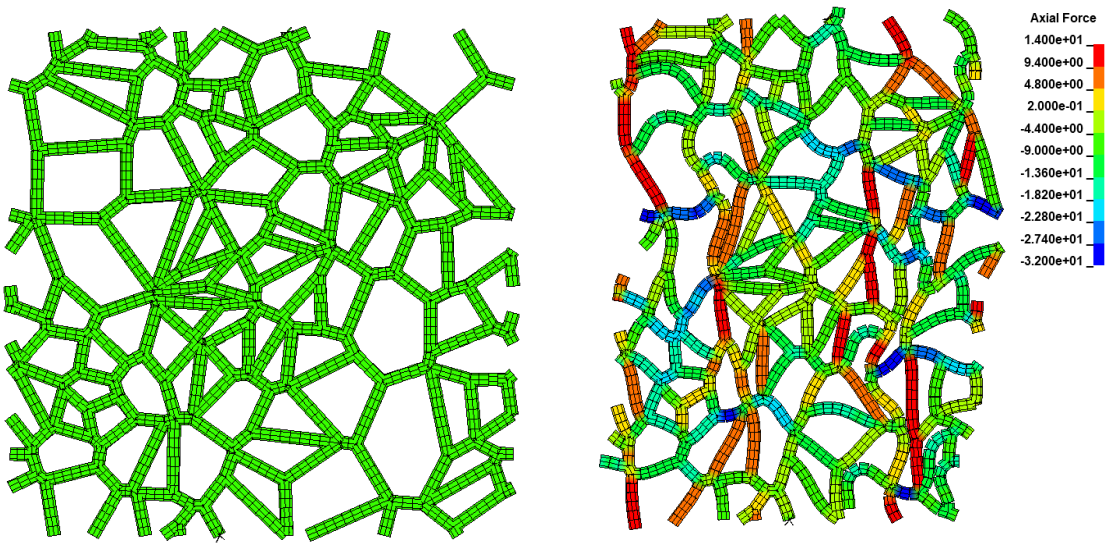

(a) RVE in the reference state

(b) Distribution of the Axial force (in nN) after compression up to 25% strain.

Figure 1. A 2-d aerogel RVE in LS-DYNA.

2 Results

Voronoi tessellation-based RVEs for different cell-size distributions and cell wall fiber diameters were generated and imported as beams in LS-DYNA. The dummy node (which controls the periodic boundary nodes) was subjected to a compression of 25% and the corresponding deformation of the RVE was studied. The contour plot of the axial force resulting in cell wall fiber is shown in Fig. 1b for aerogel with 5 wt.% cellulose concentration and a diameter of 6.4 nm .

With the increasing concentration of cellulose in aerogels the fiber diameter of the cell wall increases. Aerogels with 3, 5 and 7 wt.% cellulose concentration have diameter 5.5, 6.4 and 7.6 nm, respectively. By increasing the fiber diameter, the volume of fiber solid content increases, thereby reducing the specific surface area and affecting the pore size distribution [8]. Accordingly, the cell wall fiber diameter and the pore space can be controlled during synthesis process. By this means, tailoring the target properties and response of cellulose aerogels (CAs) using computational results is of special interest. Therefore, the sensitivity of the bulk material properties to these structural parameters was investigated and presented in Rege et al. [9].

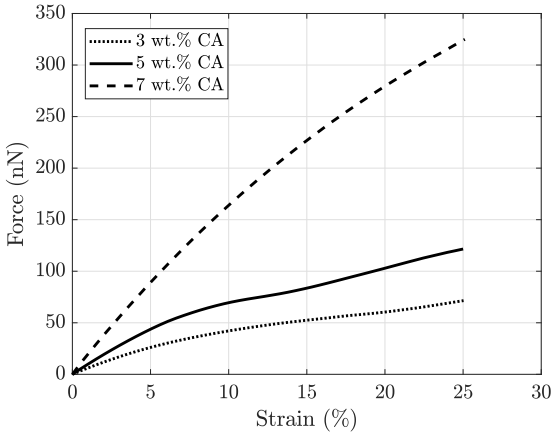

Figure 2. Model prediction of 2-d RVE-based analysis

The Voronoi based RVE model for different CA concentration with corresponding PDFs and fiber diameter was subjected to a compression of 25%, in order to investigate their actual bulk behavior. The force-strain curve predicted by the model for 3, 5 and 7 wt.% CAs are plotted in Fig.2. Accordingly, the 2-d periodic model effectively captures the trend of force-strain curves obtained in experiments. A region of linear elastic response is observed at low strains due to local bending and buckling of the cell wall fibers. Subsequently, yielding and damage occurs. Furthermore, the contact between the FE beams (i.e. cell wall fibers) affects the force-strain curve. The contact strain (i.e. the strain at which the cell wall contacts with each other within the microstructure) occurs between 12% and 18% depending on the different cellulose concentration.

3 Discussion

In this first approach, only a qualitative agreement is obtained. This is primarily because the out–of–plane connectivity is not accounted for due to the 2-d periodic RVE-based model. Although, the biopolymer aerogel network consists of open cellular structures, it has non-trivial out–of–plane connectivity which requires 3-d representation. The 2-d approach is incapable of capturing the bulk material response of a physical 3-d aerogel specimen in comparison to the macroscopic experimental data. Accordingly, a 3-d periodic RVE based on Voronoi structure was generated and simulated in LS-DYNA using larger RVE size, as a headway to this approach (Fig. 3). A Voronoi cell in 3-d space is a convex polyhedron formed by polygonal faces. Note that the cross section of a 3-d Voronoi tessellation is not based on the 2-d Voronoi tessellation. Therefore, the cell size distribution data used for generation of 2-d Voronoi does not account for the 3-d Voronoi structure.

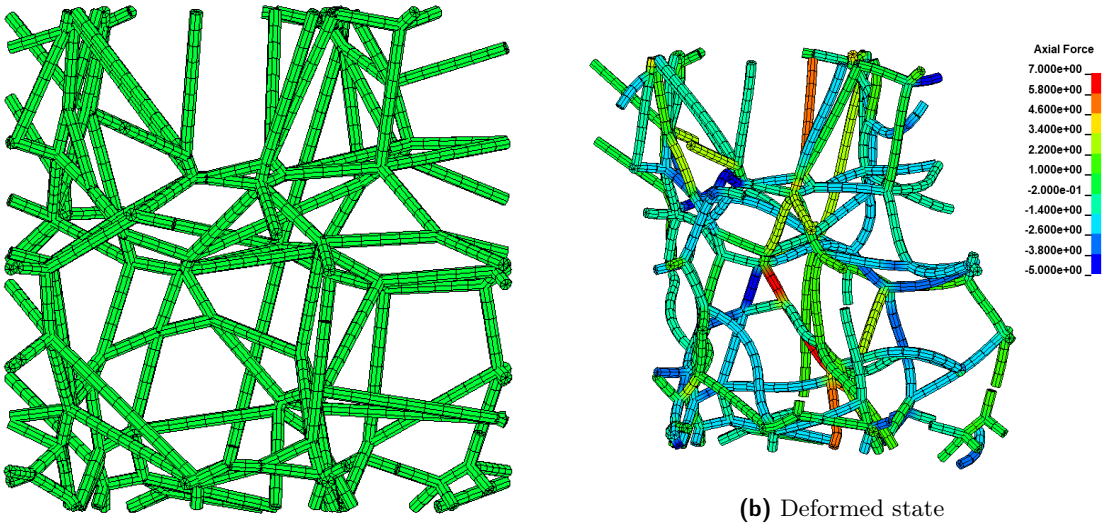

(a) Reference state

(b) Deformed state

Figure 3. 3-d voronoi based RVE in LS-DYNA

4 Conclusion

This paper describes the modeling of 2-d Voronoi tessellation-based RVEs for biopolymer aerogels and its respective finite element simulation. Application of periodic boundary conditions to the RVEs are helpful in approximating the bulk properties. The force-strain response under compression of periodic 2-d model is qualitatively in good agreement with the experimental results of biopolymer aerogels [8]. As an extension to this approach, 3-d Voronoi tessellation-based RVEs was created and tested. By using this approach, quantitative agreement, along with a qualitative one, could be obtained. Such 3-d RVEs will be generated, adhering to the experimental pore-size distribution data, and an analysis of the bulk properties based on their performance will be presented elsewhere.

References

[1] F. Aurenhammer. Voronoi diagrams—a survey of a fundamental geometric data structure. *ACM Computing Surveys (CSUR)* 23 (1991), pp. 345–405.

[2] C. B. Barber, D. P. Dobkin, and H. Huhdanpaa. The quickhull algorithm for convex hulls. *ACM Transactions on Mathematical Software (TOMS)* 22 (1996), pp. 469–483.

[3] J. L. Gurav, I. K. Jung, H. H. Park, E. S. Kang, and D. Y. Nadargi. Silica aerogel: synthesis and applications. *Journal of Nanomaterials* 2010 (2010), p. 23.

[4] J. O. Hallquist. LS-DYNA theory manual. *Livermore software Technology corporation* 3 (2006), p. 6.

[5] LS-DYNA Keyword User's Manual and I Volume. Version 11. *Livermore Software Technology Corporation* (2018), p. 11.

[6] MATLAB. *version R2018b*. M. Natick: The MathWorks Inc., 2018.

[7] A. Rege, M. Schestakow, I. Karadagli, L. Ratke, and M. Itskov. Micro-mechanical modelling of cellulose aerogels from molten salt hydrates. *Soft Matter* 12 (2016), pp. 7079–7088.

[8] A. Rege, I. Preibisch, M. Schestakow, K. Ganesan, P. Gurikov, B. Milow, I. Smirnova, and M. Itskov. Correlating Synthesis Parameters to Morphological Entities: Predictive Modeling of Biopolymer Aerogels. *Materials* 11 (2018), p. 1670.

[9] A. Rege, M. Hillgärtner, and M. Itskov. Mechanics of biopolymer aerogels based on microstructures generated from 2-d Voronoi tessellations. *The Journal of Supercritical Fluids* 151 (2019), pp. 24–29.

[10] S. Zhao, W. J. Malfait, N. Guerrero-Alburquerque, M. M. Koebel, and G. Nyström. Biopolymer aerogels and foams: Chemistry, properties, and applications. *Angewandte Chemie International Edition* 57 (2018), pp. 7580–7608.

**Proceedings of the 8th GACM Colloquium on Computational Mechanics
for Young Scientists from Academia and Industry
August 28–30, 2019 in Kassel, Germany**

Microstructural convergence analysis as basis for an efficient and accurate two-scale FE-FFT-based simulation approach

Christian Gierden * [1], Julian Kochmann[1], Johanna Waimann[1], Bob Svendsen[2,3] and Stefanie Reese[1]

[1]Institute of Applied Mechanics, RWTH Aachen University, Aachen, Germany

[2]Material Mechanics, RWTH Aachen University, Aachen, Germany

[3]Microstructure Physics and Alloy Design, Max-Planck-Institut für Eisenforschung GmbH, Düsseldorf, Germany

Abstract. We present an efficient and accurate solution scheme for a FE-FFT-based two-scale simulation which is based on a microstructural convergence analysis leading to a minimal number of grid points, which needs to be considered in terms of the two-scale simulation. While performing the entire simulation with this coarse discretized microstructure, the macroscopic deformation gradient is stored at every point of particular interest. Finally, in a post-processing step, this macroscopic deformation gradient is applied to a fine discretized microstructure to generate highly resolved microstructural data.

Introduction

To capture all the individual microstructural effects of a complex and heterogeneous material behavior in a structural finite element simulation, the usage of a two-scale simulation approach is necessary. In this context we use the FE-FFT-based method (e.g. [3]). Prakash and Lebensohn already showed that this new method is more efficient than the common FE^2 method ([10]). Nevertheless, highly resolved two-scale simulations of complex structures are still barely possible due to the high computational effort of both methods. One possibility to overcome this high computational effort is to combine the FFT-solvers with model order reduction techniques in Fourier space (e.g. [5]). Instead of that, we present the versatile use of an efficient FE-FFT-based simulation approach based on a microstructural convergence analysis in real space [4], which is also presented in a more detailed way in [1]. As a numerical example we present a bending test of a cantilever beam with polycrystalline material behaviour.

1 Two-scale simulation

Considering finite strains, the deformation of a macroscopic body $\bar{\mathcal{B}}$ is described by the macroscopic deformation gradient $\bar{\boldsymbol{F}}(\bar{\boldsymbol{X}})$ which is related to position $\bar{\boldsymbol{X}} \in \bar{\mathcal{B}}$ in the reference configuration. The macroscopic material response, e.g. the macroscopic first Piola-Kirchhoff stress $\bar{\boldsymbol{P}}(\bar{\boldsymbol{X}})$, at these points is given by the volume averaged response of a microstructure simulation. To get these microstructural responses, the microscopic boundary value problem $\mathrm{Div}\boldsymbol{P}(\boldsymbol{F}(\bar{\boldsymbol{X}}, \boldsymbol{X})) = \boldsymbol{0}$ (neglecting body forces) needs to be solved. Here, $\boldsymbol{X}$ is the local coordinate corresponding to the microstructure $\mathcal{B}$ and $\boldsymbol{P}(\boldsymbol{F}(\bar{\boldsymbol{X}}, \boldsymbol{X}))$ is the microscopic first Piola-Kirchhoff stress depending on the total deformation gradient

$$\boldsymbol{F}(\bar{\boldsymbol{X}}, \boldsymbol{X}) = \bar{\boldsymbol{F}}(\bar{\boldsymbol{X}}) + \tilde{\boldsymbol{H}}(\boldsymbol{X}) \tag{1}$$

which is additively split into $\bar{\boldsymbol{F}}(\bar{\boldsymbol{X}})$ and a microscopic spatially fluctuating part $\tilde{\boldsymbol{H}}(\boldsymbol{X}) = \nabla\tilde{\boldsymbol{u}}(\boldsymbol{X})$. The unknowns $\tilde{\boldsymbol{u}}(\boldsymbol{X})$ of the microscopic boundary value problem represent the fluctuating displacement field. Due to a better readability, the dependencies on $\bar{\boldsymbol{X}}$ and $\boldsymbol{X}$ are neglected in the following.

*Corresponding author: christian.gierden@rwth-aachen.de

2 FFT-based microstructure simulation

To overcome the dependence of the stresses on spatially varying material properties the polarisation stress

$$\boldsymbol{\tau} = \boldsymbol{P}(\boldsymbol{F}) - \mathbb{C}^0 : \boldsymbol{F} \tag{2}$$

is introduced which is the difference between the stresses in the inhomogeneous microstructure and the stresses in a homogeneous reference material $\mathbb{C}^0$. This polarisation stress leads to the reformulated microscopic balance equation $\mathrm{Div}(\mathbb{C}^0 : \boldsymbol{F}) = -\mathrm{Div}(\boldsymbol{\tau})$. To solve this balance equation Moulinec and Suquet [7] proposed to use Green's function which then leads to the Lippmann-Schwinger equation to calculate the total deformation gradient

$$\boldsymbol{F} = \bar{\boldsymbol{F}} - \mathbb{I}^0 * \boldsymbol{\tau} \tag{3}$$

where $*$ denotes the convolution integral. To solve the Lippmann-Schwinger equation it is transformed into Fourier space where it reads

$$\hat{\boldsymbol{F}}(\boldsymbol{\xi}) = \begin{cases} -\hat{\mathbb{I}}^0(\boldsymbol{\xi})\,\hat{\boldsymbol{\tau}}(\boldsymbol{\xi}) & \text{for} \quad \boldsymbol{\xi} \neq \boldsymbol{0} \\ \bar{\boldsymbol{F}} & \text{for} \quad \boldsymbol{\xi} = \boldsymbol{0} \end{cases} \tag{4}$$

and the Green operators $\hat{\Gamma}^0_{ijkl}(\boldsymbol{\xi}) = \hat{G}^0_{ik}(\boldsymbol{\xi})\,\xi_j\,\xi_l$ and $\hat{G}^0_{ik}(\boldsymbol{\xi}) = (\mathbb{C}^0_{ijkl}\,\xi_j\,\xi_l)^{-1}$ are explicitly known and just depending on the wave vectors $\boldsymbol{\xi}$ and the homogeneous reference material $\mathbb{C}^0$. To solve this problem, we use the efficient and robust FFT- and conjugate gradient-based solution scheme which is introduced in [2] in the context of finite strains and based on the linearized Lippmann-Schwinger equation

$$\left[\mathbb{I} + \mathbb{I}^0 * \left(\mathbb{C}^{\star\,(i)} - \mathbb{C}^{(0)}\right)\right] : \Delta\boldsymbol{F}^{(i+1)} = \bar{\boldsymbol{F}} - \boldsymbol{F}^{(i)} - \mathbb{I}^0 * \boldsymbol{\tau}^{(i)} \tag{5}$$

with the local tangent operator for the i-th iteration step $\mathbb{C}^{\star\,(i)} = \partial_{\boldsymbol{F}}\boldsymbol{P}|_{\boldsymbol{F}^{(i)}}$.

3 Viscoplastic polycrystalline material formulation

In a finite strain setting we assume a multiplicative split of the total deformation gradient $\boldsymbol{F} = \boldsymbol{F}_e\boldsymbol{F}_p$ into an elastic part $\boldsymbol{F}_e$ and a plastic part $\boldsymbol{F}_p$. Since elastic deformations in polycrystals are generally small, a Saint Venant-Kirchhoff model is used to capture these elastic deformations which leads to the second Piola-Kirchhoff stress $\boldsymbol{S}_e = \frac{1}{2}\mathbb{C} : (\boldsymbol{C}_e - \boldsymbol{I})$ in the intermediate configurraten with the left Cauchy-Green tensor $\boldsymbol{C}_e = \boldsymbol{F}_e^T\boldsymbol{F}_e$ and the elasticity tensor $\mathbb{C}$. Considering polycrystalline materials with n_{slip} slip systems, plastic deformations will evolve if the resolved shear stress $\tau_\alpha(\boldsymbol{M}_e) = \boldsymbol{M}_e : (\boldsymbol{d}_\alpha \otimes \boldsymbol{n}_\alpha)$ in any slip system α exeeds the critical shear stress $\tau^C(\gamma_{acc})$. Here, $\boldsymbol{M}_e = \boldsymbol{C}_e\boldsymbol{S}_e$ is the mandel stress which is related to the plastic velocity gradient $\boldsymbol{L}_p = \dot{\boldsymbol{F}}_p\boldsymbol{F}_p^{-1}$. The vectors $\boldsymbol{d}_\alpha$ and $\boldsymbol{n}_\alpha$ are the slip direction and the plane normal unit vectors, respectively. Following Peirce et al. [8], the plastic velocity gradient

$$\boldsymbol{L}_p = \sum_{\alpha=1}^{n_{slip}} \dot{\gamma}\,\boldsymbol{d}_\alpha \otimes \boldsymbol{n}_\alpha \tag{6}$$

is defined as the superposition of the plastic slip rates $\dot{\gamma}_\alpha$ in each slip system. The evolution of $\dot{\gamma}_\alpha$ is given by the Perzyna-type flow rule

$$\dot{\gamma}_\alpha = \dot{\gamma}_0 \left\langle \frac{|\tau_\alpha| - \tau^C(\gamma_{acc})}{\tau^D} \right\rangle^p \mathrm{sgn}(\tau_\alpha) \tag{7}$$

with the reference shear rate $\dot{\gamma}_0$, the drag stress τ^D and the rate sensitivity parameter p [9]. The critical resolved shear stress $\tau^C(\gamma_{acc}) = \tau_0^C + q_h(\gamma_{acc})$ is depending on the accumulated plastic slip $\gamma_{acc} = \sum_\alpha \int |\dot{\gamma}_\alpha| dt$ via the isotropic hardening function $q_h(\gamma_{acc})$ which is defined to be a Voce-type hardening behaviour:

$$q_h(\gamma_{\mathrm{acc}}) = \tau_0^c + (\tau_\infty - \tau_0)\tanh[((h_0 - h_\infty)\,\gamma_{\mathrm{acc}})/(\tau_\infty - \tau_0^c)] + h_\infty\gamma_{\mathrm{acc}} \tag{8}$$

The flow rule (7) is discretized by using an implicit time integration scheme (backward Euler) with continuously differentiable transition between the powerlaw and a linear approximation (see [11]).

4 Solution strategy and a numerical example

Let us consider a bending test of a cantilever beam consisting of pure copper with the slip systems $\boldsymbol{d}_\alpha = \{111\}$ and $\boldsymbol{n}_\alpha = \{110\}$. The material parameters for pure copper are given in table 1.

C_{11} [GPa]	C_{12} [GPa]	C_{44} [GPa]	τ_0^c [MPa]	τ^D [MPa]	τ_∞ [MPa]	h_0 [MPa]	p [-]
170.2	114.9	61.0	0.1	10	31.0	50.0	20

Table 1. Used material parameters for Copper [6] with $\dot{\gamma}_0 = 10^{-3}\,1/\mathrm{s}$.

In terms of a pre-processing step we consider a microstructure with 100 grains and a random texture. This microstructure is submitted to three different deformation gradients ($\boldsymbol{F}^\circ$, $\boldsymbol{F}^\triangle$, $\boldsymbol{F}^\square$) with $F_{max} = 0.15$ and $\Delta t = 5 \cdot 10^{-8}\,\mathrm{s}$. To determine the minimal discretization N_{min} of this microstructure, six different discretizations with $N = 7, 15, 31, 63, 127$ and 255 grid points in each direction are considered. The result is given in figure 1. It can be seen, that the error $\bar{\mathcal{E}}$ in the norm of the macroscopic first Piola-Kirchhoff stress $\bar{\boldsymbol{P}}$ of any discretization compared to the converged solution $\bar{\boldsymbol{\mathcal{P}}}$ with $N = 255$ grid points in each direction is always smaller than 1% for a minimal discretization of $N_{min} = 15$ grid points in each direction. For a convergence analysis concerning different textures see [1].

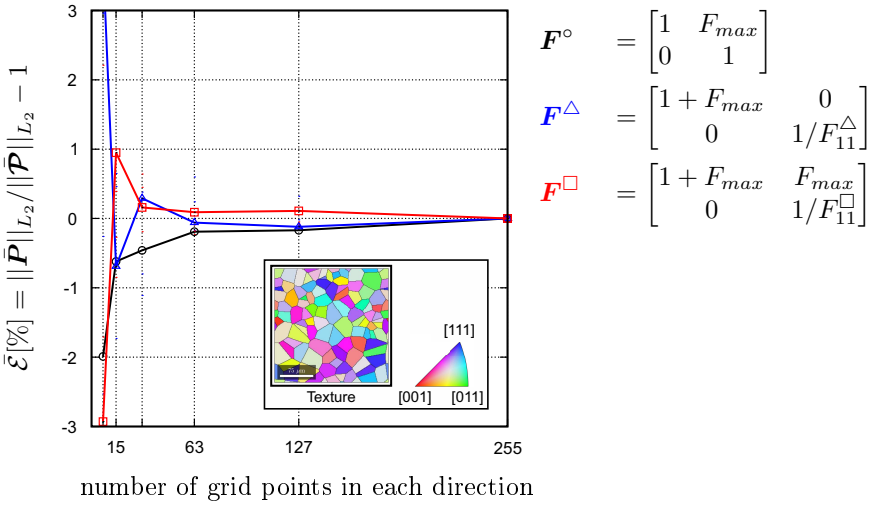

Figure 1. Convergence analysis in terms of the norm of the macroscopic first Piola-Kirchhoff stress $\bar{\boldsymbol{P}}$.

Concerning the two-scale simulation it is then possible to get sufficiently accurate macroscopic results by considering only those 15 grid points in each direction. In figure 2 the boundary conditions and the equivalant stress $\bar{\boldsymbol{\sigma}}_{eq}$ of the macroscopic boundary value problem is shown.

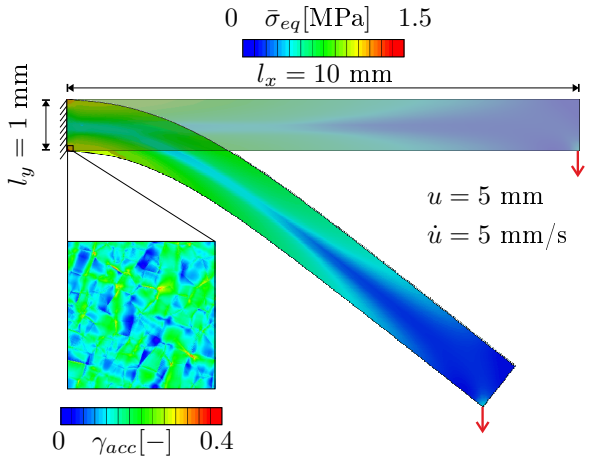

Figure 2. Macroscopic equivalant stress $\bar{\sigma}_{eq}$ computed with $N_{min} = 15$ and highly resolved microscopic accumulated plastic strain γ_{acc} computed with $N = 255$ grid points in each direction.

During the simulation the macroscopic deformation gradient of the lower right corner is stored. In a post-processing step it is then used to compute highly resolved microstructural results, e.g. for the microscopic accumulated plastic slip, with $N = 255$ grid points in each direction (see figure 2).

5 Conclusions

The proposed efficient and accurate two-scale solution scheme is decomposed into a pre-processing, a processing and a post-processing step. After finding the minimal number of grid points, which is needed to get sufficiently accurate macroscopic quantities, the entire two-scale simulation is performed with this relatively coarse discretization. Finally, in a post-processing step, high-fidelity solutions may be generated for any integration point of particular interest. By using this solution scheme high-fidility two-scale simulations can be performed in a reasonable time period.

Acknowledgements

The work is funded by the Deutsche Forschungsgemeinschaft (DFG, German Research Foundation) – Projektnummer 223500200 – TRR 136. We greatfully acknowledge the financial support of the subprojects M03 and M05.

References

[1] C. Gierden, J. Kochmann, J. Waimann, B. Svendsen, and S. Reese. Efficient two-scale FE-FFT-based mechanical process simulation of elasto-viscoplastic polycrystals at finite strains. *In preparation* (2019).

[2] M. Kabel, T. Böhlke, and M. Schneider. Efficient fixed point and Newton–Krylov solvers for FFT-based homogenization of elasticity at large deformations. *Computational Mechanics* 54 (2014), pp. 1497–1514.

[3] J. Kochmann, S. Wulfinghoff, S. Reese, J. R. Mianroodi, and B. Svendsen. Two-scale FE-FFT and phase-field-based computational modeling of bulk microstructural evolution and macroscopic material behavior. *Computer Methods in Applied Mechanics and Engineering* 305 (2016), pp. 89–110.

[4] J. Kochmann, S. Wulfinghoff, L. Ehle, J. Mayer, B. Svendsen, and S. Reese. Efficient and accurate two-scale FE-FFT-based prediction of the effective material behavior of elasto-viscoplastic polycrystals. *Computational Mechanics* 61 (2017), pp. 751–764.

[5] J. Kochmann, K. Manjunatha, C. Gierden, S. Wulfinghoff, B. Svendsen, and S. Reese. A simple and flexible model order reduction method for FFT-based homogenization problems using a sparse sampling technique. *Computer Methods in Applied Mechanics and Engineering* 347 (2018), pp. 622–638.

[6] R. A. Lebensohn, A. K. Kanjarla, and P. Eisenlohr. An elasto-viscoplastic formulation based on fast Fourier transforms for the prediction of micromechanical fields in polycrystalline materials. *International Journal of Plasticity* 32-33 (2012), pp. 59–69.

[7] H. Moulinec and P. Suquet. A numerical method for computing the overall response of nonlinear composites with complex microstructure. *Computer Methods in Applied Mechanics and Engineering* 157 (1998), pp. 69–94.

[8] D. Peirce, R. J. Asaro, and A. Needleman. Material rate dependence and localized deformation in crystalline solids. *Acta Metallurgica* 12 (1983), pp. 1951–1976.

[9] P. Perzyna. Thermodynamic Theory of Viscoplasticity. *Advances in Applied Mechanics* 11 (1971), pp. 313–354.

[10] A. Prakash and R. A. Lebensohn. Simulation of micromechanical behavior of polycrystals: finite elements versus fast Fourier transforms. *Modelling and Simulatio in Materials Science and Engineering* 17 (2009), p. 064010.

[11] S. Wulfinghoff and T. Böhlke. Equivalent plastic strain gradient crystal plasticity – enhanced power law subroutine. *GAMM-Mitteilungen* 36 (2013), pp. 134–148.

**Proceedings of the 8th GACM Colloquium on Computational Mechanics
for Young Scientists from Academia and Industry
August 28–30, 2019 in Kassel, Germany**

Large strain two-scale simulations on laptop computers

Oliver Kunc[1] and Felix Fritzen*[1]

[1]Efficient Methods for Mechanical Analysis, Institute of Applied Mechanics (CE), University of Stuttgart

Abstract. The Concentric Interpolation method is applied to structural simulations. It is based on an split of the input vector into amplitude and direction. The amplitude is interpolated by means of piecewise defined one-dimensional polynomials, while the direction is interpolated by means of spherical basis functions. This method is well-suited for application to hyperelasticity, as the material law is only state-dependent. Moreover, hyperelastic laws usually show distinct behavior with respect to the amplitude of the loading and the loading "direction", i.e. the direction of the stretch tensor in six dimensions. This very efficient evaluation of material laws renders structural two-scale simulations possible on everyday computers.

1 Introduction

Two-scale problems are known for leading to excessive computational costs if not treated efficiently. Multiple methods for addressing this problem have been proposed in the mechanics community. Most of them are projection based, see [3] for visco-plasticity, [2] for small strain hyperelasticity, and [1] for a recent numerical comparison. Among these, the authors' previous work [2] connected the projection based reduced basis approximation of homogenized hyperelastic small strain material laws with a subsequent kernel-based interpolation. This purely numerical second step is now extended to the finite strain context. By focusing on provided data samples, the evaluation of hyperelastic material laws reduces to non-iterative evaluations of elementary functions. The anticipated speed-up factors compared to the FEM are in the order of at least 10^3, while not imposing too demanding requirements on the offline phase, i.e. the amount of data samples acting as the supporting points is manageable.

2 Problem setting

Let Ω_0 be the configuration of a solid material body at rest. Under external loadings, it deforms and translates into the region Ω, see Figure 1. The kinematic quantities $\boldsymbol{X}$, $\boldsymbol{x}$ and $\boldsymbol{u}$ are the initial coordinates, the deformation and the displacement, respectively. The determinant J of the gradient $\boldsymbol{F} = \partial\boldsymbol{x}/\partial\boldsymbol{X}$ has

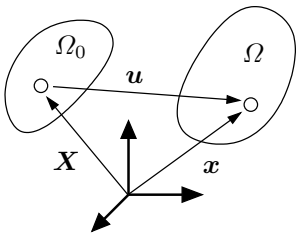

Figure 1. Material configurations and basic kinematic quantities.

to be strictly positive in order to avoid unphysical states. Via the polar decomposition of the deformation gradient, $\boldsymbol{F} = \boldsymbol{R}\boldsymbol{U}$, the rotation tensor $\boldsymbol{R}$ and the positive definite, symmetric stretch tensor $\boldsymbol{U}$ are obtained.

*Corresponding author: fritzen@mechbau.uni-stuttgart.de ORCID iD: 0000-0003-4926-0068

Hyperelastic material laws are based on the description of a free energy function only depending on the deformation gradient, $W = W(\boldsymbol{F})$. Its first and second derivative are the first Piola-Kirchhoff stress and the corresponding fourth-order stiffness, $\boldsymbol{P} = \partial W/\partial \boldsymbol{F}$, $\mathbb{C} = \partial^2 W/(\partial \boldsymbol{F})^2$, respectively.

Material objectivity implies the energy to be independent of the rotation, i.e. $W(\boldsymbol{F}) = W(\boldsymbol{U})$. Hence, the stress transforms as $\boldsymbol{P}(\boldsymbol{RU}) = \boldsymbol{RP}(\boldsymbol{U})$. The components C_{ijkl} $(i,j,k,l = 1,2,3)$ of the stiffness tensor transform as $C_{ijkl}(\boldsymbol{RU}) = \sum_{m,n=1}^{3} \delta_{ik} U^{-1}_{lm} P_{mj}(\boldsymbol{U}) + R_{im} C_{mjnl}(\boldsymbol{U}) R_{kn}$. Thus, it is obvious that the material law needs to be evaluated only at the stretch tensor, and not at the deformation gradient. This is appealing when thinking about sampling, cf. [4], as $\boldsymbol{U}$ may be represented as a six-dimensional vector while such a representation of $\boldsymbol{F}$ requires nine dimensions.

The governing balance equation of linear momentum is $\mathrm{Div}_{\boldsymbol{X}}(\boldsymbol{P}) - \boldsymbol{b} = \boldsymbol{0}$, where $\boldsymbol{b}$ compounds the body forces. Additionally, boundary conditions have to be provided. In many cases, this problem contains more degrees of freedom than can be handled by the available computer system within the given limitations of time. For instance, a full resolution of a fine-grained, heterogeneous, microscopic structure within a macroscopic structural part can quickly exceed a million nodes, with three degrees of freedom each.

Asserting the separability of length scales, a two-scale framework is introduced. Therein, macroscopic quantities are denoted by overlines, e.g. $\overline{W}, \overline{\boldsymbol{F}}, \overline{\boldsymbol{P}}, \ldots$ while microscopic quantities are not highlighted, e.g. $W, \boldsymbol{F}, \boldsymbol{P}, \ldots$ as before. Then, the microscopic and the macroscopic equations read

$$\mathrm{Div}_{\overline{\boldsymbol{X}}}(\overline{\boldsymbol{P}}) = \overline{\boldsymbol{b}}, \qquad \mathrm{Div}_{\boldsymbol{X}}(\boldsymbol{P}) = \boldsymbol{0}, \tag{1}$$

where the micro-scale equation $(1)_2$ is complemented by kinematic periodic fluctuation boundary conditions. Among certain other kinds of admissible boundary conditions, these imply the coupling relations $\overline{\boldsymbol{F}} = \langle \boldsymbol{F} \rangle$ and $\overline{\boldsymbol{P}} = \langle \boldsymbol{P} \rangle$, where the volume averaging operator $\langle \bullet \rangle = \mathrm{vol}(\Omega_0)^{-1} \int_{\Omega_0} \bullet \, \mathrm{d}V$ is employed. In the present kinematics-driven case, the macroscopic deformation gradient, $\overline{\boldsymbol{F}}$, is frequently called "the boundary condition" of the microscopic problem. Classical two-scale schemes necessitate one solution of the microscopic problem with the boundary condition $\overline{\boldsymbol{F}}(\overline{\boldsymbol{X}})$ at each macroscopic material point, $\overline{\boldsymbol{X}}$, and for each iteration of the solution of the macroscopic problem $(1)_1$. After each of these solutions of $(1)_2$, the homogenized stress response is computed by means of the volume average, $\overline{\boldsymbol{P}} = \langle \boldsymbol{P} \rangle$.

In this work, the goal is to approximate volume averages $\overline{\boldsymbol{P}}$ of solutions $\boldsymbol{P}$ to the microscopic problem $(1)_2$ very efficiently, i.e. to achieve significant speed-ups while preserving a high level of accuracy. In other words, we seek to efficiently describe the mapping $\overline{\boldsymbol{F}} \to \overline{\boldsymbol{P}}$. Exploiting the transformation rule mentioned above, attention is confined to

$$\overline{\boldsymbol{U}} \to \overline{\boldsymbol{P}}(\overline{\boldsymbol{U}}). \tag{2}$$

To this end, we introduce additional notation. The *Hencky strain* $\overline{\boldsymbol{E}}_{\mathrm{H}} = \log \overline{\boldsymbol{U}}$ is defined as the logarithm of the stretch tensor. The set of Hencky strains is a *vector space*, i.e. arbitrary linear combinations of Hencky strains are Hencky strains. This is in contrast to the stretch tensor, which may lose positive definiteness under linear combinations. The stretch tensor may be recovered by means of the exponential mapping, i.e. $\exp \overline{\boldsymbol{E}}_{\mathrm{H}} = \overline{\boldsymbol{U}}$, meaning that the correspondence $\overline{\boldsymbol{E}}_{\mathrm{H}} \leftrightarrow \overline{\boldsymbol{U}}$ is one-to-one.

Thus, the material law (2) may be alternatively expressed in terms of the Hencky strain. For an efficient description, the decomposition

$$\overline{\boldsymbol{E}}_{\mathrm{H}} = t \sum_{i=1}^{6} N_i \boldsymbol{Y}^{(i)} \qquad t = \|\overline{\boldsymbol{E}}_{\mathrm{H}}\| \tag{3}$$

into the *direction* $\underline{N} \in \mathbb{R}^6$ and the *amplitude* t is introduced. This employs the Frobenius norm $\|\bullet\|$ on the six-dimensional Hencky space (equivalent to the space $\mathrm{Sym}(\mathbb{R}^{3\times 3})$), spanned by a fixed orthonormal basis $\boldsymbol{Y}^{(1)}, \ldots, \boldsymbol{Y}^{(6)}$.

We suggest a surrogate model for the average stress $\overline{\boldsymbol{P}}$ that is based on *samples* of Hencky strains $\overline{\boldsymbol{E}}_{\mathrm{H}} \leftrightarrow t^{(i)} \underline{N}^{(j)}$, $i = 1, \ldots, N_{\mathrm{amp}}$, $j = 1, \ldots, N_{\mathrm{dir}}$, and the corresponding stresses $\overline{\boldsymbol{P}}(\exp(t_i \underline{N}^{(j)}))$. If the directions are approximately uniformly distributed, then the space of Hencky strains is sampled in a *concentric* manner, cf. Figure 2 and [2].

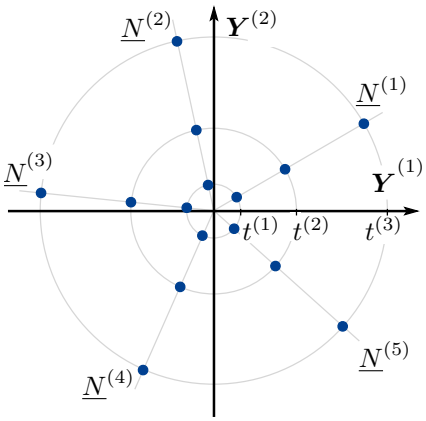

Figure 2. Concentric sampling positions within the Hencky space, exemplary along $N_{\mathrm{dir}} = 5$ directions and $N_{\mathrm{amp}} = 3$ amplitudes. This visualizes the two-dimensional case.

3 Concentric Interpolation of hyperelastic material laws

Let a macroscopic stretch tensor $\overline{\boldsymbol{U}}$ be given, for which the corresponding stress tensor $\overline{\boldsymbol{P}}$ shall be computed, cf. (2). We do so by separate interpolation of each component $\overline{P}_l$, $l = 1, \ldots, 9$, of $\overline{\boldsymbol{P}}$ in two stages, based on the *Concentric Interpolation* scheme

$$\overline{P}_l(t, \underline{N}) \approx \underline{w}(t)^{\top} \underline{k}(\underline{N}), \tag{4}$$

which differs from classical kernel interpolation on hyperspheres, cf. [5], by the fact that the weight vector, $\underline{w}$, depends on the amplitude, t. The *spherical basis functions* or *kernel functions*

$$k_j(\underline{N}) = \exp(-\gamma \operatorname{acos}^2(\underline{N} \cdot \underline{N}^{(j)})) \qquad\qquad j = 1, \ldots, N_{\mathrm{dir}} \tag{5}$$

employ the *kernel parameter* $\gamma > 0$, which needs to be determined beforehand, e.g. by a bisectional algorithm. The univariate vector of *weight functions*

$$\underline{w}(t) = \left[\widetilde{P}_l(t, \underline{N}^{(1)}) \quad \ldots \quad \widetilde{P}_l(t, \underline{N}^{(N_{\mathrm{dir}})})\right] \underline{\underline{K}}^{-1} \tag{6}$$

necessitates the *kernel matrix*

$$\underline{\underline{K}}_{ij} = \exp(-\gamma \operatorname{acos}(\underline{N}^{(i)} \cdot \underline{N}^{(j)})) \qquad\qquad i, j = 1, \ldots, N_{\mathrm{dir}} \tag{7}$$

as well as *radial interpolants* $\widetilde{P}_l(t, \underline{N}^{(j)})$. The latter are piecewise defined polynomials that interpolate the sampling values along each of the sampling directions $\underline{N}^{(j)}$. This means there is one distinct piecewise polynomial (e.g. of degree two or three) for each sampling direction, with supporting points along its respective sampling direction, e.g. along the radial lines in Figure 2.

Hence, the Concentric Interpolation scheme is an extension of the classical interpolation with spherical basis functions on hyperspheres $\mathbb{S}^{D-1}$ to the surrounding Euclidean space $\mathbb{R}^D$. In the present case, where one operates on the Hencky strain, the dimension is $D = 6$, but the scheme is generally applicable to any $D \geq 2$. In finite strain mechanics, the Concentric Interpolation method gains significant efficiency from the fact that it is sufficient to sample $\overline{\boldsymbol{U}} \leftrightarrow \overline{\boldsymbol{E}}_{\mathrm{H}}$ instead of $\overline{\boldsymbol{F}}$. This affects both the offline phase (when the data at the supporting points is generated) and the online phase (when the interpolation is performed).

The compatibility of the interpolant with the actual hyperelastic material law, $\overline{\boldsymbol{P}} = \partial \overline{W} / \partial \overline{\boldsymbol{F}}$, is only guaranteed on the supporting points, e.g. on the sampling data. It is expected that the errors due to the interpolation lie within acceptable bounds. Also, the treatment of the fourth-order stiffness, $\overline{\mathbb{C}}$, requires to be investigated.

First results are promising and actual two-scale simulations of realistic complexity, e.g. with more than 10^5 degrees of freedom on the macroscopic scale, are anticipated in the near future.

Acknowledgments

This research was funded by Deutsche Forschungsgemeinschaft (DFG) within the Emmy–Noether programm under grant DFG-FR2702/6.

References

[1] Benjamin Brands, Denis Davydov, Julia Mergheim, and Paul Steinmann. Reduced-Order Modelling and Homogenisation in Magneto-Mechanics: A Numerical Comparison of Established Hyper-Reduction Methods. *Mathematical and Computational Applications* 24.1 (2019). DOI: 10.3390/mca24010020.

[2] Felix Fritzen and Oliver Kunc. Two-stage data-driven homogenization for nonlinear solids using a reduced order model. *European Journal of Mechanics A / Solids* 69 (2018), pp. 201 –220. DOI: 10.1016/j.euromechsol.2017.11.007.

[3] Felix Fritzen and Matthias Leuschner. Reduced basis hybrid computational homogenization based on a mixed incremental formulation. *Computer Methods in Applied Mechanics and Engineering* 260 (2013). yig, pp. 143–154. DOI: 10.1016/j.cma.2013.03.007.

[4] Oliver Kunc and Felix Fritzen. Finite Strain Homogenization Using a Reduced Basis and Efficient Sampling. *Mathematical and Computational Applications* 24.2 (2019). DOI: 10.3390/mca24020056.

[5] Francis J Narcowich, Xingping Sun, Joseph D Ward, and Holger Wendland. Direct and inverse Sobolev error estimates for scattered data interpolation via spherical basis functions. *Foundations of Computational Mathematics* 7.3 (2007), pp. 369–390. DOI: 10.1007/s10208-005-0197-7.

**Proceedings of the 8th GACM Colloquium on Computational Mechanics
for Young Scientists from Academia and Industry
August 28–30, 2019 in Kassel, Germany**

Thermal Homogenization Using Image Data

Julian Lißner * [1] and Felix Fritzen[1]

[1]University of Stuttgart, Institute of Applied Mechanics (CE)

Abstract. An image based prediction of the effective heat conductivity for highly heterogeneous microstructured materials is presented. The synthetic materials under consideration show different inclusion morphology, orientation, volume fraction and topology. The prediction of the effective property is made exclusively based on image data with the main emphasis being put on the 2-point spatial correlation function. This task is implemented using both unsupervised and supervised machine learning methods. First, a snapshot proper orthogonal decomposition (POD) is used to analyze big sets of random microstructures and, thereafter, to compress significant characteristics of the microstructure into a low-dimensional feature vector. In order to manage the related amount of data and computations, incremental snapshot POD methods are proposed. In the second step, the obtained feature vector is used to predict the effective material property by using feedforward neural networks.

1 Introduction

In material analysis and design of heterogeneous materials, multiscale modeling can be used for the discovery of microstructured materials with tuned properties for engineering applications. However, the discovery of materials with the desired material property, being characterized by the microstructure of the solid, constitutes a highly challenging inverse problem. The basis for all multiscale models and simulations is information on the microstructure and on the microscale material behavior. If at hand, physical experiments can be replaced by – often costly – computations [4, 6] in order to determine the material properties by virtual testing. Separation of structural and microstructural length scales can often be assumed. This enables the use of the representative volume element (RVE) [8], characterizing the highly heterogeneous material using a single frame (or image) of the microstructured material, on which analytical or numerical computations can be conducted.

Supposing that similar images of the microstructured material yield similar effective material properties, the problem is rendered suitable for machine learning (ML) models. Although ML models usually focus on one specific task, it does not mean that the microstructure variations must be overly confined, for instance, inclusion volume fractions ranging from 20 up to 80% are considered. The main task, thus, persists in finding low-dimensional parameterizations of the images that capture the relevant information, use these parameterizations to compress the image information and build a surrogate model operating only on the reduced representation. The sampling of the data, the feature extraction and the training of the ML algorithm constitute the *offline* phase in which the surrogate model is built. Typically, the evaluation of the surrogate model can be realized almost in real-time, thereby enabling previously infeasible applications in microstructure tailoring, interactive user interfaces and computations on mobile devices.

Similarly to key ideas of the material knowledge system (MKS) approach [3], a reduced basis is deployed to reduce the dimensionality of the microstructural features contained in the 2-point correlation functions. With the sheer amount of samples required, the necessity for an incremental reduced basis computation scheme arises. With the use of synthetic microstructure data, the costly training of the reduced basis and of the artificial neural network [1] become feasible, enabling the creation of a surrogate model for the image-property linkage [5].

*Corresponding author: lissner@mechbau.uni-stuttgart.de ORCID iD: 0000-0002-2286-5211

2 Microstructure classification

The underlying bi-phasic microstructure is defined by the representative volume element (RVE), which is one periodic frame (or image) characterizing the heterogeneous material under considerations (Figure 1). The bi phasic material consists of the matrix phase of the material and insulating inclusions. The phase volume fraction, i.e. the volumetric part of each phase, suffices to describe the microstructure in a homogenized setting. However, figure 2 shows, at a constant phase volume fraction, variations beyond 50% for the effective material property, the heat conductivity $\bar{\kappa}$, are present for the underlying material. Since additional microstructural features, e.g. geometry, are characterized by randomness, a descriptor for the microstructural features is required. The 2-point spatial correlation function (2PCF) [7] induce a probability distribution describing the underlying microstructure. Roughly described, each value of the 2PCF is obtained by placing a line of a certain direction uniformly randomly distributed and computing the mean probability of finding a prescribed phase at the start and end point of the line, respectively.

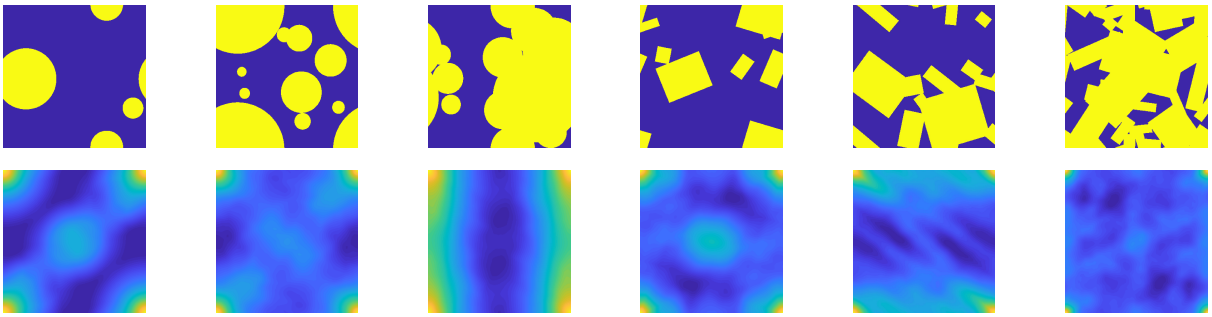

Figure 1. Depicting exemplary microstructures with their respective 2-point spatial correlation functions below.

Examples of the 2PCF (Figure 1) with the corresponding RVE above show similarities between the majorly different microstructures. Some observed characteristics of the 2PCF are:

- the maximum occurs at the corner of the domain
- preferred directions of the inclusion placement and/or orientation are captured
- the domain around the corners partially reflect the average inclusion shape

Hence, some similarities are found, particularly with respect to shape of the 2PCF at the corners and in the center. These observations hint at the existence of a low-dimensional parameterization of relevant microstructural features.

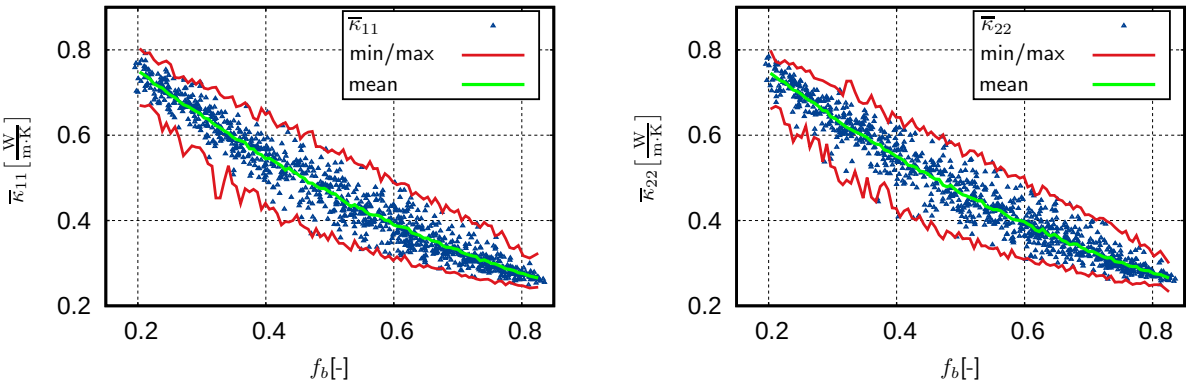

Figure 2. The range of $\bar{\kappa}_{11}$ and $\bar{\kappa}_{22}$ for 15000 RVEs for the microstructures under consideration is shown. Only 1000 values are depicted.

3 Incremental snapshot POD of the 2PCF

The properties of the 2PCF make them an excellent choice for a snapshot proper orthogonal decomposition (POD), constituting the unsupervised learning phase. The snapshot POD is used to construct a reduced basis (RB) [2] that provides an optimal subspace for approximating a given snapshot matrix. The snapshot matrix is used to compute the RB and consists of multiple individual snapshots containing the unreduced field information, i.e. the 2PCF. The RB $\underline{\underline{B}}$ is the discrete representation of a comparatively small subspace, which minimizes the relative projection error of the given snapshots. Since the considered microstructures allow for vastly different geometries, a humongous snapshots matrix would be required to ensure that the RB captures all the possibilities of microstructures. Due to storage and memory limitations this is obviously not possible and an iterative update scheme is required (Figure 3).

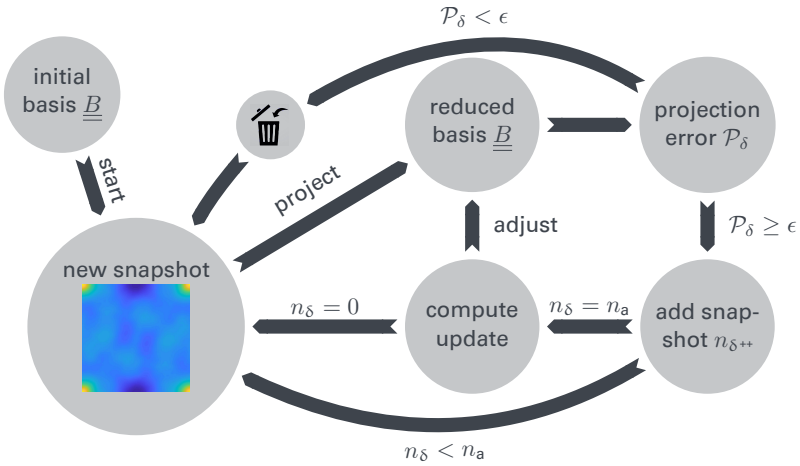

Figure 3. Iterative update scheme of the basis enrichment.

Assuming that a high projection error of a snapshot onto the RB implies a poor knowledge of the RB about the microstructural features contained in the snapshot, this snapshot is a valid candidate for the RB update. After enough candidate snapshots have been accumulated within a temporary buffer, the RB is updated. The iterative scheme is terminated once the RB is sufficiently accurate. The resulting RB $\underline{\underline{B}}$ contains a few salient eigenmodes, containing the most reocurrent information of the given snapshots it was computed with.

4 Data-driven Surrogate

The information contained within each RVE is given in voxel data, which consists of 400×400 voxels in this study. In order to have a low dimensional descriptor of the microstructure we start with the phase volume fraction f_b of the inclusion phase, where some correlation between f_b and the effective heat conductivity can be observed (Figure 2). The RB is used to extract the feature vector of each RVE, which is done for each snapshot $\underline{s}_i$ containing the 2PCF rewritten into vector format after shifting and rescaling. The input for the regression model $\underline{\xi}$ is consequently given by

$$\underline{\xi} = \begin{bmatrix} f_b \\ \underline{\underline{B}}^T \underline{s}_i \end{bmatrix} \qquad \in \mathbb{R}^{(h+1)\times 1}, \tag{1}$$

where only the first $h = 26$ eigenmodes, containing the most reoccurent patterns of $\underline{\underline{B}}$, are used. This allows a reduction of the dimension from 400×400 to just 27.

The training of the regression model constitutes the supervised learning phase. During the training the machine is provided with the inputs and their desired outputs. Dense feedforward artificial neural networks (ANN)[1] are a powerful machine learning tool to map given inputs to the desired output, suitable for this nonlinear regression task from the feature vector (Equation (1)), to the effective heat conductivity (Figure 2). Inspired the by human brain, dense feedforward ANNs propagate an input signal through various neurons to obtain an output signal. In order to achieve the desired mapping, the ANN is iteratively trained using precomputed data sets. During the training, the internal parameters of the ANN are adjusted under the premise to minimize the prediction error.

5 Preliminary Results

After the costly training of the incremental snapshot POD and the ANN is concluded, accurate and fast predictions can be made. The surrogate model has been evaluated on 2×7500 unseen test data, achieving mean relative errors, corresponding to [5], well below 2%.

Table 1. Relative errors of the surrogate models prediction

				
error measures	κ_{11}	κ_{22}	κ_{11}	κ_{22}
mean [%]	1.77	1.76	1.65	1.60
max [%]	11.7	14.1	11.6	10.5

6 Conclusions

A purely image based surrogate model to predict the effective heat conductivity has been proposed. Microstructures with topological and morphological variations with volume fractions ranging from 20 to 80% are considered. In order to handle the amount of data required to build the surrogate, an iterative snapshot POD method is deployed. The computed RB is then used to derive the extremely low dimensional feature vector used by the ANN. For most of the 15000 test data, the proposed surrogate model achieved remarkable relative errors well below 2%. A computational speedup of a factor of 40 has been achieved compared to the intrinsically fast FANS solver [4]. The most costly step of the surrogate model is the evaluation of the ANN input. Ongoing research indicates that further computational speedup can be achieved by computation of the feature vector in FFT space, boosting the speedup from 40 to at least 50. Nonetheless, the achieved accuracy is unaffected by these modifications.

Acknowledgments

Funded by the Deutsche Forschungsgemeinschaft (DFG, German Research Foundation) under Germany's Excellence Strategy – EXC-2075 – 390740016 and under grants FR2702/6, FR2702/8.

References

[1] Imad A Basheer and Maha Hajmeer. Artificial neural networks: fundamentals, computing, design, and application. *Journal of microbiological methods* 43.1 (2000), pp. 3–31.

[2] R Chris Camphouse, James Myatt, Ryan Schmit, Mark Glauser, Julie Ausseur, Marlyn Andino, and Ryan Wallace. A snapshot decomposition method for reduced order modeling and boundary feedback control. In: *4th Flow control conference*. 2008, p. 4195.

[3] Surya R Kalidindi. Computationally efficient, fully coupled multiscale modeling of materials phenomena using calibrated localization linkages. *ISRN Materials Science* 2012 (2012), pp. 1–13.

[4] Matthias Leuschner and Felix Fritzen. Fourier-Accelerated Nodal Solvers (FANS) for homogenization problems. *Computational Mechanics* 62.3 (2018), pp. 359–392.

[5] Julian Lißner and Felix Fritzen. Data-Driven Microstructure Property Relations. *Mathematical and Computational Applications* 24.2 (2019), p. 57.

[6] Christian Miehe. Strain-driven homogenization of inelastic microstructures and composites based on an incremental variational formulation. *International Journal for Numerical Methods in Engineering* 55 (2002), pp. 1285–1322.

[7] S Torquato and G Stell. Microstructure of two-phase random media. I. The n-point probability functions. *The Journal of Chemical Physics* 77.4 (1982), pp. 2071–2077.

[8] Salvatore Torquato. *Random heterogeneous materials: microstructure and macroscopic properties*. Vol. 16. Springer Science & Business Media, 2013.

**Proceedings of the 8th GACM Colloquium on Computational Mechanics
for Young Scientists from Academia and Industry
August 28–30, 2019 in Kassel, Germany**

Numerical and experimental characterization of additively manufactured mild steel under tension

Jorge Lizarazu * [1], Luise Göbel[1], Stefan Linne[1], Susanne Kleemann[1] and Tom Lahmer[1,2]

[1]Materialforschungs- und -Prüfanstalt an der Bauhaus-Universität Weimar, 99423 Weimar, Germany.
[2]Institute of Structural Mechanics, Bauhaus-University Weimar, 99423 Weimar, Germany.

Abstract. For the case of metals, Additive Manufacturing (AM), also known as 3D Printing, is a technology based on a layer-by-layer welding procedure able to create 3D products.

In the present study, the tensile behavior of additively manufactured mild steel is studied using both experimental and numerical approaches. Due to several heating and cooling cycles in the welding procedure, the microstructure of the metallic product is strongly modified and therefore, it is not as homogeneous as the original material. As a result, the product is first analyzed with optical and scanning electron microscopes, in order to identify the phases and extract the grain properties. Based on this information, the microstructure of the representative volume element (RVE) is generated by means of two approaches: The first one consists of using a Voronoi Tessellation and the second one comprises the digitization of the image obtained from the scanning electron microscope (SEM). After the definition and assignment of the constitutive laws to each phase, a subsequent numerical tensile test is carried out. The result of this simulation is compared with experimental tensile tests of specimens, which were produced using the wire arc additive manufacturing technique.

The experiments indicate that the stiffness of the additively manufactured products is similar in both parallel and perpendicular welding directions. On the contrary, the ductility exhibits more visible differences in these two directions. Besides, the material, shows a softening behavior in one direction.

Introduction.

The current applications of additively manufactured metals require a proper knowledge of the material; so that, their response under several type of loading can be estimated accurately by using numerical techniques. In pursuit of this, a study regarding uniaxial tensile behavior of 3D printed products is necessary, in order to set up the basis for the simulation under more complex loading conditions.

In this work, the procedure already proposed by [3] is applied to 3D printed mild steel products, which were created using the wire arc additive manufacturing (WAAM) technique.

WAAM is used to create middle to large sized products and has the following main advantages [4, 7]: Relative high deposition rates and a higher usage efficiency of the material. However, the technique is only able to create products of middle level of structural topology complexity with a high surface roughness; being necessary to post-process the products in a specific way [1]. Besides, since WAAM is very sensitive to the process parameters, building sequences and welding disturbances [4], repeatability of the products can be an issue; therefore, an additional investment for sensing and controlling might be necessary. The process parameters are: Wire feed speed, welding speed, layer thickness, arc voltage, arc current, wire diameter, wire type, shielding gas type and gas flow. Table 1 summarizes the typical features of WAAM.

Table 1. Typical features of WAAM

Layer thickness (mm)	Deposition rate (kg/h)	Dimensional accuracy (mm)	Surface roughness (μm)
1-2	Until 6	$\pm$ 0.2	500

*Corresponding author: jorge.lizarazu@mfpa.de

1 Study of the microstructure.

In order to analize the microstructure under the light microscope (LM) and SEM, some square samples of side 1.5 cm were cut from a plate, whose two faces were previously polished; later, the samples were etched.

1.1 Investigation under the light microscope.

The purpose of the investigation under the LM is to identify the number and boundaries of heat affected regions. Figure 1 shows that only one of such regions exists, being even impossible to identify the boundaries of each welding layer.

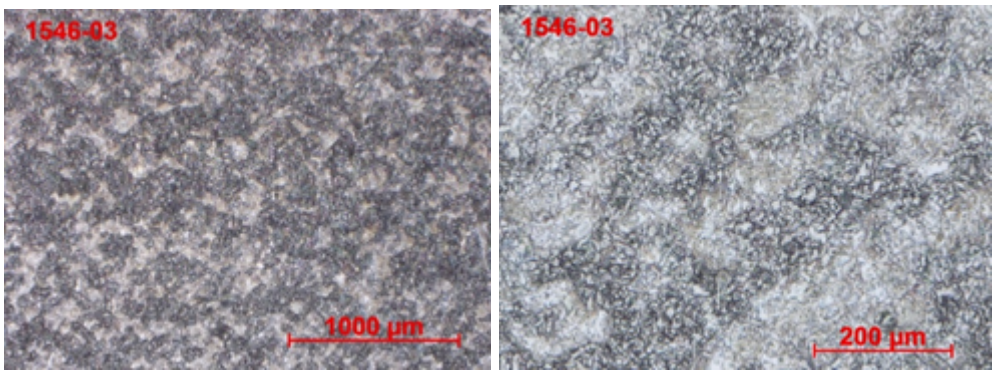

Figure 1. Images of the material under the light microscope.

1.2 Investigation under the scanning electron microscope.

The purpose of this analysis was to identify the phases of the material and extract grain parameters. Two phases were identified in Figure 2(a): Ferrite and Cementite in darker and lighter color respectively. Figure 2(b) shows the existence of several pores (in red circles) and inclusions (in red squares).

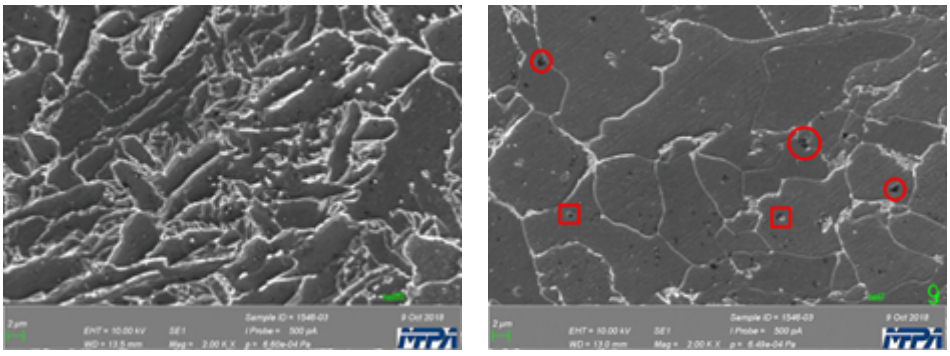

(a) Identification of phases (b) Identification of pores and inclusions

Figure 2. SEM images of the microstructure.

2 Experimental Investigation.

2.1 Microtensile test.

The purpose of this test is to extract qualitative information regarding the crack formation and propagation. All this process is depicted and self explained in Figure 3.

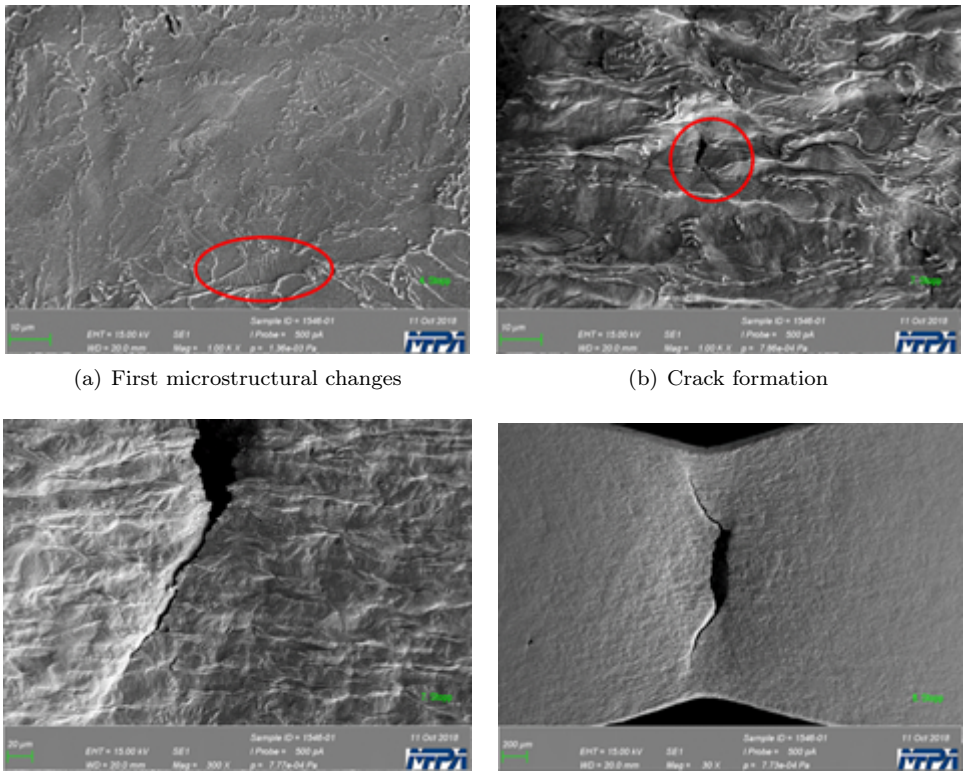

(a) First microstructural changes (b) Crack formation

(c) Crack opening (d) Break down

Figure 3. Formation and propagation of cracks in the material.

2.2 Macrotensile test.

Several specimens of rectangular shape (1 cm x 10 cm) and bottle neck shape (inscribed in a rectangle of dimensions 1.5 cm x 12 cm) were tested in order to build the stress-strain relations, observe the mechanical behavior and extract mechanical properties. The specimens were extracted from the outer boundaries of two plates, as well as from the inside part of them; additionally, the specimens were classified as parallel and perpendicular (to the welding direction).

In principle, no differences were noticed between the mechanical behavior of the specimens located at the outer boundary and the inner part of the plates. It was observed that the stiffness of the specimens, parallel and perpendicular, are similar; however, the ductility of the parallel specimens (Figure 4(d)) is twice as big as the ductility of the perpendicular specimens (Figure 4(b)). Besides, it was noticed that after converting the engineering measurements of stress and strain into the corresponding true values, the stress-strain curve exhibits a softening behaviour.

3 Numerical simulation.

3.1 Polycristaline microstructure and generation of the finite element mesh.

Two approaches were considered for the generation of the microstructure. The first one based on the Voronoi Tesselation and the second one based on the digitization of the SEM image.

3.1.1 Synthetic generation of the microstructure.

The first approach consisted on using the computer program Neper [5] to generate the microstructure. It is based on the grain parameters already extracted from the SEM image (Figure 2(a)) and the Voronoi Tesselation. The synthetically generated microstructure and the corresponding finite element mesh are shown in Figure 5.

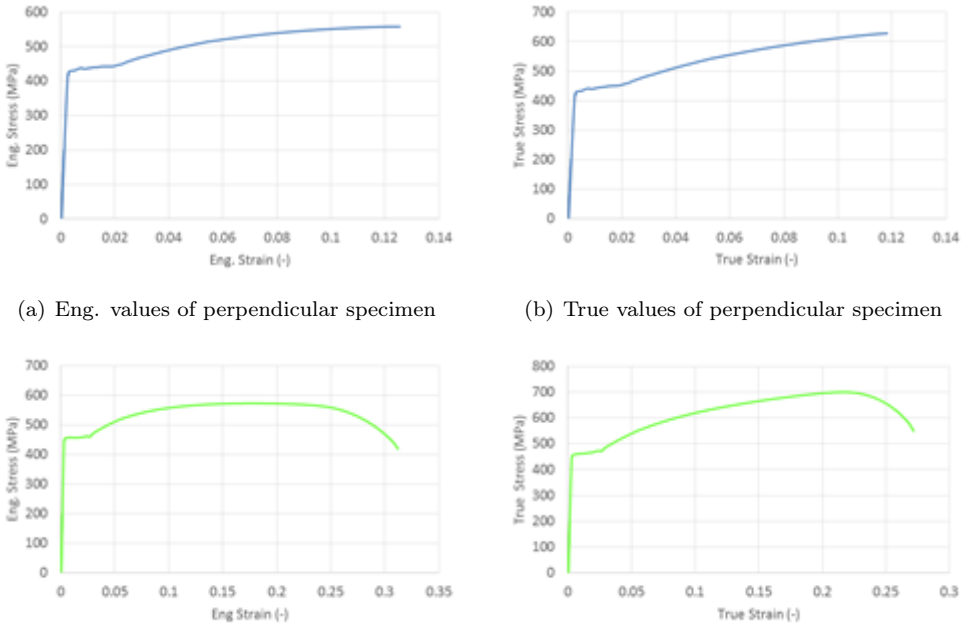

(a) Eng. values of perpendicular specimen

(b) True values of perpendicular specimen

(c) Eng. values of parallel specimen

(d) True values of parallel specimen

Figure 4. Formation and propagation of cracks in the material.

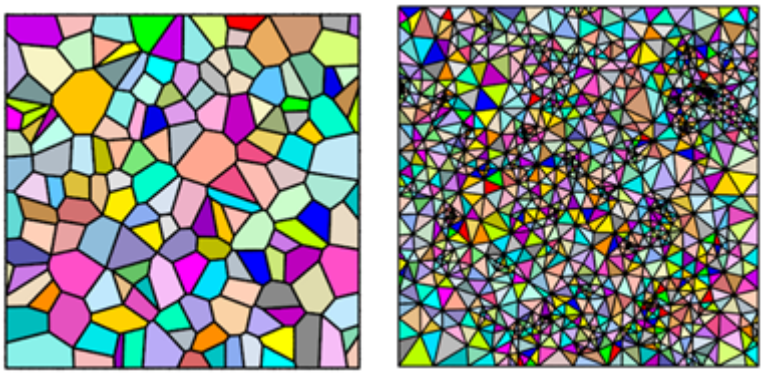

(a) Voronoi Tesselation

(b) Finite element mesh

Figure 5. Synthetic microstructure and its discretization into finite elements.

3.1.2 Image scanning based generation of the microstructure.

By using the computer program OOF2, the SEM image is automatically digitized and discretized, see Figure 6.

3.2 Constitutive relations.

After generating the microstructure and meshing each phase of the microstructure separately, the constitutive behavior to each phase is specified as follows:

3.2.1 Ferrite.

For this phase, a linear elastic behaviour with parameters $E = 200$ GPa and $\mu = 0.3$ is defined. Additionally, a plastic behaviour following Eq.(1) is considered, whose parameters are thoroughly explained

**Proceedings of the 8th GACM Colloquium on Computational Mechanics
for Young Scientists from Academia and Industry
August 28–30, 2019 in Kassel, Germany**

A Homogenization Method with Minimal RVE Boundary Conditions

Maximilian Müller * [1] and F. Gruttmann[1]

[1]TU Darmstadt, Fachgebiet Festkörpermechanik, Franziska-Braun-Straße 7, 64287 Darmstadt

Abstract. In this contribution, a homogenisation method based on the Irving Kirkwood theory is introduced. From basic assumptions for the relations between micro and macro scale mass density and linear momentum, homogenisation formulas for the stress tensor and body force vector are derived. This approach ensures compliance between the microscopic and macroscopic model without the need to fulfil the Hill condition a priori by means of a specific set of boundary conditions. Therefore a much wider variety of boundary conditions can be used in the representative volume element (RVE). As a first example, minimal boundary conditions are used. These only prevent rigid body motions. Loading of the RVE is realised through a side condition, which relates the strains of the two scales and is introduced into the weak form of equilibrium via Lagrange multipliers. Computations for three dimensional beam like structures serve as a first test. A two-scale homogenisation scheme, that uses beam elements on macro level and solid brick elements on micro level is implemented. The implementation is verified by obtaining the homogenised stiffness matrix for a homogeneous beam. Finally, structures with inhomogeneities in length direction are studied and obtained results are compared to benchmark solutions from a full-scale model.

Introduction

The existing and in FE^2 widely used approach of fulfulling the Hill-Mandel condition for homogenisation a priori by using certain sets of boundary conditions for the representative volume element (RVE), limits possible boundary conditions very strictly and often produces undesired boundary and other effects. The desire to get rid of those restrictions led to the development of a more general homogenisation method based on the Irving-Kirkwood theory [2, 3, 4]. For this contribution we apply the method to beam like structures undergoing small strains and use of beam elements on macro level. Within the RVE there will be no other boundary conditions than the ones necessary to restrict rigid body movements. The loading of the RVE will be realised with an additional constraint. For numerical examples, we study a beam with a square cross section and periodic holes perpendicular to the length direction.

1 Theoretical framework

1.1 Homogenization Theory

In order to describe a body inhomogeneities, which are much smaller than its macroscopic measurements, the heterogenous body will be described in two scales. We will assume homogeneous properties on a macroscopic scale and take account of the inhomogenieties on a microscopic scale. The homogenous properties on the macroscopic level are then derived from the microscopic level by means of homogenization.
In detail, there shall be given a body $\mathcal{B}$ inhabiting the volume $\mathcal{R}$ with boundary $\partial\mathcal{R}$. A point in $\mathcal{B}$ shall be described with coordinates $\boldsymbol{y} = [y_1, y_2, y_3]^{\mathbf{T}}$ defining the macro scale. For every point $\boldsymbol{y}$ there is an assigned surrounding volume $\mathcal{P}^{\mathrm{m}}$ of the micro scale, described with coordinates $\boldsymbol{x} = [x_1, x_2, x_3]^{\mathbf{T}}$.
For all subdivisions of $\mathcal{R}$ and all $\mathcal{P}^{\mathrm{m}}$ the mass and linear momentum balance laws hold:

$$\dot{\rho}^{\alpha} + \rho^{\alpha} \nabla_y \cdot (\boldsymbol{v}^{\alpha}) = 0, \tag{1}$$

$$\rho^{\alpha} \dot{\boldsymbol{v}}^{\alpha} = \nabla_x \cdot \boldsymbol{\sigma}^{\alpha} + \rho^{\alpha} \boldsymbol{b}^{\alpha}. \tag{2}$$

*Corresponding author: mmueller@mechanik.tu-darmstadt.de

Here, α is either m for microscopic or M for macroscopic, indicating the scale in which the quantity is defined. Further, $\nabla_x \cdot (\cdot)$ denotes the divergence of $(\cdot)$ with respect to $\boldsymbol{x}$.
These balance laws for the two scales are not independent as they describe the same body. So we postulate the following homogenization laws for mass density und linear momentum in accordance with [2]:

$$\rho^{\mathrm{M}}(\boldsymbol{y},t) = \int_{\mathcal{R}} \rho^{\mathrm{m}}(\boldsymbol{x},t) g(\boldsymbol{y},\boldsymbol{x}) \, \mathrm{d}V^{\mathrm{m}}, \tag{3}$$

$$\rho^{\mathrm{M}}(\boldsymbol{y},t)\boldsymbol{v}^{\mathrm{M}}(\boldsymbol{y},t) = \int_{\mathcal{R}} \rho^{\mathrm{m}}(\boldsymbol{x},t)\boldsymbol{v}^{\mathrm{m}}(\boldsymbol{x},t) g(\boldsymbol{y},\boldsymbol{x}) \, \mathrm{d}V^{\mathrm{m}}. \tag{4}$$

In (3) and (4) $g(\boldsymbol{y},\boldsymbol{x})$ is a weighting function, which needs to fulfill a few basic properties in order to not compromise the theory. For further information on those properties and their implications see [2]. There, it is also shown, that the postulated homogenization laws are consistent with the balance laws (3) and (4) and lead to additional homogenization laws for the body force vector and stress tensor. For the quasi static case discussed here, they are:

$$\rho^{\mathrm{M}}\boldsymbol{b}^{\mathrm{M}} := \int_{\mathcal{R}} \rho^{\mathrm{m}}\boldsymbol{b}^{\mathrm{m}} g \, \mathrm{d}V^{\mathrm{m}}, \tag{5}$$

$$\boldsymbol{\sigma}^{\mathrm{M}} := \int_{\mathcal{R}} \boldsymbol{\sigma}^{\mathrm{m}} g \, \mathrm{d}V^{\mathrm{m}}. \tag{6}$$

For this contribution we will set the weighting function $g(\boldsymbol{y},\boldsymbol{x}) = \frac{1}{V^{\mathrm{m}}}$, where V^{m} is the volume of the RVE. Also, as stated before, deformations will be limited to small strains.

1.2 Variational Formulation

With the homogenization laws for the stress tensor (5) and body force vector (6) the transition from micro to macro level is complete. We now need a transition law from macro to micro. Looking at the homogenization laws, it appears naturally to use the same homogenizational connection for the micro and macro strains:

$$\boldsymbol{\varepsilon}^{\mathrm{M}} = \int_{\mathcal{R}} \boldsymbol{\varepsilon}^{\mathrm{m}} g \, \mathrm{d}V^{\mathrm{m}} = \frac{1}{V^{\mathrm{m}}} \int_{\mathcal{R}} \boldsymbol{\varepsilon}^{\mathrm{m}} \, \mathrm{d}V^{\mathrm{m}} \qquad \Leftrightarrow \qquad \int_{\mathcal{R}} (\boldsymbol{\varepsilon}^{\mathrm{M}} - \boldsymbol{\varepsilon}^{\mathrm{m}}) \, \mathrm{d}V^{\mathrm{m}} = 0. \tag{7}$$

With given macro strains $\boldsymbol{\varepsilon}^{\mathrm{M}}$, equation (7) will be implemented as an additional constraint into the weak form of the micro problem via Lagrange multipliers. For each of the n components of the strain vector, we will need one Lagrange multiplier, which will be arranged in a vector $\bar{\boldsymbol{\lambda}} = [\bar{\lambda}_1, \cdots, \bar{\lambda}_n]$.
Variation with respect to displacements $\boldsymbol{u}$, Lagrange multipliers $\bar{\boldsymbol{\lambda}}$ and macro strains $\boldsymbol{\varepsilon}^{\mathbf{M}}$ leads with vanishing body forces to the following weak form of the problem:

$$\int_{\mathcal{R}} \delta\boldsymbol{\varepsilon}^{\mathrm{mT}} \boldsymbol{\sigma}^{\mathrm{m}} \, \mathrm{d}V^{\mathrm{m}} + \int_{\mathcal{R}} \delta\bar{\boldsymbol{\lambda}}^{\mathrm{T}} (\boldsymbol{\varepsilon}^{\mathrm{M}} - \boldsymbol{\varepsilon}^{\mathrm{m}}) \, \mathrm{d}V^{\mathrm{m}} + \int_{\mathcal{R}} \bar{\boldsymbol{\lambda}}^{\mathrm{T}} (\delta\boldsymbol{\varepsilon}^{\mathrm{M}} - \delta\boldsymbol{\varepsilon}^{\mathrm{m}}) \, \mathrm{d}V^{\mathrm{m}} = 0. \tag{8}$$

The variation with respect to $\boldsymbol{\varepsilon}^{\mathrm{M}}$ is not necessary but leads to a simpler implementation of the homogenization scheme, that can use existing code.

1.3 Application to Beams

We start with linear Timoshenko beam kinematics for the displacements $\bar{\boldsymbol{u}} = [\bar{u}_x, \bar{u}_y, \bar{u}_z]^{\mathrm{T}}$ of an arbitrary point with coordinates (x, y, z) where the coordinate x is aligned to the beam axis:

$$\bar{u}_x(x,y,z) = u_x(x) + \beta_y(x) z - \beta_z(x) y \tag{9}$$

$$\bar{u}_y(x,y,z) = u_y(x) - \beta_x(x) z \tag{10}$$

$$\bar{u}_z(x,y,z) = u_z(x) + \beta_x(x) y \tag{11}$$

Here, u_x, u_y, u_z denote the displacements of the beam axis and $\beta_x, \beta_y, \beta_z$ are rotations along their corresponding axis.
The linearized Green strains $\boldsymbol{\varepsilon}_{\mathrm{v}} = \boldsymbol{\varepsilon}^{\mathrm{M}}$ are then given by

$$\boldsymbol{\varepsilon}_{\mathrm{v}} = \begin{bmatrix} \varepsilon_x \\ \varepsilon_y \\ \varepsilon_z \\ 2\varepsilon_{xy} \\ 2\varepsilon_{xz} \\ 2\varepsilon_{yz} \end{bmatrix}_v = \begin{bmatrix} u_x' + \beta_y' \cdot z - \beta_z' \cdot y \\ 0 \\ 0 \\ u_y' - \beta_z - \beta_x' \cdot z \\ u_z' + \beta_y + \beta_x' \cdot y \\ 0 \end{bmatrix}. \tag{12}$$

They can be associated to the given macroscopic beam strains $\boldsymbol{\varepsilon}_b$:

$$\boldsymbol{\varepsilon}_{\mathrm{b}} := \begin{bmatrix} \varepsilon_{\mathrm{x}} \\ \gamma_{\mathrm{xy}} \\ \gamma_{\mathrm{xz}} \\ \vartheta_{\mathrm{x}} \\ \kappa_{\mathrm{y}} \\ \kappa_{\mathrm{z}} \end{bmatrix}_{\mathrm{b}} := \begin{bmatrix} u_x' \\ u_y' - \beta_z \\ u_z' + \beta_y \\ \beta_x' \\ \beta_y' \\ \beta_z' \end{bmatrix} \quad \Rightarrow \quad \boldsymbol{\varepsilon}_{\mathrm{v}} = \begin{bmatrix} \varepsilon_x \\ \varepsilon_y \\ \varepsilon_z \\ 2\varepsilon_{xy} \\ 2\varepsilon_{xz} \\ 2\varepsilon_{yz} \end{bmatrix}_{v} = \boldsymbol{P}_{\mathrm{b}} \boldsymbol{\varepsilon}_{\mathrm{b}} = \begin{bmatrix} 1 & 0 & 0 & 0 & z & -y \\ 0 & 0 & 0 & 0 & 0 & 0 \\ 0 & 0 & 0 & 0 & 0 & 0 \\ 0 & 1 & 0 & -z & 0 & 0 \\ 0 & 0 & 1 & y & 0 & 0 \\ 0 & 0 & 0 & 0 & 0 & 0 \end{bmatrix} \begin{bmatrix} \varepsilon_{\mathrm{x}} \\ \gamma_{\mathrm{xy}} \\ \gamma_{\mathrm{xz}} \\ \vartheta_{\mathrm{x}} \\ \kappa_{\mathrm{y}} \\ \kappa_{\mathrm{z}} \end{bmatrix}_{\mathrm{b}} . \quad (13)$$

In equation (8) the Lagrange multipliers can be indentified as a stress-like quantity. While on macroscopic level they need to represent the stress resultants $\boldsymbol{\sigma}_{\mathrm{b}} = [N, Q_y, Q_z, M_x, M_y, M_z]^{\mathrm{T}}$, on microscopic level they need to represent the cauchy stresses $\boldsymbol{\sigma}_{\mathrm{v}} = [\sigma_x, \sigma_y, \sigma_z, \tau_{xy}, \tau_{xz}, \tau_{yz}]^{\mathrm{T}}$. They can be transformed via the following equation:

$$\boldsymbol{\lambda} = \begin{bmatrix} \lambda_{\sigma_x} \\ \lambda_{\sigma_y} \\ \lambda_{\sigma_z} \\ \lambda_{\tau_{xy}} \\ \lambda_{\tau_{xz}} \\ \lambda_{\tau_{yz}} \end{bmatrix} = \boldsymbol{P}_{\lambda} \bar{\boldsymbol{\lambda}} = \begin{bmatrix} 1 & 0 & 0 & 0 & z & -y \\ 0 & 0 & 0 & 0 & 0 & 0 \\ 0 & 0 & 0 & 0 & 0 & 0 \\ 0 & f_1(y) & 0 & -z & 0 & 0 \\ 0 & 0 & f_2(z) & y & 0 & 0 \\ 0 & 0 & 0 & 0 & 0 & 0 \end{bmatrix} \begin{bmatrix} \bar{\lambda}_N \\ \bar{\lambda}_{Q_y} \\ \bar{\lambda}_{Q_z} \\ \bar{\lambda}_{M_x} \\ \bar{\lambda}_{M_y} \\ \bar{\lambda}_{M_z} \end{bmatrix} \quad (14)$$

While the Lagrange multipliers $\bar{\boldsymbol{\lambda}}$, which correspond to the macroscopic stress resultants of the beam, are constants as they are constant for each Gauss point of the RVE, the altered multipliers $\boldsymbol{\lambda}$ (and correspondingly $\boldsymbol{\sigma}_{\mathrm{v}}$) should not be constant over the cross section.
As in basic beam theory, the normal stress σ_x is linear in z and y with the gradient being dependent from the bending moments. The shear stresses τ_{xy} and τ_{xz} however, are assumed constant in basic beam theory which leads to a too stiff reaction, especially in cases like sandwich beams with a very high difference in stiffness between core and covering layers. In order to circumvent this problem we assume much more realistic quadratic shear stresses. For this contribution we use the well known formula for square cross sections and set

$$f_1(y) = \frac{3}{2A}\left(1 - 4\frac{y^2}{b^2}\right) \qquad \text{and} \qquad f_2(z) = \frac{3}{2A}\left(1 - 4\frac{z^2}{h^2}\right). \quad (15)$$

Wherein b and h are the width and height of the cross section and $A = bh$ is the area of the cross section. Inserting equations (13) and (14) into the weak form (8) gives:

$$\int_{\mathcal{R}} \delta\boldsymbol{\varepsilon}^{\mathrm{m}\mathrm{T}} \boldsymbol{\sigma}^{\mathrm{m}} \, \mathrm{d}V^{\mathrm{m}} + \int_{\mathcal{R}} \delta\boldsymbol{\lambda}^{\mathrm{T}} \boldsymbol{P}_{\lambda}^{\mathrm{T}} (\boldsymbol{P}_{\mathrm{b}} \boldsymbol{\varepsilon}_{\mathrm{b}}^{\mathrm{M}} - \boldsymbol{\varepsilon}^{\mathrm{m}}) \, \mathrm{d}V^{\mathrm{m}} + \int_{\mathcal{R}} \boldsymbol{\lambda}^{\mathrm{T}} \boldsymbol{P}_{\lambda}^{\mathrm{T}} (\boldsymbol{P}_{\mathrm{b}} \delta\boldsymbol{\varepsilon}_{\mathrm{b}}^{\mathrm{M}} - \delta\boldsymbol{\varepsilon}^{\mathrm{m}}) \, \mathrm{d}V^{\mathrm{m}} = 0. \quad (16)$$

1.4 Finite Element Formulation

For the macroscopic level, standard 3D beam elements with six degrees of freedom (three translations, three rotations) are used. On microscopic level we use 3D brick elements. A Linearization of (16) and a standard iso-parametric FE-formulation leads to:

$$L[\dots] = \delta\boldsymbol{V}^{\mathrm{m}\mathrm{T}} (\boldsymbol{K}\Delta\boldsymbol{V}^{\mathrm{m}} + \boldsymbol{A}\Delta\boldsymbol{\lambda} + \boldsymbol{F}) + \delta\boldsymbol{\lambda}^{\mathrm{T}} (\boldsymbol{A}^{\mathrm{T}}\Delta\boldsymbol{V}^{\mathrm{m}} + \boldsymbol{T}\Delta\boldsymbol{\varepsilon}^{\mathrm{M}}) + \delta\boldsymbol{\varepsilon}^{\mathrm{M}\mathrm{T}} (\boldsymbol{T}^{\mathrm{T}}\Delta\boldsymbol{\lambda}) = 0. \quad (17)$$

In which $\boldsymbol{\epsilon}^{\mathrm{m}} = \boldsymbol{B}\boldsymbol{V}^{\mathrm{m}}$, with $\boldsymbol{V}^{\mathrm{m}}$ being the displacement vector, was used and

$$\boldsymbol{K} := \int_{\mathcal{R}} \boldsymbol{B}^{\mathrm{T}} \boldsymbol{D} \boldsymbol{B} \, \mathrm{d}V^{\mathrm{m}}, \quad \boldsymbol{D} = \frac{\partial\boldsymbol{\sigma}}{\partial\boldsymbol{\varepsilon}}, \quad \boldsymbol{A} := -\int_{\mathcal{R}} \boldsymbol{B}^{\mathrm{T}} \boldsymbol{P}_{\lambda} \, \mathrm{d}V^{\mathrm{m}}, \quad \boldsymbol{T} := \int_{\mathcal{R}} \boldsymbol{P}_{\lambda}^{\mathbf{T}} \boldsymbol{P}_{\mathrm{b}} \, \mathrm{d}V^{\mathrm{m}}.$$

We also redefined $\varepsilon^{\mathrm{M}} := \varepsilon_{\mathrm{b}}^{\mathrm{M}}$ for better readability.
Next, we follow the standard homogenization scheme presented in [1], which can be used here in a very similiar, straight forward way.

2 Numerical Examples

2.1 Verification on a Homogeneous, Linear Elastic Cantilever

First, we want to verify the model on a homogeneous beam with a square cross section and linear elastic material. We use a beam with length of 16cm and height and width of 1cm. With our improvements to the shear stresses, the entries of the homogenized stiffness matrix converge towards the expected values $\boldsymbol{D}^{\mathrm{M}} = \mathrm{diag}\{EA, \kappa_y GA, \kappa_z GA, GI_p, EI_y, EI_z\}$. With E being the Youngs modulus, G the shear modulus, A the area of the cross section, I_y, I_z and $I_p = I_y + I_z$ the area moments of inertia and $\kappa_y = \kappa_z = \frac{5}{6}$ the shear correction factors.

2.2 Cantilever with Plasticity and Holes

We now investigate a beam with the same dimensions as before, but with periodic holes in y-direction with a diameter of 0.25cm. We consider a linear elastic, plastic material with linear isotropic hardening ($E = 100000\frac{\mathrm{kN}}{\mathrm{cm}^2}$, $\nu = 0$, $y_0 = 600\frac{\mathrm{kN}}{\mathrm{cm}^2}$, $\xi_h = 10000\frac{\mathrm{kN}}{\mathrm{cm}^2}$). The cantilever is loaded at the free end with a single force F in z-direction.
For a reference solution we use a full scale model with linear 3D solid elements, which consists of 16 holes over a beam length of 16cm. For our multiscale solution, we use ten beam elements on macro level and a cubic RVE with side length of 1cm and one hole, fig. 1. As a result, we compare the applied force F over displacement u_z of the free end for both models. We then see a perfect match for the linear elastic part and a good agreement for the plastic part of the structural behaviour (fig. 2).

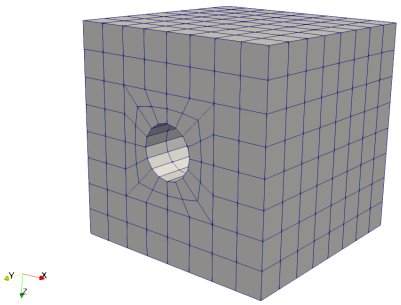

Figure 1. RVE for a beam with holes

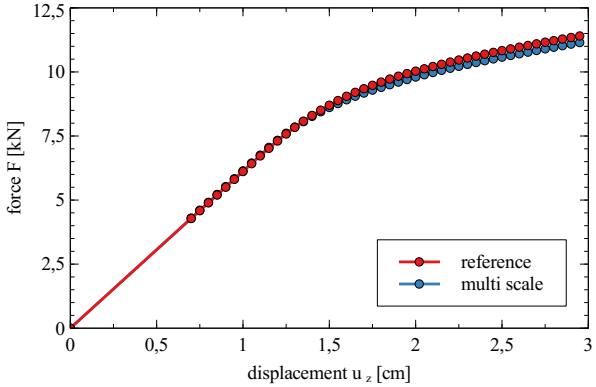

Figure 2. Load-displacement diagram of the cantilever

References

[1] F. Gruttmann and W. Wagner. A coupled two-scale shell model with applications to layered structures. *International Journal for Numerical Methods in Engineering* 94 (2013), p. 1233–1254.

[2] K. K. Mandapu, A. Sengupta, and P. Papadopoulos. A homogenization method for thermomechanical continua using extensive physical quantities. *Proceedings of the Royal Society* 468 (2012), p. 1696–1715.

[3] B. S. Mercer, K. K. Mandapu, and P. Papadopoulos. Novel Formulations of Microscopic Boundary-Value Problems in Continuous Multiscale Finite Element Methods. *Computer Methods in Applied Mechanics and Engineering* 286 (2015), p. 268–292.

[4] M. Müller and F. Gruttmann. A homogenisation method based on the Irving-Kirkwood-Theory. *Proceedings of the 7th GACM Colloquium on Computational Mechanics* (2017). URL: `http://dx.doi.org/10.18419/opus-9334`.

**Proceedings of the 8th GACM Colloquium on Computational Mechanics
for Young Scientists from Academia and Industry
August 28–30, 2019 in Kassel, Germany**

Cauchy-Born rule based continuum simulation of the mechanical properties of single-layered graphene sheets

Qige Zheng*[1] and Jens Wackerfuß[1]

[1]Institute of Structural Analysis, University of Kassel, Kassel, Germany

Abstract. Besides experiments, numerical simulations are also necessary for studying the mechanical properties of graphene sheets. In this paper, the Cauchy-Born rule is used in the formulation of the continuum mechanical model. According to the original Cauchy-Born rule, the positions of the atoms within the crystal lattice follow the overall strain of this crystalline solid in the case of small deformation. However, it is restricted to three-dimensional crystalline materials or the in-plane deformations of a two-dimensional material (like graphene). The exponential Cauchy-Born rule or the higher order Cauchy-Born rule, which are modified forms of the original and applicable to shell like structures, can be used to describe the out-of-plane deformations of a single-layered graphene.

Introduction

Due to the exceptional features of graphene sheets, many research projects are focused on them since they were discovered in 2004 [10]. Besides experiments, also numerical simulations are necessary for studying their mechanical properties. The models which are used in the simulations can be classified into two categories: molecular mechanical models and continuum mechanical models.

Effects on the atomic scale can be described explicitly with molecular mechanical models. However, this type of models is restricted to simulate structures of small sizes. For determination of the mechanical behaviors of technical relevant large graphene nanostructures at the macroscopic level, it can be calculated efficiently with continuum mechanical models. Some classical formulations of these models are able to characterize the small strain response of graphene sheets through elastic moduli such as Young's modulus, Poisson's ratio [6, 8]. The continuum mechanical models can also be derived from interatomic potentials describing the energy and the interactions within an atomistic system [1, 5]. In this way, the underlying atomistic structure is considered in the constitutive relation which is a priori valid for the scenarios of large deformations.

In this paper, a 4-node quadrilateral element with a Cauchy-Born rule based constitutive relation is formulated for studying the mechanical properties of a single-layered graphene sheet.

1 Continuum model

In this section, a continuum model is formulated based on the quasicontinuum (QC) method [12] for solving the static problems of graphene with absolute-zero temperature (0 K). In context of the QC method, the internal energy E of the whole atomistic system is equal to the strain energy which is only related to the interatomic potentials U in the situation of 0 K. And the strain energy density W is expressed as

$$W = \frac{1}{A_c} \sum_{i=1}^{n_c} U_i \ , \tag{1}$$

*Corresponding author: zheng@uni-kassel.de

where U_i and n_c denote the interatomic potential on atom i and the number of atoms in the selected domain (so-called representative cell) with radius R_c in the atomistic structure (see Fig. 1 (c)). $A_c = n_c \cdot A_{atom}$ is the area of the representative cell. A_{atom} is the area of the representative cell with only one atom and given as $A_{atom} = \frac{3\sqrt{3}}{4} {r_b}^2$ with r_b denoting here the equilibrium bond length of undeformed graphene (see Fig. 1 (b)). In context of graphene, U_i can be the Brenner potential [3], the DREIDING potential [9] or the modified Morse potential [2].

Therefore, the internal energy E of the whole atomistic system and the total energy π are formulated as

$$E = \int_{\Omega_0} W(\boldsymbol{x}, \boldsymbol{F}) \, \mathrm{d}A_0, \quad \pi = E - \sum_{i=1}^{n} \bar{\boldsymbol{f}}_i \cdot \boldsymbol{u}_i \ . \tag{2}$$

where $\bar{\boldsymbol{f}}_i$ and $\boldsymbol{u}_i$ are the external load applied to the atom i and the displacement of this atom. Ω_0 and $\mathrm{d}A_0$ denote the domain occupied by graphene and surface element in initial configuration. n is the number of atoms in the whole system. Following the original Cauchy-Born rule [4], each hexagon cell of graphene is deformed according to the local continuum deformation gradient (see Fig. 2) in the situation of in-plane deformation. This relationship is expressed as

$$\boldsymbol{r} = \boldsymbol{F} \cdot \boldsymbol{R} \quad \text{with} \quad \boldsymbol{F} = \frac{\partial \boldsymbol{x}}{\partial \boldsymbol{X}} \ , \tag{3}$$

where $\boldsymbol{R}$ is a lattice vector in the undeformed configuration and $\boldsymbol{r}$ is the corresponding lattice vector in the deformed configuration. $\boldsymbol{F}$ represents the local deformation gradient. $\boldsymbol{x}$ and $\boldsymbol{X}$ denote the positions of the atoms in undeformed and deformed configuration.

The equilibrium deformation is identified through the energy minimization process of π, as

$$\delta\pi = \sum_{i=1}^{n} (\frac{\partial E}{\partial \boldsymbol{u}_i} - \bar{\boldsymbol{f}}_i) \cdot \delta \boldsymbol{u}_i = 0 \ . \tag{4}$$

According to the QC method, n_r atoms are selected as representative atoms from the atomistic structure. The displacements and current positions of other atoms are approximated by functions of the displacements and positions of the representative atoms. Consequently, the Eq. (4) can be rewritten as

$$\delta\pi^h = \sum_{i=1}^{n_r} (\frac{\partial E}{\partial \boldsymbol{u}_i} - \bar{\boldsymbol{f}}_i) \cdot \delta \boldsymbol{u}_i = 0 \ , \tag{5}$$

where π^h is the approximate total energy. i denotes here the indexes of representative atoms. The Eq. (5) is equivalent to a closed system of $3 \cdot n_r$ equations with $3 \cdot n_r$ variables. $\boldsymbol{u}_i$ can be calculated through solving this system of equations with Dirichlet boundary conditions.

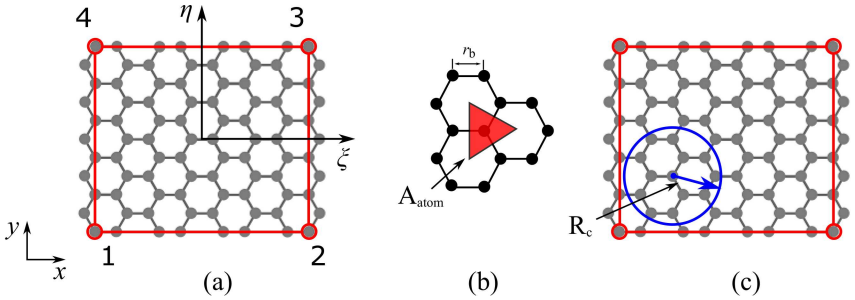

Figure 1. Schematic diagram of: (a) A 4-node quadrilateral plate/shell element (red) with underlying atomistic structure, (b) representative cell corresponding to an atom, (c) representative cell with radius R_c.

With regard to the Euler–Lagrange equation [7], the definition of first Piola-Kirchhoff stress $\boldsymbol{P}$ and Eq. (2), $\frac{\partial E}{\partial \boldsymbol{u}}$ can be transformed as following

$$\frac{\partial E}{\partial \boldsymbol{u}} = \frac{\partial E}{\partial \boldsymbol{x}} = \frac{\partial E}{\partial \boldsymbol{F}} \cdot \nabla_0 = \int_{\Omega_0} \frac{\partial W}{\partial \boldsymbol{F}} \cdot \nabla_0 \, \mathrm{d}A_0 = \int_{\Omega_0} \boldsymbol{P} \cdot \nabla_0 \, \mathrm{d}A_0 \ . \tag{6}$$

∇_0 denotes the gradient operator in undeformed configuration. The Eq. (5) is consequently rewritten as

$$\sum_{i=1}^{n_r}(\int_{\Omega_0} \boldsymbol{P}_i \cdot \nabla_0 \, \mathrm{d}A_0 - \bar{\boldsymbol{f}}_i) \cdot \delta \boldsymbol{u}_i = 0 \ , \tag{7}$$

which represents the equilibrium equations for the graphene in the situation of in-plane deformation based on QC method here.

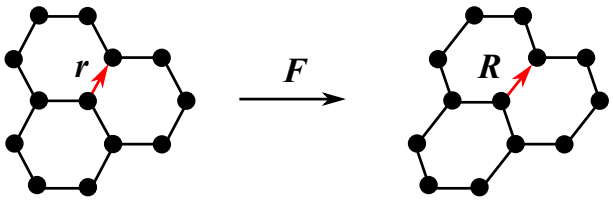

Figure 2. Schematic illustration of the original Cauchy-Born rule

Graphene is a crystalline film with the thickness of one atom. In order to consider also out-of-plane deformations of graphene, the curvature effects have to be taken into account. Therefore, a higher order Cauchy-Born rule

$$\boldsymbol{r} = \boldsymbol{F} \cdot \boldsymbol{R} + \frac{1}{2}\boldsymbol{G} : \boldsymbol{R} \otimes \boldsymbol{R} \quad \text{with} \quad \boldsymbol{G} = \nabla_0 \boldsymbol{F} \tag{8}$$

is applied [11]. The tensor $\boldsymbol{G}$ is the second-order deformation gradient. With Eq. (8) the corresponding equilibrium equations are given by

$$\sum_{i=1}^{n_r}(\int_{\Omega_0} \boldsymbol{P}_i \cdot \nabla_0 + \boldsymbol{Q}_i : \nabla_0 \nabla_0 \, \mathrm{d}A_0 - \bar{\boldsymbol{f}}_i) \cdot \delta \boldsymbol{u}_i = 0 \quad \text{with} \quad \boldsymbol{Q}_i := \frac{\partial W}{\partial \boldsymbol{G}_i} \ . \tag{9}$$

2 Finite element (FE) formulation

In the FE approximation, a 4-node finite element is formulated (see Fig. 1 (a)). The mapping from the parameter space into the physical space and the approximation of displacement are written in the usual way, namely

$$\boldsymbol{x}^h = \sum_{I=1}^{4} N_I(\xi, \eta)\boldsymbol{x}_I \ , \quad \boldsymbol{u}^h = \sum_{I=1}^{4} N_I(\xi, \eta)\boldsymbol{u}_I \ , \tag{10}$$

where $I = 1, \cdots, 4$ are the nodes in an element and $\boldsymbol{u}_I = [u_I, v_I, w_I]^T$ are the nodal DOFs. The undeformed configuration Ω_0 is partitioned into finite elements Ω_0^e with $e = 1, \cdots, n_e$, where n_e is the number of elements. Consequently, the total internal energy in Eq. (2) can be rewritten with regard to Gaussian quadrature rule as

$$E = \sum_{e=1}^{n_e} \int_{\Omega_0^e} W^e(\boldsymbol{x}) \, \mathrm{d}A_0 \approx \sum_{e=1}^{n_e} \sum_{q=1}^{n_q} \omega_q^e W^e(\boldsymbol{x}(\xi_q, \eta_q)) \ , \tag{11}$$

where ω_q^e and (ξ_q, η_q) are the quadrature weights and points for element e.

The system of equilibrium equations (Eq. (7) or (9)) is solved by applying the Newton-Raphson method. For the in-plane deformation, the global residual vector $\boldsymbol{R}_I$ and stiffness matrix $\boldsymbol{K}_{IJ}$ follow as

$$\boldsymbol{R}_I = \frac{\partial \pi^h}{\partial \boldsymbol{u}_I} - \bar{\boldsymbol{f}}_I = \sum_{e=1}^{n_e} \int_{\Omega_0^e} \boldsymbol{P}^e \cdot \nabla_0 N_I \, \mathrm{d}A_0 - \bar{\boldsymbol{f}}_I \ , \tag{12}$$

$$\boldsymbol{K}_{IJ} = \frac{\partial^2 \pi^h}{\partial \boldsymbol{u}_I \partial \boldsymbol{u}_J} = \sum_{e=1}^{n_e} \int_{\Omega_0^e} \boldsymbol{C}^e : (\nabla_0 N_I \otimes \nabla_0 N_J) \, \mathrm{d}A_0 \quad \text{with} \quad \boldsymbol{C}^e = \frac{\partial^2 W^e}{\partial \boldsymbol{F}^e \partial \boldsymbol{F}^e} \ , \tag{13}$$

where I and J are node indexes. For the out-of-plane deformation, the corresponding global residual vector and stiffness matrix are

$$\boldsymbol{R}_I = \frac{\partial \pi^h}{\partial \boldsymbol{u}_I} - \bar{\boldsymbol{f}}_I = \sum_{e=1}^{n_e} \int_{\Omega_0^e} \boldsymbol{P}^e \cdot \nabla_0 N_I + \boldsymbol{Q}^e : \nabla_0(\nabla_0 N_I)\, \mathrm{d}A_0 - \bar{\boldsymbol{f}}_I \ , \tag{14}$$

$$\begin{aligned} \boldsymbol{K}_{IJ} = \frac{\partial^2 \pi^h}{\partial \boldsymbol{u}_I \partial \boldsymbol{u}_J} = \sum_{e=1}^{n_e} \int_{\Omega_0^e} & \boldsymbol{C}_1^e : (\nabla_0 N_I \otimes \nabla_0 N_J) + \boldsymbol{C}_2^e \vdots (\nabla_0 N_I \otimes \nabla_0(\nabla_0 N_J)) \\ & + \boldsymbol{C}_3^e \vdots (\nabla_0(\nabla_0 N_I) \otimes \nabla_0 N_J) + \nabla_0(\nabla_0 N_I) : \boldsymbol{C}_4^e : \nabla_0(\nabla_0 N_J)\, \mathrm{d}A_0 \end{aligned} \tag{15}$$

$$\text{with} \quad \boldsymbol{C}_1^e = \frac{\partial^2 W^e}{\partial \boldsymbol{F}^e \partial \boldsymbol{F}^e}, \ \boldsymbol{C}_2^e = \frac{\partial^2 W^e}{\partial \boldsymbol{F}^e \partial \boldsymbol{G}^e}, \ \boldsymbol{C}_3^e = \frac{\partial^2 W^e}{\partial \boldsymbol{G}^e \partial \boldsymbol{F}^e}, \ \boldsymbol{C}_4^e = \frac{\partial^2 W^e}{\partial \boldsymbol{G}^e \partial \boldsymbol{G}^e} \ .$$

Conclusions

In this paper, a 4-node quadrilateral element with a Cauchy-Born rule based constitutive relation is presented and applied in context of the QC method for studying the mechanical properties of graphene. Compared with full atomistic simulation, this model has much less DOFs. Its constitutive relation is derived from interatomic potentials describing the energy and the interactions within an atomistic system. Therefore, it is more suitable for the scenarios of large deformations than other models based on linear elastic hypothesis. But this model is found on the precondition that the underlying atomistic structure is subjected to homogeneous deformations, i.e., non-homogeneous deformations can not be modelled. So this model should be combined with full atomistic simulation for determination of the mechanical behaviors of technical relevant large graphene nanostructures.

References

[1] M. Arroyo and T. Belytschko. Finite crystal elasticity of carbon nanotubes based on the exponential Cauchy-Born rule. *Phys. Rev. B* 69 (2004), p. 115415.

[2] T. Belytschko, S. P. Xiao, G. C. Schatz, and R. S. Ruoff. Atomistic simulations of nanotube fracture. *Phys. Rev. B* 65 (23 2002), p. 235430.

[3] Donald W. Brenner. Empirical potential for hydrocarbons for use in simulating the chemical vapor deposition of diamond films. *Phys. Rev. B* 42 (15 1990), pp. 9458–9471.

[4] J.L. Ericksen. On the Cauchy—Born Rule. *Mathematics and Mechanics of Solids* 13.3-4 (2008), pp. 199–220.

[5] C. Findeisen and J. Wackerfuß. A general approximation of the exponential Cauchy–Born hypothesis to model arbitrarily shaped shell-like nanostructures within continuum mechanics. *International Journal for Numerical Methods in Engineering* 105.10 (2016), pp. 747–780.

[6] S. Govindjee and J. L. Sackman. On the use of continuum mechanics to estimate the properties of nanotubes. *Solid State Communications* 110.4 (1999), pp. 227 –230.

[7] H. Hardy. Euler-Lagrange Elasticity: Differential Equations for Elasticity without Stress or Strain. *Journal of Applied Mathematics and Physics* 1 (2013), pp. 26–30.

[8] Jian Ping Lu. Elastic Properties of Carbon Nanotubes and Nanoropes. *Phys. Rev. Lett.* 79 (1997), pp. 1297–1300.

[9] Stephen L. Mayo, Barry D. Olafson, and William A. Goddard. DREIDING: a generic force field for molecular simulations. *The Journal of Physical Chemistry* 94.26 (1990), pp. 8897–8909.

[10] K. S. Novoselov, A. K. Geim, S. V. Morozov, D. Jiang, Y. Zhang, S. V. Dubonos, I. V. Grigorieva, and A. A. Firsov. Electric Field Effect in Atomically Thin Carbon Films. *Science* 306.5696 (2004), pp. 666–669.

[11] R. Sunyk and P. Steinmann. On higher gradients in continuum-atomistic modelling. *International Journal of Solids and Structures* 40.24 (2003), pp. 6877 –6896. ISSN: 0020-7683.

[12] E. B. Tadmor, M. Ortiz, and R. Phillips. Quasicontinuum analysis of defects in solids. *Philosophical Magazine A* 73.6 (1996), pp. 1529–1563.

**Proceedings of the 8th GACM Colloquium on Computational Mechanics
for Young Scientists from Academia and Industry
August 28–30, 2019 in Kassel, Germany**

Shear Deformations in a Multiscale Shell Formulation

Jan Zoller * [1] and Friedrich Gruttmann[1]

[1] Technische Universität Darmstadt, Fachgebiet Festkörpermechanik, Franziska-Braun-Straße 7, 64287 Darmstadt

Abstract. In this work a two-scale shell model is introduced based on the algorithm in [1], which carries out the concept of the FE^2-method. The representative volume element (RVE) is discretised with solid elements. The application of global strains to the RVE via displacement boundary conditions leads to an incorrect, and with increasing in plane size of the RVE even vanishing, shear stiffness. The reason is that the RVE reacts to shear deformations not only with shear stresses but also with bending stresses. Therefore, the theory in [2] for beams is transferred to the shell problem. In order to eliminate that resulting fallacious bending moment a constraint on the normal stress distribution is implemented. The use of periodic boundary conditions allows warping of the cross section. Thus boundary effects can be reduced or even avoided in the RVE. However, an introduced shear deformation together with permissible periodic displacements leads to a rigid body movement and, therefore, no shear stresses and stiffness are obtained. Hence, it is necessary to introduce a further constraint. To consider inhomogeneities of the material, the constraint is established with respect to the shape of the normal stress over the cross section. Both constraints are incorporated using the method of Lagrange multipliers.

Introduction

Shell elements using Reissner-Mindlin kinematics are commonly used for examining large shell structures, because they describe the kinematic behavior quite simply, and thus with few degrees of freedom. However, this assumption is not sufficient to adequately describe the deformation over the thickness direction for complex material composites.

By using the multiscale method, it is still possible to use these simple shell elements on the classical global scale. A detailed behavior of an arbitrary material distribution and structure is taken into account on an additional local scale by investigating a unit cell with a representative material composition, a so-called representative volume element (RVE). Within this RVE local effects can also be considered. This enables the calculation of large and complex structures. Further, by discretizing the unit cell with solid elements, it is possible to use existing algorithms for solid elements for the calculation in which the advantages of shell elements should be utilized. The two scales are coupled by deforming the RVE according to the shell strain $\boldsymbol{\epsilon}$ from the associated global Gauss point p and from this, the shell stress resultants $\boldsymbol{\sigma}$ and linearized stress resultants $\mathbf{D}$, with the shear stiffness record $\mathbf{D}^\gamma$, are calculated.

$$\boldsymbol{\epsilon} = \begin{bmatrix} \varepsilon_{11} & \varepsilon_{22} & \varepsilon_{12} & \kappa_{11} & \kappa_{22} & \kappa_{12} & \gamma_{13} & \gamma_{23} \end{bmatrix}^T \tag{1}$$

$$\boldsymbol{\sigma} = \begin{bmatrix} n_{11} & n_{22} & n_{12} & m_{11} & m_{22} & m_{12} & q_{13} & q_{23} \end{bmatrix}^T \tag{2}$$

$$\mathbf{D} = \begin{bmatrix} \mathbf{D}^{\varepsilon} & \mathbf{D}^{\varepsilon\kappa} & \mathbf{0} \\ \mathbf{D}^{\kappa\varepsilon} & \mathbf{D}^{\kappa} & \mathbf{0} \\ \mathbf{0} & \mathbf{0} & \mathbf{D}^{\gamma} \end{bmatrix} \tag{3}$$

1 Homogenization scheme

An algorithm for a two-scale shell formulation can already be found in [1], which is the basis for the presented model. The local boundary value problem has to be subdivided into constrained ($\mathbf{v}_b$) and unconstrained ($\mathbf{v}_a$) degrees of freedom

$$\frac{1}{A_{RVE}} \delta \mathbf{V}_p^T \left(\mathbf{K} \Delta \mathbf{V} + \mathbf{G} \right)_p = \frac{1}{A_{RVE}} \sum_{e=1}^{N} \begin{bmatrix} \delta \mathbf{v}_a \\ \delta \mathbf{v}_b \end{bmatrix}_e \cdot \left(\begin{bmatrix} \mathbf{g}_a \\ \mathbf{g}_b \end{bmatrix}_e + \begin{bmatrix} \mathbf{k}_{aa} & \mathbf{k}_{ab} \\ \mathbf{k}_{ba} & \mathbf{k}_{bb} \end{bmatrix}_e \begin{bmatrix} \Delta \mathbf{v}_a \\ \Delta \mathbf{v}_b \end{bmatrix}_e \right) = 0 \,. \tag{4}$$

*Corresponding author: zoller@mechanik.tu-darmstadt.de

For displacement boundary conditions (DBC) the applied displacements $\bar{\mathbf{u}}_I$ of a constrained node I are calculated by means of the linear map $\mathbf{A}_I$ from the global strains $\boldsymbol{\epsilon}$

$$\bar{\mathbf{u}}_I = \mathbf{A}_I \boldsymbol{\epsilon} \,, \qquad \delta\bar{\mathbf{u}}_I = \mathbf{A}_I \delta\boldsymbol{\epsilon} \,, \qquad \Delta\bar{\mathbf{u}}_I = \mathbf{A}_I \Delta\boldsymbol{\epsilon} \,. \tag{5}$$

These equations are also applied for periodic boundary conditions (PBC), which here are newly introduced for a two-scale shell formulation. This then leads to the vector $\mathbf{v}_b$ including all degrees of freedom which are involved in the PBC. In preparation for a later constraint, the shear distortion is brought into action by applying a deformation in thickness direction for PBC. This requires the consideration of the 3rd row of $\mathbf{A}_I$ and thus $\mathbf{A}_I$ differs for DBC and PBC

DBC:

$$\mathbf{A}_I = \begin{bmatrix} x & 0 & \frac{1}{2}y & xz & 0 & \frac{1}{2}yz & z & 0 \\ 0 & y & \frac{1}{2}x & 0 & yz & \frac{1}{2}xz & 0 & z \end{bmatrix},$$

PBC:

$$\mathbf{A}_I = \begin{bmatrix} x & 0 & \frac{1}{2}y & xz & 0 & \frac{1}{2}yz & 0 & 0 \\ 0 & y & \frac{1}{2}x & 0 & yz & \frac{1}{2}xz & 0 & 0 \\ 0 & 0 & 0 & -\frac{1}{2}x^2 & -\frac{1}{2}y^2 & -\frac{1}{2}xy & z & z \end{bmatrix}. \tag{6}$$

For the boundary value problem, all lines from $\mathbf{A}_I$ belonging to the constrained degrees of freedom $\mathbf{v}_b$ are combined in the matrix $\mathbf{A}_e$. The Matrix $\mathbf{a}_e$ is an incidence matrix. By making use of a static condensation process, the global shell stress resultants $\boldsymbol{\sigma}$ and the global linearized stress resultants $\mathbf{D}$ are obtained from the local boundary value problem

$$\boldsymbol{\sigma} = \frac{1}{A_{RVE}} \left(\mathbf{G}_b - \mathbf{L}^T \mathbf{K}^{-1} \mathbf{G}_a \right), \qquad \mathbf{D} = \frac{1}{A_{RVE}} \left(\mathbf{M} - \mathbf{L}^T \mathbf{K}^{-1} \mathbf{L} \right) \qquad \text{with} \tag{7}$$

$$\mathbf{K} = \bigcup_{e=1}^{N} \mathbf{a}_e^T \mathbf{k}_{aa} \mathbf{a}_e, \quad \mathbf{L} = \sum_{e=1}^{N} \mathbf{a}_e^T \mathbf{k}_{ab} \mathbf{A}_e, \quad \mathbf{M} = \sum_{e=1}^{N} \mathbf{A}_e^T \mathbf{k}_{bb} \mathbf{A}_e, \quad \mathbf{G}_a = \sum_{e=1}^{N} \mathbf{a}_e^T \mathbf{g}_a, \quad \mathbf{G}_b = \sum_{e=1}^{N} \mathbf{A}_e^T \mathbf{g}_b. \tag{8}$$

2 Eliminating the fallacious bending moments

The procedure in [1] leads to correct membrane and bending stiffnesses. However, the shear stiffness decreases with increasing RVE in-plane sizes, as can be seen in Fig. 1 (DBC) for the investigation of a homogeneous RVE. This effect corresponds to the behavior described in [3] for a two-scale beam formulation. The decrease of the shear stiffness results from the fact that the RVE reacts to the initialized shear deformation with both shear and bending stresses, thus a wave-like deformation figure is established, as illustrated in Fig. 2. This can be explained by a simplified beam model, for which the two in-plane dimensions are examined separately, $\alpha \in \{x, y\}$, Fig. 3.

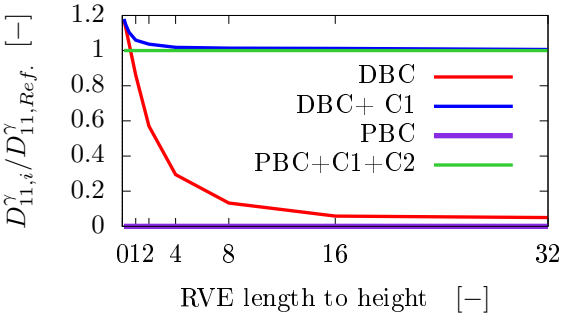

Figure 1. Relative shear stiffness versus in-plane size of a homogeneous RVE.

To prevent this, the fallacious linear moment needs to be eliminated. For this purpose, the bending stresses which conform to the linear moment are set to zero. The shape functions for the Lagrange multipliers $\lambda_{\alpha i}$ and $\mu_{\alpha i}$ correspond to the moment curve in Fig. 3. The constraint has to be implemented considering all normal stresses σ_i with $i \in \{x, y, z\}$, otherwise, because of the constitutive matrix, the stresses are shifted to another direction and the wave-like deformation remains

$$\int_{V_{RVE}} \sigma_i \cdot (z\lambda_{\alpha i} + \mu_{\alpha i}) \, \mathrm{d}V = 0 \qquad \text{with} \qquad i \in \{x, y, z\}, \, \alpha \in \{x, y\}. \tag{9}$$

The influence of boundary effects disappears with increasing RVE dimensions, Fig. 1 (DBC+C1). This constraint is also required for the use of PBC. The simplified beam element and thus also the shape functions have to be adapted, Fig. 3. As a result of these constraints, there are 12 additional degrees of freedom for the RVE.

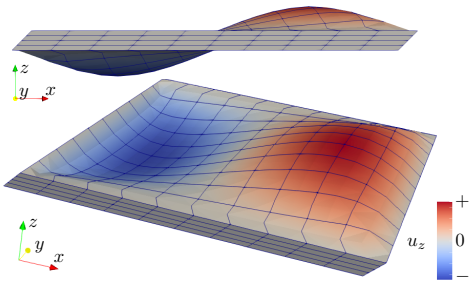

Figure 2. Wave-like deformation figure for shear loading $\gamma_{xz} = 0.1$ (scale factor: 10).

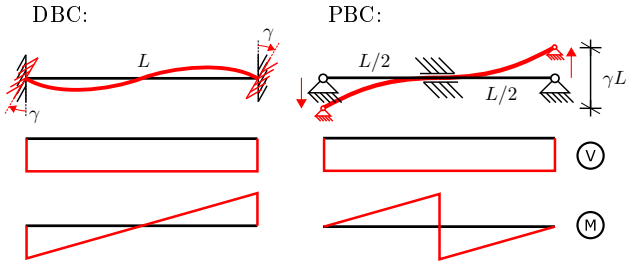

Figure 3. Simplified beam models and corresponding shear deformations, shear force (V) and bending moment (M).

3 Using periodic boundary conditions

The use of PBC allows warping of the cross section, which reduces or even avoids boundary effects in the RVE. In a two-scale shell model, the introduced displacement for a shear deformation along with permissible periodic displacements result in rigid body movements. Therefore, shear stiffness components and associated stresses are not obtained, Fig. 1 (PBC).

Due to the previously established modification of the matrix $\mathbf{A}_I$, there is no rotation of the cross section in the RVE center. The rigid body movement can be prevented by another constraint (C2 in diagrams) for the in-plane normal stress. This assumes geometrical and physical linearity. The constraint is introduced via an additional row of elements with nodes in the center plane of the RVE, Fig. 4. The constraint affects the system only via these nodes. Therefore, only for these the stresses $\bar{\sigma}_\alpha$ are determined by means of a modified kinematics, which uses a common rotation respectively translation of that plane [4]. These elements do not introduce any further stiffness to the system

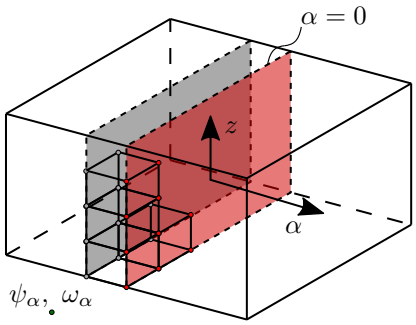

Figure 4. Additional elements to apply constraint C2.

$$\int_{\bar{V}_\alpha} (\sigma_\alpha - \bar{\sigma}_\alpha) \cdot [z\psi_\alpha + \omega_\alpha] \, \mathrm{d}V = 0 \qquad \text{with} \qquad \alpha \in \{x, y\}. \tag{10}$$

This constraint has to be established for both in-plane directions. The constraint only needs to be fulfilled on average. This still allows warping of the cross section and, thus, the algorithm obtains not only correct membrane and bending stiffnesses but also correct shear stiffnesses, Fig. 1 (PBC+C1+C2). The constraints C2 leads to four additional degrees of freedom.

4 Numerical examples

Material		Geometry
$E_1 = 2222$ N/mm^2	$\nu_1 = 0.1$	$h_1 = 1$ cm
$E_2 = 100$ N/mm^2	$\nu_2 = 0.3$	$h_2 = 3$ cm
$E_3 = 2222$ N/mm^2	$\nu_3 = 0.1$	$h_3 = 1$ cm

Figure 5. Material and geometrical properties for the three-layered RVE.

Material		Geometry
$E_1 = 3300$ N/mm^2	$\nu_1 = 0.2$	$h_1 = 2$ cm
$E_2 = 1100$ N/mm^2	$\nu_2 = 0.3$	$h_2 = 12$ cm
$E_3 = 3300$ N/mm^2	$\nu_3 = 0.2$	$h_3 = 2$ cm

Figure 6. Material and geometrical properties for the cylindrical panel.

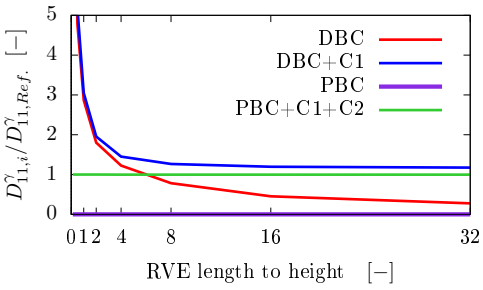

Figure 7. Relative shear stiffness of a three-layered RVE.

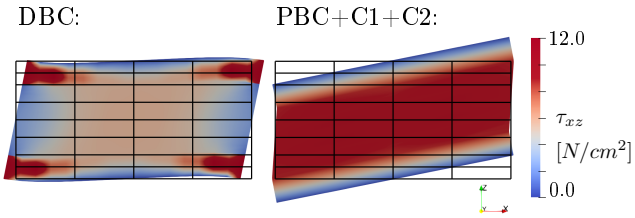

Figure 8. Shear stress for $\gamma_{xz} = 0.1$ (scale factor: 2).

The first example deals with a three-layered RVE. The two outer, stiffer layers enclose a soft core, Fig. 5. An investigation of the shear stiffness depending on the in-plane sizes is shown in Fig. 7. It shows again, that the shear stiffness for DBC decreases from a too stiff behavior to zero. Using constraint C1, the shear stiffness converges to the correct solution, although very slowly. Only the newly developed approach leads to the correct shear stiffness $\mathbf{D}^{\gamma}_{11} = 209.6$ N/cm immediately.
The influence of the boundary conditions is also evident when considering the shear stress distribution, as shown in Fig. 8. The distributions are totally different which can be of crucial importance considering local effects.

Within the second example, a cylindrical panel, Fig. 9, with a three-layered structure, Fig. 5, is subjected to a concentrated load using the arc length method, Fig. 10 . The reference solutions are computed using the model in [2].

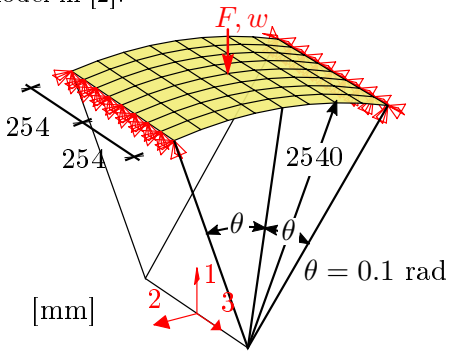

Figure 9. Cylindrical panel subjected to a concentrated load.

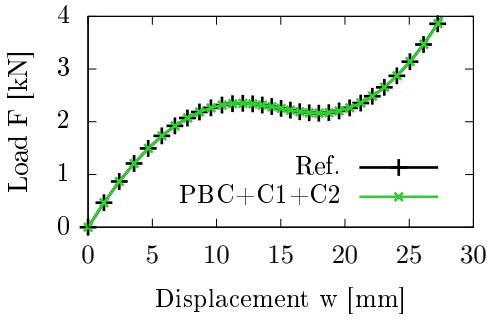

Figure 10. Load-displacement-diagram for the cylindrical panel.

Conclusion

In this contribution a coupled two-scale shell model with an application of the FE^2-method is presented. The introduced additional constraints prevent a length dependency of the shear results for DBC and enable the use of PBC. In addition to the correct membrane and bending results, this allows a correct calculation of the shear results, as shown in the examples.

References

[1] F. Gruttmann and W. Wagner. A coupled two-scale shell model with applications to layered structures. *International Journal for Numerical Methods in Engineering* 94 (2013), pp. 1233–1254.

[2] F. Gruttmann, G. Knust, and W. Wagner. Theory and numerics of layered shells with variationally embedded interlaminar stresses. *Computer Methods in Applied Mechanics and Engineering* 326 (2017), pp. 713–738.

[3] S. C. Klarmann. Geometrisch und physikalisch nichtlineare Mehrskalenmodellierung räumlicher Stabtragwerke. In: *Forschungsberichte des Instituts für Mechanik der Technischen Universität Darmstadt. Bd. 44*. Darmstadt: Technische Universität Darmstadt, 2018, pp. 1–163.

[4] S. C. Klarmann and F. Gruttmann. A homogenization approach for beam-like structures with arbitrarily shaped and deformable cross-sections. *Proceedings of the 7th GACM Colloquium on Computational Mechanics* (2017), pp. 476–479.

**Proceedings of the 8th GACM Colloquium on Computational Mechanics
for Young Scientists from Academia and Industry
August 28–30, 2019 in Kassel, Germany**

An efficient matrix-free finite element solver for the Cahn–Hilliard equation

G.F. Castelli * [1] and W. Dörfler[1]

[1]Karlsruhe Institute of Technology (KIT), Institute of Applied and Numerical Mathematics 2, Karlsruhe, Germany

Abstract.

We focus on the efficient numerical solution of the mixed formulation of the Cahn–Hilliard equation. The main challenges arise from the handling of an almost sharp moving phase boundary and processes on different time scales. We employ a higher order finite element method together with an adaptive time integrator. In particular, we use a fully parallelizable highly efficient matrix-free framework, which avoids the necessity of storing matrices.

1 Introduction

In the last few years the phase-field method has become a popular approach for modeling various types of problems with a moving phase boundary. One of the main advantages is that a sharp interface gets replaced by a smooth transition zone and thus front-tracking methods become unnecessary [5]. To name just a few examples, the phase-field method was already used to model microstructure evolution, phase separation, dendritic growth, growth of cancerous tumors and fracture, see [5] and the references cited therein.

We consider the phenomenon of phase separation in electrode particles of lithium ion batteries during the (dis-)charge process, because due to changes in the host material, for example $LiFePO_4$, a separation into lithium rich and lithium poor phases is possible. This behavior can be described with a phase-field model resulting in the Cahn–Hilliard equation, see [6, 9]. In a previous work we also considered phase transition in electrode materials of lithium ion batteries with a sharp interface model and developed a finite element solver for the coupled electrolyte-electrode system [2].

2 Model Equations

We briefly discuss the model equations introduced in [6], where the temporal evolution of the lithium concentration including the phase separation and diffusion with two coexisting phases was described with the Cahn–Hilliard equation.

Let $\Omega \subset \mathbb{R}^3$ be the domain of one electrode particle. In terms of the normalized lithium concentration $c\colon \mathbb{R}_{\geq 0} \times \overline{\Omega} \to [0,1]$ the conservation of mass yields:

$$\partial_t c - \nabla \cdot \big(M(c) \nabla \mu\big) = 0 \qquad \text{in } \mathbb{R}_{>0} \times \Omega,$$

where $M(c) = D_0 c(1-c)$ is the concentration-dependent mobility with the diffusion coefficient $D_0 > 0$ and $\mu = \delta\Psi/\delta c$ is the chemical potential, which is defined as the variational derivative of the system's free energy:

$$\Psi(c, \nabla c) = \int_\Omega \psi^{\mathrm{ch}}(c) + \psi^{\mathrm{gd}}(\nabla c)\, \mathrm{d}x.$$

*Corresponding author: fabian.castelli@kit.edu

Here the homogeneous chemical free energy density is represented by a potential of doublewell-type

$$\psi^{\mathrm{ch}}(c) = \alpha_1 c + \frac{1}{2}\alpha_2 c^2 + c\log(c) + (1-c)\log(1-c),$$

and depends on the two parameters α_1 and α_2, which control the shape of the doublewell. The gradient energy density, responsible in the end for the fourth-order derivative, is given by

$$\psi^{\mathrm{gd}}(\nabla c) = \frac{1}{2}\kappa|\nabla c|^2,$$

where the interfacial energy coefficient $\kappa > 0$ controls the width of the phase boundary.

The problem reads in its mixed formulation: Find the concentration and the chemical potential satisfying:

$$\begin{aligned}
\partial_t c &= \nabla\cdot\big(M(c)\nabla\mu\big) && \text{in } \mathbb{R}_{>0}\times\Omega,\\
\mu &= \partial_c\psi^{\mathrm{ch}}(c) - \kappa\Delta c && \text{in } \mathbb{R}_{>0}\times\Omega,\\
M(c)\nabla\mu\cdot\mathbf{n} &= \mu_{\mathrm{ext}} && \text{on } \mathbb{R}_{>0}\times\partial\Omega,\\
\nabla c\cdot\mathbf{n} &= 0 && \text{on } \mathbb{R}_{>0}\times\partial\Omega,\\
c(0,\,\cdot\,) &= c_0 && \text{in } \overline{\Omega}.
\end{aligned}$$

Note, that the lithium insertion, or extraction, is modeled by an inhomogeneous Neumann-type boundary condition. At the initial state we assume a given concentration profile $c_0\colon \overline{\Omega}\to[0,1]$, consistent with the boundary conditions.

3 Numerical Method

In the following we restrict ourself to the classical setting of the Cahn–Hilliard equation, i. e., assuming homogeneous Neumann-type boundary conditions:

$$M(c)\nabla\mu\cdot\mathbf{n} = \nabla c\cdot\mathbf{n} = 0 \qquad \text{on } \mathbb{R}_{>0}\times\partial\Omega,$$

and describe the developed finite element solver for this case. Among others, difficulties for the numerical solution are the higher order differential operator as well as the almost sharp moving phase boundary and the different time scales.

In space, we use a Lagrangian finite element method of higher order for both, the concentration and the chemical potential. Hence for curved boundaries of the triangulated domain we also have to use a correspondingly higher order boundary approximation to get the full convergence order. One advantage of the proposed mixed formulation is that we avoid the fourth-order differential operator Δ^2 and hence we can circumvent the necessity of C^1-conforming methods, see [9].

For the Cahn–Hilliard equation using an appropriate time integration scheme is very important, since several processes take place on different time scales. For example the separation of the phases and the evolution of the phase boundary happen quasi-instantaneous, while the clustering and coarsening due to the minimization of the surface free energy can take a long time. A well known time stepping scheme for the Cahn–Hilliard equation was derived by Eyre [4] and is based on a splitting of the homogeneous chemical free energy density into a convex and a non-convex part. This scheme is first-order accurate and unconditionally stable. However, we observed, that we need a very small time step to capture the correct evolution of the phase boundary. So instead we use the adaptive version of the second-order accurate unconditionally stable time integrator proposed by [5].

The fully discrete system for one time step with the implicit Euler scheme reads then as follows: Given the concentration c^k and the chemical potential μ^k at the previous time step t_k, find the concentration c^{k+1} and the chemical potential μ^{k+1} for the next time step $t_{k+1} = t_k + \tau$ such that the following weak formulation is fulfilled:

$$\begin{aligned}
\Big(v_h, c_h^{k+1} - c_h^k\Big) + \tau\Big(\nabla v_h, M\big(c_h^{k+1}\big)\nabla\mu_h^{k+1}\Big) &= 0 && \text{for all } v_h\in V_h,\\
\Big(w_h, \mu_h^{k+1} - \partial_c\psi^{\mathrm{ch}}\big(c_h^{k+1}\big)\Big) - \kappa\Big(\nabla w_h, \nabla c_h^{k+1}\Big) &= 0 && \text{for all } w_h\in V_h.
\end{aligned}$$

To this nonlinear problem we apply the Newton method. For small problems we can use direct solvers such as the LU-decomposition for the computation of the Newton updates. However, a full resolution of the three-dimensional spatial domain, respecting the almost sharp phase boundary, generates a huge amount of degrees of freedom.

3.1 Matrix-free Algorithms

For the numerical linear algebra we use the highly efficient matrix-free implementation, provided by [7], within of the open-source finite element library *deal.II* [1]. To briefly explain the idea of matrix-free algorithms we consider for a moment a generic time-dependent partial differential equation. If we use an implicit time stepping scheme, we will end up with the generic problem to solve a linear system $A\,x = b$ in almost every case. If we think of iterative methods such as the CG or the GMRES method, we know that these are based on Krylov subspaces and need matrix-vector multiplications only [8]. Now the key idea is to implement a function evaluating the matrix-vector product without storing the matrix itself. Although this makes the recomputation of the matrix entries unavoidable, every time a matrix-vector product is evaluated, this is much faster on todays modern processor architectures, since the limiting factor for matrix-vector operations is mostly not the arithmetic throughput, but the memory bandwidth [7].

To show the performance of the matrix-free implementation we solved a nonlinear test problem:

$$\begin{aligned} -\Delta u &= 3\,\exp(u) && \text{in } \Omega = (0,1)^2, \\ u &= 0 && \text{on } \partial\Omega, \end{aligned}$$

which is in some sense representative for the solution of one time step of the Cahn–Hilliard equation. In Figure 1 we plotted the computational times against the number of cores for different problem sizes. As this figure shows, we get an optimal strong scaling behavior of the parallelization.

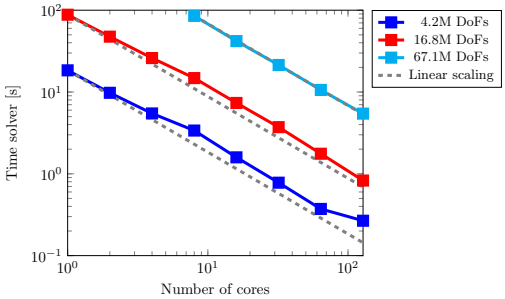

Figure 1. Strong scaling of the parallel computation.

However, since we do not have access to matrix entries, we can only use iterative Krylov subspace methods to solve the linear systems. Furthermore there is a high demand for good preconditioners, which are matrix-free implementable.

4 Numerical Results

To demonstrate the capabilities of our developed matrix-free finite element solver for the Cahn–Hilliard equation, we apply it to a test problem from the literature, Problem 4 of [3]. As domain we have $\Omega = (0,1)^2$ the two-dimensional unit square and let the final time of the simulation be $T = 10$. The homogeneous chemical free energy density is replaced by a quartic polynomial $\psi^{\mathrm{ch}}(c) = 1/4\,c^2(1-c)^2$ and the mobility by a constant $M = 0.25$. The interfacial energy coefficient is set to $\kappa = 10^{-4}$. As in Section 3 we use homogeneous Neumann-type boundary conditions and as initial condition a smooth perturbation of 0.5. We triangulate the domain with $16k$ uniform rectangles and use fourth-order Lagrangian finite elements, i. e., in total we distribute $526k$ degrees of freedom. With 16 cores of a parallel cluster we are able to solve this problem with 330 adaptive time steps in less the four hours. The initial and final state of the solution are depicted in Figure 2. The fast solution of the Cahn–Hilliard equation is also due to our new developed preconditioner, with which we need also for this large problem at maximum ~ 70 GMRES iterations and even much less as the phase separation dynamic relaxes.

5 Conclusion

Summing up, we discussed the equations modeling phase separation in electrode particles of lithium ion batteries during the (dis-)charge process. Further we presented a numerical method to solve the

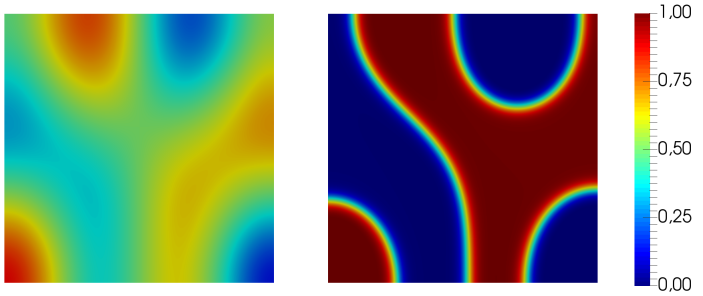

Figure 2. Concentration profile of the Cahn–Hilliard test problem at initial (left) and final (right) time.

Cahn–Hilliard equation and explained the idea of the used matrix-free framework. Finally we showed the parallel scaling behavior of the matrix-free implementation and solved a test problem for the Cahn–Hilliard equation.

With this efficient finite element solver we are now able to simulate lithium insertion into full three-dimensional electrode particles. In particular, we can now allow a tensor-valued mobility and thus investigate also anisotropic diffusion. Further we can allow general non-uniform insertion rates. In such a case, with anisotropic mobility and non-uniform insertion rate, the formation and the migration of the phase boundary through an electrode particle will be very interesting. Another advantage of our implementation is the geometry independence, this means we can also simulate arbitrary shaped particles.

To further reduce the computational time and increase the efficiency we want to incorporate spatial adaptivity based on residual-type a posteriori error estimators. In collaboration with colleagues from SiMET we currently include a new thermodynamic consistent nonlinear solid mechanics theory taking swelling and stress generation for large strains into account, however, this is part of a future work.

Acknowledgments

The authors thank M. Kamlah and T. Zhang for discussions about the model equations. G. F. Castelli acknowledges financial support by the German Research Foundation (DFG) through RTG 2218 SiMET – Simulation of mechano-electro-thermal processes in lithium-ion batteries, project number 281041241.

References

[1] W. Bangerth, R. Hartmann, and G. Kanschat. deal.II—a general-purpose object-oriented finite element library. *ACM Trans. Math. Software* 33.4 (2007), pp. 24/1–24/27.

[2] G. F. Castelli and W. Dörfler. The numerical study of a microscale model for lithium-ion batteries. *Comput. Math. Appl.* 77.6 (2019), pp. 1527–1540.

[3] M. Dehghan and V. Mohammadi. The numerical solution of Cahn–Hilliard (CH) equation in one, two and three-dimensions via globally radial basis functions (GRBFs) and RBFs-differential quadrature (RBFs-DQ) methods. *Eng. Anal. Bound. Elem.* 51 (2015), pp. 74–100.

[4] D. J. Eyre. Unconditionally gradient stable time marching the Cahn–Hilliard equation. *MRS Proceedings* 529 (1998), pp. 39–46.

[5] H. Gomez and T. J. R. Hughes. Provably unconditionally stable, second-order time-accurate, mixed variational methods for phase-field models. *J. Comput. Phys.* 230.13 (2011), pp. 5310–5327.

[6] M. Huttin and M. Kamlah. Phase-field modeling of stress generation in electrode particles of lithium ion batteries. *Appl. Phys. Lett.* 101.13 (2012), pp. 133902/1–133902/4.

[7] M. Kronbichler and K. Kormann. A generic interface for parallel cell-based finite element operator application. *Comput. & Fluids* 63 (2012), pp. 135–147.

[8] Y. Saad. *Iterative Methods for Sparse Linear Systems*. 2nd ed. SIAM, Philadelphia, PA, 2003.

[9] Y. Zhao, P. Stein, and B.-X. Xu. Isogeometric analysis of mechanically coupled Cahn–Hilliard phase segregation in hyperelastic electrodes of Li-ion batteries. *Comput. Methods Appl. Mech. Engrg.* 297 (2015), pp. 325–347.

**Proceedings of the 8th GACM Colloquium on Computational Mechanics
for Young Scientists from Academia and Industry
August 28–30, 2019 in Kassel, Germany**

Improving the numerical solution of the phase-field equation by the systematic integration of analytic properties of the phase-field profile function

Michael Fleck * [1], Felix Schleifer[1], Markus Holzinger[1] and Uwe Glatzel[1]

[1]Metals and Alloys, University of Bayreuth, Germany

Abstract. Different Allen-Cahn type phase-field models are investigated within a unified finite difference framework. We consider the stationary growth of arbitrarily oriented planar interfaces in 3D driven by a constant chemical potential. The different models are classified with respect to their individual ability to accurately reproduce the analytically exact growth behavior, with regard to the transformation velocity, the phase-field width as well as the interface energy density. We find superior behavior and accuracy for the models that have a computation-grid-dependent equilibrium potential providing translational invariance of the phase-field profile in the direction of growth, as recently suggested by A. Finel and co-workers [3]. Base on that, we propose a new phase-field model, which provides the translational invariance in the direction normal to the interface based on a local measure of the interface orientation. The new model shows the expected superior properties arbitrarily oriented planar interfaces also in the cases where the interface is not aligned with the principle directions of the numerical lattice.

Introduction

The phase-field method offers a very versatile way to setup models for the simulation of microstructure-evolution involving interfaces, that may undergo topological changes. The key point providing the versatility is the diffuse interface, where the phase-field variable varies smoothly, for instance, from zero to one about a specific length called the phase-field width. However, the rapid spatial variation of the phase-field solution naturally leads to difficulties in the numerical computation [1, 5].

Considering the stationary growth of a planar interface driven by a constant chemical potential, we quantitatively investigate the deviations of the numerical solution from the respective analytic expectations. Especially, when going over to sharper and sharper interfaces, we observe increasingly large deviations up to the extrem situation of a vanishing interface velocity that corresponds to the situation of grid pinning. Recently, A. Finel and co-workers proposed a new way to eliminate the related spurious grid-adhesion forces in 1D resulting from the spatial discretization on the numerical lattice [3].

The method of how a translationally invariant phase-field formulation in 1D is setup is briefly reviewed in section 1. Further, we quantitatively compare the growth behavior of a constantly driven planar interface using the new 1D model with respective results obtained from a conventional phase-field formulation. We find, that this new class of phase-field models provides superior properties and accuracy, even in the case of very sharp interfaces. In section 2 we discuss the stationary growth of planar interfaces with arbitrary orientation. We propose a new phase-field model of this class, which provides the translational invariance in the growth direction, based on the local measure of the interface orientation. Especially for the case of the very sharp interfaces, we also propose a new and more accurate measure of the interface position based on informations of the nonlinear phase-field profie, as discussed in section 3. Finally, in section 4, we discuss the special phase-field boundary conditions, where the interface is forced to take a specific wetting angle with the respective boundary. These boundary conditions are required for the realization of the configuration of a planar interface growing into arbitrary directions.

*Corresponding author: michael.fleck@uni-bayreuth.de ORCID iD: 0000-0002-2799-9075

1 Elimination of grid adhesion in 1D

In the simplest case, we may consider the transformation between just two phases, discriminated by a single phase-field. The starting point is a volume integral over an energy density, which locally depends on the phase-field value and gradient. The energy density is additively decomposed into a phase-field gradient contribution, an equilibrium potential contribution and a local non-equilibrium driving force contribution.

On a discrete numerical lattice the phase-field is represented by a finite array of values that are distributed on grid points within the computational lattice. We consider a planar interface in 3D with a hyperbolic tangent like profile of the following form

$$\phi_i = \frac{1}{2}\left(1 + \tanh\frac{2\,(i\Delta x - x_0)}{\xi}\right), \tag{1}$$

where i denotes the discrete locations of the grid points within the numeric lattice. The central analytic property of the hyperbolic tangent profile (1), can be easily derived form the addition theorem of the hyperbolic tangent function [3, 4]:

$$2\phi_{i\pm1} - 1 = \frac{(2\phi_i - 1) \pm a}{1 \pm (2\phi_i - 1)\, a}, \tag{2}$$

where the grid-coupling parameter a is defined as

$$a = \tanh\left(\frac{2\Delta x}{\xi}\right). \tag{3}$$

In 1D static interfaces, such as Eq. (1), have to satisfy the discrete equilibrium condition as given by

$$\frac{\xi^2}{\Delta x^2}\left(\phi_{i+1} - 2\phi_i + \phi_{i-1}\right) = \frac{\partial g(\phi_i)}{\partial \phi}. \tag{4}$$

The key point is to identify a double-well potential $g(\phi)$ such that, if $\phi_i = f(i\Delta x)$ is solution of Eq. (4), then $\phi_i = f(i\Delta x - x_0)$ is also a solution for *any real translation* x_0 [3]. Then, the phase-field profile will be obviously invariant under a translation providing an interface free of any spurious grid-adhesion. Interestingly, the analytic property Eq. (2) provides the following modification of the derivative of the equilibrium potential [3, 4]

$$\frac{\partial g(\phi)}{\partial \phi} = \frac{a^2\xi^2}{\Delta x^2}\frac{4\phi\,(1-\phi)\,(1-2\phi)}{1 - a^2\,(1-2\phi)^2}, \tag{5}$$

such that the equilibrium condition (4) is satisfied for arbitrary choices of the interface position x_0. Note, that in the continuum limit $\Delta x \to 0$, this potential converges to the original derivative of the quartic double well potential, $\partial g/\partial\phi = 16\phi\,(1-\phi)\,(1-2\phi)$, as $\lim_{\Delta x\to 0}\xi^2 a^2/\Delta x^2 = 4$.

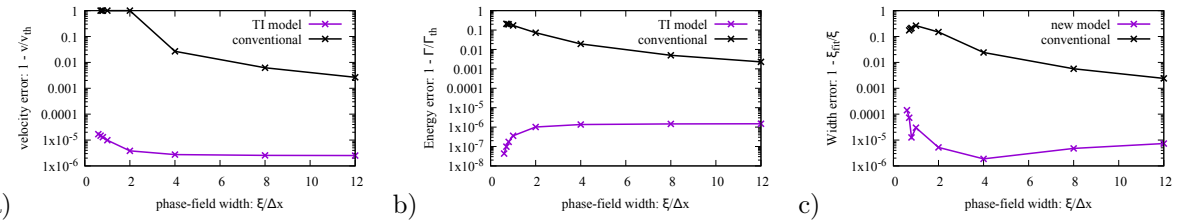

Figure 1. Comparison of the modeling behavior with and without translational-invariance during the simulation of stationary growth of the planar front in 1D.

Considering the stationary growth of the planar interface driven by a constant chemical potential, we show that the modified derivative of the equilibrium potential Eq. (5) indeed eliminates all spurious grid-adhesion forces on interfaces as represented by the profile (1). It turns out that the elimination of spurious grid-adhesion forces allows to chose the width of the diffusion interface region as small as $\xi/\Delta x = 0.6$, i.e. nearly half of the grid spacing. In Fig. 1, we compare the deviations of the resulting transformation velocity, the interface energy as well as the fitted phase-field width from the respective

analytic expectations for the conventional phase-field model with the result from the new model with translational invariance within a unique finite difference framework. It is quite surprising that, even for values of the phase-field width as small as $\xi/\Delta x = 0.6$ the error of the results from the translationally invariant model is still orders of magnitude lower than that of the conventional model for ten-times wider interfaces.

This method for the elimination of the grid-adhesion forces in the phase-field equation is related to earlier suggestions of Glasner and Weiser. Bother authors proposed the idea to improve the numerical performance of phase-field solvers via a nonlinear scaling of the phase-field equation by the profile function [5, 6]. Bother authors report about highly improved properties and accuracies of their solvers, after the nonlinear transformation using the nonlinear analytic profile function.

We point out that also for other profile-functions such as the section-wise defined sinus-profile such a modification of the equilibrium potential to diminish spurious grid-adhesion is feasible. Interestingly, we find that a respective derivation for the section-wise defined sinus profile does not provide a new function, but provides again the section-wise quadratic double obstacle potential, now with a computation-grid-dependent correction factor, as had been previously proposed by Eiken [2].

2 Arbitrarily oriented planar interfaces

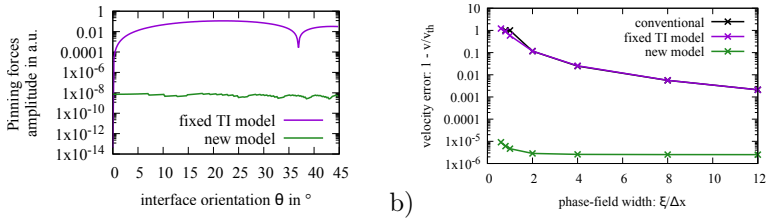

Figure 2. a) Plot of the fluctuation amplitude of the total grid-adhesion forces as function of the interface orientation angle for $\xi/\Delta x = 1$ and b) Comparison of the relative error in the resulting transformation velocity for an interface growing under an angle of $\vartheta = 45°$ with respect to the basic lattice vectors of the computational grid.

Next, we investigate the total grid-adhesion forces acting on arbitrarily oriented planar interfaces in 3D. We find that the translational invariance as well as all the related remarkable improvements provided by the modified equilibrium potential Eq. (5) is tight to an extremely sharp window of interface orientations around the initial direction, for which the translational invariance has been restored. The sharpness of this orientation window can be seen in Fig. 2a), where the solid purple curve shows the fluctuation amplitude of the total grid-adhesion forces as function of the interface orientation, when the direction of translational invariance is kept as fixed. These total grid-adhesion forces correspond to an integral over the right hand site of the phase-field equation, measured for a single interface with an ideal analytic profile. When the discrete representation of the analytic profile Eq. (1) is moved along the interface normal direction, such that its center x_0 is passing several grid points, the measured total grid-adhesion forces oscillate with the mentioned fluctuation amplitude.

In order to overcome the problems with a too sharp orientation window, we propose a new model, which measures the local interface orientation first, and then restores translational invariance for this locally measured direction. For this purpose the interface orientation has to be measures quite accurately, even for very small choices of the phase-field widths. Therefore, again we make use of the addition property Eq. (2), for the local calculation of the a_k. Moreover, we average $a_k = \left(a_k^+ + a_k^-\right)/2$, where

$$a_k^{\pm} = \frac{\pm\left(\phi_{\mathbf{i}\pm\mathbf{u}_k} - \phi_{\mathbf{i}}\right)}{\phi_{\mathbf{i}} - 2\phi_{\mathbf{i}\pm\mathbf{u}_k}\phi_{\mathbf{i}} + \phi_{\mathbf{i}\pm\mathbf{u}_k}},$$

where the lattice vector $\mathbf{u}_k$ connects two neighboring grid points in a certain direction within the numerical lattice. $\Delta x_k = |\mathbf{u}_k|$ is the distance between two neighboring grid points in the respective lattice-direction. We point out, that the orientation of the interface is uniquely described by the unit normal vector $\mathbf{n}$. This leads to respective constrains on the grid-coupling parameters a_k, that have to be satisfied. Therefore, we calculate the $k-$projections of the normal vector, with $n_k = \xi \operatorname{arctanh} a_k/(2\Delta x_k)$, enforce the unit length of the orientation vector and re-calculate the new grid-coupling parameters a_k based on the corrected interface normal vector. The green curve in Fig. 2a) shows that for the respectively new formulation the fluctuation amplitude of the grid-adhesion forces is indeed significantly reduced. Furthermore, in Fig. 2b)

we show that the relative error on the stationary phase transformation velocity for a planar front growing under an angel of $\vartheta = 45\,\mathrm{deg}$ is equally small as compared to the 1D-case shown in Fig. 1a), which proves that the new model provides grid-adhesion free motion of planar interfaces in 3D.

3 Measure of the interface position

For the results in Fig. 1 as well as Fig. 2 b), it should be mentioned that the conventional measure of the interface position by a linear interpolation of the phase-field values at neighboring grid points is not sufficiently accurate. Especially, when the phase-field width becomes very small, we have to non-linearly interpolate the interface position using the phase-field profile function 1. We propose to calculate interpolated position, where the phase-field profile takes the arbitrary contour-level l $(0 < l < 1)$, as

$$x_{\mathbf{i}}^{\mathrm{int}} = \mathbf{i}\Delta x + \frac{\lambda}{2n_k}\left|\mathsf{arctanh}\frac{l-\phi_{\mathbf{i}}}{2l\phi_{\mathbf{i}} - \phi_{\mathbf{i}} - l}\right|, \tag{6}$$

where n_k denotes the projection of the unit normal interface vector onto the $k-$th numerical lattice-direction, between which the contour position has to be calculated. In order to further regularize the resulting interface position as function of time, we impose a linear interpolation between the two slightly different interface positions x_i^{int} and $x_{i+\mathbf{u}_k}^{\mathrm{int}}$ of the two neighboring grid points, connected by the lattice vector $\mathbf{u}_k$, next to the position of the contour-level l . In this case, we have the condition $(\phi_{\mathbf{i}} - l) \cdot (\phi_{\mathbf{i}+\mathbf{u}_k} - l) \leq 0$.

4 Wetting angle boundary conditions for the phase-field

In order to realize stationary growth of the planar front with arbitrarily oriented interfaces, that are explicitly not aligned with basic lattice-vectors of our the simple cubic numerical lattice, we propose new a phase-field boundary condition, which enforces a certain wetting angle ϑ with the respective boundary. For a boundary plane with orientation k the phase-field value at a boundary grid point $\mathbf{i} + \mathbf{u}_k$ has to calculated from the respective value at the neighboring field grid point $\mathbf{i}$. The profile-shift by the length $s_n = \Delta x_k \sin\vartheta$ along the interface normal direction can be realized using the addition theorem for the hyperbolic tangent Eq. (2).

$$\phi_{\mathbf{i}+\mathbf{u}_k} = \frac{(1 - a_\vartheta)\,\phi_{\mathbf{i}}}{1 - a_\vartheta\,(2\phi_{\mathbf{i}} - 1)}, \tag{7}$$

where the grid-coupling parameter is now defined as $a_\vartheta = \tanh\left(2\Delta x_k \sin\vartheta/\lambda\right)$.

Acknowledgments

We thank the Federal Ministry for Economics and Energy (BMWi) of the Federal Republic of Germany for the financial support under the running project COORETEC: ISar (funding code: 03ET7047D). Further, we thank the Federal Ministry of Education and Research (BMBF) for the financial support under the running project ParaPhase (funding code: 01IH15005B). Also, the financial support from the German Research Foundation (DFG) within the second phase of the priority program 1713 (FL 826/3-1 | GL 181/53-1) is greatly acknowledged. Then, we are very thankful to our collaboration partners at ACCESS, especially B. Böttger and J. Eiken, MTU Aero Engines AG and Siemens AG. Finally, we would like to thank A. Finel from ONERA, CNRS, University of Paris-Saclay in France for the vivid and fruit-full discussions on this issue.

References

[1] A. Bösch, H. Müller-Krumbhaar, and O. Shochet. Phase-field models for moving boundary problems: Controlling metastability and anisotropy. *Z. Phys. B* 97 (1995), pp. 367–377. DOI: 10.1007/BF01307490. URL: https://doi.org/10.1007/BF01307490.

[2] J. Eiken. Numerical solution of the phase-field equation with minimized discretization error. *IOP Conf. Series: Materials Science and Engineering* 33 (2012), p. 012105. DOI: doi:10.1088/1757-899X/33/1/012105.

[3] A. Finel, Y. Le Bouar, B. Dabas, B. Appolaire, Y. Yamada, and T. Mohri. Sharp Phase Field Method. *Phys. Rev. Lett.* 121 (2018), p. 025501. DOI: 10.1103/PhysRevLett.121.025501. URL: https://link.aps.org/doi/10.1103/PhysRevLett.121.025501.

[4] M. Fleck, F. Schleifer, and U. Glatzel. Diminishing of numerical grid-adhesion in the phase-field equation for marginally diffuse interfaces. *Submitted to PRL* (2019).

[5] K. Glasner. Nonlinear Preconditioning for Diffuse Interfaces. *J. Comp. Phys.* 174 (2001), pp. 695–711. DOI: https://doi.org/10.1006/jcph.2001.6933. URL: http://www.sciencedirect.com/science/article/pii/S0021999101969335.

[6] M. Weiser. Pointwise nonlinear scaling for reaction–diffusion equations. *Appl. Num. Math.* 59 (2009), pp. 1858–1869. DOI: https://doi.org/10.1016/j.apnum.2009.01.010. URL: http://www.sciencedirect.com/science/article/pii/S0168927409000129.

**Proceedings of the 8th GACM Colloquium on Computational Mechanics
for Young Scientists from Academia and Industry
August 28–30, 2019 in Kassel, Germany**

Phase-field damage model coupled with ageing in polymer adhesives due to moisture diffusion

Siva Pavan Josyula * and Stefan Diebels

Applied Mechanics, Saarland University

Abstract. This paper deals with the formulation and numerical implementation of a coupled continuum model for deformation, diffusion and damage in viscoelastic materials like polymer adhesives to analyse the influence of ageing behaviour on damage phenomena. The formulation is based on a continuum mechanical model. In order to couple diffusive moisture transport with viscoelasticity, a Langmuir-type diffusion model is used, since the diffused moisture in polymers exists in two phases namely free and bound moisture. Furthermore, the coupled deformation-diffusion model takes into account the decrease in stiffness and relaxation times with increasing moisture content. Finally, the model is coupled with damage using a phase-field approach. The governing equations are obtained from supplementing balance equations with thermodynamically consistent constitutive theory, where displacements, phase-field order parameter and moisture concentration are the primary variables. Finally, degradation of the material is chosen as a fully coupled function of the moisture concentration. The numerical implementation is based on the finite element method in space and an implicit scheme for the temporal discretization. Some examples show the applicability of the presented model.

Introduction

The applications of the polymers in the commercial industry are rising especially in the manufacturing of lightweight structures. For technical applications, it is necessary to develop a computationally reliable material model to analyze the mechanical behaviour. Early ageing in the polymer adhesives showcases an important role in their application for commercial purpose, as it is apparent to lose their cohesive properties and degrades earlier than the expected lifetime.

In the current study, a polymer is considered to be exposed to humid environmental conditions at a constant temperature. These environmental conditions reflect their influences on the ageing of polymers by affecting mechanical properties, demonstrating both physical and chemical ageing. Physical ageing is due to moisture diffusion, which is reversible in the drying process. Unlike physical ageing, chemical ageing is an irreversible process caused due to breakage of the existing bonds or by the creation of new bonds. The degradation of physical ageing in polymers is modelled with a phase-field damage model.

1 Numerical formulation of a phase-field damage model for ageing in polymers

Here, we discuss the basic notations and the formulation for a phase-field damage model coupled with moisture concentration and mechanical properties [2].

The degradation of the material is described by the phase-field variable $0 \leq \phi(x) \leq 1$, where $\phi(x) = 1$ describes the damage and $\phi(x) = 0$ fully intact material, respectively.

The total potential energy function, is given by

$$\Psi_{pot} = \int_{\Omega} \Psi^m(\boldsymbol{\varepsilon}, \phi, c) + \int_{\Omega} \Psi^s(\phi, c) + \int_{\Omega} \Psi^c(c) \tag{1}$$

where the first term Ψ^m is the stored bulk energy, the second term Ψ^s refers to the surface energy associated with the formation of the crack and the last term Ψ^c refers to the relative moisture concentration.

*Corresponding author: siva.josyula@uni-saarland.de

Due to the degradation of mechanical behaviour, the material experiences the loss in the stiffness, which is characterized by the degradation function $g(\phi)$.

$$g(\phi) = (1 - \kappa)\phi^2 + \kappa \tag{2}$$

A simple quadratic function in ϕ is chosen as a degradation function such that it decreases monotonically. The degradation function $g(1) = 1$ represents the intact and $g(0) = 0$ represents fully damaged material, respectively. Furthermore, the condition $g'(0) = 0$ controls the contribution of the bulk energy in the phase-field evolution. In Equation 2 a regularization parameter κ is introduced for a well-posed stable model in case of the fully degraded material.

1.1 Moisture transport and Diffusion

The diffusion-driven moisture absorption in PU shows anomalous behaviour, and the diffused moisture exists in two phases characterized as bound and free moisture. The moisture present around the polymer network making a strong physical bond, is characterized as bound moisture. Unlike the bound moisture, the free moisture is far from the polymer network and free to diffuse.

The Ficks's second law of diffusion falls in-short to consider trapped moisture in phases. Therefore, we consider a non-Fickian diffusion model known as a Langmuir-type model. In this diffusion model, the total moisture concentration is split into free and bound moisture $c = c_f + c_b$

$$\frac{\partial c_f}{\partial t} + \frac{\partial c_b}{\partial t} = D\nabla^2 c_f \tag{3}$$

Here, the evolution equation of the bound water concentration can be formulated as

$$\frac{\partial c_b}{\partial t} = \gamma c_f - \beta c_b \tag{4}$$

where γ refers to the rate at which the mobile moisture becomes bound, and β refers to the rate at which the bound molecules of moisture become mobile.

Since, we consider that the moisture content present in the environment is free and sufficient in quantity, the value of the Dirichlet boundary condition $c_f(\Gamma_D, t)$ follows c_b in each time step from the difference between the total moisture N_{max} and the quantity of bound water at the boundary Γ_D

$$c_f(\Gamma_D, t) = N_{max} - c_b(\Gamma_D, t) \tag{5}$$

1.2 Mechanical behaviour of polymer

A material model based on the continuum approach is used to describe viscoelastic behaviour. In the simplest case, a 3-parameter rheological model can describe the viscoelastic behaviour consisting of springs and a damper, as shown in Figure 1. The moisture dependent stiffness parameters are used to describe stiffness in springs by a generalized Hookes's law [4] and the stress in the damper is governed by the strain rate.

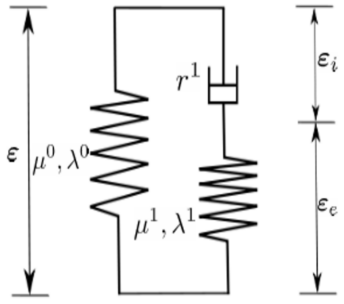

Figure 1. 3-Parameter model of viscoelasticity

A sigmoidal function $f(c) \in [0\ 1]$ is used to compute the stiffness paramters ndependent of ageing numerically. Calculation of the stiffness paramters is shown in Equation 6.

$$\begin{aligned} \lambda(c) &= f(c)\lambda_{dry} - (1 - f(c))\lambda_{sat} \\ \mu(c) &= f(c)\mu_{dry} - (1 - f(c))\mu_{sat} \\ f(c) &= 1 - \frac{k_1}{1 + \exp(-k_2(c - k_3))} \\ \text{where} \quad & c = c_f + c_b \quad \text{and} \quad k_1, k_2, k_3 \quad \text{are constants} \end{aligned} \tag{6}$$

The model reads as,

$$\begin{aligned} &\boldsymbol{\varepsilon} = \boldsymbol{\varepsilon}_e + \boldsymbol{\varepsilon}_i \quad \boldsymbol{\sigma} = \boldsymbol{\sigma}_{eq} + \boldsymbol{\sigma}_{neq} \\ &\boldsymbol{\sigma}_{eq} = 2\mu^0(c)\boldsymbol{\varepsilon} + \lambda^0(c)\mathrm{tr}\boldsymbol{\varepsilon}\mathbf{I} \\ &\boldsymbol{\sigma}_{neq} = 2\mu^1(c)(\boldsymbol{\varepsilon} - \boldsymbol{\varepsilon}_i) + \lambda^1(c)\mathrm{tr}(\boldsymbol{\varepsilon} - \boldsymbol{\varepsilon}_i)\mathbf{I}. \end{aligned} \tag{7}$$

The viscoelastic material properties used are listed in Tabel 1.

Table 1. Viscoelastic properties of polymer adhesive

		dry	50 % r.H	saturated
equilibrium	λ^0	5.3 MPa	2.82 MPa	1.2 MPa
	μ^0	3.38 MPa	1.79 MPa	0.76 MPa
nonequilibrium	λ^1	13.5 MPa	8.78 MPa	0 MPa
	μ^1	8.6 MPa	5.59 MPa	0 MPa

1.2.1 Hygroscopic swelling due to moisture diffusion

Due to the hygroscopic phenomenon in polymers, they swell due to an increase in the total volume during the absorption process.. These changes in the material due to hygroscopic swelling results in strains known as the swelling strains.

A linear function dependent on the swelling strains and relative concentration is defined to characterize the swelling behaviour [3].

$$\varepsilon_{\text{swell}} = \alpha c \tag{8}$$

where $c = c_f + c_b$ is the total moisture concentration trapped inside the material and α is the constant known as coefficient of hygroscopic swelling.

1.3 Surface energy degradation under influence of moisture

The moisture diffused into the material reduce the bonding energy by interacting with the molecules forming the polymer network. This reduction in bonding energy in-turn reduces the fracture resistance.

Here a linearly decreasing function is considered for computing the fracture energy with a change in the total concentration of moisture numerically. This function is defined from the critical energy release rate and the relative concentration [1], as shown in Equation 9.

$$\frac{G_c(c)}{G_c(0)} = 1 - \chi c \tag{9}$$

χ is an additional constant describing the influence of the moisture on the degradation process.

2 Numerical example: Cracked square plate subjected to tension in a humid environment

As an example, we consider a single-edge notched specimen of unit length with a horizontal crack starting from the left-hand side to the centre of the specimen. The specimen's bottom edge is constrained in all direction and a uniformly distributed displacement is applied on the top edge. Finally, the geometry is exposed to a humid atmosphere from all exterior edges. The applied boundary conditions to simulate the polymer adhesive at saturated condition is shown in Figure 2a.

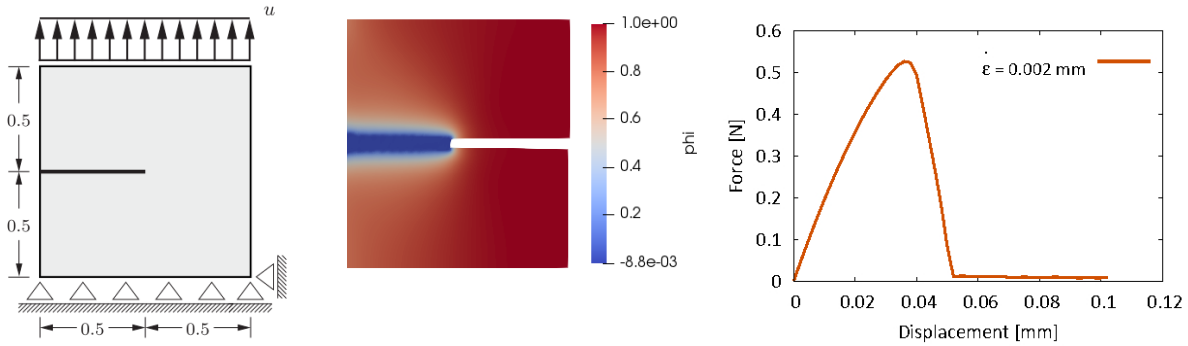

(a) Problem setup **(b)** crack pattern **(c)** load deflection curve

Figure 2. Damage in test setup under tension

Figure 2b illustrates the damage with blue and red contours. Blue contour corresponds to the damage and the red contour fully intact state of the material, respectively. Figure 2c show the damage propagation in the single-edge notched specimen under tension, where it is evident from the force versus displacement curve that the force reduces after damage.

Acknowledgement

The research project 19730 N "Berechnung des instationären mechanischen Verhaltens von alternden Klebverbindungen unter Einfluss von Wasser auf den Klebstoff" of the research association Forschungsvereinigung Stahlanwendung e.V. (FOSTA), Düsseldorf was supported by the Federal Ministry of Economic Affairs and Energy through the AiF as part of the programme for promoting industrial cooperative research (IGF) on the basis of a decision by the German Bundestag. The project is carried out at Chair of Applied Mechanics, Saarland university

References

[1] A. Alvaro, I. Thue Jensen, N. Kheradmand, O. M. Lovvik, and V. Olden. Hydrogen embrittlement in nickel, visited by first principles modeling, cohesive zone simulation and nanomechanical testing. *International Journal of Hydrogen Energy* 40 (2015), pp. 16892–16900.

[2] M. Ambati, T. Gerasimov, and L. De Lorenzis. A review on phase-field models of brittle fracture and a new fast hybrid formulation. *Computational Mechanics* 55 (2015), pp. 383–405.

[3] X. Fan. Mechanics of Moisture for Polymers: Fundamental Concepts and Model Study. *IEEE* (2008).

[4] F. Goldschmidt and S. Diebels. Modelling and numerical investigations of the mechanical behavior of polyurethane under the influence of moisture. *Archive of Applied Mechanics* 85 (2015), pp. 1035–1042.

**Proceedings of the 8th GACM Colloquium on Computational Mechanics
for Young Scientists from Academia and Industry
August 28–30, 2019 in Kassel, Germany**

An anisotropic phase-field model based on a Representative Crack Element (RCE)

Dennie Supriatna[1], Johannes Storm[1] and Michael Kaliske * [1]

[1]Institute of Structural Analysis, Technische Universität Dresden, 01062 Dresden, Germany

Abstract. To predict failure phenomena of brittle material is a challenging task. In brittle failure, no apparent deformations are visible prior to the formation of the crack. The presence of aspects such as stress concentrations, crack-growth instabilities and displacement field discontinuities yields fracture of brittle material harder to predict in an accurate way. The crack may also be a result of the fracture mode changes or even mixed of several fracture modes due to loading applications and geometry. Strobl, Seelig [4] and Steinke, Kaliske [3] have shown, that the standard phase-field approach with spectral decomposition or volumetric-deviatoric (V-D) split leads to unrealistic predictions for the stress transfer through the crack and they have developed a more realistic split for the case of isotropic elasticity and small deformations. The model is constructed from the kinematics of a discrete crack and is further derived to split the crack driving stresses and persistent stresses. In the current research, a Representative Crack Elements (RCE) concept is developed based on the kinematics of a discrete crack model. The proposed RCE approach is coupled to the phase-field method by adopting the variational homogenization concept of Blanco et al. [1]. The consistent kinematics and general variational framework enable us to extend the RCE into anisotropic material, finite deformation, dissipative material and coupled problems with other fields such as temperature. To compare the behaviour of the proposed continuum phase-field model with the RCE and a corresponding discrete model, several self consistency conditions for isotropic and anisotropic materials are employed. We demonstrate the capability of the approach by presenting several numerical examples, which cover isotropic, anisotropic and coupled problems.

Introduction

A realistic and accurate model of material degradation within the phase-field approach is currently under development. It has been shown by Strobl and Seelig [4], Schueler [2] and Steinke and Kaliske [3], that the classical V-D split and spectral decomposition lead to wrong predictions for the force transfer through the cracked body. They have proposed a more kinematically consistent approach to overcome the issue. Steinke and Kaliske [3] have proposed a directional decomposition approach, which is constructed from the kinematics of a discrete crack and is further derived to split the crack driving stresses and persistent stresses.

Inspired by the work of Steinke and Kaliske [3], a novel approach based on so-called Representative Crack Elements (RCE) is derived using the kinematics of a discrete crack model. Due to the general variational framework and consistent kinematics, this RCE allows investigations of complex crack mechanicsms: re-contacting after cracking, friction, inelasticity, anisotropy, and finite deformations.

1 Concept of Representative Crack Elements (RCE)

The proposed novel concept is based on a fully equivalent re-interpretation of the strain potential energy as the interpolation of the potential energies of the intact material ψ^0 and of the fully degraded material ψ^c using the degradation function

$$\begin{aligned}\psi^{\text{mech}} &= [1-g(s)]\,\psi^c + g(s)\psi^0 \\ &= \psi^c + g(s)\left[\psi^0 - \psi^c\right]. \end{aligned} \tag{1}$$

*Corresponding author: michael.kaliske@tu-dresden.de

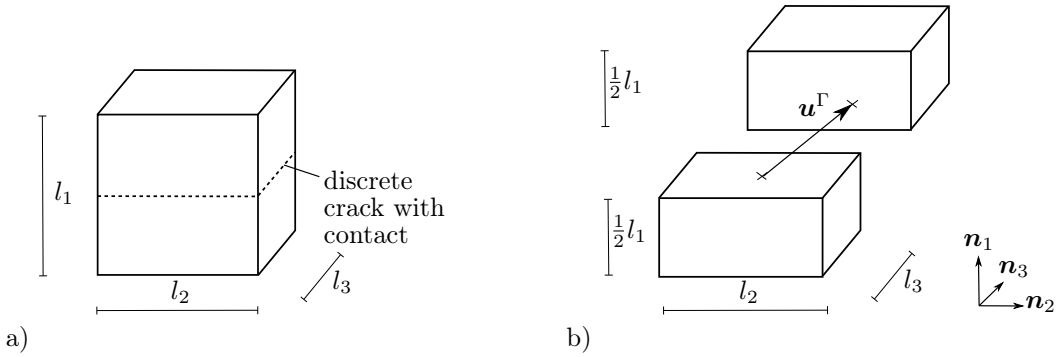

Figure 1. a) Sketch of the RCE with a discrete crack in local coordinates and b) definition of crack displacements and deformations.

Based on the clearly defined material states, the additive decomposition of stress and material tangent reads

$$\boldsymbol{S} = \boldsymbol{S}^c + g(s)\left[\boldsymbol{S}^0 - \boldsymbol{S}^c\right], \tag{2}$$

$$\mathbb{C} = \mathbb{C}^c + g(s)\left[\mathbb{C}^0 - \mathbb{C}^c\right], \tag{3}$$

which are composed of the material response without any crack ($\boldsymbol{S}^0$, $\mathbb{C}^0$) and the material response with a fully developed crack ($\boldsymbol{S}^c$, $\mathbb{C}^c$). Once, the two unique material states are identified and described, crack evolution (driving force) is the result of using the novel concept and no longer of an independent model assumption.

The fully broken material is modelled by the RCE. The following kinematic coupling operators are chosen

$$\boldsymbol{u} := \bar{\boldsymbol{u}} + \bar{\boldsymbol{H}} \cdot (\boldsymbol{\eta} - \boldsymbol{\eta}_0) + \tilde{\boldsymbol{u}}, \tag{4}$$

$$\bar{\boldsymbol{u}} := \frac{1}{V}\int_\Omega \boldsymbol{u}\ \mathrm{d}V, \tag{5}$$

$$\bar{\boldsymbol{H}} := \frac{1}{V}\int_\Omega \boldsymbol{H}\ \mathrm{d}V \quad . \tag{6}$$

Quantities with bar indicate the continuous phase-field model, whereas the rest is associated with the RCE. The displacement field of the RCE $\boldsymbol{u}$ depends on the displacement $\bar{\boldsymbol{u}}$, the displacement gradient $\bar{\boldsymbol{H}}$ of the material point in the continuous model, as well as on the position vector in the RCE $\boldsymbol{\eta}$, a constant vector $\boldsymbol{\eta}_0$ and an unknown displacement fluctuation field $\tilde{\boldsymbol{u}}$. The relations of the displacements and the displacement gradients towards the continuous model are given as their volume average on the RCE domain Ω in the reference configuration. Applying the concept of energy conservation, the first Piola-Kirchhoff stress tensor is computed as

$$\bar{\boldsymbol{P}} = \frac{1}{V}\int_\Omega \boldsymbol{P}\ \mathrm{d}V. \tag{7}$$

The variational problem of the RCE regarding the fluctuation field can be solved using various approaches. For reasons of computational efficiency, an analytical solution for elastic and thermo-elastic material behaviour is used in the following.

2 Applications

The RCE model is considered as two blocks of intact material, which are separated by a discrete crack. The crack undergoes crack contact in case of crack closure (see Fig. 1a)). With the assumption of homogeneous material and the neglect of softening behaviour in the two blocks, piecewise uniform boundary conditions yield homogeneous stress and strain states in the two blocks for the open and closed crack configurations. Thus, all outer RCE surfaces and the crack surfaces remain plane and the deformation of the blocks reads

$$\begin{aligned}\boldsymbol{F} &= \bar{\boldsymbol{F}} - \boldsymbol{\Gamma} \\ &= \bar{\boldsymbol{F}} - \sum_{i=1}^{3} \Gamma_i \boldsymbol{P}_i,\end{aligned} \tag{8}$$

where $\boldsymbol{F}$ is the deformation gradient and $\Gamma_i = u_i^\Gamma / l_1$ are the *crack deformations* obtained from the relative displacements of the crack surfaces $\boldsymbol{u}^\Gamma$ normalised by the RCE length l_1 (see Fig. 1b)). The crack projectors $\boldsymbol{P}_i$ are defined as

$$\boldsymbol{P}_1 = \boldsymbol{n}_1 \otimes \boldsymbol{n}_1, \tag{9}$$

$$\boldsymbol{P}_2 = \boldsymbol{n}_2 \otimes \boldsymbol{n}_1, \tag{10}$$

$$\boldsymbol{P}_3 = \boldsymbol{n}_3 \otimes \boldsymbol{n}_1 \tag{11}$$

using the basis vectors $\boldsymbol{n}_i$ of the local RCE coordinate system.

The unknown crack deformations Γ_i can be obtained by minimisation of the total potential energy of the RCE

$$\psi = \frac{1}{2} \int_\Omega \boldsymbol{P} : \boldsymbol{F} \, \mathrm{d}V. \tag{12}$$

Inserting the kinematic coupling Eq. (8) yields the extremal problem

$$\Gamma_i(\bar{\boldsymbol{F}}) = \arg \left\{ \min_{\Gamma_i \in \mathcal{R}} \; \hat{\psi}(\bar{\boldsymbol{F}}, \Gamma_i) \right\}, \tag{13}$$

without constraints on the crack deformations. In case of crack surface contact ($\Gamma_1 < 0$), the constrained minimisation problem is to be solved

$$\Gamma_{2,3}(\bar{\boldsymbol{F}}) = \arg \left\{ \min_{\Gamma_{2,3} \in \mathcal{R}} \; \hat{\psi}(\bar{\boldsymbol{F}}, \Gamma_2, \Gamma_3)\Big|_{\Gamma_1 = 0} \right\} \qquad \text{for} \quad \Gamma_1 < 0, \tag{14}$$

$$\Gamma_1 = 0.$$

The energy potential of the RCE for the case **linear anisotropic elasticity** reads

$$\begin{aligned} \hat{\psi}(\bar{\boldsymbol{E}}, \Gamma_i) &= \frac{1}{2} V \left[\bar{\boldsymbol{E}} : \mathbb{C} : \bar{\boldsymbol{E}} - 2 \bar{\boldsymbol{E}} : \mathbb{C} : \boldsymbol{\Gamma}^{\mathrm{sym}} + \boldsymbol{\Gamma}^{\mathrm{sym}} : \mathbb{C} : \boldsymbol{\Gamma}^{\mathrm{sym}} \right] \\ &= \frac{1}{2} V \left[\bar{\boldsymbol{E}} : \mathbb{C} : \bar{\boldsymbol{E}} - 2 \bar{\boldsymbol{E}} : \mathbb{C} : \sum_{i=1}^{3} \Gamma_i \boldsymbol{P}_i^{\mathrm{sym}} + \sum_{i=1}^{3} \Gamma_i \boldsymbol{P}_i^{\mathrm{sym}} : \mathbb{C} : \sum_{i=1}^{3} \Gamma_i \boldsymbol{P}_i^{\mathrm{sym}} \right]. \end{aligned}$$

In order to solve the unconstrained minimisation problem of Eq. (13)

$$\frac{\partial \hat{\psi}(\bar{\boldsymbol{E}}, \Gamma_i)}{\partial \Gamma_i} \stackrel{!}{=} 0 \tag{15}$$

has to hold, which yields the system of equations

$$\left[\mathbb{C}^{\Gamma_i} \right] [\Gamma_i] = \left[\boldsymbol{r}^{\Gamma_i} \right], \qquad i \in \{1, 2, 3\} \tag{16}$$

with

$$\left[\mathbb{C}^{\Gamma_i} \right] = \left[\boldsymbol{P}_i^{\mathrm{sym}} : \mathbb{C} : \boldsymbol{P}_j^{\mathrm{sym}} + \boldsymbol{P}_j^{\mathrm{sym}} : \mathbb{C} : \boldsymbol{P}_i^{\mathrm{sym}} \right], \qquad i, j \in \{1, 2, 3\} \tag{17}$$

$$\left[\boldsymbol{r}^{\Gamma_i} \right] = \left[\boldsymbol{P}_i^{\mathrm{sym}} : \mathbb{C} : \bar{\boldsymbol{E}} + \bar{\boldsymbol{E}} : \mathbb{C} : \boldsymbol{P}_i^{\mathrm{sym}} \right], \qquad i \in \{1, 2, 3\} \tag{18}$$

for the unknown crack deformation Γ_i. The inversion of the symmetrical 3x3 matrix $\left[\mathbb{C}^{\Gamma_i} \right]$ results in the crack deformations from

$$[\Gamma_i] = \left[\mathbb{C}^{\Gamma_i} \right]^{-1} \left[\boldsymbol{r}^{\Gamma_i} \right]. \tag{19}$$

For the case that $\Gamma_1 < 0$ holds, the constrained problem reads

$$\left[\mathbb{C}^{\Gamma_i} \right] [\Gamma_i] = \left[\boldsymbol{r}^{\Gamma_i} \right], \qquad i \in \{2, 3\} \tag{20}$$

with

$$\left[\mathbb{C}^{\Gamma_i} \right] = \left[\boldsymbol{P}_i^{\mathrm{sym}} : \mathbb{C} : \boldsymbol{P}_j^{\mathrm{sym}} + \boldsymbol{P}_j^{\mathrm{sym}} : \mathbb{C} : \boldsymbol{P}_i^{\mathrm{sym}} \right], \qquad i, j \in \{2, 3\} \tag{21}$$

$$\left[\boldsymbol{r}^{\Gamma_i} \right] = \left[\boldsymbol{P}_i^{\mathrm{sym}} : \mathbb{C} : \bar{\boldsymbol{E}} + \bar{\boldsymbol{E}} : \mathbb{C} : \boldsymbol{P}_i^{\mathrm{sym}} \right], \qquad i \in \{2, 3\} \tag{22}$$

$$\Gamma_1 = 0.$$

As a numerical example, the approach is applied to simulate an embedded crack in a thin plate at tensile loading. A transversely isotropic material with several fiber angles are simulated (see Fig. 2).

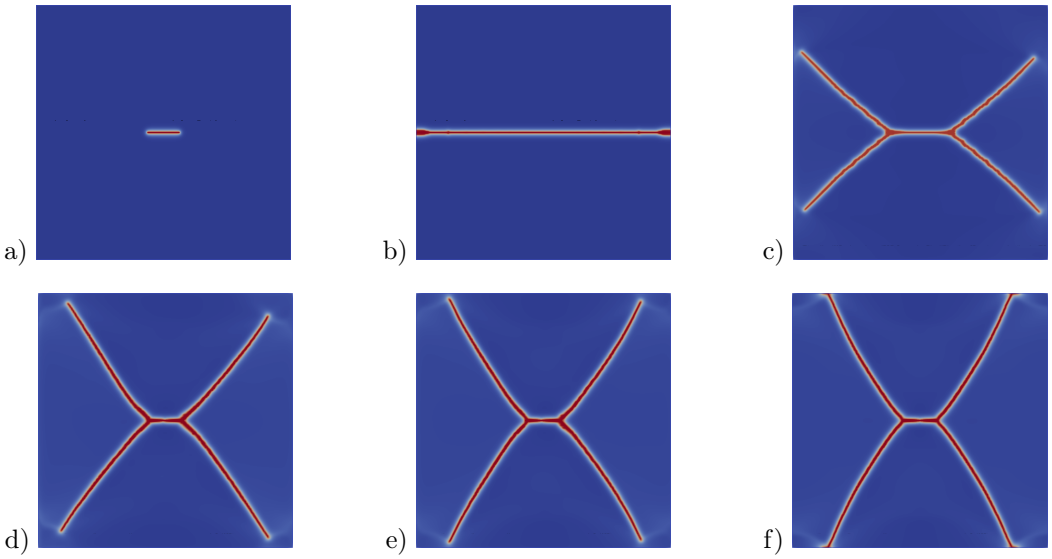

Figure 2. Comparison of crack propagation of an embedded crack in a thin plate at tensile load: a) initial crack configuration, b) isotropic material and c-f transversely isotropic material ($E_1/E_2 = 3.0$) with c) $\gamma = 70°$, c) $\gamma = 75°$, c) $\gamma = 80°$, c) $\gamma = 90°$

3 Conclusion

The proposed phase-field approach based on Representative Crack Element (RCE) is applied to transversely isotropic material. The derived fracture models can be equivalently used instead of discrete crack models due to the general variational framework and consistent kinematics.

Acknowledgments

The authors gratefully acknowledge the financial support by the German Research Foundation (DFG) within the priority program SPP 2020 (KA 1163/40).

References

[1] P. J. Blanco, P. J. Sánchez, E. A. Souza, and R. A. Feijóo. Variational Foundations and Generalized Unified Theory of RVE-Based Multiscale Models. *Archives of Computational Methods in Engineering* 23 (2014), pp. 1–63. DOI: 10.1007/s11831-014-9137-5.

[2] Alexander Schlueter. *Phase Field Modeling of Dynamic Brittle Fracture*. Technische Universität Kaiserslautern, 2018.

[3] C. Steinke and M. Kaliske. A phase-field crack model based on directional stress decomposition. *Computational Mechanics* 63 (2018), pp. 1019–1046. DOI: 10.1007/s00466-018-1635-0.

[4] M. Strobl and T. Seelig. On constitutive assumptions in phase field approaches to brittle fracture. *Procedia Structural Integrity* 2 (2016), pp. 3705–3712. DOI: 10.1016/j.prostr.2016.06.460.

**Proceedings of the 8th GACM Colloquium on Computational Mechanics
for Young Scientists from Academia and Industry
August 28–30, 2019 in Kassel, Germany**

Reconstruction of a Ferroelectric Stripe Domain Array due to Charge Defect Migration

Ivan Vorotiahin *[1], Anna Morozovska[2] and Yuri Genenko[1]

[1]Institute of Materials Science, Technische Universität Darmstadt, Otto-Berndt-Str.3, Darmstadt, Germany
[2]Institute of Physics, National Academy of Sciences of Ukraine, pr. Nauky 46, Kyiv, Ukraine

Abstract.

Introduction

Field-driven migrating charged defects, such as impurities and oxygen vacancies, are often considered as the widespread mechanism of aging in ferroelectric materials [2]. This process is usually studied within a fixed domain structure, where it is able to change charge distributions, however, it is known that domain structure is actually affected by this process [1]. This work studies the evolution of a self-organized polarization stripe-domain array induced by the movement of the oxygen vacancies throughout an acceptor-doped ferroelectric film. The processes are investigated by the Landau-Ginzburg-Devonshire theory creating a self-consistent numerical model which thoroughly describes polar, electrostatic and electromechanical properties of the film including doping-induced semiconductor properties [3]. Due to the field-driven defect migration in the domain array, the array itself undergoes changes in its charge balance which ultimately leads to domain shape modifications. The processes exhibit several characteristic times related to different mechanisms taking place inside the film, among which are the defect migration with the characteristic Maxwell time and the domain array response changing the domain configuration.

1 Problem Statement

A model of a 24-nm thin single-crystalline barium titanate film was considered, fixed on a metallic bottom electrode with a compressive misfit strain, with a free top surface exposed to the ambience (Figure 1). The film contains charged defects, namely, immobile acceptor impurities and mobile (donor) oxygen vacancies. The domain structure of the film arises spontaneously and rapidly, and then the migration of the mobile defects becomes the main mechanism of the further "self-organized" polarization evolution. The goal of this work is to establish the influence of the defect migration on the ferroelectric properties of the film.

The Landau-Ginzburg-Devonshire approach is chosen to describe polar, electrostatic, electromechanical, and semiconductor properties of the film, as well as the movement of charged defects througuout the film with time until its saturation. The Gibbs thermodynamic potential in relation to polarization, electrostatic potential, mechanical stress, electron and hole, as well as donor and acceptor concentrations comprises of a volume, a surface and dead-layer parts. The volume part consists of the Landau expansion, gradient, electrostatic, elastic, semiconductor and defect terms:

$$G_V = G_{Landau} + G_{grad} + G_{el.stat} + Gelast + G_{semi} + G_{donor} + G_{acceptor} \tag{1}$$

A system of equations consists of the Landau-Khalatnikov equation, which is given by the variation of the Gibbs free energy by polarization,

*Corresponding author: isvort@mm.tu-darmstadt.de

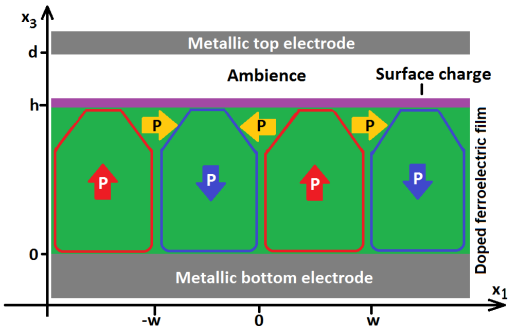

Figure 1. Schematic image of a homogeneously doped ferroelectric film of thickness , with domains of width with vertically oriented polarization (red and blue frames with arrows) and closure domains with laterally oriented polarization (yellow arrows). The film is clamped to a rigid conductive bottom electrode, has a layer of surface screening charge on the top surface and is separated by a thick ambient layer of thickness from the top electrode.

$$\Gamma \frac{\partial P_i}{\partial t} = \frac{\delta G_V}{\delta P_i} \tag{2}$$

Poisson equation for electrostatic potential, with space charge created by electrons, holes, donors and acceptors accounted for,

$$\varepsilon_0 \varepsilon_b \frac{\partial^2 \varphi}{\partial x_i \partial x_i} = \frac{\partial P_j}{\partial x_j} + e(Z_d N_d^+ - Z_a - N_a^- + p - n) \tag{3}$$

a set of four Continuity equations for each charge specie with the general form of:

$$\frac{\partial N}{\partial t} = \frac{1}{Ze} \frac{\partial J_i^N}{x_i} \tag{4}$$

and the generalized Hiike law with the elastic equilibrium condition to account for electromechanical effects, such as electrostriction and flexoeffect

$$u_i j = s_i jkl\sigma_k l + F_i jkl \frac{\partial P_k}{\partial x_l} + Q_i jkl P_k P_l \tag{5}$$

$$\frac{\partial \sigma_i j}{\partial x_i} = 0 \tag{6}$$

all accompanied with boundary conditions ensuring blocking interfaces, grounded bottom electrode, misfit strain on the bottom surface and periodicity on the side biundaries -w and w.

2 Defect-Induced Processes

Figure 2 shows the time evolution of the vertical polarization, mobile donor concentration and charge distribution over the film at the acceptor doping level of 0.1 mol-percent. At the begining, donors and acceptors distributed similarly and compensate each other's charge, however acceptors are immobile. Donors, on the other hand, redistribute over time creating areas with excess and diminished concentrations under the free top surface aligning themselves with the electrostatic potential. In response, polarization domains start changing their shape creating upon saturation the wedged or trapezoidal forms with tilted walls. Once walls are tilted, the space charge on them changes its sign.

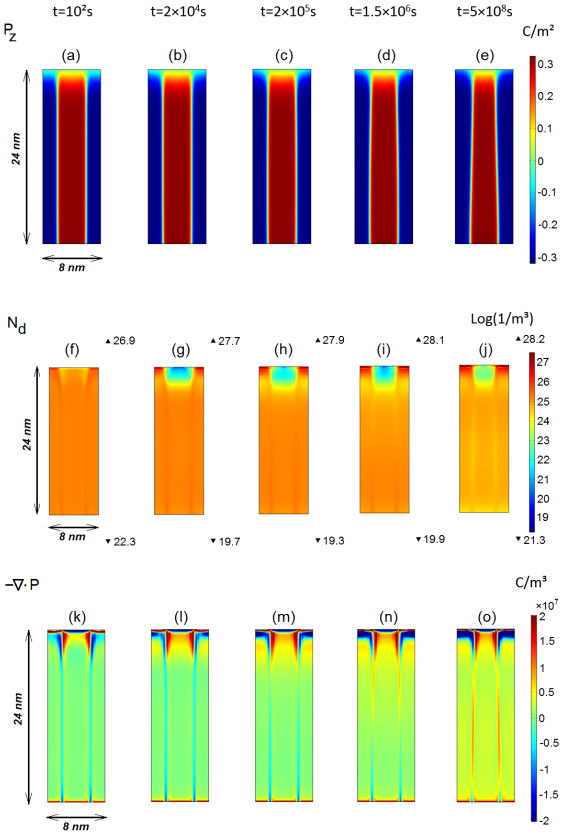

Figure 2. Time evolution of the stripe domain structure in a 24 nm thick ferroelectric film doped with a divalent acceptor of concentration 0.1 mol-percent illustrated by snapshots of two-dimensional maps of vertical polarization component (a-e), concentration of oxygen vacancies (f-j) and density of bound charge (k-o). Numbers at the top and the bottom of plots (f-j) indicate the reached limiting values of donor concentration.

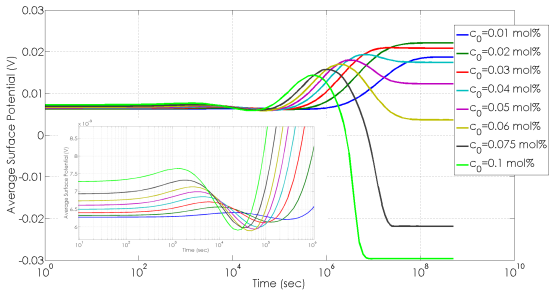

Figure 3. Time evolution of the average surface potential in a 24-nm thick ferroelectric film for a set of acceptor doping concentrations c0 from 0.01 mol-percent to 0.1 mol-percent. Inset: Zoom-in of the time development from 10 to 106 seconds.

Figure 3 shows the time evolution of the average potential on the top surface at different acceptor concentrations. The nonmonotonous shape of the curve indicates a competition between several processes occuring in the film. Comparing it to the distributions shown in Figure 2 it is possible to establish, which processes are responsible for different behaviour of the curve parts. Charge redistribution process dominates at characteristic times of 10^5 - 10^6 seconds and ultimately pulls the curve to the positive potential. Appearing first as the response, domain redistribution becomes dominant at larger timescales and ultimately pulls the curve to the negative potential.

Acknowledgments

This work was supported by the Deutsche Forschungsgemeinschaft (DFG) via the grant No. 405631895 (GE-1171/8-1).

References

[1] Z. M. Fan and X. L. Tan. In-situ TEM study of the aging micromechanisms in a BaTiO3-based lead-free piezoelectric ceramic. *Journal of European Ceramic Society* 38 (2018), pp. 3472–3477.

[2] Y. A. Genenko, J. Glaum, M. J. Hoffmann, and K. Albe. Mechanisms of aging and fatigue in ferroelectrics. *Materials Science and Engineering: B* 192 (2015), pp. 52–82.

[3] A. N. Morozovska, E. A. Eliseev, Y. A. Genenko, I. S. Vorotiahin, M. V. Silibin, Y. Kim Y. Cao, M. D. Glinchuk, and S. V. Kalinin. Flexocoupling impact on size effects of piezoresponce and conductance in mixed-type ferroelectric semiconductors under applied pressure. *Physical Review B* 94 (2016), p. 174101.

**Proceedings of the 8th GACM Colloquium on Computational Mechanics
for Young Scientists from Academia and Industry
August 28–30, 2019 in Kassel, Germany**

Phase-field simulation of the flexoelectricity in ferroelectrics

Xian-Dong Zhou *[1] and Bai-Xiang Xu[1]

[1]Division Mechanics of Functional Materials, Department of Materials Science, TU Darmstadt

Flexoelectricity describes the linear coupling between the polarization and the strain gradient or the coupling between the strain and the polarization gradient. Unlike other electromechanical coupling effects such as piezoelectricity, which require the non-central symmetry of the structure, flexoelectricity applies to all crystal symmetries. The flexoelectricity broadens the material selection arrange for electromechanical application and has received recently significant research interest [3, 4].

The flexoelectricity in ferroelectrics can be characterized by nanoindentation tests, in which large strain gradient is available. Most work focus on the estimation of the flexoelectric constants at room temperature and few work discussed about nanoindentation test at high temperature. Recent nanoindentation tests of $BaTiO_3$ shows a super compressive elasticity of the material around Curie temperature, which means a much larger indentation depth than that at room temperature under the same load. With increased indentation depth, the distribution of strain as well as strain gradient changes around the indenter tip. Therefore, it is interesting to understand how the flexoelectricity can affect the material behavior around Curie temperature in nanoindentation tests.

In this work we extend a phase-field ferroelectric model to include the flexoelectricity [2, 5]. A weak form formulation is developed. The formulation shows there are only first order derivatives in the weakest form, therefore, conventional lower order h-type finite element can be adopted for numerical implementation. The model is applied to study the nanoindentation tests of $BaTiO_3$ ferroelectrics at high temperature, particularly near Curie temperature. The reason why the material shows super compressive elasticity property is analyzed by considering different possible boundary conditions and loading in nanoindentation tests. Different temperatures below and above the Curie temperature are also considered in the simulation. In order to study how flexoelectricity affects the behavior of the material, a parametric study is performed with the three indepedent flexocoupling constants for perovskite ferroelectrics with a cubic parent phase. The domain evolution of the ferroelectrics during nanoindentation tests is analyzed with and without flexoelectricity. A flexoelectric-induced paraelectric-ferroelectric phase transition slightly above the Curie temperature is analyzed and compared with experimental results. Moreover, we simulated the flexoelectricity in nanoparticles with cation inhomogeneity and its induced strain gradient, which is successfully applied to explain the experimentally observed star-like polar regions at extremely high temperature [1].

References

[1] Leopoldo Molina-Luna, Shuai Wang, Yevheniy Pivak, Alexander Zintler, Héctor H Pérez-Garza, Ronald G Spruit, Qiang Xu, Min Yi, Bai-Xiang Xu, and Matias Acosta. Enabling nanoscale flexoelectricity at extreme temperature by tuning cation diffusion. *Nature communications* 9.1 (2018), p. 4445.

[2] D Schrade, R Mueller, BX Xu, and D Gross. Domain evolution in ferroelectric materials: A continuum phase field model and finite element implementation. *Computer methods in applied mechanics and engineering* 196.41-44 (2007), pp. 4365–4374.

[3] AK Tagantsev. Piezoelectricity and flexoelectricity in crystalline dielectrics. *Physical Review B* 34.8 (1986), p. 5883.

*Corresponding author: x.zhou@mfm.tu-darmstadt.de

[4] Bo Wang, Yijia Gu, Shujun Zhang, and Long-Qing Chen. Flexoelectricity in Solids: Progress, Challenges, and Perspectives. *Progress in Materials Science* (2019).

[5] Shuai Wang, Min Yi, and Bai-Xiang Xu. A phase-field model of relaxor ferroelectrics based on random field theory. *International Journal of Solids and Structures* 83 (2016), pp. 142–153.

**Proceedings of the 8th GACM Colloquium on Computational Mechanics
for Young Scientists from Academia and Industry
August 28–30, 2019 in Kassel, Germany**

Comparison of different rheological models in pressure-hole error simulation

Hogenrich Damanik * [1] and Stefan Turek[1]

[1]Lsiii Angewandte Mathematik, TU-Dortmund

Abstract. We present numerical techniques for the calculation of steady viscoelastic fluids given in differential form and perform numerical simulations of the hole-pressure error of different rheological models. The numerical techniques are based on a well-developed mixed Finite element approach for steady fluid flows which can deal with complex rheological models in a black-box manner. We consider rheological models from quasi Newtonian fluids, i.e with nonlinear viscosity function, as well as models from quasi linear viscoelasticity. The numerical simulation shows typical non-symmetry streamlines and a secondary vortex when increasing the viscoelasticity.

Introduction

Hole-pressure error is an interesting test problem for both numerical as well as experimental works because it has a simple geometry which can be easily fabricated and attached at the end of an extrusion process. Furthermore, there exists a theoretical work for an analytical expression of hole-pressure error, see [6], too. Hole-pressure error deals with the wrong pressure reading from the instrument due to drilling of the fluid chamber/channel. Instead of giving the actual pressure at a given point of location on the wall of the channel, a wrong pressure is measured because the tip of the pressure stick/transducer does not close the channel wall appropriately. The same situation might happen to several other points of measurement, and thus giving an inaccurate data reading. In this regard, numerical simulation can be used to provide first normal stress difference data up to a small range of elasticity.

1 Rheological models

We consider several rheological models for the numerical simulation. An incompressible steady flow of generalised Newtonian fluid needs to satisfy

$$\begin{cases} (\mathbf{u}\cdot\nabla)\mathbf{u} = -\nabla p + \nabla\cdot\mathbf{T} \\ \quad \nabla\cdot\mathbf{u} = 0 \end{cases} \tag{1}$$

with the constitutive law $\mathbf{T} = 2\eta_s(\dot\gamma, p)\mathbf{D}$, shear rate $\dot\gamma = \sqrt{\mathrm{tr}(\mathbf{D}^2)}$, and symmetric velocity gradient $\mathbf{D} = \frac{1}{2}(\nabla\mathbf{u} + \nabla\mathbf{u}^{\mathrm{T}})$. In the numerical context, the above Eq. (1) is well-known as velocity-pressure formulation $(\mathbf{u}, p)$. The fluid viscosity function can be written as, i.e., the power law model

$$\eta_s(\dot\gamma) = \eta_0\ (\epsilon + \dot\gamma^2)^{(\frac{r}{2}-1)} \tag{2}$$

with r is the constant parameter index that describes whether the fluid is in the region of shear thinning ($\frac{r}{2} < 1$) or shear thickening ($\frac{r}{2} > 1$). While there exists no normal stress difference for Newtonian fluids, we consider also fluids with elastic properties, such there is an elastic contribution to the constitutive law

$$\mathbf{T} = 2\eta_s(\dot\gamma, p)\mathbf{D} + \boldsymbol{\sigma}. \tag{3}$$

This additional elastic properties must be calculated/integrated along the historical path of each fluid particle, leading to the so-called integral model of viscoelastic fluids. Since the path for integration is

*Corresponding author: hdamanik@mathematik.tu-dortmund.de

unknown in the Eulerian frame work, Oldroyd in [8] and Giesekus in [4] provide differential forms of $\boldsymbol{\sigma}$-equation for quasi linear models where time and strain can still be separated. For numerical purposes, these original models are often reformulated. We consider the logarithm of the conformation stress $\boldsymbol{\tau}$ reformulation (LCR)

$$\boldsymbol{\tau} = \frac{\eta_p}{\Lambda}(\boldsymbol{\sigma} - \mathbf{I}), \quad \boldsymbol{\psi} = \log(\boldsymbol{\tau}) \tag{4}$$

with fluid viscosity η_p and fluid relaxation time Λ. The Oldroyd-B and Giesekus model can now be written as in the previously numerical work of [3, 7]:

$$\frac{\partial \boldsymbol{\psi}}{\partial t} + (\mathbf{u}\cdot\nabla)\boldsymbol{\psi} - (\boldsymbol{\Omega}\boldsymbol{\psi} - \boldsymbol{\psi}\boldsymbol{\Omega}) - 2\mathbf{B} = \frac{1}{\Lambda}\, f(\boldsymbol{\psi}), \quad f(\boldsymbol{\psi}) = (e^{-\boldsymbol{\psi}} - \mathbf{I}) - \alpha e^{\boldsymbol{\psi}}(e^{-\boldsymbol{\psi}} - \mathbf{I})^2 \tag{5}$$

where parameter $\alpha = 0$ gives Oldroyd-B model, and $\alpha \neq 0$ gives Giesekus model. The two models come from the kinetic theory. Other models which are also from the same theory are FENE-P and FENE-CR. In the FENE-P and FENE-CR model the maximum polymer extension is bounded by some value L, see [1]. It can be written in LCR form as

$$\frac{\partial \boldsymbol{\psi}}{\partial t} + (\mathbf{u}\cdot\nabla)\boldsymbol{\psi} - (\boldsymbol{\Omega}\boldsymbol{\psi} - \boldsymbol{\psi}\boldsymbol{\Omega}) - 2\mathbf{B} = -\frac{1}{\Lambda}\, \left(f(R,L)\mathbf{I} - \alpha_f f(R,L) e^{-\boldsymbol{\psi}}\right) \tag{6}$$

where $f(R,L) = \frac{1}{1-\frac{R^2}{L^2}}$, $\alpha_f = 0$ for FENE-P and $\alpha_f = 1$ for FENE-CR, and where $R^2 = \mathrm{tr}(\boldsymbol{\tau})$.

2 Numerical treatment

We solve the Eq. (1) for generalised Newtonian fluids, and solve the Eq. (1) and (5) or (6) for viscoelastic fluids. In this regard, finite element method is employed for space approximation. Consequently, we have to choose approriate finite element pairs which is subject to the well-known compatibility condition between the velocity and pressure space for Newtonian fluids, see [5], and between velocity-pressure and stress for viscoelastic case, see [2]. We choose the finite element pair Q_2P_1 with the following definition:

$$Q_2(T) = \left\{ q \circ \psi_T^{-1} : q \in \mathrm{span} < 1, x, y, xy, x^2, y^2, x^2y, y^2x, x^2y^2 > \right\} \tag{7}$$

with nine local degrees of freedom located at the vertices, midpoints of the edges and in the center of the quadrilateral. The space $P_1(T)$ consists of linear functions defined by

$$P_1(T) = \left\{ q \circ \psi_T^{-1} : q \in \mathrm{span} < 1, x, y > \right\} \tag{8}$$

with the function value and both partial derivatives, located in the center of the quadrilateral, as its three local degrees of freedom. Then, the interpolation functions are

$$\mathbf{V}_h = \{\tilde{\mathbf{v}}_h := (\mathbf{u}_h, \boldsymbol{\tau}_h) \in X(\Omega_h), \tilde{\mathbf{v}}_{h|T} \in [Q_2(T)]^6 \ \ \forall T \in \mathcal{T}_h\}, \tag{9}$$

$$Q_h = \{p_h \in L_0^2(\Omega_h), \quad p_{h|T} \in P_1(T) \ \ \forall T \in \mathcal{T}_h\}. \tag{10}$$

Finally, the discrete finite element formulation can be written as a nonlinear saddle point problems, namely

$$\underbrace{\begin{pmatrix} A & B^T \\ B & 0 \end{pmatrix}}_{\text{Nonlinear operator } \mathcal{A}} \begin{pmatrix} \tilde{\mathbf{u}} \\ p \end{pmatrix} = \begin{pmatrix} \text{rhs } \tilde{\mathbf{u}} \\ \text{rhs } p \end{pmatrix} \tag{11}$$

where $\tilde{\mathbf{u}}$ consists of the coefficient vector representing the velocity and LCR tensor. Here, $\mathbf{A}$ includes all convection and diffusion operators. We employ Newton iteration method to the nonlinear system of Eq. (11) and use finite differencing Jacobian as a black-box for the linearisation of Newton, see [3] for implementation aspect.

3 Numerical discussion

It is not our intention to simulate a particular fluid, so the following quantities (Tab. 1) would be used as a prototypical test problem. The degree of elasticity is controlled by Weissenberg number $\mathsf{We} = \Lambda\dot{\gamma}_w$ where $\dot{\gamma}_w$ is calculated on the channel wall.

A typical streamline of generalised Newtonian fluid for Hole-pressure error simulation is shown in Fig. 1, where one observes symmetric patterns as a typical lack of elasticity in the fluid model, although power law model with $r = 1.5$ lies in the region of shear thinning fluid.

Table 1. Material parameters

Model	Power law	Old-B	Gie	Fene-p	Fene-cr
Parameter	$r = 1.5$	$\alpha = 0$	$\alpha = 0.01$	$\alpha = 0$, $L^2 = 100$	$\alpha = 1.0$, $L^2 = 100$

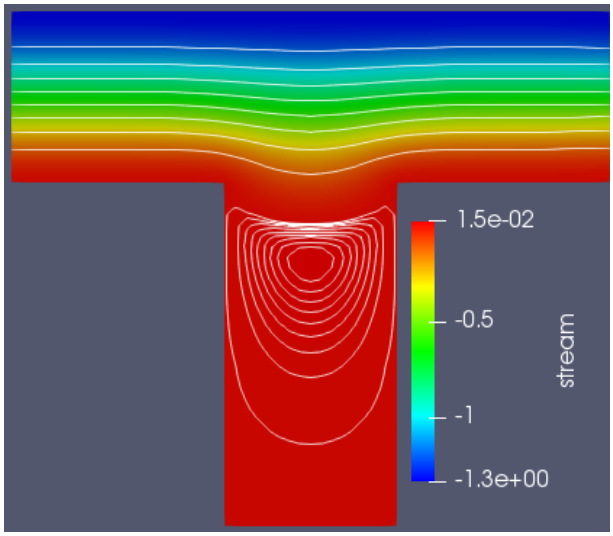

Figure 1. Streamlines

Acknowledgments

The AIF/IGF-project 18485N is gratefully acknowledged.

References

[1] Bird, R. B., Curtiss, C. F., Armstrong, R. C., and Hassager, O. *Dynamics of polymeric fluids*. Vol. 2, New York. Wiley, 1987.

[2] Brezzi, F. and Fortin, M. *Mixed and Hybrid Finite Element methods*. Springer, Berlin, 1986.

[3] Damanik, H., Hron, J., Ouazzi, A., and Turek, S. A Monolithic FEM approach for the log-conformation reformulation (LCR) of viscoelastic flow problems. *Journal of non-Newtonian Fluid Mechanics* 165 (2010), pp. 1105–1113.

[4] Giesekus, H. A simple constitutive equation for polymer fluids based on the concept of deformation-dependent tensorial mobility. *Journal of non-Newtonian Fluid Mechanics* 11 (1982), pp. 69–109.

[5] Girault, V. and Raviart, P. A. *Finite Element Methods for Navier-Stokes equations*. Berlin-Heidelberg. Springer, 1986.

[6] K. O. Higashitani and W. G. Pritchard. A kinematic calculation of intrinsic errors in pressure measurements made with holes. *Trans. Soc. Rheo.* 16 (1972), p. 687.

[7] Hulsen, M. A., Fattal, R., and Kupferman, R. Flow of viscoelastic fluids past a cylinder at high Weissenberg number: Stabilized simulations using matrix logarithms. *Journal of Non-Newtonian Fluid Mechanics* 127 (2005), pp. 27–39.

[8] Oldroyd, J. G. On the formulation of rheological equations of state. *Proc. R. Soc. London* Ser. A 200 (1950), pp. 523–541.

**Proceedings of the 8th GACM Colloquium on Computational Mechanics
for Young Scientists from Academia and Industry
August 28–30, 2019 in Kassel, Germany**

Shape Optimization in Polymer Extrusion Using Shear-Thinning Fluids

Sebastian Eusterholz * [1] and Stefanie Elgeti[1]

[1]Chair for Computational Analysis of Technical Systems (CATS), RWTH Aachen University, Germany

Abstract. Extrusion is a manufacturing process suitable for endless profiles with a fixed cross-section and is widely used in plastics processing. One key component of this process is the extruder: Its purpose is to melt, transport, and homogenize the raw material. To produce a continuous melt flow, solid polymer particles are taken in and then molten due to shear-heating as they are conveyed through the extruder. Despite other kinds of extruders also being utilized, this work focuses on single-screw extruders (SSEs). While cheap in design and operation, SSEs per se have a – compared to, e.g., twin-screw extruders – reduced mixing ability. Therefore, the resulting products often suffer from a lack of homogeneity in both temperature and material distribution. This is especially relevant if additives are introduced into the melt. As a means to increase homogeneity, it is common in the plastics processing industry to introduce flow obstacles into the screw's end section. This enhances the reordering of the essentially laminar flow. The problem with this approach is that while the mechanisms of laminar mixing are mostly understood, there is no rigorous design principle relating the mixing element geometry to certain flow characteristics. Furthermore, since single-screw extruders have to be operated at high temperatures and pressures, and thus, transparent housings for experimental studies of the flow inside those machines cannot be used; experimental data is very limited. It is our aim to replace the current, experience-based design process with shape-optimization methods. The proposed concept comprises three steps: (1) Computation of the flow field, (2) computation of the associated objective function value, and (3) determination of optimized shape parameters. While the last point is dealt with by the utilized optimization framework, this work discusses two aspects: (1) We detail on geometry modification techniques to alter given mixing-element shapes retaining boundary-conforming meshes, and (2) we review how such methods in combination with fast simulations of shear-thinning fluids can be used for the shape-optimization of industrially relevant mixing elements.

Introduction

Numerical shape optimization as a design aid has had an impact on the plastics processing industry already. The work of Elgeti et. al [1] has proven its potential to support design in areas where experimental data is rare and shape is crucial to the product's quality. A similar situation is observed in the field of mixing in single-screw extruders (SSEs).
SSEs are frequently utilized in extrusion due to their low operating and investment costs. By design, single-screw extruders, unfortunately, provide only limited mixing ability which is a likely cause for insufficiently homogeneous products. Plastics manufacturer have addressed that problem by adding flow obstacles – the mixing elements – to the rotating downstream tip of the screw to enhance reorientation within the flow. An exemplary configuration is shown in Fig. 1. Interestingly, there is no rigorous design

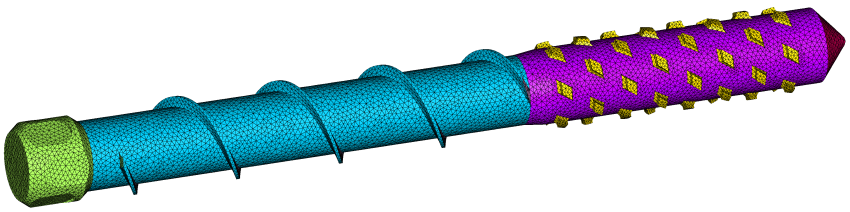

Figure 1. Exemplary SSE screw. The screw's tip is shown in purple with mixing elements of typical rhomboid shape highlighted in yellow.

pattern – also because of a lack of experimental data on the flow inside extruders. This work attempts to

*Corresponding author: eusterholz@cats.rwth-aachen.de ORCID iD: ORCID 0000-0001-7795-9760

take a first step to bridge that gap by numerical design using shape optimization. Following the approach presented in [1], we propose methods to extend the concepts utilized in die design to the numerical design of mixing elements.
The numerical design of mixing elements by shape optimization has two main building blocks: (1) A forward simulation of the physical phenomena describing mixing in extruders, and (2) the actual optimization framework. In the following sections we will first address the latter and start by proposing a technique to manipulate the computational mesh to reflect changes in the geometry. Following up on this, our setup for the flow computation of shear-thinning polymer melts is presented.

1 Geometry manipulation using free-form deformation and elasticity

The approach proposes that the update of a given geometry, and subsequently the manipulation of the mesh is composed of three steps: (1) Modification of a given spline representation of the geometry, (2) according manipulation of the boundary mesh, and (3) update of the volume mesh. Starting point of the proposed method is a spline description of some initial mixing-element geometry – as given from Computer-Aided Design. A computational domain Ω with boundary Γ is constructed around that geometry, representing a portion of the extruder's flow channel. One subdomain of Γ, called Γ_{spline}, coincides with the input geometry.
Manipulating the boundary mesh – the final goal to reflect shape changes in the simulation – is done by deforming the input spline first and then moving the mesh nodes accordingly. By accordingly we mean that mesh nodes lying on the input spline are moved such that they remain on the spline with no change in their parametric coordinate.
Previous works utilizing a similar approach rely on modifying the boundary spline by directly shifting its control points [1]. Since this approach poses restrictions on the usable input splines, we extend the method by manipulating the spline using free-form deformation. The concept, as introduced by Sederberg and Parry [3], is outlined in Fig.2.

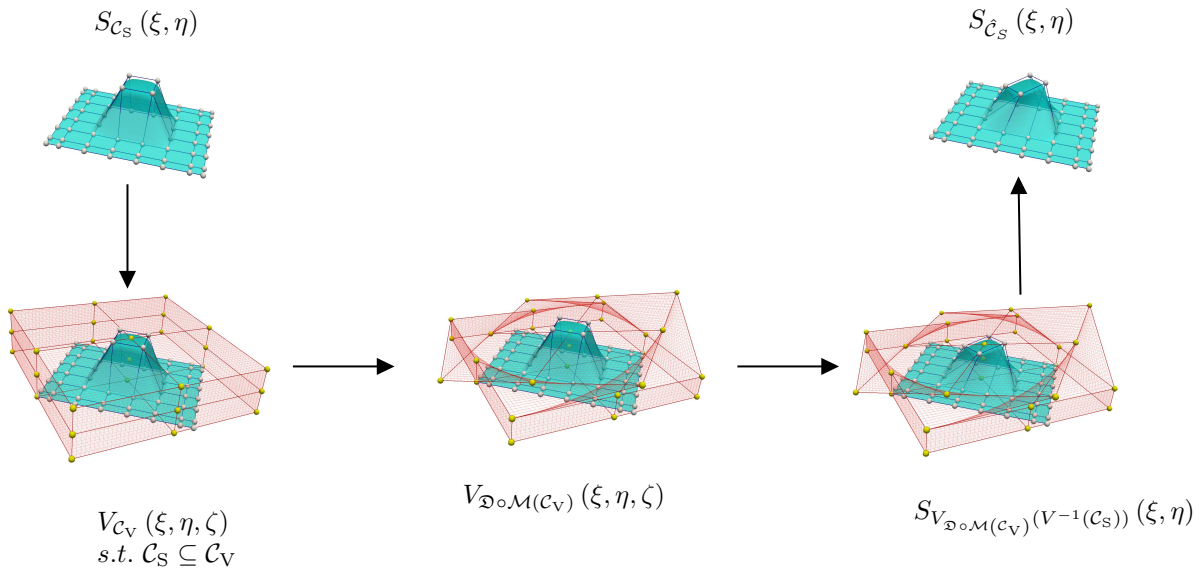

Figure 2. Free-from deformation. A volume spline $V_{\mathcal{C}_\mathrm{V}}(\xi,\eta,\zeta)$ in $\mathbb{R}^3$ is constructed around a given surface spline $S_{\mathcal{C}_\mathrm{S}}(\xi,\eta)$, such that V's control polygon $\mathcal{C}_\mathrm{V}$ encloses the surface spline's control polygon $\mathcal{C}_\mathrm{S}$. Deformation to the enclosed body is imposed by applying a deformation $\mathfrak{D}$ to a subset of V's control points, masked via $\mathcal{M}$. The deformed configuration of $S_{\mathcal{C}_\mathrm{S}}(\xi,\eta)$ is obtained by evaluating the position of the points of $\mathcal{C}_\mathrm{S}$ in the deformed configuration of V.

Once the boundary spline has been modified, and the boundary mesh nodes are shifted to the new positions, it is advantageous to update the volume mesh to retain mesh quality. We use the elastic-mesh-update method described in [2]. The deformed configuration is computed, treating the volume mesh as an elastic body that reacts to displacements imposed on its boundary. The governing equations, with the

displacement $\mathbf{z}$ being the unknown, are given in Eqs. (1) to (3).

$$\nabla \cdot \boldsymbol{\sigma}_{\text{mesh}} = \mathbf{0}\,, \tag{1}$$

$$\boldsymbol{\sigma}_{\text{mesh}}(\mathbf{z}) = \lambda_{mesh}\left(\operatorname{tr}\boldsymbol{\varepsilon}_{\text{mesh}}(\mathbf{z})\right)\mathbf{I} + 2\mu_{mesh}\boldsymbol{\varepsilon}_{\text{mesh}}(\mathbf{z})\,, \tag{2}$$

$$\boldsymbol{\varepsilon}_{\text{mesh}}(\mathbf{z}) = \frac{1}{2}\left(\nabla\mathbf{z} + (\nabla\mathbf{z})^T\right)\,. \tag{3}$$

We partition the boundary into three parts as $\Gamma = \Gamma_{spline} \cup \Gamma_{fixed} \cup \Gamma_{slip}$. Tangential movement is allowed for on Γ_{slip}, whereas we restrict any movement on Γ_{fixed}, and prescribe the displacement obtained from the spline deformation on Γ_{spline}. With this, we avoid any remeshing but still obtain a boundary-conforming mesh.

2 Simulation of shear-thinning flows

Given the deformed mesh we obtain the flow and temperature fields by solving steady incompressible Navier-Stokes equations strongly coupled to the temperature equation. We apply strong coupling between flow and temperature problem due to the material law, for which we choose the Carreau model in the following form:

$$\eta = \frac{A}{\left(1 + B\dot{\gamma}\right)^C}, \tag{4}$$

and apply a WLF temperature correction as first proposed by Williams et al. [5] and generalized by van Krevelen [4] as:

$$\eta_{0_{\text{WLF}}}(T) = \eta_0 \cdot e^{\frac{8.86\cdot\left(T_M - T_{Ref}\right)}{101.6 + T_M - T_{Ref}} - \frac{8.86\cdot\left(T - T_{Ref}\right)}{101.6 + T - T_{Ref}}}\,. \tag{5}$$

In Eq. (4), A is equal to the viscosity at zero shear η_0, B determines the transition to the shear-thinning regime and C describes the double logarithmic decay of η with increasing shear rates. In Eq. (5), T_M and T_{Ref} denote the measurement and reference temperatures. Following [4], T_{Ref} is chosen to be 43 K above the glass transition temperature. Pressure corrections are neglected so far.

3 Shape optimization in view of enhanced distributive mixing

We attempt to optimize the mixing element's geometry with regard to improved distributive mixing capabilities. Thus, we aim to maximize the re-orientations imposed by the mixing element. Instead of relying on particle tracking methods, we solve a set of n scalar concentration problems c_i, where $1 \leq i \leq n$, to estimate the material distribution within the flow domain. Given Γ_{in} and Γ_{out} as the inflow and outflow boundaries of the computational domain, we then compute the objective function J as:

$$J = \|\Delta\mathbf{d}\|_2 \quad \text{with} \quad \Delta\mathbf{d}_i = \|\mathcal{P}\left(\Delta\mathbf{x}_i\right)\|_2 = \|\mathcal{P}\left(\mathbf{x}_{i,\max,\,\text{in}} - \mathbf{x}_{i,\max,\,\text{out}}\right)\|_2 \tag{6}$$

where $\mathbf{x}_{i,\max,\,\text{in/out}}$ denotes the position of maximum concentration at $\Gamma_{in/out}$, i.e. $\mathbf{x}_{i,\max,\,\text{in/out}} \in \Gamma_{\text{in/out}}$, such that $c_i\left(\mathbf{x}_{i,\max,\,\text{in/out}}\right) \geq c_i\left(\mathbf{x}\right) \forall \mathbf{x} \in \Gamma_{\text{in/out}}$. To obtain a proper scaling, the mapping $\mathcal{P}$ ensures that only the displacement projected onto $\Gamma_{\text{in/out}}$ is taken into account, such that $\mathcal{P}\left(\Delta\mathbf{x}_i\right) \cdot \mathbf{n} = 0$ holds with $\mathbf{n}$ being the normal vector on $\Gamma_{\text{in/out}}$. It should be noted that this approach is directly applicable only to cuboid domains.

4 Summary

A new approach has been presented that enables shape optimization for mixing elements. Instead of defining one monolithic problem, a partitioned approach was chosen for both, mesh adaptation and flow computation. With the presented approach we are able to design new enhanced mixing elements by applying shape optimization to mixing elements given an arbitrary initial input geometry.

Acknowledgments

The authors gratefully acknowledge the support of DFG provided by grant "Automated design and optimization of dynamic mixing and shear elements for single-screw extruders" (EL 745/5-1)

References

[1] S. Elgeti, M. Probst, C. Windeck, M. Behr, W. Michaeli, and Ch. Hopmann. Numerical Shape Optimization As an Approach to Extrusion Die Design. *Finite Elem. Anal. Des.* 61 (2012), pp. 35–43. DOI: 10.1016/j.finel.2012.06.008.

[2] A.A. Johnson and T.E. Tezduyar. Mesh Update Strategies in Parallel Finite Element Computations of Flow Problems with Moving Boundaries and Interfaces. *CMAME* 119 (1994), pp. 73 –94.

[3] T. W. Sederberg and S. R. Parry. Free-form Deformation of Solid Geometric Models. *SIGGRAPH Comput. Graph.* 20.4 (1986), pp. 151–160. DOI: 10.1145/15886.15903.

[4] D. W. Van Krevelen and K. Te Nijenhuis. *Properties of polymers: their correlation with chemical structure; their numerical estimation and prediction from additive group contributions*. Elsevier, 2009. ISBN: 978-0-08-054819-7.

[5] M. L. Williams, R. F. Landel, and J. D. Ferry. The Temperature Dependence of Relaxation Mechanisms in Amorphous Polymers and Other Glass-forming Liquids. *Journal of the American Chemical Society* 77.14 (1955), pp. 3701–3707. DOI: 10.1021/ja01619a008.

**Proceedings of the 8th GACM Colloquium on Computational Mechanics
for Young Scientists from Academia and Industry
August 28–30, 2019 in Kassel, Germany**

Heat Dependent Thermo-Viscous Shear-Thinning Fluid Flowing around a Double-Sphere Configuration within a Pipe

Markus Rütten * [1,2]

[1]DLR - German Aerospace Center, Institute of Aerodynamics and Flow Technology, Bunsenstrasse 10, 37073 Göttingen, Germany
[2]University of Kassel, Dept. of Mechanical Engineering, Institute of Fluid Mechanics, 34125 Kassel, Germany

Abstract. Non-Newtonian fluid properties can change the flow behaviour and the resulting flow topology significantly, even for low Reynolds number laminar flows. The prediction of the flow field is even more difficult when thermal effects come into play. In particular when high shear rates occur and temperature is changing the fluid properties, unexpected flow phenomena can be observed. Focal point of this study is the laminar pipe flow of a thermo-viscous shear thinning Carreau fluid around double-sphere configurations. The two spheres are arranged in-line in pipe axial direction. In dependence of the distance between the spheres the flow topology around the sphere pair changes. The non-isothermal non-newtonian shear-thinnning fluid flows reveal temperature dependent deflections of the wake flow. Complicated flow separation and attachment structures between and behind the spheres occur. In the present CFD study sphere-wall temperature-dependent flow-structures are investigated. The temperature dependence of the fluid viscosity is modelled by applying the standard Williams-Landel-Ferry equation. It is shown that thermal-viscous shear thinning due to high shear rates and heat transfer from the sphere walls leads to a significant decrease of viscosity of three orders of magnitude in the near-field of the spheres. The locally reduced viscosity can be used to control the flow around the double sphere flow configuration. In the present simulation campaign thermal boundary conditions are varied over a wide range in order to derive relations between heat transfer, non-newtonian fluid properties and the behaviour of the double-sphere flow.

Introduction

Non-Newtonian fluids reveal a wide variety of properties due to their non-linear behaviour of viscosity in shearing flows. Since these types of fluids are widely used in technical, industrial and medical applications and also occur in biological flows, the knowledge of their complex properties and flow behaviour is necessary for the design of novel devices. The complex flow behaviour is caused by their molecular composition. Long entangled molecular chains lead to higher viscosities. High shear flow rates can tighten and align the molecular chains which leads to a decrease of the shear viscosity. This effect is called shear-thinning. The resulting flow phenomena of these processes are not easily to predict, in particular in complex flow applications [2], [3]. The flow prediction is even more difficult when additional thermal loads are playing a significant role, since middle and high-molecular-dense fluids are sensitive to the temperature influences on the viscosity [9]. Thus, heat transfer at walls, its effect on the non-linear viscosity and the resulting flow phenomena are a main focal point in the research field of non-Newtonian fluids [8], [5]. In particular, heat exchanger, lubrication systems or oil coolers are technical applications in which the properties of non-Newtonian fluids are essential for the design and layout. Since numerical simulations, conducted during the design process for such applications, have to be based on very accurately described non-Newtonian fluid models [7], experimental and numerical studies are necessary to capture all phenomena, which are related to thermal and shear-thinning viscosity properties of these fluids, in order to improve the applied fluid models. In this context the non-Newtonian flow of a shear-thinning fluid around a double-sphere configuration within a pipe is investigated.

*Corresponding author: markus.ruetten@dlr.de

1 The Non-Newtonian Fluid Model and the Double-Sphere Flow Case

In contrast to Newtonian fluids, the properties of non-Newtonian fluids play a crucial role in shearing flows due to their ability to change their viscosity by orders of magnitude in dependence of local shear rates. If thermal loads also play a role, then heat transfer can enforce the viscosity change of those fluids. Thus, the accurate modelling of the non-Newtonian fluid properties of the considered thermo-viscous shear-thinning fluid is crucial for the description of those flow problems, which is demonstrated in the present simulation campaign. Fluid viscosity modelling together with a suitable CFD grid and a strict numerical simulation strategy is a precondition for reliable simulation results.
In this study thermo-viscous shear-thinning fluids without any yield stress or temporal relaxation properties are considered: Both the temperature T and the shear rate, $\dot{\gamma} = \sqrt{\frac{1}{2}\left[\mathbf{D} : \mathbf{D}\right]}$, have an impact on the viscosity of these class of non-Newtonian fluids. The simplest shear-thinning fluid is the Ostwald - de Waele fluid [6], whose viscosity is modelled by a power law. However, fluid models purely based on the power law have the model limitation that they do not possess any lower and upper viscosity restrictions. This leads to fluid modelling errors at very low and very high shear rates, where the shear dependent viscosity reaches unrealistic values. Moreover, numerical simulations reveal that Power-Law fluids show worse convergence rates, in particular in flow regions, in which the second invariant I_2 of the strain tensor $\mathbf{D} = \frac{1}{2}\left(grad\vec{v} + grad\vec{v}^T\right)$ is small, as, for example, in nearly uniform flows. An alternative to a Power-Law fluid is the Carreau fluid model [4], which has the advantage to have both a constant zero viscosity and a constant infinite viscosity. With this model the properties of real fluids are reflected very well [2]. The flow curve of a Carreau fluid is calculated by using:

$$\eta = \eta_\infty + (\eta_0 - \eta_\infty)\left\{1 + (\lambda\dot{\gamma})^2\right\}^{\frac{n-1}{2}} \quad . \tag{1}$$

In equation (1) n is the flow index, η_0 the lower limit or zero viscosity, η_∞ the upper limit or infinite viscosity and $\dot{\gamma}$ the generalised shear rate. The parameter λ controls the transition from the Newtonian to the non-Newtonian fluid behaviour. This parameter can be determined by the characteristic stress τ_γ, at which the deformation-viscosity behaviour of the fluid changes: $\lambda = \eta_0/\tau_\gamma$. In principle, this time constant is the reciprocal value of the critical shear rate $\dot{\gamma}_c$, at which exceeding shear rates start to reduce the viscosity of the fluid. In this simulation study we used the following fluid parameters, $n = 0.2$, $\lambda = 0.5\,\mathrm{s}$, $\eta_0 = 10\,\mathrm{Pas}$, $\eta_\infty = 0.0002\,\mathrm{Pas}$, which are describing the fluid properties valid for a reference temperature $T_{ref} = 403.15\,\mathrm{K}$. The associated flow curve is depicted in Fig. 1. The small values of the time constant and the flow index are consciously chosen in order to achieve a high sensitivity of the fluid viscosity in particular to lower shear rates, so that the viscosity can drop orders of magnitude over the full range of the expected flow shear rates. This is not non-physical, since low-density polymers, carbon and silicone oils or especially synthesised engine oils just reveal such fluid properties. The reference density of the fluid is $\rho_{ref} = 1000\,\mathrm{kg/m^3}$. The density changes only slightly with temperature.

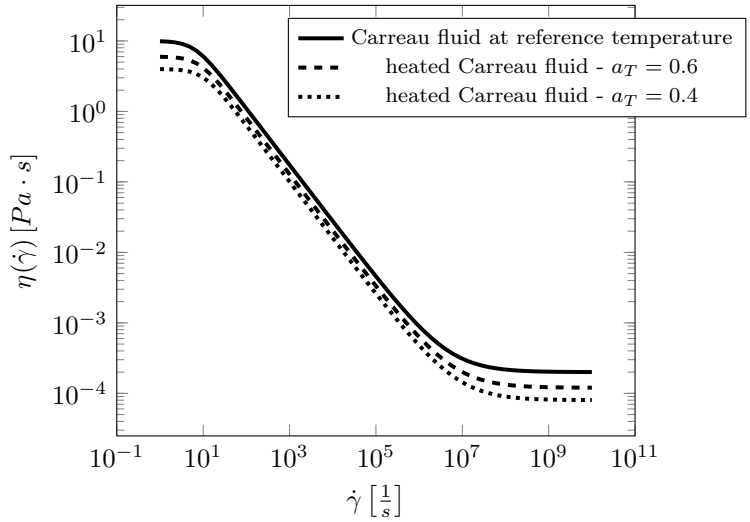

Figure 1. Fluid curves for a Carreau fluid model, $n = 0.2, \lambda = 0.5\,\mathrm{s}$, $\eta_0 = 10\,\mathrm{Pas}$, $\eta_\infty = 0.0002\,\mathrm{Pas}$, at reference temperature and for temperatures leading to viscosity-temperature shift factors of 0.6 and 0.4.

Modelling thermal-viscosity is a research field on its own and many temperature dependent viscosity models exist. However, there is an observation that for a certain group of non-Newtonian fluids, low and high density polymers or certain silicone oils, a change of the global temperature level only leads to a shift of the flow curve, whereas the basic shape of the flow curve is barely changed. This observation has led to a certain modelling concept: a so called *master flow curve* is measured for a reference temperature, thereafter, this master flow curve is adapted to the new temperature level by a viscosity-temperature shift factor a_T. This shift factor is called time-temperature superposition parameter, following the notation of [9], it is also called Andrade factor [1]. Now modelling the temperature influence on the viscosity is reduced to determine this factor. Different equations can be applied to this problem. In this work the so-called *William-Landel-Ferry equation* (WLF-equation) is used to determine the viscosity-temperature shift factor [9], [5]. The WLF-equation reads as follows:

$$log\left(a_T\right) = log\left(\frac{\eta(\dot{\gamma},T)}{\eta(\dot{\gamma},T_{ref})}\right) = \frac{-C_1\left(T-T_{ref}\right)}{C_2+\left(T-T_{ref}\right)}\,. \tag{2}$$

In this equation, T_{ref} is the reference temperature, for which, in this study, a value of 403.15 K is assumed. The fluid parameters C_1 and C_2 have to be determined experimentally for each non-Newtonian fluid, however, in this campaign the common values for polymers, $C_1 = 8.86$ and $C_2 = 101.6$ K, are used. Eventually, the thermal-viscosity model is combined with the Carreau fluid model equation leading to:

$$\eta\left(\dot{\gamma},T\right) = a_T\eta_\infty + \frac{a_T(\eta_0-\eta_\infty)}{\left(1+\left(a_T\lambda\dot{\gamma}\right)^2\right)^{\frac{1-n}{2}}}\,. \tag{3}$$

The flow around two spheres within a pipe is considered. The spheres are placed on the middle axis of the pipe and they are arranged in-line, streamdown in pipe axial direction. The pipe has a lenght of 1000 mm an a diameter D of 200 mm. The first sphere is located 300 mm streamdown of the pipe entry. The diameter d of the spheres is 60 mm. The distance between the spheres has been varied from $2d$ to $4d$ in $0.5d$ steps. In this work only the even cases are discussed. CFD grids have been generated using the commercial mesher "Centaur" from CentaurSoft. Besides the pipe inflow and outflow all boundaries are treated as viscous walls. The number of grid points and cells depends on the sphere distance, however, on average the hybrid grid consists of 18 Mio points, 15 Mio prisms, 58 Mio tetraeders, 0.5 Mio triangles and 20000 quadrilateral grid cells. The prisms are forming a structured grid close to the wall, which consists of 32 prism layers. This high number of layers is necessary for resolving both, the momentum driven boundary layer flow and also the thermal boundary layer. In order to capture the velocity profile slopes accurately the first wall normal cell height is on average 0.0032 mm, the associated growth rate in wall normal direction is 1.12.

The numerical simulations have been performed using the DLR THETA code for solving the incompressible Navier-Stokes equations. This finite volume code utilizes the so-called collocated respectively non-staggered dual grid approach storing all flow variables at the same location. An efficient coupling of the velocity and the pressure fields is ensured by using the Chorin projection method or the SIMPLE algorithm. For spatial discretisation different variations of 2nd and 3rd order upwind methods as well as 2nd order central schemes can be used. Here, a 3nd order scheme was chosen in order to get very smooth data for calculation of derived vector fields. The well-known checkerboard instability of the pressure is eliminated by a 4th order stabilisation term, which is added to the left and the right hand side of the Poisson equation. A matrix-free formulation is used for solving the linear equations. This formulation reduces the memory requirements of the code considerably. A variety of multi-grid methods ensures efficient solutions of the linear equations, even on fine grids. Domain decomposition is used as parallelisation concept. The parallel efficiency is high on desktop computers with only a few CPUs as well as on massive parallel systems with thousands of CPUs. In the considered flow case a 4-w multi-grid cycle has been performed to accelerate the CFD calculations. The projection method was used for the unsteady calculation, in which the time-step was set to 0.001 s resulting in grid cell CFL numbers less than one. The three point backward scheme, a variation of a BDF2 scheme, was used for temporal discretisation. As inflow condition a velocity block profile with 3.5 m/s was set. At the entry the local Reynold number is 70, based on the pipe diameter, zero viscosity and the reference density. The entering fluid has the reference temperature of 403.15 K. During the simulation campaign the wall temperature of the first sphere was increased from 403.15 K to 453.15 K in 10 K steps. In order to capture the impact of the heat transfer on the fluid viscosity equation (3) was implemented in the DLR-THETA code.

2 Results

The following images show the flow simulation results for three different sphere-distance cases, as mentioned above. For each only the results for the isothermal flow case with the reference temperature as the wall temperature of the first sphere and the results with the highest wall temperature of $453.15K$ are shown. For all cases contour plots of the local shear rate on the spheres and of the velocity magnitude on the mid-sectional pipe cut-plane are shown. Additionally streamlet visualisations of the flow on the cut-plane are also depicted in order to reveal local flow topologies. The lowest sphere-distance case reveals

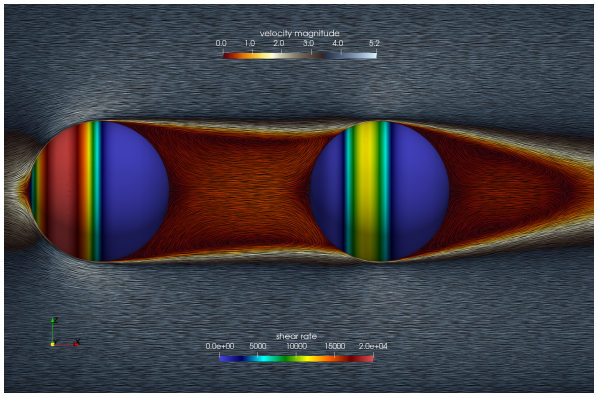

Figure 2. Visualisation of flow structures for case 1, wall temperature of the first sphere 403.15 K

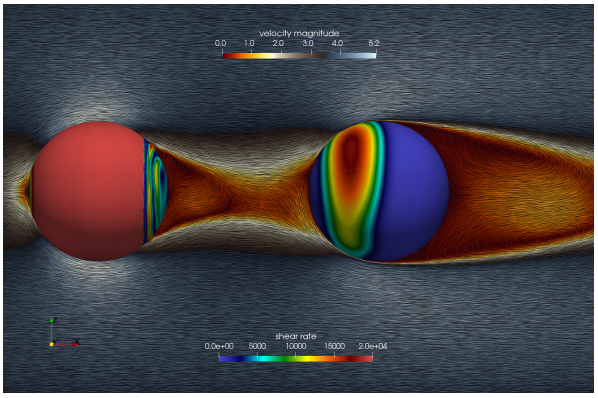

Figure 3. Visualisation of flow structures for case 1, wall temperature of the first sphere 453.15 K

a strong coupling of double-sphere flow: in the isothermal flow case the second sphere is fully attached to the wake flow of the first sphere. Its symmetrical wake vortex hits the second sphere and generates an opposite shear flow at the front part, see Fig. 2. Interestingly the wake flow separation of the second sphere is barely affected by the onflow. The increase of the wall temperature of the first sphere leads to delayed separation and, hence, to a confined asymmetric wake flow between the spheres. As depicted in Fig. 3, this results in spiraling shear stress structures on the back side of the first and the front side of the second sphere. Even the wake flow of the second sphere shows asymmetries. With increasing distance of

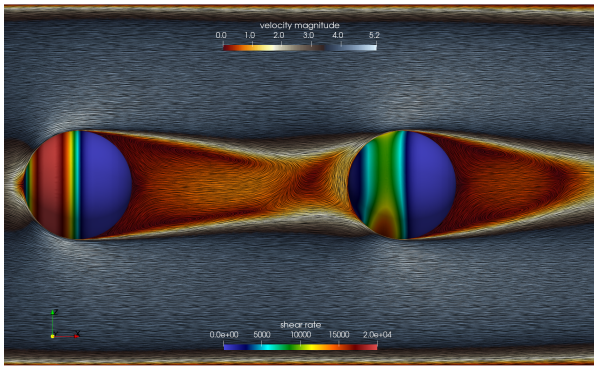

Figure 4. Visualisation of flow structures for case 2, wall temperature of the first sphere 403.15 K

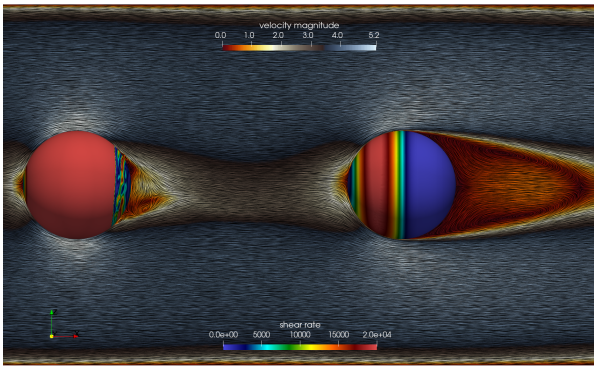

Figure 5. Visualisation of flow structures for case 2, wall temperature of the first sphere 453.15 K

the spheres the flow field interaction reduces. The middle case reveals an induced asymmetry of the first wake flow by the second sphere, although the flow in the near field of the first sphere is quite symmetric. The shear stress pattern of the second sphere reveals an unsteady spatially oscillating structure which is the foot print of the onflowing wake field of the first sphere, shown in Fig. 4. Despite this strong temporal and spatial characteristic the wake flow of the second sphere is nearly symmetric. In case of the heated wall the confined wake flow does only barely affect the flow around the second sphere, see Fig. 5. In the last sphere-distance case for both wall temperatures the flow fields around the spheres are more or less decoupled, compare the Fig. 6 and 7. The increased wall temperature of the first sphere leads again to the unstable confined wake observed before. Only a slight asymmetry is visible on the front side of the second sphere.

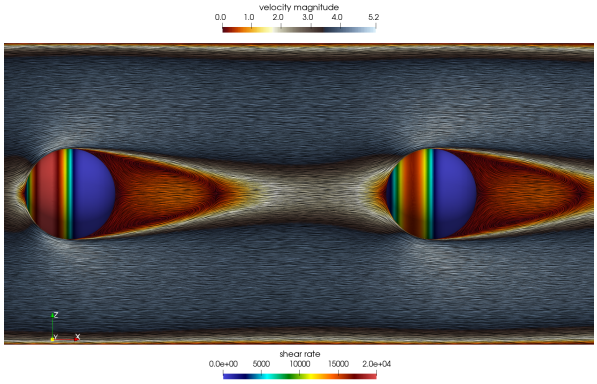

Figure 6. Visualisation of flow structures for case 3, wall temperature of the first sphere 403.15 K

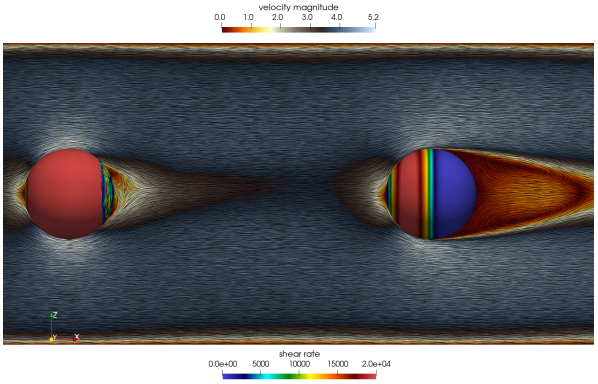

Figure 7. Visualisation of flow structures for case 3, wall temperature of the first sphere 453.15 K

3 Conclusion

In this work the flow around two spheres in a pipe was investigated. It could be observed that, when high shear rates occur and additionally heat is transferred, the fluid properties and, thereupon, the flow topology between and behind the spheres is changing drastically. The thermo-viscous shear-thinning effect of the Carreau fluid leads to a narrowed wake flow behind the first sphere, but also to a significant increase of flow instabilities and, eventually, vortical flow asymmetries. These effects are strongly dependend on the distance between the spheres. The complicated flow separation and attachment structures between and behind the spheres are a focal point of further research work.

Acknowledgments

The author would like to thank the German Aerospace Center (DLR) and the University of Kassel for greatly supporting this research work.

References

[1] E.N.D. Andrade. A theory of the viscosity of liquids. Part 1. *Philosophical Magazine* 17 (1934), pp. 497–511.

[2] R.B. Bird. Non-Newtonian behavior of polymeric liquids. *Physica A: Statistical and Theoretical Physics* 118.1–3 (1983), pp. 3–16.

[3] R.B. Bird and O. Hassager. *Dynamics of Polymeric Liquids: Vol.1: Fluid Mechanics*. Dynamics of Polymeric Liquids. London, New York: John Wiley & Sons, 1987.

[4] P.J. Carreau. Rheological equations from molecular network theories. *J. Rheol.* 16.1 (1972), pp. 99–127.

[5] J.D. Ferry. *Viscoleastic Properties of Polymers*. Third. New York: John Wiley & Sons, 1980.

[6] W. Ostwald. Über die rechnerische Darstellung des Strukturgebietes der Viskosität. *Kolloid-Z* 47.2 (1929), pp. 176–187.

[7] R.G. Owens and T.N. Phillips. *Computational Rheology*. Computational Rheology. Imperial College Press, 2002. ISBN: 9781860941863.

[8] A.H.P. Skelland. *Non-Newtonian flow and heat transfer*. New York: John Wiley & Sons, 1967.

[9] M. L. Williams, R. F. Landel, and J. D. Ferry. The Temperature Dependence of Relaxation Mechanisms in Amorphous Polymers and Other Glass-forming Liquids. *Journal of the American Chemical Society* 77 (1955), pp. 3701–3707.

Authors Index

I

J

K

L

M

N

O

P